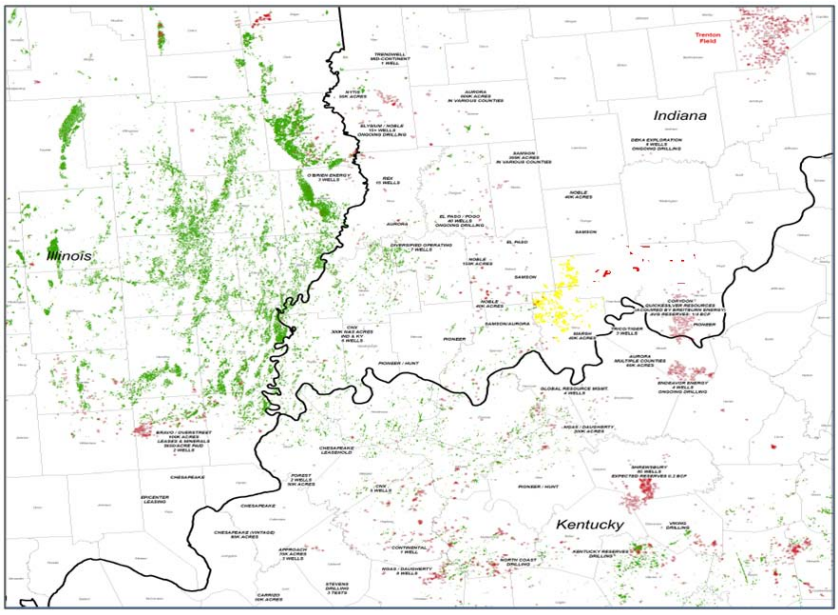
2010

New Albany Shale Gas Project

A Joint Industry Project Sponsored by Research Partnership to Secure Energy for America (RPSEA)

DRAFT

FINAL REPORT



Principal Investigator

Iraj A. Salehi

Iraj.Salehi@gastechnology.org

Gas Technology Institute

10/21/2010

SECTION 1

PROJECT SUMMARY

Disclaimer

This report was prepared as an account of work sponsored by **Research Partnership to Secure Energy for America (RPSEA)**. Neither RPSEA, Gas Technology Institute (GTI), nor any agency thereof, nor any of their employees, makes any warranty, express or implied, or assumes any legal liability or responsibility for the accuracy, completeness, or usefulness of any information, apparatus, product, or process disclosed, or represents that is use would not infringe privately owned rights. Reference herein to any specific commercial product, process, or service by trade name, trademark, manufacturer, or otherwise does not necessarily constitute or imply its endorsement, recommendation, or favoring by RPSEA, GTI, or any agency thereof. The views and opinions of authors expressed herein do not necessarily state or reflect those of RPSEA or GTI.

Acknowledgements

We acknowledge the support of RPSEA for funding the New Albany Shale Gas project. Thanks are also to many producing companies, especially NGAS, CNX, Noble, Aurora, and Trendwell, who contributed data and wells of opportunity for field data acquisition.

Funding for this project was provided by RPSEA through the Ultra-Deepwater and Unconventional Natural Gas and Other Petroleum Resources Research and Development Program authorized by the Energy Policy Act (EPAct) of 2005. RPSEA is under contract with the U.S. Department of Energy's National Energy Technology Laboratory to administer three elements of the EPAct Section 999 Program: (1) Ultra-deepwater architecture and technology; (2) Unconventional natural gas and other petroleum resources exploration and production; and (3) Technology challenges of small producers.

RPSEA is a non-profit corporation established to help meet the nation's growing need for hydrocarbon resources produced from reservoirs in America; formed by a consortium of premier U.S. energy research universities, industry and independent research organizations. The mission of RPSEA is to provide a stewardship role in ensuring the focused research, development and deployment of safe, environmentally sensitive technology that can effectively deliver hydrocarbons from domestic resources to the citizens of the United States. RPSEA will sharply focus its experience, expertise, and capabilities on meeting the program's objectives: to maximize the value of domestic natural gas and oil resources through new technologies to increase production, and to do so in less expensive, safer and more efficient and environmentally benign ways.

Report Structure

In the present report, we will present a brief summary of results and proceed to reporting details of work performed under each task. The report is voluminous and includes many details that all of them are not necessarily of interest to all readers. In addition, electronic handling of a document exceeding several hundred pages in length with graphs and diagrams usually causes problem and frustration. To avoid these issues, we are presenting the report in a binder containing seven separate sections each reporting on one major task. Care has been taken to prepare each section as a standalone document that can be detached, copied or downloaded independent of the rest of the report. The following structure will be followed in this report.

- Section 1 Project Summary
- Section 2 Data driven approach
- Section 3 Geological Studies
- Section 4 Geochemical Studies
- Section 5 Formation Evaluation
- Section 6 Hydraulic Fracturing
    - 6.1 Fracture modeling
    - 6.2 Fracture diagnostics
- Section 7 Reservoir Engineering
    - 7.1 Top-down reservoir analysis
    - 7.2 Production analysis

Table of Contents **Page**

Disclaimer 2

Acknowledgements 2

Report Structure 3

1. Summary 5

2. Data Driven Approach 7

3. Geology 7

4. Geochemistry 9

5. Formation Evaluation 10

6. Hydraulic Fracturing 11

6.1 Fracture Modeling 11

6.2 Fracture Diagnostics 12

7. Reservoir Engineering 13

7.1 Top-Down Intelligent Reservoir Modeling 14

7.2 Analytic Reservoir Analysis 15

8. Environmental Considerations 16

9. Technology Transfer 17

New Albany Shale Gas Project

A Joint Industry Project Sponsored by

Research Partnership to Secure Energy for America (RPSEA)

Final Report, October 2010

Gas Technology Institute (GTI)

1. Summary

New Albany Shale formation occurs in Illinois, Indiana, and Kentucky, but to date gas production has been primarily from western Indiana and southwest Kentucky (Figure 1). The New Albany Shale project was an industry cooperative project that combined the application of advanced exploration and development technologies with real-world data from elaborate field data acquisition and field experiments.

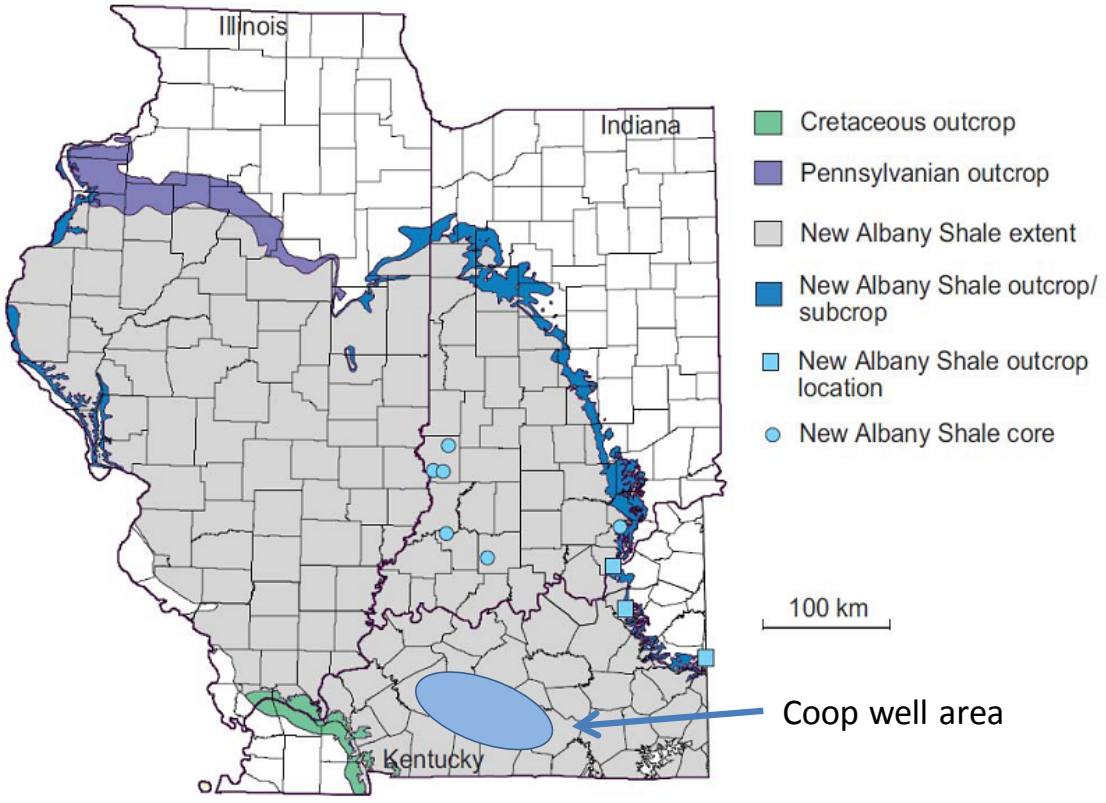


Figure 1. Area of New Albany Shale

Geologic description of New Albany shale relative to its reservoir properties and its attributes relative to natural gas generation, accumulation, and production are described in Sections 3 to 7 of this report.

The project encompassed nearly all aspects of the exploration and production technologies relevant to New Albany shale. A team of experts from nine universities and service organizations worked with nine producing companies collaborated in this project. Research teams and participating producers are shown on Table 1.

Table 1. Project Participants

Industry Partners	Research Team / Research Focus
Atlas America	Amherst College, Geochemistry
Aurora Oil and Gas	Bureau of Economic Geology (BEG), Geology
Breitburn Energy	Gas Technology Institute (GTI), Integrated Analysis, Coordination, Data Acquisition
CNXGas	Pinnacle Technologies, Fracture Diagnostics
Diversified	ResTech, Formation Evaluation
NGas	Texas A&M, Reservoir Engineering, Fracture modeling
Noble Energy	University of Arizona, Geochemistry
Rex Energy	University of Massachusetts, Geochemistry
Trendwell Energy	West Virginia University, Reservoir Engineering

The volumes of in-place and technically recoverable gas in New Albany shale have been estimated to be between 86 and 160 trillion cubic feet (tcf) and 1.9 to 19.2 (tcf) respectively. Nonetheless, current production from his resource is less than .4 bcf per year. Having realized this significant resource volume, the focus of the New Albany Shale project was on the development of techniques and methods for increasing the success ratio and productivity of New Albany shale gas wells to a level where the otherwise noncommercial wells may become commercial producers. The efforts were funded by Research Partnership to Secure Energy for America (RPSEA) and supported by nine producing companies targeting the development of the New Albany gas shale. Although the project was aimed at the development of the New Albany shale gas, results will be applicable to other gas shale formations such as the Marcellus, Woodford, and Mancos as well as other low permeability gas bearing formations.

Industry participation included donation of background data and provision of wells of opportunity for acquisition of research quality data. The culmination of data acquisition was

coring, logging, and fracture diagnostic surveys on wells provided by NGas and CNX Gas. Details data acquisition work is described in Section 2 of this report.

The New Albany Shale Gas project was a data driven fully integrated project where all data and results were shared between interfacing tasks and cross utilized for arriving at conclusions that satisfied the findings from independent studies and tests. Figure 2 depicts the information flow and integration process that governed the project.

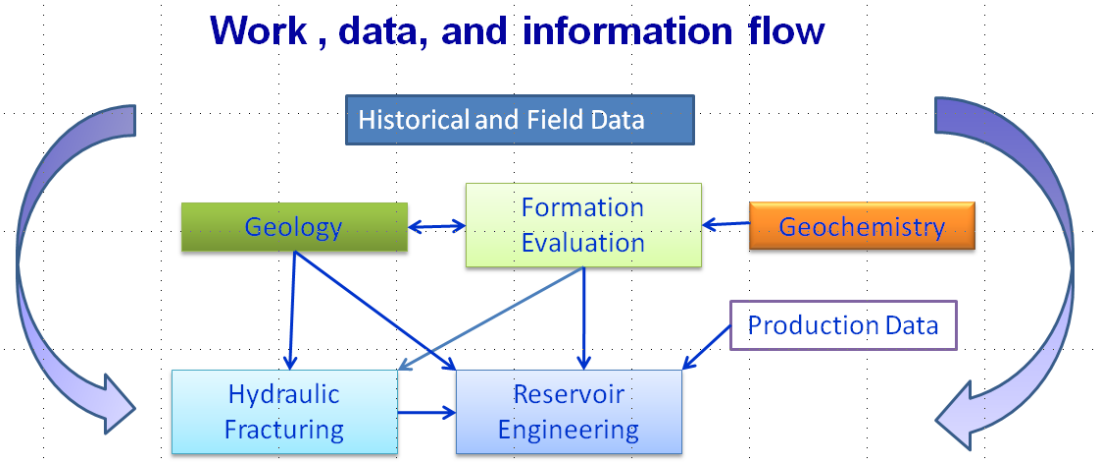


Figure 2. Cross flow of data, information, and results between team members

A summary of results from each major topic addressed in this project follows.

2. Data Driven Approach

Research Team: *Jordan Ciezobka and Angelica Chiriboga, Gas Technology Institute (GTI)*

The New Albany shale project was a field-based project in that real-world historical data were integrated with research quality data acquired as part of the project and used by the research team for calibration and verification of the analytic and interpretive results. Numerous data sets were acquired from the participating producing companies and several datasets were acquired in the field. The culmination of field data acquisition task was during coring, logging, and hydraulic fracturing on three industry cooperative wells. Summary of field data acquisition efforts is presented in Section 2, Field Data Acquisition.

3. Geology

Research Team*: Julia W. Gale, Stephen E. Laubach, and Luke J. Fidler; Bureau of Economic Geology (BEG)*

Considering the fact that in an extremely low permeability formation such as the New Albany shale natural fractures are the main contributors to flow of gas, the principal objectives of

geologic studies were to characterize the natural and to assess their relevance for natural gas production. The focus was primarily on southern Indiana and western Kentucky and to investigate whether the sealed natural fractures that are present represent weak planes that reactivate during hydraulic fracture treatments. The possibility of permeability enhancement through open natural fractures was also investigated. The full report on geological analyses is given in Section 3. A brief summary of activities and results follows.

Major activities pursued under this included:

- Synthesis of published fracture characterization data and augmentation with fracture description for 12 cores from southern Indiana, 3 cores from western Kentucky and 15 outcrop locations in both Indiana and Kentucky.
- Analysis of cores and image logs from vertical pilot wells for two well experiments both in Western Kentucky: the Daugherty Petroleum Inc. 2485-21 (Christian County), and a second well in McLean County.
- Measurement of the subcritical crack index (SCI) of core samples with the aim of understanding fracture spatial distribution and how fracture patterns differ from one layer to the next.
- Consideration of the relative orientation of maximum in situ horizontal stress (S_{Hmax})and natural fractures, and whether this geometry is favorable for reactivation.
- Assessment of whether part of the fracture population is open and would enhance permeability in the reservoir. This task includes both core and outcrop study.
- Qualitative assessment of the tensile strength of natural fracture planes.
- Estimation of key input parameters for geomechanical modeling of interaction of hydraulic and natural fractures.

Major results from these studies led to the following conclusions:

- The structural grain of the two areas studied – southern Indiana and western Kentucky – is fundamentally different. Southern Indiana is dominated by the Wabash Valley normal fault system, which trends approximately N-S and where faults are reactivated in shear in the present day stress regime. Western Kentucky is dominated by the E-W trending Rough Creek Graben, but sections of this system trend ENE-WSW.

- The present-day in situ stress must be determined on a site-specific basis. The world stress map database suggests a swing in the maximum horizontal stress direction (S_{Hmax}) from ENE-WSW in southwest Indiana to E-W in western Kentucky. In the Appalachian basin and elsewhere in the mid-continent the trend is closer to ENE-WSW. There are no data points in the World Stress map database for the McLean County location. The large differences in underlying local structure in the Illinois Basin, including a fault transfer zone in McLean County, might have a significant perturbation effect on the far-field stress orientation.

- In view of structural complexity of New Albany shale due to different faulting regimes, detailed geologic study of target areas is an imperative.

- Natural fractures are common in the New Albany Shale, but vary in character and have different properties with respect to their effect on gas production. Fractures are both opening-mode fractures and faults as observed in core and in outcrop. In many cores

there is more than one opening-mode fracture set indicating that there are different mechanisms of formation on the basis of aspect ratio, mineral fill, orientation and whether the fracture has been shortened during sediment compaction.

- The most common fracture-sealing cement is calcite, but some fractures are sealed by both calcite and quartz. Observation and testing of similar formations (e.g., the Barnett shale) indicate that hydraulically induced fracture tend to propagate from the interface between calcite filling and shale while quartz cements result in stronger fracture planes because of bonding between wall rock and cement as quartz overgrows the broken quartz of wall rock grains.

- Five samples were tested for subcritical index, fracture toughness, and Young's modulus. The samples were from cores from Sullivan County, southwestern Indiana and from western Kentucky. Subcritical indices range from 43 to 80 indicating the presence of clustering conditions in the sampled area.

Complete report on geological investigations is provided in Section 3.

4. Geochemistry

Research Team: *Anna M. Martini, Julian Damashek, Samuel E. Miller, and Mathew Kirk: Amherst College; Steven T. Petsch, University of Massachusetts; Jennifer C. McIntosh and Melissa Schlegel University of Arizona.*

Hydrocarbon gases contained in the New Albany shale consist of thermogenic gas evolved from thermally matured organic material and biogenic methane resulting from bacterial digestion of carbon compounds. While the evolution of thermogenic methane normally ceases upon uplift of the formation, bacterial activities continue as long as the environment remains amenable to bacterial growth. Characterization of bacterial and archaeal population and determination of their level of current activity plays a major role in resource characterization in that in cases where biogenic methane generation continues in the present they, the gas resource increase with time and replenished during the production life of the reservoir.

This study comprised several goals, using the NAS as a case study, including:

1. Identifying the active, modern-day community of subsurface microorganisms responsible for current methane production in shale gas plays, recognizing that methanogenesis is only the end product of a cascade of microbial metabolic functions.
2. Establishing which environmental parameter(s) limit microbial growth and activity, and thus methane generation, in shale gas reservoirs.
3. Quantifying the abundance and biodegradation indices of low molecular weight hydrocarbons in the shale that may provide substrates for microbial methanogenesis, and
4. Stimulating microbial growth and gas generation in poorly producing wells based on identification of microbial communities.

Geochemical analyses confirmed microbial methanogenesis in many of the productive fields in the NAS, with an increasing mix of abiotic gas towards the basin center. Organic geochemical analyses support only weak biodegradation of hydrocarbons in the shale, suggesting a community that has been restricted in its extent, duration or activity. Genetic information obtained from DNA isolated from NAS formation waters indicates a microbial community comprised of acetogenic Bacteria acting in syntrophy with mainly CO_2-reducing methanogenic Archaebacteria. Thus, active microbial methanogenesis in sedimentary basins may not depend on external supply of electron acceptors (e.g. sulfate, ferric iron), but instead reflects internal control limited by formation water hydrology, geochemistry, and organic matter composition.

The results of this project involving microbial community analysis in shale gas plays strongly indicate that microbial methane generation in sedimentary basins is an active process, with a high potential for stimulation and thus extension of projected well production histories. Application of these results has a direct relationship with potential targets of exploration and gas production in other sedimentary basins where methanogenesis may occur or in the future, be stimulated. Thus, this research may contribute towards development of technologies to enhance methane production in shale gas plays, and help secure natural gas resources from the extensive occurrence of fractured black shales and coal beds found throughout the U.S.A. Detailed report on geochemical analyses is presented in Section 4.

5. Formation Evaluation

Research Team: ***Don*** *Luffel, Jim Lorenzen, and Frank Caramanica, ResTech*

The focus of formation evaluation work was on the integration of core, electric log, and image measurements to develop advanced methodology that allows determination of the gas in place, shale formation characterization, and identification of fracture species and their orientation for effective completion of the highest productivity intervals of the New Albany shale.

Log analysis work performed by ResTech includes the development of advanced methodology for calculation of shale porosity, water and bitumen saturations, free gas saturation and adsorbed gas through correlation with core data. Work also performed by ResTech includes supervision of coring and core analysis including visual inspections and analyses; correlation of core and log data; quality control of porosity; water and bitumen measurements; measurement of matrix permeability, determination of total organic carbon, and adsorbed gas from isotherms. Interpretations of image logs on three wells within the study were performed to characterize natural and induced fracture species.

Report on formation evaluation work is presented as Section 5 of this report. A summary of major results follows.

- A log analysis model for determination of porosity, saturation, shale lithology, total organic carbon, matrix permeability indication, and gas in place has been calculated using available core and basic log data. Correlations on a limited basis from logs for geochem parameters of TOC, S1, S2, PI, HI, and Ro have been measured.

- A general Langmuir isotherm is developed from the data that is consistent with both the Indiana and Western Kentucky data. This can be used to derive reasonable adsorbed

gas content, which precludes the need for additional isotherm measurements in this area.

- Bulk volume adsorbed gas (BVAG) at reservoir conditions is in a pseudo liquid phase. This initial adsorbed gas in place (IGIP) occupies space. This is a significant component within the porosity and reduces the amount of free gas space. However, the total adsorbed and free gas is greater than it would have been if only free gas was present. This is essential for a more rigorous determination of both adsorbed and free gas IGIP.

- Free gas calculated in the Haley Mills field area is highest in the Grassy Creek/Clegg Creek member of the New Albany (NAB). As such, any fracture stimulation should be designed to interconnect with this member. With the restricted space available for free gas because of greater amounts of adsorbed gas and oil within the pore system, interconnected natural and induced fractures will be key to the best production.

- Although salinity appears to be variable from shale lab tests, the salinity within the range of 80,000 ppm NaCl fits best with (Sw) using the above method of log resistivity calculations compared with the core data.

6. Hydraulic Fracturing

Work in the area of hydraulic fracturing included analytic work and fracture diagnostic studies using microseismic fracture imaging. Analytic studies were focused on investigating the growth of hydraulic fractures in the vicinity of natural fractures and possible changes in the growth path as it approaches a natural fracture. Results from these studies and fracture diagnostic work are given in Sections 6.1 and 6.2. A brief summary of results follows

6.1 Fracture Modeling

Research Team: *Ahmad Ghassemi and Wenxu Xue, Texas A&M*

Because of the extreme low permeability matrix, natural fractures are the dominant pathways for natural gas to flow from shale formation and hydraulic fractures function as a gathering line that carry the gas from natural fractures to the wellbore. However hydraulic fracturing of a naturally-fractured reservoir is a great challenge for the industry, as fractures can have complex growth pattern when propagating in systems of natural fractures in the reservoir. Fracture propagation near a natural fracture (NF) considering interaction between a hydraulic fracture (HF) and a pre-existing NF is investigated comprehensively by using a two dimensional Displacement Discontinuity Method (DDM).

The numerical model developed through this project was used to first examine the mechanical response of the NF to predict potential reactivation of the NF and the resultant probable location for fracture re-initiation. Results demonstrate that:

- Before HF reaches a NF, the possibility of fracture re-initiation across the NF and with an offset is enhanced when the NF is weak.

- During the stage of fluid infiltration along the NF, a maximum tensile stress peak can be generated at the end of the opening zone along the NF ahead of the fluid front.
- Poroelastic effects, arising from fluid diffusion into the rock deformation can induce closure and compressive stress at the center of the NF ahead of the HF tip before HF arrival. Upon coalescence when fluid flows along the NF, the poroelastic effects tend to reduce the value of HF aperture and this decrease the tension peak and the possibility of fracture re-initiation with time. Next, HF trajectories near a NF were examined prior to coalesce with the NF using different joint, rock and fluid properties. Analysis shows that:
- Fracture trajectories near a NF may bend and deviate from the direction of the maximum horizontal stress when using a joint model that includes initial joint deformation.
- Fractures propagating with higher injection rate or fracturing fluid of higher viscosity propagate longer distance when turning to the direction of maximum horizontal stress.
- Fracture trajectories are less dependent on injection rate or fluid viscosity when using a joint model that includes initial joint deformation; whereas they are more dominated by injection rate and fluid viscosity when using a joint model that excludes initial joint deformation.

Fracture modeling work was carried out in part by Wenxu Xue as part of her dissertation. Draft copy of this dissertation is presented as section 6.1

6.2 Fracture Diagnostics

Research Team: ***Steve*** *Wolhart and Doug Walser, Pinnacle Technologies*

In performance of subcontract S-53 to New Albany Shale Project No. 20743, Pinnacle provided multiple services to the Gas Technology Institute (GTI). These services were initially planned as a combination of hydraulic fracture mapping, completion/stimulation practice reporting, 3-D parametric modeling, and reservoir modeling that would incorporate and/or calibrate the results of the aforementioned 3-D parametric modeling. Pinnacle provided microseismic hydraulic fracture mapping services to two GTI cooperative well partners (New Albany Shale operators) during the hydraulic fracture stimulation of one horizontal New Albany Shale gas well in Christian County, Kentucky and two parallel horizontal completions in McLean County, Kentucky. These two mapping efforts revealed a number of critical points:

- Interaction of hydraulically induced fractures with naturally occurring geological features (such as faulting) may be more common than was previously assumed.

- Interaction of hydraulically induced fractures with naturally occurring geological features may decrease Stimulated Reservoir Volume (SRV) substantially, resulting in less total induced fracture area that is exposed to potentially productive reservoir.

- Interaction of hydraulically induced fractures with naturally occurring geological features can result in significant out-of-zone penetration, thus exposing bounding layers to communication with the wellbore, and the subsequent production of undesirable fluids and/or movement of undesirable fluids into the potentially productive reservoir.

- Network azimuths were consistent with area expectations; N85°E in Christian County, Kentucky; and N60°E in McLean County, Kentucky.

- Though some degree of fracture network complexity was implied on both projects, it is possible that the completion methodology (openhole packers and ports with a "low" port count) may have limited total fracture initiation point count. A further implication is that when fracture initiation point count is low, it is possible that total surface area exposed to the potential reservoir is not as high as it could be if additional fractures were artificially induced along the wellbore.

- Christian County, Kentucky induced fractures that remained in-zone resulted in microseismic activity approximately 1,200 ft from the lateral with volumes of approximately 1.0 MMSCF N_2 per stage (no proppant).

- McLean County, Kentucky induced fractures that remained in-zone resulted in microseismic activity approximately 800 ft from the lateral, with volumes of approximately 2.6 MMSCF N_2 per stage (limited ultra-lightweight proppant and small water volumes).

- Efforts were made to forecast in advance and match pre- and post-frac mapping results with an industry respected 3D parametric model. Though it was known in advance that these models often cannot adequately simulate fracture networks (systems of parallel and oblique induced fractures), it was thought that if relatively planar bi-wing fractures were present, then such simulation could be justified. Unfortunately, it quickly became apparent as the project progressed that parametric modeling was not appropriate, as complex induced fracture networks were indeed present, and it oversimplified actual conditions to a degree that was not acceptable.

Detailed report on microseismic fracture imaging is provided in Section 6.2.

7. Reservoir Engineering

Production analysis and reserve estimation for New Albany Shale Gas wells faces severe difficulties due to the inherent low permeability manifested in low production and decline rates. In fact, analytic studies have shown that after the period of flush production, the wells will produce at very low rates for several decades. In the meantime background production rate and pressure data from existing wells were scarce and inaccurate.

Reservoir engineering and production analysis in this project were focused on two specific areas: 1) Field-scale reservoir analysis aimed at identification and characterization of inter-well reservoir variations and identification of sweet spots, and 2) Analytic reservoir engineering research focused on extremely low permeability fracture stimulated wells. The research team at West Virginia University applied their Top-Down Intelligent Reservoir Modeling approach addressing the field-level studies and the team at Texas A&M worked on analytic research on data from industry cooperative wells.

7.1 Top-Down Intelligent Reservoir Modeling

Research Team: *Shahab Mohaghegh and Amirmasoud Kalantary-Dahaghi, West Virginia University.*

The intent of this study was to reassess the potential of New Albany Shale formation using a novel and integrated workflow that incorporates field production data and well logs using a series of traditional reservoir engineering analyses complemented by artificial intelligence and data mining techniques. The model developed using this technology is a full filed model and its objective is to predict future reservoir/well performance in order to recommend field development strategies. An abstract of accomplishment follows.

- Natural fractures in the New Albany Shale were characterized by a comprehensive review of literature. Sensitivity analysis was performed on key reservoir and fracture parameters such as matrix porosity, matrix permeability, initial reservoir pressure, fracture aperture, fracture density, fracture length and well's lateral length .The impact of different reservoir characteristics such as matrix porosity, matrix permeability, initial reservoir pressure and pay thickness as well as the length and the orientation of horizontal wells on gas production in New Albany Shale have been presented.

- The study focuses on several New Albany Shale (NAS) wells in Western Kentucky. Production from these wells is analyzed and history matched. During the history matching process, natural fracture length, density and orientations as well as fracture bedding of the New Albany Shale are modeled using information found in the literature and outcrops and by performing sensitivity analysis on key reservoir and fracture parameters.

- Sensitivity analysis is performed to identify the impact of reservoir characteristics and natural fracture aperture, density and length on gas production.

- History-matched results of 87 NAS wells have been used to develop a full field reservoir model using an integrated workflow, named Top-Down, Intelligent Reservoir Modeling. In this integrated workflow unlike traditional reservoir simulation and modeling, we do not start from building a geo-cellular model. Top-Down intelligent reservoir modeling starts by analyzing the production data using traditional reservoir engineering techniques such as Decline Curve Analysis, Type Curve Matching, Single-well History Matching, Volumetric Reserve Estimation and Recovery Factor. These analyses are performed on individual wells in a multi-well New Albany Shale gas reservoir in Western Kentucky that has a reasonable production history. Data driven techniques are used to develop single-well predictive models from the production history and the well logs (and any other available geologic and petrophysical data).

- In addition, 31 recently drilled well in Christian county Western Kentucky-Halley's Mills quadrangle have been used to perform Top-down modeling. Zone manager feature of Geographix software is used .The available production data are going to be the attributes in this feature. The contours are generated and the results have been compared with the result of Top-down modeling (Fuzzy pattern recognition). Structural map, isopach map and the other geological map has been generated using Geographix.

- Additionally ,in order to indentify the effect of horizontal lateral length on well productivity from New Albany shale, fracture network has been regenerated in order to represent the distribution of natural fracture in that formation.

- Capabilities of this new technique ease of use and much shorter development and analysis time are advantages of Top-Down modeling as compared to the traditional simulation and modeling.

Results from these studies are presented in Section 7.1. FRACGEN and NFFLOW software developed by National Energy Technology Laboratories are available and will be provided upon request.

7.2 Analytic Reservoir Analysis

Research Team: *Thomas Blasingame, Christine Ehlig-Economides, Bo Sung; Texas A&M*

The original vision for New Albany shale emphasized the role of natural fractures, and there was an expectation that pressure transient tests might reveal characteristics of a natural fracture system. However, no reliable data was available from the industry and only pressure buildup data acquired in the New Albany Shale project was available. This was from A-7431 well. The A-7431 well was the first well in New Albany to adopt modern shale gas exploitation techniques based on multistage fracturing of a horizontal well. Rather than depend on natural fractures, such well designs instead create a stimulated reservoir volume (SRV) defined by a hydraulic fracture network. The horizontal segment in the A- 7431 well measured 3500 ft, and 8 fracture stages spaced about 400 ft apart were created. During this project, a second well, A- 7455, was drilled with a similar design, but in this case microseismic data were acquired while fracturing that suggest the hydraulic fractures may extend in the direction normal to the horizontal well axis as much as 1200 ft in half length.

- Low reservoir permeability and pressure of the New Albany shale inhibits the application of costly drilling and completion technologies such as extended length horizontal wells and multistage hydraulic fracturing. As such, access to a user-friendly analytic tool was found to be very attractive to the producing companies engaged in the development of New Albany shale. A package of analytic algorithms with a Microsoft Excel front-end that optimizes the length of horizontal wells and the number of hydraulic fractures as a function of reservoir parameters, cost elements, and gas price was developed. This product is available from GTI upon request.

- An integrated interpretation incorporating fracture half length of 1200 ft indicated by microseismic data acquired from the A-7455 well provides an estimate for permeability on the order of 180 nanodarcies (10^{-7} darcies) and an estimate for the SRV of 3.11 BSCF (assuming water saturation of 0.5 and including 2.2 BSCF adsorbed gas), which, in turn, gives an estimate of 2.6% for the gas recovery factor to-date.
- An independent estimate for expected ultimate recovery (EUR) based on a power law rate decline model gave an estimate of 0.136 BSCF, which would imply ultimate recovery efficiency of 5.4%. However, if the SRV is smaller than what was hypothesized

on microseismic indications from the A- 7455 well, the recovery factor could be somewhat greater. Analytical analysis of the production data suggest that the created fracture half lengths must be at least 440 ft, giving a minimum SRV of 1.63 BSCF including 1.16 BSCF adsorbed gas.

- EUR estimates were also done for 33 other New Albany shale wells for which production data were available. Most wells showed EUR estimates of less than 0.01 BSCF. The A-7431 well shows considerably higher EUR than most of the other wells, indicating that the multistage fracturing approach shows promise for this resource.
- For permeability of 180 nanodarcies the production forecast indicates that even after 30 years there will be gas between adjacent fracture stages still at the original reservoir pressure. This suggests that fracture stages should be spaced closer together. At a spacing of 50 ft instead of 440 ft, flow to adjacent fractures would interfere after 3.5 years, and much higher recovery of the gas in place could be achieved during a normal well lifetime of 30 years. However, to maintain an economic rate for 30 years, the number of fractures should be increased.

The work under this task was performed in part by Mr. Bo Song and was included in his PhD dissertation. Bo Song's thesis is included in Section 7.2. The analytic package, also developed by Bo Song, is available for download from GTI.

8. Environmental Considerations

Low reservoir pressure and production rate have hindered the development of New Albany shale gas and as such, there are no environmental concerns at the present. In addition, the low reservoir pressure has made the air drilling the method of choice. The cost of air drilling is substantially lower than that of mud drilling and at the same time, it does not cause permeability reduction that normally occurs due to formation damage caused by swelling of clay particles when in contact with water and invasion of pore space by mud filtrate. A second parameter that removes the environmental concerns relates to the fact that fracture stimulation of New Albany shale uses nitrogen as opposed to slick water or gel fracturing fluid used in other formations. The State authorities in Illinois, Indiana, and Kentucky were all contacted regarding environmental aspects of drilling and fracturing of New Albany shale. No concerns whatsoever were expressed. Specifically, Kentucky Department of Natural Resources and the Indiana Department of Environment Management clearly stated that:

- There is minimal environmental impact associated with New Albany shale production
- The volume of produced water is small and is stored in 50 bbl tanks, then transported to permitted Class II injection wells
- No or minimal flow-back water as wells are nitrogen fractured
- No volatile organic compounds or other air quality Issues are present
- Wells are drilled using air drilling technique and solid waste issues are minimal.

9. Technology Transfer

Team Members: *Research team*

Technology transfer was an integral task of the New Albany shale project and included publications and presentations at national and regional meetings of the American Association of Petroleum Geologist (AAPG), Society of Petroleum Engineers, Society of Petrophysicists and Well Log Analysts (SPWLA) and several other technical meetings as well as the RPSEA forums. In all, 25 papers and presentation were published and presented. Table 2 provides a list of papers and presentations given by the project team members.

Table 2. Technical Papers and Presentations

Title	Author	Presented at:	Date
New Albany Shale Gas Project (Featured Article)	Iraj Salehi, Angelica Chiriboga GTI	HART's Unconventional Natural Gas Report	12/2008
Identification of microbial and thermogenic gas components from Upper Devonian black shale cores, Illinois and Michigan basins. (Paper)	Anna M. Martini, Lynn M. Walter, Jennifer C. McIntosh	The American Association of Petroleum Geologists. (AAPG) Bulletin, v. 92, no. 3	3/2008
Shale Evaluation New Albany Example – RPSEA / GTI Project (Presentation)	Don Luffel, Jim Lorenzen' Restech	Spring Topical Conference Petrophysical Evaluation of Unconventional Reservoirs Philadelphia,Pa	3/15-3/19/2009
New Albany Shale Gas Project An Industry-RPSEA-GTI Cooperative Project (Presentation)	Iraj Salehi, GTI	Spring Topical Conference Petrophysical Evaluation of Unconventional Reservoirs. Philadelphia,Pa	3/15-3/19/2009
New Albany Shale Project, Project Update (Presentation)	Iraj Salehi, GTI	RPSEA Unconventional Gas Project Review Meeting, Golden, CO	4/15/2009
Implications for development of effective drilling and completion technologies (Presentation)	Julia F. W. Gale, Stephen Laubach, Bureau of Economic Geology	RPSEA Unconventional Gas Project Review Meeting, Golden, CO	4/15/2009

Title	Author	Presented at:	Date
New Albany Shale Formation Evaluation (Presentation)	Jim Lorenzen Restech	RPSEA Unconventional Gas Project Review Meeting, Golden, CO	4/15/2009
Fracture Design & Diagnostics, New Albany Shale Project (Presentation)	Steve Wolhart, Pinnacle	RPSEA Unconventional Gas Project Review Meeting, Golden, CO	4/15/2009
Analysis of Reservoir Performance in Shale Gas Reservoir Systems (Presentation)	Tom Blasingame, Texas A&M University	RPSEA Unconventional Gas Project Review Meeting, Golden, CO	4/15/2009
Natural Fractures in the New Albany Shale and their importance for shale gas production (Paper)	Julia F. W. Gale tephen E. Laubach, Bureau of Economic Geology	International Coalbed and Shale Gas Symposium Tuscaloosa, AL.	5/19- 5/ 21/2009
Formation Evaluation: Integrating Core-Geochem-Logs (Presentation)	Jim Lorenzen, Don Luffel, Frank Caramanica, ResTech	GTI Forum, Chicago, IL.	6/4/2009
Natural fractures in the New Albany Shale and their importance for shale-gas production (Presentation)	Julia F. W. Gale Stephen E. Laubach, Bureau of Economic Geology	GTI Forum, Chicago, IL.	6/4/2009
Geochemical and microbial investigation of methanogenesis in the Upper Devonian shales (Presentation)	Anna Martini & Matthew Kirk, Amherst College; Stephen Petsch, UMASS ,Jennifer McIntosh University of Arizona	GTI Forum Chicago, IL.	6/4/2009
Fracture Design & Simplistic 3-D Parametric Modeling New Albany Shale (Presentation)	Doug Walser, Steve Wolhart, Pinnacle	GTI Forum, Chicago, IL.	6/4/2009

Title	Author	Presented at:	Date
Analysis of Reservoir Performance for Shale Gas Systems, RPSEA/GTI Project(Presentation)	Tom Blasingame Department of Petroleum Engineering, Texas A&M University	GTI Forum, Chicago, IL.	6/4/2009
New Albany Shale Gas Project A Joint Industry Project Sponsored by the research Partnership to Secure Energy for America RPSEA (Paper)	Iraj Salehi & Angelica Chiriboga Gas Technology Institute (GTI)	Published by Touch Briefings Exploration & Production. Oil & Gas Volume 7 Issue 1 OTC Edition.	8/2009
Top-Down Intelligent Reservoir Modeling of New Albany Shale (Paper)	A. Kalantari Dahaghi, SPE, S.D. Mohaghegh, SPE, West Virginia University	2009 SPE Eastern Regional Meeting Charleston, West Virginia	9/23–9/25/2009
Economic Impact of Reservoir properties and Horizontal Well Length and Orientation on Production from Shale Formations, Application to New Albany Shale (Paper)	Kalantari, A., Mohaghegh, D., West Virginia University.	2009 SPE Eastern Regional Meeting. Charleston, West Virginia, USA	9/23–9/25/2009
New Albany Shale Gas Research Project. (Paper)	Kent F. Perry, Iraj Salehi	World Gas Conference Buenos Aires, Argentina	9/3-9/5/2009
Poster Presentation of New Albany shale (Poster)	Iraj Salehi	NAPE Conference Houston, Texas	02/10/10
Poster entitled Microbiology & Geochemistry of new Albany Shale	Samuel Miller, Julian Damashek, Anna Martine, Melissa Schlegel, Jennifer McIntosh & Matthew Kirk		03/20010
Poster entitled "Natural fractures in the New	Julia Gale, Stephen E. Laubach and	The AAPG 2010 New Orleans meeting. & The	04/2010

Title	Author	Presented at:	Date
Albany Shale, Illinois Basin, and their importance for shale-gas production. (Poster)	Lucas J. Fidler	poster was also displayed in the RPSEA booth in the Exhibition Hall at the meeting	

SECTION 2

DATA DRIVEN APPROACH

New Albany Shale Gas Project

Jordan Ciezobka, Angelica Chiriboga, GTI

Section 2. Data Gathering and Field Data Acquisition

Table of Contents

Section 2. Data Gathering and Field Data Acquisition 1
Introduction 2
Background Studies 3
Geology 3
Geochemical Sampling and Analysis 4
Top-Down Intelligent Reservoir Modeling 6
Well Experiments 8
Appendix 12
Z-Seis New Albany Shale RVSP Final Report 12

Introduction

Data gathering and field data acquisition tasks included obtaining well logs, cores, and production data from producing companies and public sources such the State Geological Surveys and field data acquisition. GTI and all research teams collaborated in data gathering. Field data acquisition such as logging and coring of the participating producing companies was the primary responsibility of GTI.

The field data acquisition tasks of the New Albany Shale Gas project involved the acquisition of reliable field data and timely testing of results, so that dependable data are available for analytic work and designs. Once research quality data was obtained, project subcontractors evaluated and advised on the correctness and applicability of such data. The acquired data described herein can be sorted into two categories, data that was given in-kind from project participants and data that was obtained through research that was paid for by project funding. Project funding enabled data to be collected from sampling, coring, logging, hydraulic fracturing, fracture diagnostics, pressure and rate production data, geological surveying, geochemical analysis, and best practice analysis. Data that was given in-kind consisted of production data and logs from many wells across the NAS from various participating producers.

Appreciation is given to the following participating producers that contributed in this collaborative project by providing various reservoir and production data: N-Gas, CNX, Noble Energy, Trendwell Energy, and Aurora Oil and Gas. The reservoir and production data that was given represented 47 wells in Indiana and Kentucky. The data was from vertical and horizontal wells from a wide spectrum of depths that included both biogenic and thermogenic gas. In total, 34 sets of production data were collected along with 45 sets of electric log data. Gas characterization, including methane desorption and gas content analysis was made available from 4 wells. Core pictures provided from 3 wells were used to supplement other data in natural fracture characterization. One data set of petrophysical evaluation and mineralogy analysis was also provided. Project researchers used this data to paint a clearer picture of the NAS in order to develop tools and techniques in an attempt to transform this immense resource into economically recoverable reserves.

Data acquisition is essential for current and future projects. Current projects require reliable data that is necessary for quality research so that results are accurate and lead to the development of new ideas and tools that are valid. As technology and our understanding evolve, previously acquired data that was not completely understood or evaluated can be used in future projects for analysis. Analyzing or re-analyzing previously acquired data can lead to new developments and a more thorough understanding of results. Conversely, previously acquired data needs to be properly and concisely reported and stored so that there is no redundancy or unnecessary duplication of work in future projects. For that reason, GTI has undertaken the task of compiling all acquired data and analysis, and assembling it in reports that are thorough.

For a project of this scale to be successful, a collaborative approach on every task of the project, including data acquisition, was employed. In an effort to have the best chance of solving a problem or reaching a common goal, utilizing the best experts that are on the leading edge of technology and innovation is essential. Many entities came together on this project in order to unlock the gas potential

of the New Albany Shale including, producers, service companies, academia, research institutions, and public data domains. The data set used for research in this project was greatly expanded by collaborative efforts of producers active in the NAS and by utilizing available data from core repositories including public archives. In order to ensure that we can secure energy for America that is needed currently and in the future, the collaborative approach used in this project is paramount.

The remainder of this section has been arranged according to the nature and utilization of data gathered or acquired. A brief summary of results is also included.

Background Studies

In order to assess the current status of the New Albany Shale and to ensure that prior work is not being duplicated, a thorough search on the topic was performed. Due diligence efforts included search of prior publications from both public archives in Indiana, Illinois and Kentucky, and private companies such as oil and gas producers. Efforts were made to acquire previously compiled maps and surveys. Well site visits as well as discussions with geologists and other researchers provided additional information on the current status of the NAS. Collected data is contained in a volume entitled:"Naturally Occurring Fracture Literature, Web and Available Records Review in Support of the GTI/RPSEA New Albany Shale Gas Project", and is available for viewing by contacting GTI.

Geology

In the world of unconventional gas, more specifically shale gas, natural fractures are the driving force for an economically successful play, therefore it is critical to thoroughly understand natural fracture population characteristics. Knowledge of fracture intensity and orientation is a critical factor influencing the selection of azimuth and length of horizontal wells. The geological tasks performed in this study included field trips for outcrop observation, core examination, and subcritical crack index measurements. Outcrop observations were performed in order to compare outcrop fracture characteristics to those present in the reservoir. The core examination focused on natural fracture orientation, openness, sealing material, and special distribution. Subcritical crack index and Young's modulus measurements were incorporated in this task in order to predict fracture patterns such as quantity, spacing, and clustering.

Outcrop studies were performed in southern Indiana and central and eastern Kentucky. Data from previous literature was used to supplement fracture studies and to verify location of outcrops. Joint orientation data along with fracture spacing and height, was collected from fifteen locations in Indiana and Kentucky and was used to determine if surface fracture characteristics could be correlated with subsurface fracture trends. For shallow parts of the NAS where biogenic gas exists, it may be possible that surface fracture features found in outcrops are representative of subsurface fracture systems.

Cores from Indiana Survey Core Repository were examined and sampled along with cores acquired from two well experiments. In total, fifteen vertical or slant cores from the core repository were sampled for

natural fracture characteristics. Two well experiments in Kentucky produced cores that along with formation image logs were used to determine fracture orientation, special distribution, and fracture filling material. Fracture features from the core were used to validate formation image log interpretations.

Subcritical crack index measurements were performed on samples from 3 cores in Sullivan County Indiana. In this study, mechanical rock properties were measured in order to quantify natural fracture frequency and spacing in an attempt to determine if natural fracture populations exist in clusters and may have not been sampled in cores that were obtained. Sample preparation was challenging as the cores were slant and the samples being cut were parallel to the beading planes, which had a tendency to separate. Repeatability of values from multiple tests on specimens from the same sample was inconsistent. However, stress-strain behavior and fracture toughness was consistent along with decay curves that had good fit to theoretical curves. Variability may have resulted from compositional variation between samples. The complete report on geological studies is contained in Section 3.

Geochemical Sampling and Analysis

Geochemical sampling and analysis was a two part task involving the sampling of previously sampled Antrim Shale to determine microbial population changes over time in a producing reservoir, and to sample and characterize microbial populations in the New Albany Shale. Gas, water, and cores were used as test specimens for this study, therefore field visits and laboratory work was of the essence. Geological studies, mainly natural fracture characterization, complement geochemical studies in that even though environmentally favorable conditions are needed for methanogenesis, access to natural fractures that are interconnected will ultimately lead to greater biodegradation of organic matter and higher rates of methane production.

Part 1-Antrim Shale Study

The geochemical characterization in this part of the study focused on examining changes in water chemistry and microbial populations as natural gas is produced in the Antrim Shale, enabled by a long history of development and sampling thus providing means for such observation. It is well understood that as gas is produced, geochemical adjustment of formation water may occur due to fresh water influx thereby reducing in-situ salinity and altering geochemical structure favorable for methanogenesis. In this study, eight wells were selected along the northern edge of the basin that have been sampled in the mid 1990's and re-sampled them in January 2009.

Water temperature and pH measurements were recorded from each sample in the field, and along with water samples gas samples were also collected. Gas samples were submitted for compositional and isotopic analysis, additionally the water samples were submitted for chemical, isotopic, and microbial analysis. Microbial biomass samples were collected by filtering the water through a sterile cellulose-ester membrane. Microbial biomass samples from three selected wells were chosen for genetic analysis whereby the DNA was extracted and mapped. The alkalinity of each sample was determined along with

precise concentrations of chloride, sulfate and other trace elements. Gas composition was measured by utilizing gas chromatography.

Microbial methanogenesis has continued over the last fifteen years at a significant rate, although the change in isotopic composition of gas and water cannot readily be explained. Results suggest that biogenic methane production is on the decline as a result of reservoir depletion through gas production.

Part 2-New Albany Shale Study

The NAS portion of the geochemical study was performed in order to validate if current and future bacterial methanogeneration can substantially alter the absolute and relative abundance of hydrocarbons in the New Albany Shale. Core samples of gas producing sections were examined to explore if selective removal of labile compounds and compound classes could be detected. Abundance of various aliphatic and aromatic hydrocarbons was measured for several depths from three cores in order to determine if certain locations within cores exhibit intense biodegradation of shale organic matter. Suite if biodegradation indices were calculated in order to further determine the intensity and relative stages of biodegradation, both regionally and within cores.

Another study consisted of microbial investigation of natural gas-rich black shale where microbial community structures were characterized in eight NAS sites in southwestern Indiana and northern Kentucky as well as two coal beds in Illinois and Indiana. Few previous studies of subsurface methanogenic communities have focused on sedimentary basins, and none have compared a large number of sites in gas-rich shales over a wide geographic area. This study integrates aqueous and gas geochemistry data collected from the New Albany Shale in July 2009 with a larger dataset collected by Schlegel and coworkers from 2004-2008 and McIntosh and coworkers through 2002. The expanded dataset encompasses the New Albany Shale, coal beds, and surrounding aquifers in the Illinois Basin. Natural gas extraction companies provided well log data, including formation depths, total well depths, surface level elevations, and water and gas production rates.

Natural gas wells in the expanded dataset are located in Illinois, Indiana, and Kentucky. The July 2009 sampling effort focused on Sullivan and Knox Counties in western Indiana, Harrison and Meade Counties in southern Indiana and northwestern Kentucky, respectively, and Christian County in west-central Kentucky. The GPS location of the 33 wells sampled in these counties is shown in Figure 2. Water samples were collected at the wellhead from 20 wells and natural gas samples were also collected at the wellhead from 27 wells. The collected water samples were sampled for pH, temperature, and alkalinity, while being preserved for microbial extraction. Formation water alkalinity provides a robust geochemical indicator of microbial activity in shallow shale gas systems. Collected gas samples were submitted for compositional and isotopic analysis.

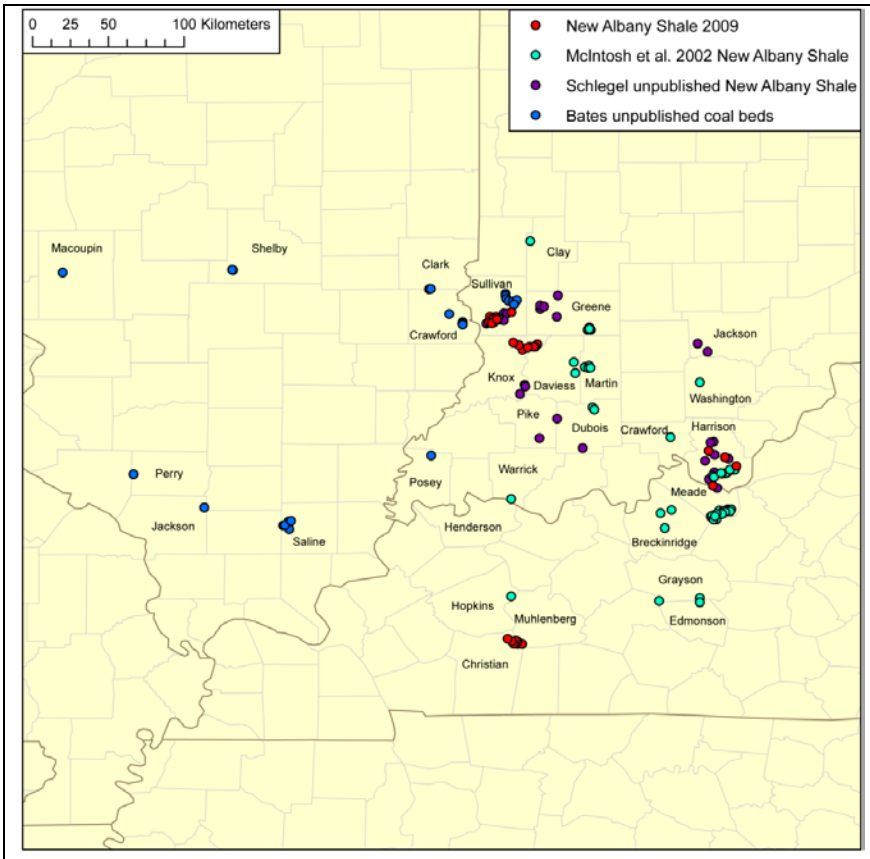


Figure 2: Map of well locations in the expanded dataset.

The geochemical and isotopic values from formation waters and gas produced in the NAS indicate a "mixed" gas, with microbial additions more prevalent in certain geographic areas, and thermogenic components generally increasing towards the more saline, deeper portions of the basin. Microbial diversity varies greatly from well to well, with no one well having one type of bacteria that accounts for more than 50% of the bacterial clone library. For the complete geochemical analysis refer to Section 4.

Top-Down Intelligent Reservoir Modeling

In order to reassess the development potential of the New Albany Shale formation in a cost effective manner, a novel and new approach was developed. Top-Down Intelligent Reservoir Modeling is an integrated workflow process, that unlike traditional reservoir simulation and modeling techniques that start with building a geo-cellular model, it begins by analyzing production data using traditional reservoir modeling techniques for a multitude of wells in a field. Along with production data, artificial intelligence and data mining techniques are used to develop a full field model in order to predict future reservoir/well performance and to ultimately optimize field development strategies. Sensitivity analysis is used to gage the impact of gas production by varying reservoir characteristics and natural fracture aperture, density and length. Production history for 87 wells in Kentucky, acquired from Kentucky Geological Survey, was used to develop a full field model using the Top-Down modeling approach. Once the reservoir model was created, well locations for future infill wells were selected based on remaining reserves, estimated production rates, and economics. Additionally, 31 recently drilled wells in Christian county Kentucky-Halley's Mill quadrangle were used to construct a reservoir model utilizing the Top-Down approach.

Sensitivity Analysis

The objective of the sensitivity analysis is to identify factors that have the most influence on production by varying the magnitude of various reservoir parameters including natural fracture characteristics. A history match was performed utilizing production data from a New Albany Shale well in Kentucky. The history match included matching the typical formation properties such as: pore pressure, matrix porosity, matrix permeability, reservoir thickness, and natural fracture orientation and aperture. The flow of a single phase fluid through a naturally fractured reservoir was modeled using a recently NETL/DOE developed simulator called NFFLOW. Natural fractures used in the analysis were generated using FRACGEN, a simulator also recently developed by NETL/DOE. Additionally, wellbore parameters such as lateral length and orientation were varied to determine the effect on gas production. Figure 3 shows the sensitivity of changing the magnitude of the various formation properties on gas production.

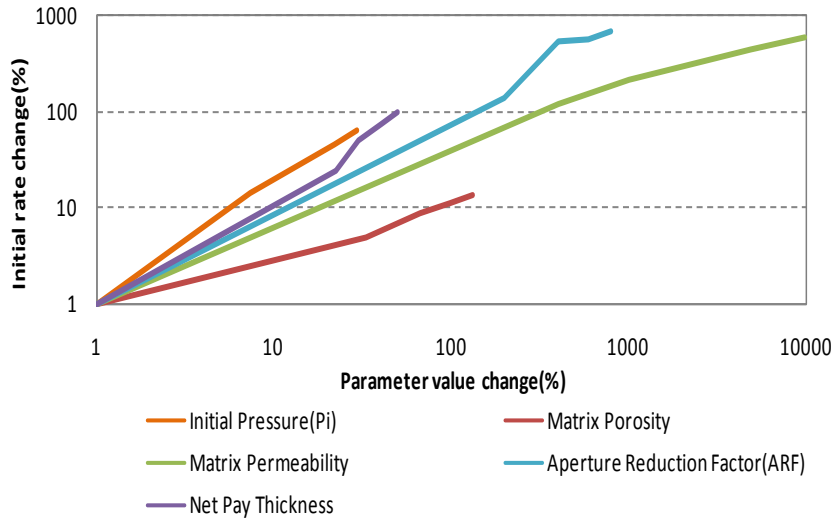


Figure 3: Sensitivity Analysis – Effect of varying reservoir and fracture properties on initial gas rate

Developing Full Field Reservoir Model

Production data from a set of 87 wells in one field in Kentucky was used to describe the reservoir. Following the Top-Down intelligent reservoir modeling approach, each set of production data was analyzed using traditional reservoir engineering techniques such as Decline Curve Analysis, Type Curve Matching, Single-well History Matching, Volumetric Reserve Estimation and Recovery Factor. By doing so, the following reservoir parameters were extracted: initial flow rate, decline rate, hyperbolic exponent, permeability, porosity, drainage area, fracture half length, and the 30 year EUR. The location of the 87 wells was plotted and each well was discretized using the Voronoi cell method while performing fuzzy pattern recognition. Spatial and temporal analysis was performed in order to plot matrix porosity and permeability distribution, sweet spots of remaining reserves, and other reservoir characteristics. Once the results of predictive modeling and fuzzy logic recognition were used to generate a complete model, the best spots for in-fill drilling were identified. Production profile along with economic analysis was generated for each site in order to determine viability.

Halley's Mill Quadrangle

In another study, production data from 31 wells in Kentucky's Haley's Mill Quadrangle was used to generate a reservoir model using the Top-Down Intelligent Model approach. Because all the wells had available log data, a second reservoir model was generated using more conventional top to bottom

techniques by utilizing Halliburton's Geographics software. Various formation properties were derived from logs by performing log analysis in the PRIZM module of Geographics. Results of discrete predictive modeling were compared with contour maps generated with Geographics so as to check for consistency. The Top-Down Intelligent Model approach is a practical way to model and simulate shale and other conventional and unconventional reservoirs using relatively small amounts of field data. As a result, optimized in-fill drilling strategies can be developed with reduced cost and resources. The complete study on Top-Down Intelligent Modeling is contained in Section 7.1.

Well Experiments

Participating Producer A

Well A-7455

Whole Core Analysis

In August 2009, a participating producer drilled a pilot well in Christian County Kentucky in the Haley's Mill Quadrangle Field to total depth of 2675' through the New Albany Shale (NAS). Between the interval 2526' MD – 2585.3' MD, 59.7 ft of whole core from the Lower New Albany Shale and the underlying Limestone was recovered and five selected samples from the NAS were sent to Core Labs in Houston, where Julia Gale, Frank Caramanica and Don Luffel examined the cores for natural fracture occurrence, openness, and orientation and compared with image analysis of the Compact Micro-Imager (CMI) log.

Samples of the core were sent to Weatherford Laboratories (Ticora Lab) for geochemical analysis, including total organic carbon (TOC), Kerogen type and thermal maturity. Three 1 ft cores were canistered and also sent to Ticora Labs for gas analysis, including gas composition, adsorbed and free gas, and methane adsorption isotherm analysis. In addition to the above collected and analyzed data, Core Lab performed X-Ray Diffraction (XRD) Analysis on five samples extracted from the core to determine rock mineralogy. Using GRI protocol, Core Lab performed core analysis on five samples in order to determine petrophysical properties. Crush and leach method was used to determine the estimated equivalent NaCl salinity and XRD analysis was used to correct for clay bound water.

Open-Hole Logging

In order to determine various formation properties that are fundamental to characterizing the reservoir a suite of logging operations conveyed via wireline were performed on the A-7455. The petrophysical approach is to use core data to build calibrated log based models that allow for determination of lithology, porosity and water saturation, oil and gas saturation, matrix permeability, total organic carbon (TOC), free adsorbed and total gas content, natural and induced fracture characterization, and geomechanical properties. Logging operations were performed in the pilot well to a measured depth (MD) of 2,675 ft. The logging program consisted of: Array Induction – Density and Neutron, Photo Density/Gas Detector, Spectral Gamma Ray, Full Array Sonic, and Compact Micro Imager. Section 5 of the report contains the detailed report.

Hydraulic Fracturing

Because the NAS has very low permeability, stimulation is vital for economical production of hydrocarbons. The operator chose to complete the horizontal section of the wellbore with open-hole packers and frac ports in order to produce as many natural fractures as possible, with the premise that hydrocarbons would converge along the horizontal section of the wellbore via natural fractures and then would enter the production tubular through the frac ports. Hydraulic fracturing was used to stimulate the reservoir and the treatment consisted of eight individual fracture stages along the horizontal section of the wellbore beginning at the toe of the well and ending at the curve. The stimulation fluid used for hydraulic fracturing was composed of nitrogen gas and a small amount of hydrochloric acid. The HCL was added to promote acid stimulation as the core testing showed that the natural fractures contained calcite deposits. No propping agent was used. Surface treating pressure, nitrogen flowrate, and HCl flowrate were recorded and collected for each individual stage. Section 6.2 contains the full report on Fracture Diagnostics.

Fracture Mapping

The main objectives of the microseismic fracture mapping survey were to determine fracture pay zone coverage along the horizontal wellbore and to measure fracture geometry. The data could also be used to determine future well placement and infill drilling strategies for optimal drainage of the reservoir. Initially, an offset monitor well close to the toe of the horizontal section of the wellbore contained the receiver array used for microseismic monitoring, with the bottom receiver located just above the NAS at a depth of 2,414 ft. This configuration was used to monitor stages 1 through 4 of the hydraulic stimulation treatment. As the fracture stages progressed closer to the heel of the wellbore, the microseismic events were at the edge of the receiver array listening distance, and as a result a second well was used to monitor the microseismic events. The second monitor well was located on the same pad as the treatment well and was used to monitor stages 5 through 8. Surface shots were used to orient the geophones once the tool array was in place. The complete fracture mapping report is contained in Section 6.2.

Participating Producer B

Well B-3

Another participating producer drilled a horizontal well (B-3) in the New Albany Shale with a lateral length of about 2,500 ft. Based on wellbore measurements the lateral did not intersect a significant amount of natural fractures, and since hydrocarbon production is thought to be primarily from natural fractures, a Reverse Vertical Seismic Profile (RVSP) was performed in order to determine natural fracture occurrence and azimuth. A surface geophone array consisted of three walk-away lines each spaced 120 degrees apart, with the first array extending north, the second array extending north 60 degrees east, and the third array extending east 30 degrees south. The walk-away lines were 4,000 ft long consisting

of four geophones spaced 1,000 ft apart, with the first geophone positioned 1,000 ft away from the wellbore. The full report on the RVSP was completed by Z-Seis and is contained in Appendix A.

Well B-15

Drilling

The B-15 is a vertical well drilled through the New Albany Shale to a depth of 3,975 ft. The well is located in McLean County Kentucky in the Jackson field and is centered between two parallel horizontal wells, B-18 and B-21. The well was drilled as an exploratory well in order to collect whole cores, electric log data, and to serve as an observation well for conducting a microseismic survey during the simultaneous stimulation of the B-18 and B-21 wells.

Whole Core Analysis

Coring operations produced 302.5 ft of core out of 312 ft of core cut between the depths of 3,572 – 3,884 ft. From the recovered cores, 28 samples were canistered for gas characterization analysis and sent to Weatherford Laboratories in Houston. Of these 28 samples, six were selected for gas composition and another three were selected for isotope determination. The NAS section of the core (3,600-3,822 ft) was visually inspected and compared to the formation image (FMI) data in order to characterize natural fractures. The comparison was also used to determine the reliability of the image log in showing natural fracture occurrence and orientation. Natural fractures found in the core were tabulated, along with the fracture depth, dip, azimuth, and fracture filler material.

The twenty-eight samples were analyzed for total organic carbon (TOC), total gas content, apparent diffusivity, and apparent sorption time. The total gas content was composed of lost, measured, and crushed gas. A report containing the results of the above analysis, the gas content of the six samples, and the gas isotope ratio analysis of the three selected samples is contained Section 5.

Open-Hole Logging

Open-hole logging operations with tools conveyed via wireline were performed to a measured depth (MD) of 3,975ft. The logging program consisted of: Triple Combo, Spectral Gamma Ray, Full Array Sonic, and Compact Micro Imager. Data from the logs is available in .LAS format.

Fracture Mapping

A microseismic survey was performed while stimulating the two parallel horizontal wells B-18 and B-21. The geophone array was positioned vertically in the B-15 well and strattled the elevation of the New Albany Shale. The tool array consisted of 16 tools in 12 positions with the bottom geophone at a depth of 3,927 ft. Five surface locations utilizing the Vibroseis unit were used to orient the tools and to produce a velocity model for locating seismic events. The microseismic survey consisted of mapping 18 fracture stages over a span of three days. The resulting microseismic data and analysis is in Section 6.2.

B-18 and B-21 Wells

Drilling

The B-18 and B-21 wells, located in McLean County Kentucky in the Jackson field, are parallel horizontal wells drilled in the New Albany Shale. B-18 has a measured depth (MD) of 6,404 ft and a true vertical depth (TVD) of 3,727 ft and is completed with a liner with nine open-hole packers and nine ball activated frac ports. B-21 has a measured depth (MD) of 6,690 ft and a true vertical depth (TVD) of 3,713 ft and is also completed with a liner with nine open-hole packers and nine ball activated frac ports. The two horizontal laterals are approximately 1,540 ft apart and were drilled in this fashion as to utilize the Zipperfrac stimulation technique.

Fracture Modeling

In order to model the created fractures a simplified conventional elastic 3-D model with limited tip effects was utilized. Because it is assumed that the formation is homogenous throughout, a single vertical fracture was modeled with the treatment parameters given by the producer. Open-hole log data along with industry accepted formation evaluation techniques were used to derive formation properties in the various rock layers. Modeled fluid and proppant properties were adjusted to coincide with the actual physical properties of the materials used. The simulation produced a fracture with a propped half length of 1290 ft and a fracture height of 502 ft. Proppant concentration in the fracture ranged from 0.004 – 0.03 lb/ft^2. A better approach would be to use a full 3-D simulator and model all eighteen fracture stages in the prescribed time interval. This way, pressure induced stress contrast and increased pore pressure would be taken into account and may show altered fracture geometry in subsequent fracture stages. However, software with these capabilities has not yet been developed. The full fracture modeling report is in Section 6.2.

Hydraulic Fracturing

The stimulation treatment was executed in a manner whereby nine adjacent fracture stages were sequentially pumped with two separate fracturing fleets at approximately the same time. Each fracturing stage was comprised of a neat nitrogen pre-pad, a 95% Mitchell Quality pad, and four proppant laden stages, utilizing Ultra Lightweight Proppant (ULP) of 30/80 mesh. The slurry stages varied from 94% to 99% foam quality. The treatment was pumped at an average bottom-hole rate of 70 bpm and each stage totaled 10,000 lbs of proppant. Once all the proppant was pumped for each stage, the well was flushed with neat nitrogen and a ball was dropped in order to isolate the previously fractured interval and to open the frac port for the next stage. This was repeated 9 times in each well with 8 balls dropped, starting at the toe of the lateral and terminating at the heel. Once each fracture stage was complete, the frac fleets shut down in order to reload nitrogen, reload the ball, and premix the proppant slurry. The treatment plots of all stages are summarized in Section 6.2.

Appendix

Z-Seis New Albany Shale RVSP Final Report

SECTION 3

GEOLOGICAL STUDIES

New Albany Shale

Bureau of Economic Geology, Fracture Characterization

Final Report

September, 2010

Julia F. W. Gale, Stephen E. Laubach and Luke J. Fidler

Table of Contents

Objectives 3

Summary of Results 3

Outcrop studies 6

Characterizing fracture orientation spacing and height growth 13

Core studies 20

Well Experiments 24

Discussion of microseismic results for the second well experiment in the context of natural fracture observations made in the pilot-hole core 32

Subcritical crack index, fracture toughness and Young's modulus tests 35

Fracture Petrography 43

Porosity examination of ion-milled surfaces 46

Alpha Gas 49

Communication of fracture characteristics for modeling hydraulic and natural fracture interaction 50

Technology Transfer 50

Acknowledgements 51

References 52

Objectives

The objectives of the study are to characterize the natural fractures in the New Albany Shale in the Illinois Basin, and to assess their relevance for natural gas production. Our focus is on the thermogenic part of the play, in southern Indiana and western Kentucky and on whether the sealed natural fractures that are present represent weak planes that reactivate during hydraulic fracture treatments. The possibility of permeability enhancement through open natural fractures is also investigated

These objectives were met through the following tasks:

1. Synthesis of published fracture characterization data and augmentation with fracture description for 12 cores from southern Indiana, 3 cores from western Kentucky and 15 outcrop locations in both Indiana and Kentucky.
2. Analysis of cores and image logs from vertical pilot wells for two well experiments both in Western Kentucky:first well in Christian County A-7455, and a second well in McLean County B-015.
3. Measurement of the subcritical crack index (SCI) of core samples with the aim of understanding fracture spatial distribution and how fracture patterns differ from one layer to the next.
4. Consideration of the relative orientation of S_{Hmax} and natural fractures, and whether this geometry is favorable for reactivation.
5. Assessment of whether part of the fracture population is open and would enhance permeability in the reservoir. This task includes both core and outcrop study.
6. Qualitative assessment of the tensile strength of natural fracture planes.
7. Estimation of key input parameters for geomechanical modeling of interaction of hydraulic and natural fractures.

Summary of Results

- Natural fractures are common in the New Albany Shale, but vary in character and have different properties with respect to their effect on gas production.

- There are both opening-mode fractures and faults in core and in outcrop.

- In many cores there is more than one opening-mode fracture set. We contend there are different mechanisms of formation on the basis of aspect ratio, mineral fill, orientation and whether the fracture has been shortened during sediment compaction.

- The majority of fractures observed in core in the Clegg Creek member (the usual gas target) in the SW Indiana part of the basin are similar to the demonstrably weak planes present in the Barnett Shale in the Fort Worth Basin (Gale et al. 2007; Gale and Holder, 2008) where calcite mineral fill is only weakly attached to the fracture walls. These fractures are undeformed, straight-sided, high height to width aspect ratios, and are commonly arranged in en echelon arrays. These fractures would be prone to reactivation during hydraulic fracture treatments.

- Partly open fractures were observed in both cores from the well experiments in western Kentucky. Calcite partly occludes these fractures, and bitumen is also present, both predating and postdating the calcite cement.

- A partly open fracture set in the lowest part of the section in the Blocher Member has been observed in both outcrop and core. These fractures have low height to width aspect ratios and irregular fracture walls. They are sealed with dolomite and have residual bitumen and large open vugs. The fractures are folded or sheared and the shale fabric has further compacted around them, indicating that they formed early in the burial history of the basin.

- The most common fracture-sealing cement is calcite, but some fractures are sealed by both calcite and quartz. We speculate that quartz cements result in stronger fracture planes because of bonding between wall rock and cement as quartz overgrows broken quartz wall rock grains.

- We tested five samples for subcritical index, fracture toughness, and Young's modulus. The samples were from cores from Sullivan County, southwestern Indiana and from western Kentucky. Sample preparation was challenging because the cores are both slant cores and are oblique to bedding. Subcritical indices range from 43 to 80.

- The structural grain of the two areas studied – southern Indiana and western Kentucky – is fundamentally different. Southern Indiana is dominated by the Wabash Valley normal fault system, which trends approximately N-S and where faults are reactivated in shear in the present day stress regime. Western Kentucky is dominated by the E-W trending Rough Creek Graben, but sections of this system trend ENE-WSW.

- The present-day in situ stress must be determined on a site-specific basis. The world stress map database suggests a swing in the maximum horizontal stress direction (S_{Hmax}) from ENE-WSW in southwest Indiana to E-W in western Kentucky. In the Appalachian basin and elsewhere in the mid-continent the trend is closer to ENE-WSW. There are no data points in the World Stress map database for the McLean County location. The large differences in underlying local structure in the Illinois Basin, including a fault transfer zone in McLean County, might have a significant perturbation effect on the far-field stress orientation.

- Previously published core data showed that some opening-mode fractures in western Kentucky (Christian County) are not parallel with the surface expression of larger faults, which trend E-W. Core from the A-7455 well contains only E-W trending fractures, but because sampling of vertical structures with a vertical core may not be representative, other orientations at this location cannot be ruled out. It is likely, however, that the E-W trend here is dominant. Microseismic results from this experiment (A-7455) indicate E-W trending zones of microseismic events. Because S_{Hmax} is also E-W trending here it is not possible to say whether the events are due to reactivation of opening-mode fractures and faults or due to small ruptures developing around hydraulic fractures that propagate through shale parallel to S_{Hmax}. Events recorded in the overlying limestone in the final frac stage may reflect reactivation of a fault.

- Core and an image log from the second well experiment reveal multiple sets of sealed opening-mode fractures although the dominant orientation is parallel to the major faults. This may reflect the location of the second well, where surface expressions of

normal faults trend 060° and are oblique to the main E-W trend of the Rough Creek Graben and possibly represent a transfer fault system. We predict that minor structures associated with this transfer zone will be more complex than structures associated with sets of parallel E-W trending faults. Faults were also observed in the core and image log. Microseismic events likely reflect a combination of reactivation of natural fractures and propagation parallel to S_{Hmax} giving a more complex fracture pattern than for the DPI well.

- The variable structure in the Rough Creek Graben and Wabash Valley Fault system makes well and completion design in the New Albany Shale challenging. Fracture patterns vary significantly from one location to another. Large faults may continue into the underlying and overlying limestones, making it difficult to keep hydraulic fractures in the target horizon. On the basis of two well experiments in western Kentucky, at the Christian County well where the underlying structure is relatively simple the problem is that S_{Hmax} and fractures are subparallel. This means that hydraulic fractures are more likely to be simple in form, as they break shale and do not encounter natural fractures because propagation is parallel to the fractures. Or, if they encounter a natural fracture they will utilize it and simplify in geometry still further. In locations where there is a more complex fault and fracture pattern although the hydraulic fracture system created is likely to be more complex, it is harder to predict, and there is greater probability of connecting with faults that continue into the limestones above and below the target

Outcrop studies

Much work has previously been published on outcrops of the New Albany Shale in the Illinois Basin and across the Cincinnati Arch into the Appalachian Basin. The stratigraphy of the New Albany Shale is well constrained and key locations are described in a field guide by Schieber and Lazar (2004) (Fig. 1). We used the locations described in the guide, together with several other locations to examine the New Albany Shale at outcrop. There is also published work on fractures at the surface of the Illinois Basin (Carr, 1981; Ault 1989; Curtis, 2002; Comer et al., 2006) (Fig. 2). Most of the fractures in these studies are barren joint systems (Fig. 3). One of the best exposures of these regional joint patterns occurs on the Indiana bank of the Ohio River at New Albany (Fig. 3). The dominant joint set trends ENE, individual fractures extending several hundreds of feet. A secondary set trends almost orthogonal to the dominant set, but abutting relationships suggest they are broadly coeval. Both joint sets are steeply dipping and have no mineralization on the joint surfaces although there are various oxide stains on the surfaces. Joint properties were also described by Comer et al. (2006). We collected data on joint orientation and spacing for several outcrops throughout southern Indiana and central and eastern Kentucky.

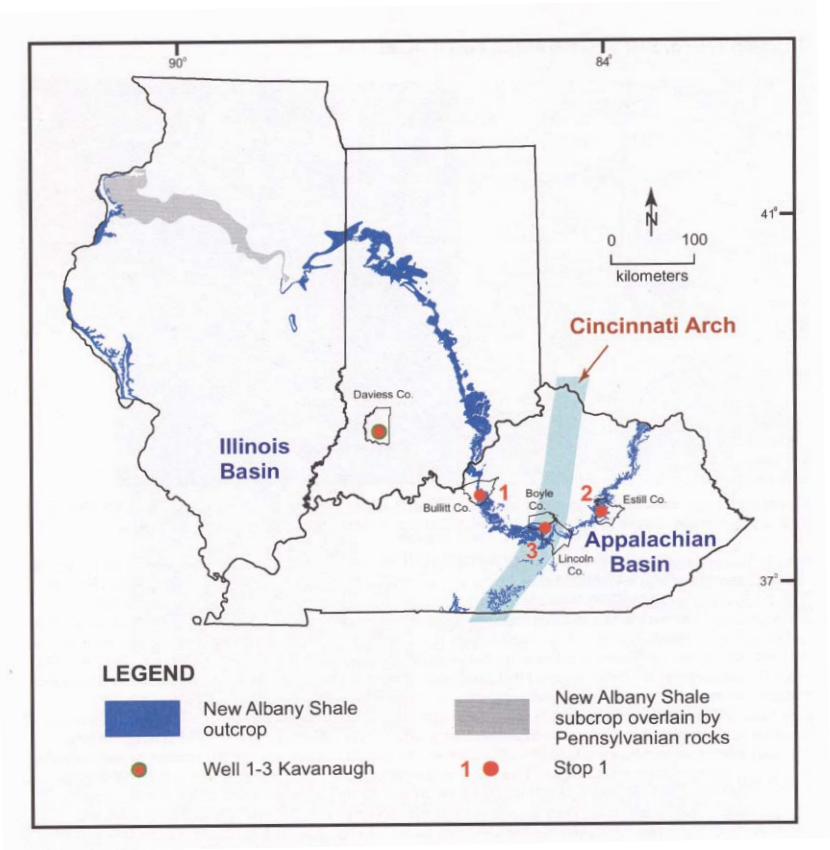


Figure 1. Map showing New Albany Shale outcrop and stops (from Schieber and Lazar, 2004). These stops were used as the basis for two field visits because the stratigraphic members are well constrained at these locations. The Kavanaugh core is described in the Schieber and Lazar (2004) field guide but we did not view it.

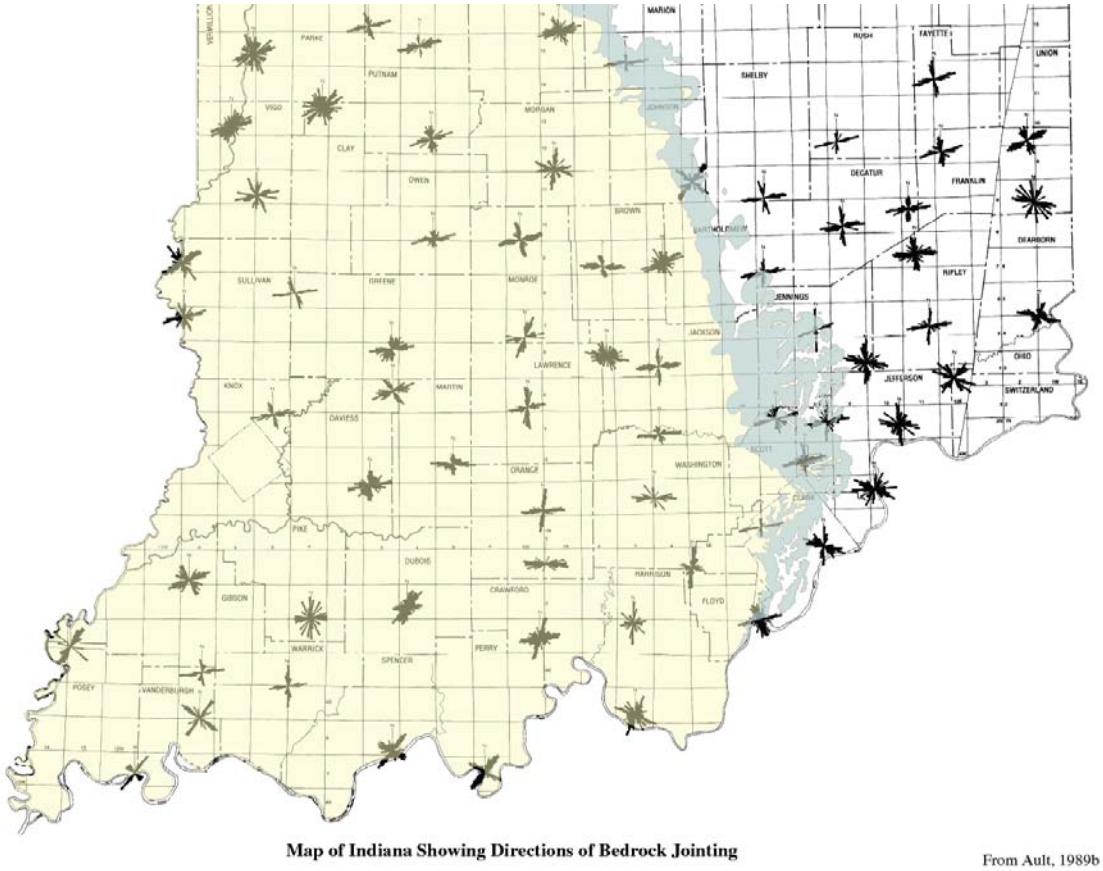


Figure 2. Map of joint orientations in bedrock in the southern Illinois Basin. Map from Comer et al. (2006) after Ault (1989).

For the shallow biogenic part of the New Albany Shale play it is possible that these orientations are representative of the fracture system in the subsurface. But for the deeper, thermogenic part of the play the subsurface fractures do not necessarily follow the surface orientations (Comer, 2006). The dominant joint orientation is subparallel to present day maximum horizontal stress. It is likely that the barren joint sets reflect this stress regime, and are the result of fracturing during uplift. The barren fractures in core that we did observe were interpreted as being induced fractures on the basis of petal centerline geometries, and the observation that they do not have the iron oxide staining that is ubiquitous in outcrop. We contend that natural fractures in the subsurface would contain cement or solid bitumen residue. The exception to this would be fractures growing as a result of recent fault movement along the Wabash Valley Fault System (Fig. 4), which would grow parallel to S_{Hmax}. Recent fractures would likely be barren because there would have been insufficient time for cements to accumulate.

Compacted fibrous quartz-dolomite-bitumen veins in the Blocher Member are described in the Schieber and Lazar (2004) field guide for their Stops 1 and 3 (Fig. 5a). We measured a bedding parallel scanline for these fractures at Stop 3 (Fig. 5b). The veins are very wide relative to their height, and commonly contain bitumen in vuggy openings, termed geodes by other workers. A vein of this type also occurs in the second experimental well from McLean Co., KY in the Blocher interval at 3760 ft (Fig. 5c). There are similar smaller deformed fractures in both outcrops and cores that are confined to pyrite-rich layers. The shale fabric and bedding are deflected around these fractures (Fig. 6). We do not know if these small fractures are related to the large fractures.

(a) (b)





(c) (d)





Figure 3. Barren joints on an outcrop on the north bank of the Ohio River at New Albany. (a) looking west, (b) looking east, (c) secondary joint trending N-S terminates and jumps to the east at a dominant set joint, (d) a short joint in the dominant ENE direction terminates against secondary joints.

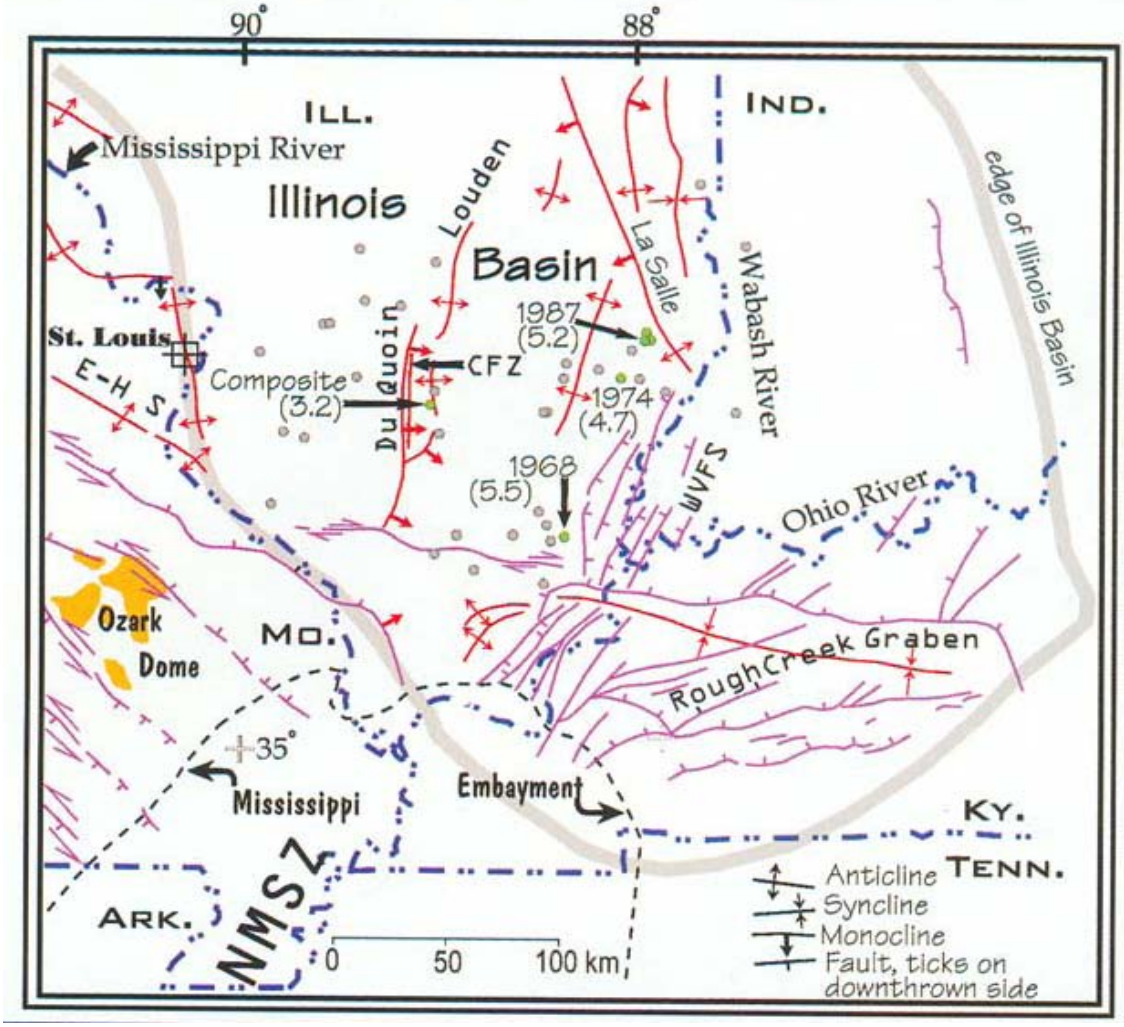
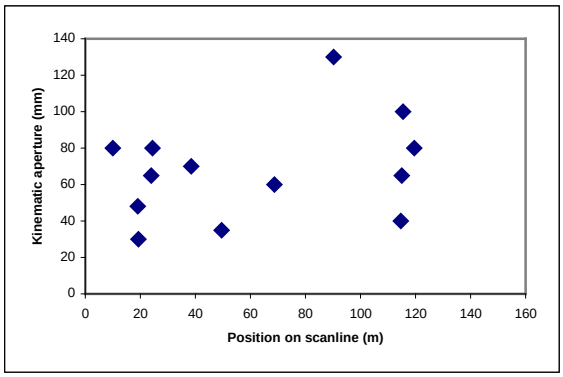


Figure 4. Structure map of the Southern Illinois Basin (from McBride (1999). WVFS = Wabash valley Fault System; NMSZ = New Madrid Seismic Zone; CFZ = Centralia Fault Zone. Earthquake epicenters for body-wave magnitude >3.0 for 1960-1995 are shown.





(b)



Figure 5. (a) Folded quartz-dolomite vein at Stop 1 (Schieber and Lazar, 2004 field guide). (b) Scanline parallel to road cut at Stop 3. Veins are clustered and are up to 14 cm wide. (c) Vuggy vein in Blocher Member in core at 3,760 ft. Core diameter 3.5 ins.

It is unlikely that these large veins will affect production as they seem to be mostly confined to the Blocher Member, which is well below the usually targeted Clegg Creek Member. The

exception is the vein seen at Stop 1, which extends up into the Camp Run Member. They merit further study, however, because they record fluid conditions at an early point in the burial of the New Albany Shale. The smaller veins are apparently more widespread, but because they are confined to pyrite layers may not affect production significantly. However, arrays of small veins can act as mechanical discontinuities for hydraulic fractures causing the hydraulic fractures to split or be deflected.

In the underlying limestone and the very base of the Blocher Member there is a second set of filled fractures. These are networks or en echelon arrays and are calcite filled (Fig. 7). These are not compacted and we interpret them to be later than the dolomite-quartz filled veins described above.

(a) (b)

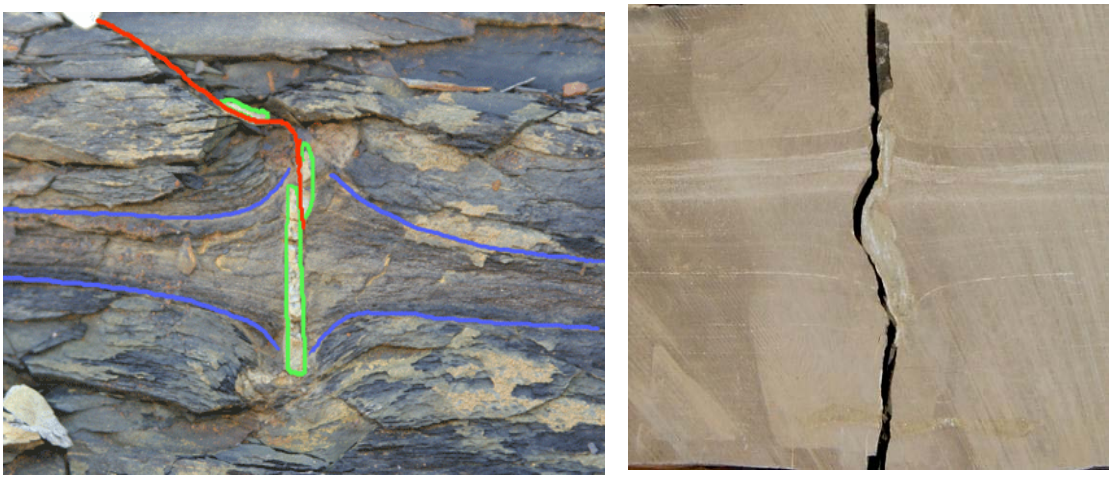


Figure 6. Small, early, compacted veins, fill likely dolomite. (a) Outcrop example at Stop 3. (b) Example from core at 2,804 ft. Height of fractures approximately 3 cm.

(a) (b)

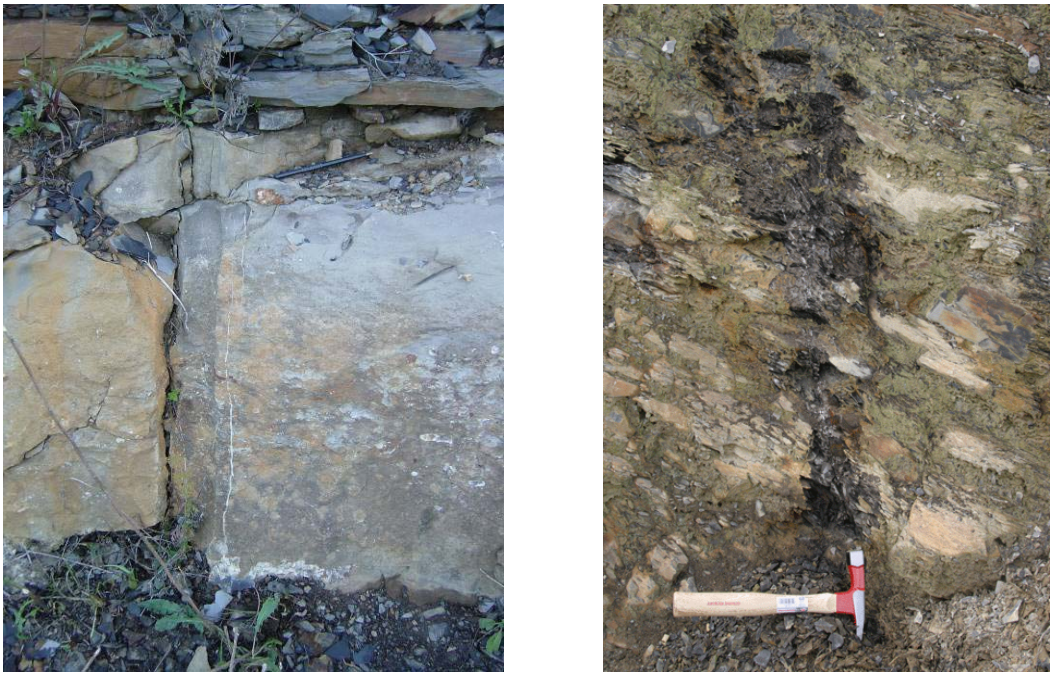


Figure 7. Narrow, calcite-filled fractures in (a) underlying Devonian limestone at Stop 3, (b) the Blocher Member at Stop 1.

Characterizing fracture orientation spacing and height growth

The objective of the second field visit of this project was to characterize the orientation, spacing and height growth parameters for different parts of the New Albany Shale section. Whilst the presence of unfilled joints in the subsurface is questionable we used the behavior of joints in outcrop to gain understanding of fracture growth. We do not use the joint character as a direct analog for the subsurface. Rather, we compare the results with core observations, where fractures are wholly or partly sealed with mineral cements.

Fracture orientation, spacing and height data were collected from outcrops in Kentucky and Indiana. Joint intensity, spacing and orientation are highly variable from outcrop to outcrop and vertically within the section. Typically, the Selmier Member contains the fewest joints, with the

Clegg Creek having the best developed sets. Most joints are of the order of 15 to 20 cm in height, terminating at bedding planes (Fig. 8).



Figure 8. Joints of various orientations in the KY 52 roadcut section opposite the Emmanuel Baptist Church west of Irvine, Kentucky. There are two dominant orientations, but other sets are also present.



Figure 9. Tall (~ 4m) intersecting joint sets in a quarry in the New Albany Shale at Shepherdstown, KY.

A few larger joints are up to 4 m high, and intersecting sets can form substantial corners in some outcrops (Fig. 9). Most joints have a skin of brown, orange or yellow weathering products along them. A few in the basal part of the roadcut west of Irvine, KY in the Appalachian basin have cement fills.

Orientation data were collected from 15 outcrops in Indiana and Kentucky. The purpose was to determine if orientations of surface joints could be correlated with subsurface fracture trends. Examination of trends of 290 joints from all outcrops shows that while there is a preferential NE-SW trend and a secondary NW-SE trend, joints occur in all orientations (Fig. 10). Commonly the dominant and secondary sets are present together as orthogonal pairs, defining erosional corners in road cuts and quarries (cf. Fig. 9).

The dominant orientation at any one outcrop can vary, even when outcrops are close by. For example, variations are found at several outcrop locations west of Irvine, KY (Stop 2, Schieber and Lazar 2004 field guide and outcrops nearby). The dominant joint trend in the roadcut outcrop opposite the Emmanuel Baptist Church on KY 52 is NE-SW (Fig. 11a). This trend is

parallel to the present day orientation of S_{Hmax} in that part of the Appalachian Basin, but we do not have subsurface data from this location. Joint orientations from a nearby outcrop 1 mile west of the church, however, are dominantly NW-SE (Fig. 11b). This is likely the orthogonal set of joints that complement the dominant regional joint trend in Figure 11a, but which form only a secondary trend in that plot.

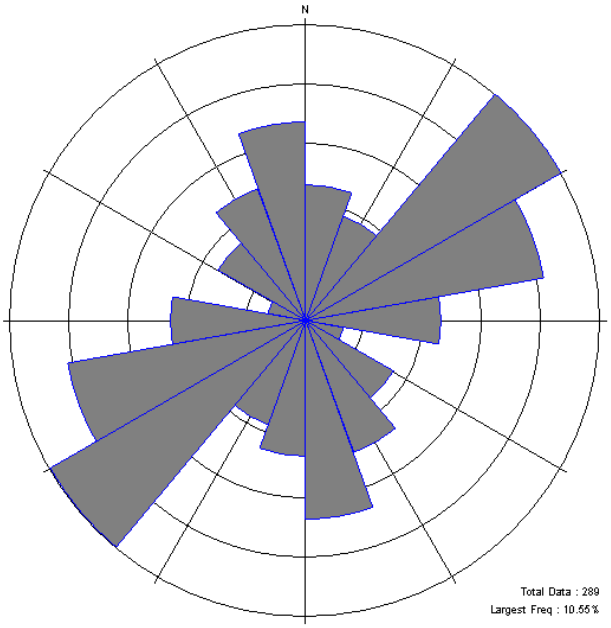


Figure 10. Rose diagram of all joint orientation measurements from Indiana and Kentucky New Albany Shale outcrops. 290 measurements.

(a) (b)

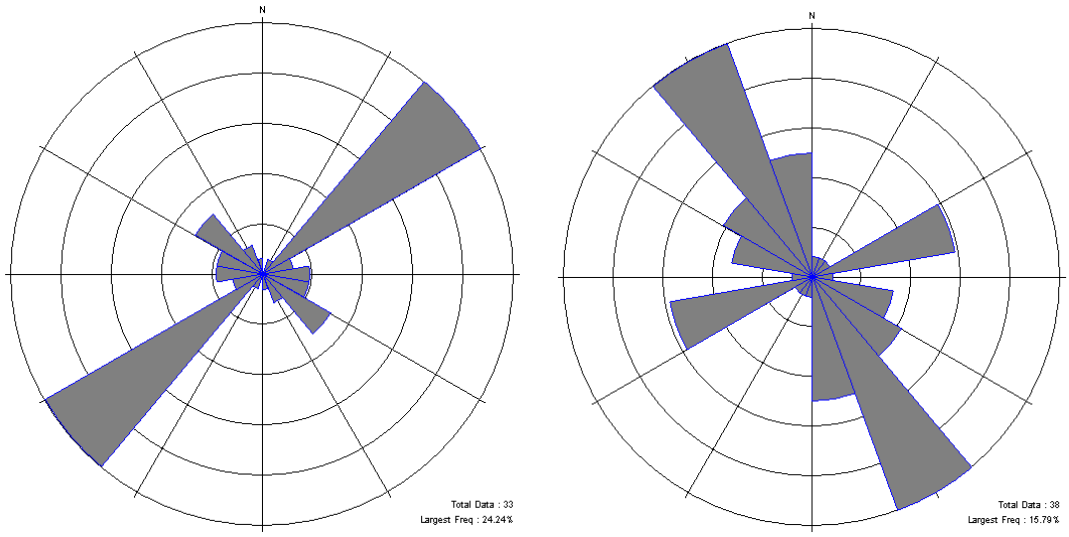


Figure 11. Rose diagrams illustrating the variability of dominant joint orientations in proximal outcrop locations. (a) Joints are consistent with regional S_{Hmax} direction, n= 33. (b) Orientations are consistent with orthogonal joint trend, n = 38.

At the type section for the Henryville Bed at the top of the New Albany Shale in southern Indiana (Fig. 12) there is a striking discordance between the orientations of dominant fractures in the shale and the overlying Rockford Limestone. The dominant joints in the limestone trend approximately N-S, but are nearly orthogonal to the joints in the shale, which trend ENE-WSW (Fig. 12). The reason for the discordance is not known, but differences in fracture orientation and spatial organization in successive layers have also been observed in limestone outcrops in central Texas.

The Henryville Bed and Rockford Limestone have clearly shared the same burial history but their diagenesis and mechanical rock property evolution would have been different. It may be that the mechanisms of formation are different for the two units. For example, the more competent limestone may have experienced flexure at some point during uplift while the more ductile shale did not fracture at that time. There are no crosscutting relations at the outcrop to provide information on the relative timing of the two fracture sets. Thus we cannot say if the fractures in the shale predate, postdate or are contemporaneous with the fractures in the limestone. This

outcrop illustrates why it is important to consider structural-diagenetic context when attempting to predict fracture orientation from limited outcrop data, and why it is dangerous to assume constant orientation with depth.



Figure 10. Joint sets in the Henryville Bed at the top of the New Albany Shale and the overlying Rockford Limestone. Dominant sets in the two lithologies are at a high angle to each other. The main set in the limestone trends towards the viewer whereas the main set in the shale crosses the photo from lower left to lower right. Exposures are in Lodge Creek on Howser Road (west of Henryville), Clark Co., Indiana (Clark Military Grant 253, T1N R7E).

Spacing between joints is highly variable in outcrops of the New Albany Shale. At a roadcut along the entrance ramp to I-65 S at Clermont Rd. (KY 245) south of Louisville, the spacing between dominant joint sets ranges from 24 to 30 feet. This is in contrast to outcrops along KY 52 west of Irvine, KY. The joints in these locations have widely varied spacings. Joints with heights up to 1m are most commonly spaced 5-50 cm apart, but can be over 3 m apart in some outcrops. Spacing for taller joints ranges from 0.5-1 m. Lithology and mechanical thickness are two important controls on joint spacing in the New Albany Shale. In outcrop, the best developed and tallest joints occur in competent grayish-green layers, while black, organic-rich

layers tend to be less competent and have fewer well-developed joints and joint sets. Thicker beds tend to have taller, more widely-spaced joints, while thin beds have short, closely-spaced joint sets (Fig. 13a). However, this correlation does not always hold true, as some thick layers contain systems of staggered, stepped joints that make spacing difficult to quantify (Fig. 13 b).

(a)



(b)



Figure 13. Photographs illustrating variations in joint height and spacing in the New Albany Shale. (a) Thicker beds have taller, wider-spaced joint sets. Joints terminate at bed boundaries, and black, organic-rich beds are devoid of well-developed joint faces. (b) In thinly-bedded layers, joints may either persist through bed boundaries, as in the 1m tall joint running from top center to center of photo, or terminate at bed boundaries, as in the numerous small joints.

Aside from the sealed fractures in the dolostone layers in the Trousdale section in the outcrop west of Irvine, and the compacted dolomite veins in the Blocher Member described above, we observed no other filled fractures. This is in contrast with the cores. Because of the general variability of joint orientations and the mismatch in fracture character between the subsurface and outcrop we think it unwise to use outcrop data for fracture characterization in the subsurface.

Core studies

Cores at Indiana Survey Core Repository examined and sampled

Diversified Operating McAtee et al. S26-IV, Pike Co. (5 samples)

Anschutz Corp. No. 16-19 Voelkel, Dubois Co.

Energy Resources of Indiana No. 1 Phegley Farms Inc., Sullivan Co. (2 samples)

Texas Gas Trans. Corp. No. 5 Pittman, Sullivan Co.

Texas Gas Trans. Corp. No. 4 Peterson et al., Sullivan Co.

Texas Gas Trans. Corp. No. 3 Peterson et al., Sullivan Co.

IGS SDH No. 180 Rothrock, Harrison Co.

IGS SDH No. 181 Deaton, Harrison Co.

IGS SDH No. 360 Don McRae, Clark Co. (1 sample)

Texas Eastern Trans Corp. No. 7, Jackson Co.

(a) (b)





(c)



Figure 14. (a) Steep, narrow sealed fracture, (b) multiphase cement, (c) sheared cement on fracture surface.

Several examples of steep, sealed, or partly sealed fractures were seen (Fig. 14 a, b). Some have smeared cement fill and have been interpreted as faults (Fig. 14 c). These sets are likely to

important either for enhancing permeability or as influences over hydraulic fracture propagation.

In addition to the above observations we examined two cores from a participating producer from Sullivan County:

1) Well C-96, Sullivan Co

2) Well C-33, Sullivan Co

Fractures in the C-96, Sullivan Co are numerous in the top part of the core but are absent in the bottom part of the core (Fig. 15). This could reflect a real difference in fracture intensity in different mechanical layers or could be the result of a sampling bias of a clustered distribution (see discussion in subcritical index section).

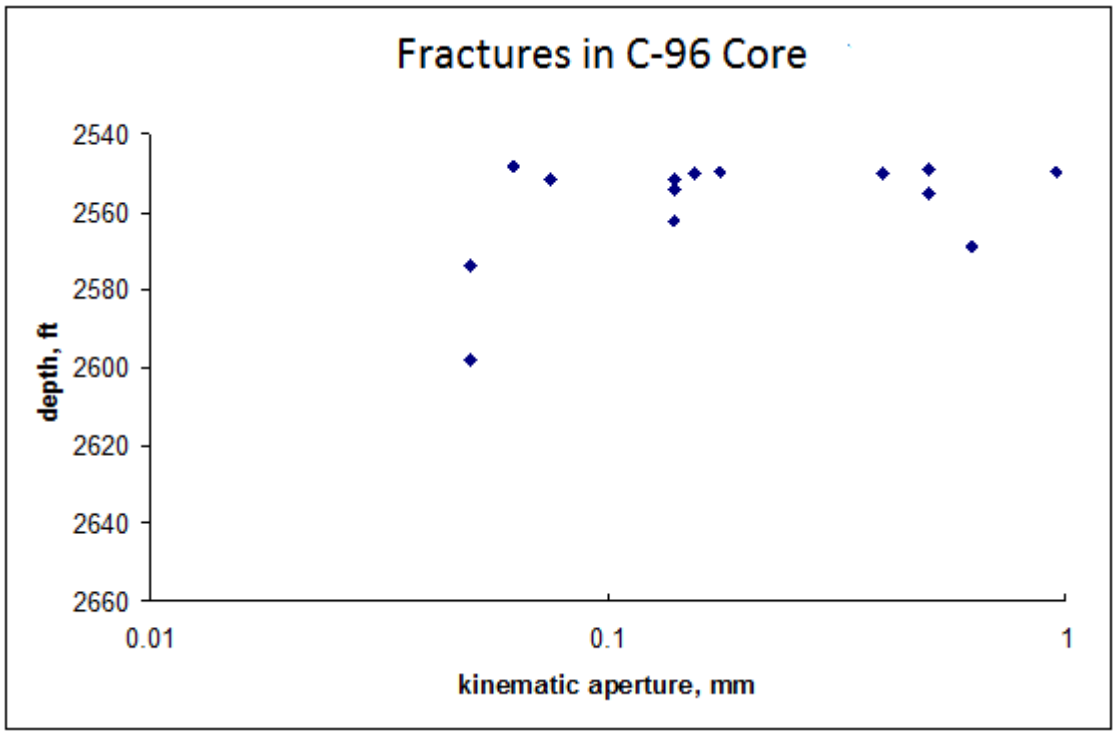


Figure 15. Fracture aperture sizes plotted against depth in the C-96 core

The natural fractures that are present are at a high angle to bedding and are sealed with calcite cement, which forms an extremely weak bond, commonly detaching from both fracture walls (Fig. 16a). The fractures mostly cross the core entirely so their height is unconstrained. Several examples have a stepped geometry, which is a commonly observed morphology in other shales (Fig. 16b).



Figure 16. Photographs of natural fractures in the C-96 core. (a) Calcite cement sliver detaching from both fracture walls at 2,568.8 ft. (b) En echelon stepped fracture planes at 2,549 ft, which are mostly calcite cemented although the cement has detached from the fracture wall in places.

There are very few fractures in the C-33 core. However, this could be a sampling artifact also. Core orientation data for the C-33 suggests the few natural fractures in the C-33 core are oriented WNW. At 2,543 ft the principal scribe line is oriented at 269.9° and a subvertical fracture trends 15° clockwise from it looking downhole, hence the fracture trends 285°. The fractures are at a high angle to bedding, are stepped and are sealed with calcite. Both the cores from Sullivan County are slant cores and there are numerous partings along bedding. Bedding-

parallel partings are all regarded as being due to stress relaxation. None have cement along them.

During the 3rd project quarter the emphasis of the project changed from southern Indiana to western Kentucky. A new fracture evaluation commenced with a focus on Christian County in anticipation that a well experiment would take place there in summer 2009. The natural fracture pattern and in situ stress field are likely to be different from that in southern Indiana, because the two areas have markedly different structure. The wells in Sullivan and Pike Counties in southern Indiana are close to the Wabash Valley Fault System, a currently active normal fault system trending NNE-SSW. Christian County in western Kentucky is close to the E-W trending Rough Creek Graben, which is not currently active. Maps of faults in the Christian County area dominantly trend E-W, although some linking faults have other trends.

Miller and Johnson's (1979) study on a cored well in Christian County (Orbit Gas Co J. Ray Clark No. 1) showed the dominant natural fracture trend is NW-SE, which does not match with the general trend of the faults, but could be local to that well. Our group strongly recommended that for the experimental well a whole diameter oriented core should be taken together with an image log so that site specific information on the natural fracture system may be gained.

Well Experiments

Core and image log analysis: Well A-7455

The unslabbed core (~ 60 ft) from the A-7455 well was examined together with an image log on 19th August, 2009 at Core Laboratories in Houston. Photographs were taken of the whole length of the core and detailed photographs taken of fractures. The core was oriented using a combination of information on the image log and the goodness of fit of the core pieces. For the most part the fit was good, and features on the image log allowed orientation. In particular, the apparent bedding dips were used. The well deviation was approximately 12° N and we assumed bedding to be horizontal. Natural fractures at the top and bottom of the core, and visible on the image log, confirmed the orientation. Core fracture occurrence, openness and orientation were compared with fractures identified using image log analysis. Tall fractures, some of which are in stepped arrays, were identified at the top and bottom parts of the core (Figs. 17 to 19). Short (< 1 in) fractures were found in a few siltstone layers e.g. at 2,530.6 ft (Fig. 20). The middle section of the core (between 2,529 ft and 2,572 ft) otherwise contains no visible natural fractures.

The dominant strike orientation (E-W) is consistent with the image log interpretation, where fractures were observed in both (Fig. 17). However, many more fractures had been picked in the image log than were present in core. In cases where a fracture had been picked on the image log but could not be seen in the core the features used to pick the fracture in the FMI were commonly a very subtle alignment of patches of low resistivity. The picks were not strongly indicative of a fracture. Thus we conclude that if fractures are present, open or sealed, they show up distinctly on the image log, and that the more subtle features generally represent something other then a natural fracture.

The image log (Fig. 17b) shows fractures with low electrical resistivity, which are usually interpreted as being due to fluid in the fracture, leading to the inference that the fractures are open in the subsurface. In this case it is indeed possible that the fractures were open prior to drilling and that the cement we observe on the fracture surfaces only partly sealed the fracture (Fig. 18). However, because the S_{Hmax} is parallel to the fractures it is also possible that they have been reactivated during drilling.

(a)



(b

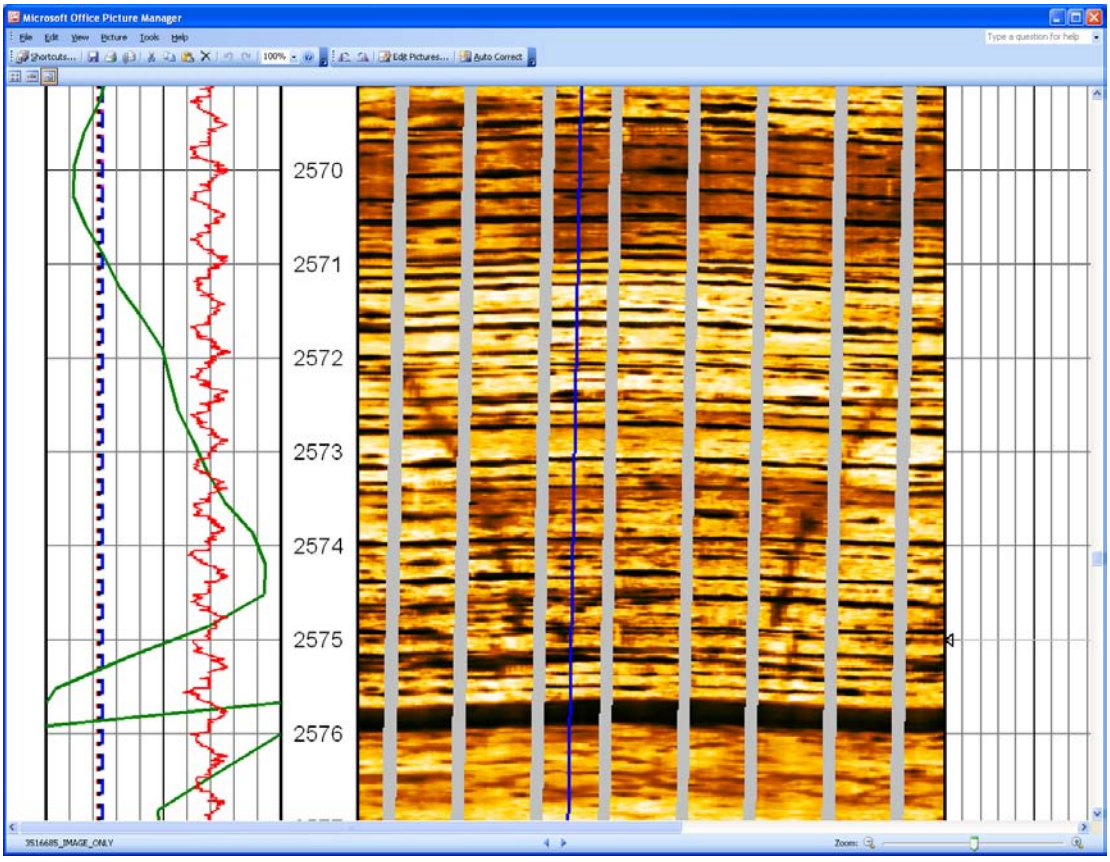


Figure 17. (a) En echelon fractures with carbonate cement at 2574-2575 ft (b) fractures on image log indicating it was partly open in the subsurface. Note offset at 2575 ft on the image log. The depth shift is less than 1 ft.

.



Figure 18. Natural fracture at 2,528 ft. Fractures are partly open in places and sealed with cement elsewhere. Here the top part of the fracture surface is decorated with calcite cement, whereas lower down the cement is absent. Propagation of natural fracture planes during drilling is possible because S_{Hmax} is close to E -W in the Rough Creek Graben.

(a)



(b)



Figure 19. (a) Stepped natural fractures at 2,574 to 2,576 ft. (b)These fractures were likely to have been partly open in the subsurface with patchy, delicate fracture cements preserved on the surface.



Figure 20. Bedding confined natural fracture in siltstone layer at 2530.6 ft. Fracture surfaces are decorated with cement.

Miller and Johnson's (1979) study on a cored well in Christian County (Orbit Gas Co J. Ray Clark No. 1) showed the dominant natural fracture trend is NW-SE, which does not match the general trend of the faults in the region. For the experimental well we had recommended that a whole diameter oriented core should be taken together with an image log so that site specific information on the natural fracture system may be gained. This was achieved and demonstrated conclusively that for the A-7455 the natural fractures trend E-W, being parallel to the regional normal faults and present day S_{Hmax}. There were no fractures trending NW-SE in either the core or the image log.

Core and image log analysis: second well experiment

An unslabbed core (~ 300 ft, of which 222 ft are in the New Albany Shale) from the well was examined by Gale and Fidler (BEG) and Caramanica (Res Tech) together with an image log on

11th August, 2010 at Weatherford Laboratories in Houston. Photographs were taken of key fracture features. The core was not oriented and because it was close to vertical in beds that are close to horizontal we could not use bedding orientation to orient the core. However, the core recovery was good and there was good agreement for the most part between fractures observed in the core and those picked on the image log.

There were a few places where fractures were present in the core although nothing had been picked on the image log, but on closer inspection there were subtle fracture signals on the log. Frank Caramanica (ResTech) made a detailed inventory of all the picks on the image log and the natural fractures in the core (Fig. 21).

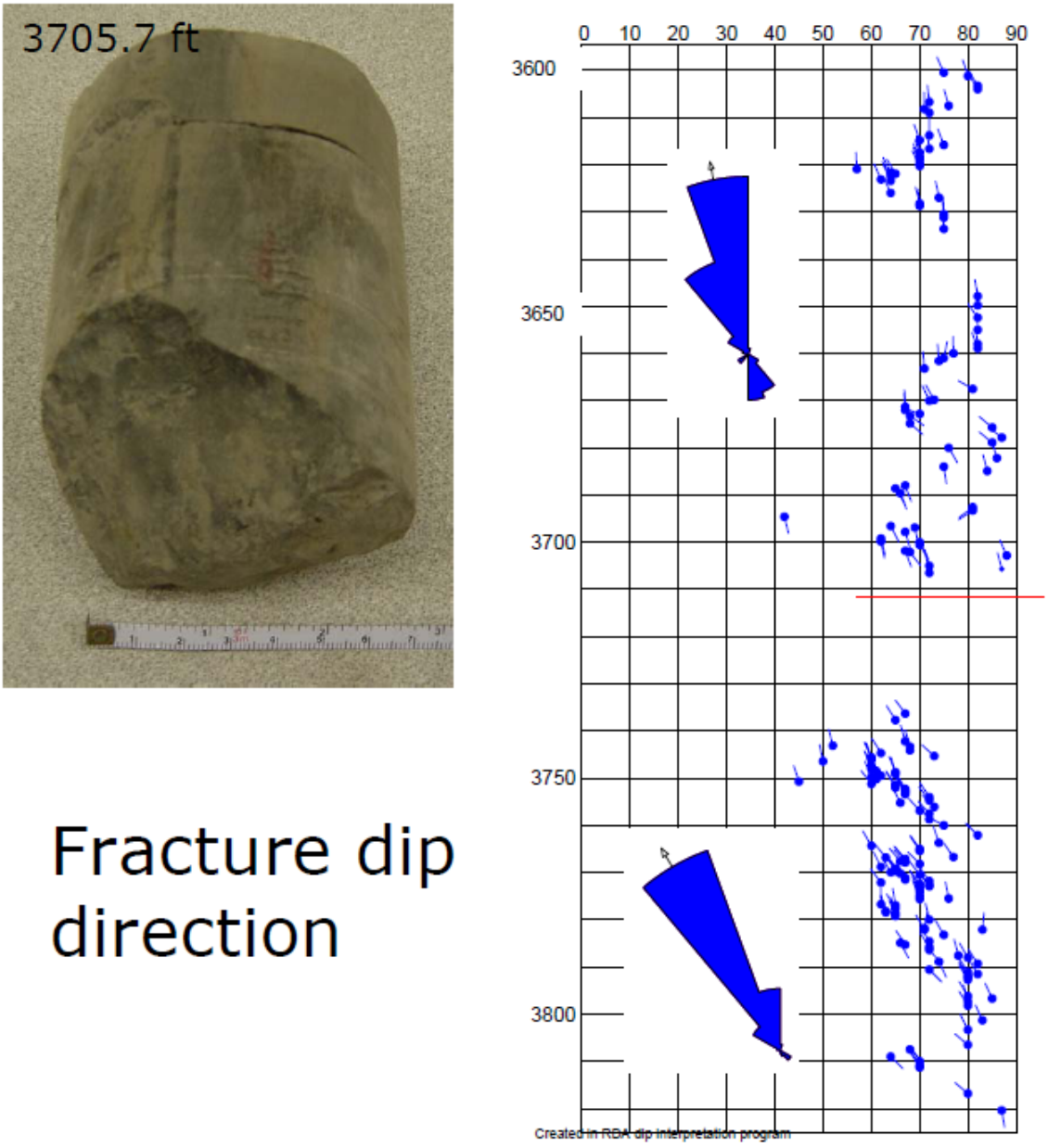


Figure 21. Plot of all induced and natural fractures in the New Albany Shale interval (3,600 – 3,822 ft MD. Plot by Frank Caramanica (ResTech). Inset: fault at 3,705.5 ft.

Dr. Caramanica noted the shift of the dominant fracture trend from approximately 085° in the upper part of the core (above 3,710 ft MD) to approximately 060° in the lower part of the core. In some locations two fracture sets are present, separated by approximately 30 to 50°, one of which is the dominant direction as described above (Fig. 22). The other could be plus or minus

30-50° from this – only one fracture trend is typically observed on the image log and the core is not oriented so we cannot tell which fracture set is being detected in the image log. We found no N-S trending fractures on the log and so deduce that where the first set trends 060° the second set trends approximately E-W. These fractures dip steeply. Interestingly, there are some conjugate sets of steeply dipping sealed fractures (approx 70° dip either way) that share a common strike orientation.

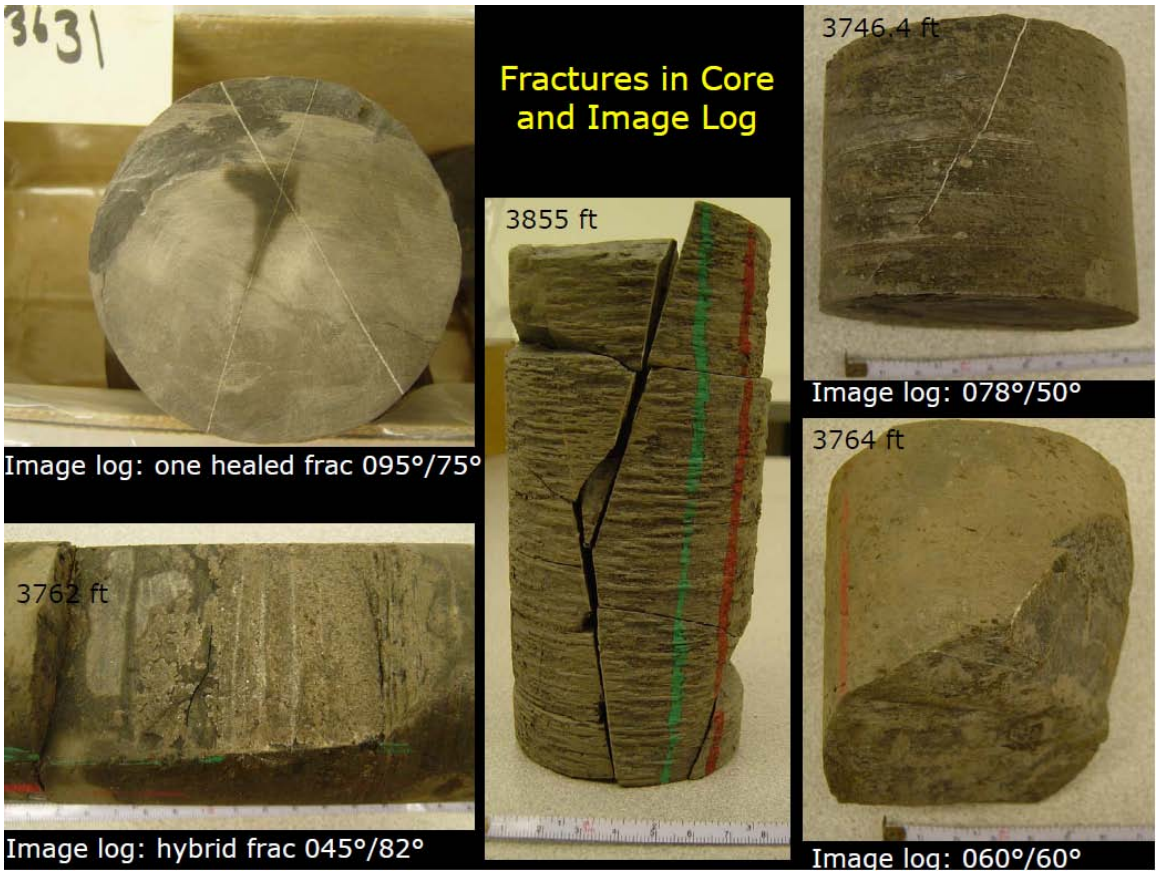


Figure 22. Sealed fractures at various depths in the second well experiment core, with orientations of image log fracture picks that we interpret to correspond to the fractures in the core at that depth.

In several instances induced and natural fracture orientations are close at around 060° so that some fractures are likely hybrid. That is, induced fractures have nucleated on natural fractures. So picking induced versus reactivated natural fractures, both of which are conductive on the image log, is a challenge. Faults trending E-W were also observed on the image log and in the core.

Discussion of microseismic results for the second well experiment in the context of natural fracture observations made in the pilot-hole core

Two trends of microseismic events were identified: 060° (more common) and 038° (one strong swath, other smaller possible swaths) by Pinnacle researchers. A possible explanation is that natural faults and fractures in that orientation enhance growth in this direction. We do not see a geologic reason why microseismic events mostly occur in the zone between the two wells. It is more likely that the distance from the observation well was too great.

The orientation of S_{Hmax} is problematic. On the basis that 060° is the most common trend for the microseismic events it is tempting to interpret this as the orientation for present day S_{Hmax} and indeed the general midcontinent S_{Hmax} orientation is ENE-WSW. The World Stress Map, however, shows a perturbation to a more E-W orientation in the vicinity of western Kentucky. In the DPI well experiment this was confirmed by induced fractures. Induced fractures in the core from the second well experiment were noted in both E-W and ENE-WSW orientations. Induced fractures commonly utilize natural fracture planes to continue propagation in the 060° direction.

In our core analysis we saw multiple fracture trends and some dip variation (steep conjugate sets). The image log interpretation (by Frank Caramanica, ResTech) shows a change in the dominant orientation with depth. Above 3,710 ft (in the Clegg Creek Member) the strike is close to E-W whereas below 3,710 ft fractures trend closer to ENE-WSW (in the Camp Run/Morgan Trial, Selmier and Blocher Members). Although these two zones were identified as having different fracture orientations there is considerable overlap of orientations. The opening-mode fracture orientations we observed in the core are consistent with the trends of larger faults at the surface in this area. There are longer sets of faults trending about 060° and a few linking faults between about 020° and 040°. The faults in the vicinity of the wells may be a transfer structure between more E-W trending segments of the Rough Creek Graben (Fig. 23).

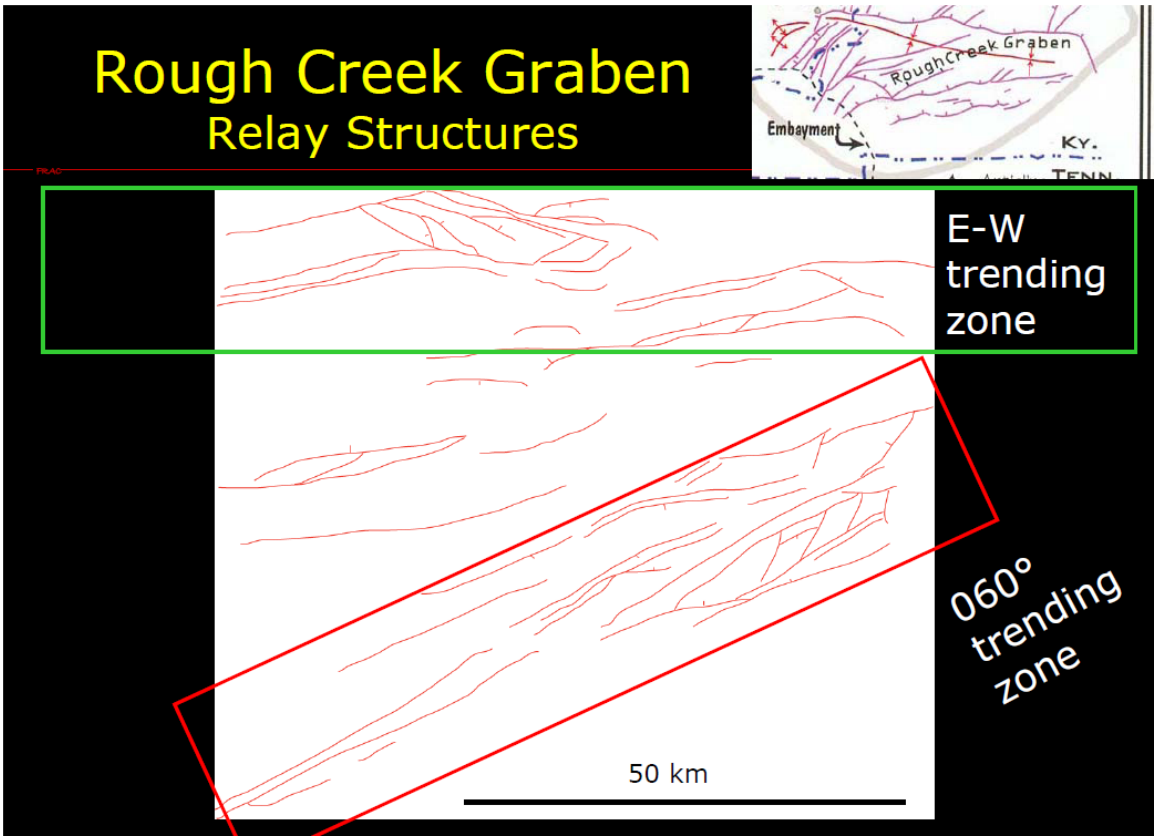


Figure 23. Variation in the orientation of surface faults (Kentucky Geological Survey map) in the Rough Creek Graben in the vicinity of McLean Co.

In the discussion of the hydraulic fracture treatment stages locations of microseismic events in map, edge and side views are made to understand the position of the events relative to the fracture orientation zones defined above. (Refer to the section of this report that explicitly documents the microseismic monitoring for these figures).

Vertical profiles show events in stages 1-4 were confined in the New Albany Shale (NAS), stages 5-7 went out of zone, down into the Devonian Limestone, and stages 7-9 went out of zone upwards into the Rockford Limestone.

Stage 1 has most events around or below 3,750 ft. In map view stage 1 events are not markedly arranged along any one direction.

For stage 2 most events are above 3,750 ft. There is a scatter in map view, as for stage 1. In stages 1, 2 and 3 the positioning of the events is closer to the well heel than the positions of the stages as marked on the well trajectories.

Stage 4 is the one with the most marked 038° trend. These events are mostly closer to the NW Well 1 (for stage 4) and in edge view they can be seen to occur near the base of the NAS. This fits with the core analysis in that the lower fractures are the more NE trending fractures. Closer to the NE well 2 the events are higher in the NAS, corresponding to the higher zone. On the map view they trend more 060°.

The stage 5 events occur in three groups: one group at the base of the NAS and into the Devonian Limestone near the observation well that seems to have a 060° trend. A second group, located at the same depth but out beyond the NE well 2, has a 038° trend and a third group at well depth between the observation well and NE well 2 that shows a 060° trend. Our fracture analysis from the image log did not extend down into the underlying limestone. The variation in trend in the stage 5 data may reflect orientation switches with depth, together with fracture clustering i.e. of the 2 deeper groups only one shows a 060° trend because natural fractures are only present in the location NE of NE well2.

Stage 7 and 8 events look like they are occurring along a fault trending 060° and dipping to the NNW down into the Rockford Lst. Other events grew up into the overlying limestone. We interpret that the treatment is getting into large faults here.

The hydraulic fractures in stage 9 from the NE well 2 are likely getting into an 060° fault up above the New Albany, but the events near the NW well1 are better confined in the New Albany. The majority of these latter events are in the lower part of the section and may reflect reactivation of 060° trending fractures.

Subcritical crack index, fracture toughness and Young's modulus tests

The subcritical index test provides results for shale samples in their current state. We need to assess whether this could also be representative of the subcritical index *at the time of fracturing*. At this stage we do not have enough information about the way that subcritical index in shales changes with composition and differing diagenesis. The measured subcritical crack indices might be close to those prevailing at the time of fracturing for the steep sealed sets, but may not be valid for the dolomite-filled fractures that predate some compaction.

In order to use these results in prediction of fracture patterns they would need to be incorporated in a geomechanical model, which includes measured parameters such as strain and mechanical layer thickness (estimated for the time of fracturing). In general, low indices indicate a less strongly clustered fracture pattern, possibly with even spacing of larger fractures at or below the mechanical layer thickness. Intermediate indices tend to have more even spacing at or above the mechanical layer thickness.

Sullivan County, IN core samples

Subcritical crack index measurements were made for two samples from the C-96 well and one sample from the C-33, both in Sullivan Co., Indiana. Sample preparation was challenging because the cores are both slant cores. For samples C-33@2528' and C-96@2630' the samples were cut parallel to bedding planes, by mounting the cores at an angle in the saw. The C-96@2630' sample was particularly difficult to cut because of bedding plane weaknesses. The C-96@2558' sample was cut perpendicular to the core axis so the slices showed some lines of failure along bedding, but several specimens were prepared between these weaknesses, which held together well and gave good decay curves. Most of the measurements were robust; stress-strain (2 load/unload cycles per specimen) behavior was consistent, fracture toughness results (three specimens for each core loaded to failure) are consistent, and decay curves for almost all subcritical index tests have good fits to theoretical curves.

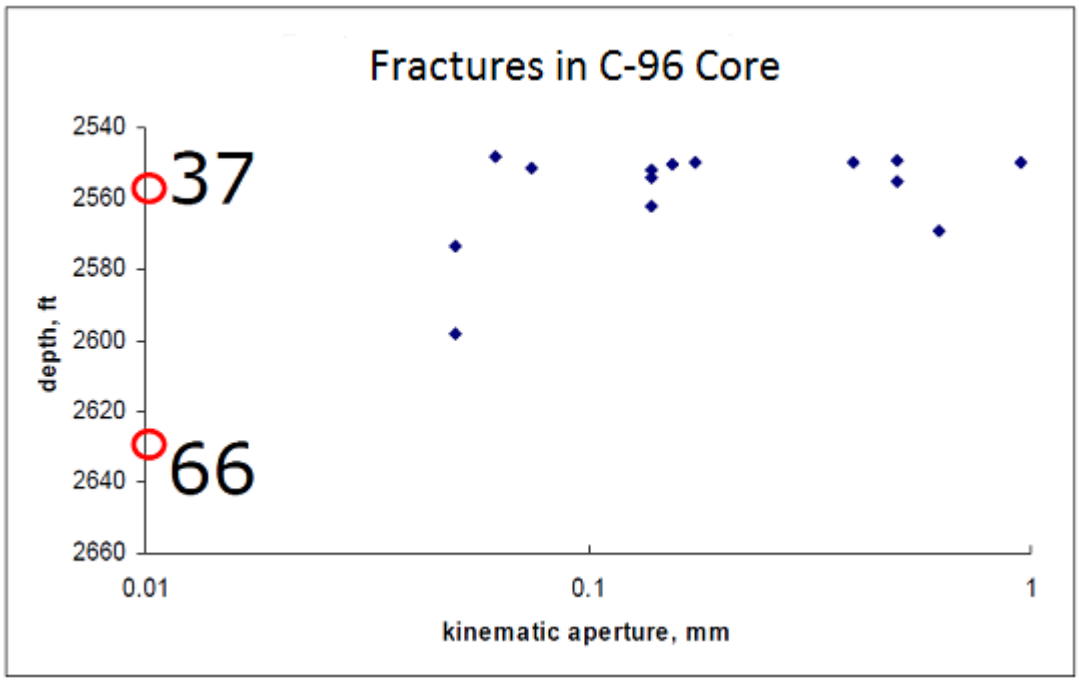
Repeatability of values from multiple tests on specimens from the same sample was inconsistent, both for multiple measurements from specimens and between specimens from the same sample. Measurements on Barnett Shale samples have been more repeatable than in this study.

Table 1: Summary of subcritical index values and relative fracture strength.

Core	E(Mpsi) 1	2	3	4	Avg	SCI 1	2	3	Avg	K_{IC} (MPa-sqrt m)	Comments
C-33-2528 ft											
3A						42	46		**44**		bedding within test area
4B	2.4	2.8	3	3.2	**3.0**	64	82	76	**74**	**1.8**	
8B	2.2	2.5	2.5	2.6	**2.5**	88	159	62	**103**	**1.5**	small decay, ragged fit
5B	2.5	3	2.8	2.9	**2.9**	59	93	76	**76**	**1.6**	
5A	1.7	2	2	2.6	**2.2**						
6A	2.5	3.5	2.9	3.4	**3.3**						
6B	2.3	2.7	2.5	2.9	**2.7**						
7A	2.8	3.6	2.9	3.5	**3.3**						
7B	2.4	2.8	2.6	2.8	**2.7**						
8A	2.7	3.5	3.1	3.4	**3.3**						
9A	3.2	4.5	3.5	3.5	**3.8**						
9B	3.2	3.9	3.5	3.7	**3.7**						
C-96-2630.6 ft											
3B	2.4	2.8	3	3.2	**3.0**						

4	3.3	3.1	3.3	3.1	**3.2**	58	66	75	**66**	**1.4**	
1A	4.3	4.4	4.5	4.7	**4.5**	70	73	92	**78**	**1.3**	
2A						71	76	88	**78**		Bump on C1
1B						40			**40**	**1.7**	Questionable (good fit)
C-96 -2558 ft											
4A	3.2	3	3.2	3	**3.1**						
10A	2.4	2.2	2.4	2.2	**2.3**					**0.9**	
8A	2.3	2.4	2.8	2.9	**2.7**					**0.8**	
10B						27			**27**		
9B						34			**34**		
6B						57	41		**49**		Bumpy on C2
5B										**1.0**	

(a)



(b)

(c)

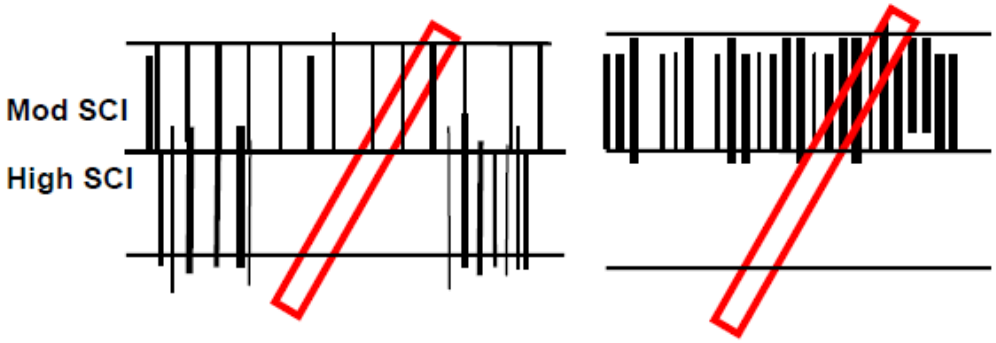


Figure 24. (a) Fracture occurrence in the C-96 core. Note the absence of fractures below 2600 ft. Depths of samples for subcritical crack index measurement together with mean values for multiple tests from each sample are shown. (b) Alternative interpretation of fracture occurrence in the core. Either (b) variation in subcritical index where clustering accounts for absence of fractures in the lower part of the core, or (c) a stratigraphic control on fracturing.

The subcritical indices for C-33@2528' and C-96@2630' are mostly moderate compared to other shale values, and range from 66 to 103 (Table 1). Other shales we have tested have a subcritical index above 100 and commonly in the 200 to 300 range (ambient air conditions). The shallower sample from the C-96 core C-96@2558' has a much lower subcritical index with measurements of 27 and 34, (discounting the irregular load decay test). The Young's modulus for all samples lies between 2.2 and 4.5 Mpsi. These are comparable with the lower values for measurements of Barnett Shale (Gale and Holder, 2008). The fracture toughness is 0.8 to 1.0 MPa-sqrt(m) for C-96@2558' tests and is substantially lower than for the other two samples, which range between 1.3 and 1.8 MPa-sqrt(m).

The higher subcritical indices were measured in the samples from the two horizons where the apparent fracture intensity is lower (Fig. 24a). Higher subcritical index generally indicates a more clustered fracture pattern. In a highly clustered pattern the chances of sampling fractures decreases, so that it is quite possible that the lower horizon in the Solsman well (2,630 ft) and the core from the C-33 well are fractured, but that the clustering has meant the fractures were not sampled (Fig. 24b). Alternatively the upper layer is actually more fractured than the lower layer (Fig. 24c).

A core sample from 2,280 ft from the Orbit J. Ray Clark #1 well in Christian Co. Kentucky was sliced parallel to bedding to provide multiple samples for subcritical index and Young's modulus testing (Fig. 25). The subcritical index values so obtained range from 43 to 80, which is lower than most Barnett Shale samples but comparable with the samples form the C-96 core (Table 2). Submillimeter layers of quartz and carbonate silt are present. It is possible that composition varies from specimen to specimen, which would explain the large variation in subcritical indices. Young's modulus is Somewhat higher than values for the C-96 well and is also higher than for Barnett shale samples we have tested (Gale and Holder, 2008).



Figure 25. Core sample from 2,280 ft from the Orbit J. Ray Clark #1 well in Christian Co. Kentucky. Samples were cut from the unfractured part of the core.

Table 2. Subcritical index (SCI) and Young's modulus measurements from the Orbit J. Ray Clark #1 well in Christian Co. Kentucky.

Core	SCI					Young's Modulus	
	1	2	3	Avg.		(Mpsi)	Avg.
Orbit J. Ray Clark # 1, 2280' Depth							
1B	64	160	260	**161**		7.3	
2A	67	65	-	**66**		-	
2B	70	191	293	**185**		3.6	
3A	46	77	-	**62**		-	

3B	47	48	-	**48**		3.4	
4	110	-	-	**110**		-	
6A	70	177	209	**152**		7.7	
6B	142	226	237	**202**		3.7	
7A	50	47	-	**49**		8.6	
7B	43	-	-	**43**		5.8	
8A	52	-	-	**52**		3.3	
8B	68	136	-	**102**		25.2	
9A	78	69	-	**74**		9.1	
9B	54	59	-	**57**		8.3	
					97		**7.8**

Subcritical crack index and Young's modulus tests were also done on two samples from the A-7455 well (Christian Co Kentucky). Subcritical index values range from 24 to 96, with the means for the samples of 46 and 53 (Table 3). As with the Orbit well samples we suspect the variability may result from compositional variation between samples. The overall range is lower than for Barnett Shale and would suggest less fracture clustering in the New Albany shale than in the Barnett. Young's modulus is comparable to the Orbit well measurements.

Table 3. Subcritical index (SCI) and Young's modulus measurements from the A-7455 well in Christian Co. Kentucky.

Core	SCI					Young's Modulus	
	1	2	3	Avg.		(Mpsi)	Avg.
A-7455, 2528.5' Depth							
1	34	24	36	**31**		6.5	
2	-	-	-			8.9	
3	36		-	**36**		9.0	
4	-	-	-			-	
5	59	64	90	**71**		8.8	
					46		**8.3**
A-7455, 2537.5' Depth							
1	37	44	32	**38**		5.8	
2	51	72	-	**62**		5.1	
3	62	91	-	**77**		5.4	
4	44	59	50	**51**		6.9	
6	61	58	96	**72**		6.1	
9	63	40	35	**46**		7.5	
10	24	41	-	**33**		7.6	
11	45	38	-	**42**		7.8	
12	60	-	-	**60**		8.5	
13	45	63	-	**54**		10.4	
					53		**7.1**

Fracture Petrography

The Corelabs XRD analyses on 5 samples from the A-7455 well (Fig. 26) show that the New Albany Shale in the lower part of the section (Selmier and Blocher Members) in Christian Co. is typical of many mudrocks, having relatively low clay content. In these samples carbonate is significant and laminae composed of dolomite rhombs are concentrated in layers (Fig. 26). These layers are likely to be more brittle than the surrounding mudstone. In the sample from the A-7455 from 2,568 ft the fracture has grown in one of these layers. The fracture contains calcite cement and also bitumen. In this and some other examples the bitumen lines the fracture (Fig. 26) whereas in other fractures the bitumen is found in the central part of the fracture (Fig. 27; sample from 2,535.5 ft). It is not clear if this represents a difference in timing of bitumen with respect to calcite or if the fracture breaks along the margin in some cases and down the center in others when bitumen is introduced. Fractures in the underlying Devonian limestone contain some porosity and might provide pathways by which hydraulic fractures could connect into this water wet limestone (Fig. 28). Fracture morphology is simple in some examples and complex in others. Both vertical and horizontal fractures have been observed (Figs. 26-29).

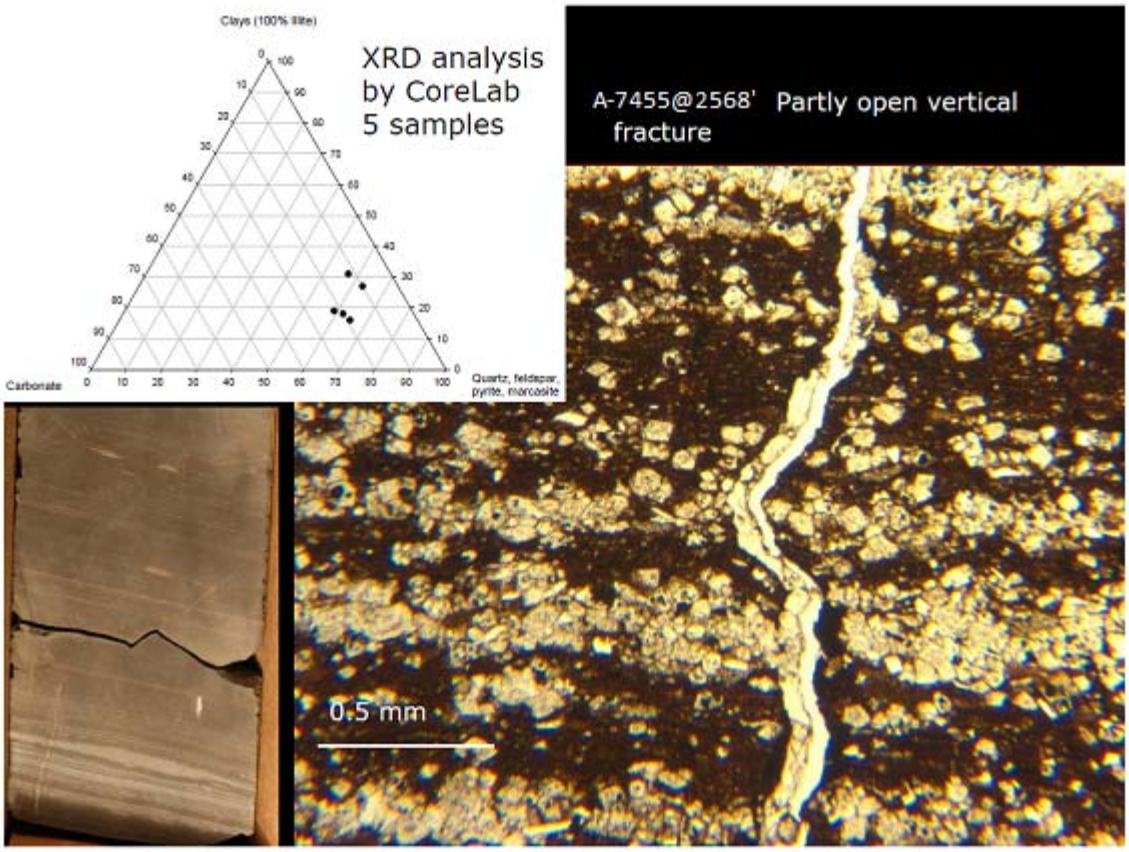


Figure 26. Fracture in laminated layer of A-7455 well from 2,568 ft. Dolomite dominates the carbonate fraction. Calcite and bitumen partly seal the fracture. The fracture opening may be induced or natural. Bitumen in this sample occurs along the fracture wall. Inset: XRD analysis conducted by CoreLabs on 5 samples from the A-7455 core.

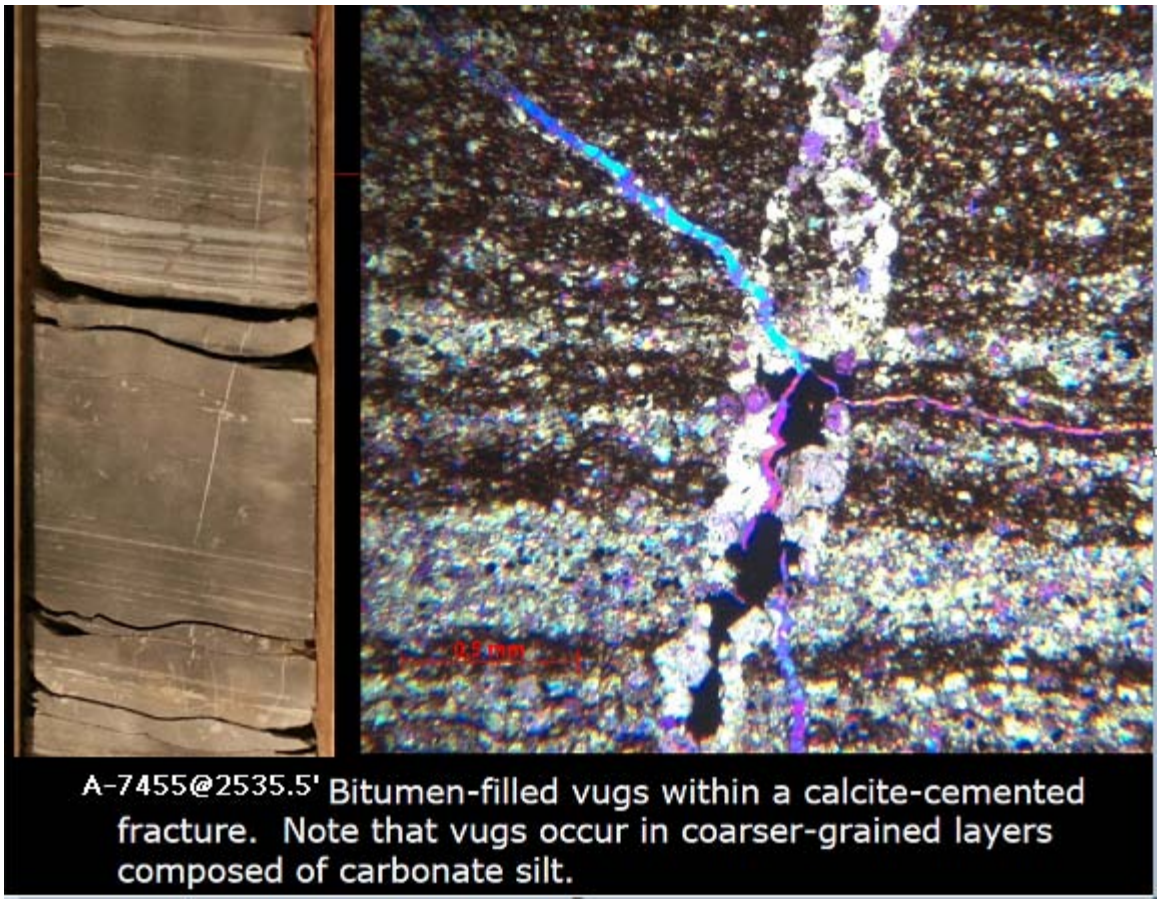


Figure 27. Fracture in laminated mudrock of A-7455 well from 2,535.5 ft. Dolomite dominates the carbonate fraction. Calcite and bitumen seal the fracture. Bitumen in this sample occurs in the central part of the fracture suggesting it postdates the calcite. The narrow, barren, irregular open fractures are likely induced. Crossed polars.

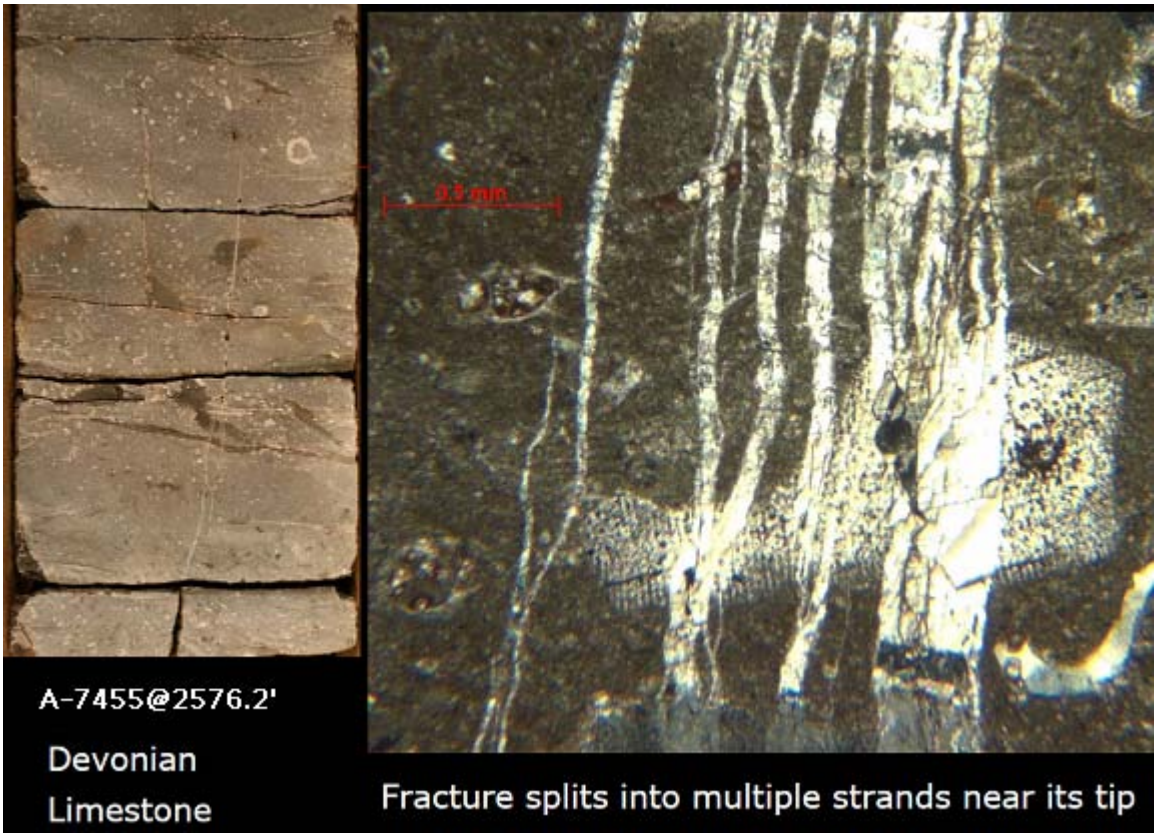


Figure 28. Fractures in the Devonian Limestone underlying the New Albany Shale of A-7455well from 2,568 ft.

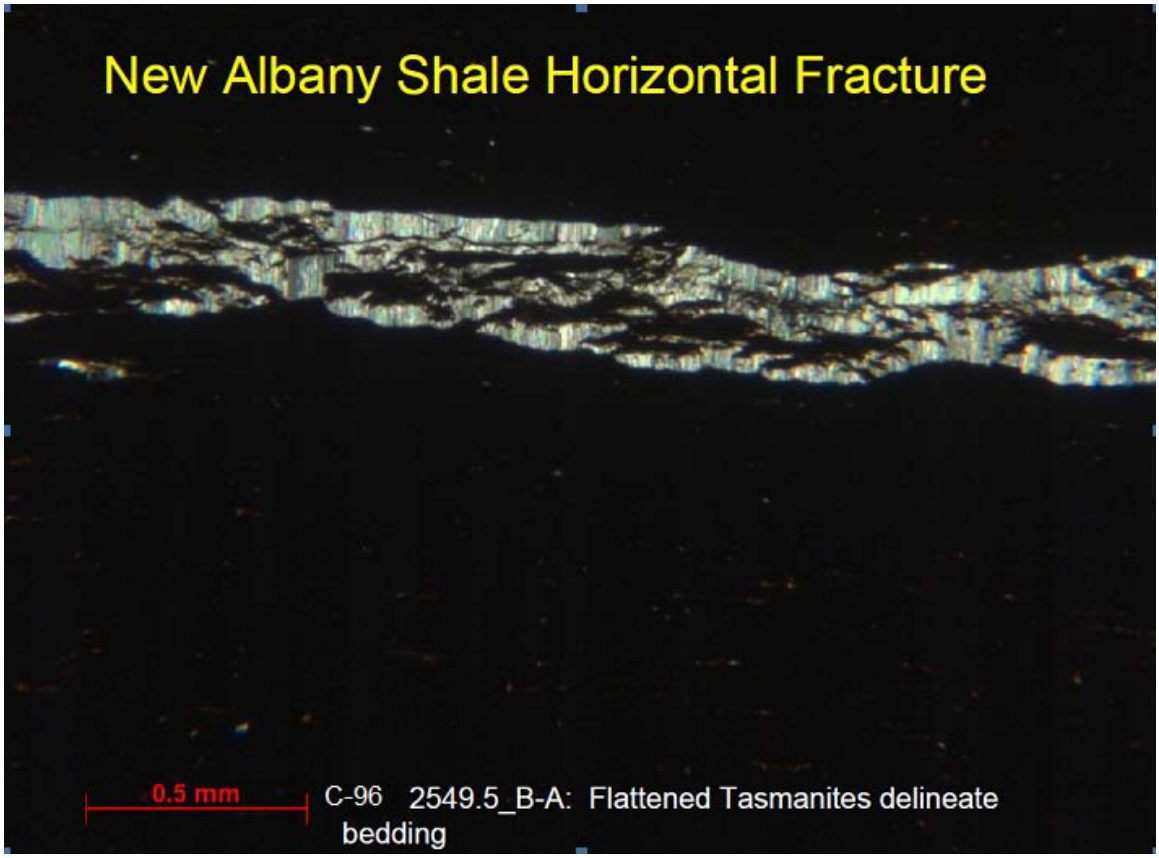


Figure 29. Horizontal fracture filled with fibrous calcite cement at 2,549.5 ft in the C-96 well, Sullivan Co. showing complex, bedding parallel fracture growth.

Porosity examination of ion-milled surfaces

A sample from the Clark Orbit #1 well in Christian Co., Kentucky was taken to examine the micro- to nanopore distribution of the host shale. A small area of the sample was prepared using an argon ion-beam milling technique that creates an extremely flat surface so that topographic effects of differential grain hardness and plucking are minimized (cf. Loucks et al., 2009). The surface can then be analyzed for pores with secondary electron detection and grain types can be distinguished using backscattered electron detection (Fig. 30). The area of the surface examined is approximately 200 µm by 500 µm and includes laminae on the order of 30 µm thick, with compositional contrast between layers. The potential for bedding-parallel openings on the micro- or nanoscale was explored but none were found in this sample.

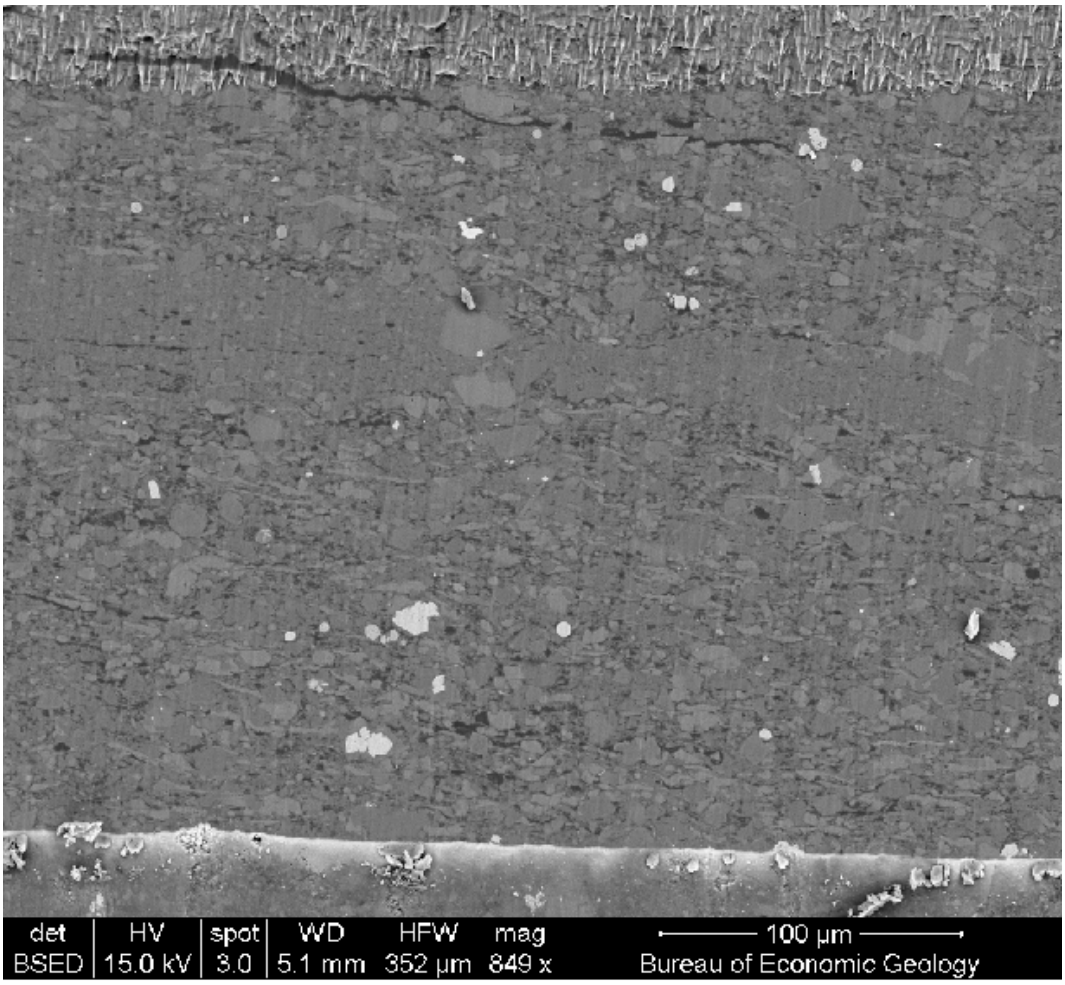


Figure 30. Ion-milled surface of sample from 4293 ft from the J. Ray Clark Orbit #1 well, imaged using backscattered electrons. Bright grains are pyrite. Clays, quartz and other minerals are grayscale; organic material and pores are dark gray to black in this image.



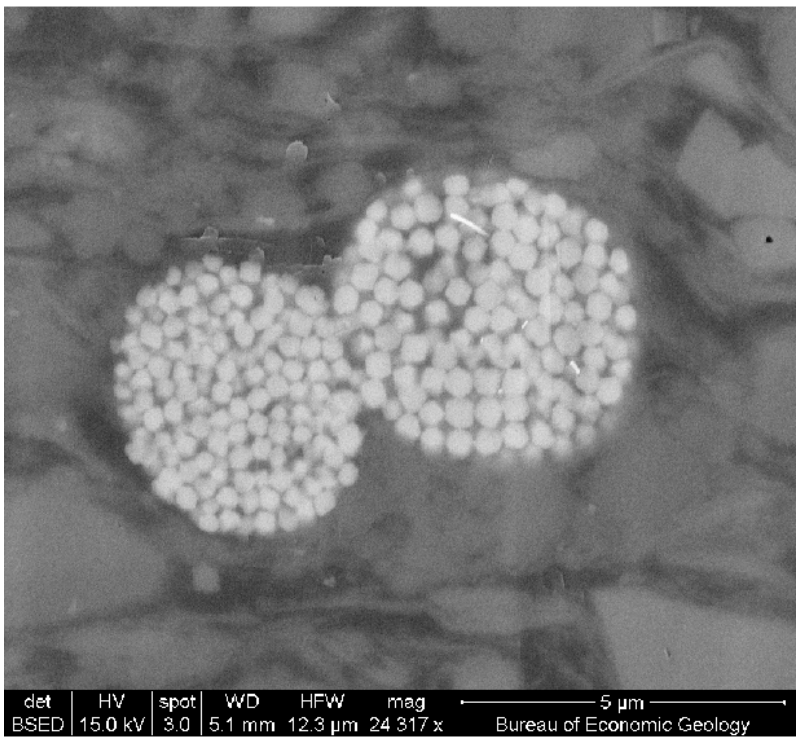


Figure 31. (a) Backscatter and (b) secondary electron images of framboidal pyrites in Fig. 30.

Small (< 5 µm) framboidal pyrites were examined, as they are known to contain intragranular porosity in some other Devonian shales (Lash and Engelder, 2008). Here the gaps between the pyrite crystals making up the framboid are filled with dark gray, probably organic material (Fig.31). A tiny pore (black) is developed at center right but is isolated. Pores in this sample are rare, generally isolated, and are volumetrically insignificant (Fig. 32). They cannot provide permeability enhancement. Unlike the Barnett Shale, the pores we did observe are not associated with organic matter. Instead they are mostly present within grains.

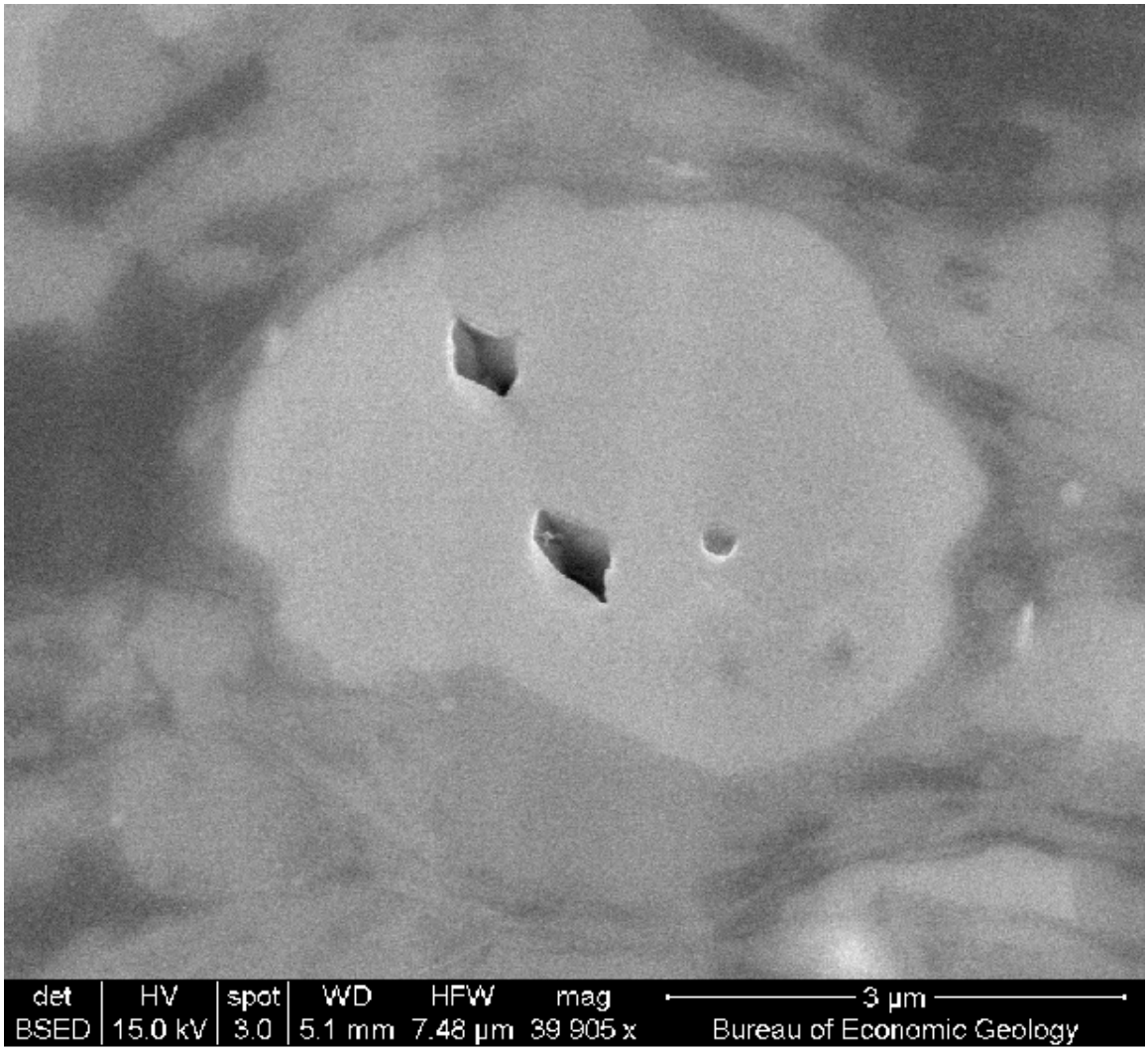


Figure 32. Intragranular pores less than one micron across.

Alpha Gas

Alpha Gas workshop

Julia Gale attended a one day workshop conducted by Dr. Frank Mango on the subject of Alpha Gas. Dr. Mango has proposed that shale gas arises due to a catalyzed equilibrium reaction that occurs at much lower temperatures than thermogenic cracking. He has used New Albany Shale samples among others in laboratory studies and is now attempting to demonstrate his ideas in

field studies. He has also proposed that the gas coming from the Antrim Shale is dominantly Alpha Gas rather than biogenic.

Most organic geochemists are skeptical of the proposal. However, the idea has gained some interest from operators in other shale gas plays and it remains to be seen if it will prove correct in the field.

Communication of fracture characteristics for modeling hydraulic and natural fracture interaction

Communication of the results to other team members was accomplished in part through participation in regular teleconference calls. In addition, for the northern Christian County location, on the basis of observations of fractures in the A-7455 core and on animage log in the well, values or ranges of values were provided for incorporation as suggested input parameters in geomechanical models (conducted by Ahmad Ghassemi, Texas A&M).

- Orientation of S_{Hmax} : E - W
- Orientation of opening-mode fractures: E - W dip N or S
- Orientation of faults: Surface faults E - W dip 60° N or S
- Kinematic aperture: 0.05 to 2 mm
- Hydraulic aperture: not known, likely 0 to 2 mm
- Strength of fracture planes: Weak but no test data. Use data from Barnett (fractures 1/2 as strong as host shale)
- Height of opening-mode fractures: 1 m fracs < 1 mm wide; 10 m fracs > 1 mm wide)
- Spacing of opening mode fractures: 1 to 10 m as base cases

Technology Transfer

Presentations were made at the following meetings:

April 14th 2009 in Golden, Colorado, project review meeting (Laubach)

May 19th 2009 in Tuscaloosa, Alabama, RPSEA forum (Gale)

June 4th 2009 in Chicago, Illinois, RPSEA forum (Gale)

April 6th 2010 in Golden, Colorado, project review meeting (Gale)

April 13th, 2010 in New Orleans, Louisiana AAPG Annual Meeting (Gale and Fidler)

June 17th, 2010 in Amsterdam, Netherlands, GTI Unconventional Gas Symposium (Gale)

A paper was published as part of the proceedings of the 2009 International Coalbed and Shale Gas Symposium, Tuscaloosa, AL, entitled "Natural fractures in the New Albany Shale and their importance for shale-gas production". The paper is attached as Appendix 1.

A University of Texas (Jackson School of Geosciences) student, Luke Fidler, has worked on the project as for his MS degree. He will graduate in 2011, at which point his thesis will be made public, archived in the Department of Geological Sciences Walter Library.

Acknowledgements

Funding for this project is provided by RPSEA through the "Ultra-Deepwater and Unconventional Natural Gas and Other Petroleum Resources" program authorized by the U.S. Energy Policy Act of 2005. RPSEA (www.rpsea.org) is a nonprofit corporation whose mission is to provide a stewardship role in ensuring the focused research, development and deployment of safe and environmentally responsible technology that can effectively deliver hydrocarbons from domestic resources to the citizens of the United States. RPSEA, operating as a consortium of premier U.S. energy research universities, industry, and independent research organizations, manages the program under a contract with the U.S. Department of Energy's National Energy Technology Laboratory.

additional funding for cost share, travel to Amsterdam, GTI, all the companies and Geological Surveys, FRAC

References

Ault, C. H. 1989b, Map of Indiana showing directions of bedrock jointing: Indiana Geological Survey Miscellaneous Map 52.

Carr, D. D. 1981. Lineament analysis. In: Hasenmueller, N. R. and Woodard, G. S. (eds.). Studies of the New Albany Shale (Devonian and Mississippian) and Equivalent Strata in Indiana. U.S. Department of Energy, contract number DE-AC 21-76MC 05204, 62–69; Morgantown, West Virginia, Morgantown Energy Research Center, U.S. Department of Energy, DOE/MC/05204-1128, 45–52.

Comer, J. B., Hasenmueller, N. R., Mastalerz, M. D., Rupp, J. A., Shaffer, N. R. & Zuppann, C. W. 2006. The New Albany Shale gas play in southern Indiana. Program with abstracts, 2006 Eastern Section. American Association of Petroleum Geologists 35th Annual Meeting, Buffalo, N.Y., 17.

Curtis, J. B. 2002. Fractured shale-gas systems. AAPG Bulletin, 86, 1921–1938.

Dumitrescu, M., Finkelstein, D. B., Lazar, R., Schieber, J. and Brassell, S. C. 2004. Origin and history of bitumen in geodes of the New Albany Shale. In: Schieber, J. and Lazar, R. (eds.) Devonian Black Shales of the Eastern U.S. Field Guide for the 2004 Annual Field Conference of the Great Lakes section of the Society for Sedimentary Geology, Indiana Geological Survey Open File Report 04-05, p. 61–67.

Gale, J. F. W. 2002. Specifying lengths of horizontal wells in fractured reservoirs. Society of Petroleum Engineers Reservoir Evaluation and Engineering, 5, 266–272.

Gale, J. F. W., Reed, R. M., and Holder, J. 2007. Natural fractures in the Barnett Shale and their importance for hydraulic fracture treatments. AAPG Bulletin, 91, 603–622.

Hamilton-Smith, T., Hasenmueller, N. R., Boberg, W. S, Smidgens, Z. and Frankie, W. T. 1994. Gas Production. In Hasenmueller, N. R. and Comer J. B. 1994, (eds.) Gas potential of the New Albany

Shale (Devonian and Mississippian) in the Illinois Basin. Final report, Illinois Basin Studies 2. For Gas Research Insitute (GRI) Contract No. 5090-213-1975. Publication no. GRI-92/0391 p. 23-40.

Hasenmueller, N. R. and Comer J. B. 1994, (eds.) Gas potential of the New Albany Shale (Devonian and Mississippian) in the Illinois Basin. Final report, Illinois Basin Studies 2. For Gas Research Insitute (GRI) Contract No. 5090-213-1975. Publication no. GRI-92/0391.

Hasenmueller, N. R., Shaffer, N. R. and Rupp, J. A. 1998, (compilers) Field Trip Log: New Albany Shale Outcrops in Southern Indiana. Gas Research Institute New Albany Shale Consortium Field Trip, August 26, 1998.

Lash, G. G. and Engelder, T., 2008, Pyrite laminae in black shale – an additional source of permeability in unconventional reservoirs. Geological Society of America Abstracts with Programs, Vol. 40, No. 6, p. 233.

Laubach, S. E., Reed, R. M., Olson, J. E., Lander, R. H. & Bonnell, L. M. 2004. Coevolution of crack-seal texture and fracture porosity in sedimentary rocks: Cathodoluminescence observations of regional fractures. Journal of Structural Geology 26, 967–982.

Loucks, R. G., Reed, R. M., Ruppel, S. C., and Jarvie, D. M., 2009, Morphology, genesis, and distribution of nanometer-scale pores in siliceous mudstones of the Mississippian Barnett Shale: Journal of Sedimentary Research, v. 79, p. 848–861.

Miller, D. D., and Johnson, R. J. E., 1979, Acoustic and mechanic analysis of a transverse anisotropy in shale: Proceedings for Third Eastern Gas Shales Symposium, October 1979, Morgantown, W. Va., Morgantown Energy Technology Center, U.S. Department of Energy, METC/SP-79/6, p. 527-542.

Olson, J. E. 2008. Multi-fracture propagation modeling: applications to hydraulic fracturing in shales and tight gas sands. In: Proceedings of the 42nd US Rock Mechanics Symposium. Paper no. ARMA 08-327.

Olson, J. E., Laubach, S. E. & Lander, R. H. 2007. Combining diagenesis and mechanics to quantify fracture aperture distributions and fracture pattern permeability. In: Lonergan, L., Rawnsley, K. & Sanderson, D. (eds.) Fractured Reservoirs. Geological Society, London, Special Publications, 270, 97–112.

Partin, T. H. 2004. Demand and high price spurs a new era of drilling for New Albany Shale gas wells in Harrison County, Indiana. In: Schieber, J. and Lazar, R. (eds.) Devonian Black Shales of the Eastern U.S. Field Guide for the 2004 Annual Field Conference of the Great Lakes section of the Society for Sedimentary Geology, Indiana Geological Survey Open File Report 04-05, p. 68–76.

Schieber, J. 2008. Non-Tectonic Aspects of Shale Fracture Formation, Permeability, and Porosity of Late Devonian Black Shales in the Eastern US. Geological Society of America Annual Meeting Abstracts with Programs, 184-14.

Schieber, J. and Lazar, R. 2004. (eds.) Devonian Black Shales of the Eastern U.S. Field Guide for the 2004 Annual Field Conference of the Great Lakes section of the Society for Sedimentary Geology, Indiana Geological Survey Open File Report 04-05, 90 p.

Sorgenfrei, H., Jr. 1952. Gas production for the New Albany Shale. Bloomington, Indiana University, M.S. thesis, 26 p.

Warpinski, N. R. and Teufel, L. W. 1987. Influence of geologic discontinuities on hydraulic fracture propagation. Journal of Petroleum Technology, 39, 209–220.

Zhang, X., Jeffrey, R. G. and Thiercelin, M. 2007. Effects of Frictional Geological Discontinuities on Hydraulic Fracture Propagation. In: Proceedings of the Society of Petroleum Engineers Hydraulic Fracturing Technology Conference, Paper SPE 106111.

SECTION 4

GEOCHEMICAL STUDIES

RPSEA# GTI#

Microbial Gas From Unconventional Reservoirs: The New Albany Shale as a case study

Final Report

March 2009 – August 2010

Prepared by:

Anna M. Martini[1], Steven T. Petsch[2], Jennifer C. McIntosh[3], Melissa Schlegel[3], Julian Damashek[1], Samuel E. Miller[1], Matthew Kirk[1]

[1]Amherst College, Department of Geology, Amherst, MA 01002

[2]University of Massachusetts Amherst, Department of Geosciences, Amherst, MA 01003

[3]University of Arizona, Department of Hydrology and Water Resources, Tucson, AZ

Prepared for:

GAS TECHNOLOGY INSTITUTE

Subcontract No. #

GTI Project Manager

Iraj Salehi

September, 2010

LEGAL NOTICE

This report was prepared by Amherst College as an account of work sponsored by Research Partnership to Secure Energy for America (RPSEA) and Gas Technology Institute (GTI). Neither RPSEA, members of RPSEA, GTI, nor any person acting on behalf of either:

a. MAKES ANY WARRANTY OR REPRESENTATION, EXPRESS OR IMLIED WITH RESPECT TO ACCURACY, COMPLETENESS, OR USEFULNESS OF THE INFORMATION CONTAINED IN THIS REPORT OR THAT THE USE OF ANY INFORMATION, APPARATUS, METHOD, OR PROCESS DISCLOSED IN THIS REPORT MAY NOT INFRINGE PRIVATELY OWNED RIGHTS, OR

b. ASSUMES ANY LIABILITY WITH RESPECT TO THE USE OF, OR FOR ANY AND ALL DAMAGES RESULTING FROM THE USE OF, ANY INFORMATION, APPARATUS, METHOD, OR PROCESS DISCLOSED IN THIS REPORT.

Reference to trade names or specific commercial products, commodities, or services in this report does not represent or constitute an endorsement, recommendation, or favoring by RPSEA, GTI or its contractors of the specific commercial product, commodity or service.

Acknowledgement

Funding for this project is provided by RPSEA through the "Ultra-Deepwater and Unconventional Natural Gas and Other Petroleum Resources" program authorized by the U.S. Energy Policy Act of 2005. RPSEA (www.rpsea.org) is a nonprofit corporation whose mission is to provide a stewardship role in ensuring the focused research, development and deployment of safe and environmentally responsible technology that can effectively deliver hydrocarbons from domestic resources to the citizens of the United States. RPSEA, operating as a consortium of premier U.S. energy research universities, industry, and independent research organizations, manages the program under a contract with the U.S. Department of Energy's National Energy Technology Laboratory.

Table of Contents

LEGAL NOTICE **2**

RESEARCH SUMMARY **4**

CHAPTER 1: THE ANTRIM SHALE AS A MODEL MICROBIAL GAS RESERVOIR **5**

1.1 The Antrim Shale: The paradigm microbial shale gas play? 5

1.2 Background on Methanogenesis 9

1.3 Methanogenesis as an agent of biogeochemistry 10

1.4 Hydrogeochemistry and methane generation in the Antrim Shale 11

1.5 Materials and methods 12

Microbial analysis 13

Field station records 15

1.6 Results 15

Microbial community composition 15

1.7 Discussion 23

CHAPTER 2: THE NEW ALBANY SHALE ORGANIC GEOCHEMISTRY **26**

2.1 Introduction and Background 26

2.2 Methods 27

2.3 Results 31

2.4 Discussion 37

2.5 Conclusions 60

CHAPTER 3: THE NEW ALBANY SHALE: FORMATION WATER, GAS GEOCHEMISTRY AND THE SUBSURFACE BIOTIC COMMUNITY **61**

Overview 61

Microbiological Investigation of a Natural Gas-Rich Black Shale 62

Materials and Methods 63

Results 70

Summary of Geochemical and Isotopic Results 84

Chapter 4: Synthesis **107**

References: **111**

Appendix **125**

RESEARCH SUMMARY

Natural gas produced from black shale and coal bed deposits is of increasing importance due to economic and political realities. At present these unconventional gas resources account for nearly 10% of total U.S. natural gas production. This is expected to grow to over 50% by 2035 (Hill et al., 2008). This study focuses on one developing shale gas play, the New Albany, and compares it to the Antrim, a mature gas play that is beginning to show signs of a decline.

This study comprised several goals, using the NAS as a case study, including:

1. identifying the active, modern-day community of subsurface microorganisms responsible for current methane production in shale gas plays, recognizing that methanogenesis is only the end product of a cascade of microbial metabolic functions.

2. establishing which environmental parameter(s) limit microbial growth and activity, and thus methane generation, in shale gas reservoirs.

3. quantifying the abundance and biodegradation indices of low molecular weight hydrocarbons in the shale that may provide substrates for microbial methanogenesis

4. stimulating microbial growth and gas generation in poorly producing wells based on identification of microbial communities.

Geochemical analyses confirmed microbial methanogenesis in many of the productive fields in the NAS, with an increasing mix of abiotic gas towards the basin center. Organic geochemical analyses support only weak biodegradation of hydrocarbons in the shale, suggesting a community that has been restricted in its extent, duration or activity. Genetic information obtained from DNA isolated from NAS formation waters indicates a microbial community comprised of acetogenic Bacteria acting in syntrophy with mainly CO_2-reducing methanogenic Archaebacteria. Thus, active microbial methanogenesis in sedimentary basins may not depend on external supply of electron acceptors (e.g. sulfate, ferric iron), but instead reflects internal control limited by formation water hydrology, geochemistry, and organic matter composition.

The results of this project involving microbial community analysis in shale gas plays strongly indicate that microbial methane generation in sedimentary basins is an active process, with a high potential for stimulation and thus extension of projected well production histories. Application of these results has a direct relationship with potential targets of exploration and gas production in other sedimentary basins where methanogenesis may occur or in the future, be stimulated. Thus, this research may contribute towards development of technologies to enhance methane production in shale gas plays, and help secure natural gas resources from the extensive occurrence of fractured black shales and coal beds found throughout the U.S.A.

CHAPTER 1: THE ANTRIM SHALE AS A MODEL MICROBIAL GAS RESERVOIR

1.1 The Antrim Shale: The paradigm microbial shale gas play?

Shale gas production was established in the Antrim Shale in northern Michigan in the 1960s but didn't rise to a major play until the 1990s when gas prices, new technology, and a tax credit fueled a rapid expansion (Figure 1; Hill et al. 2009). While the Antrim quietly overtook the Ohio Shale as the most active play, the Barnett Shale in turn, superseded it. Shale gas is expected to deliver >10% of all U.S. gas production by 2030 and to overtake coalbed deposits. Being one of the earliest plays to fully develop, there is a considerable body of research focused on the Antrim. In contrast to the Antrim, the age-equivalent New Albany Shale has yet to be fully developed into a major play, although it shares many of it's characteristics (Hill et al. 2009).

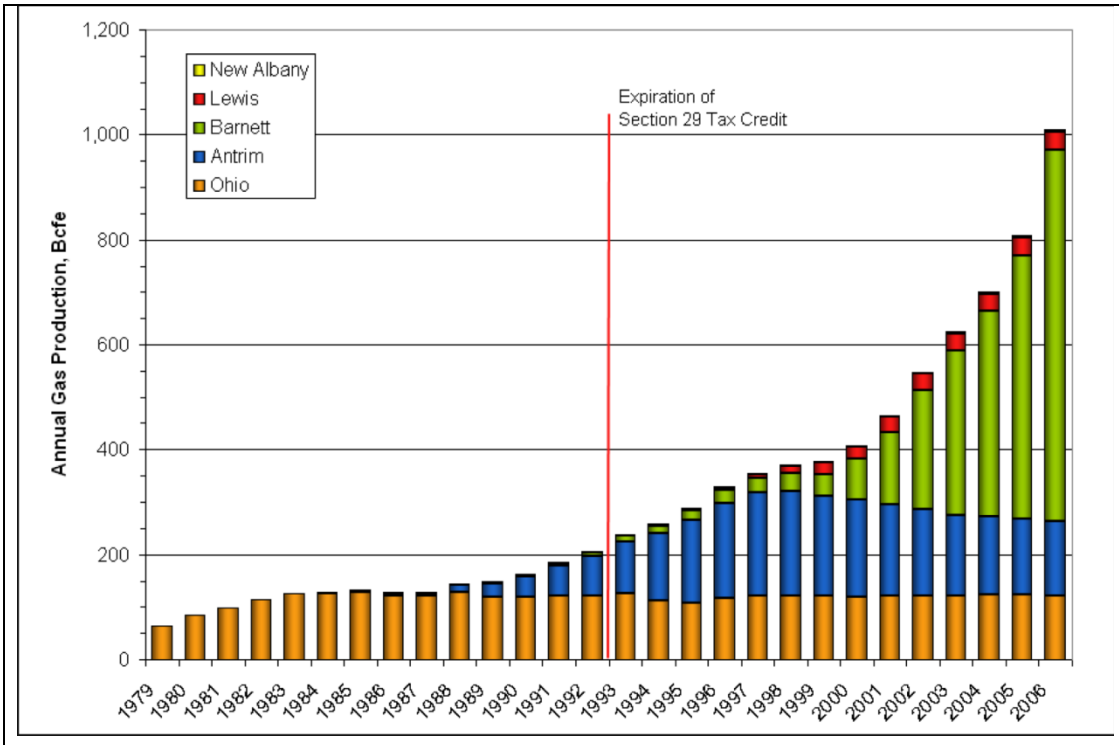


Fig. 1: Annual production from major US shale gas plays (taken from Hill et al., 2008)

Both plays also contain a mix of immature thermogenic (catagenic?) gas towards the basins' interior and dominantly microbial gas nearer to the subcrop (Martini et al., 2008; McIntosh et al., 2002). However, production in the New Albany Shale has been hampered by a natural fracture network not nearly as robust as that found in the Antrim. The major aspect of the overall GTI proposal is to develop techniques and methods for identification and characterization of natural fractures within the NAS and to provide a roadmap for effective drilling, completion, and production stimulation – all of which have undergone significant advances in recent years. Comparisons between the two late Devonian Black Shales, and the host microbial communities that generate much of the produced methane, are useful as an indicator of how a difference in fracturing can lead to significant differences in production. In other words, even given a environmentally favorable conditions for microbial methanogenesis, good access to

interconnected fractures will ultimately lead to greater biodegradation of the shale's organic matter and higher rates of gas generation.

The following table describes the key geochemical indicators for microbial methanogenesis in unconventional shale gas plays.

Table 1
Key Geochemical Indicators for Microbial Methanogenesis in Organic-rich Reservoirs

- High CH_4 concentrations, and high gas wetness values (C_1/C_{2+} >1000) – not always indicative
- High CO_2 concentrations (>1 mole %), and high $\delta^{13}C$ values of CO_2 (>10‰)
- Covariance of δD values of CH_4 and co-produced H_2O
- High dissolved inorganic carbon (DIC) values (10-70 meq/kg), with high $\delta^{13}C_{DIC}$ values (>20‰) in shale fluids
- Low Ca/Mg ratios (<1.5) associated with high DIC and alkalinity values in shale fluids
- Low SO_4 values (<10 mM) and low acetate concentrations (<1 mM) in shale fluids

* Typical values observed in the Antrim and New Albany shales (Martini et al., 1998; McIntosh et al., 2002).

Most microbial indicators overlap for the New Albany and Antrim shales; however, the salinity gradient for the Antrim is much steeper than for the New Albany (Figure 2). The Michigan Basin contains thick evaporite sequences that lead to high formation water salinities at relatively shallow depth, in stark contrast with the New Albany Shale (Figure 2b). Differences in geochemistry may also be temporal rather than spatially defined. One aspect of our study has been to examine changes in water chemistry and microbial population within the Antrim Shale, where a long history of development and repeated sampling has given us the opportunity to make such observations. For the Antrim Shale, production advances with significant depletion of the

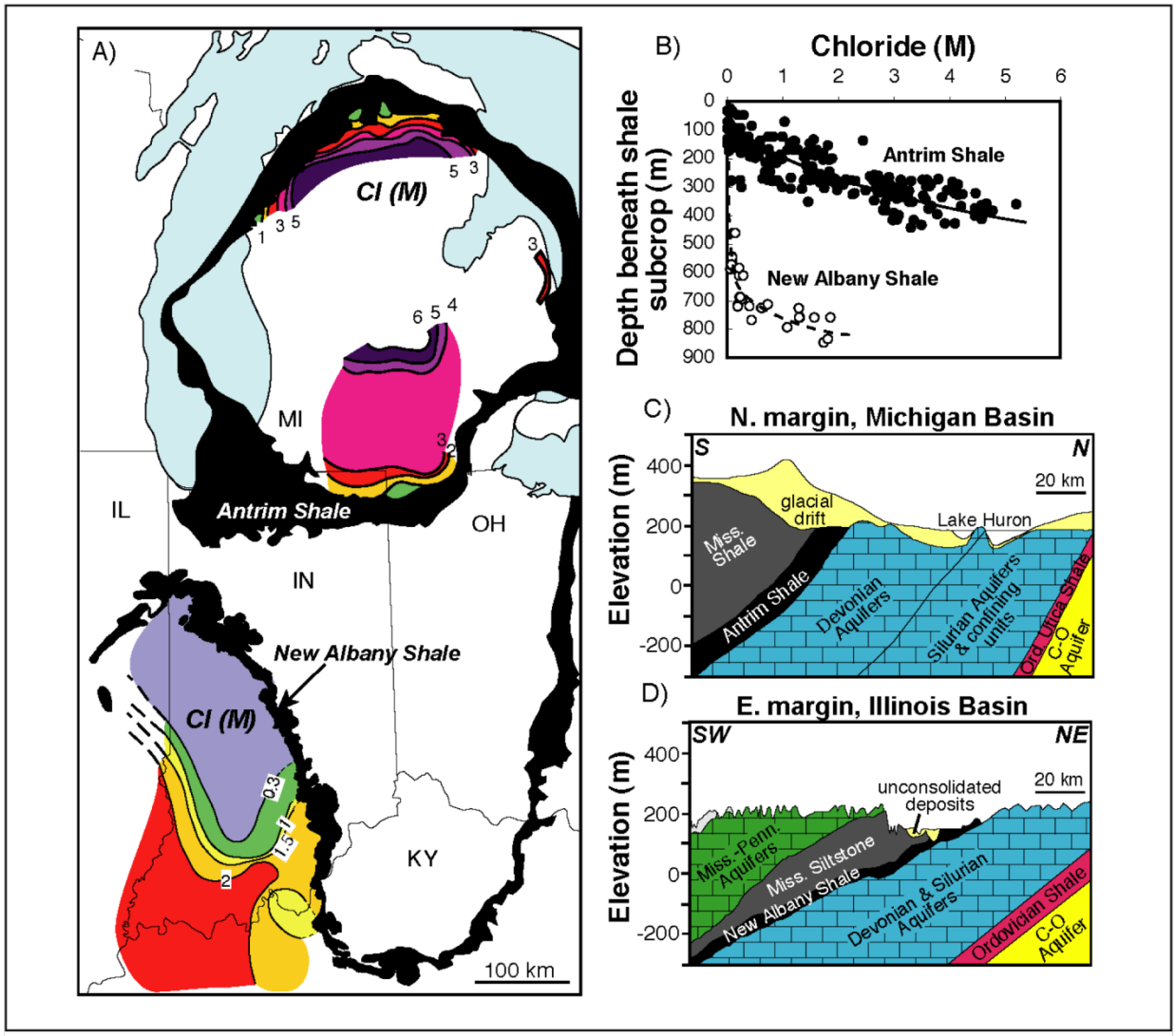


Fig 2: Spatial variations in Cl (M) across the basins. 2b) Cl concentrations with depth in the basins. Figure 2c and d show schematic views from the subcrop into each basin.

formation water. This widespread pumping from relatively closely-spaced well fields opens up a very real possibility of significant geochemical "adjustment" and commensurate changes in the microbial communities.

1.2 Background on Methanogenesis

It is widely recognized that microbiological processes impart significant and distinctive chemical signatures on sediments and sediment pore fluids. Metabolic processes such as denitrification, sulfate reduction and sulfur oxidation, and methanogenesis are each represented by an associated chemical reaction, removing reactants and leaving behind products. These reactions generate the diagnostic sediment profiles of porewater geochemistry and sediment characteristics that form the framework behind much of the paradigm of a coupled advection-diffusion-reaction conceptual model of sediment diagenesis (Berner, 1980). The depths in sediment and sedimentary rocks to which these microbial processes extend are continually being expanded and refined, as evidence accumulates for the activity of microorganisms deeply buried within marine sediments (D'Hondt et al., 2004; Orphan et al., 2001; Elvert et al., 2000; Emerson et al., 1987; Vetriani et al., 1999; Wellsbury et al., 2000), sedimentary rocks (Colwell et al.,1997; Grossman and Desrocher, 2001; Head et al., 2003; Kotelnikova, 2002; Krumholz et al., 1997; Larter et al., 2003; Ringelberg et al., 1997; Ulrich et al., 1998; Ward et al., 2004; Wilhelms et al., 2001; Vetö et al., 2004) and even metamorphosed volcanosedimentary sequences (Sherwood Lollar et al., 199; Takai et al., 2003; Ward et al., 2004). This presents the possibility the relict communities of organisms may live on in ancient sedimentary basins, continuing since burial in isolation from related surficial organisms for long expanses of geologic time. In this study, active methanogenesis within two Late Devonian black shales are investigated - the Antrim Shale, which will be the focus of this chapter, and the New Albany Shale – which will be examined in detail throughout the rest of this report. Geochemical and isotopic indicators of methanogenesis and basin fluid flow are coupled with 16S rRNA sequence analyses to provide the first characterization of the microbial populations present within these 2 black shales associated with economic production of natural gas.

1.3 Methanogenesis as an agent of biogeochemistry

Methanogenesis, the microbial generation of methane, is a common metabolic pathway observed in both freshwater and marine sediments (Sansone and Martens, 1981; Oremland et al., 1987, 1988; Zehnder, 1988; Zinder, 1993). In marine sediments, methanogenesis is observed to develop at depth, most commonly below the zones of aerobic respiration and sulfate reduction (Whiticar, 1999, Hoehler et al., 2001) or where terminal electron acceptors are otherwise depleted (D'Hondt et al., 2002, 2004). As the free energy yield per reaction is very low for methanogenesis compared with other metabolic pathways, methanogenesis tends to be found in the absence of significant quantities of alternative electron acceptors such as nitrate, Fe(III), Mn(IV), or sulfate. Methanogens are strict anaerobes that produce methane from a limited suite of simple substrates. The two most common pathways of methane generation employed by methanogens are reduction of CO_2 using H_2 (1), and decomposition of acetate, also called acetoclastic methanogenesis or methyl-type fermentation (2), with free energy yields calculated from published Gibbs free energies of formation for each aqueous species at the standard state (Amend and Shock, 2001). Other known substrates used in methyl-type fermentations include methanol, formate, and trimethylamine (Whiticar, 1999; White, 2000).

$$CO_2 + 4\ H_2 \rightarrow CH_4 + 2\ H_2O \qquad \Delta G^\circ_{rxn} = -195.6\ kJ/mol \qquad (1)$$

$$CH_3COOH \rightarrow CH_4 + CO_2 \qquad \Delta G^\circ_{rxn} = -49.3\ kJ/mol \qquad (2)$$

There is no known metabolic pathway by which methane can be produced, *directly*, from hydrocarbons found in organic matter [OM]-rich sediments or sedimentary rocks. Therefore, the main substrates required for methanogenesis (acetate, CO_2 and H_2) are supplied through the metabolic pathways of other co-existing subsurface organisms. Both H_2 and acetate are common products of fermentation (White, 2000), indicating that at a minimum, methanogenesis and fermentation must be coupled in sedimentary microbial communities.

Acetate and other volatile fatty acids are common products of fermentation (Zehnder, 1988; White, 2000) and under highly reducing conditions, fermentation leads to the generation of H_2 (Lovley and Goodwin, 1988). In young sediments, fermentation is achieved due to the high relative abundance of labile substrates within recently-buried OM. As diagenesis progresses, however, labile components of sediment OM are lost, and fermentation rates diminish (Wellsbury et al., 2002; Wellsbury et al., 2000; Baird et al., 1985; Emerson et al., 1987; D'Hondt et al., 2002, 2004). The lack of suitable substrates leads to the greatly diminished rate of overall metabolic activity and methane generation in deeply buried sediments (D'Hondt et al., 2002, 2004), although very slow rates of thymidine incorporation, acetate generation and methanogenesis have been detected in sediments hundreds of meters below the sediment-water interface (Wellsbury et al., 2000, 2002), and direct cell counts (Wellsbury et al., 2000; D'Hondt et al., 2004) and molecular evidence (Rochelle et al., 1992; Marchesi et al., 2001; Newberry et al., 2004) suggest active cells at these depths as well. These indications of metabolic activity in deeply buried sediments suggest that nearly-dormant communities of fermentative bacteria and methanogens may persist in sedimentary sequence for thousands and perhaps millions of years (Wellsbury et al., 2002). Indeed, the termination of microbial activity in sediments and sedimentary rocks comes not from the age of the sediment, but rather the temperature. Exposure to temperatures >80 °C are believed to contribute to "paleo-pasteurization" of sedimentary basins (Wilhelms et al., 2001) and inhibit further recolonization of the rocks (Colwell et al., 1997; Krumholz et al., 1997; Ringelberg et al., 1997) and degradation of sedimentary OM (Wilhelms et al., 2001;. In thermally immature sedimentary basins that contain rocks rich in OM, it is not at all clear that very low rates of metabolism might not be maintained for significant expanses of geologic time.

1.4 Hydrogeochemistry and methane generation in the Antrim Shale

Black shales are fine-grained, laminated, sedimentary rocks rich in organic matter [OM]. A growing number of black shales are recognized as unconventional natural gas resources, in which the rock has generated and continues to store large quantities of methane and other light hydrocarbons. These reservoirs include coalbeds in the Powder River Basin of Wyoming and the San Juan Basin of New Mexico, and the shales of this study, the Antrim in the Michigan Basin and the New Albany in the Illinois Basin. There are two known origins of natural gas within sedimentary basins: thermogenic processes, in which shale OM is altered and degraded as the result of heat and pressure, leading to the formation of

methane, ethane, propane, and other hydrocarbons; and microbial processes, in which metabolic pathways employed by subsurface microbial communities lead from degradation of shale OM to the generation of methane

The Antrim Shale (Upper Devonian, Michigan Basin, USA) provides an ideal setting to explore the generation of natural gas within a black shale. The Michigan Basin is a structural low on the North American craton, filled with primarily Paleozoic sedimentary rocks overlain by a thick cover of Pleistocene glacial till. Sedimentary sequences are arranged in concentric, nested bowls, such that the subcrop of the Antrim Shale occurs as a ring extending across northern Michigan, south along Lakes Michigan and Huron, and back across northern Indiana, northern Ohio and southern Michigan.

Microbial gas production is focused within a salinity gradient between approximately 0.5 to 4 M Cl-. Although most methanogenic bacteria require salinities well below 4 M Cl^- to thrive (Zinder, 1988), only salinities up to 1.8 M are tolerated in culture experiments (Ollivier et al., 1994). The highest alkalinities, greatest methane concentrations, and most enriched bicarbonate and CH_4 $\delta^{13}C$ ratios are observed in sections of the Antrim Shale along the northern margin of the Michigan Basin in which Pleistocene recharge has significantly diluted basin brines, suggesting a strong correlation between freshwater influx and generation of microbial methane in black shales (Martini et al., 2003, McIntosh et al. 2004; McIntosh and Walter, 2006).

Previous research on Antrim Shale waters and dissolved gases has demonstrated the presence of microbially-derived natural gas using geochemical and isotopic indicators. However, these indicators do not address if microbially-derived natural gas is the product of ancient subsurface communities that have long since ceased to be metabolically active, or if instead the gas derives at least in part from modern, active communities of subsurface microorganisms. In this study, molecular analysis of microbial biomass, geochemical, and isotopic analyses are used to examine microbial activity and constrain the rate of microbial methanogenesis in the Antrim Shale, Michigan Basin. Moreover, since this play is relatively mature, we can examine whether production practices have modified the microbial consortium present.

1.5 Materials and methods

Sample collection

We selected eight wells along the northern edge of the basin that had originally been sampled in the mid 1990s by Martini and others (Martini et al., 1996; Martini et al., 1998) and re-sampled them during January 14-16, 2009. Temperature and pH measurements were made in the field for a subset of wells. Gas samples were collected for compositional and isotopic analyses in Isotubes® (Isotech Laboratories, Inc.). Water samples were collected for chemical and isotopic analyses and microbial analyses in acid-washed and sterile bottles, respectively. Chemical and isotopic samples were filtered using 0.22 µm nylon syringe filters. Cation samples were preserved with trace-metal grade HNO_3. Microbial biomass samples were collected by filtering water through sterile 25 mm 0.22 µm mixed cellulose-ester filter membranes. The samples were stored in sterile 2 mL microcentrifuge tubes and preserved with 0.2 mL of sucrose lysis buffer (Giovannoni et al., 1990). All sample filtration and preservation was performed within 12 hours of sample collection rather than immediately in the field due to adverse weather conditions. Samples were stored on ice in the field. In the lab, water samples were stored at 4°C and microbial samples at –20°C.

Microbial analysis

Microbial biomass samples collected from wells 22, 147, and 150, which span a wide range in salinity, were selected for genetic analysis. DNA was extracted from the filters using a MoBio ultra-clean soil DNA kit. The alternative protocol described by the manufacturer was used to limit DNA shearing during the extraction. 16S rRNA genes were amplified from the environmental DNA using universal primers 8F (5'-AGA GTT TGA TCM TGG CTC AG-3') and 1492R (5'-GGT TAC CTT GTT ACG ACT T-3') and archaeal primers 109F (5'-ACK GCT CAG TAA CAC GT-3') and 915R (5'-GTG CTC CCC CGC CAA TTC CT-3') (Grosskopf et al., 1998). PCR products were purified using a Wizard DNA gel purification kit and ligated into a TOPO TA vector. Cloning and sequencing was performed at the Washington University Genome Center. For each sample/primer pair, partial sequences were collected from 96 clones.

The sequences were aligned using the Greengenes NAST aligner (DeSantis et al., 2006a) and checked for chimeras using Bellerophon (DeSantis et al., 2006b). Operational taxonomic units (OTUs) were defined at 97% similarity using Mothur (Schloss et al., 2009). Representative sequences within each OTU were fully sequenced. The representative sequences were aligned a second time with the NAST aligner and manually refined in ARB by comparing them to similar sequences in the Greengenes ARB database (DeSantis et al., 2006b). The sequences and selected reference sequences from the database were filtered with lanemaskPH and exported from ARB. The optimal evolutionary model for the

sequences was evaluated using jModelTest (Posada, 2008). Lastly, maximum likelihood phylogenetic trees were generated using PAUP (Swofford, 2003).

Chemical and isotopic analysis

Alkalinity was determined using Gran alkalinity titrations. Chloride and sulfate concentrations were measured at a precision of 2% using a Dionex AS50 ion chromatograph equipped with a CD20 conductivity detector, an ASRS 300 suppressor, and an IonPac AS14 column and AG14 guard column. Chloride was measured directly from diluted samples and sulfate was measured in samples that were treated with Dionex OnGuard II Ag cartridges to remove chloride. Sodium, calcium, magnesium, and strontium were measured at 3% precision and potassium at 5% precision using a Leeman Labs ICP-AES. A suite of trace elements in each sample was measured using an Agilent 7500ce ICPMS. The instrument operated in reaction gas mode for select elements to eliminate mass interference. Samples and standards were acidified with Optima high-purity nitric acid to 3% by volume prior to analysis. Results were adjusted based upon recovery of a multi-element internal standard (SPEX CertiPrep).

Gas compositional and isotopic analyses and water isotopic analyses were performed at Isotech Laboratories, Inc. Gas composition was measured using gas chromatography. The hydrogen isotopic composition of CH_4 and water was measured using dual-inlet isotope ratio mass spectrometry (DI-IRMS) at 2‰ precision. The oxygen isotopes of water and the carbon isotopes of CH_4, CO_2, dissolved inorganic carbon (DIC), and ethane were analyzed with DI-IRMS at 0.1‰ precision, with the exception of the carbon isotopes of ethane sampled from wells 147, 150, and M. In those samples, ethane carbon isotopes were measured using gas chromatography combustion isotope ratio mass spectrometry (GC-C-IRMS) at a precision of 0.3‰. Water samples were prepared for isotopic analysis using the Indiana zinc method for hydrogen, CO_2 equilibration for oxygen, and acid digestion for DIC. All isotope compositions are reported in standard δ notation. Carbon isotopes are reported relative to Vienna Pee Dee Belemnite (VPDB) and hydrogen and oxygen isotopes are reported relative to Vienna Standard Mean Ocean Water (VSMOW). The precision of CH_4 and water isotope values reported by Martini et al. (1996; 1998), are identical to the errors in our analysis. For this study, we did not consider differences between values we measured and the initial values to be significant unless they differ by more than the potential analytical error of the initial and recent value combined.

Field station records

To evaluate gas and water production over time at the field site, we gathered field station records for seven of the wells we sampled. The records start when the field stations first came online and extend through 2007. A complete record was not available for the well field containing well 73. Water and gas produced from numerous wells is delivered to each field station. Withdrawals from the individual wells sampled for this study were estimated by dividing the total monthly gas and water production by the number of wells in each field. Variation among wells in a single field, however, can be considerable.

1.6 Results

Microbial community composition

Molecular microbial analysis of the samples demonstrates a wide diversity of both archaea and bacteria species. The number of clones sequenced from each well and number of OTUs contained within those sequences is summarized in Table 3. For both archaea and bacteria clone libraries, the samples collected from the well with the highest salinity, well 22, had the fewest OTUs.

Table 3. Summary of sequence data

	Cl^-	archaea		bacteria	
well	M[a]	clones	OTUs[b]	clones	OTUs
22	2.9	91	12	64	17
147	0.9	75	25	65	29
150	0.2	68	17	84	40

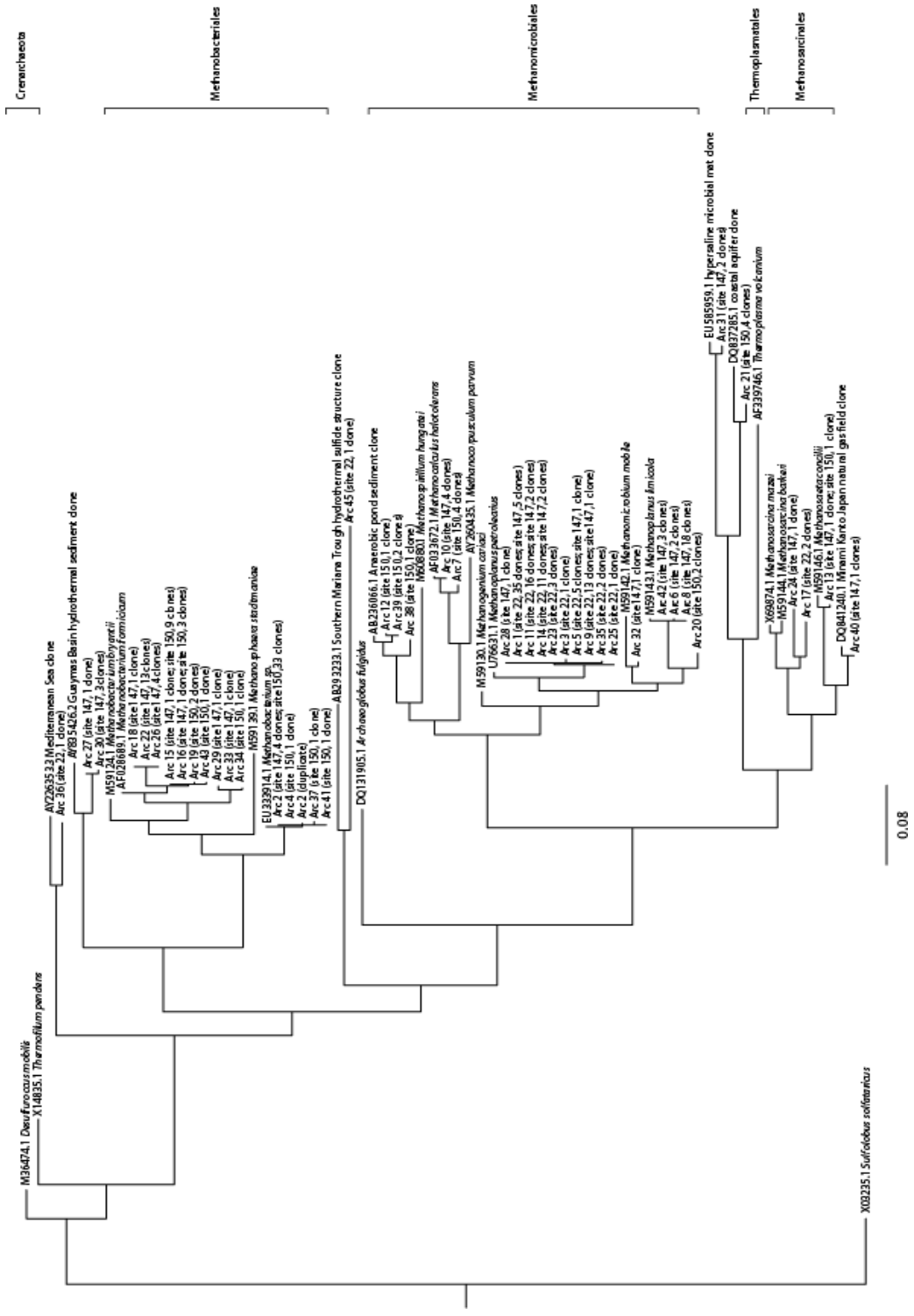
[a]Chloride concentrations measured in 2009 samples.

[b]Some OTUs contain clones from multiple samples.

Phylogenetic analysis indicates that all of the archaea species we observed are members of the *Euryarchaeota* (Fig. 4), which contains the methanogens and extreme thermophiles and halophiles (Takacs-Vesbach et al., 2001). Within this taxon, the majority of the archaeal sequences grouped within two lineages of methanogenic microorganisms; 59% of the clones grouped in order *Methanomicrobiales* and 33% grouped in order *Methanobacteriales*. Sequences grouping within the order *Methanosarcinales*, the only order of methanogens that contains species capable of using acetate, accounted for only 3% of the clones.

The proportion of methanogen lineages varied among the wells. The sample collected from well 22, the well producing the most saline water (Table 3), primarily contained *Methanomicrobiales* sequences (98%). The sample from well 150, the well producing the least saline water, largely contained *Methanobacteriales* sequences (76%). In the sample from well 147, the well with intermediate salinity, sequences from both dominant lineages were common. *Methanomicrobiales* sequences accounted for 53% of the clones and *Methanobacteriales* accounted for 40%.

Figure 4. Maximum likelihood phylogenetic tree produced from archaeal 16S rRNA gene sequences. The numbers of clones from each well is listed in parentheses for each OTU. The scale bar represents 8% sequence divergence.



Final phylogenetic analysis of the bacterial community is not yet complete. A preliminary analysis using the neighbor-joining algorithm in ARB, however, is provided in Figure 5. That analysis indicates that 30% of the sequences we observed come from the order *Desulfovibrionales*. Members of this order are primarily sulfate reducers. The next largest group of bacteria clones we observed accounts for 16% of the bacterial clones and appears to be closely related to the species *Aceobacterium woodi*. A lineage within the phylum *Firmicutes*, acetogens are fermenting microorganisms that can consume a wide variety of substrates and produce acetate and CO_2. The final major group of bacterial clones indicated by the preliminary analysis is grouped in the family *Pseudomonadaceae*. Members of this family are very widespread in nature and have versatile respiratory metabolism.

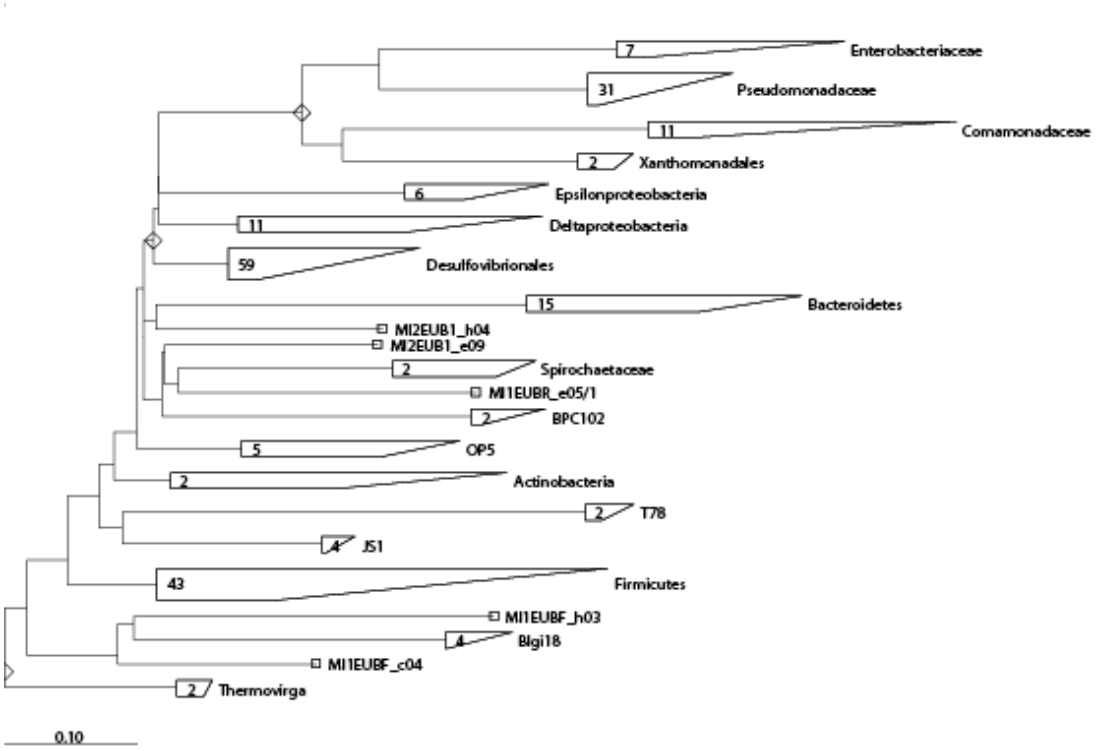


Figure 5. Preliminary neighbor joining phylogenetic tree produced from bacterial 16S rRNA gene sequences. Groups of sequences are depicted as quadrilaterals with the number of sequence listed within each quadrilateral. The scale bar approximates 10% sequence divergence.

Chemical and isotopic composition of water

Field station records demonstrate that water production has decreased sharply over time since the wells were developed. Water production peaked within the first five years of production for all of the wells (Fig. 6). Current levels of water production range from 0.2 to 14.6% of peak levels.

The pH, salinity, and bulk chemical composition of the samples we collected was largely similar to those values observed in samples collected soon after the wells were developed (Table 4). Alkalinity and sulfate concentration, however, appear to have changed significantly. Compared to the samples that were collected initially, the alkalinity content of the samples collected for this study was as much as 50% lower. The average alkalinity content of the samples we collected was 18 mM as HCO_3^- whereas initial values averaged 27.5 mM. Sulfate concentration appears to have increased. The average sulfate concentration measured in the samples we collected was 290 µM. The sulfate concentration for most of the samples collected initially was below the detection limit of those analyses (**<**20 µM) The average sulfate concentration of the three samples that did have measureable sulfate content was 48 µM.

Concurrent with these changes in chemical composition, the isotopic composition of the water also changed, as expected. Differences in δD values changed significantly in six of the eight wells (>4‰). In those samples, δD values were 13‰ lower on average than the values measured in samples collected initially (Fig. 7). In contrast to δD, $\delta^{18}O$ values were actually higher than initial values in half of the samples. Three samples had $\delta^{18}O$ values that were not significantly different from the initial values (>0.2‰), one sample had a $\delta^{18}O$ that was 0.8‰ lower, and four samples had $\delta^{18}O$ values that were 0.5‰ higher on average (Fig. 7). The $\delta^{13}C$ of DIC changed significantly (>0.2‰) in all five samples that had initial values. The $\delta^{13}C$ of DIC decreased 0.5 and 4.8‰ in two wells and increased 1.4‰ on average in three (Table 4).

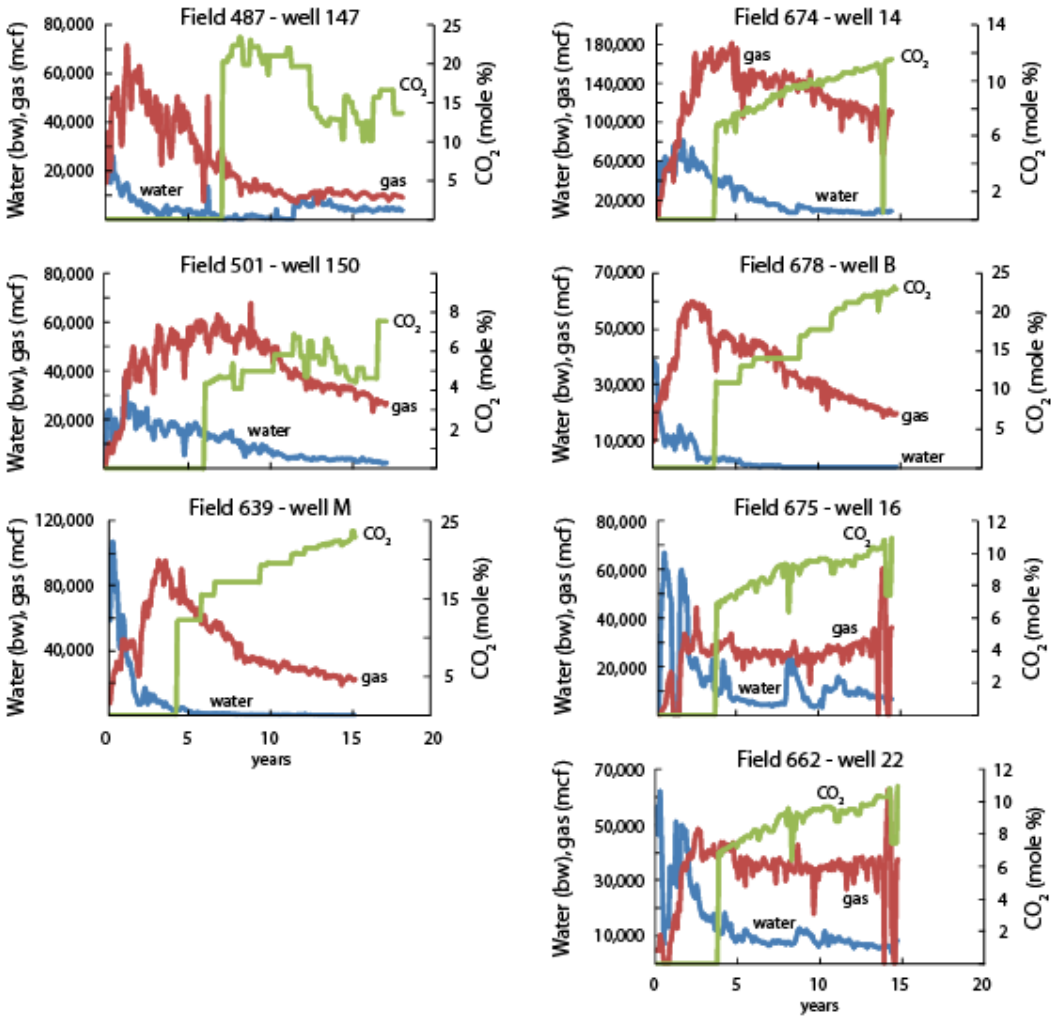
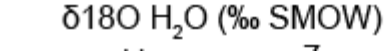


Figure 6. Field station records showing variation in water (barrels of water), gas (million cubic feet), and gas CO_2 content since the field station came online.



Chemical and isotopic composition of gas

Similar to the observed changes in water production and composition, the amount of gas being produced and its chemical and isotopic composition has shifted since the wells were developed. Field station records demonstrate that the proportion of CO_2 in produced gas has increased by as much as 15 mole% while overall natural gas production has steadily decreased (Fig. 6). Analysis of gas samples collected for this study show a similar result. Compared to samples collected initially, the CH_4 content of the gas samples collected for this study decreased by an average of 10.3 mole% in six wells while CO_2 content increased by an average of 8.6 mole% (Table 4). As CO_2 content has increased, gas wetness [$C_1/(C_2+C_3)$] has decreased in most wells. Gas wetness in samples collected for this study averaged 883 compared to 1322 in initial samples. Although the composition of gas has shifted as gas production has declined, CH_4 is still by far the largest component. The average CH_4 content of the samples we collected was 82 mole% compared to 87 mole% initially.

Shifts in the δD of CH_4 are comparable to those observed in water. As the δD of water has decreased, the δD of CH_4 has also largely decreased (Fig. 8). With the exception of one sample that did not change significantly from the value measured initially (>4‰), the δD of CH_4 was lower in all of the samples by 9‰ on average. The average difference between the δD of CH_4 and water in the samples we collected was 170‰, which is very similar to the difference observed initially, 171‰. Similarly to δD values, the δ13C of CH_4 also decreased for most wells (Fig. 8). Two samples had CH_4 δ13C values that were not significantly different from initial values (>0.2‰). The remaining six samples had δ13C values 1.3‰ lower on average. The $\delta^{13}C$ of CO_2 measured in gas samples increased for most wells (Fig. 8). Five samples had a CO_2 $\delta^{13}C$ 1.9‰ higher on average. Of the remaining three samples, one did not change significantly (>0.2‰) and two increased by 0.3 and 2.5‰. The average fractionation factor (α_c) between $\delta^{13}C$ values of CO_2 and CH_4 in the samples we collected was 1.076, where α_c is expressed as follows:

$$\alpha_c = (\delta 13C_{CO2} + 1000) / (\delta 13C_{CH4} + 1000)$$

This value is nearly identical to the fractionation observed in the samples collected from the wells shortly after they were developed, which was 1.074.

Figure 8. Variation in the hydrogen isotopic composition of CH_4 relative to co-produced water. On average, the hydrogen isotopic composition of CH_4 was depleted relative to water by 170‰ in samples collected in 2009, as depicted on the figure.

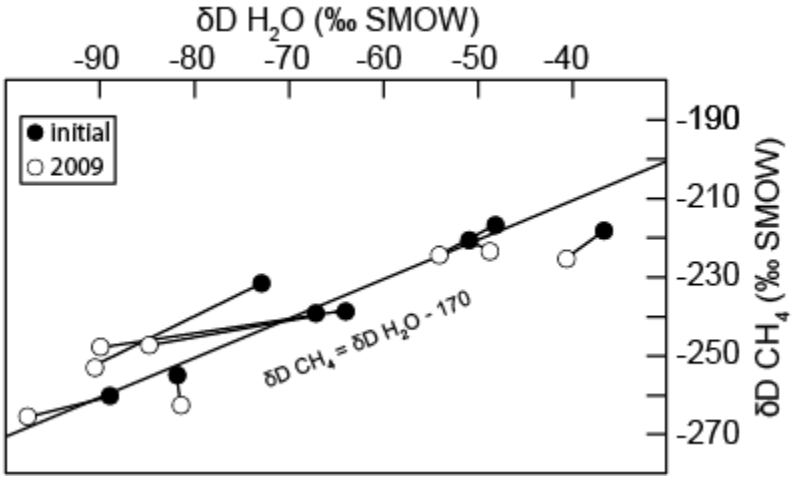
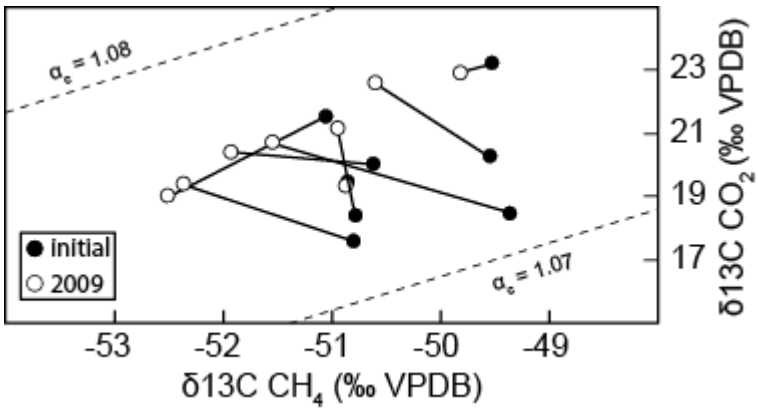


Figure 9. Variation in the carbon isotopic composition of CH_4 relative to water. The average fractionation factor (α_c) between CO_2 and CH_4 carbon isotopes in the 2009 samples was 1.076.



1.7 Discussion

Pathway of microbial methanogenesis

Martini and others (1996; 1998) originally interpreted that the CH_4 in the field area was predominately produced biologically through CO_2 reduction. The results of our isotopic and microbial analysis provide compelling support that this interpretation remains valid.

Direct analysis of the microbial community using molecular techniques indicates that hydrogentrophic methanogenic species dominate the archaeal community. At most only 3% of the archaea sequences we collected could have come from microorganisms capable of consuming acetate, those sequences that grouped in order *Methanosarcinales*. Members of the orders *Methanobacteriales* and *Methanomicrobiales*, the dominant methanogen groups present, chiefly use hydrogen (or formate) as their electron donor.

Analysis of the hydrogen isotopes of CH_4 agree with the results of our phylogenetic analysis (Fig. 8). As described in the introduction, the source of hydrogen atoms varies slightly between methanogenic pathways. This difference leads to distinct isotopic fractionations between water and CH_4 that help distinguish the pathways of biogenic methane formation. Where CH_4 is produced by CO_2 reduction, the δD of CH_4 is typically about 160‰ +/-10% lighter (i.e., more negative) than the surrounding water (Nakai et al., 1974; Schoell, 1980). CH_4 generation by acetate fermentation leads to even greater differences in δD values, reflecting the low δD typical of organic matter. The average difference in δD values we observed, 170‰, is consistent with CO_2 reduction.

The carbon isotopic composition of CH_4 also indicates CO_2 reduction as the pathway of methanogenesis (Fig. 9). Similar to water and CH_4, the carbon isotopes of coexisting CO_2 and biogenic CH_4 are related; whereas CO_2 is a reactant in the CO_2 reduction pathway, CO_2 is produced during acetate fermentation. CH_4 produced by CO_2 reduction is associated with higher fractionation factors (e.g., α_c = 1.08) whereas lower values (e.g., α_c = 1.05) are typical of acetate fermentation (Whiticar et al., 1986). The average α_c we observed, 1.076, is consistent with CO_2 reduction.

Rate of microbial methanogenesis

Variation in the isotopic composition of groundwater in the field area since the wells were initially sampled reflects the procedures used to harvest natural gas. Natural gas is produced from fractured shales like the Antrim by pumping groundwater out to lower pressures adjacent to the borehole and liberate adsorbed gas. The zone of low hydraulic potential that results favors seepage into the shale from undeveloped portions of the formation and adjacent units. Preliminary findings suggested that, in the Antrim, groundwater seepage in response to this hydraulic potential has a different isotopic composition than the groundwater that was initially present (Waldron et al., 2007). Our findings confirm that the groundwater isotopic composition has changed since the wells were initially sampled. The source of this groundwater seepage is uncertain. The apparent increase in sulfate that we observed, however, is consistent with inflow from the underlying gypsum-bearing karst aquifer, the Traverse limestone, which contains gypsum horizons.

Variation in CH_4 δD values simultaneously with the observed shift in water δD values appears to have occurred because microbial methanogenesis has continued to generate CH_4 at a significant rate over the last ca. 15 years. In other words, because the water has shifted toward lighter δD values, CH_4 produced subsequently also has lighter δD values. Other processes that could affect the isotopic composition of the CH_4 mass in the formation would likely cause the CH_4 to become isotopically heavier. During CH_4 oxidation, isotopically lighter CH_4 is consumed preferentially because it is more reactive (Whiticar, 1999). Hence, the residual pool of CH_4 gets isotopically heavier during oxidation. If CH_4 adsorption is affected by CH_4 isotopic composition, lighter CH_4 would likely desorb first, reflecting its higher kinetic energy at any given temperature. The CH_4 again would get heavier with time as a result, not lighter as we observed. Lastly, equilibrium isotope exchange between water and CH_4 could explain our data, however, this process has not been observed in low temperature systems (Schoell, 1980).

Influence of natural gas production on rate of methanogenesis

Although the isotopic analysis indicates that CH_4 has indeed been produced since the wells were initially sampled, our results also suggest that natural gas production may cause this rate to decrease, if it has not already. Like the shift in the isotopic composition of the groundwater, the observed increase in sulfate concentration likely also occurs as a result of pumping to harvest natural gas. Where sulfate concentrations exceeds as little as 30 µM, sulfate reducers can often outcompete methanogens for

electron donors (Ward and Winfrey, 1985). This relationship reflects the amount of energy that can be conserved from each groups metabolic reaction as well as microbial community dynamics (Bethke et al., 2008). Sulfate reducers, therefore, may begin to displace methanogens the shale and ultimate cause the rate of CH_4 formation to decline.

Our molecular results provide some evidence that this has started to occur already. The abundance of sulfate reducing species in our bacteria clone library sharply contrasts with the findings of Martini et al. (Martini et al., 2004), who previously analyzed the bacteria in the northern producing trend of the Antrim. In that study, the authors collected microbial biomass samples from four wells using similar methods to our own and found no evidence of sulfate reducers in any well. They were also unable to cultivate them. In our samples, however, sulfate reducers appear to be the most abundant group of bacteria. Sulfate-reducing bacteria may already be a dominant functional group of microorganism in the field area.

CHAPTER 2: THE NEW ALBANY SHALE ORGANIC GEOCHEMISTRY

2.1 Introduction and Background

Microbial methanogenesis has been implicated in natural gas generation in a growing number of economically important natural gas plays, including shale gas and coal bed methane. Detailed formation water and gas geochemical signatures of this biogenic gas are discussed elsewhere in this report. In addition to these, a number of studies have recognized signatures in the organic geochemistry of natural gas-producing shales and coals that support the concept that microbial populations in these rocks are consuming components of the shale and/or coal organic matter and using these to generate methane. The basic two-part conceptual model of the organic geochemistry of shale- and coal-hosted methanogenesis is as follows. (1) low-molecular-weight components of organic matter provide substrates for microbial fermentation reactions, yielding products such as acetate, CO_2 and H_2. (2) These fermentation products then in turn are consumed as substrates by methane-generating microorganisms. During part (1), biodegradation of shale and coal organic matter selectively consumes more labile compounds that are more susceptible to biodegradation. Thus the signatures of microbial methanogenesis in shales and coals are similar to biodegradation in general: removal of labile compounds that are most susceptible to biodegradation. For example, microbial methanogenesis associated with shale organic matter biodegradation is well-expressed in the Antrim Shale (Formolo et al., 2008a; Waldron et al., 2007). In shale samples from the northern gas-producing trend of the Antrim Shale there is nearly quantitative removal of *n*-alkanes in the most severely biodegraded samples, leaving behind an extractable residue of aliphatic hydrocarbons dominated by an unresolvable complex mixture (UCM) and much greater abundance of acyclic isoprenoids relative to *n*-alkanes. Similarly, in gas-producing coals of the Powder River and San Juan Basins there is substantial removal of both *n*-alkanes and acyclic isoprenoids relative to nominally non-biodegraded hopanes (Formolo et al., 2008b). Intriguingly at these coal bed methane sites, biodegradation of aromatic hydrocarbons such as methylated naphthalenes and methylated phenanthrenes is also observed. This observation, similar to

biodegradation of Australian coals reported by Ahmed et al. (1999) and Ahmed and Smith (2001), suggests that biodegradation of both aliphatic and aromatic hydrocarbons may occur simultaneously in coals, and that both of these compound classes (aliphatic hydrocarbons and aromatic hydrocarbons) may provide substrates for the initial fermentative steps in coal-bed microbial methanogenesis.

In this study, core samples of gas-producing sections of the New Albany Shale were examined to explore if selective removal of labile compounds and compound classes could be detected. Abundance of various aliphatic and aromatice hydrocarbons were measured for several depths from three cores, to examine if differences in compound class abundance were expressed between and within cores. These differences would then suggest locations (both regionally and within cores) where biodegradation of shale organic matter may be most intense. Secondly, a suite of biodegradation indices (*sensu* Peters et al., 2005) was calculated using the abundance of compounds less susceptible to biodegradation relative to the abundance of compounds more susceptible to biodegradation. These indices further informed the intensity and relative stages of microbial biodegradation of shale organic matter both regionally and within cores.

2.2 Methods

Sample description

Samples of the Clegg Creek member of the New Albany Shale were obtained from the Indiana Geological Survey Core repository, comprising three gas-producing sites in southern Indiana: Jackson County, Harrison County and Greene County. Jackson County samples represent the most shallowly-buried shale samples, spanning five depths between 86 to 205 feet depth. Samples were obtained from 86.5, 114.5, 147.5, 167.5 and 205.4 feet depth in Jackson County. Harrison County samples span four depths between 845 to 859 feet (845.5, 849.5, 855, and 859 feet), while Greene County samples represent the most deeply-buried shale in this study, spanning four depths between 1449 to 1511 feet (1449, 1468,

1484, and 1511 feet). Previous research indicates that kerogen in the Clegg Creek Member at these locations is a Type II kerogen dominantly marine/algal in origin. Vitrinite reflectance values support low thermal maturity thoughout the study area (R_o < 0.7%) (Comer et al., 1994).

Bitumen extraction and analysis

Shale samples of between 5-10 g mass were crushed in a steel ball mill to fine powder, then transferred to solvent extraction cells. Bitumen (solvent-extractable organic matter) was liberated from the shales into 3:1 (v/v) dichloromethane:methanol using a ASE200 Accelerated Solvent Extractor (Dionex, Sunnyvale, CA). Bitumen-bearing solvent was evaporated to near-dryness under a gentle N_2 stream. Total bitumen extracts were separated into aliphatic, aromatic and polar fractions over silica gel by sequential elution with hexane (F1), 1:1 (v/v) hexane:dichloromethane (F2) and 1:1 (v/v) dichloromethane:methanol (F3). Polar compounds (F3) were derivatized using BSTFA to generate TMS ethers of alcohols and TMS esters of fatty acids. Extracts were evaporated to near-dryness under an N_2 stream. A known mass of internal standard (20 μg 7-hexylnonadecane) was added to each extract.

Aliphatic hydrocarbons (F1), aromatic hydrocarbons (F2), and TMS-derivatives of polar compounds (F3) were redissolved in hexane analyzed by gas chromatography – mass spectrometry using an HP 6890 GC coupled to an HP 5973 Mass Selective Detector using helium as a carrier gas. The GC was equipped with a split/splitless injector run in splitless mode, and a 30m HP-5ms fused silica capillary column (0.25 mm i.d., 0.25 μm film thickness). For F1 analyses, the GC temperature program was held isothermal at 60 °C for 1.5 minutes followed by an increase at 20°C/minute to 130 °C then a 2 °C/minute increase to 300 °C, then held isothermal for 10 minutes. For F2 and F3 analyses, the GC temperature program was held isothermal at 60 °C for 2 minutes followed by an increase at 20°C/minute to 150 °C then a 2 °C/minute increase to 320 °C, then held isothermal for 10 minutes. For both F1 and F2, the mass spectrometer source was operated at 250°C in electron-impact mode at 70 eV. Identification of compounds was achieved by interpretation of mass fragmentation patterns of individual compounds and comparison with published mass spectra and retention times. Quantification of individual compounds was achieved

using total and extracted ion chromatograms and peak area integration, using m/z = 57 (for alkanes and acyclic isoprenoids), m/z = 191 (hopanes), m/z = 128, 156, 170, 184 (methylated naphthalenes), m/z = 178, 192, 206, 220, 234 (methylated phenanthrenes), m/z = 103 (TMS-derivatives of alcohols), and m/z = 117 (TMS-derivatives of fatty acids) (Peters and Moldowan, 1993; Fisher et al., 1996, 1998; Ahmed et al., 1999; Ahmed and Smith, 2001; Peters et al., 2005; Formolo et al., 2008).

Data analysis

Six classes of compounds (74 compounds total) were selected for identification and quantification: *n*-alkanes, acyclic isoprenoids, C_{31} hopanes, methylated naphthalenes, and methylated phenanthrenes. The abundance of each compounds was calculated by using the ratio of the peak are of the compound relative to the peak area of the internal standard multiplied by the mass of internal standard. Abundance values are expressed as concentrations of compound per gram of shale. Average chain length of *n*-alkanes was calculated using the formula:

$$ACL = \frac{\sum N_i C_i}{\sum C_i}$$

where ACL is the average chain length, N_i is the number of carbons in the *n*-alkane chain between 13 and 35 carbons, and C_i is the concentration of the *n*-alkane. Ratios of compound class abundance were calculated to establish patterns of biodegradation. These ratios express the abundance of compounds less susceptible to biodegradation relative to the abundance of compounds more susceptible to biodegradation; as such, higher biodegradation index values indicate *more* biodegradation. Compound abundance data and other calculated indices described in the following text are listed in Table 1.

Table 1. Summary of compound class abundance and ratio calculations discussed in text

aliphatic hydrocarbons	*aromatic hydrocarbons*
1. Σ*n*-alkanes/g_{sed} (total)	1. ΣMe-naphthalenes/g_{sed} (total)
2. Σ*n*-alkanes /g_{sed} (C_{13} – C_{19})	2. ΣMe-naphthalenes/g_{sed} (dimethyl)
3. Σ*n*-alkanes/g_{sed} (C_{20} – C_{24})	3. ΣMe-naphthalenes/g_{sed} (trimethyl)
4. Σ*n*-alkanes/g_{sed} (C_{25} – C_{30})	4. ΣMe-naphthalenes/g_{sed} (tetramethyl)
5. Average Chain Length	5. ΣMe-phenanthrenes/g_{sed} (total)
6. ΣC_{31} hopanes/g_{sed} (total)	6. ΣMe-phenanthrenes/g_{sed} (monomethyl)
7. ΣC_{31} hopanes/Σ *n*-alkanes$_{(total)}$	7. ΣMe-phenanthrenes/g_{sed} (dimethyl)
8. ΣC_{31} hopanes/Σ *n*-alkanes$_{(C13-C19)}$	8. ΣMe-phenanthrenes/g_{sed} (trimethyl)
9. ΣC_{31} hopanes/Σ *n*-alkanes$_{(C20-C24)}$	9. ΣC_{31} hopanes/ΣMe-naphthalenes$_{(total)}$
10. ΣC_{31} hopanes/Σ *n*-alkanes$_{(C25-C35)}$	10. ΣC_{31} hopanes/ΣMe-naphthalenes$_{(DMN)}$
11. Σ isoprenoids/g_{sed} (total)	11. ΣC_{31} hopanes/ΣMe-naphthalenes$_{(TrMN)}$
12. ΣC_{31} hopanes/Σ isoprenoids	12. ΣC_{31} hopanes/ΣMe-naphthalenes$_{(TeMN)}$
13. Σ isoprenoids /Σ *n*-alkanes$_{(total)}$	13. ΣC_{31} hopanes/ΣMe-phenanthrenes$_{(total)}$
14. Σ isoprenoids /Σ *n*-alkanes$_{(C13-C19)}$	14. ΣC_{31} hopanes/ΣMe-phenanthrenes$_{(MMP)}$
15. Σ isoprenoids /Σ *n*-alkanes$_{(C20-C24)}$	15. ΣC_{31} hopanes/ΣMe-phenanthrenes$_{(DMP)}$
16. Σ isoprenoids /Σ *n*-alkanes$_{(C25-C35)}$	16. ΣC_{31} hopanes/ΣMe-phenanthrenes$_{(TrMP)}$
	17. (ΣMe-naphthalenes$_{(total)}$ + ΣMe-phenanthrenes$_{(total)}$) /Σ *n*-alkanes$_{(total)}$
	18. (ΣMe-naphthalenes$_{(total)}$ + ΣMe-phenanthrenes$_{(total)}$) /Σ isoprenoids

2.3 Results

Aliphatic hydrocarbons

Straight chain saturated hydrocarbons (*n*-alkanes) were found in all analyzed samples, ranging between 13 and 35 carbons in length. The greatest abundance of total *n*-alkanes was found in samples from Greene County (range 81.0 – 134.0 $\mu g/g_{sed}$, mean = 136.9 $\mu g/g_{sed}$, n = 4) (Figure 1). The lowest abundance of *n*-alkanes was found in samples from Harrison County (range 30.6 -83.5 $\mu g/g_{sed}$, mean = 41.2 $\mu g/g_{sed}$, n = 4), while samples from Jackson County were intermediate in *n*-alkane abundance (range 45.1 – 124.2 $\mu g/g_{sed}$, mean = 93.2 $\mu g/g_{sed}$, n = 5). In all samples, abundance of *n*-alkanes was greatest in compounds between 15-20 carbons in length, with no significant odd-over-even preference in carbon chain length. Average chain length values (Figure 2) were greatest in samples from Jackson County (range 19.02 – 21.04, mean 19.59, n = 5), least in samples from Harrison County (range 17.02 – 17.76, mean 17.52, n = 4), and intermediate in samples from Greene County (range 18.09 – 19.46, mean 18.87, n = 4). The greatest overall abundance for an individual *n*-alkane is for nC_{15} from a sample from Greene County, with an abundance slightly greater than 25 $\mu g/g_{sed}$.

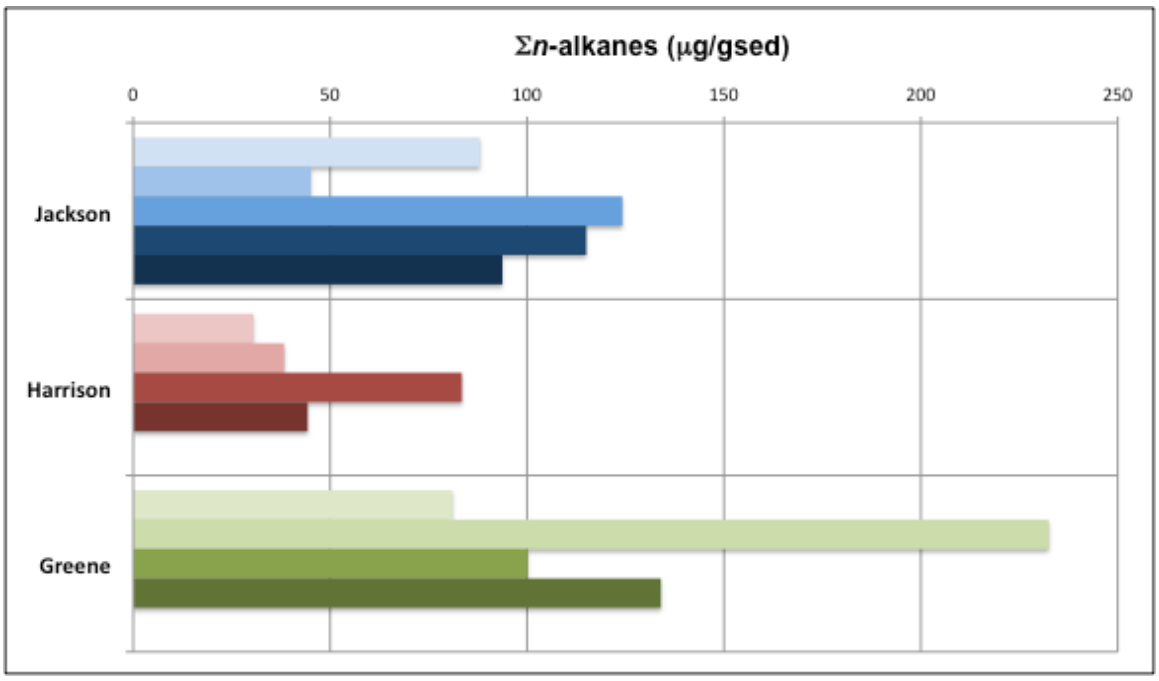


Figure 1. Abundance of total *n*-alkanes in core samples from study sites. Depths in each core (in this figure and throughout) are depicted as shallowest at top, deepest at bottom, as follows. Jackson County = 86.5', 114.5', 147.5', 167.5' and 205.4'; Harrison County = 845.5', 849.5;, 855', and 859'; Greene County = 1449', 1468', 1484', and 1511'.

Three acyclic isoprenoid saturated hydrocarbons were detected in all analyzed samples (Figure 3): norpristane (2,6,10-trimethylpentadecane), pristane (2,6,10,14-tetramethylpentadecane) and phytane (2,6,10,14-tetramethylhexadecane). All three are understood as degradation products of phytol (3,7,11,15-tetramethyl-2-hexadecen-1-ol) either during biosynthesis, diagenesis, or deeper (thermal) sedimentary processes. In all samples, norpristane and pristane exhibit approximately equal abundance, while phytane abundance is approximately 40% lower than either pristane or norpristane. The greatest abundance of total isoprenoid alkanes was found in samples from Green County (mean 35.9 $\mu g/g_{sed}$, n = 4), the lowest abundance was found in samples from Harrison County (mean 16.0 $\mu g/g_{sed}$, n = 4); samples from Jackson County exhibited intermediate isoprenoid abundance (mean = 26.0 $\mu g/g_{sed}$, n = 5). The greatest overall abundance for an individual isoprenoid alkane is for norpristane from a sample in Greene County, with an abundance slightly greater than 25 $\mu g/g_{sed}$.

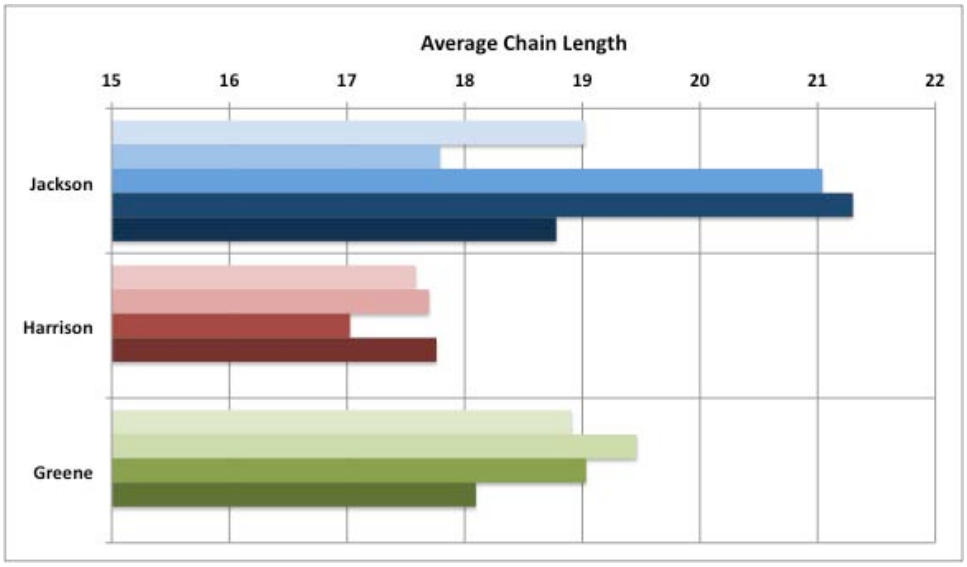


Figure 2. Average chain length of *n*-alkanes, calculated using equation provided in text.

The abundance of two isomers of the C_{31} hopane (17a(H),21b(H)-(22R)-homohopane and 17a(H),21b(H)-(22S)-homohopane) was examined in all samples (Figure 4). Total hopane abundance was overall much smaller than for total *n*-alkanes and total acyclic isoprenoids, and was comparable to the abundance of individual C_{30+} *n*-alkanes. The greatest concentration of total hopanes was found in samples from Greene County (mean = 1.8 $\mu g/g_{sed}$, n = 4), followed by samples from Jackson County (mean = 1.1 $\mu g/g_{sed}$, n = 5) and least in samples from Harrison County (mean = 0.17 $\mu g/g_{sed}$, n = 4).

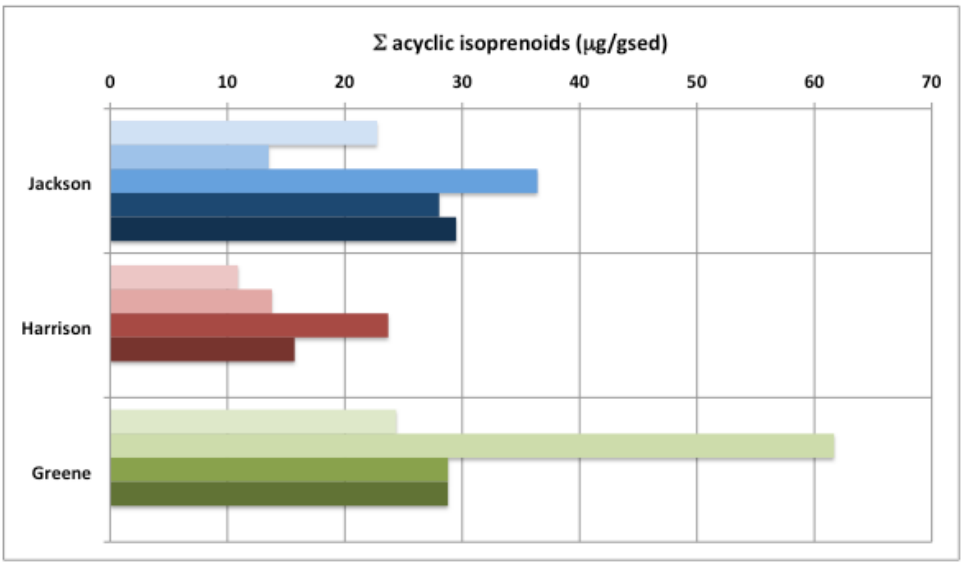


Figure 3. Concentrations of total acyclic isoprenoids (norpristane, pristane and phytane)

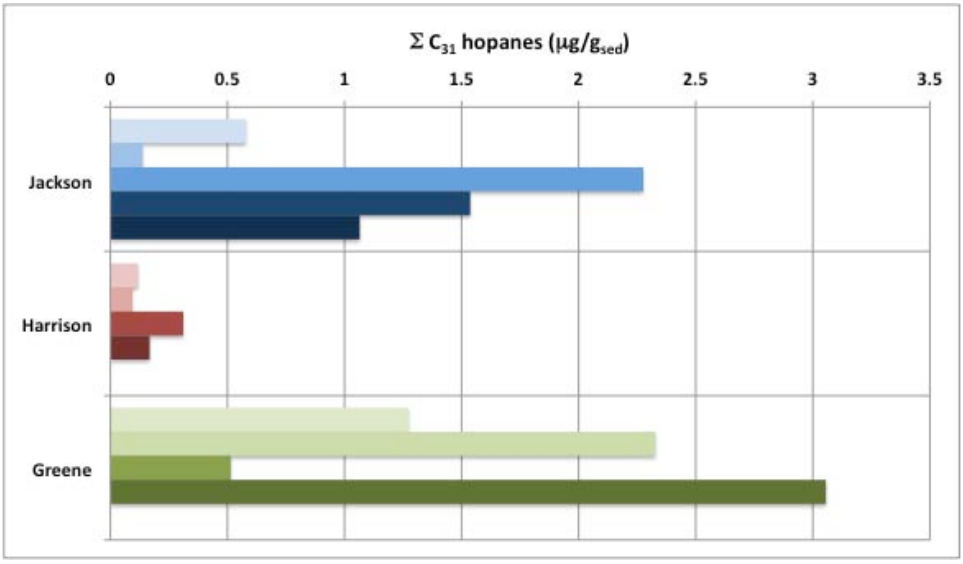


Figure 4. Concentrations of total C_{31} homohopanes.

Aromatic Hydrocarbons

Methylated naphthalenes were found in all examined samples (Figure 5). Methyl-substituted naphthalenes were found to contain between two and four methyl groups sited at various positions around the naphthalene center of the molecule, yielding a suite of six distinctly-eluting dimethylnaphthalenes (DMN), 8 distinctly-eluting trimethylnaphthalenes (TrMN), and 8 distinctly-eluting tetramethylnaphthalenes (TeMN); no monomethylnaphthalenes were detected in any samples. The greatest concentration of methylated naphthalenes was found in samples from Jackson County (range 3.2 – 9.3 $\mu g/g_{sed}$, mean = 5.9 $\mu g/g_{sed}$, n = 5). The lowest concentration of methylated naphthalenes was found in samples from Greene county (range 2.7 – 6.0 $\mu g/g_{sed}$, mean 4.5 $\mu g/g_{sed}$, n = 4), with samples from Harrison County exhibiting concentrations slightly greater than those from Greene County (range 2.6 = 6.3 $\mu g/g_{sed}$, mean = 4.8 $\mu g/g_{sed}$, n = 3). Concentrations for all individual methylated naphthalenes in all samples were less than 1 $\mu g/g_{sed}$, with the exception of one TeMN compound in one sample from Jackson County.

Methylated phenanthrenes were found in all examined samples, at concentrations similar to methylated naphthalenes (Figure 6). Methyl-substituted phenanthrenes were found to contain between one and four methyl groups sited at various positions around the phenanthrene center of the molecule, yielding a suite of four distinctly-eluting monomethylphenanthrenes (MMP), ten distinctly-eluting dimethylphenanthrenes (DMP), five trimethylphenanthrenes (TrMP), and six distinctly-eluting tetramethylphenanthrenes (TeMP). The greatest concentration of methylated phenanthrenes was found in samples from Greene County (range 12.1 – 26.3 $\mu g/g_{sed}$, mean = 17.0 $\mu g/g_{sed}$, n = 4). The lowest concentration of methylated phenanthrenes was found in samples from Jackson County (range 6.0 – 12.4 $\mu g/g_{sed}$, mean = 10.1 $\mu g/g_{sed}$, n = 5), with samples from Harrison County exhibiting concentrations slightly greater than those from Jackson County (of methylated phenanthrenes was found in samples from Greene County (range 5.9 – 14.8 $\mu g/g_{sed}$, mean = 11.8 $\mu g/g_{sed}$, n = 3).

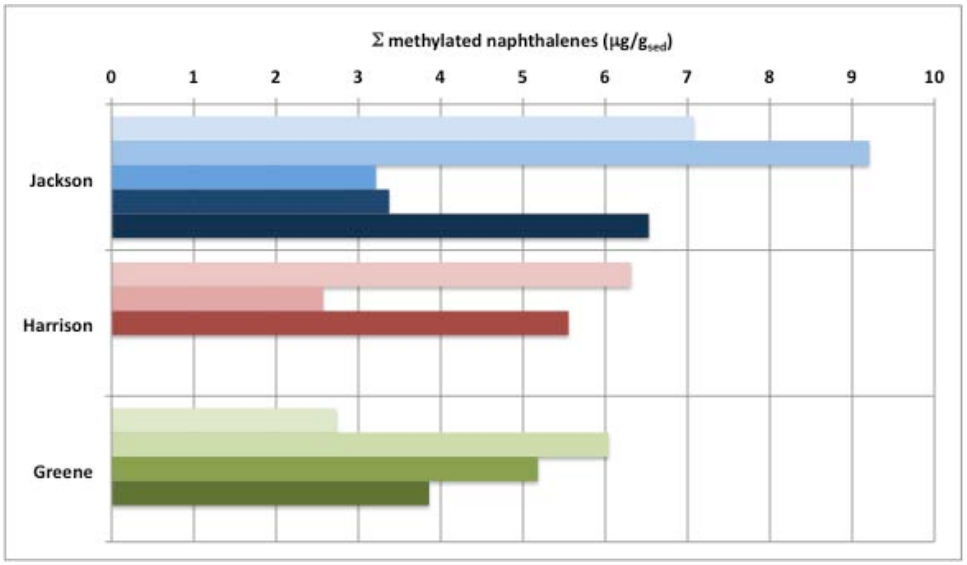


Figure 5 Concentrations of total methylated naphthalenes.

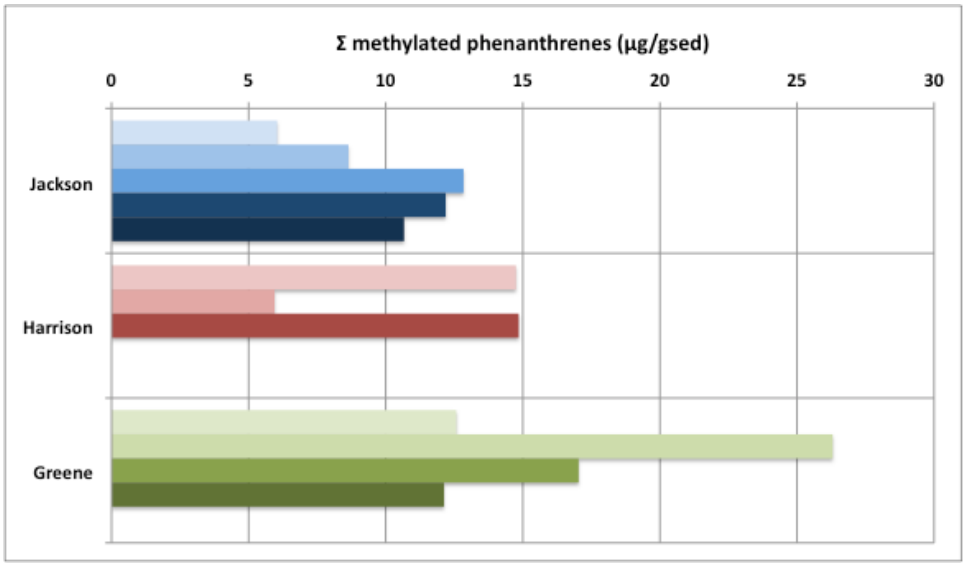


Figure 6. Concentrations of total methylated phenanthrenes.

2.4 Discussion

Absolute and relative abundance of aliphatic hydrocarbons

Samples of the Clegg Creek Member of the New Albany Shale from three cores were examined in this study. Samples from Jackson County represent the shallowest examples of shale, ranging between 86 to 205 feet depth. Harrison County samples span four depths between 845 to 859 feet, while Greene County samples represent the most deeply-buried shale in this study, spanning four depths between 1449 to 1511 feet. In spite of this range of depths, concentrations of *n*-alkanes are fairly uniform across all samples, with lowest concentrations measured in samples from the core of intermediate depth in Harrison County.

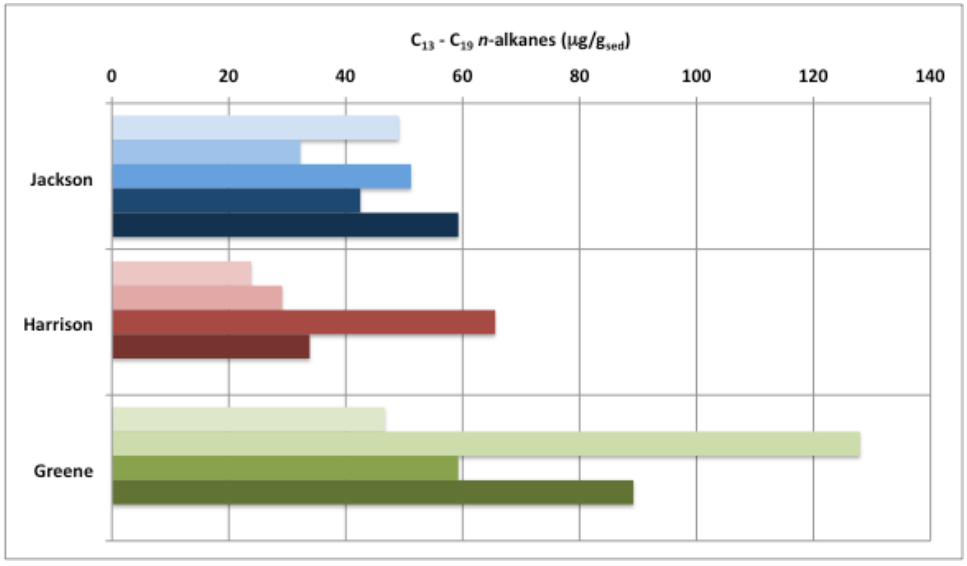


Figure 7. Abundance of C_{13} – C_{19} *n*-alkanes.

In all samples, *n*-alkanes between 13-19 carbons in length make up the largest fraction of total *n*-alkanes (Figure 7). In Jackson County, the relative abundance of these short-chain *n*-alkanes ranges between 37-

71% of total *n*-alkanes, with the lowest relative concentrations observed in samples in the middle depths of the Jackson County core samples. C_{13}-C_{19} *n*-alkanes exhibit a narrow range of relative abundance in samples from Harrison County (between 76-78% of total *n*-alkanes) with no clear trend with depth in the Harrison County core samples. C_{13}-C_{19} *n*-alkanes exhibit a narrow range of relative abundance in samples from Greene County as well (between 55-67% of total *n*-alkanes) with lowest relative abundance observed in samples from the upper portions of the Greene County core.

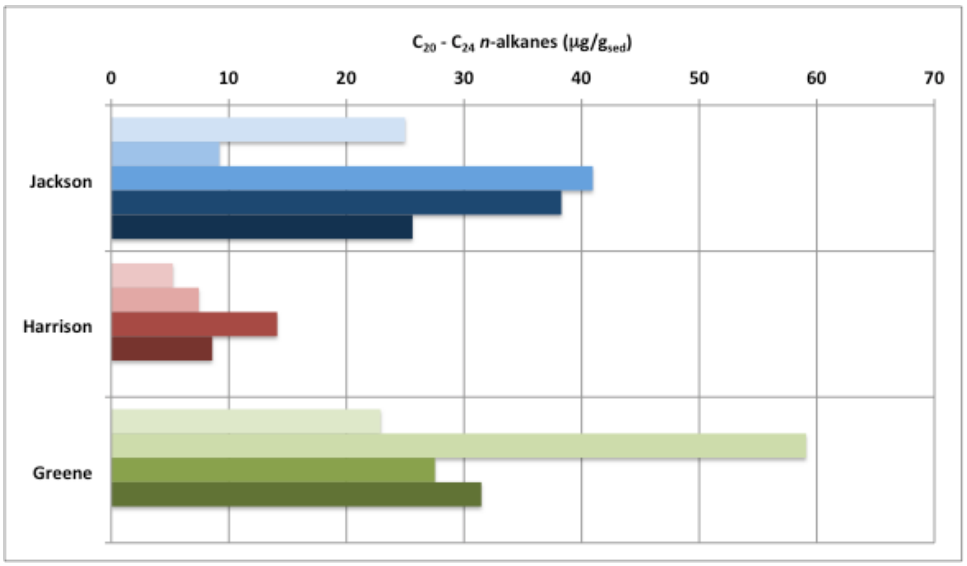


Figure 8. Abundance of C_{20} – C_{24} *n*-alkanes.

C_{20}-C_{24} *n*-alkanes comprise between 17-27% of all *n*-alkanes in the samples (Figure 8). The greatest relative abundance of these mid-chain-length *n*-alkanes is observed in samples from Jackson County (between 20.3 – 33.2% of total *n*-alkanes), in which the greatest relative abundance of C_{20}-C_{24} *n*-alkanes is found in the middle depth of the Jackson County core. The lowest relative abundance of C_{20}-C_{24} *n*-alkanes is observed in samples from Harrison County (between 17-19.4% of total *n*-alkanes) with no clear trend with depth in the Harrison County core samples. C_{20}-C_{24} *n*-alkanes exhibit a narrow range of relative abundance in samples from Greene County as well (between 23.5-28.2% of total *n*-alkanes) with no clear trend with depth in the Greene County core samples.

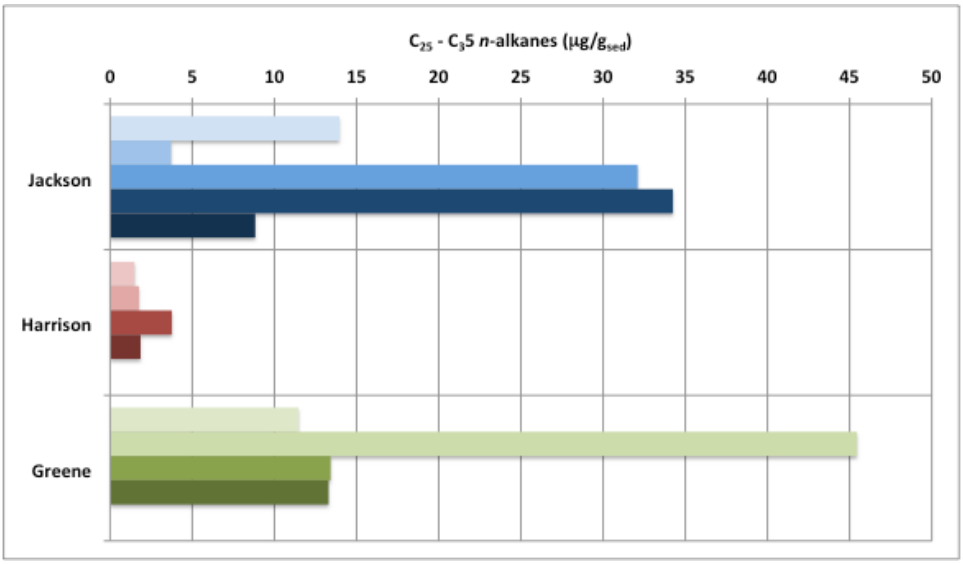


Figure 9. Abundance of C_{25} – C_{35} *n*-alkanes.

C_{25}-C_{35} *n*-alkanes make up the smallest fraction of total *n*-alkanes in all samples (Figure 9). The greatest relative abundance of these long-chain *n*-alkanes is observed in samples from Jackson County (between 8-30% of total *n*-alkanes), with highest relative concentrations in middle depths of the Jackson County Core, and in samples from Greene County (between 10-19% of total *n*-alkanes), with highest concentrations in the upper portions of the Greene County Core. Lowest relative concentrations of C_{25}-C_{35} *n*-alkanes are observed in the core from Harrison County, where relative abundances fall in a narrow range between 4.2-4.9% of total *n*-alkanes.

The relative abundance of *n*-alkanes of varying chain length is verified by calculation of average chain length (ACL) for each sample. As described in *Results*, ACL values are lowest in samples from Harrison County. Within each core, however, there are few signatures of variations in chain length with depth. The largest ACL values in the Greene County samples are found in upper portions of that sample set, while largest ACL values for Jackson County are found in middle depths of that sample set.

The relative abundance of various *n*-alkanes reveals that there is no obvious trend in *n*-alkanes with lateral distance or burial depth between the three cores. Thus biodegradation of *n*-alkanes cannot simply be assigned as greater in one core compared to another along a trend that corresponds to burial depth. The low relative abundance of mid- and long-chain *n*-alkanes found in samples from Harrison County compared to both Jackson and Greene County suggests that biodegradation of *n*-alkanes may be least intense in Harrison County, as short-chain *n*-alkanes are thought to be biodegraded more readily than longer chain *n*-alkanes. Within each core, the relative abundance of *n*-alkanes may suggest that biodegradation is uniform throughout the Harrison County section of the Clegg Creek Member of the New Albany Shale, may be most intense in the lowermost section of the Greene County core, and may be least intense in the middle section of the Jackson County core.

The acyclic isoprenoid hydrocarbons norpristane, pristane and phytane exhibit lowest abundance in samples from Harrison County, while samples from Jackson County and Greene County (excepting one outlier) exhibit similar and higher concentrations (see Figure 3). Thus, similar to *n*-alkane abundance, little trend can be recognized in isoprenoid abundance across the study sites reflecting lateral distance and/or burial depth. Concentrations of isoprenoids within each core are variable, making assignment of depth-related trends in abundance within single cores problematic.

C31-homohopanes represent the compounds that are least susceptible to biodegradation, within currently understood metrics of subsurface hydrocarbon biodegradation. Overall hopane abundances are substantially lower in samples from Harrison County compared to either Jackson County or Greene County. Within each core, absolute hopane abundance is greatest in middle depths of the Jackson County core. In the other two cores, hopane abundance is highly variable, making interpretation of abundance changes with depth problematic (see Figure 4).

Ratios of the abundance of various aliphatic hydrocarbon compound classes can be interpreted as biodegradation indices, in which differences in ratio values among samples reflect differing extents of biodegradation. Because hopanes are understood to be least susceptible to biodegradation, the ratio of

hopane abundance to various compound class abundances provides a suite of indices in which greater numeric values indicate greater extents of biodegradation. Other indices that calculate the abundance of methyl-branched alkanes (i.e. isoprenoids) to straight-chain alkanes similarly indicate extents of biodegradation. This ratio-index approach removes the bias of variations in the absolute abundance of compound classes among samples. Values of biodegradation indices reveal differences in biodegradation among the three cores examined in this study, as well as differences within each core that indicate where biodegradation at a single site may be most severe.

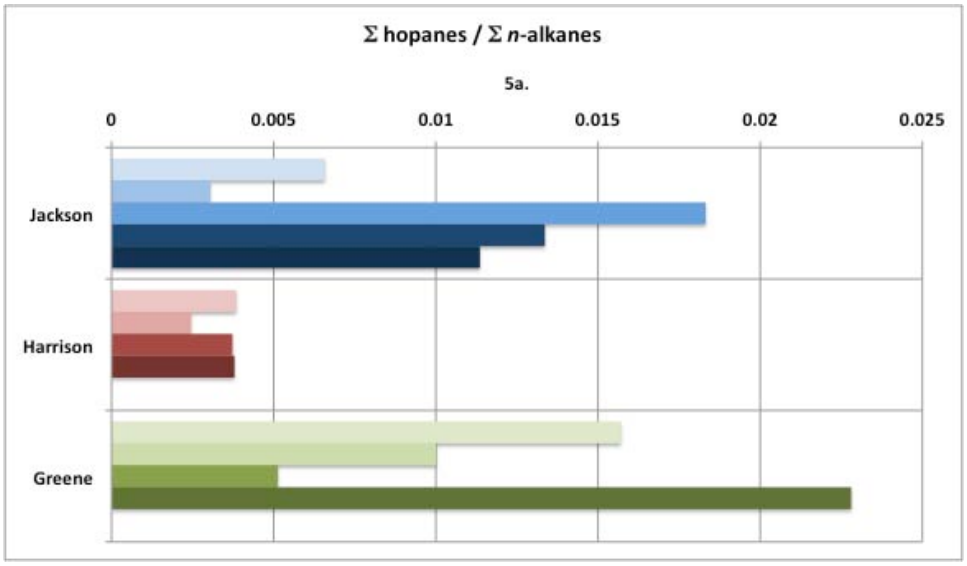


Figure 10. Biodegradation index of total hopanes to total *n*-alkanes.

The ratio of total hopanes to total *n*-alkanes (Figure 10) varies from low values in samples from Harrison County (mean = 0.003) to intermediate values in samples from Jackson County (mean = 0.011) to highest values in samples from Greene County (mean = 0.013). Similar trends emerge in evaluating total hopane abundance compared to abundance of C_{13}-C_{19} *n*-alkanes (Jackson County mean = 0.023; Greene County mean = 0.022; Harrison County mean 0.004), hopanes/C_{20}-$_{24}$ (Jackson County mean = 0.035; Greene County mean = 0.053; Harrison County mean = 0.019), and hopanes/C_{25}-C_{35} (Jackson County mean = 0.062; Greene County mean = 0.107; Harrison County mean = 0.076). Differences in hopane/*n*-alkane biodegradation indices among different cores are most extreme in values calculated for short-chain *n*-alkanes (Figure 11) and converge to similar values among all cores for long-chain alkanes, (Figures 12 and

13) corroborating that biodegradation is most extensive among short-chain *n*-alkanes. The ratio of hopanes to total acyclic isoprenoids follows trends observed for hopanes/*n*-alkane indices (Figure 14): lowest values in Harrison County (mean = 0.01), intermediate values in Jackson County (mean = 0.038), and highest values in Greene County (mean = 0.053). These indices thus suggest that biodegradation is most severe for total *n*-alkanes and isoprenoids in the Greene County core, and least severe in Harrison County.

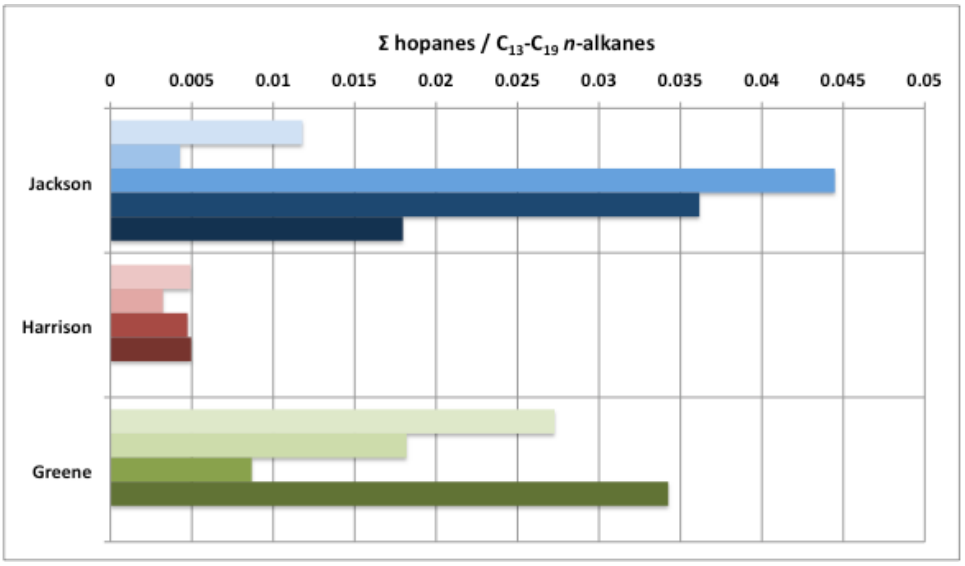


Figure 11. Biodegradation index of total hopanes to C_{13} – C_{19} *n*-alkanes.

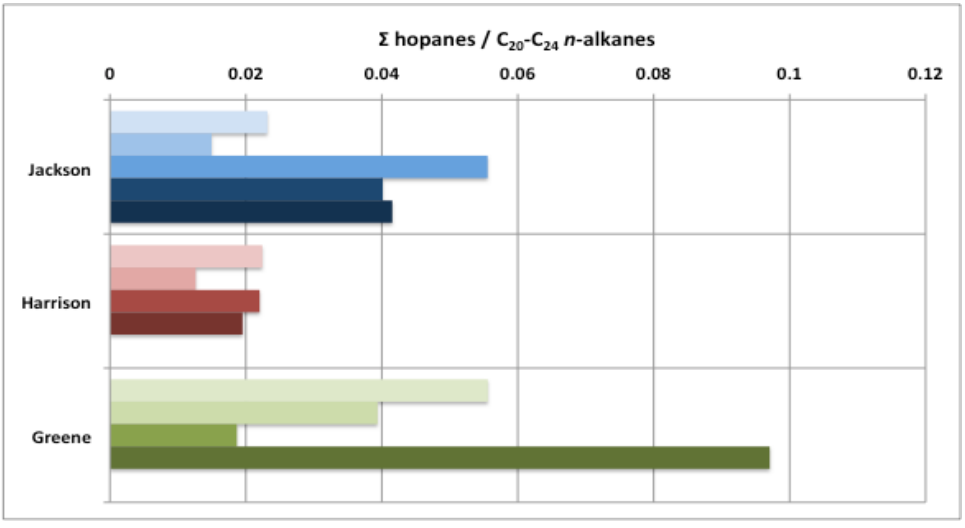


Figure 12. Biodegradation index of total hopanes to C_{20} – C_{24} *n*-alkanes.

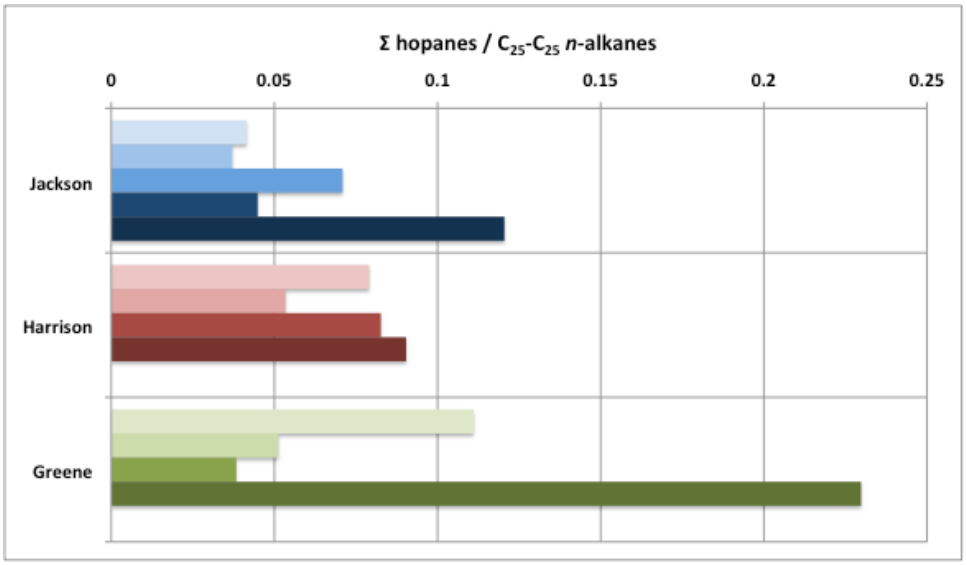


Figure 13. Biodegradation index of total hopanes to C_{25} – C_{35} *n*-alkanes.

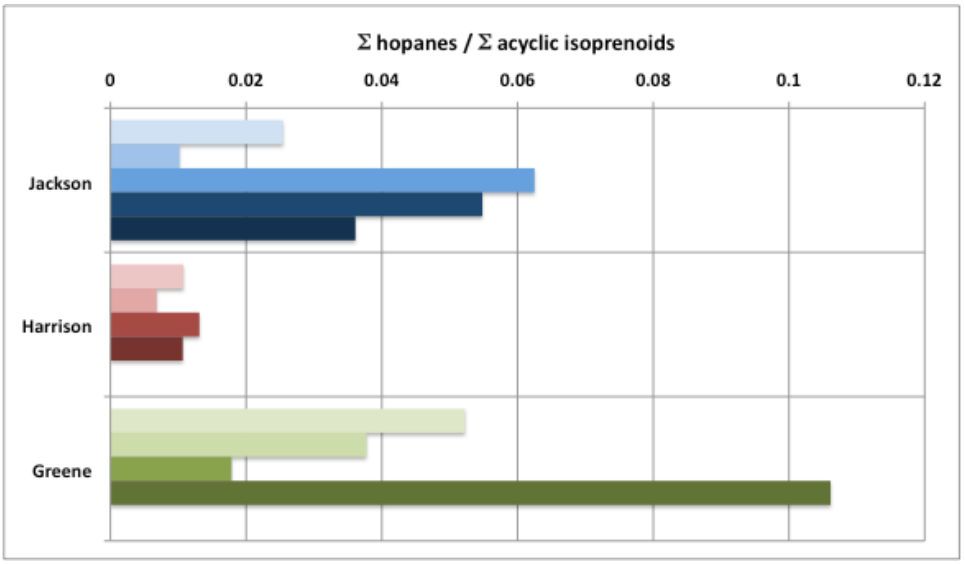


Figure 14. Biodegradation index of total hopanes to total acyclic isoprenoids.

Within each core, trends in aliphatic hydrocarbon biodegradation indices are not obvious. Hopanes/total *n*-alkanes appears to indicate most intense biodegradation in the middle- to lower sections of the Jackson County core, and least intense biodegradation in the middle sections of the Greene County core (see Figure 10). However, these signatures are not smoothly varying with depth. Biodegradation indices

are low and uniform throughout the Harrison County core. Similarly subtle trends with depth are observed in the ratios of hopanes to specific *n*-alkane subsets (C_{13}-C_{19}, C_{20}-C_{24}, and C_{25}-C_{35}) (see Figures 11, 12 and 13) as well as hopanes/isoprenoids (see Figure 14), suggesting most extensive biodegradation at middle-lower depths in the Jackson County core, least extensive biodegradation in the middle of the Greene County core, and uniformly low throughout the Harrison County core.

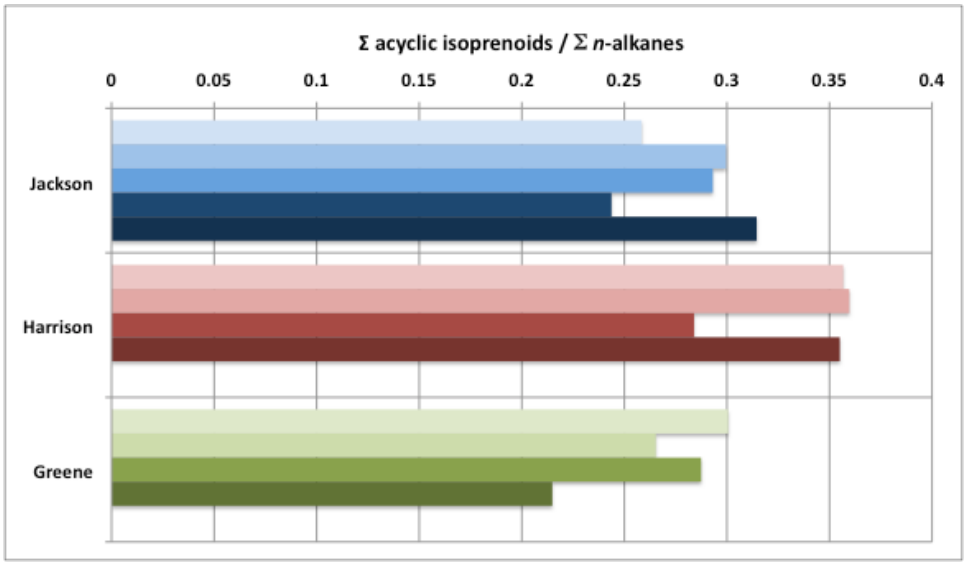


Figure 15. Biodegradation index of total acyclic isoprenoids to total *n*-alkanes.

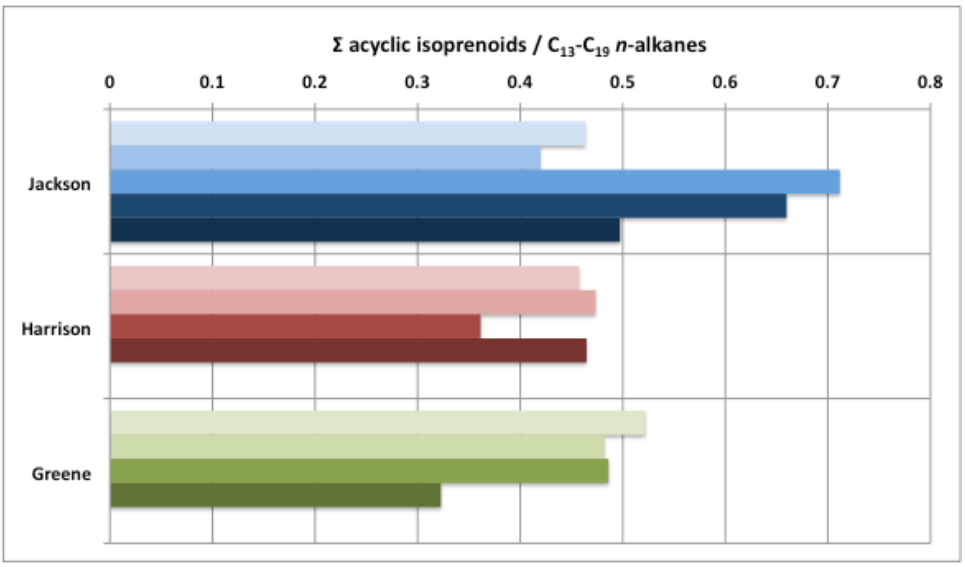


Figure 16. Biodegradation index of total acyclic isoprenoids to C_{13} – C_{19} *n*-alkanes.

Both *n*-alkanes and acyclic isoprenoids are understood to be susceptible to biodegradation in shales and coals at rates greater than hopane biodegradation proceeds. Thus, ratios of the abundance of isoprenoids to *n*-alkanes reveal information about the intensity of aliphatic hydrocarbon biodegradation not seen in comparisons to nominally non-degraded hopanes (Figure 15). For example, the ratio of isoprenoid to total *n*-alkane abundance is greatest in samples from Harrison County and lowest in Greene County. This pattern is not seen in the ratios of isoprenoids to C_{13}-C_{19} *n*-alkanes (Figure 16), but is modest for the C_{20}-C_{24} *n*-alkanes (Figure 17) and quite severe in the C_{25}-C_{35} *n*-alkanes. (Figure 18) These trends can be interpreted as extensive aliphatic hydrocarbon biodegradation in both Greene and Jackson Counties, in which differences in the relative abundance of *n*-alkanes and isoprenoids are not longer apparent because both compound classes have been extensively lost through degradation, and the initial stages of biodegradation in Harrison County, in which *n*-alkanes are just beginning to be lost through biodegradation.

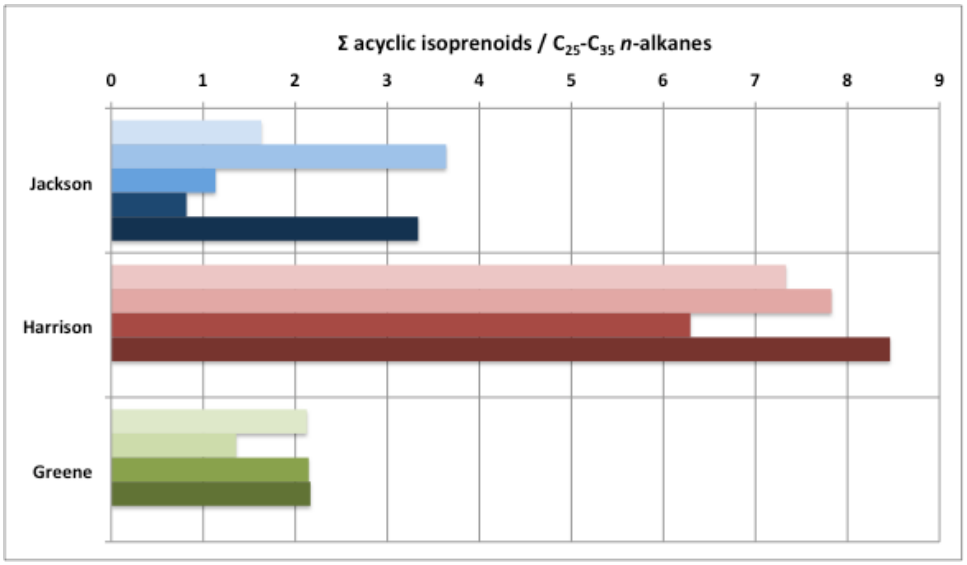


Figure 17. Biodegradation index of total acyclic isoprenoids to C_{20} – C_{24} *n*-alkanes.

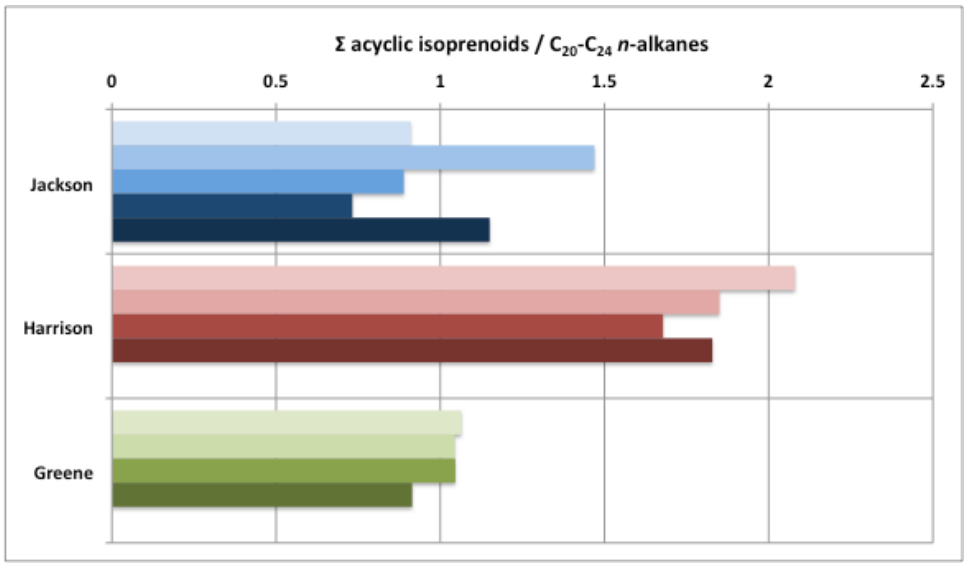


Figure 18. Biodegradation index of total acyclic isoprenoids to C_{25} –C_{35} *n*-alkanes.

Absolute and relative abundance of aromatic hydrocarbons

Samples of the Clegg Creek Member of the New Albany Shale from three cores were examined in this study. Samples from Jackson County represent the shallowest examples of shale, ranging between 86 to 205 feet depth. Harrison County samples span four depths between 845 to 859 feet, while Greene County samples represent the most deeply-buried shale in this study, spanning four depths between 1449 to 1511 feet. In spite of this range of depths, concentrations of methylated naphthalenes and methylated phenanthrenes are fairly uniform across all samples (see Figures 5 and 6), with highest concentrations of methylated naphthalenes in uppermost sections of the Jackson County core, and highest concentrations of methylated phenanthrenes in middle sections of the Greene County core.

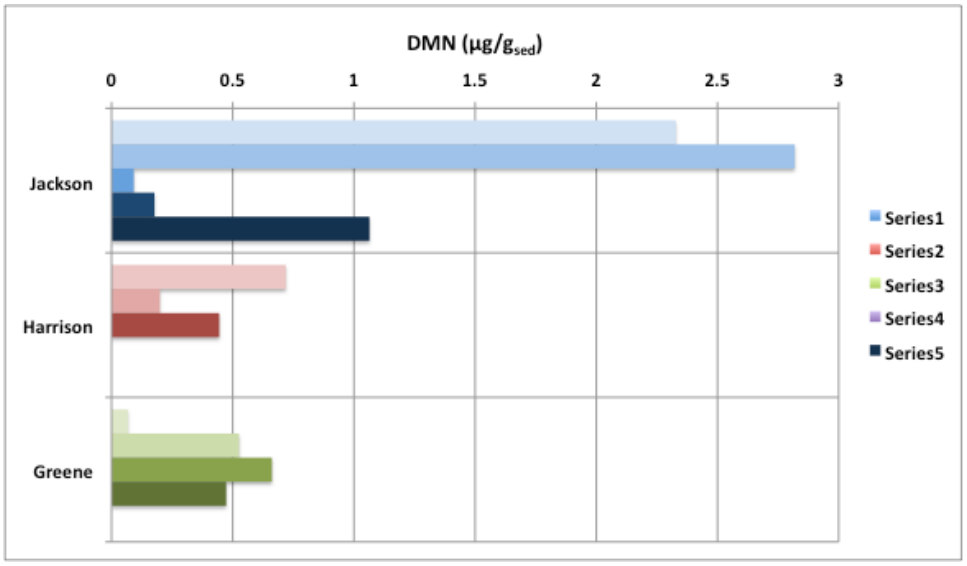


Figure 19. Abundance of dimethylnaphthalenes (DMN).

There are varying relative abundances of specific methylated naphthalenes both between cores and within cores in this study. In Jackson County, the relative abundance of DMN ranges widely between 3-33% of total methylated naphthalenes, with the lowest relative concentrations observed in samples in the middle depth of the Jackson County core (Figure 19). DMN abundances range between 8-11% of total methylated naphthalenes in the three analyzed samples from Harrison County, with lowest abundance measured in the middle depth sample from Harrison County. DMN abundance ranges between 2.5-13% of total methylated naphthalenes in samples from the Greene County core, with greatest relative concentrations observed in the lower depths of the core.

In Jackson County, the relative abundance of TrMN ranges between 35-38% of total methylated naphthalenes, with the lowest relative concentrations observed in samples in the middle depth of the Jackson County core (Figure 20). TrMN abundances range between 45-53% of total methylated naphthalenes in the three analyzed samples from Harrison County, with lowest abundance measured in the middle depth sample from Harrison County. TrMN abundance ranges between 36-53% of total methylated naphthalenes in samples from the Greene County core, with greatest relative concentrations observed in the middle depths of the core.

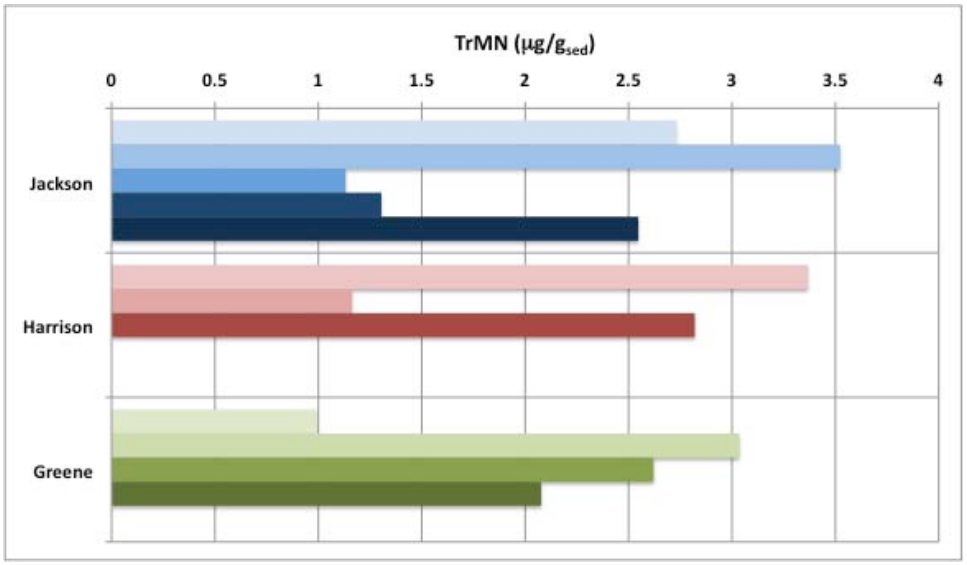


Figure 20. Abundance of trimethylnaphthalenes (TrMN).

In Jackson County, the relative abundance of TeMN ranges widely between 28-62% of total methylated naphthalenes, with the greatest relative concentrations observed in samples in the middle depth of the Jackson County core (Figure 21). TeMN abundances range between 35-47% of total methylated naphthalenes in the three analyzed samples from Harrison County, with greatest abundance measured in the middle depth sample from Harrison County. TeMN abundance ranges between 33-61% of total methylated naphthalenes in samples from the Greene County core, with greatest relative concentrations observed in the uppermost depths of the core.

There are varying relative abundances of specific methylated phenanthrenes both between cores and within cores in this study. Mono-, di-, tri- and tetramethylphenanthrenes are approximately equal in abundance among the three cores, with tetramethyalphenanthrenes comprising no more than 11% of total methylated phenanthrenes in any sample. Samples from Jackson County exhibit the greatest relative concentrations of TeMP. In Jackson County, MMP concentrations range between 22-34% of total methylated phenanthrenes, with greatest relative concentrations in the middle sections of this core (Figure 22). MMP concentrations exhibit a narrow range in samples from the Harrison County core (31.6-32.2%), while MMP relative concentrations in the Greene County core range between 27-36% with no clear trend with depth. DMP and TrMP concentrations exhibit ranges and depth patterns similar to MMP (Figures 23, 24, and 25).

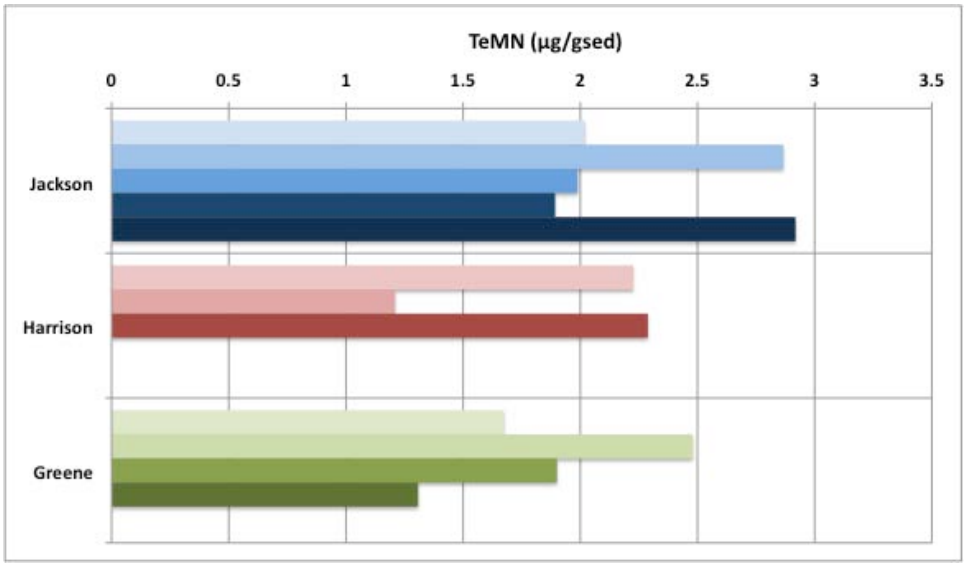


Figure 21. Abundance of tetramethylnaphthalenes (TeMN).

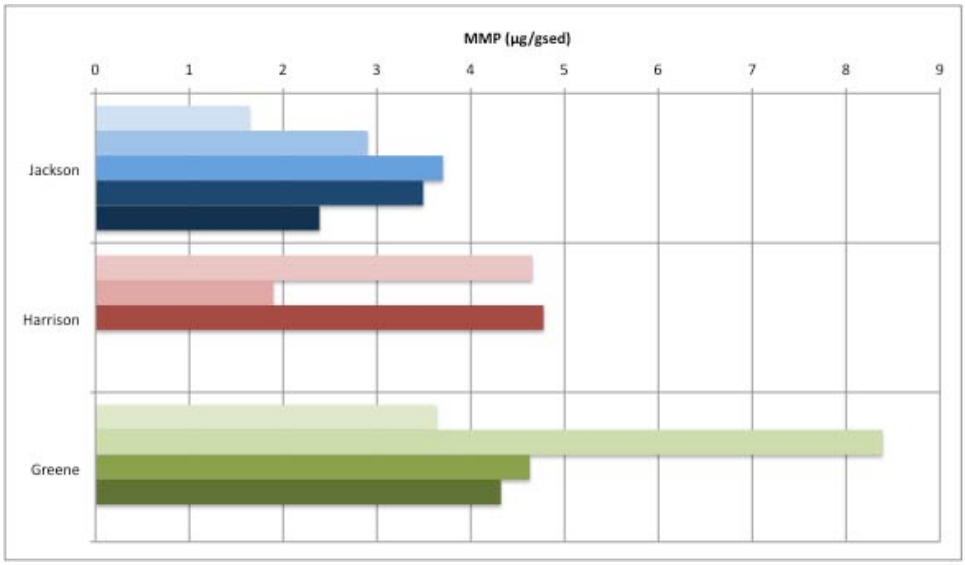


Figure 22. Abundance of monomethylphenanthrenes (MMP).

The relative abundance of various methylated naphthalenes and phenanthrenes reveals that there is no obvious trend in aromatic hydrocarbon absolute abundance with lateral distance or burial depth between the three cores. Thus biodegradation of aromatic hydrocarbons cannot simply be assigned as greater in one core compared to another along a trend that corresponds to burial depth. The high relative abundance of tetramethyl-substituted naphthalenes and phenanthrenes found in samples from Jackson County compared to both Harrison and Greene County suggests that biodegradation of aromatic hydrocarbons may be least extensive in Jackson County (see Figure 21), as mutiply-substituted aromatics are thought to be less susceptible to biodegradation. Within each core, the relative abundance of methylated aromatic hydrocarbons may suggest that biodegradation is uniform throughout the Harrison County section of the Clegg Creek Member of the New Albany Shale, may be most intense in the lowermost section of the Greene County core, and may be least intense in the middle section of the Jackson County core.

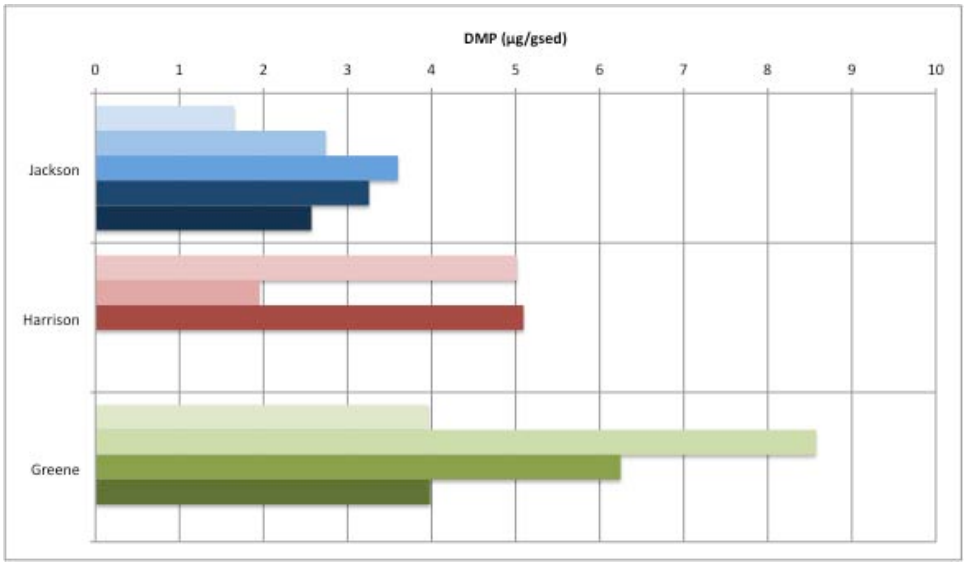


Figure 23. Abundance of dimethylphenanthrenes (DMP).

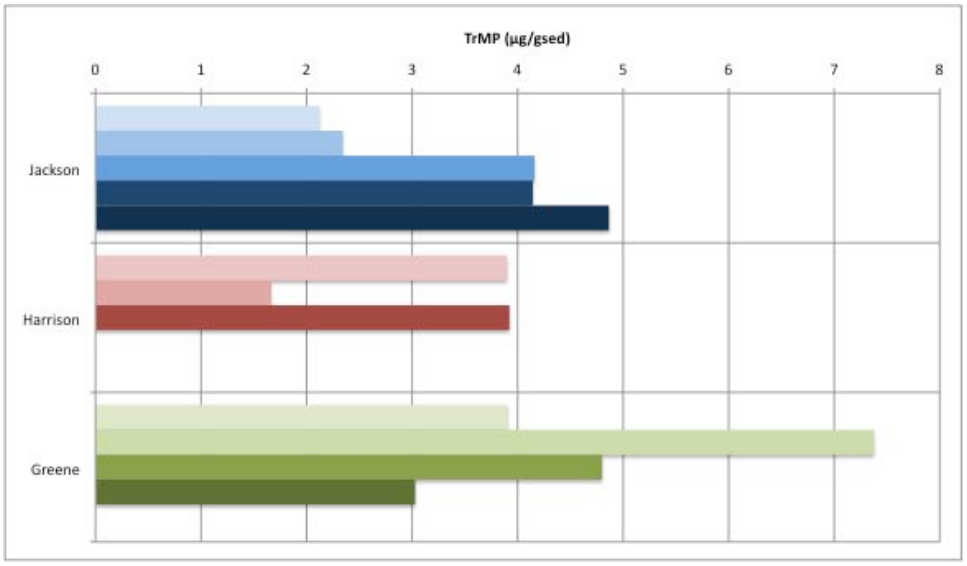


Figure 24. Abundance of trimethylphenanthrenes (TrMP).

Similar to the approach used to examine biodegradation of aliphatic hydrocarbons, ratios of the abundance of various aromatic hydrocarbon compound classes can be interpreted as biodegradation indices, in which differences in ratio values among samples reflect differing extents of biodegradation. Because hopanes are understood to be least susceptible to biodegradation, the ratio of hopane abundance to various compound class abundances provides a suite of indices in which greater numeric

values indicate greater extents of biodegradation. Other indices that calculate the abundance of methylated aromatic hydrocarbons to isoprenoids and *n*-alkanes similarly indicate extents of biodegradation. This ratio-index approach removes the bias of variations in the absolute abundance of compound classes among samples. Values of biodegradation indices reveal differences in biodegradation among the three cores examined in this study, as well as differences within each core that indicate where biodegradation at a single site may be most severe.

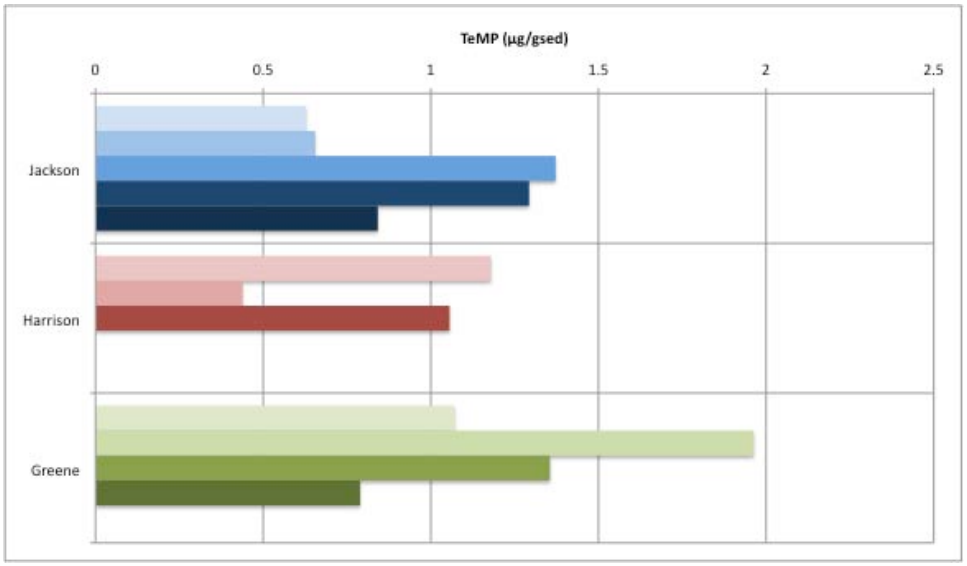


Figure 25. Abundance of tetramethylphenanthrenes (TeMP).

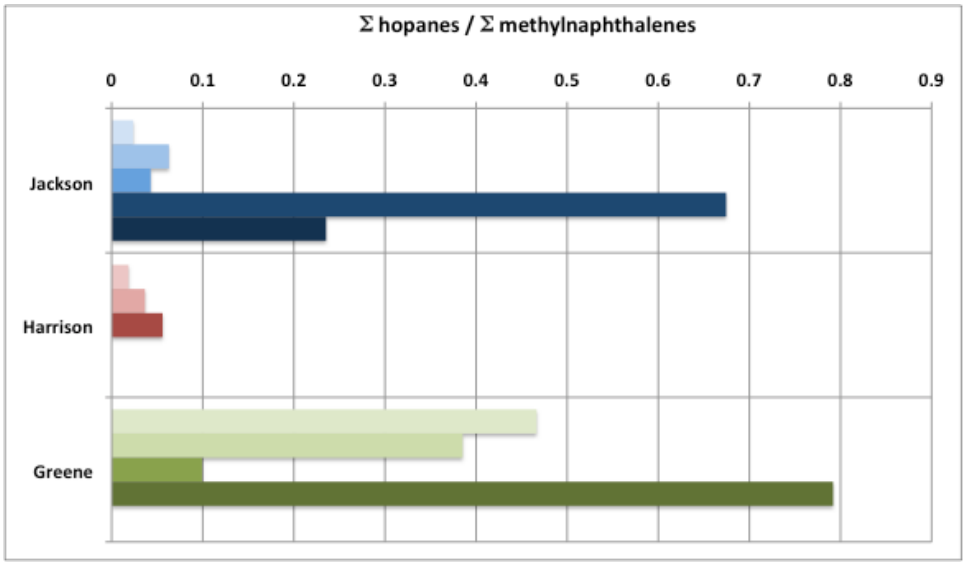


Figure 26. Biodegradation index of total hopane to total methylated naphthalenes.

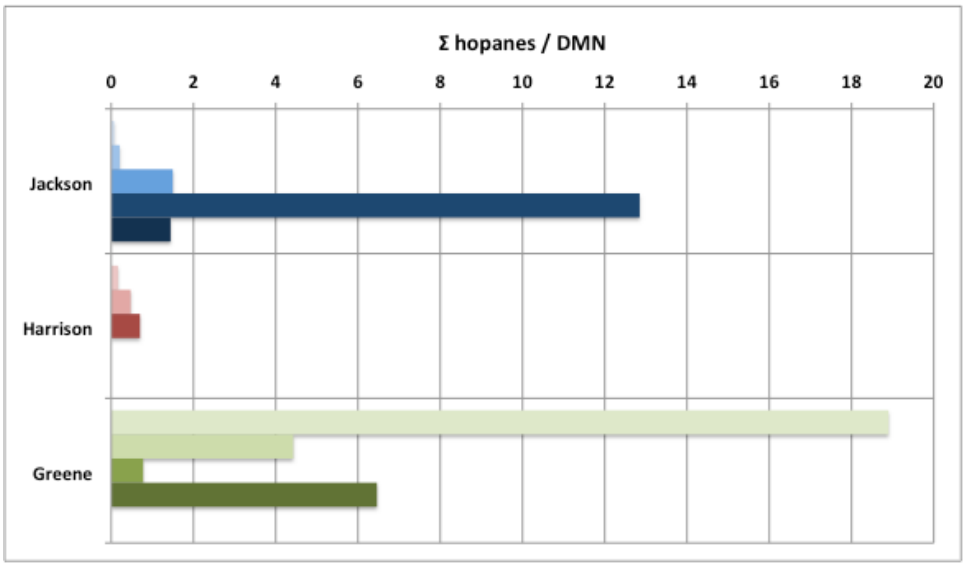


Figure 27. Biodegradation index of total hopanes to DMN.

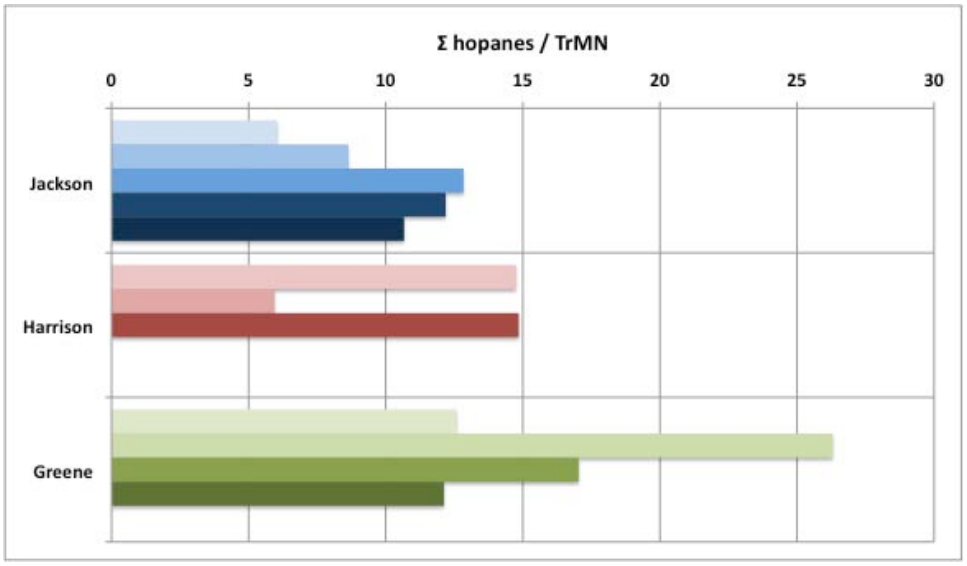


Figure 28. Biodegradation index of total hopanes to TrMN.

The ratio of total hopanes to total methylated naphthalenes varies from low values in samples from Harrison County (mean = 0.04) to intermediate values in samples from Greene County (mean = 0.21) to highest values in samples from Jackson County (mean = 0.44) (Figure 26). Similar trends emerge in evaluating total hopane abundance compared to abundance of DMN (Figure 27) (Jackson County mean = 7.64; Greene County mean = 3.21; Harrison County mean 0.45), hopanes/TrMN (Figure 28) (Jackson County mean = 0.93; Greene County mean = 0.54; Harrison County mean = 0.075), and hopanes/TeMN (Figure 29) (Jackson

County mean = 1.08; Greene County mean = 0.42; Harrison County mean = 0.09). Differences in hopane/methylated naphthalene biodegradation indices among different cores are most extreme in values calculated for dimethylnaphthalenes and converge to similar values among all cores for TrMN and TeMN, corroborating that biodegradation is most extensive among aromatic hydrocarbons with fewer methyl substitutions.

The ratio of total hopanes to total methylated phenanthrenes also varies (Figure 30), with lowest values in samples from Harrison County (mean = 0.015) to intermediate values in samples from Greene County (mean = 0.087) to highest values in samples from Jackson County (mean = 0.12). Similar trends emerge in evaluating hopane/MMP indices (Figure 31) (Jackson County mean = 0.36; Greene County mean = 0.33; Harrison County mean = 0.04), hopane/DMP (Figure 32) (Jackson County mean = 0.44; Greene County mean = 0.24; Harrison County mean = 0.05), and hopane/TrMP (Figure 33) (Jackson County mean = 1.66; Greene County mean = 0.97; Harrison County mean = 0.20).

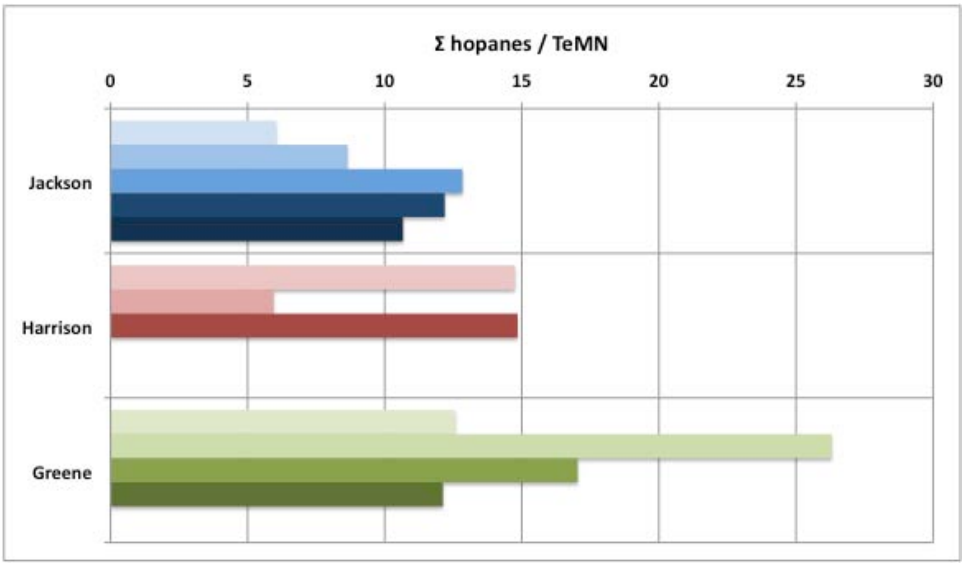


Figure 29. Biodegradation index of total hopanes to TeMN.

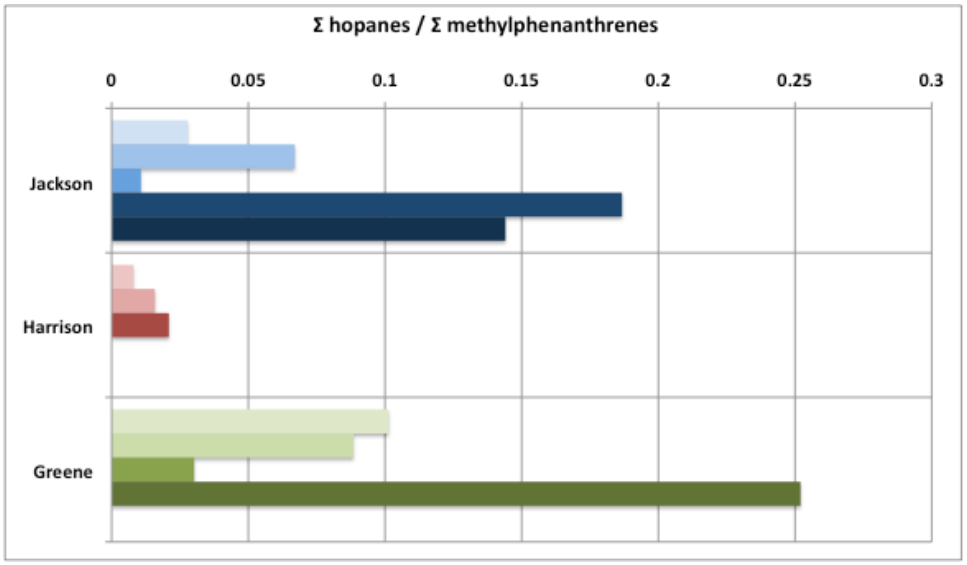


Figure 30. Biodegradation index of total hopanes to total methylated phenanthrenes.

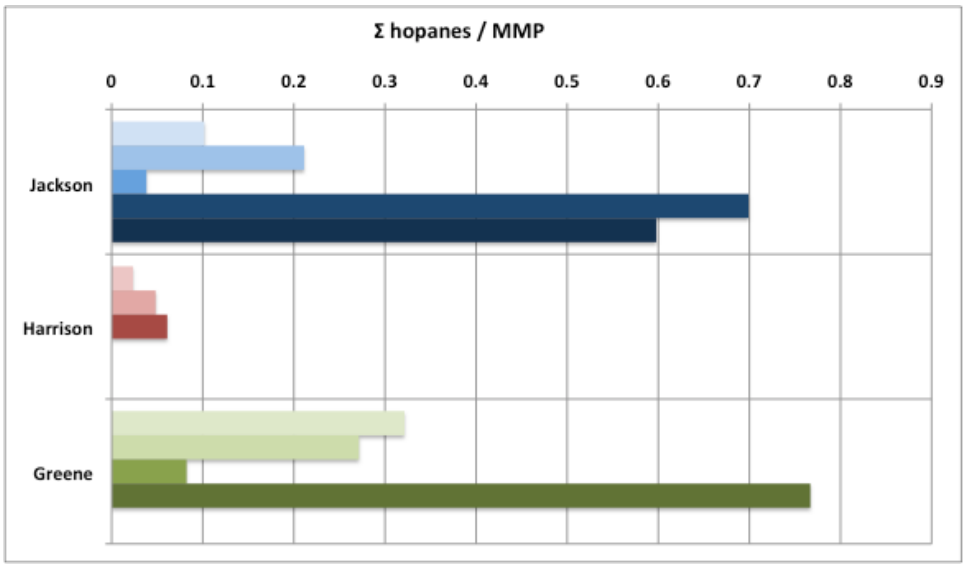


Figure 31. Biodegradation index of total hopanes to MMP.

Within each core, trends in aromatic hydrocarbon biodegradation indices are not obvious. Hopanes/methylated naphthalenes and hopanes/methylated phenanthrenes ratio appear to indicate

most intense biodegradation in the middle- to lower sections of the Jackson County core, and least intense biodegradation in the middle sections of the Greene County core (see Figures 26 and 30). However, these signatures are not smoothly varying with depth. Biodegradation indices are low and uniform throughout the Harrison County core.

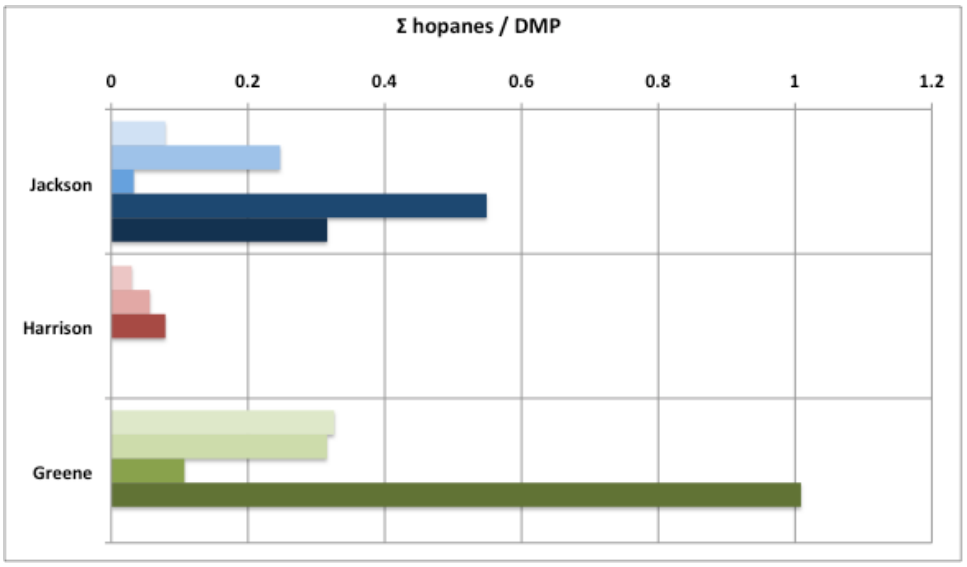


Figure 32. Biodegradation index of total hopanes to DMP.

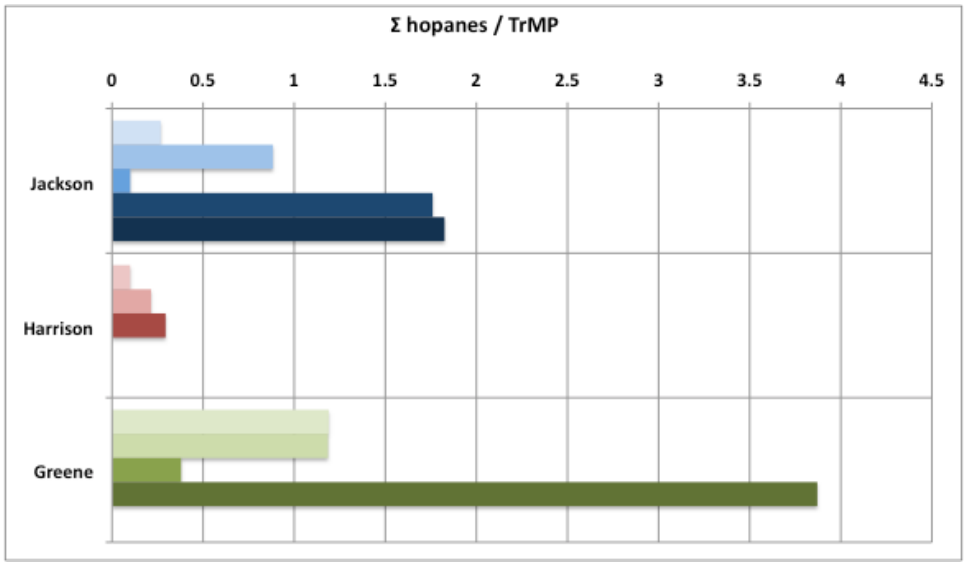


Figure 33. Biodegradation index of total hopanes to TrMP.

Aliphatic hydrocarbons are traditionally understood to be susceptible to biodegradation in shales and coals at rates greater than aromatic hydrocarbon biodegradation proceeds. However, recent research calls this assumption into question (Ahmed et al., 1999; Ahmed and Smith, 2001; Formolo et al., 2008), indicating that aliphatic and aromatic hydrocarbon biodegradation may occur simultaneously in methane-generating coals. Ratios of the abundance of aromatic to aliphatic hydrocarbons may reveal information about the intensity of hydrocarbon biodegradation not seen in comparisons to nominally non-degraded hopanes. For example, the ratios of total methylated naphthalenes+phenanthrenes to total *n*-alkane abundance (Figure 34) and to total isoprenoids abundance (Figure 35) are greatest in samples from Harrison County and lowest in Greene County. This pattern is not seen in the ratios of hopanes to these aromatic compounds. These trends can be interpreted as extensive hydrocarbon biodegradation in both Greene and Jackson Counties, in which differences in the relative abundance of hopane compared to aliphatic and aromative hydrocarbons are not longer apparent because both compound classes have been extensively lost through degradation, and the initial stages of biodegradation in Harrison County, in which *n*-alkanes are just beginning to be lost through biodegradation.

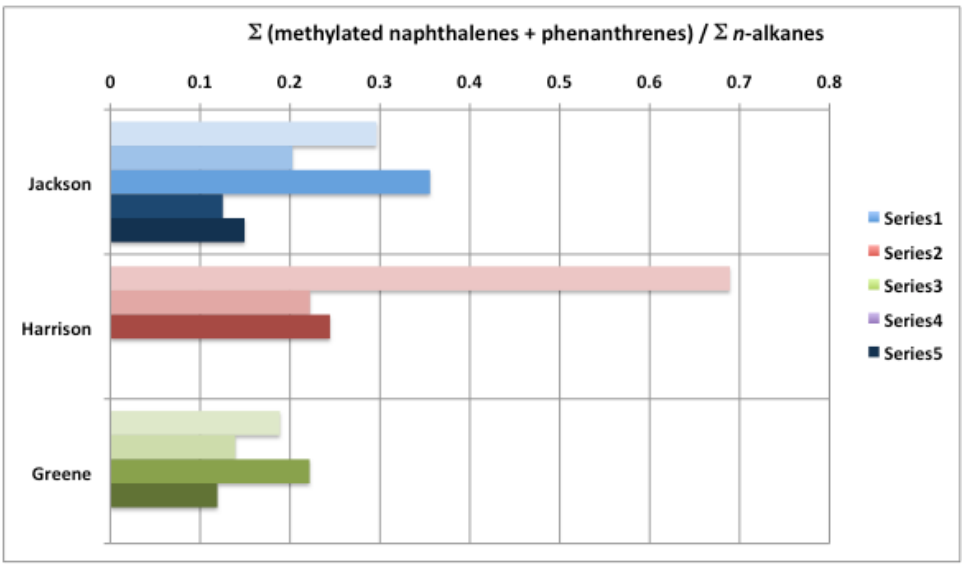


Figure 34. Biodegradation index of total methylated naphthalenes and methylated phenanthrenes to total *n*-alkanes.

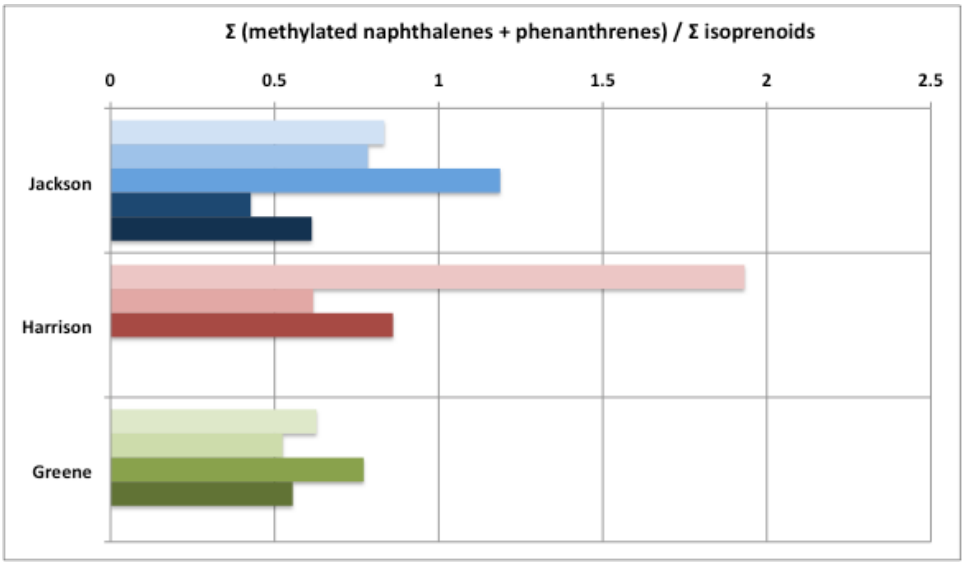


Figure 35. Biodegradation index of total methylated naphthalenes and methylated phenanthrenes to total acyclic isoprenoids.

2.5 Conclusions

The overall high abundance of *n*-alkanes, acyclic isoprenoids, and methylated aromatic hydrocarbons points to only weak biodegradation in the New Albany Shale at all three core locations in this study. Moderate or severe biodegradation would have shown more significant losses of *n*-alkanes, as well as selective loss of methylated naphthalenes and phenanthrenes with the least amount of methyl-group substitution. This conclusion is further supported by very low values for all biodegradation indices. For example, values for the hopane/Σ*n*-alkane biodegradation index are all less than 0.025, while values of biodegradation indices comparing hopane abundance to subclasses of *n*-alkanes are all less than 0.25 (in most cases, much less). This stands in contrast to results for biodegradation indices from biodegraded coals in the Powder River and San Juan Basins, where these biodegradation indices are 10- to 100-fold greater (Formolo et al., 2008a). Similarly, biodegradation indices for acyclic isoprenoids compared to *n*-alkanes range between 0.2 and 0.4 in these New Albany Shale samples, while similar indices calculated for the methane-generating Antrim Shale are 2-5 times greater (Formolo et al., 2008b). Biodegradation indices that compare hopanes to methylated aromatic hydrocarbons are also lower in these New Albany Shale samples compared to similar values in the gas-producing coal beds of the Powder River and San Juan Basins (Formolo et al., 2008a). In summary, while microbial gas generation has clearly occurred in the New Albany Shale, indicated via geochemical signatures in formation water and gas and the microbial ecology of the subsurface supporting a diverse community of Bacteria and methane-generating Archaea, this community has not been sufficiently active (compared to analogous communities in the Antrim Shale and coals from the Powder River Basin) to substantially alter the absolute and relative abundance of hydrocarbons in the New Albany Shale.

CHAPTER 3: THE NEW ALBANY SHALE: FORMATION WATER, GAS GEOCHEMISTRY AND THE SUBSURFACE BIOTIC COMMUNITY

Overview

The primary focus of this study was to investigate the microbial populations within and various environmental controls for the generation of methane in the New Albany Shale. Previous research had found most microbial gas generation to be associated with a plume of dilute waters sourced from Pleistocene meteoric recharge that penetrated deep into basinal brines (McIntosh et al., 2002). Biogenic gas indicators, associated with the depressed salinity include enriched $\delta^{13}C_{DIC}$ values (as high as 29.4‰), elevated concentrations of alkalinity (up to 29.4meq/kg), low SO_4^{2-} levels (<5mM), and a high percentage of CH_4 (up to 94.87%) with depleted $\delta^{13}C_{CH4}$ values (as low as -65.4‰; McIntosh et al., 2002). In contrast, thermogenic methane in western Kentucky, as well as the Antrim Shale in the Michigan Basin, is associated with increased salinity (>1.5MCl^-), $\delta^{13}C_{DIC}$ values ≤0‰, and low concentrations of alkalinity (<6meq/kg; McIntosh et al., 2002; McIntosh and Martini, 2008). Compilations from research of methanogenic environments in sedimentary basins world-wide have expanded the set of geochemical indicators for microbial methane in organic-rich reservoirs (e.g. Rice and Claypool, 1981; McIntosh and Martini, 2008) to include waters that have exceptionally high alkalinity and dissolved inorganic carbon (DIC) values (up to 70 meq/kg), enriched $\delta^{13}C_{DIC}$ values (>+20‰), low Ca/Mg ratios (<1.5), low concentrations of SO_4^{2-} (<10mM) and acetate (<1mM), high percentages of CO_2 (>1%), low percentages of O_2 (anoxic conditions), and low percentages of C_{2+} hydrocarbons (<2%). Importantly, microbial methanogenesis is also associated with a co-variance of δD values of methane and water, demonstrating that the microbes use water to produce methane *in situ* (Schoell, 1980; McIntosh et al., 2002). The combination of geochemical indicators with microbial studies from organic-rich reservoirs has demonstrated that microbial methanogenesis has produced economic accumulations of natural gas in several sedimentary basins world-wide, including the Illinois Basin. This study adds to the geochemical database a direct identification of the microbial population now present in this reservoir. For each selected well, complete geochemical and isotopic analysis were also performed to allow comparisons

between the signals of microbial activity in the water and gas produced and the actual consortium of organisms present.

Microbiological Investigation of a Natural Gas-Rich Black Shale

Elucidation of the geochemistry of biogenic shale gas systems has not been accompanied by a thorough investigation of the microbial community structure responsible for degradation of shale organic matter into methane, although researchers and companies have long speculated that methanogens may pressurize underproducing petroleum wells and coal beds with natural gas (Gray et al., 2009; Jones et al., 2008; Bhupathiraju et al., 1993). The present study characterizes the microbial community structures of eight New Albany Shale sites in southwestern Indiana and northern Kentucky as well as two coal beds in Illinois and Indiana. All ten sites produce economic quantities of natural gas. Few previous studies of subsurface methanogenic communities have focused on sedimentary basins, and none have compared a large number of sites in gas-rich shales over a wide geographic area (Takai et al., 2003; Krumholz et al., 1997; Waldron et al., 2007; Huang, 2008). Some recent studies have analyzed the microbial community structure of coal bed methane accumulations, including the Powder River Basin of Wyoming, coal beds in Alberta, and one Illinois Basin coal bed (Green et al., 2008; Penner et al., 2010; Strapoc et al., 2008).

Comparison of microbial DNA sequences from environmental samples with publically available reference sequences provides information on the phylogenetic, or evolutionary, relationships between sampled organisms. These relationships uncover physiological and ecological characteristics of microbes without resort to difficult culture experiments (Woese, 1987). Microbial community determination through molecular phylogenetics also has the advantage of pseudorandom sampling, as opposed to culture experiments, which select for organisms adapted to the enrichment medium (Woese, 1987).

Microbial molecular phylogenetics frequently makes use of the sequence encoding for the 16S fragment of the ribosome (16S rDNA). All organisms of the two microbial domains of life, Bacteria and Archaea, share this gene, yet distinct differences between the 16S genes in each domain necessitate the separate sequencing of bacterial and archaeal 16S rDNA. The 16S gene, known as a molecular clock, evolves at a relatively constant rate and therefore allows for the reconstruction of evolutionary relationships between disparate organisms (Woese, 1987). Comparison of 16S gene sequences enables estimation of the degree of evolutionary divergence between organisms and inference of a common ancestor. On a phylogenetic tree, the ends of branches represent sampled organisms and are called operational taxonomic units (OTUs), while branching points (internal nodes) represent inferred common ancestors.

Materials and Methods

Sample Collection

This study integrates aqueous and gas geochemistry data collected from the New Albany Shale in July 2009 with a larger dataset collected by Schlegel and coworkers from 2004-2008 and McIntosh and coworkers through 2002. The expanded dataset encompasses the New Albany Shale, coal beds, and surrounding aquifers in the Illinois Basin. Natural gas extraction companies provided well log data, including formation depths, total well depths, surface level elevations, and water and gas production rates.

Natural gas wells in the expanded dataset are located in Illinois, Indiana, and Kentucky. The July 2009 sampling effort focused on Sullivan and Knox Counties in western Indiana, Harrison and Meade Counties in southern Indiana and northwestern Kentucky, respectively, and Christian County in west-central Kentucky. The GPS locations of the 33 wells sampled in these counties are shown in Figure 1. We collected water samples at 20 wells and natural gas samples at 27 wells.

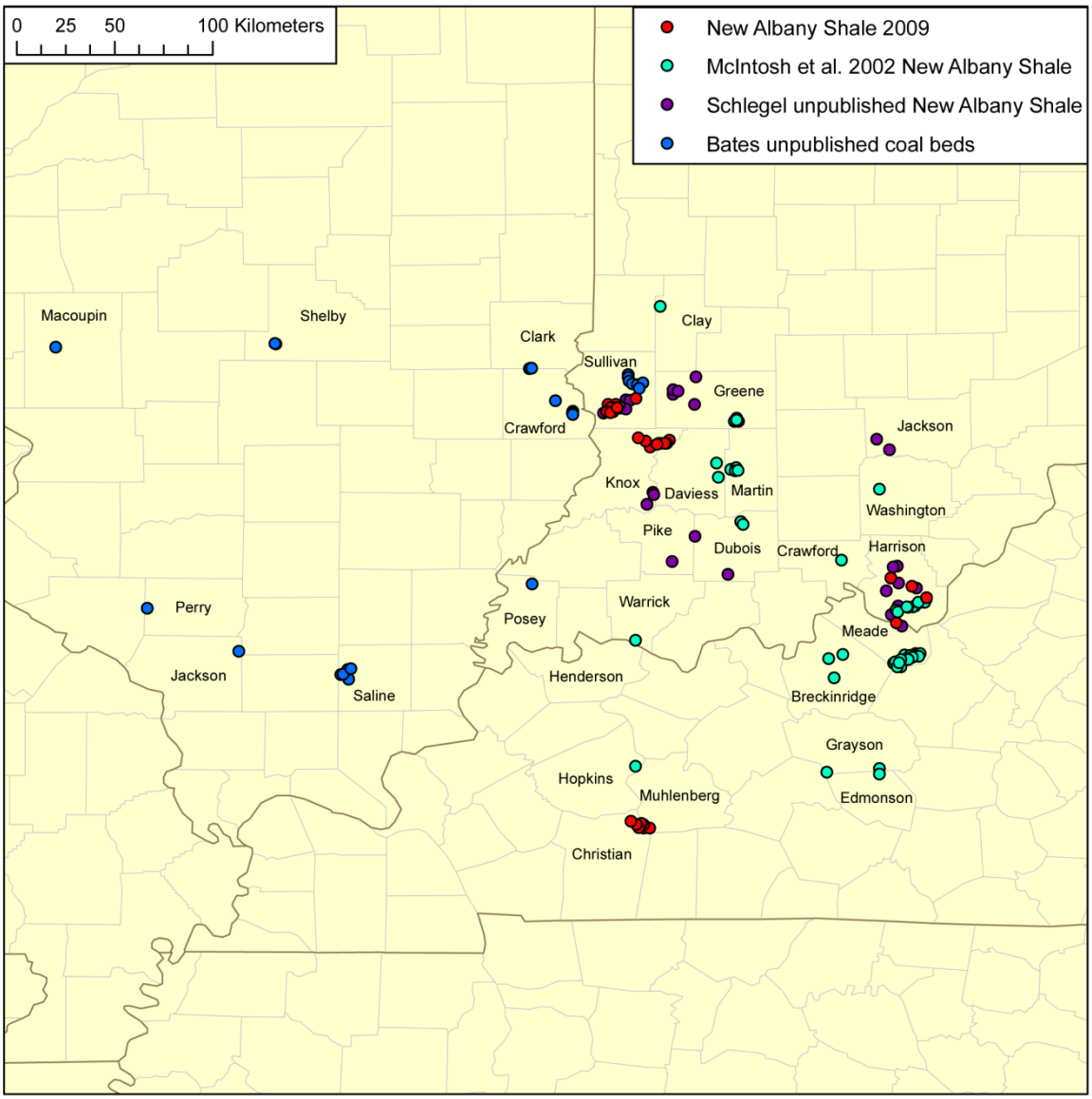


Figure 1: Map of all well locations in the expanded dataset.

Formation water samples were collected from the wellhead, with temperature and pH measured immediately. Samples were filtered through 0.45 µm nylon filters (Fisher Scientific, Pittsburgh, PA) and preserved as follows: alkalinity, major and trace cation, and anion samples were stored in polyethylene Nalgene bottles (Thermo Fisher Scientific, Rochester, NY) with no head space; cation samples were acidified with nitric acid, to inhibit microbial growth prevent chemical reactions; dissolved organic carbon (DIC) and carbon isotope samples were stored in glass serum bottles and treated with $CuCl_2$ to inhibit

microbial growth; and hydrogen/oxygen isotope samples were stored in glass scintillation bottles. All formation water samples were immediately stored on ice, and refrigerated in the laboratory prior to use. Alkalinity measurements were made within hours of sample collection by titration with 0.1 M HCl, using a Contiburette µ10-c digital burette (Finemech Inc., Portola Valley, CA), and entering titration data into an online alkalinity calculator (USGS Oregon Water Science Center; http://or.water.usgs.gov/alk/). DIC contributes the majority of the alkalinity of NAS formation waters, as levels of acetate and hydrogen sulfide are low. Given moderate formation water pH values of 6.31-7.47 and high chloride concentrations of 889-2077 mM, the principal DIC species is bicarbonate (McIntosh et al. 2002).

Microbial samples were collected by filtering formation water through sterile 0.2 µm Isopore membrane filters (Millipore, Billerica, MA) until the filters clogged (typically 100-300 mL). Samples were placed immediately on ice and were stored at -20°C upon return to the laboratory.

Gas samples were taken from the wellhead using IsoTubes (Isotech Laboratories, Champaign, IL), following the manufacturer's instructions. Tubes were thoroughly flushed prior to sample collection, and capped immediately after collection. Isotube samples were sent to Isotech Laboratories for bulk compositional and isotopic analysis.

Laboratory Measurements

In the laboratory, we measured the density of water samples from each well. Anion concentrations were then analyzed on a Dionex DX 500 ion exchange chromatography system (IC). In the variant of IC that measures anion concentrations, a positively charged resin coats beads in the chromatography column. Anions from the analyte bind to the resin until higher anion concentrations in the eluent displace them. Elution occurs at different times for different anions in the analyte based on the acid dissociation constant (pK_a) of the conjugate acid. For instance, formate elutes earlier than chloride, because the pK_a of formic acid is 3.7, whereas the pK_a of hydrochloric acid is -8.0. In our analysis, 0.5 M Na_2CO_3 was used as the eluent. Carbonate/bicarbonate buffers are commonly used for the separation of inorganic anions. The IC system neutralizes the eluent with a suppressor, reducing the background conductivity and lowering the detection limit. We used one concentration of eluent (isocratic) and not a gradient because of our choice of Na_2CO_3. Field aliquots were prepared for IC by a 1:50 dilution with distilled deionized water (DDI). Dilution drove the concentrations of certain anionic species likely present, such as acetate and bromide, below the detectable limit.

Major cation concentrations (Na^+, Ca^{2+}, Mg^{2+}, K^+, and Sr^{2+}) were measured in the Martini lab using inductively coupled plasma-atomic emission spectroscopy (ICP-AES) on a Leeman Labs Direct Reading Echelle instrument. ICP-AES measures cation abundances by comparing the intensity of characteristic atomic emissions in a sample to those in a standard. We used four standards containing varying cation concentrations to interpolate sample concentrations. Software automatically performs calibration to the standard. Atomic emissions spectra are produced when excited electrons in the ionized sample return to the ground state. The high temperature of the argon plasma ionizes the nebulized sample. Passage of an electrical current through argon gas in a strong electromagnetic field initially transforms the gas into plasma at a temperature of nearly 10000 K. The Direct Reading Echelle is a grating that separates emissions spectra by wavelength and intensity, allowing measurement of specific atomic concentrations, even among overlapping spectral lines.

Trace cation concentrations (Fe, Ba, Mn, Al, V, Cr, Co, Ni, Cu, Zn, As, Mo, Ag, Pb, U) were measured in the Martini laboratory using inductively coupled plasma-mass spectrometry (ICP-MS) on an Agilent 7500 ce instrument. Sample introduction is the same for ICP-AES and ICP-MS – a high-temperature plasma flame ionizes the nebulized sample. In MS, an ion lens then transmits positively charged ions to the octopole reaction system. In this cell, He collides with interfering polyatomic molecules, breaking the molecules into ions separable in the quadrupole mass analyzer. Application of different voltages across the four metal rods of the quadrupole selects for ions with varying mass to charge ratios. Other ions collide with the rods and do not reach the detector. The detector produces a mass spectrum by measuring the current induced by ions with specific mass to charge ratios. Comparison of sample to standard measurements allows for quantification of concentration data. We used multiple standard solutions to minimize specific mass interferences in calibration. Regression lines were generated from standards data. The lowest R^2 value of a regression line was 0.9481 for Al. We did not analyze boron, because the regression line for that element's standard did not have a mass to charge ratio of approximately zero at a boron concentration of zero. No samples had concentrations higher than the detectable limit for a number of elements (Be, Cd, Se, Tl, Th, and W).

Microbiology Methods

Two approaches were taken to study the microbial community structure in the NAS. The first was using TRFLP techniques for a overview of the diversity profile. The second was species identification using DNA sequencing methods.

TRFLP Methods

DNA samples were analyzed for TRFLP at the Department of Biology Laboratory, University of New Mexico to determine microbial diversity (Liu et al., 1997). TRFLP data was obtained for 1 shallow aquifer sample (screened in glacial drift), 9 coal samples (plus one duplicate), 11 shale samples, and 1 limestone aquifer sample (screened in Devonian limestone). Because thermogenic gas wells rarely produce water, no thermogenic methane endmembers for TRFLP analysis were obtained. DNA was extracted from the sample filters using a MoBio UltraClean™ soil DNA kit. Generally the manufacturer instructions were followed, with the exception of excluding the bead-beating step (to limit shearing of DNA molecules), which was replaced by moderate vortexing for 5 seconds to mix the samples. Each sample was then incubated each for 10 minutes at 70°C. Archaeal 16s rRNA gene fragments were amplified using the primer pair 109F-915R (Grosskopf et al., 1998) in 50µL PCR reactions with a Promega *Taq* DNA polymerase. Because primers were specific for archaea, the 16S rRNA genes that were amplified are unlikely to be exclusively methanogens. Following PCR, the reaction products were purified with a Qiagen PCR purification kit, and then DNA concentration and purity were quantified using a NanoDrop 2000c spectrophotometer. Subsequently, 100ng of purified PCR product were digested using Promega restriction enzyme *HhaI* according to manufacturer instructions and then were purified using an ethanol precipitation. The dried DNA fragments were re-suspended and denatured by adding 10µL of formamide and 0.20µL of BioVentures, Inc. Mapmarker™ 1000 size standard and incubating at 95°C for 10 minutes. The fragments were analyzed on an Applied Biosystems 3130xl Genetic Analyzer and sized with Applied Biosystems GeneMapper™ (v 4.0) software. To statistically compare samples, the TRFLP data was manipulated following two methods. One method, described in Rees et al. (2004), eliminates peaks less than 1% of the total normalized area for each sample, and then aligns peaks by rounding the base pair size. This method retained the maximum variability in the TRFLP fingerprint for each sample. The other method, described in Abdo et al. (2006), eliminates peaks less than 1% of the total normalized area for each sample, and then aligns peaks by combining base pair lengths within ±1 base pair into the same group, greatly reducing variability between samples. The two data sets were imported into the multivariate statistical software package, Primer v6 (Primer-E Ltd, Plymouth, UK) to compare methanogen communities in the different samples and organic-rich reservoirs via non-metric multi dimensional scaling (MDS), an analysis of similarity (ANOSIM), similarity percentages (SIMPER), and dispersion indices as described in Rees et al. (2004).

DNA Extraction, Amplification

DNA was extracted from the filters using the MoBio UltraClean soil DNA kit (MoBio Laboratories, Carlsbad, CA), following the manufacturer's instructions but substituting a 5 second vortex and 10 minute incubation at 70°C instead of the bead-beating step, to prevent excess shearing of the DNA. Extracted DNA was stored at -20°C.

Archaeal 16S rRNA gene fragments were amplified with polymerase chain reaction (PCR; Saiki et al. 1988) using the primers 109F (5'-ACK GCT CAG TAA CAC GT-3') and 915R (5'-GTG CTC CCC CGC CAA TTC CT-3'; Grosskopf et al. 1998); numbers correspond to the position of the primer on the 16S gene of *E. coli*. PCR reactions were 50 µL and included 1.25 units/µL GoTaq Flexi polymerase (Promega Corp., Madison, WI), 0.20 mM deoxyribonucleotide triphosphates (dNTPs), 1.5 mM $MgCl_2$, and 30 ng bovine serum albumin (BSA), and were performed in an Applied Biosystems 2720 Thermal Cycler (Life Technologies Corp., Carlsbad, CA) using the following program: denaturation at 94°C for 5 minutes, 30 cycles at 94°C for 30 seconds, at 52°C for 30 seconds, and at 72°C for 1 minute 30 seconds, and a final elongation at 72°C for 7 minutes. Bacterial 16S rRNA fragments were amplified using the primers 8F (5'-AGA GTT TGA TCM TGG CTC AG-3') and 1492R (5'-GGT TAC CTT GTT ACG ACT T-3'; Reysenbach et al. 1994), with reactions otherwise identical to those described for archaeal amplifications. Bacterial amplifications were performed using the following program: denaturation at 94°C for 5 minutes, 30 cycles at 94°C for 30 seconds, at 50°C for 30 seconds, and at 72°C for 1 minute 30 seconds, and a final elongation at 72°C for 7 minutes.

The quantity and length of completed PCR reactions was visually checked via gel electrophoresis, using 50 mL of a 1.0% agarose solution (0.5 g agarose, 50 mL Tris/Borate/EDTA buffer, 5 µL ethidium bromide); 1.0 µL of a PCR reaction solution was combined with 2.0 mN loading buffer and was run on the gel for 45 minutes at 60 volts. Bands on a gel were visualized with an ultraviolet light. Samples with low yields or bands at incorrect lengths were discarded

Cloning and Sequencing, Phylogenetic Tree Construction

PCR products containing strong bands of the desired length were purified using the MinElute PCR Purification kit (Qiagen Inc., Valencia, CA), following the manufacturer's instructions, and were stored at -20°C. Cleaned products were ligated for cloning using the TOPO TA Cloning kit and pCR2.1-TOPO vector (Invitrogen Corp., Carlsbad, CA), following the manufacturer's instructions. Ligation products were sent to the Genome Sequencing Center at Washington University (St. Louis, MO), where transformation, cloning, and sequencing was performed.

Upon return, sequences were manually edited, the cloning vector sequence was removed, and imprecise sequence ends were clipped using CodonCode Aligner (version 3.5.2; CodonCode Corp., Dedham, MA). OrientationChecker (Ashelford et al. 2000) was used to put the sequences in the same orientation, and Greengenes (DeSantis et al. 2006) was used to create multiple sequence alignments, identify and eliminate chimeras using Bellerophon (version 3 as implemented in Greengenes; Huber et al. 2004), and assemble distance matrices. Using Mothur (version 1.8.0; Schloss et al. 2009), operational taxonomic units (OTUs) were defined at 97% sequence similarity (Schloss and Handelsman 2005), and representative clones from each OTU were selected and manually assembled into a single alignment. Sequences is this alignment were aligned with the Fast Aligner Tool as implemented in ARB (version 5.1; Ludwig et al. 2004), manually edited, and added to the most recent Greengenes ARB database (published November 2008) using ARB Parsimony. Reference sequences were manually selected, and both reference and OTU-representative sequences were exported as a single alignment. Phylogenetic trees were grown in PAUP* (version 4.0b10; Sinauer Associates, Sunderland, MA; Swofford 2002) using a neighbor-joining algorithm, and 1000-replicate neighbor joining bootstrap analyses were performed. Nodes with a bootstrap value <70 were collapsed.

Results

Appendix A contains the water and gas compositional and isotopic data for this report.

Carbon Stable Isotopes in Methane

The carbon stable isotopic signature of methane can distinguish between microbial and thermal sources. Typical $\delta^{13}C_{CH_4}$ values of biogenic methane range from -110‰ to -50‰, and typical thermogenic values range from -50‰ to -20‰ (Whiticar, 1999). Exceptions to these classifications exist in shallow sedimentary basins, where immature (low-temperature) thermogenic methane commonly exhibits $\delta^{13}C_{CH_4}$ values of less than -50‰. Biogenic methane may have $\delta^{13}C_{CH_4}$ values of greater than -50‰ where relatively closed hydrologic systems allow for the build up of ^{13}C-rich HCO_3^-, as in the New Albany Shale (Martini et al., 1998; McIntosh et al., 2002). Methanogens preferentially metabolize lighter carbon substrates, leading to ^{13}C depletion relative to ^{12}C in the methane they produce. A number of factors determine specific $\delta^{13}C_{CH_4}$ values of biogenic methane, including the $\delta^{13}C$ value of the carbon precursor, the metabolic pathway used in methanogenesis, and environmental variables influencing metabolic efficiency, such as temperature, pH, and hydrogen gas concentration (Whiticar et al., 1986). The temperature of pyrolysis and $\delta^{13}C$ value of the source largely determines specific $\delta^{13}C_{CH_4}$ values of thermogenic methane, with lower values characteristic of immature gases. To further complicate reliance on $\delta^{13}C_{CH_4}$ values as an indicator of gas origin, microbial hydrocarbon oxidation raises $\delta^{13}C_{CH_4}$ values and is thought to occur in the New Albany and Antrim Shales (Whiticar, 1999; Martini et al., 2003; Martini et al., 2008).

The gas samples we collected from the eastern margin of the New Albany Shale have $\delta^{13}C_{CH_4}$ values ranging from -54.27‰ to -49.13‰, with an average value of -52.0‰. Other studies of the same area report values ranging from -64.30‰ to -45.03‰, with an average value of -52.0‰ (McIntosh et al., 2002; Schlegel, unpublished). The observed distribution of New Albany Shale $\delta^{13}C_{CH_4}$ values is remarkably similar to the distribution of $\delta^{13}C_{CH_4}$ values observed in the margins of the Antrim Shale, suggesting that similar processes are responsible for methane formation in both basins (Figure 2) (Martini et al., 1998; Martini et al., 2003). Excluding one anomalously low value from a sample collected by Schlegel in 2008 (-64.30‰), the minimum $\delta^{13}C_{CH_4}$ value in both formations is about -58‰. In addition, both distributions have a significant left-skew and very few values greater than -47‰. Analysis of the

distribution of $\delta^{13}C_{CH_4}$ by geographic area reveals relatively higher values in western Indiana (average of -49.9‰ for 27 samples from Sullivan and Knox Counties) and relatively lower values in southern Indiana and northern Kentucky (average of -53.4‰ for 22 samples from Harrison and Meade Counties) (Figure 3).

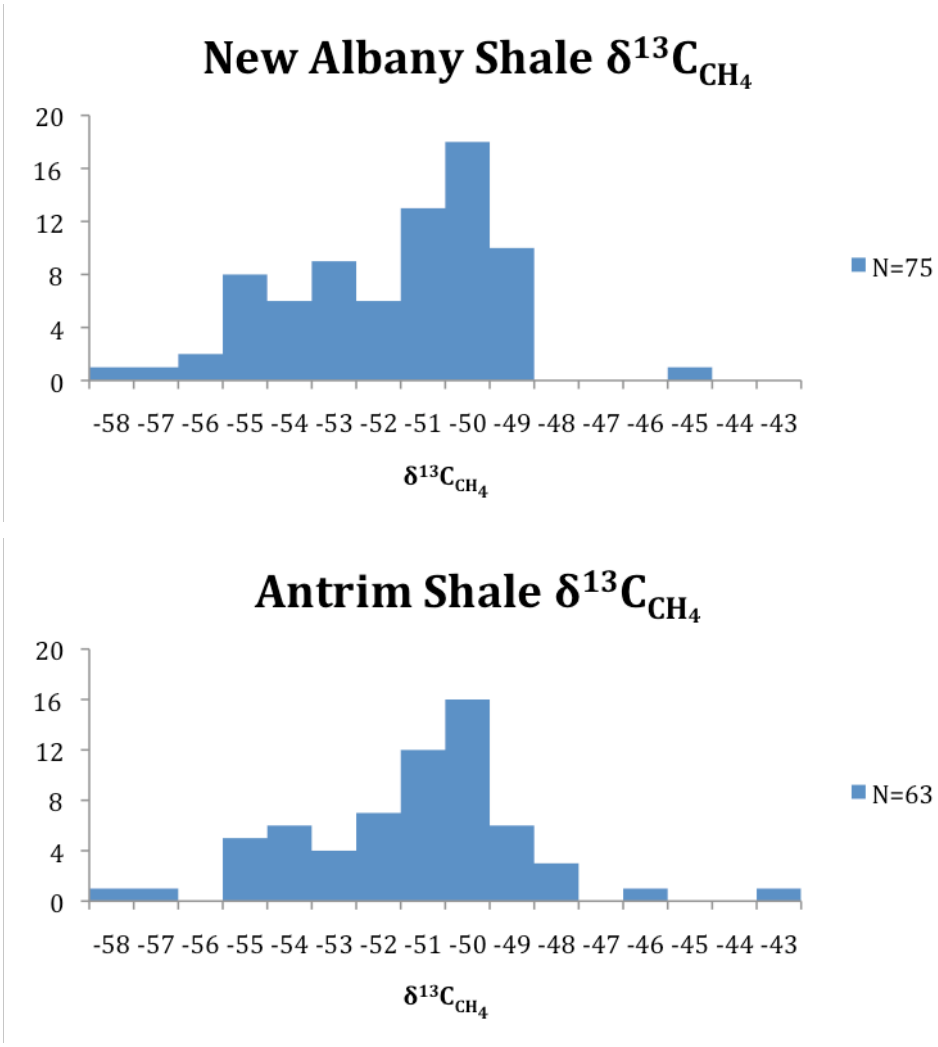
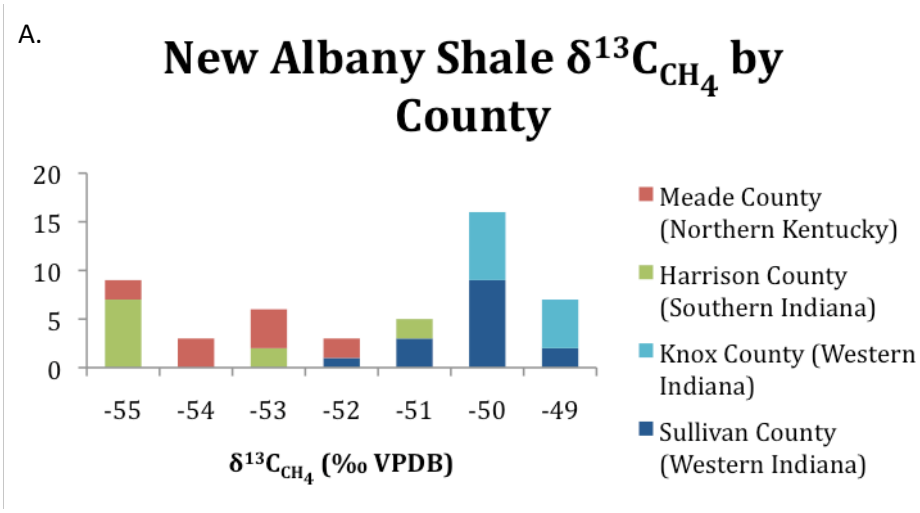


Figure 2: Histograms of all reported $\delta^{13}C_{CH4}$ values of samples collected from the margins of the Antrim Shale and the eastern margin of the New Albany Shale (Martini et al., 1998; Martini et al., 2003; McIntosh et al., 2002; Schlegel, unpublished).

A.



B.

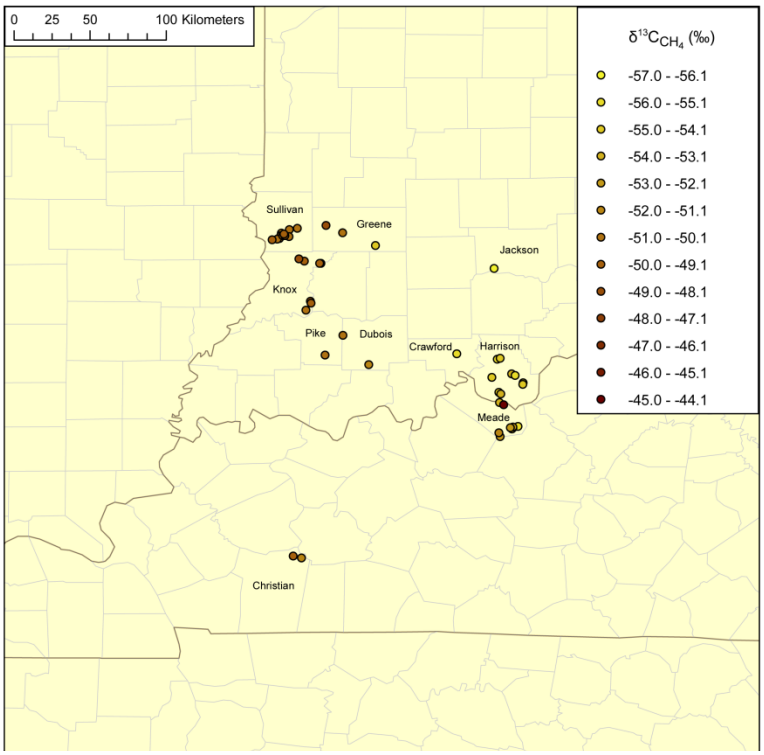


Figure 3: A. Histogram of $\delta^{13}C_{CH4}$ values for the four most heavily sampled counties in the field area (McIntosh et al., 2002; Schlegel, unpublished). B. Map of $\delta^{13}C_{CH4}$ values at sampled sites. Note the relatively higher $\delta^{13}C_{CH4}$ values in western Indiana and relatively lower values in southern Indiana and northern Kentucky.

$\delta^{13}C_{CH4}$ values of thermogenic methane in the eastern margin of the New Albany Shale are anomalously low compared to the typical minimum of about -50‰ (Martini et al., 2008). (Geochemical

evidence for the thermogenic origin are presented below.) The eastern margin of the New Albany Shale, based on its temperature and pressure history, would not normally be expected to produce thermogenic methane (Werner-Zwanziger et al., 2005). Metamorphism of shale kerogen, or insoluble organic matter, into oil and natural gas occurs in a "generation window" of thermal maturity. In general, vitrinite reflectance (R_o) greater than 0.7% indicates that kerogen lies within the generation window (Werner-Zwanziger et al., 2005). Vitrinite reflectance for the New Albany Shale in our field area is generally less than 0.7%, and cores extracted in western Indiana have R_o values of about 0.6% (Werner-Zwanziger et al., 2005) (Figure 4). Despite the thermal immaturity of the western margin of the New Albany Shale, natural gas produced at many wells in the area has the chemical fingerprint of thermogenic gas (both in $\delta^{13}C_{CH4}$ and indicators such as low HCO_3^-). Moreover, shale less thermally mature than the New Albany (R_o < 0.4%) has been known to generate thermogenic gas, possibly due to transition-metal or mineral catalysis (Rowe and Muehlenbachs, 1999).

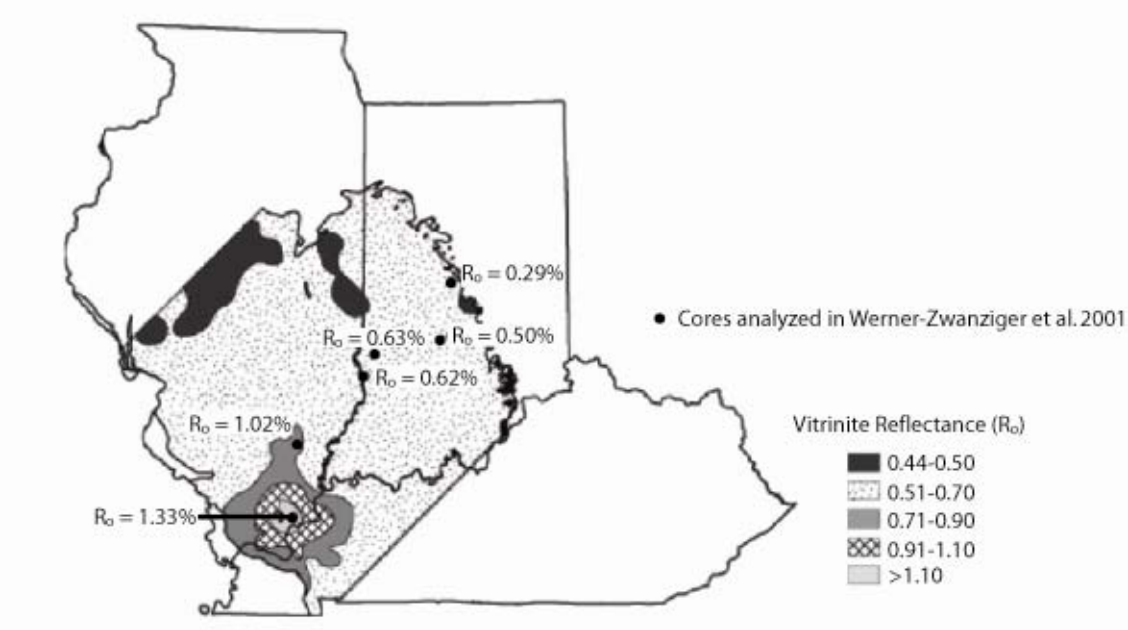


Figure 4: Vitrinite reflectance in the eastern margin of the New Albany Shale is lower than the typical "generation window" of 0.7%, although other geochemical evidence indicates the presence of thermogenic methane (R_o values are averages for each core; modified from Werner-Zwanziger et al., 2005).

Variations in $\delta^{13}C_{CH4}$ values observed between geographic areas and between biogenic and thermogenic methane have several potential explanations. One possible cause for variability between sites involves kinetic isotope fractionation during gas desorption from shale organic matter (Zhang and Krooss,

2001). Large amounts of methane and carbon dioxide are absorbed onto organic matter in the New Albany Shale. Many wells pump water out of the formation to reduce pressure and desorb natural gas. Production histories show that as water outflow levels out over time, the rate of natural gas extraction slowly falls from its peak (Figure 5). In the Antrim Shale, approximately 70-75% of extracted gas desorbs from the shale, and the rest comes out of pore space and fractures (Martini et al., 2003). A similar production pattern exists in the New Albany Shale, as indicated by the inverse relationship between water and gas production rates (Curtis, 2002).

Methane absorbed to shale has lower $\delta^{13}C_{CH_4}$ values than gaseous methane in solution, although an experiment conducted on a shale sample with total organic carbon (TOC) content of 5.74% only found a -1.37‰ equilibrium fractionation between gaseous and absorbed methane (Zhang and Krooss, 2001). The New Albany Shale has up to 15% TOC content in the uppermost Clegg Creek member (McIntosh et al., 2002). Higher levels of TOC are expected to produce a larger equilibrium fractionation between gaseous and absorbed methane (Zhang and Krooss, 2001). Initial extraction efforts remove ^{13}C-depleted gaseous methane from pore spaces and fractures. As continued production dewaters the shale and lowers pressure in the formation, $\delta^{13}C_{CH_4}$ values of the desorbed methane increase (Zhang and Krooss, 2001). Variability in the isotopic composition of methane with pressure in the formation complicates comparison of $\delta^{13}C_{CH_4}$ values between sites with different production histories.

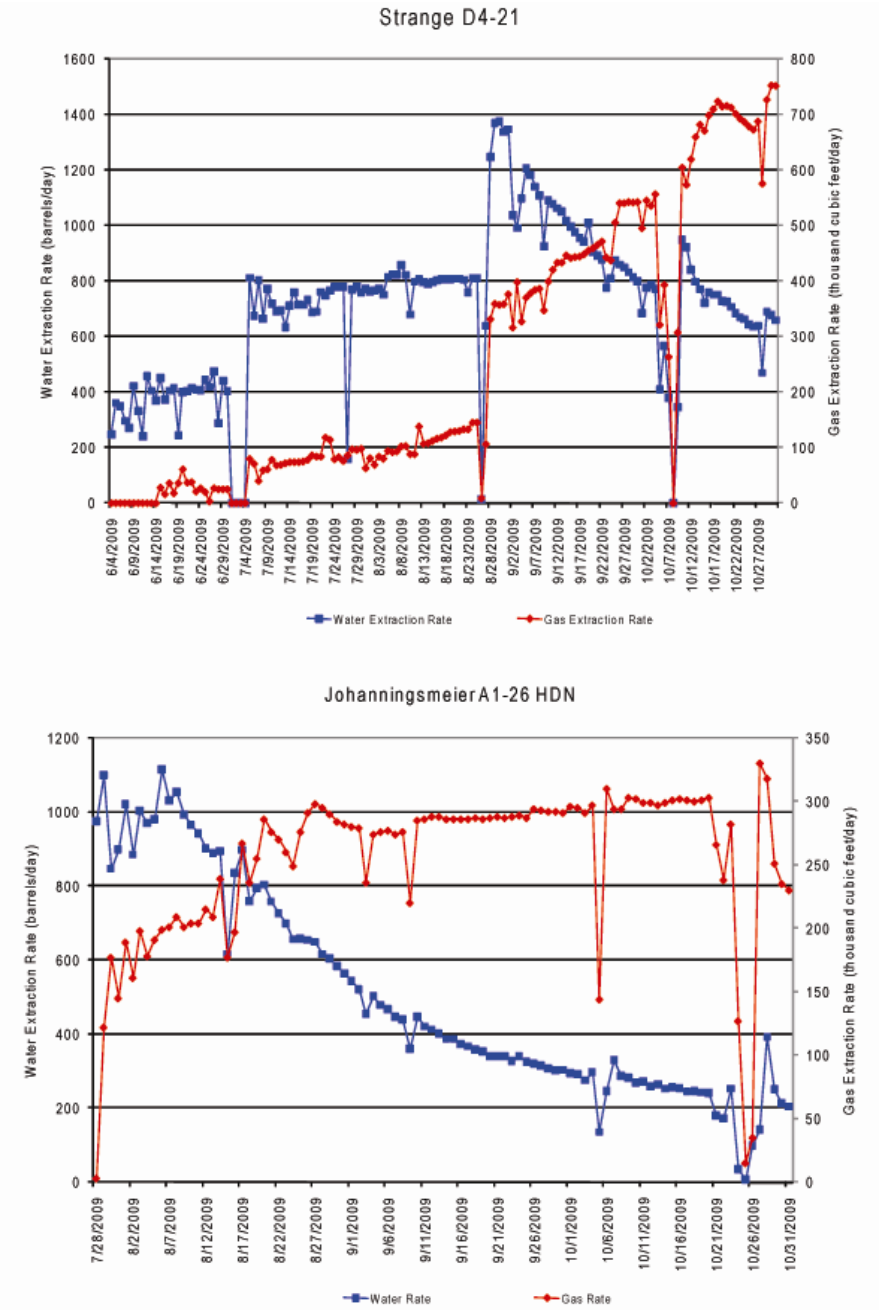


Figure 5: Inverse relationship between water and gas extraction rates at two sampled wells. As the water extraction rate increased over time at Strange, extraction rate of sorbed gas also increased. At Johanningsmeier, water and gas extraction approached steady state.

phic and source differences in $\delta^{13}C_{CH_4}$ values (Whiticar, 1999). Oxidation of C_{1-5} hydrocarbons both decrease the concentration of these gases, and also leave behind a ^{13}C-enriched residual that can be mistaken as a more thermogenically mature gas component. It is interesting to note that the oxidation is usually not observable with respect to methane in the produced gas. This is likely due to both there being a far greater amount of

methane available and that more is constantly being produced by the microorganisms in the shale (Martini et al., 2003; Martini et al., 2008). It may also be true that there is simply preferential oxidation of longer-chain hydrocarbons due to thermodynamic constraints. Microbial hydrocarbon oxidation of this variety should generate an isotopic effect. Favorable oxidation of three-carbon propane over two-carbon ethane and ethane over one-carbon methane leads to a relative increase in $\delta^{13}C$ for longer-chain versus shorter-chain hydrocarbons. Cross-plots of $\delta^{13}C_{CH_4}$ versus $\delta^{13}C_{C_2H_6}$ (Figure 6) and $\delta^{13}C_{C_2H_6}$ versus $\delta^{13}C_{C_3H_8}$ (Figure 7) display a relative enrichment of longer-chain hydrocarbons due to the lower concentrations of methane than ethane and ethane than propane. The expected positive correlation between $\delta^{13}C$ values of different hydrocarbon species is also observed.

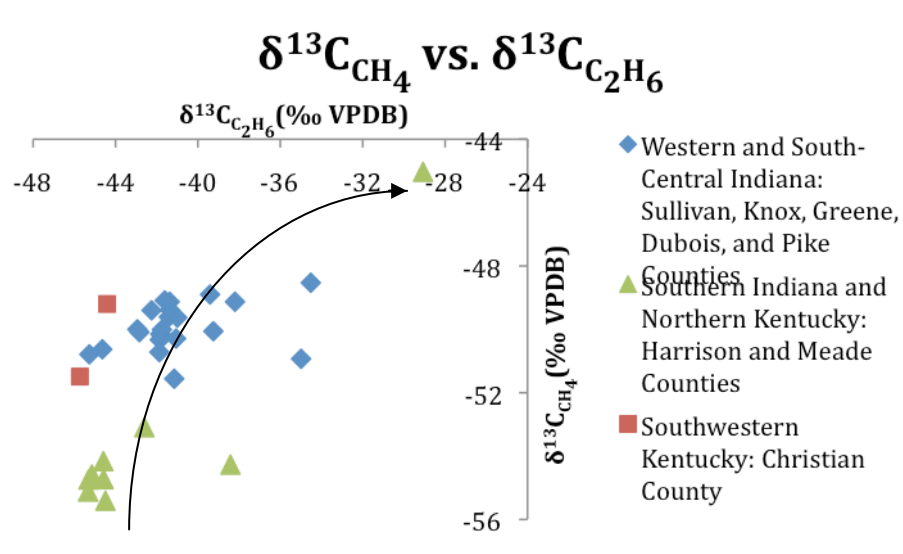


Figure 6: Positive correlation between $\delta^{13}C_{CH_4}$ and $\delta^{13}C_{C_2H_6}$. Microbial hydrocarbon oxidation would increase both $\delta^{13}C_{CH_4}$ and $\delta^{13}C_{C_2H_6}$. Consumption of methane and ethane at equal rates would lead to more positive $\delta^{13}C_{C_2H_6}$ compared to $\delta^{13}C_{CH_4}$ due to the relative scarcity of ethane.

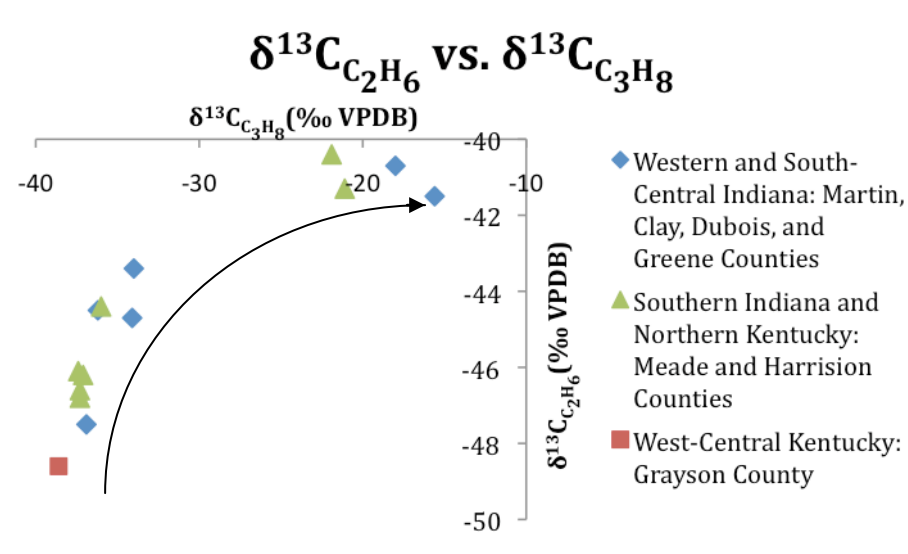


Figure 7: Positive correlation between $\delta^{13}C_{C_2H_6}$ and $\delta^{13}C_{C_3H_8}$. Microbial hydrocarbon oxidation would increase both $\delta^{13}C_{C_2H_6}$ and $\delta^{13}C_{C_3H_8}$ and likely lead to the more positive $\delta^{13}C_{C_3H_8}$ than $\delta^{13}C_{C_2H_6}$ due, as in Figure 6, to the reservoir effect.

Lastly, environmental constraints on methanogenesis and the efficiency of different metabolisms used by methanogenic organisms influence the carbon isotopic signature of methane (Whiticar, 1999). Inorganic factors can also generate small levels of variability in $\delta^{13}C_{CH_4}$ values. The fractionation factor between bicarbonate substrate and methane produced via hydrogenotrophic methanogenesis can vary by at least 1‰ over the range of water temperatures observed in the field area (Whiticar, 1999).

Stable Carbon Isotopes in Carbon Dioxide

Different groups of methanogens use different carbon substrates and thereby influence aqueous geochemistry in distinguishable ways. Hydrogenotrophic methanogens generate methane and water through the reduction of carbon dioxide and the oxidation of hydrogen gas.

$$CO_2 + 4\,H_2 \rightarrow CH_4 + 2\,H_2O$$

This pathway illustrates that the only carbon input in hydrogenotrophic methanogenesis is CO_2, and the only carbon output is methane. In closed systems with significant amounts of hydrogenotrophic methanogenesis, the isotopic signature of CO_2 therefore reflects the preferential uptake of light carbon. Dissolved CO_2 in New Albany Shale formation waters, largely found as HCO_3^-, is significantly enriched in ^{13}C relative to ^{12}C. This study confirms that some of the most enriched $\delta^{13}C_{DIC}$ values found in sampled

subsurface formation waters come from the New Albany Shale (Martini et al., 1998). $\delta^{13}C_{DIC}$ values range from 26.0‰ to 31.5‰, with an average value of 28.1‰. Deeper parts of the shale and surrounding carbonate aquifers exhibit much lower $\delta^{13}C_{DIC}$ values typical of groundwater.

Gaseous carbon dioxide and bicarbonate ions are in carbon isotopic equilibrium on the eastern margin of the New Albany Shale (Figure 8). An equation for equilibrium isotopic fractionation of carbon relates the ratio of $\delta^{13}C_{DIC}$ values for these two species to temperature (Zhuang et al., 1994).

$$\varepsilon_{\text{bicarbonate-carbon dioxide gas}} = -(0.141 \pm 0.003) * T(°C) + 0.05)‰$$

$$/(1000 + \delta^{13}C_{CO2}) - 1) * 1000$$

The average temperature of formation waters extracted from the New Albany Shale was 19.6°C. At this temperature, $\delta^{13}C_{CO_2}$ is enriched by 8.02‰ relative to $\delta^{13}C_{HCO_3^-}$.

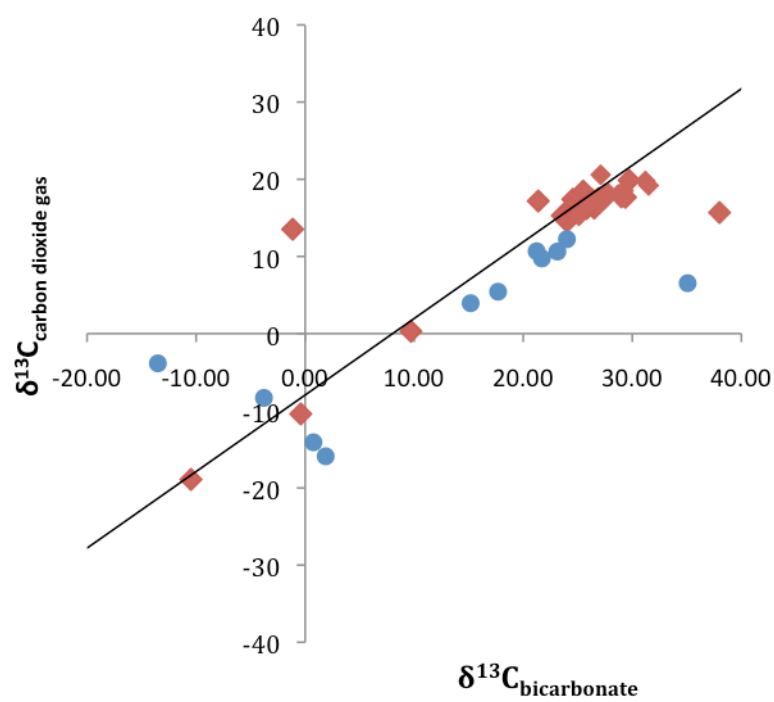


Figure 8: Temperature-controlled carbon isotopic equilibrium in carbon dioxide gas and dissolved bicarbonate. The line represents an 8.02‰ fractionation between gaseous CO_2 and HCO_3^-.

Hydrogen Stable Isotopes

Hydrogen stable isotopes provide another indication of significant biogenic gas production in the eastern margin of the New Albany Shale. The heavier stable of isotope of hydrogen has a single neutron and is called deuterium (D). Saline basinal brine and dilute waters (glacial recharge in western Indiana or meteoric recharge in southern Indiana and northern Kentucky) define endmember δD_{H_2O} values in the field area. Brines in the New Albany Shale have a δD_{H_2O} value of about -5‰, while dilute recharge has a value of about -40‰ (McIntosh et al., 2002). In areas containing biogenic gas, the hydrogen isotopic value of methane covaries with that of water. Certain methanogens produce this effect by linking δD_{CH_4} to δD_{H_2O} via hydrogen species in isotopic equilibrium with water. Hydrogenotrophic methanogens derive all hydrogen produced in methane from dissolved hydrogen gas, as shown by the metabolic pathway employed by these organisms.

$CO_2 + 4\ H_2 \rightarrow CH_4 + 2\ H_2O$

Biogenic methane in a closed system containing only hydrogenotrophic methanogens would follow a linear relationship between δD_{CH_4} and δD_{H_2O} in which δD_{CH_4} is approximately 160‰ more negative than δD_{H_2O} (Whiticar, 1999).

Acetoclastic methanogens consume two substrates containing hydrogen – acetate and hydronium ions (protons) – and they incorporate hydrogen from both sources into methane.

$CH_3COO^- + H^+ \rightarrow CH_4 + CO_2$

Acetate in this reaction originates in shale organic matter and only partially equilibrates with water (de Graaf et al., 1996). The different proportions of water-derived hydrogen in methane produced by hydrogenotrophic and acetoclastic methanogens result in different relationships between δD_{CH_4} and δD_{H_2O} in the two groups. In other words, a change in δD_{H_2O} causes a larger response in δD_{CH_4} for hydrogenotrophic methanogens than acetoclastic methanogens, because not all hydrogen consumed by acetoclastic methanogens is in isotopic equilibrium with water.

All other types of methanogens, collectively called methylotrophic methanogens, derive either none or about one-quarter of hydrogen in produced methane from reducing agents in isotopic equilibrium with water (Whiticar, 1999). The proportion of hydrogen incorporated into methane from substrates in isotopic equilibrium with water and substrates derived from shale organic matter is not immediately apparent from the overall metabolic pathways of many methylotrophic methanogens. A representative subset of methylotrophic methanogens uses water to reduce dimethylsulfide.

$2\ (CH_3)_2S + 2\ H_2O \rightarrow 3\ CH_4 + CO_2 + 2\ H_2S$

Some methylotrophic species only use substrates derived from shale organic matter. For example, methanol reducers derive all hydrogen in produced methane from the methanol substrate.

$4\ CH_3OH \rightarrow 3\ CH_4 + CO_2 + 2\ H_2O$

δD_{CH_4} values of methane produced in the thermogenic degradation of shale organic matter reflect δD values of shale organic matter and the temperature of production. Therefore, no clear relationship exists between thermogenic δD_{CH_4} values and δD_{H_2O} values of associated formation waters. δD_{CH_4} values of methane produced by microbial methanogenesis show a clear relationship with associated δD_{H_2O} values. Hydrogenotrophic methanogens consistently fractionate deuterium by about -180‰ to -160‰, while methylotrophic and acetoclastic methanogens fractionate deuterium by about -370‰ to -300‰ (Whiticar, 1999). All hydrogen in methane produced by hydrogenotrophic methanogens comes from a substrate in isotopic equilibrium with water, suggesting that a 1‰ change in δD_{H_2O} results in a 1‰ change in δD_{CH_4}. At minimum, one-quarter of the hydrogen in methane produced by acetoclastic methanogens comes from a substrate in isotopic equilibrium with water, suggesting that a 1‰ change in δD_{H_2O} results in a 0.25‰ change in δD_{CH_4}. δD_{H_2O} and δD_{CH_4} values from the eastern margin of the New Albany Shale display a linear relationship similar to that described for hydrogenotrophic methanogenesis (Figure 9). Mixing between thermogenic and biogenic gas components and the presence of other methanogenic metabolisms could cause the lower observed slope compared to the predicted slope for hydrogenotrophic methanogenesis.

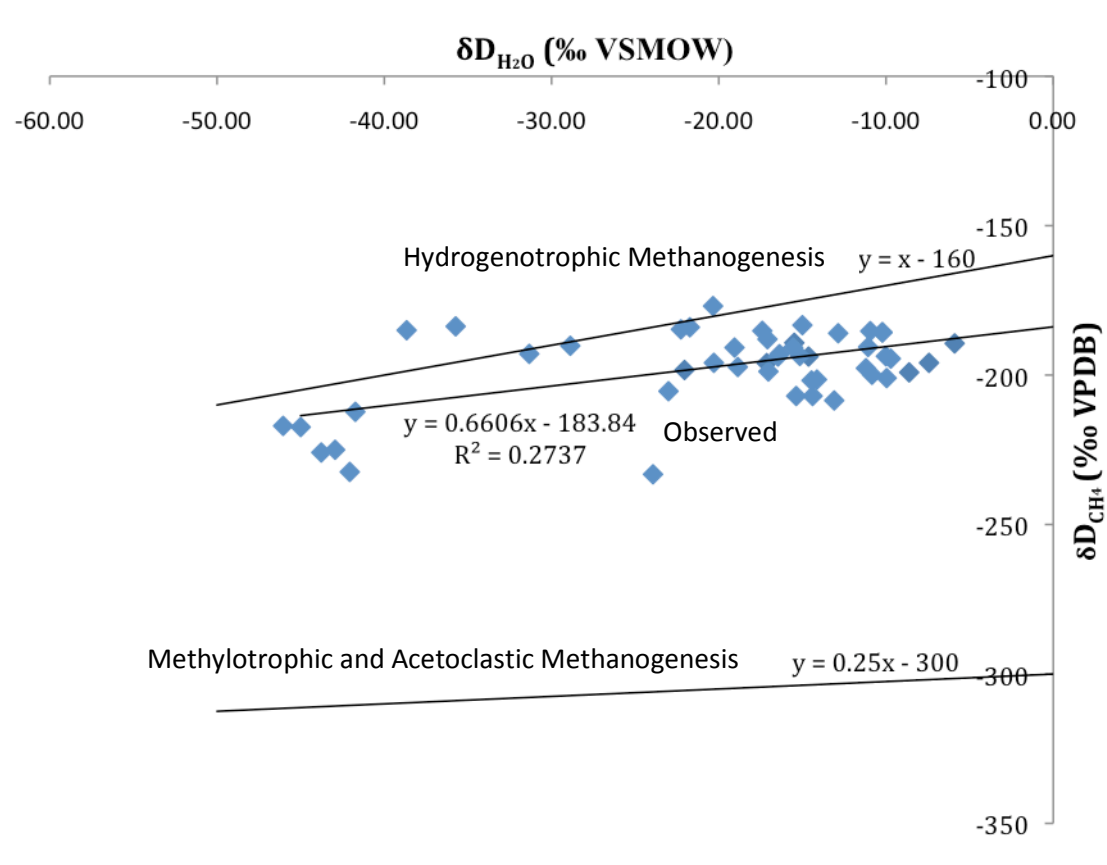


Figure 9: δD_{H_2O} and δD_{CH_4} values of all samples from the extended Illinois Basin dataset. The fitted line falls near the empirical fit for hydrogenotrophic methanogenesis.

Natural Gas Hydrocarbon Composition

Microbial methanogenesis does not produce longer-chain hydrocarbons than methane, as shown by the metabolic pathways listed above. Thermogenic natural gas contains a mixture of hydrocarbons of different sizes. Therefore, the ratio of methane to longer-chain hydrocarbons in a natural gas (gas wetness) yields information about its source (Martini et al., 1998). Gas wetness decreases with depth in the New Albany Shale, a consequence of pyrolysis associated with higher temperatures at greater depths (Figure 10).

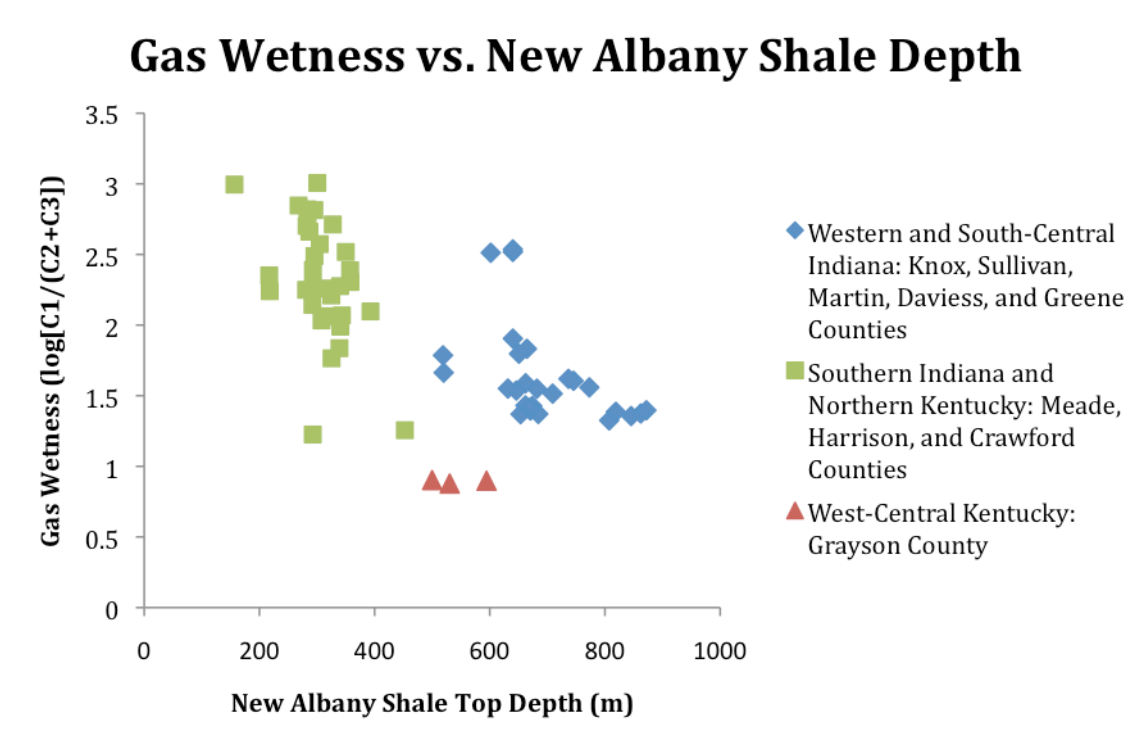


Figure 10: Gas wetness decreases with depth due to increasing thermogenic gas production. West-central Kentucky wells are associated with tectonic activity toward the Rough Creek Graben (McIntosh et al., 2002).

Formation Water Composition

Formation water alkalinity also provides a robust geochemical indicator of microbial activity in shallow shale gas systems. Although methanogenesis consumes HCO_3^-, the main source of alkalinity, high levels of shale organic matter degradation by *Bacteria* generate abundant HCO_3^- (Martini et al., 1998). Salinity is a primary control on microbial abundance and alkalinity (Figure 11). Chloride concentrations greater than 1500 mM are associated with alkalinities less than 20 mM, whereas chloride concentrations between 300 mM and 1500 mM are associated with the highest alkalinities. As the hydrologic system becomes more open toward the New Albany Shale outcrop, microbially-derived bicarbonate cannot accumulate to high concentrations (Clay County, Greene County, and Jackson County). An enclave of elevated alkalinity in Harrison County, Indiana and Meade County, Kentucky is associated with the infusion of dilute meteoric recharge through Mississippian carbonates directly

overlying the New Albany Shale. This zone of dilute recharge occurs in an area too far south to be influenced by glacial recharge through the northeast margin of the Illinois Basin. Therefore, areas adjacent to the zone of meteoric recharge have high salinities associated with basinal brine and low alkalinities.

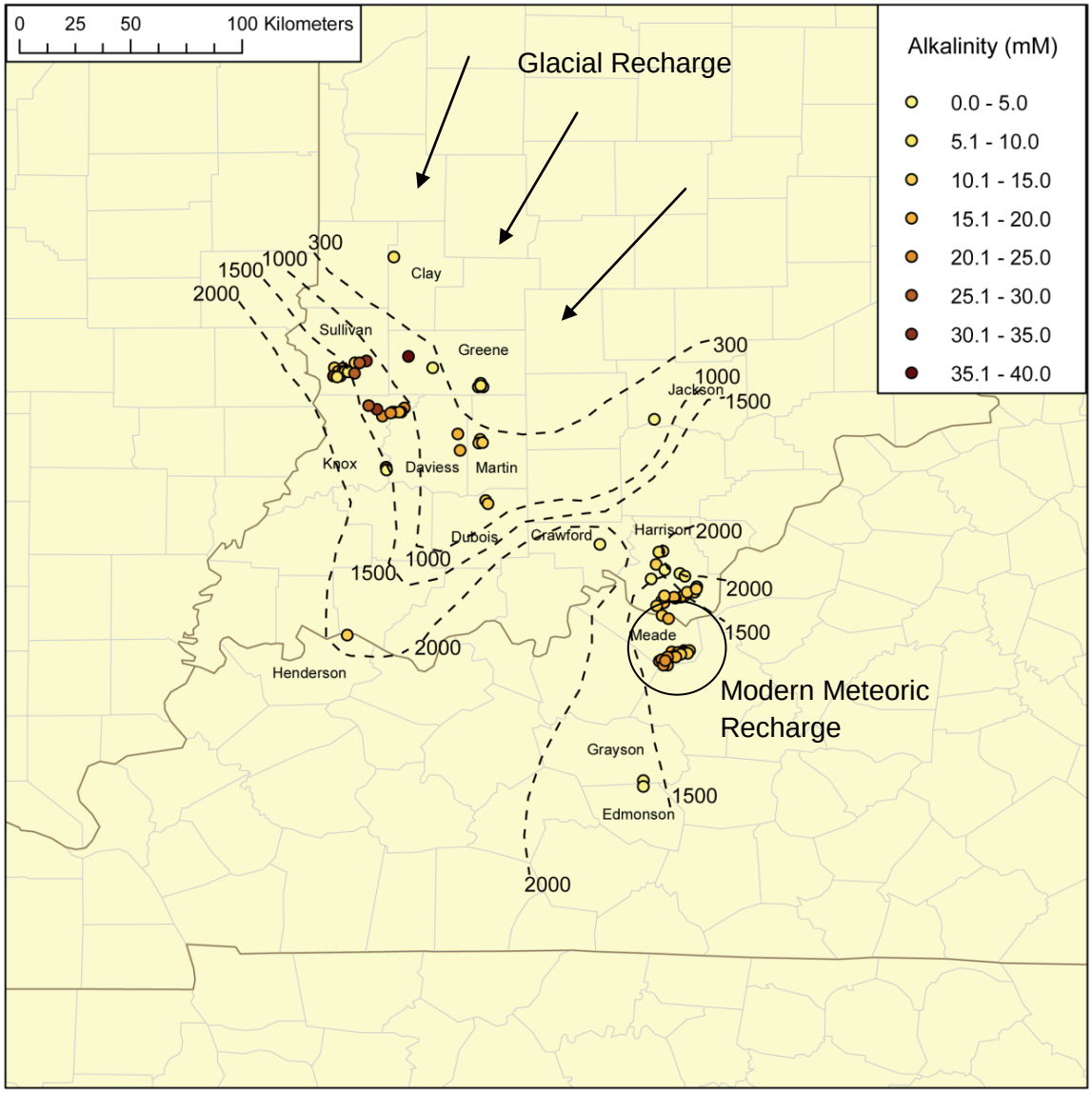


Figure 11: Map of alkalinity values and lines of equal chloride concentration in the New Albany Shale determined from the total set of New Albany Shale formation water samples.

Summary of Geochemical and Isotopic Results

The geochemical and isotopic values from formation waters and gas produced in the New Albany Shale indicate a "mixed" gas, with microbial additions more prevalent in certain geographic areas and thermogenic components generally increasing towards the more saline, deeper, portions of the basin. These results are generally consistent with previous studies.

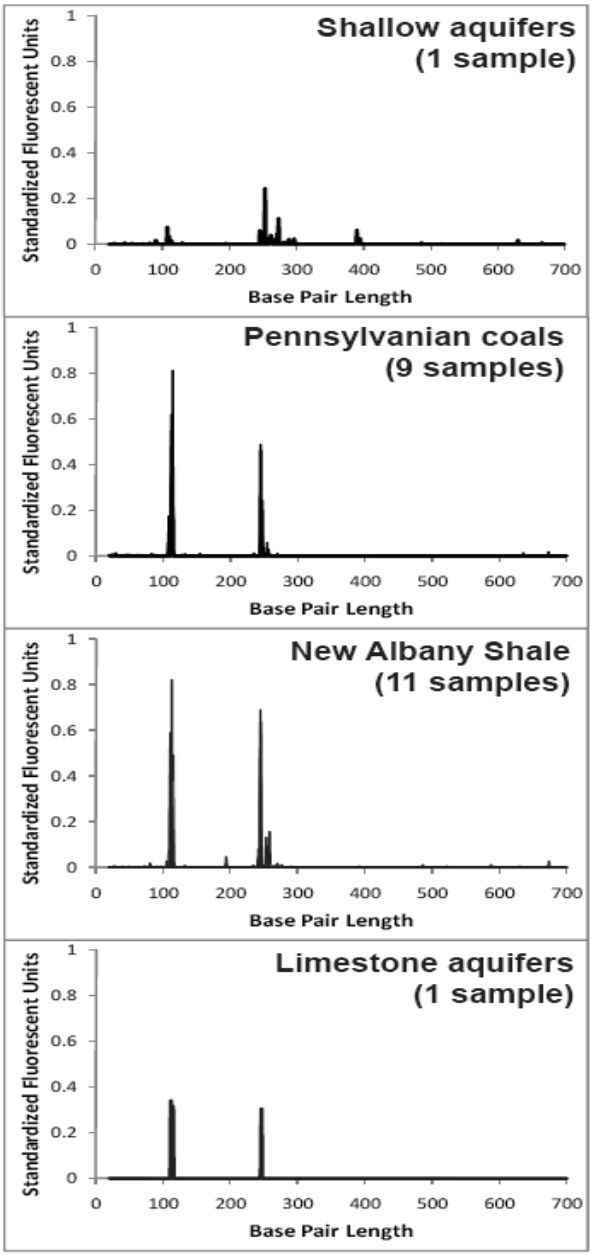
Microbiology

TRLFP analysis

TRFLP results show low numbers of archaea with just two groups of base pairs dominant in shale, coals, and limestone aquifer samples (Figure 12). This compares favorably with previous clone library studies of deep subsurface methanogenic environments, which showed multiple methanogenic species in one or two groups (Waldron et al., 2007; Green et al., 2008; Strąpoć et al., 2008; Ehinger et al., 2009). However, these results could be affected by PCR bias due to choice of primers, as well as digestion of the sample by only one restriction enzyme, suggesting that perhaps more than one species may be represented in a peak. The shallow aquifer sample shows multiple TRFLP peaks, including relatively large peaks consistent with the dominant peaks in the other reservoirs. To statistically compare samples, the TRFLP data was manipulated following methods described in Rees et al. (2004) and Abdo et al. (2006; see section 3 for brief descriptions).

MDS results for the Rees data reduction have stresses of 0.17 and 0.11 for 2 and 3 dimensions, respectively. For the Rees data reduction, the coal and shale samples cluster near each other, but there is considerable overlap between the two groups (Fig. 13). In addition, a formation water sample from the limestone aquifer plots within the coal cluster, whereas the shallow aquifer sample plots apart from both the coal and the shale clusters. MDS results for the Abdo data reduction have stresses of 0.01 for both 2 and 3 dimensions. With the exception of one coal and one shale sample, all the samples plot in a

single tight cluster, indicating that all samples, regardless of organic-rich reservoir, contained similar communities of archaea (Fig. 12). The different MDS results demonstrate that the method used to reduce the data greatly influences results.



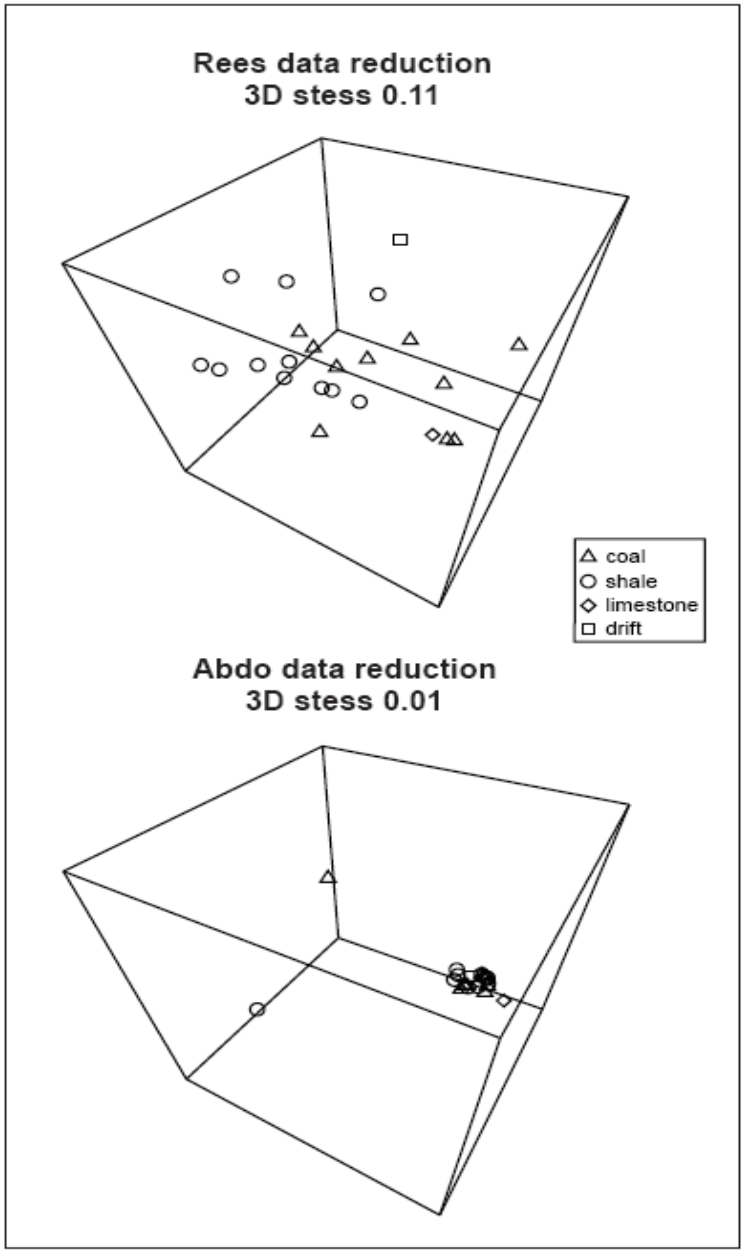


Fig. 12. Terminal restrictive fragment length polymorphism (TRFLP) results are displayed as plots of base pair length versus standard fluorescent units for all samples for shallow aquifers, coals, shale, and limestone aquifers. Note dominant peaks in all reservoirs at base pairs approximately 100 and 250 units long, suggesting that all reservoirs are dominated by only a few types of similar methanogens.	**Fig. 13.** Three dimensional multi dimensional scaling (MDS) plots using the Rees and Abdo reduction methods show that for the Rees data reduction, the coal and shale samples cluster near each other, but there is considerable overlap between the two groups. In addition, a formation water sample from the limestone aquifer plots within the coal cluster, whereas the shallow aquifer sample plots apart from both the coal and the shale clusters. Results for the Abdo data reduction show that with the exception of one coal and one shale sample, all samples plot in a single tight cluster, indicating that all samples, regardless of organic-rich reservoir, have similar groups of base pairs.

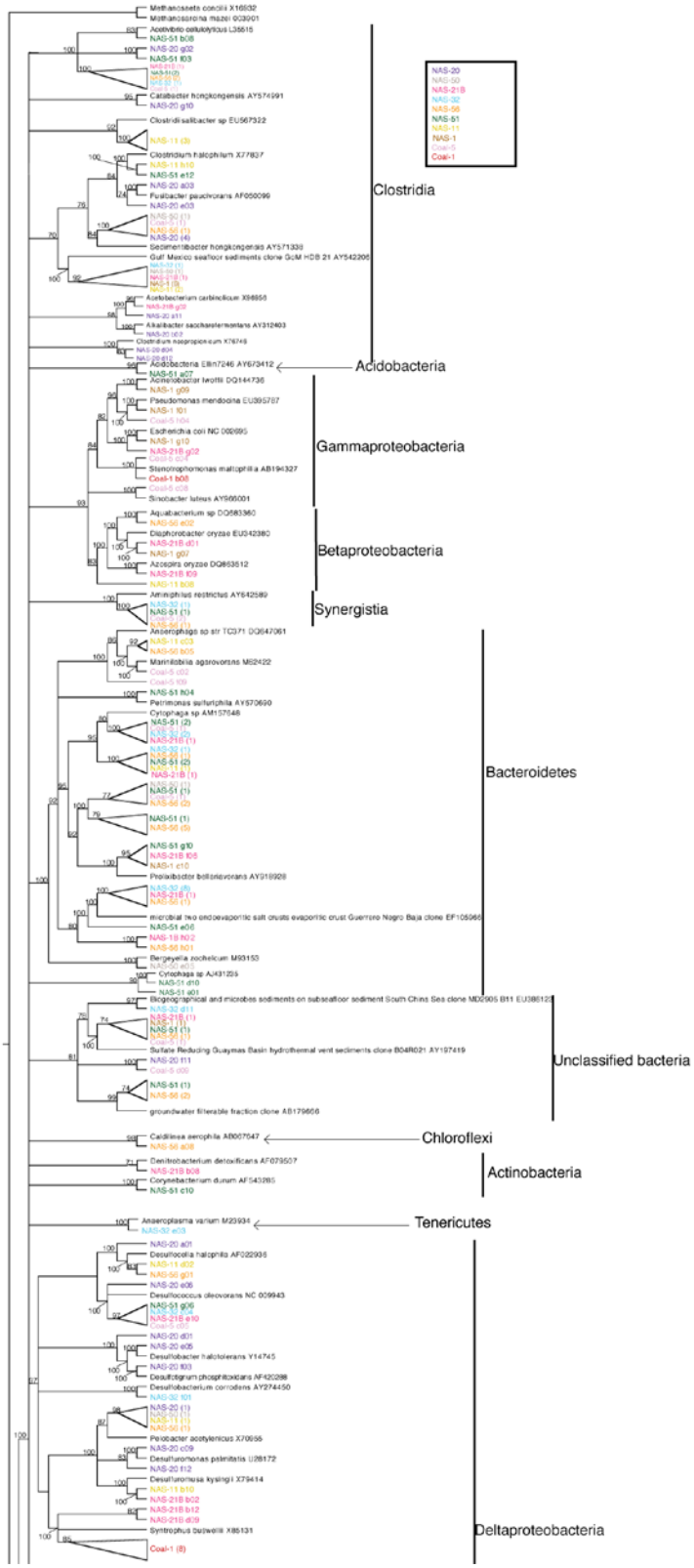
ANOSIM results are a measure of statistical significance between samples, ranging from -1 to 1. Positive values indicate that the samples are more dissimilar between groups than within group (in our case the groups are by organic-rich reservoir); whereas negative values indicate that the samples are more similar between groups than within groups. Values near 0 indicate that samples have the same similarity within groups as between groups. Our values are 0.348 ($p = 0.002$) for the Rees reduced data and 0.004 ($p = 0.441$) for the Abdo reduced data. This means that for the Rees reduced data, the general difference between organic-rich reservoirs is moderate, and somewhat statistically significant, whereas for the Abdo reduced data there is no difference between the organic-rich reservoirs, and the results are not statistically significant.

Statistics indicate that the coal and shale groups are moderately different from each other, even though heterogeneity within each group is large. Archaea from soil samples exhibit an analogous pattern in which samples from similar climates are statistically different from each other, but more similar to each other than samples from different climates (Angel et al., 2010). In addition, the coal and shale groups are different from the limestone aquifer and shallow aquifer samples, and the limestone aquifer and shallow aquifer samples are also different from each other. However the dominance of two groups of archaea, regardless of organic-rich reservoir, and the only moderate difference between the shale and coal groups suggest a similarity between methanogen populations in all the reservoirs, including the limestone and shallow aquifers. This could be achieved by inoculation of the coals, shale, and limestone aquifer by groundwater that migrated through the shallow aquifer prior to recharging the deeper aquifers of the Illinois Basin.

16S Sequencing

Due to the bias inherent in pure-culture studies (Woese 1987; Amann et al. 1995; Hugenholtz et al. 1998), this study used phylogenetics to assess the microbial community structure at NAS well sites by amplifying the 16S ribosomal RNA gene fragment (16S rRNA) from environmental samples, cloning and sequencing the products, and using the sequences to grow phylogenetic trees. Comparison of environmental sequences with publicly available reference sequences gives basic information regarding the microbial community composition, allowing for inferences of the metabolic processes and ecological roles of the microbes to be made. While 16S rRNA clone libraries are far from a perfect representation of a microbial community (Wintzingerode et al. 1997), they do provide a general overview of the microbes

present, and are therefore a solid first step in characterizing a microbial community. Although the geochemistry of biogenic shale gas systems has been studied extensively (Schoell 1980; Martini et al. 1998; Shurr and Ridgley 2002), comparatively little effort has focused on the microbes themselves, though there has been a recent flurry of activity investigating the microbiology related to methane production in unconventional gas systems (Green et al. 2008; Strąpoć et al. 2008; Gray et al. 2009; Penner et al. 2010). In this study, we sequenced environmental samples from eight NAS shale gas wells in southwest Indiana/northern Kentucky, as well as two coalbed wells in Illinois and Indiana; all ten wells sampled produce, or have produced, economic quantities of natural gas.Clustering our sequences into 97% similarity OTUs gave 259 bacterial OTUs (Fig. 14) and 252 archaeal OTUs (Fig. 15). Forty bacterial OTUs (~15%) and 137 archaeal OTUs (~54%) did not cluster with named reference species. The bacterial phyla *Firmicutes*, *Bacteroidetes*, and *Proteobacteria* contained the highest number of OTUs, though a number of OTUs were affiliated with the phyla *Acidobacteria*, *Synergistetes*, *Tenericutes*, *Chloroflexi, Actinobacteria*, *Spirochaetes*, and *Deferribacteres*. *Proteobacteria* present included *Beta-*, *Delta-*, *Gamma-*, and *Epsilonproteobacteria* (Fig. 14). All unknown archaeal OTUs clustered in the phylum *Euryarchaeota*; OTUs related to classified species were within the classes *Methanomicrobia*, *Methanobacteria*, and *Methanococci*. Most OTUs associated with *Methanomicrobia* were within the order *Methanomicrobiales*, although a small number clustered with *Methanosarcinales*, *Methanococcales*, *Methanobacteriales*, or *Thermoplasmatales* (Fig. 15). 16S sequence data alone did not provide enough information to resolve the relationships between these archaeal orders and the four unclassified clusters in our tree.


NAS-20
NAS-50
NAS-21B
NAS-32
NAS-56
NAS-51
NAS-11
NAS-1
Coal-5
Coal-1
Clostridia
Acidobacteria
Gammaproteobacteria
Betaproteobacteria
Synergistia
Bacteroidetes
Unclassified bacteria
Chloroflexi
Actinobacteria
Tenericutes
Deltaproteobacteria

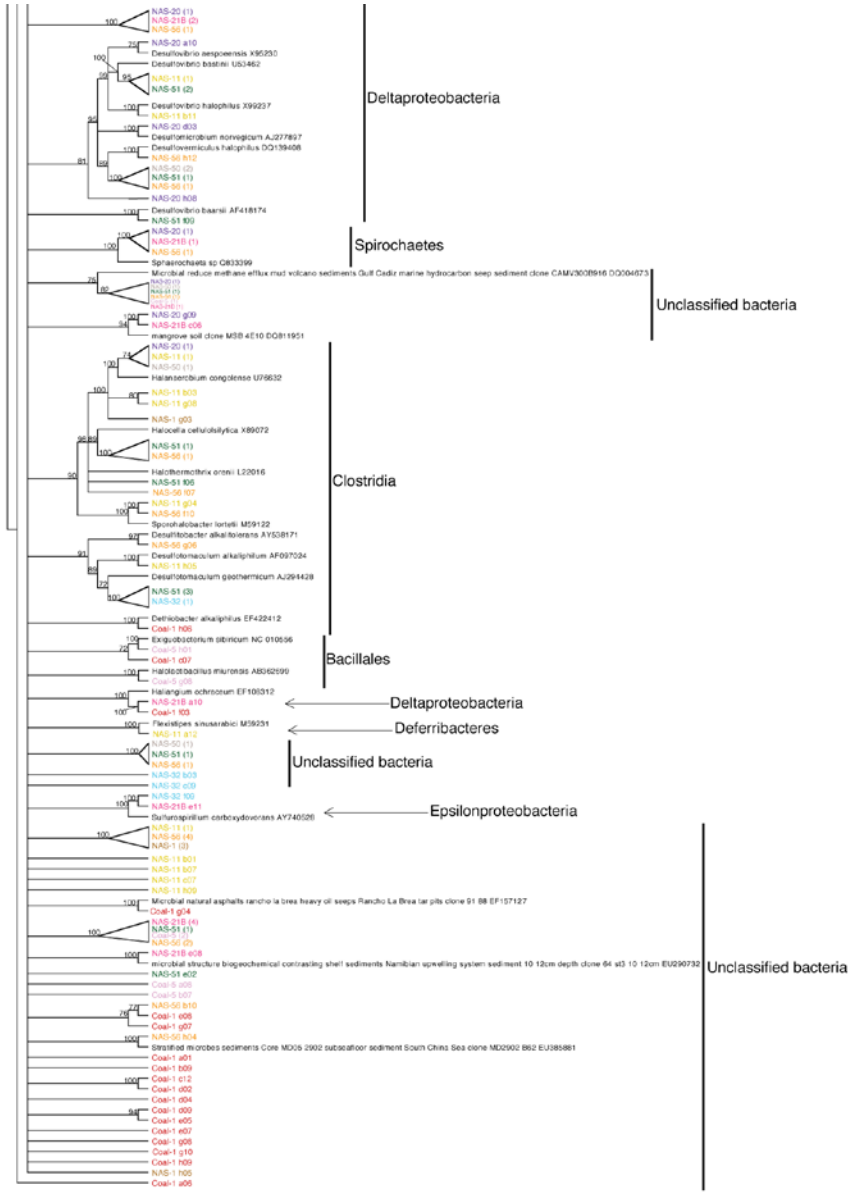


Figure 14: *Bacteria* OTU trees

Bacteria: Phylum Firmicutes, Class Clostridia

Among the bacterial clone libraries, the paraphyletic phylum *Firmicutes* was the most profuse; every well had sequences clustering within *Firmicutes* (Fig. 14). Many of these clustered within the class *Clostridia*, which predominantly contains obligate fermentative anaerobes. Many *Clostridia* species produce appreciable concentrations of organic acids or alcohols as metabolic byproducts (Wiegel et al. 2006).

Many OTUs within *Clostridia* clustered with the order *Clostridiales*. Sequences from NAS-51, NAS-20, NAS-21B, NAS-56, and NAS-32, as well as the coalbed Coal-5, grouped with the *Clostridiales* species *Acetivibrio cellulolyticus* (Fig. 14), which ferments cellulose to hydrogen, CO_2, acetate, and ethanol (Patel et al. 1980; Laube and Martin 1981). OTUs from NAS-21B and NAS-20 also clustered with *Clostridiales* species from the genera *Acetobacterium* and *Alkalibacter*. *Acetobacterium* species degrade alcohols to fatty acids and are homoacetogenic, converting CO_2 to acetate (Willems and Collins 1996; Drake et al. 2006), and *Alkalibacter saccharofermentans* degrades glucose to CO_2, hydrogen, formate, acetate, and ethanol (Garnova et al. 2004).

OTUs from NAS-11, NAS-51, and NAS-20 clustered within *Clostridiales* genera *Clostridium* and *Fusibacter*. *Clostridium* is a diverse genus that has continually undergone a significant amount of taxonomic revision; the *Clostridium* reference species used in our analysis were part of *Clostridium* "cluster XI" (Collins et al. 1994), which includes a number of alkaliphilic species (Garnova et al. 2003); however, species in this *Clostridium* cluster have enough metabolic variety (Collins et al. 1994) to make it difficult to deduce the likely metabolism of these OTUs without further investigation. The reference species from *Fusibacter* is also part of *Clostridium* cluster XI and produces acetate, butyrate, CO_2, and hydrogen during glucose fermentation (Ravot et al. 1999).

One OTU from NAS-20 grouped with the *Clostridiales* species *Catabacter hongkongensis*, an obligate anaerobe that converts many sugars into acids (Lau et al. 2007). Three OTUs from NAS-11 clustered with the *Clostridiales* genus *Clostridiisalibacter*, sequences of which have been found in hypersaline environments. *Clostridiisalibacter* species are halophilic and can ferment amino acids and other organic molecules to acetate and isobutyrate, among other products (Liebgott et al. 2008). Additionally, *Clostridiisalibacter* were first isolated from olive mill wastewater, which contains significant

concentrations of polyphenols, polyalcohols, and aromatic compounds; these compounds are also generated during shale and coal biodegradation (Strąpoć et al. 2008).

OTUs from NAS-50, NAS-56, NAS-20, and the coalbed Coal-5 clustered with the *Clostridiales* genus *Sedimentibacter*, a genus that can ferment amino acids, producing acetate and butyrate (Breitenstein et al. 2002; Wiegel et al. 2006). OTUs from NAS-56, NAS-11, NAS-32, and NAS-51 also grouped with the *Clostridiales* genera *Desulfitobacter* and *Desulfotomaculum*. *Desulfitobacter* contains a diverse array of anaerobic microbes that metabolize a variety of chlorinated substances by reductive dehalogenation (Spring and Rosenzweig 2006). *Desulfotomaculum* display a wide variety of metabolisms, including species that consume hydrogen, alcohols, sugars, or organic acids. Many can also reduce sulfate. If sulfate is not present, some species can ferment glucose, fructose, or pyruvate, using hydrogen/CO_2 or formate and creating acetate (Widdel 2006). The presence of OTUs clustering with *Desulfotomaculum* may simply represent additional acetogenic metabolism, but could also indicate the presence of sulfate reduction. There may be evidence of non-sulfate sulfur reduction, as well: one OTU from the coalbed Coal-1 grouped with the *Clostridiales* genus *Dethiobacter*, a genus of alkaliphilic, moderately halophilic species that can reduce non-sulfate sulfur compounds while metabolizing hydrogen, acetate, ethanol, and a variety of sugars (Sorokin et al. 2008).

A number of OTUs within *Clostridia* from NAS-20, NAS-11, NAS-50, and NAS-1 grouped with the order *Haloanaerobiales*, which consists of fermentative, halophilic, obligate anaerobes. Most *Haloanaerobiales* species ferment sugars and produce acetate, ethanol, hydrogen, and CO_2 (Rainey et al. 1995; Oren 2006). Some OTUs clustered with species from the *Haloanaerobiales* genus *Halanaerobium*, many species of which can additionally produce acetate or trimethylamine, ferment glucose, and reduce thiosulfate or sulfur (Ravot et al. 1997; Oren 2006). OTUs from NAS-51 and NAS-56 clustered with the *Haloanaerobiales* genus *Halocella*, species of which can ferment cellulose, starch, and a number of carbohydrates, producing acetate, ethanol, lactate, hydrogen, and CO_2 (Simankova et al. 1993; Oren 2006). Two OTUs from NAS-11 and NAS-56 grouped with the *Haloanaerobiales* genus *Sporohalobacter*. Like other genera in this order, *Sporohalobacter* is a halophilic, anaerobic, fermentative bacterium; however, it differs from the others in that it ferments amino acids (Oren et al. 1987; Oren et al. 1989; Oren 2006).

Bacteria: Phylum Firmicutes, Class Bacillales

Single OTUs from the coalbeds Coal-5 and Coal-1 within *Firmicutes* were closely related to the order *Bacillales*, specifically the genus *Exiguobacterium*. Organisms in this genus can be aerobic or anaerobic, and metabolize a variety of carbohydrates, including glucose, fructose, and maltose (Frühling et al. 2002). One OTU from Coal-5 grouped strongly with the *Bacillales* genus *Halolactibacillus*, which contains halophilic and alkaliphilic species that can metabolize glucose and a number of carbohydrates aerobically or anaerobically, producing lactic acid, formate, acetate, and ethanol (Ishikawa et al. 2005).

Bacteria: Phylum Bacteroidetes

A significant number of OTUs grouped with reference sequences from the phylum *Bacteroidetes*, including OTUs from all NAS wells except NAS-20, and from the coalbed Coal-5. Organisms in this phylum can anaerobically degrade cellulose, proteins, polysaccharides, and some polyaromatic hydrocarbons, and many are thought to be involved in oil biodegradation (Strąpoć et al. 2008).

A large number of OTUs clustered with the related *Bacteroidetes* genera *Cytophaga* and *Prolixibacter*, including at least one OTU from all wells containing sequences related to *Bacteroidetes*. Species within *Cytophaga* are mesophilic anaerobes that ferment a variety of polysaccharides, producing acetate, propionate, succinate, hydrogen, and CO_2 (Haack and Breznak 1993). *Prolixibacter* consists of anaerobic microbes that can ferment sugars through acid fermentation, producing acetate, succinate, and propionate (Holmes et al. 2007). Closely related to these genera is an OTU from NAS-51 that grouped with the genus *Petrimonas*, which consists of mesophilic anaerobes that ferment carbohydrates and organic acids, producing acetate, hydrogen, and CO_2 (Grabowski et al. 2005). Additionally, a number of OTUs from NAS-50, NAS-51, NAS-56, NAS-21B, and NAS-1, as well as the coalbed Coal-5, were in a clade containing unclassified but presumably *Bacteroidetes* sequences from mud volcanoes and salt crust evaporates, positioned basal to the *Cytophaga/Prolixibacter* clade; though these OTUs do not group with classified species, it in reasonable, due to their positions on our tree, to infer that they have a similar metabolism to *Cytophaga*, *Prolixibacter*, and *Petrimonas* species. Finally, one OTU from NAS-50 grouped with the genus *Bergeyella*. This genus is within the class *Flavobacteria*, which is related to *Cytophaga*. *Flavobacteria* can anaerobically degrade polysaccharides, and have been grown on *n*-hexane and long-chain oil droplets (Rahman et al. 2002; Strąpoć et al. 2008).

OTUs from NAS-11 and NAS-56, as well as the coalbed Coal-5, grouped with sequences from the *Bacteroidetes* genera *Anaerophaga* and *Marinilabilia*. *Anaerophaga* have been shown to ferment carbohydrates, producing acetate, propionate, and succinate, and are moderately halophilic and moderately thermophilic (Denger et al. 2002). *Marinilabilia* species can also ferment a variety of sugars and carbohydrates (Nakagawa and Yamasato 1996).

Bacteria: Phylum Proteobacteria

A number of OTUs within *Proteobacteria* clustered monophyletically with the classes *Beta-* and *Gammaproteobacteria*. As *Betaproteobacteria* includes a diverse range of phenotypes and metabolic processes (Kersters et al. 2006), it is difficult to assign metabolic properties to environmental organisms using only 16S sequence data; however, there do appear to be some metabolic traits shared among the *Betaproteobacteria* species on our phylogeny. *Betaproteobacteria* reference sequences came from the genera *Aquabacterium*, *Diaphorobacter*, and *Azospira*; OTUs grouped with these genera were from NAS-1, NAS-21B, NAS-56, and NAS-11, as well as both coalbeds. One OTU from NAS-56 grouped strongly with the *Aquabacterium* reference sequence; *Aquabacterium* are microaerophilic, non-fermentative, and can use nitrate as an alternative electron acceptor, producing nitrite (denitrification; Kalmbach et al. 1999; Ward 2000). Likewise, the genus *Diaphorobacter* contains aerobic and anaerobic denitrifying bacteria (Khan and Hiraishi 2002), but also includes bacteria capable of nitrification (sequential oxidation of ammonia to nitrite and then nitrate; Ward 2000); consorts of *Diaphorobacter* have been shown to be capable of simultaneous nitrification and denitrification (Khardenavis et al. 2007). On our phylogeny, OTUs grouped with *Diaphorobacter* came from NAS-21B and NAS-1. The genus *Azospira* consists of bacteria that can reduce oxygen, nitrogen, and perchlorate (Reinhold-Hurek and Hurek 2006); the single OTU associated with *Azospira* was from NAS-21B. The three genera of *Betaproteobacteria* used as reference species all contain species that can live in anaerobic or slightly aerobic environments, and are capable of reducing nitrogen compounds; this suggests that some of the bacteria present in NAS-21B, NAS-1, and NAS-56 may be involved in nitrogen cycling.

The *Gammaproteobacteria* reference sequences in our phylogeny came from the genera *Acinetobacter*, *Pseudomonas*, *Escherichia*, *Stenotrophomonas*, and *Sinobacter*. *Gammaproteobacteria* species also display a wide variety of metabolic phenotypes, but many are chemoorganotrophes (Kersters et al.

2006). *Acinetobacter* species are mesophilic chemoorganotrophs that utilize glucose, pentose, and a number of other organic molecules for growth (Rossau et al. 1991; Kersters et al. 2006; Towner 2006). An OTU from NAS-1 grouped strongly with *Acinetobacter*. The genus *Pseudomonas* has been found in a wide variety of terrestrial and aquatic ecosystems, and is known for its wide metabolic diversity; *Pseudomonas* species can metabolize a number of carbon compounds, including carbohydrates, alcohols, fatty acids, amino acids, and a number of aromatic compounds (Moore et al. 2006). OTUs from NAS-1 and the coalbed Coal-5 grouped with *Pseudomonas*. OTUs from NAS-1 and NAS-21B grouped with the genus *Escherichia*, species of which are usually found in the mammalian intestine. *Escherichia* are typically facultative anaerobes that can ferment glucose and other carbohydrates, and can reduce nitrate to nitrite (Welsh 2006). OTUs from the coalbeds Coal-5 and Coal-1 grouped with the genus *Stenotrophomonas*, which can metabolize various carbohydrates, and may be able to utilize hydrocarbons as a carbon source (Palleroni and Bradbury 1993). An OTU from Coal-5 also grouped with the genus *Sinobacter*, which consists of aerobic microbes that can metabolize a variety of carbohydrates (Zhou et al. 2008).

A large number of OTUs from all NAS wells except NAS-1, and from the coalbeds Coal-5 and Coal-1, fell in one of two clades within the *Proteobacteria* class *Deltaproteobacteria*. While there is significant phenotypic diversity within *Deltaproteobacteria*, a substantial number of species in the class are obligate anaerobes that reduce sulfur and/or sulfate, consuming an electron donor such as hydrogen or acetate in the process (Kersters et al. 2006). Many of the OTUs that grouped within *Deltaproteobacteria* were closely related to reference species with such metabolisms.

The genera *Desulfocella* and *Desulfococces* are within the *Deltaproteobacteria* order *Desulfobacterales*; *Desulfocella* are halophilic sulfate-reducing bacteria (SRBs) that also consume fatty acids, pyruvate, and a few other organic molecules (Brandt et al. 1999), and *Desulfococces* are SRBs that grow on long-chain alkanes (Aeckersberg et al. 1998). Reference sequences from these two genera grouped in a single clade, along with OTUs from NAS wells NAS-20, NAS-11, NAS-56, NAS-51, NAS-32, and NAS-21B, as well as the coalbed Coal-5. Other *Desulfobacterales* genera in this clade included *Desulfobacter*, *Desulfotignum*, and *Desulfobacterium*. *Desulfobacter* are SRBs that also consume acetate (Brandt and Ingvorsen 1997); *Desulfotignum* are SRBs that can utilize a wide variety of electron donors, including many organic molecules and aromatic compounds, producing acetate and CO_2 (Kuever et al. 2001); and

Desulfobacterium are SRBs that produce acetate (Brysch et al. 1987). OTUs that grouped in the *Desulfobacter/Desulfotignum/Desulfobacterium* clade are from NAS-20 and NAS-32.

Reference sequences from the *Deltaproteobacteria* order *Desulfovibrionales* were also present, including the genera *Desulfovibrio*, *Desulfomicrobium*, and *Desulfovermiculus*. Species within this order are moderately halophilic SRBs, and many of them utilize the same substrates as methanogens, such as hydrogen, acetate, and formate (Magot et al. 2004; Belyakova et al. 2006). OTUs associated with this order came from NAS-51, NAS-20, NAS-56, NAS-50, and NAS-11, all of which had elevated salinity.

Our phylogeny also contained reference sequences from the *Deltaproteobacteria* order *Desulforomonadales*, including sequences from the genera *Pelobacter*, *Desulfuromonas*, and *Desulfuromusa*. Unlike most *Deltaproteobacteria*, species within these genera do not reduce sulfate: *Pelobacter* species ferment alcohol and produce acetate (Schink 2006); *Desulfuromonas* species reduce sulfur, consuming acetate, lactate, succinate, and fatty acids, and producing CO_2 (Coates et al. 1995); and *Desulfuromusa* species reduce sulfur, consuming acetate, dicarboxylic acids, and fatty acids, and producing CO_2 (Liesack and Finster 1994). Additionally, OTUs from NAS-21B and Coal-1 clustered with the *Deltaproteobacteria* genus *Haliangium*, a moderately halophilic aerobe that can metabolize a number of organic molecules (Fudou et al. 2002).

Also included in the phylogeny are reference sequences from the genera *Syntrophus*, species of which also do not reduce sulfate. Instead, *Syntrophus* species reduce an electron acceptor, such as hydrogen or formate, to compounds that get immediately consumed by a syntrophic partner, such as a methanogen (Wallrabenstein et al. 1995). OTUs associated with *Syntrophus* were from NAS-21B and the coalbed Coal-1. Previous research has suggested that *Syntrophus* species may be involved in anaerobic oil degradation (Zengler et al. 1999; Jones et al. 2008). Notably, our data shows far fewer OTUs related to *Syntrophus* in the NAS than in oil degradation cultures (Jones et al. 2008).

There is one clade of OTUs that grouped with the *Proteobacteria* class *Epsilonproteobacteria*. The genus of the reference sequence is *Sulfurospirillum*, species of which can metabolize CO and acetate, and can reduce sulfur or nitrogen species (Jensen and Finster 2005). OTUs grouping with *Epsilonproteobacteria* were from NAS-21B and NAS-32.

Bacteria: Additional Phyla

In addition to the dominant bacterial orders described above, some OTUs clustered with reference sequences from bacterial orders in which far fewer reference sequences were included. For example, one clade of OTUs clustered with a reference sequence from the genus *Aminiphilus*, which is in the phylum *Synergistetes* and the order *Synergistales*. OTUs in this clade were from NAS-32, NAS-51, and NAS-56, as well as the coalbed Coal-5. *Aminiphilus* species are primarily mesophilic anaerobes that ferment an array of organic molecules, producing acetate (Díaz et al. 2007). One OTU from NAS-51 grouped with the genus *Acidobacteria* (phylum *Acidobacteria*, order *Acidobacteriales)*. Species from this genus are acidophilic, growing optimally in pH ranging from 3.0 to 6.0, and metabolize a number of organic molecules (Kishimoto et al. 1991). One OTU from NAS-32 grouped weakly the genus *Anaeroplasma* (phylum *Tenericutes*, order *Anaeroplamatales*). *Anaeroplasma* are obligate anaerobes that ferment starch, maltose, and cellubiose, producing CO_2, ethanol, and a variety of organic acids (Robinson et al. 1975). One OTU from NAS-56 grouped strongly with the genus *Caldilinea* (order *Chloroflexi*). *Chloroflexi* species are thermophiles that can metabolize a variety of organic molecules, including acetate (Sekiguchi et al. 2003), and are thought to use chlorinated compounds as electron acceptors in syntrophic associations with hydrogenotrophic microbes such as methanogens (Inagaki et al. 2006). One OTU from NAS-51 grouped with the genus *Corynebacterium* (order *Actinobacteria*). *Corynebacterium* species grow aerobically and produce acids by metabolizing organic molecules (Riegel et al. 1997). An OTU from NAS-21B also grouped with the *Actinobacteria* genus *Denitrobacterium*, which is metabolically similar to other *Actinobacteria*, but can also reduce nitrogen compounds (Anderson et al. 2000). One OTU from NAS-11 grouped with the genus *Flexistipes* (phylum *Deferribacteres*), a halophilic, heterotrophic genus first isolated from deep Red Sea sediments (Fiala et al. 1990). OTUs from NAS-20, NAS-21B, and NAS-56 grouped with the genus *Sphaerochaeta* (phylum *Spirochaetes*). Species in this genus ferment carbohydrates, producing acetate, ethanol, and CO_2 (Leschine et al. 2006).

Bacteria: Unclassified Clades

A number of bacterial OTUs clustered with reference sequences from uncultured bacteria. This is not surprising, since studies of other subsurface microbial communities have found that a majority of environmental sequences are distantly related to any cultured organisms (Sørensen and Teske 2006).

Our bacterial phylogeny contains four distinct groups of unclassified sequences, labeled unclassified bacteria I, II, III, and IV. A number of OTUs, including all grouped in “unclassified bacteria III” and many designated as “unclassified bacteria IV,” do not group with any reference sequences (Fig. 14); therefore, we have no information about their identity or metabolic properties. Sources for the reference sequences in “unclassified bacteria I” provide no phylogenetic or taxonomic information (Dhillon et al. 2003; Miyoshi et al. 2005), yielding no clues as to the metabolisms of the OTUs in this group. “Unclassified bacteria II” contains two unrelated branches, one with a reference sequence from a mud volcano and the other with a reference sequence from mangrove sediments; however, neither of these sequences are from published articles, so we were unable to clarify their phylogenetic identity or metabolic roles.


Thermoproteus_tenax_AY538182
Desulfurococcus_mobilis_M36474
Sulfolobus_metallicus_U40813
Methanogen_Evidenced_MethylCoenzymeMReductase_mcrA_Genes_Hydrothermal_Sediments_Guaymas_Basin_hydrothermal_sediment_clone_AY835428
NAS-11 e02
NAS-1 g11
NAS-50 (9)
NAS-56 (11)
NAS-51 (22)
NAS-11 (23)
NAS-1 (26)
NAS-51 e06
NAS-11 d07
NAS-1 f06
NAS-11 a06
NAS-11 g06
NAS-50 e03
NAS-11 g10
NAS-1 a04
Methanothermococcus_sp_AB260042
Methanococcus_maripaludis_U38485
NAS-21B (3)
NAS-20 (1)
NAS-21B b05
Methanococcales
Methanobacterium_subterraneum_DQ649330
Coal-1 d09
Coal-1 e12
Methanobacterium_sp_EU333014
Coal-1 (3)
Methanobacteriales
Cultivation_methanogens_shal_sediments_Hydrate_Ridge_Oregon_marine_sediment_clone_DQ058804
NAS-21B e12
NAS-50 (2)
NAS-56 (4)
NAS-11 (7)
NAS-1 (3)
NAS-1 c10
NAS-1 d09
NAS-11 b05
NAS-1 e07
NAS-11 c10
NAS-11 d10
NAS-1 (1)
NAS-51 (1)
NAS-51 d10
Methanosaeta_concilii_X16932
Coal-1 (4)
Coal-1 c05
Coal-1 d08
Coal-1 d10
Coal-1 h12
Coal-1 e04
Methanosarcina_mazei_AY196685
NAS-50 (3)
NAS-21B (1)
NAS-50 e04
NAS-21B b09
NAS-50 b11
NAS-21B a01
Methanosarcinales
NAS-20
NAS-50
NAS-21B
NAS-32
NAS-56
NAS-51
NAS-11
NAS-1
Coal-5
Coal-1

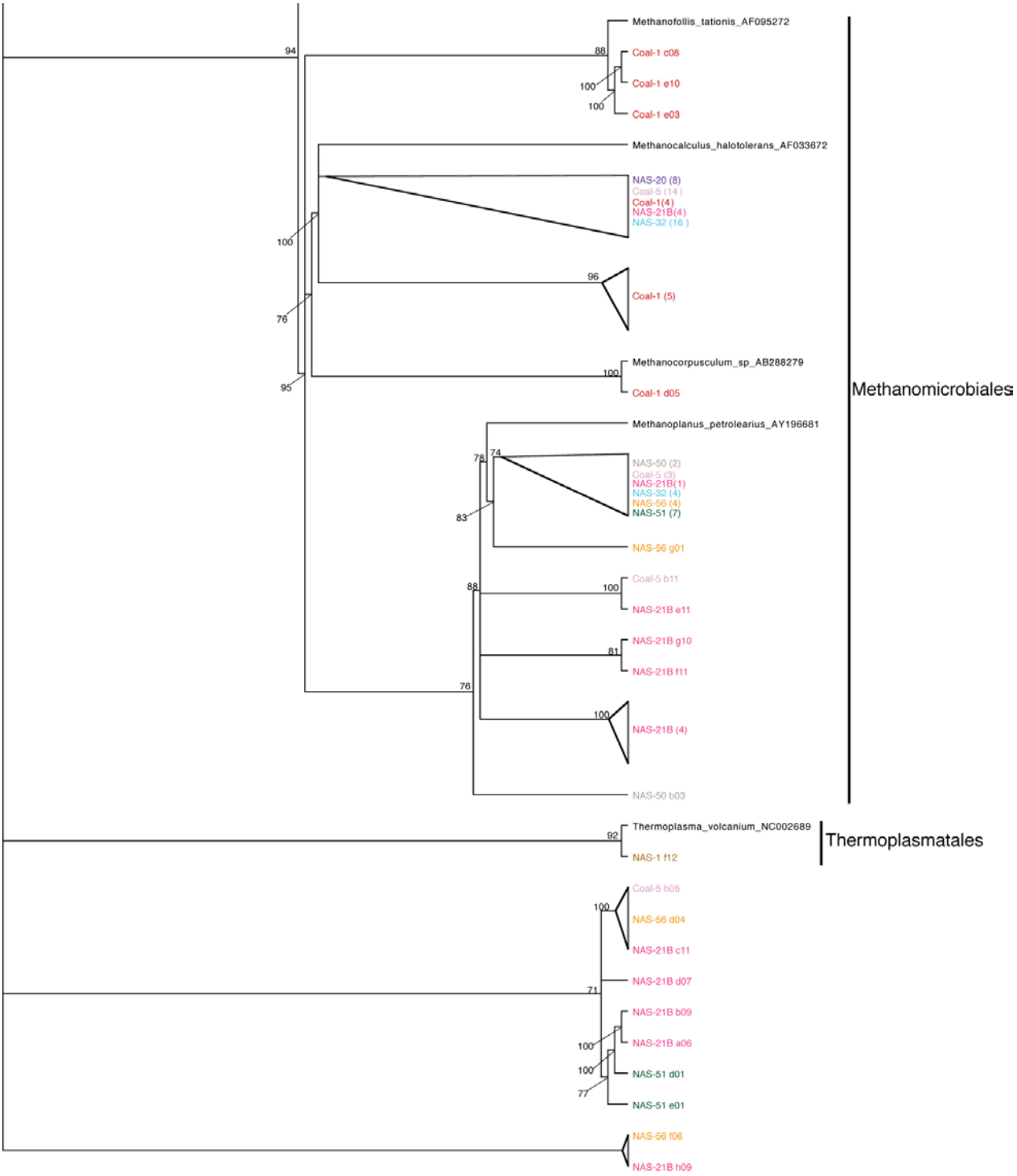


Figure 15: Archaea OTU tree

Archaea: Order Methanomicrobiales

About 35% (86/252) of the archaeal OTUs fell within the *Methanomicrobia* order *Methanomicrobiales* (Fig. 15), which consists entirely of mesophilic obligate anaerobes that use hydrogen/CO_2, formate, or alcohols as a substrate for methanogenesis, but not acetate or methylated C-1 compounds. Additionally, many species within this order have been isolated from subsurface ecosystems, including oil fields, groundwater, and drilling waste (Garcia et al. 2006). Three OTUs from the coalbed Coal-1 clustered with the genus *Methanofollis*, which consists of microbes that largely utilize hydrogen/CO_2 or formate for methanogenesis (Zellner et al. 1999). A number of OTUs, including sequences from NAS-20, NAS-21B, and NAS-32, as well both coalbeds, grouped with the genus *Methanocalculus* (Fig. 15); *M. halotolerans*, the reference species used, is a hydrogenotrophic methanogen with a wide salinity tolerance (Ollivier et al. 1998; Waldron et al. 2007). The genus *Methanoplanus* is another that incorporated OTUs from numerous wells, including NAS-50, NAS-21B, NAS-32, NAS-56, NAS-51, and the coalbed Coal-5 (Fig. 15). The reference species, *M. petrolearius*, was isolated from an oil field, and grows optimally at 1-3% NaCl. *Methanoplanus* species use formate for methanogenesis, although some are thought to be in symbiotic relationships that provide hydrogen for methanogenesis, and some species exhibit methanogenesis in the presence of CO_2 and hydrogen/2-propanol (Ollivier et al. 1997; Waldron et al. 2007). Finally, one OTU from the coalbed Coal-1 grouped strongly with the genus *Methanocorpusculum*, which consists of organisms that use hydrogen/CO_2, formate, and sometimes CO_2/2-propanol for methanogenesis, and have been isolated from a variety of ecosystems (Waldron et al. 2007). Additionally, *Methanocorpusculum* are thought to be the dominant archaeal genus in an Illinios Basin coalbed (Strąpoć et al. 2008), and were identified in an enrichment culture from the Antrim Shale (Waldron et al. 2007). *Methanocorpusculum* cannot inhabit waters with high salinity (Strąpoć et al. 2008); as Coal-1 has dramatically lower chloride concentrations than any other wells in this study, the absence of *Methanocorpusculum* sequences from the other wells may be due to salinity constraints. Six of the eight NAS wells, as well as both coalbeds, contained OTUs that group within *Methanomicrobiales*, species of which are methanogens that predominantly utilize hydrogen/CO_2 and formate as substrates.

Archaea: Orders Methanobacteriales, Methanococcus

Five archaeal OTUs from the coalbed Coal-1 clustered with sequences from the order *Methanobacteriales*. Species in this order are strict anaerobes that have been found in a wide variety of anoxic ecosystems, and use hydrogen/CO_2 to produce methane, although a few can also use formate, secondary alcohols, or CO (Bonin and Boone 2006).

OTUs from NAS-21B and NAS-20 clustered with reference species from the order *Methanococcales*. Species from this order also primarily use the hydrogen/CO_2 methanogenesis pathway. NAS sequences clustered close to *Methanococcus maripaludis*, a mesophile isolated from salt marshes that thrives in moderately saline environments (Whitman and Jeanthon 2006; Keswani et al. 2006). Chloride concentrations in NAS-21B and NAS-20 were quite high (889 mM and 687 mM, respectively); salinity may be a factor that constrains their archaeal community composition.

Overall, the majority of our archaeal OTUs clustered within the orders *Methanobacteriales*, *Methanomicrobiales*, and *Methanococcales*. As species from these groups predominantly use the hydrogen/CO_2 methanogenesis pathway, this may be the primary pathway for methanogenesis in the NAS and neighboring coalbeds.

Archaea: Order Methanosarcinales

The archaeal order *Methanosarcinales* contains two families: *Methanosarcinaceae* and *Methanosaetaceae*. In this study, the coalbed Coal-1 was the only site to have OTUs grouped within the genus *Methanosaeta* (Family *Methanosaetaceae*); species within this genus exclusively use acetate for methanogenesis, and have been found in a variety of anaerobic environments (Patel and Sprott 1990; Kendall and Boone 2006a). Multiple OTUs from NAS-50 and NAS-21B clustered with a reference sequence from the genus *Methanosarcina* (Family *Methanosarcinaceae*). Many members of *Methanosarcina* use acetate for methanogenesis, though they are outcompeted by *Methanosaeta* species; other *Methanosarcina* can use acetate or hydrogen/CO_2 for methanogenesis. Additionally, many *Methanosarcina* species are halotolerant (Kendall and Boone 2006a). Despite the lack of acetate found in any of the wells in this study, grouping of OTUs from NAS-50, NAS-21B, and Coal-1 within *Methanosarcinales* suggests that there may be an appreciable amount of acetate methanogenesis in these wells. This is highly likely in Coal-1, due to the grouping of Coal-1 OTUs within *Methanosaeta*. It is, however, important to remember that many *Methanosarcina* species can also use hydrogen/CO_2 for

methanogenesis, so the precise amount of acetoclastic methanogenesis cannot be deduced from *Methanosarcina*-bearing wells without further investigation.

Archaea: Order Thermoplasmatales

Interestingly, one OTU from NAS-1 clustered strongly (BS=92) with a reference sequence from the class *Thermoplasmatales*. The reference species, *Thermoplasma volcanium*, is a facultative anaerobe that grows optimally at 60°C and at a pH of 2. Some *Thermoplasma* species have been grown in culture using coal extract material. *Thermoplasma* species are different from the other archaea reference species not only in being thermophilic and acidophilic, but also in their metabolism: while the other archaeal reference species in our phylogeny are methanogens, *Thermoplasma* species typically grow via sulfur respiration (Segerer et al. 1988; Huber and Stetter 2006).

Archaea: Unclassified Clades

While many archaeal OTUs clustered with classified reference species, a large percentage of OTUs clustered with sequences from unclassified, uncultured organisms (Fig. 15). Unclassified archaeal clades were designated "unclassified I, II, III, and IV". A significant number of OTUs from NAS-11, NAS-1, NAS-50, NAS-56, and NAS-51 clustered in "unclassified I." The reference sequence in this clade was from a hydrothermal sediment in the Guaymas basin, and is part of an unclassified but distinct division of archaea called SAGMEG-1 (Dhillon et al. 2005), sequences of which were originally isolated from an African gold mine (Takai et al. 2001) but are now thought to be ubiquitous in subsurface environments (Mochimaru et al. 2007; Fry et al. 2009). Sequences from NAS-21B, NAS-50, NAS-56, NAS-11, NAS-1, and NAS-51 clustered within "unclassified II," which included a reference sequence isolated from marine sediments at Hydrate Ridge, Oregon. This reference sequence is in an unclassified archaeal division known as ANME-1, which, interestingly, is thought to consist of anaerobic methane oxidizing archaea (Hinrichs et al. 1999; Kendall and Boone 2006b). While ANME-1 sequences are commonly found in subsurface marine sediments, they have only recently been isolated from subsurface terrestrial sediments (Fry et al. 2009). While more evidence is needed to make any firm conclusions, the presence of ANME-1 sequences from a number of NAS wells suggests that there may be some level of anaerobic

methane oxidation at these sites. Certainly the geochemical and isotopic evidence from the produced gas would suggest anaerobic hydrocarbon oxidation.

The final two unclassified division of archaea, unclassified III and IV, did not cluster with any reference sequences. These groups include sequences from NAS-56, NAS-21B, and NAS-51, as well as the coalbed Coal-5. With these data, we are unable to speculate about their metabolic function in the ecosystem.

Summary of Microbial Diversity

In the eight NAS wells and two coalbed wells sampled in this study, the relative abundances of bacterial groups displayed no clear patterns between wells. Indeed, a striking characteristic of the bacterial libraries is the pervasive overall diversity; in none of the wells does one type of bacteria (excluding unclassified bacteria) account for over half of the bacterial clone library. *Clostridia* are present in all wells sampled, *Deltaproteobacteria* are present in all except the NAS well NAS-1, and *Bacteroidetes* is present in all except for the NAS well NAS-20 and the coalbed Coal-1. Additionally, all of the wells contain at least three different classes of bacteria, with many containing five classes or more. This rife bacterial diversity may simply reflect the high level of phenotypic and metabolic diversity among bacterial lineages, but may also suggest that comparable groups of bacteria fulfill similar niches at each location. Classified bacteria recovered within *Firmicutes*, *Deltaproteobacteria*, *Gammaproteobacteria*, and *Bacteroidetes* metabolize substrates derived from organic molecules present in shales, such as alkanes and hydrocarbons, producing products such as acetate, carbon dioxide, hydrogen, and bicarbonate. Many other bacteria recovered metabolize other organic intermediates such as amino acids.

The relative abundances of archaeal groups do not appear to display a clear pattern either. However, a significant proportion of archaeal OTUs clustered with sequences from unclassified organisms. While there appear to be distinct clades within these unclassified archaea, it is unclear what their metabolic roles and ecological significance are. However, it is important to note that most archaea recovered from NAS wells grouped with hydrogenotrophic methanogens (only NAS-50 had sequences clustered with acetotrophic methanogens), while the coalbed Coal-1 had both hydrogenotrophic and acetotrophic methanogens.

It is interesting to note that our data shows a similarity between the microbial communities of the wells NAS-1 and NAS-11; the only major difference between these two wells is in the *Proteobacteria* (NAS-11 has *Beta-* and *Deltaproteobacteria*, while NAS-1 has *Beta-* and *Gammaproteobacteria*). Since these wells are less than five kilometers apart and have analogous gas and aqueous geochemistry, they provide a control that many environmental microbiology studies do not include; the relative similarity of their communities suggests that the community composition of microbes is not random.

Though this study is the first known characterization of the microbial diversity of the NAS, a similar study was recently undertaken in the Antrim Shale (Michigan Basin, USA; Waldron et al. 2007). Archaeal 16S data from a low-salinity (12.8 mM Cl^-) Antrim Shale well suggested the exclusive presence of a single phylotype from the *Methanomicrobiales* genus *Methanocorpusculum*. In contrast, the high-salinity well (2,269 mM Cl^-) contained sequences from orders *Methanomicrobiales* and *Methanosarcinales*, weakly related to the genera *Methanoplanus* and *Methanohalophilus*, respectively (Waldron et al. 2007). Unfortunately, no bacterial data were generated, so we can only relate our archaeal data to this study.

In addition to the breakdown of shale, methane can be generated from the degradation of coal. A study of a methanogenic coalbed culture from the Powder River Basin (WY, USA; Green et al. 2008) suggested a dominant bacterial clade of *Firmicutes*, as well as clades of *Deltaproteobacteria* and *Spirochaeta*. The archaeal data showed a single clade closely related to the *Methanosarcinales* genus *Methanosarcina*. On the basis of these clone libraries, the authors argued that fermentation, acetogenesis, and acetoclastic methanogenesis were present, and emphasized the importance of acetogenic bacteria that convert intermediates such as organic molecules and carbohydrates into the substrates needed for methanogenesis (Green et al. 2008). Another recent coalbed study investigated western Canadian coalbeds (Penner et al. 2010). Most bacterial sequences from the coal were associated with *Alpha-*, *Beta-*, or *Gammaproteobacteria*; no archaeal sequences could be amplified directly from the coal. Enrichment experiments were also performed, which displayed a microbial assemblage closer to that of the present study: abundant *Firmicutes*, and significant but fewer numbers of *Betaproteobacteria*, *Gammaproteobacteria*, and *Bacteroidetes*. Archaea from the enrichments grouped exclusively with *Methanosarcina* (Penner et al. 2010). A third coalbed study investigated the microbial diversity present in both coal and cultured well water (Li et al. 2008). The only archaeal clade recovered from the coal was related to the genus *Archaeoglobus*, an anaerobic, hyperthermophilic, sulfate-reducing Euryarchaeoen

(Klenk et al. 1997). Bacterial sequences recovered from the coal were dominated by *Alpha-* and *Gammaproteobacteria*. No archaeal sequences could be recovered from the water, while bacterial sequences related to *Clostridiales*, *Bacillales*, *Gammaproteobacteria*, and *Betaproteobacteria* were abundant (Li et al. 2008). Generally, it appears that many coalbed communities contain bacterial assemblages potentially capable of breaking down organic matter, many of which metabolize organic molecules into methanogenic substrates such as acetate or carbon dioxide; similar assemblages were recovered in our bacterial clone libraries. The methanogenic communities in coalbeds appear to contain acetate-utilizing *Methanosarcinales* species. However, contrary to this hypothesis, dominance of archaeal sequences related to the hydrogenotrophic genis *Methanocorpusculum* have also been reported from coalbed samples (Strąpoć et al. 2008); therefore, more data are needed to make any generalizations about "typical" methanogenesis in coalbeds.

Similar to coal biodegradation, methane can also be naturally generated from the degradation of oil. A recent study investigating the microbial communities of methanogenic oil-degradation cultures (Gieg et al. 2008) predominantly found archaea similar to the acetotrophic genus *Methanosaeta*, although a few cultures suggested that hydrogenotrophic methanogens similar to *Methanobacterium* may also be present. Bacterial communities in these cultures contained a number of SRBs (*Desulfobulbus*, *Desulfosporosinus*, *Desulfovibrio*), fermentative bacteria (*Chloroflexi*, *Clostridiales*, *Bacteroidetes*), and syntrophic bacteria (*Desulfotomaculum*, *Smithella*; Gieg et al. 2008). Another study of oil-degrading cultures (Jones et al. 2008), bacterial communities were dominated by species from the genus *Syntrophus*, which participate in the syntrophic oxidation of alkanes and acetate; such reactions could produce the carbon dioxide and hydrogen needed for hydrogenotrophic methanogenesis. Archaeal data from the same cultures suggested the dominance of hydrogenotrophic methanogens, though some acetotrophic methanogens were present as well. The authors suggested that the hydrogen and carbon dioxide produced in the bacterially mediated oxidation of alkanes and acetate were utilized as substrates for methanogenesis. They coined this process "methanogenic alkane degradation dominated by CO_2 reduction (MADCOR)," and inferred that it is the predominant biodegradation pathway in oil reservoirs (Jones et al. 2008).

Though the studies summarized here only provide a cursory glance at the literature pertaining to methanogenic biodegradation, there appear to be a few trends in the microbial communities present at sites of degradation. The methanogenic degradation of any of the substrates appears to be accompanied

by a relatively diverse suite of bacteria that can metabolize organic molecules from the parent substrate, producing either the acetate or hydrogen/CO_2 needed for methanogenesis. Bacteria related to *Chloroflexi*, *Clostridiales*, *Proteobacteria*, *Firmicutes*, and *Bacteroidetes* appear to be widespread in these environments, though perhaps with significant differences in diversity at the genus or species level. However, it appears that there may be a difference in the type of methanogenesis present, depending on the parent substrate: tentatively, while biodegradation from coal may predominantly support acetotrophic methanogens, that of shale and oil appears to load to dominance of hydrogenotrophic methanogens. The eight NAS wells sampled in the present study show a clear dominance of hydrogenotrophic methanogens, although two of these wells (NAS-50 and NAS-21B) appear to contain sequences related to *Methanosarcinales*, as well. However, since the archaeal sequences recovered from the oil degradation cultures of Jones et al. (2008) also contained a small percentage (13-14%) of sequences closely related to acetotrophic methanogens, it is perhaps not surprising that we recovered some from shale as well.

Chapter 4: Synthesis

The microbial inhabitants of methane bearing strata in the Illinois Basin leave a fingerprint on natural gas and formation water chemistry. Low $\delta^{13}C_{CH_4}$ relative to $\delta^{13}C_{DIC}$ suggest high levels of hydrogenotrophic methanogenesis. The preponderance of hydrogenotrophic *Archaea* in clone libraries validates this geochemical proxy. Hydrogenotrophic methanogenesis in conjunction with lower levels of acetoclastic and methylotrophic methanogenesis leads to strong but imperfect covariance between δD_{H_2O} and δD_{CH_4} along a fractionation line predicted by the hydrogenotrophic pathway (Whiticar 1999). Admixtures of thermogenic methane can also skew this relationship. A finite pool of bicarbonate in the New Albany Shale as well as anaerobic methane oxidation may result in elevated $\delta^{13}C_{CH_4}$ in comparison to typical biogenic methane. Similarity between unclassified sequences from environments known to contain anaerobic methane-oxidizing consortia and clone library sequences affiliated with sulfate-reducers and methanogens suggests the presence of anaerobic methane oxidation in the New Albany

Shale. Unclassified *Archaea* thought to be related to methane-oxidizing consortia are more abundant at sites with elevated $\delta^{13}C_{CH_4}$. Although sulfate reduction maintains sulfate concentrations at a low level in the New Albany Shale compared to surrounding carbonates, non-competitive sulfate reduction via electron donors such as fatty acids and aromatics enables the coexistence of sulfate-reducers and *Archaea* above limiting sulfate concentrations, even in the absence of methane-oxidizing consortia. An increase in the ratio of methane to longer-chain hydrocarbons with depth, among other geochemical proxies, indicates that both thermogenic and biogenic natural gas sources contribute significantly to production in western Indiana.

Formation water geochemistry also leaves a fingerprint on the microbial communities of the New Albany Shale. This study confirms the implications of archaeal enrichments from the Antrim Shale of the Michigan Basin – methanogenic consortia adapt to formation waters of variable salinities (Waldron et al., 2007). Many clone library sequences are affiliated with reference species from hypersaline environments. Clone library sequences related to low halotolerance reference species, such as acetoclastic methanogens, most often inhabit wells with relative dilute formation waters. Archaeal group ecology changes over the regional salinity gradient. Unclassified *Archaea* dominate high salinity sites in western Indiana, whereas classified *Archaea* comprise the majority of sequences at lower salinity coal beds and New Albany Shale sites exposed to meteoric recharge.

Finally, this study for the first time proposes detailed pathways of anaerobic rock organic matter degradation based on the molecular phylogenetic evidence of many environmental samples (Figure 16). Microbial consortia in the New Albany Shale and Illinois Basin coal beds may be able to degrade organic molecules from multiple sources in the rock and reuse nearly every metabolic product (Swain and Rogers, 1966). Shale and coal organic matter degradation can produce molecular intermediates utilized in a metabolic chain reaction. (Refer to the pathway on the right side of Figure 16: oil alkane → fatty acid → propionate → formate → methane.) Rock organic matter degradation can alternatively proceed to completion through one metabolic reaction. (Refer to the pathway in the right-center of Figure 16: toluene → bicarbonate.) A suite of bacterial groups participate at all levels of biodegradation. In Figure 16, *Firmicutes*, *Bacteroidetes*, *Deltaproteobacteria*, and *Gammaproteobacteria* all metabolize substrates derived from the rock, and numerous organisms consume molecular intermediates. Moreover, traditional end-products bound for methanogenic consumption do not have a predetermined fate. Bicarbonate and acetate – to name two of the more common methanogenic substrates – cycle between each other through processes including homoacetogenesis and sulfate reduction (Figure 16, bottom and

left-center). Various organisms identified in clone libraries likely play a role in degrading microbial biomass such as amino acids (Figure 16, bottom-left). Lastly, anaerobic methane oxidation may remobilize the traditional terminal metabolic product, methane, under favorable thermodynamic conditions (Figure 16, bottom-left).

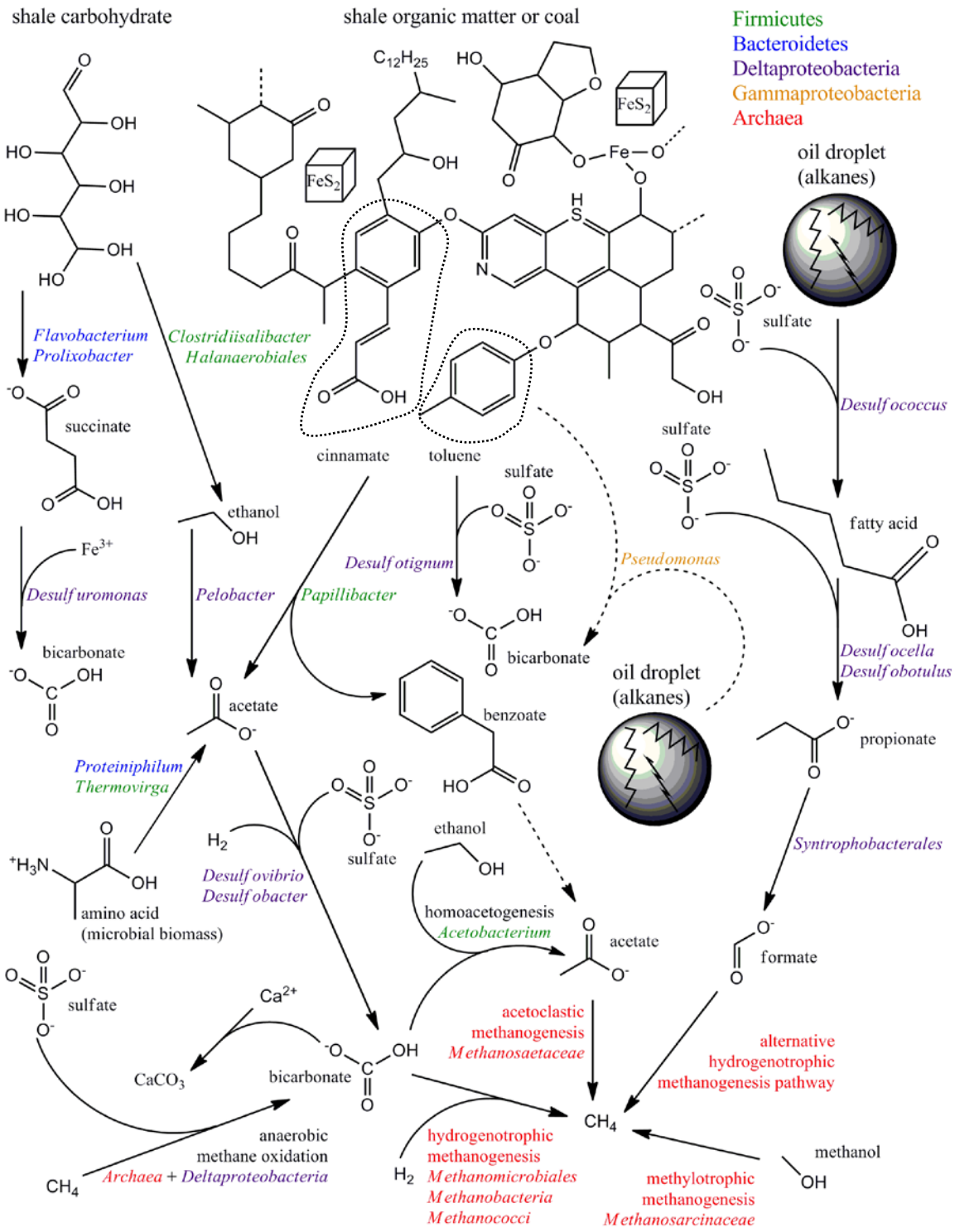


Figure 36: Anaerobic biogeochemistry in the Illinois Basin. Organisms can degrade a variety of organic compounds in shale and coal, including carbohydrates in the shale matrix and oil droplets. There are no end metabolites – methane, CO_2 (bicarbonate), and biomass all recycle. (Structure of coal adapted from Catcheside and Ralph, 1999.)

References:

Abdo, A., Schuette, U.M.E., Bent, S.J., Williams, C.J., Forney, L.J., Joyce, P., 2006, Statistical methods for characterizing diversity of microbial communities by analysis of terminal restriction fragment length polymorphisms of 16s rRNA genes, *Environmental Microbiology*, 8:5:929-938.

Allen, T.D., P.A. Lawson, M.D. Collins, E. Falsen, and R.S. Tanner. (2006). "*Clocaibacterium normanense* gen. nov., sp. nov., a Novel Bacterium in the Family *Flavobacteriaceae* Isolated from Municipal Wastewater." International Journal of Systematic and Evolutionary Microbiology 56, p. 1311-1316.

Amend, J.P. and Shock, E.L. (2001) Energetic of overall metabolic reactions of thermophilic and hyperthermophilic Archaea and Bacteria. *FEMS Microbiology Reviews* **25**, 175-243.

Angel, R., Soares, M.I.M., Ungar, E.D., Gillor, O., 2010, Biogeography of soil archaea and bacteria along a steep precipitation gradient, International Society for Microbial Ecology (ISME) Journal, 4, 552-563.

Baird, B. H., Nivens, D. E., Parker, J. H., and White, D. C. (1985) The biomass, community structure, and spatial distribution of the sedimentary microbiota from a high-energy area of the deep sea. *Deep Sea Research* **32**, 1089-1099.

Barrows, M.H. and R.M. Cluff, 1984, *New Albany Shale Group (Devonian-Mississippian) source rocks and hydrocarbon generation in the Illinois Basin*, in *AAPG Memoir: Petroleum geochemistry and basin evaluation*, G. Demaison and R.J. Murris, Editors, American Association of Petroluem Geologists. p. 111-138.

Berner, R.A. (1980) *Early Diagenesis: A Theoretical Approach.* Princeton Univ. Press. 237 p.

Bethke, C.M., Ding, D., Jin, Q., and Sanford, R.A., 2008, Origin of microbiological zoning in groundwater flows: Geology, v. 36, p. 739-742.

Bhupathiraju, V.K., M.J. McInerney, and R.M. Knapp. (1993). "Pretest Studies for a

Microbially Enhanced Oil Recovery Field Pilot in a Hypersaline Oil Reservoir." Geomicrobiology Journal 11:1, p. 19-34.

Bhupathiraju, V.K., M.J. McInerney, C.R. Woese, and R.S. Tanner. (1999). "*Haloanaerobium kushneri* sp. nov., an Obligately Halophilic, Anaerobic Bacterium from an Oil Brine." International Journal of Systematic and Evolutionary Microbiology 49, p. 953-960.

Boetius, A., K. Ravenschlag, C.J. Schubert, D. Rickert, F. Widdel, A. Gieseke, R. Amann, B.B. Jorgenen, U. Witte, and O. Pfannkuche. (2000). "A Marine Microbial Consortium Apparently Mediating Anaerobic Oxidation of Methane." Nature 407, p. 623-626.

Bonin, A.S. and D.R. Boone. (2006). "The Order *Methanobacteriales.*" *in* The Prokaryotes: A Handbook on the Biology of Bacteria, Third Edition 3:11, p. 231-243. Singapore: Springer.

Brandt, K.K., B.K.C. Patel, and K. Ingvorsen. (1999). "*Desulfocella halophila* gen. nov., sp. nov., a Halophilic, Fatty-Acid-Oxidizing, Sulfate-Reducing Bacterium Isolated from Sediments of the Great Salt Lake." International Journal of Systematic Bacteriology 49, p. 193-200.

Budai, J.M., A.M. Martini, L.M. Walter, and T.C.W. Ku. (2002). "Fracture-Fill Calcite as a Record of Microbial Methanogenesis and Fluid Migration: A Case Study from the Devonian Antrim Shale, Michigan Basin." Geofluids 2:3, p. 163-183.

Caldwell, S.L., J.R. Laidler, E.A. Brewer, J.O. Eberly, S.C. Sandborgh, and F.S. Colwell. (2008). "Anaerobic Oxidation of Methane: Mechanisms, Bioenergetics, and the Ecology of Associated Microorganisms." Environmental Science and Technology 42:18, p. 6791-6799.

Catcheside, D.E.A. and J.P. Ralph. (1999). "Biological Processing of Coal." Applied Microbiology and Biotechnology 52:1, p. 16-24.

Chao, A. (1989). "Estimating Population Size for Sparse Data in Capture-Recapture Experiments." Biometrics 45, p. 427-438.

Chen, S., and X. Dong. (2005). "*Proteiniphilum acetatigenes* gen. nov., sp. nov., from a UASB Reactor Treating Brewery Wastewater." International Journal of Systematic and Evolutionary Microbiology 55, p. 2257-2261.

Coates, J.D., D.J. Lonergan, E.J.P. Philips, H. Jenter, D.R. Lovley. (1995). "*Desulfuromonas palmitatis* sp. nov., a Marine Dissimilatory Fe(III) Reducer that can Oxidize Long-Chain Fatty Acids." Archives of Microbiology 164:6, p. 406-413.

Coates, J.D., J. Woodward, J. Allen, J., P. Philp, and D.R. Lovley. (1997). "Anaerobic Degradation of Polycyclic Aromatic Hydrocarbons and Alkanes in Petroleum-Contaminated Marine Harbor Sediments." Applied Environmental Microbiology 63:9, p. 3589-3593.

Colwell, F. S., Onstott, T. C., Delwiche, M. E., Chandler, D., Fredrickson, J. K., Yao, Q.-J., McKinley, J. P., Boone, D. R., Griffiths, R., Phelps, T. J., Ringelberg, D., White, D. C., LaFreniere, L., Balkwill, D., Lehman, R. M., Konisky, J., and Long, P. E. (1997) Microorganisms from deep, high temperature sandstones: constraints on microbial colonization. *FEMS Microbiology Reviews* **20**, 425-435.

Conrad, R. (2006). "Contribution of Hydrogen to Methane Production and Control of Hydrogen Concentrations in Methanogenic Soils and Sediments." FEMS Microbiology Ecology 28:3, p. 193-202.

Craig, H., 1961, Isotopic variations in meteoric waters: Science, v. 133, p. 1702-&.

Curtis, J. (2002). "Fractured Shale-Gas Systems." AAPG Bulletin 86:11, 2002, p. 1921-1938.

Dahle, H. and N.-K. Birkeland. (2006). "*Thermovirga lienii* gen. nov., sp. nov., a Novel Moderately Thermophilic, Anaerobic, Amino-Acid-Degrading Bacterium Isolated from a North Sea Oil Well." International Journal of Systematic and Evolutionary Microbiology 56, p. 1539-1545.

Davidson, R. (1994). "Nitrogen in Coal." International Energy Agency 32 pp. http://www.caer.uky.edu/iea/ieaper08.shtml.

Defnoun, S., M. Labat, M. Ambrosio, J.-L. Garcia, and B.K.C. Patel. (2000). "*Papillibacter cinnamivorans* gen. nov., sp. nov., a Cinnamate-Transforming Bacterium from a Shea Cake Digester." International Journal of Systematic and Evolutionary Microbiology 50 p. 1221-1228.

de Graaf, W., P. Wellsbury, R.J. Parkes, T.E. Cappenberg. (1996). "Comparison of Acetate Turnover in Methanogenic and Sulphate-Reducing Sediments by Radiolabelling and Stable Isotope Labelling and by Use of Specific Inhibitors: Evidence for Isotopic Exchange." Applied and Environmental Microbiology 62, p. 772-777.

Denger, K., R. Warthmann, W. Ludwig, and B. Schink. (2002). "*Anaerophaga thermohalophila* gen. nov., ap. nov., a Moderately Thermohalophilic, Strictly Anaerobic Fermentative Bacterium." International Journal of Systematic and Evolutionary Microbiology 52, p. 173-178.

DeSantis, T.Z., P. Hugenholtz, N. Larsen, M. Rojas, E.L. Brodie, K. Keller, T. Huber, D. Dalevi, P. Hu, and G.L. Andersen. (2006a). "Greengenes, A Chimera-Checked 16S rRNA Gene Database and Workbench Compatible with ARB." Applied and Environmental Microbiology 72:7, p. 5069-5072.

DeSantis, T.Z., P. Hugenholtz, K. Keller, E.L. Brodie, N. Larsen, Y.M. Piceno, R. Phan, and G.L. Andersen. (2006b). "NAST: A Multiple Sequence Alignment Server

for Comparative Analysis of 16S rRNA Genes." Nucleic Acids Research 34, p. W394-W399.

D'Hondt, S., Rutherford, S., and Spivack, A.J. (2002) Metabolic activity of subsurface life in deep-sea sediments. *Science* **295**, 2067-2070.

D'Hondt, S., Jorgensen, B. B., Miller, D. J., Batzke, A., Blake, R., Cragg, B. A., Cypionka, H., Dickens, G. R., Ferdelman, T., Hinrichs, K.-U., Holm, N. G., Mitterer, R., Spivack, A., Wang, G., Bekins, B., Engelen, B., Ford, K., Gettemy, G., Rutherford, S. D., Sass, H., Skilbeck, C. G., Aiello, I. W., Guerin, G., House, C. H., Inagaki, F., Meister, P., Naehr, T., Niitsuma, S., Parkes, R. J., Schippers, A., Smith, D. C., Teske, A., Wiegel, J., Padilla, C. N., and Acosta, J. L. S. (2004) Distributions of Microbial Activities in Deep Subseafloor Sediments. *Science* **306**(5705), 2216-2221.

Dinh, H.T., J. Kuever, M. Mussmann, A.W. Hassel, M. Stratmann, and F. Widdel. (2004). "Iron Corrosion by Novel Anaerobic Microorganisms." Nature 427, p. 829-832.

Drake, H.L., K. Kusel, and C. Matthies. (2006). "Acetogenic Prokaryotes." *in* The Prokaryotes: A Handbook on the Biology of Bacteria, Third Edition 2:1.13, p. 354-420. Singapore: Springer.

Economic Report of the President. (2010). Washington, D.C., Government Printing Office. http://www.whitehouse.gov/sites/default/files/microsites/economic-report-president.pdf.

Elvert, M., Suess, E., Greinert, J., and Whiticar, M. J. (2000) Archaea mediating anaerobic methane oxidation in deep-sea sediments at cold seeps of the eastern Aleutian subduction zone. *Organic Geochemistry* **31**, 1175-1187.

Emerson, S., Stump, C., Grootes, P. M., Stuiver, M., Farwell, G. W., and Schmidt, F. H. (1987) Estimates of degradable organic carbon in deep-sea surface sediments from ^{14}C concentrations. *Nature* **329**, 51-53.

Fiala, G., C.R. Woese, T.A. Langworthy, and K.O. Stetter (1990). "*Flexistipes sinusarabici*, a Novel Genus and Species of Eubacteria Occurring in the Atlantis II Deep Brines of the Red Sea." Archives of Microbiology 154, p. 120-126.

Formolo, M.J., J.M. Salacup, S.T. Petsch, A.M. Martini, and K. Nusslein. (2008). "A New Model Linking Atmospheric Methane Sources to Pleistocene Glaciation via Methanogenesis in Sedimentary Basins." Geology 36:2, p. 139-142.

Formolo, M., Martini, A., and Petsch, S. (2008) Biodegradation of sedimentary organic matter in the Powder River and San Juan Basins: The impact of thermal maturity. *International Journal of Coal Geology,* **76**, 86-97. invited submission.

Garcia, J.-L., B. Ollivier, W. Whitman. (2006). "The Order *Methanomicrobiales.*" *in* The Prokaryotes: A Handbook on the Biology of Bacteria, Third Edition 3:10, p. 208-230. Singapore: Springer.

Garnova, E.S., T.N. Zhilina, T.P. Tourova, N.A. Kostrikina, and G.A. Zavarzin. (2004). "Anaerobic, Alkaliphilic, Saccharolytic Bacterium *Alkalibacter saccharofermentans* gen. nov., sp. nov. from a Soda Lake in the Transbaikal Region of Russia." Extremophiles 8:4, p. 309-316.

Gluskoter, H.J. and O.W. Rees. (1964). "Chlorine in Illinois Coal." Illinois State Geological Survey Circular 372. Urbana: State of Illinois Department of Registration and Education.

Giovannoni, S.J., Delong, E.F., Schmidt, T.M., and Pace, N.R., 1990, Tangential Flow Filtration and Preliminary Phylogenetic Analysis of Marine Picoplankton: Applied and Environmental Microbiology, v. 56, p. 2572-2575.

Gray, N.D., A. Sherry, S.R. Larter, M. Erdmann, J. Leyris, T. Liengen, J. Beeder, and I.M. Head. (2009). "Biogenic Methane Production in Formation Waters from a Large Gas Field in the North Sea." Extremophiles 13:3, p. 511-519.

Green, M.S., K.C. Flanegan, and P.C. Gilcrease. (2008). "Characterization of a Methanogenic Consortium Enriched from a Coalbed Methane Well in the Powder River Basin, U.S.A." International Journal of Coal Geology 76:1-2, p. 34-45.

Grosskopf, R., Janssen, P.H., and Liesack, W., 1998, Diversity and structure of the methanogenic community in anoxic rice paddy soil microcosms as examined by cultivation and direct 16S rRNA gene sequence retrieval: Applied and Environmental Microbiology, v. 64, p. 960-969.

Grossman, E. L. and Desrocher, S. (2001) Microbial sulfur cycling in terrestrial subsurface environments. In *Subsurface Microbiology and Biogeochemistry* (ed. J. K. Fredrickson and M. Fletcher), pp. 219-247. Wiley-Liss, Inc.

Head, I.M., Jones, D.M., and Larter, S.R. (2003) Biological activity in the deep subsurface and the origin of heavy oil. *Nature* **426**, 344-352

Hill, D.G., J. Curtis and P. Lillis. (2008). "Update on North American Shale-Gas Exploration and Development" Rocky Mountain Association Guidebook p. 13-42

Hoehler, T. M., Alperin, M. J., Albert, D. B., and Martens, C. S. (2001) Apparent minimum free energy requirements for the methanogenic Archaea and sulfate reducing bacteria in an anoxic marine sediment. *FEMS Microbiology* **38**, 33-41.

Holmes, D.E., N.P. Nevin, T.L. Woodard, A.D. Peacock, and D.R. Lovley. (2007). "*Prolixibacter bellariivorans* gen. nov., sp. nov., a Sugar-Fermenting, Psychrotolerant Anaerobe of the Phylum *Bacteroidetes*, Isolated from a Marine-Sediment Fuel Cell." International Journal of Systematic and Evolutionary Microbiology 57, p. 701-707.

Horsley, S. (2010). "Obama Opens Up East Coast for Offshore Drilling." NPR, March 31, 2010. http://www.npr.org/templates/story/story.php?storyId=125420241.

Howarth, R. (2010). "Preliminary Assessment of the Greenhouse Gas Emissions from Natural Gas Obtained by Hydraulic Fracturing." 2010. http://www.eeb.cornell.edu/howarth/GHG%20emissions%20from%20Marcellus%20Shale%20--%20April%201,%202010%20draft.pdf.

Huang, R. (2008). Shale-Derived Dissolved Organic Matter as a Substrate for Subsurface Methanogenic Communities in the Antrim Shale, Michigan Basin, USA. M.Sc., University of Massachusetts.

Huber, T., G. Faulkner, and P. Hugenholtz. (2004). "Bellerophon: A Program to Detect Chimeric Sequences in Multiple Sequence Alignments." Bioinformatics 20:14, p. 2317-2319.

Hubert, C. and G. Voordouw. (2007). "Oil Field Souring Control by Nitrate-Reducing *Sulfurospirillum* spp. that Outcompete Sulfate-Reducing *Bacteria* for Organic Electron Donors." Applied Environmental Microbiology 73:8, p. 2644-2652.

Inagaki, F., T. Nunoura, S. Nakagawa, A. Teske, M. Lever, A. Lauer, M. Suzuki, K. Takai, M. Delwiche, F.S. Colwell, K.H. Nealson, K. Horikoshi, S. D'Hondt, and B.B. Jorgenson. (2006). "Biogeographical distribution and Diversity of Microbes in methane Hydrate-Bearing Deep Marine Sediments on the Pacific Ocean Margin." Proceedings of the National Academy of Sciences 103:8, p. 2815-2820.

Jones, D.M., I.M. Head, N.D. Gray, J.J. Adams, A.K. Rowan, C.M. Aitken, B. Bennett, H. Huang, A. Brown, B.F.J. Bowler, T. Oldenburg, M. Erdmann and S.R. Larter. (2008). "Crude-Oil Biodegradation via Methanogenesis in Subsurface Petroleum Reservoirs." Nature 451, p. 178-180.

Kanagawa, T. (2003). "Bias and Artifacts in Multitemplate Polymerase Chain Reactions (PCR)." Journal of Bioscience and Bioengineering 96:4, p. 317-323.

Kemp, P.F. and J.Y. Aller. (2004). "Estimating Prokaryotic Diversity: When Are 16S rDNA Libraries Large Enough?" Limnology and Oceanography: Methods 2, p. 114-125.

Kendall, M.M. and D.R. Boone (2006). "The Order Methanosarcinales" *in* The Prokaryotes: A Handbook on the Biology of Bacteria, Third Edition 3:12, p. 244-256. Singapore: Springer.

Khan, S.T. and A. Hiraishi. (2002). "*Diaphorobacter nitroreducens* gen nov, sp nov, a Poly(3-hydroxybutyrate)-Degrading Denitrifying Bacterium Isolated from Activated Sludge." The Journal of General and Applied Microbiology 48:6, p. 299-308.

Kirk, M.F., A.M. Martini, J.C. McIntosh, S.T. Petsch, and C. Takacs-Vesbach. (2009). "Effect of Natural Gas Production on Geochemistry and Microbiology in a Fractured Organic-Rich Shale." Goldschmidt Conference Abstracts 2009.

Kotelnikova, S. (2002) Microbial production and oxidation of methane in deep subsurface. *Earth-Science Reviews* **58**, 367-395.

Krumholz, L. R., McKinley, J. P., Ulrich, G. A., and Suflita, J. M. (1997) Confined subsurface microbial communities in Cretaceous rock. *Nature* **386**, 64-66.

Krumholz, L.R., S.H. Harris, and J.M. Suflita. (2002). "Anaerobic Microbial Growth from Components of Cretaceous Shales. Geomicrobiology Journal 19, p. 593-602.

Kuever, J., F.A. Rainey, and F. Widdel. (2005a). "Genus IV. *Desulfobotulus* gen. nov." *in* Bergey's Manual of Systematic Bacteriology: Second Edition 2, p. 970. Singapore: Springer.

Kuever, J., F.A. Rainey, and F. Widdel. (2005b). "Genus I. *Desulfarculus* gen. nov." *in* Bergey's Manual of Systematic Bacteriology: Second Edition 2, p. 1004-1005. Singapore: Springer.

Lai, M.-C., T.-Y. Hong, and R.P. Gunsalus. "Glycine Betaine Transport in the Obligate Halophilic Archaeon *Methanohalophilus portucalensis*." Journal of Bacteriology 182:17, p. 5020-5024.

Larter, S. R., Wilhelms, A., Head, I., Koopmans, M., Aplin, A., Di Primio, R., Zwach, C., Erdmann, M., and Telnaes, N. (2003) The controls on the composition of biodegraded oils in the deep subsurface - part 1: biodegradation rates in petroleum reservoirs. *Organic Geochemistry* **34**, 601-613.

Leschine, S., B.J. Paster, and E. Canale-Parola. (2006). "Free-Living Saccharolytic Spirochaetes: The Genus *Spirochaeta*" *in* The Prokaryotes: A Handbook on the Biology of Bacteria, Third Edition 7:4.1, p. 195-210. Singapore: Springer.

Liebgott, P.-P., M. Joseph, M.-L. Fardeau, J.-L. Cayol, E. Falsen, F. Chamkh, A.I.-

Qatibi, and M. Labat. (2008). "*Clostridiisalibacter paucivorans* gen. nov., sp. Nov., A Novel Moderately Halophilic Bacterium Isolated from Olive Mill Wastewater." International Journal of Systematic and Evolutionary Microbiology 58, p. 61-67.

Lien, T. and J. Beeder. (1997). "*Desulfobacter vibrioformis* sp. nov., a Sulfate Reducer from a Water-Oil Separation System." International Journal of Systematic Bacteriology 47:4, p. 1124-1128.

Lloyd, K.G., L. Lapham, and A. Teske. (2006). "An Anaerobic Methane-Oxidizing Community of ANME-1b Archaea in Hypersaline Gulf of Mexico Seidments." Applied and Environmental Microbiology 72:11, p. 7218-7230.

Lovley, D.R. and Goodwin, S. (1988) Hydrogen concentration as an indicator of the terminal-electron-accepting reactions in aquatic sediments. *Geochimica et Cosmochimica Acta* **52**, 2993-3003.

Madigan, M.T., J.M. Martinko, P.V. Dunlap, and D.P. Clark. (2009). Brock Biology of Microorganisms. San Francisco, Pearson Benjamin Cummings.

Magot, M., O. Basso, C. Tardy-Jacquenod, and P. Caumette. (2004). "*Desulfovibrio bastinii* sp. nov. and *Desulfovibrio gracilis* sp. nov., Moderately Halophilic, Sulfate-Reducing Bacteria Isolated from Deep Subsurface Oilfield Water." International Journal of Systematic and Evolutionary Microbiology 54, p. 1693-1697.

Martini, A.M., L.M. Walter, J.M. Budai, T.C.W. Ku, C.J. Kaiser, and M. Schoell. (1998). "Genetic and Temporal Relations between Formation Waters and Biogenic Methane: Upper Devonian Antrim Shale, Michigan Basin, USA." Geochimica et Cosmochimica Acta 62:10, p. 1699-1720.

Martini, A.M., L.M. Walter, T.C.W. Ku, J.M. Budai, J.C. McIntosh, and M. Schoell. (2003). "Microbial Production and Modification of Gases in Sedimentary Basins: A Geochemical Case Study from a Devonian Shale Gas Play, Michigan Basin." AAPG Bulletin 87:8, p. 1355-1375.

Martini, A.M., L.M. Walter, and J.C. McIntosh. (2008). "Identification of Microbial and Thermogenic Gas Components from Upper Devonian Black Shale Cores, Illinois and Michigan Basins." AAPG Bulletin 92:3, p. 327-339.

Martini, A.M., Budai, J.M., Walter, L.M., and Schoell, M., 1996, Microbial generation of economic accumulations of methane within a shallow organic-rich shale: Nature, v. 383, p. 155-158.

Martini, A.M., Nusslein, K., and Petsch, S., 2004, Enhancing microbial gas from unconventional reservoirs: Geochemical and microbiological characterization of methane-rich fractured black shales, RPSEA-0024-04 / GRI-05/0023, Research Partnership to Secure Energy for America, p. 43.

McClay, K., S.H. Streger, and R.J. Steffan. (1995). "Induction of Toluene Oxidation Activity in *Pseudomonas mendocina* KR1 and *Pseudomonas* sp. Strain ENVPC5 by Chlorinated Solvents and Alkanes." Applied and Environmental Microbiology 61:9, p. 3479-3481.

McIntosh, J.C., L.M. Walter, and A.M. Martini. (2002). "Pleistocene Recharge to Midcontinent Basins: Effects on Salinity Structure and Microbial Gas Generation." Geochimica et Cosmochimica Acta 66:10, p. 1681-1700.

McIntosh, J. C., Walter, L. M., and Martini, A. M. (2004) Extensive modification of formation water geochemistry : Case study from a Midcontinent sedimentary basin, United States. *GSA Bulletin* **116**, 743-759.

McIntosh, J.C., and L.M. Walter. (2005). "Volumetrically Significant Recharge of Pleistocene Glacial Meltwaters into Epicratonic Basins: Constratins Imposed by Solute Mass Balances." Chemical Geology 222:3-4, p. 292-309.

McIntosh, J.C. and L.M. Walter, (2006), *Paleowaters in Silurian-Devonian carbonate aquifers: geochemical evolution of groundwater in the Great Lakes region since the Late Pleistocene.* Geochimica et Cosmochimica Acta, **70**: p. 2454-2479.

Mechichi, T., M. Labat, B.K.C. Patel, T.H.S. Woo, P. Thomas, and J.-L. Garcia. (1999). "*Clostridium methoxybenzovorans* sp. nov., a New Aromatic o-Demethylating Homoacetogen from an Olive Mill Wastewater Treatment Digestor." International Journal of Systematic Biology 49, p. 1201-1209.

Nakai, N., Yoshida, Y., and Ando, N., 1974, Isotopic studies on oil and natural gas fields in Japan: Chikyakaya, v. 7/8, p. 87-89.

Ollivier, B., Caumette, P., Garcia, J.-L. & Mah, R. A. (1994). Anaerobic bacteria from hypersaline environments. *Microbiology Reviews* **58**, 27-38.

Oremland, R.S., Keine, R.P., Mathrani, I., Whiticar, M.J., and Boone, D.R. (1988) Descripion of an estuarine methylotrophic methanogen which grows on dimethylsulfide. *Applied and Environmental Microbiology* **55**, 994-1002.

Oremland, R.S., Miller, L.G. and Whiticar, M.J. (1987) Sources and flux of natural gases from Mono Lake, California. *Geochimica et Cosmochimica Acta* **51**, 2915-2929.

OilTracers LLC. (2009). "Determining the Origin of Hydrocarbon Gas Shows and Gas

Seeps (Bacterial Gas vs. Thermogenic Gas) Using Gas Geochemistry." http://www.gaschem.com/determ.html.

Ommedal, H. and T. Torsvik. (2007). "*Desulfotignum toluenicum* sp. nov., a Novel Toluene-Degrading, Sulphate-Reducing Bacterium Isolated from an Oil-Reservoir Model Column." International Journal of Systematic and Evolutionary Microbiology 57, p. 2865-2869.

Oremland, R.S. and S. Polcin. (1982). "Methanogenesis and Sulfate Reduction: Competitive and Noncompetitive Substrates in Estuarine Sediments." Applied and Environmental Microbiology 44:6, p. 1270-1276.

Oren, A. (2006). "The Order *Haloanaerobiales*." *in* The Prokaryotes: A Handbook on the Biology of Bacteria, Third Edition 4:1.2.27, p. 809-822. Singapore: Springer.

Orphan, V. J., Hinrichs, K.-U., Ussler III, W., Paull, C. K., Taylor, L. T., Sylva, S. P., Hayes, J. M., and DeLong, E. F. (2001) Comparative analysis of methane-oxidizing archaea and sulfate-reducing bacteria in anoxic marine sediments. *Applied and Environmental Microbiology* **67**, 1922-1934

Parkes, R.J., Cragg, B.A., Bale, S.J., Goodman, K., and Fry, J.C. (1995) A combined ecological and physiological approach to studying sulfate reduction within deep marine sediment layers. *Journal of Microbiological Methods* **23**, 235-249.

Penner, T.J., J.M. Foght, and K. Budwill. (2010). "Microbial Diversity of Western Canadian Subsurface Coal Beds and Methanogenic Coal Enrichment Cultures." International Journal of Coal Geology 82, p. 81-93.

Petsch, S.T., R.J. Smernik, T.I. Eglinton, and J.M. Oades. (2001). "A Solid State ^{13}C-NMR Study of Kerogen Degradation during Black Shale Weathering." Geochimica et Cosmochimica Acta 65:12, p. 1867-1882.

Posada, D., 2008, jModelTest: Phylogenetic model averaging: Molecular Biology and Evolution, v. 25, p. 1253-1256.

Quaiser, A., T. Ochsenreiter, C. Lanz, S.C. Schuster, A.H. Treusch, and C. Schleper. (2003). "*Acidobacteria* Form a Coherent but Highly Diverse Group within the Bacterial Domain: Evidence from Environmental Genomics." Molecular Microbiology 50:2 p. 563-575.

Rahman, K.S.M., J. Thahira-Rahman, P. Lakshmanaperumalsamy, and I.M. Banat. (2002). "Towards Efficient Crude Oil Degradation by a Mixed Bacterial Consortium." Bioresource Technology 85:3, p. 257-261.

Riegel, P., R. Heller, G. Prevost, F. Jehl, and H. Monteil. "*Corynebacterium durum* sp. nov., from Human Clinical Specimens." International Journal of Systematic Bacteriology 47:4, p. 1107-1111.

Ringelberg, D. B., Sutton, S., and White, D. C. (1997) Biomass, bioactivity and biodiversity: microbial ecology of the deep subsurface: analysis of ester-linked phospholipid fatty acids. *FEMS Microbiology Reviews* **20**, 371-377.

Rogers, J.E., R.G. Riley, S.W. Li, D.C. Mann, and R.E. Wildung. (1981). "Microbiological Degradation of Organic Components in Oil Shale Retort Water: Organic Acids." Applied and Environmental Microbiology 42:5, p. 830-837.

Romond, C. (1980). "The Taxonomy of the Peptococcaceae." Infection 8:S2, p. 153-154.

Ronquist, F. and J.P. Huelsenbeck. (2003). "MrBayes 3: Bayesian Phylogenetic Inference under Mixed Models." Bioinformatics 19, p. 1572-1574.

Rowe, D. and A. Muehlenbachs. (1999). "Low-Temperature Thermal Generation of Hydrocarbon Gases in Shallow Shales." Nature 398, p. 61-65.

Schink, B. (2006). "The Genus *Pelobacter*" *in* The Prokaryotes: A Handbook on the Biology of Bacteria, Third Edition 7:3.4.1, p. 5-11. Singapore: Springer.

Schloss, P.D., S.L. Westcott, T. Ryabin, J.R. Hall, M. Hartmann, E.B. Hollister, R.A. Lesniewski, B.B. Oakly, D.H. Parks, C.J. Robinson, J.W. Sahl, B. Stres, G.G. Thallinger, D.J. Van Horn, and C. F. Weber. (2009). "Introducing mothur: Open-Source, Platform-Independent, Community-Supported Software for Describing and Comparing Microbial Communities." Applied and Environmental Microbiology 75:23, p. 7537-7541.

Schloss, P.D. and J. Handelsman. (2005). "Introducing DOTUR, A Computer Program for Defining Operational Taxonomic Units and Estimating Species Richness." Applied and Environmental Microbiology 71:3, p. 1501-1506.

Schwarz, J.I.K., W. Eckert, R. Conrad. (2007). "Community Structure of Archaea and Bacteria in a Profundal Lake Sediment Lake Kinneret (Israel)." Systematic and Applied Microbiology 30, p. 239-254.

Schoell, M. (1980). "The Hydrogen and Carbon Isotopic Composition of Methane from Natural Gases of Various Origins." Geochimica et Cosmochimica Acta 44:5, p. 649-661.

Shaw, J. (2002). "The Great Global Experiment." Harvard Magazine November-December 2002. http://harvardmagazine.com/2002/11/the-great-global-experim.html.

Simankova, M.V., N.A. Chernych, G.A. Osipov, and G.A. Zavarzin. (1993). "Halocella cellulolytica gen. nov., sp. nov., A New Obligately Anaerobic, Halophilic, Cellulolytic Bacterium." Systematic and Applied Microbiology 16:3, p. 385-389.

So, M.C., C.D. Phelps, and L.Y. Young. (2003). "Anaerobic Transformation of Alkanes

to Fatty Acids by a Sulfate-Reducing Bacterium, Strain Hxd3." Applied and Environmental Microbiology 69:7 p. 3892-3900.

Sobieraj, M. and D.R. Boone. (2005). "Genus IV. *Smithella* Liu, Balkwill, Aldrich, Drake and Boone 1999, 553." *in* Bergey's Manual of Systematic Bacteriology: Second Edition 2, p. 1039. Singapore: Springer.

Strapoc, D., F.W. Picardal, C. Turich, I. Schaperdoth, J.L. Macalady, J.S. Lipp, Y.-S. Lin, T.F. Ertefai, F. Schubotz, K.-U. Hinrichs, M. Mastalerz, and A. Schimmelmann. (2008) "Methane-Producing Microbial Community in a Coal Bed of the Illinois Basin." Applied and Environmental Microbiology 74:8, p. 2424-2432.

Swain, F.M. and M.A. Rogers. (1966). "Stratigraphic Distribution of Carbohydrate Residues in Middle Devonian Onondaga Beds of Pennsylvania and Western New York. Geochimica et Cosmochimica Acta 30:5 p. 490-502.

Swofford, D.L., 2003, PAUP*, Phylogenetic Analysis Using Parsimony (*and other methods): Sunderland, MA, USA, Sinauer Associates, Inc.

Takai, K., M.R. Mormile, J.P. McKinley, F.J. Brockman, W.E. Holben, W.P. Kovacik, and J.K. Fredrickson. (2003). "Shifts in Archaeal Communities Associated with Lithological and Geochemical Variations in Subsurface Cretaceous Rock." Environmental Microbiology 5, p. 309-320.

Tardy-Jacquenod, C., M. Margot, B.K.C. Patel, R. Matheron, and P. Caumette. (1998). "*Desulfotomaculum halophilum* sp. nov., a Halophilic Sulfate-Reducing Bacterium Isolated from Oil Production Facilities." International Journal of Systematic Bacteriology 48, p. 333-338.

Ulrich, G. A., Martino, D., Burger, K., Routh, J., Grossman, E. L., Ammerman, J. W., and Suflita, J. M. (1998) Sulfur cycling in the terrestrial subsurface: Commensal interactions, spatial scales, and microbial heterogeneity. *Microbial Ecology* **36**, 141-151

U.S. Department of Energy. (2009). Modern Shale Gas Development in the United States: A Primer. http://fossil.energy.gov/programs/oilgas/publications/naturalgas_general/Shale_Gas_Primer_2009.pdf.

Valentine, D.L. and W.S. Reeburgh. (2008). "New Perspectives on Anaerobic Methane Oxidation." Environmental Microbiology 2:5, p. 477-484.

Vetö, I., Futo, I., Horvath, I., and Szanto, Z. (2004) Late and deep fermentative methanogenesis as reflected in the H-C-O-S isotopy of the methane-water system in deep aquifers of the Pannonian Basin (SE Hungary). *Organic Geochemistry* **35**, 713-723.

Vetriani, C., Jannasch, H. W., MacGregor, B. J., Stahl, D. A., and Reysenback, A.-L. (1999) Population structure and phylogenetic characterization of marine benthic Archaea in deep sea sediments. *Applied and Environmental Microbiology* **65**, 4375-4384.

Waldron, P.J., S.T. Petsch, A.M. Martini, and K. Nusslein. (2007). "Salinity Constraints on Subsurface Archaeal Diversity and Methanogenesis in Sedimentary Rock Rich in Organic Matter." Applied and Environmental Microbiology 73, p. 4171-4179.

Ward, D.M., and Winfrey, M.R., 1985, Interactions between methanogenic and sulfate-reducing bacteria in sediments: Advances in Aquatic Microbiology, v. 3, p. 141-179.

Werner-Zwanziger, U., G. Lis, M. Mastalerz, and A. Schimmelmann. (2005). "Thermal Maturity of Type II Kerogen from the New Albany Shale Assessed by ^{13}C CP/MAS NMR." Solid State Nuclear Magnetic Resonance 27:1-2, p. 140-148.

Wellsbury, P., Goodman, K., Cragg, B.A., and Parkes, R.J. (2000) The geomicrobiology of deep marine sediments from Blake Ridge containing methane hydrates (Sites 994, 995, and 997). *Proceedings of the Ocean Drilling Program, Scientific Results* **164**, 379-391.

Wellsbury, P., Mather, I., and Parkes, R. J. (2002) Geomicrobiology of deep, low organic carbon sediments in the Woodlark Basin, Pacific Ocean. *FEMS Microbiology Ecology* **42**, 59-70. White, 2000

Whiticar, M.J., E. Faber, and M. Schoell (1986). "Biogenic Methane Formation in Marine and Freshwater Environments: CO_2 Reduction versus Acetate Fermentation – Isotopic Evidence." Geochimica et Cosmochimica Acta 50:5, p. 693-709.

Whiticar, M.J. (1999). "Carbon and Hydrogen Systematics of Bacterial Formation and Oxidation of Methane." Chemical Geology 161:1-3, p. 291-314.

Whitman, W.B. and C. Jeanthon. "Methanococcales." *in* The Prokaryotes: A Handbook on the Biology of Bacteria, Third Edition 3:13, p. 257-273.

Wiegel, J., R. Tanner, and F.A. Rainey. (2006). "An Introduction to the Family *Clostridiaceae*." *in* The Prokaryotes: A Handbook on the Biology of Bacteria, Third Edition 4:1.2.20, p. 654-678.

Wilhelms, A., Larter, S. R., Head, I., Farrimond, P., di-Primio, R., and Zwach, C. (2001) Biodegradation of oil in uplifted basins prevented by deep-burial sterilization. **411**(6841), 1034-1037.

Woese, C.R. (1987). "Bacterial Evolution." Microbiological Reviews 51:2, p. 221-271.

Zehnder, A.J.B, (1988) *Biology of Anaerobic Microorganisms*. Wiley, New York.

Zhang, T. and B.M. Krooss. (2001). "Experimental investigation on the Carbon Isotope Fractionation of Methane during Gas Migration by Diffusion through Sedimentary Rocks at Elevated Temperature and Pressure." Geochimica et Cosmochimica Acta 65:16, p. 2723-2742.

Zhang, J., P.D. Quay, and D.O. Wilbur. (1994). "Carbon Isotope Fractionation during Gas-Water Exchange and Dissolution of CO_2." Geochimica et Cosmochimica Acta 59:1, p. 107-114.

Appendix

Table 1. List of wells used in geochemical analysis.

Suggested Sample ID	Depth m	County	State	Date	Temperature °C	Alkalinity mM	pH	Density g/cm³	Cell count cells/mL	$\delta^{18}O$ ‰	δD ‰	$\delta^{13}C_{DIC}$ ‰
NAS-1	628	Knox	IN	7/24/2013	22.895	24.2	7.1	1.047		-2.22	-8.00	28.98
NAS-2	644	Knox	IN	7/24/2013	19.3	32.8	7.3	1.019		-2.63	-8.62	29.22
NAS-3	654	Knox	IN	7/24/2013	20.8	19.3	6.7	1.039		-1.80	-7.43	27.77
NAS-4	661	Knox	IN	7/24/2013	19.2	26.9	7.5	1.023		-1.64	-16.19	29.45
NAS-5	674	Knox	IN	7/24/2013	19.8	22.2	6.4	1.044		-1.29	-6.15	28.63
NAS-6	680	Knox	IN	7/25/2013	20.67	22.7	7.0	1.034		-0.99	-16.37	28.13
NAS-7	684	Knox	IN	7/25/2013	17.8	12.8	6.8	1.046		-1.50	-14.38	27.67
NAS-8	707	Knox	IN	7/25/2013	21.95	23.3	7.0	1.040		-1.23	-15.68	27.97
NAS-9	736	Knox	IN	7/25/2013	29.7	30.9	6.4	1.036		-3.02	-14.63	26.86
NAS-10	743	Knox	IN	7/25/2013	29.6	27.5	6.5	1.054		-1.61	-5.90	28.73
NAS-11	652	Knox	IN	7/25/2013	22.33	34.1	6.7	1.021		-2.11	-4.00	28.47
NAS-12	789	Knox	IN	1/12/2012	10.7	32.5	6.0	1.091		-3.5	-10	24.3
NAS-13	491	Knox	IN	1/12/2012	9	1.9	7.6	1.089		-1.7	-8	30.5
NAS-14	753	Knox	IN	1/12/2012		18.0	8.0	1.092		-2.8	-20	29.2
NAS-15	805	Knox	IN	1/12/2012		10.1	7.6	1.055		-2.4	-11	28.7
NAS-16	797	Knox	IN	5/14/2012		24.8	7.6	1.051		-3.9	-17	30.5
NAS-17	747	Knox	IN	5/14/2012		17.1	8.5	1.085		-1.9	-11	32.2
NAS-18	564	Greene	IN	6/17/2012	17.2	36.6	5.7	1.022	3.26E+06	-5.0	-29	27.6
NAS-19	514	Greene	IN	6/17/2012								
NAS-20	472	Greene	IN	6/17/2012	16.3	4.5	6.3	1.031				
NAS-21	233	Meade	KY	1/10/2012	14.7	13.9	6.6	1.039	1.35E+06	-4.6	-23	29.7
NAS-22	175	Meade	KY	1/10/2012	15.6	15.8	6.8	1.047	2.20E+05	-3.9	-20	29.4
NAS-23	302	Harrison	IN	1/10/2012	13.2	10.7	6.5	1.069		-1.1	-10	25.5
NAS-24	290	n - Webst	IN	1/10/2012	12.9	6.7	6.4	1.088	2.75E+05	-0.9	-13	26.4
NAS-25	411	Harrison	IN	1/10/2012	12.9	7.5	6.8	1.075	3.06E+06	-2.3	-14	24.5
NAS-26	283	Harrison	IN	1/10/2012	11.5	8.5	6.7	1.076		-1.0	-14	27.4
NAS-27	366	Harrison	IN	1/10/2012	12.9	3.1	6.6	1.081		-0.2	-11	21.4
NAS-28	265	Harrison	IN	6/15/2012	15.5	11.6	6.4	1.069		-0.1	-8	28.2
NAS-29	300	Harrison	IN	6/15/2012	14.2	4.7	6.7	1.079		-0.2	-11	29.4
NAS-30	312	Harrison	IN	6/15/2012	16.3	14.4	6.1	1.023		-3.7	-24	27.9
NAS-31	337	Harrison	IN	6/15/2012	16.7	13.7	6.0	1.049		-2.8	-19	27.0
NAS-32	310	Harrison	IN	7/23/2013	15	7.0	6.6	1.044		-0.41	-11.13	31.50
NAS-33	309	Harrison	IN	7/23/2013	14.7	4.9	6.3	1.059		-0.44	-11.89	27.08
NAS-34	761	Christian	KY	7/22/2013								
NAS-35	805	Christian	KY	7/22/2013								
NAS-36	759	Christian	KY	7/22/2013								
NAS-37	821	Christian	KY	7/22/2013								
NAS-38	759	Christian	KY	7/22/2013								
NAS-39	822	Christian	KY	7/22/2013								
NAS-40	734	Christian	KY	7/22/2013								
NAS-41	745	Sullivan	IN	1/8/2012		17.6	5.9	1.075		-2.1	-19	25.8
NAS-42	773	Sullivan	IN	1/8/2012					8.98E+05			
NAS-43	737	Sullivan	IN	1/8/2012	18.2	18.2	6.5	1.062		-4.7	-22	24.0
NAS-44	764	Sullivan	IN	6/12/2012	21.9	8.1	6.2	1.082	8.69E+03	-1.4	-11	26.5
NAS-45	711	Sullivan	IN	6/12/2012	28.9	10.7	6.1	1.028	6.61E+05	-4.7	-31	-1.1
NAS-46	704	Sullivan	IN	6/12/2012	23.4	25.3	6.4	1.080	1.42E+05	-2.5	-13	25.6
NAS-47	749	Dubois	IN	6/13/2012								
NAS-48	789	Pike	IN	6/13/2012								
NAS-49	705	Dubois	IN	6/13/2012								
NAS-50	738	Sullivan	IN	7/25/2012	16.7	25.4	7.7	1.086		-1.8	-10	26.0
NAS-51	733	Sullivan	IN	7/21/2013	21.6	19.6	7.0	1.037		-2.75	-22.05	25.09
NAS-52	766	Sullivan	IN	7/21/2013	24.6	13.7	7.1	1.034		-2.14	-23.68	26.25
NAS-53	765	Sullivan	IN	7/21/2013	26.6	10.2	6.6	1.036		-1.28	-20.65	26.32
NAS-54	763	Sullivan	IN	7/21/2013	19.04	31.0	6.8	1.034		-1.69	-13.44	27.20
NAS-55	736	Sullivan	IN	7/21/2013	21.3	25.8	6.8	1.040		-1.43	-15.48	29.02
NAS-56	697	Sullivan	IN	7/21/2013	23.1	32.8	7.0	1.041		-3.24	-17.13	27.01
NAS-57	525	Vigo	IN	11/22/11	NA	9.5	7.4	1.005		-7.1	-45	9.7
Coal-1	149	Sullivan	IN	7/24/2013						-5.20	-33.09	-13.51
Coal-2	135	Sullivan	IN	7/24/2013						-7.01	-44.92	0.76
Coal-3	199	Sullivan	IN	7/24/13					1.62E+05	-7.01	-45.22	1.88
Coal-4	137	Maricopin	IL	7/31/12	13.1	6.1	7.4	1.008		-6.68	-38.37	35.07
Coal-5	402	Shelby	IL	7/31/12	20.3	2.3	6.5	1.073		-2.03	-13.59	15.18
Coal-6	402	Shelby	IL	7/31/12	20.5	3.0	6.8	1.075		-1.93	-12.85	14.87
Coal-7	334	Crawford	IL	6/18/12	18.7	6.0	7.8	1.036	2.26E+05	-5.19	-32.85	21.71
Coal-8	306	Crawford	IL	6/18/12	16.5	13.9	7.8	1.020	7.15E+05	-5.60	-37.31	23.13
Coal-9		Crawford	IL	8/1/12	19.2	6.3	7.4	1.042		-5.14	-29.77	21.23
Coal-10	341	Gibson	IN	6/14/12	19.1	12.0	7.4	1.015		-4.61	-27.58	17.69
GW-1	11	Johnson	IN	6/19/12	18.5	8.2	6.9	1.001		-7.1	-42	-15.0

DIC	^{14}C		Tritium		Cl^-	Br^-	SO_4^{2-}	Ca	Mg	Na	K	Sr	Be	B
meq/kg	FMC	error	TU	error	mM	mM	mM	mM	mM	mM	mM	mM	µg/L	µg/L
22.55					1508.79	2.73	0.07	35.95	74.42	1401.03	7.11	3.20	bdl	bdl
26.98					1179.17	2.12	1.69	45.83	57.10	1095.13	4.81	2.45	bdl	bdl
18.25					1673.67	2.92	0.20	40.16	84.32	1622.18	8.80	4.66	bdl	bdl
23.48					1487.11	2.48	0.09	23.76	57.91	1486.08	7.11	2.86	bdl	bdl
22.97					1760.95	3.66	0.14	39.27	78.38	1518.66	9.03	4.27	bdl	bdl
18.62					1554.67	2.83	0.10	31.37	75.61	1543.83	7.85	3.11	bdl	bdl
11.44					1765.51	3.36	0.14	37.59	94.51	1652.23	9.10	3.96	bdl	bdl
20.51					1841.34	3.53	0.11	44.38	83.73	1603.75	10.22	4.23	bdl	bdl
31.22					1163.85	2.25	0.00	33.52	63.98	1066.79	5.76	2.74	bdl	bdl
28.79					1533.21	2.64	0.00	36.62	79.08	1462.80	7.83	2.84	bdl	bdl
34.13					1231.14	2.38	0.10	23.93	55.09	1136.86	33.15	2.37	bdl	bdl
37.19	0.0149	0.0012			1949.24	0.00	0	10.22	79.52	1746.51	9.85	2.46	bdl	bdl
1.26					1844.24	2.85	0.21	12.01	78.99	1630.16	9.22	1.60	bdl	bdl
					1923.91	2.92	0.28	12.93	79.81	1779.45	9.36	2.16	bdl	bdl
					1170.15	2.27	0.66	13.10	32.05	1177.35	13.77	0.91	bdl	bdl
					1050.50	2.08	0.25	27.92	51.93	967.27	10.54	2.34	bdl	198
					1772.14	2.90	1.83	9.93	78.17	1673.20	9.07	1.03	bdl	bdl
9.60	0.0023	0.0011			435.10	1.46	0.10	9.66	14.14	460.59	2.43	0.36	bdl	585
	0.1508	0.0016	2.8	0.38	646.68	2.02	0.38	37.37	20.53	574.37	5.05	0.75	bdl	76
16.21	0.005	0.001			849.08	1.59	0	33.89	35.38	756.51	4.00	1.43	bdl	bdl
16.99					1022.96	1.56	0	34.31	39.27	912.81	4.42	1.15	bdl	bdl
11.59					1484.50	2.50	0.23	69.37	58.89	1249.72	4.98	2.60	bdl	bdl
6.65	0.0121	0.001			1880.45	2.98	0.05	114.73	95.21	1496.60	5.89	5.00	bdl	bdl
7.75	0.0083	0.001			1641.84	2.78	0.08	74.65	97.63	1345.88	6.70	3.42	bdl	bdl
8.82					1637.19	2.79	0.04	77.54	94.44	1306.89	6.77	2.68	bdl	bdl
3.07					1761.28	3.13	0.07	101.28	87.10	1537.29	7.96	4.76	bdl	bdl
10.52					1465.43	2.89	5.17	37.75	82.62	1253.38	6.73	1.31	bdl	bdl
6.47					1631.19	3.50	0.10	82.61	89.94	1368.60	5.91	3.96	bdl	bdl
18.21					478.76	1.80	0	17.31	18.01	472.45	2.23	0.89	bdl	13
					1044.77	2.47	0.11	37.58	51.38	918.71	3.92	1.58	bdl	bdl
6.17					1761.41	3.21	0.00	101.26	106.09	1467.47	7.13	4.30	bdl	bdl
4.19					1798.00	3.90	0.06	122.73	100.09	1492.23	6.17	6.30	bdl	bdl
18.00	0.0027	0.0011	1.4	0.40	1576.52	2.90	0.10	97.80	67.07	1276.86	8.50	4.28	bdl	213
20.28					1296.68	2.63	0.33	88.72	56.52	1068.37	7.80	3.39	bdl	369
					1747.14	3.45	0.14	48.37	72.82	1563.67	8.62	3.70	bdl	bdl
					600.19	2.03	0.12	44.61	26.27	501.90	4.80	1.46	bdl	416
26.04					1699.70	2.89	0.09	31.49	68.27	1531.45	7.48	2.98	bdl	bdl
24.45					1776.97	2.83	0.10	28.16	89.89	1616.30	7.84	1.82	bdl	bdl
18.85					1386.14	2.39	0.00	46.28	59.53	1211.40	6.07	3.25	bdl	bdl
8.76					1519.31	3.16	0.07	78.06	74.26	1151.04	7.65	4.60	bdl	bdl
8.58					1657.42	3.58	0.08	110.18	94.26	1439.64	11.23	6.35	bdl	bdl
28.23					1833.10	3.05	0.00	44.69	92.86	1618.81	7.33	4.05	bdl	bdl
22.72					1816.21	3.28	0.07	78.35	85.75	1578.56	8.78	5.72	bdl	bdl
32.18					1426.70	2.58	0.07	33.73	69.30	1383.37	5.99	3.04	bdl	bdl
					128.74	0.18	0.06	4.01	3.49	108.79	0.80	0.13	bdl	267
	0.0026	0.0010			88.06	0.03	0.02	0.38	0.34	121.23	0.24	0.01		
					15.51	0.03	2.79	0.16	0.44	37.00	0.05	0.01		
	0.0029	0.0010			1.81	0.01	0.03	0.06	0.02	20.69	0.00	0.00		
3.74					181.96	0.30	0	0.36	1.23	185.25	0.38	0.09		
2.19					1696.31	1.86	0	54.34	40.18	1350.45	1.93	2.14		
2.10					2169.24	1.75	0	83.92	59.67	1850.82	2.55	3.25		
5.80					813.70	0.79	0	13.90	13.10	771.77	1.21	0.42		
13.23					434.00	0.42	0	4.13	4.56	448.39	0.88	0.14		
5.51					941.54	0.00	1.58	18.77	18.92	878.33	1.33	0.57		
10.94					316.32	0.48	0.02	3.98	2.90	323.90	0.63	0.05		
					0.26	0.00	0.15	1.74	1.70	1.36	0.04	0.18	bdl	82

Al	V	Cr	Mn	Fe	Co	Ni	Cu	Zn	As	Se	Mo	Ag	Cd	Ba	W	Tl	Pb	Th
µg/L	µg/L	µg/L	µg/L	µg/L	µg/L	µg/L	µg/L	µg/L	µg/L	µg/L	µg/L	µg/L	µg/L	µg/L	µg/L	µg/L	µg/L	µg/L
47	3.15	bdl	86	10075	5.33	bdl	bdl	bdl	bdl	bdl	2.02	bdl	bdl	21770	bdl	bdl	bdl	bdl
55	2.71	1.09	4505	78350	6.32	bdl	bdl	bdl	0.85	bdl	1.87	0.28	bdl	12045	bdl	bdl	bdl	bdl
133	6.08	0.77	74	13425	5.63	2.48	bdl	72.45	1.89	bdl	6.16	bdl	bdl	15000	bdl	bdl	bdl	bdl
555	2.89	bdl	65	4815	4.45	43.49	bdl	bdl	bdl	bdl	22.54	bdl	bdl	16985	bdl	bdl	bdl	bdl
181	3.69	bdl	302	32335	6.72	bdl	bdl	12.71	0.86	bdl	6.37	0.31	bdl	12530	bdl	bdl	bdl	bdl
94	3.38	bdl	82	4686	5.24	bdl	bdl	bdl	bdl	bdl	15.45	bdl	bdl	17965	bdl	bdl	bdl	bdl
12	3.81	bdl	113	15305	5.51	bdl	bdl	bdl	0.79	bdl	2.65	0.60	bdl	10500	bdl	bdl	bdl	bdl
99	4.12	bdl	349	7005	6.05	6.53	5.94	23.74	0.81	bdl	2.60	bdl	bdl	16195	bdl	bdl	1.93	1.44
129	3.13	0.42	168	14125	5.91	bdl	bdl	bdl	bdl	bdl	1.52	bdl	bdl	36205	bdl	bdl	bdl	bdl
1189	3.30	0.24	139	16170	6.24	bdl	bdl	10.20	0.65	bdl	60.90	0.29	bdl	31705	bdl	bdl	bdl	bdl
167	2.89	bdl	257	16245	4.84	6.70	bdl	188.90	1.04	bdl	13.09	0.25	1.79	20500	bdl	bdl	14.05	13.77
bdl	4.163	bdl	540	206850	2.051	bdl	41.730	bdl	1.805	bdl	5.228	5.954	bdl	19530	bdl	0.434	bdl	bdl
bdl	3.284	bdl	133	bdl	2.189	bdl	bdl	bdl	0.868	bdl	bdl	2.954	bdl	13638	bdl	0.365	bdl	bdl
bdl	3.530	bdl	1276	3756	8.795	39.075	bdl	bdl	1.150	bdl	bdl	0.939	bdl	20100	bdl	0.334	bdl	bdl
bdl	2.546	bdl	692	53392	2.750	bdl	bdl	120.400	0.744	bdl	bdl	1.178	bdl	4513	5.706	bdl	bdl	bdl
bdl	1.771	bdl	751	60690	3.402	bdl	bdl	bdl	0.663	bdl	bdl	2.159	bdl	33060	bdl	0.271	bdl	bdl
bdl	4.021	bdl	118	bdl	2.101	bdl	bdl	bdl	1.040	bdl	bdl	1.446	bdl	9238	bdl	0.100	bdl	bdl
bdl	7.660	bdl	111	117444	5.708	bdl	bdl	bdl	2.848	bdl	bdl	3.364	bdl	52116	bdl	0.181	bdl	bdl
bdl	1.157	bdl	2677	73640	5.632	bdl	bdl	bdl	1.175	bdl	1.407	1.808	bdl	2205	bdl	0.036	bdl	bdl
bdl	1.691	bdl	177	17115	3.987	bdl	bdl	bdl	0.645	bdl	bdl	2.241	bdl	41740	bdl	0.086	0.226	bdl
bdl	1.970	bdl	83	10712	4.137	bdl	bdl	bdl	0.724	bdl	bdl	1.294	bdl	12680	bdl	0.078	0.579	bdl
bdl	4.106	bdl	673	43010	9.864	3.844	bdl	bdl	5.567	bdl	bdl	2.847	bdl	13370	bdl	0.112	bdl	bdl
bdl	4.043	bdl	225	10116	12.471	73.775	130.500	bdl	1.500	bdl	bdl	2.396	bdl	22188	bdl	bdl	0.585	bdl
bdl	3.253	bdl	464	37940	8.202	bdl	bdl	bdl	1.135	bdl	bdl	3.194	bdl	20470	bdl	bdl	bdl	bdl
bdl	3.594	bdl	623	61120	9.247	bdl	bdl	bdl	1.588	bdl	bdl	2.763	bdl	22210	bdl	bdl	bdl	bdl
bdl	3.701	bdl	152	3415	11.436	bdl	bdl	bdl	1.878	bdl	bdl	2.604	bdl	20600	bdl	0.244	0.469	bdl
bdl	3.126	bdl	219	17860	5.196	bdl	bdl	bdl	1.060	bdl	bdl	2.955	bdl	2226	bdl	0.104	bdl	bdl
bdl	3.755	bdl	749	46810	10.070	bdl	61.730	bdl	1.330	bdl	bdl	4.226	bdl	13310	bdl	bdl	bdl	bdl
bdl	1.023	bdl	35	2848	1.874	bdl	bdl	bdl	0.317	bdl	bdl	1.133	bdl	28520	bdl	bdl	bdl	bdl
bdl	2.361	bdl	199	11905	4.489	bdl	bdl	bdl	0.752	bdl	bdl	1.735	bdl	25390	bdl	0.081	0.194	bdl
242	4.85	0.93	1331	109500	12.66	5.60	bdl	9.99	1.61	bdl	7.62	0.68	bdl	20460	bdl	bdl	bdl	bdl
170	4.90	3.88	320	26975	19.38	0.94	bdl	bdl	1.27	bdl	3.82	0.73	bdl	12580	bdl	bdl	bdl	bdl
bdl	3.416	bdl	500	17500	11.430	6.235	bdl	bdl	6.051	bdl	30.940	3.525	bdl	39740	bdl	0.197	3.629	bdl
bdl	2.483	bdl	1577	40570	10.010	bdl	bdl	bdl	0.975	bdl	bdl	6.069	bdl	22170	bdl	0.061	bdl	bdl
bdl	3.945	bdl	132	16900	5.863	bdl	bdl	bdl	1.388	bdl	bdl	2.480	bdl	54600	bdl	0.154	bdl	bdl
bdl	1.228	bdl	235	816	6.420	bdl	186.640	bdl	0.648	bdl	6.464	0.545	bdl	10496	0.415	0.047	bdl	bdl
bdl	3.848	bdl	129	11534	4.160	bdl	44.475	bdl	1.060	bdl	bdl	1.139	bdl	43950	bdl	0.080	bdl	bdl
bdl	4.120	bdl	559	41775	4.074	bdl	bdl	bdl	1.139	bdl	bdl	3.580	bdl	14838	bdl	0.272	bdl	bdl
69	2.55	4.65	414	39390	7.13	bdl	bdl	bdl	bdl	bdl	16.49	bdl	bdl	31850	bdl	bdl	bdl	bdl
198	1.99	bdl	1000	70210	12.32	3.16	bdl	bdl	bdl	bdl	7.11	bdl	bdl	22020	bdl	bdl	bdl	bdl
57	5.32	28.36	357	15400	15.46	6.29	bdl	bdl	bdl	bdl	3.23	bdl	bdl	26180	bdl	bdl	bdl	bdl
5	4.65	2.01	2542	206600	8.38	17.61	bdl	20.52	bdl	bdl	5.59	bdl	bdl	34870	bdl	bdl	bdl	bdl
222	6.76	11.87	1875	176700	10.26	1.80	bdl	bdl	bdl	bdl	bdl	bdl	bdl	46090	bdl	bdl	bdl	bdl
bdl	2.76	3.20	549	48310	5.16	2.69	bdl	bdl	bdl	bdl	4.72	bdl	bdl	25410	bdl	bdl	bdl	bdl
bdl	0.396	bdl	84	69	0.411	bdl	bdl	bdl	0.174	bdl	1.857	0.139	bdl	2430	0.105	0.046	0.093	bdl
bdl	0.024	bdl	11	778	0.075	bdl	0.176	11.900	15.030	bdl	66.570	0.059	0.104	599	0.026	0.003	0.026	bdl

U	He	H_2	Ar	O_2	CO_2	N_2	CO	C_1	C_2	C_2H_4	C_3	iC_4	nC_4	iC_5
µg/L	%	%	%	%	%	%	%	%	%	%	%	%	%	%
bdl	0.0149	0		0.057*	3.95	0.75	0	92.55	2.48	0	0.125	0.0417	0.0168	0.0079
bdl	0.0093	0		0.033*	4.68	0.71	0	91.83	2.57	0	0.0995	0.0346	0.0154	0.009
0.57	0.0116	0.0063		0.029*	3.11	1.04	0	91.73	3.46	0	0.457	0.0553	0.0586	0.0151
bdl	0.0107	0		0.044*	4.39	0.61	0	92.51	2.33	0	0.0572	0.0325	0.0066	0.0051
bdl	0.0109	0.0022		0.039*	3.54	0.87	0	91.98	3.14	0	0.302	0.0527	0.0346	0.0116
bdl	0.0101	0		0.032*	4.19	0.65	0	92.45	2.52	0	0.0873	0.0379	0.0093	0.0056
bdl	0.0113	0		0.05*	3.19	1.13	0	91.58	3.49	0	0.409	0.0566	0.052	0.0134
1.64	0.0109	0		0.039*	3.95	0.83	0	92.27	2.69	0	0.131	0.0444	0.0141	0.0069
bdl	0.0187	0.0041		0.022*	3.34	0.75	0	93.55	2.21	0	0.0372	0.0471	0.0036	0.0046
bdl	0.013	0.0022		0.012*	3.24	0.87	0	93.48	2.28	0	0.0381	0.0459	0.0038	0.0051
14.12	0.011	0		0.023*	3.72	0.57	0	93.13	2.41	0	0.0736	0.0335	0.0099	0.008
bdl	0.0348	0.0378	0.0066	0.0091	3.55	2.03	0	90.22	3.51	0	0.415	0.0725	0.0537	0.0217
bdl	0.0171	3.61	0	0.0078	4.33	1.23	0	87.30	3.03	0	0.322	0.0636	0.0390	0.0212
0.326	0.0081	0.284	0.0539	0.453	4.24	5.34	0	86.18	2.97	0	0.313	0.0633	0.0361	0.0225
bdl	0.0479	0	0.0100	0.0114	2.22	3.00	0	90.22	3.93	0	0.373	0.0893	0.0299	0.0254
0.118	0.0285	0.0092	0.0053	0	4.36	1.44	0	90.72	3.02	0	0.270	0.0618	0.0425	0.0160
0.098	0.0025	0.0457	0	0.0182	7.37	0.79	0	86.98	2.9	0	1.71	0.0826	0.0363	0.0221
6.161	0.0497	0	0.0168	0.127	2.59	3.53	0	92.08	1.32	0	0.19	0.0649	0.0116	0.0159
bdl	0.0424	0.125	0.0466	0.116	0.014	8.26	0	84.66	4.29	0	1.82	0.113	0.369	0.0443
0.770	0.0069	0	0.0117	0.184	7.37	1.10	0	91.24	0.076	0	0.0068	0.0033	0	0
2.116	0.0160	0.0016	0.0129	0.233	5.70	1.36	0	91.08	1.32	0.0013	0.180	0.0369	0.0289	0.0137
bdl	0.0035	0.0013	0.0959	2.32	5.81	9.33	0	81.67	0.650	0	0.0846	0.0232	0.0038	0.0029
0.185	0.0077	0.0200	0.0213	0.378	4.68	2.14	0	91.67	0.854	0	0.168	0.0345	0.0147	0.0045
1.720	0.0211	0.0018	0.0126	0.0824	3.57	1.71	0	93.97	0.510	0	0.0915	0.0239	0.0052	0.0019
0.090	0.0239	0.0028	0.0101	0.0349	4.63	1.19	0	93.28	0.670	0	0.128	0.0237	0.0064	0.0028
0.083	0.0113	0	0.0280	0.523	4.20	2.93	0	91.32	0.776	0	0.168	0.0269	0.0124	0.0040
0.944														
0.219														
0.048														
0.789														
bdl	0.0041	0.0161		0.038*	4.28	0.78	0	94.44	0.366	0	0.0539	0.0221	0.0027	0.0016
bdl	0.003	0		0.18*	10.39	1.14	0	87.75	0.459	0	0.0459	0.0284	0.0024	0
	0.271	0.148	0.0141	0.0243	0.22	7.98	0	87.2	3.64	0	0.374	0.0468	0.0455	0.0147
	0.135	0.164	0.0098	0.0243	0.37	4.04	0	90.34	4.28	0	0.453	0.0664	0.0604	0.025
	0.173	0.154	0.0141	0.0242	0.22	7.5	0	87.06	4.08	0	0.57	0.0629	0.0802	0.0244
	0.211	0.288	0.0221	0.1	0.075	8.74	0	83.96	5.14	0	1.09	0.0849	0.187	0.0328
	0.187	0.0972		0.025*	1.31	5.13	0	88.25	4.19	0	0.603	0.0678	0.0848	0.024
	0.16	0.106		0.037*	0.68	8.82	0	85.72	3.89	0	0.432	0.0636	0.0487	0.0223
	0.15	0.0771		0.041*	2.1	7.51	0	85.01	4.25	0	0.638	0.0698	0.0946	0.0258
13.830	0.0149	0	0	0.0165	6.03	0.88	0	89.44	3.41	0	0.0970	0.0713	0.0050	0.0126
	0.0159	0.0839	0	0.0057	4.20	1.26	0	90.61	3.50	0	0.182	0.0902	0.0106	0.0154
11.610	0.0161	0.0153	0.0695	1.31	4.21	7.62	0	83.58	2.99	0	0.0743	0.0740	0.0045	0.0103
0.073	0.0154	0.0016	0.0139	0.224	5.50	1.46	0	89.23	3.36	0	0.0964	0.0675	0.004	0.0117
5.784	0.0160	0.0011	0.0089	0.123	3.39	1.11	0	94.40	0.865	0	0.0278	0.029	0.0027	0.005
0.125														
	0.0423	0.0374	0.0135	0.112	3.04	2.71	0	90.54	3.11	0	0.286	0.0354	0.0319	0.0126
	0.0289	0.557	0.0223	0.117	0.28	5.31	0	87.53	4.99	0	0.804	0.104	0.138	0.0458
	0.0058	0.0047	0.855	19.36	0.079	76.2	0	3.21	0.201	0	0.0613	0.0043	0.0124	0.0034
0.620	0.0147	0	0.0047	0.0136	5.51	0.88	0	90.07	3.26	0	0.134	0.065	0.0112	0.0104
bdl	0.0127	0.0028	0.0058	0.0155	5.96	1.02	0	88.67	4.06	0	0.136	0.065	0.0153	0.0134
bdl	0.0134	0.0053	0.0058	0.0182	5.02	1.08	0	89.77	3.74	0	0.214	0.0686	0.027	0.0151
bdl	0.0101	0.0024	0	0.0181	5.3	0.74	0	90.11	3.59	0	0.114	0.0661	0.0121	0.0134
bdl	0.0091	0.002	0	0.0178	5.7	0.69	0	89.88	3.5	0	0.105	0.0627	0.0054	0.014
bdl	0.0139	0	0.0054	0.0122	6.4	0.84	0	88.87	3.64	0	0.114	0.0644	0.0056	0.0128
bdl	0.008	0	0	0.0234	5.82	0.55	0	90.99	2.42	0	0.092	0.0533	0.012	0.0101
0.053	0.0478	0.0207	0.0535	0.0237	1.91	4.21	0	93.52	0.0569	0	0.0017	0.0082	0	0
	0.003	0	0.037	0.23	0.67	4.68		94.34	0.04		0	0	0	0
	0.004	0.002	0.081	0.21	0.09	5.89		93.72	0.01		0	0	0	0
	0.004	0	0.089	0.90	0.07	7.05		91.88	0.01		0	0	0	0
	0.046	0.002	0.046	0.20	0.25	7.95		91.29	0.17		0.040	0.006	0.003	0
	0.300	0.003	0.073	0.39	0.81	19.49		78.51	0.39		0.031	0.008	0.003	0
	0.034	0.002	0.031	0.24	0.32	4.44		94.89	0.04		0.002	0	0	0
	0.006	0.002	0.046	0.28	0.62	7.91		90.96	0.18		0.010	0	0	0
	0.108	0.002	0.052	0.25	0.63	11.07		87.68	0.20		0.015	0.002	0	0
	0.044	0	0.197	3.86	0.46	25.84		69.59	0.01		0	0	0	0
0.018			1.02	8.2	2.22	70.2	0	18.36	0	0	0	0	0	0

nC_5 %	C_6+ %	$\delta^{13}CO_2$ ‰	$\delta^{13}C_1$ ‰	δDC_1 ‰	$\delta^{13}C_2$ ‰	$\delta^{13}C_3$ ‰	Specific Gravity	BTU dry
0.0031	0.0063						0.61	988
0.0029	0.0063	18.53	-50.29	-199	-41.06		0.617	982
0.0111	0.0155	18.18	-50.00	-196	-42.94		0.612	1009
0	0.0047						0.612	983
0.0061	0.0114						0.612	1000
0.0019	0.0051						0.611	987
0.0104	0.0123						0.613	1006
0.0025	0.0082						0.611	990
0	0.0157	17.67	-49.13	-194	-38.20		0.602	992
0	0.014	18.03	-48.90	-189	-39.41		0.601	992
0.0024	0.0081						0.606	991
0.0117	0.0257	16.30	-49.61	-195	-41.41	-30.37	0.621	995
0.0115	0.0208	15.69	-49.39	-185	-41.35	-25.94	0.604	965
0.0125	0.0254	16.35	-49.09	-184	-41.61		0.639	941
0.0112	0.0339	16.25	-50.15	-197	-41.82	-24.56	0.614	1001
0.0099	0.0177		-49.39	-199			0.622	986
0.0122	0.0273		-50.27	-191			0.662	984
0	0.0042	17.90	-48.53	-190	-34.52		0.604	965
0.0558	0.0399		-50.63	-205	-44.64	-36.60	0.637	1003
0	0.0059	19.86	-53.64	-205			0.631	927
0.0044	0.0082	17.66	-45.03	-177	-29.07	-25.90	0.626	955
0	0.0042	18.46	-54.58	-194	-45.15		0.667	843
0.0024	0.0096	17.32	-55.41	-209	-44.49		0.617	951
0	0	17.40	-54.73	-202	-44.58		0.600	965
0	0	17.50	-55.12	-202	-45.33		0.609	962
0	0.0010	17.18	-54.74	-200	-45.31		0.616	945
0	0						0.601	966
0	0						0.663	900
0.006	0.0155						0.611	963
0.0111	0.0205						0.601	1011
0.0125	0.0227						0.614	977
0.0342	0.0347						0.631	984
0.0132	0.0132						0.616	992
0.0096	0.0108						0.622	955
0.0183	0.0158						0.635	962
0.0018	0.0170	16.21	-50.33	-191	-41.85	-16.24	0.635	974
0.0030	0.0253	16.39	-49.40	-183	-42.25	-19.62	0.620	991
0.0012	0.0235	14.56	-49.63	-185	-41.00	-16.58	0.651	907
0	0.0115	16.31	-50.16	-185	-41.82		0.633	970
0.0039	0.0188	13.52	-50.93	-193	-34.99		0.598	976
0.0073	0.0167	17.44	-50.09	-190	-42.84		0.614	985
0.0349	0.0335		-50.79	-193	-45.27	-32.74	0.614	1011
0.0039	0.0011		-51.23	-205			0.985	39
0.0027	0.021	16.86	-50.01	-186	-41.75		0.630	979
0.0028	0.0186	15.25	-51.56	-198	-41.15		0.639	979
0.0051	0.0213						0.629	987
0.0028	0.0194						0.629	985
0.0027	0.015						0.632	980
0	0.0213	17.55	-50.72	-189	-41.87		0.64	973
0.0034	0.0203	16.87	-50.06	-196	-39.25		0.627	972
0	0.0045	0.30	-55.73	-217			0.591	951
0	0	12.23	-58.23	-230				
0	0	-14.09	-66.59	-227				
0	0	-15.90	-66.49	-222				
0	0	6.53	-61.23	-220				
0	0	3.94	-60.71	-210				
0	0	9.74	-52.15	-212				
0	0	10.63	-58.19	-219				
0	0	10.67	-58.44	-212				
0	0	5.43	-58.31	-210				
0	0							

SECTION 5

FORMATION EVALUATION

Final Report

New Albany Shale Gas in the Illinois Basin – Formation Evaluation

Prepared by:

Res Tech Inc.

Subcontract S-45

Funded by:

Research Partnership to Secure Energy for America

DE-AC26-07NT42677

Funding for this project is provided by RPSEA through the "Ultra-Deepwater and Unconventional Natural Gas and Other Petroleum Resources" program, authorized by the U.S. Energy Policy Act of 2005. RPSEA (www.rpsea.org) is a nonprofit corporation whose mission is to provide a stewardship role in ensuring the focused research, development and deployment of safe and environmentally responsible technology that can effectively deliver hydrocarbons from domestic resources to the citizens of the United States. RPSEA, operating as a consortium of premier U.S. energy research universities, industry, and independent research organizations, manages the program under a contract with the U.S. Department of Energy's National Energy Technology Laboratory.

Gas Technology Institute

October 2010

FINAL REPORT

New Albany Shale Gas in the Illinois Basin – Formation Evaluation

Principle researchers:
Mr. Don Luffel, Mr. Jim Lorenzen and Mr. Frank Caramanica
Res Tech Inc.

A Research Partnership to Secure Energy for America Project

For
GAS TECHNOLOGY INSTITUTE
Contract No. 07122-16
Subcontract S-45
Mr. Iraj Salehi, Manager
October 2010

Table of Contents

List of Illustrations …… (4)

List of Tables …… (6)

Executive Summary …… (7)

Objectives …… (7)

Technical Perspective …… (7)

Results …… (8)

Introduction …… (11)

Formation Evaluation …… (17)

Core Analysis …… (17)

Core Data and Analysis Adjusted to Reservoir …… (23)

Conditions …… (24)

Langmuir Isotherm Equation …… (26)

Log Analysis of Adsorbed, Free Gas, and Total Gas …… (28)

Logging and Log Analysis …… (30)

Log Analysis Methodology …… (45)

Total Organic Carbon …… (45)

Kerogen Volume …… (46)

Pyrite Volume …… (48)

Clay Volume …… (49)

Quartz, Carbonate and Porosity …… (50)

Saturation Determination …… (51)

Synthetic Sonic Equations …… (59)

Natural and Induced Fracture Characterization …… (62)

Core-Image Comparisons McLean County KY …… (66)

Production of Free, Adsorbed, Total Gas From Average Reservoir Pressure …… (72)

General Methane Isotherm …… (74)

Measurement of Matrix Permeabilities of Shale Cores …… (79)

Appendix A …… (85)

Graphical Log Section New Albany Shale …… (85)

Illustrations

Figure

1 Kentucky County map …….. (12)

2 Indiana County map …….. (12)

3 As received gas saturation versus Dean Stark result, well A-7455, oil density 0.8 …….. (20)

4 As received gas saturation versus Dean Stark result, well A-7455, oil density 0.9 …….. (21)

5 Ambient bulk volume histogram A-7455 …….. (25)

6 Bulk volume histogram at reservoir conditions A-7455 …….. (26)

7 Methane isotherm A-7455 …….. (28)

8 NAB log section characterizing porosity, TOC, Lithology, saturations and permeability …….. (31)

9 Methane isotherm and free gas compared to canister total gas, Daugherty Well A-7455 …….. (34)

10 Osburn Trust total gas content histogram from canister …….. (35)

11 Osburn Trust core histogram of bulk volume at ambient conditions ……. (36)

12 Osburn Trust histogram of bulk volume at reservoir conditions ……. (37)

13 Noble wells Osburn Trust and Solsman isotherm with free gas Compared to total canister gas …….. (38)

14 B 15 Canister results histogram of lost, free and crushed Gas …….. (41)

15 Bulk density versus TOC correlation from W. KY …….. (45)

16 Rock Eval. TOC versus XRD Kerogen volume from Noble Energy Solsman well, Sullivan Co., Indiana …….. (47)

17 Bulk density correlation to kerogen volume from Western Ky. Wells Frazer and Orbit Clark #1 …….. (48)

18 Major lithologic components of the NAB shale …….. (49)

19 Correlation of water saturation to oil saturation from Noble Energy Solsman #1 core data …….. (52)

20 Correlation of water saturation to oil saturation from core data, Western Kentucky wells…….. (53)

21 Orbit Clark #1 well, Christian County, KY. displaying computed to core saturation results …….. (54)

Illustrations
Continued

Figure

22	*Log section A-7455* ……	*(56)*
23	*Crossplot of measured versus synthetic compressional sonic as a function of density – neutron and density and deep resistivity* …..……..	*(60)*
24	*Crossplot of measured versus synthetic shear sonic as a function of density – neutron and density and deep resistivity* ……..	*(61)*
25	*Log plot of Poisson's ratio, Young's modulus, bulk modulus, shear modulus, brittleness and closure stress* …….	*(62)*
26	*FMI image of open natural fractures from the Noble Energy, Osburn Trust well, Sullivan Co., IN* …….	*(63)*
27	*Stereo plot of interpreted fracture dips Osburn Trust* ……..	*(63)*
28	*Stick plot suggesting interconnectivity of fractures, Osburn Trust*…….	*(64)*
29	*Stereo dip plot of interpreted fractures A-7455* …….	*(65)*
30	*Stick plot suggesting interconnectivity of fractures, A-7455* ……..	*(66)*
31	*Dip plot from the B-15 well, McLean Co., KY* ……..……..	*(71)*
32	*Forecast derivative of total, free, and adsorbed gas with average reservoir pressure* …….	*(73)*
33	*NAB methane isotherms with small normalization in different areas* …….	*(76)*
34	*NAB methane isotherms normalized with best fit general isotherm* …….	*(77)*
35	*Isotherm from the Big Sandy formation* …….	*(78)*
36	*Core permeability from the NAB and the Haynesville* …….	*(81)*
37	*Travis Peak tight gas sand line for permeability compared to NAB and Haynesville* …….	*(82)*
38	*Permeability with core plugs from Appalachian Devonian shale added* …….	*(83)*
39	*Permeability with plug chips from the Appalachian Devonian shale added* …….	*(84)*

Tables

Table

1	*Key wells with initial gas in place (IGIP) and rate, with pressure and temperature……*	*(13)*
2	*Available electric log data……..*	*(16)*
3	*A-7455 as received core results……*	*(19)*
4	*Gas content at reservoir conditions A-7455……*	*(22)*
5	*A-7455 canister data……*	*(24)*
6	*Table of example XRD results……*	*(33)*
7	*GRI protocol core results……*	*(33)*
8	*Osburn Trust ambient core results adjusted to reservoir conditions……..*	*(39)*
9	*B-15 canister gas composition results……*	*(42)*
10	*B-15 additional canister gas composition results……..*	*(43)*
11	*Example geo-chemistry report with definitions……..*	*(44)*
12	*Multi-mineral inputs and outputs for log analysis model……*	*(50)*
13	*Formation brine salinity table from NAB samples A-7455……*	*(52)*
14	*Bed summary of log analysis results……*	*(57)*
15	*Interpreted fracture table* from NAB of B-15 well……	*(69)*

Executive Summary

Title	New Albany Shale Gas (Formation Evaluation)
Contractor	Res Tech Inc.
Project Manager	Jim Lorenzen
Principal Investigators	Don Luffel, Frank Caramanica, Jim Lorenzen, Res Tech Inc.
Report Period	August 2008-July 2010
Objectives	The objective is the integration of core, electric log, and image measurements to develop advanced methodology that allows determination of the gas in place, shale formation characterization, and through the identification of fracture species and orientation the delineation and effective completion of the highest productivity intervals of the New Albany shale.
Technical Perspective	The New Albany shale of the Illinois Basin is one of the most complex potential resource plays of North America. Although extensive throughout the basin, inherent characteristics make it more of a challenge to successfully evaluate and complete. Among these are lower maturity, kerogen type II/III and vitrinite reflectance in the 0.6-1.2 range (oil window), sub-normal pressure as low as .26 psi/ft from data available, a high adsorbed gas volume with the presence of heavy components, more than one hydrocarbon phase, both oil and gas, with oil volumes being significant, and typically low matrix permeability requiring all wells to be fracture stimulated and/or drilled horizontally and fracture stimulated.

Technical Perspective (continued)

Log analysis work performed by ResTech includes the development of advanced methodology for calculation of shale porosity, water and bitumen saturations, free gas saturation and adsorbed gas through correlation with core data. Work also performed by ResTech includes supervision of coring and core analysis including visual inspections and analyses; correlation of core and log data; quality control of porosity; water and bitumen measurements; measurement of matrix permeability, determination of total organic carbon, and adsorbed gas from isotherms. Interpretations of image logs on three wells within the study were performed to characterize natural and induced fracture species. Technology transfer was achieved through presentations at two SPWLA Topical conferences; one in Philadelphia, Pa. in 2009 and the other in Austin, TX in 2010. Also participation in the GTI sponsored producer's forum in June 2009 and finally by compilation and distribution of this final report.

Results

A review of all available core and log data provided by operating partners was completed along with review of previous GRI studies including the 1999 Producibility Consortium and the GIS Compilation of Gas Potential of the New Albany Shale in the Illinois Basin. In addition, the drill wells cored and completed as part of the study were evaluated. These wells were the A-7455 and the B-15. In the B-15 well only partial data were available for release in this report. From these data and associated evaluations were the following results:

- A log analysis model for determination of porosity, saturation, shale lithology, total organic carbon, matrix permeability indication, and gas in place has been calculated using available core and basic log data. A basic logging suite is shown to effectively evaluate the resource.

- Correlations on a limited basis from logs for geochem parameters of TOC, S1, S2, PI, HI, and Ro have been measured.

- A resistivity based Archie model is used to calculate water saturation (Sw) which is calibrated to core results. From core correlations the Sw is then related to oil saturation (So) and is compared to core analysis. Examples of results are presented. All related (So) efforts from correlation of S1 from pyrolysis of core samples have been ineffective.

- Although salinity appears to be variable from shale lab tests, the salinity within the range of 80,000 ppm NaCl fits best with (Sw) using the above method of log resistivity calculations compared with the core data.

- A general Langmuir isotherm is developed from the data that is consistent with both the Indiana and Western Kentucky data. This can be used to derive reasonable adsorbed gas content, which precludes the need for additional isotherm measurements in this area. Data from other areas may not fit with this result, as an example from the Big Sandy which is shown.

- As Received Gas (ARG) technique is the preferred methodology to determine gas saturation of cores at ambient conditions prior to lab extraction of fluids with methods. It has been found significant conflict with Dean Stark results and is still under investigation by some labs.

- Bulk volume adsorbed gas (BVAG) at reservoir conditions is a pseudo liquid phase. This initial adsorbed gas in place (IGIP) occupies space. This is a significant component within the porosity and reduces the amount of free gas space. However, the total adsorbed and free gas is greater than it would have been if only free gas was present. This is essential for a more rigorous determination of both adsorbed and free gas IGIP.

- A generalized matrix permeability model of crushed shale samples developed by GRI method is used by all labs. Trends of NAB shales and other data including Haynesville and Devonian

shales are presented. One of the three main labs has distinctly higher permeabilities, but appears to be incorrect. However, all of the lab results of the matrix permeabilities are generally considered to be too low to account for shale producibilities. The bulk permeability of the system can only be estimated from well tests, modeling of natural and induced fracturing, and reservoir simulation.

- Free gas calculated in the Haley Mills field area is highest in the Grassy Creek/Clegg Creek member of the New Albany (NAB). As such, any fracture stimulation should be designed to interconnect with this member. With the restricted space available for free gas because of greater amounts of adsorbed gas and oil within the pore system, interconnected natural and induced fractures will be key to the best production.

- Fractures are characterized from the FMI data of the Osburn Trust #1-1H in Sullivan County, Indiana. Natural fractures both open and partially open exist in conjugate sets with high angle dip. The dip direction is NNW-SSE and the strike is ENE-WSW. Few induced fractures are interpreted. Results from the well A-7455 in Christian County, Kentucky the CMI interpreted fractures have dominant N-S dip with E-W strike while the fracture dip and strike in McLean County, Kentucky is NNW-SSE and ENE-WSW respectively. Although the area is structurally complex a fairly consistent dip – strike orientation is observed from the available well log image data.

Introduction

Log analysis has been advanced in New Albany (NAB) shale with methodology using correlation with core analysis data. In the area of Southwest Kentucky and in part of Indiana (see Maps Fig. 1 and 2), results of log and core analysis data were calculated with eight wells, and from the Haley's Mill Field log data were calculated from 19 wells. Adsorbed gas contents in NAB correlate effectively with just TOC in this area, and this was used from the log data. Gas was then calculated at reservoir conditions with free, adsorbed, and total initial gas-in-place (IGIP) at each depth/ft in Mcf/AcFt and cumulative for IGIP of Mcf/Ac from the entire NAB thickness. For NAB at reservoir conditions the free gas is initially less than 20 – 40 % of the total IGIP. This is because of the large amount of bitumen/oil and the space occupied with the adsorbed gas/liquid. Two Noble wells in Sullivan County, Indiana, the well A-7455 in Southwestern Kentucky, Christian County, and the B-3 in Webster County, KY mostly provided thorough canisters, log data, core analyses, and other lab data. The total initial IGIP in cumulative Mcf/Ac is shown in **Table 1**. Production rates of Noble wells and B-3 well aren't available.

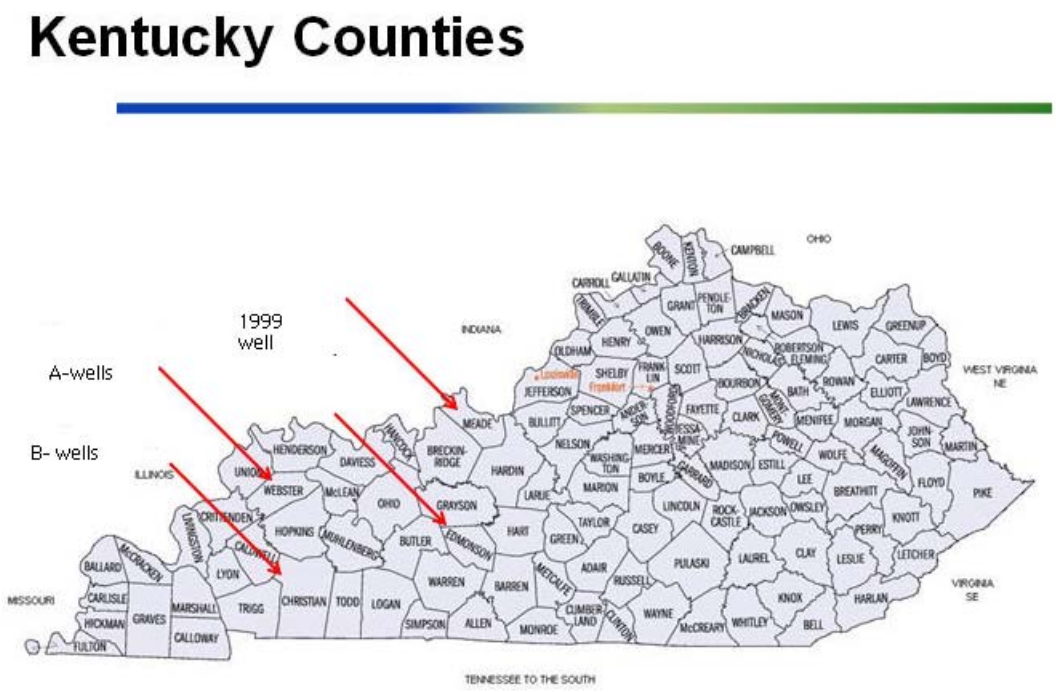


Figure – 1 Kentucky Counties showing general location of primary study wells

Indiana Counties



Figure - 2 Indiana County map wells in Vigo and Sullivan County

Table 1

IGIP Calculated from Log Analysis of Major Wells in the GTI NAB Project

Operator	Well Name	Total IGIP (Mcf/Ac)	Initial daily rate (Mcf)	NAB Thickness (Ft)	Average Depth (Ft)	Pressure (Psig)	Temperature (Deg F)
Noble Energy	Osburn Trust 1-11H	34,810.6	N/A	160	2,566	1,155	86
Noble Energy	Solsman 1-32 H	46,378.4	N/A	189.5	2,591	1,166	86
Company A	A- 7455	20,716.1	90	145	2,503	665	90
Company B	Island Creek BF-001	77,384.2	N/A	387	4,110	1,192	101
Trendwell	Dalton C2-22	16,542.3	N/A	112.5	1835	826	85
Trendwell	Jeffries C3-21	13,064.4	N/A	110.5	1730	779	84
Orbit	Clark #1	19,157.7	N/A	147	2250	607	87
Exxon	Jimmy Bell	54,479.8	N/A	243	3213	932	92

We have developed a derivative graphical method for forecast of cumulative gas production as reservoir pressure declines. This shows cumulative adsorbed gas, free gas, and total gas with average reservoir pressure. Since the initial reservoir pressures of the NAB are usually less than 2000 psig, the Langmuir Equations of adsorbed gas will be active as the reservoir pressure declines, and the adsorbed gas will convert to free gas. This should move through the same permeability and fracture paths with the free gas. However, from canister cores there are evidence that significant amounts of gas content usually are collected only with crushed shales. As a result the permeability is much lower than permeability initial in the canister cores. This will be discussed later.

Core and image log data for three wells are a part of the GTI Project A-7455, Noble Energy Osburn Trust 1-11H, and B-15 wells. These were studied and interpreted of natural, partially natural, healed fractures, induced fractures, and faults. The fracture data and faults with the image log were interpreted separately in tables, Rose plots with dip directions, and cumulative development of stick plots of natural fractures to show potential for intersection of conjugate fracture sets.

With the NAB core analysis data from the GTI Project, we have developed important advanced log analysis and adsorbed/free gas as shown above. However, there are several added, important features that still need to be researched with the improved lab data.

- Permeability (Km of matrix permeability) of free gas is routinely used with ambient crushed shale chips with pulse pressure measurements. Core Lab results of NAB from two Noble wells have 0.01 to 1.0 nanodarcies with Bulk Volume Gas of 1 to 3 %. Schlumberger/TerraTek lab results of NAB of sidewall cores from B-3, have about 100 nanodarcies with BVG of 1.5 to 2.5 %. There is a strong argument from operating companies that the shale chip permeabilities are too low with every lab. Ning, X., et al, in Topical Report, GRI-93/103, March 1993, used Devonian core plugs at reservoir overburden stress and pore pressure and developed method of measurement of Km even though fractures had to be discounted. Km results were similar with chips from core end pieces. A similar approach has been taken with various gas porosity and shale lithology from several shale basins.

- As Received Gas (ARG) is gas porosity from as-received density of shale samples prior to extraction of water and oil/bitumen. This is routinely done by TerraTek and Weatherford Lab, but Core Lab only provides ARG on request. TerraTek did ARG measurements with B-3, but can't validate this compared to Dean Stark since their method of water and oil/bitumen extraction is retorted. With our request Core Lab, ARG results were measured from five shale samples of the core data of the well A-7455, but Dean Stark extraction showed less gas porosity than ARG. Currently, Core Lab is doing research on over 100 core samples, including NAB, all showing significantly higher amount of gas porosity.

- Formation Water Salinity – Cores were drilled with air in well A-7455. Core Lab calculated salinity of the formation water in five cores. Salinity was 19,586 to 83,541 ppm NaCl from total water and 28,860 to 139,961 ppm NaCl from only free water, i.e., bound water in clays has no NaCl. Log analysis was adjusted to match water content with the core analysis data. There are water salinities from very few shale cores drilled from air. Previously similar air drilled core data were published in the GRI-95/0496 Final Report. Since these salinities vary widely, more data are needed to broaden our understanding of salinity variations and how this impacts log analysis.

GTI Project data from recent wells with log and core data, and data from previous wells are as follows:

- B-15 drilled well January 2010 with 312' conventional cores from 3,572 – 3,884' in McLean County, KY.

- B-15 drilled well April 2007 with 25 sidewall cores of five clusters in depth of 3,941 – 4,294' and logs in Webster County, KY.

- Well 7455 drilled in August 2009 with 60' conventional cores from 2,526 – 2,586' and logs in Christian County, KY.

- Twenty nine vertical and two horizontal wells from Haley's Mill Field in Christian County, KY with production rates from August 2008 – April 2009. Nineteen of these wells have log data. Production data from five wells has gas compositions.

- Trendwell Dalton C2 – 22 drilled well June 2007 with 19 cores/canisters, gas content, two compositions, Rock Eval, TOC, logs, in Vigo City, IN.

- Trendwell Jeffries C3 – 21 drilled well August 2007, logs, in Vigo City, IN.

- Noble Osburn Tr 1-11H drilled well August 2006 with 85' conventional cores from 2,495 – 2,580' with logs in Sullivan County, IN.

- Noble Solsman Tr 1-32H drilled well December 2006 with conventional cores from 2,547 – 2,638' with logs in Sullivan County, IN.

- Three core samples from Orbit Clark #1 well drilled in Christian County, KY with log data (ca 1975 ?) were collected from Kentucky Geological Survey, by Global Exploration, and from Zinc Frazer #1 well drilled in Crittenden County, KY (ca 1975 ?) with three core samples from KGS but no log data available. Three core samples of NAB were also collected from an archive of Exxon J. Bell #1, from a well drilled (ca 1975?) in Webster County, KY. GE provided core data analysis (2006) from labs of Core Lab, Humble Geochem, and Ticora, and the log analyses done by ResTech, Inc.

Available log data is summarized in **Table 2** below.

Table 2

Available Electric Log Data

Well Name	Log Service Provider	Available Electric log data
B-15	Schlumberger	AIT-TLD-MCFL-CNL-HNGS-FMI-ECS-SONIC SCANNER
B-5	Schlumberger	HALS-TLD-MCFL-CNL-DSI
A-7455	Weatherford	DEN-NEUT-IND-NGT-DIPOLE SONIC-CMI
Company A (19 wells of 29)	Unknown	DEN-IND-GR OR DEN-IND-NEUT-GR
Noble Osburn 1-11H	Schlumberger	PI-CNL-TLD-MCFL-FMI-DSI
Noble Solsman 1-1H	Schlumberger	PI-CNL-TLD-MCFL-DSI
Orbit Clark #1	Schlumberger	IND-LL8-FDC-CNL-DT-DTS

Exxon #1 Jimmy Bell	Schlumberger	IND-FDC-CNL-BHC
Trendwell Jeffries C3-21	Baker Atlas	DEN-NEUT-IND-GR
Trendwell Dalton C2-22	Baker Atlas	DEN-NEUT-IND-SPECTRAL GR

Core data results and log analysis will be shown for the eight wells (B-15 core and full log suite not available for this report) above and the Haley's Mill Field wells. Initially with the first well, analysis of the core and log data will be shown with some of the equations required. For the rest of the NAB wells, the evaluated log analysis results are shown in Appendix 1. The last features covered in the report are already improved lab data, and features that labs need improvements. This includes adjusted core results to reservoir conditions. The improvements are matrix permeability (Km) of shale chips, As Received Gas porosity (ARG), and formation water salinity.

Formation Evaluation – New Albany Shale

Well A- 7455, Christian County, KY

This well was vertically drilled in August 2009, with 60' conventional core in the depth 2,526 – 2,586' drilled with air, in the low part of NAB. With the cores, three canisters were collected for gas content, gas composition, isotope measurements, and methane isotherm with Weatherford Lab. Water-base fluid was then added in the well for running logs. A horizontal well was then drilled, and nitrogen was used for frac stimulation with monitor of microseismic data in a nearby vertical well and surface tilt measurements. In the following are core data, analysis with reservoir conditions, and log analysis including image log interpretation.

Core Analysis

Ambient Core Data and Analysis

Table 3 shows the measurements of five cores from Core Lab using the GRI Protocol of shale. Core lab analyses were requested measuring As Received fresh-state grain densities from crushed shale samples along with crushed shale samples with measurements of the matrix permeabilities (Km). As Received Gas (ARG) method was originally used along with Km as shown in the GRI Final Report, GRI-95/0496. Now a simpler equation of calculating ARG is with the grain densities of crushed samples as follows:

$$Ø^*S_g = 100^*(1 - \rho_b/\rho_{bc}) \quad \text{..... (1)}$$

Where: $Ø^*S_g$ = ARG filled porosity, percent bulk volume (%BVG),

ρ_b = shale bulk density, gm/cc,

ρ_{bc} = with crushed shale, pseudo grain density includes as both grains and presence of fluids.

This measurement of As Received Gas filled porosity of the fresh-state is useful since the gas porosity is prior to Dean Stark extraction of fluids (water, bitumen/oil) and oven drying the crushed shale samples. Since the initial calculated gas porosities from the dry shale samples are the same as the As Received Gas porosities, and this allows the bitumen/oil volume to be calculated from the Dean Stark fluid weight so the bitumen/oil density can be obtained. Currently, the bitumen/oil fluid densities are only estimated. Note in **Table 3** the average gas filled porosities from Dean Stark extraction are 0.38 %BVG less than As Received Gas porosities. If the density of the bitumen/oil was 0.90 gm/cc instead of 0.8 gm/cc (normally used), the Dean Stark gas filled porosities would be higher, with an average of only 0.16 %BVG less than the As Received Gas average. In Figure 3, the five cores of As Received Gas with normal bitumen/oil densities of 0.80 gm/cc, and in Figure 4, with oil/bitumen densities of 0.9 gm/cc. Assumptions regarding bitumen/oil density may be significant discrepancy between ARG and Dean Stark gas filled porosity. However, from Core Lab data in other shale basins where there are virtually no bitumen/oil present, results of As Received Gas porosities are still significantly higher than gas porosities from Dean Stark. Core Lab is currently with research to understand the problems with a variety of shales, and they plan to share with us the lab data.

Table 3
Well A-7455
Core Lab Analyses of Fresh State Shale As Received Gas and Adjacent Shale with GRI Protocol

	As Received				Dean Stark Extracted Conditions & Dry					
Depth (ft)	Bulk Density (gm/cc)	Matrix Perm (mD)	Fresh State Grain Density (g/cc)	Fresh State Gas-filled Porosity (%BV)	Gas-filled Porosity (%BV)	Gas Sat'n (%PV)	Porosity (%BV)	Oil Sat'n (%PV)	Water Sat'n (%PV)	Grain Density (gm/cc)
2533.0	2.356	2.03E-06	2.420	2.64	2.20	40.1	5.49	41.9	18.1	2.463
2537.9	2.187	1.99E-06	2.240	2.32	2.12	35.9	5.91	34.8	29.3	2.288
2553.0	2.308	2.35E-09	2.326	0.75	0.26	5.7	4.63	62.8	31.6	2.380
2562.0	2.439	4.13E-10	2.448	0.34	0.15	6.0	2.45	34.0	60.0	2.479
2573.0	2.339	1.00E-08	2.362	0.95	0.38	10.4	3.71	41.8	47.8	2.398
			Average	**1.40**	**1.02**					

Footnotes

Matrix perm is from pressure decay results on the fresh, crushed, 20/35 mesh size sample, and measured grain density

Dean Stark extracted sample (20/35 mesh size) dried at 110 deg C.

Oil volume computed assuming an oil density of 0.8 g/cc

Water volume corrected assuming a brine concentration of 30,000 ppm NaCl with an ambient density of 1.018 g/cc

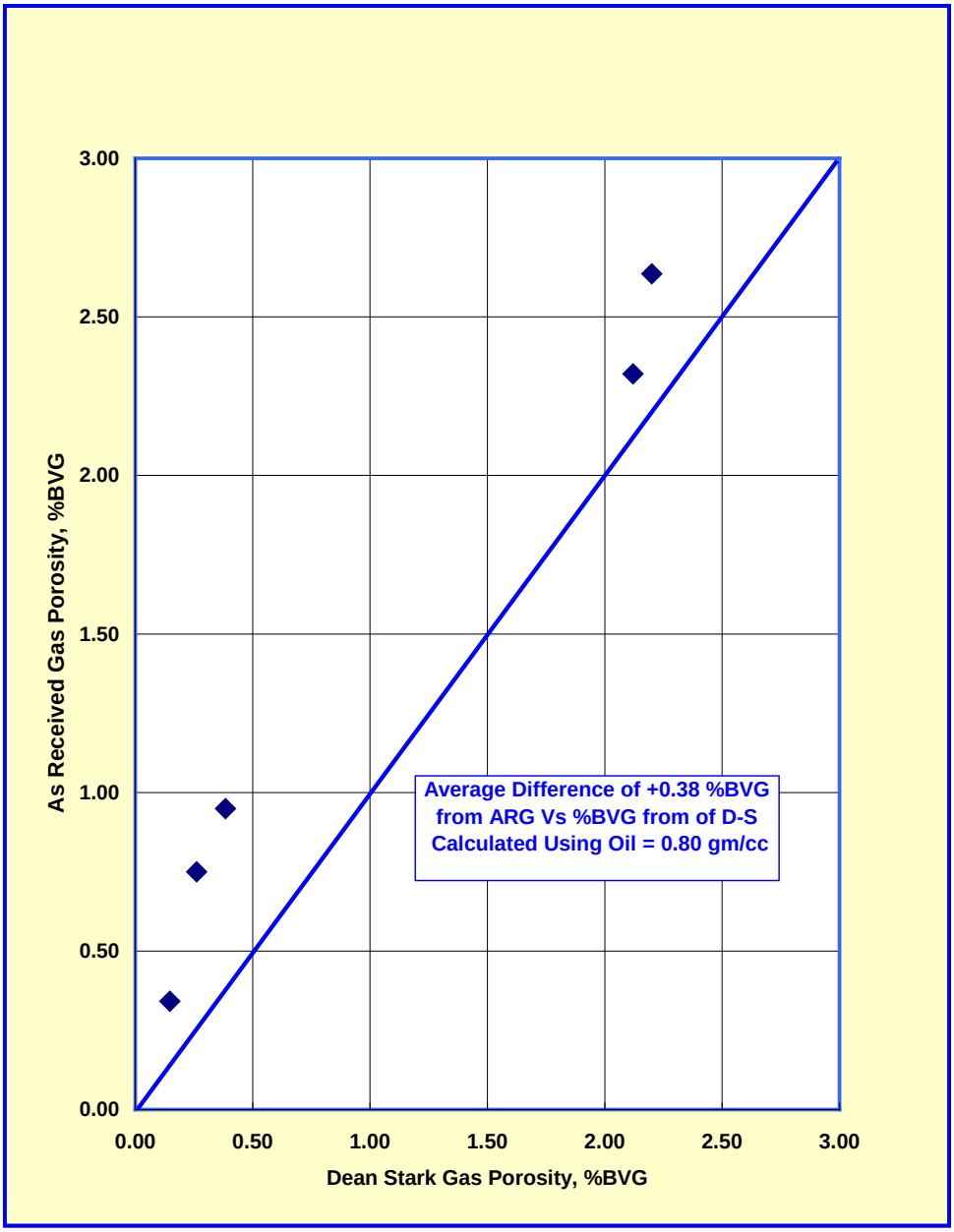


Figure 3 – As Received Gas Porosity from Core Lab Compared with Dean Stark Gas assuming oil of 0.80 gm/cc, Well A-7455, NAB Cores, Christian County, KY

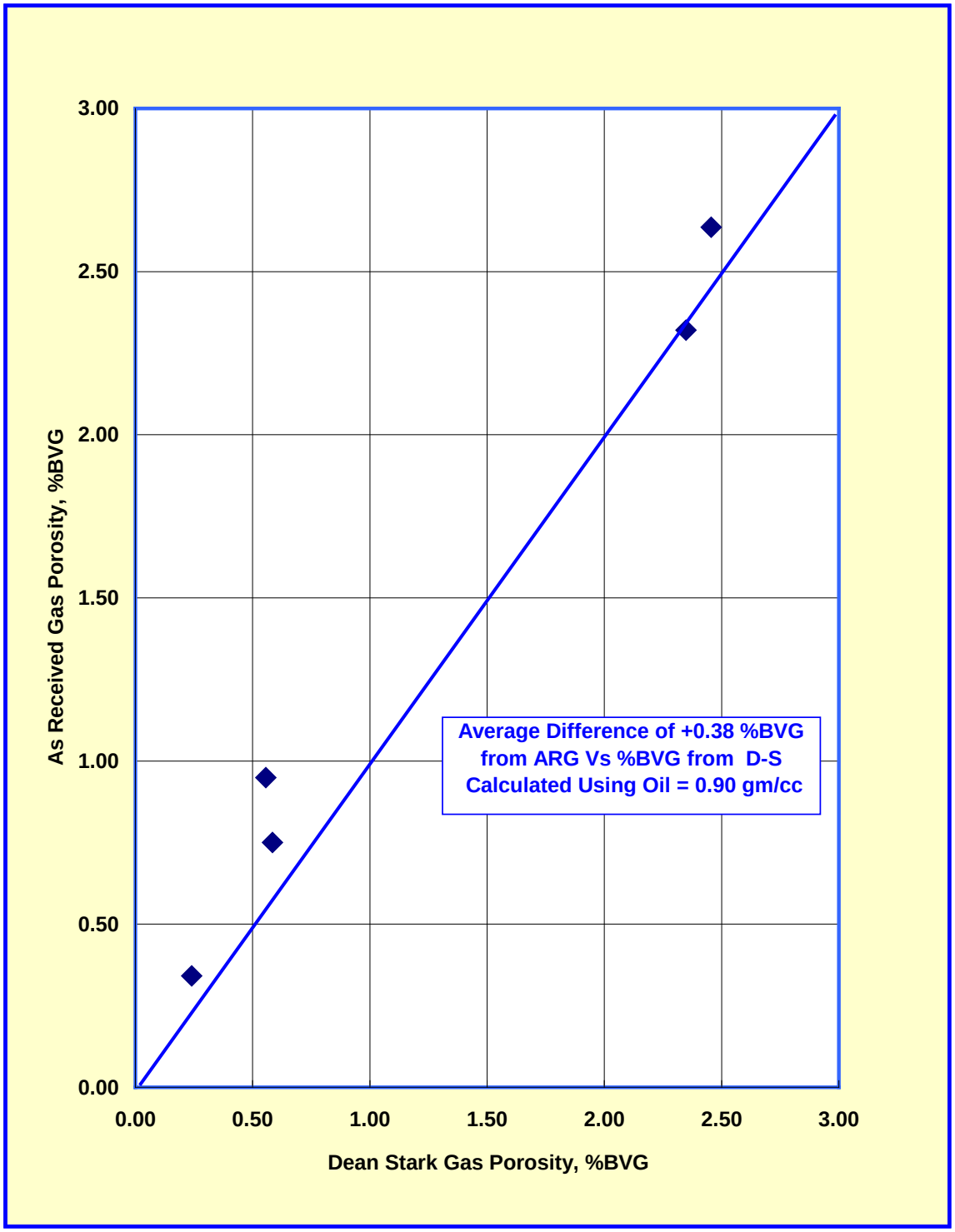


Figure 4 – As Received Gas Porosity from Core Lab Compared with Dean Stark Gas assuming oil of 0.90 gm/cc, Well A-7455, NAB Cores, Christian County, KY

Table 4

Gas Content from Free Gas, Dissolved Gas, and Adsorbed Gas at Reservoir Conditons
Cores from Well 2485-21, NAB Christian County, Kentucky

	Ambient							Adjusted to Reservoir Conditions											
Depth Ft	Phi %PV	Sw %PV	So %PV	Sg %PV	Bulk Dens gm/cc	Shale Vol CuFt/ton	TOC wt %	Phi %BV	Sw %PV	So %PV	Sg %PV	Sgads % PV	Free Gas scf/ton	Adsorb Gas Excl Diss Gas scf/ton	Adsorb Gas Incl Diss Gas scf/ton	Adsorb Gas Plus Free Gas scf/ton	Canister Total Gas (Incl Free Gas) scf/ton	Ads Gas MCFG per AcFt	Canister Total Gas (Incl Free Gas) MCFG per AcFt
2533.0	5.49	18.1	37.2	44.7	2.356	13.617	8.73	5.22	19.0	40.9	25.0	15.1	8.8	36.8	41.7	52.0	58.4	133.5	187.1
2537.9	5.91	29.3	30.9	39.8	2.187	14.664	NA	5.61	30.9	34.0									
2553.0	4.63	31.6	55.8	12.6	2.308	13.894	10.40	4.40	33.2	61.3	-15.5	20.9	-4.6	43.3	49.6	47.4	57.7	155.8	181.1
2562.0	2.45	60.0	30.2	9.8	2.439	13.145	NA	2.33	63.1	33.2									
2573.0	3.71	47.8	37.2	15.0	2.339	13.709	7.22	3.52	50.3	40.8	-9.5	18.4	-2.3	31.1	34.5	33.9	52.6	109.6	167.3
Average	4.44	37.3	38.3	24.4	2.326	13.805	8.78	4.22	39.3	42.1	0.0	18.1	0.6	37.7	41.9	44.4	56.2	132.5	178.5

Footnote

Estimate of porosity at Net Overburden Pressure = 0.95 * Ambient Porosity.

Pi = 665 psig, Temp = 90 deg F

Assumed that the bitumen/oil is 26 deg API with GOR = 99 scf/stbo

Initial free gas has 0.679 specific gravity, with CO2 = 0.36 % and FVF = 49.3 scf/rcf

Ads gas liquid density = 0.42 gm/cc (26.2 lb/cu ft) with 59.8 % of C1, 20.5% C2, 19.2 % C3, 0.47 % CO2 with MW = 25.56

Langmuir Eq'n for 10 %TOC: scf/ton = 127.0*Pi/(Pi+1129.6)

Core Data and Analysis Adjusted to Reservoir Conditions

Ambient core lab data of Well A-7455 were adjusted to reservoir conditions for better correlations of log analysis and to determine free and adsorbed gas in place. **Table 4** shows the "Ambient" core data from Core Lab with the water, bitumen/oil, and gas from GRI Protocol, shale bulk density, converted to shale volume of cu ft/ton, and TOC. Note that TOC's were only available from the Weatherford Lab with three canisters adjacent to three of the five cores used by Core Lab. Reservoir pressure is 665 psig and 90 deg F provided by the oprating Company. With reservoir overburden pressure, a factor of 0.95 is estimated to reduce ambient porosity. Volume of water and bitumen/oil was assumed to have negligible change of compressibility. However, bitumen/oil was assumed to be 26 deg API and GOR of 99 scf/stbo. From PVT of bitumen/oil of this density, the FVF (formation volume factor) is 1.044 rb/stb. That is, the bitumen/oil volume expands 4.4 %. The remaining space in the porosity is then occupied of free and adsorbed gas.

The amount of the adsorbed gas in the reservoir is calculated from the Langmuir Equation using a methane isotherm. The adsorbed gas occupying within the reservoir porosity at initial pressure is a pseudo of liquid gas phase. The volume of the liquid depends on its density and the molecular weight of the gas. This will be shown later with Equations (2), (3), and (4). Initial production is free gas and mostly methane from NAB shale. However, the total gas of NAB is a complex of methane and heavier aliphatic hydrocarbons. Adsorbed gas usually has significant amount of heavier components. This is primarily based of gas content of canister cores. Three canisters were used in the A company well. These gas contents are shown in Figure 9. With the canister at 2,532 ft a gas composition was measured with chromatography shown in Table 5. After 25 days collecting gas contents and compositions (with about 83 % methane), a shale sample was crushed. The crushed gas composition had only 59.8 % methane, with larger amounts of heavier components as shown in Table 5. In Table 4 above in the footnotes the initial free gas composition is shown with specific gravity of 0.679 including 0.36 % of CO2 (correlated with ambient molecular air density = 1.00) and reservoir space of FVF = 49.3 scf/rcf from PVT calculations at initial reservoir pressure and temperature. Also with the footnote in Table 4, we estimated the density of 0.42 gm/cc (26.2 lb/cu ft) with the liquid phase of the adsorbed gas and the molecular weight (MW) of 25.56 similar to the crushed shale composition. Weatherford Lab (Ticora) has provided their estimate of the liquid density. These parameters are at best estimated, and probably varied throughout the NAB formations.

Table 5

Well A-7455

Canister at 2,532 Ft

Corrected Gas Composition with O2. N2, and H2 Removed

Date/Time	C1 Mol Frac	C2 Mol Frac	C3+ Mol Frac	N2 Mol Frac	CO2 Mol Frac
08/06/2009 00:15:00	0.8227	0.1113	0.0582	0.0000	0.0078
08/06/2009 04:00:00	0.8346	0.1104	0.0550	0.0000	0.0000
08/06/2009 15:01:59	0.8377	0.1075	0.0523	0.0000	0.0025
08/24/2009 08:10:00	0.8077	0.1224	0.0658	0.0000	0.0041
08/31/2009 13:28:00 Crushed Spl	0.5977	0.2049	0.1923	0.00000	0.0052
Sum Lump	0.7504	0.1437	0.1012	0.0000	0.0047

Adsorbed gas liquid density is estimated depending on the composition of gas in the crushed shale sample. The gas composition is methane of 59.8 % and remaining components as shown. The liquid density accounting for the heavier components is estimated to be 0.42 gm/cc compared to 0.375 gm/cc for methane only. In **Table 4** for the three cores, adsorbed gas is calculated from the Langmuir Equation as related to TOC and is mostly attached to kerogen. Additionally, some gas may adsorb in clays such as illite, and may also dissolve in the presence of bitumen/oil. For example, at the core with depth of 2,533 ft and TOC of 8.73 %, adsorbed gas is 41.7 scf/ton shale. With the adsorbed gas liquid of 0.42 gm/cc, the space occupies 15.1 % of pore volume (Sg ads %PV), the remaining space occupied by water Sw of 19.0 %PV, and bitumen/oil So of 40.9 %PV. The remaining is then free gas Sg of 25.0 %PV. However, for the other two cores (2,553.0 ft and 2,573.0 ft'), Sg's are negative -15.5 and -9.5 %PV respectively. This may be due to several reasons: (a) bitumen/oil density is higher than assumed, (b) As Received Gas is higher than Dean Stark protocol at ambient conditions, (c) adsorbed isotherm equations using only methane will be inaccurate for complex heavy gas components, and (d) the ambient free gas is not enough to saturate the bitumen/oil and adsorption of the kerogen.

These inaccuracies are more pronounced due to the combination of water and large amounts of bitumen/oil in the NAB shale compared to other shale basins where bitumen/oil is often negligible. As such, inaccuracies may not be evident. Figure 5 shows core lab data for pore space at ambient conditions using Bulk Volume (%BV) from the A company well. Figure 6 shows the pore space for the core data at reservoir conditions including the negative space of two of the cores. Two cores were unavailable of TOC, so the space of the combination of both the adsorbed gas and the free gas are separately shown of these two cores.

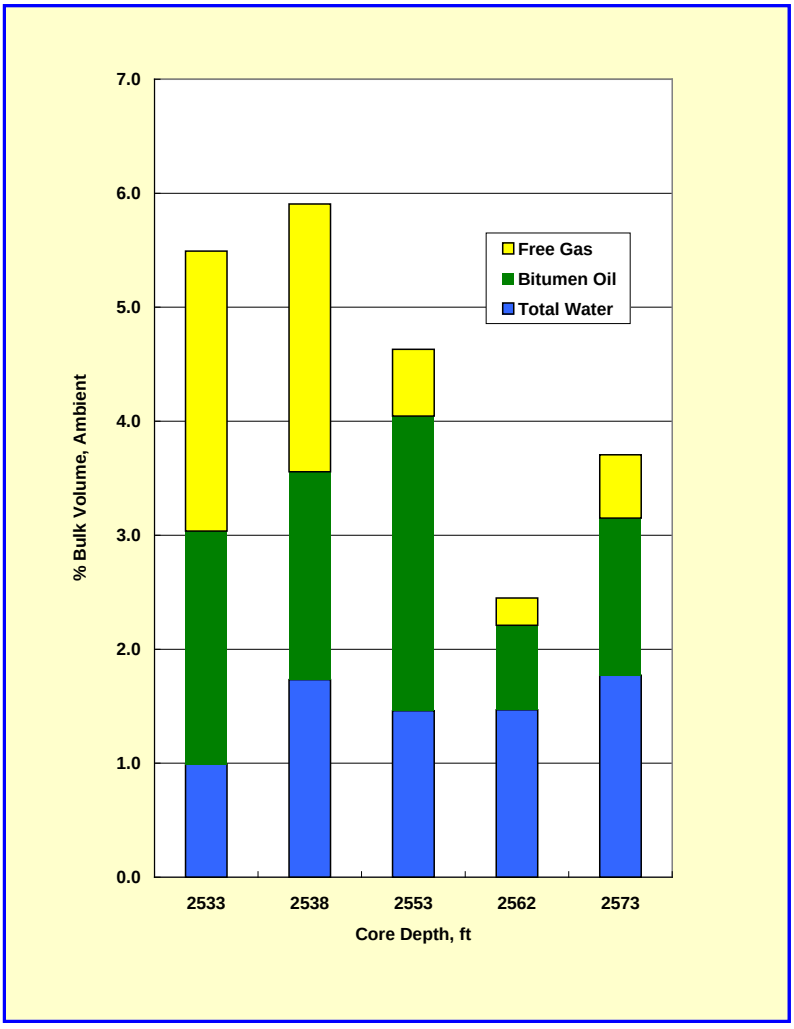


Figure 5 - Ambient NAB Core Lab Analysis from Well A-7455, Christian County, KY

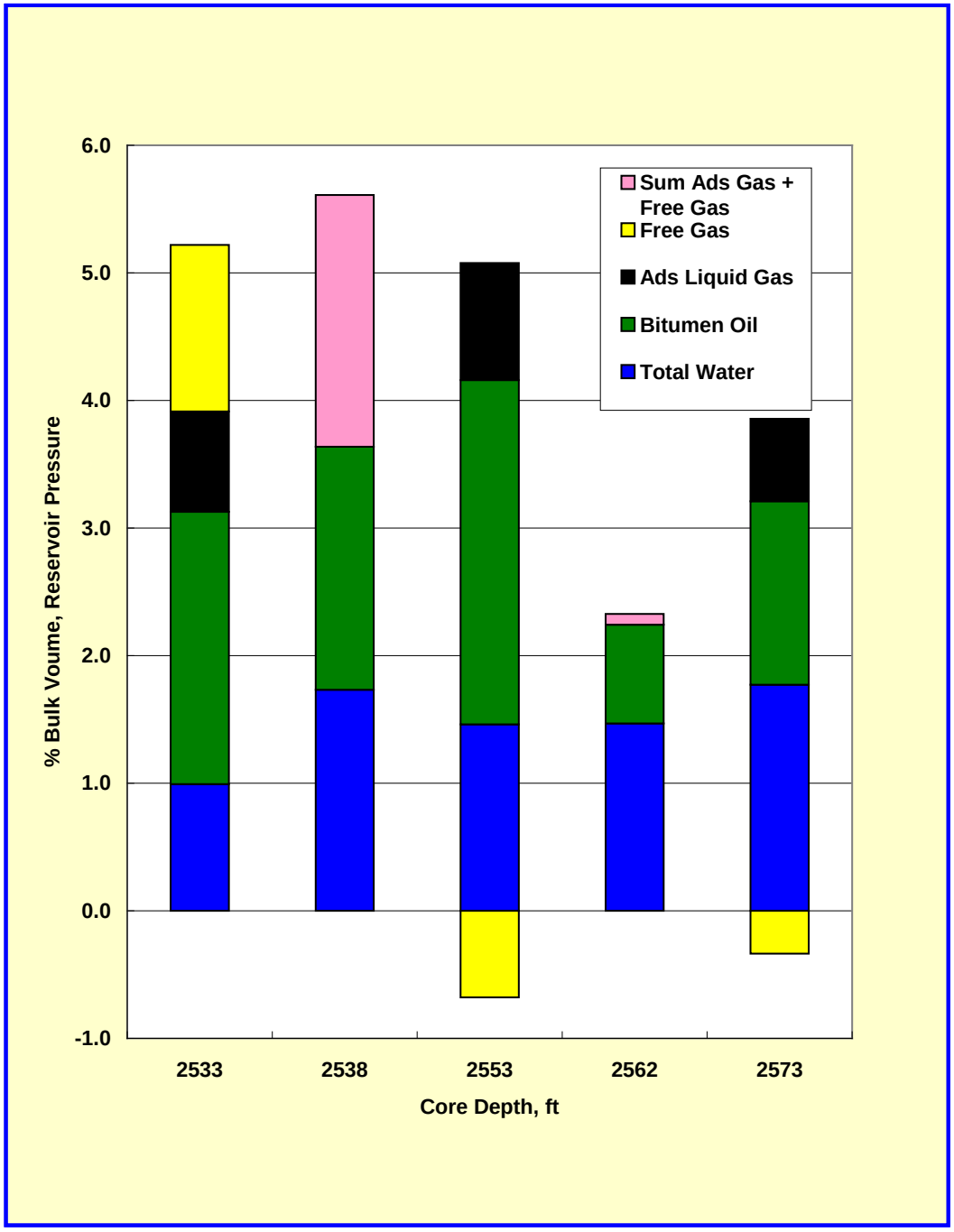


Figure 6 – Adjusted Core Lab Analysis for Reservoir Condition, from Well A- 7455, Christian County, KY

Langmuir Isotherm Equation – As mentioned above, adsorbed gas primarily attaches to kerogen; small amounts of gas may be dissolved in bitumen/oil; and remaining portion of the total gas is free gas in the pore system of the shale. The amount and gas composition of the adsorbed gas depend on the reservoir pressure, temperature, and primarily the character and amount of the kerogen. The overall character of the kerogen is complex and usually TOC (Total Organic Carbon) is measured from shale samples as a major correlation of kerogen.

In the Well A-7455, only the core in the canister of 2553' was used by Weatherford Lab for a shale sample for methane isotherm at initial reservoir pressure of 665 psig and 90 deg F. The TOC is 10.4 wt% with the brown open triangle symbols in Figure 7. A maximum lab pressure of 898 psia and maximum lab methane is a content of 58.7 scf/ton shale. Brown filled color symbols are a linear reduction of the gas content with TOC of 10.0 wt%. This normalized isotherm of TOC of 10.0 wt% is useful to calculate gas content at various cores with TOC's from log analysis with variations at each depth. Gas content with a TOC from the normalized Langmuir Equation is:

V = (TOC/10.0)*(127.0*P/(P+1129.6)) …….. (2)

where: V = volume gas content of scf/ton shale (scf at 60 ^{O}F and one atm pressure),

P = reservoir pressure, psia,

TOC = Total Organic Carbon, wt%.

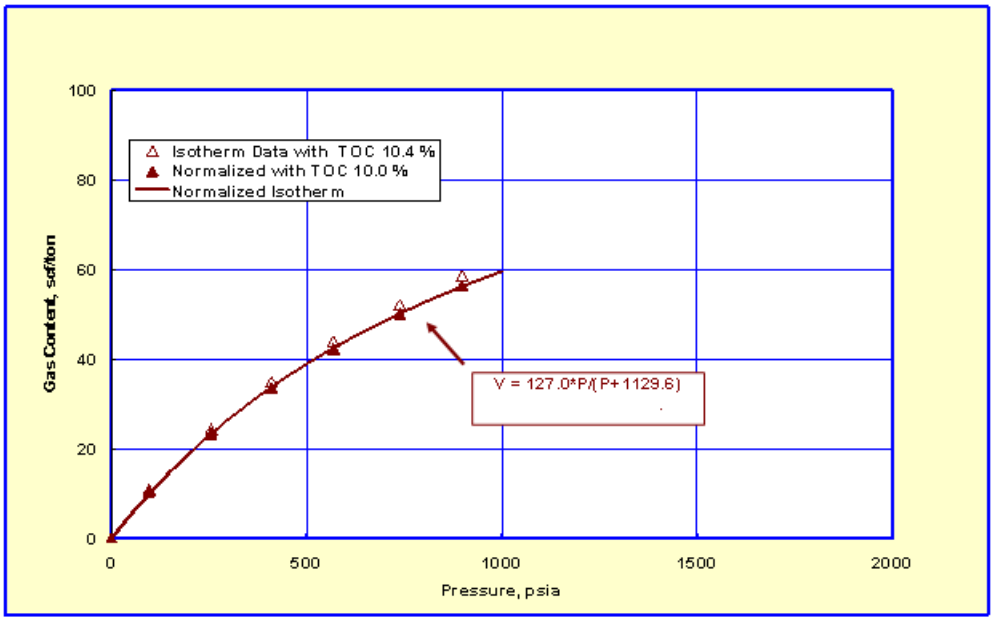


Figure 7 – Methane Adsorption Isotherm Data from one core with Well A-7455, Christian County, KY

Equation 2 represents the Langmuir shale gas volume of 127 scf/ton at infinite pressure with TOC of 10 wt%. For the pressure of 1129.6 psia the Langmuir shale gas volume content (with TOC of 10 wt%) is one half the Langmuir volume, i.e., 127/2 = 63.5 scf/ton.

Log Analysis of Adsorbed, Free Gas, and Total Gas – Adsorbed gas at reservoir conditions for the Well A-7455 is calculated every half foot as Mscf/AcFt:

$$Vads = 1.36*((12.7*(Pi+15))/((Pi+15)+1129.6))*Rhob*TOC \quad \ldots\ldots\ldots\ldots\ldots\ldots\ldots\ldots(3)$$

where Vads = Adsorbed gas phase, Mscf/AcFt,

Pi = Reservoir initial pressure, 665 psig,

Rhob = Log bulk density, gm/cc,

TOC = Total organic carbon, wt%.

For liquid phase of the adsorbed gas:

BVAG = (MW*Vads)/(32.067*379.5*LD*1.36) …… (4)

where BVAG = Adsorbed liquid phase, BV(frac) of the shale volume,
MW = Molecular weight of mixed gas compositions, lb/lb mol,
Vads = From Eq'n (3), Mscf/AcFt,
LD = Liquid Density of adsorbed gas, lb/cu ft.

In this equation, in the numerator the MW of the mixed adsorbed liquid gas (lb/lb mol) is multiplied by the adsorbed gas in Mscf/AcFt (Eq'n 3). Then it is divided in the denominator with the following items: 32.067 is multiplied by 379.5 for the volume of cu-ft per ton of shale with multiply of the molar gas volume in scf at standard conditions per lb mol. This is multiplied with LD (lb liquid of adsorbed gas/cu ft liquid). The multiplier 1.36 is then used to convert Mscf/AcFt for BVAG to be BV (BV Ads Gas/BV Shale), i.e., fraction of the adsorbed liquid gas in the shale volume.

The remaining of the total gas is free gas at the initial Pi of psig:

FG = (Phi - BVW - BVO - BVAG)* (1542*(Pi+15)/(Z*(460+T))) …… (5)

where FG = Free Gas, Mcf/AcFt,
Phi = Porosity, BV (frac),
BVW = Water saturation, BV (frac),
BVO = Bitumen/Oil, BV (frac),
BVAG = Adsorbed liquid gas phase, BV (frac),
Z = Compressibility factor of gas with MW, CO2, N2 (dimensionless),
T = Reservoir temperature, °F.

These log analysis equations are used for calculation of IGIP (Initial Gas in Place) Mcf/AcFt of free gas, adsorbed gas, and total gas at each half-foot of depth from the log data. In addition, cumulative gases are then calculated for IGIP of free gas, adsorbed gas, and total gas in Mcf/Ac for selected vertical sections or with the entire vertical shale section.

Logging and Log Analysis

The New Albany (NAB) resource play is a very complex formation to evaluate and complete successfully. This is because the kerogen, the main component of the total organic carbon (TOC) is relatively immature type II to type II-III with vitrinite reflectance (Ro) of from 0.6 – 1.2, putting it in the oil window. With significant amounts of oil/bitumen in the system, along with water and adsorbed gas, in many instances the space available for free gas is restricted. In some portions of the NAB thickness the gas is entirely adsorbed. Since, as with all resource shale plays the matrix permeability is low, generally 0.001- 100 nano-Darcy little or no oil or water are produced and free and adsorbed gas must be delivered to a well bore as a function of inherent matrix porosity, matrix permeability, natural fractures, induced fractures, and natural or induced micro-fractures or some form of plane of weakness allowing flow after fracture stimulation.

Despite this complexity, it is possible to adequately characterize the NAB using basic logs of resistivity, density-neutron-gamma ray-caliper for TOC, primary lithologic components, porosity, oil, water, and gas saturation, adsorbed gas content, a general matrix permeability, and calculated GIP. Figure 8 is an example from the Noble Energy Osburn Trust 1-11H well where the only log inputs are those mentioned above. This is important as many areas have older logs that only consist of these basic data. These should be considered a potential source for prospecting within the basin. For example, a regional petrophysical analysis of these basic log data would allow the mapping of free gas. To be certain other electric logs may provide needed information such as dipole sonic for rock mechanical properties and completion fracture design, or image devices to locally determine natural or induced fracture orientations and intensity, or elemental capture logs to provide additional lithology inputs. The point however, is that a basic evaluation is possible for determining GIP, the amount of adsorbed and free gas, the amount of TOC, the primary lithology, where within the formation thickness the free gas resides, and the porosity, saturation, and permeability (if only generally) of the NAB section.

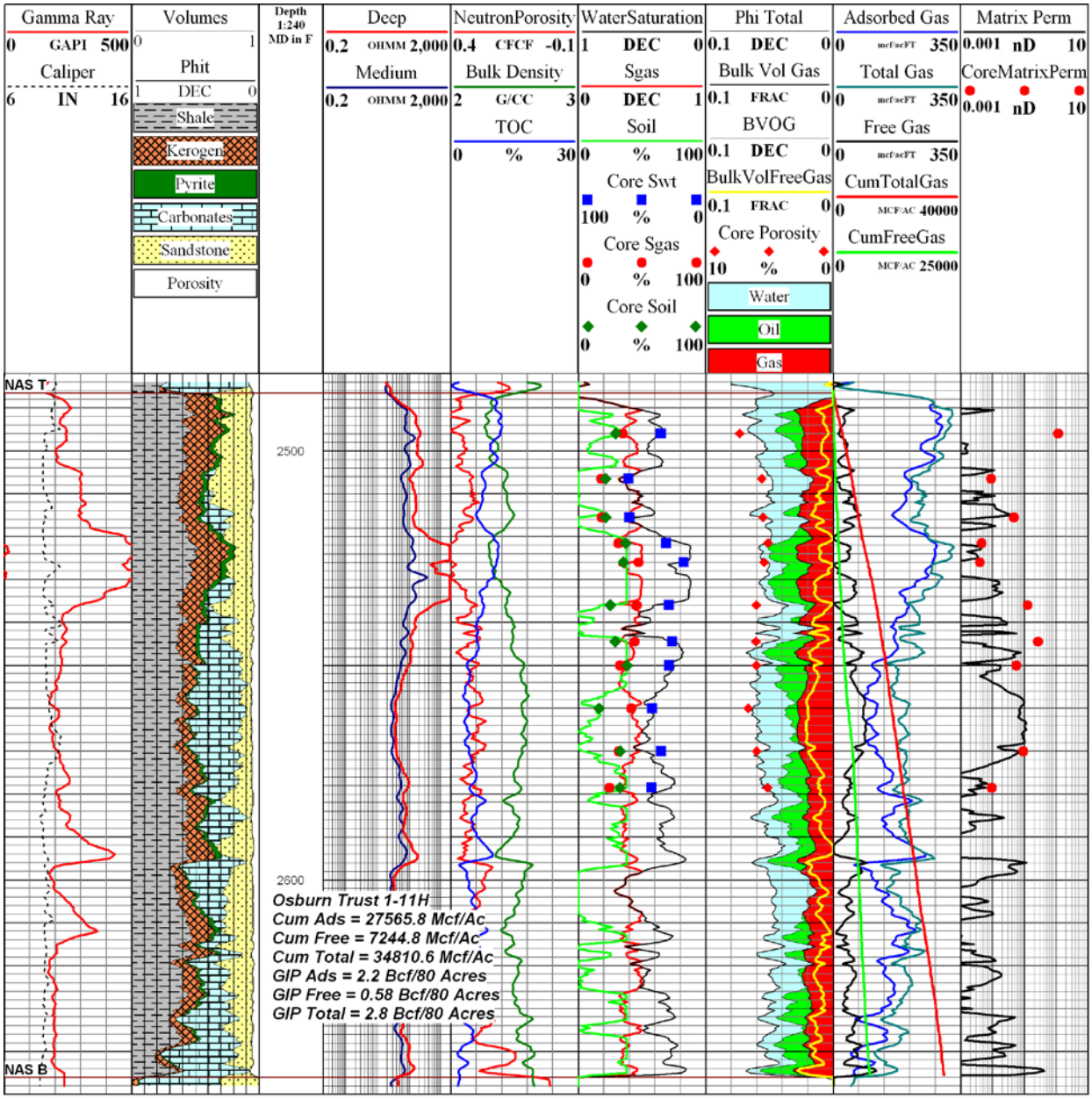


Figure 8 - Resulting New Albany characterization from Analysis of Basic Logs Resistivity, Density, Neutron, with Caliper and Gamma Ray

Where some of the more advanced electric logs may not be absolutely critical in making a log evaluation, core analysis is critical at least initially in an area. The petrophysical approach is to use the core data to build log based models that allow the determination of the following:

- Lithology of the shale
- Porosity and water saturation
- Oil and gas saturation
- Matrix permeability

- Total organic carbon, and geochem parameters S1, S2, S3, Ro, HI, OI, and PI
- Free, adsorbed, and total gas content
- Geomechanical properties –Young's modulus, Poisson's ratio, stress

Once the petrophysical models are built (as for example the best fit general isotherm shown later in this report) coring may not be necessary on subsequent development wells. However new areas may require adjustment to the models, and additional core may be needed.

These core analyses should consist of Rock Eval-pyrolysis which provides the TOC and geochemical parameters as shown in Table xx. The table below was originally compiled by Humble Geochem with blue columns added by ResTech. The kerogen density that is added to this table is calculated using results from the GRI Devonian shale project "Development of Laboratory and Petrophysical Techniques for Evaluating Shale Reservoirs". The equation relates vitrinite reflectance (Ro) to kerogen density and is restated in equation 6 below:

$$\mathbf{RhoK = 0.3491 * Ro + 0.9626} \quad \ldots\ldots\ldots\ldots\ldots\ldots\ldots\ldots\ldots\ldots\ldots\ldots\ldots\ldots \mathbf{(6)}$$

where

RhoK = Kerogen density, (g/cc),

Ro = Vitrinite reflectance, (%).

In addition to the Rock Eval and pyrolysis, XRD or other methods such as Fourier Transform Infrared Spectroscopy (FTIR) or x-ray fluorescence (SPE 131768 Sondergeld,et al) should be employed to delineate primary shale lithology. Also, the GRI protocol core analysis for bulk density, grain density, porosity, gas, oil and water saturation, and matrix permeability should be developed. As part of these analyses the as received gas technique (ARG discussed previously) ought to be requested if not routinely supplied by lab of choice. These data are used to calibrate a multi-mineral model for porosity and the resistivity based Archie model to water saturation. The oil saturation is estimated as shown in the methodology section of this report, with the remainder being gas, each of which are compared to the GRI core result. **Table 6** displays an example of XRD data presented in weight % for the A-7455 well. These are typical results for the core components of the lithology of the NAB shale, largely made of quartz-feldspar-plagioclase, carbonates, pyrite/marcasite, and clay which is dominated by illite. **Table 7** is gas saturation, bitumen/oil, and water from Core Lab using GRI Protocol.

Table 6

Example XRD results

Daugherty Petroleum, Inc.
DPI - 2485-21
Christian County, Kentucky

XRD Analysis by Core Lab of the Five NAB Shale Samples

	Whole Rock Mineralogy (Weight %)								Relative Clay Abundance (Normalized to 100%)		
Depth	Quartz	K-Feldspar	Plagioclase	Calcite	Dolomite & Fe-Dolomite	Pyrite	Marcasite	Total Clay	Illite & Mica	Kaolinite	Chlorite
2533.00-33.50	37	4	10	0	20	7	4	18	100	0	0
2537.90-38.35	39	7	6	0	12	3	2	31	100	0	0
2553.00-53.50	37	6	9	0	10	6	5	27	100	0	0
2562.00-62.50	41	6	5	5	17	5	2	19	100	0	0
2573.00-73.50	50	5	4	7	12	4	2	16	100	0	0

Table 7

Gas Saturation from Dean Stark Analysis from GRI protocol

Daugherty Petroleum, Inc.
DPI - 2485-21
Christian County, Kentucky

CL File No.: HOU-090730
Date: September 21, 2009
Analyst(s): MS-JH

Gas Shale Core Analysis

		As received				Dry & Dean Stark Extracted Conditions [2]			
Sample	Depth (ft)	Bulk Density (g/cc)	Matrix Permeability [1] (mD)	Gas-filled Porosity (%)	Gas Saturation (%)	Grain Density (g/cc)	Porosity (%)	Oil Saturation [3] (%)	Water Saturation [4] (%)
G-1	2533.00 - 2533.50	2.356	2.03E-06	2.20	40.1	2.463	5.49	41.9	18.1
G-2	2537.90 - 2538.35	2.187	1.99E-06	2.12	35.9	2.288	5.91	34.8	29.3
G-3	2553.00 - 2553.50	2.308	2.35E-09	0.26	5.7	2.380	4.63	62.8	31.6
G-4	2562.00 - 2562.50	2.439	4.13E-10	0.15	6.0	2.479	2.45	34.0	60.0
G-5	2573.00 - 2573.50	2.339	1.00E-08	0.38	10.4	2.398	3.71	41.8	47.8

Footnotes:

(1) Matrix Permeability is an effective Kg determined from pressure decay results on the fresh, crushed, 20/35 mesh size sample.
(2) Dean Stark extracted sample (20/35 mesh size) dried at 110 °C. Porosity and saturations are relative to total interconnected pore space.
(3) Oil volume computed assuming an oil density of 0.8 g/cc
(4) Water volume corrected assuming a brine concentration of 30,000 ppm NaCl with an ambient density of 1.018 g/cc

Reference: "Development of Laboratory and Petrophysical Techniques for Evaluating Shale Reservoirs", GRI-95/0496, Gas Research Institute, April 1996

Additional core measurements from gas canisters can be made for gas content and composition. The NAB lends itself to these type measurements as the formation is shallow, trip times are short, and low reservoir pressures minimize the impact of lost gas. The gas content can be used to compare with methane isotherm results of adsorbed gas content for insight into the relationship of adsorbed gas to the total.

Also, free gas will be a part of the total desorbed gas content. Previous Figure 5 shows the gas content of three NAB canister cores of ambient gas in the Well A-7455. Previous Figure 6 shows the adjusted Core Lab analysis for reservoir condition for each three cores, and two of the cores calculate negative free gas. Figure 9 shows comparisons of methane isotherm (from one of the three cores), absorbed gas plus free gas (two negative), and gas content from the three canisters. This is shown in previous **Table 4**.

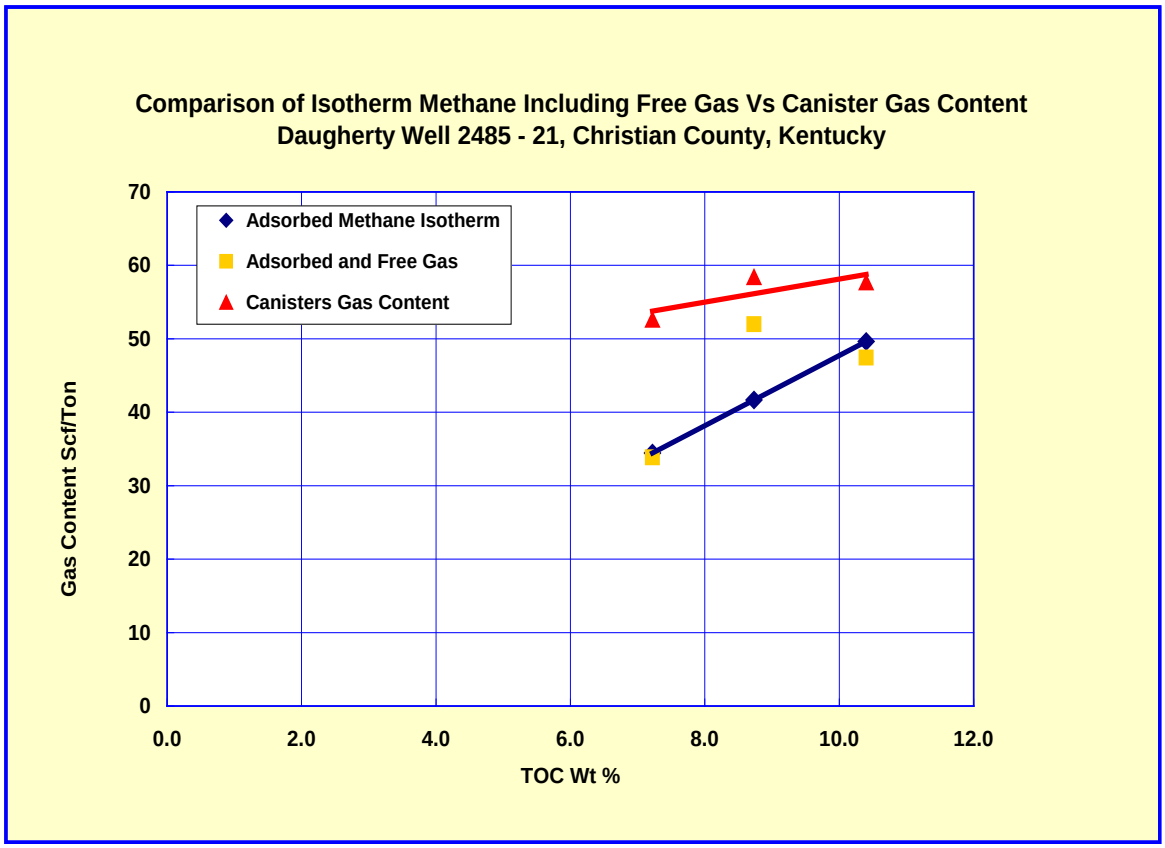


Figure 9 – Comparison of Isotherm Methane Including Reservoir Free Gas with Canister Gas Content in 2533 – 2573 ft, Well A-7455, Christian County, KY

A key observation from these data results is that the total gas content from canisters often have adsorbed gas compositions heavier than methane gas. Usually core labs use only isotherm measurements with methane even though present heavy components are present, especially for heavy compositions associated with adsorbed gas. These cases will cause the isotherm results to be different with the heavy components, and is common in the New Albany of the Illinois basin.

With the Noble Osburn Well 1 – 11H of Sullivan County, Indiana is ten canisters shown in Figure 10.

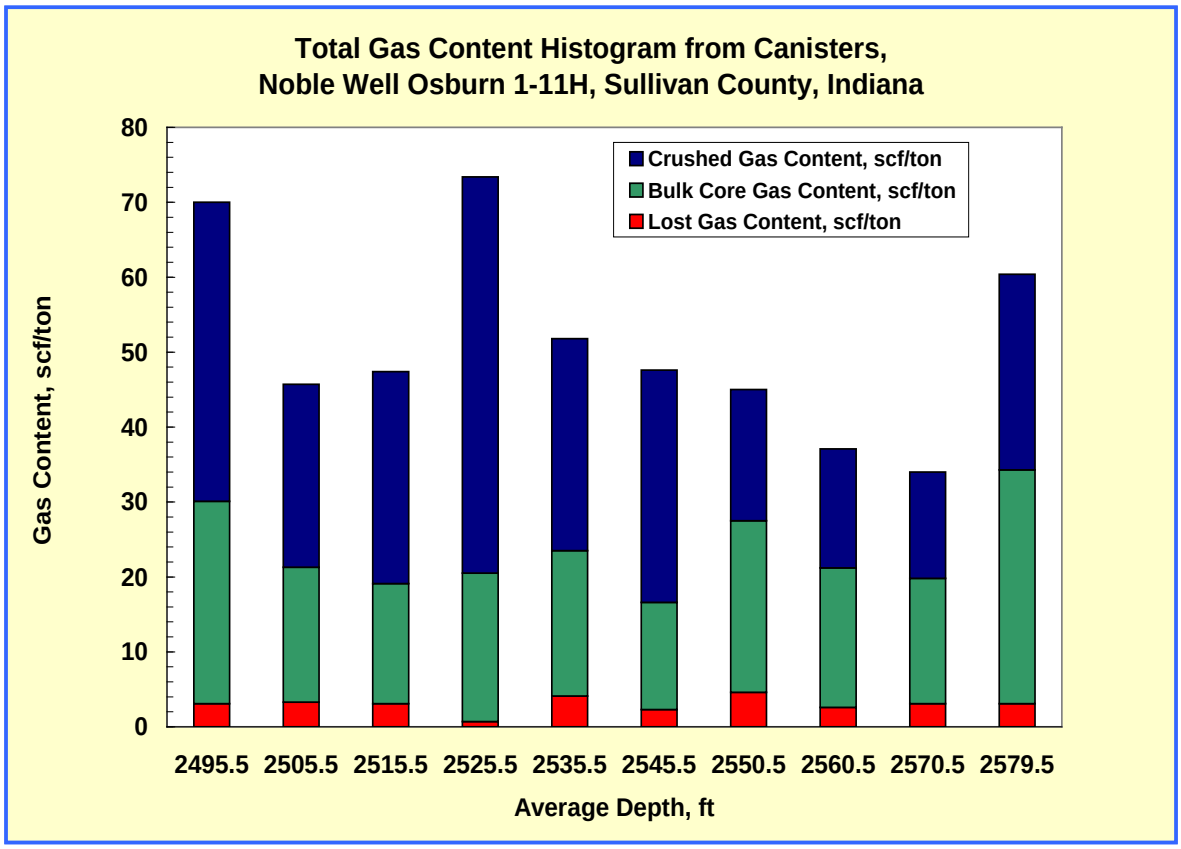


Figure 10 – Ambient Canister Gas: Lost gas, Bulk Core Gas, and Crushed Gas Combined to Estimate Total Gas Content

The red color shows lost gas before the conventional cores were tripped to surface. The green color shows amount of gas content that has freed from the bulk cores and into the head space of the canisters (about 1500 hours), and blue color is then gas content measured from crush of an aliquot of each core. From these canister cores, the gasses from the crushed samples are about 60 % of the total gas contents.

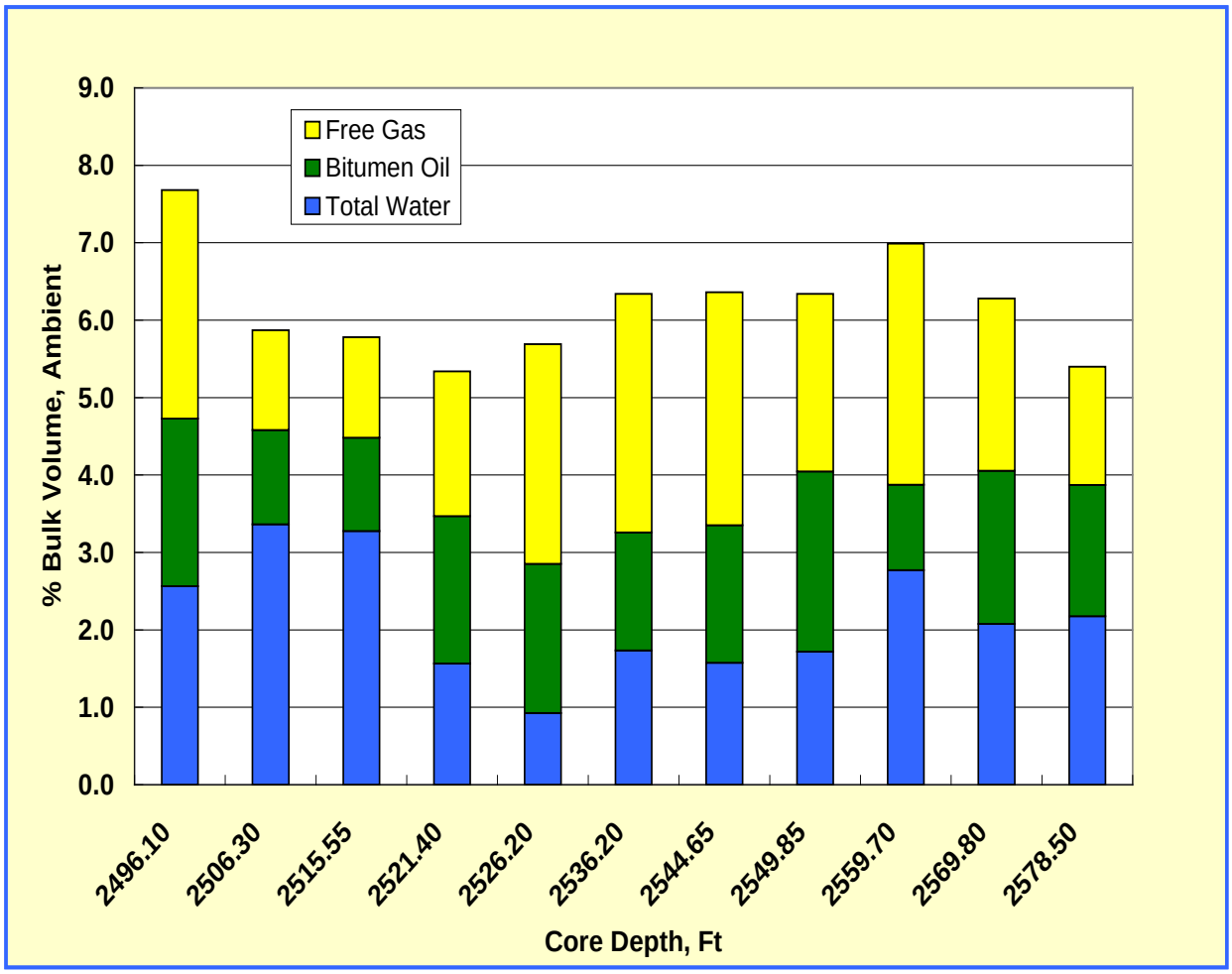


Figure 11 – Ambient Core Lab Analysis from Noble Osburn 1-11H, Sullivan County, Indiana

The core analysis results show the space of the ambient gas, water, and bitumen/oil and the relationship with the canister cores shown in Figure 10.

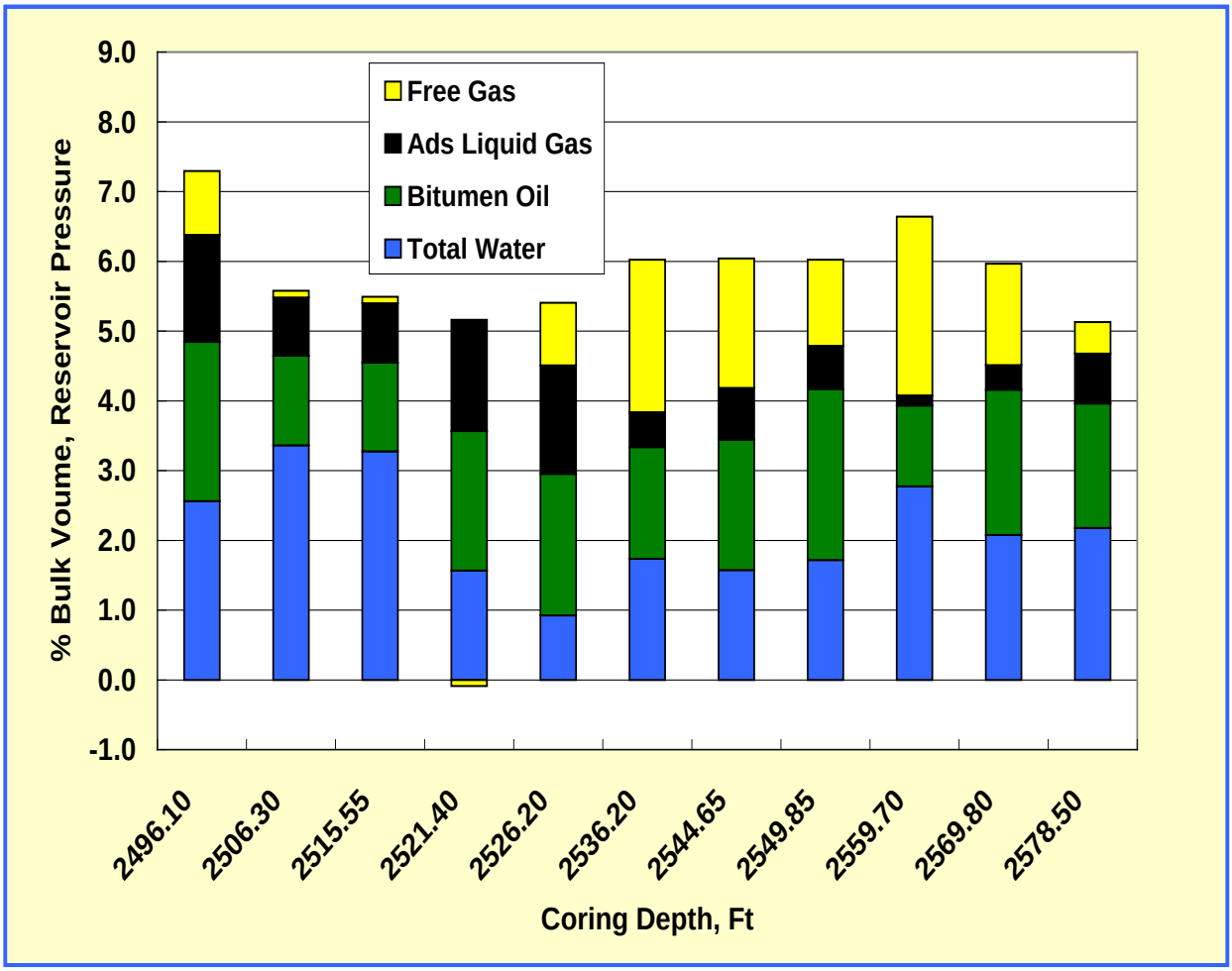


Figure 12 – Adjusted Core Lab Analysis at Reservoir Condition Noble Osburn 1-11H, Sullivan County, IN

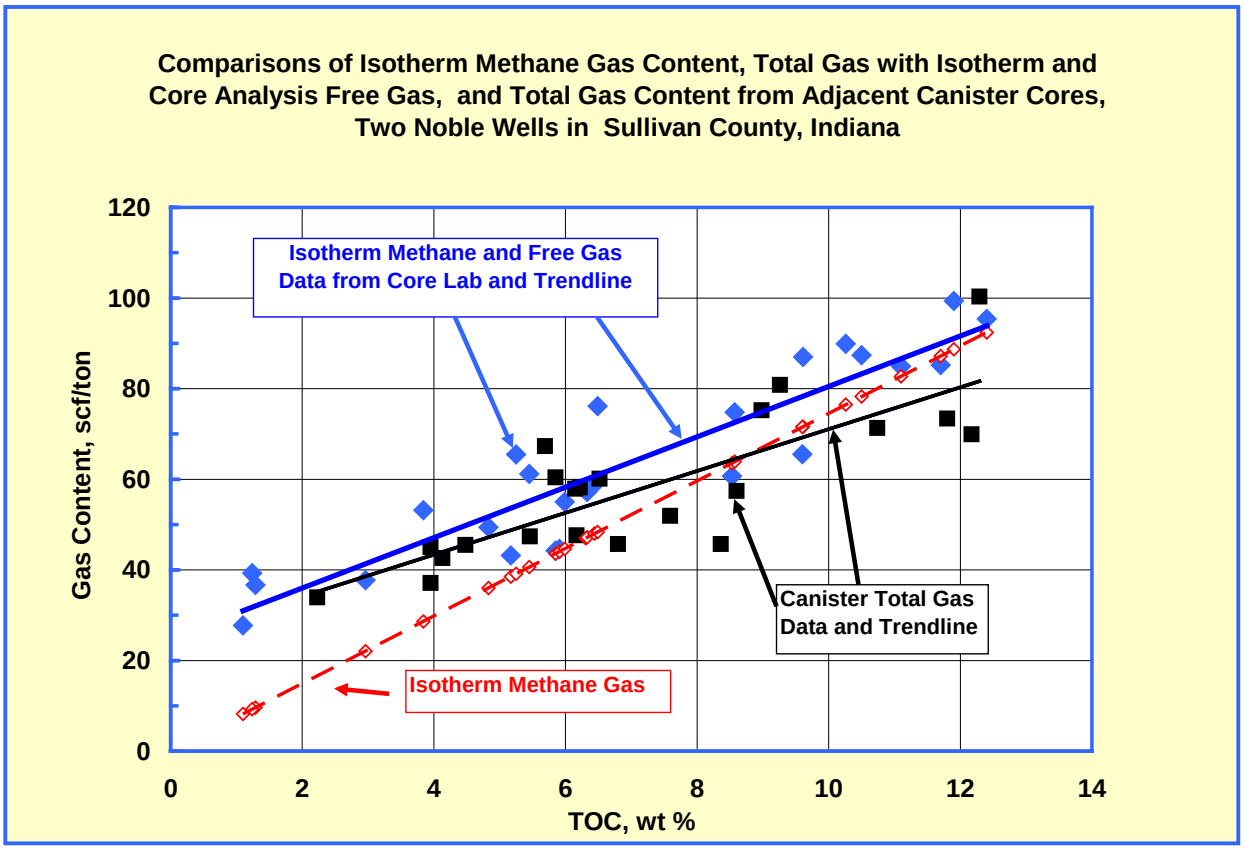


Figure 13 – Red Trendline of Methane Isotherm, Canisters Core Gas, and Methane Isotherm Including Free Gas from Core Analyses, Two Noble wells, Indiana gasses

In Figure 13 there is a blue Trendline of isotherm including free gas of a small higher total. The black symbols and a black Trendline show canister of total gas contents. Overall, the adsorbed gas content from the methane isotherm is reasonable considering that when added free gas at reservoir condition, total gas more or less matches the canister total gas. Note some of the NAB shales have little or none of the free gas in reservoir conditions. This shows in the graph in Figure 12, in **Table 8**, and in other wells.

The variation and heavy components of the gas are illustrated in **Table 8** below. This compares with the method used for data from company A. Core Lab analyzed at ambient pressure and temperature with 11 cores adjacent to the canister cores. These data were then adjusted to reservoir pressure and temperature.

TABLE 8

AMBIENT CORE LAB ANALYSIS DATA ADJUSTED TO RESERVOIR CONDITIONS FOR FREE GAS AND ADSORBED GAS WITH SHALE FROM NOBLE OSBURN 1-11H

	Ambient Lab Analyses								Adjusted to Reservoir Conditions										
Well Sample Depth, Ft	Amb Phi, %BV	Amb Sw, %PV	Amb So %PV	Amb Sg %PV	K E+06 md	Bulk Dens gm/cc	Grain Dens gm/cc	Core Anal TOC %wt	OB Phi %BV	OB Sw %PV	OB So %PV	OB Sgads %PV	OB Sg %PV	Free Gas scf/ton	Ads Gas Excl Diss Gas scf/ton	Ads Gas with Diss Gas scf/ton	Total Gas with Free Gas scf/ton	Ads Gas w/Diss MCFG per AcFt	Total Gas w/Free MCFG per AcFt
Osburn Tr 1-11H																			
2496.10	7.68	33.4	28.2	38.4	1.1700	2.185	2.316	11.90	7.30	35.1	31.3	22.0	11.6	10.66	81.05	88.68	99.34	263.52	295.20
2506.30	5.87	57.3	20.8	21.9	0.0091	2.420	2.523	5.85	5.58	60.3	23.0	15.6	1.0	0.66	39.72	43.59	44.25	143.48	145.64
2515.55	5.78	56.7	20.9	22.4	0.0473	2.443	2.546	5.91	5.49	59.7	23.1	16.2	0.9	0.58	40.24	44.04	44.62	146.33	148.26
2521.40	5.34	29.4	35.6	35.1	0.0046	2.276	2.369	11.70	5.07	30.9	39.5	32.9	-3.2	-1.99	80.76	87.19	85.20	269.88	263.74
2526.20	5.69	16.3	33.8	49.9	0.0041	2.484	2.605	10.50	5.41	17.1	37.5	30.1	15.2	9.13	72.28	78.25	87.38	264.33	295.18
2536.20	6.34	27.4	24.0	48.6	0.1260	2.427	2.557	3.84	6.02	28.8	26.6	8.7	35.9	24.55	23.79	28.62	53.16	94.45	175.47
2544.65	6.36	24.8	27.9	47.3	0.2670	2.442	2.573	5.45	6.04	26.1	30.9	12.8	30.1	20.56	35.02	40.61	61.18	134.88	203.18
2549.85	6.34	27.1	36.7	36.2	0.0558	2.481	2.607	4.83	6.02	28.5	40.7	10.8	20.0	13.40	28.77	35.99	49.39	121.45	166.66
2559.70	6.99	39.7	15.8	44.6	16.6000	2.607	2.762	1.29	6.64	41.7	17.5	2.3	38.5	27.03	6.36	9.61	36.65	34.08	129.93
2569.80	6.28	33.1	31.5	35.4	0.0912	2.529	2.657	2.96	5.97	34.8	34.9	6.2	24.1	15.67	16.03	22.06	37.73	75.87	129.76
2578.50	5.40	40.3	31.4	28.3	0.0096	2.478	2.579	5.17	5.13	42.4	34.8	14.6	8.2	4.67	33.26	38.53	43.19	129.84	145.56

Note: Ambient Conditions
Oil bitumen was adjusted to 0.93 gm/cc

Note: Adjusted to Reservoir Conditions
Pi = 1110 psia, T = 80 deg F

Previously shown in Equations (2), (3), (4), and (5) used to calculate the adsorbed gas, the reservoir pressure and temperature of the liquid phase adsorbed gas and its space, fractional space of the water, the space of the total porosity, and the rest of the space available in the total porosity is then the free gas. The methane isotherm equation for the Noble Osburn and Solsman wells was used for six isotherm cores (three in each well). Previous Figure 13 shows the close data of the average gas content as function of the TOC. The Langmuir Equation is shown later in Figure 17.

The gas composition is an important consideration in the calculation of the molecular weight used to determine the bulk volume adsorbed gas, using Equation 2. Methane isotherm results are still the most direct way to estimate adsorbed gas when canister data are not available or not trustworthy. As such isotherm data are used in both the Indiana and Western Kentucky areas to estimate adsorbed gas content and is combined with free gas determined from either the core or log based model to delineate total gas in place. A general best fit isotherm for the Western Indiana, Southwestern Kentucky area is presented later in this report.

Recently there are added data from 28 canisters in B-15 in McLean County, Kentucky, with cores from 3,572 – 3,884 ft. Figure 14 shows the 28 canister data. Also, gas composition is shown from six canister cores in **Table 9** and **Table 10**. These data show variation of the compositions, but generally in the crushed samples there are heavy compositions and significant final gas contents.

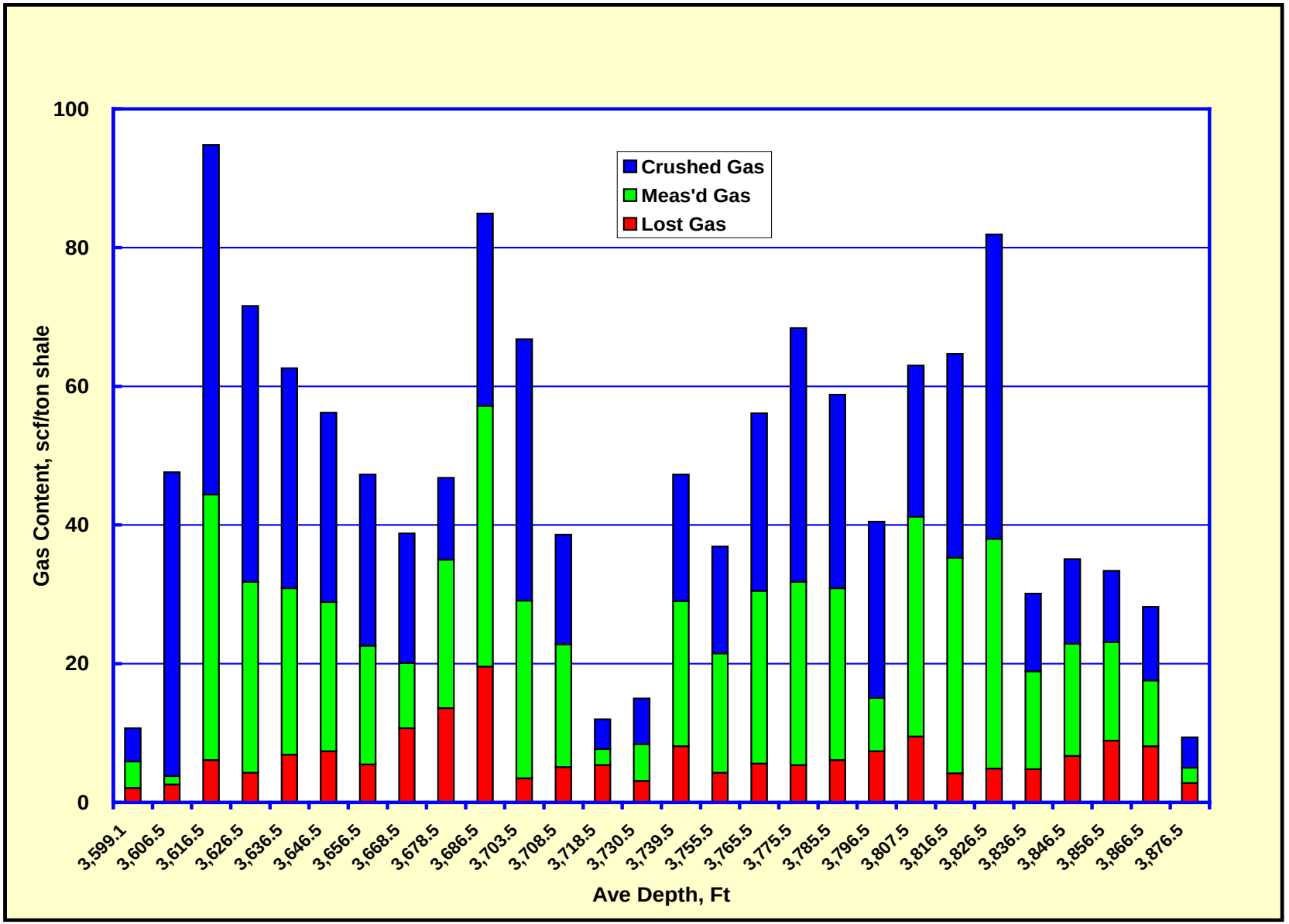


Figure 14 – Total Canister Gas Content Histograms, B-15, McLean County, KY

Table 9

Canister Composition of Gas Analysis, Well B-15, McLean County, Kentucky

Sample Number	Collection Point	As-Received Gas Content	Incremental Gas Content	Gas Analysis (O_2, N_2 and H_2 Mole Fractions Omitted)[1]					Calorific Value	
				C_1	C_2	C_3-C_{10}	CO_2	Total	Dry	Saturated
	hours	scf/ton	scf/ton	mole %	mole %	mole %	mole %	mole %	Btu/ft^3	Btu/ft^3
Average Depth (ft): 3,636.5				**Lost Gas Content: 11.02%**				**New Albany Shale**		
46152-5-1	1.72	8.16	8.16	83.01	11.75	4.09	1.15	100.00	1,160.5	1,140.4
46152-5-2	2.01	8.71	0.55	83.30	12.10	3.95	0.65	100.00	1,165.4	1,145.1
46152-5-3	2.49	9.44	0.73	82.72	12.50	4.27	0.52	100.00	1,176.2	1,155.7
46152-5-4	3.04	10.05	0.61	82.50	12.69	4.38	0.44	100.00	1,180.2	1,159.7
46152-5-5	4.07	10.89	0.84	81.42	13.42	4.74	0.43	100.00	1,192.5	1,171.8
46152-5-6	33.56	18.48	7.58	80.37	14.69	4.74	0.20	100.00	1,204.9	1,183.9
46152-5-A[3]	337.17	62.56	44.08	49.09	28.45	21.82	0.64	100.00	1,604.4	1,576.5
Apparent Gas Composition[2]				**58.76**	**23.91**	**16.68**	**0.65**	**100.00**	**1,479.5**	**1,453.8**
Average Depth (ft): 3,678.5				**Lost Gas Content: 29.13%**				**New Albany Shale**		
46152-9-1	3.34	17.47	17.47	74.90	15.79	8.52	0.78	100.00	1,273.5	1,251.3
46152-9-2	4.31	19.33	1.86	76.81	15.00	7.81	0.38	100.00	1,260.5	1,238.5
46152-9-3	10.24	23.86	4.53	75.21	16.26	8.21	0.32	100.00	1,278.6	1,256.4
46152-9-4	29.19	27.83	3.97	72.49	18.30	8.94	0.27	100.00	1,306.4	1,283.7
46152-9-5	352.53	35.01	7.18	52.53	29.11	18.35	0.00	100.00	1,548.0	1,521.1
Apparent Gas Composition[2]				**70.19**	**18.83**	**10.51**	**0.48**	**100.00**	**1,333.5**	**1,310.3**
Average Depth (ft): 3,739.5				**Lost Gas Content: 17.12%**				**New Albany Shale**		
46152-15-1	1.93	9.38	9.38	79.37	12.62	5.34	2.67	100.00	1,172.5	1,152.1
46152-15-2	2.47	10.43	1.05	78.55	14.30	6.42	0.73	100.00	1,225.9	1,204.5
46152-15-3	2.95	11.12	0.68	79.29	13.99	6.23	0.50	100.00	1,222.5	1,201.3
46152-15-4	3.53	11.75	0.64	79.02	14.19	6.30	0.49	100.00	1,225.2	1,203.9
46152-15-5	4.52	12.66	0.91	78.79	14.39	6.43	0.39	100.00	1,230.4	1,209.0
46152-15-A[3]	387.52	47.31	34.65	57.75	21.13	21.13	0.00	100.00	1,542.7	1,515.9
Apparent Gas Composition[2]				**63.50**	**18.96**	**16.97**	**0.57**	**100.00**	**1,447.4**	**1,422.2**
Average Depth (ft): 3,765.5				**Lost Gas Content: 9.92%**				**New Albany Shale**		
46152-17-1	2.02	6.51	6.51	76.85	15.28	7.87	0.00	100.00	1,265.3	1,243.3
46152-17-2	2.43	7.12	0.61	76.29	14.99	6.95	1.77	100.00	1,227.4	1,206.0
46152-17-3	2.97	7.90	0.77	77.01	14.90	7.20	0.89	100.00	1,242.7	1,221.0
46152-17-4	3.43	8.47	0.57	77.48	14.86	7.01	0.66	100.00	1,240.7	1,219.1
46152-17-5	4.43	9.33	0.86	74.26	16.53	8.58	0.63	100.00	1,282.3	1,260.0
46152-17-6	383.05	30.42	21.09	74.43	16.08	9.49	0.00	100.00	1,306.7	1,284.0
46152-17-A[3]	383.05	55.99	25.57	32.52	25.04	42.43	0.00	100.00	2,065.4	2,029.5
Apparent Gas Composition[2]				**55.65**	**20.05**	**24.25**	**0.05**	**100.00**	**1,645.6**	**1,617.0**

Table 10

Canister Composition of Gas Analysis, Well B-15, McLean County, Kentucky

Sample Number	Collection Point	As-Received Gas Content	Incremental Gas Content	Gas Analysis (O_2, N_2 and H_2 Mole Fractions Omitted)[1]					Calorific Value	
				C_1	C_2	C_3-C_{10}	CO_2	Total	Dry	Saturated
	hours	scf/ton	scf/ton	mole %	mole %	mole %	mole %	mole %	Btu/ft^3	Btu/ft^3
Average Depth (ft): 3,807.5				**Lost Gas Content: 15.13%**				**New Albany Shale**		
46152-21-1	2.73	11.18	11.18	74.32	16.31	8.40	0.97	100.00	1,273.0	1,250.8
46152-21-2	3.45	12.41	1.22	73.93	16.63	8.92	0.52	100.00	1,289.3	1,266.8
46152-21-3	451.81	41.27	28.87	65.56	22.35	12.08	0.00	100.00	1,389.3	1,365.2
46152-21-A[3]	451.81	63.08	21.81	55.24	22.38	19.58	2.80	100.00	1,500.0	1,473.9
Apparent Gas Composition[2]				**63.71**	**21.18**	**13.96**	**1.15**	**100.00**	**1,405.0**	**1,380.6**
Average Depth (ft): 3,846.5				**Lost Gas Content: 19.00%**				**New Albany Shale**		
46152-25-1	3.94	9.14	9.14	75.87	14.92	8.23	0.98	100.00	1,261.6	1,239.7
46152-25-2	465.81	22.89	13.76	64.82	21.83	13.34	0.00	100.00	1,412.8	1,388.3
46152-25-A[3]	465.81	35.12	12.23	64.00	16.00	20.00	0.00	100.00	1,503.3	1,477.1
Apparent Gas Composition[2]				**67.41**	**18.00**	**14.33**	**0.25**	**100.00**	**1,405.0**	**1,380.5**

Table 11 Example Geo Chem Result with Definitions

County	State	Operator	Well Name	Top Depth (ft.)	Bottom Depth (ft.)	Median Depth (ft.)	Leco TOC	S1	S2	S3	Core Lab Meals Rhob gm/cc	RTI** Calc'd % BVO	Tmax (°C)	Calc. %Ro	Meas. %Ro	RTI Calc'd from Calc'd Ro Kero Dens	RTI Calc'd from Meas'd Ro Kero Dens	HI	OI	S2/S3	S1/TOC	PI
Crittenden	KY	Savage Zinc	#1 Frazer	1585.7		1585.7	8.31	1.45	19.45	0.28	2.423	0.39	448	0.90	0.64	1.278	1.186	234	3	69	17	0.07
Crittenden	KY	Savage Zinc	#1 Frazer	1711.8		1711.8	5.15	1.49	7.98	0.22	2.560	0.42	450	0.94		1.291		155	4	36	29	0.16
Crittenden	KY	Savage Zinc	#1 Frazer	1920.2		1920.2	5.39	2.02	9.52	0.25	2.487	0.56	454	1.01		1.316		177	5	38	37	0.18
Christian	KY	Orbit Gas	#1 Clark	2188.7		2188.7	6.67	3.72	47.73	0.31	2.409	1.00	444	0.83		1.253		716	5	154	56	0.07
Christian	KY	Orbit Gas	#1 Clark	2244.7		2244.7	9.89	5.88	54.81	0.31	2.384	1.56	436	0.69		1.203		554	3	177	59	0.10
Christian	KY	Orbit Gas	#1 Clark	2284.3		2284.3	13.31	7.14	76.30	0.30	2.219	1.76	445	0.85	0.55	1.259	1.155	573	2	254	54	0.09

Assumption is that oil density is 0.90 gm/cc

Note: "-1" indicates not measured or meaningless ratio

* Tmax data not reliable due to poor S2 peak

TOC = weight percent organic carbon in rock
S1, S2 = mg hydrocarbons per gram of rock
S3 = mg carbon dioxide per gram of rock
Tmax = °C

**BVO calc'd by RTI using S1 as oil with density of 0.9 gm/cc

HI = hydrogen index = S2 x 100 / TOC
OI = oxygen index = S3 x 100 / TOC
S1/TOC = normalized oil content = S1 x 100 / TOC
PI = production index = S1 / (S1+S2)
Calculcated%VRo = 0.0180 x Tmax - 7.16 (Jarvie et al., 2001)
Measured %Ro = measured vitrinite reflectance

Log Analysis Methodology

Below are presented the steps and methods used to characterize the resource leading to calculation of gas in place and then a derived synthetic shear sonic (when measurements are not available) used in calculating mechanical rock properties.

Total Organic Carbon (TOC) - Determination of TOC in resource plays takes various forms from multi-mineral calculations using spectrometry tools, Quinn Passey's delta log R technique, back calculation from kerogen volumes and core correlation to measured bulk density from core. This last procedure is used in this study because it works well in the NAB and because the density measurement is so prevalent. Figure 15 below shows the core correlation of TOC to overburden adjusted core bulk density from the Western Kentucky area.

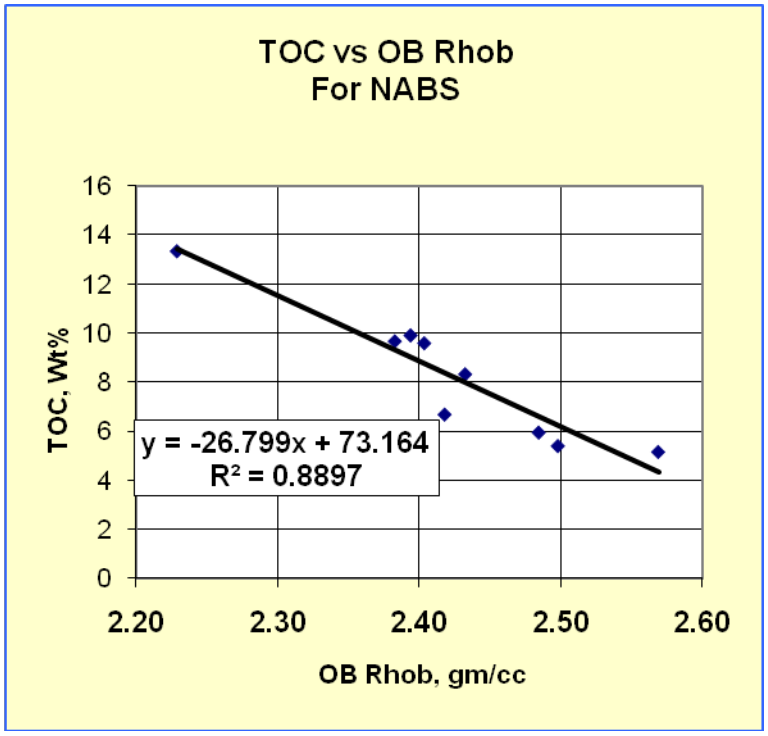


Figure 15 - Three Western Kentucky wells. Note the Core Bulk Density Has Been Adjusted to Overburden Pressure.

Similar correlations are used when specific core data are available. As shown in Equation 7 from the Osburn Trust well in Indiana, the correlations are very similar. It is suggested that without core data the equation in Figure 15 above will work well in both the Indiana and Western Kentucky areas.

TOC= -27.335*Rhob+72.281 ……..(**7)**

The TOC is important as an indicator of kerogen volume, and can be directly related to other geochemistry parameters, such as S1 and S2 (see **Table 11** for definitions).

Kerogen Volume (Vk) - In the NAB the kerogen is Type II to Type II/III as has been stated earlier. It is in the oil window with Ro of 0.6-1.2 typically. Because of its effects on logging devices such as density and neutron it is important to quantify the volume present and having done that, assign an appropriate density to that volume. As with TOC several techniques are available for the kerogen volume determination. In previous work with GRI in the Devonian shale a correlation of uranium yield to kerogen volume was derived GRI-95/0496. The uranium yield from spectral gamma ray was attempted but the data available did not give reasonable results. Also used is the direct correlation of TOC to kerogen volume from core XRD evaluations. And additionally because kerogen volume drives density measurements of the shale whether core or log related, the kerogen volume can be related to density or calculated from equation 8 below which is also from the GRI report cited above.

$$Vk = [(Ct - S1*Cs1)/Ck]*(rhob/rhok) \quad \text{.....(8)}$$

where:

	Vk	=	Kerogen volume, frac,
	Ct	=	TOC, wt frac,
	S1	=	free oil in the rock sample, wt frac,
	Cs1	=	carbon in the bitumen, wt frac,
	Ck	=	carbon in the kerogen, wt frac,
	Rhob	=	bulk density of rock sample g/cc,
	Rhok	=	density of the kerogen, g/cc.

Typically the kerogen density is determined using Equation 6, Ct can come from core or log calculations, S1 is from pyrolysis results, Cs1 is taken as 0.87, and Ck as 0.53 (see GRI-95/0496) .

For the log analysis of the wells in this study, the correlation of Vk to TOC was used and also a correlation directly to density was attempted. Figure 16 below is the correlation of TOC from Rock Eval results to Vk from XRD data in volume % from the Solsman well in Indiana.

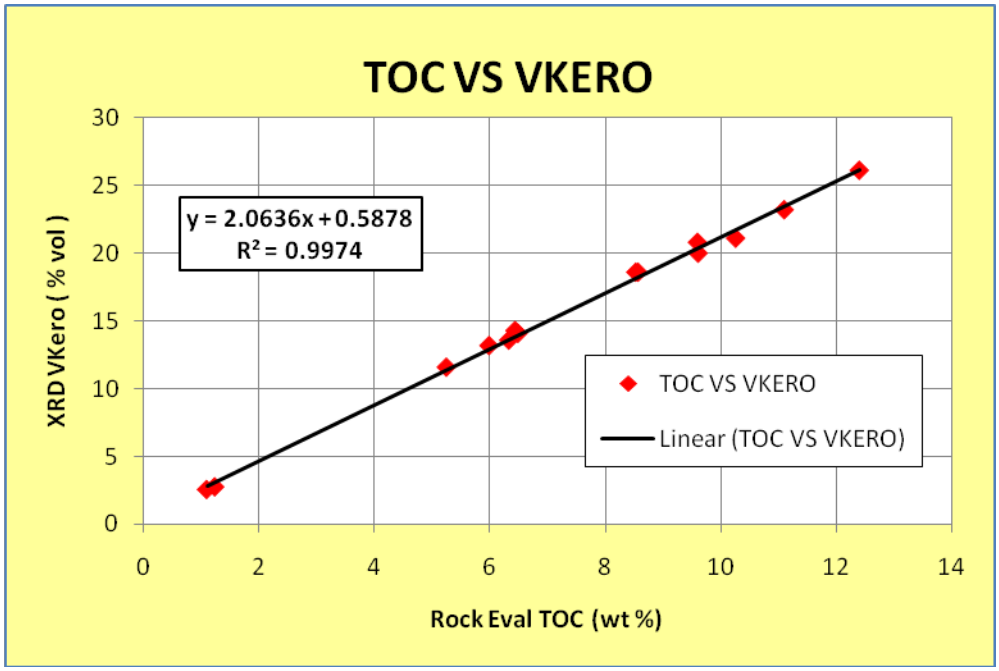


Figure 16 - Rock Eval TOC in wt % vs XRD Kerogen in % Volume, Almost a 2 to 1 Relationship

Equation 8 suggests a relationship of kerogen volume to bulk density can be developed as shown below in Figure 17, but since TOC may also be correlated to Rhob as we have previous seen, it is suggested that the TOC relationship above be used for kerogen volume.

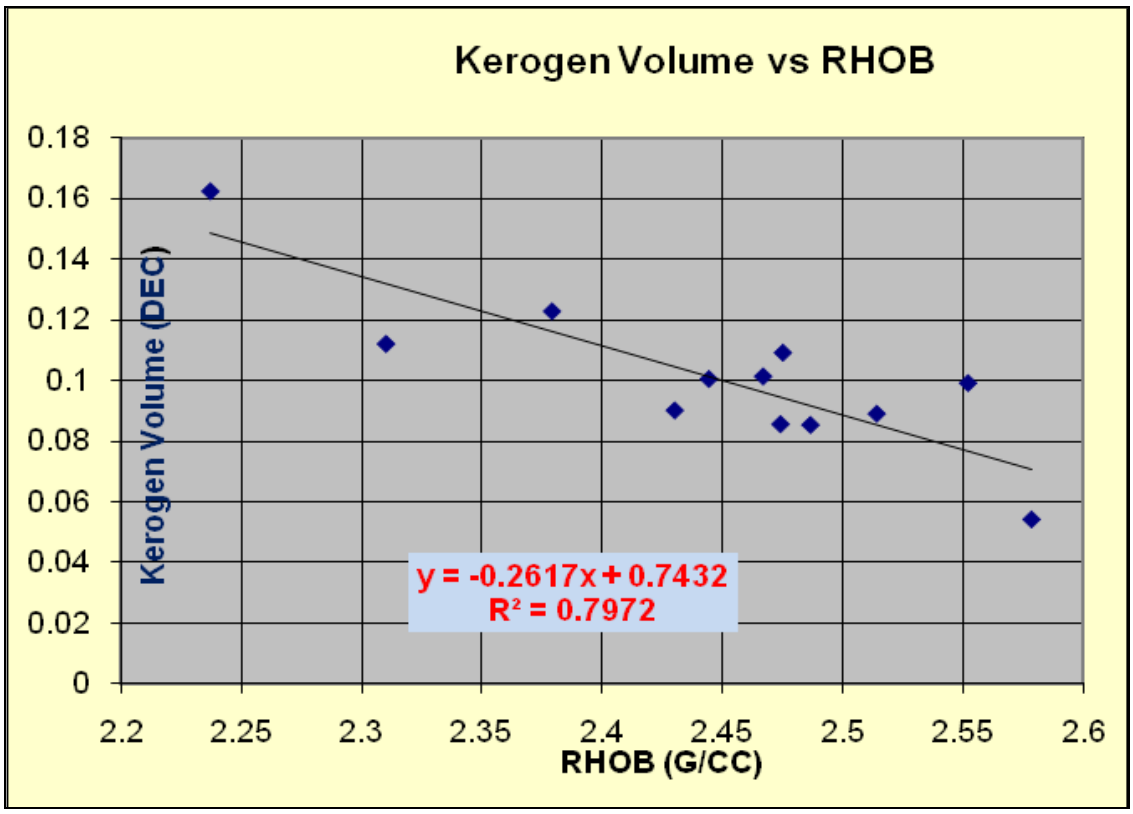


Figure 17 – Computed VK As it Relates to Core Bulk Density from the Frazer and Clark #1 Wells in Western KY

Pyrite Volume (Vpyr) - The pyrite volumes as observed in XRD results can be approximated using spectral elemental capture results for iron and sulfur if these data are available. Lacking these data the pyrite volume may be assumed to be a function of the kerogen volume. In the case of the NAB the assumption is that pyrite is generally about 25% of the kerogen volume. This works reasonably well and is the same assumption made for Devonian shale derived from previous Appalachian studies. The operator will need to determine if the added logging cost of running the elemental capture tool is worth the benefit. It is suggested that it be used sparingly only as a check of the assumption made above. No data for direct comparison is available at the time of this report, but it is observed in other resource plays that fit for purpose results may be obtained from volumetric analysis not requiring the acquisition of elemental capture data (R. W. Spears, S. L. Jackson; Petrophysics, Vol. 50, No.1, February 2009).

Clay Volume (Vclay) - Clay volume in the NAB is made up predominantly of Illite (see **Table 6**), and although XRD results may identify other clay components it has not been adequately shown that breaking these components out in a volumetric analysis adds to the quality of the answer. Theoretically, if you have enough log inputs of the spectral gamma ray or spectral neutron type, and density results, all various clay components could be derived and hopefully will lead to a more robust porosity determination and/or allow an improved completion design. Unfortunately, seldom are these data available or will the well operator be willing to bear the added expense of acquiring these data, in light of the fact that this hypothesis has not been adequately demonstrated. With these statements being made, a very basic calibration of total clay volume to scaled neutron response is used to determine log derive clay volume. It is recommended that operators environmentally correct and normalize the log response of the neutron tool in a given area for best results. In the example below the scaled neutron provides reasonable results for the B-3 well in Webster County, Kentucky, Figure 18.

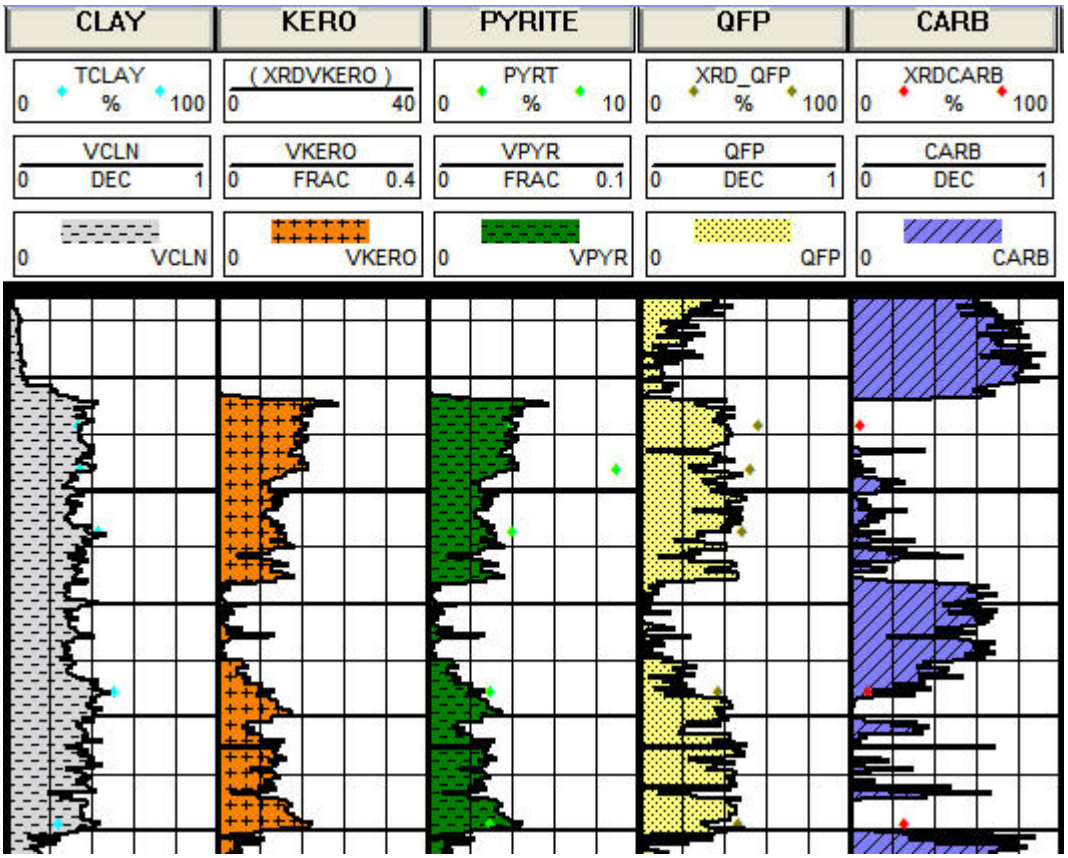


Figure 18 – Calculated Total Clay Volume Matches Well with the XRD Results from Sidewall Core Data. The Pyrite Volume Agrees Fairly Well Except For a Single Point. Quartz, which is a Combination of Quartz, Feldspar and Plagioclase, and the Carbonate Volume are Reasonable.

Quartz, Carbonate, and Porosity - Once we have determined the unique component volumes of the shale resource, kerogen, pyrite, and clay, we still need to determine the other more conventional volumes of quartz and carbonates and combine these results through a multi-mineral model to derive porosity. To do this we have employed a multi-mineral solver software. Further, we have grouped feldspars and plagioclase with the quartz and generally group the calcite and dolomite together as carbonates. Again with additional log inputs it would be possible to separate these components, but we have purposely kept the model basic so that typical log suites can be used. Along with density and neutron input we also use the volumes determined above. The software then produces output results for these volumes accounting for the added quartz and carbonate fractions and the porosity. End points for the mineral components are adjusted such that porosity and lithology match core results. **Table 12** below displays a typical input-output model setup. The kerogen density input is from Equation 6 and is based on Ro.

Table 12

Multi-Mineral Statmin Model NAB

Output / **Input**	**VSS**	**VCARB**	**VCLAY**	**KERO_V**	**PYR_V**	**PHI**	
NPHI	EPNSD	-.01	.3	.95	-.02	1	
	.01	.02	.05	.02	.02	.02	
RHOB	2.64	2.83	2.65	1.17	4.99	1.0	
	.02	.03	.02	.01	.02	.01	
UMA	4.8	11	8	.27	90	0	
	1	1	1	.05	1	.05	
VCLA	0	0	1	0	0	0	
	.02	.02	.001	.02	.02	.02	
VK	0	0	0	1	0	0	
	.01	.01	.01	.001	.01	.01	
VPYR	0	0	0	0	1	0	
	.01	.01	.01	.01	.001	.01	

Saturation Determination - The pore space of the NAB is a complex system. It contains not only water, gas, and adsorbed gas, but also because of its maturity varying and significant amounts of oil (see **Table 7**). The oil saturation reported in the core data for this study range anywhere from 6% in the Webster County, Ky B-3 well to 70% in the Orbit Clark #1 well in Christian County, KY. Core from the wells in Indiana had oil saturations 16 to 38%. This oil must be account for because it occupies significant space and in so doing restrict the pore space available to gas. Equation 9 below summarizes the components of the pore space in term of bulk volumes.

$$\mathbf{Phi = Bvw + Bvo + Bvag + Bvfg} \quad \text{.....(9)}$$

Where:

Phi	=	Total porosity determine from core or log analysis, (frac) BV,
Bvw	=	Bulk volume water, (frac),
Bvo	=	Bulk volume oil, (frac),
Bvag	=	Bulk volume adsorbed gas, (frac),
Bvfg	=	Bulk volume free gas, (frac).

To determine saturation again we must depend on core and make the assumption that the core reported water saturation generally from Dean Stark analysis is correct. We then compute water saturation Sw using the Archie model and adjust the electrical properties such that a match to the core is achieved. It is generally observed that the lowest member of the NAB, the Blocher, will have different m and n values than the Selmeir and Grassy Creek/Clegg Creek members. Observed values of “m” range from 1.8 to 2.13 and with “n” values from 1.4 to 2. The salinity used in both the Indiana and Western Kentucky areas is 80,000 ppm NaCl. This value is based upon produced waters from the NAB in this area and fits with the results presented in **Table 13** below which are derived from core in the air drilled A-7455 well in Christian County, Kentucky.

The air drilling provided at unique opportunity to analyze core for salinity in the absence of drilling fluid. The results show a large spread from roughly 28,000 to 140,000 ppm NaCl, once the bound water fraction correction is applied. This variable salinity was also observed in the Devonian shale study conducted by GRI in the early 1990’s. The explanation for this variation, particularly in the air drilled well is unresolved. Since the produced NAB water is very nearly the mean result from the data it is selected as the most reasonable salinity.

Table 13

Formation Salinity

Formation Brine Salinity
Partition of Fluids Method

Company: **Daugherty Petroleum, Inc.**
Well: DPI - 2485 - 21
Location: Christian County, Kentucky

Date: 10/12/09
File: HOU-090730

Sample No.	Depth	Permeability Klinkenberg (md)	Porosity He fraction	CEC From XRD	Q_v From XRD	Dean Stark Water Total	Dean Stark Water CBW Corr'td	Chloride as-is	Chloride CBW Corr'td	Calculated NaCl as-is	Calculated NaCl CBW Corr'td	Resistivity as-is	Resistivity CBW Corr'td
	feet	Ambient	Ambient	meq/100g	meq/ml	cc	Formation Water	mg/l	mg/l	mg/l	mg/l	Ohm-meters @ 75F	
1	2533.00 - 2533.50	2.03E-06	0.055	4.500	1.908	0.303	0.181	50667.68	84886.27	83540.92	139960.57	0.09	0.06
2	2537.90 - 2538.35	1.99E-06	0.059	7.750	2.823	0.505	0.403	38944.12	48721.25	64211.12	80331.66	0.11	0.09
3	2553.00 - 2553.50	2.35E-09	0.046	6.750	3.309	0.505	0.457	15856.92	17503.48	26144.91	28859.76	0.23	0.21
4	2562.00 - 2562.50	4.13E-10	0.025	4.750	4.688	0.404	0.000	11878.98	*	19586.08	*	0.30	0.36
5	2573.00 - 2573.50	1.00E-08	0.037	4.000	2.490	0.606	0.440	14091.72	19404.66	23234.45	31994.43	0.26	0.19

*** Clay Bound Water fractions are calculated from XRD Q_v values.**

***Mean CBW Corr'td NaCl, mg/l : 70286.61**

Once Sw is determined hydrocarbon saturation cannot simply be calculated as 1-Sw because there are both oil and gas present. To determine oil saturation independent of gas saturation a correlation to core water saturation is shown in the specific case of the Noble Solsman well in Sullivan County, Indiana Figure 19 and a more general correlation from multiple wells shown in Figure 20**.**

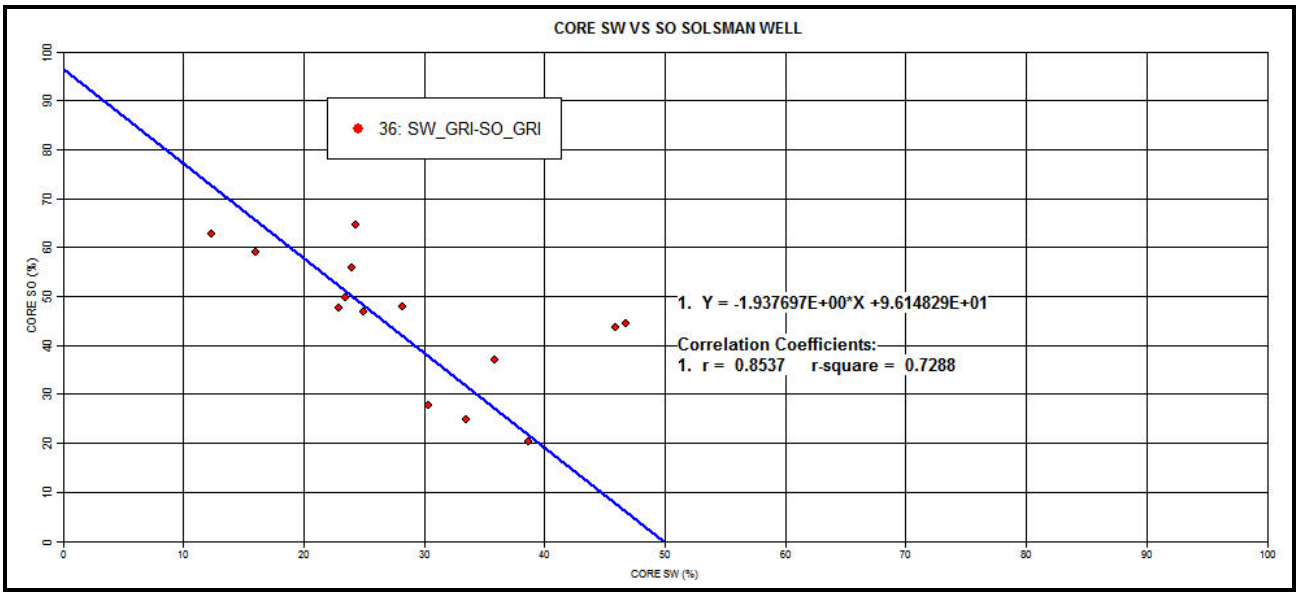


Figure 19 –Core Water Saturation Plotted Vs Core Oil Saturation, Noble Solsman Well, Sullivan County, Indiana

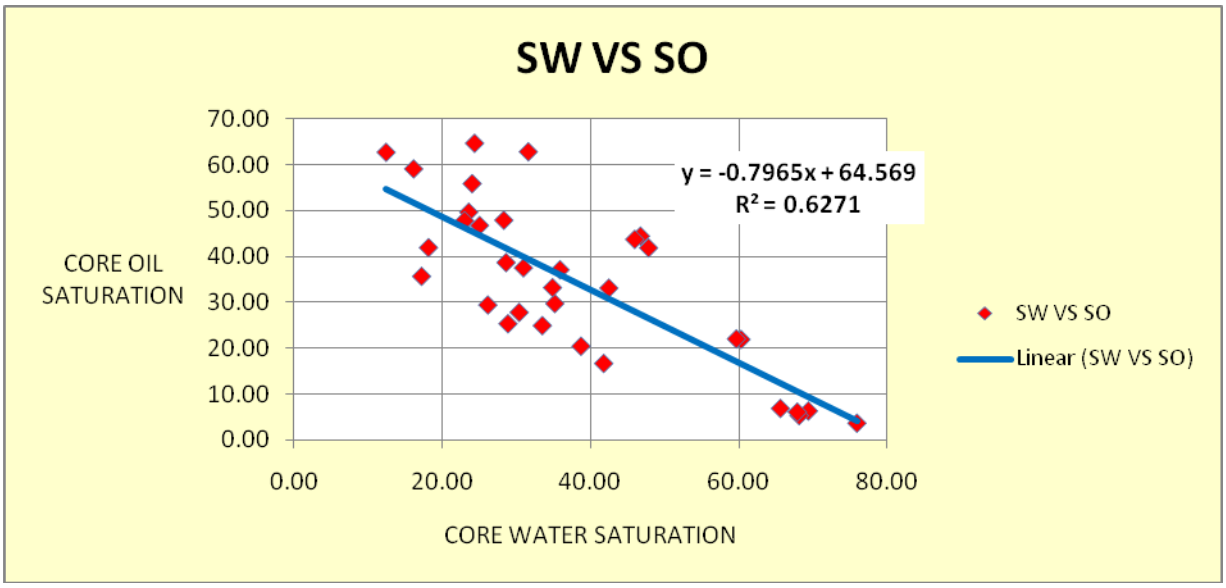


Figure 20 –Core Water Saturation Related to Core Oil Saturation in Multiple Wells, Western Kentucky Area.

When oil saturation is established, from the above plots, the gas saturation is the resulting balance. An example is shown below for the Orbit Clark #1 well.

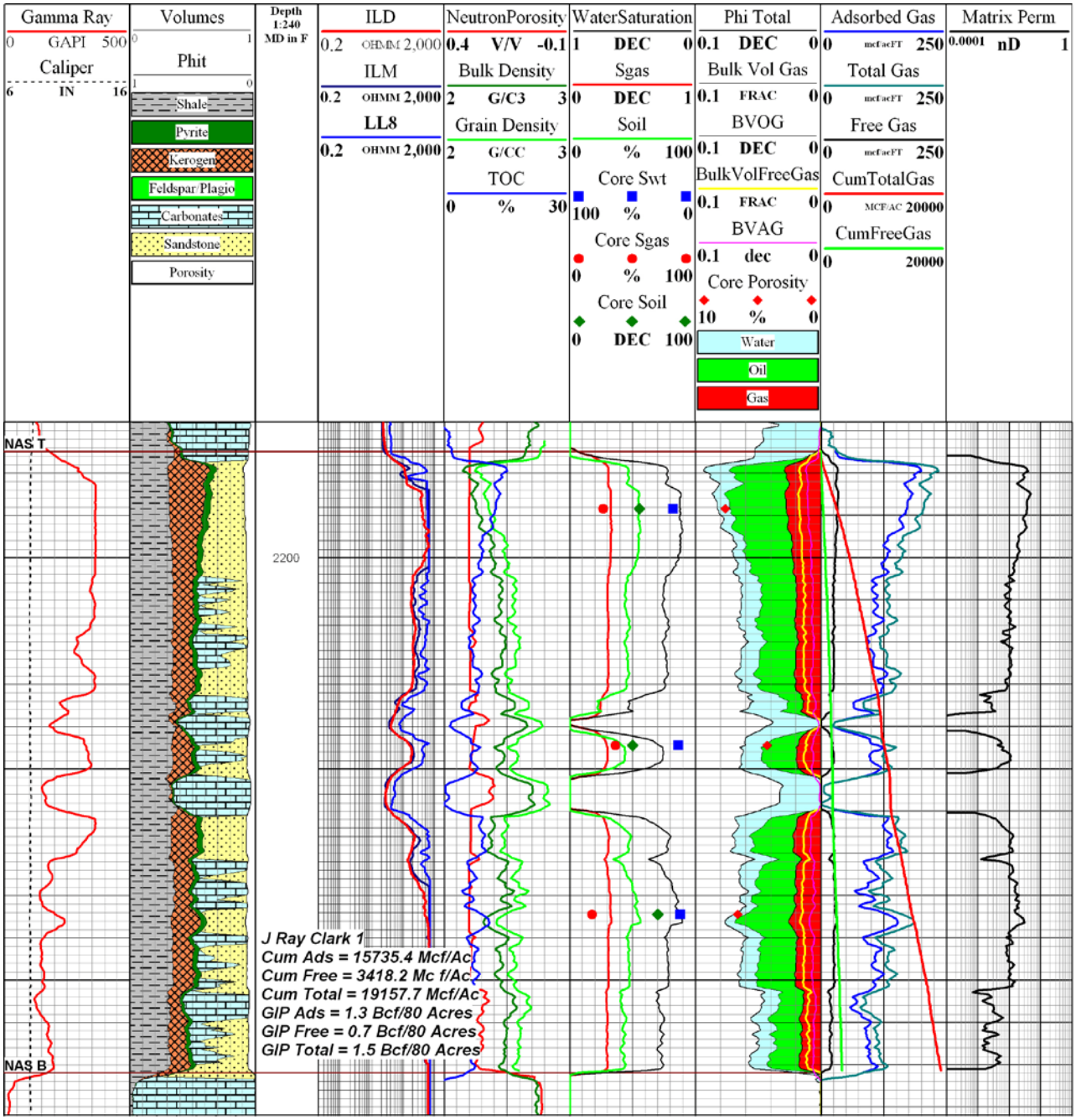


Figure 21 – Log Analysis Saturations Show Sw, So, and Sgas Compared with the Limited Core Data Available, Orbit Clark Well

Once the individual saturations are determined then bulk volumes are calculated in the normal fashion as the product with porosity. The next consideration is the correction of the bulk volume gas for the adsorbed portion, this is achieved using Equations 3 and 4 with either a measured isotherm or the generalized result for this region present below in Figure 22. The final corrected bulk volume free gas is then obtained from Equation 10 below.

BVFG = PHI - BVW – BVO – BVA …… (10)

where: BVFG = Bulk volume free gas, (frac),
PHI = Porosity, (frac),
BVW = Bulk volume water, (frac),
BVO = Bulk volume oil, (frac),
BVAG = Bulk volume adsorbed gas, (frac).

Free gas then determined using Equation 5 and the sum of the adsorbed gas and free gas, both in MCF/acre is total gas. The initial gas in place (IGIP) for each component, adsorbed, free, and total are then obtained by accumulation on a foot by foot basis. This is presented graphically in log form for each well in Appendix A. Figure 22 shows a display of the result for well A-7455.

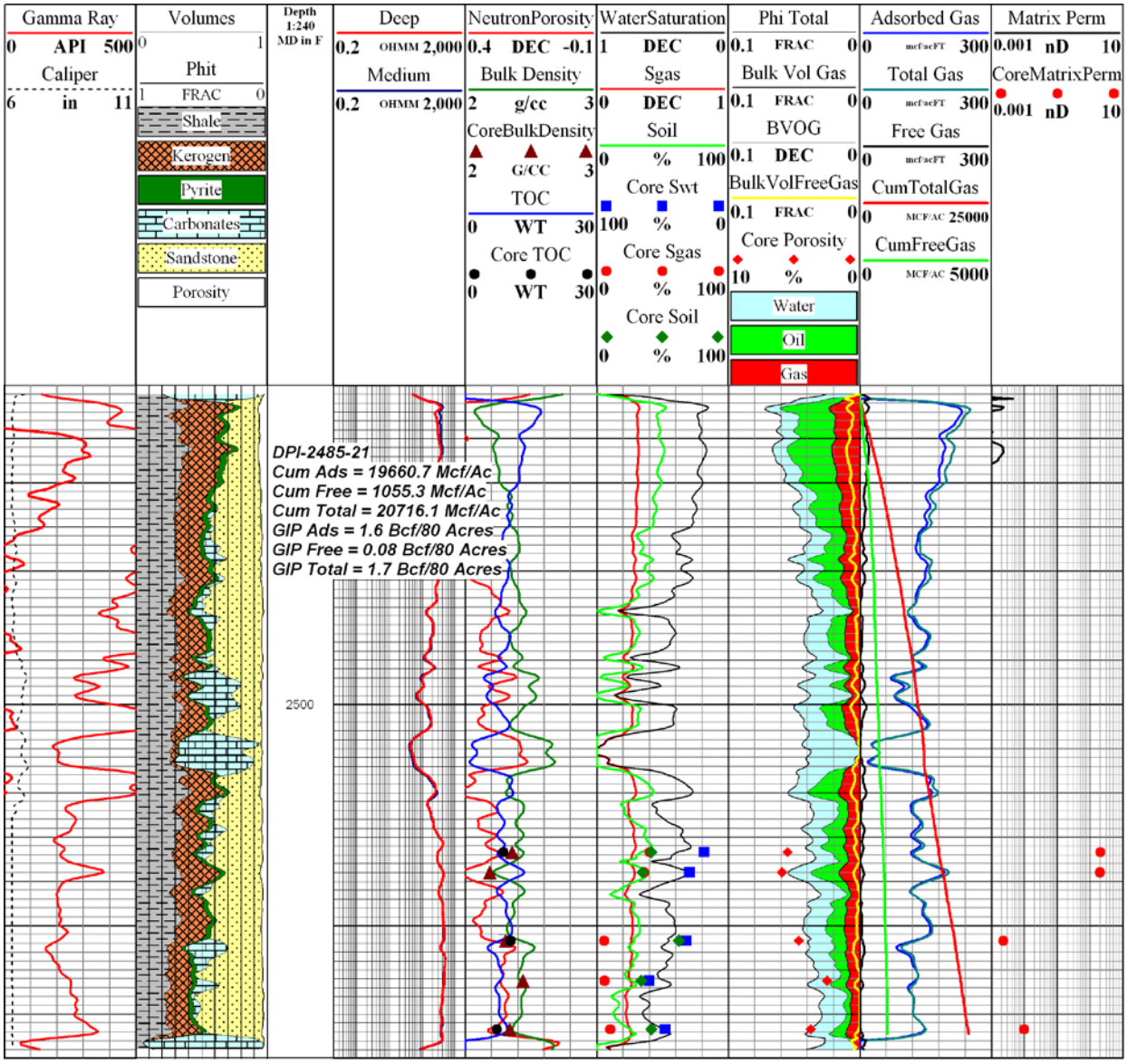


Figure 22 –A-7455 Gas Content and Cumulative Gas in Place Per 80 acres

TABLE 14

NEW ALBANY CUMGAS-ADSORBED –FREE-TOTAL

					Averages										Cumulative					
Well Name	Zone Name	Top Depth (MD)	Bot Depth (MD)	Gross Interval	PHIT	TOC	RHOB	BVFG	BVAG	SGAS	SO	ADS_GAS	FREE GAS	TOTAL GAS	CUM ADS	CUM FREE	CUM TOTAL	ADS GIP	FREE GIP	TOTAL GIP
		(ft)	(ft)	(ft)	(frac)	(wt%)	(g/cc)	(frac)	(frac)	(frac)	(%)	(mcf/acft)	(mcf/acft)	(mcf/acft)	(MCF/AC)	(MCF/AC)	(MCF/AC)	(BCF/80 ACRES)	(BCF/80 ACRES)	(BCF/80 ACRES)
A-7218	NEW ALBANY	2198	2317	119	0.045	8.462	2.404	0.004	0.008	0.232	23.553	138.311	8.465	146.776	16313	1007.3	17320.5	1.3	0.08	1.4
A-7227	NEW ALBANY	2238	2395	157	0.086	8.534	2.401	0.017	0.008	0.267	36.927	139.962	40.682	180.644	21414.8	6224.4	27638.6	1.7	0.50	2.2
A-7242	NEW ALBANY	2404	2544	140	0.046	8.575	2.4	0.003	0.009	0.245	27.452	146.947	8.431	155.377	20500.9	1177.1	21675.1	1.6	0.09	1.7
A-7260	NEW ALBANY	2250	2404	154	0.045	8.601	2.399	0.002	0.009	0.216	18.631	142.314	5.284	147.597	21703.4	805.8	22508.6	1.7	0.06	1.8
A-7269	NEW ALBANY	2454	2607	153	0.048	8.632	2.398	0.004	0.009	0.244	28.487	149.891	10.3	160.19	22708.4	1560.4	24268.8	1.8	0.12	1.9
A-7275	NEW ALBANY	2237	2435	198	0.064	7.53	2.439	0.009	0.007	0.247	27.582	124.805	21.606	146.411	24648.9	4267.2	28916.1	2.0	0.34	2.3
A-7420	NEW ALBANY	2408	2556	148	0.046	9.203	2.376	0.002	0.009	0.225	24.636	156.76	6.387	163.147	23200.4	945.3	24145.7	1.9	0.08	1.9
A-7426	NEW ALBANY	2390	2536	146	0.051	9.04	2.382	0.005	0.009	0.255	30.896	153.366	11.691	165.056	22391.4	1706.8	24098.2	1.8	0.14	1.9
A-7432	NEW ALBANY	2238	2388	150	0.042	9.146	2.378	0.002	0.009	0.204	19.86	149.405	4.379	153.785	22410.8	656.9	23067.7	1.8	0.05	1.8
A-7435	NEW ALBANY	2237	2388	151	0.049	8.934	2.386	0.004	0.009	0.255	30.054	146.293	10.202	156.495	22090.3	1540.5	23630.8	1.8	0.12	1.9
A-7447	NEW ALBANY	2485	2635	150	0.048	8.981	2.385	0.004	0.009	0.228	25.979	156.333	10.533	166.866	23450.2	1580	25030	1.9	0.13	2.0
A-7366	NEW ALBANY	2254	2404	150	0.046	8.744	2.393	0.003	0.009	0.236	26.28	144.352	7.85	152.202	21652.7	1177.6	22830.3	1.7	0.09	1.8
A-7389	NEW ALBANY	2245	2392	147	0.047	8.74	2.394	0.003	0.009	0.235	26.454	143.76	7.815	151.576	21132.8	1148.8	22281.6	1.7	0.09	1.8
A-7392	NEW ALBANY	2249	2398	149	0.044	9.002	2.384	0.003	0.009	0.242	28.132	147.678	7.156	154.835	22004	1066.3	23070.3	1.8	0.09	1.8
A-7401	NEW ALBANY	2349	2500	151	0.048	8.239	2.412	0.004	0.008	0.241	26.429	140.249	10.142	150.391	21177.6	1531.5	22709.1	1.7	0.12	1.8
A-7416	NEW ALBANY	2251	2402	151	0.047	8.359	2.408	0.004	0.008	0.229	25.953	138.574	9.288	147.862	20716.8	1388.6	22105.4	1.7	0.11	1.8
A-7419	NEW ALBANY	2389	2534	145	0.04	8.018	2.421	0.001	0.008	0.215	21.267	138.841	3.786	142.627	14994.9	408.8	15403.7	1.2	0.03	1.2
A-7434	NEW ALBANY	2254	2406	152	0.044	8.305	2.41	0.003	0.008	0.235	25.848	138.276	6.8	145.076	20953.7	1033.6	21987.3	1.7	0.08	1.8

TABLE 14 - Continued

NEW ALBANY CUMGAS-ADSORBED –FREE-TOTAL

A-7437	NEW ALBANY	2274	2426	152	0.045	8.027	2.42	0.002	0.008	0.181	14.822	135.155	5.975	141.131	20543.6	908.3	21451.9	1.6	0.07	1.7
DALTON C2-22	NEW ALBANY	1780	1892.5	112.5	0.078	5.138	2.454	0.016	0.007	0.211	16.45	104.52	46.207	150.728	11642.7	5108	16542.3	0.9	0.41	1.3
JEFFERIES C3-21	NEW ALBANY	1667	1777.5	110.5	0.079	4.073	2.484	0.015	0.005	0.254	26.271	80.471	40.495	120.967	9005.2	4450	13064.4	0.7	0.36	1.0
#1 JIMMY BELL	NEW ALBANY	3091	3334	243	0.064	5.75	2.505	0.029	0.007	0.57	5.023	132.659	91.538	224.197	32247.3	22243.7	54479.8	2.6	1.78	4.4
Island Creek BF-001	NEW ALBANY	3913	4300	387	0.048	4.463	2.554	0.025	0.006	0.618	11.214	103.056	102.75	205.809	38783.8	38653	77384.2	3.1	3.09	6.2
DPI - 2485-21	NEW ALBANY	2430	2575	145	0.043	8.914	2.386	0.003	0.008	0.258	29.429	136.061	6.23	143.364	19660.7	1055.3	20716.1	1.6	0.08	1.7
J RAY CLARK 1	NEW ALBANY	2175	2322	147	0.062	7.276	2.448	0.012	0.006	0.28	40.702	107.409	23.361	130.769	15735.4	3418.2	19157.7	1.3	0.27	1.5
OSBURN TRUST 1-11H	NEW ALBANY	2486	2646	160	0.053	6.452	2.479	0.011	0.011	0.405	20.197	172.286	45.28	217.566	27565.8	7244.8	34810.6	2.2	0.58	2.8
SOLSMAN 1-32H	NEW ALBANY	2547.5	2737	189.5	0.07	6.686	2.411	0.018	0.008	0.371	32.742	174.939	69.802	244.741	33150.9	13227.5	46378.4	2.7	1.06	3.7

Graphical displays for each well are included in Appendix A

Some observations from these results are that in the Haley's Mill, Christian County, Kentucky area the free gas distribution is highest in the Grassy Creek/Clegg Creek interval, upper NAB. This is not the case in Webster County, Ky. or in the wells in Indiana where free gas distribution in more uniform across the NAB thickness. The B-3 well in Webster County, KY has much lower reported oil saturation from core than either the Indiana wells or the wells in Christian County. The lower oil saturation and somewhat higher pressure, (as these wells are deeper) allows more space for free gas, as such the BF 001 and the compute of Jimmy Bell well for the highest cumulative GIP. Also, the higher total GIP results are associated with the deeper wells but some wells have lower average TOC.

Identifying the distribution of gas across the NAB thickness and characterizing lithology, porosity, saturations, and TOC are important. The gas effective completions must be designed to maximize interconnectivity of natural and induced fractures since matrix permeability is low (see discussion later).

Synthetic Sonic Equations

To aid in completion design rock mechanical properties are computed from logs using compressional and shear sonic input. From measured data in the A-7455 well, synthetic compressional and shear sonic data were generated to create synthetic sonic results for all study wells and these results were provided to our research partners, Pinnacle. The equations make use of density-neutron as input and also density and deep resistivity where no neutron data are available. **Figures 23** and **24** compare the measured compressional and shear to the synthetic results of both models. The equations are given below.

DTP_SYN=64.7002+113.904*NPHI-80428*RHOB……(11)

DTPD_SYN=397.23-110.405*RHOB-18.366*LOG(RDEEP)……(12)

DTS_SYN=111.112+163.457*NPHI-8.7719*RHOB……(13)

DTSD_SYN=591.818-157.975*RHOB-27.2926*LOG(RDEEP)……(14)

where:

DTP_SYN	=	Synthetic compressional sonic f(D,N) (us/ft),
DTPD_SYN	=	Synthetic compressional sonic f(D,RD) (us/ft),
DTS_SYN	=	Synthetic shear sonic f(D, N) (us/ft),
DTSD_SYN	=	Synthetic shear sonic f(D, RD) (us/ft),

NPHI	=	Neutron porosity (dec),
RHOB	=	Bulk density (g/cc),
RDEEP	=	Deep resistivity (ohm.)

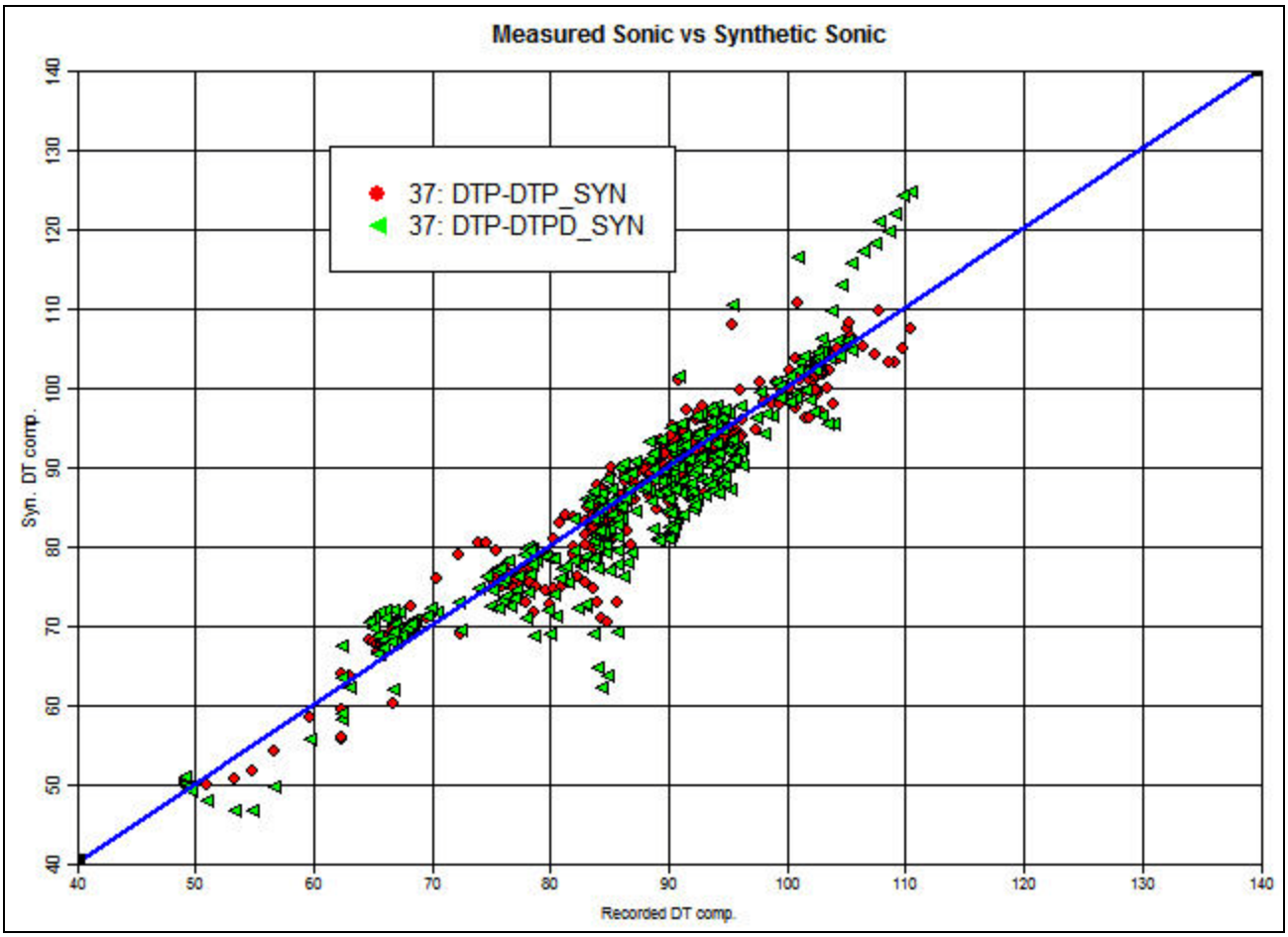


Figure 23 - Recorded Compressional Sonic (A-7455) Compared to the Derived Synthetic Compressional Result. Red is a Function of Density and Neutron, and Green a Function of Density and Deep Resistivity.

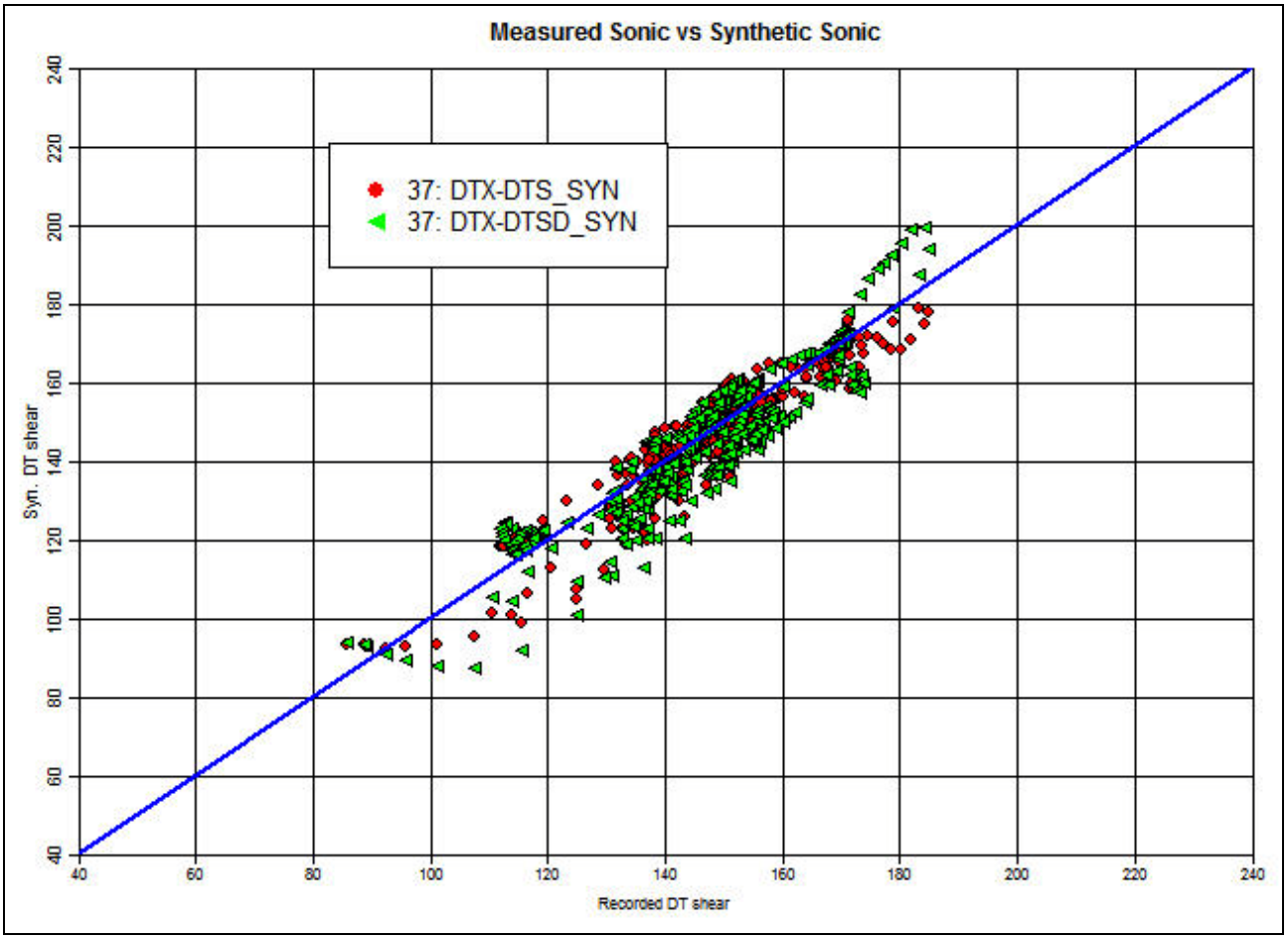


Figure 24 - Recorded Shear Sonic in the A-7455 Well Versus the Generated Synthetic Shear Result. Red is a Function of Density and Neutron, the Green a Function of Density and Deep Resistivity.

Having compressional and shear sonic data allow the routine calculation of rock mechanical properties Poisson's ratio, Young's, shear, and bulk moduli, brittleness, and closure stress. Figure 25 below is an example from the B-3 well. The closure stress is uncalibrated and the brittleness is computed as from SPE 115258 (Rickman, Mullen, Petre,Griesser, and Kundert, 2008).

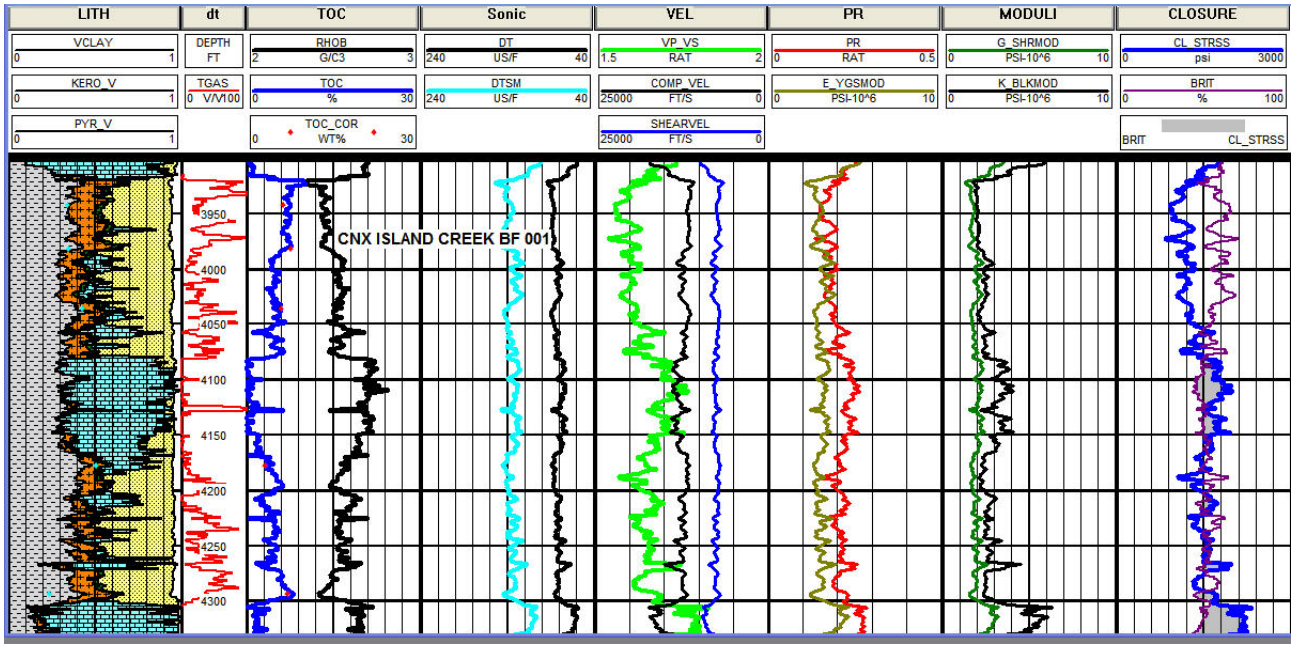


Figure 25 – Calculated basic rock mechanical properties using compressional and shear sonic inputs. Stress calculated is isotropic and uncalibrated.

Natural and Induce Fracture Characterization - To effectively design a drilling or completion in the NAB or any resource play, knowledge of the naturally occurring fractures and induced fractures is vitally important, as the matrix permeability by itself cannot provide economic gas rates and fracture stimulations must take advantage of any permeability pathways.

Fractures are characterized from the FMI data of the Osburn Trust #1-1H in Sullivan County, Indiana. Natural fractures both open and partially open exist in conjugate sets with high angle dip. The dip direction is NNW-SSE and the strike is ENE-WSW. Few induced fractures are interpreted. Results from the well A-7455 in Christian County, Kentucky the CMI interpreted fractures have dominant N-S dip with E-W strike while the fracture dip and strike in McLean County, Kentucky is NNW-SSE and ENE-WSW respectively. Although the area is structurally complex a fairly consistent dip – strike orientation is observed from the available well log image data.

Figure 26 below shows an FMI image of natural fractures and Figure 27 the dip stereo plot from the Osburn Trust.

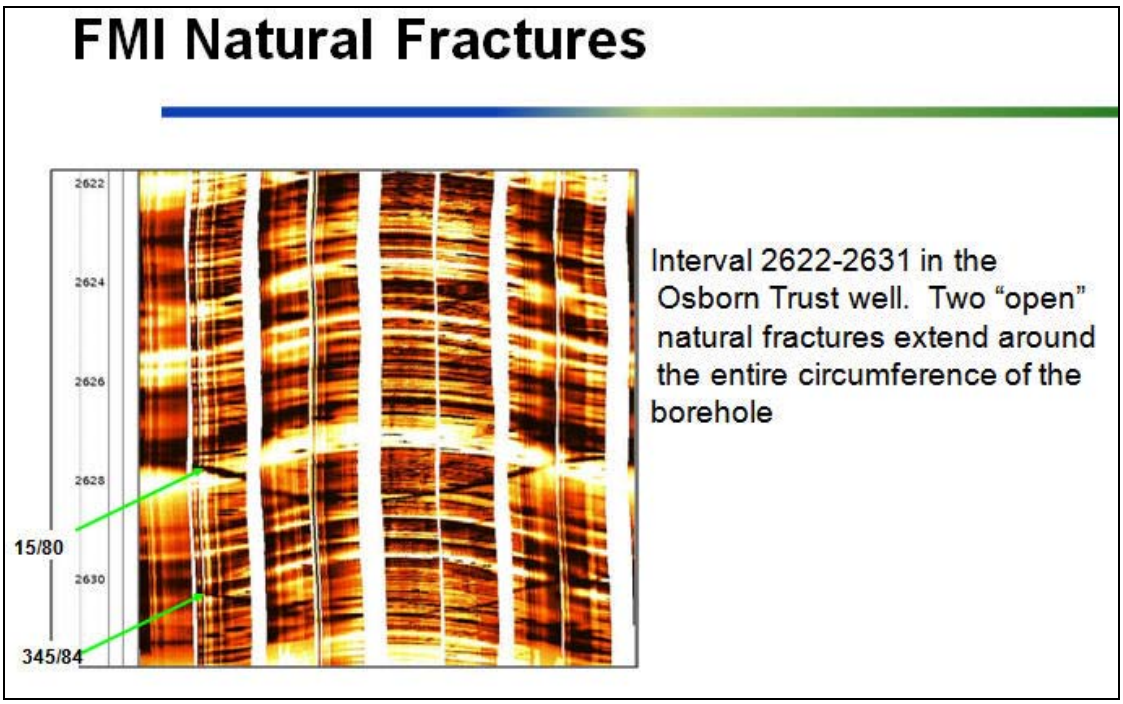


Figure 26 – FMI Image of Natural Fractures Sullivan County, Indiana

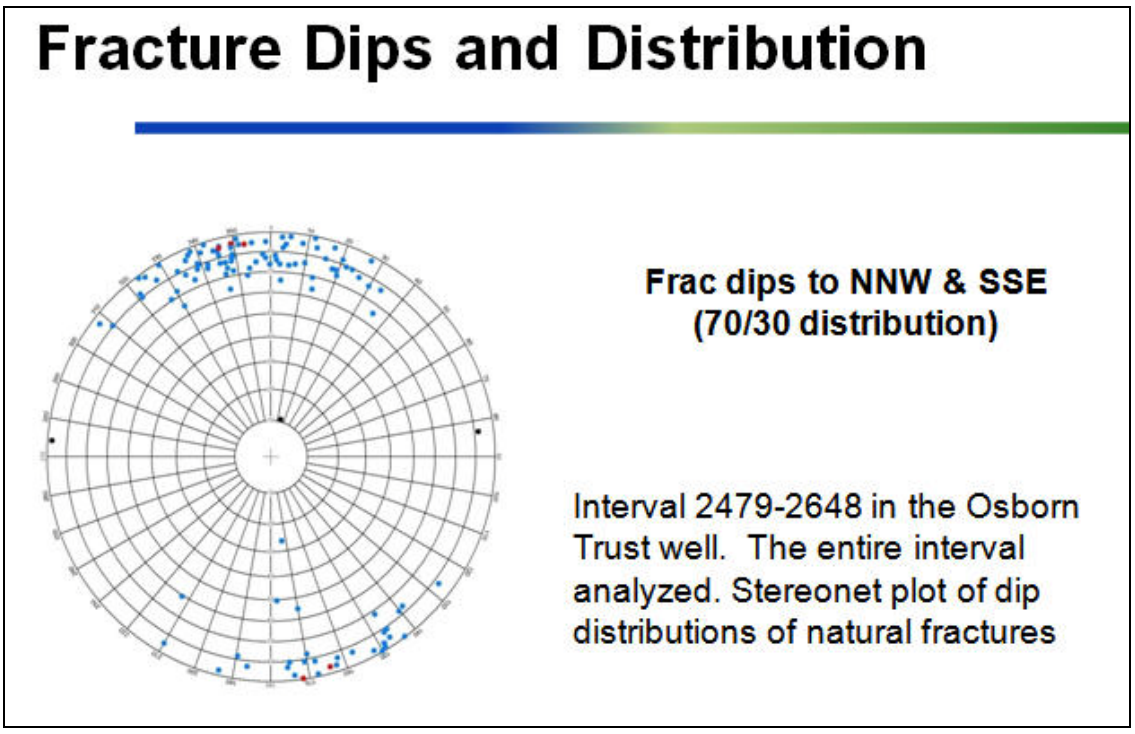


Figure 27 – Sullivan County, Indiana Natural Fracture Have Strike in the ENE-WSW Direction.

The distribution of the fractures interpreted in the Osburn well can best be illustrated using a intersection or stick plot that suggest potential connectivity, Figure 28 below.

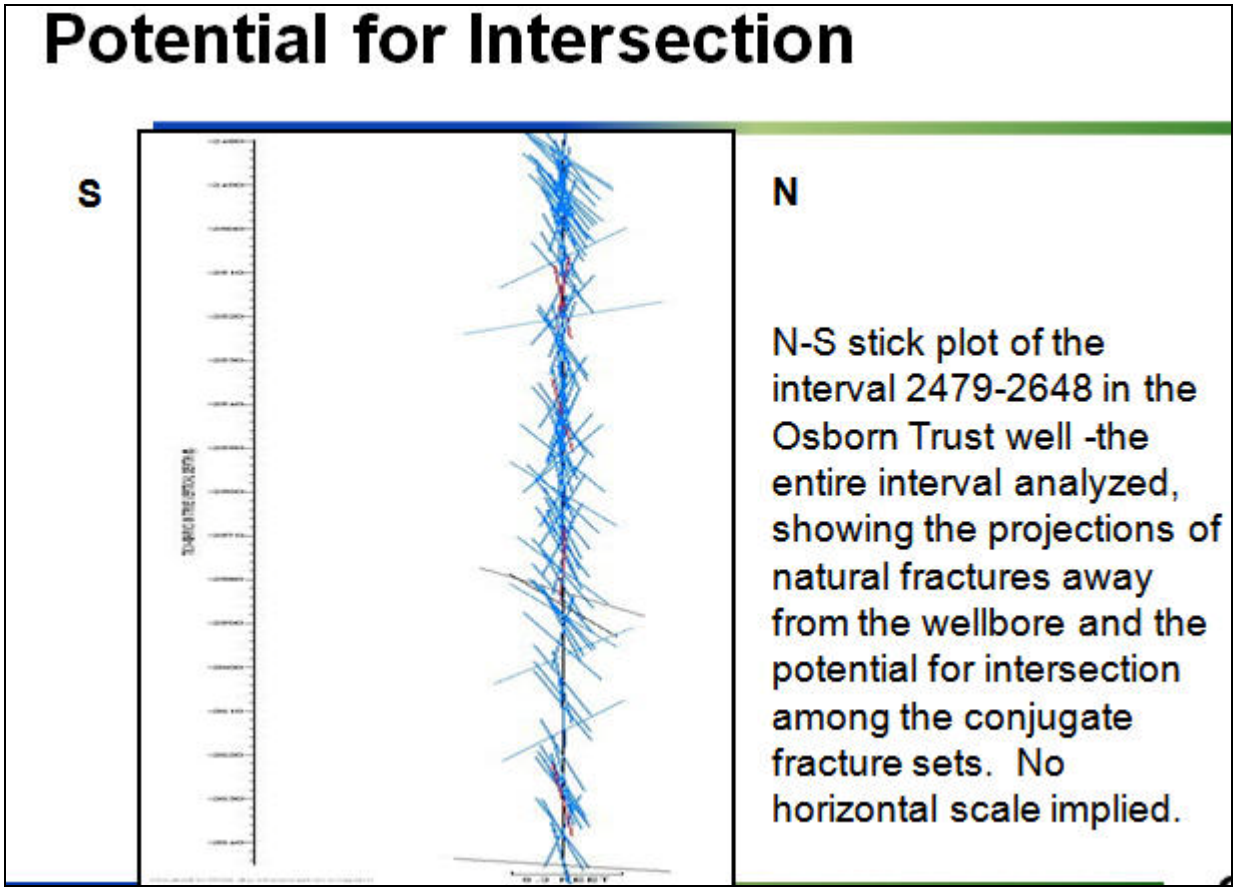


Figure 28 –The Upper Portion of the NAB Interpreted Interval Appears to be intensely Fractured with Conjugate Components. The Lower Part of the NAB Has Less Fracture Connectivity.

In the well A-7455 in Christian County, Kentucky we observe a very similar orientation of naturally occurring fractures as interpreted from the compact micro-imager (CMI), Figure 29.

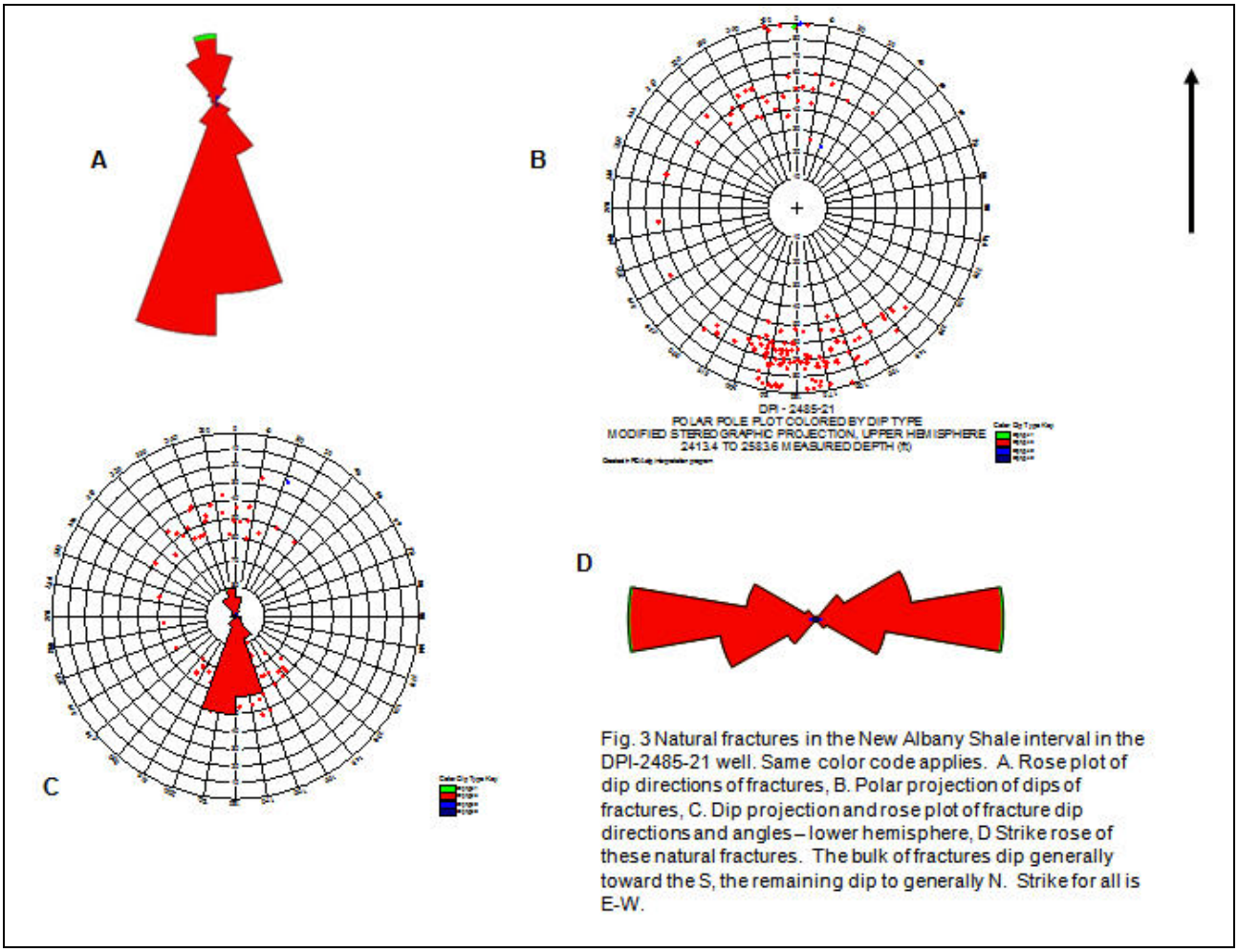


Figure 29 – Displays Dip and Strike Directions of Interpreted Natural Fractures as Seen on the CMI in Christian County, Kentucky. The Directions of Dip and Strike Are Similar Observed in Sullivan County, Indiana, Even Though the Structure in the Kentucky Area is Quite Complex.

A stick plot suggesting potential interconnectivity is shown in Figure 30.

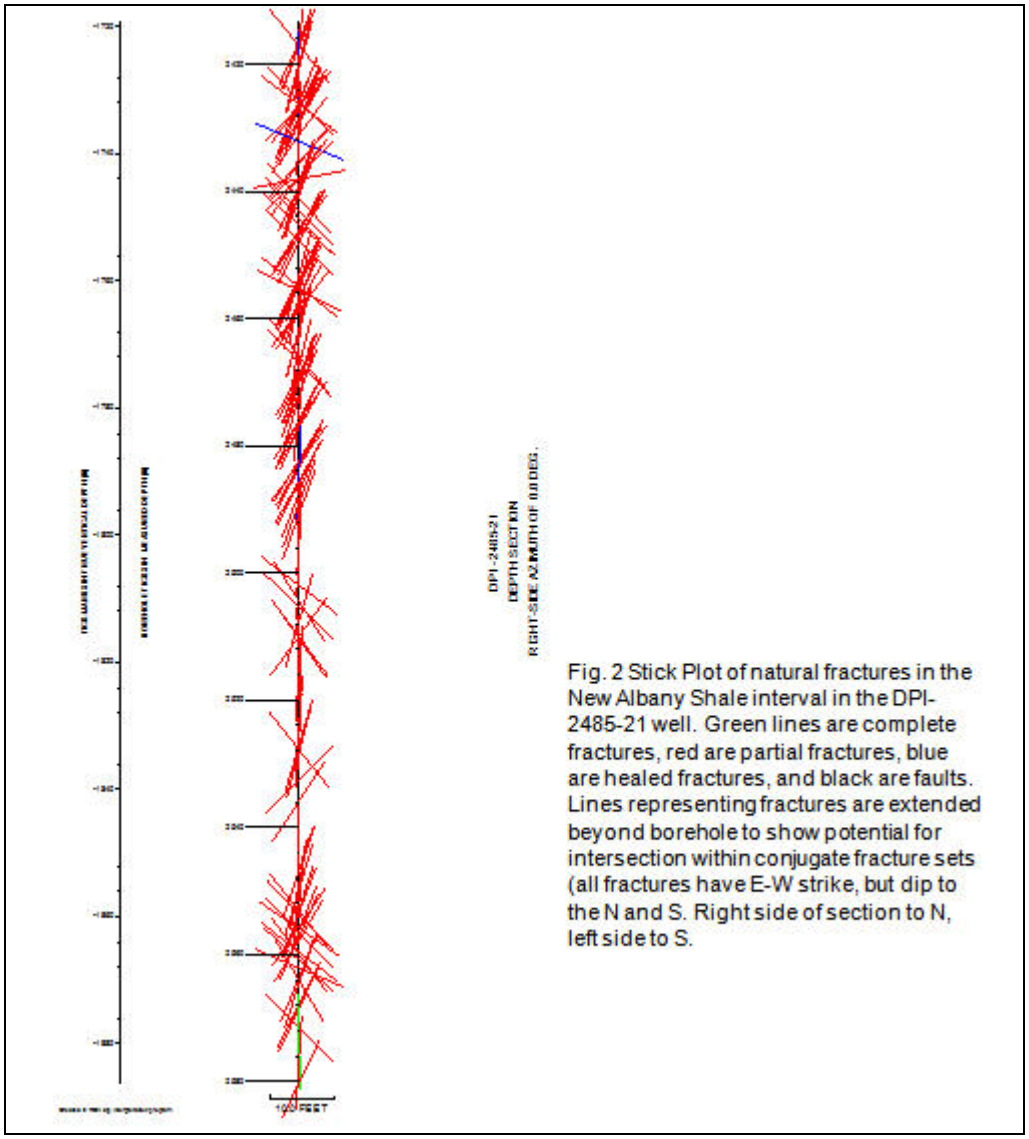


Fig. 2 Stick Plot of natural fractures in the New Albany Shale interval in the DPI-2485-21 well. Green lines are complete fractures, red are partial fractures, blue are healed fractures, and black are faults. Lines representing fractures are extended beyond borehole to show potential for intersection within conjugate fracture sets (all fractures have E-W strike, but dip to the N and S. Right side of section to N, left side to S.

Figure 30 –The Upper and Lower NAB, Grassy Creek and Blocher Respectively Display Better Potential Interconnectivity Than Does the Middle Selmier Member.

In addition to these two wells core and FMI fracture analysis was performed in the B 15 well in McLean County, Ky., those results and procedures are summarize below.

Core - Image Comparisons McLean County, Kentucky

Summary - Comparison of formation image (FMI) data with the conventional core cut in the subject well showed that there is a particularly high degree of reliability concerning the quality of the image interpretation. The New Albany portion of the conventional core (3600 - 3822' MD) was examined at the Houston, Texas core facility of Weatherford International. There was a very close correspondence between the fractures delineated on the image log, from those features occurring on the borehole wall, and the fractures noted on the core. In addition, the

depths that the fractures noted on the core material corresponded very closely to the depths for the same feature noted on the formation image log – the core material and image logs are very closely on depth. It is the opinion of this analyst that the formation image data and interpretation are an indispensable method of fracture analysis.

Introduction - Computed formation image data were available from 2851 to 3950' MD, and conventional core material spanning the interval 3572-3884' were laid out for analysis at the Weatherford facility. Time restraints and the scope of this portion of the project limited the comparison of the core with image data to the interval of the New Albany Shale (3600 - 3822' MD), which in the area or the subject well consists of the Clegg Creek, Camp Run/Morgan Trail, Selmeir, and Blocher members. All depths cited in this report are measured depth (MD) and are predicated on depths tied to the formation image log. Due to the very low angles of bedding dips (5 deg. and less) and the deviation angle of the borehole (2 to 7 deg), it was not possible at this time to be able to determine the orientation of the core.

Method - The core material was housed within elongate "zip lock" plastic bags that were nested within three foot (3') length boxes. Intervals of missing core were represented by segments of "noodles", foam plastic recreational flotation devices. In addition, there were several segments of core that were sealed within bags for possible fluid analysis. This core material was not sampled or analyzed, since it would have involved breaking the integrity of the seal. Observation of the core and its contained fractures was accomplished by careful removal of each available core segment, visually examined for the presence of fractures, then replaced in its respective position from which it was taken. The fractures were then classified into those which could be determined as being of "natural" or induced origin. Natural fractures are those that were formed by tectonic/depositional processes prior to drilling of the subject well. Induced fractures are those formed by stresses caused by the drilling process. Observation shows that there are certain fractures whose natural/induced origins cannot be determined. Analysis by Dr. Julia Gayle of the Texas Bureau of Economic Geology determined the classification of the fractures occurring on the core material.

Table 15 is a summary of fractures occurring on the core material that were compared with the fracture analysis based on the formation image log (FMI), as well as the fracture traces on the formation image data. Hybrid is used to describe drill-induced fractures that have evidently nucleated on natural fractures (ref. Dr. Julia Gale), but in this table, those fractures that are of indeterminate origin were also included under the term hybrid. Those fractures observed on the core material that were classified under "observed on image log" are those that

were selected by the Mr. Elliot Wiltse of Schlumberger Wireline Services or were observed on the formation image data.

Table 15

Observation of Fractures in Core Material B-15 Well

Measured Depth of Fracture On Core Material	Fracture Types						Observed On Image Log	Orientation from Image Log (est.)		Comments
	Natural				Induced	Hybrid				
	Open	Partial	Healed	Fault				Dip Az	Dip Angle	
3590.0-3591								308	88	
New Albany Shale										
Clegg Creek Mem.										
3604.0-3605.5								329	82	
3609.0-3611.0								358	75	Petal
3618								Indet	Indet	Petal
3623.1								Indet	Indet	Petal
3623.1			**Partial**					338	63	
3628			**Partial**					345	70	Pyrite Fill
3629										
3631.2-3631.4								355	75	Orthog.
3632.0-3632.2										Orthog.
3633.0-3633.2										
3633.6-3633.8								355	75	
3639.5			**Partial**							
3649.8-3650.4								358	82	Calcite
3650.4										Orthog.
3658								352	82	
3633.2-3363.6								355	71	
3667.5										Calcite
3670.0-3671.0								335	72	Orthog.
3671.3-3671.8			**Partial**					357	67	Calcite
3673.2								290	67	Calcite
3675.7-3675.9								310	85	Calcite
3676.2-3676.3										
3676.4-3677.2										
3680.0-3682.0								150	76	Calc, Orth
3682.2-3684.6			**Partial**					343	85	
3687.7-3691.4				**Zone**				148-165	65-67	
3693.3-3694.3								238	81	Orthog.
3694.3-3695.6										Orthog.
3694.6								166	81	
3700.6-3701.5		**Fault**						154	70	
3701.8-3703.8								142	70	
3705.7								165	39	
Camp Rn-Morgan Tr.										
3706.5								345	72	
3709.1-3712.4								Indet.	80-90	
3712.4-3715.0								Indet.	80-90	

Measured Depth of Fracture On Core Material	Fracture Types						Observed On Image Log	Orientation from Image Log (est.)		Comments
	Natural				Induced	Hybrid				
	Open	Partial	Healed	Fault				Dip Az	Dip Angle	
3723.7-3726.2								Indet.	80-90	
3726.7-3728.4								Intet.	Indet.	
3729-3729.8								Intet.	80-90	
Selmeir Mem.										
3737.7-3737.9			**Partial**					327	65	
3742.2-3742.3								344	67	
3743.3-3743.6								338	67	
3764-3746.7								347	50	Calcite
3757.5-3757.7		**2 Fracs**						318	72	
3761		**Fault**						Indet.	Low Angle	
3762.1-3762.5								315	82	
3764.3-3764.5								Indet.	60	
3766.7								322	67	
3767.6								320	66	
3767,7-3767.9					**2 Petal**					
3768.2-3768.7					**4 Petal**					
3770.1					**Petal**					
3772.4					**Petal**					
3772.9					**Petal**					
3780.4					**Petal**					
3780.7					**Petal**					
3782.1-3783.3								Indet.	80-90	
3787.0-3787.3								143	72	
3788.0-3788.8								330	80	
3789.3					**Petal**					
3789.8					**Petal**					
3790.1					**Petal**					
3790.6-3791.0								328	82	
3791.5-3791.8								328	80	
3792.2-3792.5								328	80-90	
3792.7-3792.9								328	80-90	
Blocher Mem.										
3801.3-3801.6								335	83	
3803.3-3303.6								333	80	Shl Inj
3810.0-3810.6			**Partial**					328	70	
3810.9-3812.0								328	70	
3812.1-3813.2										Orthog.
3813.3-3813.8										Conjugate
3815.55-3815.9										
3822.6-3823.6										

The dips of natural and induced fractures are shown in the tadpole plot of Figure 31 below.

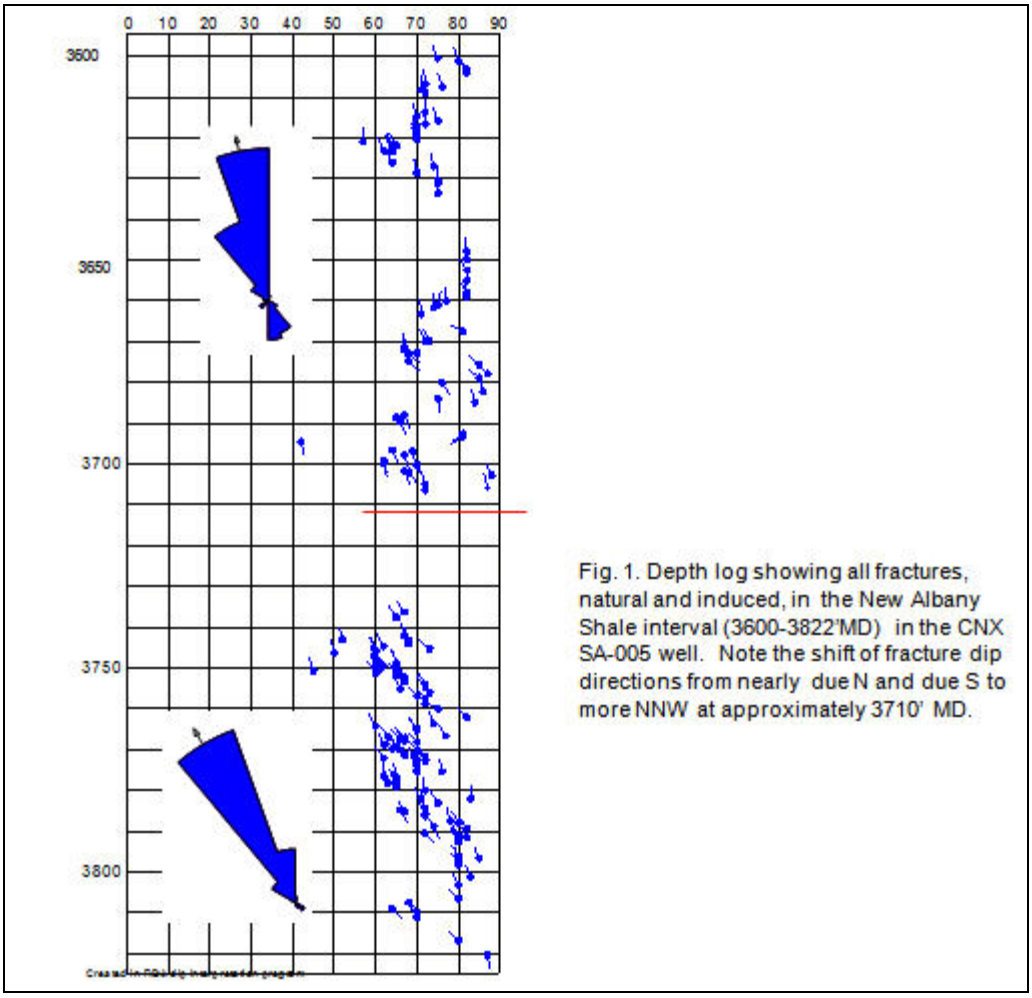


Figure 31- Conjugate North –South Dipping Fractures, the Lower NAB Appears to Have Fewer Conjugate Fractures.

A general observation might be the relative consistency of the strike direction of the fractures interpreted, basically E-W. Also few induced fractures were interpreted. In an exploration sense more effective fracture stimulations could be performed in areas where current day stress directions are conjugate to the naturally occurring fracture. Additionally a combination of mapped free or total gas distribution from log analysis combined with shear seismic technique to identify area of anisotropy caused by natural fracturing could help locate sweet spots of production. However the economics of such an exploration study would need to be evaluated.

Production of Free, Adsorbed, Total Gas from Average Reservoir Pressure

As described in the Summary, for forecast of cumulative gas production as reservoir pressure declines, we have developed a derivative graphical method. This shows cumulative adsorbed gas, free gas, and total gas with average reservoir pressure. Since the initial reservoir pressures of the NAB are usually less than 2000 psig, the Langmuir Equations of adsorbed gas are active as the reservoir pressure declines, and the adsorbed gas will convert to free gas. The adsorbed gas should move through the same permeability and fracture paths with the free gas.

Figure 32 shows the forecast of the total, adsorbed, and free gas for the A-7455 well as related to the average reservoir pressure. For this well, an example of core data is used with a depth of 2,533 ft and is shown in **Table 3**. Rhob is 2.356 gm/cc, and TOC = 8.73 wt% shown in **Table 4**. In this case the adsorbed gas is 82.6 % and the free gas is 17.4 % of the total at zero reservoir pressure. For the method, a derivative of the Langmuir Equation is used for calculating the adsorbed gas declining and the decline is converting to free gas:

$$dV/dP = (G_L*(P+P_L) - (G_L*P))/(P+P_L)^2*1.36*Rhob*TOC \quad \text{..... (15)}$$

where

	dV/dP	=	Mcf/AcFt/psi
	G_L	=	Langmuir Eq'n constant, scf/ton (12.7 with this well, TOC = 1.0 wt%),
	P	=	Average reservoir pressure, psia,
	P_L	=	Langmuir Eq'n constant (1129.6 psi),
	Rhob	=	Shale density, gm/cc,
	TOC	=	Wt%.

The method of the forecast, however, is complex. For example, the average reservoir pressure has to be calculated with reservoir simulation within a drainage area, and the variation of the composition at the variation of the reservoir pressure, especially with NAB shales. The gas contents of the canisters are measured over several days collecting fair amounts of gas. When the gas collections are virtually zero, aliquot canister shale samples are crushed in order to collect the remaining gas content. With the NAB shales these crushed gasses usually have heavier compositions, and often have a significant amount of the crushed gas content. Overall, with NAB shales most of the gas content is from the adsorption isotherm from the beginning and declining of the reservoir pressure. Since initially the canister gas collection flows significantly into the canister head space, this must be related to fair permeability. However, at the time of

the shale crushed, this must be related to low permeability. In the reservoir with this low shale permeability, it will likely need micro-fractures to recover these adsorption gas contents.

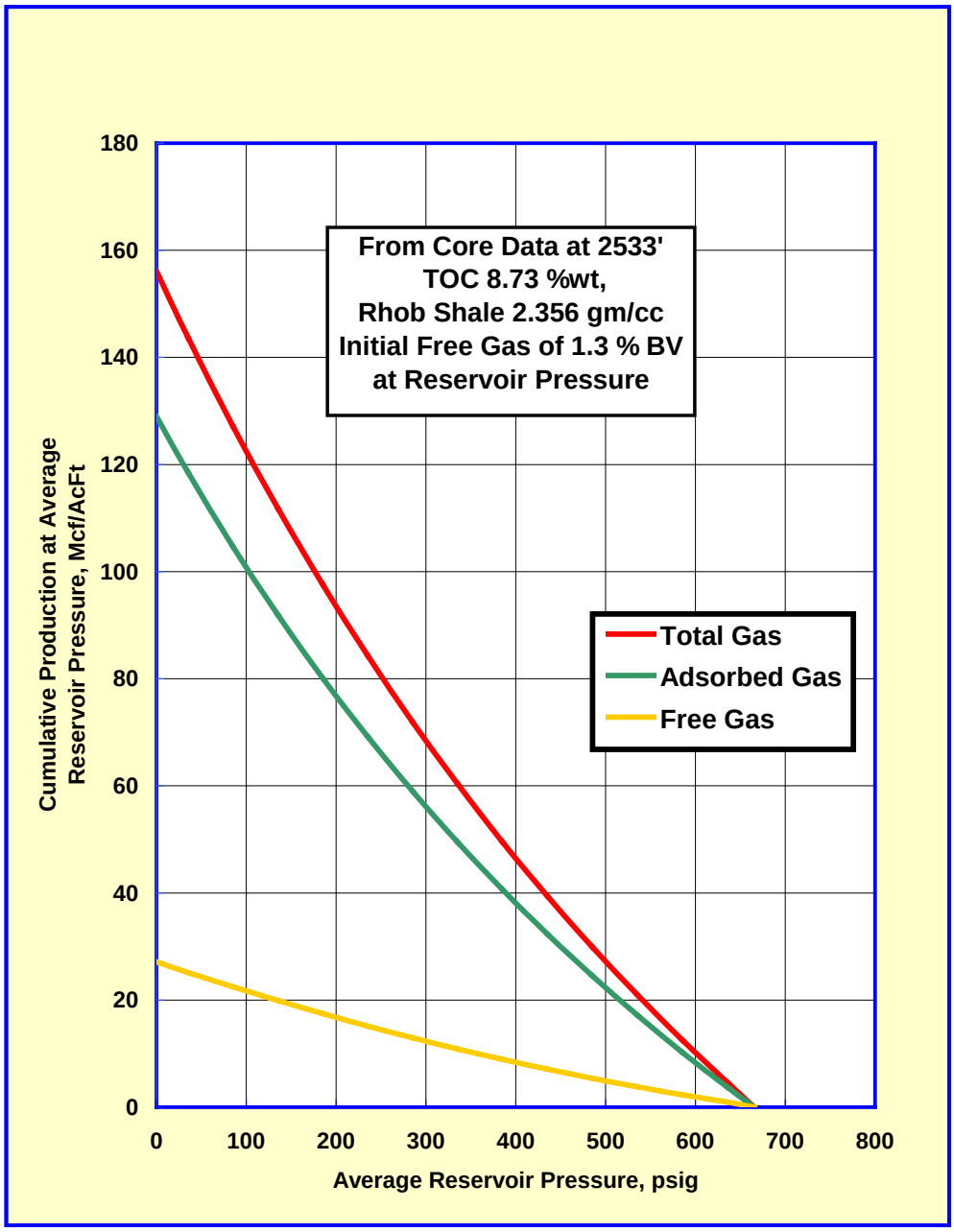


Figure 32 - Forecast Gas in NAB, Well 7455 in Christian County, KY

From Equation 15, the derivative was calculated as a function of reservoir pressure at delta pressures of 50 psi with 0.1225 Mcf/AcFt/psi at initial reservoir pressure at 680 psia and 0.3063 Mcf/AcFt/psi at final reservoir pressure of 15 psia. The declined adsorbed gas is calculated with delta pressures of the average reservoir pressure of Mcf/AcFt at the depth of 2,533 ft. As the adsorbed gas declines, cumulative gas is produced at the average reservoir pressures as shown in Figure 32. As the adsorbed gas pseudo liquid declines, added space becomes part of the free gas. This is a benefit since larger free gas space should improve matrix permeability (Km).

The graph in Figure 32 deals with several issues. First, the graph presents that when a well is put in production both adsorbed gas and free gas are present. Our position is that an amount of adsorbed gas responds to reduced reservoir pressure rapidly. This is evident with labs doing isotherms with crushed shale samples, such that the time-equilibrated periods are usually shorter than an hour or so. As described above, the adsorbed gas and free gas should move through the same permeability and fracture paths with the normal free gas. With new well tests, it is difficult to tell the difference of the adsorbed gas and free gas and normal free gas. In NAB tests with canisters the initial gas compositions usually show mostly methane. As mentioned above, when gas is collected from canisters when shale samples are crushed, the compositions usually show lower methane components and larger amounts of ethane, propane, and other heavier components.

General Methane Isotherms in NAB

Methane isotherm data from one canister core from well A-7455, was shown with a Langmuir Equation shown in **Table 4** as footnote and the isotherm and equation are shown in Figure 7. Added isotherm data were also provided from canisters and cores from eight other wells in SW Kentucky and four wells in Indiana. In Figure 33 measured isotherm data are shown with raw, variations of TOC for each isotherm of 4.0 to 13.3 % TOC and these symbols have no filled color. These data are then linearly adjusted to normalize with 10 % TOC. The same symbols are used but with filled color. Langmuir Equation curves are shown best fit with these symbols. Although the linear adjustment with a normalization of TOC to represent the Langmuir Equation is not perfect, it is reasonable to use. Note that normalizing for just TOC for methane adsorption may differ with some shales of different kerogens and/or clays. However, with NAB in Figure 34 in the SW of Kentucky and in part of Indiana, the normalized curves with TOC data of 10 % are reasonably close.

From these data a generalized composite best fit isotherm for this area is shown in red Figure 34. Gas content with a TOC from the normalized Langmuir Equation is:

V = (TOC/10.0)*(162.12*P/(P+1345.94)) ……..... (16)

where: V = volume gas content of scf/ton shale (scf at 60 ^{o}F, one atm pressure),
P = reservoir pressure, psia,
TOC = Total Organic Carbon, wt%.

However, in some other shale basins normalization of isotherms for Langmuir Equations, TOC may need to be combined with one or more parameters such as kerogen maturity.

Data of methane isotherms from Big Sandy/Devonian shale for nine cores from four wells in Eastern Kentucky and West Virginia were provided from Nuttall and Bustin Report from the Kentucky Geological Survey. Figure 35 shows the raw data which has low amounts of TOC of 0.7 to 4.7 %. Normalized data curve to 10 % TOC has a wide scatter of gas content demonstrating how in other areas the use of the generalized isotherm is inappropriate. Even with a smaller TOC %, the scatter of gas content would still be wide. For comparisons with Figure 35 of a normalized Langmuir Equation from the NAB isotherm data in SW of Kentucky, it shows that the NAB normalized gas content is significantly higher than the Big Sandy gas content.

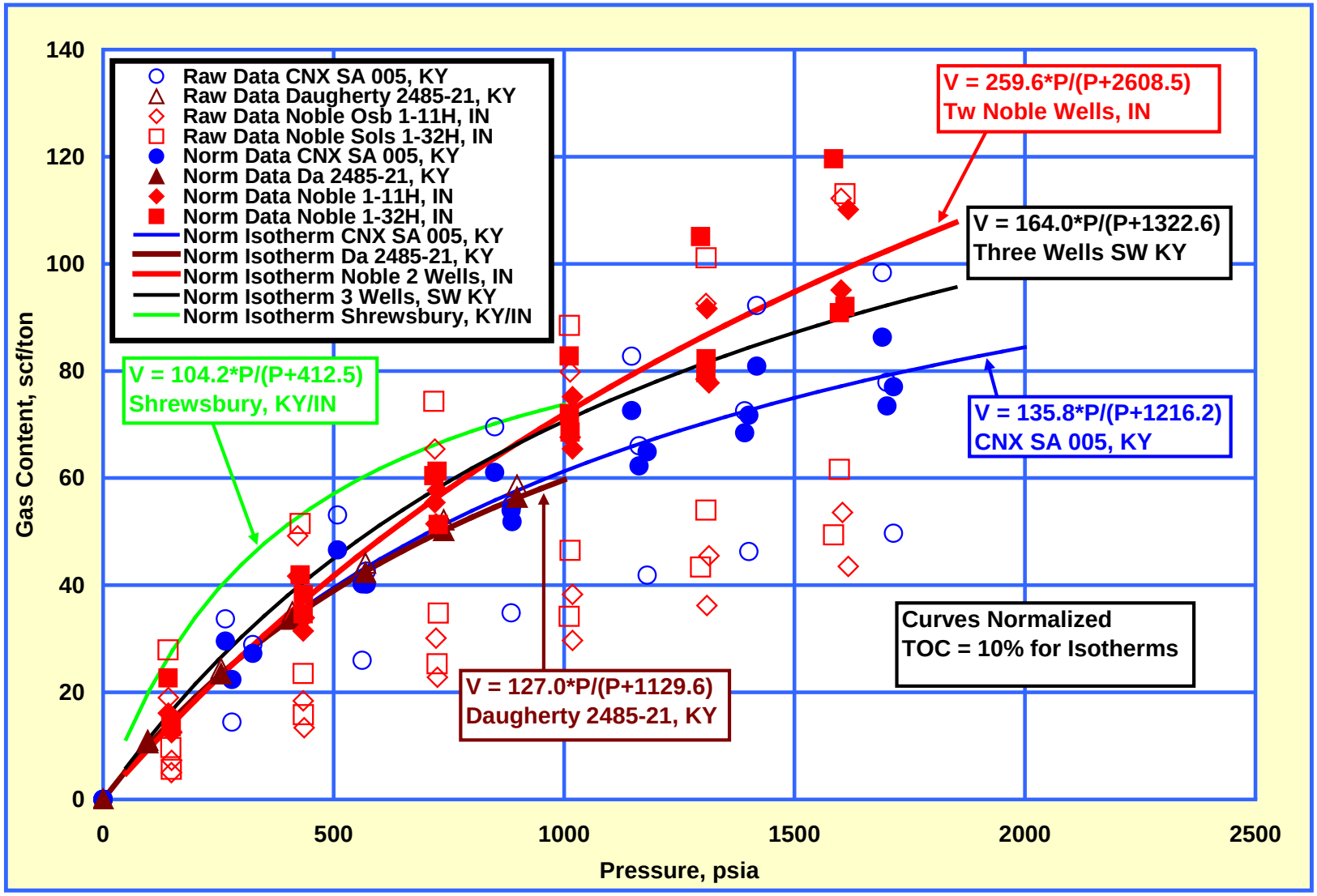


Figure 33 - NAB Methane Isotherms: B-15, KY; A-7455, KY; Three Wells, SW KY; Shrewsbury, KY/IN; Two Noble Wells, IN

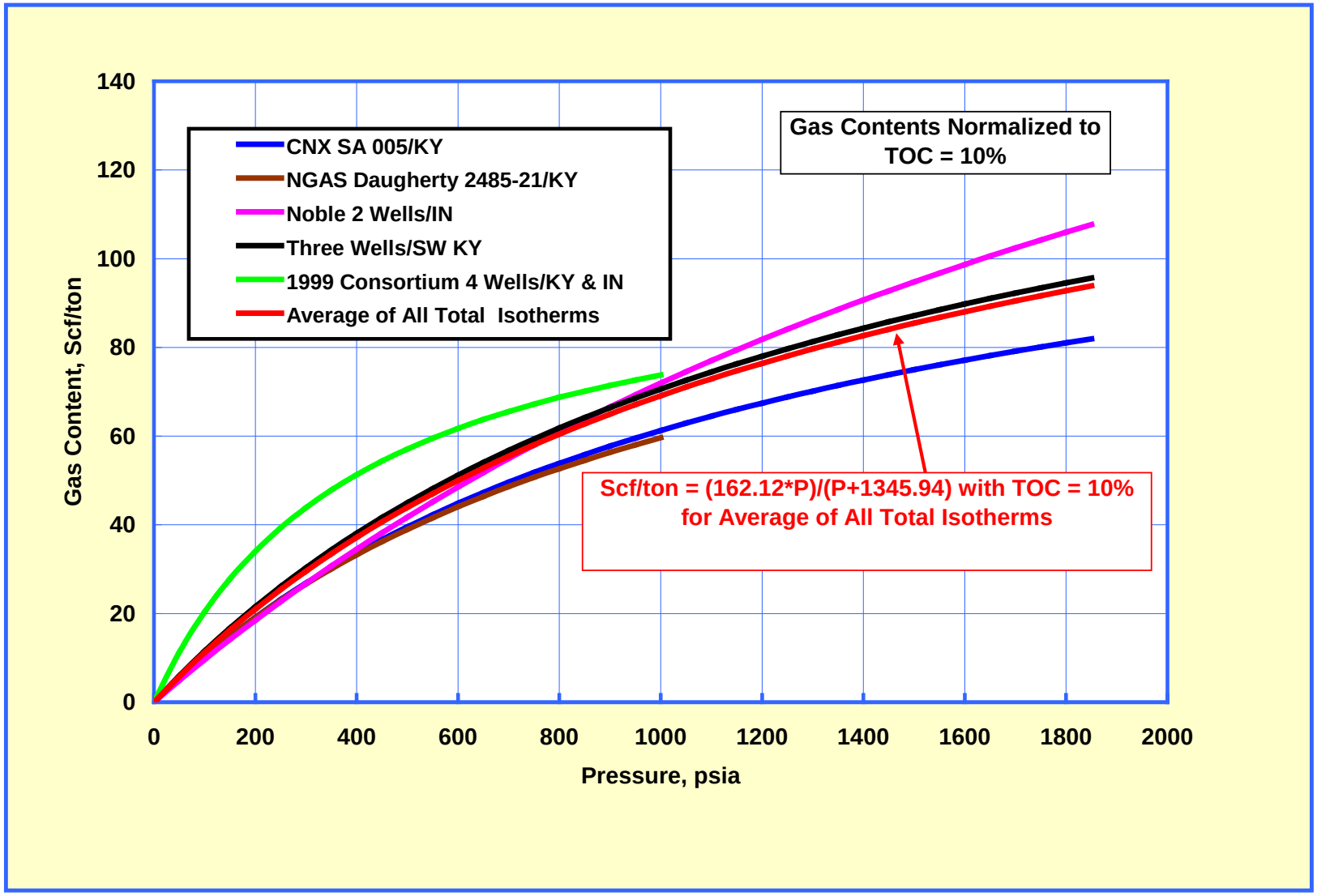


Figure 34 - Average Normalized Isotherm Models from Five Areas in Western Kentucky and Indiana

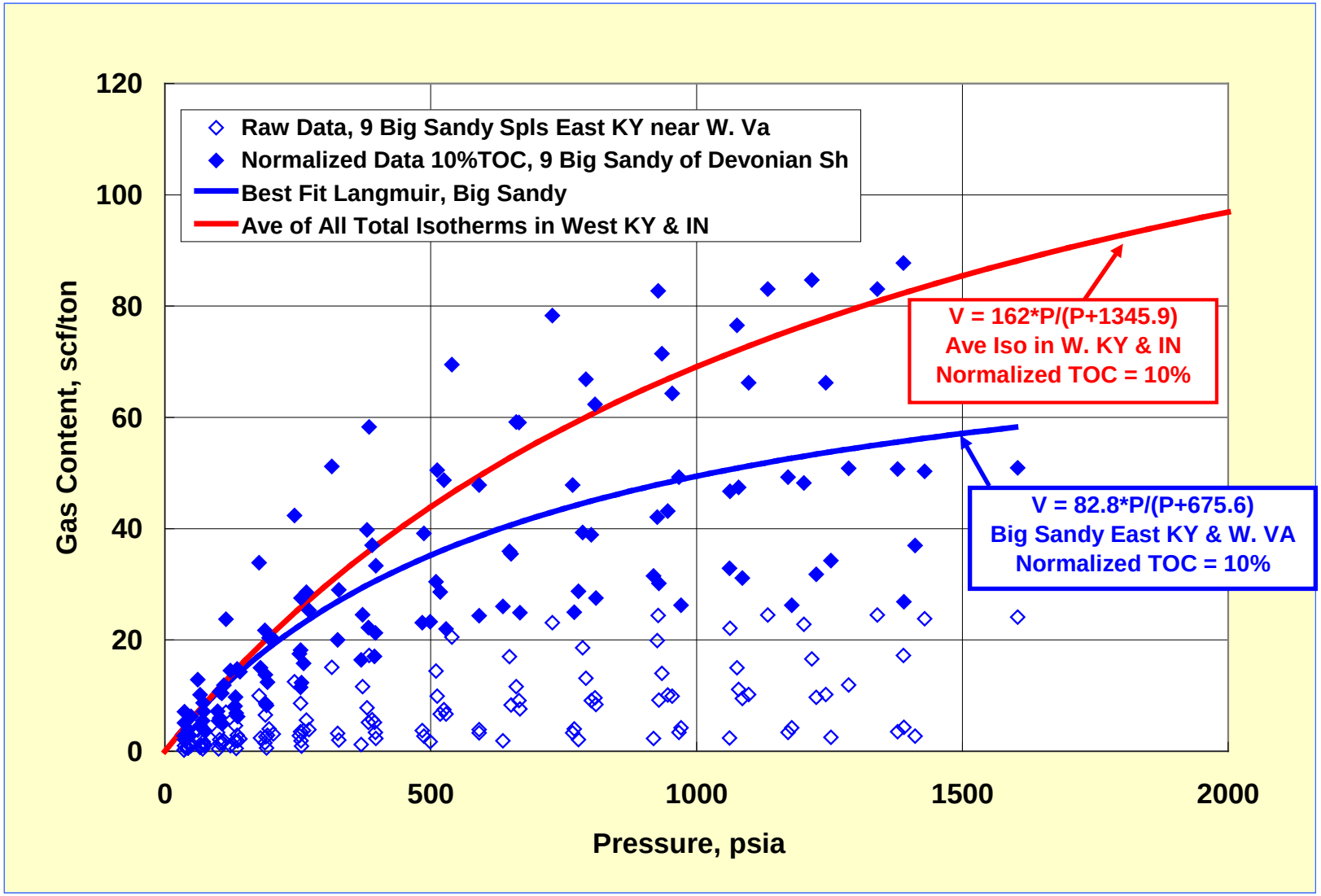


Figure 35 - Methane Adsorption Isotherms With Shale from Big Sandy/Devonian from Nuttall & Bustin Report (KGS), East Kentucky - West Virginia

Measurement of Matrix Permeabilities of Shale Cores

As described previously in the **Introduction**, gas permeabilities (Km matrix permeability) of free gas are routinely obtained using crushed shale chips with pulse pressure measurements. Figure 36 shows permeability results of NAB shale samples. Conventional Core Lab (Lab 1) results from 25 samples of the two Noble wells in Indiana (symbols of brown diamonds) are shown of 0.0001 to 1.0 nanodarcy (Km of 0.0001 10-06 to 1.0 10-06 md) with Bulk Volume Gas (BVG) of 0.1% to 3%. Schlumberger/TerraTek (Lab 3) shows permeability results of NAB from 5 sidewall core clusters from B-3 in SW Kentucky (symbols of brown triangles), which has significantly higher of about 66 to 93 nanodarcy with BVG of 1.5 to 2.5 %. In Figure 36 there are also Haynesville shale samples of permeability results shown to compare with the NAB results and to include a larger amount of shale chips, larger amount of gas porosity, and a third lab. Lab 1 is shown of permeabilities from 128 Haynesville (HVL) shale samples (symbols of blue diamonds), 31 HVL shale samples of Lab 2 from Weatherford Lab (symbols of pink squares), and 120 HVL shale samples of Lab 3 (symbols of green triangles). A red average Trendline is shown of the HVL shale permeability with Lab 1 and Lab 2, whereas a green Trendline is shown for Lab 3 of the higher permeabilities and yet about the same range of BVG%.

With Km matrix permeability of Lab 3 significantly higher than Lab 1 and Lab 2, a large group of operational companies consider that Lab 3 method is more reliable. As a result we have included previous published permeability measurements of East Texas Travis Peak shale core plugs. Also published are Appalachian Devonian shale permeability measurements of both permeability of shale plugs and crushed/chips of the plug ends. From these data which of the Labs are most compatible. In Figure 37 the black upper Trendline represents gas permeability of core plug analyses of East Texas Travis Peak siltstones and mudstones from a SPE 19008 paper of “Relationships of Permeability, Porosity, and Overburden Stress Derived from an Extensive Core Analysis Data Base in the Travis Peak Formation” D. L. Luffel, W. E. Howard, and E. R. Hunt, ResTech, published in 1989 funded by GRI. There was a total of 2100 core plugs from nine wells. However, only 905 core plugs were used after 1195 core plugs were rejected because of induced or natural fractures. There were three rock environments, one of which is siltstone/mudstones of 144 core plugs. The Kg data were measured at an average of 4700 psi net overburden (NOB) stress, pore pressures of about 100 psig, with cores dried from oven. The Travis Peak 144 plugs of the siltstone/mudstones have low permeabilities but are about 100 times greater than the matrix permeability of the shale.

Part of this is due to the Travis Peak Kg as higher because connate water saturation was not included. Also, the Travis Peak environment shown probably does not fully match shale even though it had siltstone/mudstone, so the permeability is likely to be higher. Note that the Travis Peak slope of the permeability data is about the same slope of the data from the shale samples from Labs 1 and 2. The slope of the Lab 3 shale sample results is rather flat of only one decade (about 100 to 1000 nanodarcy) with a large spread of gas porosity of 1 to 10 %BVG. The Lab 3 results seem unreasonable, but information isn't available.

As mentioned above, a paper was SPE 25898 "The Measurement of Matrix and Fracture Properties in Naturally Fractured Cores," X. Ning, J. Fan, S. A. Holditch, and W. J. Lee, Texas A&U, published in 1993 funded by GRI. A new lab apparatus was developed to measure matrix permeability with induced fractures in shale core plugs from cores in Huron shale from new wells in Appalachian area. Plugs were 1 ½ inch diameter and 2.0 inch length. Pore pressure was 500 to 1000 psig of He, with sleeve of 4000 psig. The plug was equilibrated for two days. It was first tested with Berea core of matrix of 0.001 md, then the plug was cracked lengthwise, and it was Km 0.0013 md. With the developed measurements, fracture(s), matrix permeability (Km), and gas porosity were measured in the shale plugs, usually less than one day.

Twenty-three core plugs were used from air drilled cores from two wells with Devonian Appalachian shales. Core plugs had end trims used for thin sections to identify fractures, which were all induced fractures with parallel to bedding. In Figure 38 the Km's are shown with symbols of red squares of the 23 core plugs with Km of about 0.002 – 0.08 nanodarcy and gas porosity of 1.6 – 6 %. Adjacent shale samples of chips from ends of the plugs were also used for Km measurements as shown in Figure 39 with symbols of red squares but not with red filling. The chips have about the same range of Km with 0.005 – 0.2 but with gas porosity of only 1 – 3%. It is unclear but the core plug gas porosities appear to be too high. The paper of SPE 20575 of "Characterization of Core Scale Heterogeneities Using Laboratory Pressure Transients," J. Kamath, R. E. Boyer, and F. M. Nakagawa, published 1990, first showed the calculation of Km with fractured cores. They reported that the porosity could be in error if the upstream and downstream volumes are not the same size as the gas pore volume sample. In general, the Km of the core plugs and the Km of plug ends of chips are in same Km range. The results are evident that the Km is about within the results of the methods used of Lab 1 and 2. However, some additional lab research is further needed for both Km and gas porosity.

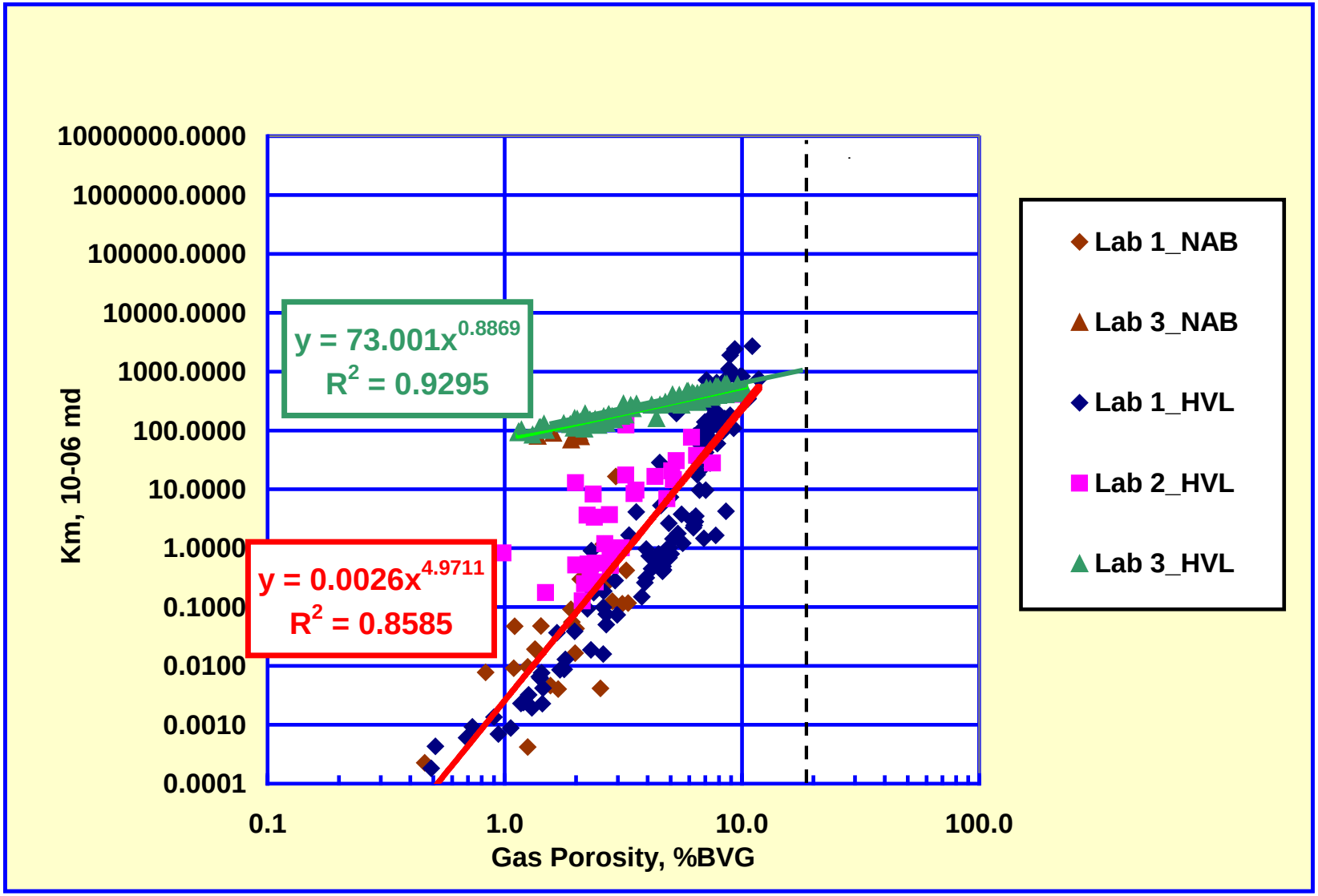


Figure 36 - Matrix Shale Permeability of Km = f (GasPorosity)

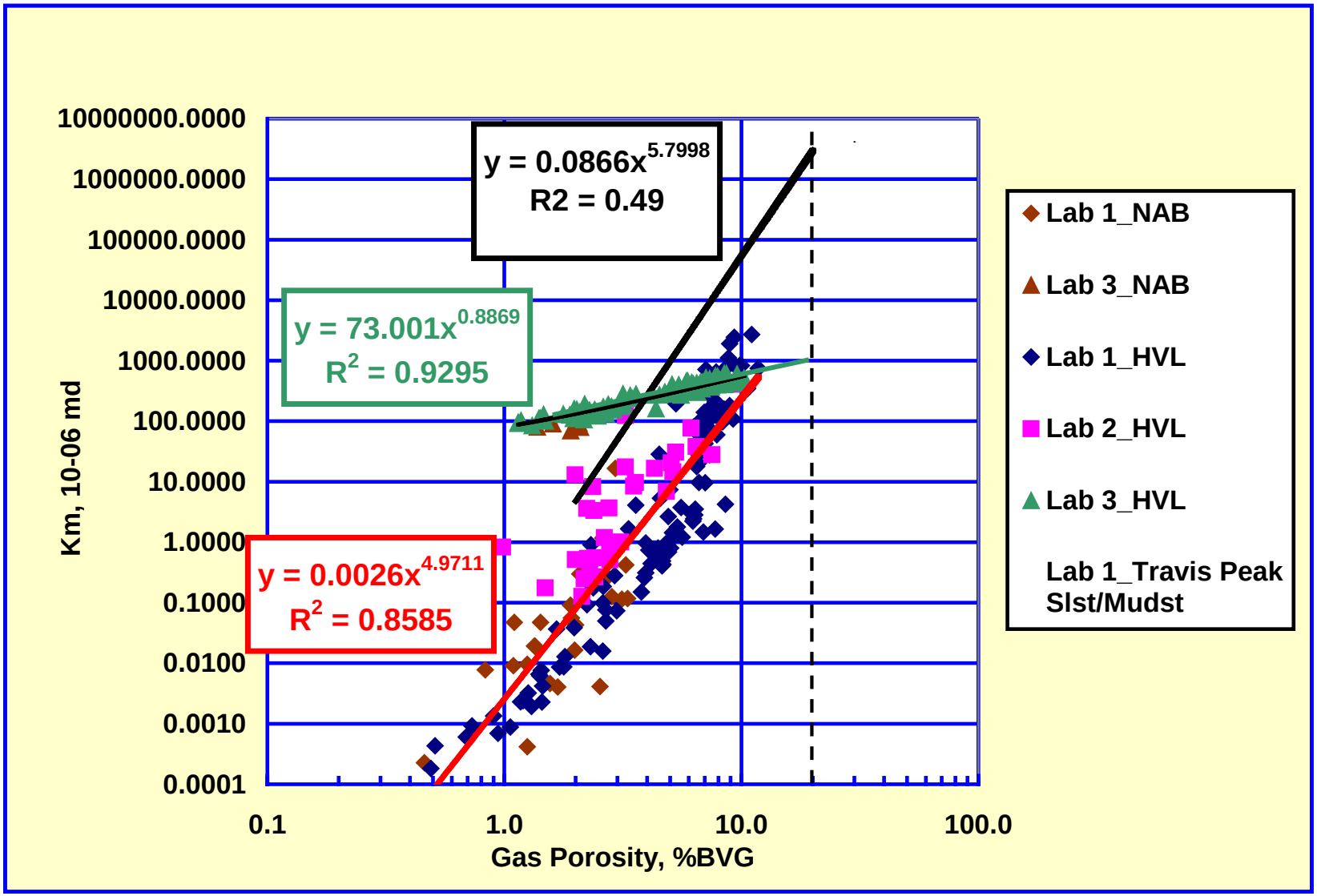


Figure 37 - Added East Travis Peak Slst/Mudst of Core Kg

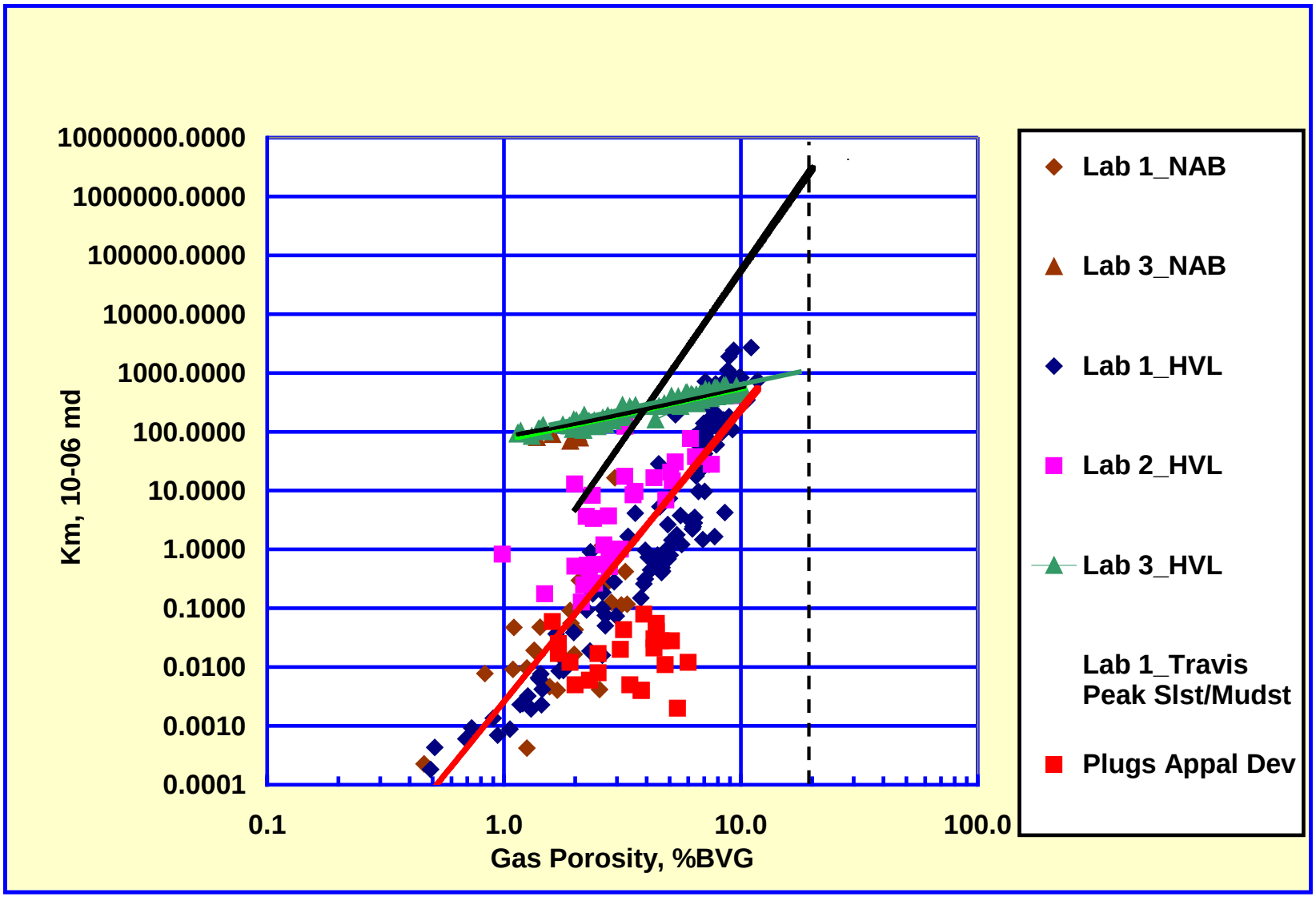


Figure 38 - Appalachian Devonian Shale Plugs with Km

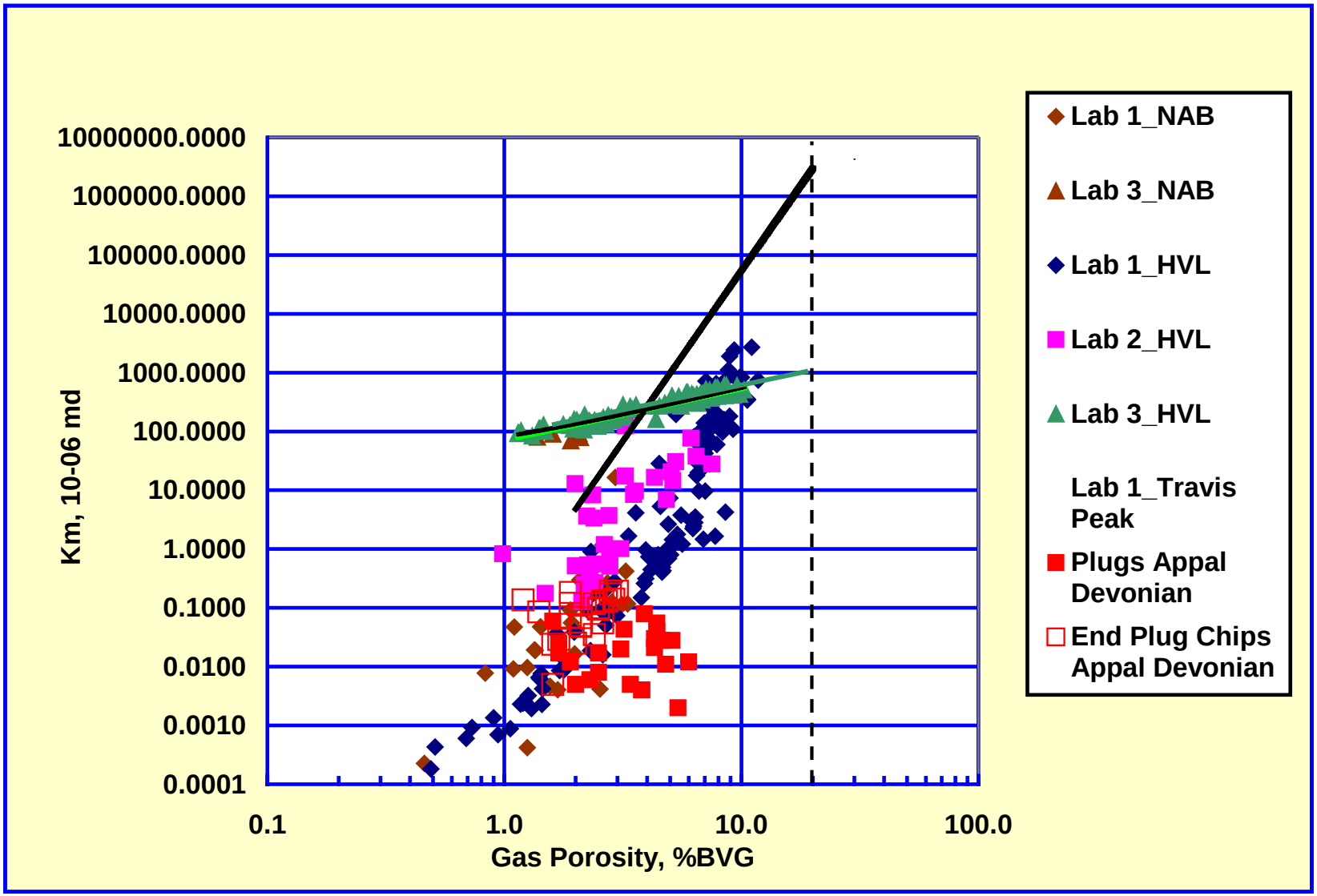


Figure 39 – Appalachian Devonian Plugs and End Plug Chips of Km

Appendix A

Graphical Log Sections New Albany Shale

Track Definitions:

Track 1-Gamma Ray (0-500 API, red), caliper (6-11 inches)

Track 2-Lithology and porosity (0-1)

Track 3-Depth track (ft)

Track 4-Resistivity scaled logarithmically (.2-2000 ohmm, deep-red, medium dark blue, shallow lt. blue)

Track 5- bulk density (Rhob 2-3 g/cc dark green), neutron (0.4--.10 red), total organic carbon (TOC 0-30 wt %, blue)

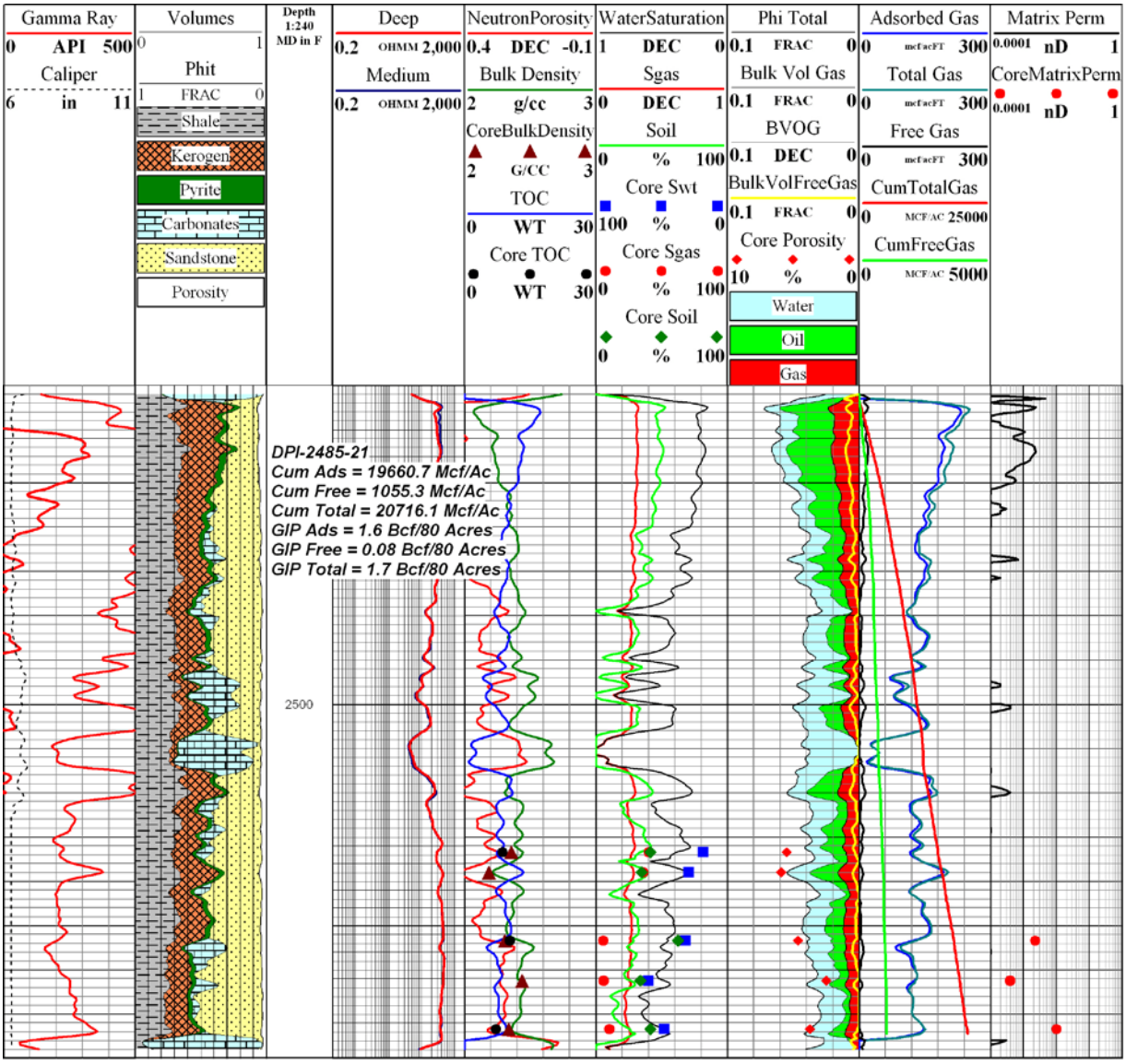
Track 6-Saturations (Sw 1-0 black), (So 0-100% green), (Sgas 0-1 red)

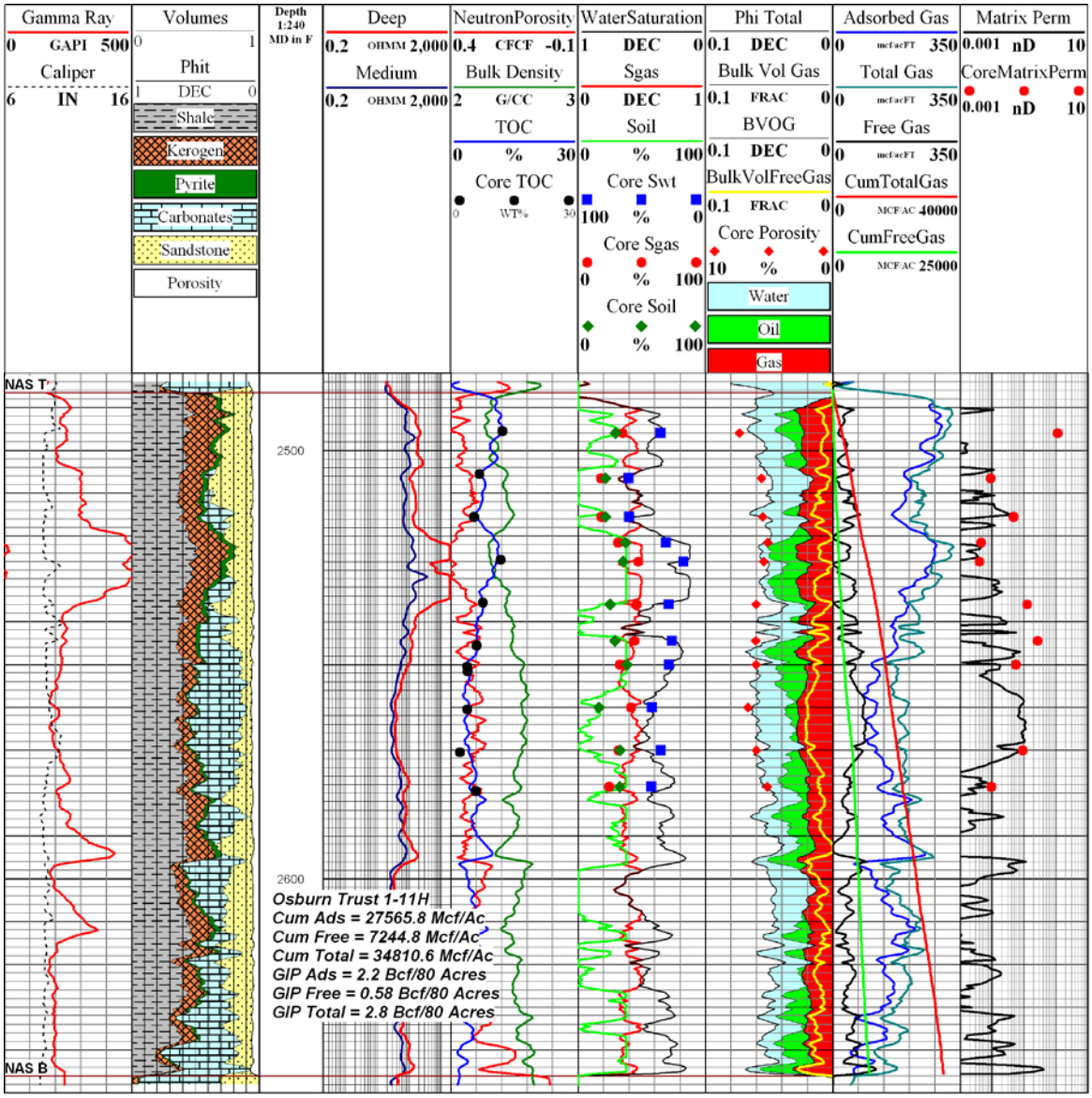
Track 7- Bulk volume analysis of porosity (0.1-0, black), water- lt. Blue, oil -green, gas- red, bulk volume free gas –yellow, corrected for adsorbed gas space

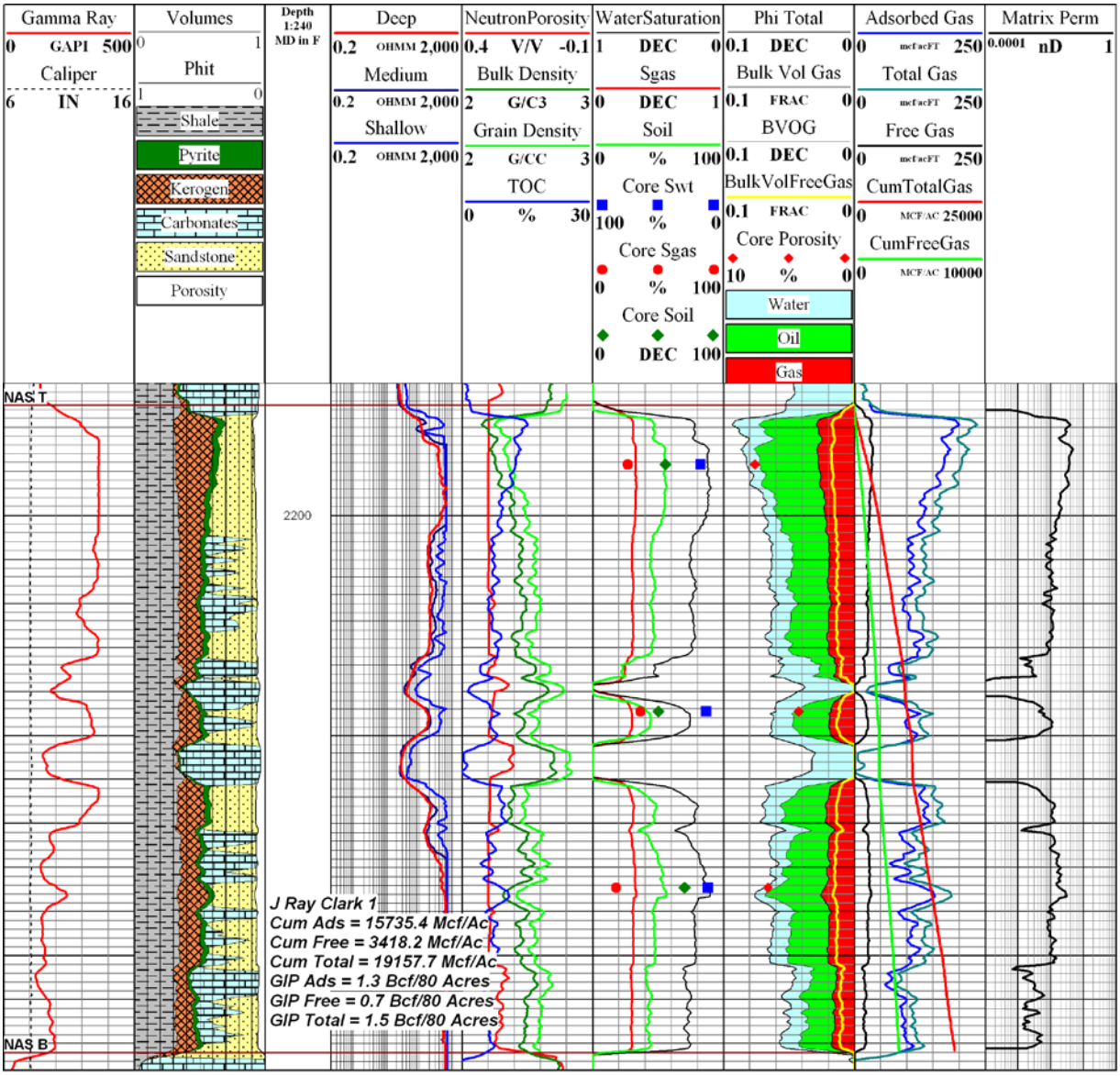
Track 8-Gas content (scale varies MCF/ACFT), adsorbed gas-blue, free gas – black, total gas-dark green, Cumulative gas (scale varies, MCF/AC) free gas lt. green, and total gas-red

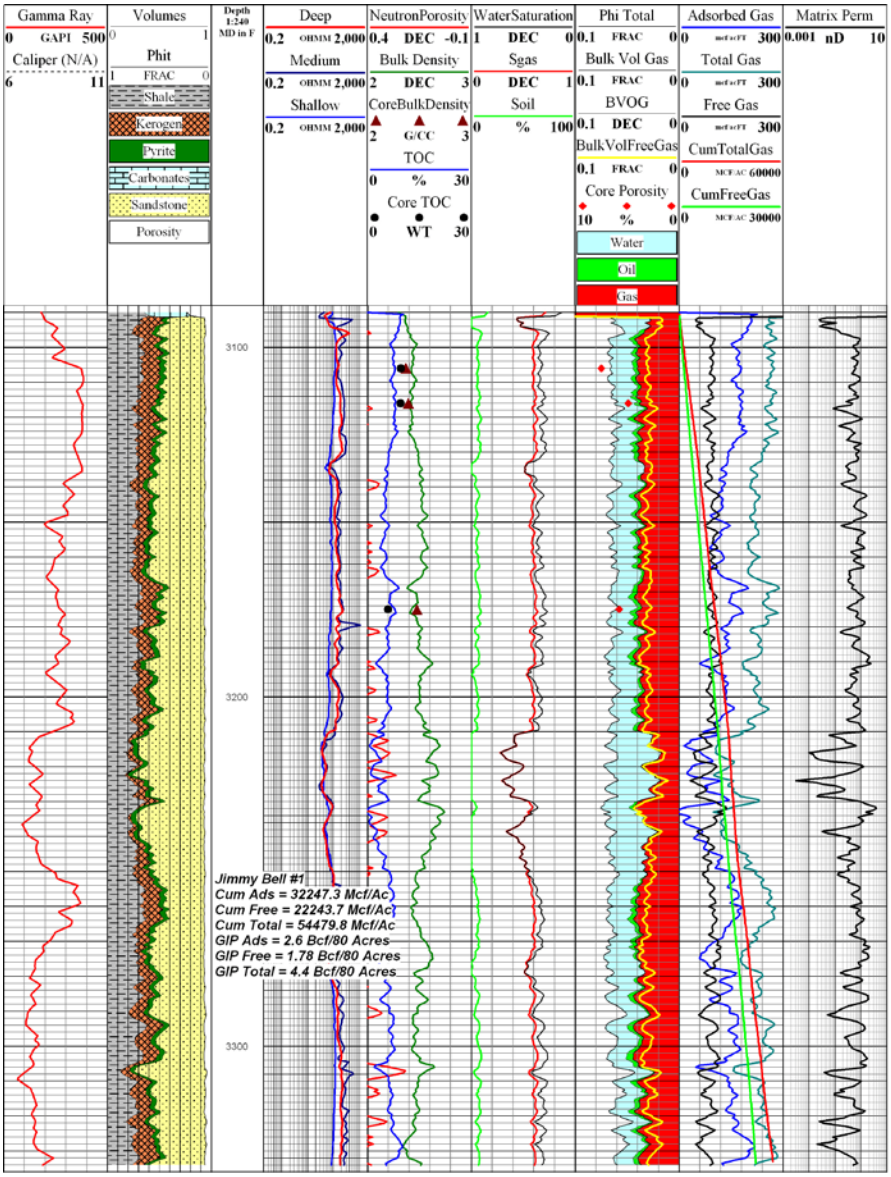
Track 9-Matrix permeability (log scale 0.0001-1 nano-darcy)

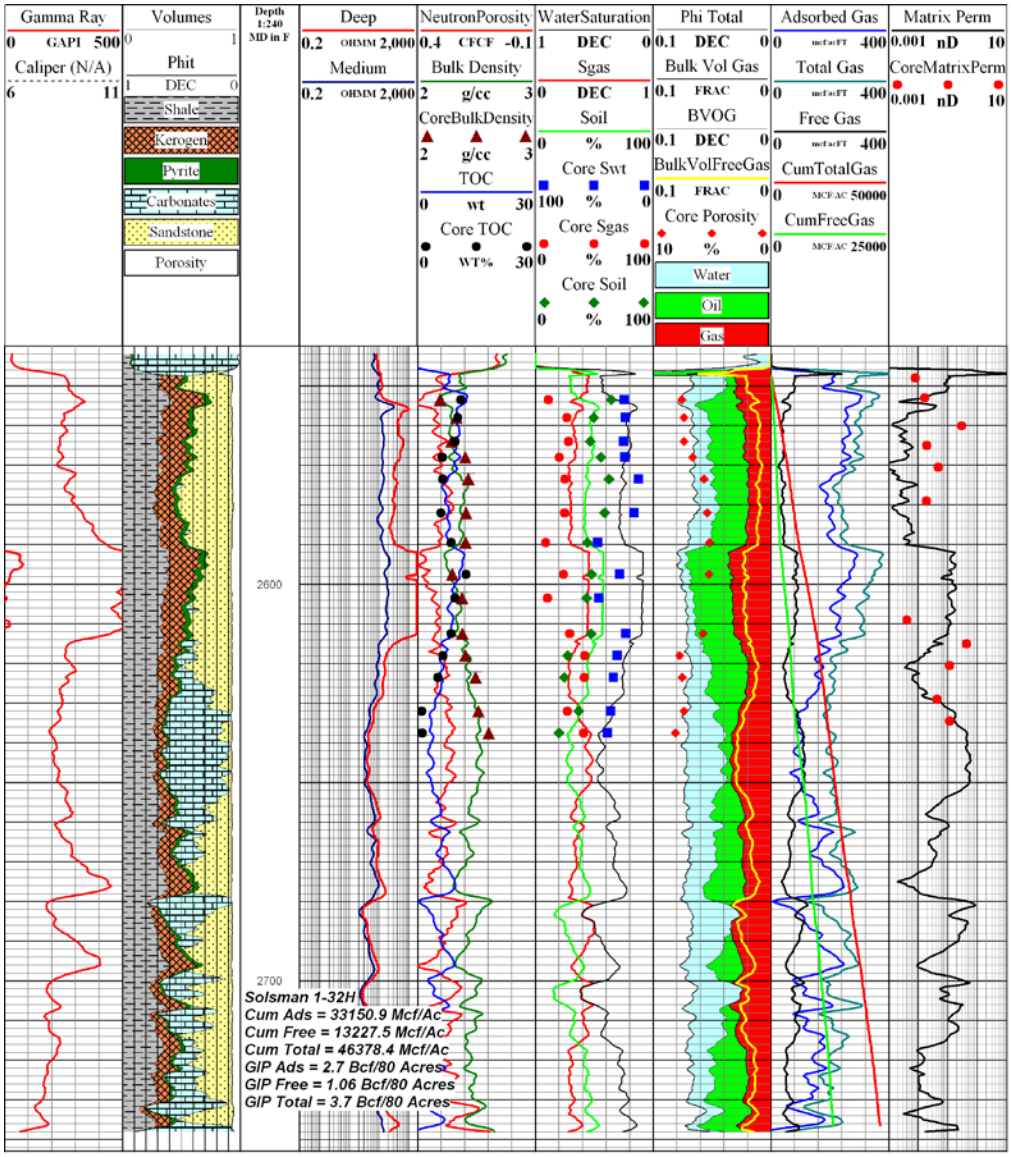
All available core data is posted on the log section.

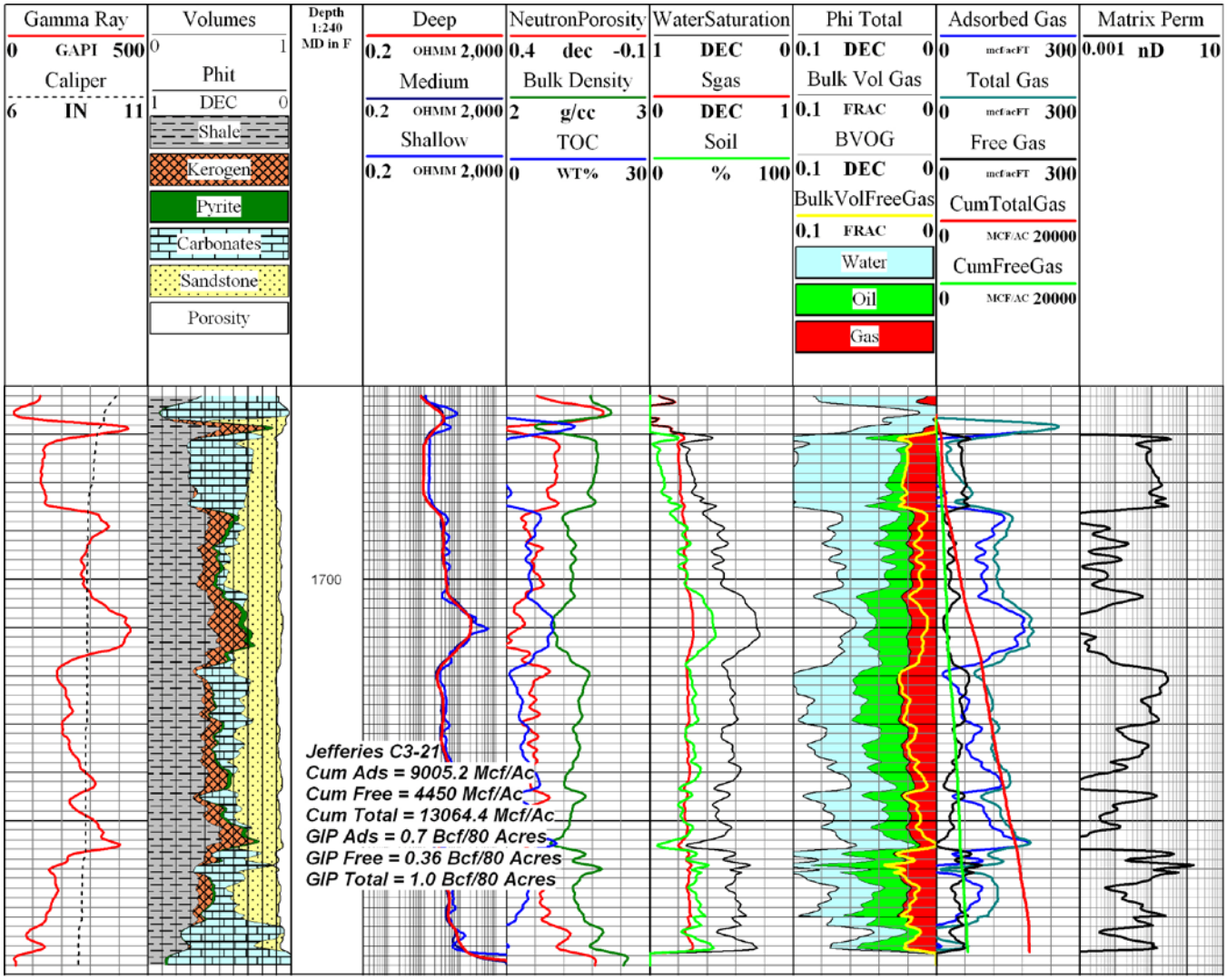

Gamma Ray
0 API 500
Caliper
6 in 11
Volumes
0 1
Phit
1 FRAC 0
Shale
Kerogen
Pyrite
Carbonates
Sandstone
Porosity
Depth
1:240
MD in F
Deep
0.2 OHMM 2,000
Medium
0.2 OHMM 2,000
NeutronPorosity
0.4 DEC -0.1
Bulk Density
2 g/cc 3
CoreBulkDensity
2 G/CC 3
TOC
0 WT 30
Core TOC
0 WT 30
WaterSaturation
1 DEC 0
Sgas
0 DEC 1
Soil
0 % 100
Core Swt
100 % 0
Core Sgas
0 % 100
Core Soil
0 % 100
Phi Total
0.1 FRAC 0
Bulk Vol Gas
0.1 FRAC 0
BVOG
0.1 DEC 0
BulkVolFreeGas
0.1 FRAC 0
Core Porosity
10 % 0
Water
Oil
Gas
Adsorbed Gas
0 mcf/acFT 300
Total Gas
0 mcf/acFT 300
Free Gas
0 mcf/acFT 300
CumTotalGas
0 MCF/AC 25000
CumFreeGas
0 MCF/AC 5000
Matrix Perm
0.0001 nD 1
CoreMatrixPerm
0.0001 nD 1
DPI-2485-21
Cum Ads = 19660.7 Mcf/Ac
Cum Free = 1055.3 Mcf/Ac
Cum Total = 20716.1 Mcf/Ac
GIP Ads = 1.6 Bcf/80 Acres
GIP Free = 0.08 Bcf/80 Acres
GIP Total = 1.7 Bcf/80 Acres
2500

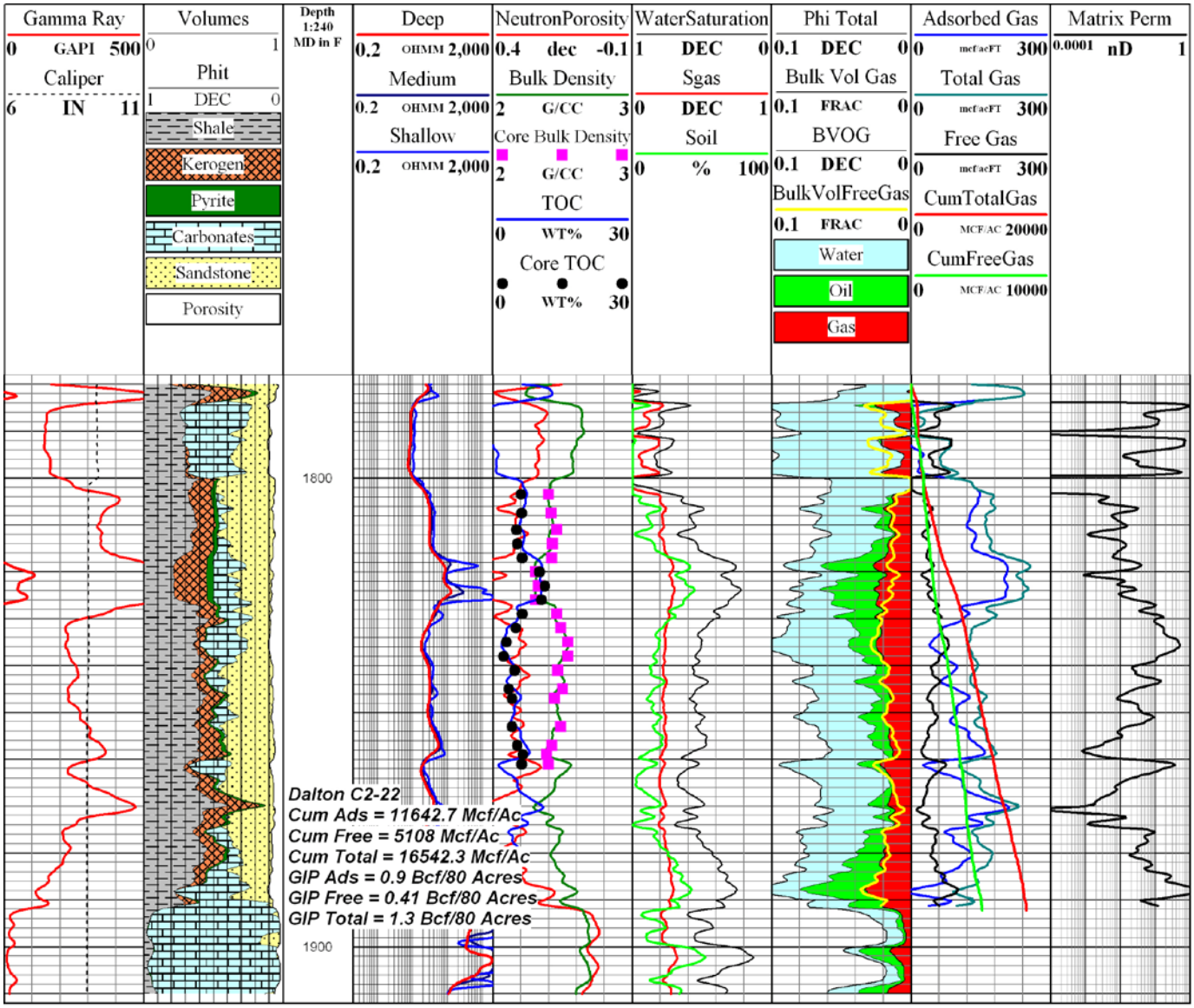

Gamma Ray
0 GAPI 500
Caliper
6 IN 16
Volumes
0 1
Phit
1 DEC 0
Shale
Kerogen
Pyrite
Carbonates
Sandstone
Porosity
Depth 1:240 MD in F
Deep
0.2 OHMM 2,000
Medium
0.2 OHMM 2,000
NeutronPorosity
0.4 CFCF -0.1
Bulk Density
2 G/CC 3
TOC
0 % 30
Core TOC
0 WT% 30
WaterSaturation
1 DEC 0
Sgas
0 DEC 1
Soil
0 % 100
Core Swt
100 % 0
Core Sgas
0 % 100
Core Soil
0 % 100
Phi Total
0.1 DEC 0
Bulk Vol Gas
0.1 FRAC 0
BVOG
0.1 DEC 0
BulkVolFreeGas
0.1 FRAC 0
Core Porosity
10 % 0
Water
Oil
Gas
Adsorbed Gas
0 mcf/acFT 350
Total Gas
0 mcf/acFT 350
Free Gas
0 mcf/acFT 350
CumTotalGas
0 MCF/AC 40000
CumFreeGas
0 MCF/AC 25000
Matrix Perm
0.001 nD 10
CoreMatrixPerm
0.001 nD 10
NAS T
2500
2600
NAS B
Osburn Trust 1-11H
Cum Ads = 27565.8 Mcf/Ac
Cum Free = 7244.8 Mcf/Ac
Cum Total = 34810.6 Mcf/Ac
GIP Ads = 2.2 Bcf/80 Acres
GIP Free = 0.58 Bcf/80 Acres
GIP Total = 2.8 Bcf/80 Acres

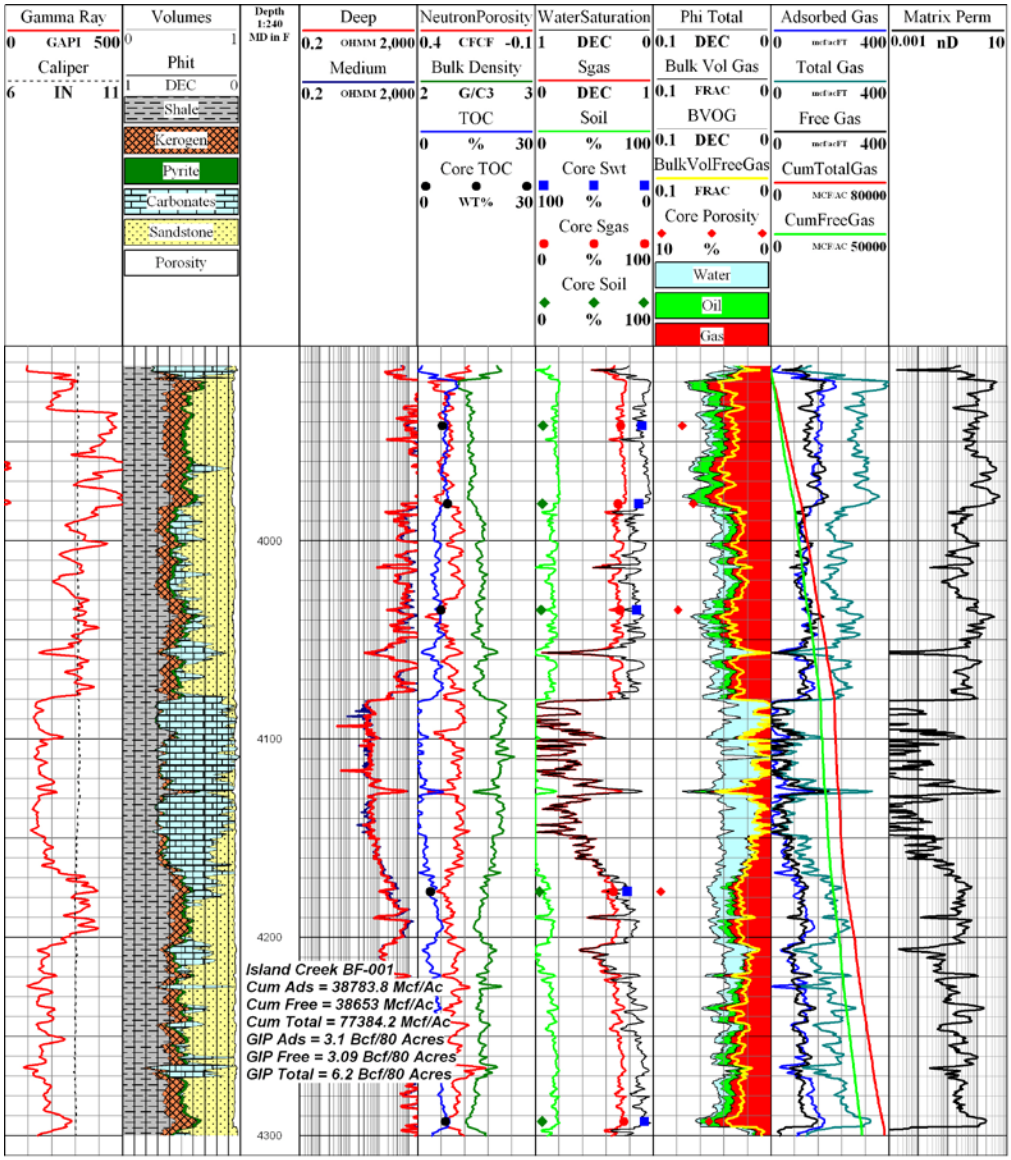

Gamma Ray
0 GAPI 500
Caliper
6 IN 16
Volumes
0 1
Phit
1 0
Shale
Pyrite
Kerogen
Carbonates
Sandstone
Porosity
Depth
1:240
MD in F
Deep
0.2 OHMM 2,000
Medium
0.2 OHMM 2,000
Shallow
0.2 OHMM 2,000
NeutronPorosity
0.4 V/V -0.1
Bulk Density
2 G/C3 3
Grain Density
2 G/CC 3
TOC
0 % 30
WaterSaturation
1 DEC 0
Sgas
0 DEC 1
Soil
0 % 100
Core Swt
100 % 0
Core Sgas
0 % 100
Core Soil
0 DEC 100
Phi Total
0.1 DEC 0
Bulk Vol Gas
0.1 FRAC 0
BVOG
0.1 DEC 0
BulkVolFreeGas
0.1 FRAC 0
Core Porosity
10 % 0
Water
Oil
Gas
Adsorbed Gas
0 mcf/acFT 250
Total Gas
0 mcf/acFT 250
Free Gas
0 mcf/acFT 250
CumTotalGas
0 MCF/AC 25000
CumFreeGas
0 MCF/AC 10000
Matrix Perm
0.0001 nD 1
NAS T
2200
NAS B
J Ray Clark 1
Cum Ads = 15735.4 Mcf/Ac
Cum Free = 3418.2 Mcf/Ac
Cum Total = 19157.7 Mcf/Ac
GIP Ads = 1.3 Bcf/80 Acres
GIP Free = 0.7 Bcf/80 Acres
GIP Total = 1.5 Bcf/80 Acres

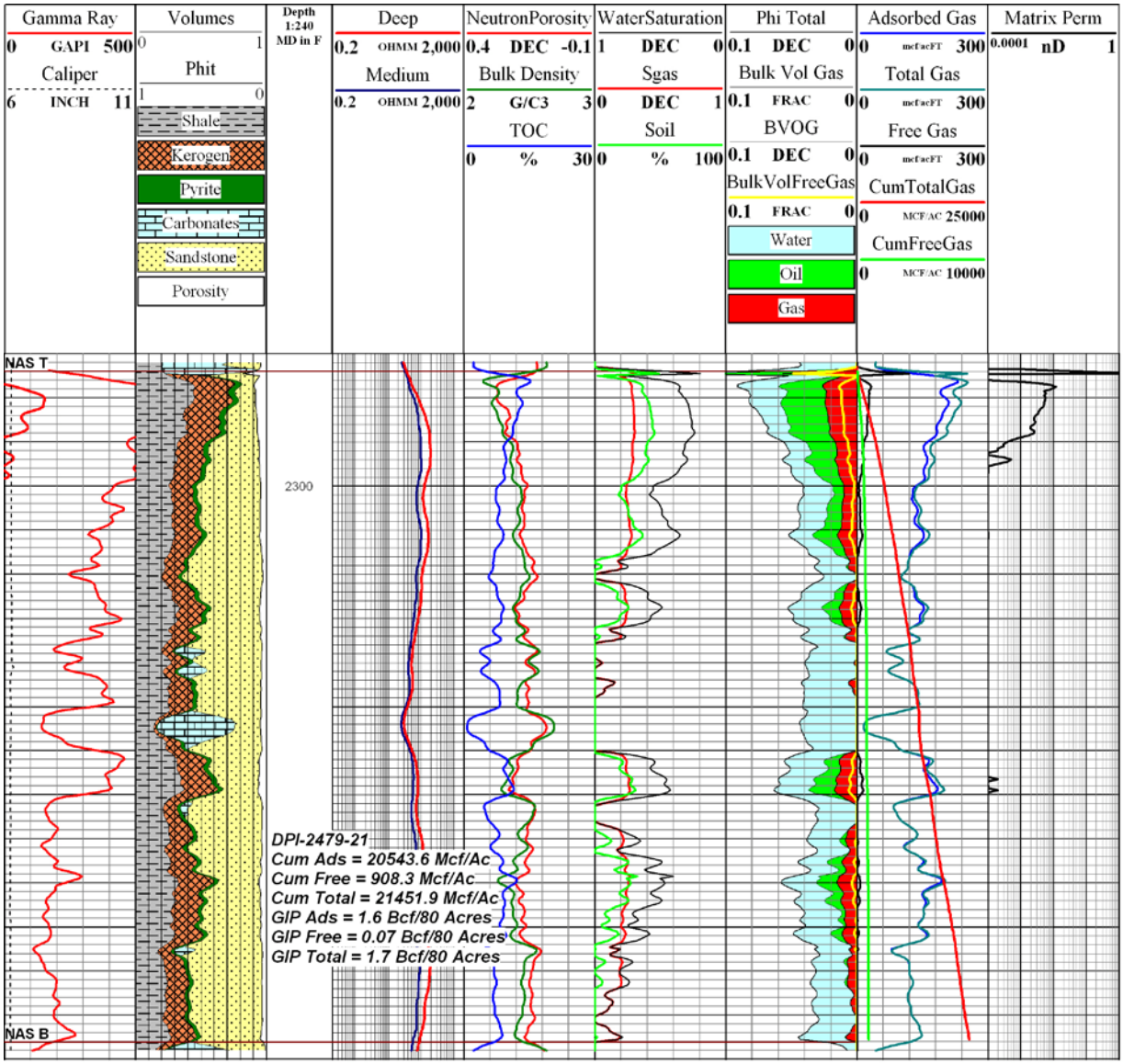

Gamma Ray
0 GAPI 500
Caliper (N/A)
6 11
Volumes
0 1
Phit
1 FRAC 0
Shale
Kerogen
Pyrite
Carbonates
Sandstone
Porosity
Depth 1:240 MD in F
Deep
0.2 OHMM 2,000
Medium
0.2 OHMM 2,000
Shallow
0.2 OHMM 2,000
NeutronPorosity
0.4 DEC -0.1
Bulk Density
2 DEC 3
CoreBulkDensity
2 G/CC 3
TOC
0 % 30
Core TOC
0 WT 30
WaterSaturation
1 DEC 0
Sgas
0 DEC 1
Soil
0 % 100
Phi Total
0.1 FRAC 0
Bulk Vol Gas
0.1 FRAC 0
BVOG
0.1 DEC 0
BulkVolFreeGas
0.1 FRAC 0
Core Porosity
10 % 0
Water
Oil
Gas
Adsorbed Gas
0 mcf/cft 300
Total Gas
0 mcf/cft 300
Free Gas
0 mcf/cft 300
CumTotalGas
0 MCF/AC 60000
CumFreeGas
0 MCF/AC 30000
Matrix Perm
0.001 nD 10
3100
3200
3300
Jimmy Bell #1
Cum Ads = 32247.3 Mcf/Ac
Cum Free = 22243.7 Mcf/Ac
Cum Total = 54479.8 Mcf/Ac
GIP Ads = 2.6 Bcf/80 Acres
GIP Free = 1.78 Bcf/80 Acres
GIP Total = 4.4 Bcf/80 Acres

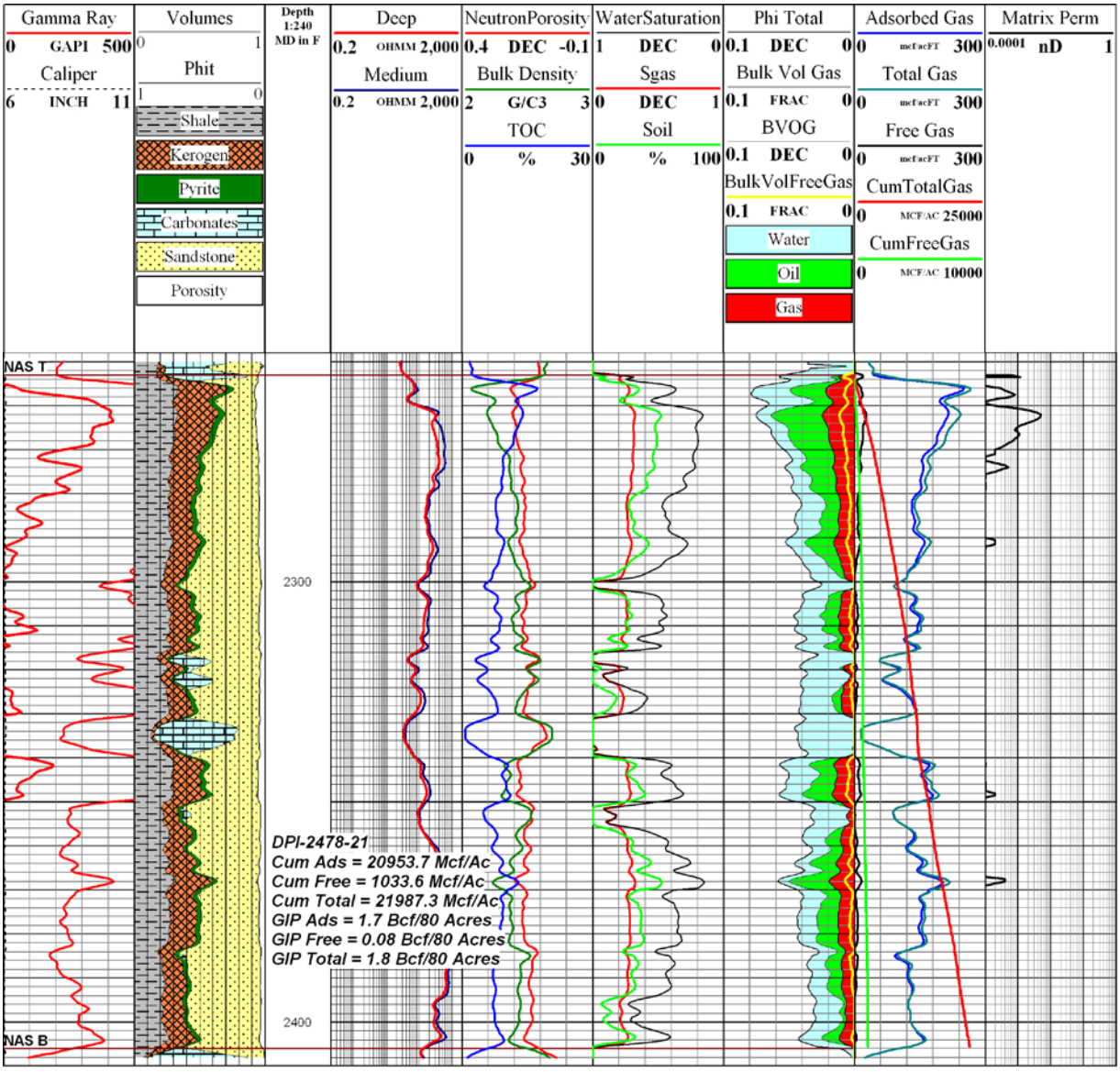

Gamma Ray
0 GAPI 500
Caliper (N/A)
6 11
Volumes
Phit
1 DEC 0
Shale
Kerogen
Pyrite
Carbonates
Sandstone
Porosity
Depth 1:240 MD in F
Deep
0.2 OHMM 2,000
Medium
0.2 OHMM 2,000
NeutronPorosity
0.4 CFCF -0.1
Bulk Density
2 g/cc 3
CoreBulkDensity
2 g/cc 3
TOC
0 wt 30
Core TOC
0 WT% 30
WaterSaturation
1 DEC 0
Sgas
0 DEC 1
Soil
0 % 100
Core Swt
100 % 0
Core Sgas
0 % 100
Core Soil
0 % 100
Phi Total
0.1 DEC 0
Bulk Vol Gas
0.1 FRAC 0
BVOG
0.1 DEC 0
BulkVolFreeGas
0.1 FRAC 0
Core Porosity
10 % 0
Water
Oil
Gas
Adsorbed Gas
0 mcf/cFT 400
Total Gas
0 mcf/cFT 400
Free Gas
0 mcf/cFT 400
CumTotalGas
0 MCF/AC 50000
CumFreeGas
0 MCF/AC 25000
Matrix Perm
0.001 nD 10
CoreMatrixPerm
0.001 nD 10
2600
2700
Solsman 1-32H
Cum Ads = 33150.9 Mcf/Ac
Cum Free = 13227.5 Mcf/Ac
Cum Total = 46378.4 Mcf/Ac
GIP Ads = 2.7 Bcf/80 Acres
GIP Free = 1.06 Bcf/80 Acres
GIP Total = 3.7 Bcf/80 Acres

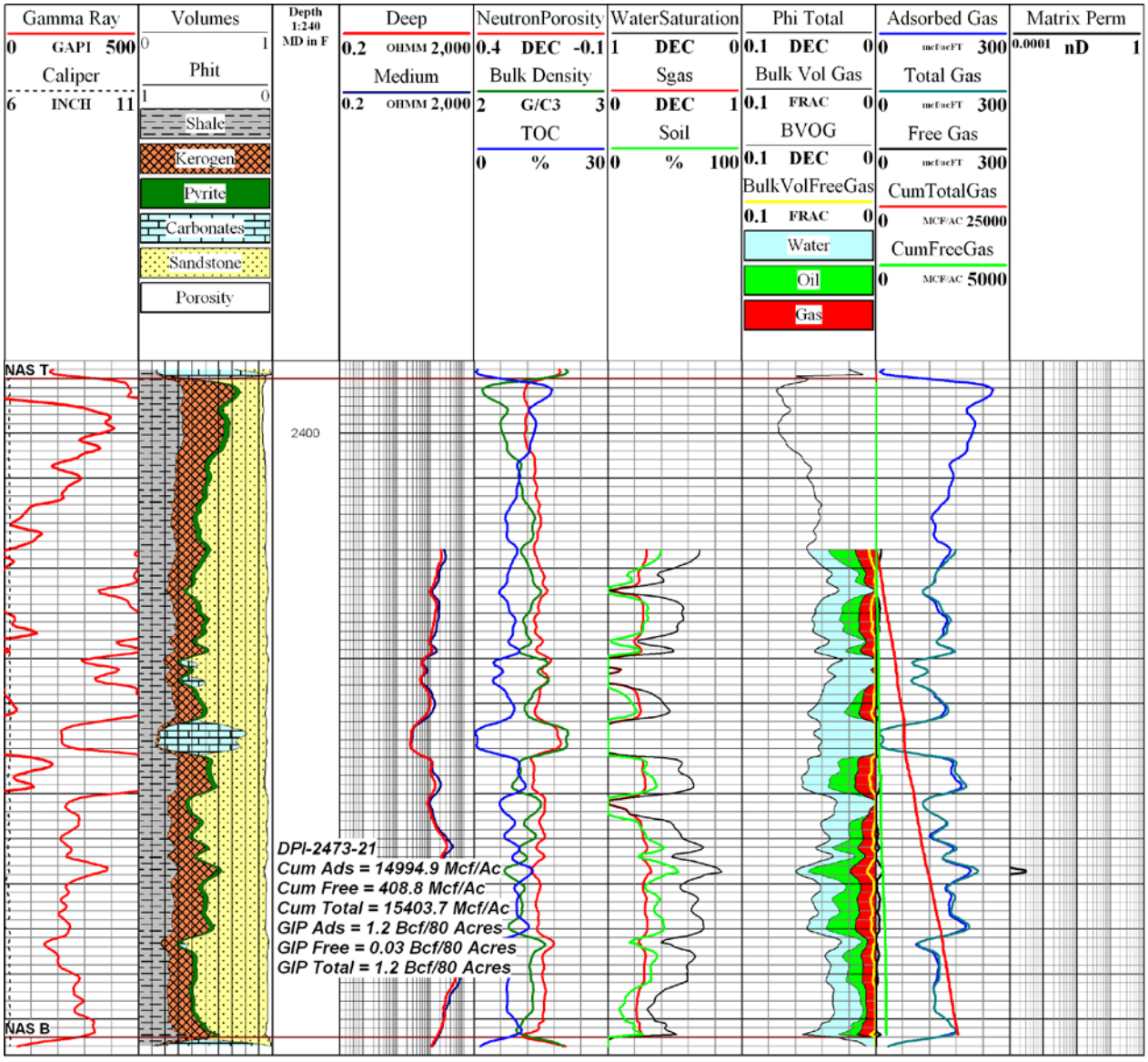

Gamma Ray
0 GAPI 500
Caliper
6 IN 11
Volumes
0 1
Phit
1 DEC 0
Shale
Kerogen
Pyrite
Carbonates
Sandstone
Porosity
Depth 1:240 MD in F
Deep
0.2 OHMM 2,000
Medium
0.2 OHMM 2,000
Shallow
0.2 OHMM 2,000
NeutronPorosity
0.4 dec -0.1
Bulk Density
2 g/cc 3
TOC
0 WT% 30
WaterSaturation
1 DEC 0
Sgas
0 DEC 1
Soil
0 % 100
Phi Total
0.1 DEC 0
Bulk Vol Gas
0.1 FRAC 0
BVOG
0.1 DEC 0
BulkVolFreeGas
0.1 FRAC 0
Water
Oil
Gas
Adsorbed Gas
0 mcf/acFT 300
Total Gas
0 mcf/acFT 300
Free Gas
0 mcf/acFT 300
CumTotalGas
0 MCF/AC 20000
CumFreeGas
0 MCF/AC 20000
Matrix Perm
0.001 nD 10
1700
Jefferies C3-21
Cum Ads = 9005.2 Mcf/Ac
Cum Free = 4450 Mcf/Ac
Cum Total = 13064.4 Mcf/Ac
GIP Ads = 0.7 Bcf/80 Acres
GIP Free = 0.36 Bcf/80 Acres
GIP Total = 1.0 Bcf/80 Acres

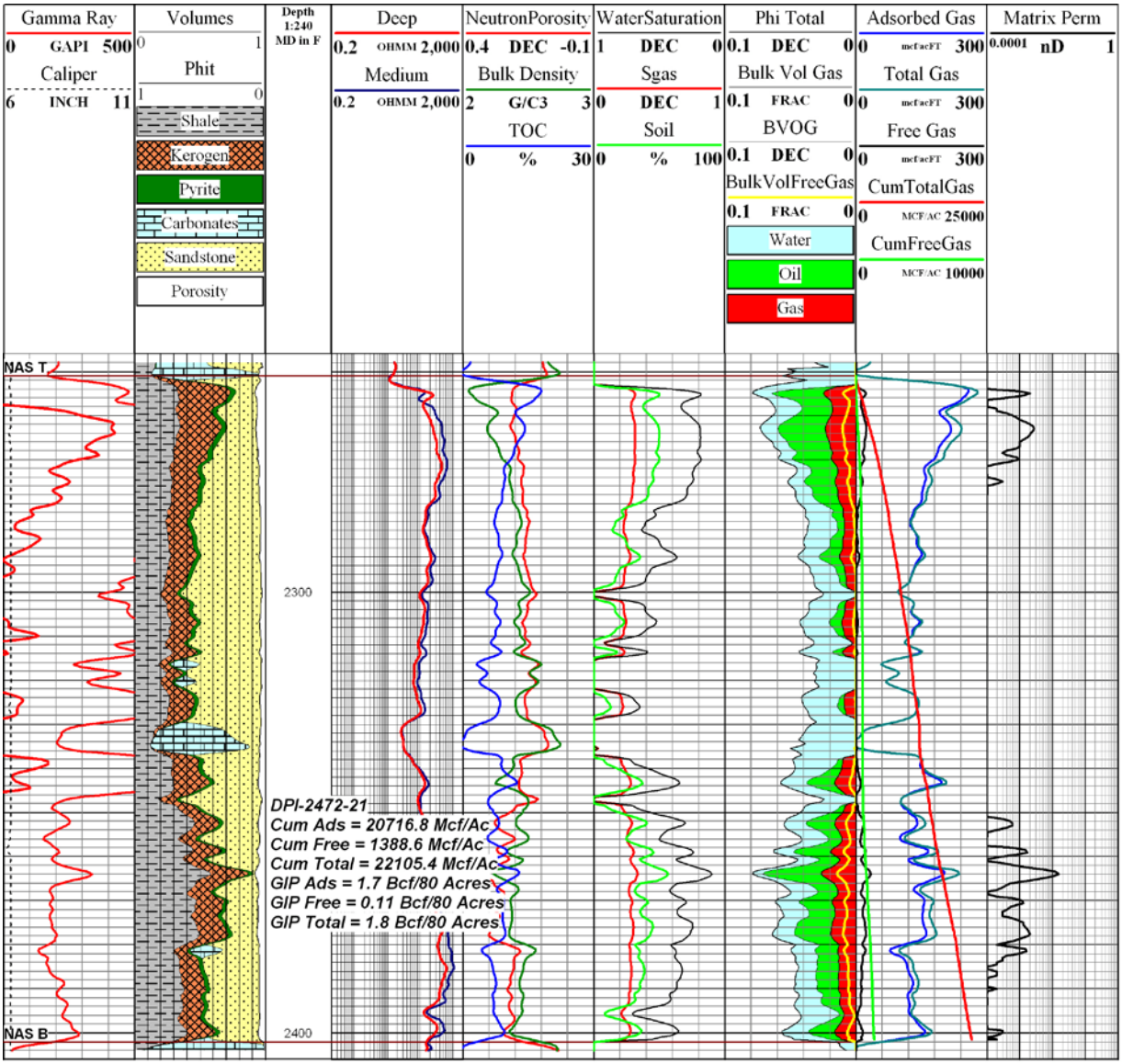

Gamma Ray
0 GAPI 500
Caliper
6 IN 11
Volumes
0 1
Phit
1 DEC 0
Shale
Kerogen
Pyrite
Carbonates
Sandstone
Porosity
Depth
1:240
MD in F
Deep
0.2 OHMM 2,000
Medium
0.2 OHMM 2,000
Shallow
0.2 OHMM 2,000
NeutronPorosity
0.4 dec -0.1
Bulk Density
2 G/CC 3
Core Bulk Density
2 G/CC 3
TOC
0 WT% 30
Core TOC
0 WT% 30
WaterSaturation
1 DEC 0
Sgas
0 DEC 1
Soil
0 % 100
Phi Total
0.1 DEC 0
Bulk Vol Gas
0.1 FRAC 0
BVOG
0.1 DEC 0
BulkVolFreeGas
0.1 FRAC 0
Water
Oil
Gas
Adsorbed Gas
0 mcf/acFT 300
Total Gas
0 mcf/acFT 300
Free Gas
0 mcf/acFT 300
CumTotalGas
0 MCF/AC 20000
CumFreeGas
0 MCF/AC 10000
Matrix Perm
0.0001 nD 1
1800
Dalton C2-22
Cum Ads = 11642.7 Mcf/Ac
Cum Free = 5108 Mcf/Ac
Cum Total = 16542.3 Mcf/Ac
GIP Ads = 0.9 Bcf/80 Acres
GIP Free = 0.41 Bcf/80 Acres
GIP Total = 1.3 Bcf/80 Acres
1900

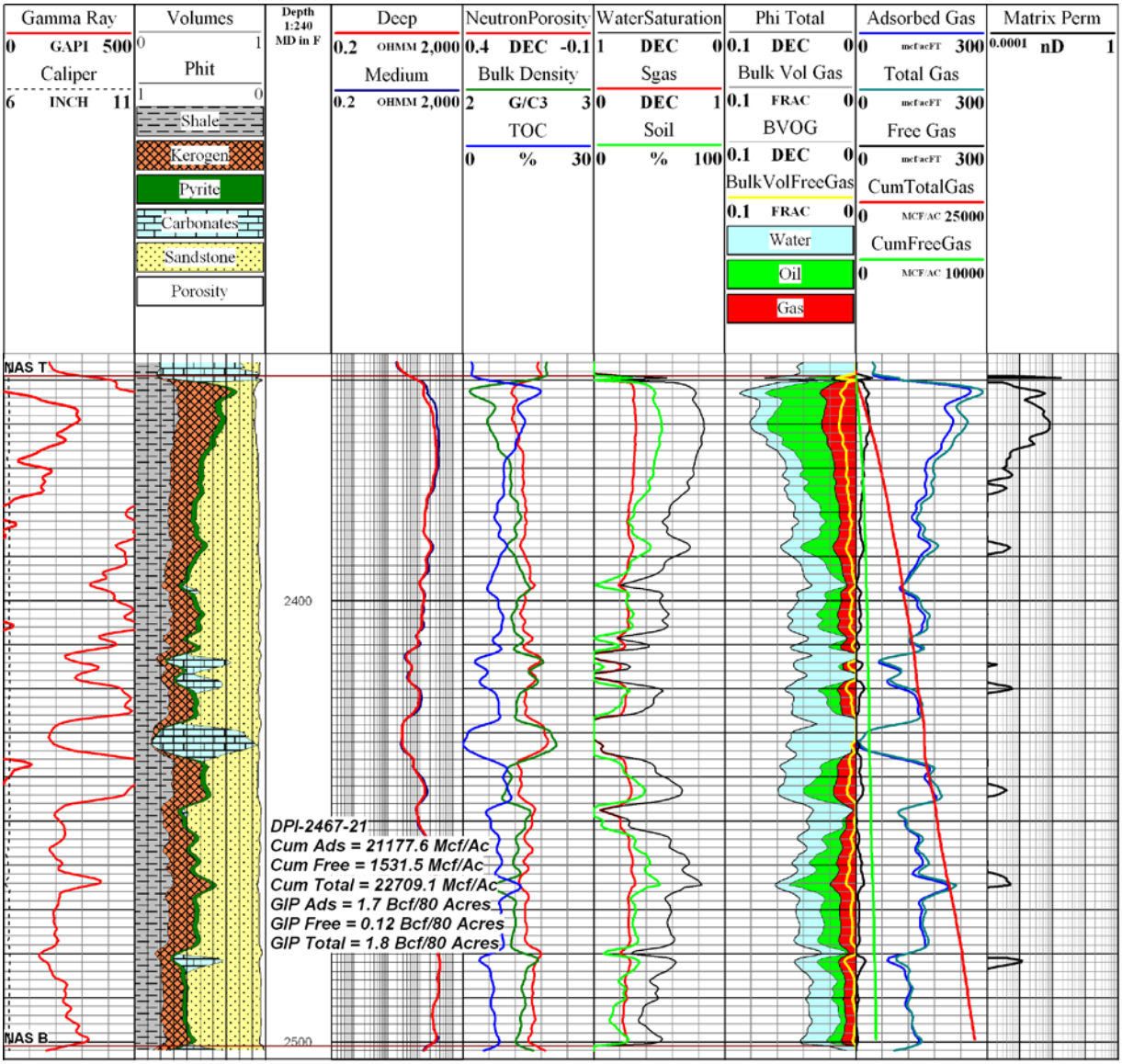

Gamma Ray
0 GAPI 500
Caliper
6 IN 11
Volumes
Phit
DEC
Shale
Kerogen
Pyrite
Carbonates
Sandstone
Porosity
Depth 1:240 MD in F
Deep
0.2 OHMM 2,000
Medium
0.2 OHMM 2,000
NeutronPorosity
0.4 CFCF -0.1
Bulk Density
2 G/C3 3
TOC
0 % 30
Core TOC
0 WT% 30
WaterSaturation
1 DEC 0
Sgas
0 DEC 1
Soil
0 % 100
Core Swt
100 % 0
Core Sgas
0 % 100
Core Soil
0 % 100
Phi Total
0.1 DEC 0
Bulk Vol Gas
0.1 FRAC 0
BVOG
0.1 DEC 0
BulkVolFreeGas
0.1 FRAC 0
Core Porosity
10 % 0
Water
Oil
Gas
Adsorbed Gas
0 mcf/cFT 400
Total Gas
0 mcf/cFT 400
Free Gas
0 mcf/cFT 400
CumTotalGas
0 MCF/AC 80000
CumFreeGas
0 MCF/AC 50000
Matrix Perm
0.001 nD 10
4000
4100
4200
4300
Island Creek BF-001
Cum Ads = 38783.8 Mcf/Ac
Cum Free = 38653 Mcf/Ac
Cum Total = 77384.2 Mcf/Ac
GIP Ads = 3.1 Bcf/80 Acres
GIP Free = 3.09 Bcf/80 Acres
GIP Total = 6.2 Bcf/80 Acres

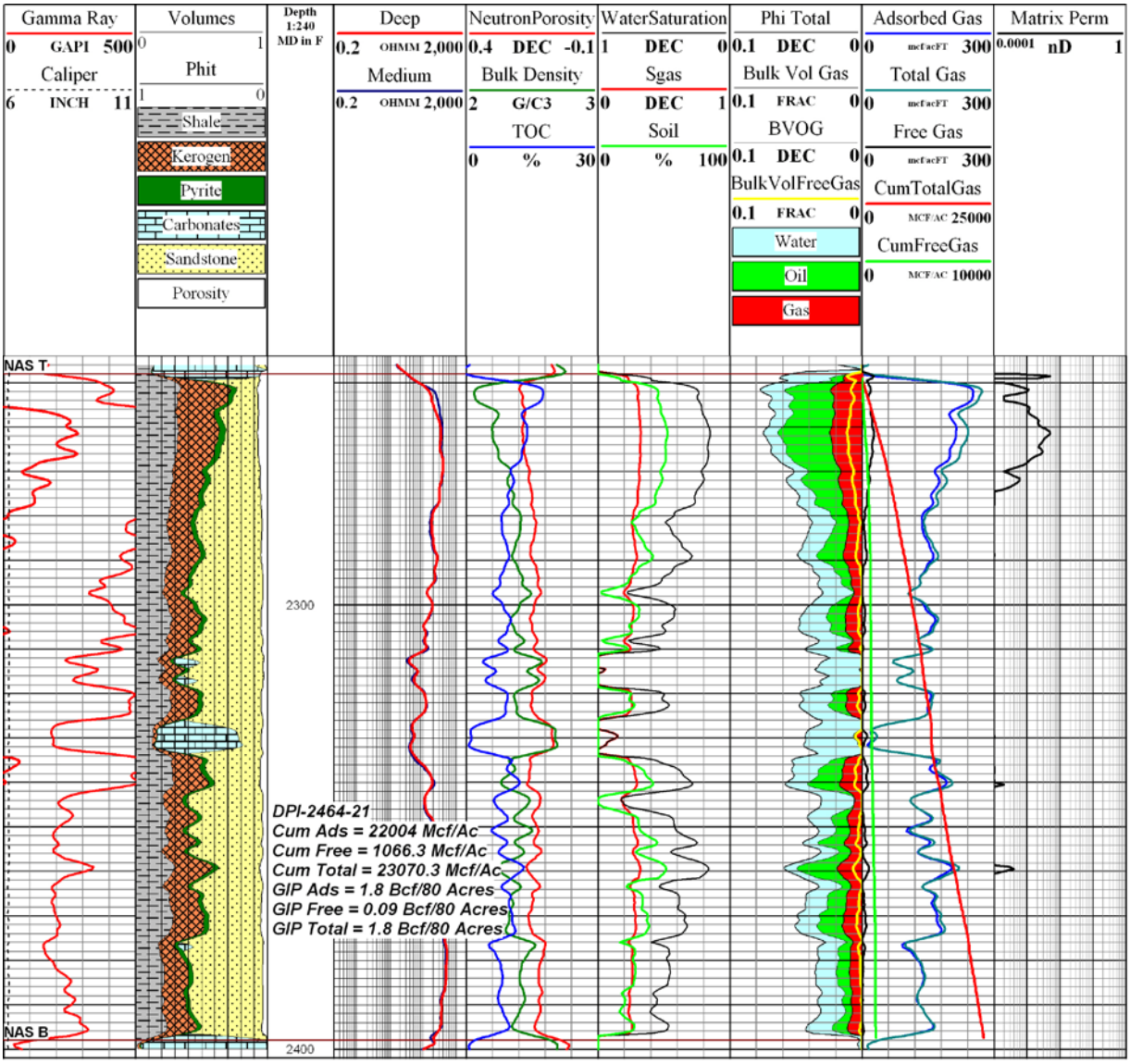

Gamma Ray
0 GAPI 500
Caliper
6 INCH 11
Volumes
0 1
Phit
1 0
Shale
Kerogen
Pyrite
Carbonates
Sandstone
Porosity
Depth
1:240
MD in F
Deep
0.2 OHMM 2,000
Medium
0.2 OHMM 2,000
NeutronPorosity
0.4 DEC -0.1
Bulk Density
2 G/C3 3
TOC
0 % 30
WaterSaturation
1 DEC 0
Sgas
0 DEC 1
Soil
0 % 100
Phi Total
0.1 DEC 0
Bulk Vol Gas
0.1 FRAC 0
BVOG
0.1 DEC 0
BulkVolFreeGas
0.1 FRAC 0
Water
Oil
Gas
Adsorbed Gas
0 mcf/acFT 300
Total Gas
0 mcf/acFT 300
Free Gas
0 mcf/acFT 300
CumTotalGas
0 MCF/AC 25000
CumFreeGas
0 MCF/AC 10000
Matrix Perm
0.0001 nD 1
NAS T
2300
DPI-2479-21
Cum Ads = 20543.6 Mcf/Ac
Cum Free = 908.3 Mcf/Ac
Cum Total = 21451.9 Mcf/Ac
GIP Ads = 1.6 Bcf/80 Acres
GIP Free = 0.07 Bcf/80 Acres
GIP Total = 1.7 Bcf/80 Acres
NAS B

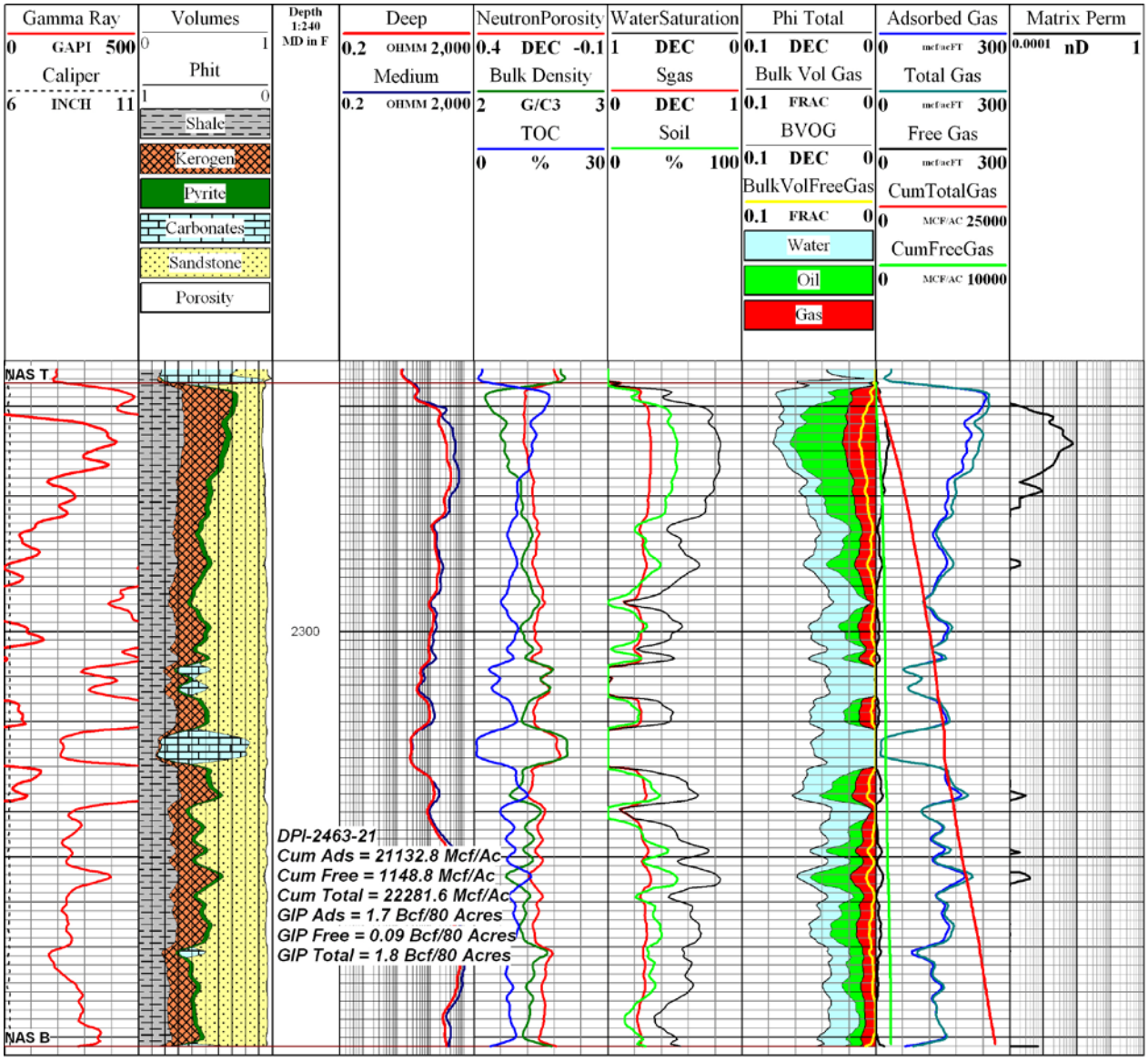

Gamma Ray
0 GAPI 500
Caliper
6 INCH 11
Volumes
0 1
Phit
1 0
Shale
Kerogen
Pyrite
Carbonates
Sandstone
Porosity
Depth
1:240
MD in F
Deep
0.2 OHMM 2,000
Medium
0.2 OHMM 2,000
NeutronPorosity
0.4 DEC -0.1
Bulk Density
2 G/C3 3
TOC
0 % 30
WaterSaturation
1 DEC 0
Sgas
0 DEC 1
Soil
0 % 100
Phi Total
0.1 DEC 0
Bulk Vol Gas
0.1 FRAC 0
BVOG
0.1 DEC 0
BulkVolFreeGas
0.1 FRAC 0
Water
Oil
Gas
Adsorbed Gas
0 mcf/acFT 300
Total Gas
0 mcf/acFT 300
Free Gas
0 mcf/acFT 300
CumTotalGas
0 MCF/AC 25000
CumFreeGas
0 MCF/AC 10000
Matrix Perm
0.0001 nD 1
NAS T
2300
DPI-2478-21
Cum Ads = 20953.7 Mcf/Ac
Cum Free = 1033.6 Mcf/Ac
Cum Total = 21987.3 Mcf/Ac
GIP Ads = 1.7 Bcf/80 Acres
GIP Free = 0.08 Bcf/80 Acres
GIP Total = 1.8 Bcf/80 Acres
2400
NAS B

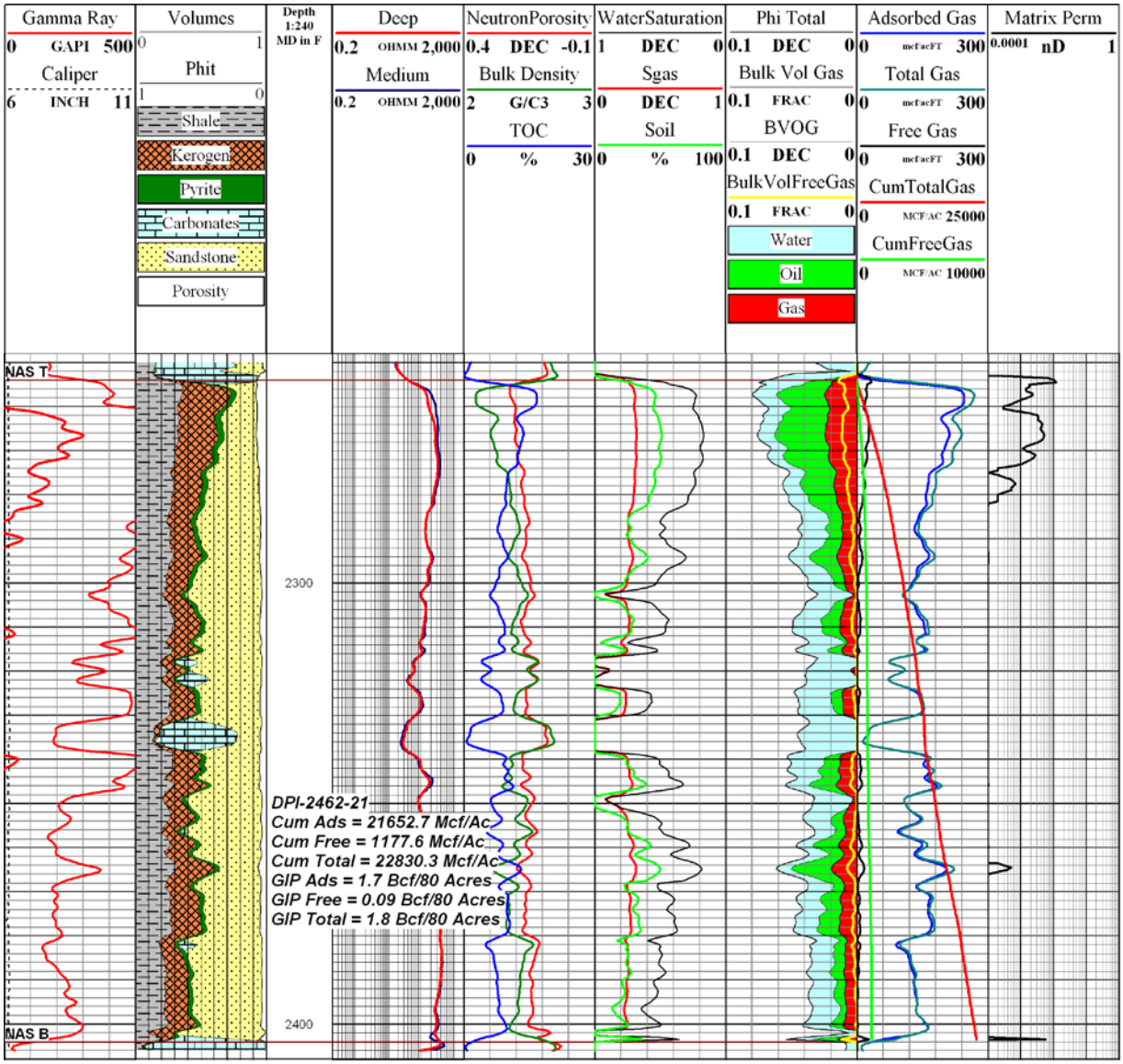

Gamma Ray
0 GAPI 500
Caliper
6 INCH 11
Volumes
0 1
Phit
1 0
Shale
Kerogen
Pyrite
Carbonates
Sandstone
Porosity
Depth 1:240 MD in F
Deep
0.2 OHMM 2,000
Medium
0.2 OHMM 2,000
NeutronPorosity
0.4 DEC -0.1
Bulk Density
2 G/C3 3
TOC
0 % 30
WaterSaturation
1 DEC 0
Sgas
0 DEC 1
Soil
0 % 100
Phi Total
0.1 DEC 0
Bulk Vol Gas
0.1 FRAC 0
BVOG
0.1 DEC 0
BulkVolFreeGas
0.1 FRAC 0
Water
Oil
Gas
Adsorbed Gas
0 mcf/acFT 300
Total Gas
0 mcf/acFT 300
Free Gas
0 mcf/acFT 300
CumTotalGas
0 MCF/AC 25000
CumFreeGas
0 MCF/AC 5000
Matrix Perm
0.0001 nD 1
NAS T
2400
DPI-2473-21
Cum Ads = 14994.9 Mcf/Ac
Cum Free = 408.8 Mcf/Ac
Cum Total = 15403.7 Mcf/Ac
GIP Ads = 1.2 Bcf/80 Acres
GIP Free = 0.03 Bcf/80 Acres
GIP Total = 1.2 Bcf/80 Acres
NAS B

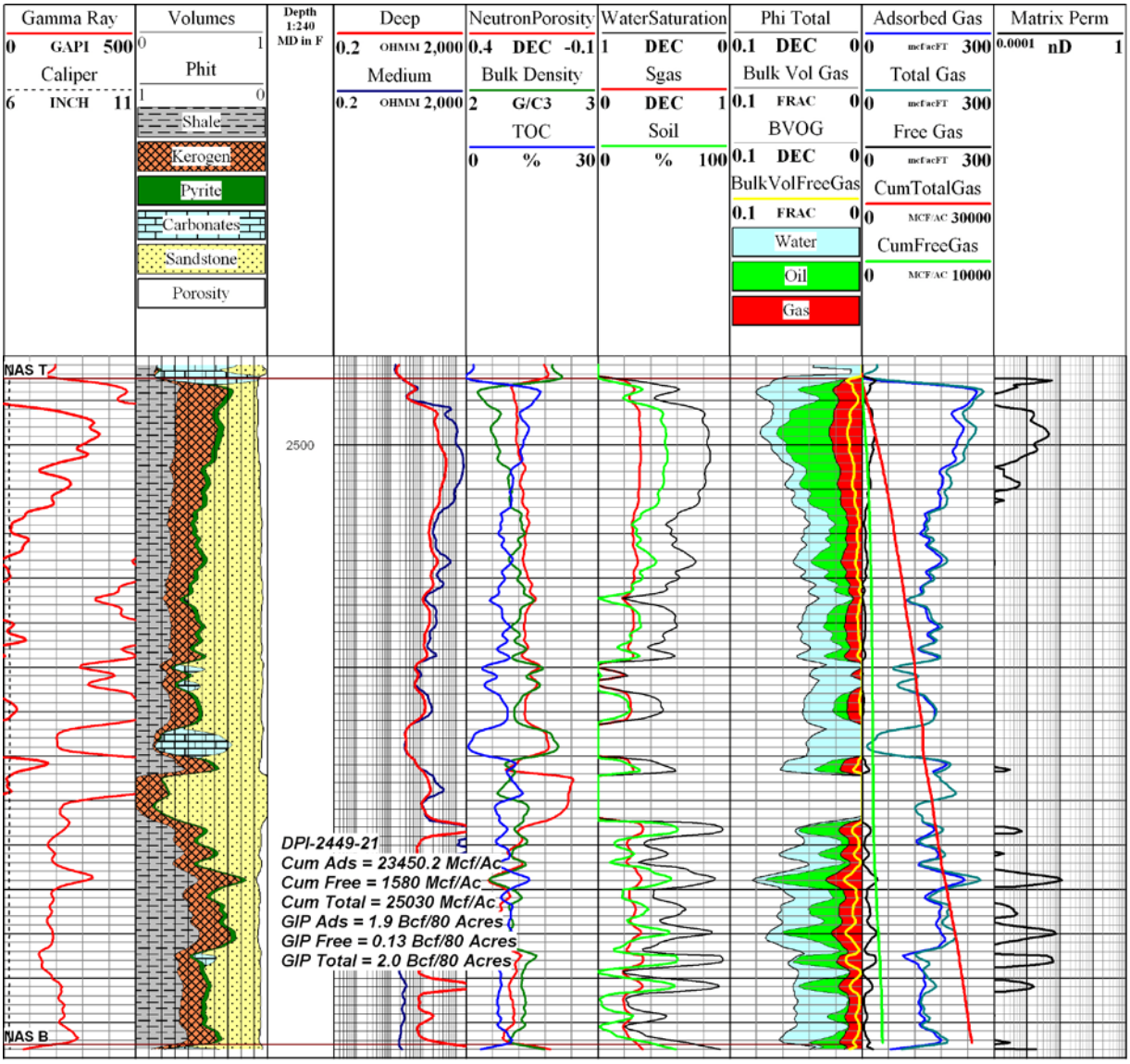

Gamma Ray
0 GAPI 500
Caliper
6 INCH 11
Volumes
0 1
Phit
1 0
Shale
Kerogen
Pyrite
Carbonates
Sandstone
Porosity
Depth 1:240 MD in F
Deep
0.2 OHMM 2,000
Medium
0.2 OHMM 2,000
NeutronPorosity
0.4 DEC -0.1
Bulk Density
2 G/C3 3
TOC
0 % 30
WaterSaturation
1 DEC 0
Sgas
0 DEC 1
Soil
0 % 100
Phi Total
0.1 DEC 0
Bulk Vol Gas
0.1 FRAC 0
BVOG
0.1 DEC 0
BulkVolFreeGas
0.1 FRAC 0
Water
Oil
Gas
Adsorbed Gas
0 mcf/acFT 300
Total Gas
0 mcf/acFT 300
Free Gas
0 mcf/acFT 300
CumTotalGas
0 MCF/AC 25000
CumFreeGas
0 MCF/AC 10000
Matrix Perm
0.0001 nD 1
NAS T
NAS B
2300
2400
DPI-2472-21
Cum Ads = 20716.8 Mcf/Ac
Cum Free = 1388.6 Mcf/Ac
Cum Total = 22105.4 Mcf/Ac
GIP Ads = 1.7 Bcf/80 Acres
GIP Free = 0.11 Bcf/80 Acres
GIP Total = 1.8 Bcf/80 Acres

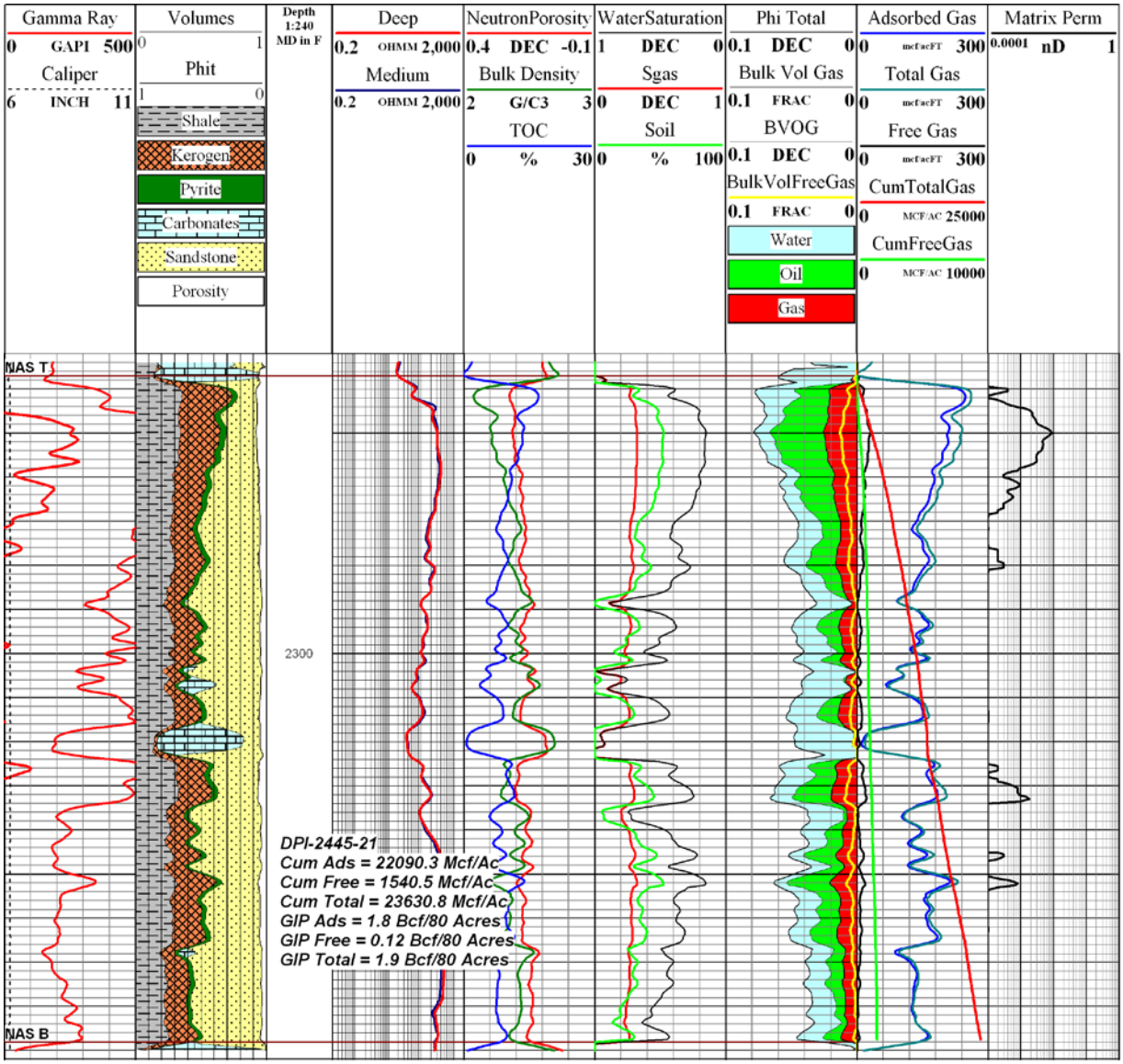

Gamma Ray
0 GAPI 500
Caliper
6 INCH 11
Volumes
0 1
Phit
1 0
Shale
Kerogen
Pyrite
Carbonates
Sandstone
Porosity
Depth 1:240 MD in F
Deep
0.2 OHMM 2,000
Medium
0.2 OHMM 2,000
NeutronPorosity
0.4 DEC -0.1
Bulk Density
2 G/C3 3
TOC
0 % 30
WaterSaturation
1 DEC 0
Sgas
0 DEC 1
Soil
0 % 100
Phi Total
0.1 DEC 0
Bulk Vol Gas
0.1 FRAC 0
BVOG
0.1 DEC 0
BulkVolFreeGas
0.1 FRAC 0
Water
Oil
Gas
Adsorbed Gas
0 mcf/acFT 300
Total Gas
0 mcf/acFT 300
Free Gas
0 mcf/acFT 300
CumTotalGas
0 MCF/AC 25000
CumFreeGas
0 MCF/AC 10000
Matrix Perm
0.0001 nD 1
NAS T
NAS B
2400
2500
DPI-2467-21
Cum Ads = 21177.6 Mcf/Ac
Cum Free = 1531.5 Mcf/Ac
Cum Total = 22709.1 Mcf/Ac
GIP Ads = 1.7 Bcf/80 Acres
GIP Free = 0.12 Bcf/80 Acres
GIP Total = 1.8 Bcf/80 Acres

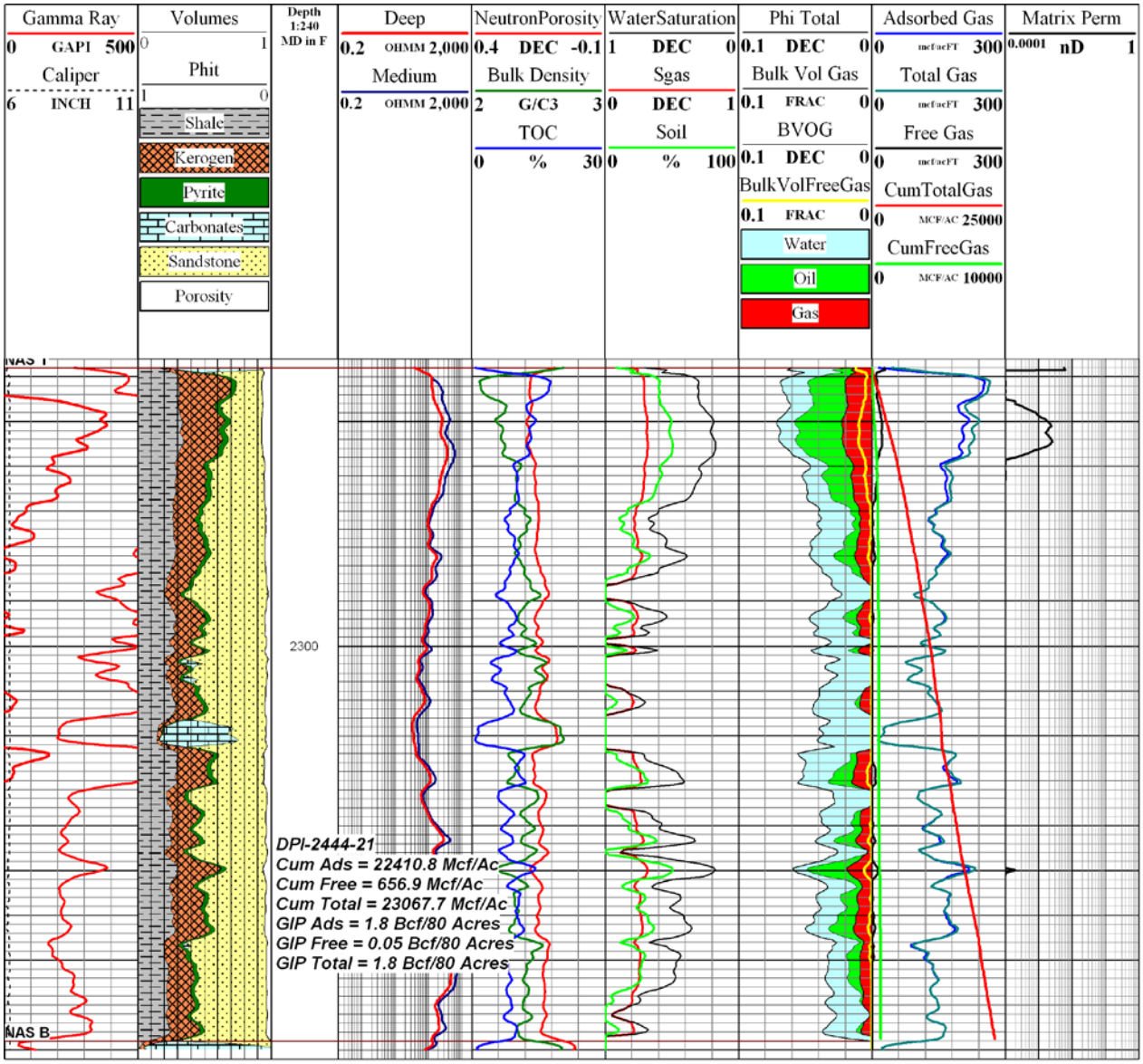

Gamma Ray
0 GAPI 500
Caliper
6 INCH 11
Volumes
0 1
Phit
1 0
Shale
Kerogen
Pyrite
Carbonates
Sandstone
Porosity
Depth
1:240
MD in F
Deep
0.2 OHMM 2,000
Medium
0.2 OHMM 2,000
NeutronPorosity
0.4 DEC -0.1
Bulk Density
2 G/C3 3
TOC
0 % 30
WaterSaturation
1 DEC 0
Sgas
0 DEC 1
Soil
0 % 100
Phi Total
0.1 DEC 0
Bulk Vol Gas
0.1 FRAC 0
BVOG
0.1 DEC 0
BulkVolFreeGas
0.1 FRAC 0
Water
Oil
Gas
Adsorbed Gas
0 mcf/acFT 300
Total Gas
0 mcf/acFT 300
Free Gas
0 mcf/acFT 300
CumTotalGas
0 MCF/AC 25000
CumFreeGas
0 MCF/AC 10000
Matrix Perm
0.0001 nD 1
NAS T
NAS B
2300
2400
DPI-2464-21
Cum Ads = 22004 Mcf/Ac
Cum Free = 1066.3 Mcf/Ac
Cum Total = 23070.3 Mcf/Ac
GIP Ads = 1.8 Bcf/80 Acres
GIP Free = 0.09 Bcf/80 Acres
GIP Total = 1.8 Bcf/80 Acres

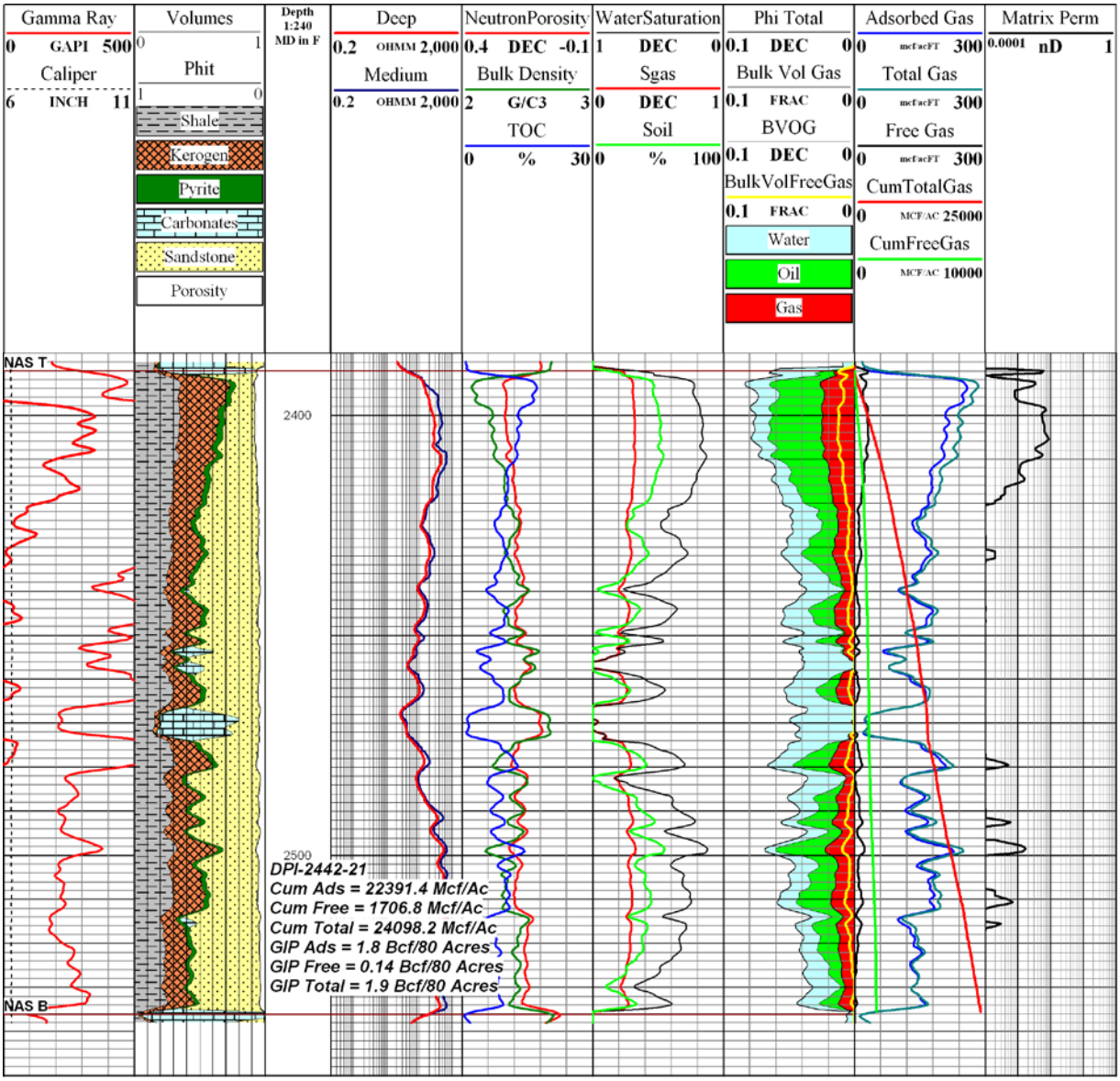

Gamma Ray
0 GAPI 500
Caliper
6 INCH 11
Volumes
0 1
Phit
1 0
Shale
Kerogen
Pyrite
Carbonates
Sandstone
Porosity
Depth 1:240 MD in F
Deep
0.2 OHMM 2,000
Medium
0.2 OHMM 2,000
NeutronPorosity
0.4 DEC -0.1
Bulk Density
2 G/C3 3
TOC
0 % 30
WaterSaturation
1 DEC 0
Sgas
0 DEC 1
Soil
0 % 100
Phi Total
0.1 DEC 0
Bulk Vol Gas
0.1 FRAC 0
BVOG
0.1 DEC 0
BulkVolFreeGas
0.1 FRAC 0
Water
Oil
Gas
Adsorbed Gas
0 mcf/acFT 300
Total Gas
0 mcf/acFT 300
Free Gas
0 mcf/acFT 300
CumTotalGas
0 MCF/AC 25000
CumFreeGas
0 MCF/AC 10000
Matrix Perm
0.0001 nD 1
NAS T
2300
DPI-2463-21
Cum Ads = 21132.8 Mcf/Ac
Cum Free = 1148.8 Mcf/Ac
Cum Total = 22281.6 Mcf/Ac
GIP Ads = 1.7 Bcf/80 Acres
GIP Free = 0.09 Bcf/80 Acres
GIP Total = 1.8 Bcf/80 Acres
NAS B

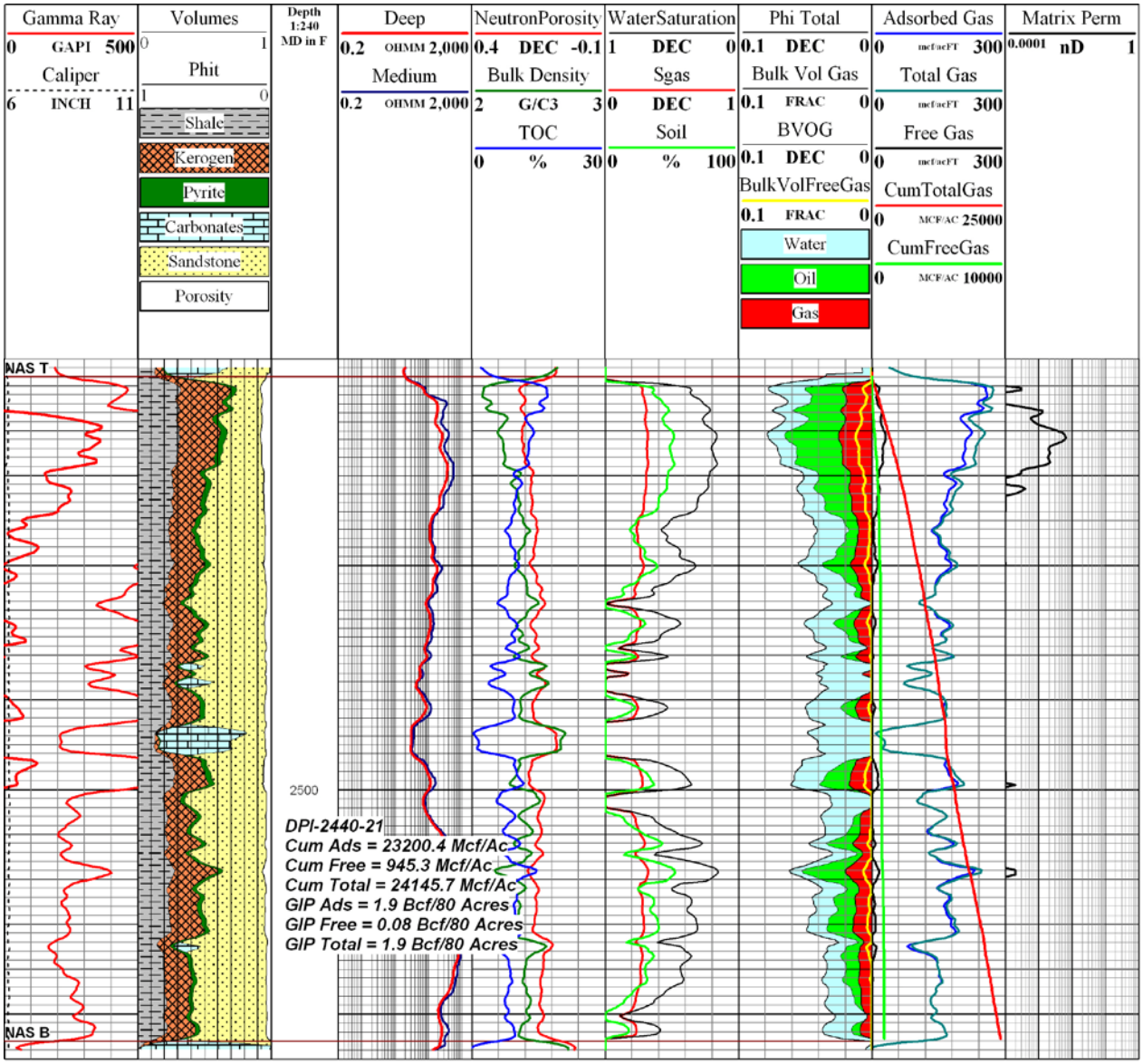

Gamma Ray
0 GAPI 500
Caliper
6 INCH 11
Volumes
0 1
Phit
1 0
Shale
Kerogen
Pyrite
Carbonates
Sandstone
Porosity
Depth 1:240 MD in F
Deep
0.2 OHMM 2,000
Medium
0.2 OHMM 2,000
NeutronPorosity
0.4 DEC -0.1
Bulk Density
2 G/C3 3
TOC
0 % 30
WaterSaturation
1 DEC 0
Sgas
0 DEC 1
Soil
0 % 100
Phi Total
0.1 DEC 0
Bulk Vol Gas
0.1 FRAC 0
BVOG
0.1 DEC 0
BulkVolFreeGas
0.1 FRAC 0
Water
Oil
Gas
Adsorbed Gas
0 mcf/acFT 300
Total Gas
0 mcf/acFT 300
Free Gas
0 mcf/acFT 300
CumTotalGas
0 MCF/AC 25000
CumFreeGas
0 MCF/AC 10000
Matrix Perm
0.0001 nD 1
NAS T
NAS B
2300
2400
DPI-2462-21
Cum Ads = 21652.7 Mcf/Ac
Cum Free = 1177.6 Mcf/Ac
Cum Total = 22830.3 Mcf/Ac
GIP Ads = 1.7 Bcf/80 Acres
GIP Free = 0.09 Bcf/80 Acres
GIP Total = 1.8 Bcf/80 Acres

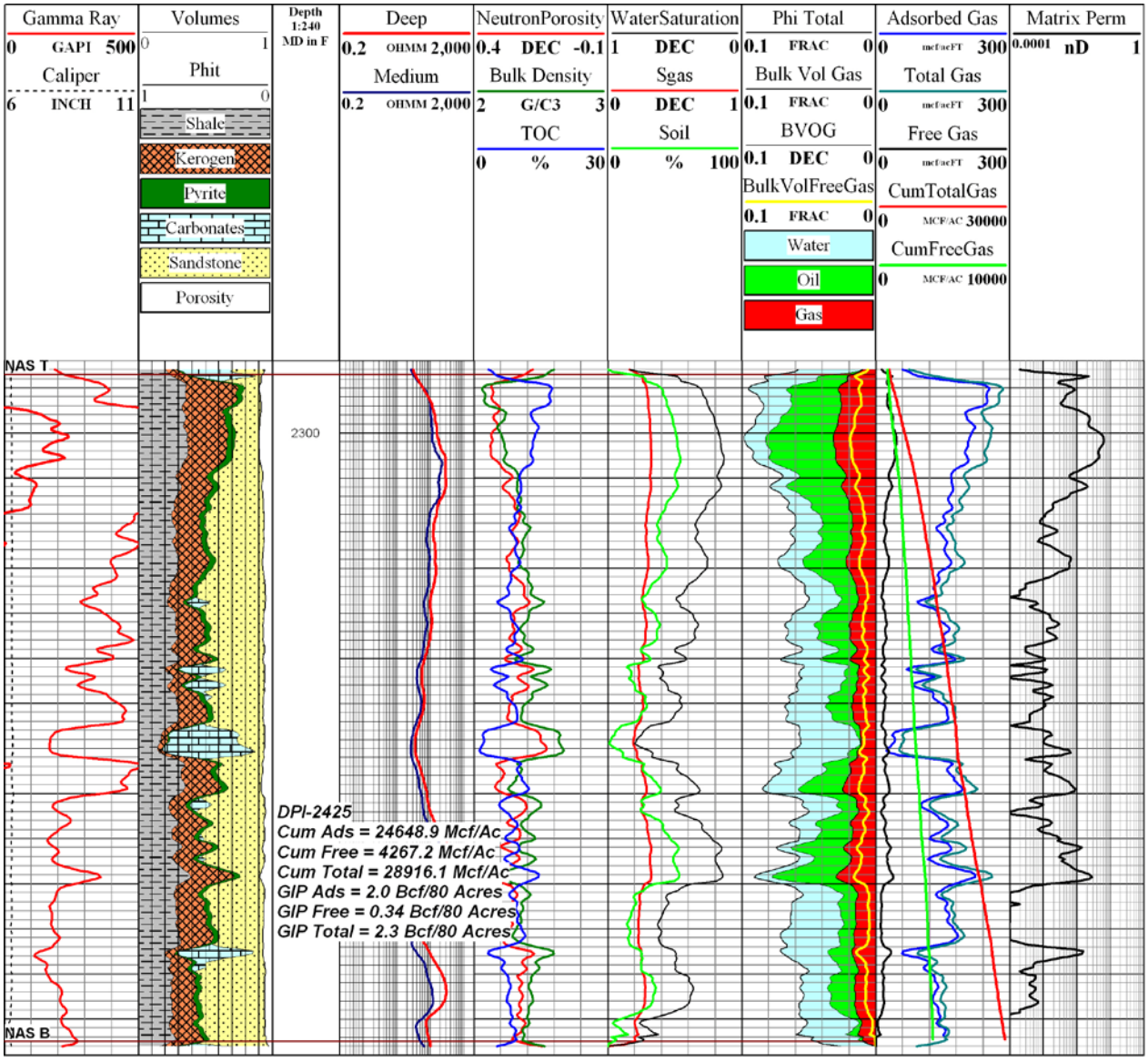

Gamma Ray
0 GAPI 500
Caliper
6 INCH 11
Volumes
0 1
Phit
1 0
Shale
Kerogen
Pyrite
Carbonates
Sandstone
Porosity
Depth 1:240 MD in F
Deep
0.2 OHMM 2,000
Medium
0.2 OHMM 2,000
NeutronPorosity
0.4 DEC -0.1
Bulk Density
2 G/C3 3
TOC
0 % 30
WaterSaturation
1 DEC 0
Sgas
0 DEC 1
Soil
0 % 100
Phi Total
0.1 DEC 0
Bulk Vol Gas
0.1 FRAC 0
BVOG
0.1 DEC 0
BulkVolFreeGas
0.1 FRAC 0
Water
Oil
Gas
Adsorbed Gas
0 mcf/acFT 300
Total Gas
0 mcf/acFT 300
Free Gas
0 mcf/acFT 300
CumTotalGas
0 MCF/AC 30000
CumFreeGas
0 MCF/AC 10000
Matrix Perm
0.0001 nD 1
NAS T
2500
DPI-2449-21
Cum Ads = 23450.2 Mcf/Ac
Cum Free = 1580 Mcf/Ac
Cum Total = 25030 Mcf/Ac
GIP Ads = 1.9 Bcf/80 Acres
GIP Free = 0.13 Bcf/80 Acres
GIP Total = 2.0 Bcf/80 Acres
NAS B

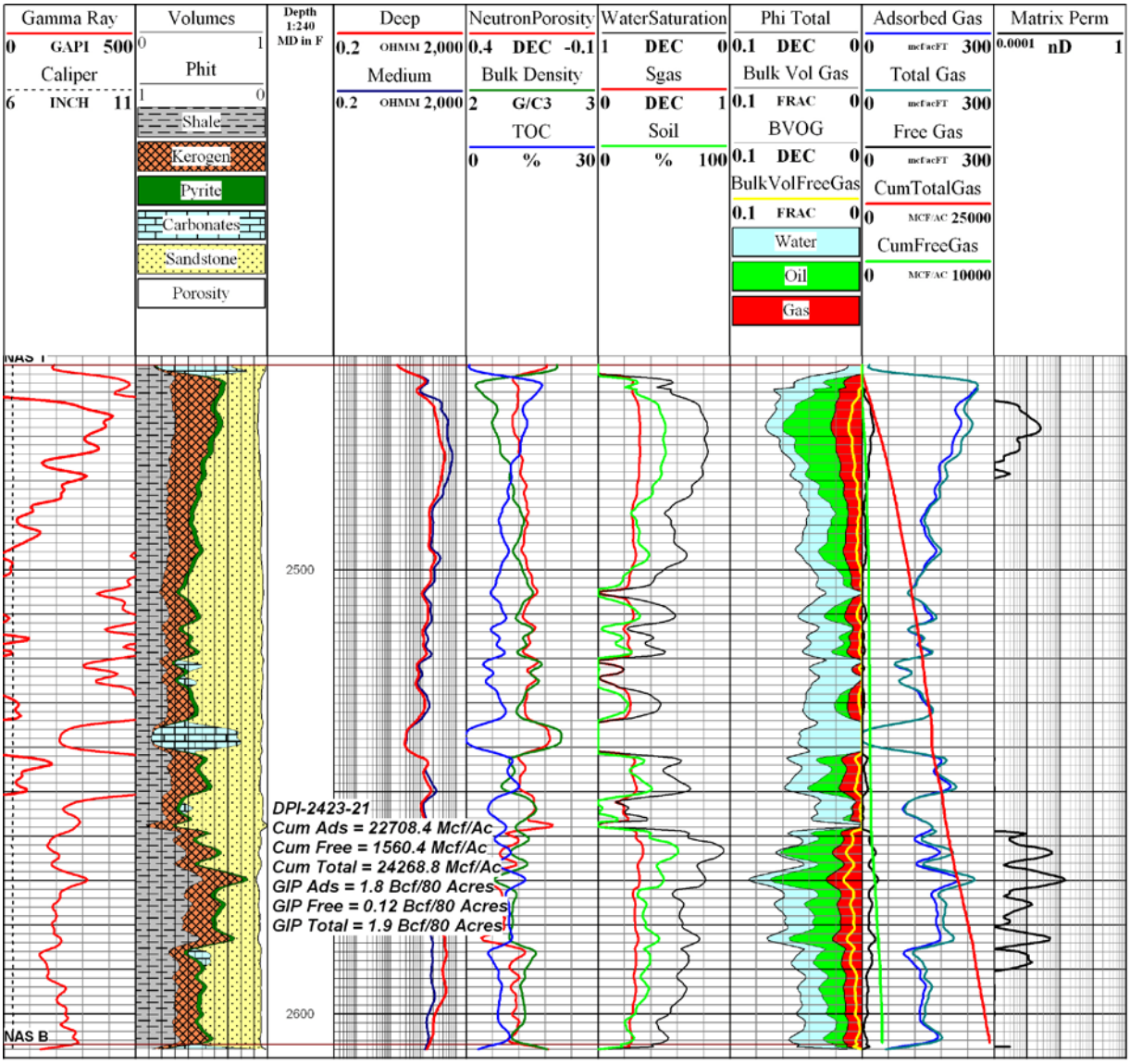

Gamma Ray
0 GAPI 500
Caliper
6 INCH 11
Volumes
0 1
Phit
1 0
Shale
Kerogen
Pyrite
Carbonates
Sandstone
Porosity
Depth
1:240
MD in F
Deep
0.2 OHMM 2,000
Medium
0.2 OHMM 2,000
NeutronPorosity
0.4 DEC -0.1
Bulk Density
2 G/C3 3
TOC
0 % 30
WaterSaturation
1 DEC 0
Sgas
0 DEC 1
Soil
0 % 100
Phi Total
0.1 DEC 0
Bulk Vol Gas
0.1 FRAC 0
BVOG
0.1 DEC 0
BulkVolFreeGas
0.1 FRAC 0
Water
Oil
Gas
Adsorbed Gas
0 mcf/acFT 300
Total Gas
0 mcf/acFT 300
Free Gas
0 mcf/acFT 300
CumTotalGas
0 MCF/AC 25000
CumFreeGas
0 MCF/AC 10000
Matrix Perm
0.0001 nD 1
NAS T
2300
NAS B
DPI-2445-21
Cum Ads = 22090.3 Mcf/Ac
Cum Free = 1540.5 Mcf/Ac
Cum Total = 23630.8 Mcf/Ac
GIP Ads = 1.8 Bcf/80 Acres
GIP Free = 0.12 Bcf/80 Acres
GIP Total = 1.9 Bcf/80 Acres

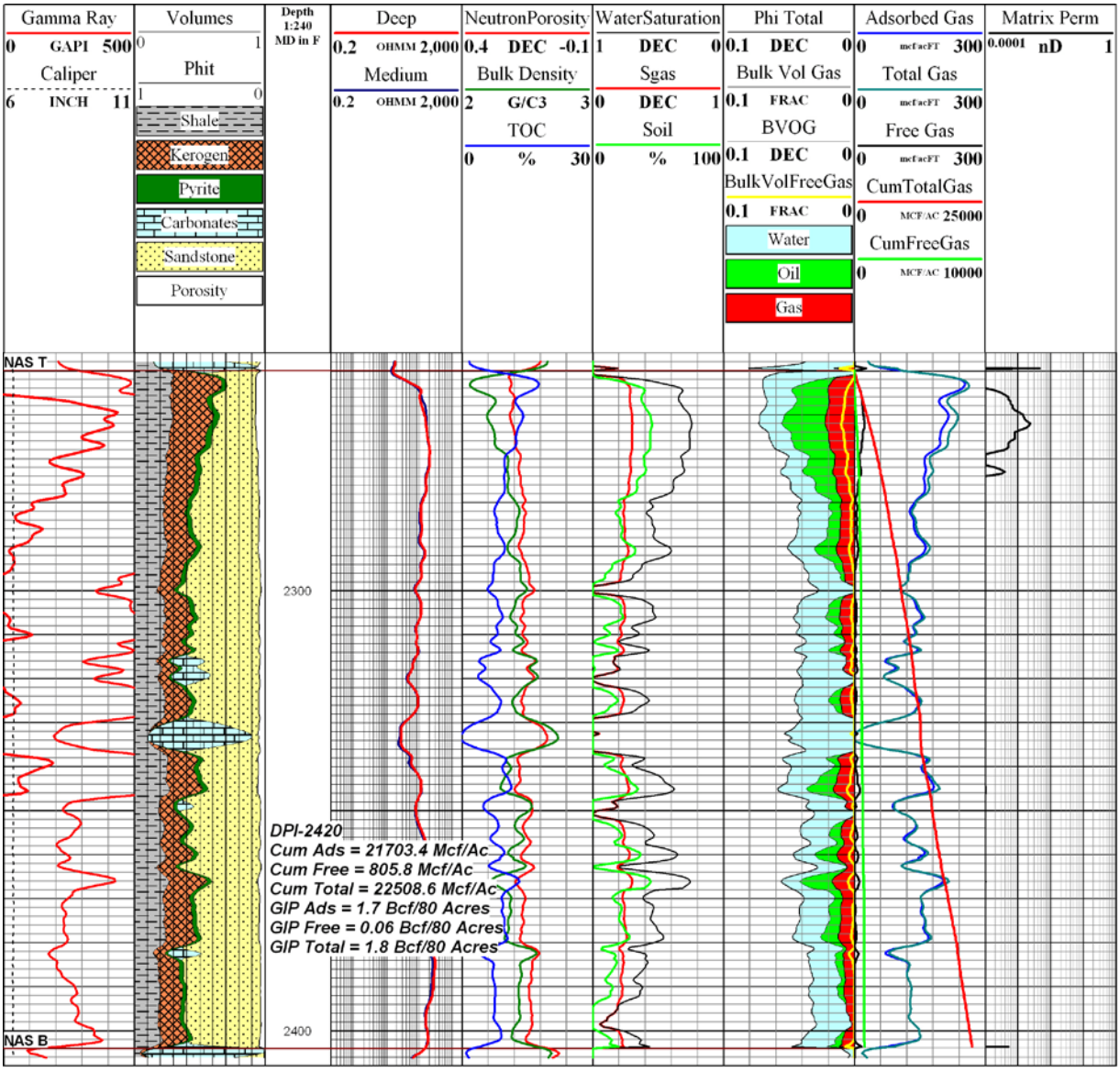

Gamma Ray
0 GAPI 500
Caliper
6 INCH 11
Volumes
0 1
Phit
1 0
Shale
Kerogen
Pyrite
Carbonates
Sandstone
Porosity
Depth 1:240 MD in F
Deep
0.2 OHMM 2,000
Medium
0.2 OHMM 2,000
NeutronPorosity
0.4 DEC -0.1
Bulk Density
2 G/C3 3
TOC
0 % 30
WaterSaturation
1 DEC 0
Sgas
0 DEC 1
Soil
0 % 100
Phi Total
0.1 DEC 0
Bulk Vol Gas
0.1 FRAC 0
BVOG
0.1 DEC 0
BulkVolFreeGas
0.1 FRAC 0
Water
Oil
Gas
Adsorbed Gas
0 mcf/acFT 300
Total Gas
0 mcf/acFT 300
Free Gas
0 mcf/acFT 300
CumTotalGas
0 MCF/AC 25000
CumFreeGas
0 MCF/AC 10000
Matrix Perm
0.0001 nD 1
2300
DPI-2444-21
Cum Ads = 22410.8 Mcf/Ac
Cum Free = 656.9 Mcf/Ac
Cum Total = 23067.7 Mcf/Ac
GIP Ads = 1.8 Bcf/80 Acres
GIP Free = 0.05 Bcf/80 Acres
GIP Total = 1.8 Bcf/80 Acres
NAS B

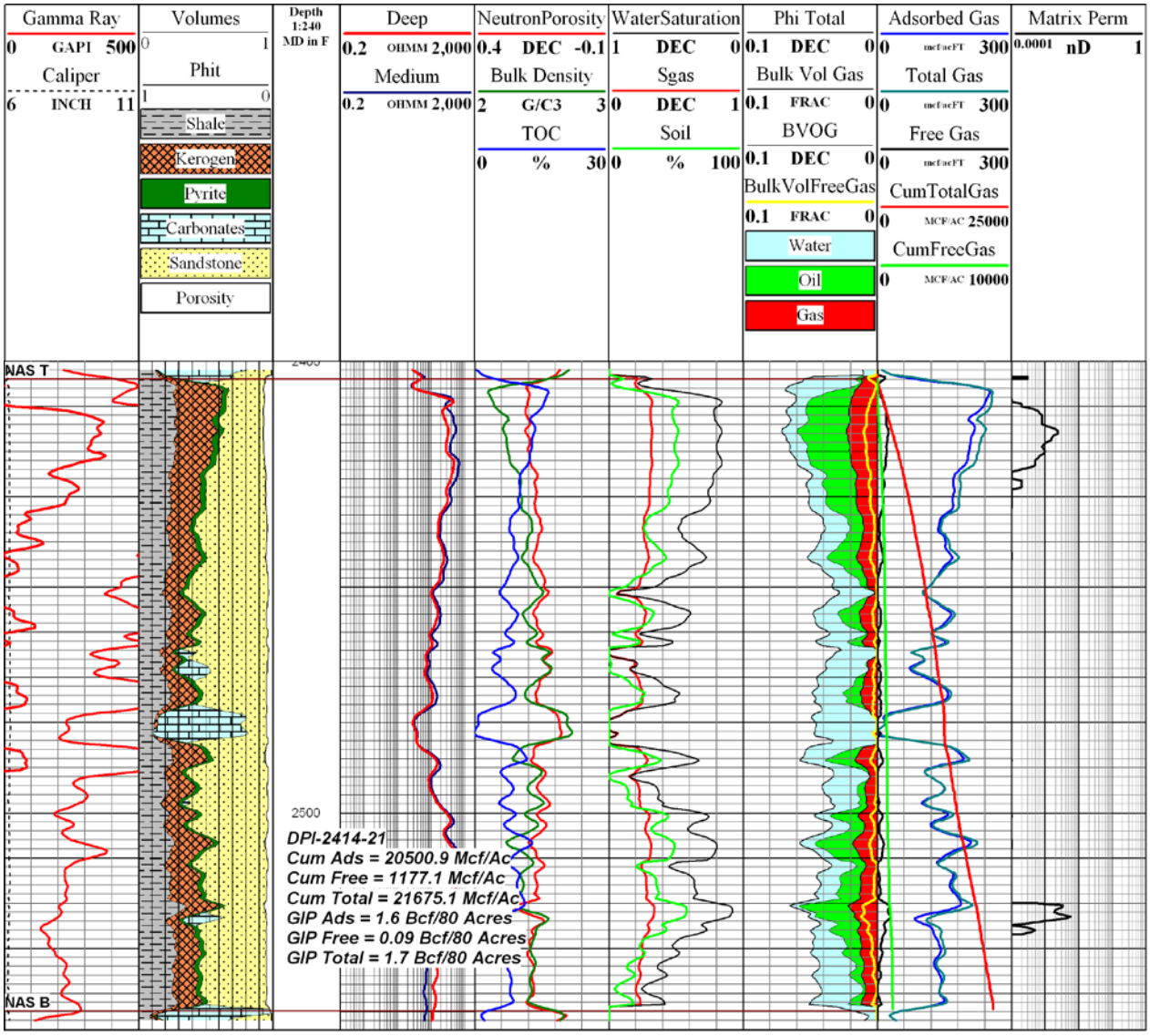

Gamma Ray
0 GAPI 500
Caliper
6 INCH 11
Volumes
0 1
Phit
1 0
Shale
Kerogen
Pyrite
Carbonates
Sandstone
Porosity
Depth 1:240 MD in F
Deep
0.2 OHMM 2,000
Medium
0.2 OHMM 2,000
NeutronPorosity
0.4 DEC -0.1
Bulk Density
2 G/C3 3
TOC
0 % 30
WaterSaturation
1 DEC 0
Sgas
0 DEC 1
Soil
0 % 100
Phi Total
0.1 DEC 0
Bulk Vol Gas
0.1 FRAC 0
BVOG
0.1 DEC 0
BulkVolFreeGas
0.1 FRAC 0
Water
Oil
Gas
Adsorbed Gas
0 mcf/acFT 300
Total Gas
0 mcf/acFT 300
Free Gas
0 mcf/acFT 300
CumTotalGas
0 MCF/AC 25000
CumFreeGas
0 MCF/AC 10000
Matrix Perm
0.0001 nD 1
NAS T
2400
2500
DPI-2442-21
Cum Ads = 22391.4 Mcf/Ac
Cum Free = 1706.8 Mcf/Ac
Cum Total = 24098.2 Mcf/Ac
GIP Ads = 1.8 Bcf/80 Acres
GIP Free = 0.14 Bcf/80 Acres
GIP Total = 1.9 Bcf/80 Acres
NAS B

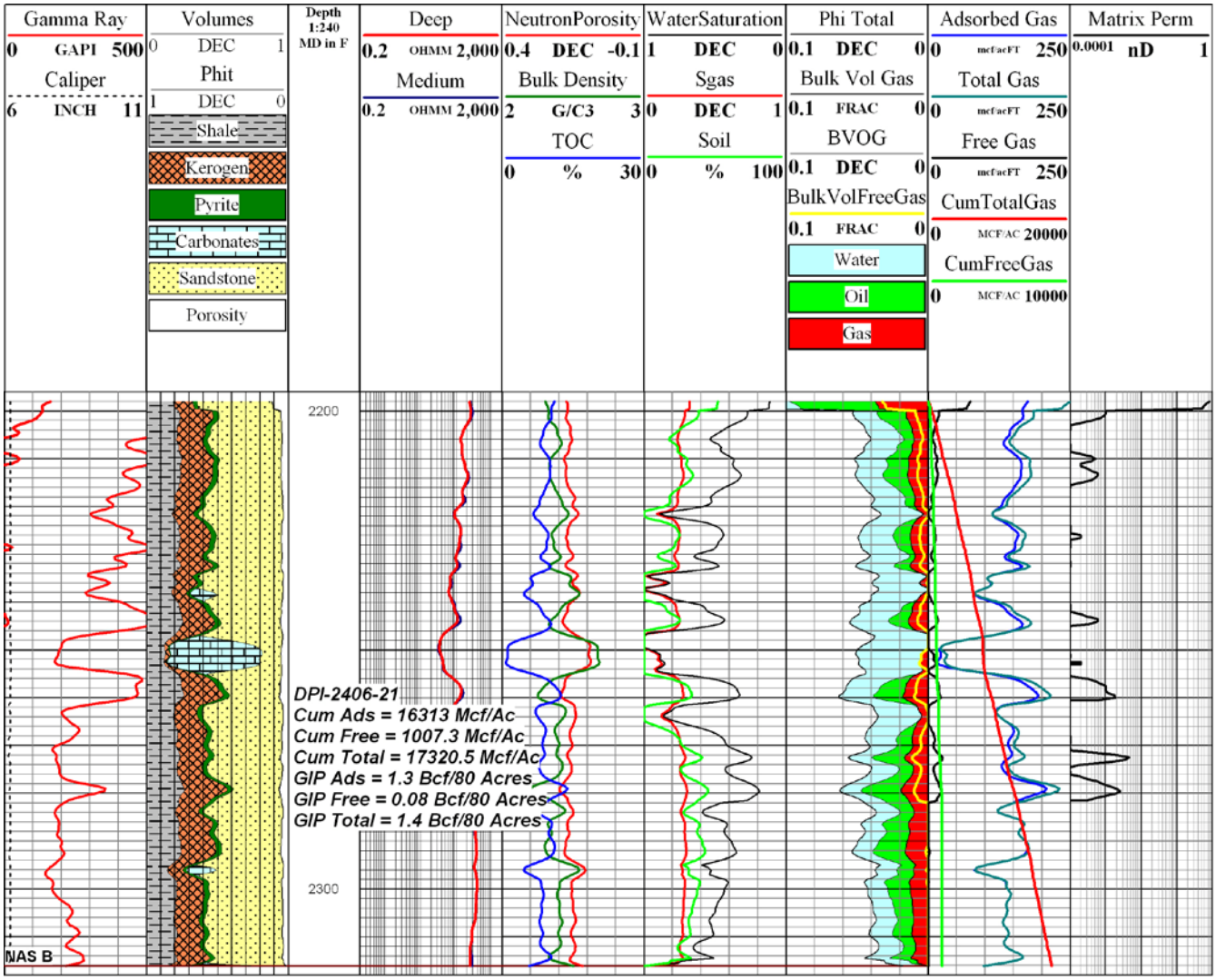

Gamma Ray
0 GAPI 500
Caliper
6 INCH 11
Volumes
0 1
Phit
1 0
Shale
Kerogen
Pyrite
Carbonates
Sandstone
Porosity
Depth 1:240 MD in F
Deep
0.2 OHMM 2,000
Medium
0.2 OHMM 2,000
NeutronPorosity
0.4 DEC -0.1
Bulk Density
2 G/C3 3
TOC
0 % 30
WaterSaturation
1 DEC 0
Sgas
0 DEC 1
Soil
0 % 100
Phi Total
0.1 DEC 0
Bulk Vol Gas
0.1 FRAC 0
BVOG
0.1 DEC 0
BulkVolFreeGas
0.1 FRAC 0
Water
Oil
Gas
Adsorbed Gas
0 mcf/acFT 300
Total Gas
0 mcf/acFT 300
Free Gas
0 mcf/acFT 300
CumTotalGas
0 MCF/AC 25000
CumFreeGas
0 MCF/AC 10000
Matrix Perm
0.0001 nD 1
NAS T
NAS B
2500
DPI-2440-21
Cum Ads = 23200.4 Mcf/Ac
Cum Free = 945.3 Mcf/Ac
Cum Total = 24145.7 Mcf/Ac
GIP Ads = 1.9 Bcf/80 Acres
GIP Free = 0.08 Bcf/80 Acres
GIP Total = 1.9 Bcf/80 Acres

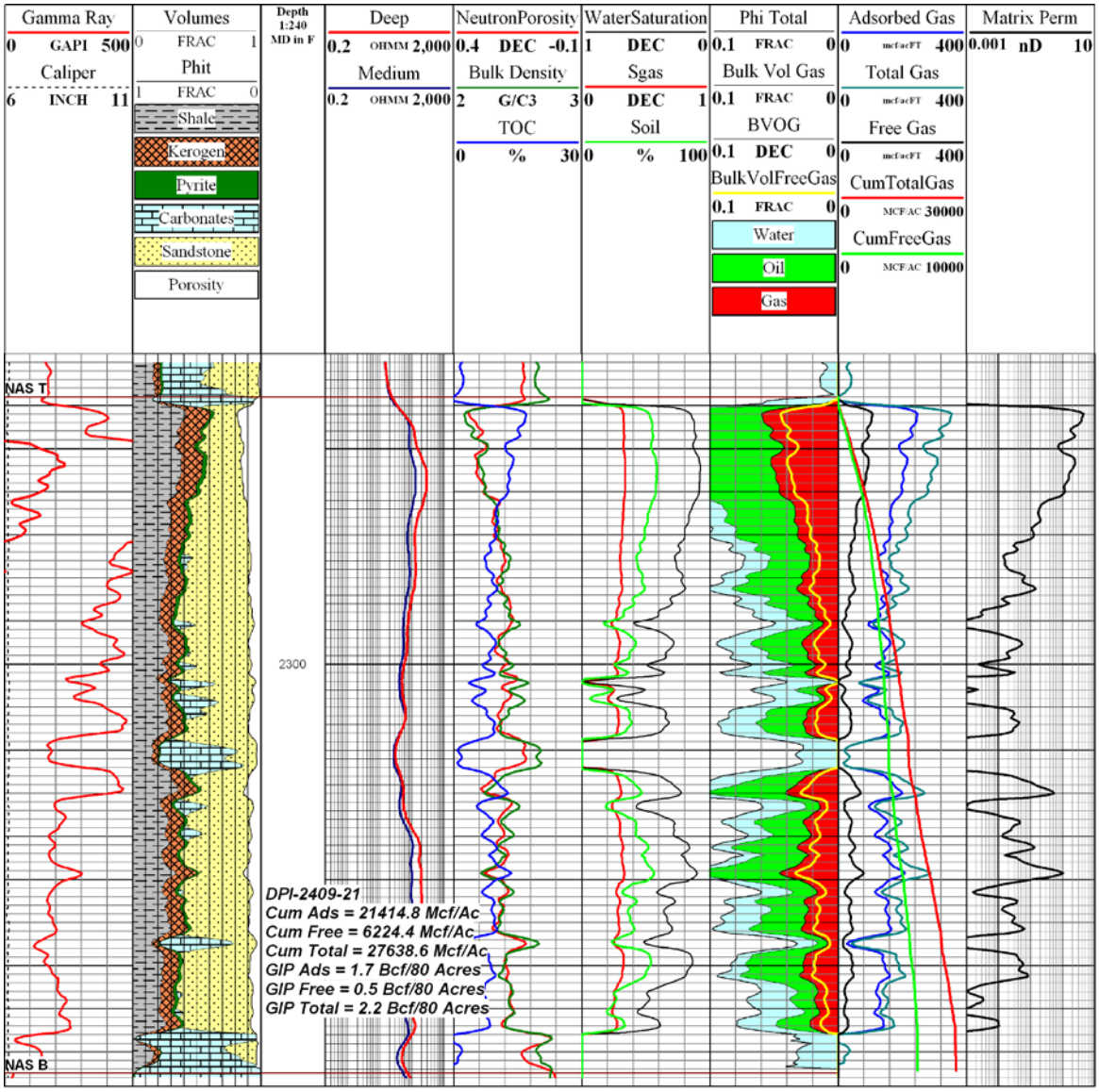

Gamma Ray
0 GAPI 500
Caliper
6 INCH 11
Volumes
0 1
Phit
1 0
Shale
Kerogen
Pyrite
Carbonates
Sandstone
Porosity
Depth 1:240 MD in F
Deep
0.2 OHMM 2,000
Medium
0.2 OHMM 2,000
NeutronPorosity
0.4 DEC -0.1
Bulk Density
2 G/C3 3
TOC
0 % 30
WaterSaturation
1 DEC 0
Sgas
0 DEC 1
Soil
0 % 100
Phi Total
0.1 FRAC 0
Bulk Vol Gas
0.1 FRAC 0
BVOG
0.1 DEC 0
BulkVolFreeGas
0.1 FRAC 0
Water
Oil
Gas
Adsorbed Gas
0 mcf/acFT 300
Total Gas
0 mcf/acFT 300
Free Gas
0 mcf/acFT 300
CumTotalGas
0 MCF/AC 30000
CumFreeGas
0 MCF/AC 10000
Matrix Perm
0.0001 nD 1
NAS T
2300
DPI-2425
Cum Ads = 24648.9 Mcf/Ac
Cum Free = 4267.2 Mcf/Ac
Cum Total = 28916.1 Mcf/Ac
GIP Ads = 2.0 Bcf/80 Acres
GIP Free = 0.34 Bcf/80 Acres
GIP Total = 2.3 Bcf/80 Acres
NAS B


Gamma Ray
0 GAPI 500
Caliper
6 INCH 11
Volumes
0 1
Phit
1 0
Shale
Kerogen
Pyrite
Carbonates
Sandstone
Porosity
Depth 1:240 MD in F
Deep
0.2 OHMM 2,000
Medium
0.2 OHMM 2,000
NeutronPorosity
0.4 DEC -0.1
Bulk Density
2 G/C3 3
TOC
0 % 30
WaterSaturation
1 DEC 0
Sgas
0 DEC 1
Soil
0 % 100
Phi Total
0.1 DEC 0
Bulk Vol Gas
0.1 FRAC 0
BVOG
0.1 DEC 0
BulkVolFreeGas
0.1 FRAC 0
Water
Oil
Gas
Adsorbed Gas
0 mcf/acFT 300
Total Gas
0 mcf/acFT 300
Free Gas
0 mcf/acFT 300
CumTotalGas
0 MCF/AC 25000
CumFreeGas
0 MCF/AC 10000
Matrix Perm
0.0001 nD 1
NAS T
2500
DPI-2423-21
Cum Ads = 22708.4 Mcf/Ac
Cum Free = 1560.4 Mcf/Ac
Cum Total = 24268.8 Mcf/Ac
GIP Ads = 1.8 Bcf/80 Acres
GIP Free = 0.12 Bcf/80 Acres
GIP Total = 1.9 Bcf/80 Acres
2600
NAS B


Gamma Ray
0 GAPI 500
Caliper
6 INCH 11
Volumes
0 1
Phit
1 0
Shale
Kerogen
Pyrite
Carbonates
Sandstone
Porosity
Depth
1:240
MD in F
Deep
0.2 OHMM 2,000
Medium
0.2 OHMM 2,000
NeutronPorosity
0.4 DEC -0.1
Bulk Density
2 G/C3 3
TOC
0 % 30
WaterSaturation
1 DEC 0
Sgas
0 DEC 1
Soil
0 % 100
Phi Total
0.1 DEC 0
Bulk Vol Gas
0.1 FRAC 0
BVOG
0.1 DEC 0
BulkVolFreeGas
0.1 FRAC 0
Water
Oil
Gas
Adsorbed Gas
0 mcf/acFT 300
Total Gas
0 mcf/acFT 300
Free Gas
0 mcf/acFT 300
CumTotalGas
0 MCF/AC 25000
CumFreeGas
0 MCF/AC 10000
Matrix Perm
0.0001 nD 1
NAS T
2300
DPI-2420
Cum Ads = 21703.4 Mcf/Ac
Cum Free = 805.8 Mcf/Ac
Cum Total = 22508.6 Mcf/Ac
GIP Ads = 1.7 Bcf/80 Acres
GIP Free = 0.06 Bcf/80 Acres
GIP Total = 1.8 Bcf/80 Acres
2400
NAS B


Gamma Ray
0 GAPI 500
Caliper
6 INCH 11
Volumes
0 1
Phit
1 0
Shale
Kerogen
Pyrite
Carbonates
Sandstone
Porosity
Depth 1:240 MD in F
Deep
0.2 OHMM 2,000
Medium
0.2 OHMM 2,000
NeutronPorosity
0.4 DEC -0.1
Bulk Density
2 G/C3 3
TOC
0 % 30
WaterSaturation
1 DEC 0
Sgas
0 DEC 1
Soil
0 % 100
Phi Total
0.1 DEC 0
Bulk Vol Gas
0.1 FRAC 0
BVOG
0.1 DEC 0
BulkVolFreeGas
0.1 FRAC 0
Water
Oil
Gas
Adsorbed Gas
0 mcf/acFT 300
Total Gas
0 mcf/acFT 300
Free Gas
0 mcf/acFT 300
CumTotalGas
0 MCF/AC 25000
CumFreeGas
0 MCF/AC 10000
Matrix Perm
0.0001 nD 1
NAS T
2500
DPI-2414-21
Cum Ads = 20500.9 Mcf/Ac
Cum Free = 1177.1 Mcf/Ac
Cum Total = 21675.1 Mcf/Ac
GIP Ads = 1.6 Bcf/80 Acres
GIP Free = 0.09 Bcf/80 Acres
GIP Total = 1.7 Bcf/80 Acres
NAS B


Gamma Ray
0 GAPI 500
Caliper
6 INCH 11
Volumes
0 DEC 1
Phit
1 DEC 0
Shale
Kerogen
Pyrite
Carbonates
Sandstone
Porosity
Depth 1:240 MD in F
Deep
0.2 OHMM 2,000
Medium
0.2 OHMM 2,000
NeutronPorosity
0.4 DEC -0.1
Bulk Density
2 G/C3 3
TOC
0 % 30
WaterSaturation
1 DEC 0
Sgas
0 DEC 1
Soil
0 % 100
Phi Total
0.1 DEC 0
Bulk Vol Gas
0.1 FRAC 0
BVOG
0.1 DEC 0
BulkVolFreeGas
0.1 FRAC 0
Water
Oil
Gas
Adsorbed Gas
0 mcf/acFT 250
Total Gas
0 mcf/acFT 250
Free Gas
0 mcf/acFT 250
CumTotalGas
0 MCF/AC 20000
CumFreeGas
0 MCF/AC 10000
Matrix Perm
0.0001 nD 1
2200
DPI-2406-21
Cum Ads = 16313 Mcf/Ac
Cum Free = 1007.3 Mcf/Ac
Cum Total = 17320.5 Mcf/Ac
GIP Ads = 1.3 Bcf/80 Acres
GIP Free = 0.08 Bcf/80 Acres
GIP Total = 1.4 Bcf/80 Acres
2300
NAS B


Gamma Ray
0 GAPI 500
Caliper
6 INCH 11
Volumes
0 FRAC 1
Phit
1 FRAC 0
Shale
Kerogen
Pyrite
Carbonates
Sandstone
Porosity
Depth 1:240 MD in F
Deep
0.2 OHMM 2,000
Medium
0.2 OHMM 2,000
NeutronPorosity
0.4 DEC -0.1
Bulk Density
2 G/C3 3
TOC
0 % 30
WaterSaturation
1 DEC 0
Sgas
0 DEC 1
Soil
0 % 100
Phi Total
0.1 FRAC 0
Bulk Vol Gas
0.1 FRAC 0
BVOG
0.1 DEC 0
BulkVolFreeGas
0.1 FRAC 0
Water
Oil
Gas
Adsorbed Gas
0 mcf/acFT 400
Total Gas
0 mcf/acFT 400
Free Gas
0 mcf/acFT 400
CumTotalGas
0 MCF/AC 30000
CumFreeGas
0 MCF/AC 10000
Matrix Perm
0.001 nD 10
NAS T
NAS B
2300
DPI-2409-21
Cum Ads = 21414.8 Mcf/Ac
Cum Free = 6224.4 Mcf/Ac
Cum Total = 27638.6 Mcf/Ac
GIP Ads = 1.7 Bcf/80 Acres
GIP Free = 0.5 Bcf/80 Acres
GIP Total = 2.2 Bcf/80 Acres

SECTION 6

HYDRAULIC FRACTURING

6.1

FRACTURE MODELING

NUMERICAL INVESTIGATION OF INTERACTION BETWEEN

HYDRAULIC FRACTURES AND NATURAL FRACTURES

ABSTRACT

Hydraulic fracturing of a naturally-fractured reservoir is a great challenge for industry, as fractures can have complex growth pattern when propagating in systems of natural fractures in the reservoir. Fracture propagation near a natural fracture (NF) considering interaction between a hydraulic fracture (HF) and a pre-existing NF is investigated comprehensively by using a two dimensional Displacement Discontinuity Method (DDM) in this thesis.

The rock is first considered as an elastic impermeable medium, and then pore pressure and poroelastic stresses are considered. A uniform pressure fluid model and a Newtonian fluid flow model are used to calculate the fluid flow, fluid pressure and width distribution along the fracture. Joint elements are implemented to describe different NF contact modes (stick, slip, and open mode). The structural criterion is used for predicting the direction and mode of fracture propagation.

The numerical model was used to first examine the mechanical response of the NF to predict potential reactivation of the NF and the resultant probable location for fracture re-initiation. Results demonstrate that:

- Before HF reaches a NF, the possibility of fracture re-initiation across the NF and with an offset is enhanced when the NF is weak.

- During the stage of fluid infiltration along the NF, a maximum tensile stress peak can be generated at the end of the opening zone along the NF ahead of the fluid front.
- Poroelastic effects, arising from fluid diffusion into the rock deformation can induce closure and compressive stress at the center of the NF ahead of the HF tip before HF arrival. Upon coalescence when fluid flows along the NF, the poroelastic effects tend to reduce the value of HF aperture and this decrease the tension peak and the possibility of fracture re-initiation with time.

Next, HF trajectories near a NF were examined prior to coalesce with the NF using different joint, rock and fluid properties. Analysis shows that:

- Fracture trajectories near a NF may bend and deviate from the direction of the maximum horizontal stress when using a joint model that includes initial joint deformation.
- Fractures propagating with higher injection rate or fracturing fluid of higher viscosity propagate longer distance when turning to the direction of maximum horizontal stress.
- Fracture trajectories are less dependent on injection rate or fluid viscosity when using a joint model that includes initial joint deformation; whereas they are more dominated by injection rate and fluid viscosity when using a joint model that excludes initial joint deformation.

ACKNOWLEDGEMENTS

Support from RPSEA (through GTI), DOE, and Crisman Institute of Texas A&M University is appreciated.

TABLE OF CONTENTS

Page

ABSTRACT iv

LIST OF TABLES xiii

1 INTRODUCTION 1

1.1 Hydraulic Fracturing 1
1.2 Hydraulic Fracture Modeling 1
1.3 Interaction of Hydraulic Fractures and Natural Fractures 7
1.4 Research Objectives 10
1.5 Sign Convention 11

2 MODEL SETUP 12

2.1 Constant Displacement Discontinuity Method 12
2.2 Crack Tip Element 14
2.3 Fracture Propagation Scheme 15
2.4 Newtonian Fluid Flow Within the Hydraulic Fracture 19

3 MODEL VERIFICATION 24

3.1 Evaluation of SIF 24
3.2 Fracture Propagation (Elastic Case) 33

4 JOINT ELEMENT 38

4.1 Joint Element 38
4.2 Numerical Procedure 49
4.3 Numerical Examples 51

5 HYDRAULIC FRACTURE AND NATURAL FRACTURE INTERACTION 62

5.1 Introduction 62
5.2 Mechanical Responses of a Natural Fracture 62
5.3 Hydraulic Fracture Trajectories Near a Natural Fracture 85
5.4 Hydraulic Fracture Propagation by Using Newtonian Fluid Flow 93

6 SUMMARY AND CONCLUSIONS 102

6.1 Summary 102
6.2 Conclusions 103

NOMENCLATURE 105

LIST OF FIGURES

Page

Fig. 1.1 Mode I, Mode II, and Mode III cracks (Wikipedia). 5

Fig. 2.1 Constant displacement discontinuity components over a line segment. 12

Fig. 2.2 Special crack tip displacement discontinuity at the left crack tip. 15

Fig. 2.3 Structural criterion: average stress over the segment *d* (length of FPZ) in the small vicinity of the crack tip (after Dobroskok et al. 2005). 17

Fig. 2.4 Stress state in the vicinity of the crack tip. 19

Fig. 2.5 Geometry for a plane strain fracture and the fluid flow within the fracture. 19

Fig. 3.1 SIF calculated based on the stresses ahead of the crack tip. 25

Fig. 3.2 A slanted pressurized crack under biaxial stresses in an infinite elastic medium. 26

Fig. 3.3 A fracture process zone (Gdoutos 2005) 30

Fig. 3.4 Fracture trajectories calculated with different *d* for a slanted pressurized crack under biaxial stresses in an infinite elastic medium. 32

Fig. 3.5 An initially straight pressurized crack under biaxial stresses. 33

Fig. 3.6 Crack trajectories under different internal pressures. 34

Fig. 3.7 Crack trajectories under different maximum horizontal stresses. 35

Fig. 3.8 A line crack under uniaxial stress in an infinite elastic medium. 36

Fig. 3.9 Crack growth under uniaxial stress in an infinite elastic medium. 37

Fig. 4.1 Representation of an elastic joint element (a) normal stiffness; (b) shear stiffness. 38

Fig. 4.2 Mohr diagram for a MC joint element under different contact mode under different stress conditions. 44

Fig. 4.3 Compression of a single joint. 51

Fig. 4.4 Shear and normal displacement (D_s, D_n) along the joint surface (initial joint deformation included) 52

Fig. 4.5 Shear and normal stress along the joint surface (initial joint deformation included) 52

Fig. 4.6 Shear and normal displacement (D_s, D_n) along the joint surface (initial joint deformation not included). 54

Fig. 4.7 Shear and normal stress along the joint surface (initial joint deformation not included). 54

Fig. 4.8 A slanted joint under biaxial stresses. 55

Fig. 4.9 Shear and normal displacement (D_s , D_n) along the joint surface. 56

Fig. 4.10 Shear and normal stress along the joint surface. 56

Fig. 4.11 Shear of a single joint. 57

Fig. 4.12 Normal and shear displacement (D_n, D_s) along a joint surface under plastic deformation. 58

Fig. 4.13 Normal and shear stress along a joint surface under plastic deformation. 58

Fig. 4.14 A rectangular opening subjected to far-field compressive stress. 59

Fig. 4.15 Dimensionless normal displacements at y=0 using joint element solution. 60

Fig.4.16 Dimensionless normal stresses at y=0 obtained using joint element solution. 60

Fig. 5.1 A hydraulic fracture located near a natural fracture. 62

Fig. 5.2 Stress distribution along a weak joint (at x=0, d_0=0.1m, θ=90°). 66

Fig. 5.3 Normal and shear displacement (D_n, D_s) along a weak joint (at x=0, d_0=0.1m, θ=90°). 66

Fig. 5.4 Maximum tensile stress along a weak joint (x=0) at different tip distances (d_0) (θ=90°). 67

Fig. 5.5 Stress distribution along a strong joint (at x=0, d_0=0.1m, θ=90°). 68

Fig. 5.6 Normal and shear displacement (D_n, D_s) along a strong joint (at x=0, d_0=0.1m, θ=90°). 68

Fig. 5.7 Maximum tensile stress along a strong joint (x=0) at different tip distances (d_0) (θ=90°). 69

Fig. 5.8 Stress distribution along a moderate joint (at x=0, d_0=0.1m, θ=90°)..... 71

Fig. 5.9 Normal and shear displacement (D_n, D_s) along a moderate joint (at x=0, d_0=0.1m, θ=90°). 71

Fig. 5.10 Maximum tensile stress along a moderate joint (x=0) at different tip distances (d_0) (θ=90°). 72

Fig. 5.11 Sketch of mesh arrangement for the NF and HF. Dashed part of the NF is negligible in the interaction between HF and NF, and therefore can be omitted in the modeling. 73

Fig. 5.12 Normalized normal/shear displacements (d_n, d_s) along the NF (x=0)..... 76

Fig. 5.13 Normalized values of normal stress (s_n), shear stress (s_t), and maximum tensile stress (s_p) along NF (x=0). 76

Fig. 5.14 Normalized maximum tensile stress along NF (x=0) at different fluid invaded lengths of NF (b) (p=3.0MPa). 78

Fig. 5.15 Normalized normal displacement (d_n) along NF (x=0) at different fluid infiltrated lengths of NF (b) (p=3.0MPa). 78

Fig. 5.16 Normalized maximum tensile stress along NF (x=0) at different fluid pressures (p) (b=0.2). 80

Fig. 5.17 Distribution of normal displacement (D_n) along a moderate joint (x=0) at different time (t) considering poroelastic effects (d_0=0.1m, θ=90°). 81

Fig. 5.18 Distribution of normal stress along a moderate joint (x=0) at different time (t) considering poroelastic effects (d_0=0.1m, θ=90°). 81

Fig. 5.19 Distribution of maximum tensile stress along a moderate joint (x=0) at different time (t) considering poroelastic effects (d_0=0.1m, θ=90°). 82

Fig. 5.20 Normalized maximum tensile stress along NF at different fluid invaded lengths along NF (b) and time (t) considering poroelastic effects (p=3.0MPa, C_f=6.16×10^{-6}). 84

Fig. 5.21 Normalized maximum tensile stress along NF at different fluid invaded lengths along NF (b) and time (t) considering poroelastic effects (p=3.0MPa, C_f=6.16×10^{-5}). 84

Fig. 5.22 A HF propagating towards a NF. 85

Fig. 5.23 Deflection of HFs at different orientation angles (α) when propagating towards a NF. 87

Fig. 5.24 Fracture trajectories propagating under biaxial stresses without the presence of a NF for HF at different slant angles (α). 88

Fig. 5.25 Fracture trajectories under different net pressures (Δp). 89

Fig. 5.26 Fracture trajectories under different distances from fracture tip to NF. 90

Fig. 5.27 Fracture trajectories under different far-field stress differences (Δs). 91

Fig. 5.28 Trajectories of HF propagating towards a NF at different slant angles (α). 92

Fig. 5.29 An initially straight pressurized crack under biaxial stresses. 93

Fig. 5.30 Fracture trajectories under different fluid injection rates (q) at the wellbore (μ=1.0cp). 94

Fig. 5.31 Fracture trajectories under different fluid viscosities (μ) (q=1.0bbl/min). 95

Fig. 5.32 Fracture trajectories for HF propagating under biaxial stresses at different slant angles (α) using Newtonian fluid flow model. 96

Fig. 5.33 Fluid pressure at the wellbore (x=0) with time by using Newtonian fluid model for HF at different slant angles (α). 97

Fig. 5.34 Deflection of HFs at different orientation angles (α) when propagating towards a NF simulated by using a joint model that includes initial deformation and a Newtonian fluid model. 98

Fig. 5.35 Deflection of HFs at different orientation angles (α) when propagating towards a NF simulated by using a joint model that excludes initial deformation and a Newtonian fluid model. 99

Fig. 5.36 Deflection of HF (α=30˚) under different injection rates at the wellbore (q) when propagating towards a NF simulated by using a joint model that includes initial deformation and a Newtonian fluid model. 100

Fig. 5.37 Deflection of HF (α=30˚) under different injection rates at the wellbore (q) when propagating towards a NF simulated by using a joint model that excludes initial deformation and a Newtonian fluid model. 101

LIST OF TABLES

Page

Table 2.1 Different possibility, mode and direction of crack propagation (Dobroskok et al. 2005)..... 18

Table 3.1 SIFs calculated by using DDs and stresses 27

Table 3.2 SIFs calculated based on DDs..... 28

Table 3.3 Input parameters in Section 3.2.1..... 33

Table 5.1 Input parameters in Section 5.2.2..... 64

Table 5.2 Input parameters in Section 5.2.3..... 74

Table 5.3 Input parameters in Section 5.2.4..... 77

Table 5.4 Input parameters in Section 5.3..... 86

Table 5.5 Input parameters for simulating a HF using Newtonian fluid model..... 94

1 INTRODUCTION

1.1 Hydraulic Fracturing

Hydraulic fracturing is a process by which a fracture initiates and propagates in response to hydraulic loading (i.e., pressure applied by a fluid) of the wellbore wall, and the fracture. Fracturing of oil and gas reservoirs by mixing viscous hydraulic fluids and sorted proppant is a technique widely used in the petroleum industry to enhance the recovery of oil and gas from underground hydrocarbon reservoirs. Other applications include (but are not limited to) heat extraction from geothermal reservoirs, fault reactivation in mining and the measurement of in situ stress.

1.2 Hydraulic Fracture Modeling

Numerous analytical and numerical models have been developed to simulate hydraulic fracturing. The early efforts focused on analytical solutions for fractures of simple geometry, either straight in plane strain or penny-shaped (Geertsma and de Klerk 1969; Khristianovic and Zheltov 1955; Nordgren 1972; Perkins and Kern 1961; Sneddon 1946). All these solutions are approximate, and they contain strong simplifications in relation to either the opening or the pressure field within the crack. In recent years, research efforts have been directed towards the development of numerical algorithms to model the propagation of hydraulic fractures in rocks characterized by different mechanical properties and/or in-situ stresses, and natural discontinuities.

This thesis follows the style of *SPE Journal.*

Hydraulic fracturing is a complicated and challenging process to model, as it involves the coupling of at least three components:

1) Mechanical deformation in rock induced by the fluid pressure on fracture surface
2) Fluid flow within the fracture
3) Fracture propagation in the rock formation.

In the following sections, the modeling consideration of these three components is discussed in detail.

1.2.1 Reservoir Rock

In most current models, the mechanical deformation in the rock mass due to the fluid pressure on the fracture surfaces is assumed to be linear elastic. However, many natural substances such as rocks and soils are porous and their matrix is permeated by a fluid such as liquid or gas. Usually both solid matrix and the pore network (pore space) are assumed to be continuous and form two interpenetrating continua. Porous media whose solid matrix/fluid system behaves linearly under applied loads is called poroelastic.

The theory of poroelasticity was introduced by Biot in 1941. Biot's equations of the linear theory of poroelasticity are derived from: Equations of linear elasticity for the solid matrix; Navier–Stokes equations for the viscous fluid; Darcy's law for the fluid flow through the porous matrix. The coupled poroelastic effects of the deformation of fluid-saturated porous media can be summarized as follows (Vandamme et al. 1989):

- Volumetric variations caused by changes in pore pressure: an increase of the pore pressure can induce a volumetric expansion of the porous rock
- Pore pressure variations due to changes in mean stress: pore pressure is increased from the application of a confining pressure if the fluid is prevented from escaping (undrained condition)
- The sensitivity of the volumetric response of the rock to the rate of loading: the rock stiffness ranges from K_u (undrained bulk modulus) to K (drained bulk modulus), depending on the loading rate. In fast loading, the fluid has not enough time to dissipate so the rock is undrained and appears stiffer.

The poroelastic effects, which arise from coupling of the fluid flow and rock deformation, are mostly ignored in the previous fracture modeling. The inherent assumptions are that the time scale of the problem (diffusion) is such that poroelastic effects have not had time to develop and that the magnitude of the effect is small enough to be neglected (Boone et al. 1991). However, in many instances, such as injection into highly permeable sands or naturally fractured reservoirs, there is large leakoff into the formation during fracturing treatment so that poroelastic effects of significant magnitude can develop and need be considered. The poroelastic influences of neighboring producing/inject well can create a heterogeneous stress field in the reservoir, and cause a hydraulic fracture to propagate deviating from its expected path of propagation (perpendicular to the minimum far-field compressive stress) (Berchenko and Detournay 1997). Also, pore pressure diffusion can decrease the effective stress in natural fractures promoting slip.

The influences of coupled poroelastic processes on fracture opening have also been addressed previously (Detournay and Cheng 1991; Ghassemi and Zhang 2006; Vandamme et al. 1989). It has been shown that poroelastic effects could cause the crack opening to decrease with time and that the opening and closure of the crack in response to poroelastic loads would have a corresponding influence on the stress intensity factor (SIF) at the crack tip. Therefore, it is of interest to simulate fracture propagation considering poroelastic effects of the host rock.

A few analytical procedures have been developed and used to solve the poroelastic effects on fracture propagation (Huang and Russell 1985; Ruina 1978). However, these analytical approaches are limited in solving many practical problems. Researchers have been continuing the efforts in developing various robust numerical methods such as the Boundary Element Method (BEM) (Crouch and Starfield 1983; Dong and de Pater 2001; Yan 2004) and the Finite Element Method (FEM) to solve crack problems. In terms of computational resources, BEM is more efficient than other methods, including FEM, for crack problems where surface/volume ratio is small, as in the BEM one only needs to construct a "mesh" over the modeled surface.

The displacement discontinuity (DD) method lends itself nicely to solving problems involving injection/production using hydraulically induced or natural fractures and provides for more flexibility. The square root crack tip element (Yan 2004) in the 2D real DD method greatly improves the accuracy of evaluation of stress/displacement and the SIF at the crack tip. In our present work, the 2D real DD BEM is used to model fracture deformation and propagation considering poroelastic effects of the rock.

1.2.2 Fluid Flow Within the Fracture

Although actual fluids used for hydraulic fracturing treatments have very complicated rheologies, such as viscoelasticity, usually the fluid flow within the fracture is modeled using relatively simple model. Typical underlying assumptions include: the fracturing fluid has a uniform pressure distribution inside the fracture; the fracturing fluid is an incompressible Newtonian fluid such that the pressure gradient within the fracture is related to the flow rate and the fracture width governed by the Poiseuille's Law (Batchelor 1967); the fracturing fluid can be approximated by a power-law model. In our current study both assumptions of constant pressure distribution and Newtonian fluid are used as our focus is stimulation of unconventional gas reservoirs that are mostly treated with water.

1.2.3 Fracture Propagation

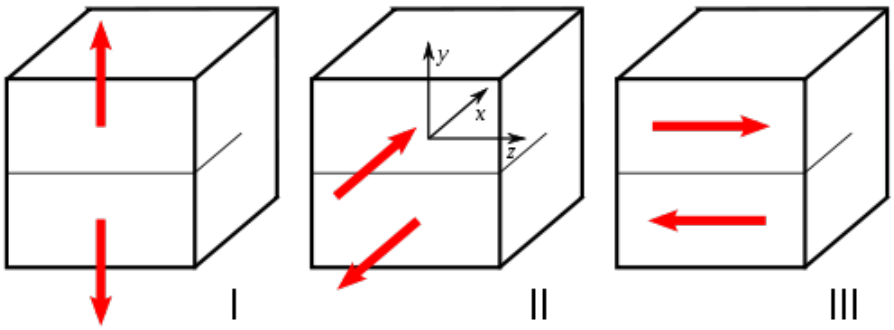


Fig. 1.1 Mode I, Mode II, and Mode III cracks (Wikipedia).

There are three different basic modes of fracture propagation as shown in **Fig. 1.1.** Mode I is opening or tensile mode, where the crack surfaces move apart in a direction perpendicular to the surfaces. Mode II is sliding or in-plane shear mode, where the crack surfaces slide over one another in a direction perpendicular to the leading edge of the crack. Mode III is tearing or antiplane shear mode, where the crack surfaces move relative to one another in a direction parallel to the leading edge of the crack.

The fracture propagation process is mostly modeled using linear elastic fracture mechanics (LEFM) theory, which assumes that the material is isotropic and linear elastic. Based on this assumption, the stress field near the crack tip is calculated using the theory of elasticity. LEFM is valid only when the zone of inelastic deformation at the crack tip is small compared to the size of the crack. The criterion of fracture propagation is mostly given by the maximum tangential tensile stress approach, conventional energy-release rate approach or stress intensity factor (SIF) approach.

The model we used here differs from those of previous studies in that it includes a more flexible crack initiation and propagation criterion - structural criterion (Dobroskok et al. 2005). This criterion is a unified criterion capable of predicting both Mode I (tensile, opening) and Mode II (sliding, shear) fracture propagation. Since Griffith's (1924) paper on fracture of brittle materials, immense literature has appeared on this subject. Most of these works have focused on Mode I propagation. And most previous hydraulic fracture propagation model were based on Mode I or mixed-mode propagation, without considering the possibility of Mode II propagation. However, in many cases in rock mechanics, Mode II propagation may prevail, or appear at some

stage of crack growth. The importance of Mode II crack propagation in rock can be found in literature using both analytical (Bobet and Einstein 1998; Rao et al. 2003) and numerical (Bobet 2001; Tang et al. 2001) approaches.

1.3 Interaction of Hydraulic Fractures and Natural Fractures

The increased interest in exploration and production of low permeability reservoirs makes the design and evaluation of hydraulic fracturing treatments in these reservoirs a new challenge for industry. Many of the low permeability gas reservoirs, such as gas-bearing shales, and methane-bearing coals, are usually found crisscrossed by one more or sets of natural fractures where fracture can grow in a complicated manner.

Under these circumstances, it is often found that the fracturing fluid and proppant can reopen and flow through the pre-existing fractures, as well as create new fractures in the rock (Fisher et al. 2002). Also, shear stresses accumulated in the rock mass (due to the natural anisotropy of stresses and the presence of discontinuities such as natural fractures and faults) tend to be released during a treatment, triggering shear slippage along the discontinuities (Warpinski et al. 2004).

The problem of induced and natural fracture interaction has been the subject of many theoretical (Potluri et al. 2005), experimental/analytical (Blanton 1982; Warpinski and Teufel 1987), and numerical (Cooke and Underwood 2001; Koshelev and Ghassemi 2003; Thiercelin and Makkhyu 2007; Wu et al. 2004; Zhang and Jeffrey 2006) studies.

Blanton (1982) presented a simple analytical fracture interaction criterion relating differential stress and angle of interaction to extrapolate the lab results to field simulations. Warpinski and Teufel (1987) derived a fracture interaction criterion to

predict whether the hydraulic fracture causes a shear slippage on the natural fracture plane causing arrest of the propagating fracture or dilates the natural fracture leading to excessive leakoff. Renshaw and Pollard (1995) provided a criterion for crack behavior that is near and orthogonal to un-bonded interfaces.

Potluri et al. (2005) reviewed various fracture interaction criteria and presented a systematic criteria for different types of fracture propagation modes near natural fractures, based on the conditions of differential stress, angle of intersection, and fracture toughness, and pressure drop within the natural fractures. However, these analytical attempts, the in-situ stress along the natural discontinuities were assumed not to have been affected by the hydraulic fracture, i.e., the mechanical interactions between the hydraulic fracture and the natural fracture were not considered.

Cooke and Underwood (2001) investigated the local sliding, de-bonding and the subsequent opening along bedding contacts using a Displacement Discontinuity (DD) method to study the probable fracture intersection modes with natural bedding contacts. The bedding contacts they considered were sliding-only interfaces, opening-only interfaces, and both sliding and opening interfaces. However the fracture considered in their study is far-field tension stress driven instead of fluid driven.

Koshelev and Ghassemi (2003) simulated the trajectory of a hydraulically driven crack near natural fractures, and interface between two inhomogeneous blocks using the complex variable hypersingular boundary element method (BEM). They demonstrated that natural fractures and other inhomogeneities can generate unstable fracture configurations under different initial crack inclination, loading, and geometry. But the

pressure distribution along the hydraulic fracture was assumed to be constant and fluid flow remained to be solved in their simulated process.

Wu et al. (2004) studied fracture behavior crossing a bi-material interface. They used Griffith type global fracture criterion with anisotropic specific fracture energy, in addition to conventional mass and energy balances. The basic assumption in their study that fluid within the fracture follows a uniform pressure and that the interface is welded and no-slipping remained to be improved.

Zhang et al. (2006) considered fluid flow in the hydraulic fracture and obtained the resulting pressure distribution as it intersected the natural fracture and examined the conditions for further fracture propagation. The rock formation was modeled as an impermeable homogeneous elastic medium, and the fluid was modeled as an incompressible, Newtonian fluid injected at a constant rate. The frictional stress on the surfaces of pre-existing fractures was assumed to obey the Coulomb law. The DD method and the finite difference method were employed to deal with this coupling mechanism of rock fracture and fluid flow.

Thiercelin and Makkhyu (2007) presented a semi-analytical model based on the dislocation theory to predict the reactivation of a natural fault with an approaching hydraulic fracture. They assumed that re-initiation occurs prior to fracture touching the interface. They analyzed the maximum tensile stress on the opposite side of the natural fractures to determine the most probable location of fracture re-initiation. However, the influence of natural fracture reactivation on the change of in-situ stress and the resultant change of fracture response and interaction mode were not considered.

As a result of the complex nature of the problem, these investigations have been limited to the case of one HF approaching a single joint. The results have shown that the fracture patterns that can occur for hydraulically induced fractures propagating near natural fractures can be complex, and are determined by the state of stress in the neighborhood of the intersection and joint material properties. Generally, four types of interaction have been recognized using the 2D plain strain studies; a hydraulic fracture can across the natural fracture without changing direction or it can be terminated by the natural fracture, it can propagate along the natural fracture, or reinitiate across the with an offset or jog (Zhang and Jeffrey 2006).

Despite their limitations, numerical modeling has become an indispensable tool for researchers to obtain a more complete picture of the detailed process of fracture propagation near natural discontinuities.

Hydraulic fracture growth behavior in a naturally-fracture rock differs greatly from that of an intact rock. Models that can couple fluid flow, rock deformation, frictional and opening behavior of the natural interface and fracture propagation mechanics are needed to allow estimation of the stimulated volume when fracturing unconventional energy resources. Often, the model ought to consider poroelastic the effects of pore fluid diffusion on rock deformation to better understand the pressure history recorded during stimulation jobs.

1.4 Research Objectives

The main objectives of this study are:

- To study the interaction between a hydraulic fracture and a natural fracture. To study (via a parametric analysis) the effect of the model input parameters, such as rock, joint, and fluid properties, on the stresses/displacements distribution and the possible slipping/opening along the joint. To observe the general behavior of natural fractures and hydraulic fractures.
- To model the process of hydraulic fracture tip approaching pre-existing natural fractures. To quantify the orientation and extension of the stimulated fracture.

1.5 Sign Convention

In rock mechanics, compressive stresses are generally considered as positive for the convenience of engineering use. In this thesis, in order to be consistent with the rock mechanics literature, all equations are presented using the *compression positive convention*. This sign convention is adopted for the remainder of this thesis. However, in Chapter 5, a *tension positive sign convention* is used as the maximum tensile stress along the NF is of interest and is checked.

2 MODEL SETUP

2.1 Constant Displacement Discontinuity Method

Consider a line crack over a line segment $|x| \le a, y = 0$ in an infinite elastic material. There is a constant displacement discontinuity when crossing over the crack, which can be defined as (Crouch and Starfield 1983):

$$\begin{aligned} D_x &= u_x(x,0_-) - u_x(x,0_+) \\ D_y &= u_y(x,0_-) - u_y(x,0_+) \end{aligned} \quad \text{..... (2.1)}$$

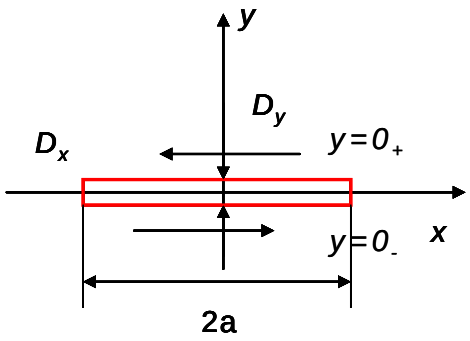


Fig. 2.1 Constant displacement discontinuity components over a line segment.

The displacements and stresses at a point (x,y) due to the constant displacement discontinuity D_x, D_y over the line segment are given by Crouch (1983):

$$\begin{aligned} u_x &= D_x\left[2(1-\nu) f_{,y} - y f_{,xx}\right] + D_y\left[-(1-2\nu) f_{,x} - y f_{,xy}\right] \\ u_y &= D_x\left[(1-2\nu) f_{,x} - y f_{,xy}\right] + D_y\left[2(1-\nu) f_{,y} - y f_{,yy}\right] \end{aligned} \quad \text{..... (2.2)}$$

$$\sigma_{xx} = 2GD_x\left[2f_{,xy} + yf_{,xyy}\right] + 2GD_y\left[f_{,yy} + yf_{,yyy}\right]$$
$$\sigma_{yy} = 2GD_x\left[-yf_{,xyy} + yf_{,xyy}\right] + 2GD_y\left[f_{,yy} - yf_{,yyy}\right] \quad \text{..... (2.3)}$$
$$\sigma_{xy} = 2GD_x\left[f_{,yy} + yf_{,yyy}\right] + 2GD_y\left[-yf_{,xyy}\right]$$

where

$$f(x,y) = -\frac{1}{4\pi(1-\nu)}[y(\arctan\frac{y}{x-a} - \arctan\frac{y}{x+a}) - \quad \text{..... (2.4)}$$
$$(x-a)In\sqrt{(x-a)^2+y^2} + (x+a)In\sqrt{(x+a)^2+y^2}]$$

Knowing the analytical solution for a single, constant elemental displacement discontinuity (DD), we can find the numerical solution to any problem by discretizing a curved crack with enough elements and by summing the effects of all N elements. The discretized form of displacement discontinuity equation can be formed as (Crouch and Starfield 1983):

$$\overset{i}{\sigma}_s = \sum_{j=1}^{N} \overset{ij}{A}_{ss}\overset{j}{D}_s + \sum_{j=1}^{N} \overset{ij}{A}_{sn}\overset{j}{D}_n$$
$$\overset{i}{\sigma}_n = \sum_{j=1}^{N} \overset{ij}{A}_{ns}\overset{j}{D}_n + \sum_{j=1}^{N} \overset{ij}{A}_{nn}\overset{j}{D}_n \quad \text{..... (2.5)}$$

, and

$$\overset{i}{u}_s = \sum_{j=1}^{N} \overset{ij}{B}_{ss}\overset{j}{D}_s + \sum_{j=1}^{N} \overset{ij}{B}_{sn}\overset{j}{D}_n$$
$$\overset{i}{u}_n = \sum_{j=1}^{N} \overset{ij}{B}_{ns}\overset{j}{D}_n + \sum_{j=1}^{N} \overset{ij}{B}_{nn}\overset{j}{D}_n \quad \text{..... (2.6)}$$

where $\overset{j}{D}_s$ and $\overset{j}{D}_n$ are the shear and normal components of discontinuity with respect to the local co-ordinates *s* and *n* at the j^{th} element. $\overset{i}{\sigma}_s$ and $\overset{i}{\sigma}_n$ are the shear and normal stress

at the midpoint of the i^{th} element. u_s^i and u_n^i are the shear and normal displacement at the midpoint of the i^{th} element. *A* and *B* are the influence coefficient matrix accounting for the different positions and orientations of each element.

Given the boundary conditions on each element, we can solve the system of algebraic equations of Eq. (2.5) and (2.6), and get the values of elemental DD that are necessary to produce the boundary condition, element by element along the crack. Once the displacement discontinuities D_s^j and D_n^j along the crack are found, the displacements and stresses at any point in the body can be determined by using Eq. (2.5) and (2.6) with the influence coefficients calculated for the point of interest.

2.2 Crack Tip Element

The theory of linear elastic fracture mechanics shows that the relative displacement between the crack surfaces in the small vicinity of the crack tip is proportional to $r^{1/2}$ (r is measured from the tip along the crack). Therefore, the constant DD method cannot produce accurate estimate of the stresses and displacements near the crack tip. To account for the $r^{1/2}$ variation, we used a special crack tip element at the crack tip. The schematic for a left crack tip is shown in **Fig. 2.2** and the DD for a left crack tip element can be written as (Yan 2004):

$$D_x = H_s\left(\frac{a+\xi}{a}\right)^{0.5}$$
$$D_y = H_n\left(\frac{a+\xi}{a}\right)^{0.5} \quad \text{..... (2.7)}$$

where H_s and H_n are the tangential and normal displacement discontinuity quantities at the center of the crack tip element.

Substitution of Eq. (2.7) into Eq. (2.2) and (2.3), the displacements and stresses at the crack tip then can be expressed in terms of H_s and H_n.

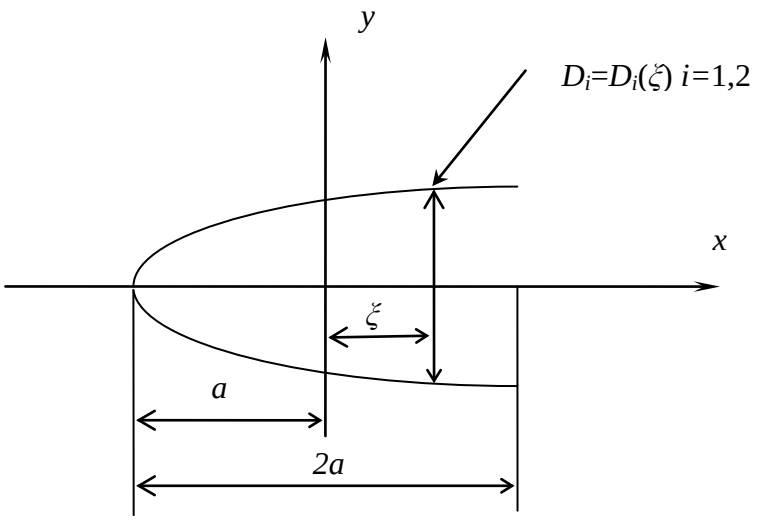


Fig. 2.2 Special crack tip displacement discontinuity at the left crack tip.

2.3 Fracture Propagation Scheme

We used the structural criterion (which has been described in detail in Dobroskok's (2005) paper) for modeling and automatic tracking of tensile and shear mode crack propagation.

The tensile driving force f_I is defined as averaged tangential stress ahead of the crack tip (Dobroskok et al. 2005):

$$f_I = \bar{\sigma}_{\theta\theta} = \frac{1}{d}\int_0^d \sigma_{\theta\theta}(r)dr\ ,\ \bar{\sigma}_{\theta\theta} < 0 \quad \text{..... (2.8)}$$

where d is the characteristic size of the fracture process zone (FPZ) (see Section **3.1.2** for definition).

The shear driving force f_{II} is defined using Mohr-Coulomb criterion, relating to the averaged shear stress and tangential stress ahead of the crack tip (Dobroskok et al. 2005):

$$f_{II} = sign(\bar{\sigma}_{r\theta})\bar{\sigma}_{r\theta} - \tan\phi(-\bar{\sigma}_{\theta\theta}) = c\ ,\ \bar{\sigma}_{\theta\theta} \geq 0 \quad \text{..... (2.9)}$$

where ϕ is rock friction angle, c is rock cohesion, and

$$\bar{\sigma}_{r\theta} = \frac{1}{d}\int_0^d \sigma_{r\theta}(r)dr \quad \text{..... (2.10)}$$

The normalized driving forces can be defined as (Dobroskok et al. 2005): Mode I (normalized tensile driving force, F_I):

$$F_I = \frac{f_I}{\sigma_t} = \frac{\bar{\sigma}_{\theta\theta}}{\sigma_t}, \bar{\sigma}_{\theta\theta} < 0 \quad \text{..... (2.11)}$$

where σ_t is rock tensile strength; Mode II (normalized shear driving force, F_{II}):

$$F_{II} = \frac{f_{II}}{c} = \frac{sign(\bar{\sigma}_{r\theta})\bar{\sigma}_{r\theta} - \tan\phi(-\bar{\sigma}_{\theta\theta})}{c}, \bar{\sigma}_{\theta\theta} \geq 0 \quad \text{..... (2.12)}$$

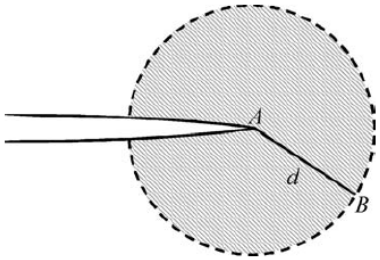


Fig. 2.3 Structural criterion: average stress over the segment *d* (length of FPZ) in the small vicinity of the crack tip (after Dobroskok et al. 2005).

To find the direction of crack propagation, normalized tensile and shear driving forces ahead of the crack tip are evaluated over a distance equal to the length of a FPZ, in directions comprising angles from $-\pi$ to $+\pi$ with the current tip element. The directions and the values of the maximum normalized tensile or shear driving force are determined and a new element is added according to the criterion summarized in **Table 2.1**.

For Mode I (tensile mode) propagation, the propagation direction is the direction in which the normalized tensile driving force is maximum:

$$\theta_I = \left\{\theta : \max_{\theta} F_I(\theta)\right\} \quad \text{..... (2.13)}$$

For Mode II (shear mode) propagation, the propagation direction is in the direction in which the normalized shear driving force is maximum:

$$\theta_{II} = \left\{\theta : \max_{\theta} F_{II}(\theta)\right\} \quad \text{..... (2.14)}$$

The corresponding maximum normalized tensile and shear driving forces at θ_I and θ_{II} are denoted as $F_{IMAX} = F_I(\theta_I)$ and $F_{IIMAX} = F_{II}(\theta_{II})$, respectively.

Table 2.1 Different possibility, mode and direction of crack propagation (Dobroskok et al. 2005)

Maximum Normalized Driving Forces	Mode	Direction
$F_{\text{IMAX}}<1, F_{\text{IIMAX}}<1$	does not propagate	
$F_{\text{IMAX}}>1, F_{\text{IIMAX}}<1$	Mode I	$\theta_p = \theta_I$
$F_{\text{IMAX}}<1, F_{\text{IIMAX}}>1$	Mode II	$\theta_p = \theta_{II}$
$F_{\text{IMAX}} > F_{\text{IIMAX}} >1$	Mode I	$\theta_p = \theta_I$
$F_{\text{IIMAX}} > F_{\text{IMAX}} >1$	Mode II	$\theta_p = \theta_{II}$

In the case of a small FPZ ($d / \ell \leq 0.1$), the stresses at the crack tip are calculated by the asymptotic analytical equation, which can be written as (Dobroskok et al. 2005):

$$\sigma_{\theta\theta}(r,\theta) = \frac{1}{\sqrt{2\pi r}} \cos^3 \frac{\theta}{2} (K_I - 3K_{II} a) \quad \text{..... (2.15)}$$

$$\sigma_{r\theta}(r,\theta) = \frac{1}{\sqrt{2\pi r}} \cos^3 \frac{\theta}{2} [K_I a + K_{II}(1 - 2a^2)] \quad \text{..... (2.16)}$$

where $a = \tan(\theta / 2)$.

As Eq. (2.15) and (2.16) are only valid at a small vicinity near the tip region, in the case of a large FPZ ($d / \ell > 0.15$ (ℓ : half length of the crack)), the stresses at the crack tip are calculated as stresses at field points based on Eq. (2.5).

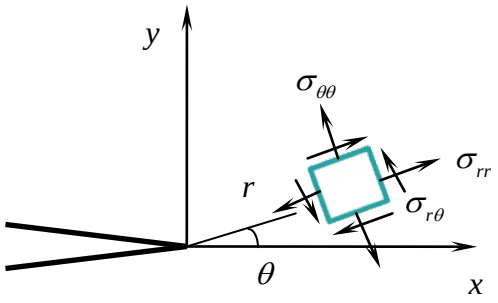


Fig. 2.4 Stress state in the vicinity of the crack tip.

While evaluating the driving forces, the induced stresses at a point in the current time step are calculated by summing the influence of the fictitious fluid sources over all elements in the system and over all preceding time steps. The boundary conditions on a newly added element are considered to be the same as those of the initial crack.

2.4 Newtonian Fluid Flow Within the Hydraulic Fracture

Apart from the assumption of constant fluid pressure distribution along the hydraulic fracture, we also model the fluid flow within the fracture as an incompressible Newtonian fluid in our study, as our focus is stimulation of unconventional gas reservoirs that are mostly treated with water.

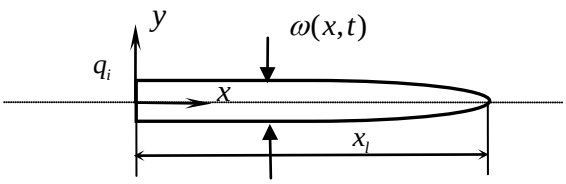


Fig. 2.5 Geometry for a plane strain fracture and the fluid flow within the fracture.

Ignoring the fracture leakoff term, the continuity equation for flow of an incompressible fluid in the hydraulic fracture can be written as:

$$\frac{\partial \omega}{\partial t} = \frac{\partial q}{\partial x} \quad \text{..... (2.17)}$$

where ω is the hydraulic fracture width, and q is the fluid flux through a cross-section of the fracture. Fluid flux can be expressed with respect to the fracture width and pressure gradient along the hydraulic fracture based on Poiseuille's law (Batchelor 1967):

$$q = \frac{\omega^3}{12\mu} \frac{\partial p_f}{\partial x} \quad \text{..... (2.18)}$$

where p_f is the fluid pressure within the hydraulic fracture.

The boundary condition of the problem is:

$$q(0,t) = q_i = const \quad \text{..... (2.19)}$$

where q_i is the fluid injection rate at the wellbore (x=0). At the fracture tip, it is assumed that the net fluid pressure becomes zero, which can be expressed as:

$$p_f(x_l,t) - \sigma_n = 0 \quad \text{..... (2.20)}$$

where σ_n is the far-field stress normal to the fracture surface. Initially, the fracture is closed, so the initial condition is:

$$\omega(x,0) = 0 \quad \text{..... (2.21)}$$

Eq. (2.17) is discretized using the implicit finite difference method from time t_m to t_{m+1}:

$$\frac{\omega_i^{m+1} - \omega_i^m}{\Delta t} = \frac{q_{i+1/2}^{m+1} - q_{i-1/2}^{m+1}}{\Delta x} \quad \text{..... (2.22)}$$

where $\Delta t = t_{m+1} - t_m$ and $\Delta x = x_{i+1/2} - x_{i-1/2}$.

Let $\omega_{i+1/2}^{m+1} = \frac{\omega_{i+1}^{m+1} + \omega_i^{m+1}}{2}$, and $\omega_{i-1/2}^{m+1} = \frac{\omega_{i-1}^{m+1} + \omega_i^{m+1}}{2}$. According to Eq. (2.18) we can get:

$$q_{i+1/2} = \frac{(\omega_{i+1}^{m+1} + \omega_i^{m+1})^3}{8 \times 12\mu} \frac{p_{i+1}^{m+1} - p_i^{m+1}}{\Delta x} \quad \text{..... (2.23)}$$

$$q_{i-1/2} = \frac{(\omega_i^{m+1} + \omega_{i-1}^{m+1})^3}{8 \times 12\mu} \frac{p_i^{m+1} - p_{i-1}^{m+1}}{\Delta x} \quad \text{..... (2.24)}$$

Substituting Eq. (2.24) into Eq. (2.22) yields:

$$\omega_i^{m+1} - \omega_i^m = \frac{\Delta t}{(8) \times 12\mu (\Delta x)^2} \left[(\omega_{i+1}^{m+1} + \omega_i^{m+1})^3 p_{i+1}^{m+1} - (\omega_{i+1}^{m+1} + \omega_i^{m+1})^3 p_i^{m+1} - (\omega_i^{m+1} + \omega_{i-1}^{m+1})^3 p_i^{m+1} + (\omega_i^{m+1} + \omega_{i-1}^{m+1})^3 p_{i-1}^{m+1} \right] \quad (2.25)$$

The boundary conditions in Eq. (2.19) and (2.20) can be written in discretized form into:

For *i*=1,

$$q^m{}_{1/2} = q_l \quad \text{..... (2.26)}$$

For *i*=*n*,

$$p^m{}_n = \sigma_n \quad \text{..... (2.27)}$$

Initial condition can be written into:

$$\omega_i^0 = \omega(x_i, 0) = 0 \quad \text{..... (2.28)}$$

Combining Eq. (2.25), (2.26), (2.27) and (2.28) yields:

$$a_i p_{i-1}^{m+1} + b_i p_i^{m+1} + c_i p_{i+1}^{m+1} = d_i \quad \text{..... (2.29)}$$

where

$$a_i = (\omega_i^{m+1} + \omega_{i-1}^{m+1})^3$$
$$b_i = -(\omega_i^{m+1} + \omega_{i+1}^{m+1})^3 - (\omega_i^{m+1} + \omega_{i-1}^{m+1})^3 \quad \text{for } i=2 \text{ to } n\text{-}1 \quad \text{..... (2.30)}$$
$$c_i = (\omega_i^{m+1} + \omega_{i+1}^{m+1})^3$$
$$d_i = \frac{\omega_i^{m+1} - \omega_i^m}{(\Delta t / 8\mu'(\Delta x)^2)}$$

where $\mu' = 12\mu$

$$a_n = 0, b_n = 1, d_n = \sigma_{\infty,n} \quad \text{..... (2.31)}$$

and

$$a_1 = 0$$
$$b_1 = -(\omega_1^{m+1} + \omega_2^{m+1})^3 \quad \text{..... (2.32)}$$
$$c_1 = (\omega_1^{m+1} + \omega_2^{m+1})^3$$
$$d_1 = \frac{\omega_1^{m+1} - \omega_1^m - \frac{\Delta t}{\Delta x} q_l}{(\Delta t / 8\mu'(\Delta x)^2)}$$

When the fluid pressure along the fracture has a prescribed value and uniformly distributed, the fracture width can be explicitly solved for by using the DD method as described Section **2.1.** However, the main challenge for modeling a Newtonian fluid flow model is to determine two unknown and dependent variables, the fracture width and the fluid pressure distribution along the fracture. The two underlying coupling mechanisms are: 1) the fracture aperture (as mechanical response of the reservoir rock) changes with the applied loading which is imposed on the fracture surfaces by the fluid pressure; 2) the fluid pressure and the resultant pressure gradient along the fracture are related to the fracture width according to the Poiseuille's law. An iterative process is needed to solve for the pressure distribution and the fracture aperture.

The iteration process can be explained as follows. During each time step, at k^{th} iteration between width and fluid pressure along the fracture, a trial solution for the fluid pressure $p_i^{m+1(k)} = p^{(k)}(x_i, t_{m+1})$ along the fracture is first used then, the DD method as described in Section **2.1** is used to solve the fracture width $\omega_i^{m+1(k)} = \omega^{(k)}(x_i, t_{m+1})$**.** This fracture width $\omega_i^{m+1(k)} = \omega^{(k)}(x_i, t_{m+1})$ is then substituted into Eq. (2.29) to solve for a new fluid pressure distribution $p_i^{m+1(k+1/2)} = p^{(k+1/2)}(x_i, t_{m+1})$ along the fracture. The process is continued within each time step until convergence i.e., when the difference between the two sets of width/fluid pressure approaches zero (or is less than a very small value).

To shorten and stabilize the iteration process, a relaxation factor α is used to get the fluid pressure for the next cycle of iteration.

$$p_i^{m+1(k+1)} = p_i^{m+1(k)} + \alpha(p_i^{m+1(k+1/2)} - p_i^{m+1(k)}) \quad \text{..... (2.33)}$$

3 MODEL VERIFICATION

3.1 Evaluation of SIF

3.1.1 Different SIF Calculated by Using Different Lengths of Tip Element, Lengths of Ordinary Element and *d* (Length of FPZ)

Stress intensity factor (SIF) is a parameter used to characterize the stress field near the crack tip, and it is used to evaluate the stress ahead of the crack tip and further determine fracture propagation direction and mode according to the structural criterion as explained in Section **2.3**. The magnitude of SIF depends on the geometric configuration, the size and location of the crack and loading conditions of the body. SIF can be obtained by using analytical, numerical and experimental methods. In a boundary element modeling, SIF is usually calculated in two approaches. One is using the DD at the crack tip as expressed by the following equation (Yan 2004):

$$K_I = \frac{G}{4(1-\nu)}\sqrt{\frac{2\pi}{r}}D_n(r)$$
$$K_{II} = \frac{G}{4(1-\nu)}\sqrt{\frac{2\pi}{r}}D_s(r) \quad \text{..... (3.1)}$$

where $D_n(r)$ and $D_s(r)$ are the normal and shear components of DD at a distance r from the crack tip.

The other approach of calculating SIF at the crack tip is using the stresses ahead of the crack tip by the following equation (Rice 1968):

$$K_I = \sigma_n(r)\sqrt{2\pi r}$$
$$K_{II} = \sigma_s(r)\sqrt{2\pi r} \quad \text{..... (3.2)}$$

where $\sigma_n(r)$ and $\sigma_s(r)$ are the normal and shear components of the stresses at the point located along the tangent of the crack, and at a distance r from the crack tip as shown in **Fig. 3.1.**

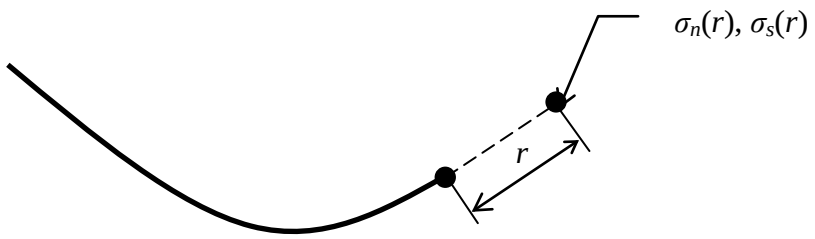


Fig. 3.1 SIF calculated based on the stresses ahead of the crack tip.

The program has been extended to include tip element at each crack tip, and fracture propagation has been enabled from both crack tips. To verify the accuracy of the code for calculating SIF at the crack tip, the SIF of a straight crack in an infinite elastic space was checked against the analytical value by using different lengths of tip element, lengths of ordinarily element and *d* (length of FPZ).

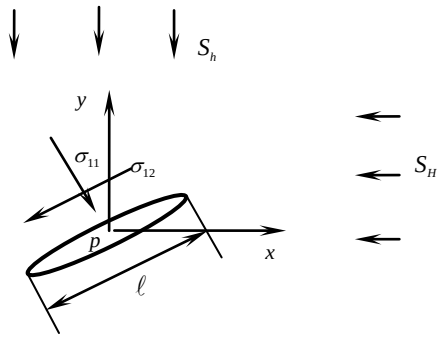


Fig. 3.2 A slanted pressurized crack under biaxial stresses in an infinite elastic medium.

The analytical solution for SIF at the crack tip is (Woo and Ling 1984):

$$K_I = \sigma_I \sqrt{\pi a} \quad \text{..... (3.3)}$$

$$K_{II} = \sigma_{II} \sqrt{\pi a} \quad \text{..... (3.4)}$$

where $a = \frac{\ell}{2}$ and

$$\sigma_I = \sigma_{11} - p \quad \text{..... (3.5)}$$

$$\sigma_{II} = \sigma_{12} \quad \text{..... (3.6)}$$

σ_{11} and σ_{12} are far-field stresses with respect to the local coordinates of the crack. SIFs calculated based on DDs by using Eq. (3.1) and on stresses by using Eq. (3.2) are shown and compared in **Table 3.1**.

Table 3.1 SIFs calculated by using DDs and stresses

SIF calculated based on DDs										
	$\ell_{tip}=0.6\ell$		$\ell_{tip}=0.5\ell$		$\ell_{tip}=0.4\ell$		$\ell_{tip}=0.3\ell$		$\ell_{tip}=0.2\ell$	
	$\ell_{ord}=0.1\ell$		$\ell_{ord}=0.1\ell$		$\ell_{ord}=0.1\ell$		$\ell_{ord}=0.1\ell$		$\ell_{ord}=0.1\ell$	
K_I	1.34E+06	0.71%	1.30E+06	0.69%	1.25E+06	0.78%	1.21E+06	1.17%	1.17E+06	2.35%
K_{II}	1.06E+06	0.70%	1.02E+06	0.68%	9.86E+05	0.78%	9.51E+05	1.16%	9.21E+05	2.34%
	$\ell_{tip}=0.1\ell$		$\ell_{tip}=0.075\ell$		$\ell_{tip}=0.05\ell$		$\ell_{tip}=0.05\ell$			
	$\ell_{ord}=0.1\ell$		$\ell_{ord}=0.1\ell$		$\ell_{ord}=0.1\ell$		$\ell_{ord}=0.05\ell$			
K_I	1.17E+06	7.22%	1.19E+06	10.89%	1.26E+06	18.43%	1.17E+06	7.61%		
K_{II}	9.20E+05	7.26%	9.40E+05	10.90%	9.91E+05	18.43%	9.24E+05	7.69%		
SIF calculated based on stresses, *d*=0.01*l*										
	$\ell_{tip}=0.2\ell$		$\ell_{tip}=0.1\ell$		$\ell_{tip}=0.075\ell$		$\ell_{tip}=0.05\ell$		$\ell_{tip}=0.05\ell$	
	$\ell_{ord}=0.1\ell$		$\ell_{ord}=0.1\ell$		$\ell_{ord}=0.1\ell$		$\ell_{ord}=0.1\ell$		$\ell_{ord}=0.05\ell$	
K_I	1.02E+06	-10.34%	1.02E+06	-6.75%	1.03E+06	-4.05%	1.08E+06	1.28%	1.01E+06	-7.30%
K_{II}	8.07E+05	-10.35%	8.00E+05	-6.72%	8.13E+05	-4.04%	8.47E+05	1.29%	7.96E+05	-7.23%
SIF calculated based on stresses, *d*=0.05*l*										
	$\ell_{tip}=0.2\ell$		$\ell_{tip}=0.1\ell$		$\ell_{tip}=0.075\ell$		$\ell_{tip}=0.05\ell$		$\ell_{tip}=0.05\ell$	
	$\ell_{ord}=0.1\ell$		$\ell_{ord}=0.1\ell$		$\ell_{ord}=0.1\ell$		$\ell_{ord}=0.1\ell$		$\ell_{ord}=0.05\ell$	
K_I	8.6E+05	-25.05%	8.40E+05	-22.88%	8.47E+05	-21.34%	8.65E+05	-18.60%	8.27E+05	-24.15%
K_{II}	6.7E+05	-25.06%	6.62E+05	-22.86%	6.67E+05	-21.33%	6.81E+05	-18.59%	6.51E+05	-24.10%

It can be observed that SIFs calculated by stress formulae generally improve as the length of tip element gets smaller. The optimum ratio of ℓ_{tip} to ℓ_{ord} when the error is the smallest is 0.5. The error is the smallest when ℓ_{tip}=0.05ℓ, ℓ_{ord}=0.1ℓ, and d=0.01ℓ, which is about 1.28% when compared with the analytical values. However, the results are not very good for SIFs calculated by using large d values (when d=0.05ℓ), as SIF calculated based on the stress formulae is only valid in a very mall vicinity of the crack

tip. The type of DD we used is real DD with equal length ordinary elements, so it is less accurate in estimating the stress ahead of the crack tip compared with the complex variable Boundary Element Method used by Dobroskok et al. (2005).

SIFs calculated based on DDs at the crack tip element are also within reasonable range. The accuracy of SIF calculation is dependent on the selection of ℓ_{tip} and ℓ_{ord}. The most accurate estimate of K_I and K_{II} are obtained when $\ell_{tip} = 0.5\ell$ and $\ell_{ord} = 0.1\ell$. The SIF calculated by using DD formulae when $\ell_{tip} = 0.1\ell_{ord}$ and $l_{ord} = 0.1\ell$ gives an error of about 7.22%, which is acceptable for numerical estimates of rock engineering problems, and that is what we used in the following numerical calculation in this thesis.

Table 3.2 also shows that SIFs calculated by DD formulae have the same error for cracks slanted at different angles with respect to *x*-axis. Therefore the crack propagation direction, which is determined by the value of K_I /K_{II}, can be modeled exactly.

Table 3.2 SIFs calculated based on DDs

	Analytical			Numerical			Error (%)		
Angle	KI	KII	KII/KI	KI	KII	KII/KI	KI	KII	KII/KI
30	0.4431	0.7675	1.7321	0.4752	0.8230	1.7320	7.23%	7.23%	0.00%
45	0.8862	0.8862	1.0000	0.9503	0.9503	1.0000	7.23%	7.23%	0.00%
60	1.3293	0.7675	0.5774	1.4254	0.8230	0.5774	7.23%	7.23%	0.00%
90	1.7725	0.0000	0.0000	1.9006	0.0000	0.0000	7.23%	0.00%	0.00%

For both simplicity and accuracy, in the following numerical examples in this thesis, SIFs are calculated by choosing ℓ_{tip} and ℓ_{ord} to be 0.1ℓ (ℓ: the original half crack length) to avoid remeshing of the elements with crack growth, and by using DD formulae, as SIFs calculated by this approach is independent on the selection of *d*. SIF calculated by the stress formulae will be dependent on the selection of *d*, so this approach is not adopted in the following numerical examples.

3.1.2 Selection of *d* (Length of FPZ)

Another important parameter in the modeling of the crack propagation process is *d*, the characteristic length of the fracture process zone. **Fig. 3.3** illustrates a macro-crack (continuous traction-free crack) with its surrounding zone in a rock. The damaged zone ahead of the traction-free crack is referred to as the fracture process zone (FPZ) and it plays an important role in the analysis of growth of the crack. Within the FPZ many micro-failure mechanisms including matrix microcracking, matrix interface debonding, crack deviation and branching take place. A FPZ is called a small FPZ if $d/\ell \le 0.1$ and non-small for $d/\ell > 0.15$ (ℓ: half length of the crack) (2005).

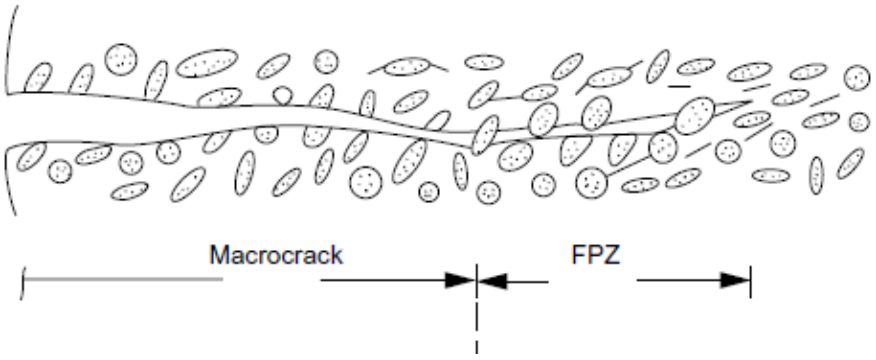


Fig. 3.3 A fracture process zone (Gdoutos 2005)

The length of the FPZ, *d*, depends on the geometry and size of the structure, the type of material, and the considered scale of study, and in practice they are to be found experimentally. As shown in Dobroskok et al (2005), fracture would display different propagation trajectories for a small FPZ case ($d/\ell = 0.05$) and a non-small FPZ case ($d/\ell = 0.25$). It is important to carefully select this value in order to get reliable modeling results.

As another test case, the propagation of a slanted pressurized crack under biaxial stresses in an elastic space was modeled using different values of *d*, and the results are plotted in **Fig. 3.4.** (The input parameters were: half crack length ℓ =1m, minimum horizontal stress S_h=-0.5MPa, maximum horizontal stress S_H=-3MPa, internal fluid pressure within the fracture p=2.5MPa, cohesion c=2.2MPa, and tensile strength T_0=2.0MPa). The calculated crack trajectories are similar and crack propagates in Mode I in three cases of small FPZ: d=0.1 ℓ, d=0.05 ℓ, and d=0.01 ℓ. The modeling results are not sensitive to the variation of *d* as long as *d* falls in the small FPZ category.

However, when d is set to 0.5ℓ (non-small FPZ), the fracture does not propagate forward. Due to the singularity of the stress distribution around the crack tip, the calculated averaged driving forces around the tip is a function depending strongly on d. The averaged normal and shear driving force will decline very rapidly with the increase of d. Therefore, propagation may not occur if a very large d is selected.

Zhang (2002) showed that there is an empirical relation between Mode I fracture toughness and the tensile strength of the rock:

$$T_0 = 6.88\, K_{IC} \quad (3.7)$$

which is valid for general rocks from soft to hard under the condition of quasi-static or low-speed impact loading. As pointed by Dobroskok (2005) for a small FPZ,

$$K_{IC} = \sqrt{\frac{\pi d}{2}} T_0 \quad (3.8)$$

Therefore, it can be estimated that $d \approx 0.013\text{m}$. For most cracks of length over 1m, d is within the range of a small FPZ. As we use real DD with equal length ordinary elements, the stress ahead of the crack tip determined by SIF formulae Eq.(2.15) and (2.16) is only valid for the very small vicinity of the crack tip. Therefore, in this thesis we only focused on cases of small FPZ.

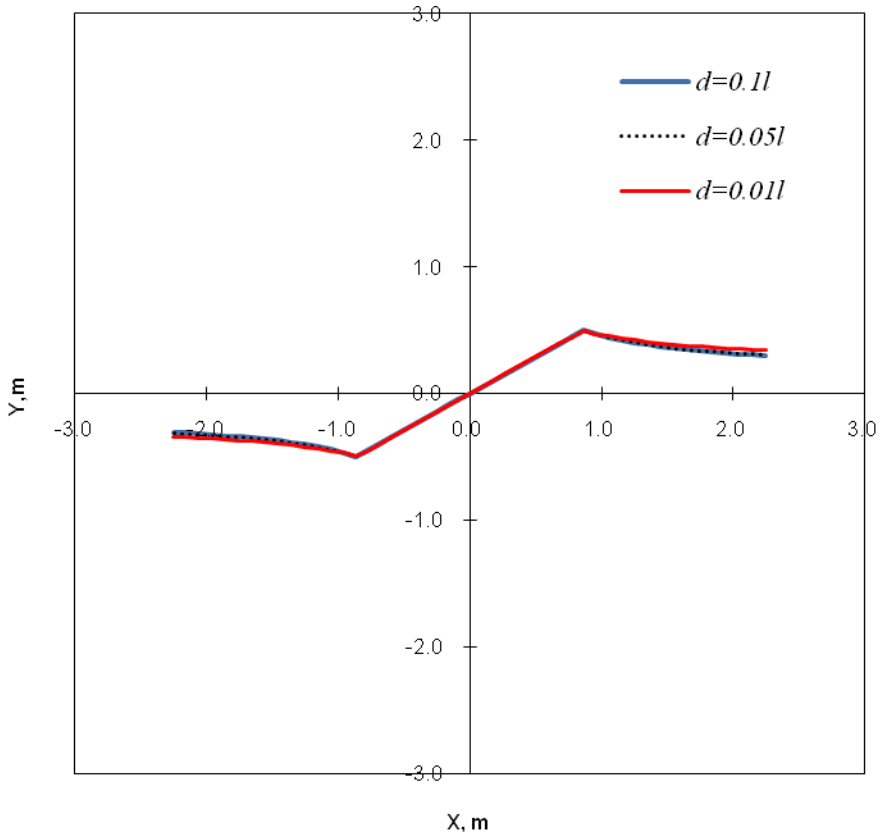


Fig. 3.4 Fracture trajectories calculated with different *d* for a slanted pressurized crack under biaxial stresses in an infinite elastic medium.

3.2 Fracture Propagation (Elastic Case)

3.2.1 Crack Propagation Under Biaxial Stress in an Infinite Elastic Rock

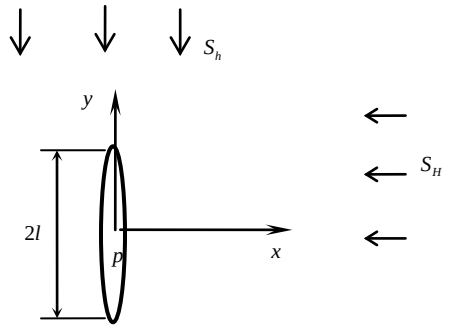


Fig. 3.5 An initially straight pressurized crack under biaxial stresses.

Using the example in Dong and de Pater's paper (2001), the propagation path of a pressurized crack under biaxial compressive stresses in an infinite elastic rock is simulated. The input parameters are listed in **Table 3.3**. The maximum circumferential stress criterion was used in our example as in Dong and de Pater's paper. Constant pressure distribution inside the crack was assumed.

Table 3.3 Input parameters in Section 3.2.1

E	Young's modulus	2.0×10^{04}	MPa
l	initial half crack length	0.02	m
υ	Poisson's ratio	0.2	
K_{IC}	Mode I critical stress intensity factor	0.6	$MPa\cdot m^{1/2}$

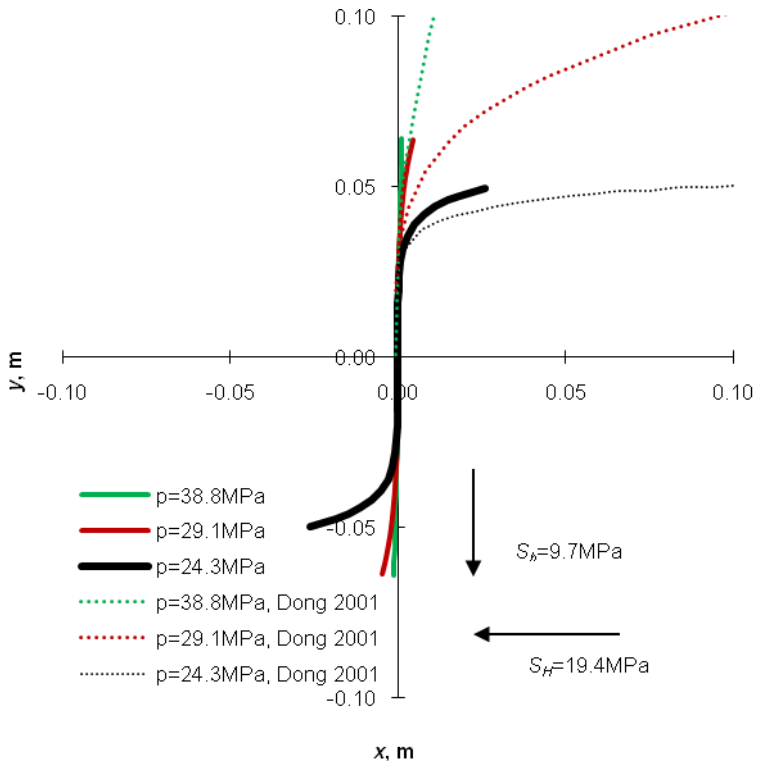


Fig. 3.6 Crack trajectories under different internal pressures.

Fig. 3.6 shows the reorientation of crack trajectories under different internal pressures (p=24.3, 29.1 38.8 MPa) in the crack. **Fig. 3.7** shows the reorientation of crack trajectories under different maximum horizontal stresses (S_H=22.6, 19.4, 9.7 MPa). Similarly as those obtained by Dong (2001), the crack would reorient from its original direction (the direction of S_h) and propagate along the direction of S_H under the far-field compressive stresses. Different curves show that for crack with lower internal pressure or for a stress field with bigger difference between maximum horizontal stress S_H and minimum horizontal stress S_h (higher degrees of anisotropy of the stress field), the direction of the crack path change more quickly.

As quadratic boundary elements were used by Dong while we used constant elements along the crack and tip element implemented at the crack tip, the preciseness of the fracture tip SIF calculation and our model results of fracture paths are slightly from those predicted by Dong.

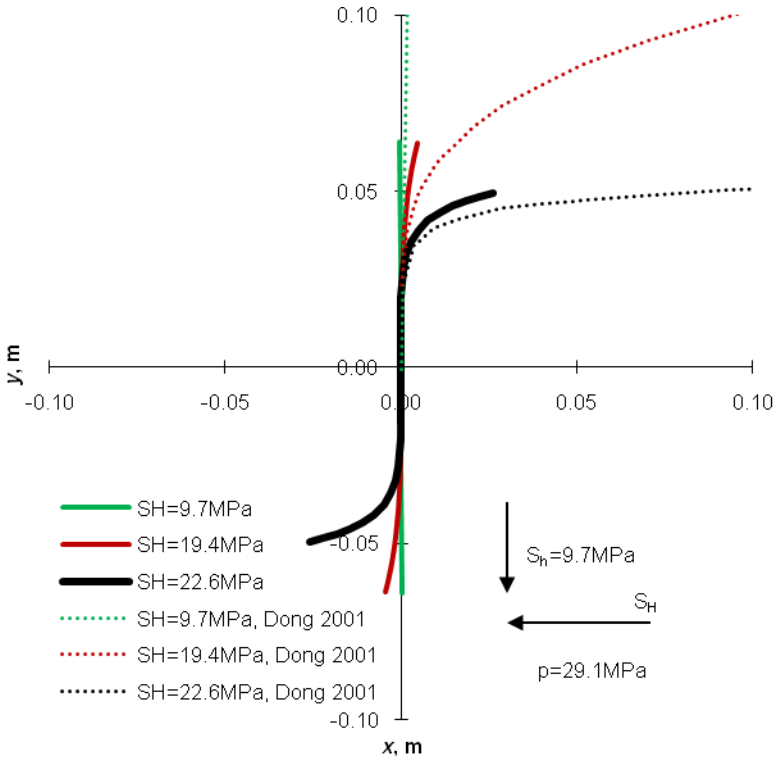


Fig. 3.7 Crack trajectories under different maximum horizontal stresses.

3.2.2 Crack Propagation Under Uniaxial Stress in an Infinite Elastic Medium

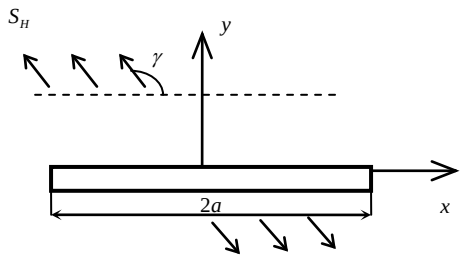


Fig. 3.8 A line crack under uniaxial stress in an infinite elastic medium.

We also investigated the propagation of a straight line crack with a length of $2a = 2\text{m}$ in an infinite elastic space under plane-strain conditions as shown in **Fig. 3.8.** The crack surfaces are subjected to far-field tension, S_H, at different angles γ with respect to the x-axis. We modeled the crack with l_{tip} and l_{ord} equal to $0.1l$ and d=$0.01l$. To compare our results with previous studies, the maximum circumferential stress criterion was also used in the program. In view of the symmetry in geometry and mechanical loading of the problem, only half of the crack is plotted in **Fig. 3.9.** The crack grows in the direction perpendicular to the direction of far-field uniaxial tension as the crack is subjected to the greatest tension at this direction and can propagate most easily. The model results match the results in Mogilevskaya's (2005) paper.

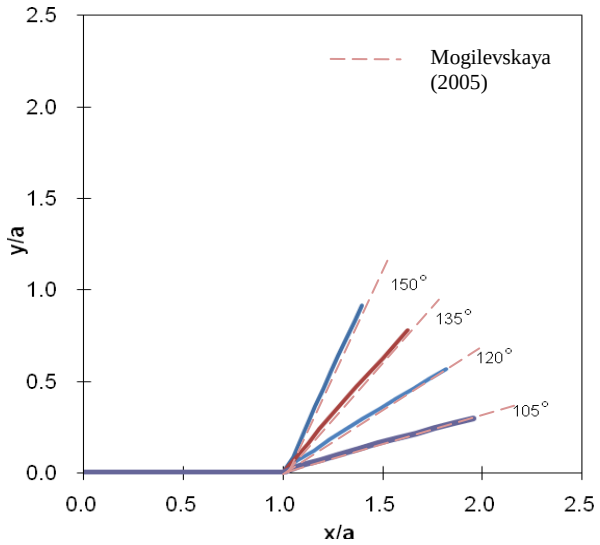


Fig. 3.9 Crack growth under uniaxial stress in an infinite elastic medium.

4 JOINT ELEMENT

4.1 Joint Element

For many problems in rock mechanics, the total stresses at any point in the rock can be represented as the sum of the **initial stresses** and the stress changes at that point, which is usually called the **induced stress** (Crouch and Starfield 1983).

$$\sigma_{ij} = (\sigma_{ij})_0 + \sigma'_{ij} \quad \text{..... (4.1)}$$

Similarly, total displacement can be represented as the **initial displacement** and the **induced displacement**.

$$\sigma_{ij} = (\sigma_{ij})_0 + \sigma'_{ij} \quad \text{..... (4.2)}$$

4.1.1 Joint Stick Mode (Elastic Joint Element)

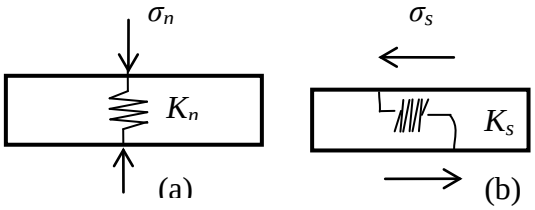


Fig. 4.1 Representation of an elastic joint element (a) normal stiffness; (b) shear stiffness.

4.1.1.1 Joint Element Excluding Initial Joint Deformation

For an elastic joint element (shown in **Fig. 4.1)** with zero initial deformations, the joint elements deform only in response to the induced stress caused for example by an approaching hydraulic fracture. The relation between tractions and the DD's on the joint surface are (Crouch and Starfield 1983):

$$\begin{bmatrix} \overset{i}{\sigma_n'} \\ \overset{i}{\sigma_s'} \end{bmatrix} = -\begin{bmatrix} K_n^i & 0 \\ 0 & K_s^i \end{bmatrix} \begin{bmatrix} \overset{i}{D_n'} \\ \overset{i}{D_s'} \end{bmatrix} \quad \text{.....(4.3)}$$

where $\overset{i}{\sigma_n'}$, $\overset{i}{\sigma_s'}$ are the induced normal and shear stresses, and $\overset{i}{D_n'}$, $\overset{i}{D_s'}$ are the components of induced normal and shear DD vector on the i^{th} element of the joint surface. $K_n^{\,i}$ and $K_s^{\,i}$ are the normal and the shear rigidity of the joint. For a joint (having N elements) undergoing elastic deformation, the induced stresses on any element *i* are given by (Crouch and Starfield 1983):

$$\begin{aligned} \overset{i}{\sigma_s'} &= \sum_{j=1}^{N} \left(\overset{ij}{A_{ss}} \overset{j}{D_s'} + \overset{ij}{A_{sn}} \overset{j}{D_n'} \right) \\ \overset{i}{\sigma_n'} &= \sum_{j=1}^{N} \left(\overset{ij}{A_{ns}} \overset{j}{D_s'} + \overset{ij}{A_{nn}} \overset{j}{D_n'} \right) \end{aligned} \quad \text{for } i\text{=1 to N} \text{..... (4.4)}$$

where $\overset{ij}{A_{ss}}$, $\overset{ij}{A_{sn}}$, $\overset{ij}{A_{ns}}$, $\overset{ij}{A_{nn}}$ are the boundary influencing coefficients as defined in Eq. (2.5). From Eq. (4.3) and (4.4), we can rewrite the system of equations in the following form:

$$0 = (\overset{i}{K_s})(\overset{i}{D_s'}) + \sum_{j=1}^{N}\left[\overset{ij}{A_{ss}}\overset{j}{D_s'} + \overset{ij}{A_{sn}}\overset{j}{D_n'}\right]$$
$$0 = (\overset{i}{K_n})(\overset{i}{D_n'}) + \sum_{j=1}^{N}\left[\overset{ij}{A_{ns}}\overset{j}{D_s'} + \overset{ij}{A_{nn}}\overset{j}{D_n'}\right]$$
for i=1 to N ..... (4.5)

which can be simplified as:

$$\begin{bmatrix}0\\0\end{bmatrix} = \begin{bmatrix}A_{ss}+K_s & A_{sn}\\ A_{ns} & A_{nn}+K_n\end{bmatrix}\begin{bmatrix}D_s'\\D_n'\end{bmatrix} = [A+K]\begin{bmatrix}D_s'\\D_n'\end{bmatrix} \quad \text{..... (4.6)}$$

By introducing the **total joint deformation (** $\overset{i}{D_s}$ and $\overset{i}{D_n}$), which can be expressed as the sum of the **initial total joint deformation** ($(\overset{i}{D_s})_0$ and $(\overset{i}{D_n})_0$) and the **induced deformation** (Crouch and Starfield 1983):

$$\overset{i}{D_s} = (\overset{i}{D_s})_0 + \overset{i}{D_s'}$$
$$\overset{i}{D_n} = (\overset{i}{D_n})_0 + \overset{i}{D_n'} \quad \text{..... (4.7)}$$

, as the **initial joint deformation** was assumed zero for a joint in this case, we write Eq. (4.5) as:

$$0 = (\overset{i}{K_s})(\overset{i}{D_s}) + \sum_{j=1}^{N}\left[\overset{ij}{A_{ss}}\overset{j}{D_s} + \overset{ij}{A_{sn}}\overset{j}{D_n}\right]$$
$$0 = (\overset{i}{K_n})(\overset{i}{D_n}) + \sum_{j=1}^{N}\left[\overset{ij}{A_{ns}}\overset{j}{D_s} + \overset{ij}{A_{nn}}\overset{j}{D_n}\right]$$
for i=1 to N ..... (4.8)

This type of joint element has the assumption that the natural fracture under consideration has already reached equilibrium with geologic time and is closed and does

not slip under far-field stress prior to the process of hydraulic fracturing. As the initial deformation on a fault was assumed to be zero, the initial stress field around a hydraulic fracture was not affected by the presence of the fault (Crouch and Starfield 1983).

4.1.1.2 Joint Element Including Initial Joint Deformation

In Section **4.1.1.1**, we used a joint element without considering the initial joint deformation, which means the initial stress field prior to fracture propagation was not affected by the presence of the fault. Another type of joint element would include initial joint deformation prior to fracture propagation process. In this type of scenario, the initial stress field was disturbed by the initial deformation of the fault under the action of the far-field stress prior to the fracture propagation process. The joint has deformed (possibly plastically) under initial far-field stresses prior to the process of hydraulic fracturing.

The **initial total stress** can be expressed as the sum of the far-field stress and the **initial induced stress** (Crouch and Starfield, 1983).

$$(\sigma_{ij})_0 = (\sigma_{ij})_0^{\infty} + (\sigma_{ij}^{'})_0 \quad \text{..... (4.9)}$$

(For a joint **exclude initial joint deformation**, we can obtain that

$$(\sigma_{ij})_0 = (\sigma_{ij})_0^{\infty} \quad \text{..... (4.10))}$$

Similarly, the **initial displacements** can be expressed as the sum of the far-field displacements and the **initial induced displacements**.

$$(u_i)_0 = (u_i)_0^{\infty} + (u_i^{'})_0 \quad \text{..... (4.11)}$$

For a joint system of N elements with elastic deformation, the **initial total stresses** at element *i* are (Crouch and Starfield, 1983):

$$\begin{aligned} (\sigma_s^{i})_0 &= -(K_s^{i})(D_s^{i})_0 \\ (\sigma_n^{i})_0 &= -(K_n^{i})(D_n^{i})_0 \end{aligned} \quad \text{..... (4.12)}$$

where $(D_s^{i})_0$ and $(D_n^{i})_0$ are the **initial total joint deformation**. The initial induced stresses at element *i* are (Crouch and Starfield 1983):

$$\begin{aligned} (\sigma_s^{i'})_0 &= \sum_{j=1}^{N}\left[A_{ss}^{ij}(D_s^{j})_0 + A_{sn}^{ij}(D_n^{j})_0 \right] \\ (\sigma_n^{i'})_0 &= \sum_{j=1}^{N}\left[A_{ns}^{ij}(D_s^{j})_0 + A_{nn}^{ij}(D_n^{j})_0 \right] \end{aligned} \quad \text{..... (4.13)}$$

where A_{ss}^{ij}, A_{sn}^{ij}, A_{ns}^{ij}, A_{nn}^{ij} are the boundary influencing coefficients as defined in Eq. (2.5). Combining Eq. (4.9), (4.12) and (4.13), we can obtain:

$$\begin{aligned} -(\sigma_s^{i})_0^{\infty} &= (K_s^{i})(D_s^{i})_0 + \sum_{j=1}^{N}\left[A_{ss}^{ij}(D_s^{j})_0 + A_{sn}^{ij}(D_n^{j})_0 \right] \\ -(\sigma_n^{i})_0^{\infty} &= (K_n^{i})(D_n^{i})_0 + \sum_{j=1}^{N}\left[A_{ns}^{ij}(D_s^{j})_0 + A_{nn}^{ij}(D_n^{j})_0 \right] \end{aligned} \quad \text{for } i\text{=1 to N} \text{..... (4.14)}$$

which can be simplified as

$$\begin{bmatrix} -(\sigma_s)_0^{\infty} \\ -(\sigma_n)_0^{\infty} \end{bmatrix} = \begin{bmatrix} A_{ss} + K_s & A_{sn} \\ A_{ns} & A_{nn} + K_n \end{bmatrix} \begin{bmatrix} (D_s)_0 \\ (D_n)_0 \end{bmatrix} = [A + K] \begin{bmatrix} (D_s)_0 \\ (D_n)_0 \end{bmatrix} \quad \text{..... (4.15)}$$

Initial total joint deformation $(\overset{i}{D_s})_0$ and $(\overset{i}{D_n})_0$ can therefore be solved. The same form of equation can also be derived in relation to the total joint deformation D_s and D_n (Crouch and Starfield 1983):

$$\begin{aligned} -(\overset{i}{\sigma_s})_0^{\infty} &= (\overset{i}{K_s})(\overset{i}{D_s}) + \sum_{j=1}^{N} \left[\overset{ij}{A_{ss}} (\overset{j}{D_s}) + \overset{ij}{A_{sn}} (\overset{j}{D_n}) \right] \\ -(\overset{i}{\sigma_n})_0^{\infty} &= (\overset{i}{K_n})(\overset{i}{D_n}) + \sum_{j=1}^{N} \left[\overset{ij}{A_{ns}} (\overset{j}{D_s}) + \overset{ij}{A_{nn}} (\overset{j}{D_n}) \right] \end{aligned} \quad \text{for } i\text{=1 to N..... (4.16)}$$

In this assumption, the mechanical response of a natural fracture under far-field stresses would distort the initial stress field prior to the propagation of hydraulic fracture.

4.1.2 Joint Slip Mode

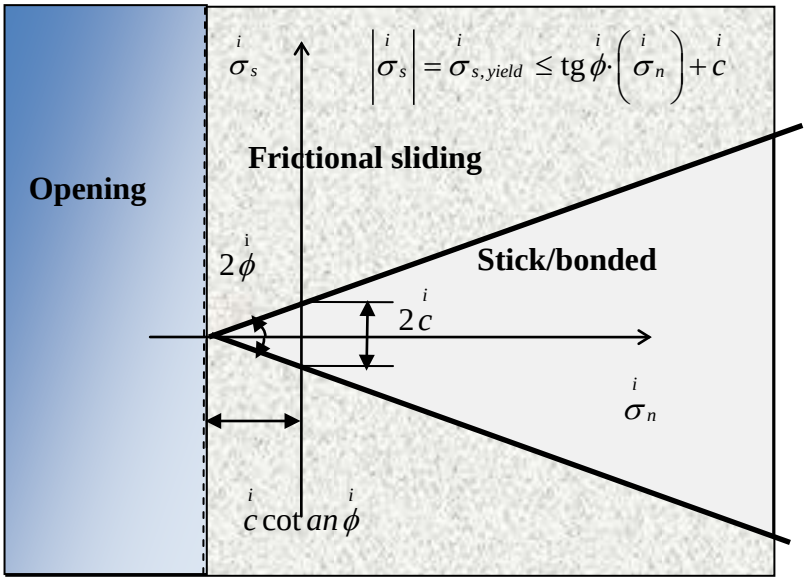


Fig. 4.2 Mohr diagram for a MC joint element under different contact mode under different stress conditions.

During elastic deformation, there is a constraint between the normal and shear stresses across the joint, which is given by the Mohr-Coulomb condition as plotted in **Fig. 4.2.** The total shear stress across a M-C joint element cannot exceed the valued specified by Eq. (4.17) (Crouch and Starfield 1983)**.**

$$\left|\sigma_s^i\right| \le \sigma_{s,yield}^i = \mathrm{tg}\phi^i \cdot \left(\sigma_n^i\right) + c^i \quad \text{..... (4.17)}$$

where ϕ^i is the angle of friction, and c^i is the cohesion. It requires that the element be allowed to undergo a certain amount of inelastic deformation or permanent slip, when the total shear stress on a joint element, $\left|\sigma_s^i\right|$, exceeds the total yield stress $\sigma_{s,yield}^i$.

The simulation of the joint displacements and stresses under yield condition is explained as follows. Suppose the current values of the DD components on element *i* are $\overset{i}{D}_n^{'}$, $\overset{i}{D}_s^{'}$ (**if initial joint deformation is excluded**), if no inelastic deformation occurred during this or any previous loading the total normal stress and shear stress are

$$\begin{aligned}(\overset{i}{\sigma}_s)_{total}^{(k)} &= (\overset{i}{\sigma}_s)_0 + \overset{i}{\sigma}_s^{'} \\ (\overset{i}{\sigma}_n)_{total}^{(k)} &= (\overset{i}{\sigma}_n)_0 + \overset{i}{\sigma}_n^{'}\end{aligned} \quad \text{..... (4.18)}$$

Combining Eq. (4.18) with Eq. (4.4), we can get

$$\begin{aligned}(\overset{i}{\sigma}_s)_{total} &= (\overset{i}{\sigma}_s)_0 + \sum_{j=1}^{N}\left[\overset{ij}{A}_{ss}\overset{j}{D}_s^{'} + \overset{ij}{A}_{sn}\overset{j}{D}_n^{'}\right] \\ (\overset{i}{\sigma}_n)_{total} &= (\overset{i}{\sigma}_n)_0 + \sum_{j=1}^{N}\left[\overset{ij}{A}_{ns}\overset{j}{D}_n^{'} + \overset{ij}{A}_{nn}\overset{j}{D}_n^{'}\right]\end{aligned} \quad \text{..... (4.19)}$$

According to Eq. (4.17), the yield stress is:

$$\overset{i}{\sigma}_{s,yield} = \overset{i}{c} + (\overset{i}{\sigma}_n)_{total} \cdot \tan\overset{i}{\phi} \quad \text{..... (4.20)}$$

The magnitude of the shear stress $(\overset{i}{\sigma}_s)_{total}$ calculated from Eq. (4.19) cannot exceed the yield stress defined in Eq. (4.20). If the element is yielding, the total shear stress must equal the yield stress, so combining Eq. (4.19) and (4.20), we can get the governing equation for the shear deformation at the i^{th} joint element if joint yield occurs:

$$\pm\overset{i}{\sigma}_{s,yield} = (\overset{i}{\sigma}_s)_0 + \sum_{j=1}^{N}\left[\overset{ij}{A}_{ss}\overset{j}{D}_s^{'} + \overset{ij}{A}_{sn}\overset{j}{D}_n^{'}\right] \quad \text{..... (4.21)}$$

The positive value of the yield stress $\overset{i}{\sigma}_{s,yield}$ is used if the total shear stress $(\overset{i}{\sigma}_s)_{total}$ is positive, and the negative value is used if it is negative.

$$sign(\overset{i}{\sigma}_{s,yield}) = sign((\overset{i}{\sigma}_s)_{total}) \quad \text{..... (4.22)}$$

(In a convention system where compression is positive, σ_s is positive if point to the left with respect to the outward of a surface.)

The governing equation for the normal deformation is obtained from Eq. (4.5) for a joint element **excluding initial joint deformation:**

$$0 = (\overset{i}{K}_n)(\overset{i}{D}_n^{'}) + \sum_{j=1}^{N}\left[\overset{ij}{A}_{ns}\overset{j}{D}_s^{'} + \overset{ij}{A}_{nn}\overset{j}{D}_n^{'}\right] \quad \text{..... (4.23)}$$

The **initial joint deformation** is zero for a joint in this case, so $\overset{i}{D}_s = \overset{i}{D}_s^{'}$ and $\overset{i}{D}_n = \overset{i}{D}_n^{'}$ and Eq. (4.21), (4.23), and (4.10) can be written as:

$$\pm\overset{i}{\sigma}_{s,yield} - (\overset{i}{\sigma}_s)^{\infty} = \sum_{j=1}^{N}\left[\overset{ij}{A}_{ss}\overset{j}{D}_s + \overset{ij}{A}_{sn}\overset{j}{D}_n\right]$$
$$0 = (\overset{i}{K}_n)(\overset{i}{D}_n) + \sum_{j=1}^{N}\left[\overset{ij}{A}_{ns}\overset{j}{D}_s + \overset{ij}{A}_{nn}\overset{j}{D}_n\right] \quad \text{..... (4.24)}$$

Similarly, the governing equation for the normal deformation is obtained from Eq. (4.14) for a joint element **including initial joint deformation:**

$$-(\overset{i}{\sigma_n})_0^{\infty} = (\overset{i}{K_n})(\overset{i}{D_n})_0 + \sum_{j=1}^{N}\left[\overset{ij}{A_{ns}}(\overset{j}{D_s})_0 + \overset{ij}{A_{nn}}(\overset{j}{D_n})_0\right] \text{ for } i\text{=1 to N} \quad \text{..... (4.25)}$$

Therefore, the corresponding system of equations is:

$$\begin{bmatrix} \pm\sigma_{s,yield}^{\infty} - \sigma_s^{\infty} \\ -\sigma_n^{\infty} \end{bmatrix} = \begin{bmatrix} A_{ss} & A_{sn} \\ A_{ns} & A_{nn} + K_n \end{bmatrix} \begin{bmatrix} (D_s)_0 \\ (D_n)_0 \end{bmatrix} \quad \text{..... (4.26)}$$

Similarly, the positive value of the yield stress $\overset{i}{\sigma}_{s,yield}$ is used if the total shear stress $(\overset{i}{\sigma_s})_{total}$ is positive, and the negative value is used if it is negative, as expresses in Eq. (4.22).

The same form of equation can also be derived in relation to the total joint deformation D_s and D_n (Crouch and Starfield 1983):

$$\begin{aligned} \pm\overset{i}{\sigma}_{s,yield} - (\overset{i}{\sigma_s})^{\infty} &= \sum_{j=1}^{N}\left[\overset{ij}{A}_{ss}\overset{j}{D}_s + \overset{ij}{A}_{sn}\overset{j}{D}_n\right] \\ -(\overset{i}{\sigma_n})^{\infty} &= (\overset{i}{K_n})(\overset{i}{D_n}) + \sum_{j=1}^{N}\left[\overset{ij}{A}_{ns}\overset{j}{D}_s + \overset{ij}{A}_{nn}\overset{j}{D}_n\right] \end{aligned} \quad \text{..... (4.27)}$$

4.1.3 Joint Opening Mode

Joint separation or tensile cracking is another possible failure mode for the joint element, as shown in **Fig. 4.2**. According to the Mohr-Coulomb condition, the tensile strength of a joint element can be expresses as:

$$\overset{i}{\sigma}_n = \overset{i}{c}\cot an\overset{i}{\phi} \quad \text{..... (4.28)}$$

When the tensile stress across an element is greater than the tensile strength $\overset{i}{\sigma}_n$, the element needs to be allowed to crack open, in which the total normal and shear stresses become zero.

The total stress on element *i* is equal to the summation of far-field stress and induced stress:

$$\left(\overset{i}{\sigma}\right)^{total} = \left(\overset{i}{\sigma}\right)^{\infty} + \left(\overset{i}{\sigma}\right)^{ind} \quad \text{..... (4.29)}$$

For a joint with N element, if element *i* becomes an open joint element, the equation takes the form:

$$\begin{aligned} 0 - (\overset{i}{\sigma_s})^{\infty} &= (\overset{i}{\sigma_s})^{ind} = \sum_{j=1}^{N} \left[\overset{ij}{A}_{ss} \overset{j}{D}_s + \overset{ij}{A}_{sn} \overset{j}{D}_n \right] \\ 0 - (\overset{i}{\sigma_n})^{\infty} &= (\overset{i}{\sigma_n})^{ind} = \sum_{j=1}^{N} \left[\overset{ij}{A}_{ns} \overset{j}{D}_s + \overset{ij}{A}_{nn} \overset{j}{D}_n \right] \end{aligned} \quad \text{..... (4.30)}$$

where A_{ss}, A_{sn}, A_{ns}, A_{nn} are the influence coefficient matrix accounting for the different positions and orientations of each element as defined in Eq. (2.5).

The simulation of the joint displacements and stresses under opening mode is as follows. Suppose the current values of the DD components at element *i* are $\overset{i}{D}_n$, $\overset{i}{D}_s$, if no opening mode occurred during this or any previous loading, calculate the total normal stress and shear stress along the joint. If $(\overset{i}{\sigma_n})_{total} \geq \overset{i}{c} \cdot \cot \overset{i}{\phi}$, governing Eq. (4.30) is used to calculate $\overset{i}{D}_n$ and $\overset{i}{D}_s$.

4.2 Numerical Procedure

For problems involving joint elements, the contact type (stick, yield or open) and the displacements/stresses of each element along the joint are unknown. But if the contact mode is known, the corresponding governing equations relating the stresses and DD in Section 4.1 can be used to solve the DD at each element. Then the stresses along the joint can be obtained and used to check the contact state again. If the new and the old contact modes are not in agreement, the assumed contact mode must be changed and DD must be solved again. The process will be stopped when the new and the assumed contact modes are the same and resultant DD and stresses along the joint converge. The iterative procedure can be summarized and listed as follows:

1) Within each time step, at k^{th} iteration and at element i, first a joint contact type (for example stick mode) is assumed and the corresponding k^{th} estimates for the normal and shear displacements $\overset{i}{D}_n^{(k)}$, $\overset{i}{D}_s^{(k)}$ at the i^{th} element are obtained using Eq.(4.8) or (4.16).

2) The total normal and shear stresses at the i^{th} element $(\overset{i}{\sigma}_n)_{total}^{(k)}$ and $(\overset{i}{\sigma}_s)_{total}^{(k)}$ are calculated by Eq. (4.31) as followed:

   The total stress on a joint element in the system is obtained by adding the far-field stress σ^{∞} and the induced stress σ^{ind} resulting from the deformation of all elements present in the system which is:

$$(\overset{i}{\sigma_s})^{(k)}_{total} = (\overset{i}{\sigma_s})^{\infty}_{0} + \sum_{j=1}^{N}\left[\overset{ij}{A_{ss}}\ \overset{j}{D_s}^{(k)} + \overset{ij}{A_{sn}}\ \overset{j}{D_n}^{(k)} \right]$$

$$(\overset{i}{\sigma_n})^{(k)}_{total} = (\overset{i}{\sigma_n})^{\infty}_{0} + \sum_{j=1}^{N}\left[\overset{ij}{A_{ns}}\ \overset{j}{D_s}^{(k)} + \overset{ij}{A_{nn}}\ \overset{j}{D_n}^{(k)} \right] \quad \text{..... (4.31)}$$

3) Calculate the yield stress at the k^{th} iteration according to Eq. (4.20). Then a check is made to see whether the yield/opening condition is met or not according to Eq. (4.20) and (4.28).

4) If the yield condition is met, Eq. (4.24) or (4.27) is used to compute the next approximation of the normal and shear displacements at the i^{th} elements $\overset{i}{D_n}^{(k+1)}$ and $\overset{i}{D_s}^{(k+1)}$.

5) If the yield condition is not met, Eq.(4.8) or (4.16) are used to compute the next approximation of the normal and shear displacements at the i^{th} elements, $\overset{i}{D_n}^{(k+1)}$ and $\overset{i}{D_s}^{(k+1)}$.

6) If the opening condition is met, Eq.(4.30) is used to compute the next approximation of the normal and shear displacements at the i^{th} elements, $\overset{i}{D_n}^{(k+1)}$ and $\overset{i}{D_s}^{(k+1)}$.

7) Continue to step 2) and check the contact mode again. If the new contact mode does not match the old one, the assumed contact mode must be changed and DD must be solved again. Continue the iterative process until

DD and stresses at each element *i* converges (the difference between the stresses of two iteration cycles (between $(\overset{i}{\sigma}_n)_{total}^{(k)}$ and $(\overset{i}{\sigma}_n)_{total}^{(k+1)}$, $(\overset{i}{\sigma}_s)_{total}^{(k)}$ and $(\overset{i}{\sigma}_s)_{total}^{(k+1)}$) approaches zero or less than a certain small value).

8) We then continue to simulate the next time step and repeat the entire procedure.

4.3 Numerical Examples

4.3.1 Compression of a Single Joint

As an example, consider the initial deformation of a horizontal joint of length 2m under in-situ compressive stress S_h=1MPa. The normal and shear rigidity of the joint is set to be $K_n = 0.5\text{MPa/m}$ and $K_s = 0.25\text{MPa/m}$.

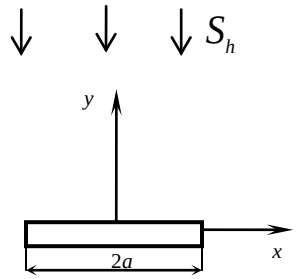


Fig. 4.3 Compression of a single joint.

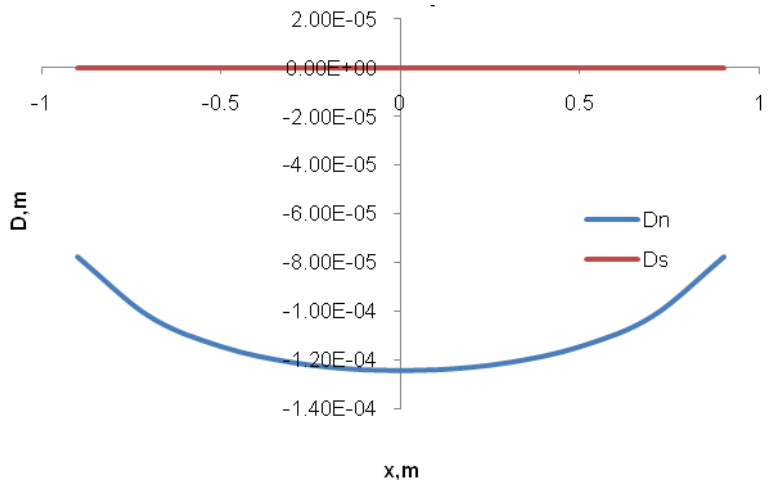


Fig. 4.4 Shear and normal displacement (D_s, D_n) along the joint surface (initial joint deformation included)

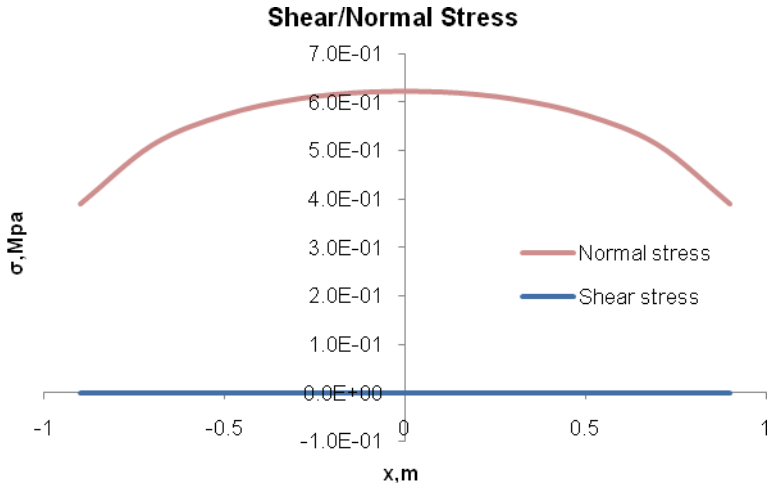


Fig. 4.5 Shear and normal stress along the joint surface (initial joint deformation included)

The mechanical response of a horizontal natural fracture under far-field compressive stresses calculated by using 10 equal length joint elements including initial joint deformation is shown in **Fig. 4.6** and **Fig. 4.7**. The governing equation **Eq. (4.15)**

in this case is reduced to $-(\overset{i}{\sigma}_n)_0^{\infty} = (\overset{i}{K}_n)(\overset{i}{D}_n) + \sum_{j=1}^{N} \overset{ij}{A}_{nn}(\overset{j}{D}_n)$ or $[\sigma_n^{\infty}] = [A_{nn} + K_n][-D_n]$.

Therefore, uniaxial compressive stress will cause a negative D_n, indicating joint closure (it is assumed here that the initial aperture of the joint is much bigger than the maximum relative closure of the two joint surfaces, which is only at the order of 10^{-4}m. Therefore, the two joint surfaces have not come into contact or penetrated into each other.) The total normal stress along the joint surface is positive (compressive) and is smaller than the magnitude of the far-field compressive stress, as the joint acts like a spring that it absorbs some of the external force/energy by deformation (relative joint closure). (A joint with higher value of normal stiffness would deform less, and the degree of stress absorption is less.) Shear displacement and shear stress in this case is zero along the joint surface.

In comparison, the mechanical response of a horizontal natural fracture under far-field compressive stresses without considering the initial joint deformation is shown in **Fig. 4.6** and **Fig. 4.7**. As can be seen, the total normal and shear stresses on the joint corresponds to the far-field compressive stress S_h and zero far-field shear stress, respectively. As we have excluded the initial joint deformations under far-field stresses, assuming the joint has reached equilibrium under geological time, so the model yields results that there is no slippage or relative normal displacement along the joint.

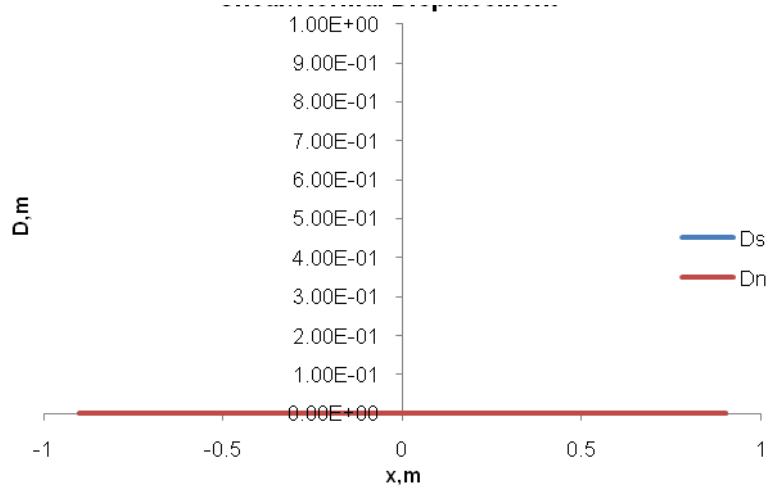


Fig. 4.6 Shear and normal displacement (D_s, D_n) along the joint surface (initial joint deformation not included).

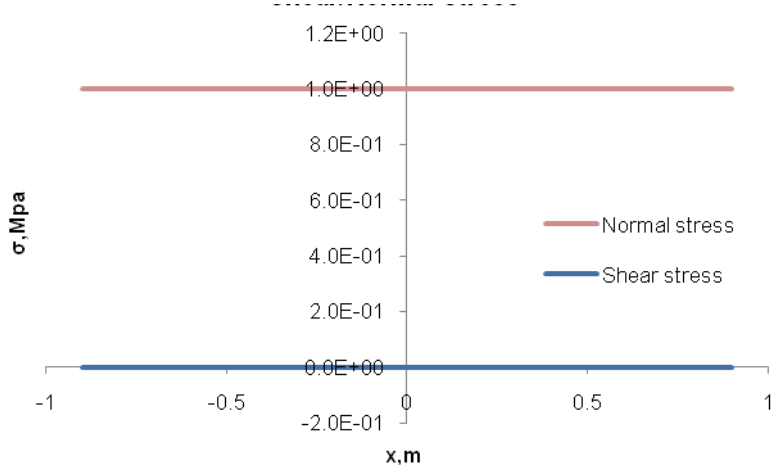


Fig. 4.7 Shear and normal stress along the joint surface (initial joint deformation not included).

In summary, both two models can be used for describing joint behaviors under far-field stresses. But the selection of which model to use depends on the specific considerations for the particular fracturing situations. For fracturing in a naturally-

fractured reservoir of long geological history, the second model in which initial joint deformation is excluded seems to have a better representation of the mechanical response (stresses/displacements) of the natural joints as we could expect. And especially when investigating the induced stresses/displacements along the natural joint due to fracturing, the initial joint deformation probably is of less importance to the problem, and can therefore be ignored or regarded as zero.

Therefore more examples were simulated by using the second approach and shown in the following sections, to verify whether this approach can give us reasonable and good approximations for simulating problems involving joint deformation.

4.3.2 A Slanted Single Joint under Biaxial Stresses

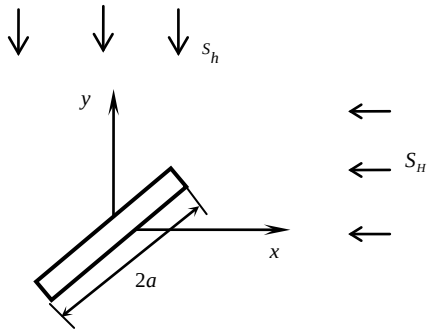


Fig. 4.8 A slanted joint under biaxial stresses.

The mechanical response of a slanted single joint under far-field biaxial stress S_H=4MPa, S_h=3MPa is checked. The slant angle of the joint relative to the direction of

SH is 45°, and the normal and shear rigidity of the joint is $K_n = 0.5\text{MPa/m}$ and $K_s = 0.25\text{MPa/m}$. The half length of the joint *a*=1m.

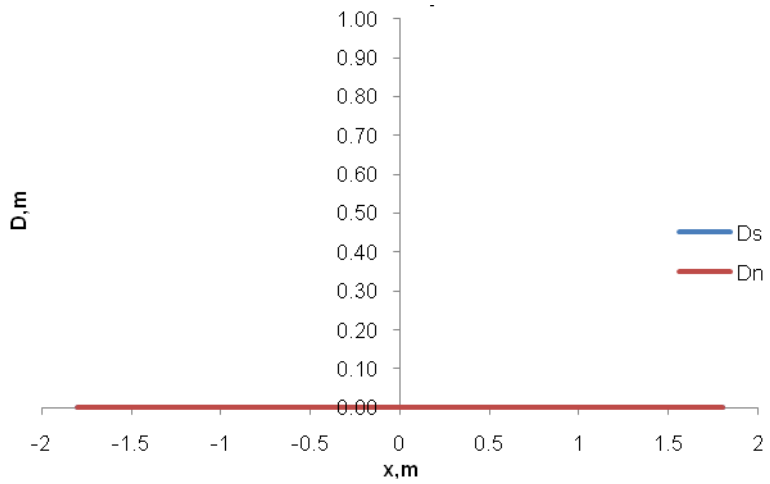


Fig. 4.9 Shear and normal displacement (D_s, D_n) along the joint surface.

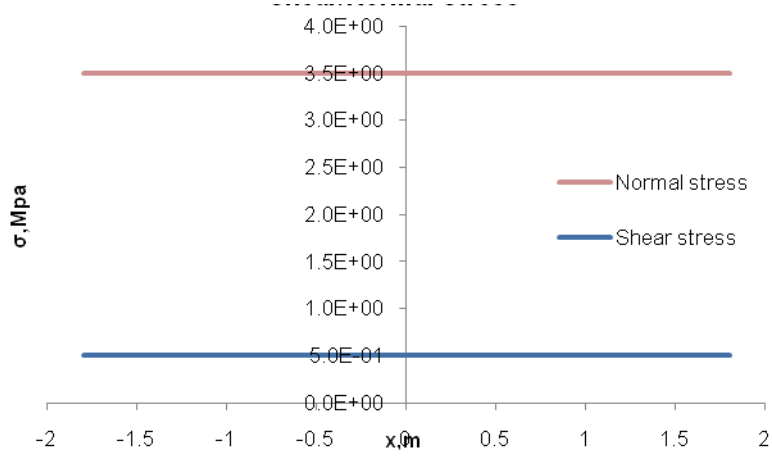


Fig. 4.10 Shear and normal stress along the joint surface.

As can be seen from **Fig. 4.9** and **Fig. 4.10**, the total shear and normal stresses on the joint are the far-field stresses in the joint direction. The joint is closed and has not slipped under far-field stresses.

4.3.3 Shear of a Single Joint

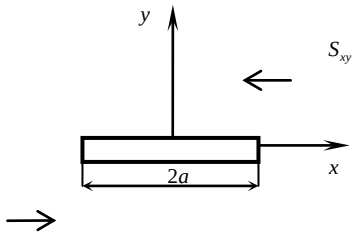


Fig. 4.11 Shear of a single joint.

The mechanical response of a horizontal joint under far-field shear stress is checked in this example. The normal and shear rigidity of the joint is assumed to be $K_n = 0.5\text{MPa/m}$ and $K_s = 0.25\text{MPa/m}$. The frictional angle $\phi = 30°$, far-field stress S_{xy}=2.2MPa, and cohesion $c = 0.22\text{MPa}$.

The stresses and displacements along the joint are shown in **Fig. 4.12** and **Fig. 4.13**. As far-field shear stress has exceeded the yield stress of the joint, which in this case is equal to the cohesion 0.22 MPa, the joint would undergo permanent slippage along the surface, so that the total shear stresses stay at the value of the yield stresses. As can be seen from **Fig. 4.12**, the normal closure and normal stresses are zero in this case. Slippage along the joint is symmetric and parabolic.

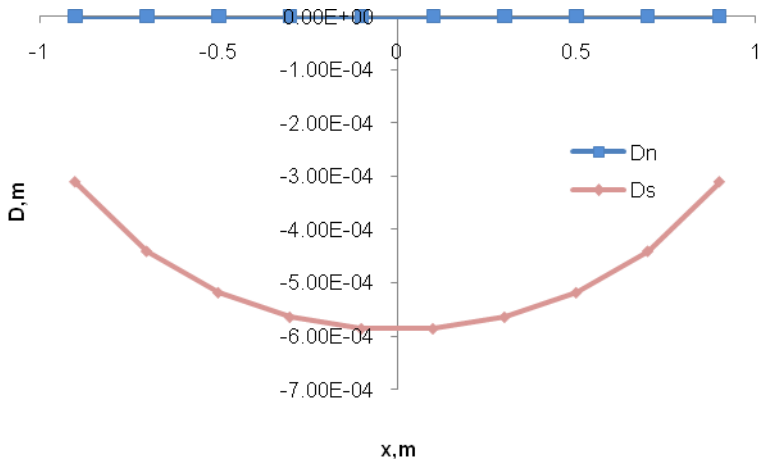


Fig. 4.12 Normal and shear displacement (D_n, D_s) along a joint surface under plastic deformation.

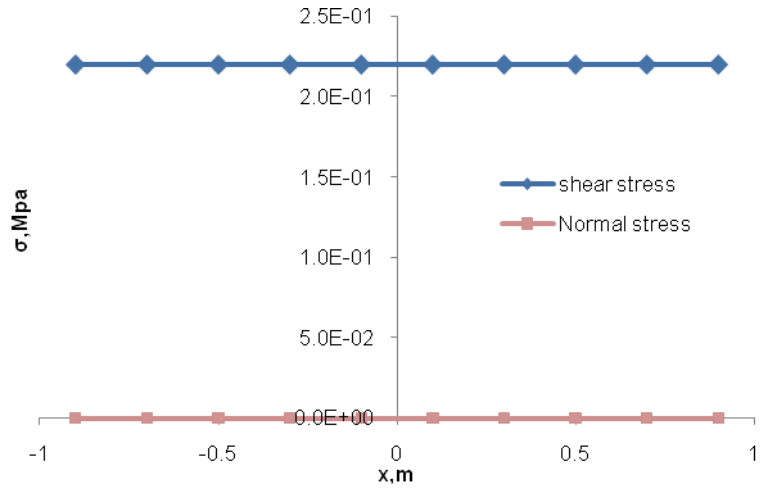


Fig. 4.13 Normal and shear stress along a joint surface under plastic deformation.

4.3.4 Assessment of Accuracy

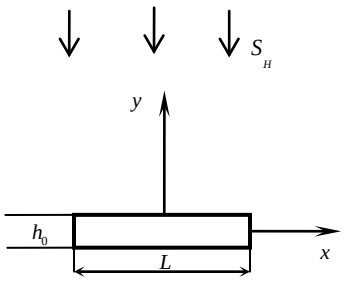


Fig. 4.14 A rectangular opening subjected to far-field compressive stress.

The accuracy of the joint element approach can be checked by using the numerical example in p.137 of Crouch's book (Crouch 1976), which essentially examines the stresses and displacement in the vicinity of an excavation in an infinite elastic medium. As shown in **Fig. 4.14**, a single rectangular opening of width *L* and height h_0, in an infinite body is subjected to a uniaxial stress $S_H = p$. The stresses and displacements in the vicinity of the opening and along the x axis are checked. This problem is solved by using joint element method. I used 10 elements to model the rectangular opening with "**mined" joint elements** (crack elements) and 10 elements along *x*-axis at each side of the rectangular opening as "**unmined" joint elements**. Poisson's ration of the rock is $v = 0.2$.The rectangular length to height ratio is $L/h_0 = 10$. The far field stress *p* to the shear modulus *G* was taken as $p/G = 2.4 \times 10^{-3}$.

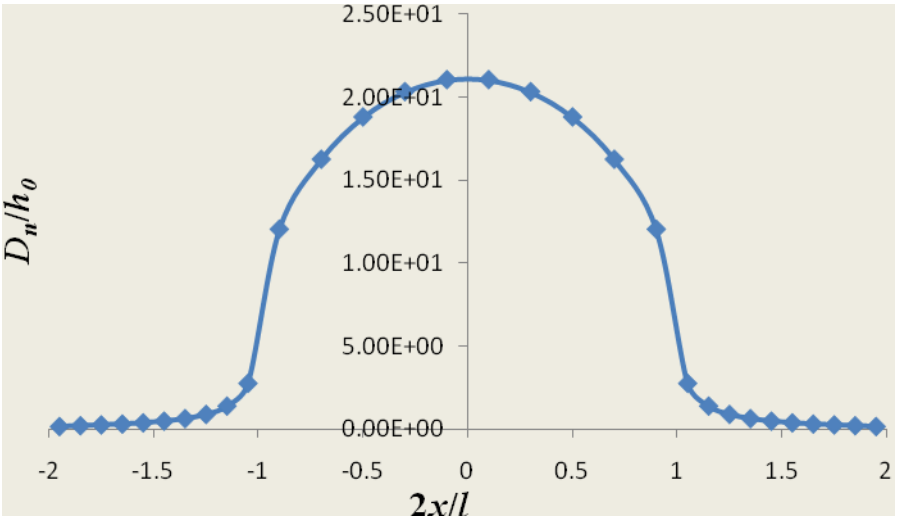


Fig. 4.15 Dimensionless normal displacements at *y*=0 using joint element solution.

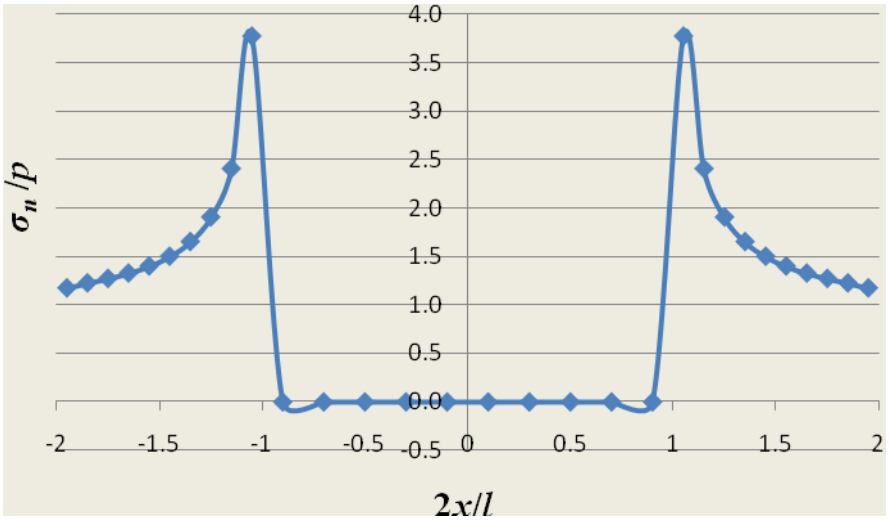


Fig.4.16 Dimensionless normal stresses at *y*=0 obtained using joint element solution.

Dimensionless normal displacement and stresses along *y*=0 are shown in **Fig. 4.15** and **Fig.4.16**. We can see that the two surfaces of the rectangular excavation are closed relative to each other under far-field compressive stress (positive D_n indicating

relative closure) and that two surfaces outside the excavation approaches zero displacement. The total normal stress distribution is zero along the excavation and approaches to far-field compressive stress outside the excavation. At locations near the excavation, there are stress localization which is about 3.77 times of the far-field stress. This value matches well with results when only crack element of DD method is used to model the stresses within and outside the excavation along y=0 (Crouch 1976). Therefore, we may come to the conclusion that joint element method can give us fairly accurate results when determining the stress and displacement distribution for problems involving natural fractures and hydraulic fractures (which can be regarded as mined elements with nonzero total normal stresses imposed on the surface).

5 HYDRAULIC FRACTURE AND NATURAL FRACTURE INTERACTION

5.1 Introduction

The objectives of the initial phase of modeling are:

- To study the interaction between a hydraulic fracture (HF) and a natural fracture (NF). Carry out a parametric analysis to explore the effect of model input parameters on the displacements and stresses, and the possible slipping or opening of a pre-existing NF (observe NF and HF mechanical interaction).
- To model the process of HF tip approaching a NF to trace the orientation and extension of the HF.

5.2 Mechanical Responses of a Natural Fracture

5.2.1 Problem Definition

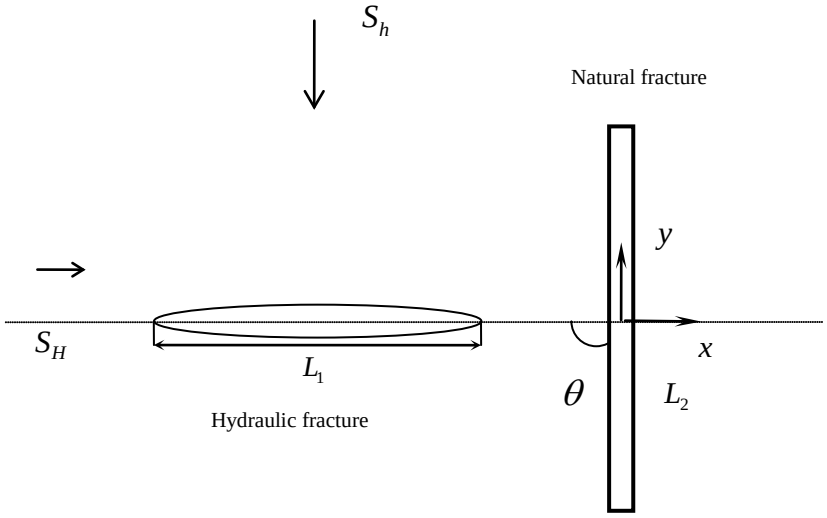


Fig. 5.1 A hydraulic fracture located near a natural fracture.

The first modeling was done assuming a stationary hydraulically induced fracture located near a NF that is oriented θ degrees to the maximum horizontal in-situ stress S_H. The fracture is assumed to be subjected to a constant pressure distribution along its length. The stress and displacement distributions along the NF are checked. The natural fractures/faults are considered to have reached mechanical equilibrium under far-field stresses with geological time (joint model as described in Section **4.1.1.1**). With the introduction of a new HF, the stress field near the NF would experience perturbation, possibly leading to slip/opening. This process along with the most probable location for fracture re-initiation along the NF is investigated below.

For a given rock tensile strength, T_0, the criterion for the tensile crack initiation is (Chuprakov et al. 2010):

$$\sigma_p > T_0 \quad \text{..... (5.1)}$$

where σ_p is the maximum tensile stress. When the joint is considered ideally smooth and without any secondary flaws along its surface, the zones of tension are the probable locations for new tensile crack re-initiation.

A complete investigation of the interaction between a HF and a NF should include stages of HF tip approaching, fracture coalescence, fluid flow into the NF, and the subsequent initiation of the secondary fracture from the NF. In this thesis, the HF induced stress change and the resultant slippage or tensile opening along the NF are

---

In this chapter, a *tension positive sign convention* is used for convenience as the maximum tensile stress is of interest along the back side of the NF. So, a positive stress indicates tension and positive normal displacement indicates relative opening of the two joint surfaces.

studied for the stage of an approaching HF tip (Section 5.2.2 and 5.2.3), and the stage of fluid flow into the NF (Section 5.2.4).

5.2.2 Parametric Studies

The model inputs are listed in **Table 5.1.** Joints with different magnitude of bonding strengths were investigated in our study. We considered three sets of joint properties: a weak joint (c=0, T_0=0), an infinitely strong joint (c=∞, T_0=∞), and a joint with moderate strength (ϕ=26.6°, c=2.2MPa, T_0=0.2MPa). The distance between the HF tip and NF was modeled to be 0.2m, 0.1m, and 0.05m. The NF (length of 2m) was modeled with 50 constant DD elements with equal length and the HF (length of 2m) was modeled with 20 constant DD elements with equal length. Modeling results are discussed in details as follows.

Table 5.1 Input parameters in Section 5.2.2.

Joints	Rock	HF
Geometry: • Orientation $\theta = 90°$ • Length $L_2 = 2\text{m}$	In-situ Stresses: • $S_H = -2.1\text{MPa}$ • $S_h = -1.9\text{MPa}$	Geometry • Length $L_1 = 2m$ • Distance with NF d_0
Mechanical Properties: • Friction angle: ϕ • Cohesion: c • Tensile strength: T_0 • Normal stiffness $K_n = 0.5\times10^6\,\text{MPa/m}$ • Shear stiffness $K_s = 0.25\times10^6\,\text{MPa/m}$	Mechanical Properties: • Young's modulus $E = 1.4\times10^4\,\text{MPa}$ • Poisson's ratio $v = 0.1$	Fluid Properties: • Fluid pressure $p = 3.9\text{MPa}$

The weak joint has zero cohesion and tensile strength, so it cannot sustain any shear and tensile forces and is always ready to slip or open. In **Fig. 5.2**, the stress distribution along a weak joint, when d_0=0.1m and θ=90° is plotted. The shear stress in this case is zero, and yield stress is zero in this case, so fault is in a plastic yield condition or "permanent slip" mode. The normal stress and shear stress are zero near the center of the joint, which is an indication of joint opening (normal to the joint surface) at this segment. The maximum tensile stress becomes positive near the center of the opposite side of the joint, and has two peak values located at two locations with symmetry to the x axis. As the tensile limit of the joint is zero and has been exceeded in this case, these two locations could become most probable location for new tensile crack onset before the coalescence of the HF with the NF.

However, the induced tensile crack may not have a sufficient capability to grow further without fluid infiltration. Once the HF coalesces with the NF, and fluid penetrates into the NF, the stress distribution along the joint and the zones of stress localization for new crack re-initiation may change. Therefore, a complete study of HF interaction with NF involving all the subsequent stages is needed for us to have a complete picture of this problem.

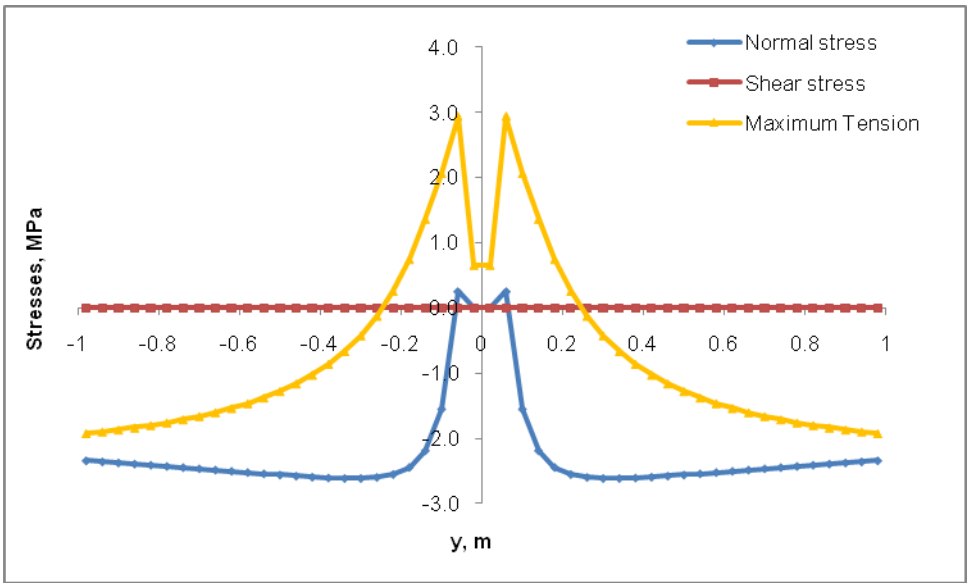


Fig. 5.2 Stress distribution along a weak joint (at x=0, d_0=0.1m, θ=90°).

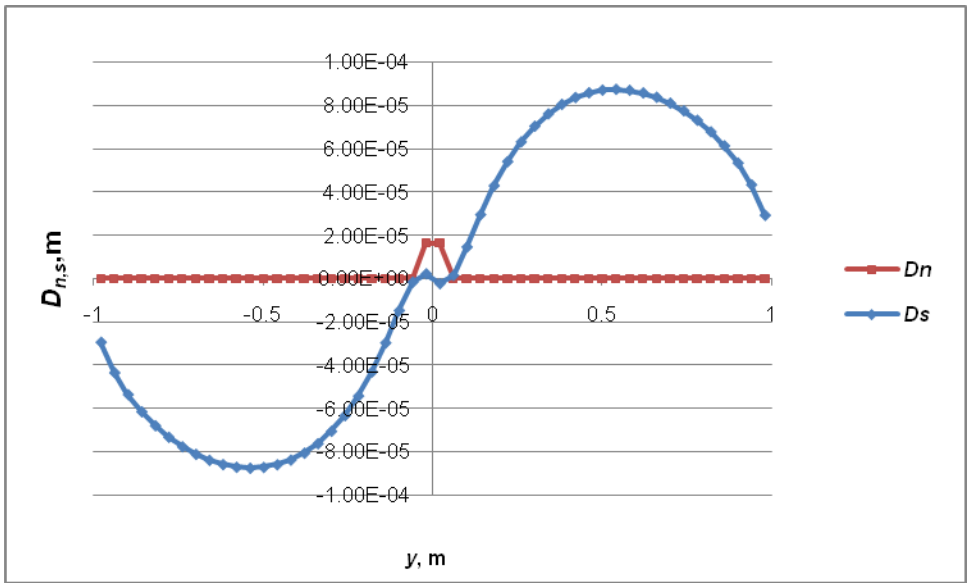


Fig. 5.3 Normal and shear displacement (D_n, D_s) along a weak joint (at x=0, d_0=0.1m, θ=90°).

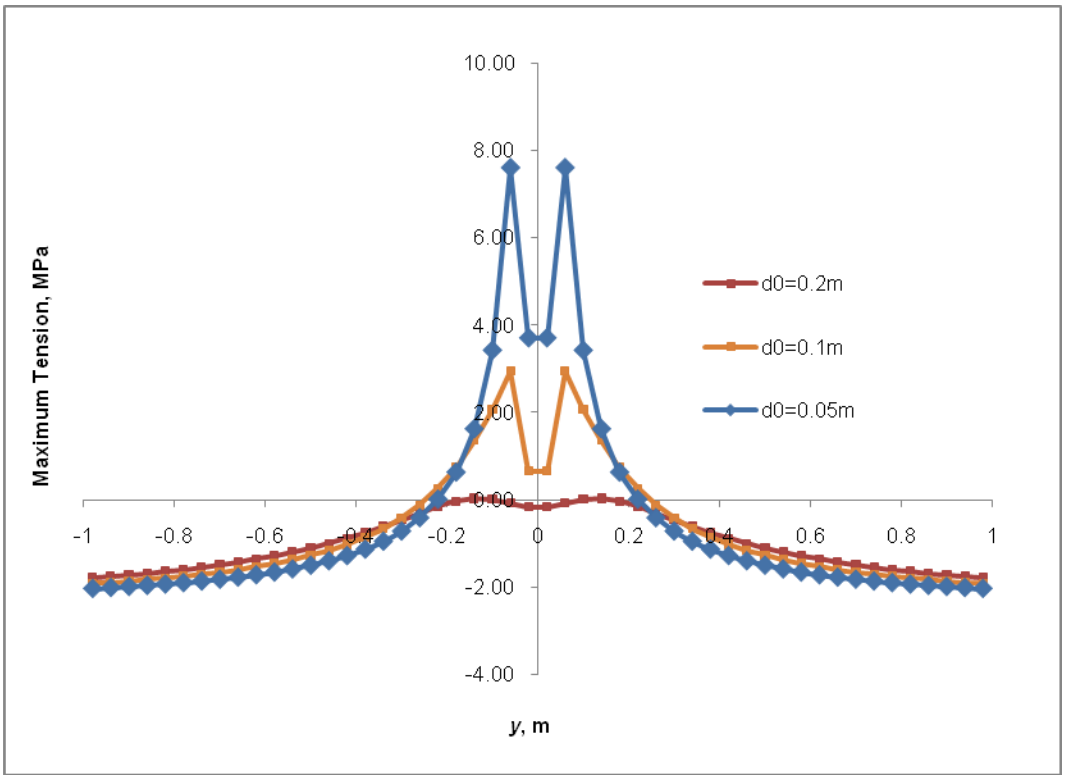


Fig. 5.4 Maximum tensile stress along a weak joint (x=0) at different tip distances (d_0) (θ=90°).

The shear slip and normal displacement is shown in **Fig. 5.3**. The normal displacement is positive, which indicates that HF can induce normal opening near the HF tip region along the joint. Curves of maximum tensile stress generated along the back side of the joint at different distances from the HF tip and NF are plotted in **Fig. 5.4**. With the approaching of HF tip to the NF, the influence of fracture tip is stronger and the tension force gets bigger. The two peak locations move closer to the center of the NF, with the decreasing of the distance between HF tip and NF.

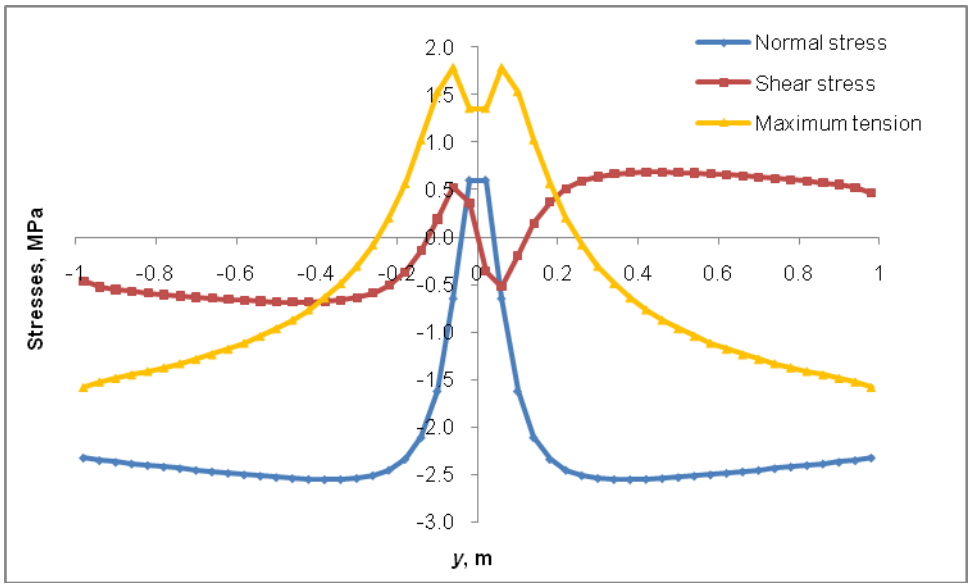


Fig. 5.5 Stress distribution along a strong joint (at x=0, d_0=0.1m, θ=90°).

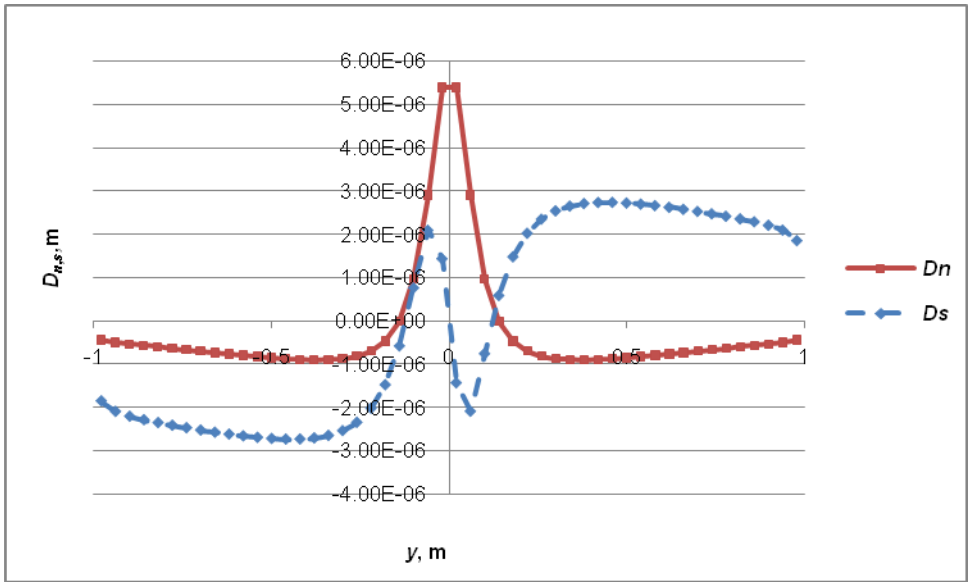


Fig. 5.6 Normal and shear displacement (D_n, D_s) along a strong joint (at x=0, d_0=0.1m, θ=90°).

Stresses and displacements along a strong joint ($c=\infty$, $T_0=\infty$) are calculated and plotted in **Fig. 5.5** and **Fig. 5.6**. A joint with infinite strength is bonded so strongly that tensile failure (joint crack open) and shear failure (joint permanent slip) will never occur to it. From **Fig. 5.5** we can see that everywhere along the joint the shear and normal stress are nonzero, and that yield stress has not been reached (infinite in this case), so everywhere along the joint is in the "stick" contact mode. For a very strong joint, the HF cannot induce enough stresses that can lead to the joint "open" and "permanent slip" contact mode. The shear slip and normal closure for a strong joint is at the order of 10^{-6}m as shown in **Fig. 5.6**, which is much smaller than those for a weak joint. As could be expected, the induced displacements are much less for a joint with stronger strength.

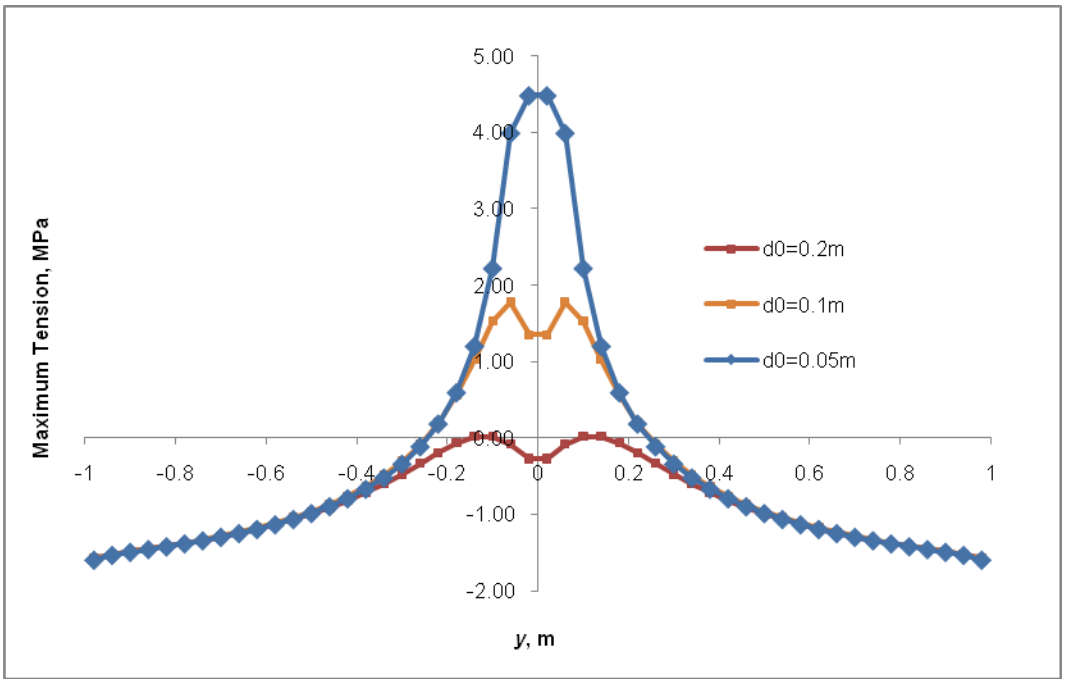


Fig. 5.7 Maximum tensile stress along a strong joint (x=0) at different tip distances (d_0) (θ=90°).

From **Fig. 5.7** we can see that the maximum tensile stress generated at the back side of the strong joint also increase with the decrease of the distance between HF tip and NF. The joint has an infinite tensile strength in this case, so the induced tension is not big enough to pull the back side of the joint rock open. In comparison with a weak joint, the magnitude of the peak value gets smaller and the location of the two peak values gets closer for a strong joint.

In most practical cases, a natural joint is of moderate strength between these two above limiting cases. Therefore a joint with intermediate strength values (α=26.6°, c=2.2MPa, T_0=0.2MPa) is also simulated to check its mechanical responses. The stress distribution for on the joint is shown in **Fig. 5.8**. It can be seen that one small segment at the center of joint has zero shear and normal stress corresponding to an "open" contact mode (when the normal stress exceeds the tensile limit of the joint and the joint surfaces open like a crack). When d_0=0.1m, the peak values of maximum tensile stress at the opposite side of the NF is about 2 MPa which exceeds the tensile limit of the joint (0.2 MPa) in this case. So, the onset of new tensile cracks can begin there before the HF coalesces with the NF. Again **Fig. 5.10** shows that the maximum tensile stress increases with the approach of HF tip, and the peak tension becomes more localized near the tip region when the tip is closer to the NF.

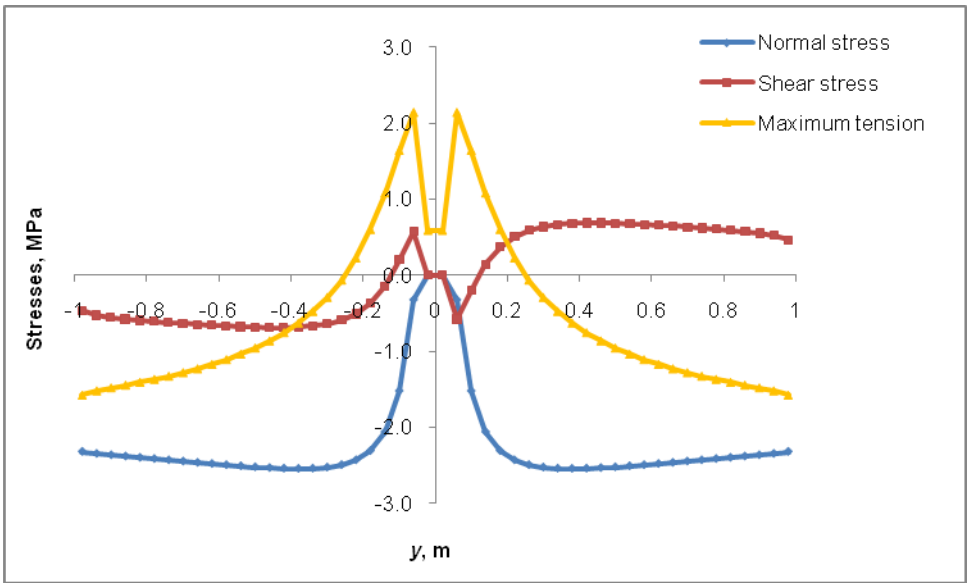


Fig. 5.8 Stress distribution along a moderate joint (at x=0, d_0=0.1m, θ=90°).

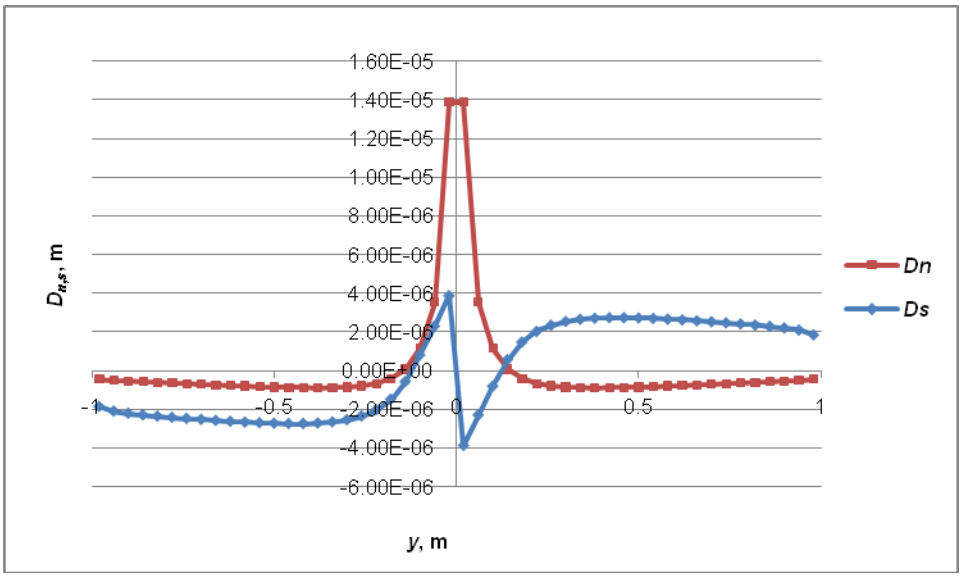


Fig. 5.9 Normal and shear displacement (D_n, D_s) along a moderate joint (at x=0, d_0=0.1m, θ=90°).

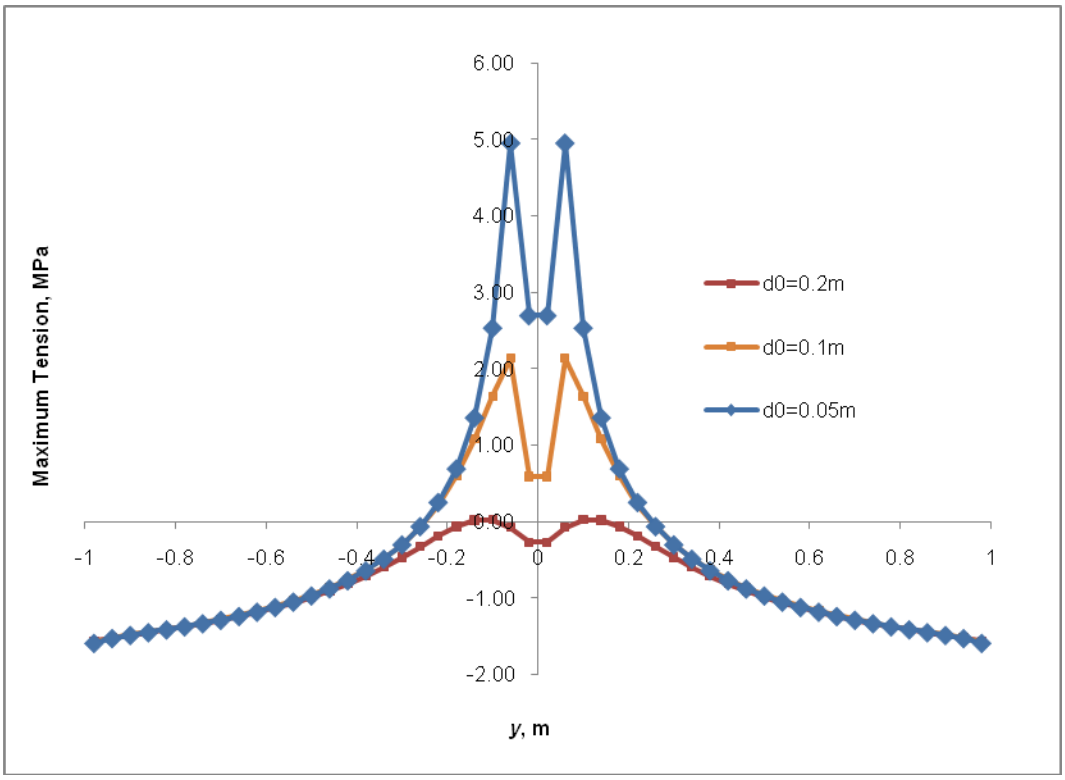


Fig. 5.10 Maximum tensile stress along a moderate joint (x=0) at different tip distances (d_0) (θ=90°).

By comparing **Fig. 5.4**, **Fig. 5.7** and **Fig. 5.10**, it can be concluded that: 1) before HF reaches the NF, fracture re-initiation is more encouraged when the joint is weaker because the induced tension is more likely to exceed the tension limit of the rock; a stronger joint tends to inhibit fracture re-initiation as the induced tension is usually smaller and the tensile strength; 2) in terms of re-initiation location, a fracture step-over (offset) is more likely to happen for HF interacting with a weak joint because the joint slips so that the stress localization on the joint tends to be mitigated by NF sliding; direct crossing of the HF is more likely to occur when interacting with a stronger joint.

5.2.3 Discussion

The mechanical response along a joint was compared with a previous study (Chuprakov et al. 2010) of a stationary HF located near a NF. The geometry of the problem is shown in **Fig. 5.1**. The main parameters used are listed in **Table 5.2**.

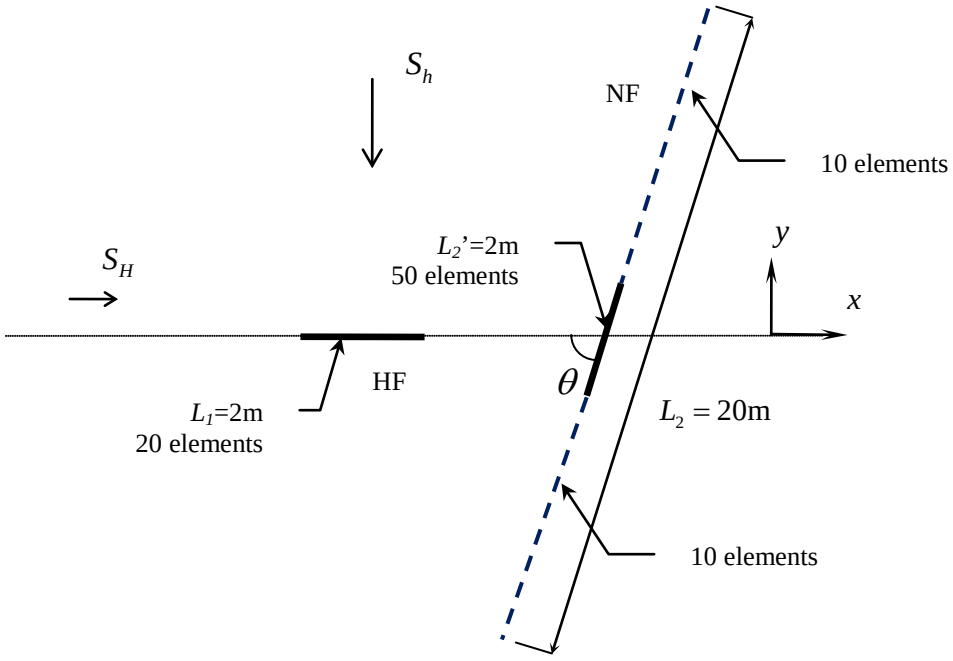


Fig. 5.11 Sketch of mesh arrangement for the NF and HF. Dashed part of the NF is negligible in the interaction between HF and NF, and therefore can be omitted in the modeling.

Seventy elements were used in the simulation of the NF of 20m length, with 50 elements distributed over the central region of the NF (with a length of 2m); 20 equal length elements were used along the HF of length of 2m. Similar results were obtained for modeling only the center of the NF with a length of 2m using 50 equal length

elements. The modeling results indicate that the interaction between HF and NF is negligible in regions outside the central portions of the NF (dashed part of NF as sketched in **Fig. 5.11**) and that excluding these regions in the model will not affect the model outputs.

The shear and normal displacement along the joint $D_{s,n}$ are normalized as following: $d_{s,n} = \frac{D_{s,n}}{L_1}\frac{G}{(1-\nu)\sigma_m}$, in which $\sigma_m = \frac{1}{2}(\sigma_1 + \sigma_3)$ is the mean far-field stress. The shear and normal stresses $S_{t,n}$ along the joint are normalized by the mean far-field stress: $s_{t,n} = \frac{S_{t,n}}{\sigma_m}$.

Table 5.2 Input parameters in Section 5.2.3

Joints	Rock	HF
Geometry: • Orientation $\theta = 40°$ • Length $L_2 = 20\text{m}$	In-situ Stresses: • $S_H = -2.1\text{MPa}$ • $S_h = -1.9\text{MPa}$	Geometry • Length $L_1 = 2\text{m}$ • Distance with NF $d = 0.1\text{m}$
Mechanical Properties: • Friction angle: $\phi = 26.6°$ • Cohesion $c = 2.2\text{MPa}$ • Tensile strength: $T_0 = 0.2\text{MPa}$ • Normal stiffness $K_n = 0.5\times10^6\,\text{MPa/m}$ • Shear stiffness $K_s = 0.25\times10^6\,\text{MPa/m}$	Mechanical Properties: • Young's modulus $E = 1.4\times10^4\,\text{MPa}$ • Poisson's ratio $\nu = 0.1$	Fluid Properties: • Fluid pressure $p = 3.9\text{MPa}$

From **Fig. 5.12**, it can be seen that along most part of the joint the shear slip and normal displacement are nearly zero, and that the HF tip would induce a relative joint opening (positive d_n) and shear slip (d_s) near the center of the NF. In **Fig. 5.13**, the normalized stresses along the joint are plotted. At the lower side (y<0) of the NF, there is an opened segment where shear stress and normal stress come to zero. The maximum tensile stress generated along the opposite side of the joint reaches two peak values near the two ends of the opening section (the maximum tensile stress are normalized by the far-field compressive stress, so the sign of the maximum tensile stress is negative). Similar results can be found in Chuprakov et al. (2010). The magnitude and location of the peak of maximum tensile stress are actually very sensitive to various model input parameters. The difference might result from: 1) in Chuprakov et al., the normal opening for the "closed" part sof NF was set to zero. But in this thesis, the relative normal closure/opening could occur along the entire length of the joint (it is assumed that the NF has an initial aperture that is much larger than the induced relative normal displacements (either positive or negative) so that two surfaces of NF will not come into contact or overlap)). Therefore, in our results, the boundary between the HF influenced zone (with nonzero shear and normal displacments) and the closed part of the NF are less disdinct; 2) The shear and normal rigidity of the joint were not considered/mentioned in Chuprakov et al. while a relatively large rigidity is assumed in this thesis to prevent significant normal/shear displacement outside the HF influenced zone; 3) The tensile strength of the rock was not mentioned in Chuprakov et al. The strength of the rock will

afftect the jog position (tension peak may occur either at the right or left side of NF (Chuprakov et al. 2010)).

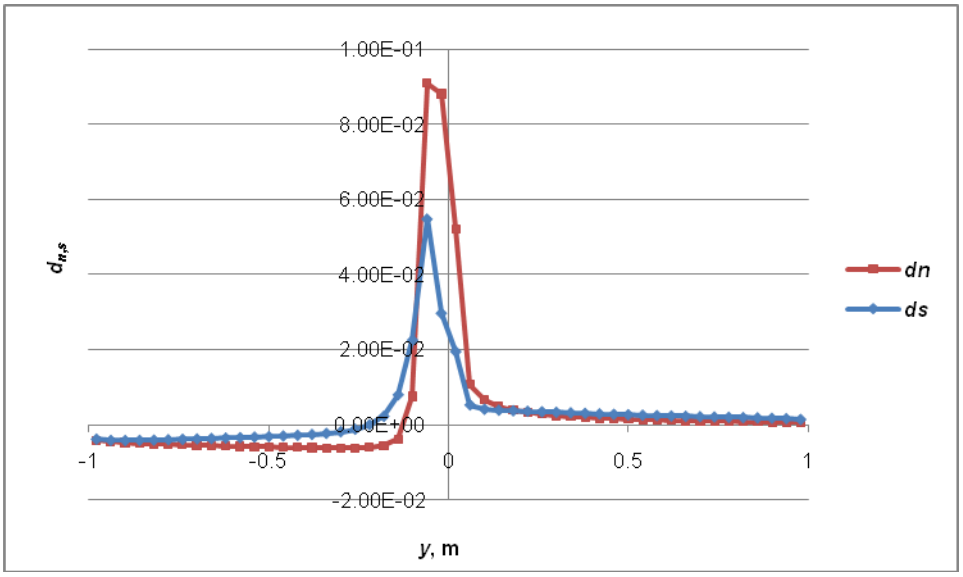


Fig. 5.12 Normalized normal/shear displacements (d_n, d_s) along the NF (x=0).

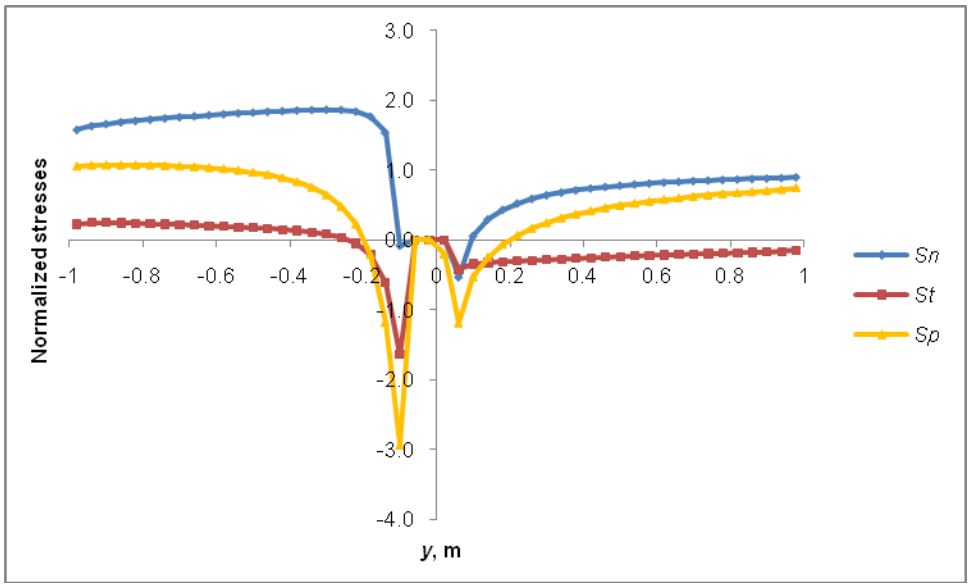


Fig. 5.13 Normalized values of normal stress (S_n), shear stress (S_t), and maximum tensile stress (S_p) along NF (x=0).

5.2.4 Interaction at the Stage when Fluid Flows into the Natural Fracture

The mechanical response of a NF once the fluid is flowing from the HF into the NF is considered in this section. It is assumed that the HF has coalesced with NF, and that the injected fluid propagates along the (y>0) part of the NF (why not y<0 or both shouldn't make nay difference for an acute orientation angle θ) (**Fig. 5.1**). Fluid is assumed that flow is steady and a constant pressure distribution has been established along both the HF and the infiltrated part of the NF. The input parameters are listed in **Table 5.3**.

Table 5.3 Input parameters in Section 5.2.4

Joints	Rock	HF
Geometry: • Orientation $\theta = 40°$ • Length $L_2 = 2\text{m}$ • Invaded length b	In-situ Stresses: • $S_H = -2.0\text{MPa}$ • $S_h = -2.0\text{MPa}$	Geometry • Length $L_1 = 2\text{m}$ • Distance with NF $d = 0.0\text{m}$
Mechanical Properties: • Friction angle: $\phi = 26.6°$ • Cohesion $c = 0.1\text{MPa}$ • Tensile strength: $T_0 = 0.2\text{MPa}$ • Normal stiffness $K_n = 0.5\times10^6\,\text{MPa/m}$ • Shear stiffness $K_s = 0.25\times10^6\,\text{MPa/m}$	Mechanical Properties: • Young's modulus $E = 1.4\times10^4\,\text{MPa}$ • Poisson's ratio $v = 0.1$	Fluid Properties: • Fluid pressure p

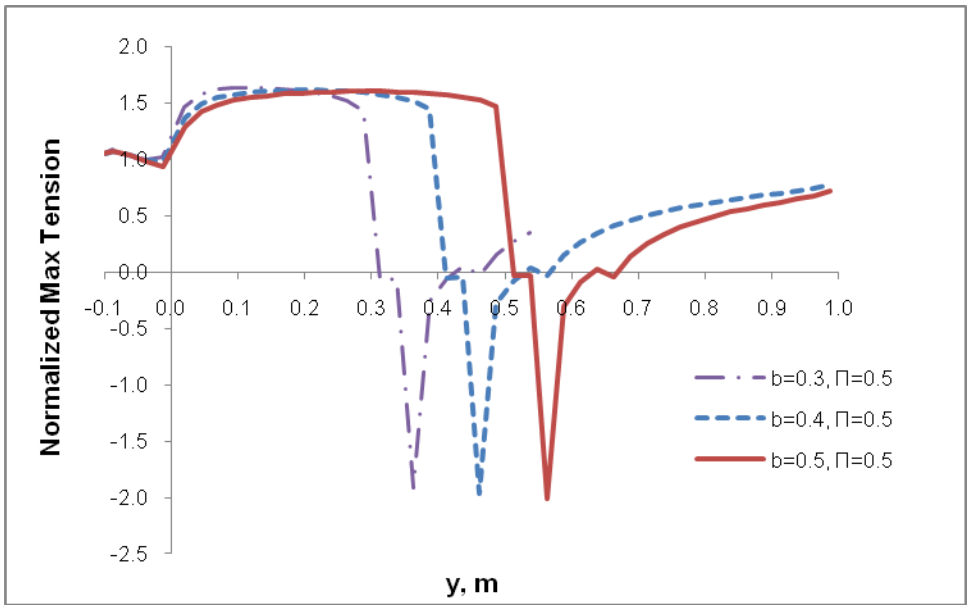


Fig. 5.14 Normalized maximum tensile stress along NF (*x*=0) at different fluid invaded lengths of NF (*b*) (*p*=3.0MPa).

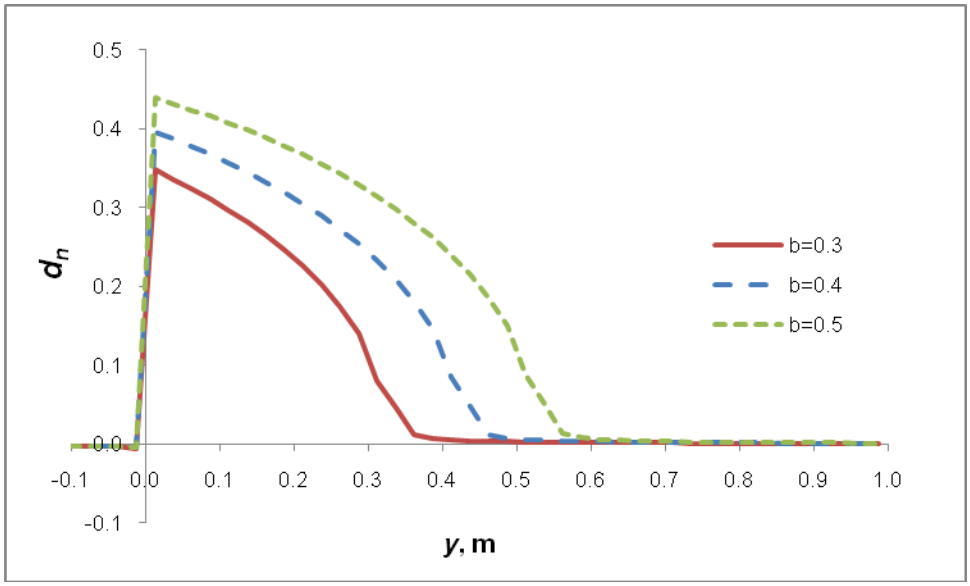


Fig. 5.15 Normalized normal displacement (d_n) along NF (*x*=0) at different fluid infiltrated lengths of NF (*b*) (*p*=3.0MPa).

First consider the normalized maximum tensile stress that develops along the NF when the fluid infiltrated length of NF is increased without changing the fluid pressure. As can be seen from **Fig. 5.14**, a tensile peak is generated along the NF ahead of the fluid front (the maximum tensile stress, S_p, along the joint is normalized by the mean far-field stress, $s_p = \frac{S_p}{\sigma_m}$ in which $\sigma_m = \frac{1}{2}(\sigma_1 + \sigma_3)$ is the mean far-field stress. The fluid infiltrated length of the NF L_b is normalized with half length of the HF, $b = \frac{L_b}{0.5L_1}$). The value of the tensile peak is about 4MPa, and does not change with increased fluid infiltrated length. The location of the tension peak moves along the NF with the increasing of the fluid infiltrated length.

As can be seen from **Fig. 5.15**, the fluid pressure, which is set to higher than the far-field compressive stress (by 1MPa), creates an open zone (d_n>0) along the NF. The length of the open zone is always longer than the fluid infiltrated zone which means there is a fluid lag between the fluid front and end of the open zone. In addition, the tension peak is located at the end of the NF open zone. Therefore, the tension peak is always ahead of the fluid front, and moves with the open zone while fluid infiltrates along the NF. These results are consistent with those of Cooke and Underwood 2001 and Chuprakov et al. 2010. The location of the maximum tensile stress peak is a probable location for further fracture re-initiation.

As another example, let's fix pressurized length of the HF while increasing the fluid pressure along the HF and NF. The normalized maximum tensile stress along the

NF is plotted in **Fig. 5.16**. It can be seen that the value of the tension peak increases and its location moves further to the right part of the NF (y>0) with increasing fluid pressure.

Based on these two example simulations, it can be concluded that the location of peak tension is dependent on both the fluid pressure and fluid infiltrated length of the NF, and its value depends mostly on the fluid pressure.

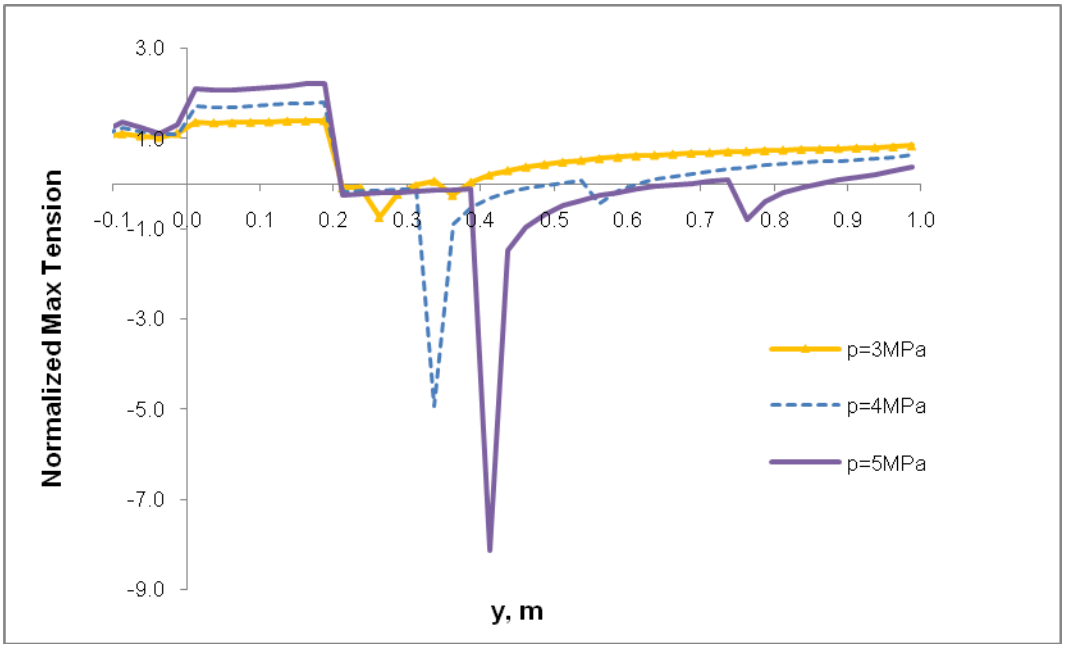


Fig. 5.16 Normalized maximum tensile stress along NF (x=0) at different fluid pressures (p) (b=0.2).

5.2.5 Poroelastic Effects on Mechanical Responses of Natural Fracture

In all previous numerical examples, the rock formation was considered to be elastic and impermeable. In this section, the pore pressure effects on the mechanical responses of the NF are investigated. Again, a uniform pressure distribution along the HF is assumed.

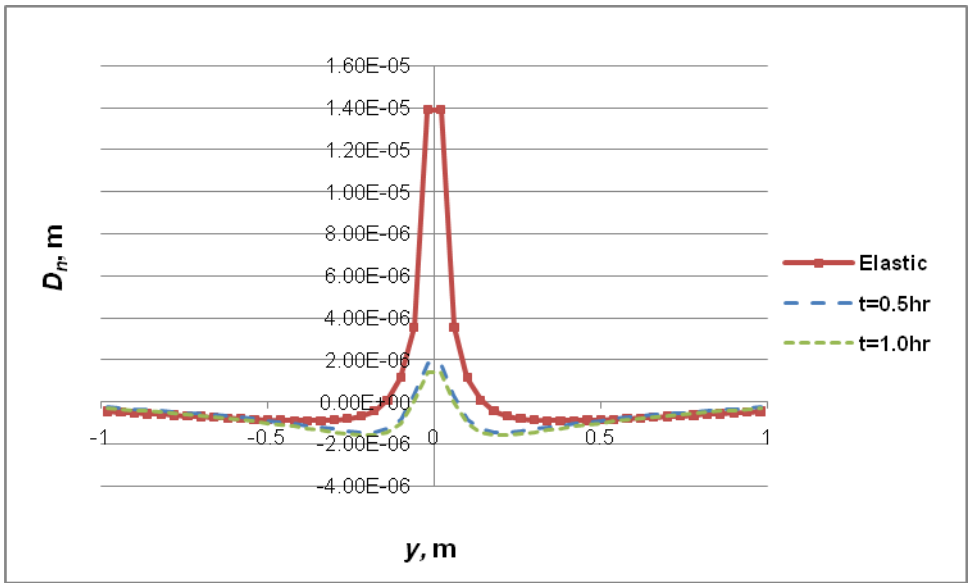


Fig. 5.17 Distribution of normal displacement (D_n) along a moderate joint (x=0) at different time (t) considering poroelastic effects (d_0=0.1m, θ=90°).

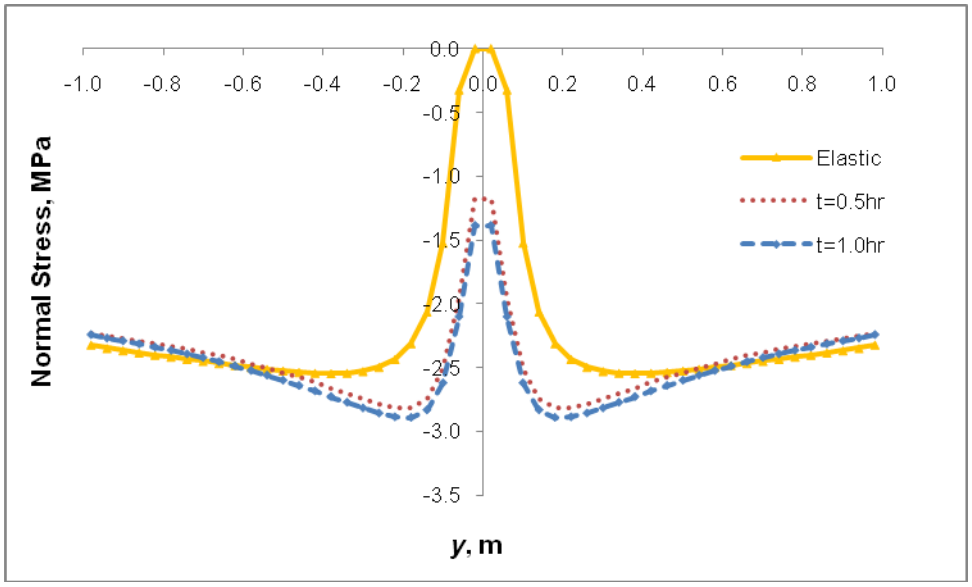


Fig. 5.18 Distribution of normal stress along a moderate joint (x=0) at different time (t) considering poroelastic effects (d_0=0.1m, θ=90°).

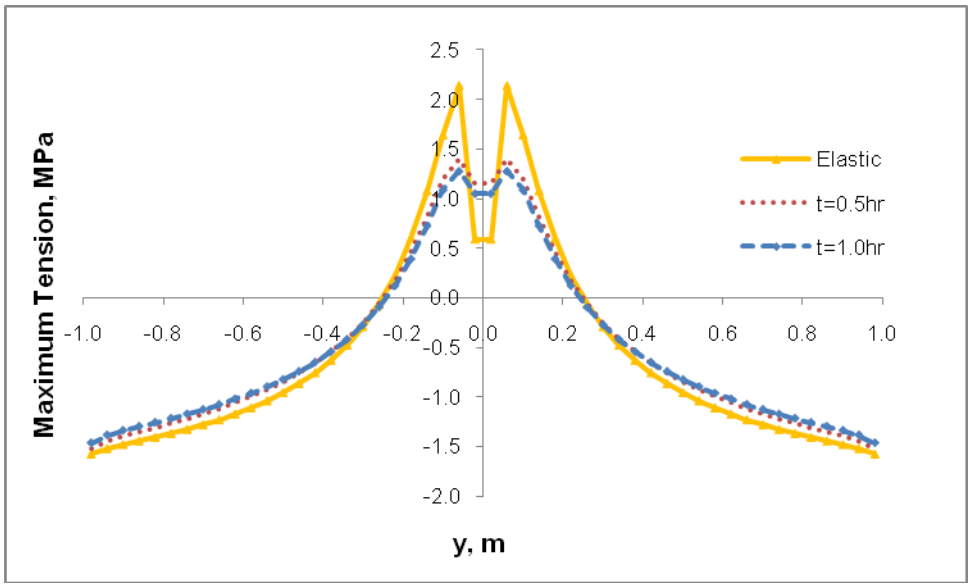


Fig. 5.19 Distribution of maximum tensile stress along a moderate joint (x=0) at different time (t) considering poroelastic effects (d_0=0.1m, θ=90°).

First consider the stage prior to HF coalescing with NF by assuming a stationary HF located near the NF, and monitor the mechanical response of the NF with fluid diffusion from fracture surface into the rock with time. The natural fracture is slanted at 90° (θ=90°) and has a moderate strength (α=26.6°, c=2.2MPa, T_0=0.2MPa); the distance between fracture tip and NF d is 0.1m. Other input parameters are listed in **Table 5.1.**

Distribution of normal displacement (D_n), normal stress, and maximum tensile stress generated along the joint at different times are plotted in **Fig. 5.17**, **Fig. 5.18** and **Fig. 5.19**, respectively. It can be observed that with fluid diffusion from the fracture into the rock matrix, the HF tip induced normal displacement, normal stress and maximum tensile stress all decrease with time near the center of the NF, and slightly increase outside the center region of the NF. The normal stress at the center of the NF decreases

from zero to negative value (compressive). The value of HF tip induced maximum tensile stress decreases with time. Therefore, the possibility for fracture re-imitation is less if pore pressure diffusion is included.

Near the center of the NF, HF tip induced stresses are weakened because HF aperture decreases with fluid diffusion into the rock, which is much more influential than the effective stress decrease with pore pressure increase. However, further away from the HF tip influenced region, outside the center of the NF, the factor of effective stresses decrease gradually dominates so the maximum tensile stress and normal stress become more tensile.

The poroelastic effects on the mechanical response of the NF during the stage when fracturing fluid penetrates part of the NF are then considered by assuming a sequence of fluid with moving fluid front. The input parameters are listed in **Table 5.3**. The model ideally should couple the fluid infiltrated length, pressure distribution and time together, but the simulation is simplified by assuming a fluid infiltrated length at each time, and by assuming a uniform pressure distribution along the HF and NF.

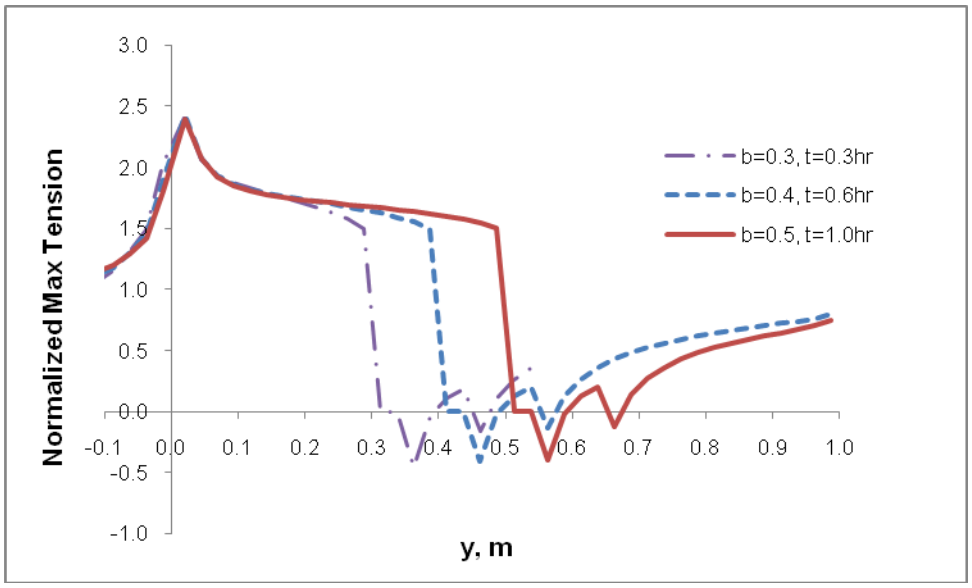


Fig. 5.20 Normalized maximum tensile stress along NF at different fluid invaded lengths along NF (*b*) and time (t) considering poroelastic effects (*p*=3.0MPa, C_f=6.16×10^{-6}).

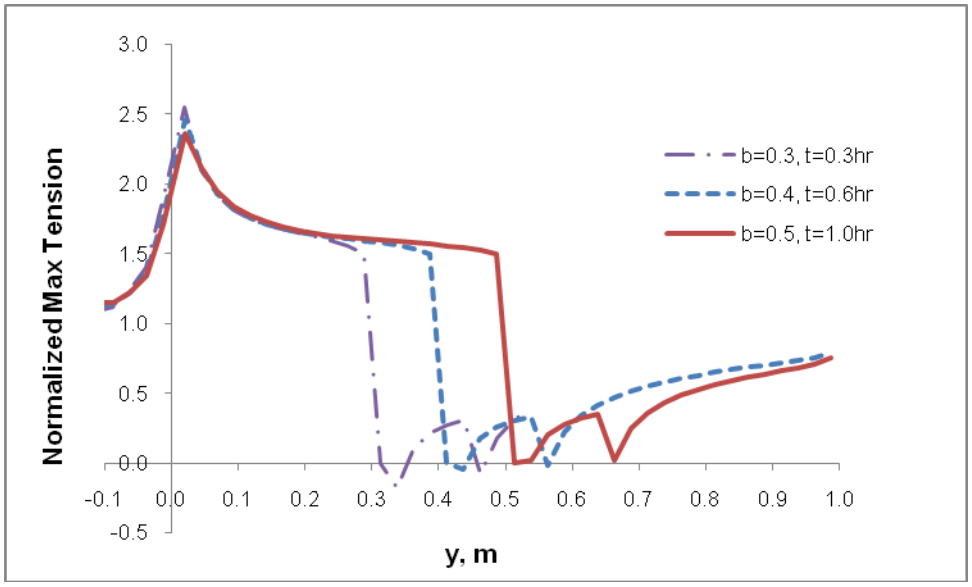


Fig. 5.21 Normalized maximum tensile stress along NF at different fluid invaded lengths along NF (*b*) and time (t) considering poroelastic effects (*p*=3.0MPa, C_f=6.16×10^{-5}).

The normalized maximum tensile stress generated along the NF with increasing time and fluid infiltration (for a fluid diffusivity, C_f , of $6.16\times10^{-6}m^2/s$ and $6.16\times10^{-5}m^2/s$) are plotted in **Fig. 5.20** and **Fig. 5.21**, respectively. Compared with **Fig. 5.14**, it can be seen that poroelastic effects caused by fluid diffusion can significantly decrease the value of tension peak at each time step, decreasing the possibility for fracture re-initiation along the NF. For a fluid with higher value of diffusivity, poroelastic effects are more significant. As shown in **Fig. 5.21**, tension peak diminishes with time and approaches zero, and the values of tension peaks are reduced more when compared to those plotted in **Fig. 5.20**.

5.3 Hydraulic Fracture Trajectories Near a Natural Fracture

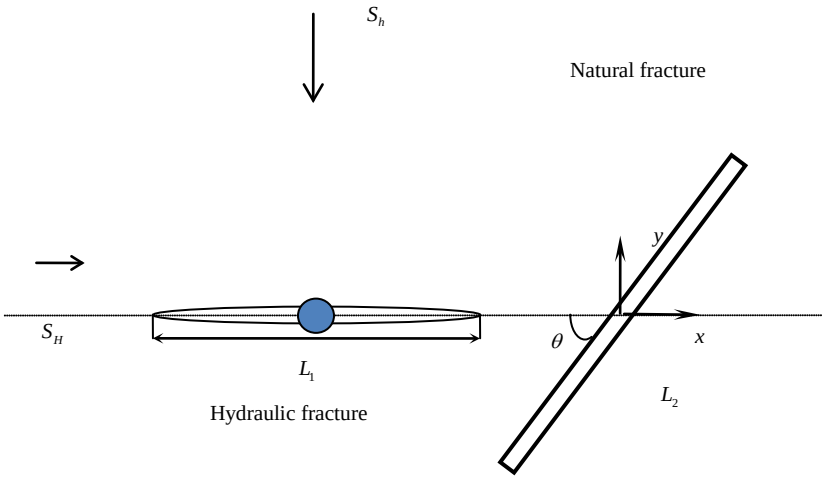


Fig. 5.22 A HF propagating towards a NF.

Table 5.4 Input parameters in Section 5.3.

Joints	Rock	HF
Geometry: • Orientation $\theta = 76°$ • Length $L_2 = 2.06\text{m}$	In-situ Stresses: • $S_H = -43\text{MPa}$ • $S_h = -39\text{MPa}$	Geometry • Length $L_1 = 2\text{m}$ • Distance with NF $d = 1\text{m}$ • Slant angle α
Mechanical Properties: • Friction angle: $\phi = 31°$ • Cohesion $c = 2.2\text{MPa}$ • Tensile strength: $T_0 = 2.0\text{MPa}$ • Normal stiffness $K_n = 0.5\times10^4\,\text{MPa/m}$ • Shear stiffness $K_s = 0.25\times10^4\,\text{MPa/m}$	Mechanical Properties: • Young's modulus $E = 2.07\times10^4\,\text{MPa}$ • Poisson's ratio $\nu = 0.25$	Fluid Properties: • Fluid pressure $p = 44\text{MPa}$

The second modeling attempt was done to model the trajectories of a HF emanating from a wellbore and propagating towards a NF, which is oriented θ degree to the axis of maximum horizontal stress S_H. Fluid pressure distribution along the HF is assumed constant. The input parameters are for Barnett shale (Palmer et al. 2007) as listed in **Table 5.4**. We first checked the fracture trajectories by using joint models that include initial joint deformation (as described in Section **4.1.1.2**).

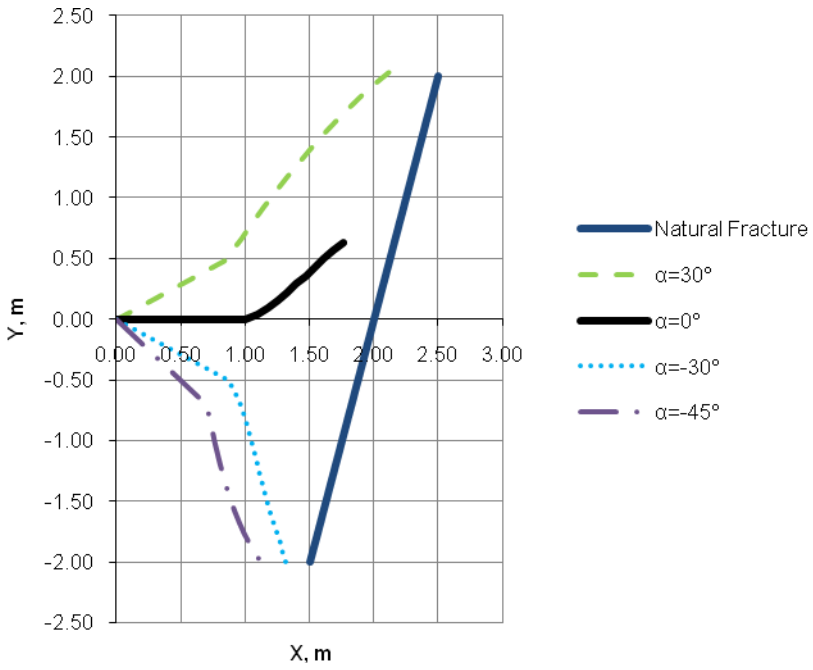


Fig. 5.23 Deflection of HFs at different orientation angles (α) when propagating towards a NF.

As can be seen from **Fig. 5.24**, fractures initially slanted at different angles (due to stress localization and ruptures at local flaws or micro-cracks in the rock formation immediately adjacent to the wellbore, fracture could initiate in certain direction initially. Another scenario would be for an inclined well, fracture would initially have an angle with respect to the direction of maximum horizontal stress) would propagate perpendicular to the direction of minimum far-field stresses under biaxial stresses without the presence of a NF. With NF located in front of the HF, the HF would deviate from its original path and bend near the NF, as shown in **Fig. 5.23**. In this case, as the joint model that includes initial deformation under far-field stresses was used, the

deformation along the joint can change the stress field around the HF tip, and therefore change its propagation path. It will be shown later that whether the deformation along the joint due to the far-field stresses is considered or not can affect the simulation results of HF trajectories.

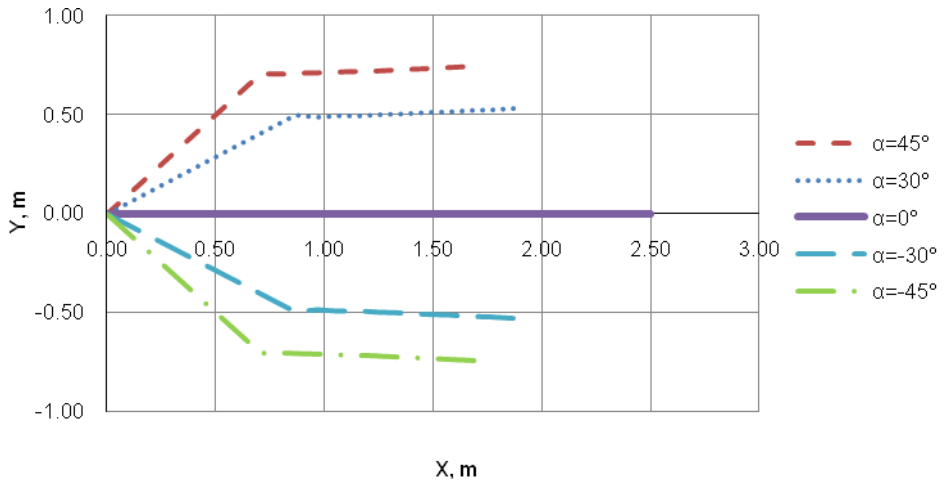


Fig. 5.24 Fracture trajectories propagating under biaxial stresses without the presence of a NF for HF at different slant angles (α).

The fracture deviation behavior would be of great importance for us to predict or monitor during the stimulation practice. Ideally we would like to design a fracturing treatment to create as much as conductive paths as possible, either by directly crossing NF or reinitiating new fractures from the NF. HF fracture bending or blunting at the NF are what we aim to avoid. Therefore, the following parametric studies are conducted to investigate the influence of different rock or fluid properties on the fracture trajectories.

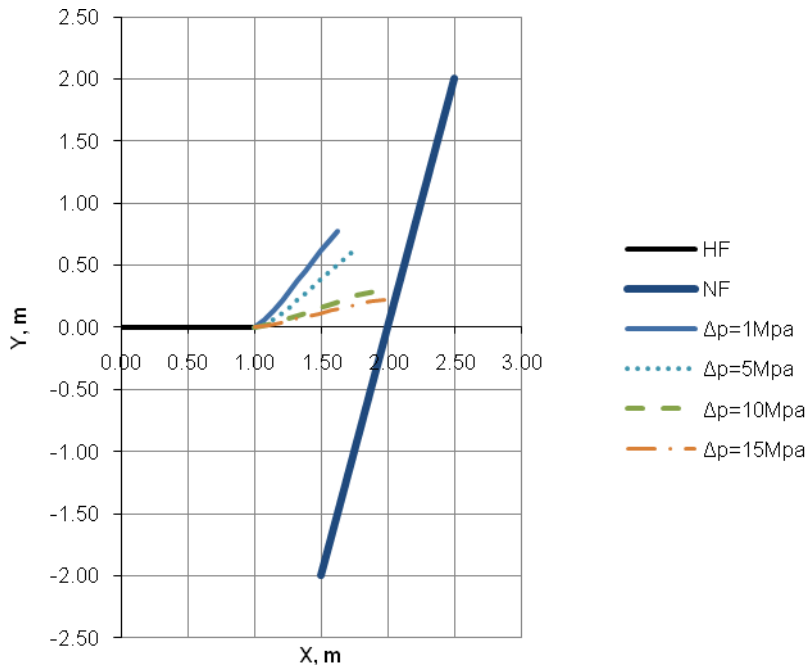


Fig. 5.25 Fracture trajectories under different net pressures (*Δp*).

Net pressure of the HF is a factor that can affect fracture propagation near a NF as shown in **Fig. 5.25**. A fracture under higher net pressure deviates less from its original path**.** A tensile fracture under a higher net pressure has a higher driving force at the fracture tip, so perturbation of the stress field induced by the NF appears to be less influential. The implication for stimulation practices is that fractures with higher net fluid pressure have less bending and are more likely to propagate towards a naturally-fractured reservoir. Once the fracture coalesces with NF, we could expect the onset of even greater pressure drop along the fracture paths; therefore higher net fluid pressure is needed when fracturing naturally-fractured reservoirs.

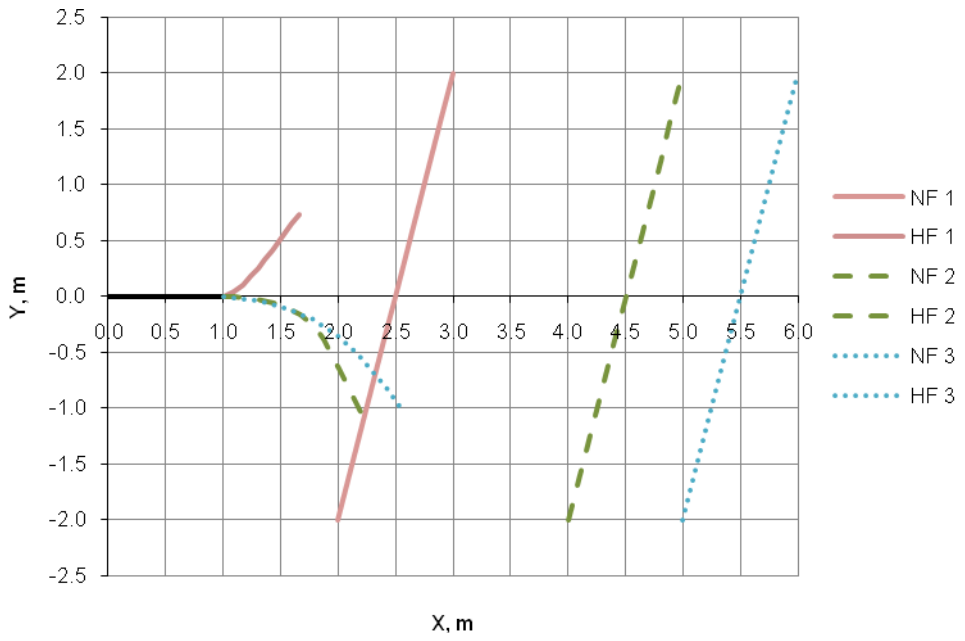


Fig. 5.26 Fracture trajectories under different distances from fracture tip to NF.

The NF may be located at different distances relative to the HF tip. As plotted in **Fig. 5.26**, the smaller the distance between NF and the fracture tip, the greater deviation exhibited at the fracture tip. When the NF is located further from the HF, the influence of deformation along the NF on the stress field around the HF tip gets smaller, so HF deviation becomes smaller. The fracture trajectory may either go to the left or the right side of the original path, depending on the specific in-situ stress field at the fracture tip.

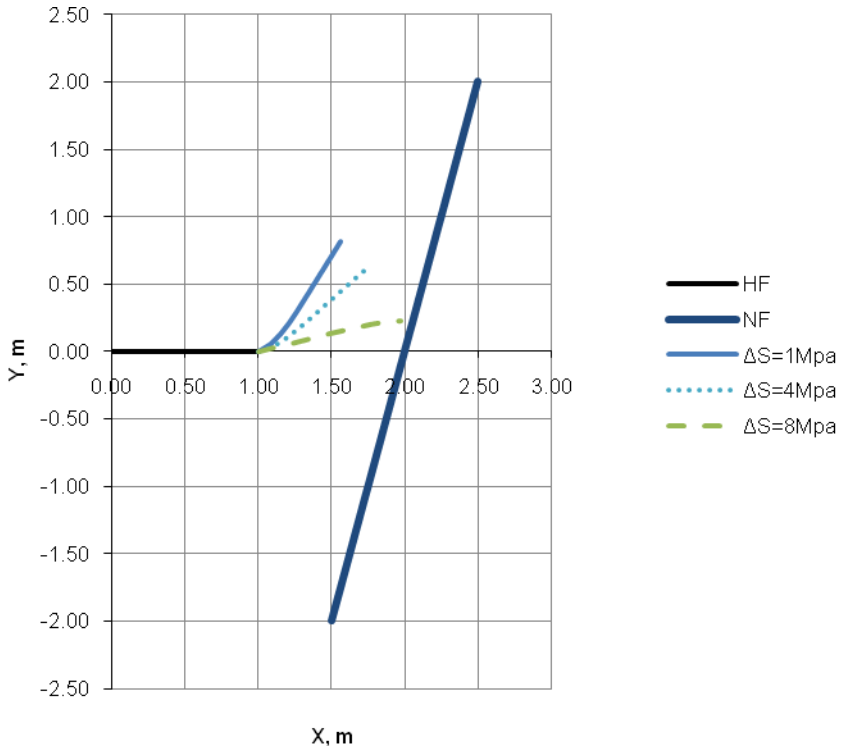


Fig. 5.27 Fracture trajectories under different far-field stress differences (*Δs*).

HF also shows different degrees of deviation from its original paths under different differences between the maximum in-situ stress (S_H) and minimum in-situ stress (S_h), as shown in **Fig. 5.27**. When the difference is small (the stress-field approaches isotropic condition), the perturbation of the stress field at the HF tip brought by the NF is more significant, so the bending of the HF is more significant.

Fracture trajectories calculated by using joint models that do not consider initial joint deformation (as described in 4.1.1.1) are shown in **Fig. 5.28**. As compared with **Fig. 5.23**, fracture paths are not influenced by the presence of NF. Because in this case,

joint deformation due to far-field stresses is zero (as demonstrated in Section **4.3.2**, a joint model that excludes initial joint deformation would have zero normal/shear displacements and normal/shear stresses corresponding to the action of the far-field stresses). HF tip-induced joint deformation and stresses are also negligible as the tip is far enough from the NF (about 1m). Therefore, the joint does not perturb the stress-field around HF until the HF tip arrives very close to the NF, so that HF will not deviate significantly from its original path.

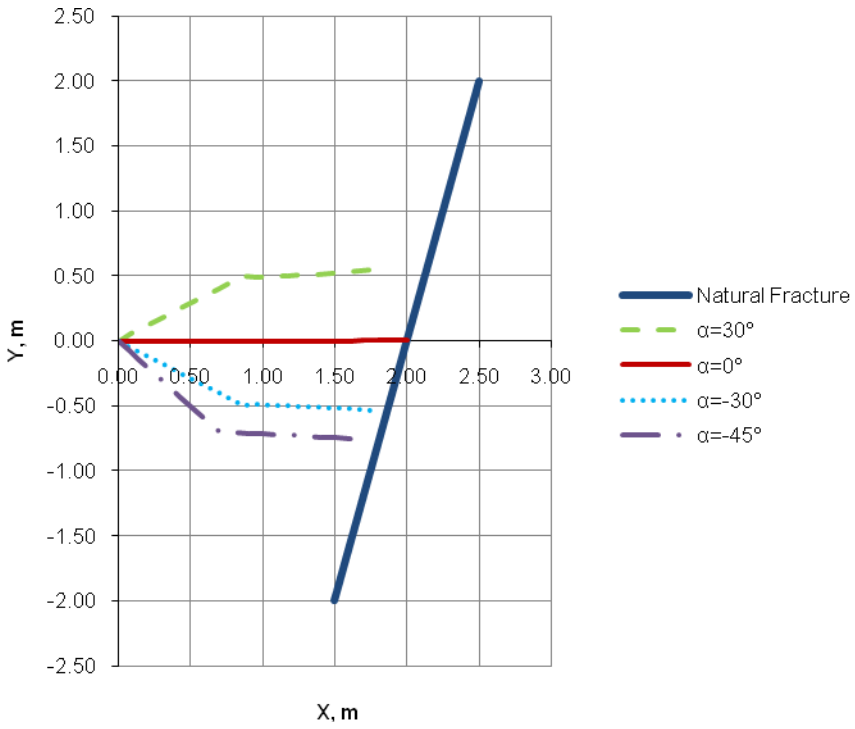


Fig. 5.28 Trajectories of HF propagating towards a NF at different slant angles (*α*).

Analysis based on this type of joint model might give a better representation for formations where the pre-existing fractures have been subjected to the far-field stresses for long time and have reached mechanical equilibrium prior to the process of hydraulic fracturing. Selection of joint model would have direct impact on the modelling results of fracture propagation near NFs. Therefore, carefully consideration of geomechanical characteristics of the reservoir is needed to get reliable modelling results.

5.4 Hydraulic Fracture Propagation by Using Newtonian Fluid Flow

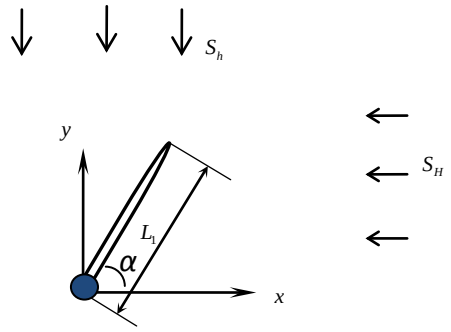


Fig. 5.29 An initially straight pressurized crack under biaxial stresses.

Simulation of the hydraulically induced fracture (**Fig. 5.29**) is carried out assuming a Newtonian fluid flow model. The input parameters are listed in **Table 5.5**. The fracture trajectories were calculated under different fluid injection rates and viscosities, and the results are plotted in **Fig. 5.30** and **Fig. 5.31**.

Table 5.5 Input parameters for simulating a HF using Newtonian fluid model

Rock	HF
In-situ Stresses: • $S_H = -2.0$MPa • $S_h = -0.5$MPa	Geometry • Length $L_1 = 2$m • Slant angle α=80˚
Mechanical Properties: • Young's modulus $E = 1.4\times10^4$MPa • Poisson's ratio $v = 0.1$	Fluid Properties: • Injection rate q • Viscosity μ

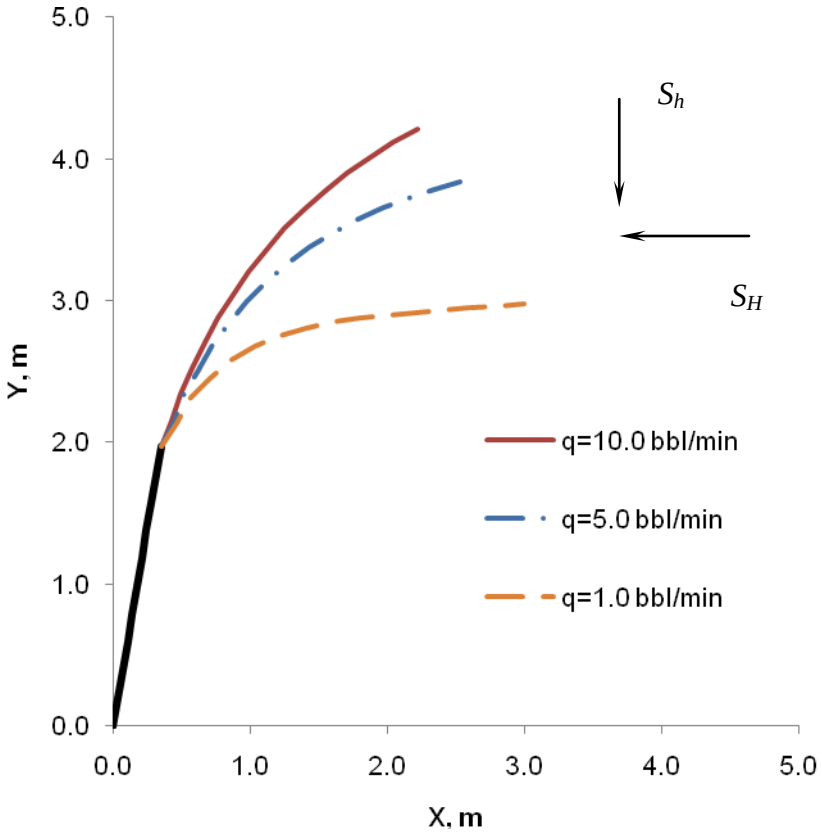


Fig. 5.30 Fracture trajectories under different fluid injection rates (q) at the wellbore (μ=1.0cp).

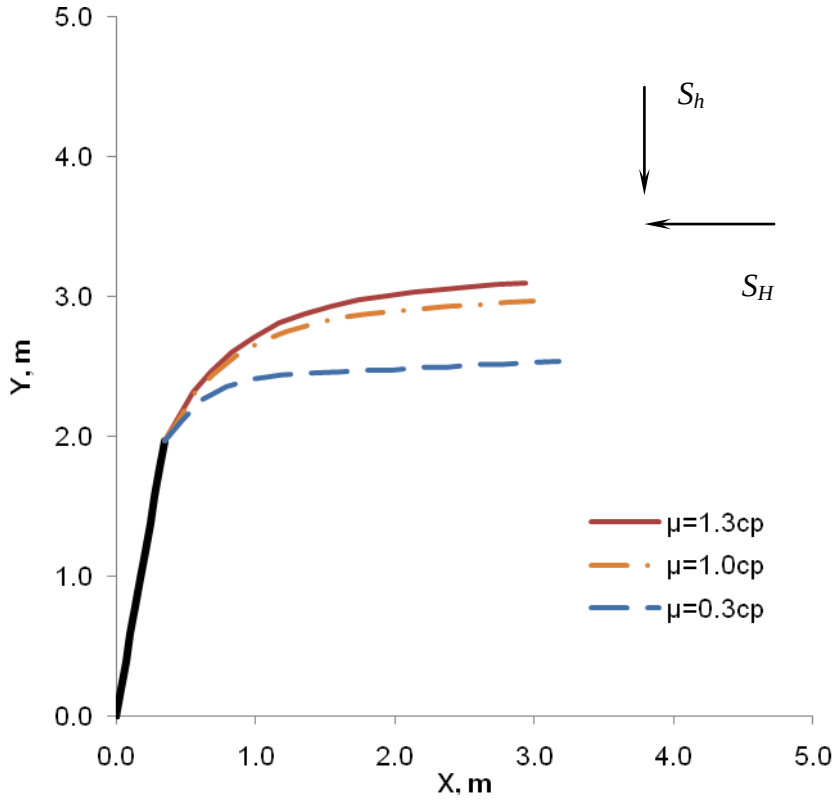


Fig. 5.31 Fracture trajectories under different fluid viscosities (μ) (q=1.0bbl/min).

As can be seen from **Fig. 5.30**, the fracture, which initially slanted at 80˚ with the direction of maximum horizontal stress S_H, will gradually turn and propagate along the direction of maximum horizontal stress under the influence of far-field stresses. When the injection rate is higher, which is 10.0bbl/min, the fracture travels longer distance before turning to the direction of maximum horizontal stress, as a fracture under higher injection rate has bigger resistance against the far-field compressive stresses. For lower injection rate, which is 5.0bbl/min and 1.0bbl/min, the fracture will travel shorter distance while turning. Similarly, as shown in **Fig. 5.31**, when the fracturing fluid has higher viscosity (1.3cp, viscosity of water at 10˚C), the hydraulic fracture will travel

longer distance before turning than those with a lower viscosity (1.0cp and 0.3cp, viscosity of water at 20 ˚C and 90 ˚C respectively).

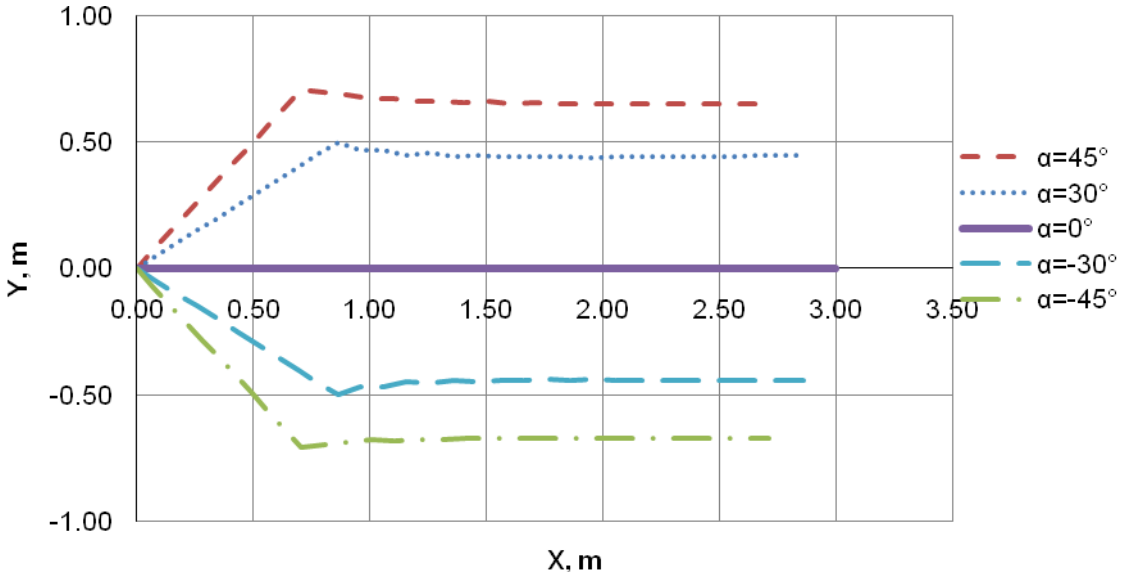


Fig. 5.32 Fracture trajectories for HF propagating under biaxial stresses at different slant angles (α) using Newtonian fluid flow model.

The trajectories for HF propagating under biaxial stresses at different slant angles using a Newtonian fluid flow model are plotted in **Fig. 5.32**. As compared with **Fig. 5.24**, the fractures follow similar trajectories as results simulated by using constant pressure model. Hence the model outputs for fracture footprints by using Newtonian fluid model are stable and reliable. It predicts that HF will propagate along the direction of maximum horizontal stress, S_H.

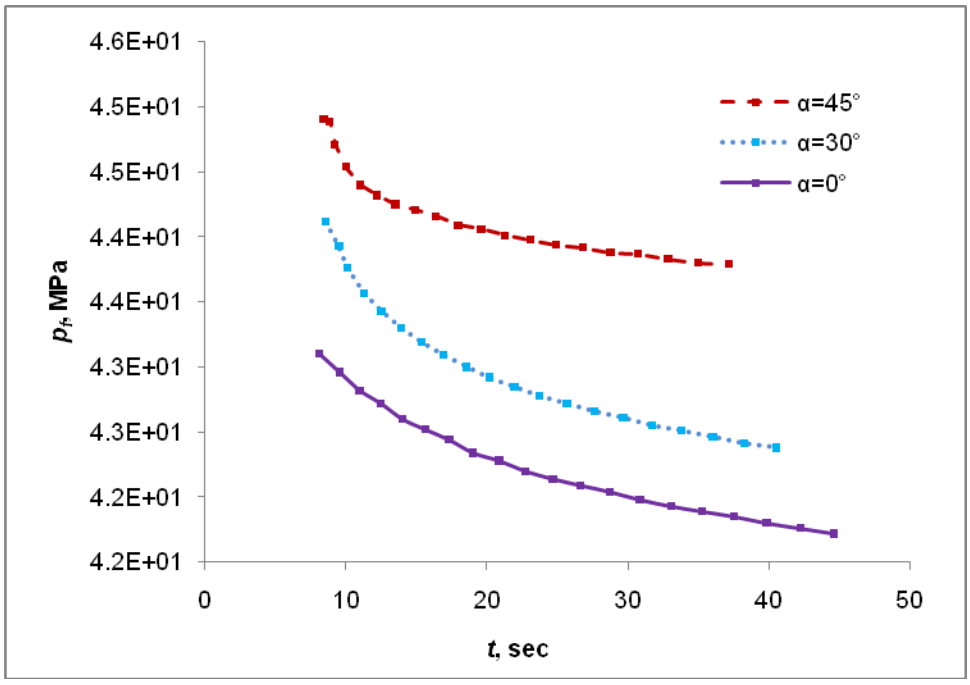


Fig. 5.33 Fluid pressure at the wellbore (x=0) with time by using Newtonian fluid model for HF at different slant angles (α).

The variation of fluid pressure at the wellbore with time for HF at different slant angles α is plotted in **Fig. 5.33**. Under the boundary condition of constant injection rate at the wellbore, the pressure at the wellbore required for the fracture to propagate decreases with time. As the fracture grows and the fracture aperture increases, less energy is required to propagate the HF and the pressure is decreasing. It can also be observed that for a HF with bigger slant angle, the pressure at the wellbore is higher than those with a smaller slant angle.

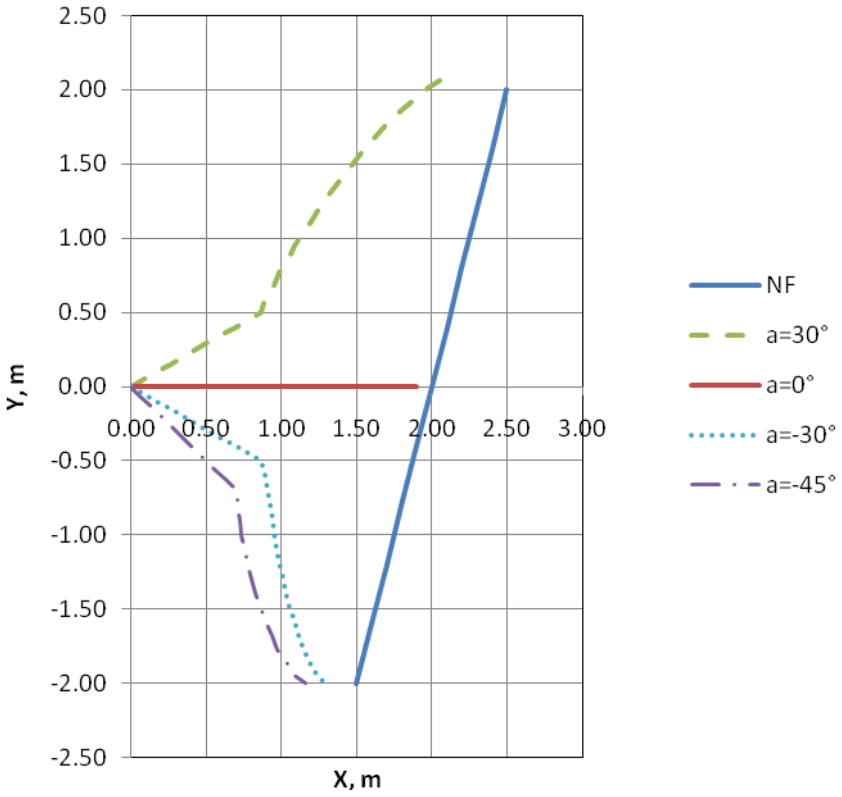


Fig. 5.34 Deflection of HFs at different orientation angles (α) when propagating towards a NF simulated by using a joint model that includes initial deformation and a Newtonian fluid model.

HF trajectories near a NF by using a Newtonian fluid model and joint models that include and exclude initial joint deformations are simulated and plotted in **Fig. 5.34** and **Fig. 5.35**, respectively. The input parameters are similar as listed in **Table 5.4** except that the fluid is modeled to have a viscosity μ=1.0cp and the injection rate at the wellbore q=1.0 bbl/min. As can be seen, fracture trajectories are identical as those plotted in **Fig. 5.23** and **Fig. 5.28**. The model outputs for fracture footprints by using Newtonian fluid model near NF are stable and reliable.

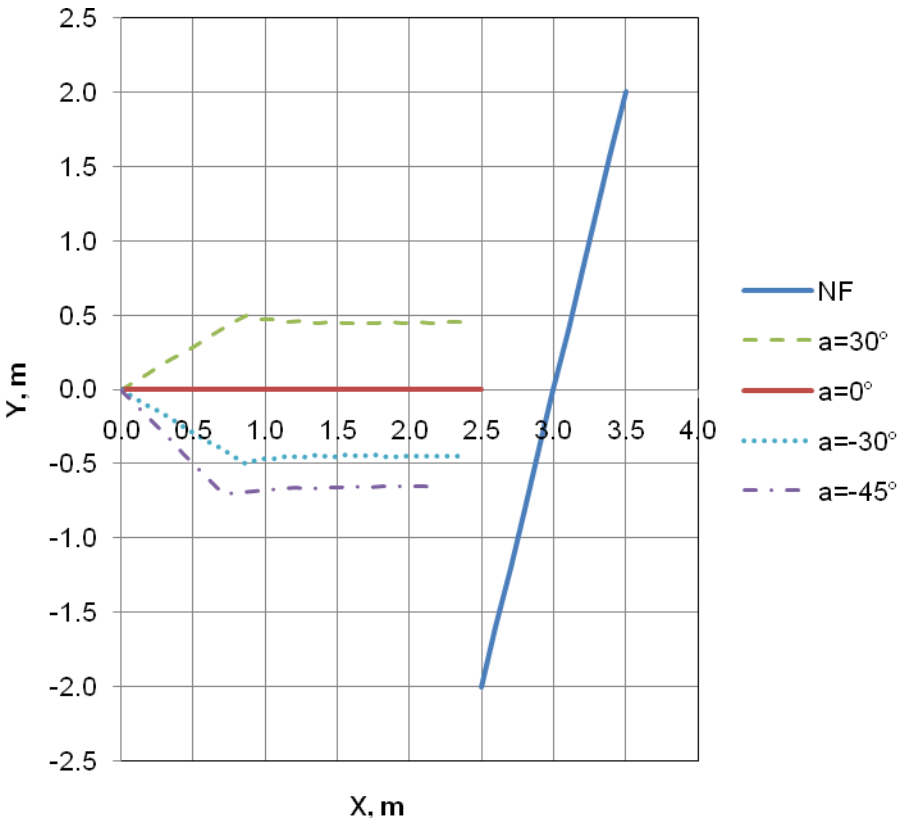


Fig. 5.35 Deflection of HFs at different orientation angles (α) when propagating towards a NF simulated by using a joint model that excludes initial deformation and a Newtonian fluid model.

Fracture trajectories under different fluid injection rates at the wellbore by using a Newtonian fluid model and joint models that include and exclude the initial joint deformation are simulated and plotted in **Fig. 5.36** and **Fig. 5.37**, respectively. It can be observed from **Fig. 5.36** that fracture trajectories are identical under three different injection rates and that they are not sensitive to the fluid injection rates when using a joint model that include initial deformation. In this type of joint model, we can see that the NF is a predominant factor in controlling the HF trajectory. The initial deformation

along the NF (when included) is much more influential to the stress field around the HF than the fluid flow within the HF.

In contrast, HF shows three different routes under different injection rates when a joint model that excludes the initial joint deformation is used, as plotted in **Fig. 5.37**. We can observe that fracture under higher injection rate deviates more from the direction of maximum horizontal stress (S_H). Simulation results from this type of joint model exhibits that the NF has a much smaller influence on the stress field around the HF and that the influence of fluid flow within the HF overweighs and can thereby affect the fracture trajectory.

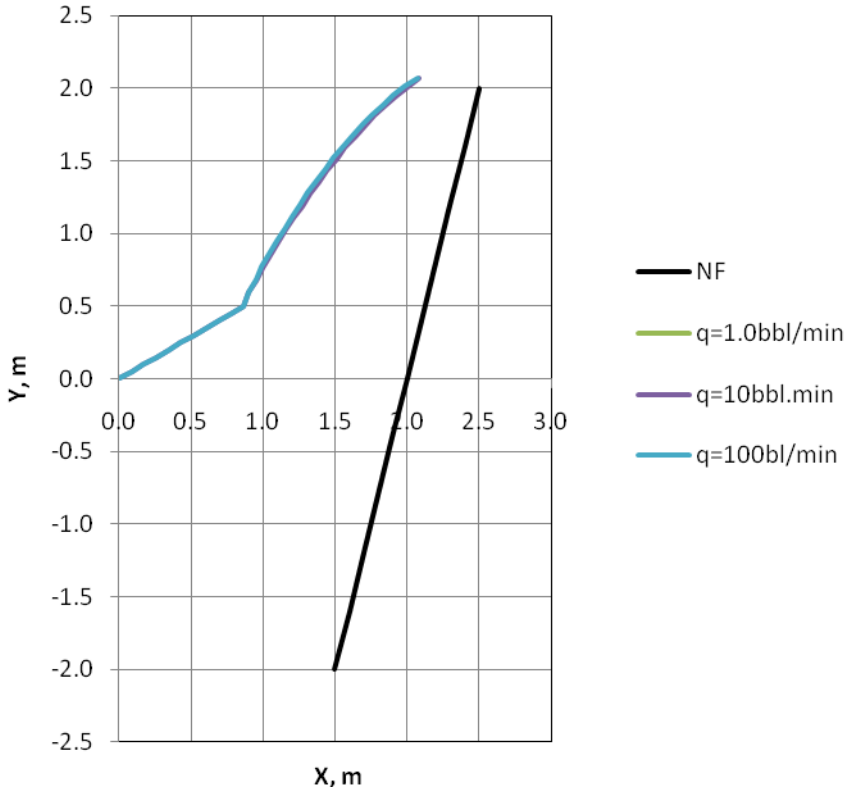


Fig. 5.36 Deflection of HF (α=30˚) under different injection rates at the wellbore (q) when propagating towards a NF simulated by using a joint model that includes initial deformation and a Newtonian fluid model.

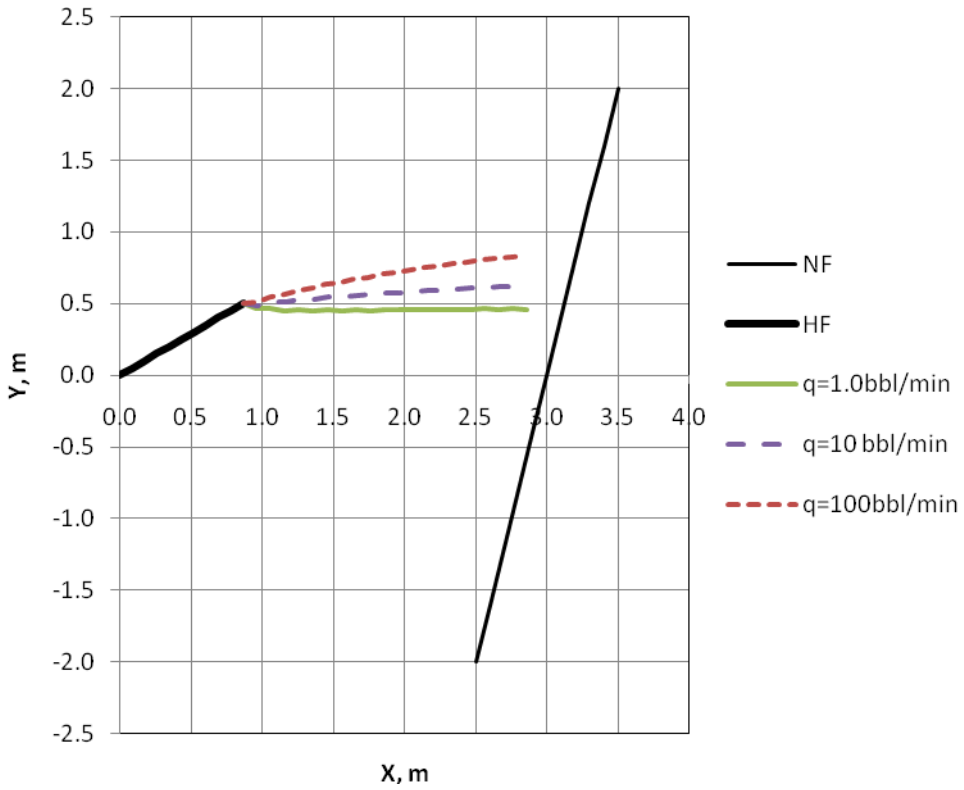


Fig. 5.37 Deflection of HF (α=30˚) under different injection rates at the wellbore (*q*) when propagating towards a NF simulated by using a joint model that excludes initial deformation and a Newtonian fluid model.

6 SUMMARY AND CONCLUSIONS

6.1 Summary

In this thesis, the interaction between a HF and a NF are investigated numerically by considering the three coupling components of this problem: the mechanical deformation of the rock in response to the fluid pressure acting on the fracture surface; the fluid flow within the fracture; and the fracture propagation in the formation. Rock deformation is simulated to be elastic while poroelastic effects associated with pore pressure diffusion are included. Fluid pressure is first modeled be uniformly distributed in the HF, and then flow of a Newtonian fluid is considered. Fracture propagation is modeled using the stress structural criterion. A special type of DD element (joint element) is used to describe different joint contact modes (stick, open and yield) for numerical analysis of HF interaction with NF.

The mechanical response of the NF to a static HF is studied to predict the probable location for the onset of new tensile crack before HF coalesces with the NF. The stage when the fluid invades the NF is also considered by simulating a sequence of static states of fluid with uniform pressure distribution along the HF and NF.

Hydraulic fracture trajectories near a NF before HF coalesces with the NF under different joint, rock and fluid properties were modeled using two different joint models (which exclude or included initial joint deformation) and two different fluid flow models (prescribed uniform pressure model or Newtonian fluid flow model).

Future research on the interaction between a HF and a NF can be done by modeling a complete set of stages of HF and NF interaction: HF approaching NF, coalescence, subsequent fluid infiltration, and fracture re-initiation from the NF.

6.2 Conclusions

1. During the stage of HF approaches a NF before coalescence, the possibility of fracture re-initiation across the NF is enhanced when the NF is weak; a stronger NF tends to inhibit fracture re-initiation. In terms of re-initiation location, a step-over (offset) is more likely to occur for HF interacting with a weaker joint, as the stress localization tends to be mitigated by sliding of the NF; a strong joint that does not slip promotes direct crossing.
2. During the stage of fluid infiltration along the NF, a maximum tensile stress peak is generated at the end of the opening zone along the NF ahead of the fluid front. The location and value of the tension peak is a function of fluid pressure and fluid infiltrated length.
3. Poroelastic effects, arising from fluid diffusion into the rock deformation can induce closure and compressive stress near the center of the NF ahead of the HF tip before HF reaches NF. While fluid flows along the NF, poroelastic effects can reduce the value of tension peak, decreasing the possibility of fracture re-initiation with time.
4. Hydraulic fractures subjected to higher injection rates or fracturing fluids of higher viscosity propagate longer distance before turning to the direction of maximum horizontal stress.

5. Fracture trajectories near a NF tend to bend and deviate from the direction of maximum horizontal stress when using a joint model that includes the initial joint deformation.
6. Fracture trajectories are less dependent on the injection rate or fluid viscosity as the influence of NF is more predominant when using a joint model that includes initial joint deformation; whereas fracture trajectories are more dominated by the HF variables such as injection rate and fluid viscosity. This is because the influence of NF is smaller when using a joint model that excludes initial joint deformation.

NOMENCLATURE

$\overset{ij}{A}_{ns}$ = boundary influence coefficients (gives the normal stress at the midpoint of the i^{th} element due to a constant shear DD over the j^{th} element)

B = Skempton's pore pressure coefficient

c = cohesion, MPa

C_f = Fluid diffusivity, m^2/s

d = characteristic length of fracture process zone, m

D_x = displacement discontinuity with respect to x-axis, m

D_y = displacement discontinuity with respect to y-axis, m

$\overset{j}{D}_s$ = total shear components of discontinuity with respect to the local co-ordinates s and n at the j^{th} element, m

$\overset{j}{D}_n$ = total normal components of discontinuity with respect to the local co-ordinates s and n at the j^{th} element, m

$(\overset{i}{D}_s)_0$ = shear component of initial total joint deformation, m

$(\overset{i}{D}_n)_0$ = normal component of initial total joint deformation, m

$\overset{i}{D}_s'$ = shear component of the induced deformation, m

$\overset{i}{D}_n'$ = normal component of the induced deformation, m

E = Young's modulus, MPa

f_I = tensile driving force, MPa

f_{II} = shear driving force, MPa

F_I = normalized tensile driving force

F_{II} = normalized shear driving force

G = shear modulus of rock formation, MPa

k = dynamic permeability, md

K_u = undrained bulk modulus, MPa

K = rock's bulk modulus, MPa

K_I = Mode I stress intensity factor, MPa·m$^{1/2}$

K_{II} = Mode II stress intensity factor, MPa·m$^{1/2}$

K_{IC} = Mode I critical stress intensity factor, MPa·m$^{1/2}$

l = initial crack half length, m

L_1 = fracture length, m

L_2 = joint length, m

p = pressure, MPa

p_f = fluid pressure, MPa

$p(0,t)$ = pressure at the wellbore at time t, MPa

$p(x,t)$ = pressure at coordinate x at time t, MPa

Δp = pressure drop, MPa

q = fracturing fluid flow rate, bbl/min

$q(0,t)$ = injection rate at the wellbore (x=0) at time t, bbl/min

S_H = maximum horizontal stress, MPa

S_h = minimum horizontal stress, MPa

t = time point during a fracture treatment, s

T_0 = tensile strength, MPa

u_x = displacement with respect to *x*-axis, m

u_y = displacement with respect to *y*-axis, m

$\overset{i}{u}_s$ = shear displacement at the midpoint of the i^{th} element, m

$\overset{i}{u}_n$ = normal displacement at the midpoint of the i^{th} element, m

w = fracture width, m

w_j = level weighting factor

x = coordinate along direction of fracture propagation, m

y = coordinate along direction of fracture propagation, m

α = Biot's effective stress coefficient

μ = fluid viscosity, cp

ν = Poisson's ratio

ρ = density of the fracturing fluid, kg/m^3

ϕ = angle of friction, $^\circ$

σ_n = in-situ normal rock stress perpendicular to fracture face, MPa

$\sigma_{\theta\theta}$ = tangential stress in radial coordinate, MPa

$\sigma_{r\theta}$ = shear stress in radial coordinate, MPa

σ_{rr} = radial stress in radial coordinate, MPa

$\overset{i}{\sigma}_s$ = shear stress at the midpoint of the i^{th} element, MPa

$\overset{i}{\sigma}_n$ = normal stress at the midpoint of the i^{th} element, MPa

REFERENCES

Batchelor, G.K. 1967. *An Introduction to Fluid Dynamics*. Cambridge, UK.: Cambridge University Press. Original edition. ISBN 0521 66396 2.

Berchenko, I. and Detournay, E. 1997. Deviation of Hydraulic Fractures through Poroelastic Stress Changes Induced by Fluid Injection and Pumping. *International Journal of Rock Mechanics and Mining Sciences* **34** (6): 1009-1019.

Biot, M.A. 1941. General Theory of Three-Dimensional Consolidation. *J. Appl. Phys.* **26**: 182-185.

Blanton, T.L. 1982. An Experimental Study of Interaction between Hydraulically Induced and Pre-Existing Fractures. Paper presented at the SPE Unconventional Gas Recovery Symposium, Pittsburgh, Pennsylvania. SPE of AIME 10847-MS. DOI: 10.2118/10847-MS.

Bobet, A. 2001. Numerical Simulation of Initiation of Tensile and Shear Cracks. Paper presented at the The 38th U.S. Symposium on Rock Mechanics (USRMS), Washington D.C. Swets & Zeitlinger Lisse.

Bobet, A. and Einstein, H.H. 1998. Fracture Coalescence in Rock-Type Materials under Uniaxial and Biaxial Compression. *Int. J. Rock Mech. Min. Sci.* **35**: 863-888.

Boone, T.J., Ingraffea, A.R., and Roegiers, J.C. 1991. Simulation of Hydraulic Fracture Propagation in Poroelastic Rock with Application to Stress Measurement Techniques. *International Journal of Rock Mechanics and Mining Sciences & Geomechanics Abstracts* **28** (1): 1-14.

Chuprakov, D.A., Akulich, A., Siebrits, E. et al. 2010. Hydraulic Fracture Propagation in a Naturally Fractured Reservoir. Paper presented at the SPE Oil and Gas India Conference and Exhibition, Mumbai, India. SPE 128715-MS. DOI: 10.2118/128715-MS.

Cooke, M.L. and Underwood, C.A. 2001. Fracture Termination and Step-over at Bedding Interfaces Due to Frictional Slip and Interface Opening. *Journal of Structural Geology* **23** (2-3): 223-238.

Crouch, S.L. 1976. *Analysis of Stresses and Displacements around Underground Excavations: An Application of the Displacement Discontinuity Method*: Dept. of Civil and Mineral Engineering, University of Minnesota. Original edition. ISBN.

Crouch, S.L. and Starfield, A.M. 1983. Boundary Element Methods in Solid Mechanics, London: George Allen & Unwin.

Detournay, E. and Cheng, A.H.D. 1991. Plane Strain Analysis of a Stationary Hydraulic Fracture in a Poroelastic Medium. *International Journal of Solids and Structures* **27** (13): 1645-1662.

Dobroskok, A., Ghassemi, A., and Linkov, A. 2005. Extended Structural Criterion for Numerical Simulation of Crack Propagation and Coalescence under Compressive Loads *International Journal of Fracture* **133**: 223-246.

Dong, C.Y. and de Pater, C.J. 2001. Numerical Implementation of Displacement Discontinuity Method and Its Application in Hydraulic Fracturing. *Computer Methods in Applied Mechanics and Engineering* **191** (8-10): 745-760.

Fisher, M.K., Wright, C.A., Davidson, B.M. et al. 2002. Integrating Fracture Mapping Technologies to Optimize Stimulations in the Barnett Shale. Paper presented at the SPE Annual Technical Conference and Exhibition, San Antonio, Texas. Copyright 2002, Society of Petroleum Engineers Inc. 77441.

Gdoutos, E.E. 2005. *Fracture Mechanics: An Introduction*: Springer Netherlands. Original edition. ISBN 1-4020-3153-X.

Ghassemi, A. and Zhang, Q. 2006. Porothermoelastic Analysis of the Response of a Stationary Crack Using the Displacement Discontinuity Method. *Journal of Engineering Mechanics* **132**: 26-33.

Griffith, A.A. 1924. The Theory of Rupture. *Proceedings 1st International Congress Applied Mechanics*: 55-63.

Huang, N.C. and Russell, S.G. 1985. Hydraulic Fracturing of a Saturated Porous Medium-Ii: Special Cases. *Theoretical and Applied Fracture Mechanics* **4** (3): 215-222.

Koshelev, V. and Ghassemi, A. 2003. Hydraulic Fracture Propagation near a Natural Discontinuity. In *Twenty-Eight Workshop on Geothermal Reservoir Engineering*. Stanford University, Stanford, California.

Palmer, I.D., Moschovidis, Z.A., and Cameron, J.R. 2007. Modeling Shear Failure and Stimulation of the Barnett Shale after Hydraulic Fracturing. Paper presented at the SPE Hydraulic Fracturing Technology Conference, College Station, Texas, U.S.A. SPE.

Potluri, N.K., Zhu, D., and Hill, A.D. 2005. The Effect of Natural Fractures on Hydraulic Fracture Propagation. Paper presented at the SPE European Formation Damage Conference, Sheveningen, The Netherlands. SPE 94568-MS.

Rao, Q., Sun, Z., Stephansson, O. et al. 2003. Shear Fracture (Mode Ii) of Brittle Rock. *Rock Mech. Mining Sci.* **40**: 355-375.

Renshaw, C.E. and Pollard, D.D. 1995. An Experimentally Verified Criterion for Propagation across Unbounded Frictional Interfaces in Brittle, Linear Elastic Materials. *International Journal of Rock Mechanics and Mining Science & Geomechanics Abstracts* **32** (3): 237-249.

Rice, J.R. 1968. Mathematical Analysis in the Mechanics of Fracture. In *Fracture, an Advanced Treatise.*, New York: Academic Press. II: Mathematical fundamentals.

Ruina, A.L. 1978. Influence of Coupled Deformation-Diffusion Effects on the Retardation of Hydraulic Fracture. In *19th US Rock Mechanics Symposium (USRMS)*:274-282. University of Nevada Press, Reno, Nevada: ARMA.

Tang, C.A., Lin, P., Wong, R.H.C. et al. 2001. Analysis of Crack Coalescence in Rock-Like Materials Containing Three Flaws - Part Ii: Numerical Approach. *Int. J. Rock Mech. Min. Sci.* **38**: 925-939.

Thiercelin, M.J. and Makkhyu, E. 2007. Stress Field in the Vicinity of a Natural Fault Activated by the Propagation of an Induced Hydraulic Fracture, Rock Mechanics: Meeting Society's Challenges and Demands: Taylor & Francis Group, London.

Vandamme, L., Detournay, E., and Cheng, A.H.-D. 1989. A Two-Dimensional Poroelastic Displacement Discontinuity Method for Hydraulic Fracture Simulation. *International Journal for Numerical and Analytical Methods in Geomechanics* **13** (2): 215-224.

Warpinski, N.R. and Teufel, L.W. 1987. Influence of Geologic Discontinuities on Hydraulic Fracture Propagation (Includes Associated Papers 17011 and 17074). *SPE Journal of Petroleum Technology* **39** (2): 209-220. DOI: 10.2118/13224-pa

Warpinski, N.R., Wolhart, S.L., and Wright, C.A. 2004. Analysis and Prediction of Microseismicity Induced by Hydraulic Fracturin. *SPE Journal* **9** (1): 24-33. DOI: 10.2118/87673-pa

WOO, C.W. and LING, L.H. 1984. On Angled Crack Initiation under Biaxial Loading. *The Journal of Strain Analysis for Engineering Design* **19** (1): 51-59. DOI: 10.1243/03093247V191051

Wu, H., Chudnovsky, A., Dudley, J.W. et al. 2004. A Map of Fracture Behavior in the Vicinity of an Interface. Paper presented at the Gulf Rocks 2004, the 6th North America Rock Mechanics Symposium (NARMS), Houston, Texas. ARMA 04-620.

Yan, X. 2004. A Special Crack Tip Displacement Discontinuity Element. *Mechanics Research Communications* **31** (6): 651-659.

Zhang, X. and Jeffrey, R.G. 2006. The Role of Friction and Secondary Flaws on Deflection and Re-Initiation of Hydraulic Fractures at Orthogonal Pre-Existing Fractures. *Geophysical Journal International* **166**: 1454-1465.

Zhang, Z.X. 2002. An Empirical Relation between Mode I Fracture Toughness and the Tensile Strength of Rock. *International Journal of Rock Mechanics and Mining Sciences* **39** (3): 401-406.

6.2

FRACTURE DIAGNOSTICS

Pinnacle, A Halliburton Service
9949 W. Sam Houston Pkwy N.
Houston, TX 77064
Phone: 281.876.2323
Fax: 281.876.4455
www.pinntech.com

Bakersfield 661.335.7711
Beijing 86.13838562150
Calgary 403.516.2260
Ft. Worth 817.333.1130
Denver 720.344.3464
Houston 281.876.2323
Midland 432.386.6791
Oklahoma City 405.604.5634
Pittsburgh 1.800.786.1097
San Francisco 415.861.1097

September 30, 2010

Mr. Iraj A. Salehi
Manager, Shale Gas Research
Gas Technology Institute
1700 South Mount Prospect Road
Des Plaines, Illinois 60018-1804
Office: 847-768-0902
Mobile: 847-312-4363
Iraj.Salehi@gastechnology.org

Re: New Albany Shale Subcontract S-53 Project 20743 Final Report

Please find the final report for the deliverables provided by Pinnacle for the above-referenced project.

Objectives:

- Evaluate current completion/stimulation practices in the New Albany Shale;
- Design and perform field experiments to measure hydraulic fracture geometry and evaluate stimulation effectiveness;
- Integrate the results of field experiments with geologic, geophysical, completion and production data to optimize development of the New Albany Shale;
- Transfer the results of the study to the natural gas industry.

Deliverable: Report on current New Albany Shale stimulation practices.

Deliverable: Plan for field experiments and perform them.

Deliverable: Report on the field experiments (Microseismic, Surface Tiltmeter, or Distributed Temperature Sensing).

Deliverable: Final report in electronic format; preparation of one technical paper or article and one 1-day workshop.

Funding for this project is provided by RPSEA through the "Ultra-Deepwater and Unconventional Natural Gas and Other Petroleum Resources" program authorized by the U.S. Energy Policy Act of 2005. RPSEA (www.rpsea.org) is a non-profit corporation whose mission is to provide a stewardship role in ensuring the focused research, development and deployment of safe and environmentally responsible technology that can effectively deliver hydrocarbons from domestic resources to the citizens of the United States. RPSEA, operating as a consortium of premier U.S. energy research universities, industry, and independent research organizations, manages the program under a contract with the U.S. Department of Energy's National Energy Technology Laboratory.

Table of Contents

LIST OF FIGURES ..... **III**

1. EXECUTIVE SUMMARY **1**

2. DISCUSSION OF COMPLETION AND STIMULATION PRACTICE **3**

3. DISCUSSION OF 3-D PARAMETRIC MODELING EFFORTS IN THE NEW ALBANY SHALE 7

4. DISCUSSION OF CHRISTIAN COUNTY MICROSEISMIC **13**

4.1 DISCUSSION, MAPPING EFFORT ON THE TOEWARD STAGES 19

4.2 DISCUSSION, MAPPING EFFORT ON THE HEELWARD STAGES 22

4.3 QUALITY ASSURANCE, CHRISTIAN COUNTY MICROSEISMIC 36

5. DISCUSSION OF MCLEAN COUNTY MICROSEISMIC **43**

5.1 FRACTURE MAPPING DISCUSSION 48

5.2 QUALITY ASSURANCE 94

List of Figures

Figure 1. Raw data and calculated mechanical data used in parametric modeling 8
Figure 2. Forecast geometry of a single stage, McLean County 10
Figure 3. Map view, all stages 16
Figure 4. Lateral side view (orthogonal to lateral), all stages 17
Figure 5. Lateral end-on view (along lateral), all stages 18
Figure 6. Typical raw digitized data from a near event, first observation well 19
Figure 7. Typical raw digitized data from a far event, first observation well 20
Figure 8. Typical raw digitized data from a high event, first observation well 20
Figure 9. Typical raw digitized data from a low event, first observation well 21
Figure 10. Typical raw digitized data from a low event, second observation well 22
Figure 11. Map view, stage 6 23
Figure 12. Lateral side view (orthogonal to lateral), stage 6 24
Figure 13. Map view, stage 7 25
Figure 14. Lateral side view (orthogonal to lateral), stage 7 26
Figure 15. Map view, stage 8 28
Figure 16. Lateral side view (orthogonal to lateral), stage 8 29
Figure 17. Lateral end-on view (along lateral), stage 8 30
Figure 18. Comparison of event moment magnitudes (stages 1 to 4 on left, 5 to 8 on right) 31
Figure 19. Stage definitions, stages 1 to 4 32
Figure 20. Stage definitions, stages 5 to 8 33
Figure 21. Treatment record, stages 1 to 4 34
Figure 22. Treatment record, stages 5 to 8 35
Figure 23. Project setup map view 37
Figure 24. Project setup side view 38
Figure 25. Toolstring diagram, first observation well 39
Figure 26. Velocity model, stages 1 to 4 40
Figure 27. Velocity model, stages 5 to 8 41
Figure 28. Event location uncertainty, stages 1 to 4 42
Figure 29. Event location uncertainty, stages 5 to 8 42
Figure 30. Map view, all stages 47
Figure 31. Lateral side view (orthogonal to lateral), all stages 47
Figure 32. Lateral end-on view (along lateral), all stages 48

Figure 33. Events colored by relative time during individual stages, map view 49
Figure 34. Events colored by relative time during individual stages, side view 50
Figure 35. Moment magnitude, map view 51
Figure 36. Moment magnitude, side view, looking down major azimuth trend (N60°E) 51
Figure 37. Moment magnitude, side view, looking down secondary azimuth trend (N39°E) 52
Figure 38. Moment magnitude bubble plot, map view 53
Figure 39. Signal-to-Noise ratios for the project 55
Figure 40. Example of background noise for a stage close to the observation well 55
Figure 41. Listening distance, all stages, both wells 56
Figure 42. Event depth uncertainty, side view 57
Figure 43. Map view, stage 1 58
Figure 44. Lateral side view (orthogonal to lateral), stage 1 58
Figure 45. Lateral end-on view (along lateral), stage 1 59
Figure 46. Treatment record, stage 1 (SW treatment well) 60
Figure 47. Treatment record, stage 1 (NE treatment well) 61
Figure 48. Map view, stage 2 62
Figure 49. Lateral side view (orthogonal to lateral), stage 2 62
Figure 50. Lateral end-on view (along lateral), stage 2 63
Figure 51. Treatment record, stage 2 (SW treatment well) 64
Figure 52. Treatment record, stage 2 (NE treatment well) 65
Figure 53. Map view, stage 3 66
Figure 54. Lateral side view (orthogonal to lateral), stage 3 66
Figure 55. Lateral end-on view (along lateral), stage 3 67
Figure 56. Treatment record, stage 3 (SW treatment well) 68
Figure 57. Treatment record, stage 3 (NE treatment well) 69
Figure 58. Map view, stage 4 70
Figure 59. Lateral side view (orthogonal to lateral), stage 4 70
Figure 60. Lateral end-on view (along lateral), stage 4 71
Figure 61. Treatment record, stage 4 (SW treatment well) 72
Figure 62. Treatment record, stage 4 (NE treatment well) 73
Figure 63. Map view, stage 5 74
Figure 64. Lateral side view (orthogonal to lateral), stage 5 74
Figure 65. Lateral end-on view (along lateral), stage 5 75
Figure 66. Treatment record, stage 5 (SW treatment well) 76

Figure 67. Treatment record, stage 5 (NE treatment well) 77
Figure 68. Map view, stage 6 78
Figure 69. Lateral side view (orthogonal to lateral), stage 6 78
Figure 70. Lateral end-on view (along lateral), stage 6 79
Figure 71. Treatment record, stage 6 (SW treatment well) 80
Figure 72. Treatment record, stage 6 (NE treatment well) 81
Figure 73. Map view, stage 7 82
Figure 74. Lateral side view (orthogonal to lateral), stage 7 82
Figure 75. Lateral end-on view (along lateral), stage 7 83
Figure 76. Treatment record, stage 7 (SW treatment well) 84
Figure 77. Treatment record, stage 7 (NE treatment well) 85
Figure 78. Map view, stage 8 86
Figure 79. Lateral side view (orthogonal to lateral), stage 8 86
Figure 80. Lateral end-on view (along lateral), stage 8 87
Figure 81. Treatment record, stage 8 (SW treatment well) 88
Figure 82. Treatment record, stage 8 (NE treatment well) 89
Figure 83. Map view, stage 9 90
Figure 84. Lateral side view (orthogonal to lateral), stage 9 90
Figure 85. Lateral end-on view (along lateral), stage 9 91
Figure 86. Treatment record, stage 9 (SW treatment well) 92
Figure 87. Treatment record, stage 9 (NE treatment well) 93
Figure 88. Project setup, map view 95
Figure 89. Project setup side view 96
Figure 90. Map view, Vibroseis shot positioning 97
Figure 91. Toolstring diagram 98
Figure 92. Velocity model, stages 1 – 3 99
Figure 93. Velocity model, stages 4 – 9 100

1. Executive Summary

In performance of subcontract S-53 to New Albany Shale Project No. 20743, Pinnacle provided multiple services to the Gas Technology Institute (GTI). These services were initially planned as a combination of hydraulic fracture mapping, completion/stimulation practice reporting, 3-D parametric modeling, and reservoir modeling that would incorporate and/or calibrate the results of the aforementioned 3-D parametric modeling. Pinnacle provided microseismic hydraulic fracture mapping services to two GTI cooperative well partners (New Albany Shale operators) during the hydraulic fracture stimulation of one horizontal New Albany Shale gas well in Christian County, Kentucky and two parallel horizontal completions in McLean County, Kentucky. These two mapping efforts revealed a number of critical points:

- Interaction of hydraulically induced fractures with naturally occurring geological features (such as faulting) may be more common than was previously assumed.
- Interaction of hydraulically induced fractures with naturally occurring geological features may decrease Stimulated Reservoir Volume (SRV) substantially, resulting in less total induced fracture area that is exposed to potentially productive reservoir.
- Interaction of hydraulically induced fractures with naturally occurring geological features can result in significant out-of-zone penetration, thus exposing bounding layers to communication with the wellbore, and the subsequent production of undesirable fluids and/or movement of undesirable fluids into the potentially productive reservoir.
- Network azimuths were consistent with area expectations; N85°E in Christian County, Kentucky; and N60°E in McLean County, Kentucky.
- Though some degree of fracture network complexity was implied on both projects, it is possible that the completion methodology (openhole packers and ports with a "low" port count) may have limited total fracture initiation point count. A further implication is that when fracture initiation point count is low, it is possible that total surface area exposed to the potential reservoir is not as high as it could be if additional fractures were artificially induced along the wellbore.
- Christian County, Kentucky induced fractures that remained in-zone resulted in microseismic activity approximately 1,200 ft from the lateral with volumes of approximately 1.0 MMSCF N_2 per stage (no proppant).
- McLean County, Kentucky induced fractures that remained in-zone resulted in microseismic activity approximately 800 ft from the lateral, with volumes of approximately 2.6 MMSCF N_2 per stage (limited ultra-lightweight proppant and small water volumes).

Efforts were made to forecast in advance and match pre- and post-frac mapping results with an industry respected 3D parametric model. Though it was known in advance that these models often cannot adequately simulate fracture networks (systems of parallel and oblique induced fractures), it was thought that if relatively planar bi-wing fractures were present, then such simulation could be justified. Unfortunately, it quickly became apparent as the project progressed that parametric modeling was not appropriate, as complex induced fracture networks were indeed present, and it oversimplified actual conditions to a degree that was not acceptable.

The primary venue for transfer of the results of this work will be the Society of Petroleum Engineers (SPE) 2011 Eastern Regional Meeting. A second public disclosure will be through an Appalachian conference hosted by The Energy Forum, LLC., in 2011. A copy of this report, or more information may be obtained by contacting FracHouston@pinntech.com or (800) 786-1097.

2. Discussion of Completion and Stimulation Practice

The New Albany Shale has been marginally attractive as a producer for a number of years, pre-dating most unconventional shale development efforts by a wide margin[1]. The first drilling targeting New Albany Shale gas in Indiana occurred in 1885, and a relatively large number of fields were drilled in the first half of the 20th century in all three Illinois Basin States.

Traditional completion and stimulation practice involved the use of gelatinated nitroglycerine charges and/or hydrochloric acid in openhole sections of vertical wellbores, and success appeared to be related to the connection of the wellbore with naturally occurring open fractures. Experimentation with water-based fracturing fluids over a large number of years led to a general consensus that techniques involving water were not fiscally viable, possibly due to less-than-normal static pressure gradients and the propensity of water to adsorb on various clay-rich surfaces. With the introduction of nitrogen foam fracturing processes, it quickly became apparent that treatments with gaseous fluids were statistically out-performing near-wellbore treatments involving explosives and/or acid. Vertical completions involving straight nitrogen (with no water or proppant) became popular, and slowly began to replace foam as a fluid of choice. Clearly, there are localized portions of NAS properties where 100% N_2 treatments result in superior acceleration of reserve recovery, but there is not enough statistical data to indicate whether or not this type of stimulation fluid outperforms foam fracture treatments across wide swaths of the play.

The gradual acceptance of horizontal drilling and multi-stage completions led to the realization that these processes generally resulted in higher reserve recovery efficiency per D&C dollar. Though at the time of this study there were still a number of operators working with vertical completions, the preponderance of clearly commercial completions have been associated with horizontal wellbores within a wide range of gaseous commodity prices.

In several North American horizontal shale plays, the shift from complex fluids (high loadings of hydroxypropyl guar, carboxymethyl hydroxypropyl guar, carboxymethyl guar, or carboxymethyl hydroxyethyl cellulose crosslinked with various organometallic compounds) to slickwater (fresh or lightly salted water with ultra-low concentrations of polyacrylamide) resulted in substantial and measureable improvements in gaseous hydrocarbon well net present value. Though the relative contribution of each of the following is still uncertain, it is probable that one or more of these is a dominating root cause of the improvement in other resource plays:

1. Slickwater fluids are on the order of 100 to 1,000 times less viscous than complex [crosslinked] non-Newtonian power law fluids, thereby promoting the far-field development of more complex fracture systems, and, by implication, more total surface area exposed to potentially productive reservoir.

2. Slickwater fluids are materially more cost-effective per unit of volume pumped.

[1]Illinois Basin Consortium, Illinois State Geological Survey, Indiana Geological Survey, and Kentucky Geological Survey: "Final Report, Gas Potential of the New Albany Shale", GRI-92/0391, funded by the Illinois Basin Consortium and the Gas Research Institute, Exploration and Production Technology Research Department, January 1994)

3. Slickwater fluids are quite a bit "cleaner" than complex fluids, leaving significantly less polymer in the closed fracture, and less solids.

Verifiable success with slickwater in the Ft. Worth Basin Barnett and other horizontal plays led to renewed speculation and a short resurgence of experimentation with large volumes of slickwater in the new Albany Shale. To date, no known successes involving slickwater completions in this formation have been reported in the literature or in public data.

The sporadic success of 100% N_2 treatments [as compared to foams and other completion methods] in the play has led to an industry consensus that root causes (1) and (3) above may be "drivers" of success in other plays. Nitrogen has approximately 80 -100 times less viscosity than typical slickwater formulations (possibly promoting even more far-field fracture complexity), and it is essentially inert in terms of its physical and chemical interaction with typical New Albany shale mineralogy.

Though completions involving 100% nitrogen-based fluids statistically outperform near-wellbore stimulation and stimulation with large volumes of liquid, there is no evidence to demonstrate that they a) out-perform foam-based systems uniformly across the play, or b) that they regularly result in commercial completions comparable to other domestic plays for a given commodity and D&C cost structure. A major concern of industry participants with respect to 100% N_2 treatments was that the lack of proppants could theoretically lead to rapid and premature closure of some large percentage of induced fractures, thus limiting the total exposed induced fracture surface area. Two methods to address this concern were employed on the selected project participant's completions:

1. On the Christian County Kentucky project, small spearheads of treated HCl were pumped ahead of the N_2 fracturing fluid on each stage. It was known from core processing activities that non-negligible quantities of calcium carbonate lined a large percentage of both open and closed natural fracture faces. The process was recommended with the thought that some limited etching would be better than no etching at all, and the damage caused by leaving small quantities of high-chloride saltwater [spent acid] would be overwhelmed by the stimulation resulting from the etching.

2. In McLean County Kentucky, the fracturing fluid eventually chosen and pumped was a 92 – 99 Downhole Slurry Quality (DHSQ) nitrogen/water mist. 30/80-mesh ultra-lightweight proppant (a thermoplastic bead with a specific gravity of ±1.05) was slurried in a KCl water solution, and batch-pumped at several concentrations ranging from 0.05 ppa to 0.25 ppa. This type of system is radically different from conventional true "foams" (water-based fluids with between 65 and 85% N_2 by volume), in that a) effective apparent viscosities are lower, b) proppant-carrying capabilities are limited, even with ultra-lightweight proppants, and c) the total quantities of water per unit volume of fracturing fluid are much, much lower. The process was recommended with the assumption that damage caused by the small volumes of water would be overwhelmed by the extra stimulation that would result by placing some limited quantities of proppant into the induced fracture system network.

Though approaches (1) and (2) above (with respect to fluid choice) may have had technical merit, poor production results (discussed elsewhere in this report) from both projects were such that they might have masked any improvements that might have been attributable to the process changes.

Horizontal completion practice in other domestic shale plays has generally dovetailed toward two basic methods of exposing the formation to the wellbore. The first (and most common) method involves cementing the lateral in place, then pumping various combinations of plug and perforating charges to particular points along the lateral. Current industry consensus is that this method allows relatively precise control of fracture initiation, and it becomes possible to promote extremely high induced fracture surface area (at least close to the wellbore) via high fracture initiation point count. The second completion method involves running casing or a liner into the open hole, and not placing cement behind pipe. Stages are isolated with open hole packers, and access to the annulus between packers is controlled by various configurations of ports and sliding sleeves. Advantages of this particular process is that (unlike pumping plugs and guns):

- Gaseous fracturing fluids may statistically be employed with lower risk of early treatment termination due to screenout or high fracture initiation pressure associated with total entry friction (perforation/port friction + near wellbore friction). It is thought that the cause of this observations is rooted in the much higher formation surface area that is exposed to any given lateral exit point (in this case ports, as opposed to perforations).

- Total completion time is shorter, because interstage "down time" is much shorter or nonexistent, which can have a material impact on the D&C component of net present value.

- Once the lateral, packers, and ports/sleeves are in place, then the degree of on-location operational complexity during stimulation activities is substantially reduced, again contributing to an improved [lower] D&C component of net present value.

A primary disadvantage of packer/port/sleeve completions is the relatively low fracture initiation point count that can be ensured. Recently, and after both of the subject wells were completed, various industry providers of these mechanical systems announced that improvements in system design has resulted in the doubling of possible stages in a single wellbore, and it is possible that this technology could be utilized in future attempts to raise the fracture initiation point count per unit of lateral length.

3. Discussion of 3-D Parametric Modeling Efforts in the New Albany Shale

Various three dimensional parametric fracturing models have been employed for a number of years in order to:

1. Simulate a proposed hydraulically induced fracture as a predictive tool in order to optimize future stimulation process(es).
2. Simulate a fracture in real-time [that is ongoing at the time of simulation].
3. Simulate a historical hydraulic fracturing operation by matching pressure response, in turn implying a particular geometry associated with a given reservoir layering schema.
4. Simulate a historical hydraulic fracturing operation by matching both net pressure response and fracture geometry observed by a fracture mapping procedure.

One of the primary objectives of this project was to provide a schema or methodology for utilizing commercially available 3D parametric modeling in "routine" New Albany Shale hydraulic fracture design efforts. Such a schema would take the form of a set of guidelines for petrophysical interpretations and log channel manipulations for use in model layer creation, recommendations for "typical" model propagation parameters, leakoff parameters, and proppant transport parameters. It was intended that the microseismic monitoring efforts would be utilized (along with net pressure data) to modify and "calibrate" a simulation of a typical stage on each of the fracture mapping operations.

By the end of the first quarter of 2009, sufficient log evaluation by another GTI subcontractor had been completed for Christian County, Kentucky wells, that took a closer look at the utilization of logging tool response to develop lithological layering for 3-D parametric stimulation modeling.

During the process of reviewing area fracture mapping results not associated with this project, it became evident that occasionally induced fractures appeared to be relatively simple, and other times looked more like shale "networks" that are observed in competitive or analogous domestic shale plays. Often, these networks are composed of multiple parallel and oblique or orthogonal networks of natural and/or induced fractures. Three-dimensional parametric stimulation models simulate the geometry of simple, bi-wing induced fractures, so it was concluded that the only cases where 3-D parametric modeling would be applicable would be those where it was known that induced fractures were relatively "simple". At the time of this study, a number of attempts had been made by other researchers to develop workarounds to this problem utilizing existing parametric or grid-based [bi-wing] software packages, but reasonable, stable, or duplicatable solutions had not been made public. Several corporate or other entities are in various stages of development and commercialization of more robust software that attempts to simulate the geometry of fracture networks with multiple parallel and/or oblique or orthogonal fractures, when the frequency of such fractures can be estimated or calibrated to an existing fracture mapping effort. The nature of such efforts is such that these solutions must necessarily involve simulation of the induced fractures, in-situ natural fractures, directional in-situ stress conditions, and Darcy parameters associated with the reservoir.

In other domestic shale plays, it has been noted that the most successful wells exhibit relatively large induced or naturally fractured networks, with the inference that the better production was

associated with the higher degree of fracture surface area exposed to the reservoir. It follows that the effort described below to develop adequate 3D parametric modeling techniques will only apply to those cases where fracturing is simple, the degree of networking is low, and therefore in cases where the relative area of fracture face exposed to the reservoir is low.

Several logs from New Albany Shale penetrations in Christian County, KY were examined by the primary GTI logging interpretation contractor. One log, in particular, was analyzed, and the available monopole sonic channel was combined with an industry-accepted routine to develop reasonable values for both shear and compressional velocities in lithologies in and above the New Albany shale. Utilizing these channels, values for Young's modulus, Poisson's ratio and stress were calculated (again, using industry-accepted equations), and these values were utilized to develop lithological layering for a series of 3D parametric modeling runs. The calculated stress for this case within the New Albany shale was slightly higher than the boundary lithologies. The result was a fundamental instability in the modeling result. This occurs frequently when a target interval lies within a layer or series of layers in which the calculated stress is higher than the boundaries. Subsequent fracture mapping efforts demonstrated that (when naturally occurring pre-stressed features were not dominating) relative fracture containment was indeed noted within the shale. The suggestion, then, was that actual dipole measurements may be required to adequately describe the in-situ stress regime to a degree that is acceptable for 3-D parametric model layering.

A dipole sonic logging suite was run on the McLean County, KY vertical observation wellbore prior to placement and cementing of casing. Calculation of mechanical properties from Δt_{shear} and $\Delta t_{compressional}$ (including static Young's Modulus, Poisson's Ratio, shear modulus, uniaxial compressive strength and horizontal minimum principle stress) was performed with industry-accepted expressions, and utilized in the 3-D parametric predictive modeling associated with the McLean County completion.

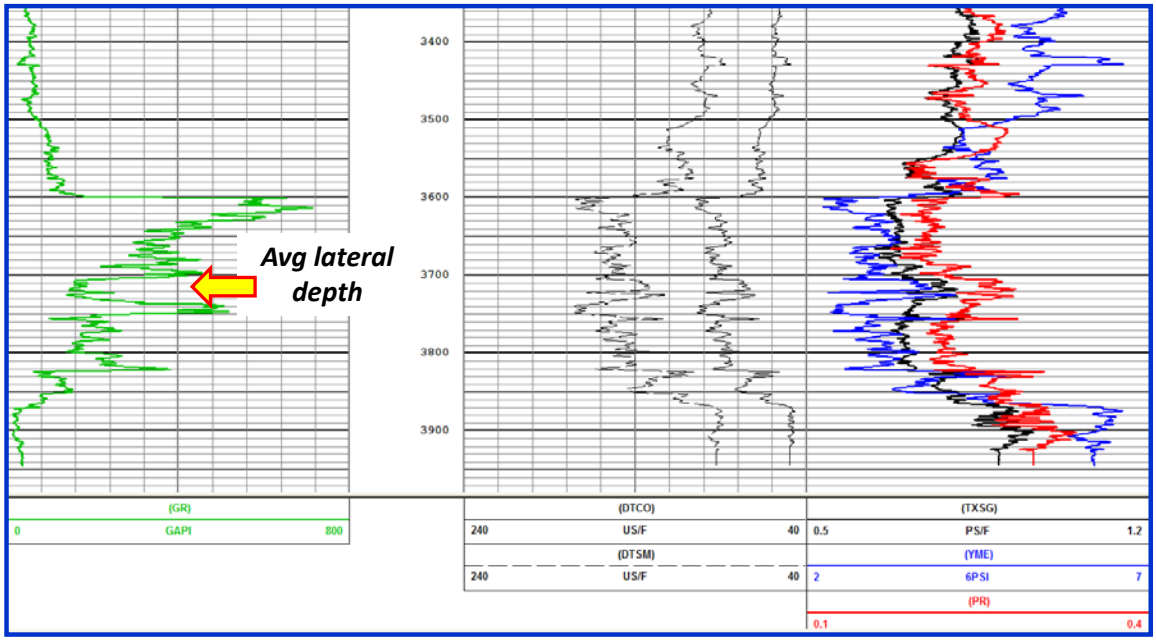


Figure 1. Raw data and calculated mechanical data used in parametric modeling

Figure 1 is a graphical representation of the log data utilized in layer simulation for 3-D parametric modeling. The following conventions were employed in forward modeling efforts:

- Values for from Δt_{shear} and $\Delta t_{compressional}$ were assumed to represent wave properties not only at the wellbore where they were measured, but throughout the surrounding reservoir in the volumes adjacent to the two horizontal wells to be stimulated (homogeneous layering).

- Values for shear moduli were calculated from

$$G = \rho_b \frac{d^2}{\Delta t_S^2}$$

values of Poisson's Ratio from

$$\nu = \frac{\frac{1}{2}\left(\frac{\Delta t_S}{\Delta t_C}\right)^2 - 1}{\left(\frac{\Delta t_S}{\Delta t_C}\right)^2 - 1}$$

and values of static Young's Modulus from

$$E = 2G(1+\nu)$$

Though the calculated Young's Moduli might have been a bit low in the high-TOC portion of the lithological column, no adjustment was made, because there was no hard evidence available that it needed to be shifted. There is some experimental evidence by Papanastasiou and Cook (*Modes of Fracture Initiation in Thick-wall Cylinder Experiments*, ARMA, 1999) and van Dam, de Pater, and Romijn (*Analysis of Hydraulic Fracture Closure in Laboratory Experiments*, SPE 47380,1998), that suggest that the relevant Young's Modulus for hydraulic fracturing is the "unloading modulus" measured during laboratory experiments, which lies somewhere in between the tangent modulus measured from core testing and that of the static Young's Modulus calculated from sonic measurements. Plona and Cook (*Effects of Stress Cycles on Static and Dynamic Young's Moduli in Castlegate Sandstone*, ARMA, 1995) reported this same observation. Poisson's ratios were left alone for the same reason, and closure stresses (assumed equal to the horizontal minimum principle stresses) were left as calculated, in the absence of any pre-fracture pump-in/leak-off calibrating data.

- The [vertical] values of Δt_{shear} and $\Delta t_{compressional}$ measured during logging operations were assumed to represent their respective horizontal values.

- A conventional elastic 3-D model with limited tip effects was utilized. Previous mapping experience had suggested that relatively confined, very long fracture half-lengths were probable.

- Values for permeability in a dual-porosity reservoir are necessarily simplified when performing 3-D parametric modeling. It is normal practice to utilize an effective permeability that takes into account both matrix and natural/induced fracture permeability

over the volume stimulated. For purposes of this simulation (and in the absence of better information), log-derived permeabilities were employed.

- Values for fracture toughness (a measure of how much energy is required to actually break rock at the induced fracture tip) were estimated (in the absence of better information) from K_{Ic} = 20 X (SQRT(gamma ray^10)) + 200. Fracture toughness is considered an important parameter only during very early pumping operations, possibly only after a very few feet of fracture have been induced. In the case of the New Albany Shale, it was thought that this can occur in just a few seconds after breakdown, and then values for K_{Ic} after that point may have little or no impact on either pressure response or fracture geometry.

- Pore pressure was not known, but it was assumed that the reservoir and its bounding layers were substantially under-pressured. A gradient of 0.29 psi/ft was utilized during pre-completion modeling.

- Water saturations calculated by the logging subcontractor may have averaged higher than were desirable, but were retained for modeling purposes in the absence of contrary evidence.

An example of the pre-completion forecast of a single stage geometry utilizing the above conventions is shown in **Figure 2**.

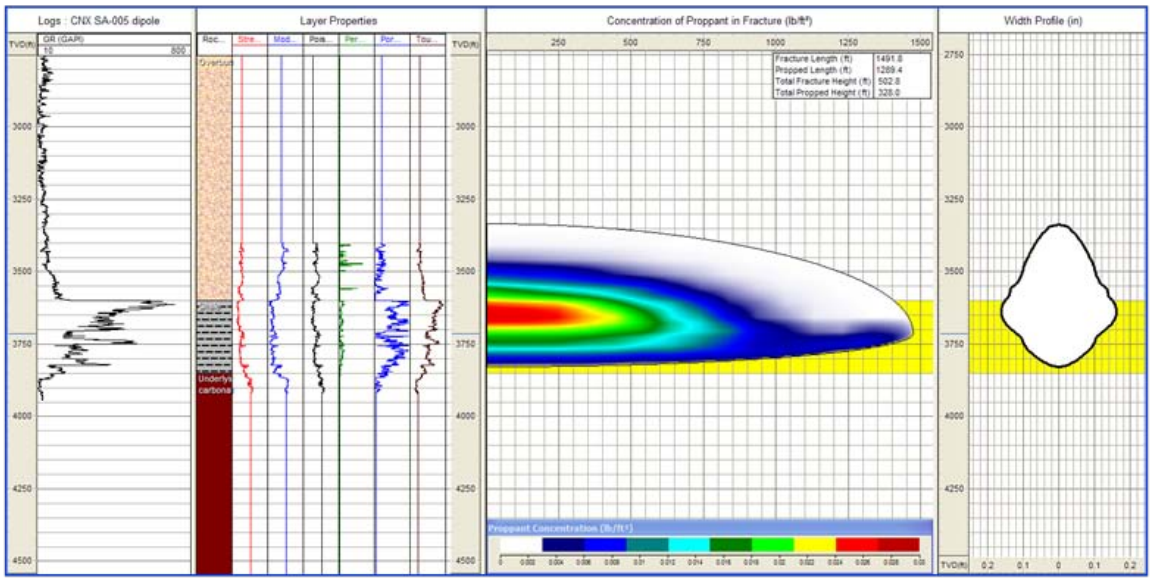


Figure 2. Forecast geometry of a single stage, McLean County

In typical logging operations in this play, values for Δt_{shear} and $\Delta t_{compressional}$ are not typically available, due to D&C cost considerations. However, various "triple combo" suites are run in a large percentage of New Albany shale E&P efforts. A method was proposed by which realistic and stable 3-D parametric modeling might be accomplished in the New Albany Shale for cases where induced fracturing is relatively simple, and where only a triple combo suite was available. This method relies on utilizing gamma ray, photoelectric constant, and [calculated] effective porosity in conjunction with known area fracture gradients or closure stresses, and/or calibrating

with fracture mapping efforts, when available. Examples were constructed for the case of straight nitrogen fracturing treatments, but the approach was eventually discarded due to the high quantity of arbitrary assumptions that were required.

Once both fracture mapping efforts were completed, it quickly became evident that the only uniquely "planar" induced fractures were those associated with interaction with naturally occurring geological features, such as faulting. Fractures that did *not* interact with such features generated microseismic responses consistent with complex network fracturing; groups of parallel and oblique cross-cutting geometries that remained largely confined to the New Albany Shale were the rule in this case. Attempting to force fit a simple bi-wing simulator to model multiple parallel and oblique fractures was not considered a reasonable engineering practice, and so the effort was terminated.

4. Discussion of Christian County Microseismic

Pinnacle provided FracSeis[SM] microseismic mapping services as a subcontractor of the Gas Technology Institute to an industry participant during the hydraulic fracture stimulation of the horizontal gas well located in Christian County, Kentucky. The well was drilled transverse (perpendicular to the expected fracture azimuth) in the objective New Albany Shale Formation (NAS) and completed as an uncemented lateral with a series of open hole packers and sliding sleeves. The well was stimulated for gas production using eight nitrogen hydraulic fracture treatment stages, with a minimal quantity of nitrified HCl in front of each stage, and no proppant.

The objectives of the fracture mapping service were to:

- Determine fracture pay zone coverage along the horizontal wellbore
- Measure fracture geometry (height, length and azimuth)
- Determine the relative degree of induced fracture complexity and fracture network width
- Provide immediate information that could be used for future well placement and infill drilling strategies
- Contribute to the understanding of the effectiveness of openhole isolation packer processes

The receiver array was first located in a temporarily abandoned adjacent vertical well (See **Figure 23**). Placement of the array in the observation well was above the New Albany Shale, with the bottom tool at 2,414 ft, as shown in **Figure 25**. As the stages progressed to the south in the heelward direction, the locations of sliding sleeves and events exceeded the listening distance of the geophones, so after the fourth stage was complete, the toolstring was rigged out and placed into the intermediate string of a vertical [future horizontal] offset, which was located on the same surface pad as the treatment well. The geophones were oriented with a series of surface (dynamite) shots located as per **Figure 23**.

Microseismic fracture mapping results for those stages that recorded enough events to adequately define fracture network geometry are summarized in **Table 1** and **Table 2**. The spatial mapping of microseisms for all stages is presented graphically in **Figure 3**, **Figure 4** and **Figure 5**. Fracture network heights were quite limited during the first three stages, with the top of the networks contained within the lower portions of the Ft. Payne, and the lowest activity in the upper portions of the Sellersburg. Fracture half-lengths X_f for these three stages ranged from about 1,200 ft to over 1,600 ft. The azimuth of the networks was N85°E, which was consistent with area near-wellbore measurements of induced fractures. It appeared as if network widths were wide enough that communication in the New Albany Shale (or bounding lithologies) around openhole packers could have occurred after initiation, and substantial volumetric overlap of microseismic activity was noted during these stages. The relatively high degree of confinement in the softer shale lithologies suggest that toe-ward horizontal stresses σ_{min} and σ_{max} are lower in the NAS than in bounding layers, or that the ultra-low apparent viscosity of the fracturing fluid contributed to better confinement than would have been otherwise expected.

After the geophone array was pulled from the first observation well and placed in the second, it became clear that surface noise from the nitrogen pumps was substantial enough that microseismic activity from the last four stages would be difficult, if not impossible to hear. Low signal-to-noise ratios (SNR) prevented the clear determination of fracture network geometry during stages 5, 6 and 7; however, during stages 6 and 7, it became obvious that there was significant upward growth up through the Ft. Payne and into (at least) the Warsaw series of carbonate lithologies. During stage 8, enough events were recorded to clearly define upward growth through the Payne, the Warsaw and up into the Salem. Because few events were sourced in the New Albany Shale, it was not evident at what position nitrogen was exiting the casing or lateral during any of the last four stages.

Some events noted during a particular stage (after the first) could have been associated with earlier pumping activity and it was not possible to quantify the percentage of such.

Given the positioning of events from the last three out of four stages, it is possible that the New Albany Shale was not adequately stimulated adjacent to the heelward portions of the lateral. Many of the heelward events were of larger moment magnitude, a condition often associated with interaction between induced fluids and naturally occurring geological features such as faulting. In other unconventional plays, it has been noted that when significant interaction between stimulation fluids and geological features is observed, often early–history well performance is less than when such features are not encountered.

The event moment magnitudes of events from the first four stages fit into a log-normal distribution, averaging about -3.5 on the Richter scale and ranging from about -3 to -4.2. Events recorded from the last four stages (dominated by stage 8) did not fit a log-normal distribution, as stage 8 had disproportionate number of high-magnitude events. Average magnitude -3.5 events were detectable up to about 1,600 ft distance from the toolstring. The uncertainties of event locations are less than 25 ft for both depth and tool-to-event distance and average less than 70 ft for azimuth error.

Table 1. Job Summary Stages 1 – 4

County:	Christian	**State/Province:**	KY
Services Provided:	☒ Fracture Microseismic	Downhole Tilt Mapping: ☐ TWT ☐ OWT	☐ Surface Tilt Mapping
	☐ Reservoir Monitoring	Consulting Services: ☐ Engineering ☐ Supv. & QC	

	Units	**Stage 1**	**Stage 2**	**Stage 3**	**Stage 4**
Treatment Date:		9/21/2009	9/21/2009	9/21/2009	9/21/2009
Formation:		New Albany Shale	New Albany Shale	New Albany Shale	New Albany Shale
Sleeve Depth (MD):	ft	5,741 ft	5,241 ft	4,786 ft	4,327 ft
No. of holes:	ea	1 port	1 port	1 port	1 port
Treatment Volumes:					
Nitrogen	scf	1,001,884	999,300	999,680	1,004,000
Proppant:					
None	lbm	0	0	0	0
Rates & Pressures:					
Average Rate	scfm	105,090	103,900	106,200	103,674
Average WHTP	psi	4,948	4,607	4,522	4,086
Diagnostic ISIP	psi	2,589	2,127	2,213	N/A
Final ISIP	psi	N/A	N/A	N/A	2,019
Results & Analysis:					
Geometry:					
Fracture Half-length	ft	1,190	1,650	1,260	Unknown
Fracture Network Height	ft	188	250	184	Unknown
Fracture Network Width	ft	520	750	600	Unknown
Fracture Azimuth		N85°E	N85°E	N85°E	Unknown
Stimulated Reservoir Volume	ft^3	Not calculated			
Fracture Dip		No	No	No	Unknown
Asymmetry Assumed		No	No	No	Unknown
Complexity		Yes	Yes	No	Unknown

Table 2. Job Summary Stages 5 – 8

	Units	**Stage 5**	**Stage 6**	**Stage 7**	**Stage 8**
Treatment Date:		9/21/2009	9/21/2009	9/21/2009	9/21/2009
Formation:		New Albany Shale	New Albany Shale	New Albany Shale	New Albany Shale
Sleeve Depth (MD):	ft	3,781 ft	3,614 ft	2,964 ft	2,554 ft
No. Perforations:	ea	1 port	600	1 port	1 port
Treatment Volumes:					
Nitrogen	scf	1,002,882	1,002,000	1,007,179	1,007,094
Proppant:					
None	lbm	0	0	0	0
Rates & Pressures:					
Average Rate	scfm	101,928	104,228	104,009	104,859
Average WHTP	psi	3,854	3,714	3,718	3,520
Diagnostic ISIP	-	2,135	2,076	2,096	N/A
Final ISIP	psi	N/A	N/A	N/A	2,107
Results & Analysis:					
Geometry:					
Fracture Half-length	ft	Unknown	At least 540	At least 800	1,000
Fracture Network Height	ft	Unknown	At least 552	At least 558	840
Fracture Network Width	ft	Unknown	Unknown	Unknown	750
Fracture Azimuth		Unknown	N85°E	Unknown	N85°E
Stimulated Reservoir Volume	ft^3	Not calculated			
Fracture Dip		Unknown	Unknown	Unknown	No
Asymmetry Assumed		Unknown	Unknown	Unknown	No
Complexity		Unknown	Unknown	No	No

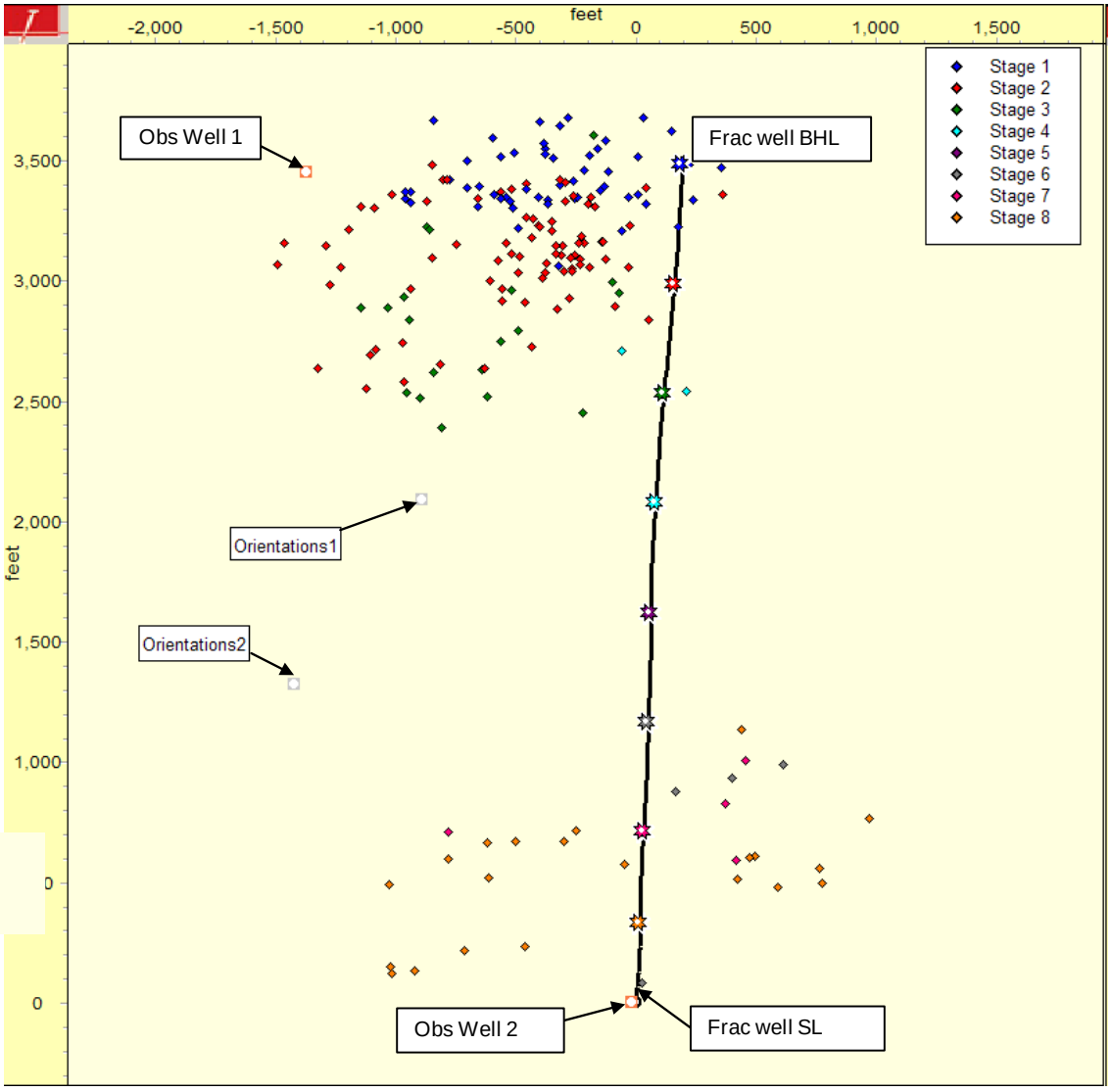


Figure 3. Map view, all stages

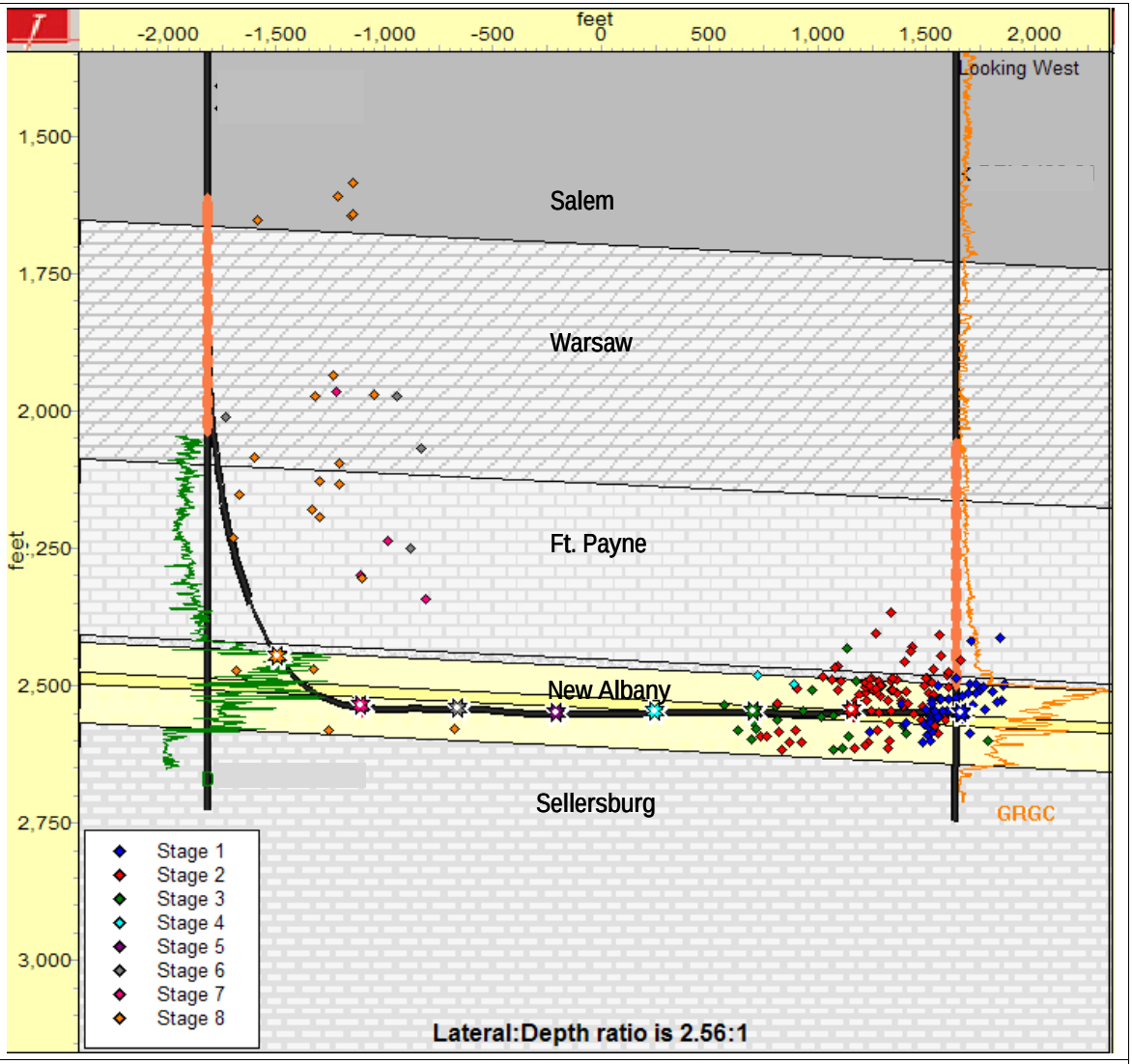


Figure 4. Lateral side view (orthogonal to lateral), all stages

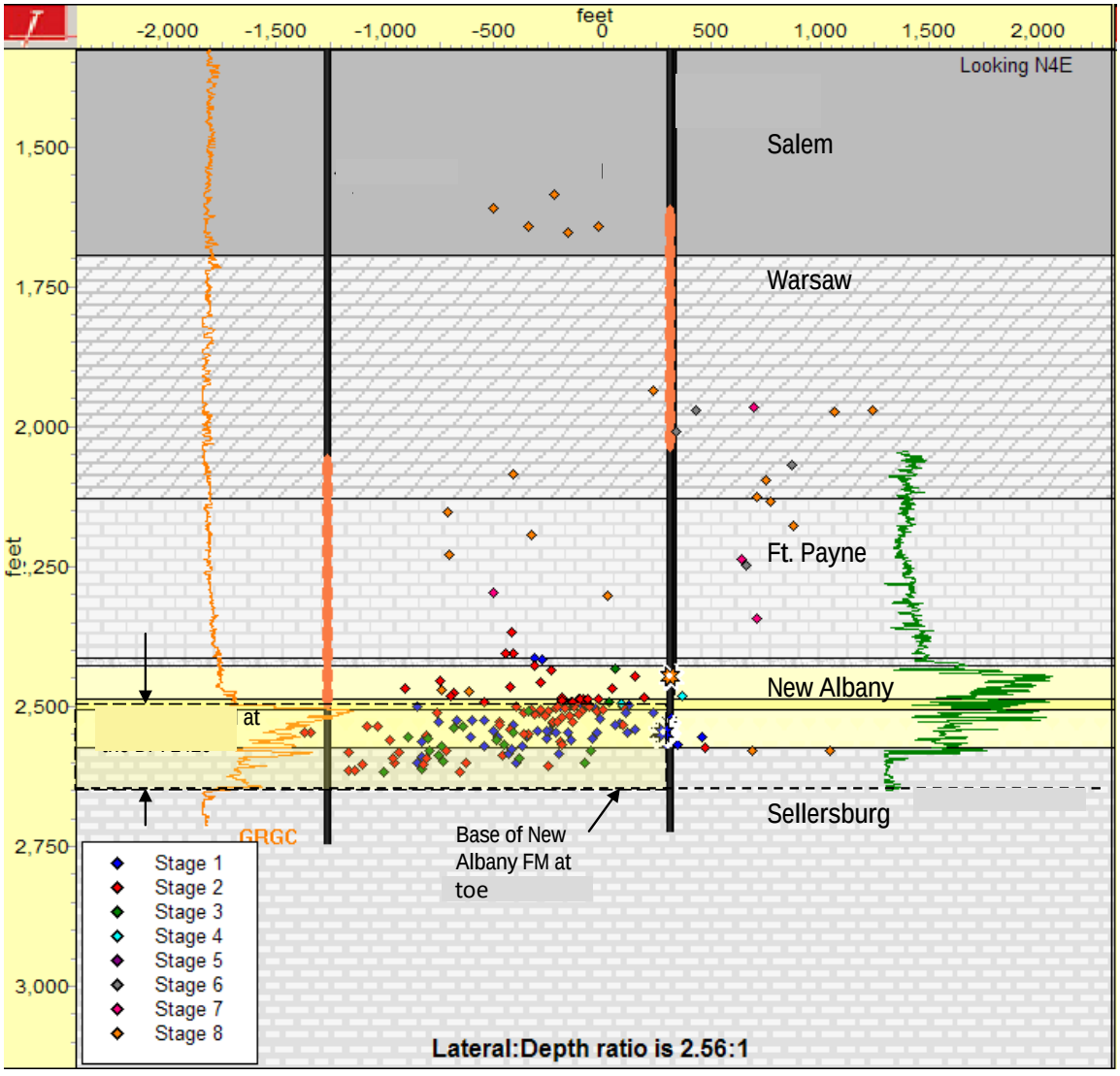


Figure 5. Lateral end-on view (along lateral), all stages

4.1 Discussion, Mapping Effort on the Toeward Stages

The geophones were first placed in a vertical cemented wellbore that had collapsed casing just above the New Albany Shale. During the completion effort, the surface noise was somewhat limited; the signal-to-noise ratio was high enough that relatively low-magnitude microseisms were detected and therefore the western wings of stages 1 and 2 were well-defined. Stage 3 was nearing the limits of listening distance, but the geometry of the layout was such that it was thought that the western extremities of this stage were reasonably distinct.

Figure 6 is an example of data from an event that was close to the observation well. Though low-frequency background noise and/or changes in lithology interfered with the selection of compressional wave signals from the top six tools, the shear wave is clearly distinguishable on all 12 tools, and the short spread between P- and S-signatures places the source close to the observation well. **Figure 7** is an example of a "far" event (one that was close to the stimulated lateral, near the heel). Events with high and low elevations are depicted in **Figure 8** and **Figure 9,** and the move-out (changing differential between compressional and shear wave arrivals) can be seen on about half the tools in each case.

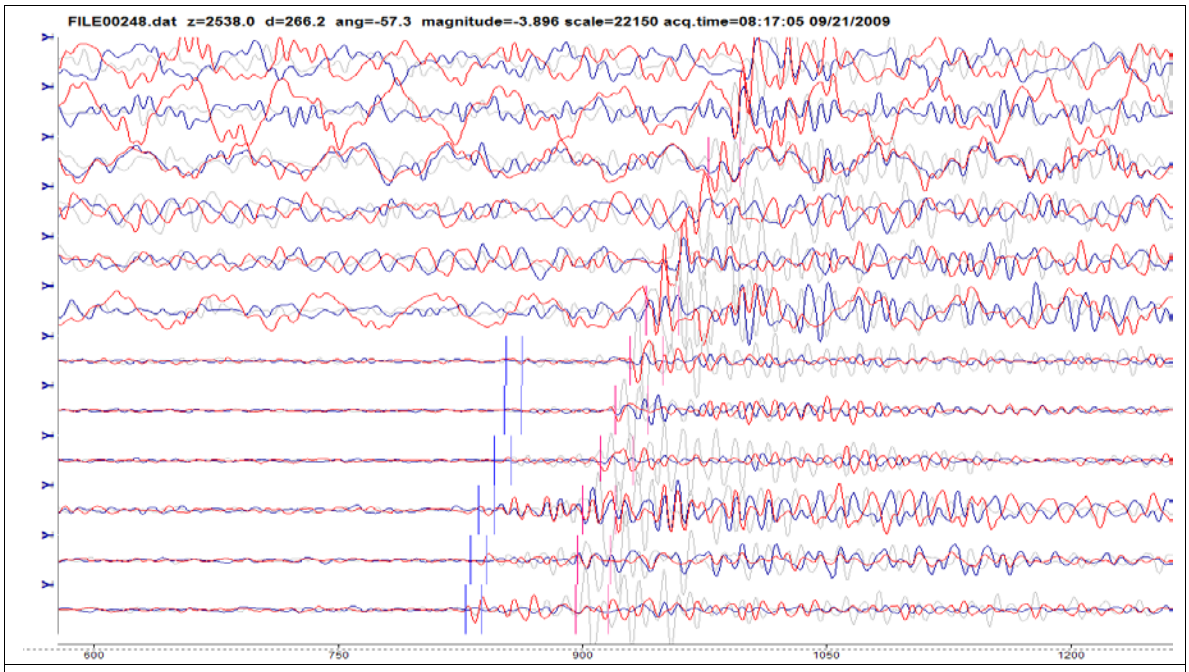


Figure 6. Typical raw digitized data from a near event, first observation well

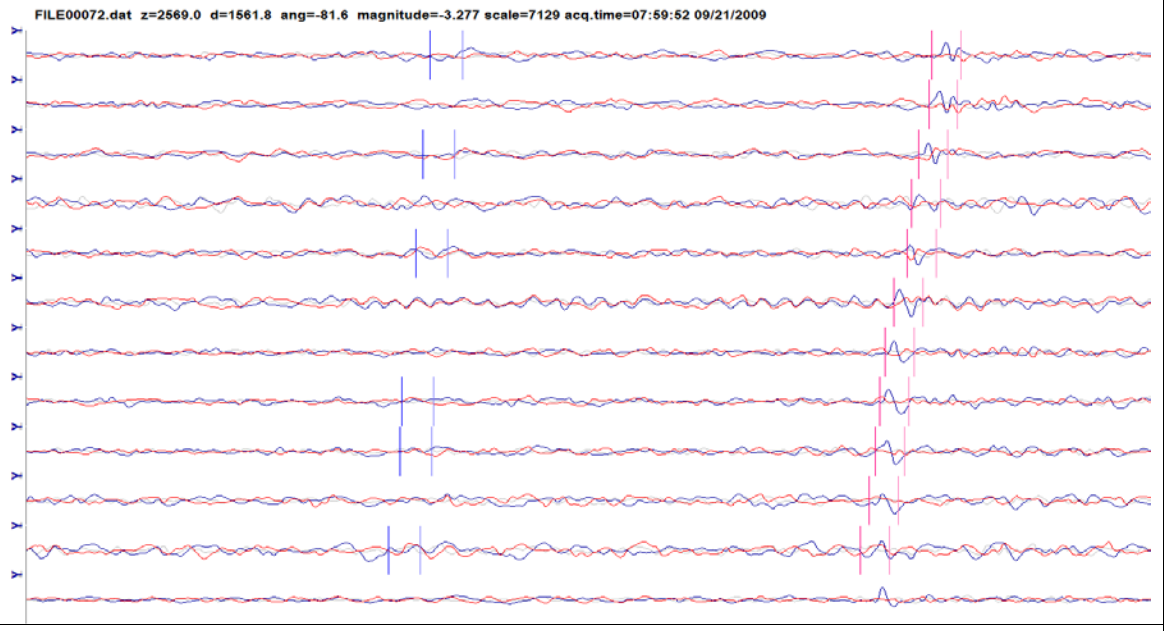


Figure 7. Typical raw digitized data from a far event, first observation well

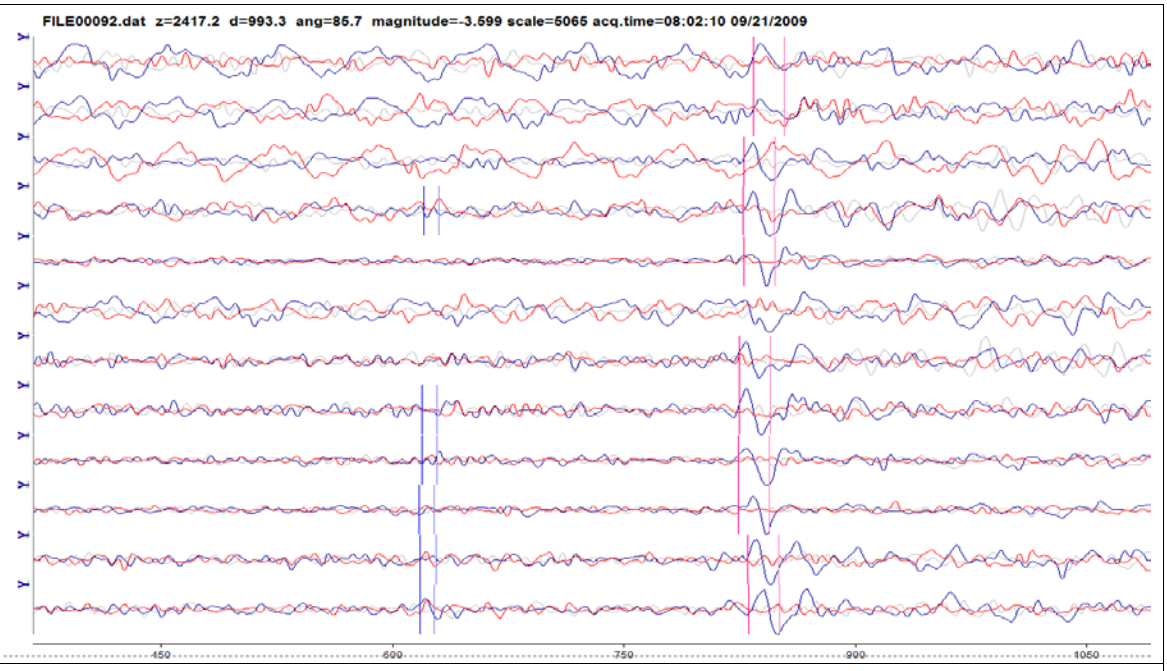


Figure 8. Typical raw digitized data from a high event, first observation well

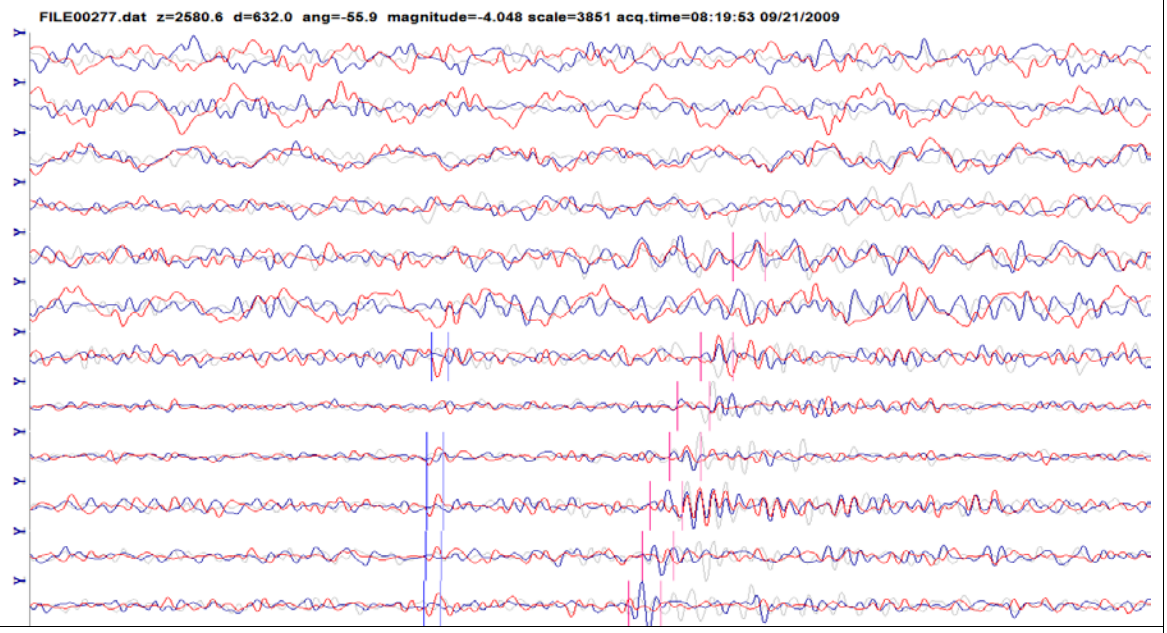


Figure 9. Typical raw digitized data from a low event, first observation well

Microseismic fracture mapping results for the tow-ward stages showed that fractures were relatively confined in the New Albany Shale. Fracture half-lengths were at least 1,200 ft (symmetry assumed), with a primary fracture azimuth of N85°E, a potential secondary azimuth of N52°E, and a network width of 500 - 700 ft.

The relatively good confinement (from a fracture network height growth perspective) suggests that that horizontal stresses σ_{min} and σ_{max} are lower in the NAS than in the bounding Ft. Payne and Sellersburg, and that effective stimulation would not be effectively shut down by radical growth outside the New Albany Shale, unless natural geological features were present that could promote such height growth.

Events were located primarily on the west side of the lateral, but it is thought likely that distance-related bias was responsible for not hearing events on the eastern side. Some of the events seen in stage 2 could have been associated with leak-off activity from the previous stage. It is clear that there is interaction between stage 1 and stage 2, and that there was communication between them. It is likely that such communication occurred away from the wellbore, but it is not possible to quantify how much activity was associated with the stage 2 pumping operation, and how much was "left over" from stage 1.

A portion of the network "width" could have been associated with multiple fracture initiation points in the openhole between the two packers, as it was known that there existed a number of open natural fractures approximately perpendicular to the azimuth of the lateral orientation. It was not possible to verify this possibility.

Stage 3 total event count was substantially lower than previous stages. Though some of this observation may be explained by distance-related signal attenuation, it is a logical assumption that more events would normally be expected, as the area to the west of the sliding sleeve is within the previously demonstrated listening distance. This suggests a number of potential scenarios: a) re-pressurization of existing induced fractures from previous stages, b) increased

count of open natural fractures connecting the stage 3 openhole wellbore, c) simultaneous exit of some portion of the volume of nitrogen exiting the casing or lateral at a different location outside the range of the array listening distance or d) some combination of the above. As in stage 2, it was not known how much of the observed activity was associated with the stage 3 pumping operation, and how much was "left over" from previous stages.

Microseismic fracture mapping results for stages 4 and 5 were outside the listening distance of both geophone array positions, and zero events stage 5 were recorded.

4.2 Discussion, Mapping Effort on the Heelward Stages

After the fourth stage, the geophones were moved to the intermediate casing in the second observation well, the vertical portion of a new wellbore that had not yet had the horizontal portion drilled at the time of the stimulated well's completion. The observation well's surface location was approximately 15 ft away from the surface location of the stimulated well, and tools were set above the New Albany Shale. During the stimulation of stages 5 through 8, low-frequency surface noise associated with pumping operations was substantial. The signal-to-noise ratio was high and many low-magnitude events were likely obscured by the surface noise. Only the last stage (8) had enough events to clearly define fracture geometry, but the few events detected during stages 6 and 7 are presented, because the positioning of them from an elevation perspective is material to the overall evaluation of the mapping effort.

Figure 10 is an example of data from an event that was below the observation toolstring. Low-frequency background noise interfered with the selection of compressional wave signals from several tools, but the shear wave is clearly distinguishable on 11 out of 12 tools.

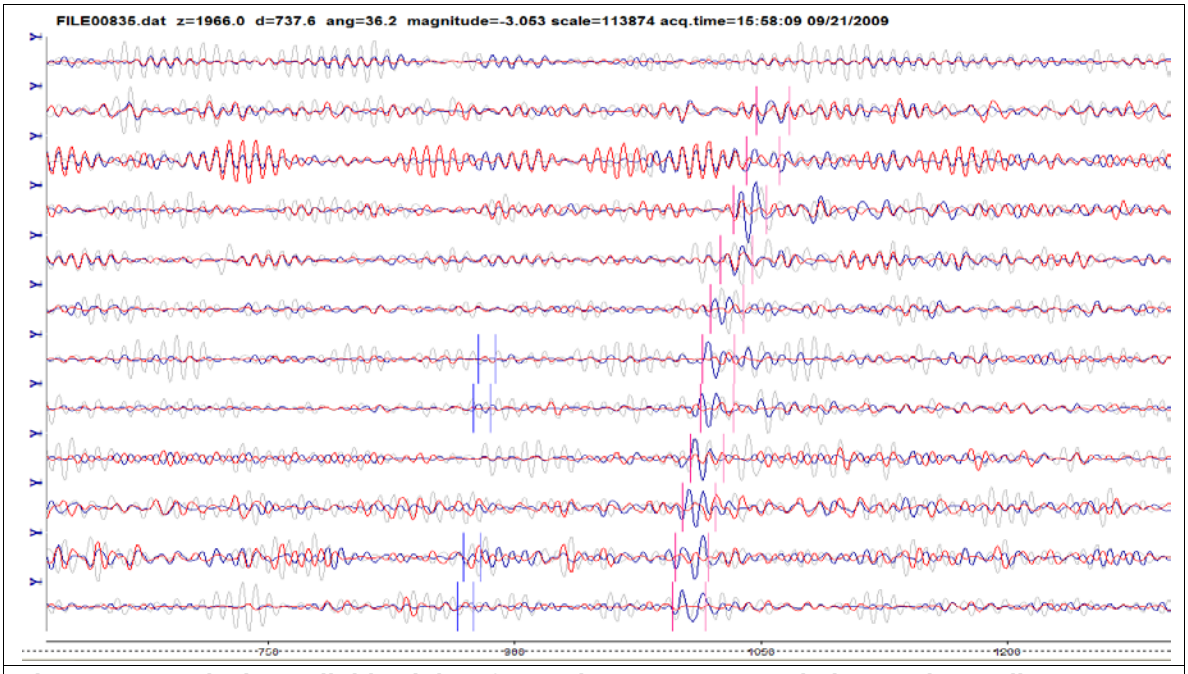


Figure 10. Typical raw digitized data from a low event, second observation well

Microseismic fracture mapping results for stage 6 in the New Albany Shale (with sliding sleeve at 3,416 ft and confining packers at 3,364 and 3,818 ft) are summarized in **Table 2**. The spatial mapping of the four microseisms that were recorded is presented graphically in **Figure 11** and **Figure 12**. A fracture height of at least 552 ft is suggested, with the top of the fracture at about 1,972 ft TVD and the exit point of the casing at about 2,524 ft TVD. Fracture half-length was at least 540 ft, but could have been longer.

Though the low event count precludes the defining of fracture geometry for this stage, these four events have been displayed because they are all located well above the lateral in the Ft. Payne and Warsaw. The exit point from the lateral or casing is unknown, though one event was located very close to the kick-off point of the horizontal section.

A cause of the high growth is not determinable from unique information gathered during this stage.

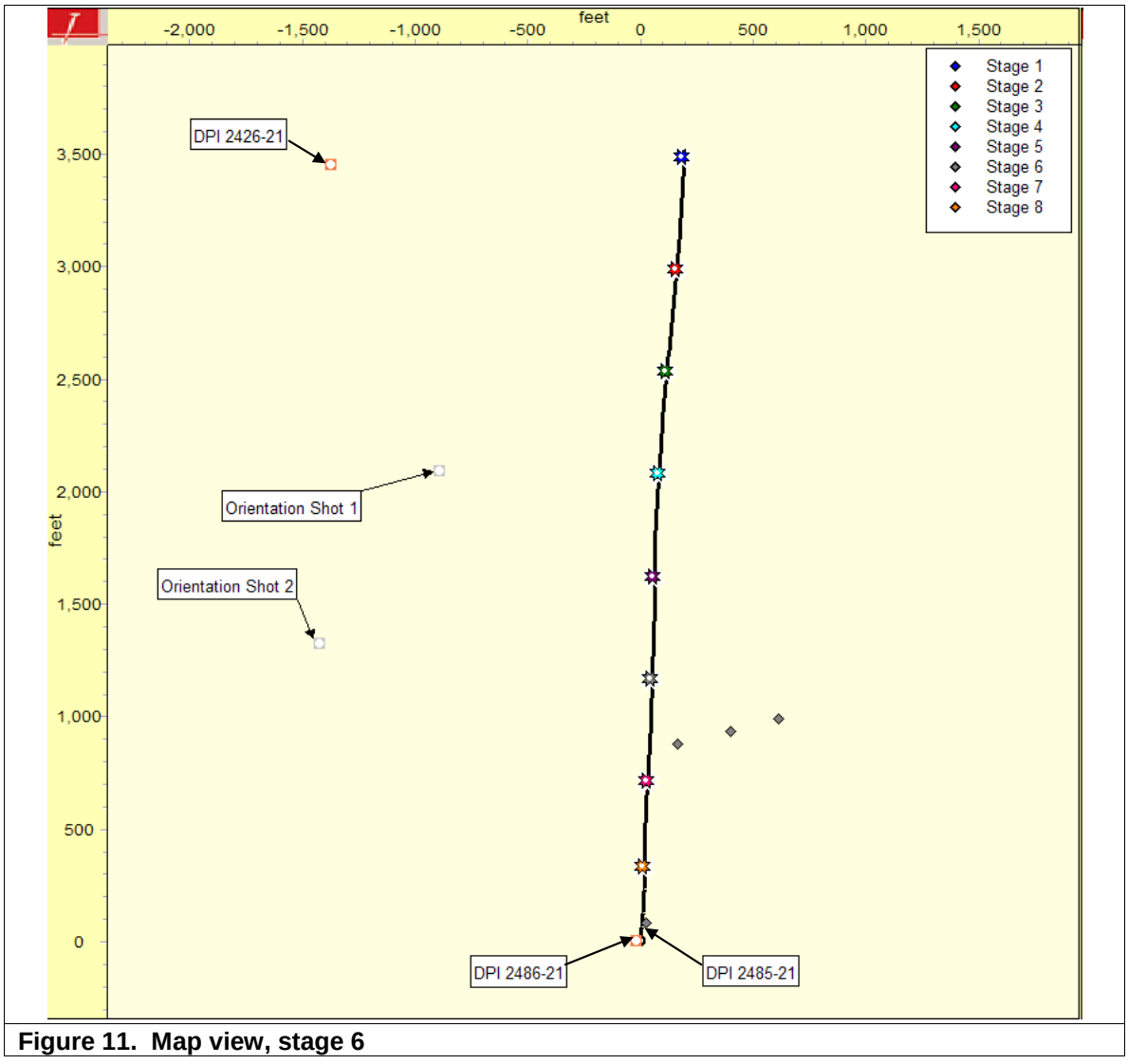


Figure 11. Map view, stage 6

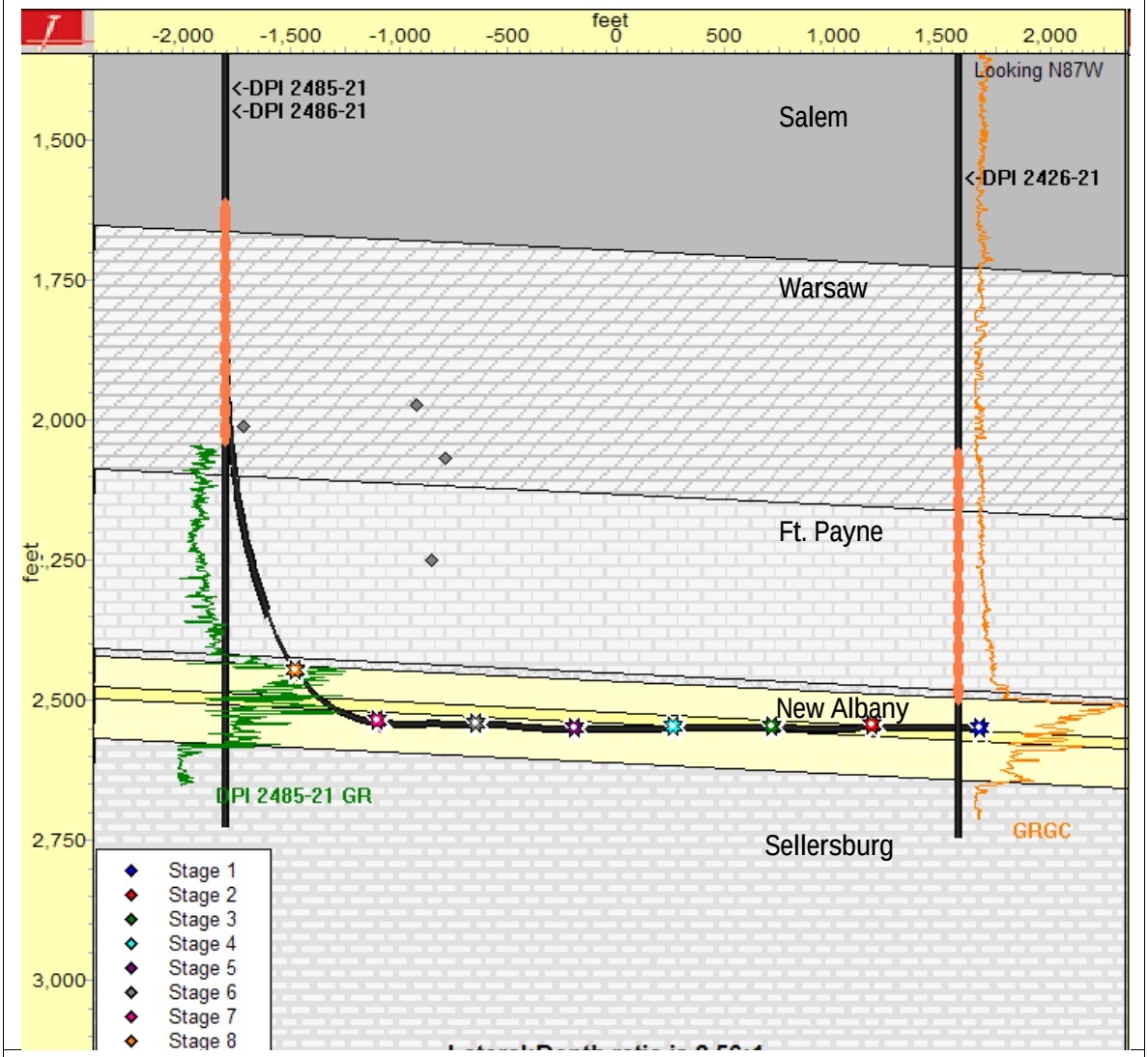


Figure 12. Lateral side view (orthogonal to lateral), stage 6

Microseismic fracture mapping results for stage 7 in the New Albany Shale (with sliding sleeve at 2,963 ft and confining packers at 2,911 and 3,364 ft) are summarized in **Table 2**. The spatial mapping of microseisms is presented graphically in **Figure 13** and **Figure 14**. Again, a fracture height of at least 558 ft is implied, with the top of the fracture at about 1,966 ft TVD and the lateral sleeve at about 2,524 ft TVD. Fracture half-length was at least 800 ft.

Like stage 6, the low event count precludes a clear definition of fracture geometry. Again, the four events have been displayed because they are all located well above the lateral, in the Ft. Payne and Warsaw. Again, as in the previous stage, the exit point from the lateral or casing is unknown.

A root cause of the high growth is not determinable from just the information gathered during this stage.

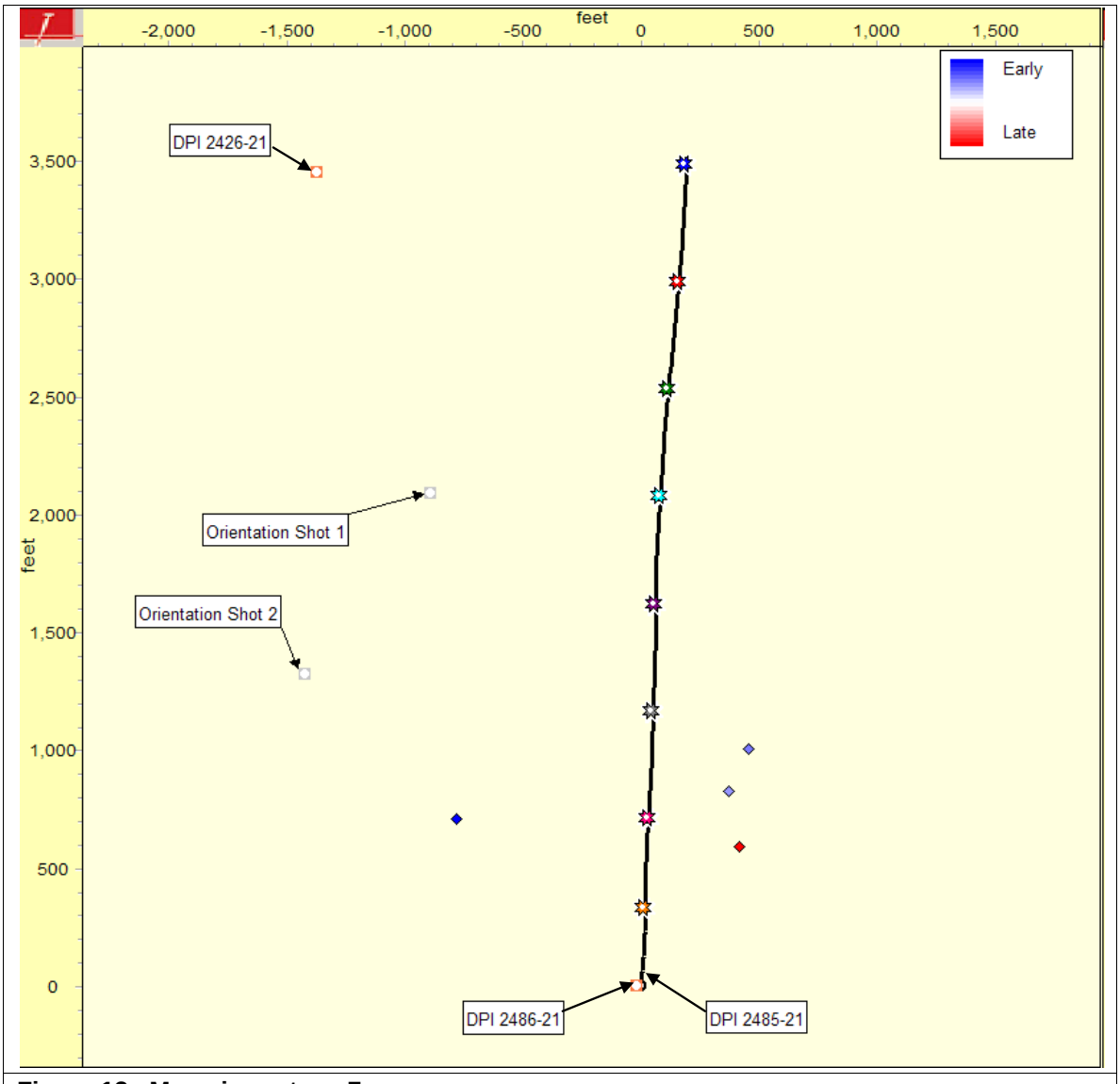


Figure 13. Map view, stage 7

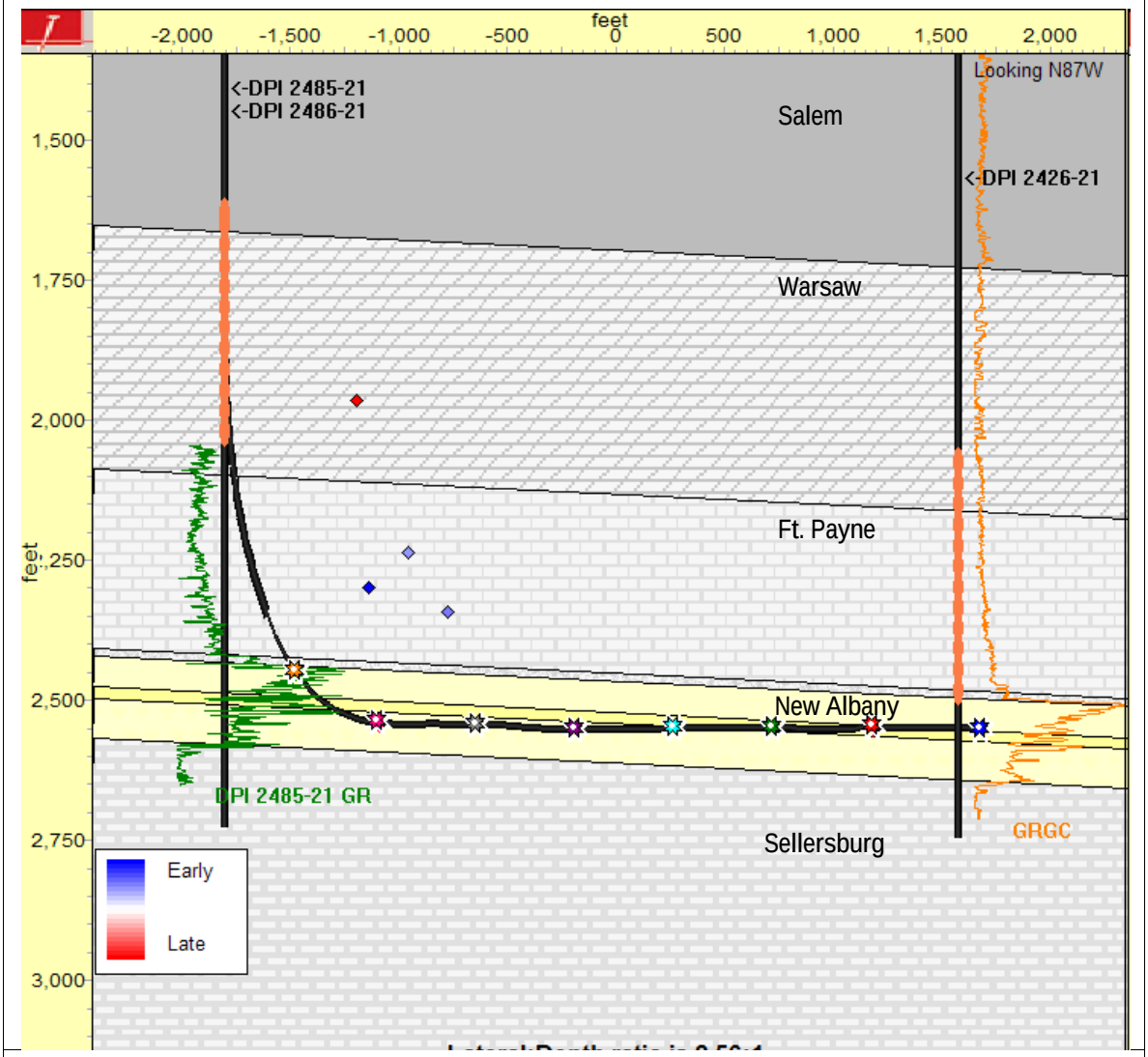


Figure 14. Lateral side view (orthogonal to lateral), stage 7

Microseismic fracture mapping results for stage 8 in the New Albany Shale (with sliding sleeve at 2,555 ft and confining packers at 2,502 and 2,911 ft) are summarized in **Table 2**. The spatial mapping of microseisms is presented graphically in **Figure 15**, **Figure 16** and **Figure 17**. A fracture height of at least 841 ft is indicated, with the top of the fracture at about 1,585 ft TVD and the lowest events at about 2,426 ft TVD. Fracture half-length was at least 1,000 ft, with a primary fracture azimuth of N85°E.

This stage was unique, in that a lower degree of complexity is implied. Though an overall network width of 750 ft is measured from northern-most to southern-most events, there are clear "fingers" of activity that can be seen in the map view (**Figure 15**).

Fracture height growth was extensive, with events locating in the Ft. Payne, Warsaw and Salem zones. Very few events were heard in the New Albany Shale, suggesting that stimulation in the NAS may not have been as extensive as desired in the heel-most portion of the lateral. Too few events were seen next to the wellbore to adequately isolate the location of the fluid exit point, and therefore it is not possible to evaluate the effectiveness of the openhole isolation process in this portion of the wellbore. It is possible that fracturing of the NAS did occur, but that event magnitude of the associated activity was obscured by the high background noise associated with

A second observation unique to this stage was the magnitude of events relative to other stages. **Figure 18** displays a pair of histograms with moment magnitude (microseism amplitude normalized for distance to the geophone array) of all events recorded for all stages. It is evident that the average moment magnitude for stage 8 is about 50% higher than for stages 6 and 7, and about 40% higher when compared to stages 1 through 4. In other shale gas plays, high-magnitude events have been associated with the presence of geological "features" or irregularities such as faulting. In addition, there is loose evidence that induced fractures that interact with faults often expend much of their energy doing so and it is probable that in such cases, less energy is directed toward breakup of the shale of interest.

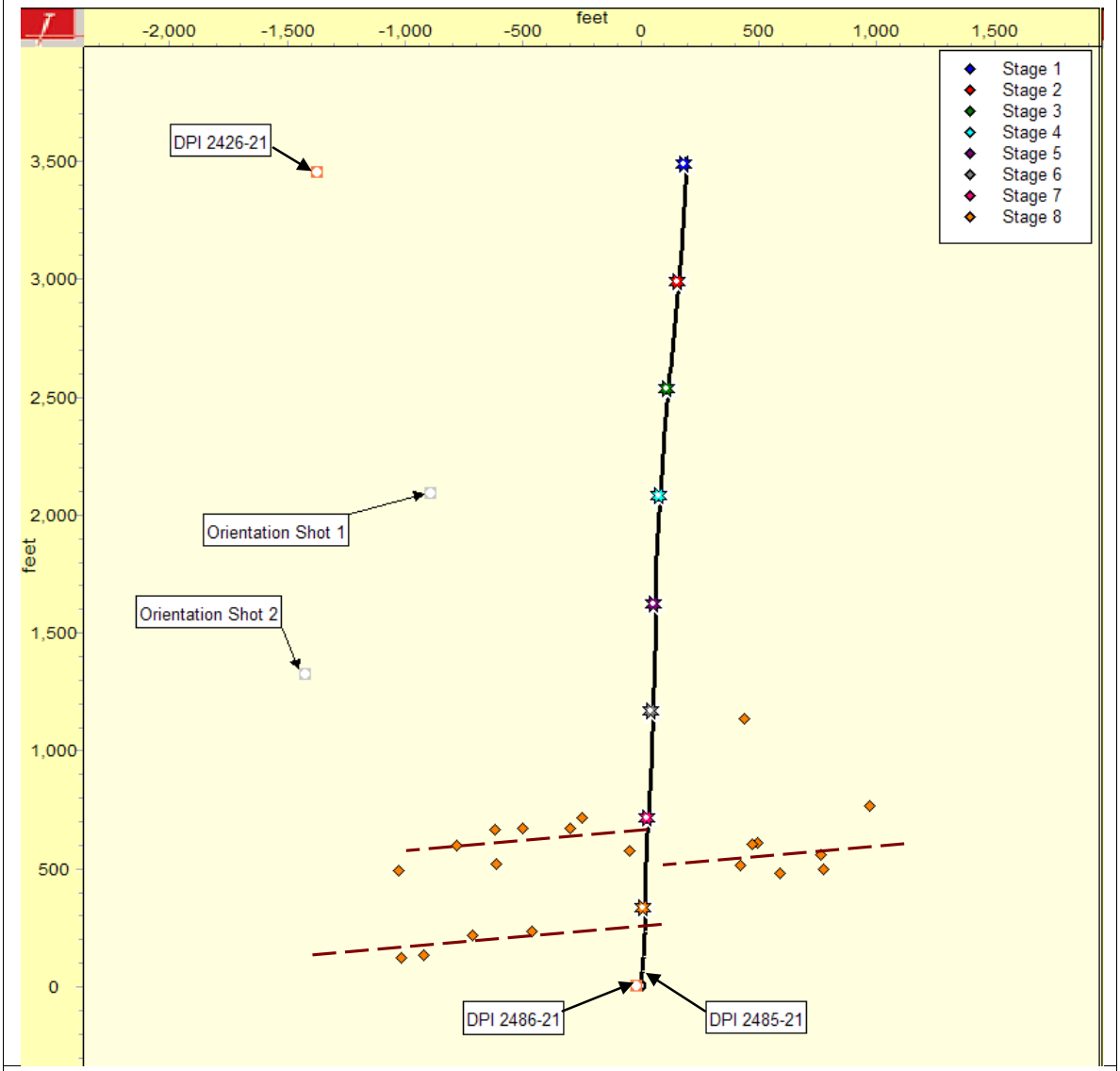


Figure 15. Map view, stage 8

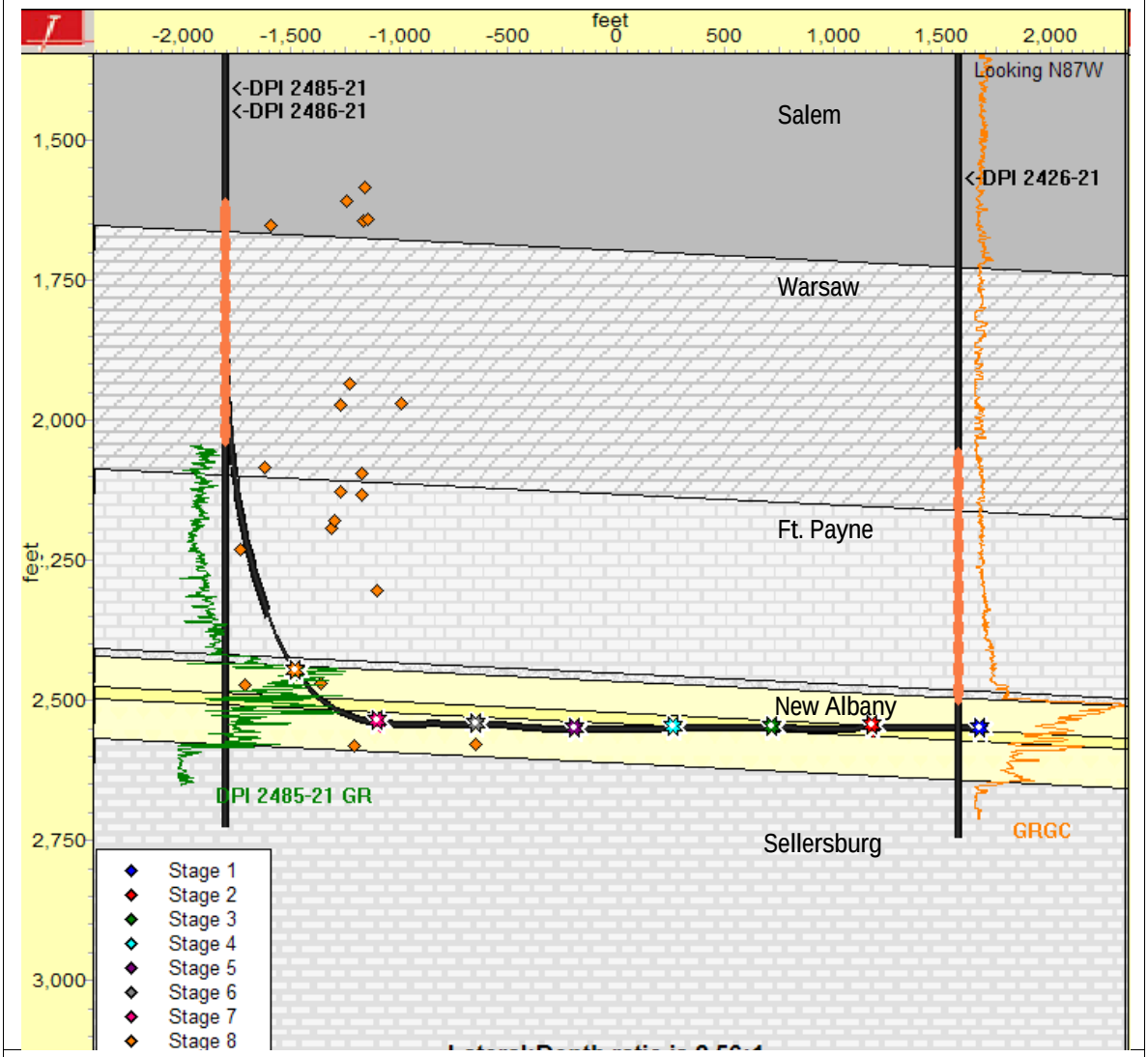


Figure 16. Lateral side view (orthogonal to lateral), stage 8

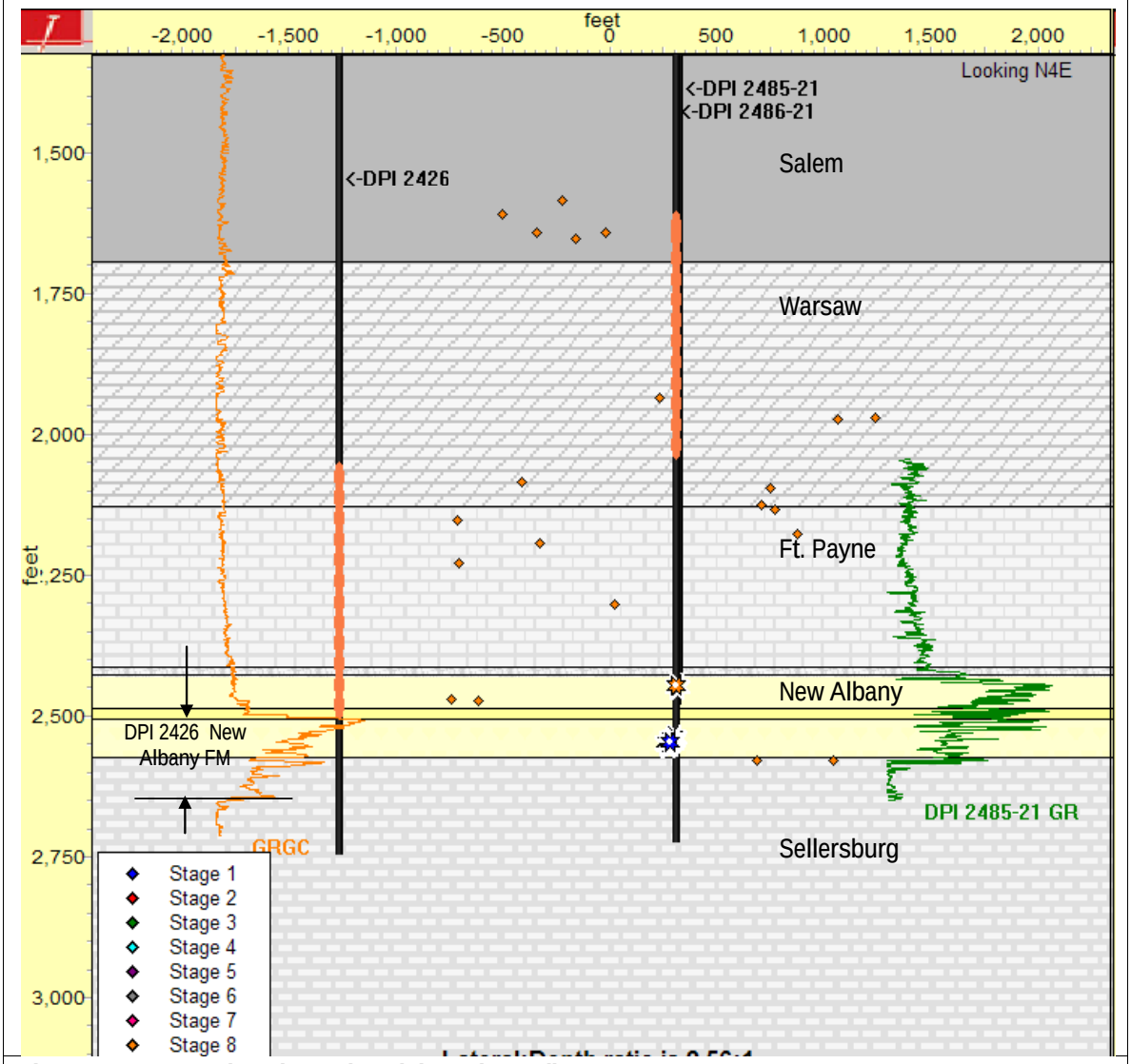


Figure 17. Lateral end-on view (along lateral), stage 8

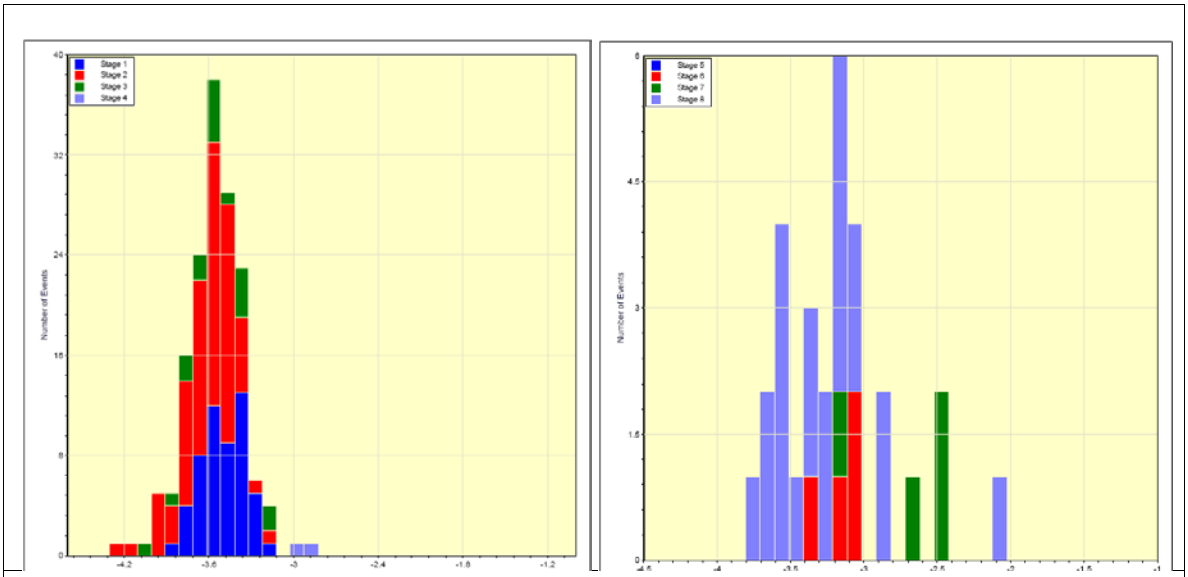


Figure 18. Comparison of event moment magnitudes (stages 1 to 4 on left, 5 to 8 on right)

In an openhole packers-style completion, often there are continuous pumping operations, with no shutdowns between stages as the fluid is diverted from one sleeve to the next. During this completion, there were two exceptions to this: First, stages 1 to 3 and 5 to 7 had planned shutdowns after sleeve opening and about 10 minutes of pumping at full rate, in order to record instantaneous shut-in pressures. Second, a planned shutdown of several hours after stage 4 was implemented in order to re-supply an additional 4 million scf of nitrogen and allow the geophones to be pulled from the first observation well and moved over and into to the intermediate string of the vertical [future horizontal] well located on the same surface pad as the treatment well. It became important, then, to define with some degree of precision, the start and stopping point of each stage. **Figure 19** and **Figure 20** clearly define the stage transition, which was called as the ball seated on the sleeve shoulder, exposing the annulus between packers for the subsequent stage to treating fluid(s).

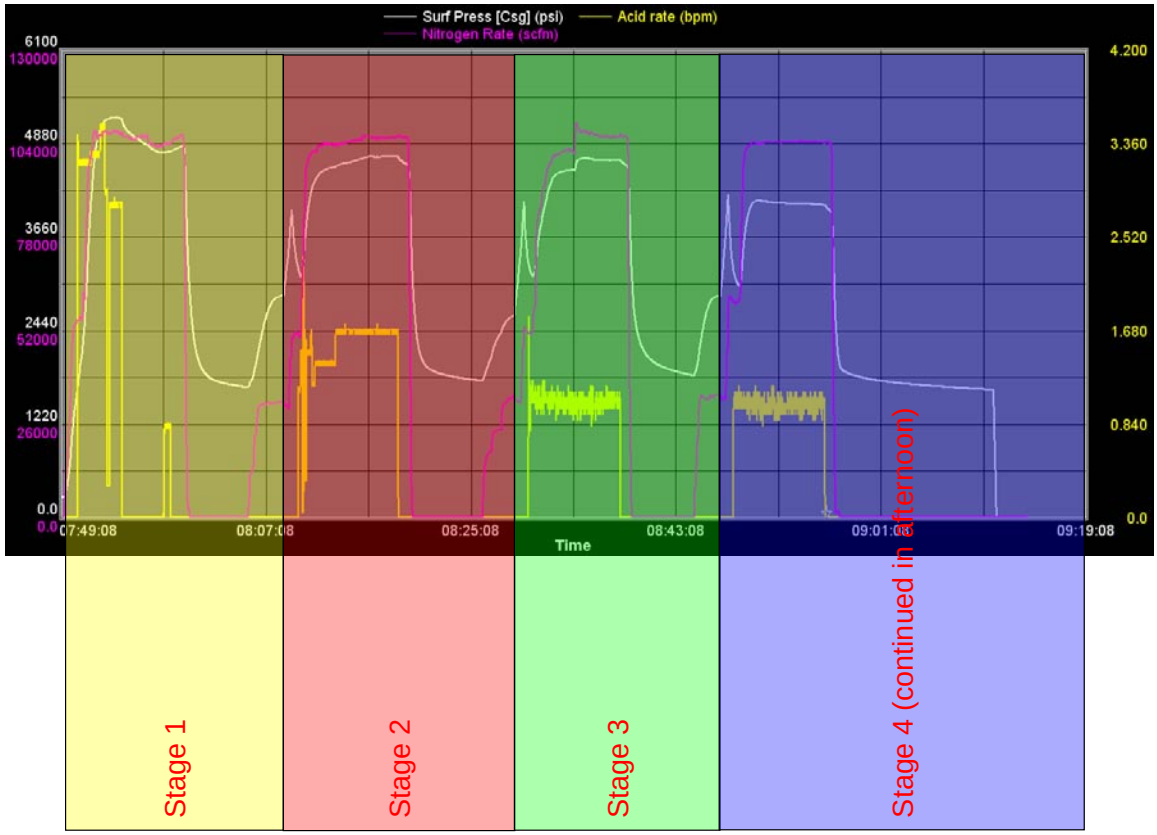


Figure 19. Stage definitions, stages 1 to 4

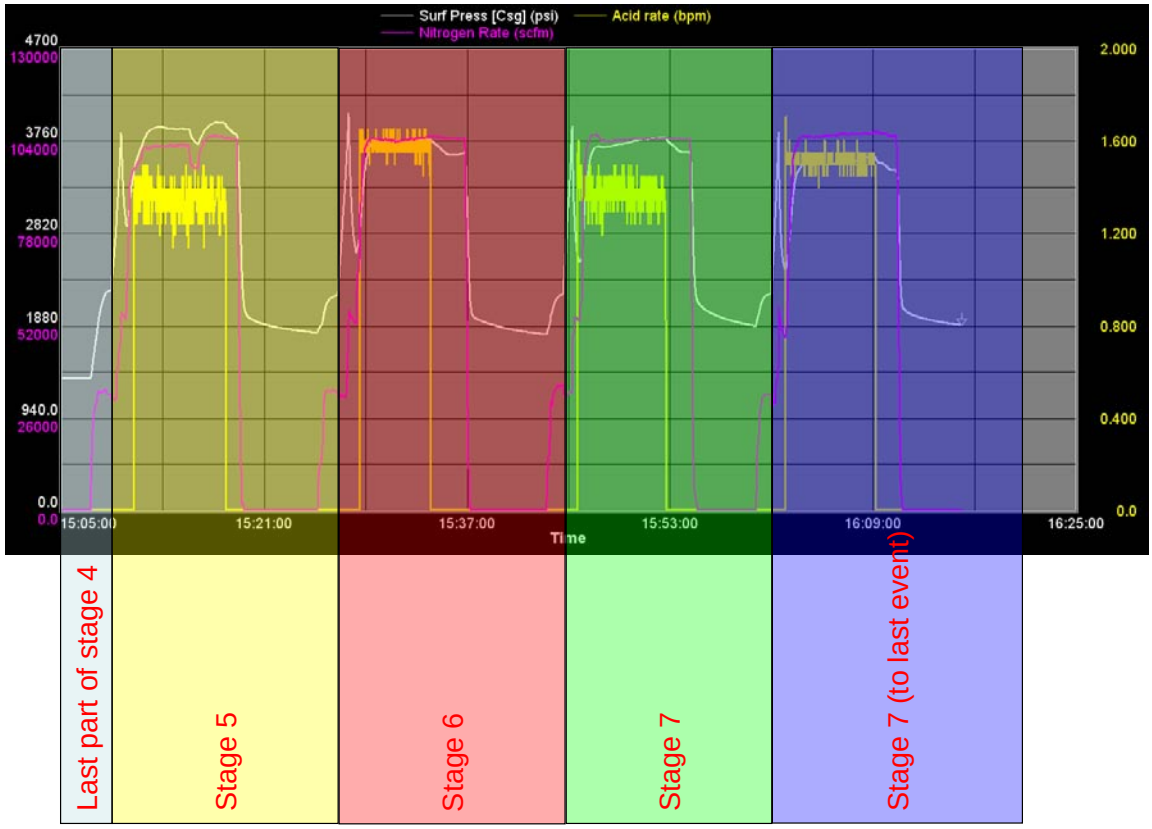


Figure 20. Stage definitions, stages 5 to 8

On 9/21/2009, a pre-job safety meeting was held, and the pumping service company primed and tested surface treating lines as per instructions. Surface treating pressures, acid and nitrogen rates are shown as functions of treating time in **Figure 21** and **Figure 22**. Treatment operations started at 07:48 hrs with an initial wellhead pressure of 276 psi. 1,500 gallons of 15% HCl was pumped at about 1.6 bpm as nitrogen was ramped up to about 105,000 scf/min. The recorded acid rates as depicted for stage 1 in **Figure 21** were not accurate due to an electronic problem, but confidence in the 1.6 bpm estimate was high due to reports from the pump operator. The acid was flushed, and a total of 1,001,884 scf was pumped before shutting down for an ISIP, then seating the ball on the first sleeve shoulder.

Stages 2, 3 and 4 were pumped in a similar manner, with treating parameters as recorded in **Table 1** At 08:54 hrs, operations were halted for the tool move and nitrogen re-supply. After microseismic tools had been clamped into the new observation wellbore7, a surface dynamite shot was fired in order to orient the geophones.

At 14:50 hrs, pumping resumed and a ball was dropped and seated against the stage 5 sleeve shoulder. Stages 6, 7 and 8 were pumped in a similar manner, with treating parameters as recorded in **Table 2**. At 16:10 hrs, operations were completed and load recovery began approximately one-half hour later.

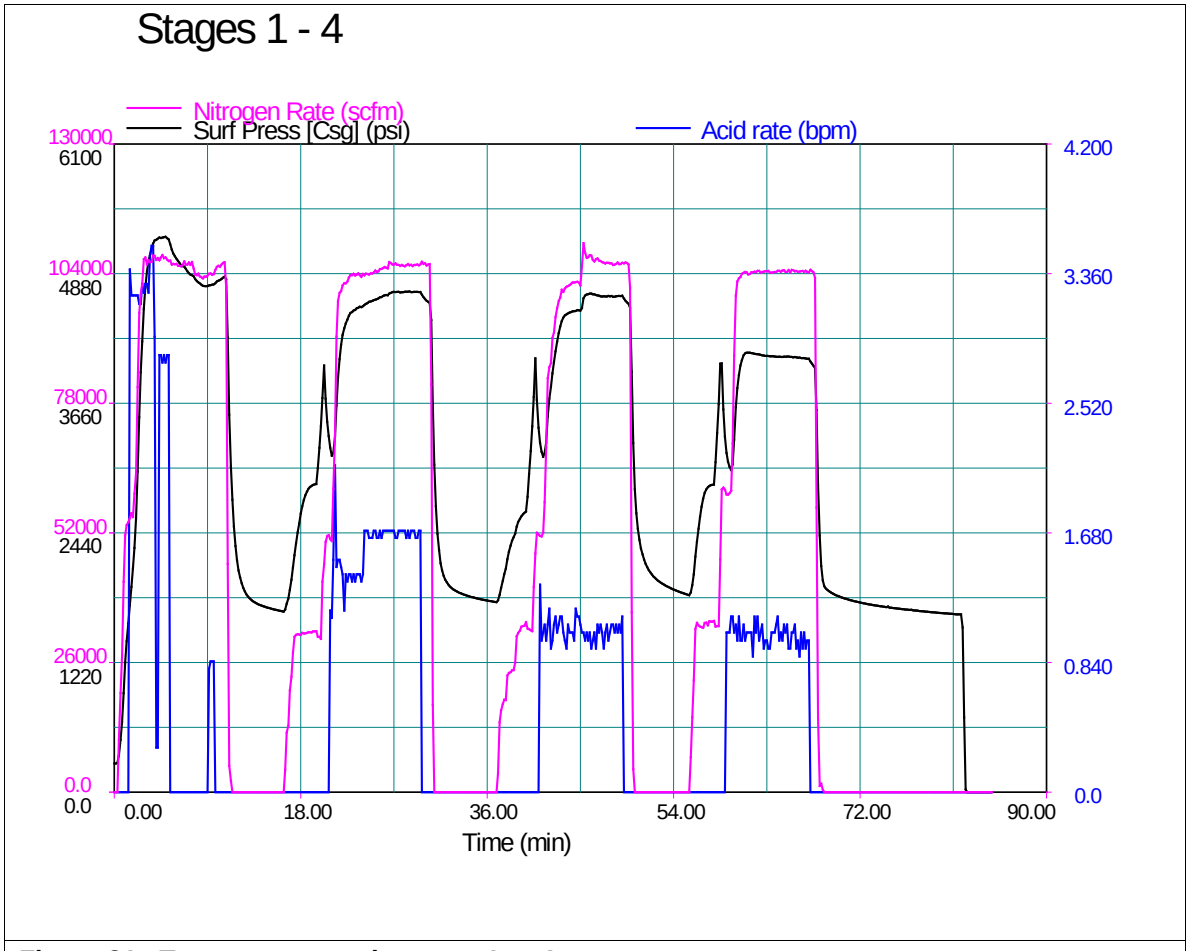


Figure 21. Treatment record, stages 1 to 4

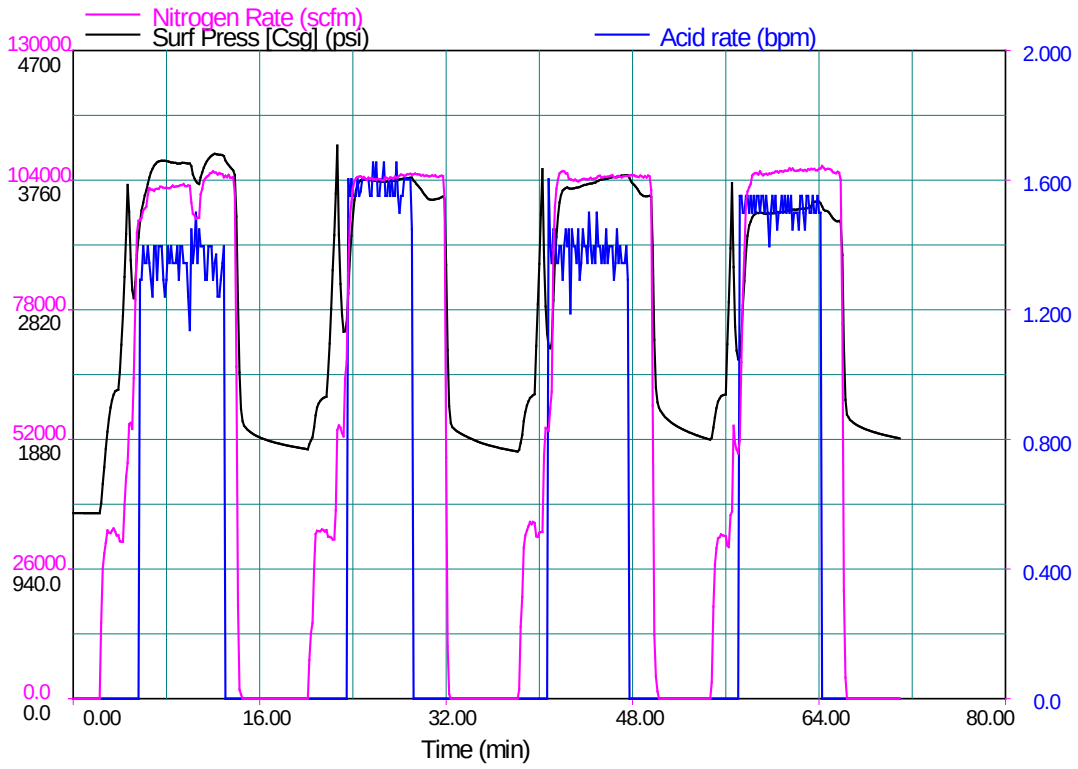


Figure 22. Treatment record, stages 5 to 8

4.3 Quality Assurance, Christian County Microseismic

The general setup is portrayed in **Figure 23** and **Figure 24**. The key areas for quality assurance in analysis are microseismic tool position and accuracy of event location. These two areas are addressed in this section.

The toolstring in the first observation well placed the bottom of the string at 2,414 ft, and is shown in **Figure 25**. Placement of the array was above the New Albany Shale. The vertical distance between the bottom tool and the furthest perforation was 122 ft. The approximate vertical distance between the bottom tool and furthest event was less than 100 ft. The estimated horizontal distance between the bottom tool and the furthest recordable event was 1,850 ft.

The second area of quality assurance is the location of orienting events with respect to the wellbore. Two surface dynamite shots (4 lb in 20-ft backfilled ratholes) were utilized to orient the toolstring in each observation well. The velocity model used in the determination of the microseismic events placement for the toeward stages is shown in **Figure 26**, and heelward stages in **Figure 27**. This model was initially developed with the dipole sonic information off an observation well, and then correlated to GR depths in the three wellbores in question.

Figure 28 shows the event location uncertainty (depth, azimuth and radius errors) for the toe-most stages. In general, the location accuracy is moderate to high. The average depth (elevation) error is less than 25 ft, the average azimuth error is about 50 ft and the average radius (tool-to-event distance) error is less than 25 ft. **Figure 29** is the location error for stages 5 to 8. Further information on this subject matter may be found in the included Quality Control report.

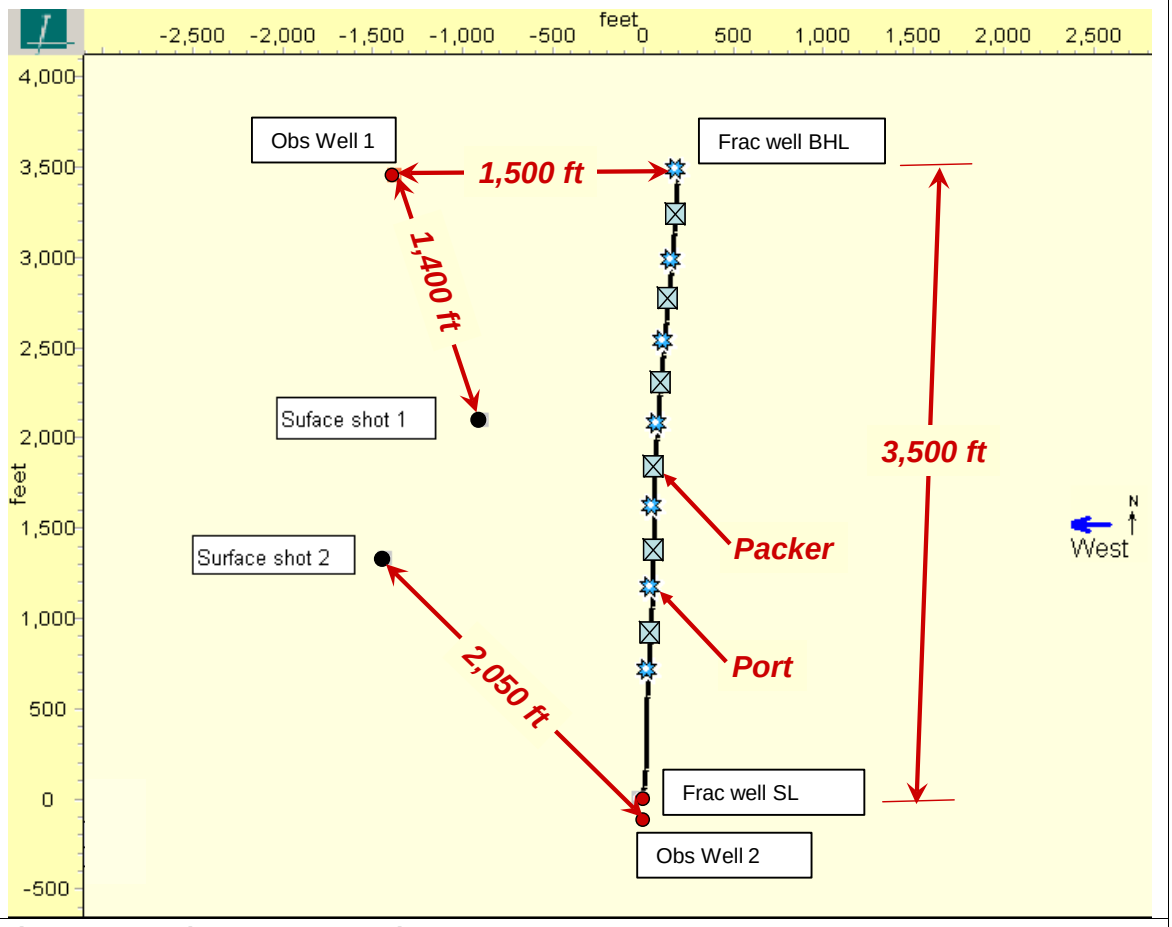


Figure 23. Project setup map view

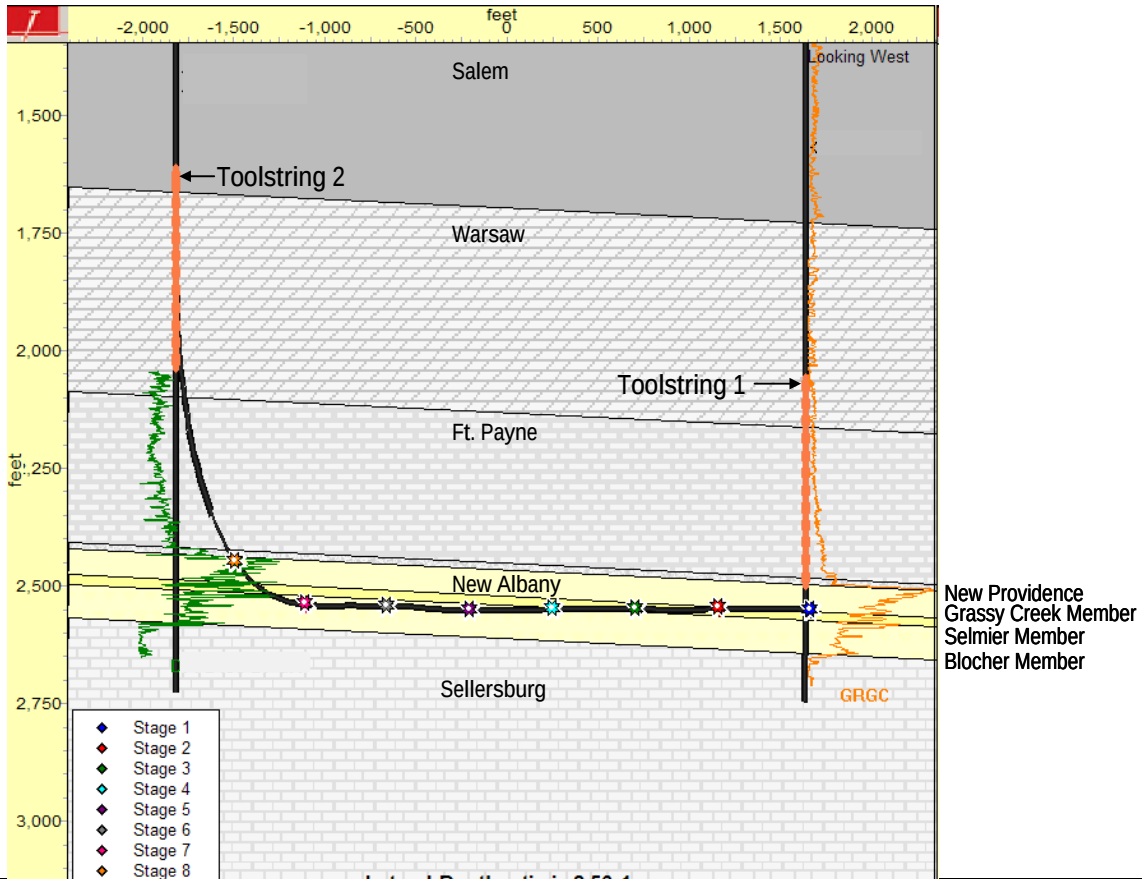


Figure 24. Project setup side view

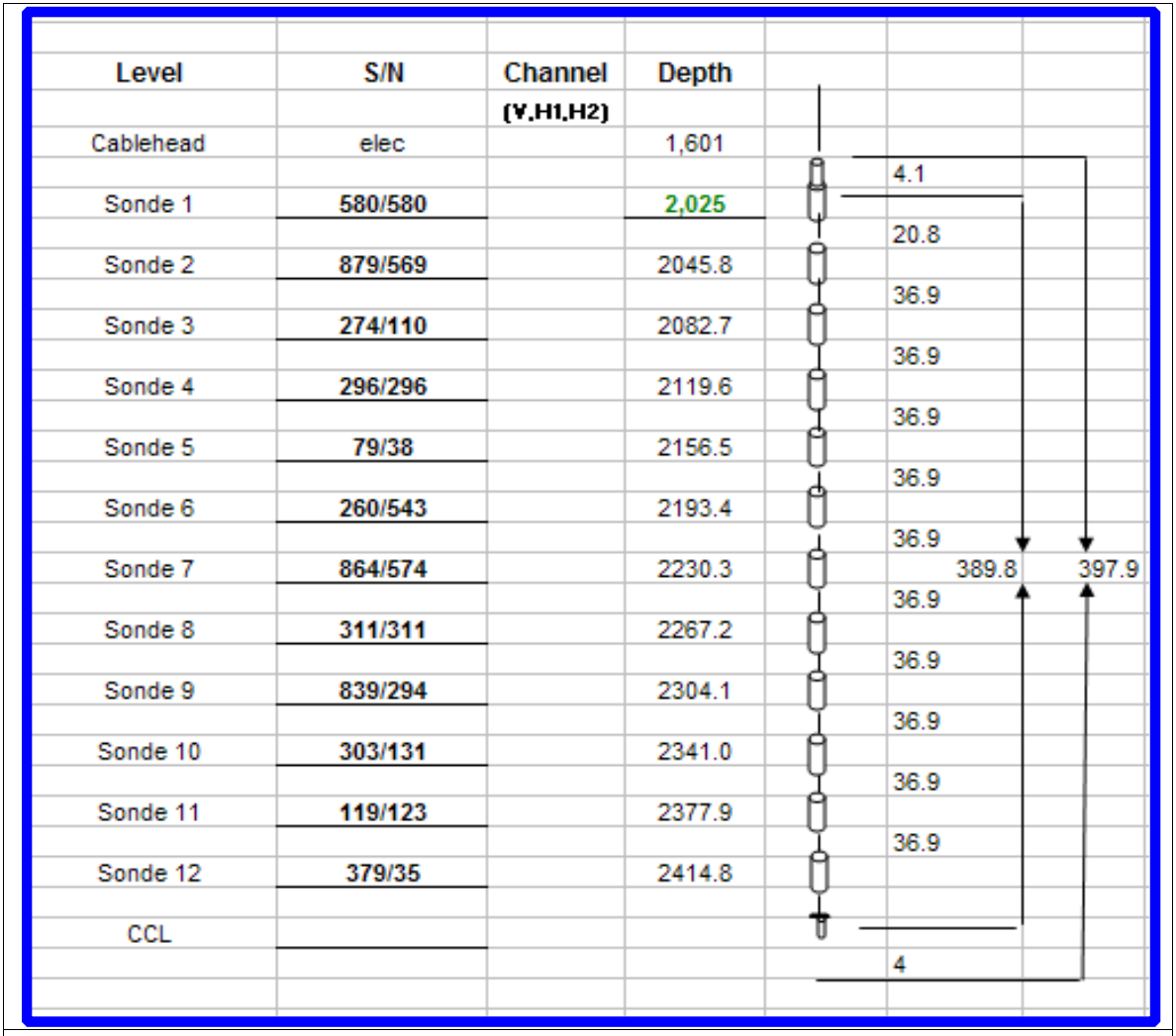


Figure 25. Toolstring diagram, first observation well

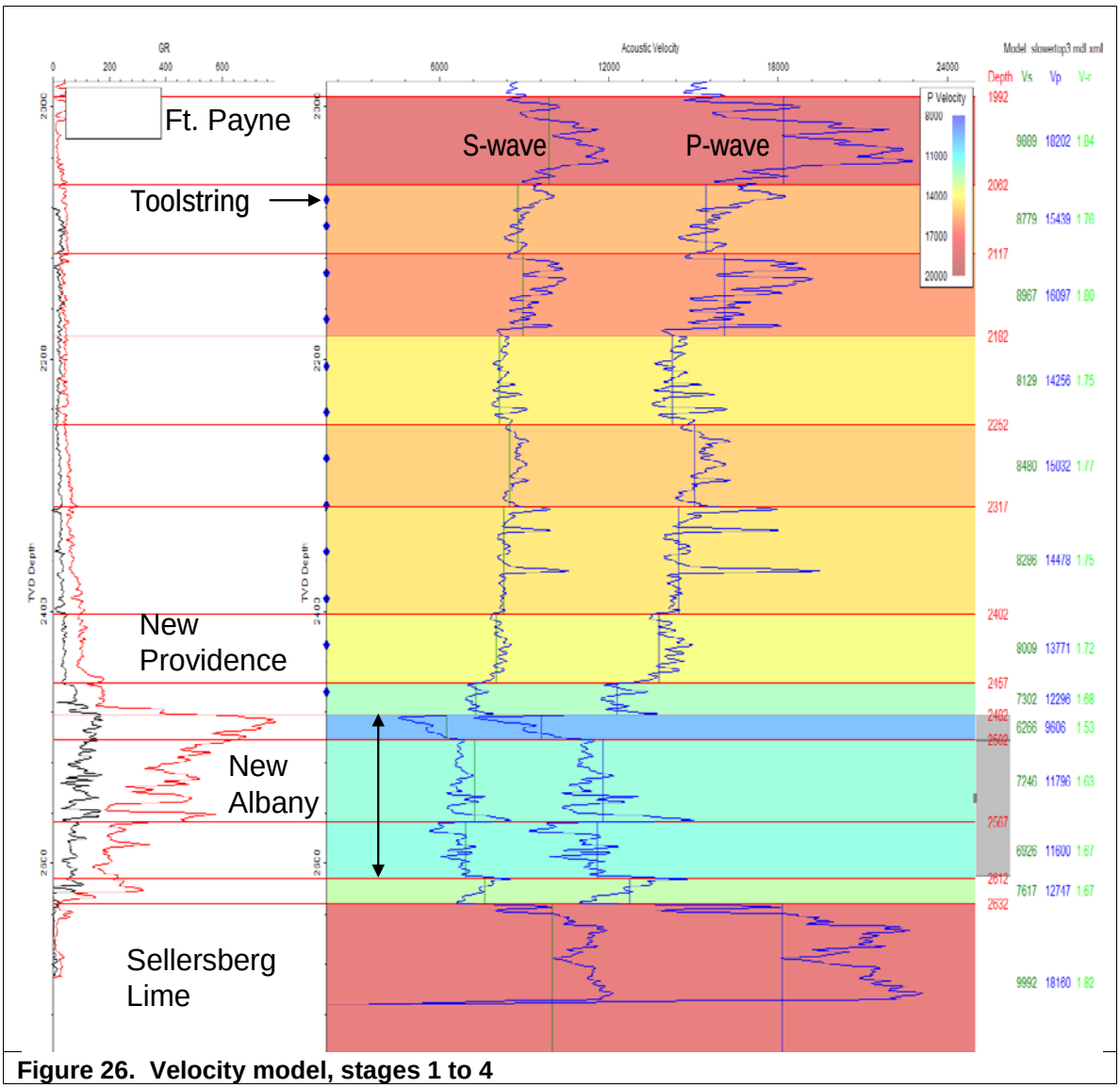


Figure 26. Velocity model, stages 1 to 4

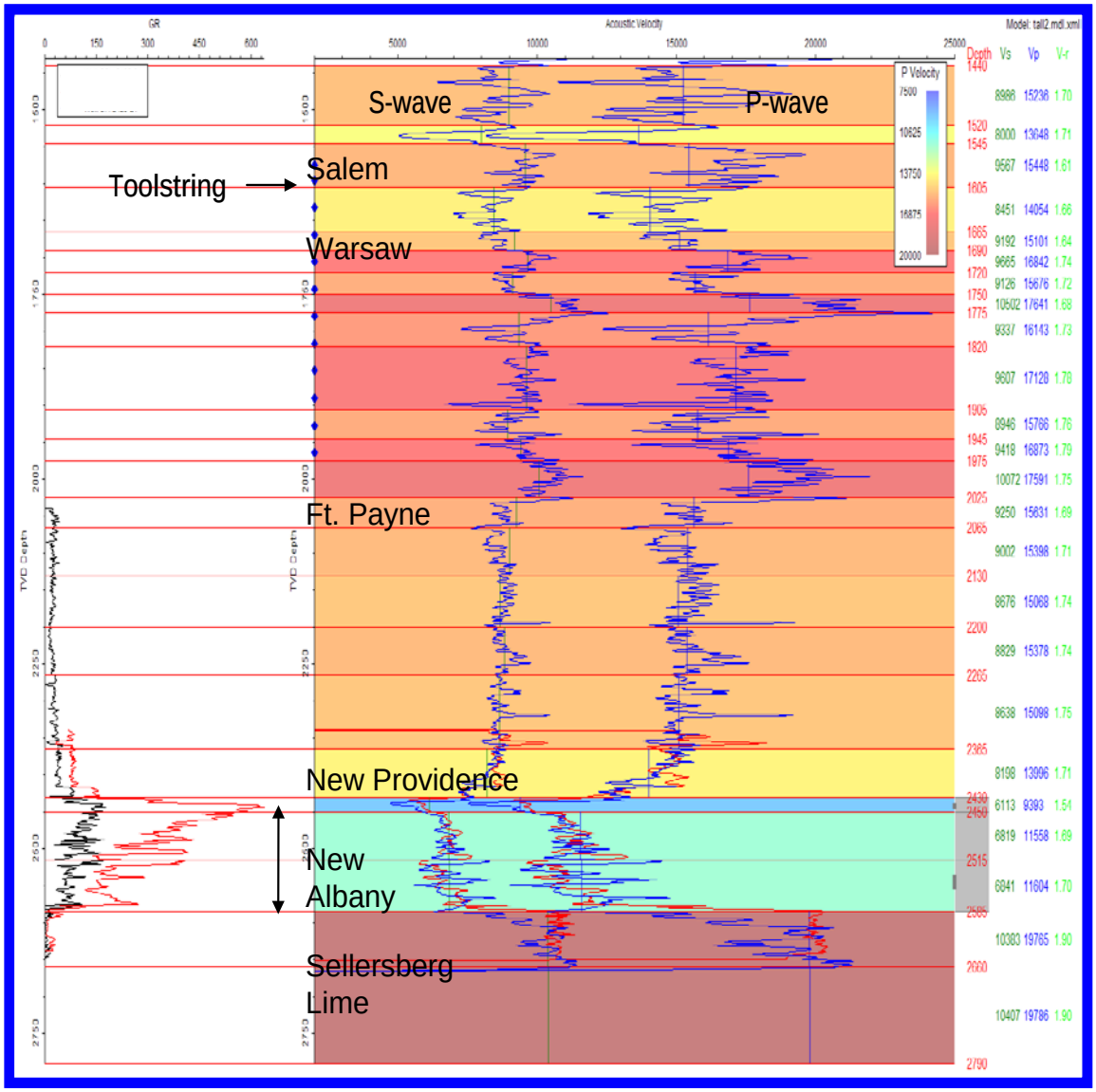


Figure 27. Velocity model, stages 5 to 8

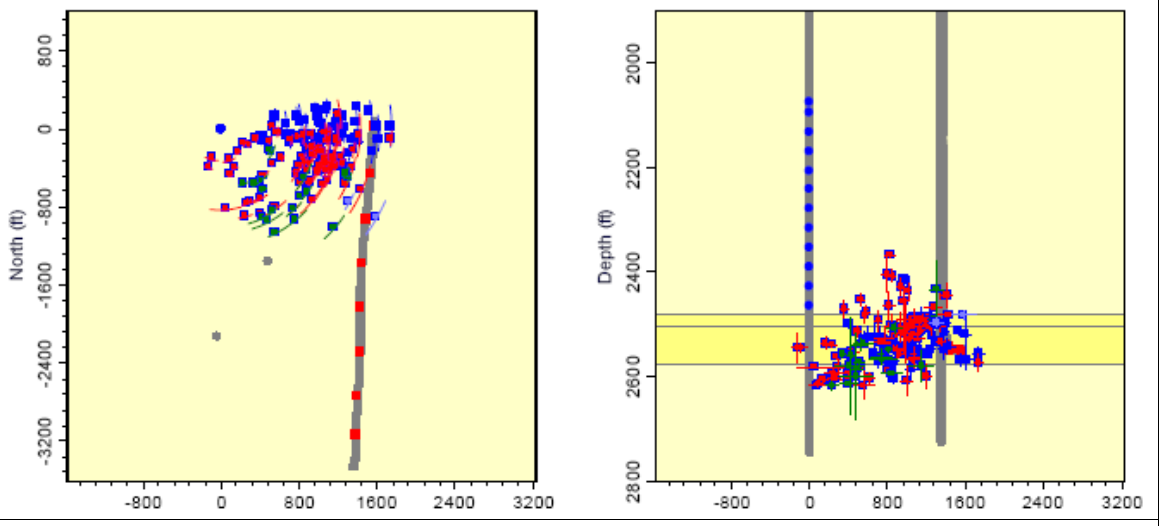


Figure 28. Event location uncertainty, stages 1 to 4

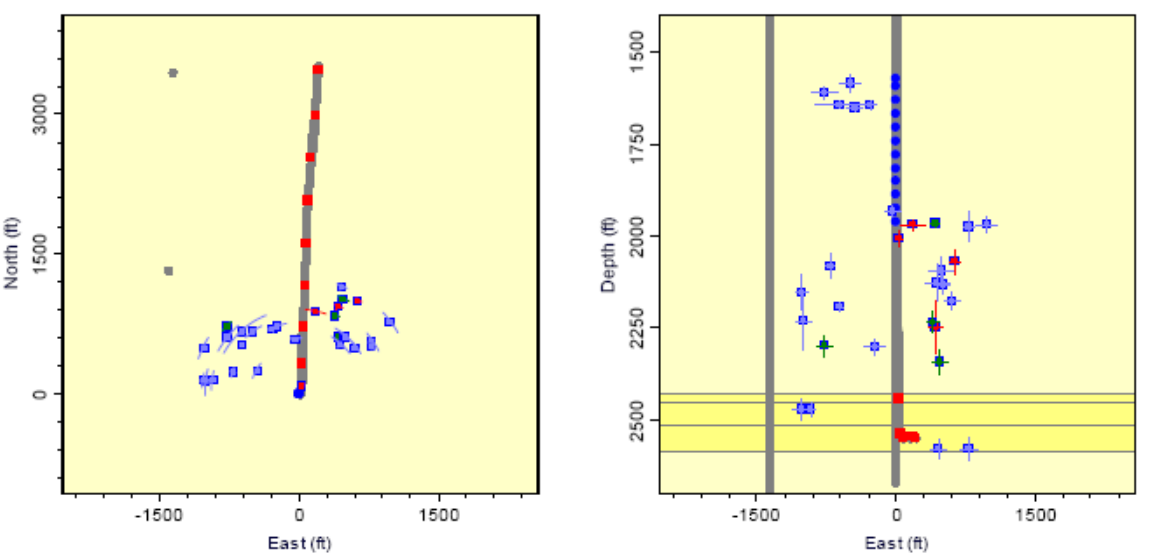


Figure 29. Event location uncertainty, stages 5 to 8

5. Discussion of McLean County Microseismic

Two parallel wells in McLean County, KY were drilled transverse (perpendicular to the expected fracture azimuth) in the objective New Albany Shale Formation and completed with openhole packers isolating individual portions of each wellbore. The pair of wells was stimulated for gas production using 18 hydraulic fracture treatment stages in a "simulfrac" process, whereby nine adjacent stages were sequentially pumped in each wellbore with two separate fracturing fleets at approximately the same time.

A dedicated vertical observation well (the Observation well) was drilled between the two laterals, and the geophone array was placed in such a manner as to straddle the elevation of the expected fractures.

The objectives of the fracture mapping service were to:

- Determine fracture pay zone coverage along the horizontal wellbore
- Measure fracture geometry (height and length) and azimuth
- Determine the relative degree of induced fracture complexity and fracture network width
- Provide immediate information that could be used for future well placement and infill drilling strategies
- Observe the interaction between fractures initiating in different wellbores at the same time, and potentially validate the simulfrac process

Results of the monitoring effort are summarized in **Table 3** through **Table 7**, and in **Figure 30**, **Figure 31**, and **Figure 32**.

The mapping exercise led to a number of conclusions. During most stages, propagation away from both wellbores was extremely rapid (full extent of length observed only a few minutes after individual stage initiation), leading to the supposition that pre-existing open natural fractures were connected to the wellbore. There was very little activity observed during the first three stages to the southwest of the SW treatment well, or to the northeast of the NE treatment well laterals. Observation wellbore bias was likely a major factor, implying that the fractures initiated during these three stages were actually symmetric in nature. The first three stages were contained within the New Albany shale and fracture half-lengths were approximately 800 ft. These same first three stages on each wellbore likely stimulated the New Albany Shale adequately, but later stages may have had substantial interaction with non-productive reservoir above, and with the potentially wet Devonian carbonate underlying the New Albany shale. The primary fracture network azimuth was N60ºE, and a secondary azimuth of approximately N38ºE was noted.

Previous fracture mapping in other shales such as the Barnett has shown that well performance is directly related to the Stimulated Reservoir Volume (SRV). Although there have not been enough projects in the New Albany Shale play to clearly establish an association between SRV and production, it is possible or even probable that some type of link does exist. The SRV for the mapped fracture stages for this project was not calculated. It is likely that the 1st three stages produced values for SRV that might be useful, but only if the apparent observation wellbore bias was known to be present with certainty, and symmetry of fractures was assumed. Subsequent stages showed significant interaction with either open natural fracturing, or pre-stressed geological features, and therefore would not be appropriate for analysis more suited to wide fracture networks.

Microseismic event moment magnitudes (Mw) ranged from -4.7 to -1.0 Mw, and the average was -3.1 Mw. Microseismic events of average magnitude were imaged up to 1909 ft away from the toolstring. The

average-maximum microseismic event was -1.9 Mw, and these events were imaged up to 1,653ft away from the toolstring. Azimuthal location uncertainties ranged from 6 ft to 212 ft, and the average was 49 ft. Distance location uncertainties ranged from 4 ft to 76 ft, and the average was 17 ft. Depth location uncertainties ranged from 2 ft to 161 ft, and the average was 13 ft. There were additional intangible uncertainties associated with event locations that were not included in the location error calculations, and these are discussed further elsewhere in this report.

Table 3. Job Summary

County:	McLean	**State/Province:**	Kentucky
Services Provided:	☒ Fracture Microseismic	Downhole Tilt Mapping: ☐ TWT ☐ OWT	☐ Surface Tilt Mapping
	☐ Reservoir Monitoring	Consulting Services: ☐ Engineering ☐ Supv. & QC	

	Units	**Stage 1 (SW treatment well)**	**Stage 2 (SW treatment well)**	**Stage 3 (SW treatment well)**	**Stage 4 (SW treatment well)**
Treatment Date:		7/14/10	7/14/10	7/14/10	7/14/10
Formation:		New Albany Shale	New Albany Shale	New Albany Shale	New Albany Shale
Port Depth (MD):	ft	6,241	5,955	5,643	5,383
Treatment Volumes:					
Nitrogen	scf	2,339,042	2,645,170	2,747,095	2,600,312
Proppant:					
30/80 LiteProp	lbm	10,000	8,814	10,000	10,000
Rates & Pressures:					
Average Rate	bpm	53.4	51.6	54.1	53.5
Average WHTP	psi	4,238	4,621	4,220	4,298
Diagnostic ISIP	psi	N/A	N/A	N/A	N/A
Final ISIP	psi	2,502	2,579	2,668	2,990
Results & Analysis:					
Geometry:					
Fracture Half-length (symmetry)	ft	810	810	810	805
Fracture Network Height	ft	245	140	250	270
Fracture Network Width	ft	615	610	630	600
Fracture Azimuth (Primary)		N60ºE	N60ºE	N60ºE	N60ºE
Fracture Azimuth (Secondary)		N38ºE	Unknown	Unknown	N38ºE
Stimulated Reservoir Volume	ft^3	Not Applicable			
Fracture Dip		No	No	No	No
Asymmetry		Unknown	Unknown	Unknown	Unknown
Complexity		Yes	Yes	Yes	Yes

Table 4. Job Summary

	Units	Stage 5 (SW treatment well)	Stage 6 (SW treatment well)	Stage 7 (SW treatment well)	Stage 8 (SW treatment well)
Treatment Date:		7/15/10	7/15/10	7/16/10	7/16/10
Formation:		New Albany Shale	New Albany Shale	New Albany Shale	New Albany Shale
Port Depth (MD):	ft	5,097	4,773	4,487	4,202
Treatment Volumes:					
Nitrogen	scf	2,528,014	2,680,362	2,905,225	2,661,629
Proppant:					
30/80 LiteProp	lbm	10,000	10,000	10,000	10,000
Rates & Pressures:					
Average Rate	bpm	51.9	53.1	56.1	53.1
Average WHTP	psi	4,452	4,339	4,001	4,151
Diagnostic ISIP	psi	N/A	N/A	N/A	N/A
Final ISIP	psi	3,068	2,829	4,868	5,021
Results & Analysis:					
Geometry:					
Fracture Half-length (symmetry)	ft	810	810	810	1,240
Fracture Network Height	ft	305	415	590	785
Fracture Network Width	ft	525	470	650	800
Fracture Azimuth (Primary)		N60ºE	N60ºE	N60ºE	N60ºE
Fracture Azimuth (Secondary)		N38ºE	N38ºE	Unknown	N38ºE
Stimulated Reservoir Volume	ft^3	Not Applicable			
Fracture Dip		No	No	No	No
Asymmetry		Unknown	Unknown	Unknown	Unknown
Complexity		Yes	Yes	Yes	Yes

Table 5. Job Summary

	Units	Stage 9 (SW treatment well)	Stage 1 (NE treatment well)	Stage 2 (NE treatment well)	Stage 3 (NE treatment well)
Treatment Date:		7/16/10	7/14/10	7/14/10	7/14/10
Formation:		New Albany Shale	New Albany Shale	New Albany Shale	New Albany Shale
Port Depth (MD):	ft	3,915	6,539	6,213	5,933
Treatment Volumes:					
Nitrogen	scf	2,570,835	2,577,535	2,415,572	2,776,187
Proppant:					
30/80 LiteProp	lbm	10,000	10,000	10,000	10,000
Rates & Pressures:					
Average Rate (liquid equiv)	bpm	57	50	50.1	52
Average WHTP	psi	3,810	4,735	4,867	4,634
Diagnostic ISIP	psi	N/A	N/A	N/A	N/A
Final ISIP	psi	2,835	3,055	3,036	3,096
Results & Analysis:					
Geometry:					
Fracture Half-length (symmetry)	ft	1,180	810	810	810
Fracture Network Height	ft	575	245	140	250
Fracture Network Width	ft	505	615	610	630
Fracture Azimuth (Primary)		N60ºE	N60ºE	N60ºE	N60ºE
Fracture Azimuth (Secondary)		N38ºE	N38ºE	Unknown	Unknown
Stimulated Reservoir Volume	ft^3	Not Applicable			
Fracture Dip		No	No	No	No
Asymmetry		Unknown	Unknown	Unknown	Unknown
Complexity		Yes	Yes	Yes	Yes

Table 6. Job Summary

	Units	Stage 4 (NE treatment well)	Stage 5 (NE treatment well)	Stage 6 (NE treatment well)	Stage 7 (NE treatment well)
Treatment Date:		7/14/10	7/15/10	7/15/10	7/16/10
Formation:		New Albany Shale	New Albany Shale	New Albany Shale	New Albany Shale
Port Depth (MD):	ft	5,609	5,281	4,954	4,663
Treatment Volumes:					
Nitrogen	scf	2,654,132	2,530,378	1,313,375	2,968,195
Proppant:					
30/80 LiteProp	lbm	10,000	10,000	2,000	10,000
Rates & Pressures:					
Average Rate	bpm	52	53.5	53	57.5
Average WHTP	psi	4,152	4,355	5,941	4,038
Diagnostic ISIP	psi	N/A	N/A	N/A	N/A
Final ISIP	psi	2,865	3,330	2,829	2,289
Results & Analysis:					
Geometry:					
Fracture Half-length (symmetry)	ft	810	810	810	810
Fracture Network Height	ft	270	305	415	590
Fracture Network Width	ft	600	525	470	650
Fracture Azimuth (Primary)		N60ºE	N60ºE	N60ºE	N60ºE
Fracture Azimuth (Secondary)		N38ºE	N38ºE	N38ºE	Unknown
Stimulated Reservoir Volume	ft^3	Not applicable			
Fracture Dip		No	No	No	No
Asymmetry		Unknown	Unknown	Unknown	Unknown
Complexity		Yes	Yes	Yes	Yes

Table 7. Job Summary

	Units	Stage 8 (NE treatment well)	Stage 9 (NE treatment well)
Treatment Date:		7/16/10	7/16/10
Formation:		New Albany Shale	New Albany Shale
Port Depth (MD):	ft	4,339	4,052
Treatment Volumes:			
Nitrogen	scf	2,688,725	2,561,476
Proppant:			
30/80 LiteProp	lbm	10,000	10,000
Rates & Pressures:			
Average Rate	bpm	61	56
Average WHTP	psi	3,649	4,044
Diagnostic ISIP	psi	N/A	N/A
Final ISIP	psi	2,880	2,668
Results & Analysis:			
Geometry:			
Fracture Half-length (symmetry)	ft	810	1,010
Fracture Network Height	ft	785	575
Fracture Network Width	ft	800	505
Fracture Azimuth (Primary)		N60ºE	N60ºE
Fracture Azimuth (Secondary)		N38ºE	N38ºE
Stimulated Reservoir Volume	ft^3	Not Applicable	
Fracture Dip		No	No
Asymmetry		Unknown	Unknown
Complexity		Yes	Yes

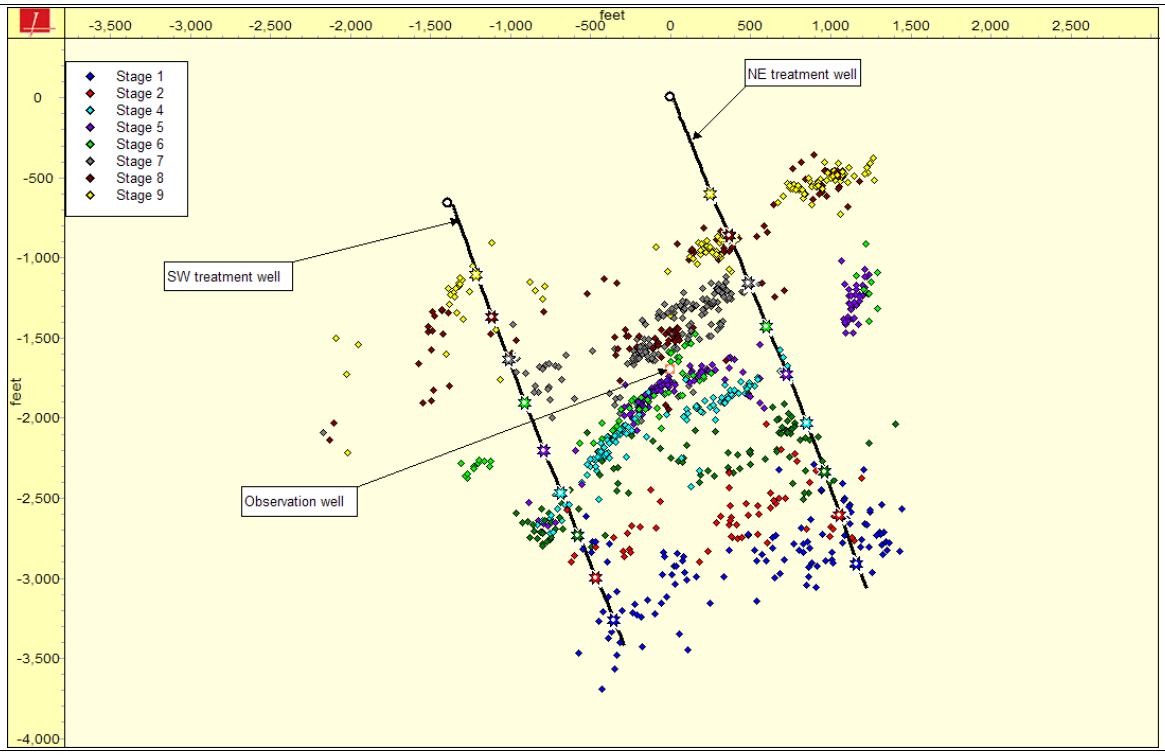


Figure 30. Map view, all stages

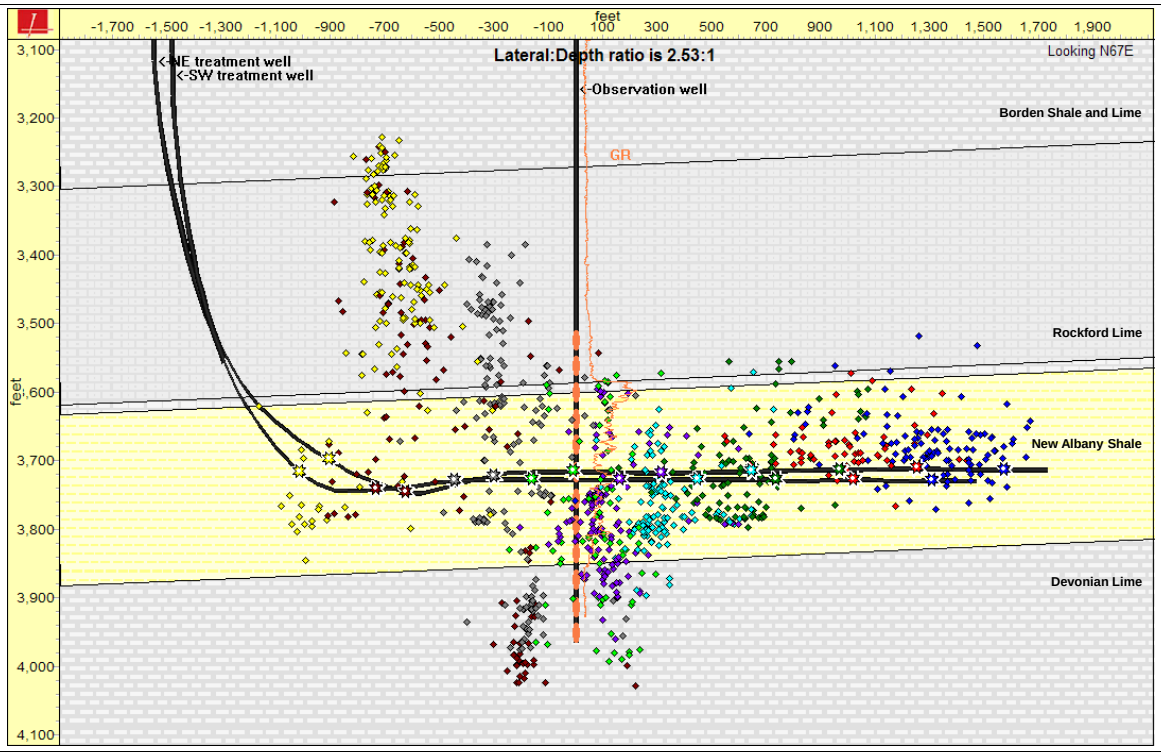


Figure 31. Lateral side view (orthogonal to lateral), all stages

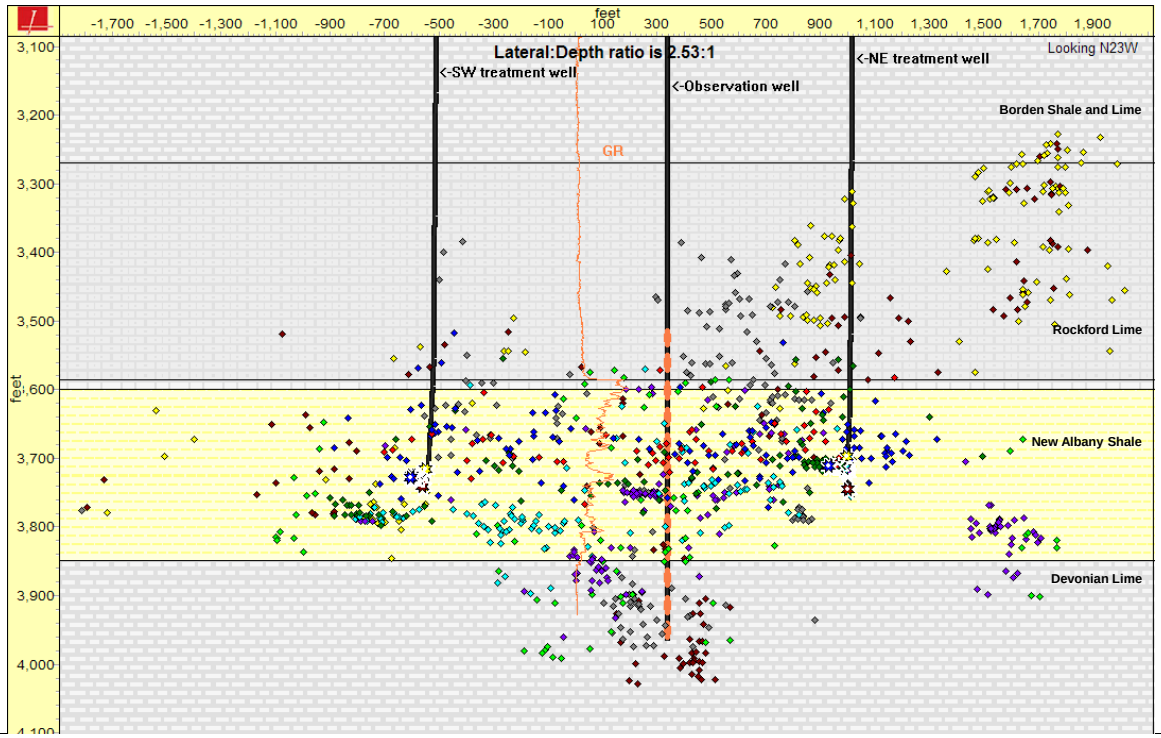


Figure 32. Lateral end-on view (along lateral), all stages

5.1 Fracture Mapping Discussion

During the planning stages of the completion of the two parallel horizontal producers, it was decided to locate and drill a single dedicated vertical observation well situated between the two laterals in order to most effectively map the proposed simulfrac. **Figure 88** shows the relative positioning of the three wells with respect to each other. The two laterals were completed in an un-cemented manner with open hole packers and nine ports each.

The completion involved pumping nine stages simultaneously in each wellbore, starting at the toe of each lateral, and moving toward the heel. The fracturing fluid was a 92 – 99 Downhole Slurry Quality (DHSQ) nitrogen foam. A 30/80-mesh ultra-lightweight proppant (a thermoplastic bead with a specific gravity of ±1.05) was slurried in a KCL water solution, and batch-pumped at several concentrations ranging from 0.05 lb/gal to 0.25 lb/gallon. The treatments had inter-stage periods of "no pumping" that were utilized to batch-mix additional proppant and re-load nitrogen.

The geophone array was placed into the observation wellbore, and clamped into place straddling the New Albany Shale, with 16 tools in 12 positions as per **Figure 89** and **Figure 91**. There were no portions of the wellbore that had sufficient connection with the formation (via cementing) to perform stringshots for geophone orientation or velocity model calibration, so a Vibroseis unit was utilized to generate a continuous energy source, which was correlated in such a manner as to convert the extended source signal into an impulse, and finally orient tools. This exercise was performed five times in five different locations, as shown in **Figure 90**. Unfortunately, there was not a deviation survey available on the observation well, and therefore some unknown degree of intangible error was introduced into event positioning. Since this well was just under 4,000 ft deep, it is likely that a worst-case offset would be

bottom-hole location of a radius of about 100 ft off the surface location, or a diameter of 200 ft off the surface location.

Mapping results for all stages are summarized in **Table 3** through **Table 7**, and in **Figure 30**, **Figure 31**, and **Figure 32**. Early stages (1 through 3) demonstrated fractures initiating near the two wellbores, and proceeding outward, in directions approximately transverse to the individual laterals as the treatments progressed. Subsequent stages (4 through 9) generated "full" fracture lengths very early in the pumping operations, suggesting that open natural fractures may have been encountered during these stages. Monitoring of events prior to initiation of pumping some stages resulted in the mapping of some events that might have been associated with the previous stage(s). **Figure 33** and **Figure 34** show all events colored by relative time in each stage.

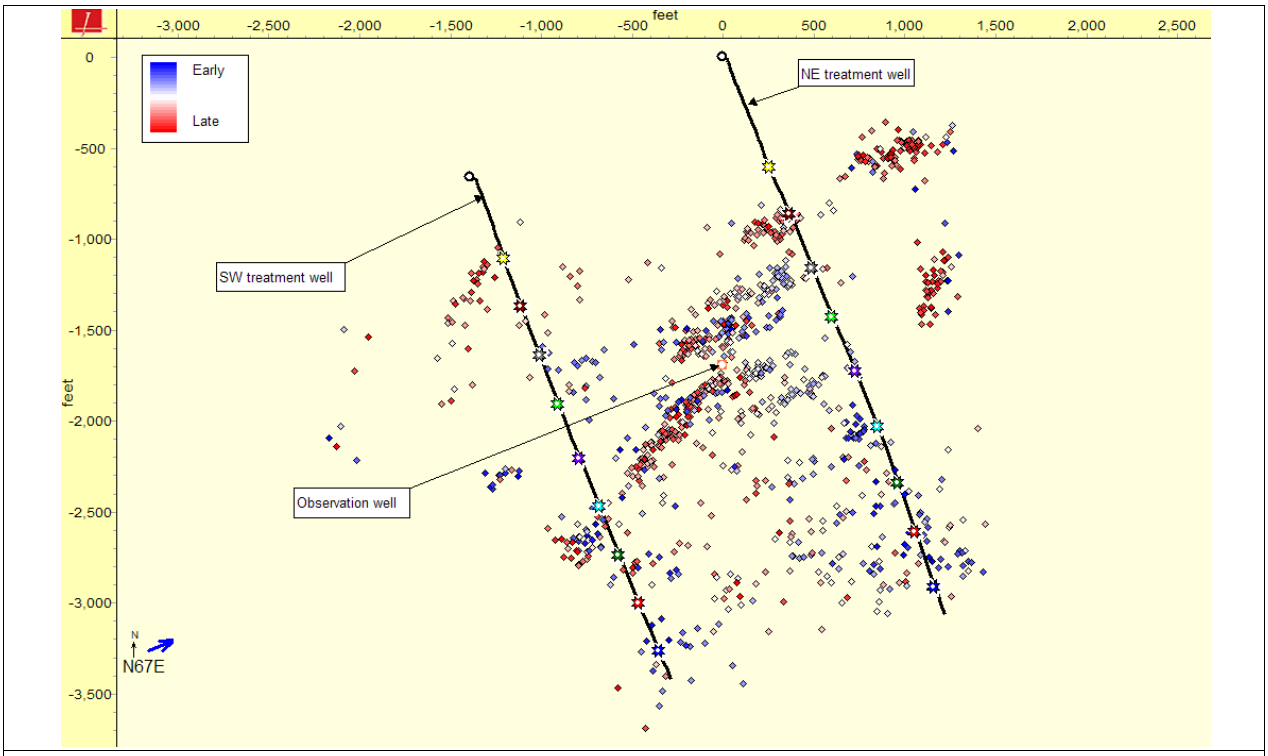


Figure 33. Events colored by relative time during individual stages, map view

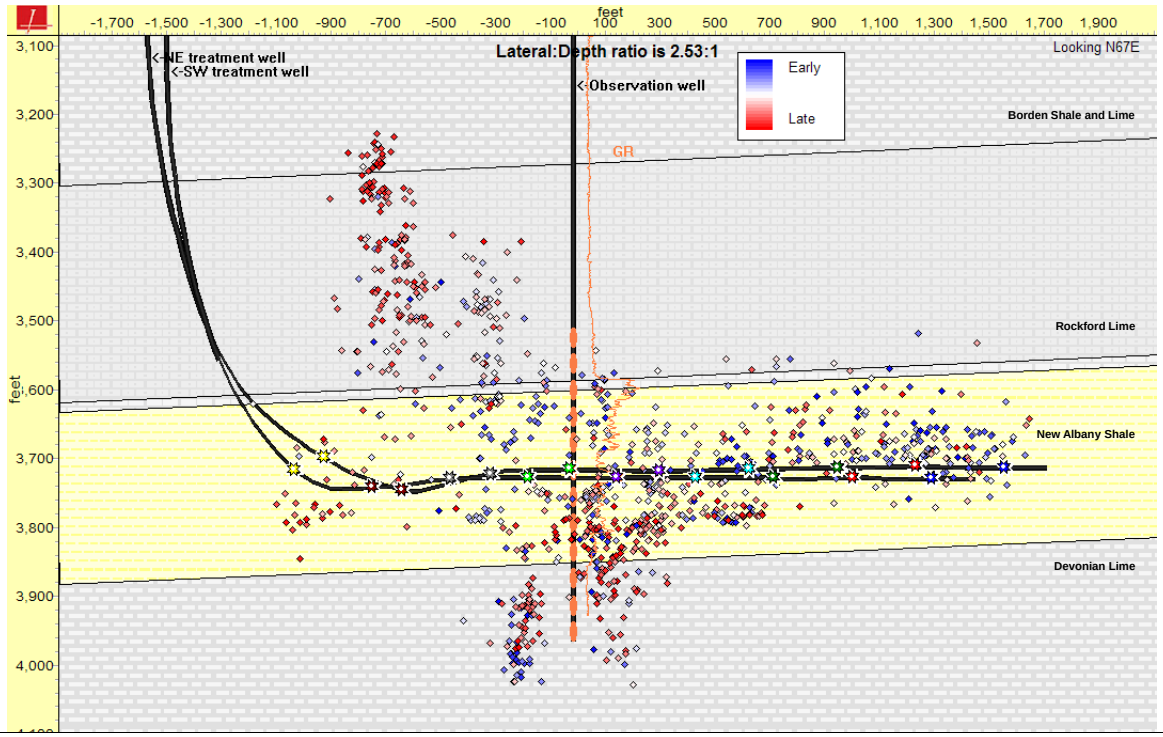


Figure 34. Events colored by relative time during individual stages, side view

Stages were defined by start and stop times on one of the wells, and it was not possible to operationally have each stage start and stop at exactly the same time. The result was that there was not an exact match between event generation and the initiation of pumping on both wells. It addition, stage ports were not located normal to each other along the N60°E regional direction of horizontal maximum principle stress σ_{max}, resulting in an "offset" for stage port locations that ranged from 285 ft to 435 ft.

There appeared to be two overall trends with respect to induced fracture or fracture network azimuth. Early stages demonstrated relatively wide "clouds" of events consistent with a fractured shale network, oriented at approximately N60°E. Cloud widths for these stages were wider than the available OH section + location error + microseismicity associated with nanodarcy rock + the intangible error associated with the lack of a deviation survey on the Observation well. Later stages generally had simpler groupings of events with narrower "widths", suggesting that fractures may not have been as complex, and may have been associated with interaction with naturally occurring geological features, such as in-situ low differential stress faulting, or open natural fracturing. Interaction with pre-stressed faulting is normally correlated with planar grouping of events and increases in observed event moment magnitude. **Figure 35, Figure 36,** and **Figure 37** are graphical representations of moment magnitude (microseism amplitude normalized for distance to the receiver array). Some planar groupings of events along "features" had higher average moment magnitudes consistent with a conventional interpretation of faulting, and some did not. There appeared to be a secondary grouping of relatively planar event clouds oriented along an azimuth of approximately N39°E. **Figure 38** is a bubble plot with moment magnitude presented in a slightly different way for clarity.

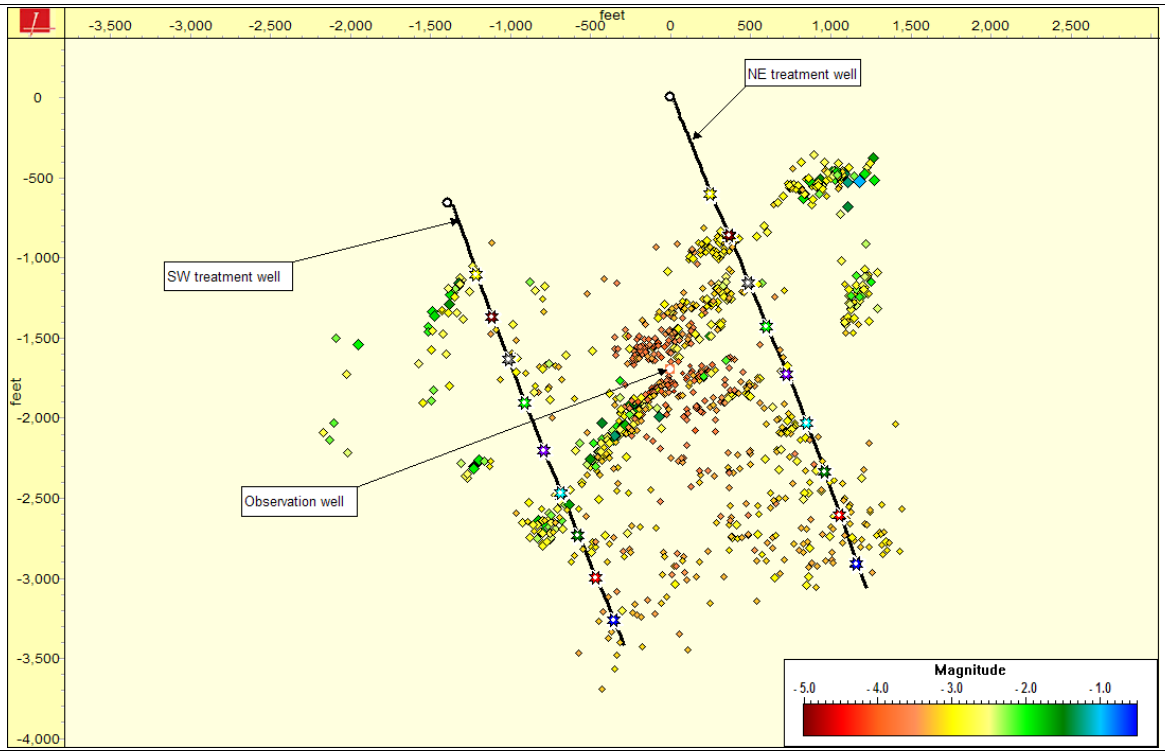


Figure 35. Moment magnitude, map view

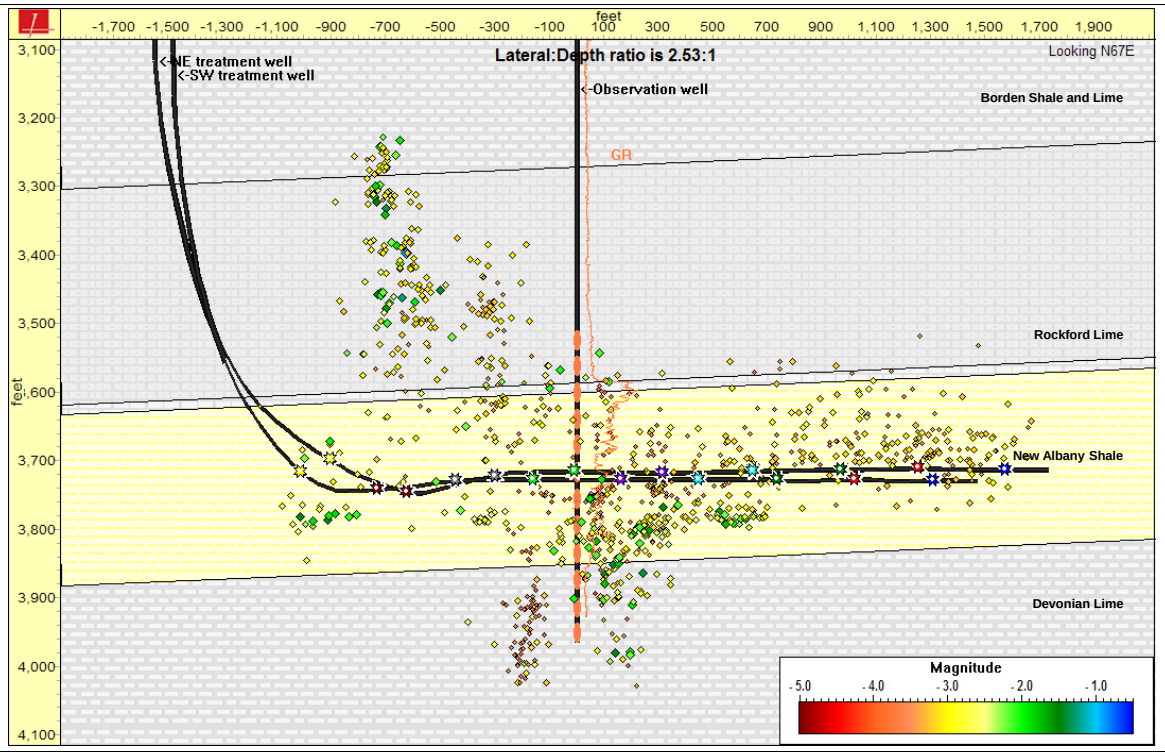


Figure 36. Moment magnitude, side view, looking down major azimuth trend (N60°E)

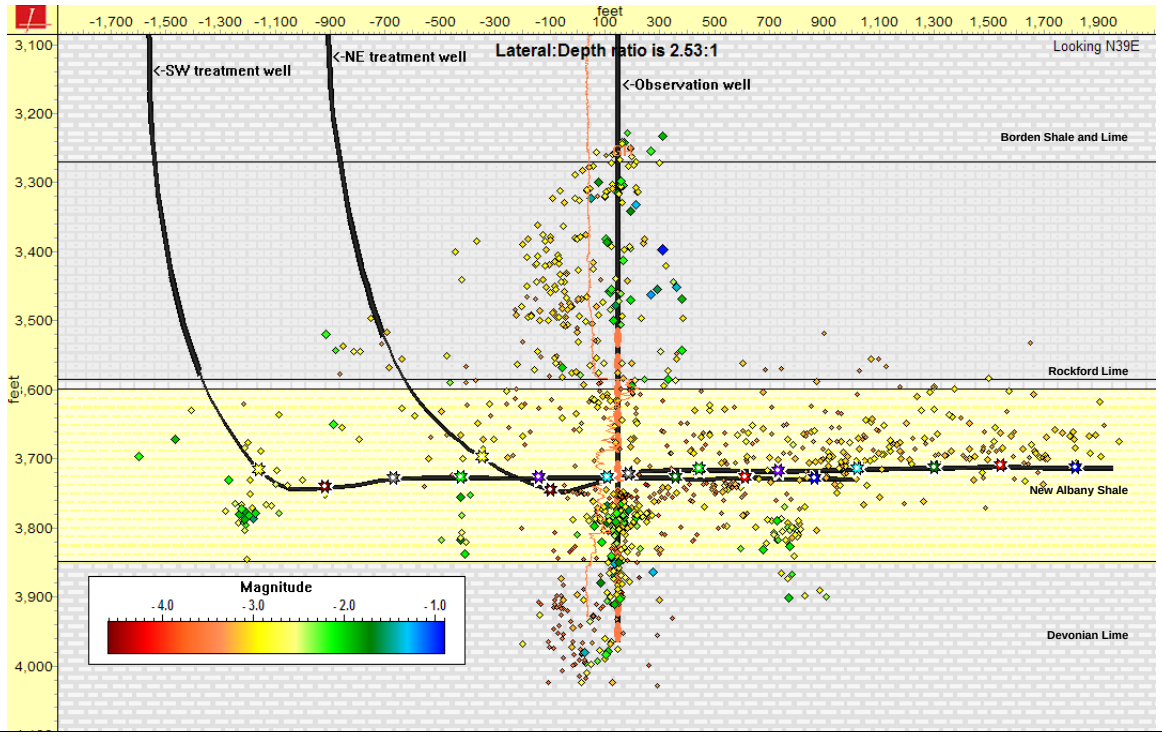


Figure 37. Moment magnitude, side view, looking down secondary azimuth trend (N39°E)

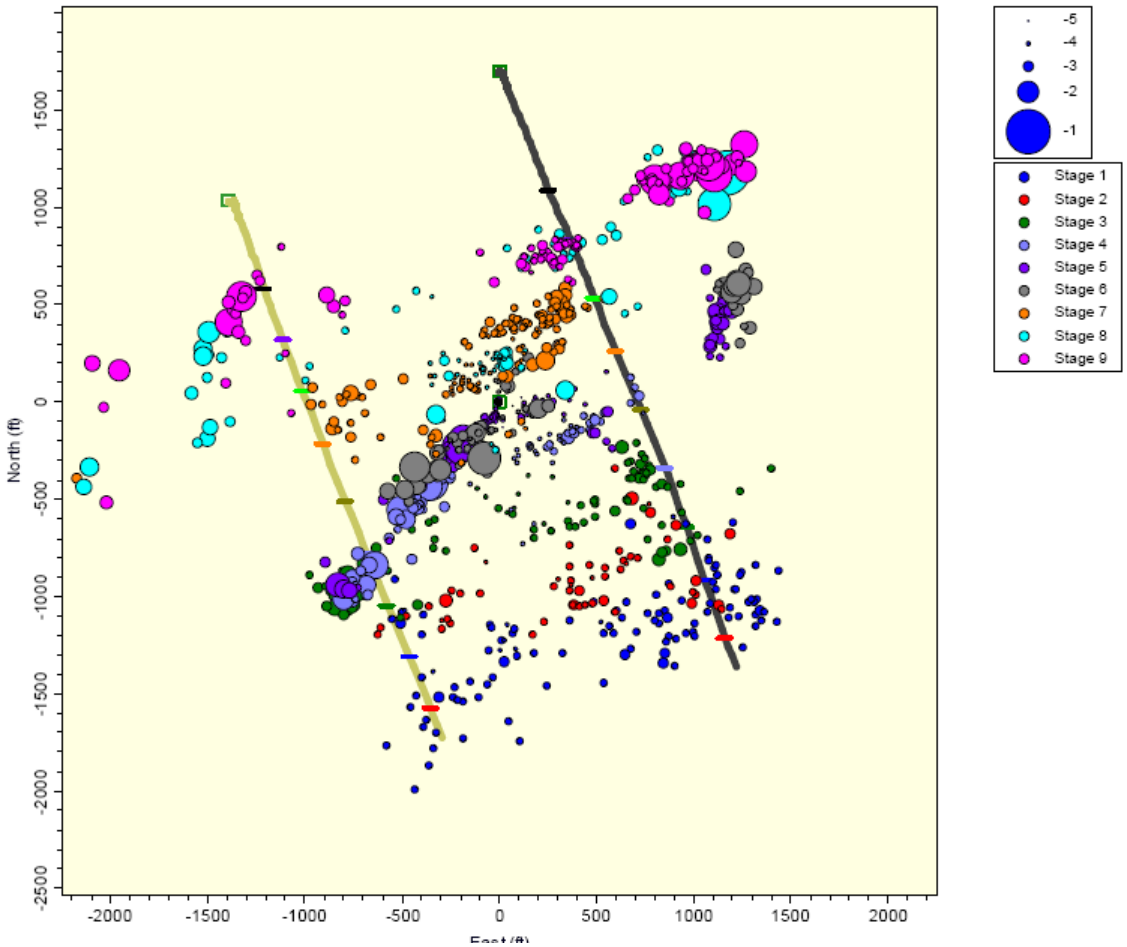


Figure 38. Moment magnitude bubble plot, map view

The measurement of X_f is dependent upon the assumption of symmetry vs. asymmetry. After observing many hundreds of microseismic mapping operations, Pinnacle has coined a phrase, "observation wellbore bias", which refers to the tendency for an observation well to hear events preferentially on the observation-well side of a given lateral, independently of listening distance. The root cause of this is not known, but it is hypothesized that signals on the far side of a lateral are attenuated by water or gas-filled induced fractures, by proppant, or sometimes by drilling-induced fractures, or increased fracture density near a given wellbore's path. Most events (especially in the first 3 stages) were mapped between the two stimulated wellbores, and it is probable that observation wellbore bias was partially or fully responsible. "Typical" fracture half lengths X_f were measured assuming symmetry, and were just over 800 ft for those cases where very little activity was noted to the southwest of the southwest treatment well and to the northeast of the northeast treatment well. The basis for this claim:

1. There is a statistical preponderance of observation wellbore bias in other mapping efforts, and repeated verification of the phenomena with dual geophone arrays positioned on opposite sides of a given lateral.

2. Signal-to-Noise Ratios (SNR's) for the first three stages on each well were significantly higher, on average, than on the remaining six stages (see **Figure 39**), and listening distances were likely substantially more than the distance between the geophone array and the furthest microseisms to

the south (**Figure 41**). The implication, then, is that if observation wellbore bias were not a factor, then events would have been heard on either side of the two wellbore had they existed.

3. Events in the first 3 stages initiating from each independent wellbore showed no evidence of connecting with each other early in their respective treatments. These early events were clearly biased toward the reservoir volume between the two laterals, and so interaction between the two wellbore's induced fractures was not likely during the early portions of each of these 3 stages.

As the completion progressed closer to the observation well, background noise increased. **Figure 40** is an example of measured background noise for a stage that was located close to the observation wellbore. Stages near the beginning and end of the completion had lower background noise levels. Background noise also generally increased during pumping operations, and tapered off dramatically gat the cessation of pumping on both wells.

Fractures for the first three or four stages were generally contained vertically within the New Albany Shale. Subsequent stages appeared to interact with naturally occurring geological features, and there was significant growth upwards into the Rockford Limestone, and on at least two stages, substantial downward penetration into the potentially wet Devonian below the New Albany Shale.

Experience in other unconventional shale plays has shown that when there is extensive interaction with naturally occurring geological features, often early historical production profiles are not as favorable when feature count/100 acres is low, or is zero.

Two velocity models were employed for this project. The first (**Figure 92**) was used for the 3 initial stages, and the second (**Figure 93**) was used for all remaining stages. The difference between the two is that S-wave velocities were increased just slightly on the model for the first 3 stages.

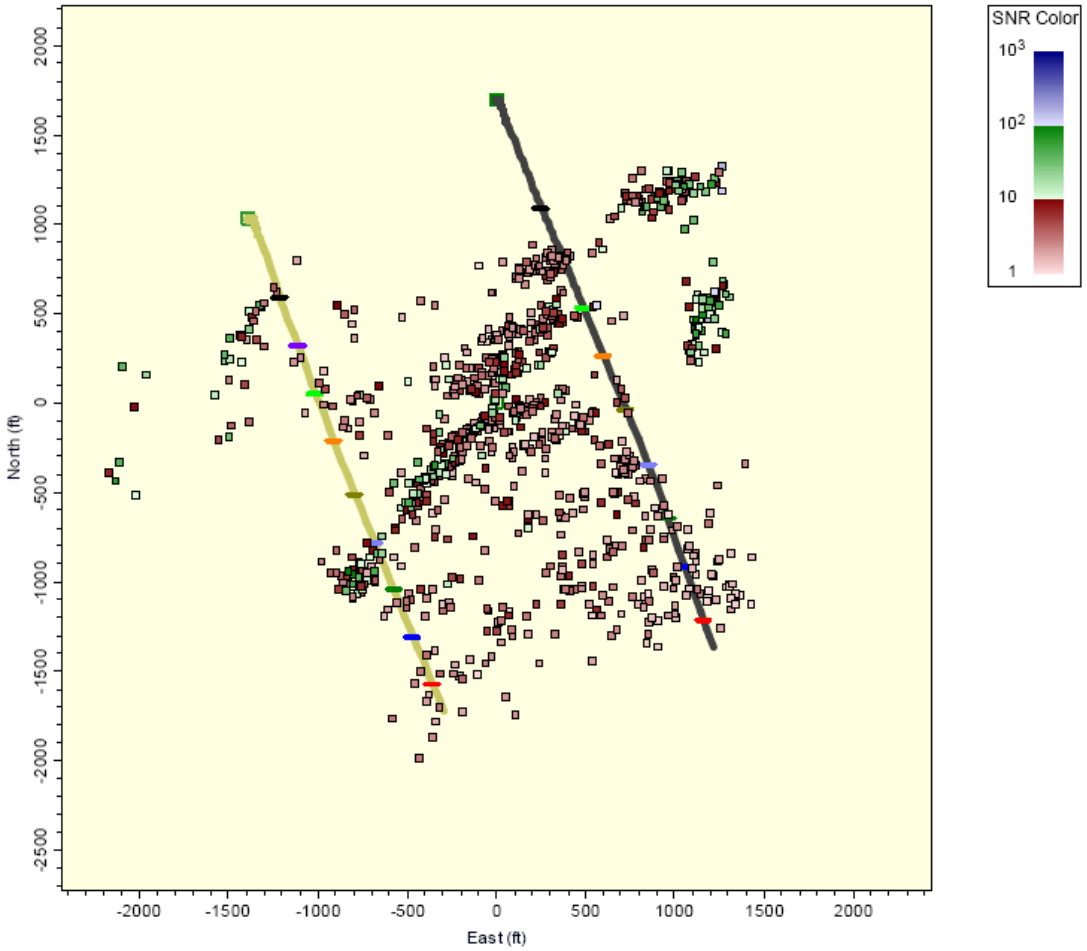


Figure 39. Signal-to-Noise ratios for the project

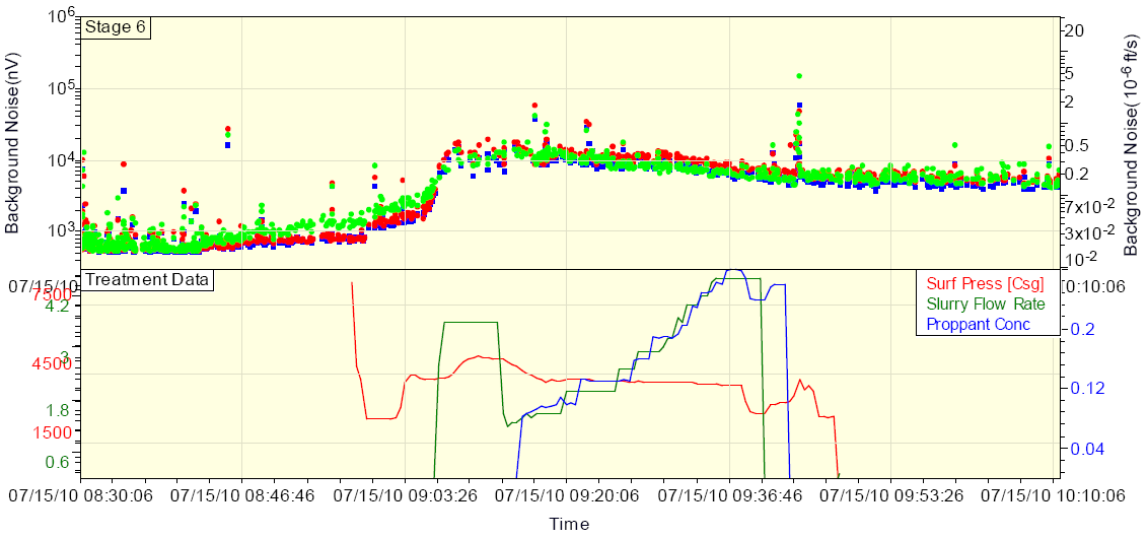


Figure 40. Example of background noise for a stage close to the observation well

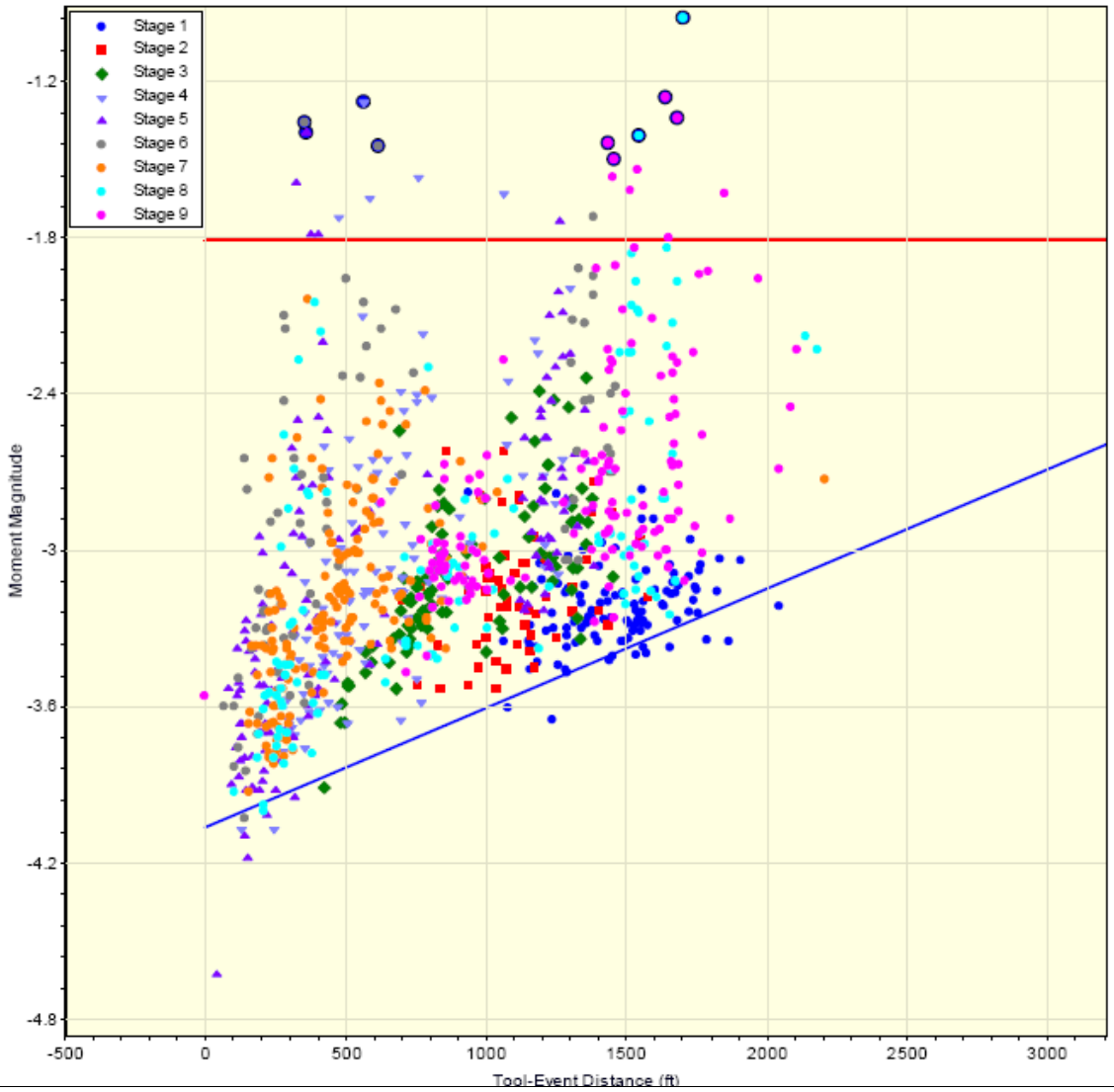


Figure 41. Listening distance, all stages, both wells

The two models that were used to position and display event locations were simple 2-dimensional layered representations that took into account a slight regional dip, but not specific variations along or normal to the wellbores. **Figure 43** through **Figure 87** are stage-specific graphics.

Figure 42 is an example event location uncertainty plot that visually depicts depth error. The largest component of location uncertainty was azimuthal. Azimuthal location uncertainties ranged from 0 ft to 212 ft, and the average was 49 ft. Distance location uncertainties ranged from 4 ft to 76 ft, and the average was 17 ft. Depth location uncertainties ranged from 2 ft to 161 ft, and the average was 13 ft. Note that uncertainty increases with increased distance from the observation array.

There were a number of additional sources of intangible uncertainty for this project that were not included in the calculated values of uncertainty. These include, but are not limited to:

1. There was no deviation survey performed on the observation well, and therefore, there is 100% certainty that the tool array was actually in a different position from what was depicted. The amount of deviation from vertical is unknown, but there is a strong likelihood that the bottom-hole location has an offset of between 20 and 100 ft from the surface location. Event errors associated with unknown [X-Y, or map-view] geophone locations do not vary directly with each other.

2. A method to tie into collars on the observation well was not available, so tool positioning from a vertical standpoint was estimated by a) tagging the top rubber plug at its assumed depth, then adjusting with conventional stretch curves. Like X-Y error, event errors associated with unknown geophone depths do not vary directly with each other.

3. The final velocity models (**Figure 92** and **Figure 93)** used for event positioning were assumed to be 100% correct, when in fact it is well known that horizontal velocities can often vary somewhat from the vertical velocities that are measured during the OH logging process. Because the 4-1/2" casing in both treatment wells had no cemented connection with the formation, it was not possible to generate downhole signals that could be utilized to calibrate either velocity model.

4. Directional surveys on the two treatment wells were assumed to be 100% correct, when in fact, there was some [unknown] error associated with both of those surveys.

5. There was approximately 14 ft of potential error in all horizontal directions with respect to all three wellhead surface locations.

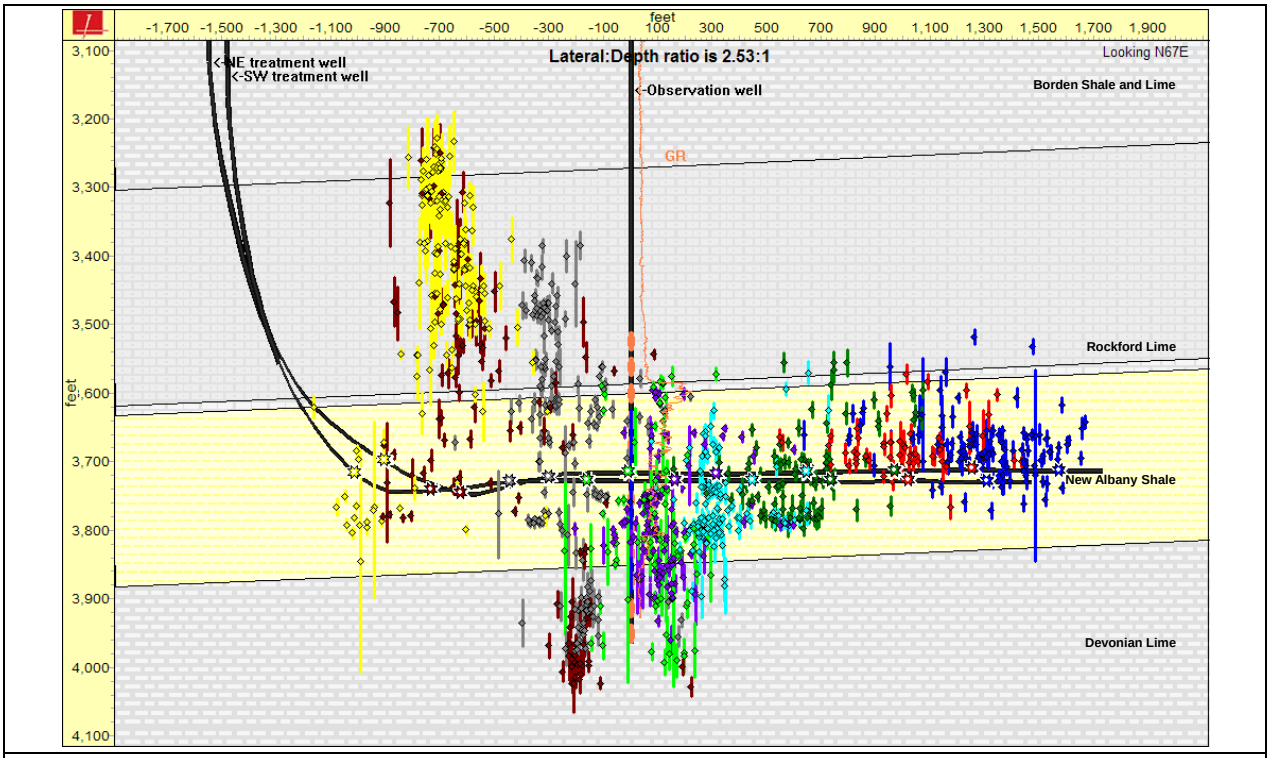


Figure 42. Event depth uncertainty, side view

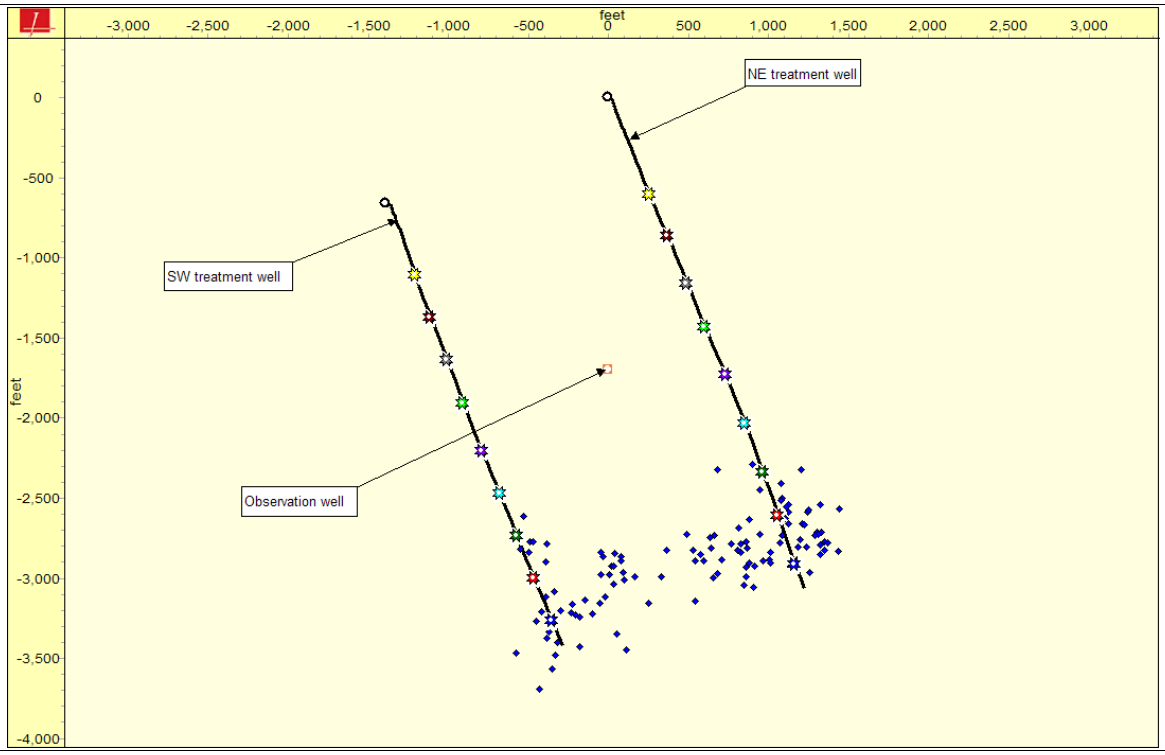


Figure 43. Map view, stage 1

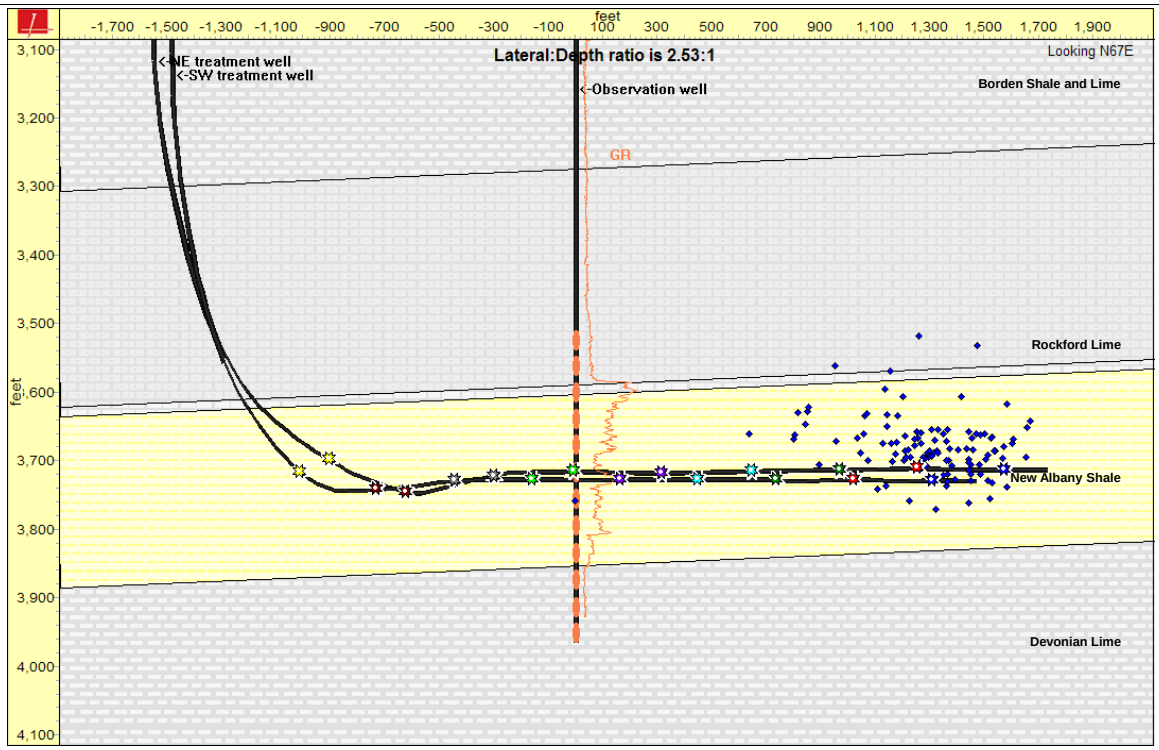


Figure 44. Lateral side view (orthogonal to lateral), stage 1

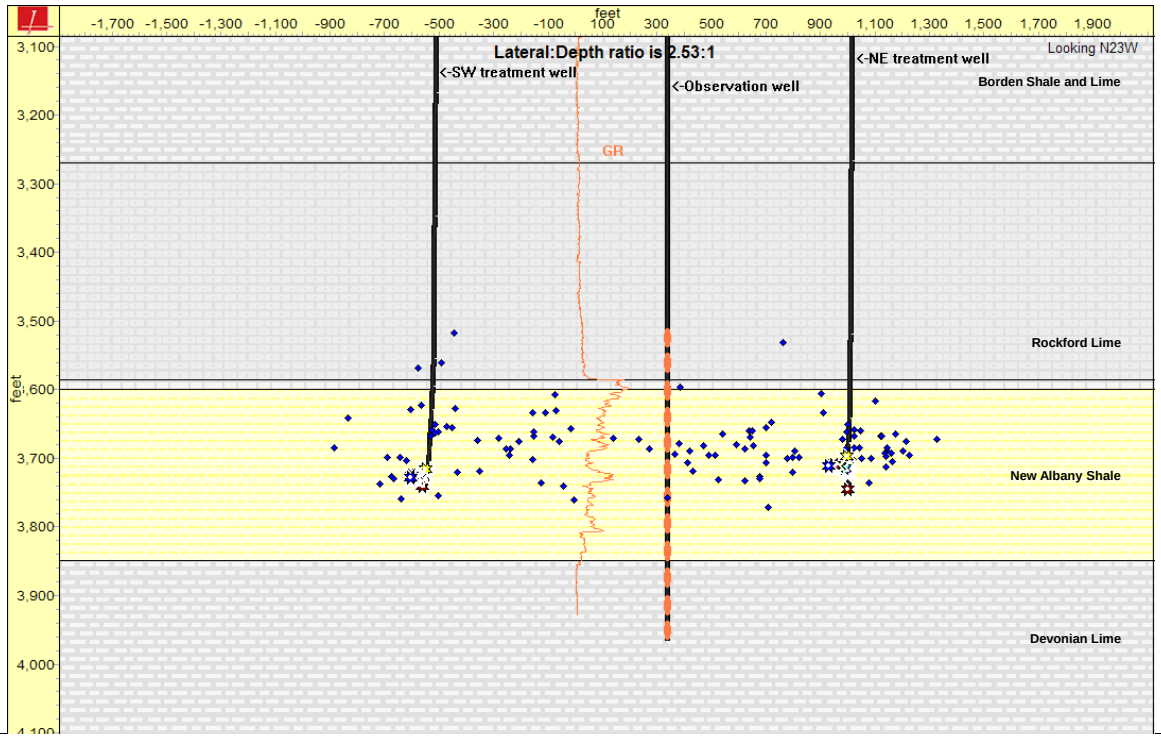


Figure 45. Lateral end-on view (along lateral), stage 1

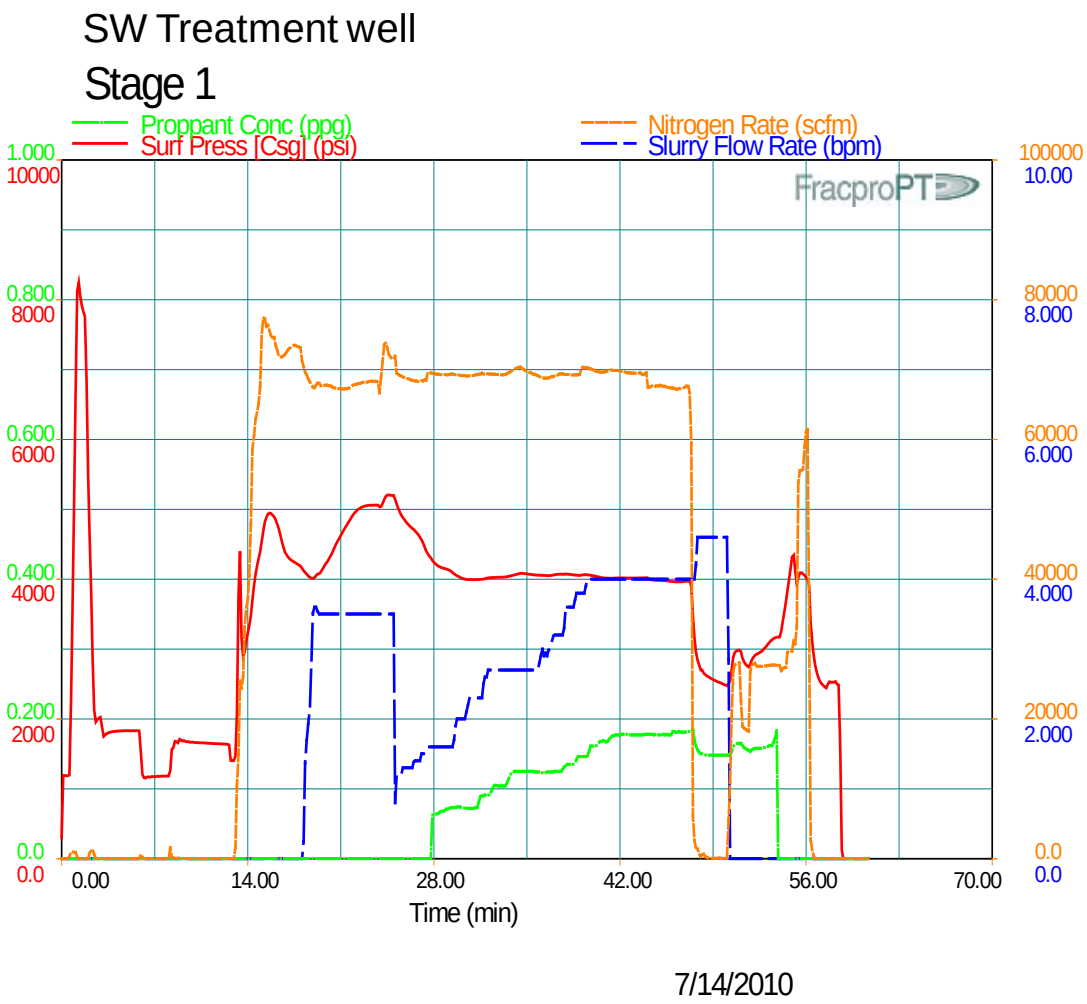


Figure 46. Treatment record, stage 1 (SW treatment well)

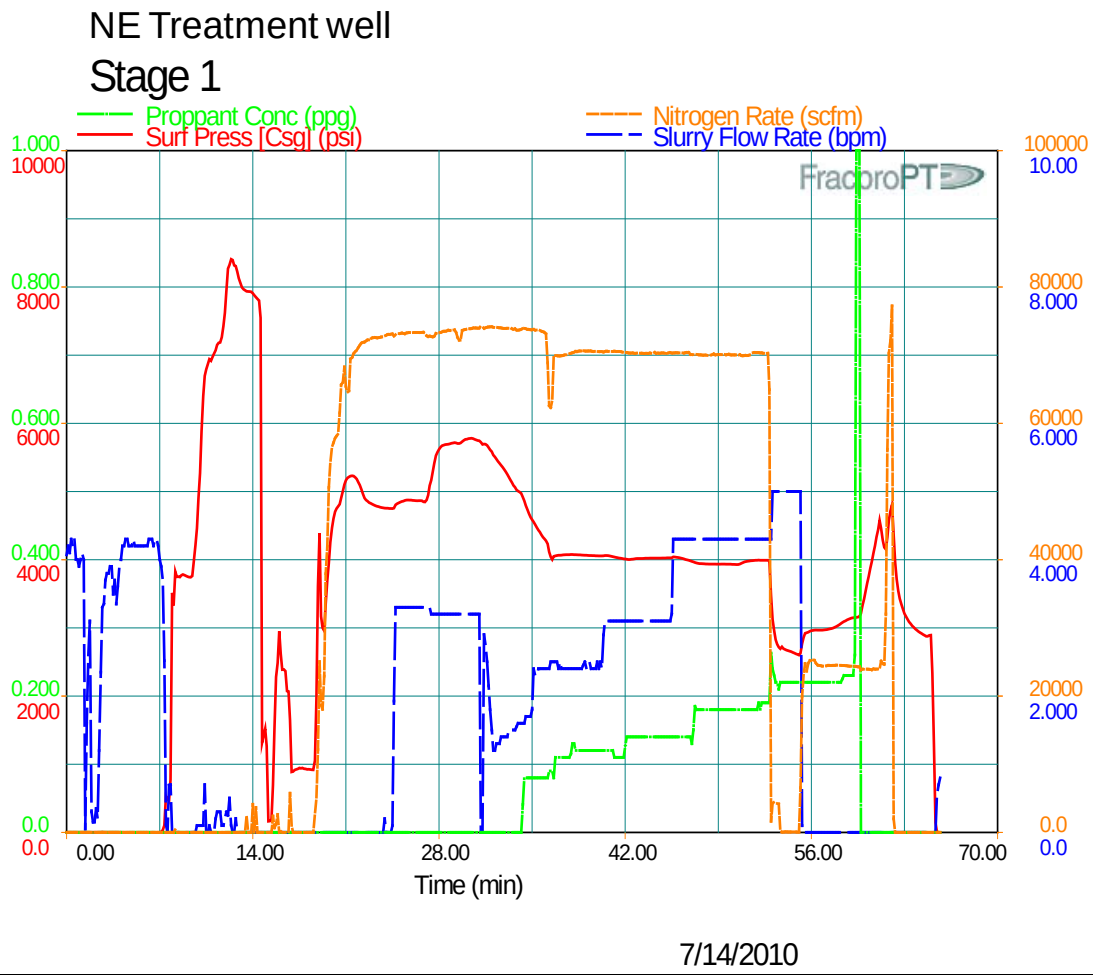


Figure 47. Treatment record, stage 1 (NE treatment well)

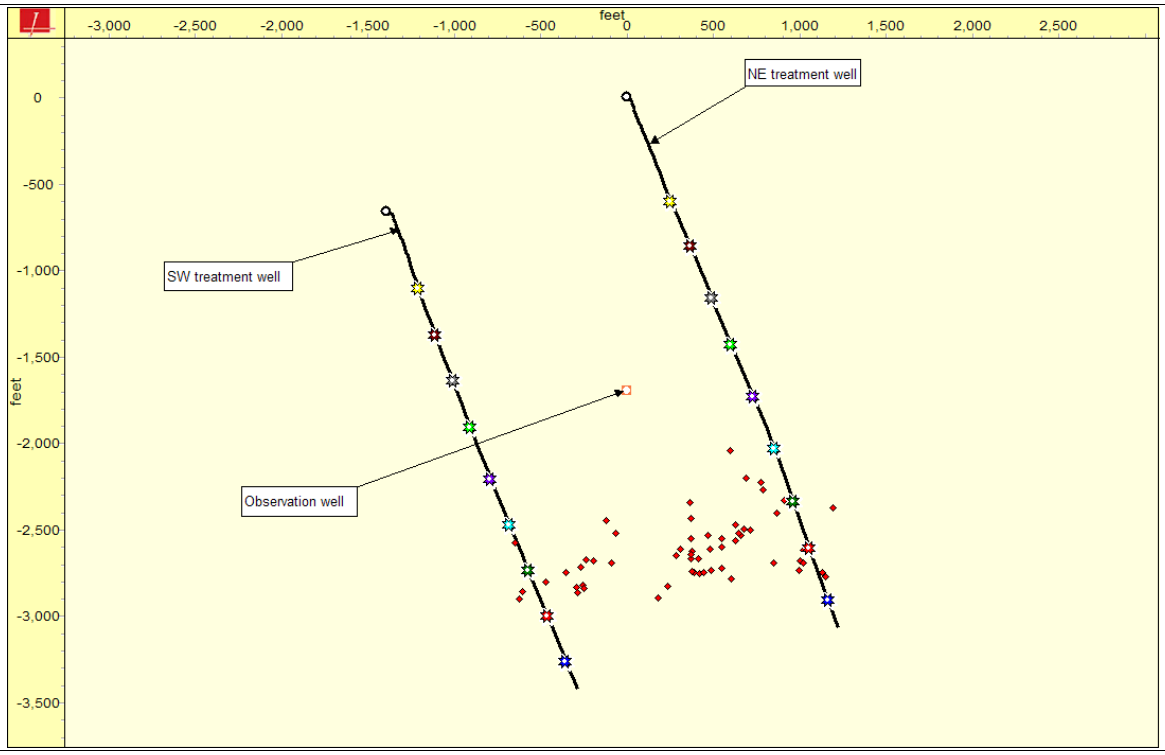


Figure 48. Map view, stage 2

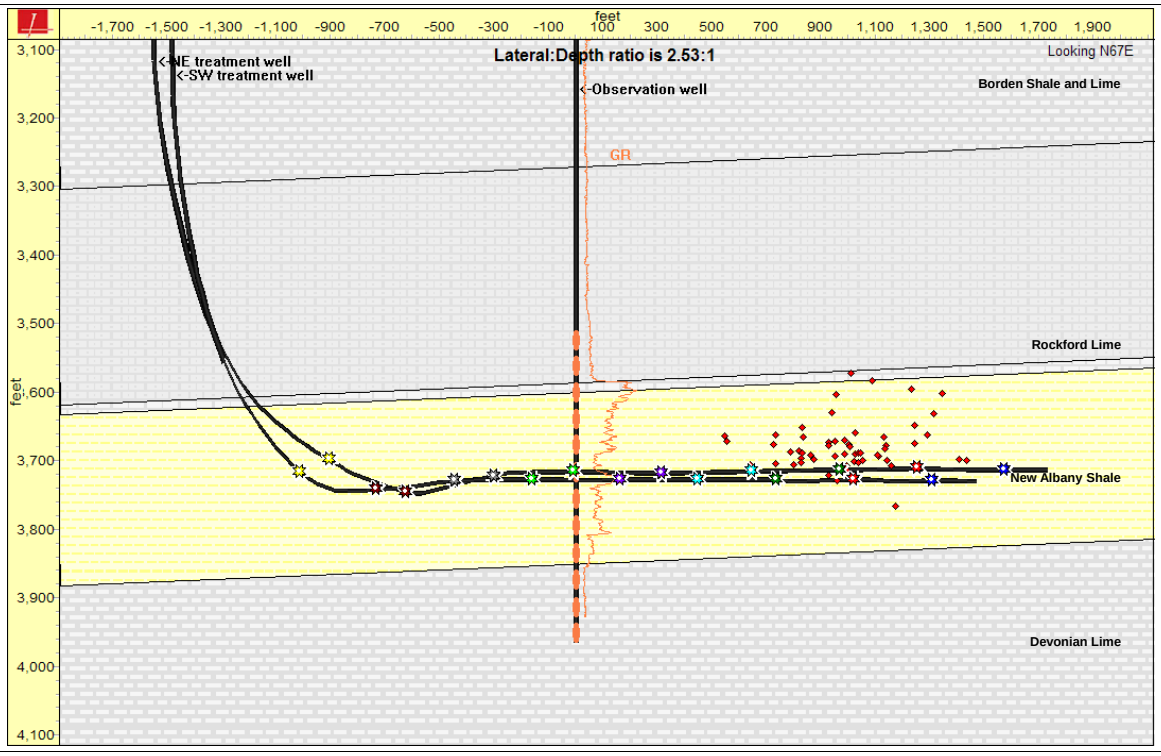


Figure 49. Lateral side view (orthogonal to lateral), stage 2

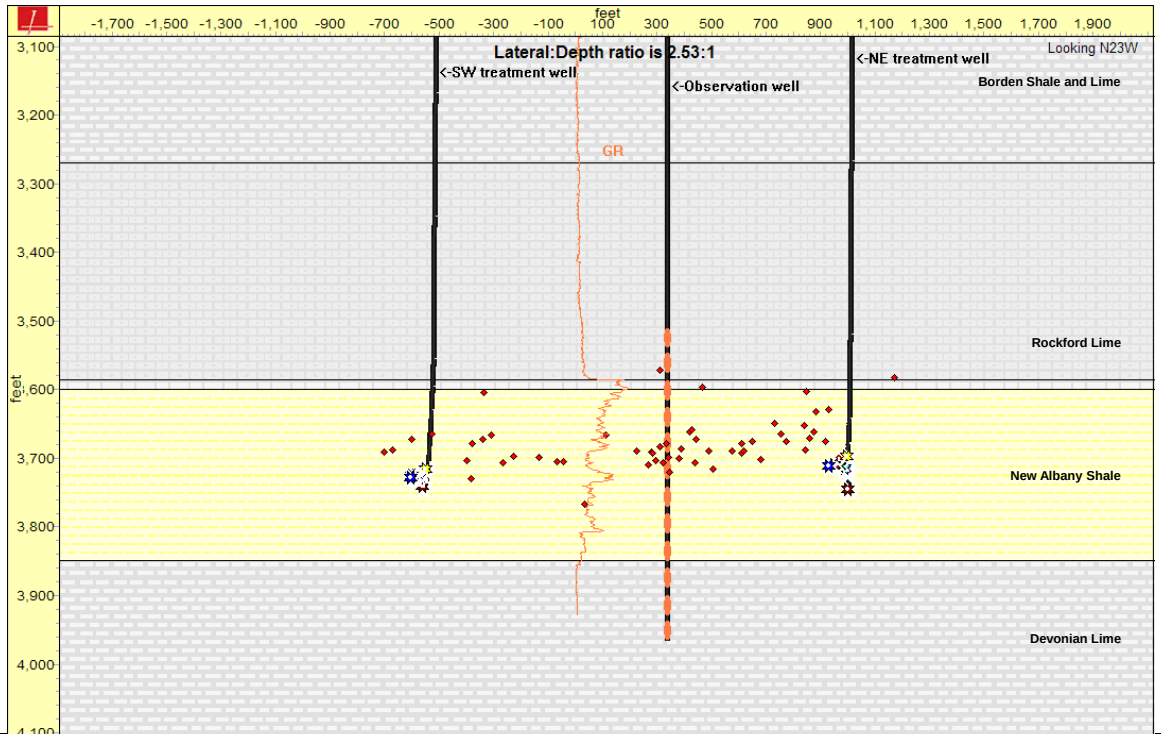


Figure 50. Lateral end-on view (along lateral), stage 2

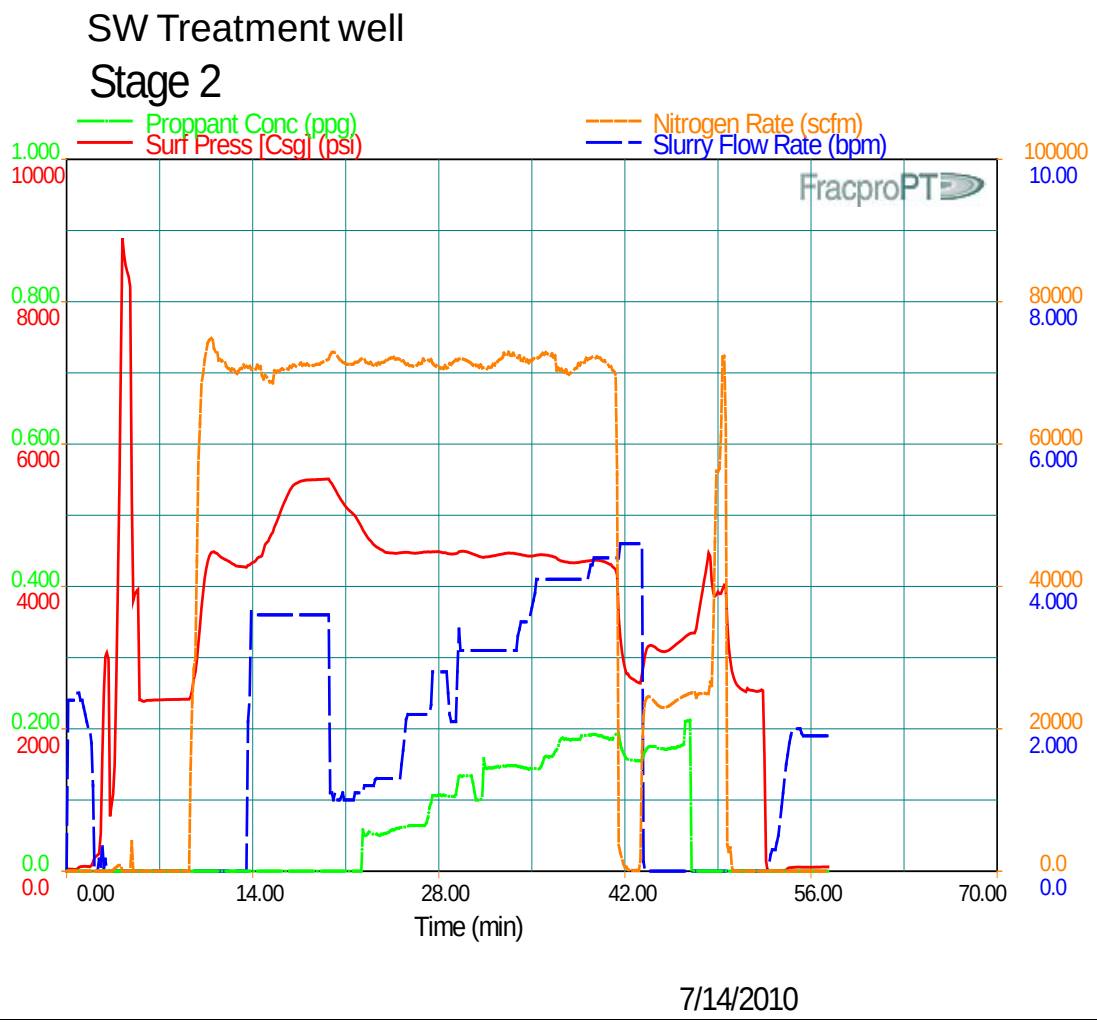


Figure 51. Treatment record, stage 2 (SW treatment well)

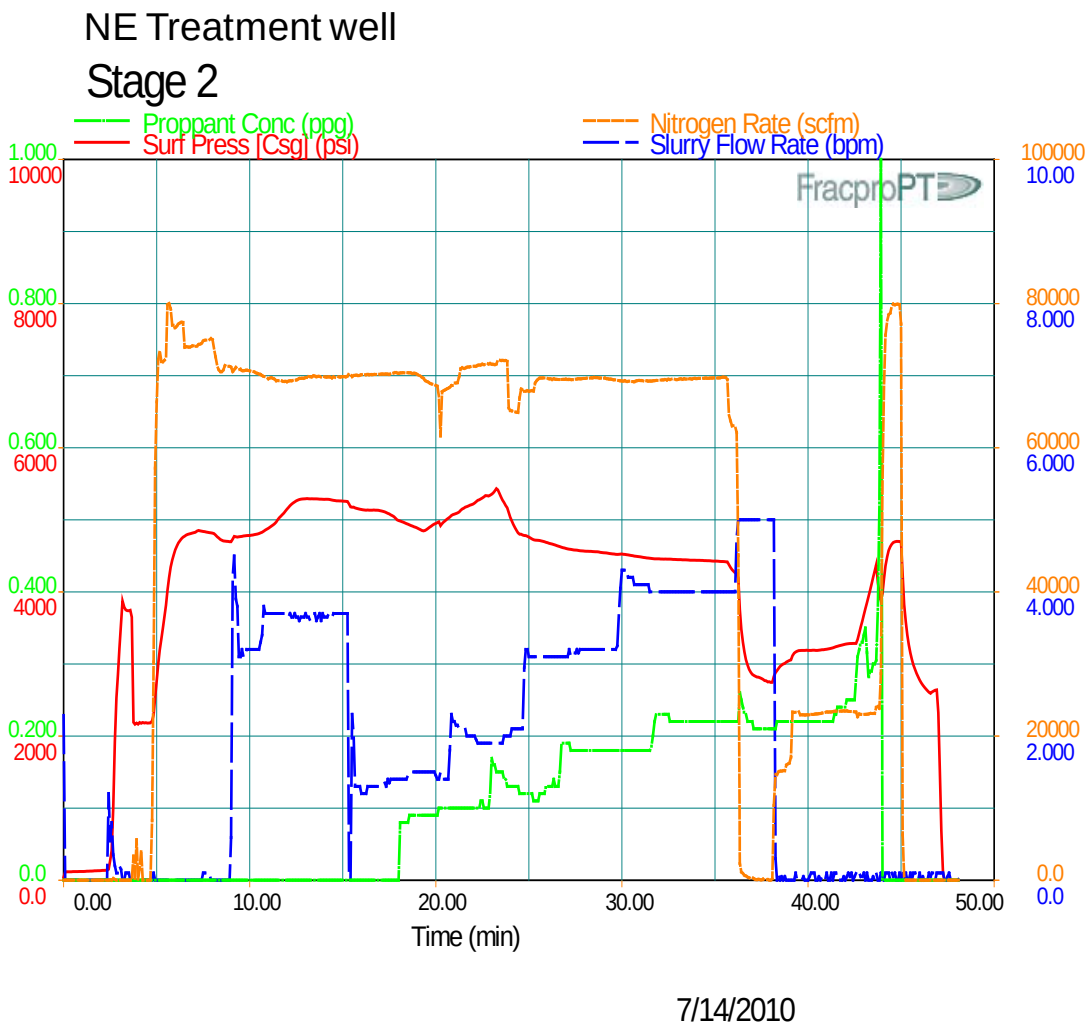


Figure 52. Treatment record, stage 2 (NE treatment well)

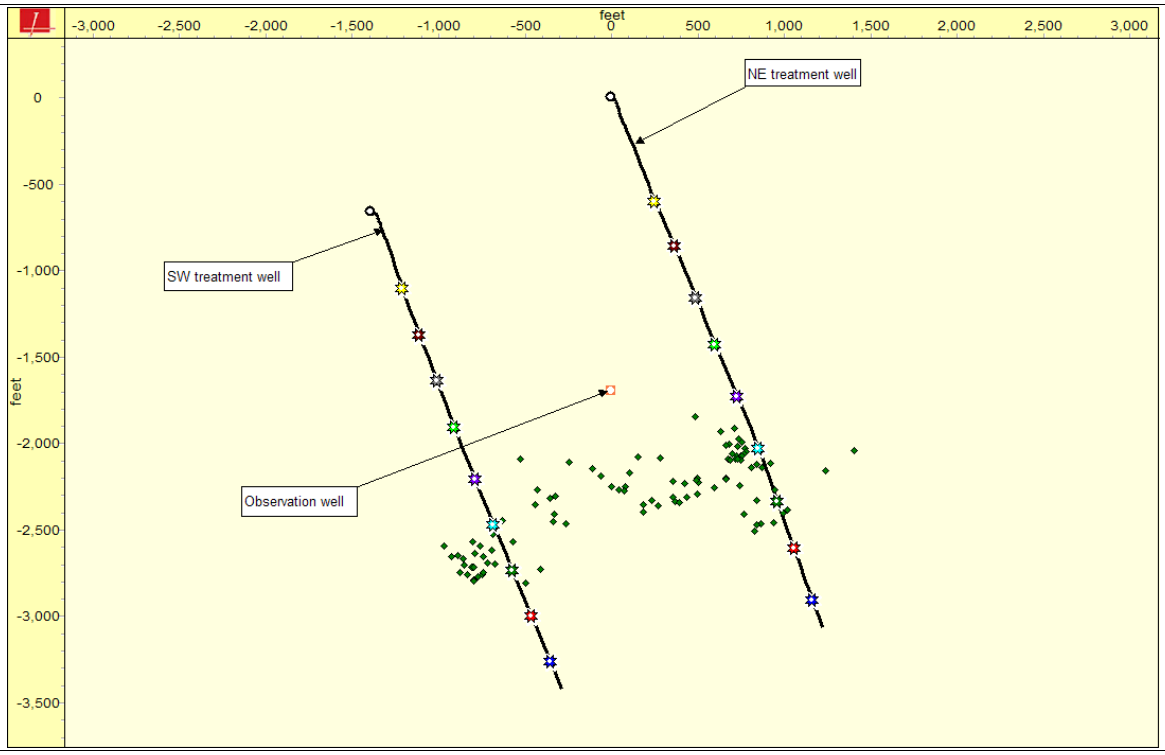


Figure 53. Map view, stage 3

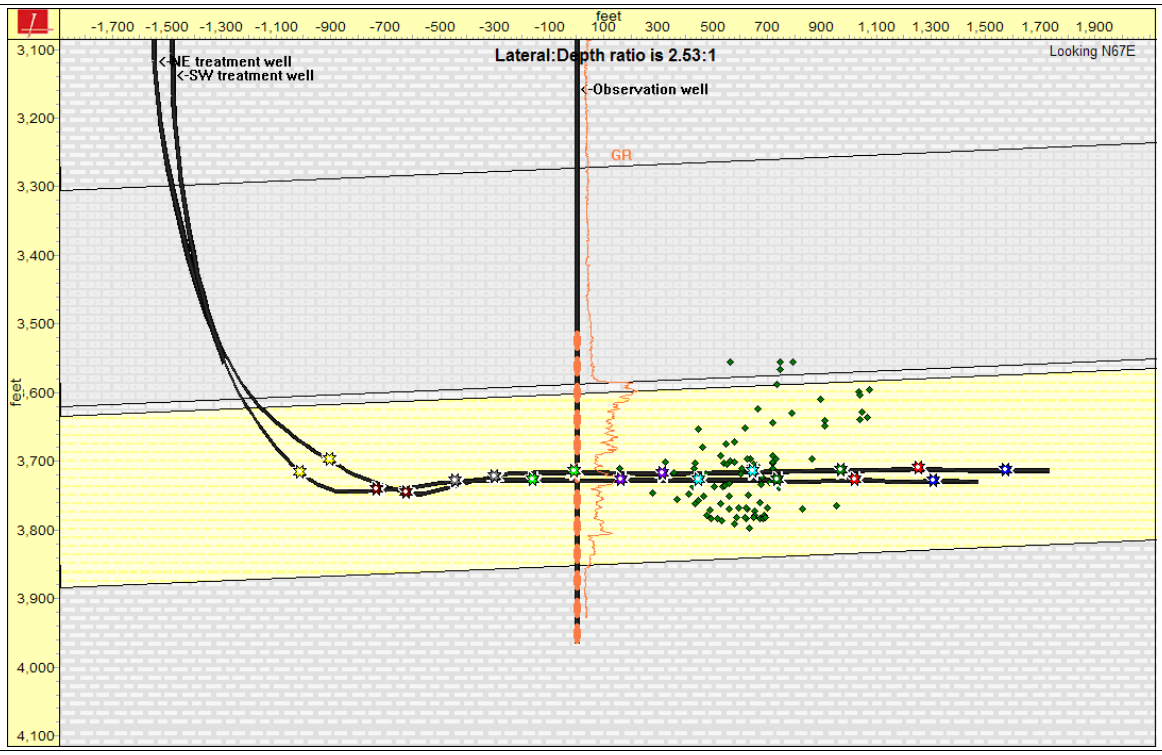


Figure 54. Lateral side view (orthogonal to lateral), stage 3

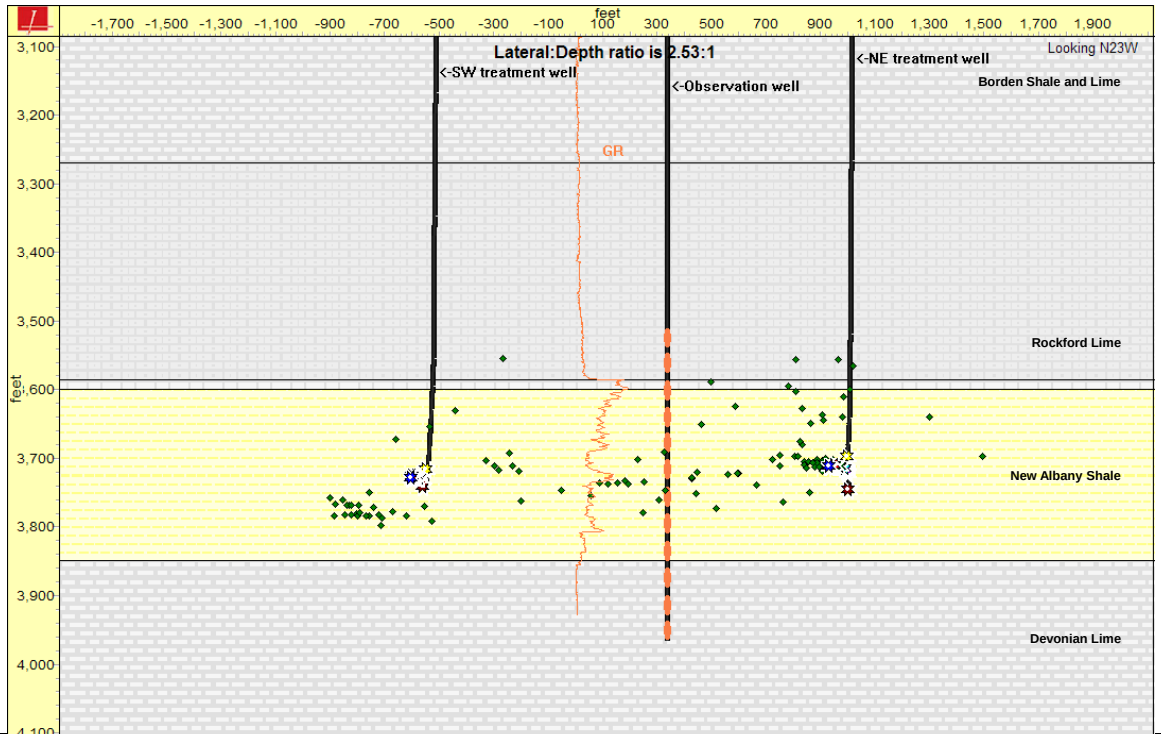


Figure 55. Lateral end-on view (along lateral), stage 3

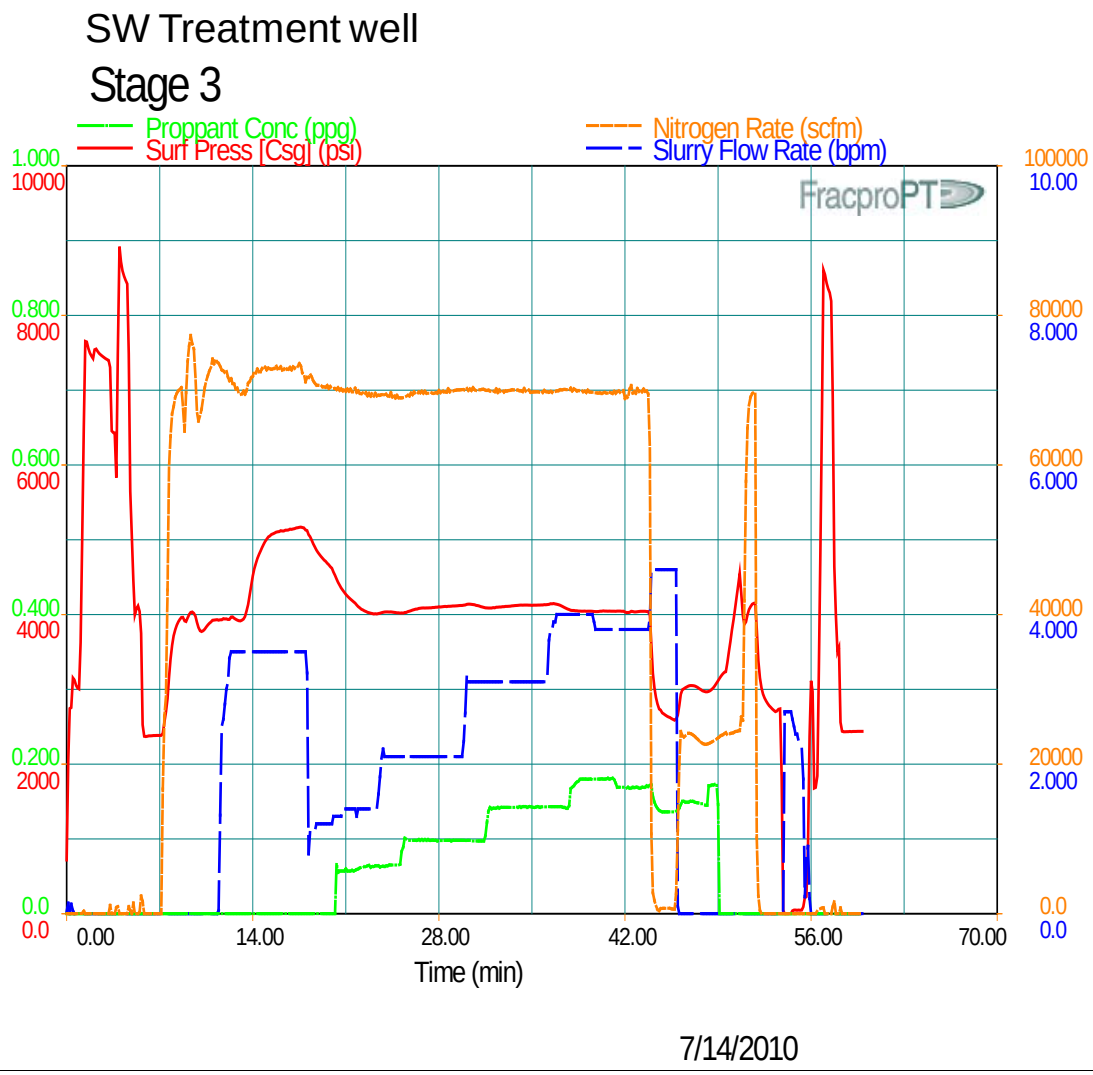


Figure 56. Treatment record, stage 3 (SW treatment well)

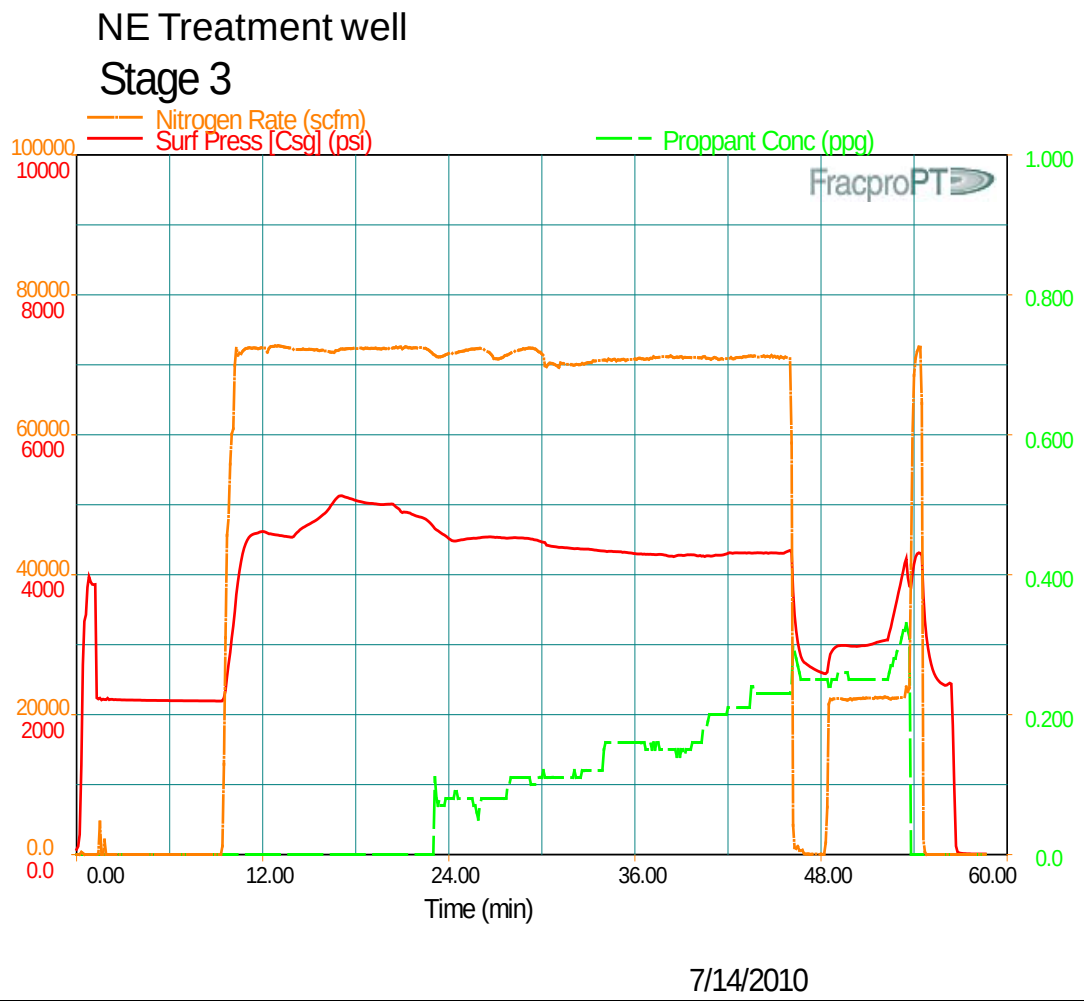


Figure 57. Treatment record, stage 3 (NE treatment well)

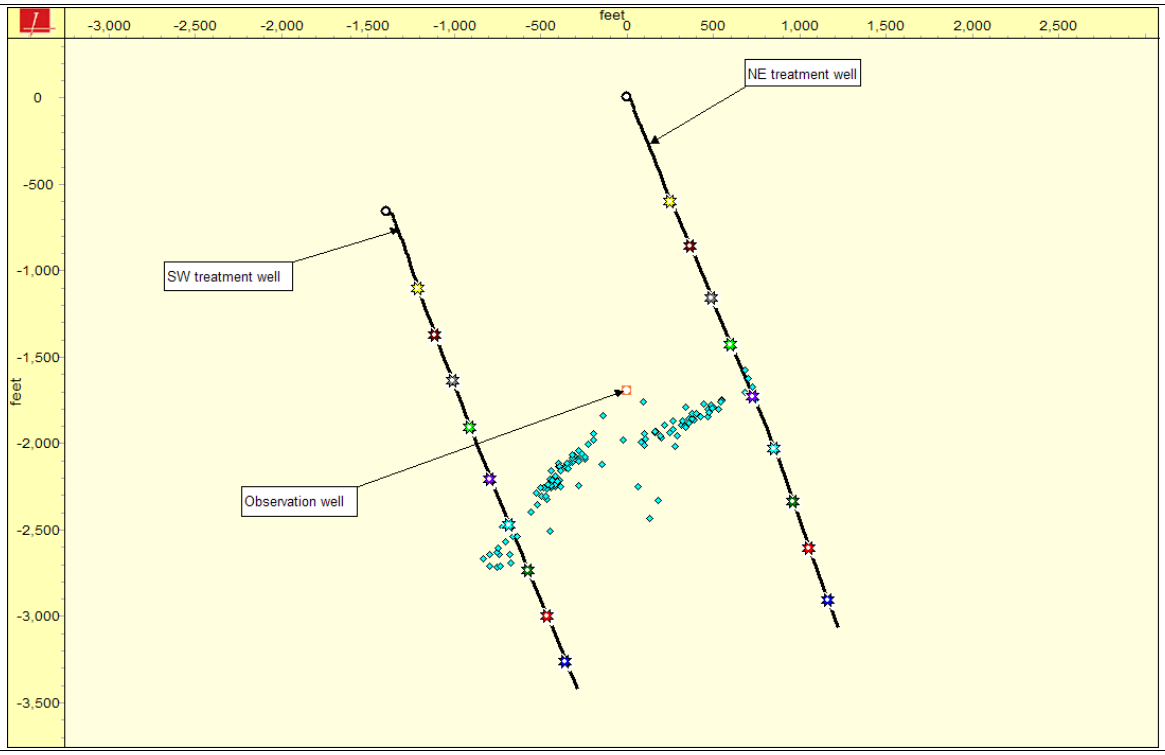


Figure 58. Map view, stage 4

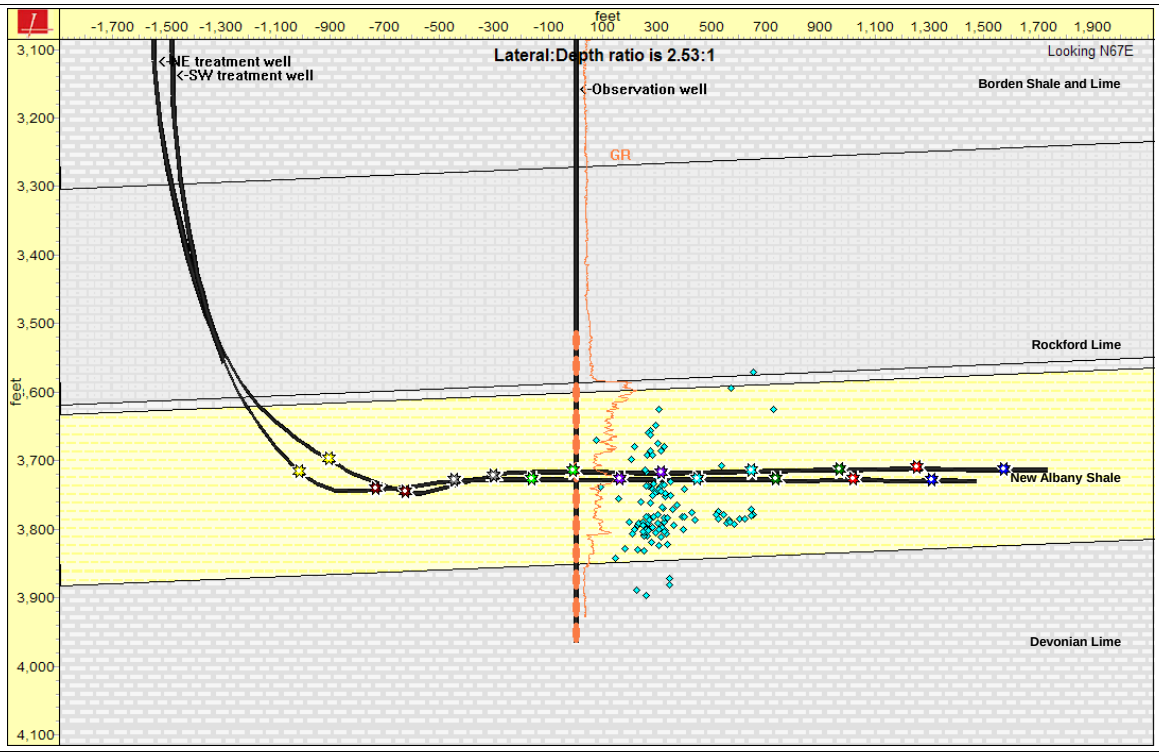


Figure 59. Lateral side view (orthogonal to lateral), stage 4

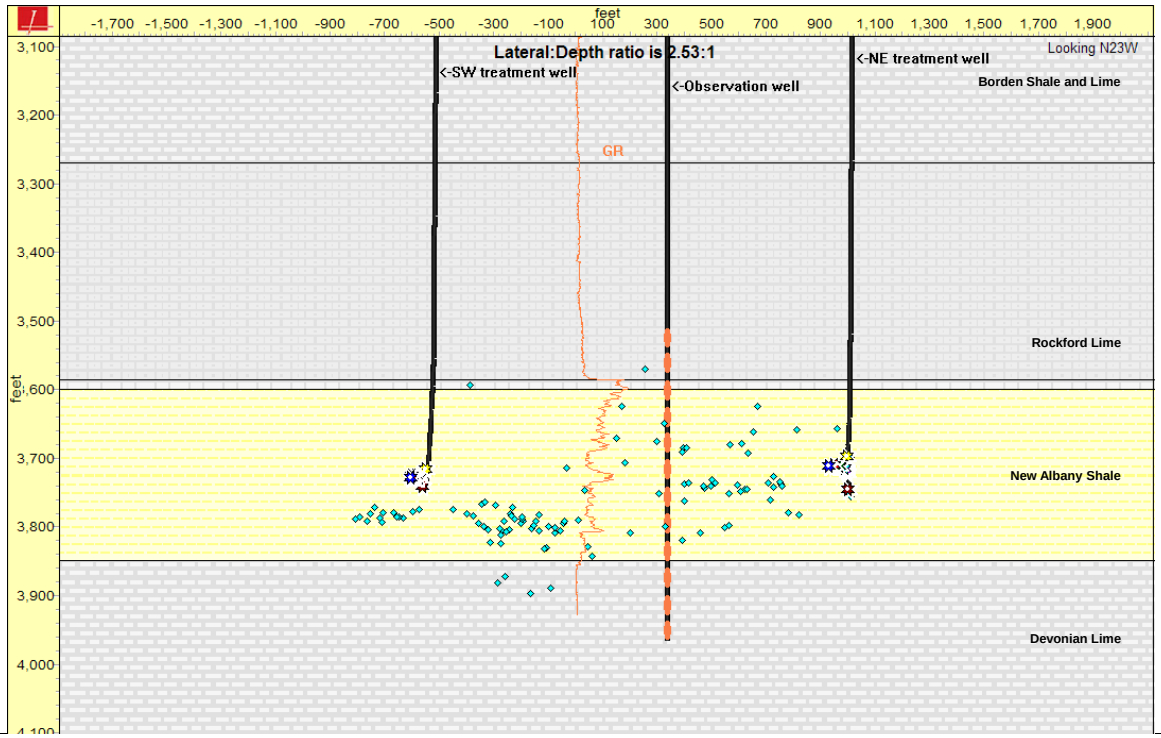


Figure 60. Lateral end-on view (along lateral), stage 4

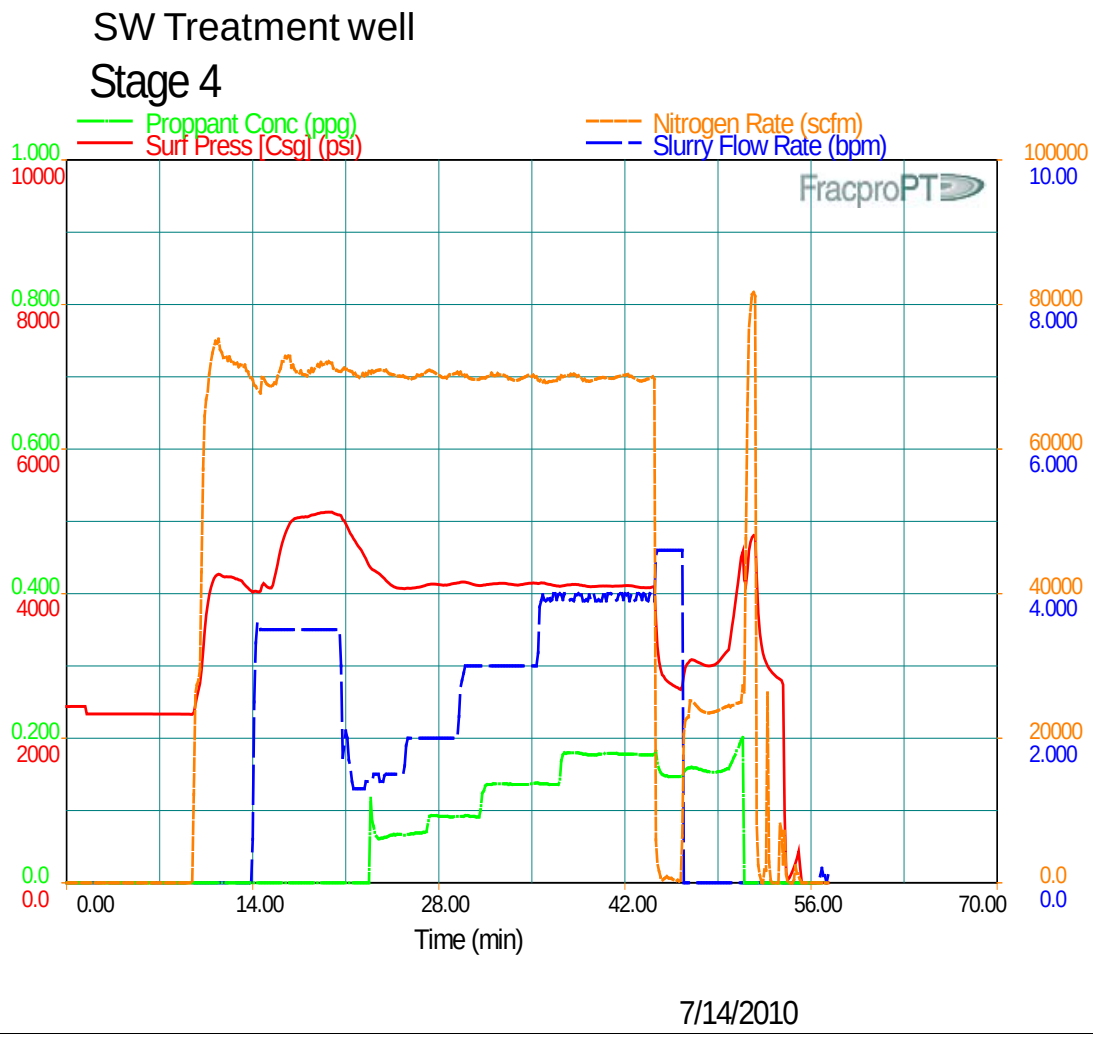


Figure 61. Treatment record, stage 4 (SW treatment well)

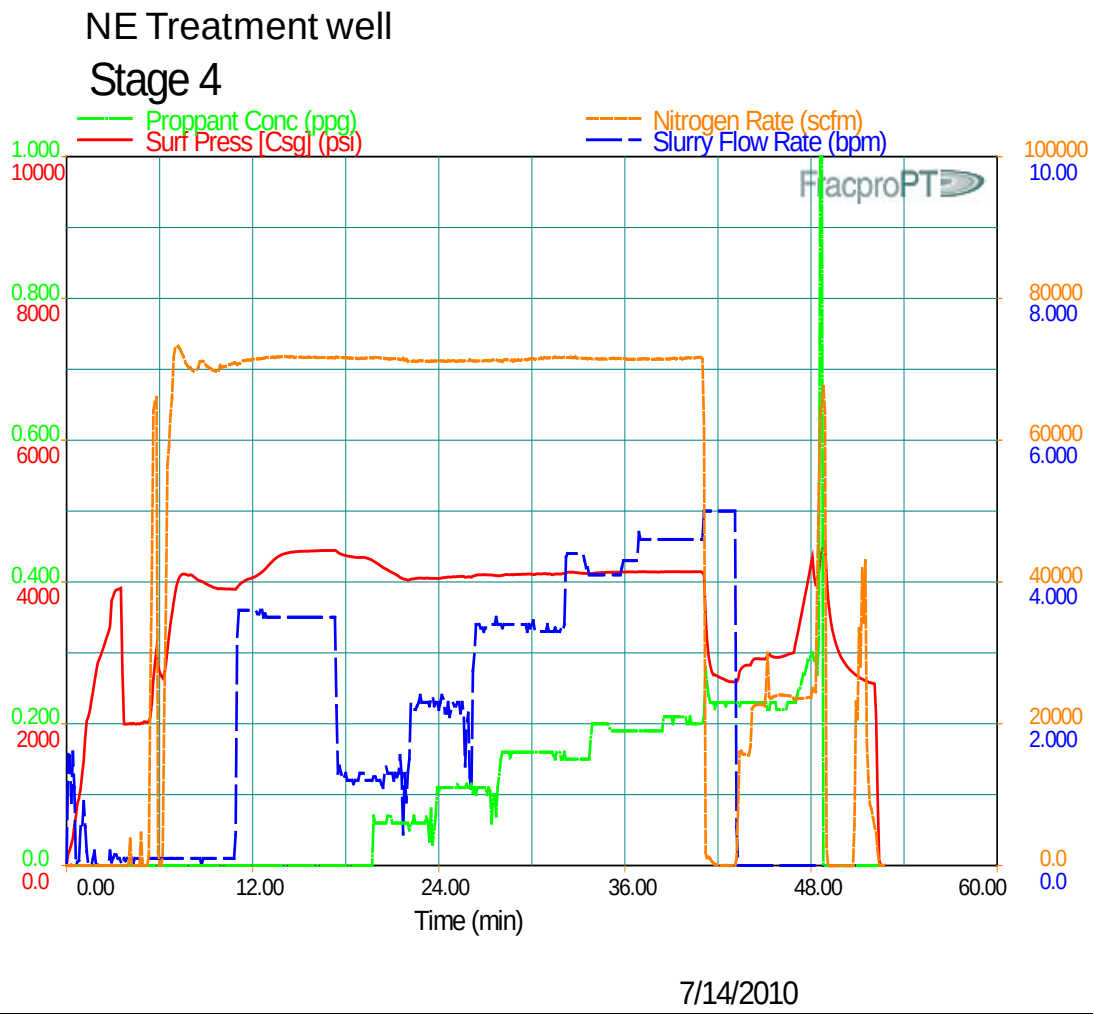


Figure 62. Treatment record, stage 4 (NE treatment well)

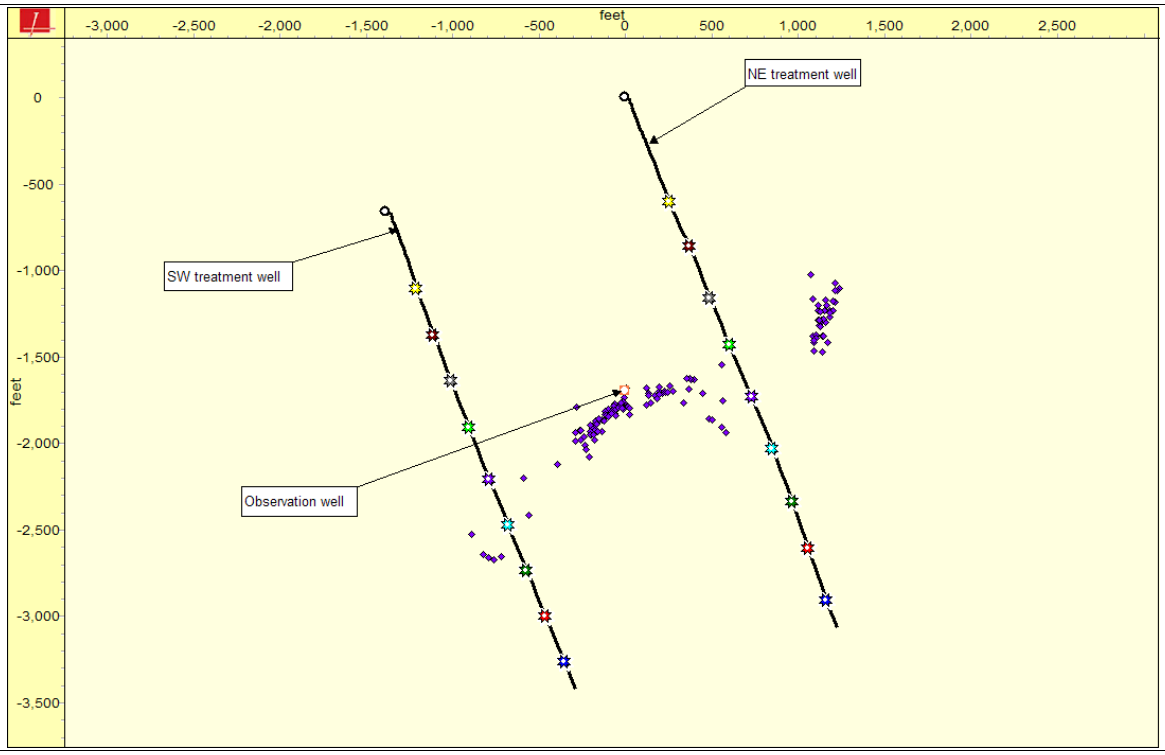


Figure 63. Map view, stage 5

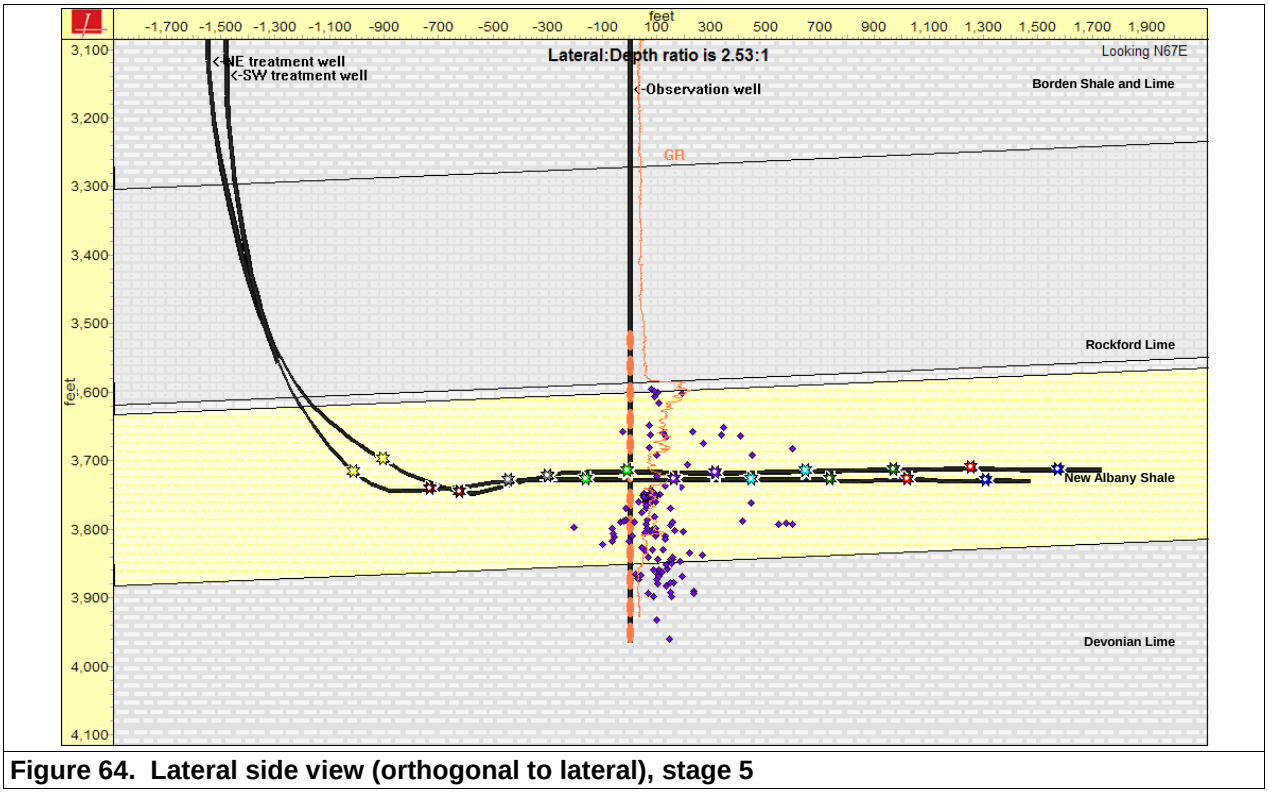


Figure 64. Lateral side view (orthogonal to lateral), stage 5

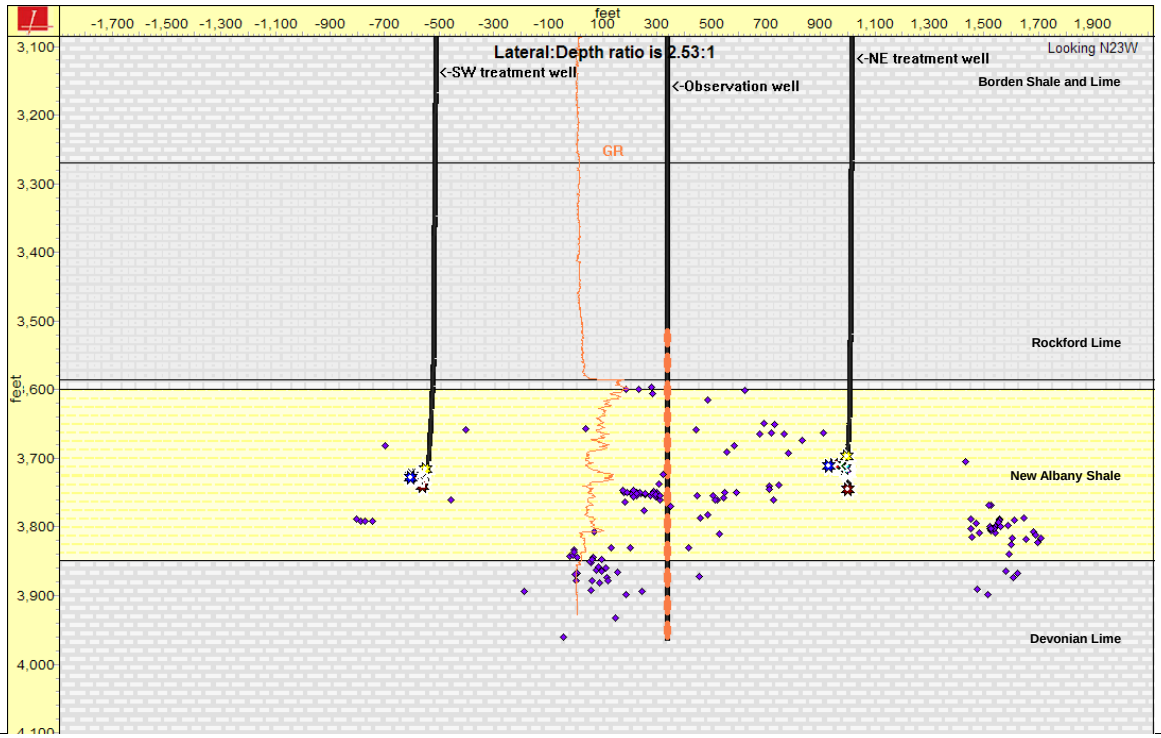


Figure 65. Lateral end-on view (along lateral), stage 5

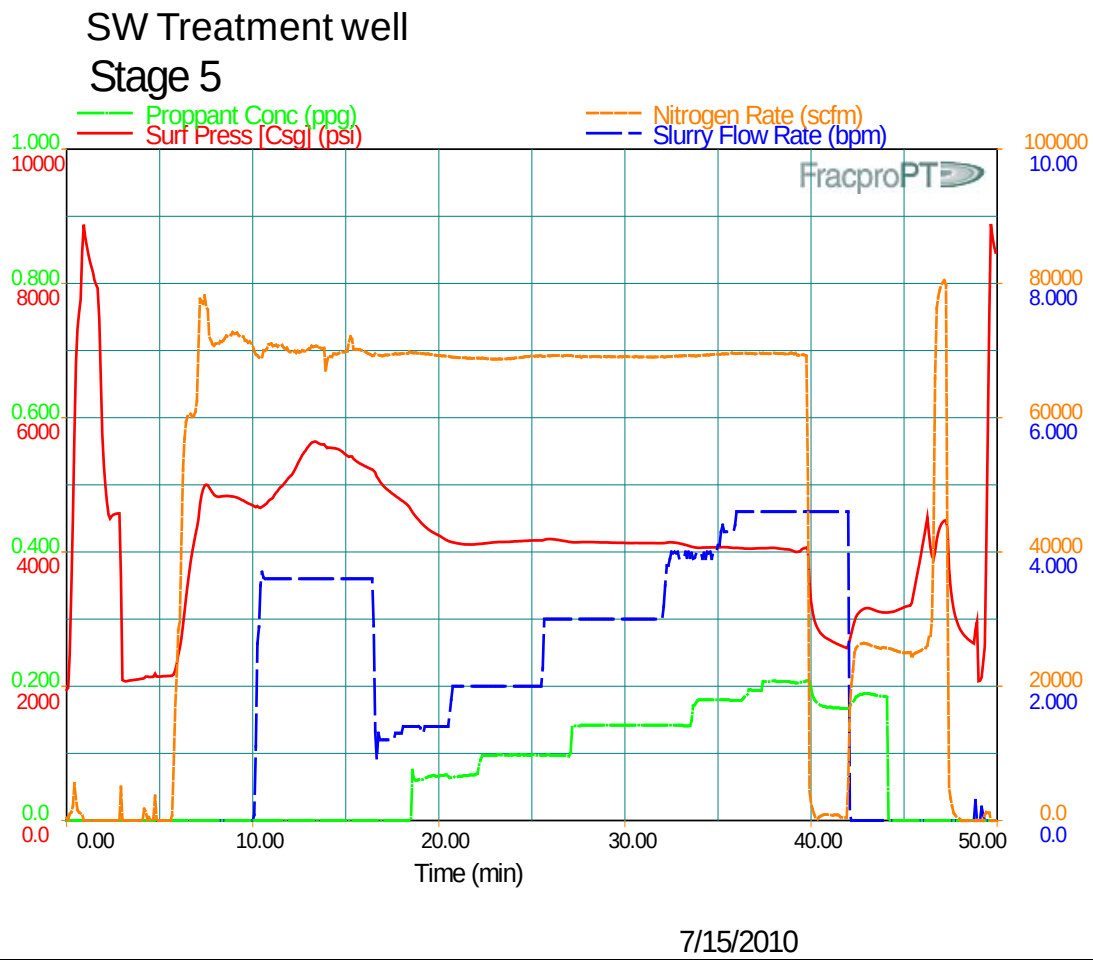


Figure 66. Treatment record, stage 5 (SW treatment well)

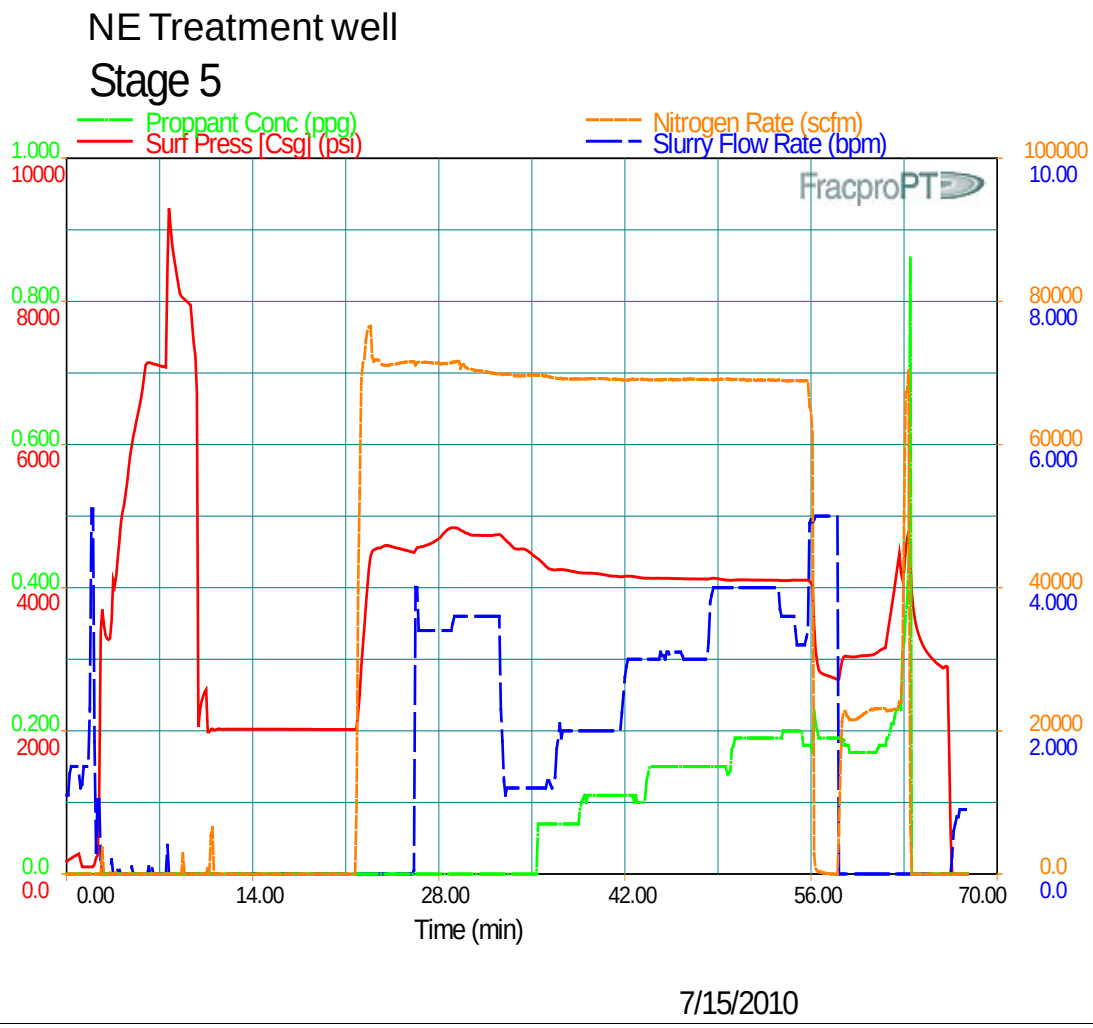


Figure 67. Treatment record, stage 5 (NE treatment well)

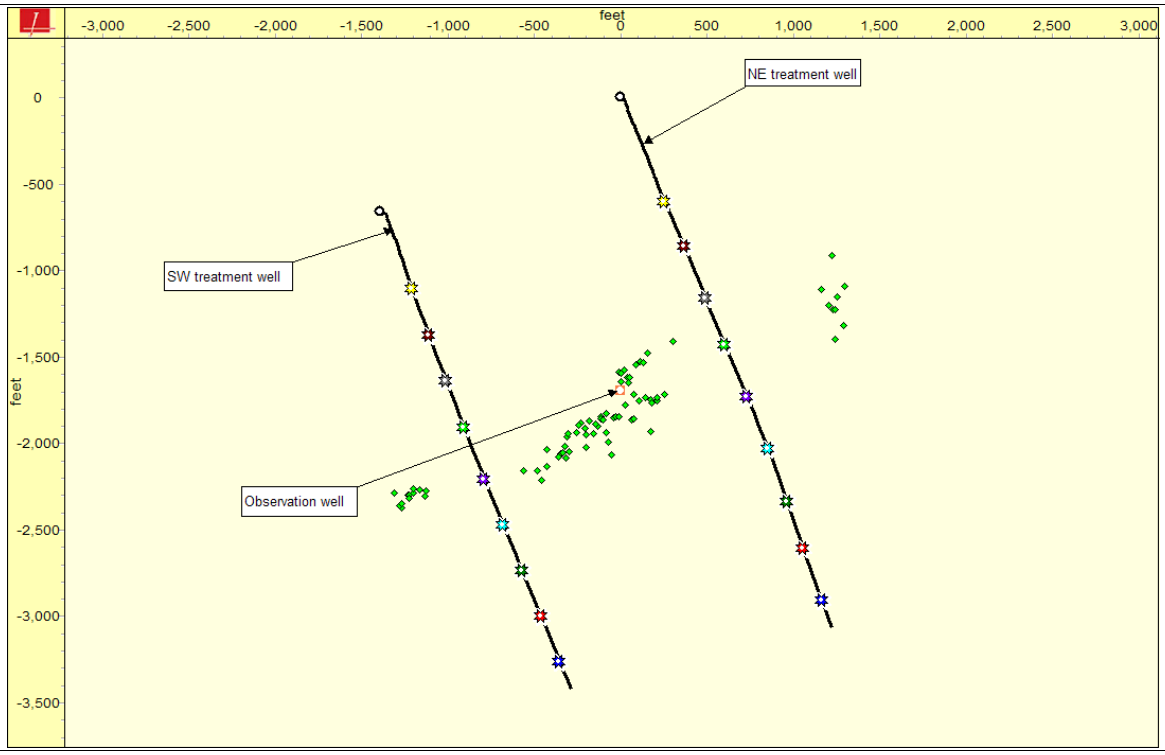


Figure 68. Map view, stage 6

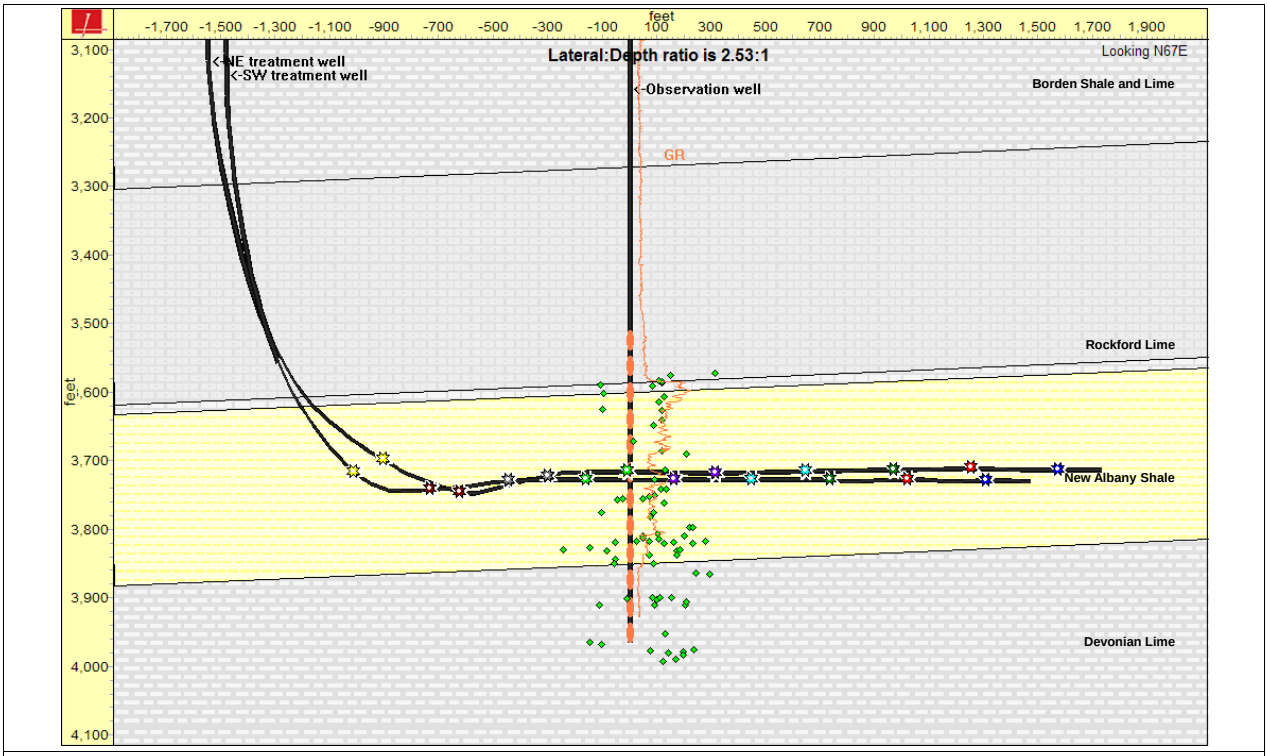


Figure 69. Lateral side view (orthogonal to lateral), stage 6

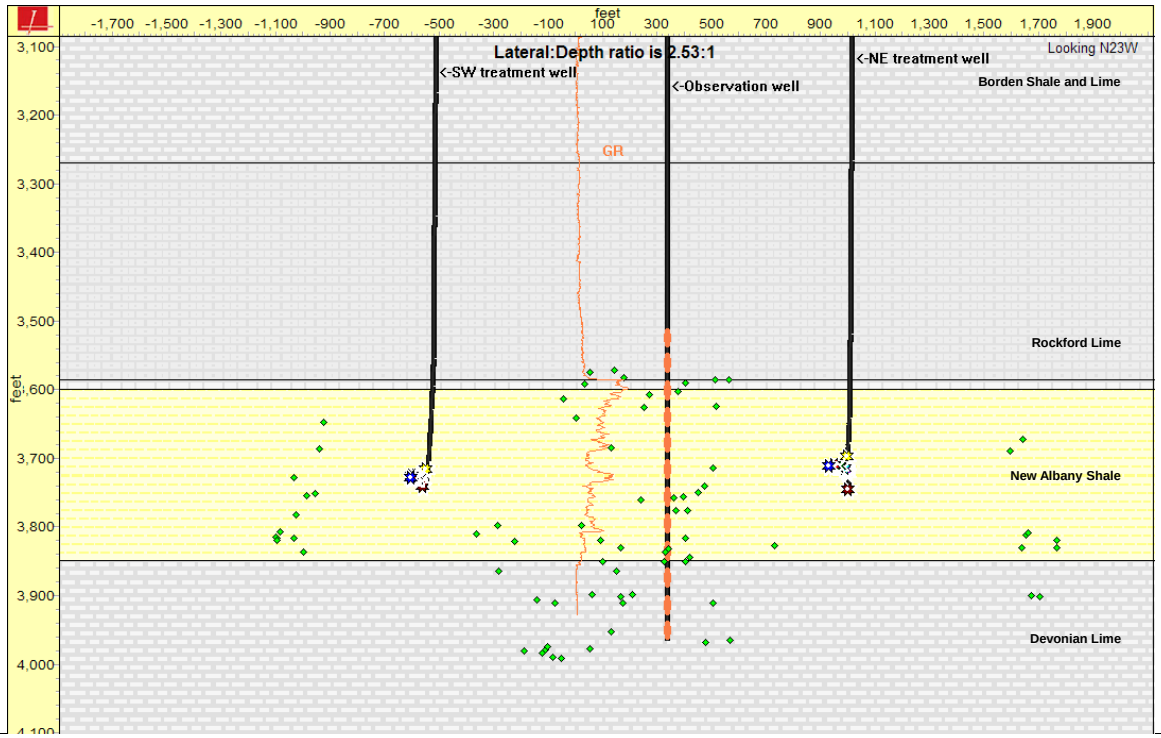


Figure 70. Lateral end-on view (along lateral), stage 6

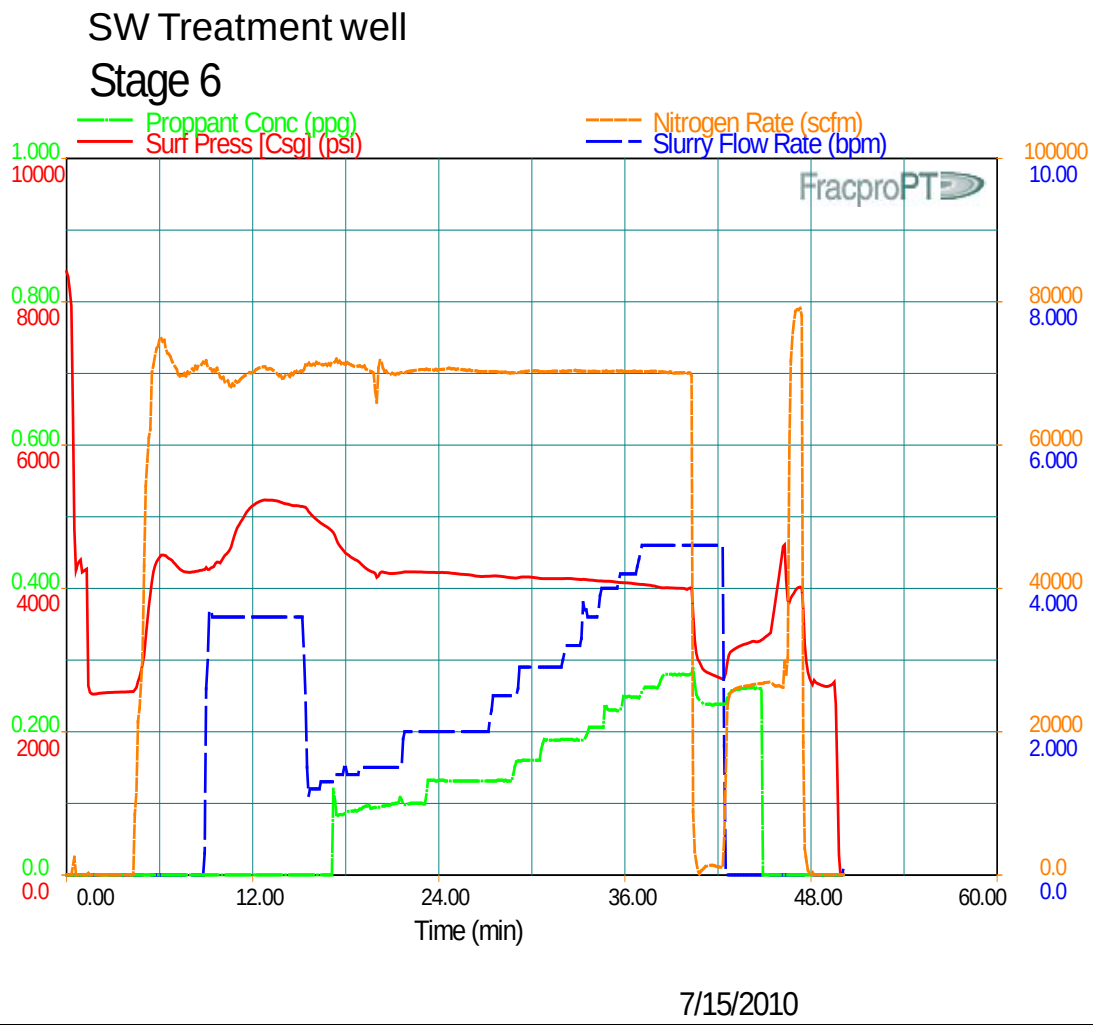


Figure 71. Treatment record, stage 6 (SW treatment well)

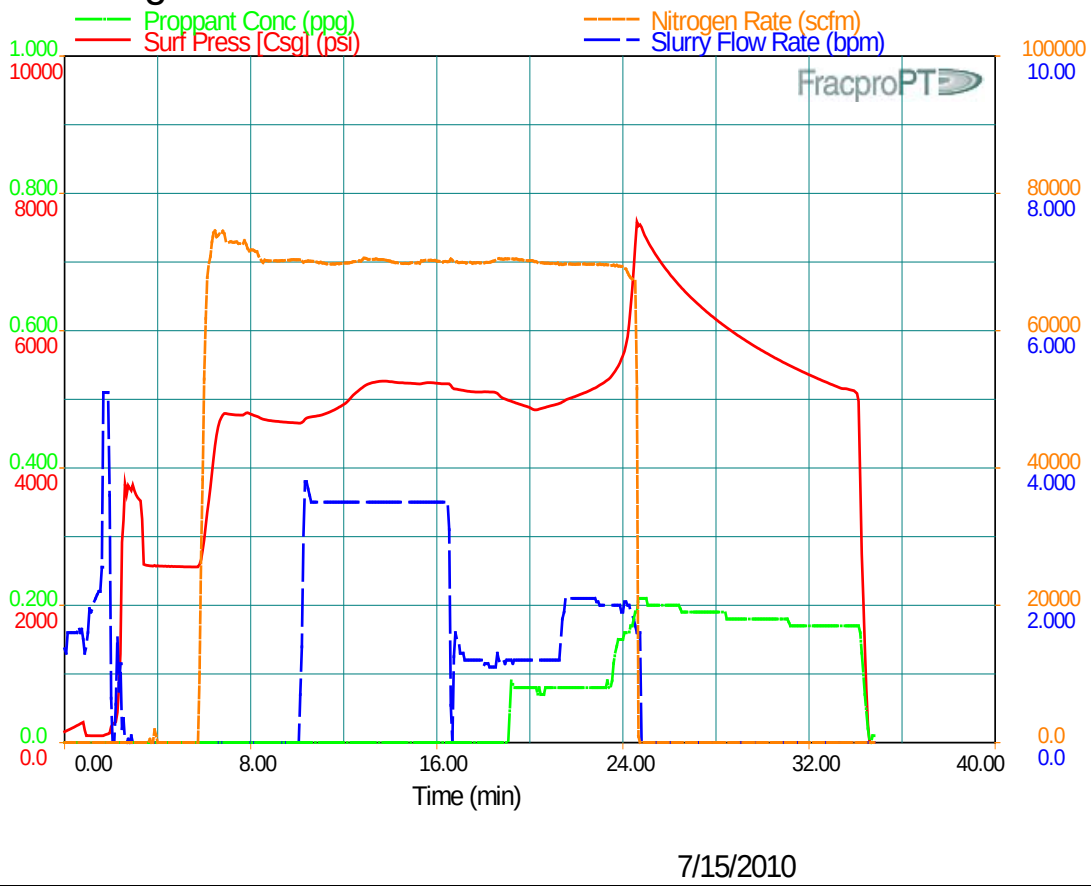


Figure 72. Treatment record, stage 6 (NE treatment well)

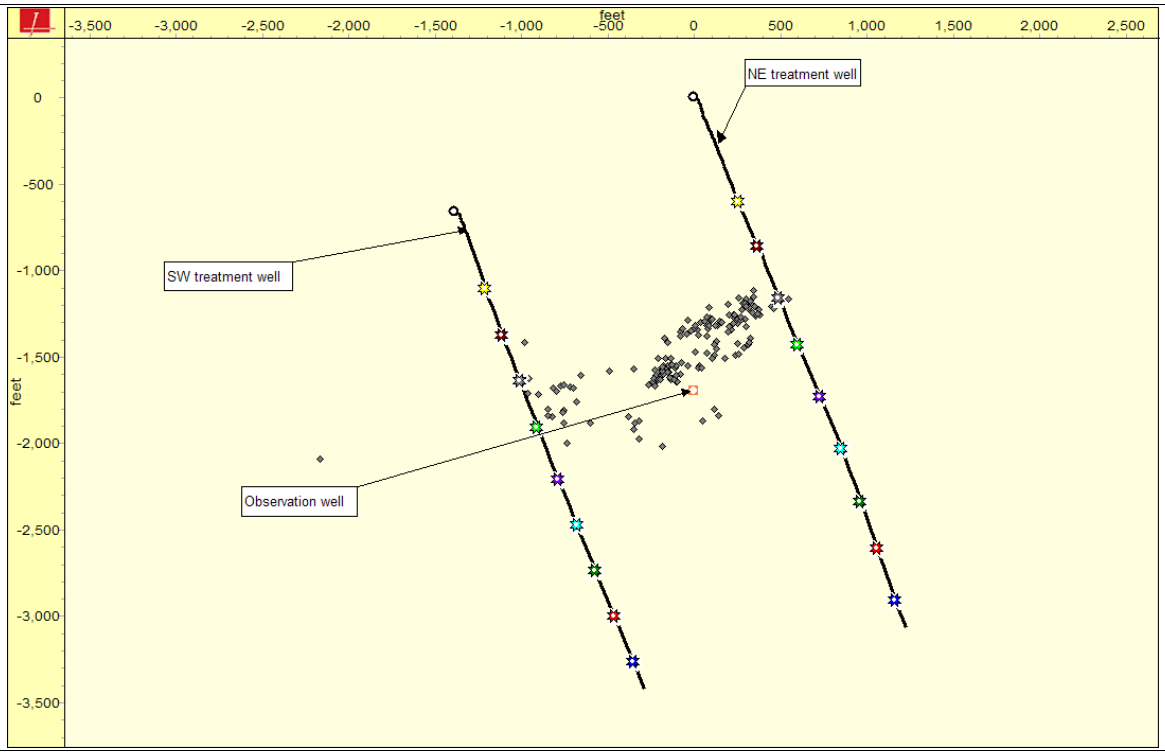


Figure 73. Map view, stage 7

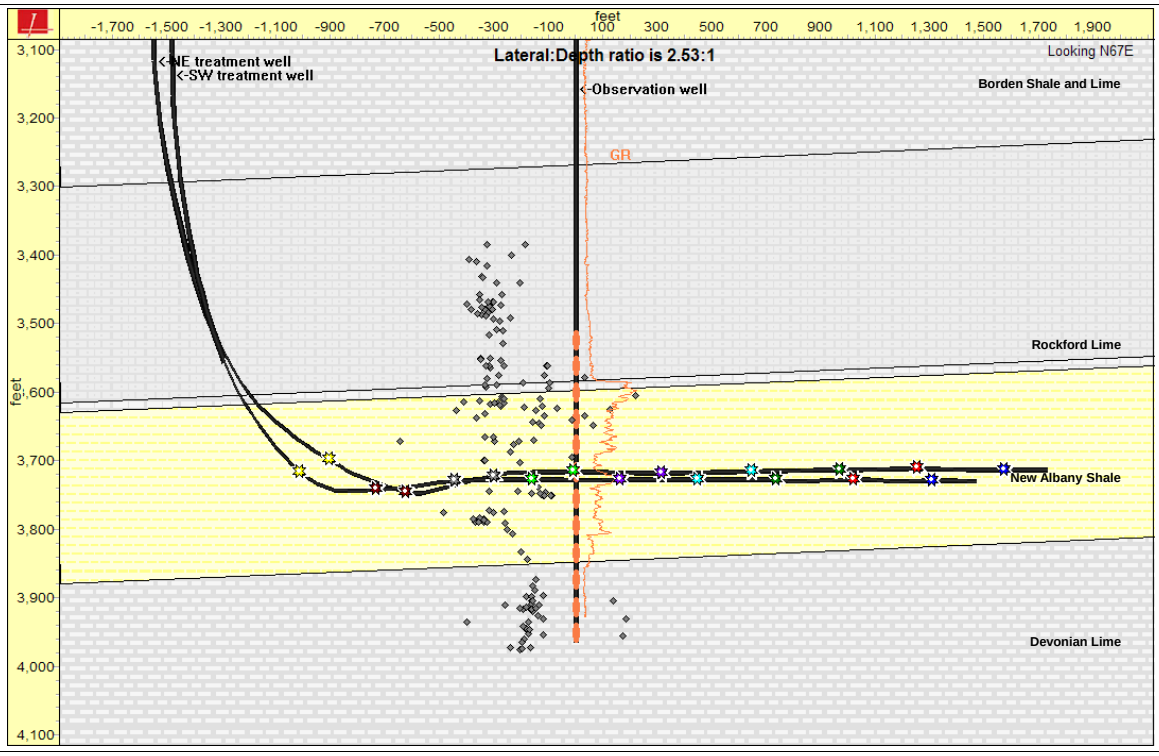


Figure 74. Lateral side view (orthogonal to lateral), stage 7

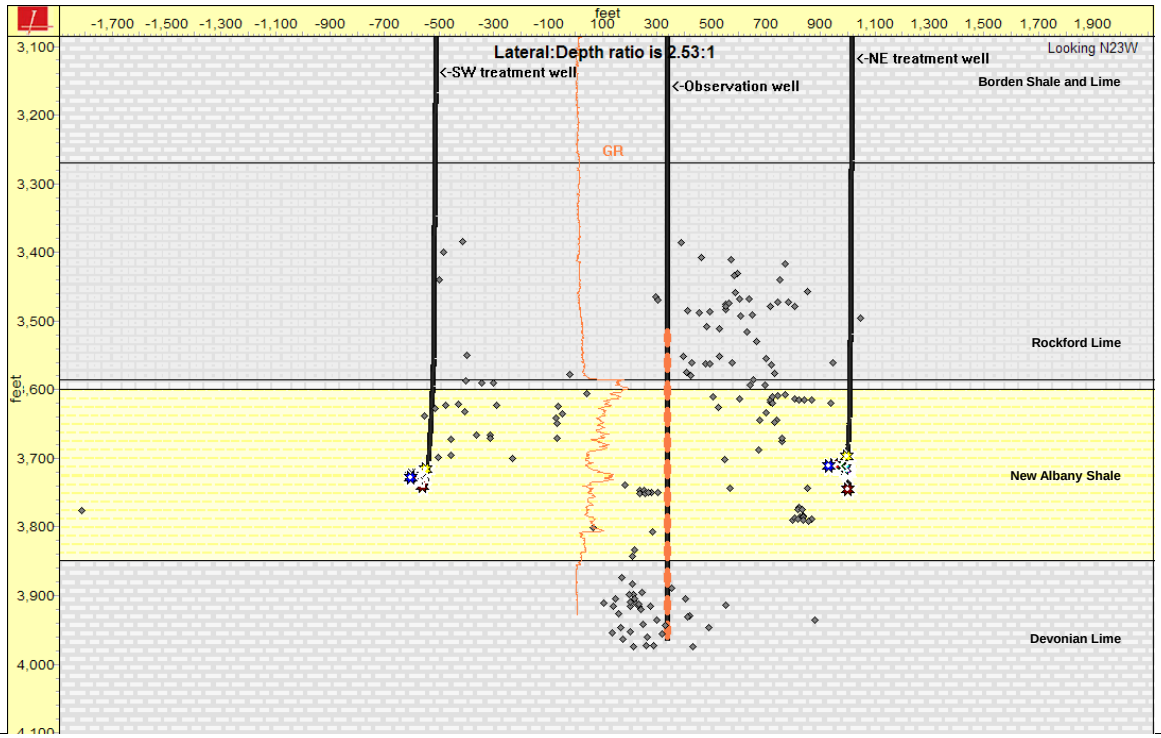


Figure 75. Lateral end-on view (along lateral), stage 7

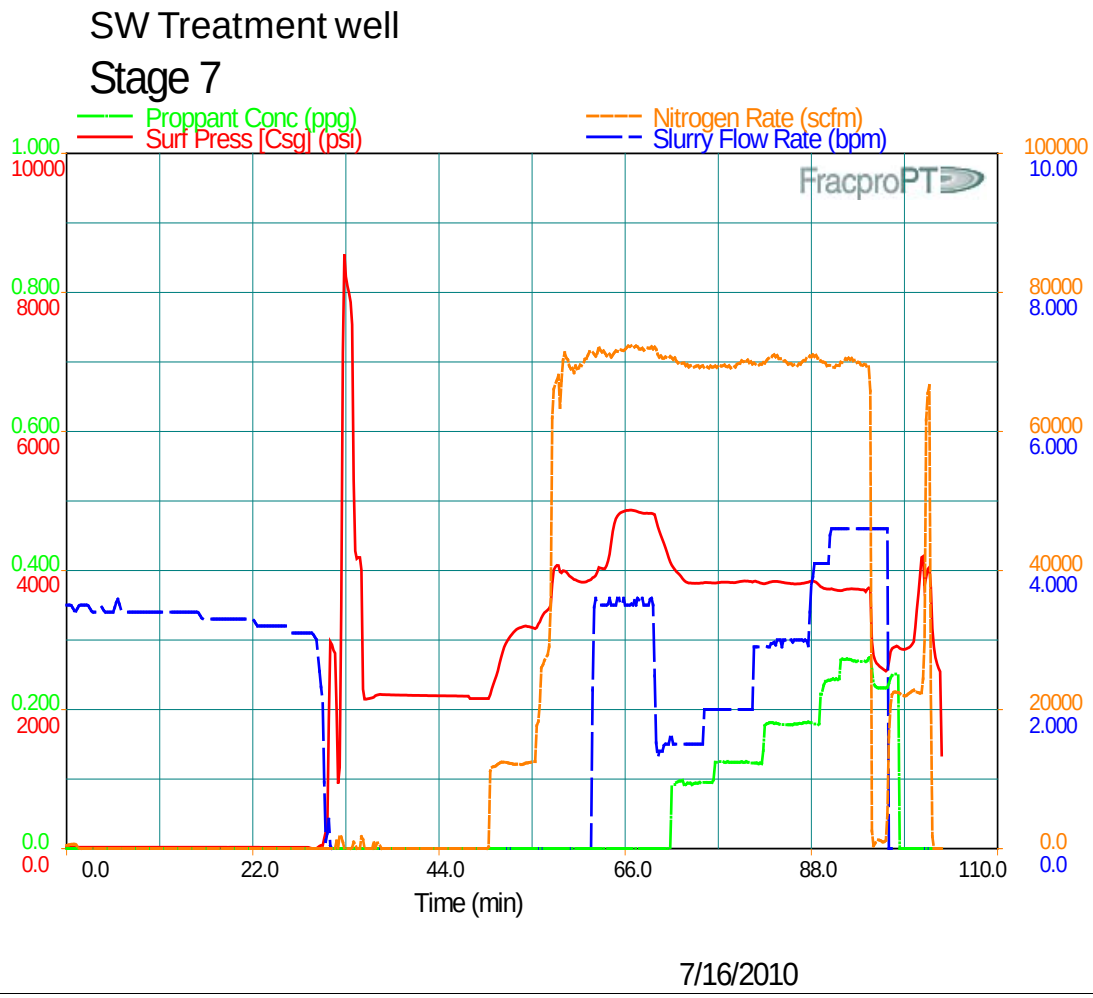


Figure 76. Treatment record, stage 7 (SW treatment well)

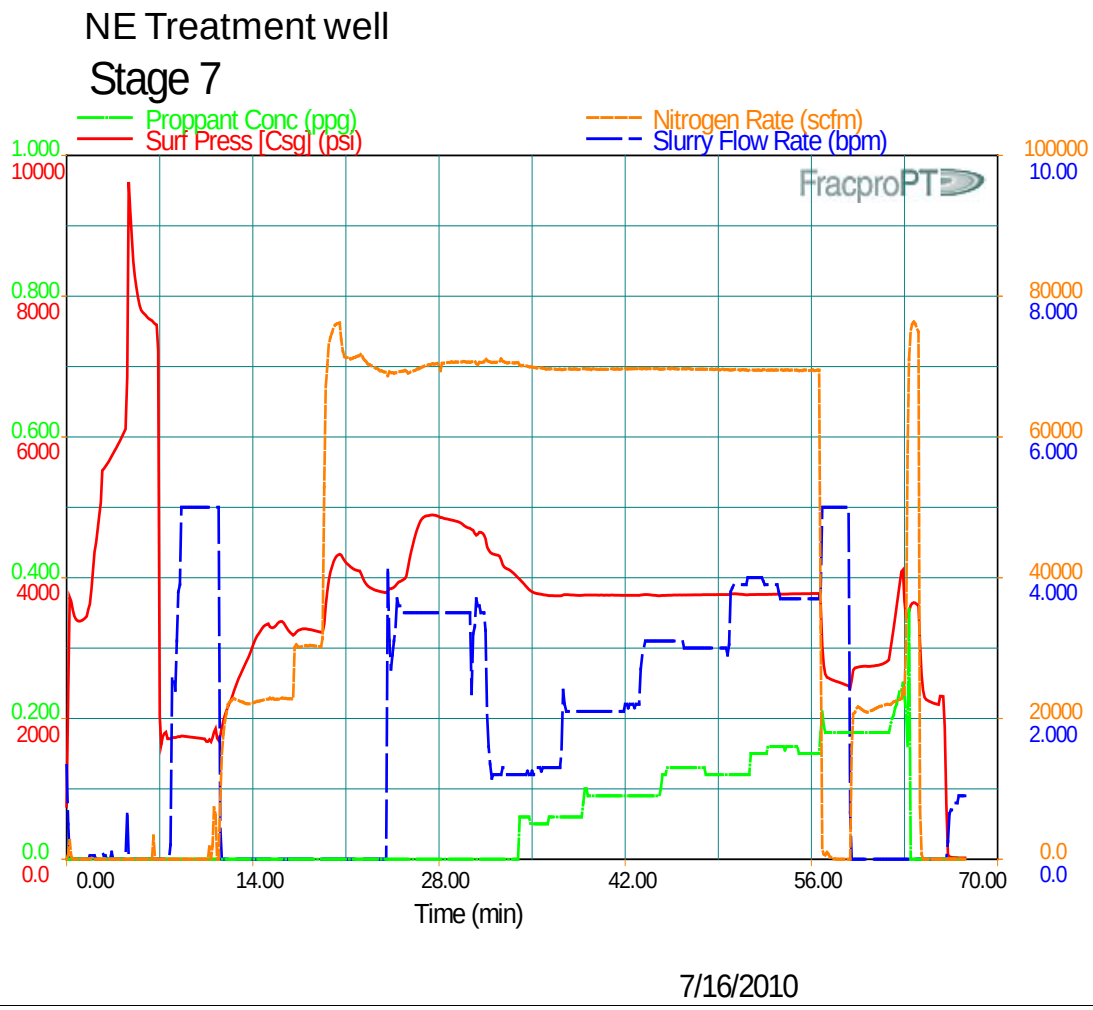


Figure 77. Treatment record, stage 7 (NE treatment well)

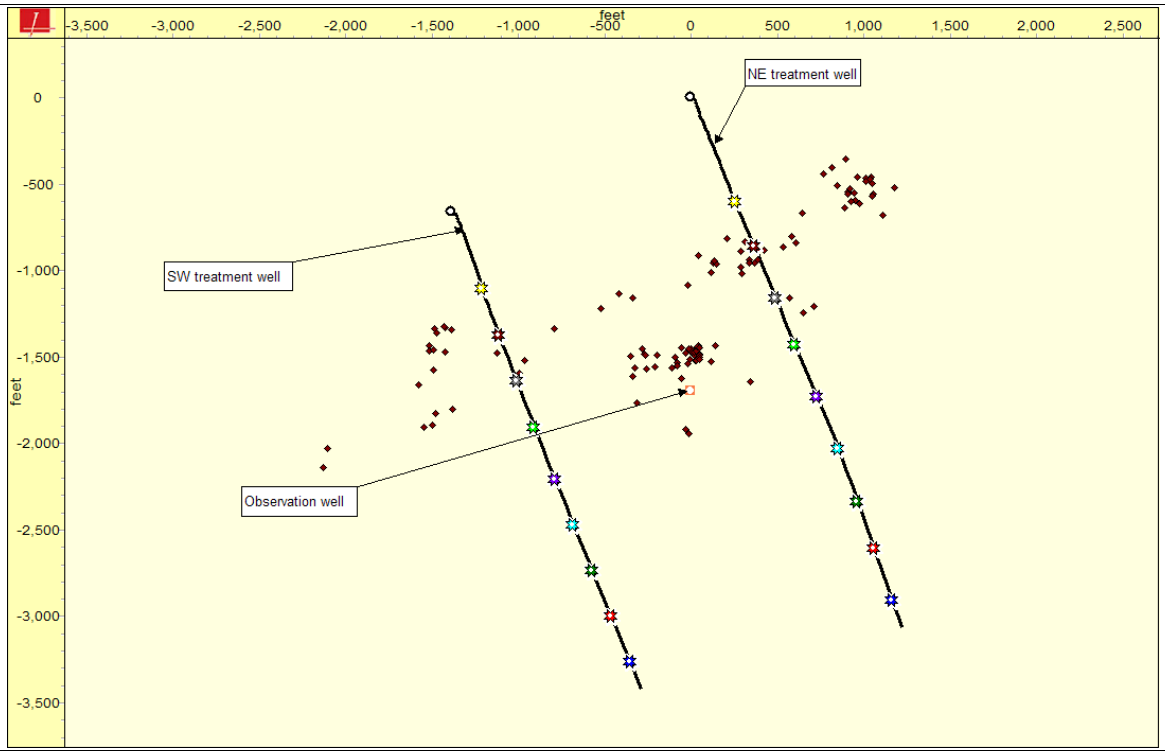


Figure 78. Map view, stage 8

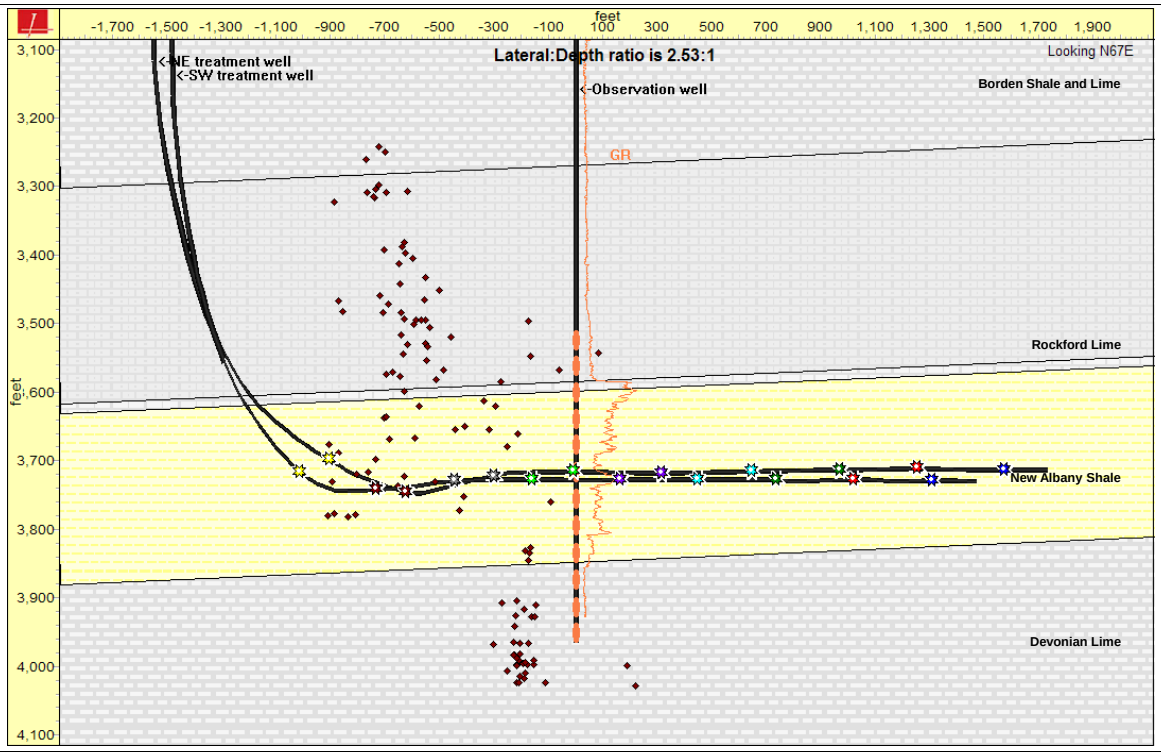


Figure 79. Lateral side view (orthogonal to lateral), stage 8

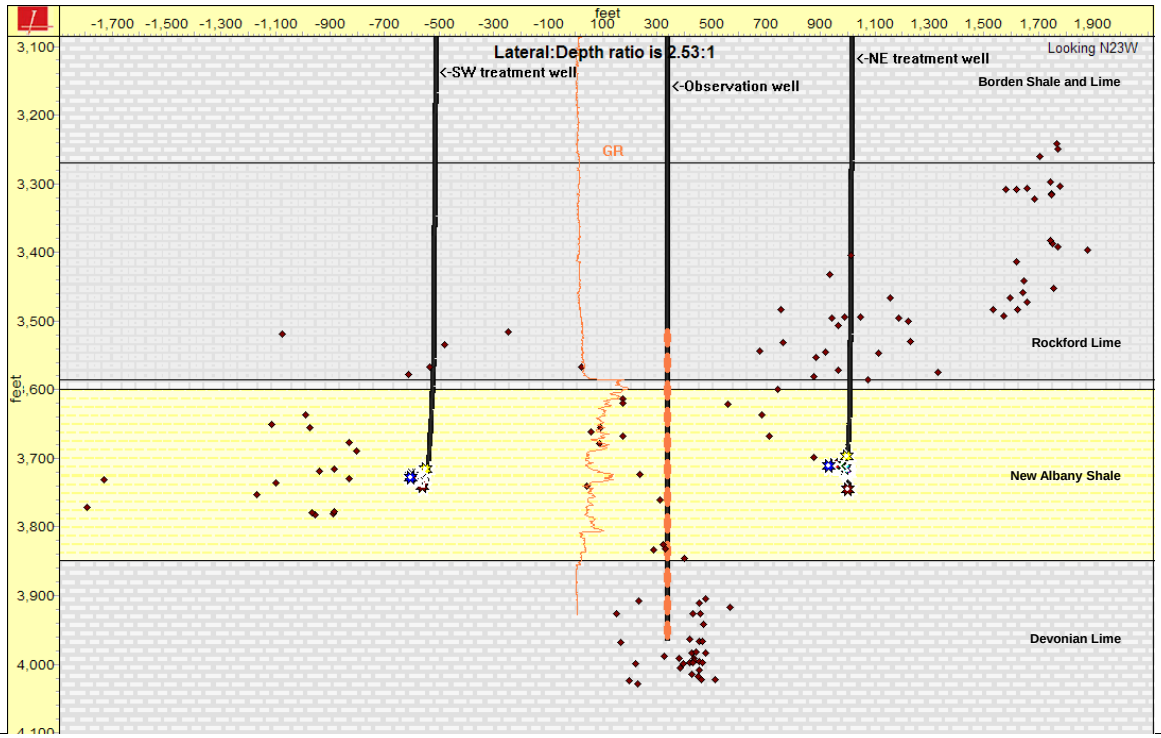


Figure 80. Lateral end-on view (along lateral), stage 8

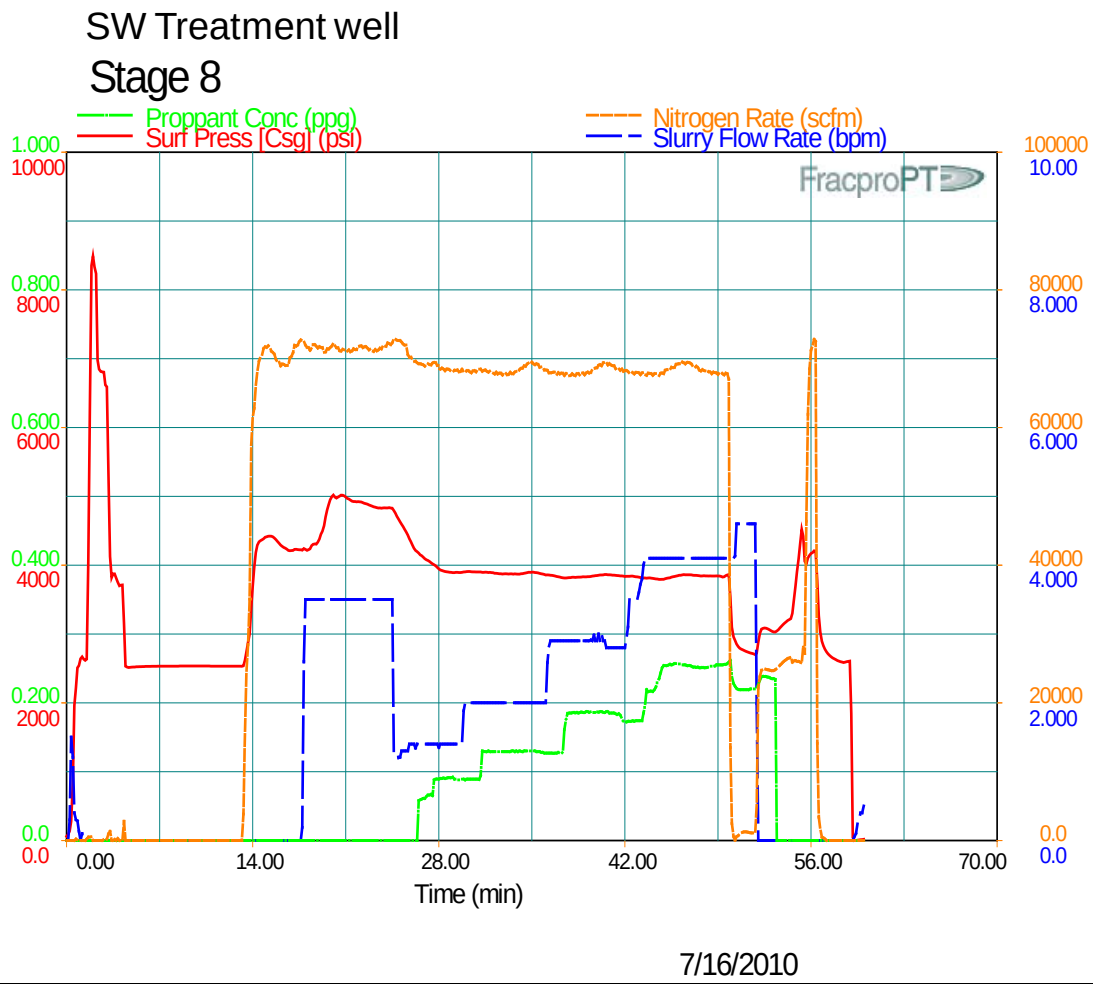


Figure 81. Treatment record, stage 8 (SW treatment well)

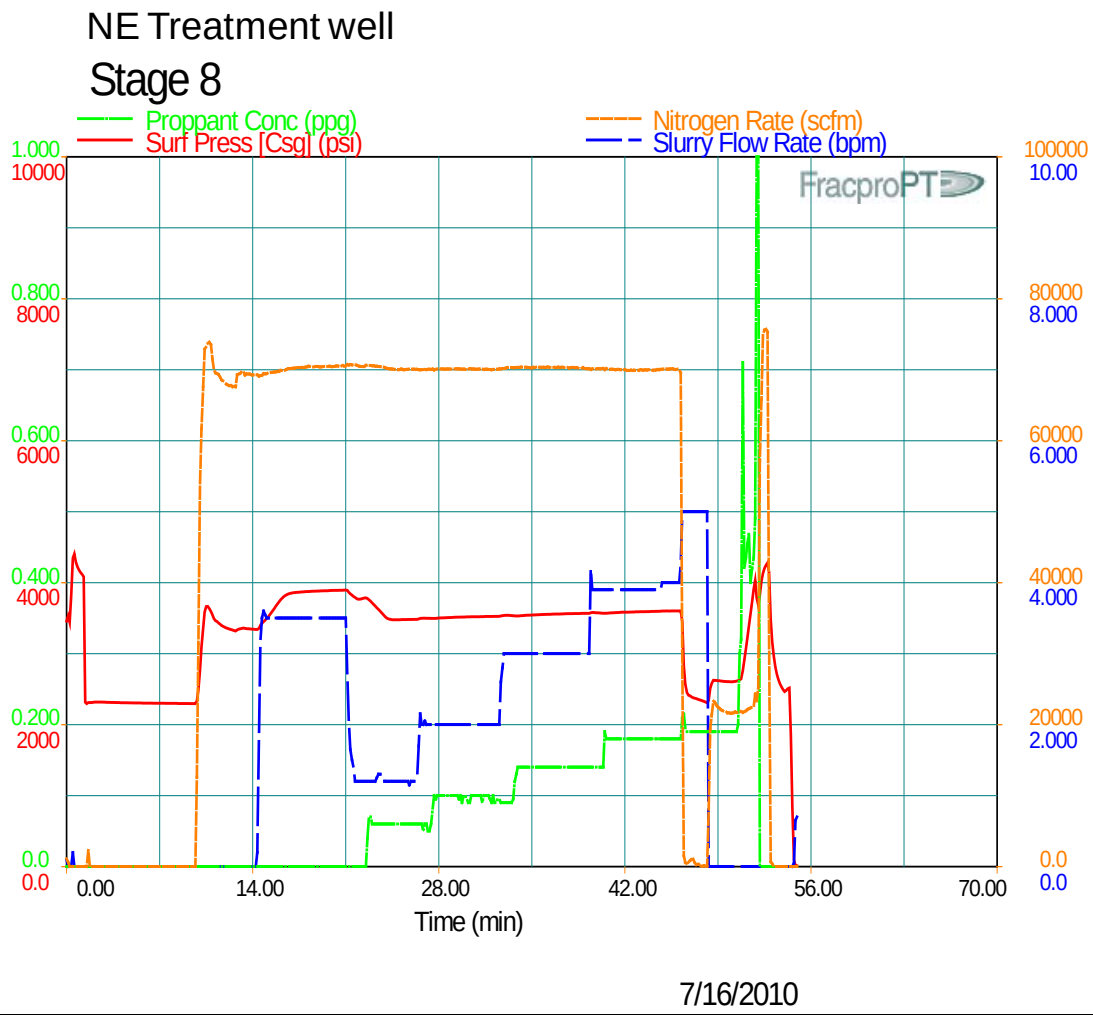


Figure 82. Treatment record, stage 8 (NE treatment well)

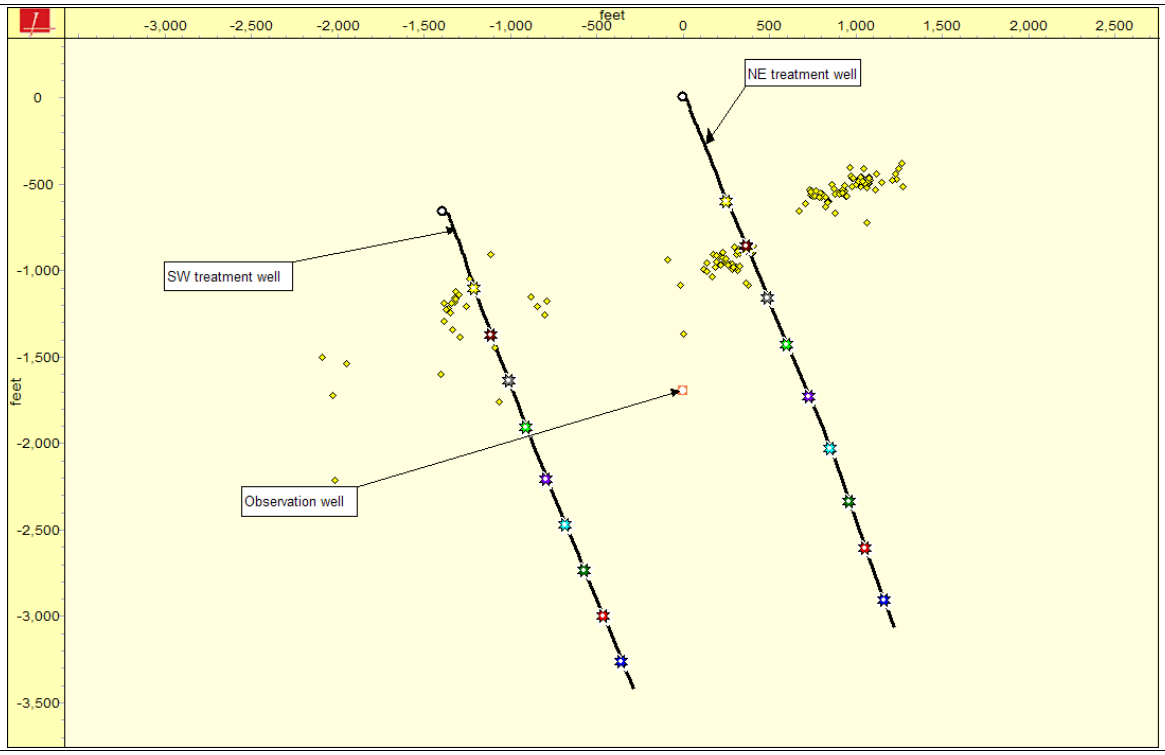


Figure 83. Map view, stage 9

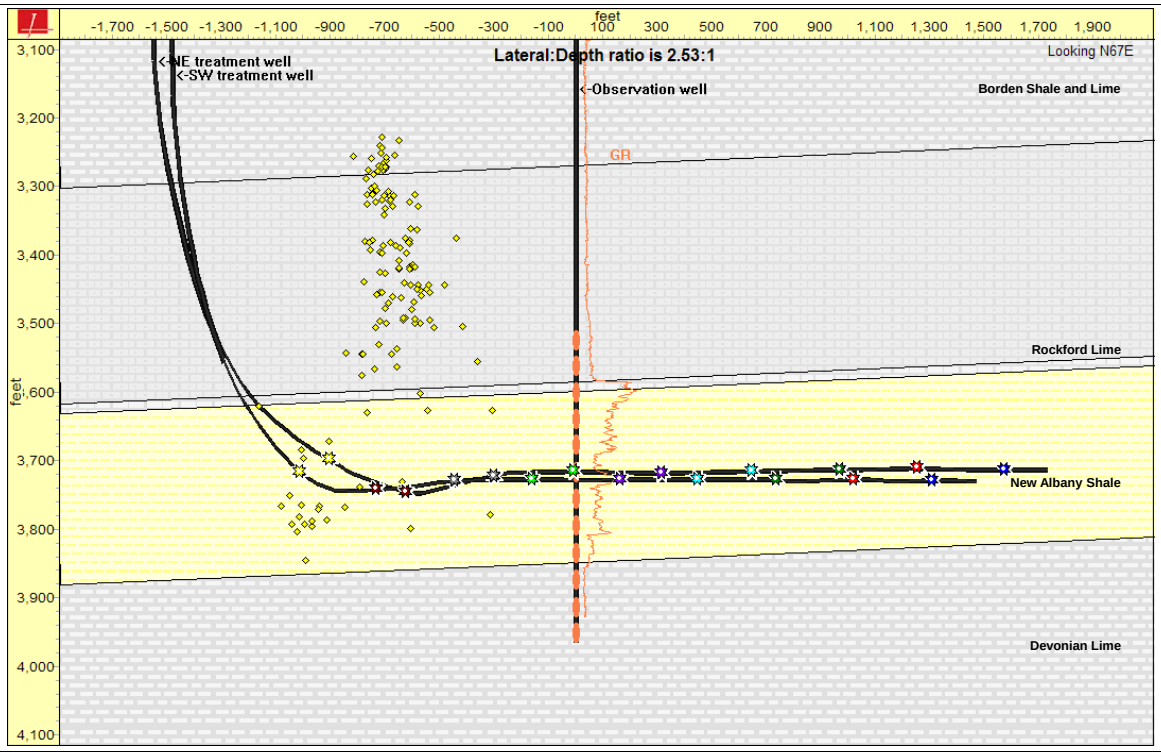


Figure 84. Lateral side view (orthogonal to lateral), stage 9

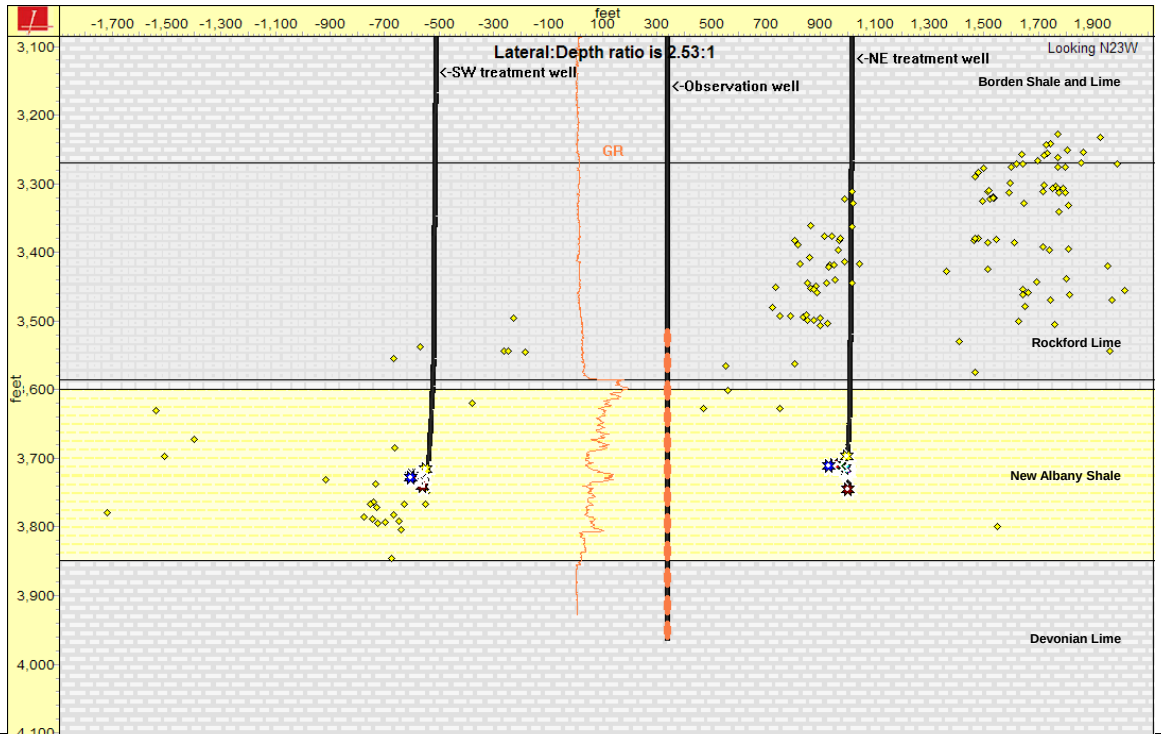


Figure 85. Lateral end-on view (along lateral), stage 9

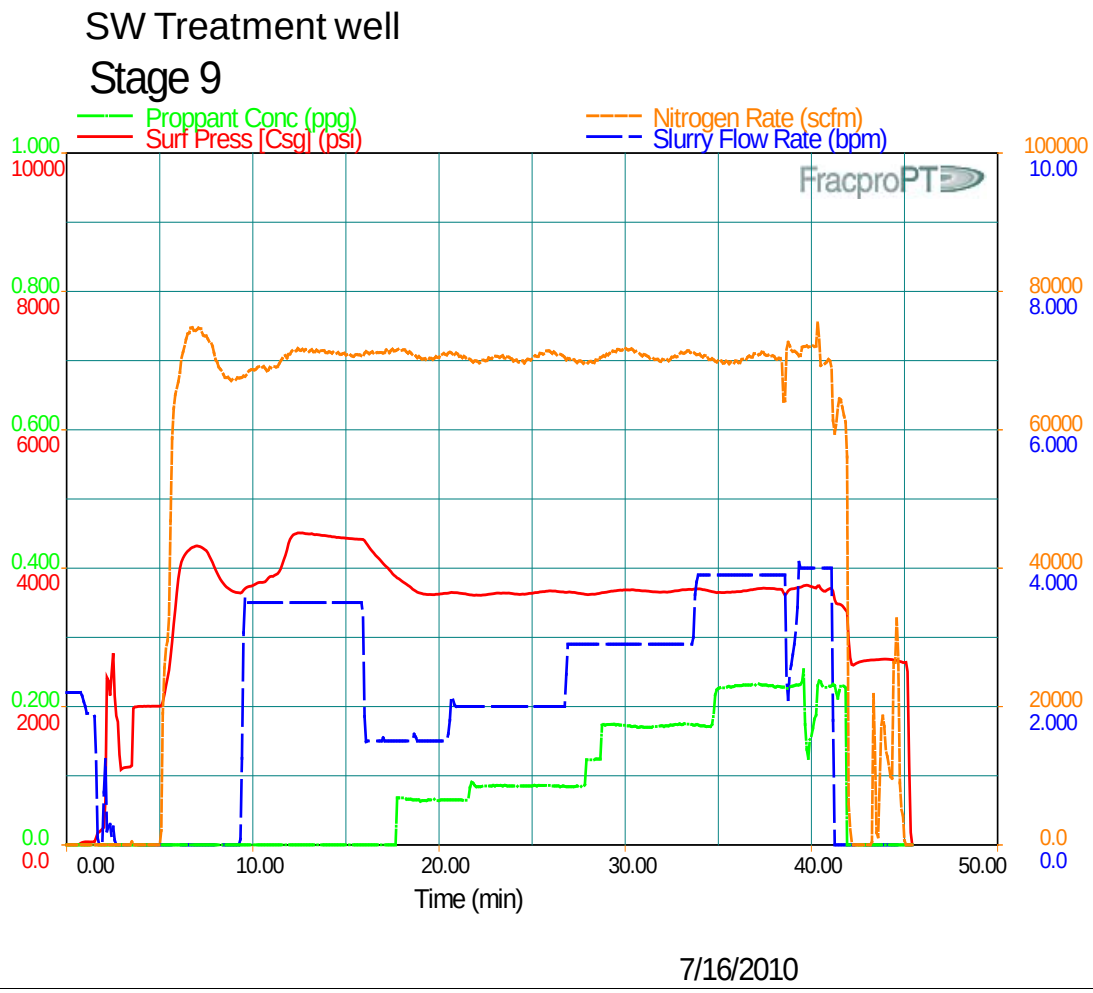


Figure 86. Treatment record, stage 9 (SW treatment well)

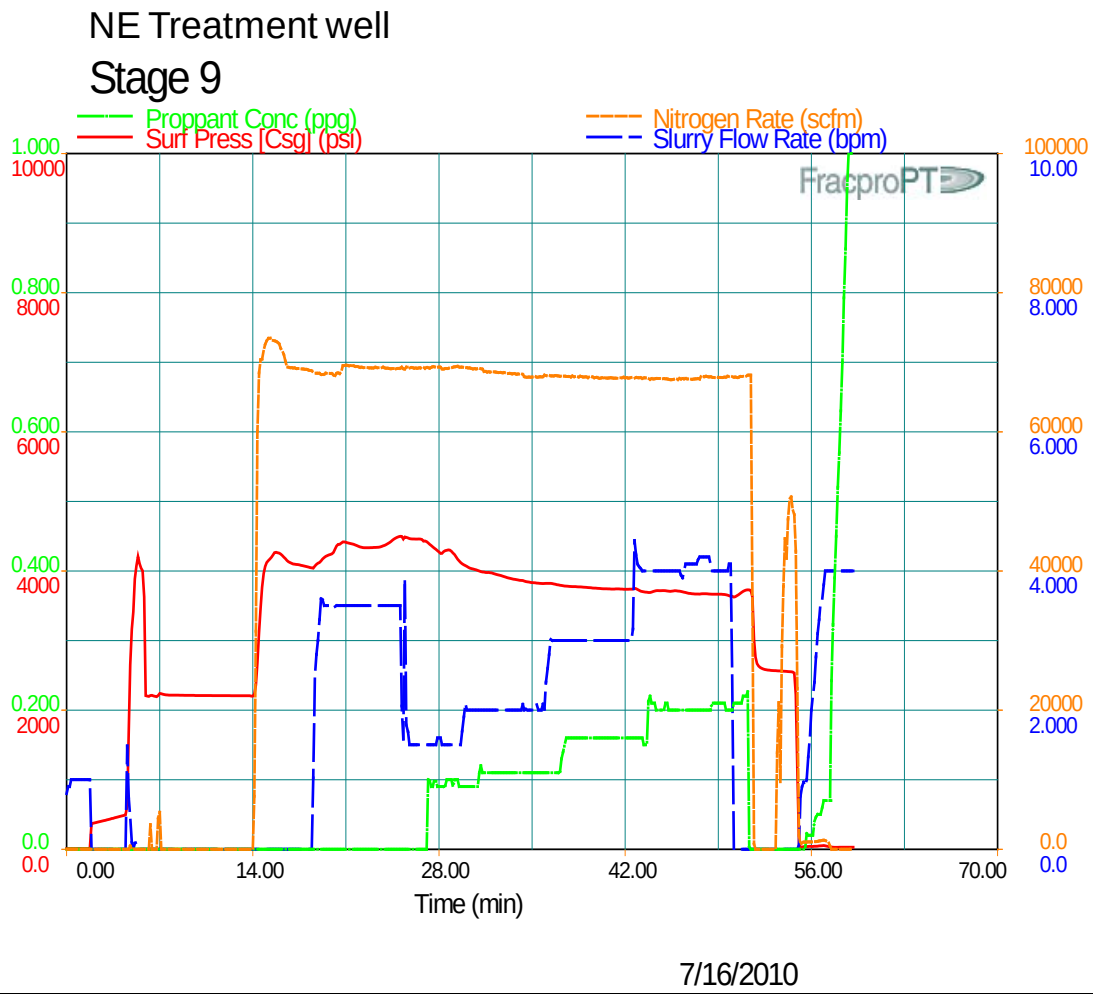


Figure 87. Treatment record, stage 9 (NE treatment well)

5.2 Quality Assurance

The key areas for quality assurance in analysis are microseismic tool position and accuracy of event location. These two areas are addressed in this section. The general setup is shown in **Figure 88** and **Figure 89**.

The toolstring is shown in **Figure 91**. The toolstring in the observation well (Observation well) placed the bottom of the string at 3,927 ft. Placement of the array in the observation well was in a good position for the primary mapping target, the New Albany Shale. The vertical distance between the bottom tool and the furthest port was 240 ft. The horizontal distance between the bottom tool and the furthest perforation was 1,680 ft. The approximate vertical distance between the bottom tool and furthest event was 180 ft. The estimated horizontal distance between the bottom tool and the furthest recordable event was 2,165 ft.

The second area of quality assurance is the location of events with respect to the observation wellbore; in this particular case, due to absence of perforation shots, a Vibroseis unit was used prior to the job to orient the tools. The map view presented in **Figure 90** shows the locations of the Vibroseis unit from above. The velocity model that was used in the determination of the microseismic event placement for stages 1 – 3 is shown in **Figure 92**, and stages 4 – 9 in **Figure 93**.

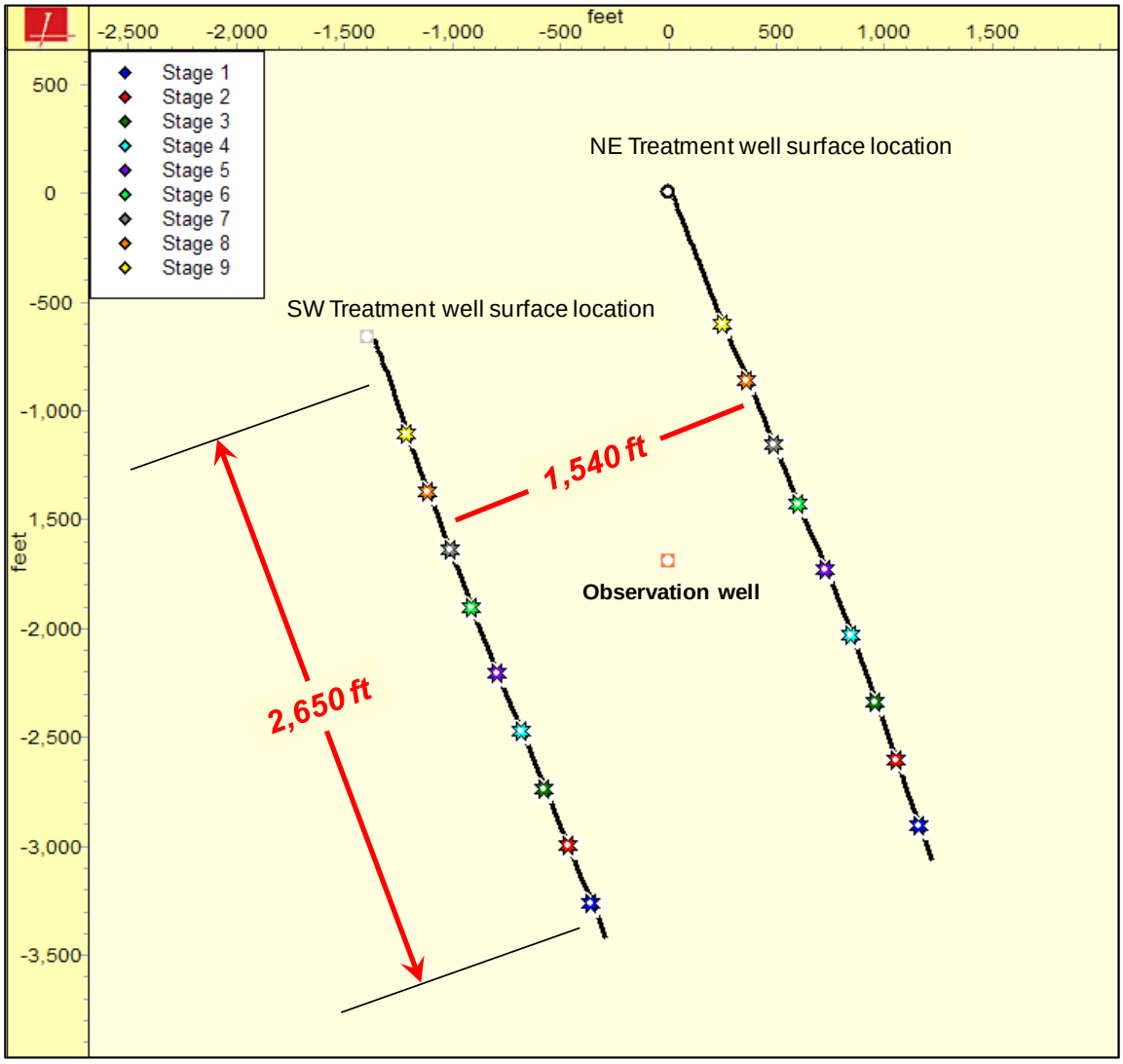


Figure 88. Project setup, map view

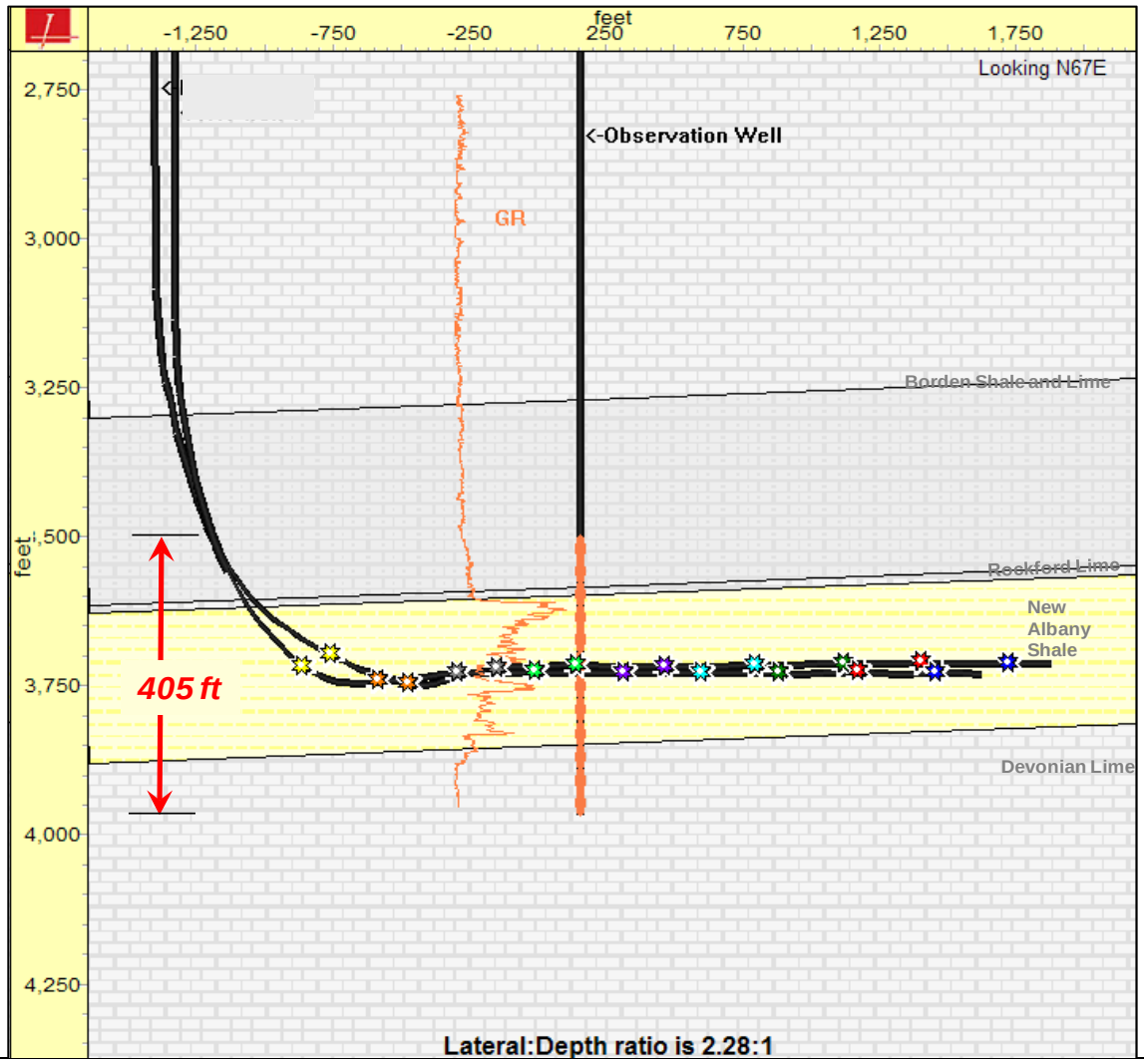


Figure 89. Project setup side view

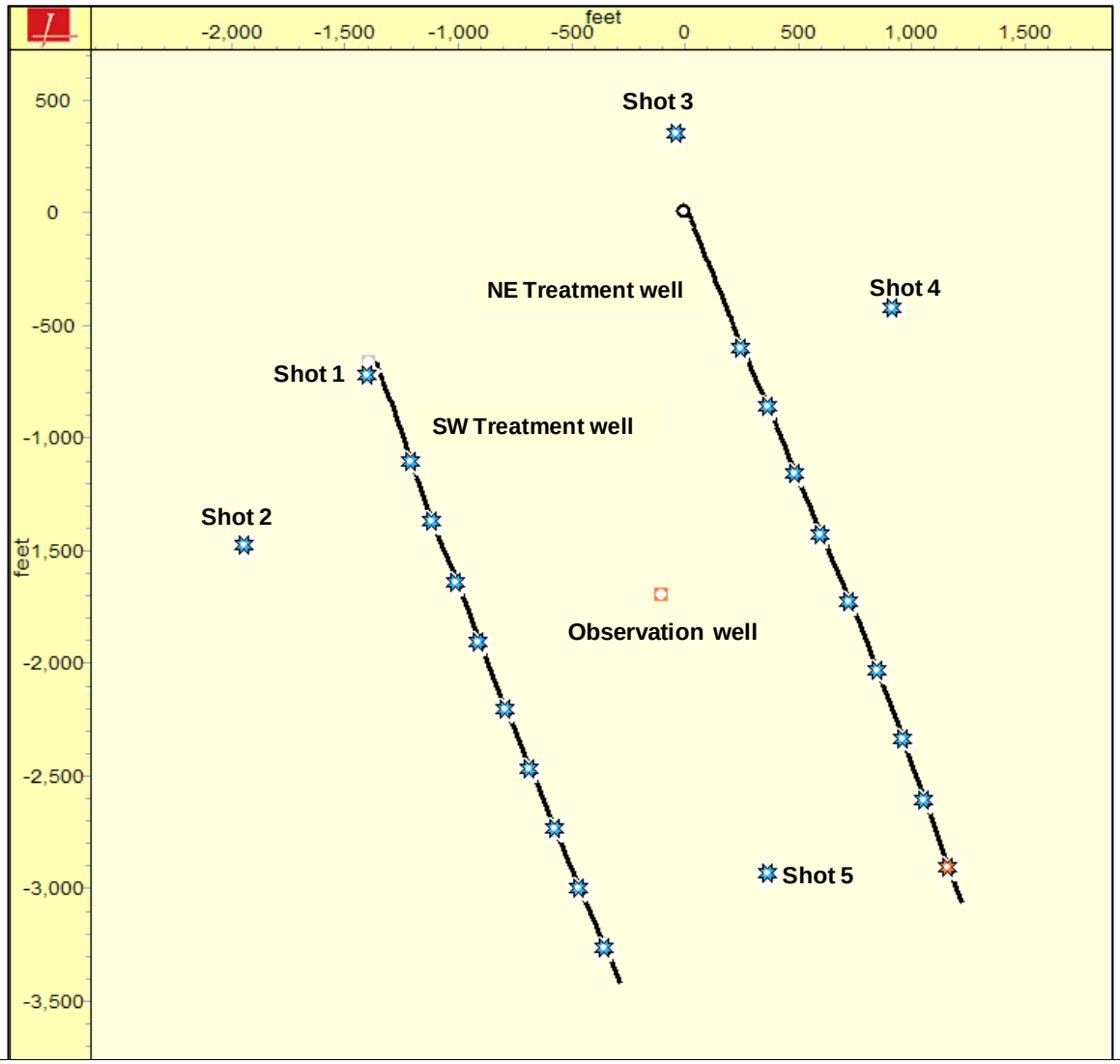
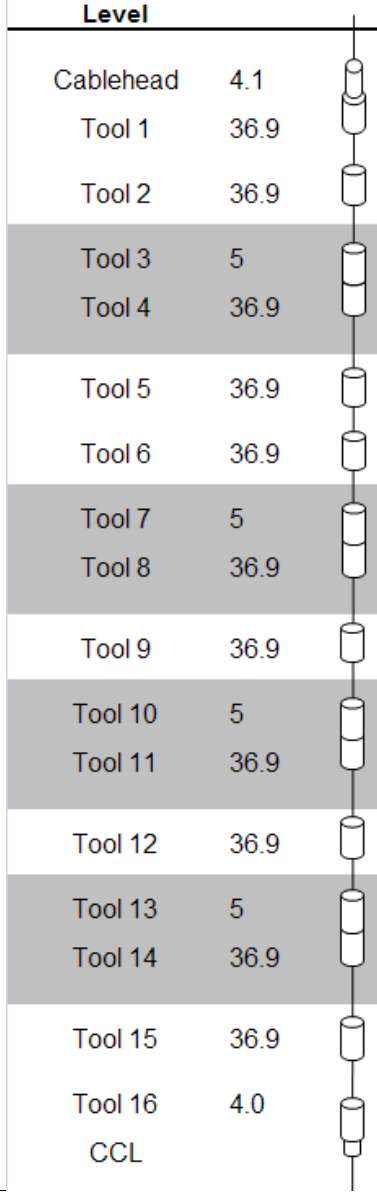


Figure 90. Map view, Vibroseis shot positioning



Level		Depth	Channel (V,H1,H2)	Elec SN	Tube SN
Cablehead	4.1	3492.9			
Tool 1	36.9	3497.0	1,2,3	859	859
Tool 2	36.9	3533.9	4,5,6	934	934
Tool 3	5	3570.8	7,8,9	930	930
Tool 4	36.9	3575.8	10,11,12	913	913
Tool 5	36.9	3612.7	13,14,15	607	518
Tool 6	36.9	3649.6	16,17,18	891	891
Tool 7	5	3686.5	19,20,21	990	990
Tool 8	36.9	3691.5	22,23,24	916	916
Tool 9	36.9	3728.4	25,26,27	915	915
Tool 10	5	3765.3	28,29,30	936	936
Tool 11	36.9	3770.3	31,32,33	822	822
Tool 12	36.9	3807.2	34,35,36	925	925
Tool 13	5	3844.1	37,38,39	922	922
Tool 14	36.9	3849.1	40,41,42	823	823
Tool 15	36.9	3886.0	43,44,45	880	880
Tool 16	4.0	3922.9	46,47,48	926	926
CCL		3926.9			

Figure 91. Toolstring diagram

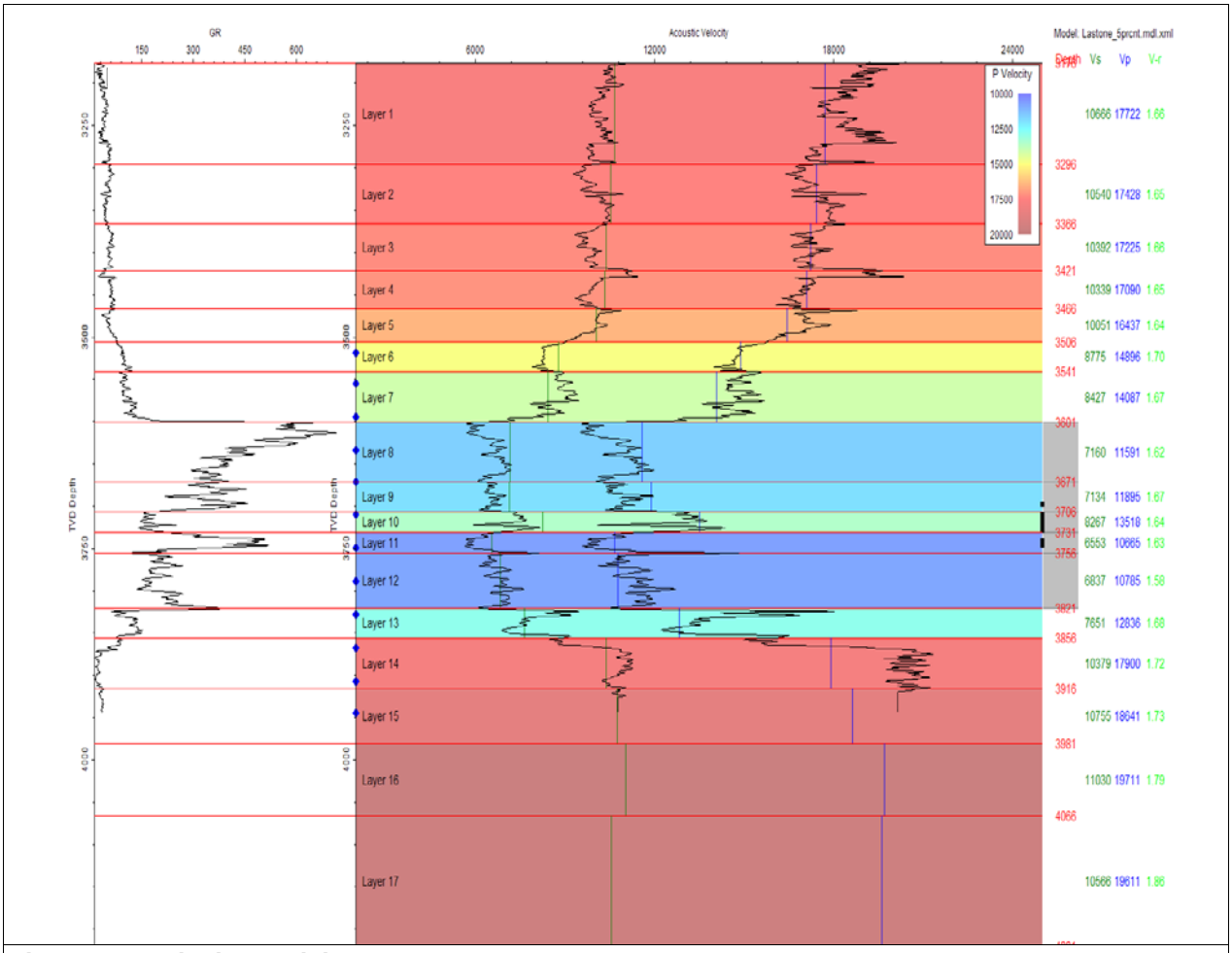


Figure 92. Velocity model, stages 1 – 3

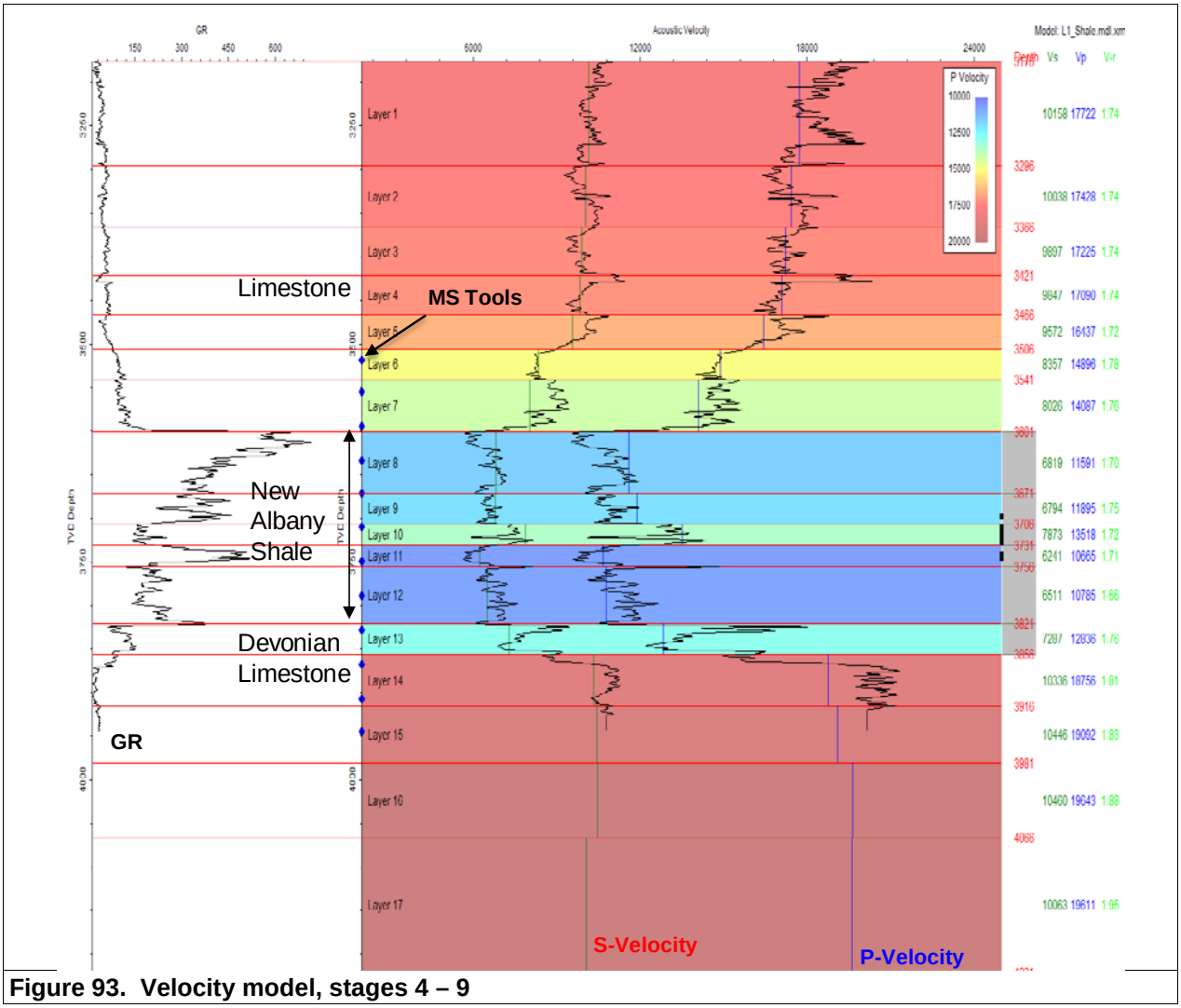


Figure 93. Velocity model, stages 4 – 9

SECTION 7

RESERVOIR ENGINEERING

7.1

TOP-DOWN RESERVOIR ANALYSIS

WEST VIRGINIA UNIVERSITY

A Novel Approach in New Albany Shale Reservoir Modeling

Best Practices Analysis in New Albany Shale

FINAL REPORT

Shahab D. Mohaghegh - Amirmasoud Kalantari-Dahaghi
Petroleum & Natural Gas Engineering Department
West Virginia University

June 2010

THIS PROJECT WAS FUNDED BY:
RESEARCH PARTNERSHIP TO SECURE ENERGY FOR AMERICA

Project Manager: Iraj Salehi

Summary

The intent of this study is to reassess the potential of New Albany Shale formation using a novel and integrated workflow, which incorporates field production data and well logs using a series of traditional reservoir engineering analyses complemented by artificial intelligence & data mining techniques. The model developed using this technology is a full filed model and its objective is to predict future reservoir/well performance in order to recommend field development strategies.

The impact of different reservoir characteristics such as matrix porosity, matrix permeability, initial reservoir pressure and pay thickness as well as the length and the orientation of horizontal wells on gas production in New Albany Shale have been presented.

The study was conducted using publicly available numerical model, specifically developed to simulate gas production from naturally fractured reservoirs.

The study focuses on several New Albany Shale (NAS) wells in Western Kentucky. Production from these wells is analyzed and history matched. During the history matching process, natural fracture length, density and orientations as well as fracture bedding of the New Albany Shale are modeled using information found in the literature and outcrops and by performing sensitivity analysis on key reservoir and fracture parameters.

Sensitivity analysis is performed to identify the impact of reservoir characteristics and natural fracture aperture, density and length on gas production.

Then, the history-matched results of 87 NAS wells have been used to develop a full field reservoir model using an integrated workflow, named Top-Down, Intelligent Reservoir Modeling. In this integrated workflow unlike traditional reservoir simulation and modeling, we do not start from building a geo-cellular model. Top-Down intelligent reservoir modeling starts by analyzing the production data using traditional reservoir engineering techniques such as Decline Curve Analysis, Type Curve Matching, Single-well History Matching, Volumetric Reserve Estimation and Recovery Factor. These analyses are performed on individual wells in a multi-well New Albany Shale gas reservoir in Western Kentucky that has a reasonable production history. Data driven techniques are used to develop single-well predictive models from the production history and the well logs (and any other available geologic and petrophysical data).

Upon completion of the abovementioned analyses a large database is generated .This database includes a large number of spatio-temporal snap shots of reservoir behavior. Artificial intelligence and data mining techniques are used to fuse all these information into a cohesive reservoir model. The reservoir model is calibrated (history matched) using the production history of the most recent set of wells that have been drilled in the field. The calibrated reservoir model is utilized for predictive purposes to identify the most effective field development strategies including locations of infill wells, remaining reserves, and under-

performer wells. Capabilities of this new technique, ease of use and much shorter development and analysis time are advantages of Top-Down modeling as compared to the traditional simulation and modeling.

In addition, 31 recently drilled well in Christian county Western Kentucky-Halley's Mills quadrangle have been used to perform Top-down modeling. Zone manager feature of Geographix software is used .The available production data are going to be the attributes in this feature. The contours are generated and the results have been compared with the result of Top-down modeling (Fuzzy pattern recognition). Structural map, isopach map and the other geological map has been generated using Geographix.

Additionally ,in order to indentify the effect of horizontal lateral length on well productivity from New Albany Shale, fracture network has been regenerated in order to represent the distribution of natural fracture in that formation.

Table of Contents

Summary.....**Error! Bookmark not defined.**

List of Figures..... viii

List of Tables..... xii

Chapter 1..... 1

Introduction..... 1

1.1 Unconventional Gas Reservoirs..... 1

1.2 Naturally fractured Shale gas Reservoirs..... 3

1.3 New Albany Shale Formation..... 10

Chapter 2..... 14

Methodology..... 14

2.1 New Albany Shale Natural Fracture Network Modeling and Simulation..... 14

2.2 Top-Down Intelligent Reservoir Modeling of New Albany Shale..... 14

2.2.1 Traditional Reservoir Simulation & Modeling..... 14

2.2.2 Top-Down Intelligent Reservoir Modeling as an Alternate/Complement to Conventional Reservoir Modeling Techniques..... 16

Chapter 3..... 20

Results and Discussion..... 20

3.1 Sensitivity Analysis on Reservoir and Fracture Properties..... 22

3.2 History Matched Model..... 27

3.3 Effect of lateral orientation on well productivity..... 29

3.4 Horizontal Lateral Length Effect on Well Productivity..... 30

3.5 Economic Analysis..... 35

3.6 Data Preparation Procedure for Top-down Modeling..... 38

3.7 Model Calibration and Validation..... 46

3.8 Model Calibration and Validation..... 50

3.9 New Albany Shale Subsurface Modeling-Recently Completed Gas Wells..... 52

3.10 Model Calibration and Validation..... 65

Chapter 4..... 68

Concluding Remarks 68

Technology Transfer..... 68

Acknowledgment..... 68

References 69

Appendix A..... 72

List of Figures

Figure 1.Gas shale storage and flow capacity diagram showing pore type, flow type, dominant particle motion within a given flow regime.(12) 7
Figure 2.Major shale gas basins in the United States with total resource potential of 500 to 1,000 tcf.(13) 8
Figure 3. New Albany Shale formation throughout the Illinois basin and Under-study area... 10
Figure 4. Conventional Reservoir Simulation &Modeling-A Bottom-Up Approach..... 16
Figure 5. Top-down Intelligent Reservoir Modeling Workflow 17
Figure 6. Integrated workflow for New Albany Shale Reservoir Modeling 19
Figure 7. Schematic showing outcrop fracture features of the New Albany shale..... 20
Figure 8. Simulation result examples for one history-matched New Albany Shale Gas well.. 22
Figure 9. Sensitivity analysis on initial reservoir pressure
Figure 10. Sensitivity analysis on matrix porosity 23
Figure 11. Sensitivity analysis on matrix permeability
Figure 12. Sensitivity analysis on pay thickness 24
Figure 13. Sensitivity analysis on Aperture reduction
Figure 14. Sensitivity analysis - Effect of reservoir and fracture properties variation on initial gas rate factor (Monthly gas production)..... 24
Figure 15 . Fracture Length Values
Figure 16. Fracture Density Values ……. 25
Figure 17. Sensitivity analysis results (Monthly gas production)
Figure 18. Sensitivity analysis results (Monthly gas production) 26
Figure 19. Sensitivity analysis results (Monthly gas production)
Figure 20. Sensitivity analysis results (Monthly gas production) (Medium fracture network density with variable length)(High fracture network density with variable length)..... 26
Figure 21. Sensitivity analysis results (Monthly gas production) 26
Figure 22. Single well history matching result, after changing the key 27
Figure 23. The well and fracture intersection for the history matched model (Based on 320 acre spacing)..... 29
Figure 24. Horizontal well orientations in Y direction (0, 30, 45, 60, and 90 degrees) 29
Figure 25. Single well history matching result-Zero and 30-degree well orientation (From left to right)..... 30
Figure 26.Effect of horizontal lateral length on well productivity from New Albany Shale ... 31
Figure 27.Cumulative gas production as a function of horizontal lateral length for 1, 3,5,10, and 30 years of Cum. Production 32
Figure 28. Initial rate as a function of horizontal lateral length..... 32
Figure 29.Pressure distribution in the reservoir as a function of time (2nd month and 30th years of production..... 33

Figure 30.Pressure distribution in the reservoir as a function of time (2nd month and 30th years of production-from left to right) (Green represent the lower pressure and red shows max reservoir pressure)(5 mile lateral length)..... 33
Figure 31.Pressure distribution in the reservoir as a function of time (2nd month and 30th years of production-from left to right) (Green represent the lower pressure and red shows max reservoir pressure)(7.5 mile lateral length)..... 34
Figure 32.Pressure distribution in the reservoir as a function of time (2nd month and 30th years of production-from left to right) (Green represent the lower pressure and red shows max reservoir pressure) (9 mile lateral length)..... 34
Figure 33.Pressure distribution in the reservoir as a function of time (2nd month and 30th years of production-from left to right) (Green represent the lower pressure and red shows max reservoir pressure) (12 mile lateral length)..... 35
Figure 34. Sensitivity analysis on effect of normalized reservoir and fracture properties on normalized initial gas rate..... 36
Figure 35.Effect of initial reservoir pressure on NPV
Figure 36.Effect of fracture aperture reduction factor on NPV..... 36
Figure 37.Effect of horizontal lateral length on NPV
Figure 38.Comparison the effect of different parameters on NPV..... 37
Figure 39.NPV profile for different initial reservoir pressure values
Figure 40.NPV profile for different fracture aperture reduction factor values..... 37
Figure 41.NPV profile for different horizontal lateral length values..... 37
Figure 42. Simulation result examples for two history-matched New Albany Shale Gas wells (Out of 87 wells)..... 39
Figure 44.Two clusters of NAS wells for analysis (Case 1&2)..... 39
Figure 43. Location of under-study NAS gas wells..... 39
Figure 45. Decline curve analysis sample for one of NAS Figure 46.Type curve matching sample for one of NAS Gas wells 40
Figure 47.History matching results in comparison with DCA
Figure 48.Generating the Voronoi cells for 55 NAS for one of the wells(Case 1)..... 41
Figure 49. Calculated recovery factor for individual wells as well as field recovery factor 41
Figure 50. Results of discrete predictive modeling showing the distribution of matrix porosity, and matrix permeability for the entire field (From left to right)..... 42
Figure 51. Results of discrete predictive modeling showing the distribution of total permeability from type curve and initial gas in place for the entire field (From left to right).. 42
Figure 52. Results of Fuzzy Pattern Recognition showing the sweet spots in the field for the remaining reserve (MMCF) as of 2006, 2020 and 2040..... 43
Figure 53. Remaining reserve as a function of time..... 43
Figure 54. Proposed infill drilling locations and drainage area before and after placement of new wells (From left to right)..... 44
Figure 55. Results of Fuzzy Pattern Recognition showing the sweet spots in the field for the remaining reserve (MMCF) as of 2006, 2020 and 2040 (After drilling 6 extra wells) 44
Figure 56. Remaining reserve as a function of time (After drilling 6 extra wells)..... 45
Figure 57. Economic analysis result for new well#3..... 46

Figure 58. Results of Fuzzy Pattern Recognition showing the sweet spots in the field for the 1 Year cum for 55 wells (left) and 1Year cum. Production for 49 wells (right).(Case 1) 47
Figure 59. DCA sample for one of NAS Gas wells…….....50
Figure 60. TCM sample for one NAS Gas wells……...48
Figure 61. HM results in comparison with DCA
Figure 62. Generating the Voronoi cells for 32 NAS wells (Case 2) 48
Figure 63. Results of discrete predictive modeling showing the distribution of first 3 months, 5 year cum. Production and fracture half length for the entire field (From left to right)..... 49
Figure 64. Results of Fuzzy Pattern Recognition showing the sweet spots in the field for the first 3 months, 5-year cum. Production, and the fracture half-length (From left to right)..... 49
Figure 65. Results of discrete predictive modeling showing the distribution of total porosity, matrix porosity, and net pay thickness for the entire field (From left to right) 49
Figure 66. Results of Fuzzy Pattern Recognition showing the sweet spots in the field for the matrix porosity and total permeability from type curve and matrix permeability (From left to right) 50
Figure 67. Remaining reserve as a function of time 50
Figure 68. Results of Fuzzy Pattern Recognition showing the sweet spots in the field for the 1Year cum for 32 wells (left) and 1Year cum. Production for 28 wells (right).(Case 2 52
Figure 69. Making a New Project and Setting the Datum 53
Figure 70.Well Records and Formation List. 54
Figure 71.Interpreting the Shale Formations and Gas Effect in Prizm. 55
Figure 72. Four cross sections were created for analyzing the well logs. 55
Figure 73. Picking the top and bottom of formations in Cross Section D. 56
Figure 74.Picking the top and bottom of formations in Cross Section B. 57
Figure 75. NAS Top Subsea 58
Figure 76. Devonian LS Top Subsea 59
Figure 77. NAS Isochore map 59
Figure 78.Decline curve analysis sample for one of New Albany
Figure 79.Type curve matching sample for one of New Albany..... 60
Figure 80.History matching results
Figure 81.Generating the Voronoi cells for 31 NAS wells..... 60
Figure 82.Calculated recovery factor for individual wells as well as field recovery factor 61
Figure 83.Results of discrete predictive modeling in comparison with contour map (Geographix result) showing the distribution of total porosity, and gas saturation for the entire field..... 62
Figure 84.Results of discrete predictive modeling showing the distribution of total permeability from type curve and fracture aperture for the entire field (From left to right) 62
Figure 85.Results of Fuzzy Pattern Recognition showing the sweet spots in the field based on initial water saturation in comparison with the Geographix generated contour map. 63
Figure 86.Results of Fuzzy Pattern Recognition showing the sweet spots in the field based on initial reservoir pressure in comparison with the Geographix generated contour map. 63
Figure 87.Results of Fuzzy Pattern Recognition showing the sweet spots in the field based on matrix porosity in comparison with the Geographix generated contour map..... 63

Figure 88.Results of Fuzzy Pattern Recognition showing the sweet spots in the field for the first 3, 6 and 9 month of Cum.gas production in comparison with the corresponding contour maps from geographix. 64
Figure 89.Results of Fuzzy Pattern Recognition showing the sweet spots in the field for the remaining reserve (MMCF) as of 2006, 2020, and 2040..... 65
Figure 90. Results of Fuzzy Pattern Recognition showing the sweet spots in the field for the first 3-month cum. production for 31 wells (left) and first 3-month cum. Production for 28 wells (right)..... 67

List of Tables

Table 1.Distribution of worldwide unconventional gas reservoirs. (2) 3
Table 2.List of common reservoir attributes used for force ranking gas-shale portfolios 4
Table 3.List of common sources for the reservoir property list of Table2. 5
Table 4. Fracture network properties (Base model) 21
Table 5. The input variable for single well history matching 22
Table 6. Multiple values for fracture length and density 24
Table 7. Shows the input parameters for single well history matching (Best match) 27
Table 8. Fracture network properties (History matched model) 28
Table 9. Initial rates based on different well orientation-History matched model 29
Table 10. NPV for New infill drilling location 45
Table 11. Results of Top-Down modeling (Case 1) 47
Table 12. Results of Top-Down modeling (Case 2) 51
Table 13.Results of Top-Down modeling- Model Calibration 66

Chapter 1

Introduction

1.1 Unconventional Gas Reservoirs

Unconventional Gas reservoirs continue to be a fast growing sector within the petroleum industry. These reservoirs include Coal Bed Methane, Shale Gas, and Tight Gas Sands.

Outside of the United States, with a few exceptions, unconventional gas resources have largely been overlooked and understudied. In most of the world, the natural gas industry is focusing on producing gas from conventional reservoirs and has yet to turn its attention to unconventional gas reservoirs. These unconventional gas reservoirs represent a vast, long-term, global source of natural gas and have not been appraised in any systematic way. Unconventional gas resources—including tight sands, coalbed methane, and gas shales—constitute some of the largest components of remaining natural gas resources in the United States. Research and development concerning the geologic controls and production technologies required to evaluate and produce these unconventional gas resources has provided many new technologies during the past several decades. These new technologies have enabled operators in the United States to unlock the vast potential of these challenging resources, boosting production levels to an estimated 30% of the natural gas production in the United States.

Around the world, unconventional gas resources are widespread, but with several exceptions, they have not received close attention from natural gas operators.This is due in part because geologic and engineering information on unconventional resources is scarce, and natural gas policies and market conditions have been unfavorable for development in many countries. In addition, there is a chronic

shortage of expertise in the specific technologies needed to develop these resources successfully. As a result, only limited development has taken place to date outside of North America.

Interest is growing, however, and during the last decade development of unconventional gas reservoirs has occurred in Canada, Australia, Mexico, Venezuela, Argentina, Indonesia, China, Russia, Egypt, and Saudi Arabia. Many of those who have estimated the volumes of gas in place within unconventional gas reservoirs agree on one aspect: that it is a large resource. In Table 1, Kawata and Fujita summarized the work of Rogner, who estimated the worldwide unconventional gas resource (1) .Using the United States as an analogy, there is good reason to expect that unconventional gas production will increase significantly around the world in the coming decades for the following reasons:

- A significant number of geologic basins around the world contain unconventional gas reservoirs.
- Rogner estimates that in the world there are around
    - ✓ 9,000 Tcf of gas in place in coalbed methane,
    - ✓ 16,000 Tcf of gas in place in shale gas, and
    - ✓ 7,400 Tcf of gas in place in tight gas sands.
- Any reasonable recovery efficiency leads one to the conclusion that there is an ample opportunity in the future to develop unconventional gas worldwide.
- Tight gas sand development in the United States, critical to future U.S. gas supply, has to over 4 Tcf/year and is supported by ongoing technological development.
- The technology developed in the United States over the past 3 to 4 decades will be available for application around the world.
- New technology is rapidly becoming a worldwide commodity through efforts of major service companies.
- The global need for energy, particularly natural gas, will continue to be an incentive for worldwide unconventional gas resource development.
- Tight gas sands, gas shales, and coalbed methane are already critical to North America today and will be an important energy source worldwide during the 21st Century.

Unconventional Reservoir System Definition. Similar to conventional hydrocarbon systems, unconventional gas reservoirs are characterized by complex geological and petrophysical systems as well as heterogeneities — at all scales. However, unlike conventional reservoirs, unconventional gas reservoirs typically have very fine grain rock texture, exhibit gas storage and flow characteristics

which are uniquely tied to nano-scale pore throat and pore size distribution and possess common organic and clay content that serve as gas sorption sites. The clays and organics impart an anisotropic

Table 1.Distribution of worldwide unconventional gas reservoirs. (2)

Region	Coalbed Methane (Tcf)	Shale Gas (Tcf)	Tight-Sand Gas (Tcf)	Total (Tcf)
North America	3,017	3,842	1,371	8,228
Latin America	39	2,117	1,293	3,448
Western Europe	157	510	353	1,019
Central and Eastern Europe	118	39	78	235
Former Soviet Union	3,957	627	901	5,485
Middle East and North Africa	0	2,548	823	3,370
Sub-Saharan Africa	39	274	784	1,097
Centrally planned Asia and China	1,215	3,528	353	5,094
Pacific (Organization for Economic Cooperation and Development)	470	2,313	705	3,487
Other Asia Pacific	0	314	549	862
South Asia	39	0	196	235
World	9,051	16,112	7,406	32,560

fabric to gas shales which affects their mechanical and transport properties. Gas-shale reservoir pore structures are defined in terms of nanometers to micrometers, whereas most tight gas reservoirs are described at a micrometer or larger scale. Both gas-shale and tight gas systems have free gas stored within the pores of the rock matrix. Gas-shale differs in possessing the characteristic of gas adsorption on surface areas associated with organic content and clay. Bustin et al. (2008)(3) states that the relative importance of adsorbed versus free gas varies as a function of the amount of organic matter present, pore size distribution, mineralogy, digenesis, rock texture and reservoir pressure and temperature. We choose to define unconventional systems simply as those systems, which have a sorbed gas component. This includes gas-shale, coal bed methane and gas hydrates but does not include tight gas sand which is henceforth considered as conventional.

1.2 Naturally fractured Shale gas Reservoirs

A Brief History of Gas Shale Assessment. Gas has been produced from shale since the first shale-gas well in the organic rich Devonian Dunkirk Shale in New York in 1821. Shallow, low pressure wells first were concentrated in New York and Ohio. By 1935, operators recognized the dual role of matrix and fractures in shale systems (Browning 1935 and Lafferty 1935)(4). From 1927-1962, the

Columbia Gas System Service Corp (now Chesapeake Energy), drilled tens to hundreds of wells per year into Devonian shales and promoted shale research (5). The interest in characterizing gas-shale systems began in earnest in the 60's when the Bureau of Mines (later to become ERDA, the Energy Research and Development Administration) defined and funded the Eastern Gas Shales Project which began in 1976(6). The objectives of ERDA were to determine the gas reserves potential, provide shale characterization, improve stimulation practices and permeability measurement. Expansion of interest in gas shale outside of the Appalachians began in 1981 with the first Barnett Shale well, drilled in the Fort Worth Basin in northern Texas by Mitchell Energy Corporation(7). Starting in the late 80's and into the early 90's, pioneering work on the measurement of shale properties was sponsored by the Gas Research Institute (GRI) resulting in numerous publications that describe new core analysis methods(8).Since the mid-90's, gas shales have advanced to economic gas play status thanks to a combination of high gas prices, improved shale reservoir characterization and advances in drilling and completion technology and environmental pressures.

Gas-shale Assessment Criteria. Gas-shale well productivity depends upon reservoir quality and successful execution of an effective hydraulic stimulation. Defining the quality of gas-shale reservoirs is based on a broad range of parameters. Most gas-shale operators have developed internal criteria by which to rank their portfolio of gas shale systems. Table 2 is a list of the most common gas shale reservoir attributes used for ranking purposes. The list is in alphabetical order and reflects no priority ranking.

Table 3 is a partial list of common sources for the reservoir property list of Table 2. We can measure reservoir properties from different sources and at multiple scales. The primary measurement sources include core tests, well logs, and pressure test methods (e.g. injection fall off tests). Of the core-based methods for measuring shale pore systems, gas storage capacity, flow capacity and elastic properties, many are borrowed from the coal bed methane and conventional reservoir protocols (9).The American Petroleum Institute (API) has not set any standard of measurement for shale systems such as exists for conventional core testing in the Recommended Practices 40 (API 1998). The result is an evolution of core test methods that differ from lab to lab for any given test type. This work will document some of these inconsistencies in measurement of rock storage, flow capacity, and provide a recommendation for future standards of testing.

Table 2.List of common reservoir attributes used for force ranking gas-shale portfolios

Parameter	Desired Result
Dehydration Effects (Sw)	< 40% Sw

Depth	Shallowest Depth in Dry gas Window
Fracture Fabric and Type	Vertical vs. horizontal orientation
	Open vs. Filled with silica or calcite
Gas Composition	low CO2, N, and H2S
Gas-Filled Porosity (Bulk volume gas)	> 2% Gas Filled Porosity
Gas type (biogenic, thermogenic, or mixed)	Thermogenic
Internal Vertical Heterogeneity	Less is better
Mineralogy	> 40% Quartz or Carbonates
	< 30% Clays
	Low expandablilty
	Biogenic vs. detrital silica
OGIP (free and sorbed)	> 100 BCF/section
Permeability	> 100 nanoDacry
Poisson's Ratio (static)	< 0.25
Pressure	> 0.5 psi /ft
Reservoir Temperature	> 230 F
Seals	Fracture Barriers Present Top and Base
Shows	High gas Readings-Production
Stress	< 2000 psia Net Lateral Stress
Thermal Maturity	Dry gas window > 1.4 Ro
Thickness	> 30 m
Total Organic Content (and Type)	> 2%
Wettability	Oil prone wetting of kerogen
Young's Modulus	> 3.0 MMPSIA

Table 3.List of common sources for the reservoir property list of Table2.

Reservoir Property Data Source	Reservoir Property Data Source

Elastic Properties	DSI (dynamic), Core-based compressiontest (static)
Fluid Properties	Mud log, PVT, PDA, pressure gradients
Fracture and Closure Stress	IFOT, Frac job, log-based (DSI)
Free & Sorbed Gas	Canister desorption & Langmuir Adsorption
Maturity	Visual Ro, maserals, RockEval (calc)
Permeability	SS & USS, IFOT, MICP, PDA, & NMR (calc)
Pore Pressure	IFOT, PDA, log-based, “dip-in”
Porosity	Gas expansion, MICP, NMR, & logbased
Rock Composition	XRD, TS point counts, FTIR, ICP-MS, EDAS (SEM)
Temperature	OHL & PL, frac job, & IFOT
TOC	Leco TOC & RockEval (calc)
Water Saturation	Core extraction, Pc, & log-based

Gas Storage and Flow Regime Model. Shale gas storage and flow are controlled by the network of pores ranging in size from micrometers (10-6 m) to Å (10-10 m). Gas is stored as free compressed gas in the open pores and cracks, as adsorbed gas on the surfaces of kerogen and clay and as diffuse gas stored within the solid organic matter. Flow from larger connected pores and throats generally follow the Darcy equation and are referred to as continuum or no slip flow. When we consider gas flow in nanopores, both non-continuum effects (gas slippage) and surface interactive forces (diffusion) dominate. Javadpour et. al. 2007(10) and Javadpour 2009(11) present shale gas storage and flow schematics of gas evolution and production at different length scales. Figure 1 is another schematic of shale gas storage and flow capacity describing the range of pore types, flow type, the expected particle motion associated with each flow type and the Knudsen flow regime boundaries for each. The scale is relative but the inferred range is from angstroms to micrometers.

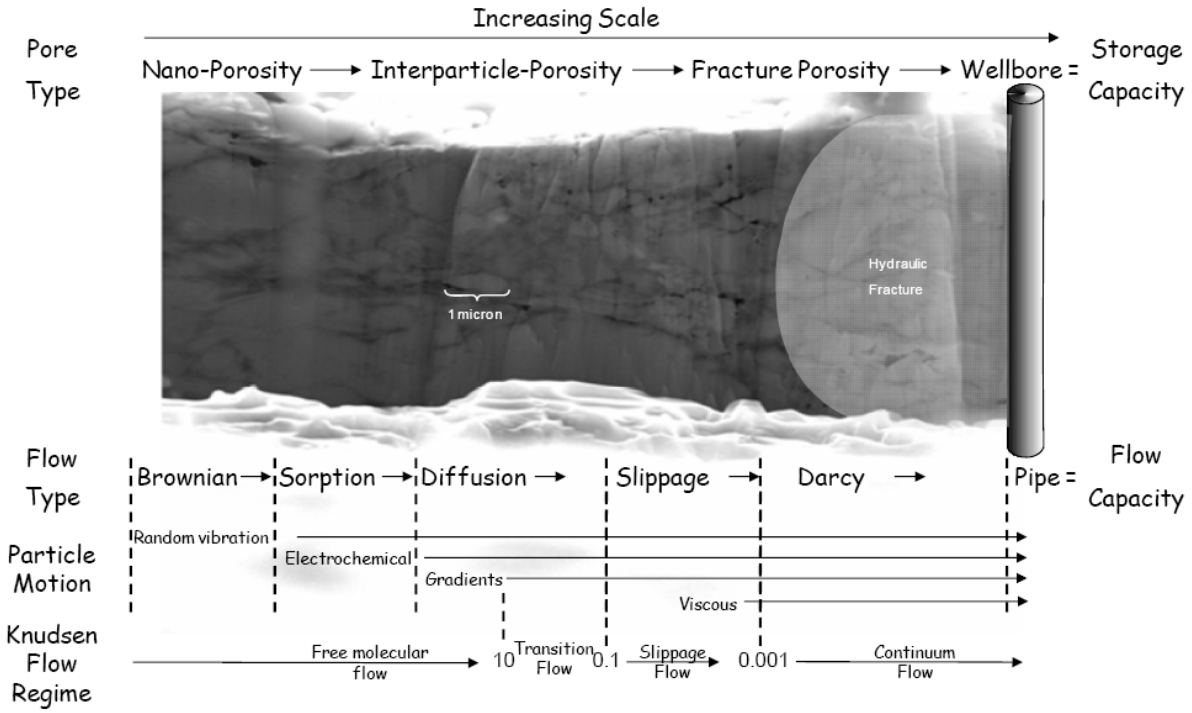


Figure 1.Gas shale storage and flow capacity diagram showing pore type, flow type, dominant particle motion within a given flow regime.(12)

Although it is difficult to extract, most shale gas is fairly clean and dry. That is because over time, there has been enough heat in the reservoir rock to break down any liquid hydrocarbons. The relative amounts of oil and gas contained in shale are one indication of how much heat has been in the reservoir, and for how long. Thermally mature shales have had enough heat and pressure to produce hydrocarbons. The most thermally mature shales will contain only dry gas. Less mature shales will have wetter gas, and the least thermally mature shales may contain only oil. In rare cases, the produced methane may have small percentages of carbon dioxide, nitrogen, ethane, and even propane. Carbon dioxide is more commonly found in biogenic gas shales.

Gas shale reservoirs in the United States tend to be found within three depth ranges between 250 and 8,000 ft. The New Albany and Antrim shales, for example, have some 9,000 wells in the range of 250 to 2,000 ft. In the Appalachian basin shales and the Devonian and Lewis shales, there are about 20,000 wells from 3,000 to 5,000 ft. Although the Barnett and Woodford shales are much deeper, the Caney and Fayetteville shales are from 2,000 ft to 6,000 ft, with most of the reservoirs between 2,500 and 4,500 ft. A good shale gas prospect has a shale thickness between 300 and 600 ft.

Shale has such low permeability that it releases gas very slowly, which is why shale is the last major source of natural gas to be developed.

The good news is that shale can hold an enormous amount of natural gas. The most prolific shales are relatively flat, thick, and predictable, and the formations are so large that their wells will continue producing gas at a steady rate for decades.

Currently Producing Gas Shale Reservoirs-The Barnett Shale in the Fort Worth basin of North Central Texas is by far the most active shale gas play in the United States. The reservoir ranges from 100 ft to more than 1,000 ft in gross thickness and holds from 50 × 109 ft3 (50 bcf) to 200 bcf of gas per square mile. The Gas Technology Institute estimates that organic shale reservoirs in the United States contain up to 780 trillion (780 × 1012) ft3 of gas. Equally, gas-rich organic shales almost certainly exist elsewhere around the world, but so far, the United States is the only country with a large shale gas industry.

Thomas Jefferson was still alive when the first commercial shale gas well was drilled in 1821. True, it was only 27 ft deep into the Devonian Dunkirk shale, but residents of the nearby village of Fredonia, New York, were happy to use the gas to illuminate their homes. Until recently, however, shale has been seen as only a source rock or seal for oil and gas. Gas shale reservoirs were not considered significant or producible. Supply and demand has always driven the oil and gas business, so natural gas did not become an important commodity until after World War II. Figure 2 shows the main shale gas reservoirs in US.

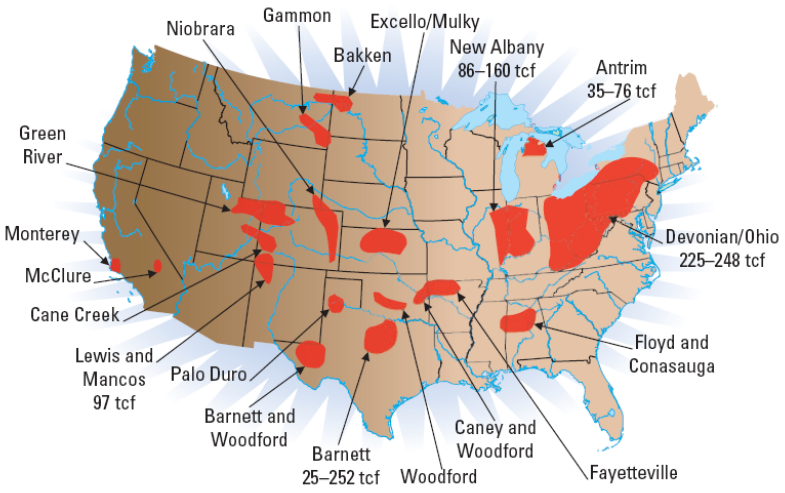


Figure 2.Major shale gas basins in the United States with total resource potential of 500 to 1,000 tcf.(13)

Shale gas wells are not hard to drill, but they are difficult to complete. In almost every case, the rock around the wellbore must be hydraulically fractured before the well can produce significant amounts of gas. Fracturing involves isolating sections of the well in the producing zone, then pumping fluids

and proppant (grains of sand or other material used to hold the cracks open) down the wellbore through perforations in the casing and out into the shale. The pumped fluid, under pressures up to 8,000 psi, is enough to crack shale as much as 3,000 ft in each direction from the wellbore. In the deeper high-pressure shales, operators pump slickwater (a low-viscosity waterbased fluid) and proppant. Nitrogen-foamed fracturing fluids are commonly pumped on shallower shales and shales with low reservoir pressures.

Fractures are the key to good production. The more fractures in the shale around the wellbore, the faster the gas will be produced. Because of shale's extremely low permeability, the best fracture treatments are those that expose as much of the shale as possible to the pressure drop that allows the gas to flow. The natural formation pressure of a large gas shale reservoir will decline only slightly over decades of production. Any pressure drop on individual wells is likely the result of fractures closing up, rather than depletion of the reservoir. The key to good shale gas production over time is having the proper distribution and placement of proppant to keep the fractures open.

Economics of Shale Gas-There are fundamental differences in the production of gas from shale and gas produced from other unconventional sources. Many tight gas sands, for example, yield a tremendous amount of gas for the first few months, but then production declines significantly and often becomes uneconomical after a relatively short time.

Shale gas is completely different. Shale gas wells do not come on as strong as tight gas, but once the production stabilizes, they will produce consistently for 30 years or more. Suppose that new horizontal wells in a typical shale gas play produce 1 million ft3 per day (1 MMcf/d). If the operator puts 10 such wells on 1 square mile, that section will produce 10 MMcf/d. With an estimated 120 bcf of gas per square mile in the ground, these gas shale reservoirs will be producing gas for a very long time. That realization, plus increasingly effective horizontal drilling tools, 3D seismic imaging, and advanced reservoir modeling software, has many people looking at shale gas as an important new resource.

The price of gas is linked to oil and based on each fuel's heating value. The ratio is about 6 to 1. In other words, 1 bbl of oil contains about 6 times more heat energy than 1,000 ft3 of gas. If a barrel of oil sells for USD 50.00, then 1,000 ft3 of gas is worth about USD 8.00. As long as oil prices remain high, there is no reason for natural gas prices to go down. Although gas is abundant in much of the world, it is expensive and potentially dangerous to transport internationally.

1.3 New Albany Shale Formation

The name New Albany Black Slate was originally proposed by Borden (1874) for brownish-black shale exposed along the Ohio River at New Albany, Floyd County, Indiana. This unit is currently designated the New Albany Shale. The New Albany consists of brownish-black, organic-rich and greenish-gray, organic-poor shale and is present in the subsurface throughout much of the Illinois Basin. The New Albany Shale formation occurs in Illinois, Indiana, and Kentucky, but to date gas production has been primarily from western Indiana and southwest Kentucky.

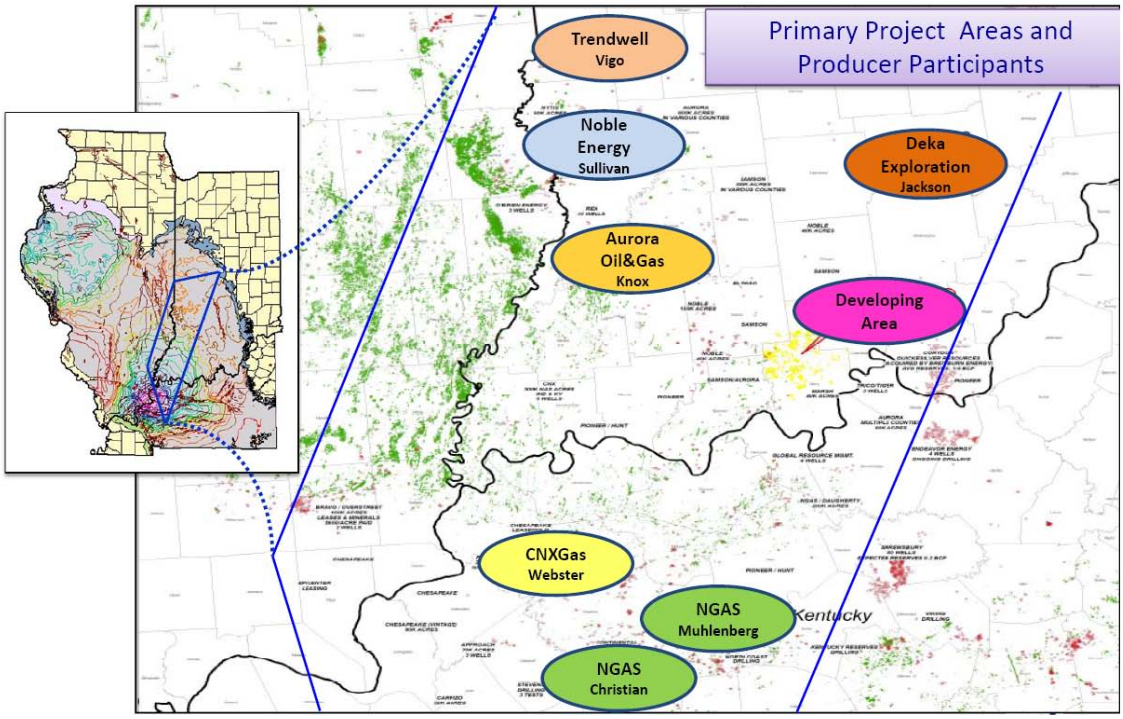


Figure 3. New Albany Shale formation throughout the Illinois basin and Under-study area.(14)

The elevation of the top of the New Albany ranges from about 750 feet above sea level near the outcrop to more than 4,500 feet below sea level in southeastern Illinois (Hamilton County). Unlike many other shale plays, the New Albany Shale in the Illinois Basin has a continuous 100-foot thick pay zone of shale, capped by very thick, dense, gray-green shale (Borden Shale). Prior to 1994, over 600 New Albany Shale wells had been produced commercially in the Illinois Basin. Vertical fractures in the shale fed the gas flow at the top of the shale.

Porosity of the New Albany Shale in a core from Christian County, Kentucky, varies from 0.5 to 3.1 percent, averaging 1.8 percent. Porosity of the New Albany Shale in a core from Sullivan County, Indiana, varies from 0.6 to 9.3 percent, averaging 4.0 percent (Kalyoncu and others, 1979). Matrix permeability values in a core of the New Albany Shale from Clark County, Indiana, varied from$2.5e^{-6}$ to 1.9 millidarcies and had a geometric average of 1.4 e^{-3} millidarcies (Zielinski and Moteff, 1980).

The New Albany Shale is affected by complex faulting in Western Kentucky and adjacent parts of Illinois and Indiana. Elsewhere, less intense deformation has locally produced folds and faults that influence its elevation and thickness.(15)

Natural fracturing is essential for effective reservoir permeability. In fields where detailed studies have been undertaken, fracturing appears to be related to structures such as faults, flexures, and local or regional carbonate buildups over which the shale is draped and compacted.

The dark-colored shale layers typically have parallel laminae, more than 2.5 weight percent organic carbon, amorphous (Type II) kerogen, high radioactivity, and high concentrations of natural gas released from cores. The lighter-colored shale layers commonly have bioturbated fabric, 1 to 2 weight percent organic carbon, humic (Type III) kerogen, moderate radioactivity, and lower concentrations of natural gas released from cores.(15)

The New Albany Shale in the Illinois Basin has promising gas production potential because of its high estimated gas content (86 TCF) and long history of production. Gas-in-place (GIP) measures from 8 bcfg/square mile to 20 or more bcfg/square mile, depending on locations and depths.

Gas has been produced from the New Albany Shale since 1858, from at least 40 fields in Kentucky, 19 in Indiana, and 1 in Illinois. Production data are not publicly available, and none have been disclosed by operators to date. Only IP data are generally available. Measured IP values for New Albany Shale wells range from less than 10 to 4,500 MCFGPD and average 187 MCFGPD.

Gas production is developed mainly in relatively organic rich shale beds of the Grassy Creek (Shale), Clegg Creek, and Blocher (Shale) Members. The limited evidence that production, where known, comes from the most organic-rich shale beds suggests that the gas produced from the New Albany is indigenous.

New Albany Shale gas is predominantly methane with significant and variable amounts of heavier hydrocarbons. Oil is occasionally produced in small amounts from the New Albany and the stratigraphically equivalent Chattanooga Shale in south-central Kentucky. Water generally is not produced in Kentucky, but is co-produced with gas in Indiana and along the Indiana and Kentucky border.(15)

The New Albany Shale reservoir contains natural gas both as free gas in open pore space, and as adsorbed gas on interior clay and kerogen surfaces. Analyses of New Albany Shale core samples from Sangamon, Effingham, and Tazewell Counties, Illinois, and from Christian County, Kentucky, indicate that between 30 and 80 percent of the methane in the shale was adsorbed gas, with the fraction of adsorbed gas showing a strong dependence on pressure.

Commercial production of gas from the New Albany Shale requires well stimulation that interconnects the well bore with the natural fracture system. Effective stimulation maintains permeability by introducing a proppant into the pressure-sensitive fractures near the well bore. Current stimulations are hydraulic-fracture treatments using nitrogen foam with a proppant; these treatments have replaced the older gelatinated nitroglycerine explosive shots.

The amount of organic carbon in the New Albany Shale is quite variable, ranging from near 0 weight percent in greenish-gray beds to 25 weight percent in brownish-black organic-rich beds; 86 percent of the samples analyzed by Frost (1980)(16) contain more than 1.0 weight percent organic carbon and 97 percent contain more than 0.5 weight percent organic carbon. More than 90 percent of the organic matter is amorphous; the remainder is composed of vitrinite, liptinite, and inertinite. Rock-Eval® data indicate that the New Albany Shale contains mostly Type II kerogen that still has substantial oil- and gas-generating potential.

The inorganic portion of the New Albany Shale is relatively uniform in composition, except for the carbonate and pyrite content, which are variable. The mineralogy and inorganic chemistry vary stratigraphically from bed to bed, but they are typically uniform within a given bed. (15)

Criteria that operators may use to identify areas where the New Albany Shale is likely to have the greatest gas-production potential are the presence of: (1) high organic-carbon content in the shale (2) thick organic-rich shale intervals (3) high radioactivity on the gamma-ray log and low density on the density log, which are generally indicative of organic-rich intervals, (4) natural fractures in the shale, (5) structural features where associated fracturing is likely, (6) proximity to historic production.

In general, deterrent to gas exploration and development in the New Albany Shale that need to be overcome include: (1) absence of current exploration and production activity, (2) inadequate gas pipeline infrastructure, (3) lack of gas production data, and (4) large tracts of acreage leased by coal companies.

Chapter 2

Methodology

2.1 New Albany Shale Natural Fracture Network Modeling and Simulation

The modeling of fluid flow through fractured formations can be based on deterministic, stochastic or fractal formulations of flow paths and matrix volumes. Deterministic models, however, are generally unable to effectively describe many naturally fractured formations with respect to the distributions of flow path length, flow path connectivity, and matrix block size and shape. (17)

NFFLOW™ is a numerical model for naturally fractured gas reservoirs (Developed by NETL/DOE) that permits the modeling of irregular flow paths mimicking the complex system of interconnected natural fractures in such reservoirs. This type of natural fracture reservoir simulation permits a more accurate and realistic representation of fractured porous media when modeling fluid flow compared to the traditional deterministic formulations. The NFFLOW™ simulator is a single-phase (dry-gas), two-dimensional numerical model that solves fluid flow equations in the matrix and fracture domains sequentially for wells located in a bounded naturally fractured reservoir. The mathematical model "decouples" fluid flow in fractures and matrix, and solves a one-dimensional unsteady state flow problem in the matrix domain to compute the volumetric flow rates from matrix into fractures and wellbores.(18)

FRACGEN™, the fracture network generator (Developed by NETL/DOE), implements four Boolean models of increasing complexity through a Monte Carlo process that samples fitted statistical distributions for various network attributes of each fracture set. Three models account for hierarchical relations among fracture sets, and two generate fracture swarming. Termination/intersection frequencies may be controlled implicitly or explicitly.

In this study, FRACGEN/NFFLOW is being used to model gas production from New Albany shale.

2.2 Top-Down Intelligent Reservoir Modeling of New Albany Shale

2.2.1 Traditional Reservoir Simulation & Modeling

Reservoir simulation is the industry standard tool to understand the reservoir behavior and predict future performance. It is used in all phases of field development in the oil and gas industry. In order to predict reservoir performance, a series of models of reservoir process are constructed which yield information about the complex phenomena accompanying different recovery methods.

Full field reservoir simulation models which has been built by integration of static and dynamic measurements into the reservoir model have become the major source of information for analysis, prediction and decision making. Traditional reservoir simulation and modeling is a bottom-up approach that starts with building a geo-cellular model of the reservoir. Using modeling and geo-statistical manipulation of the data the geo-cellular model is populated with the best available petrophysical and geophysical information at the time of development. Engineering fluid flow principles are then added and solved numerically in order to generate a dynamic reservoir model. Figure 4 shows the Conventional reservoir simulation workflow (A bottom-up approach).

Usually, the full field model is calibrated using historic pressure and production data in a process referred to as "history matching." Once the full field subsurface reservoir model has been successfully calibrated, it is used to predict future reservoir production under a series of potential scenarios, such as drilling new wells, injecting various fluids or stimulation.

For economical and technical point of view, building a complex geological model, which serves as the foundation of the reservoir simulation model, needs a significant investment (time and money).On the other hand, the history matching process itself can be very time consuming and frustrating. This is due to uncertainty about the reservoir, and the fact that a history match can usually be achieved through various configurations - a set of unique and distinctly different simulation models (which all condition to input data) can produce the same history match. How do we know which one is correct? (19)

Despite aforementioned issues, conventional reservoir simulation and modeling is a well understood technology that usually works well in the hand of an experienced team of engineers and geoscientists.

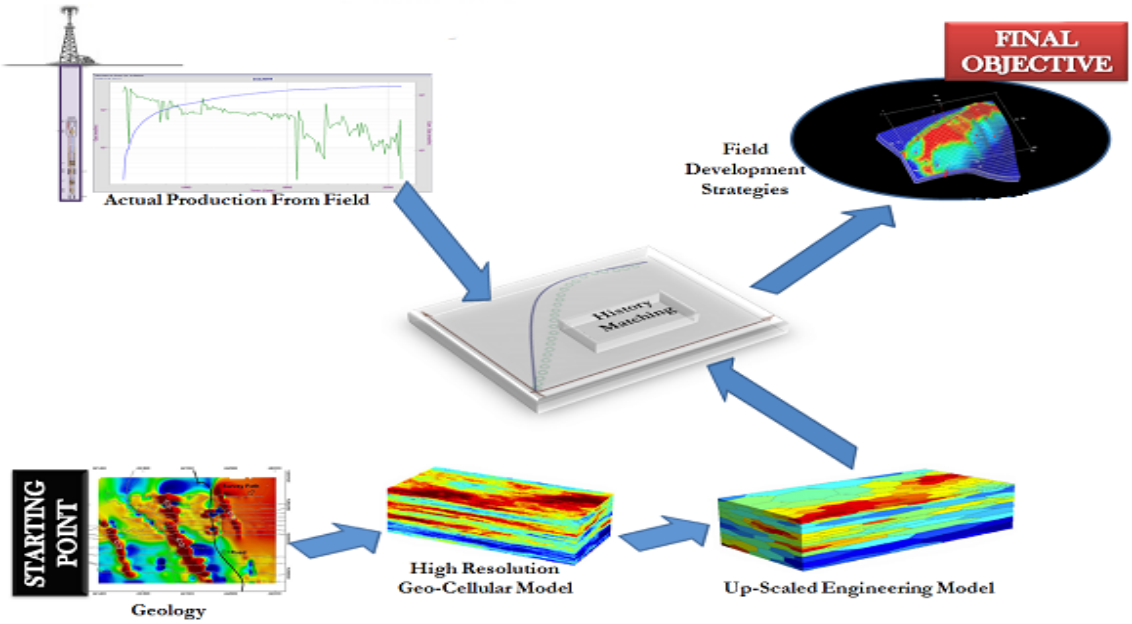


Figure 4. Conventional Reservoir Simulation &Modeling-A Bottom-Up Approach

2.2.2 Top-Down Intelligent Reservoir Modeling as an Alternate/Complement to Conventional Reservoir Modeling Techniques

Top-Down modeling can be used as an alternative for short-term reservoir modeling and/or as a complementary method for long term, reservoir behavior modeling.

Top-Down Intelligent Reservoir Modeling approaches the reservoir simulation and modeling from reverse standpoint by attempting to make an insight into reservoir by starting with actual field measurements (well production history). The production history is augmented by core, log, well test, and seismic data in order to increase the accuracy of the Top-Down modeling technique. Although not intended as a substitute for the conventional reservoir simulation of large, complex fields, this unique approach to reservoir modeling can be used as an alternative (at a fraction of the cost) to traditional reservoir simulation and modeling in cases where performing conventional modeling is cost and man-power prohibitive specially for independent producer of mature fields. In cases where a conventional model of a reservoir already exists, Top-Down modeling should be considered a compliment to the conventional technique, to provide an independent look at the data coming from the reservoir/wells for optimum development strategy and recovery enhancement.

Top-Down Intelligent Reservoir Modeling starts with well-known reservoir engineering techniques such as Decline Curve Analysis, Type Curve Matching, and History Matching using single well numerical reservoir simulation, Volumetric Reserve Estimation, and calculation of Recovery Factors.

Using statistical techniques, multiple Production Indicators (First 3, 6, and 9 month cumulative production as well as 1, 3, 5, and 10-year cumulative oil, gas and water production and Gas Oil Ratio and Water Cut) are calculated. These analyses and statistics generate a large volume of data and information that are spatio-temporal snap shots of reservoir behavior. This large volume of data is processed using the state-of-the-art in artificial intelligence and data mining (neural modeling(20), genetic optimization(21), and fuzzy pattern recognition(22)) in order to generate a complete and cohesive model of the entire reservoir. This is accomplished by using a set of discrete modeling techniques to generate production related predictive models of well behavior, followed by intelligent models that integrate the discrete models into a cohesive picture and model of the reservoir as a whole, using a continuous fuzzy pattern recognition algorithm.

The Top-Down Intelligent Reservoir Model is calibrated using the most recent set of wells that have been drilled in the field. The calibrated model is then used for field development strategies and reservoir management to improve and enhance hydrocarbon recovery. Figure 5 shows the Top down intelligent reservoir modeling workflow.

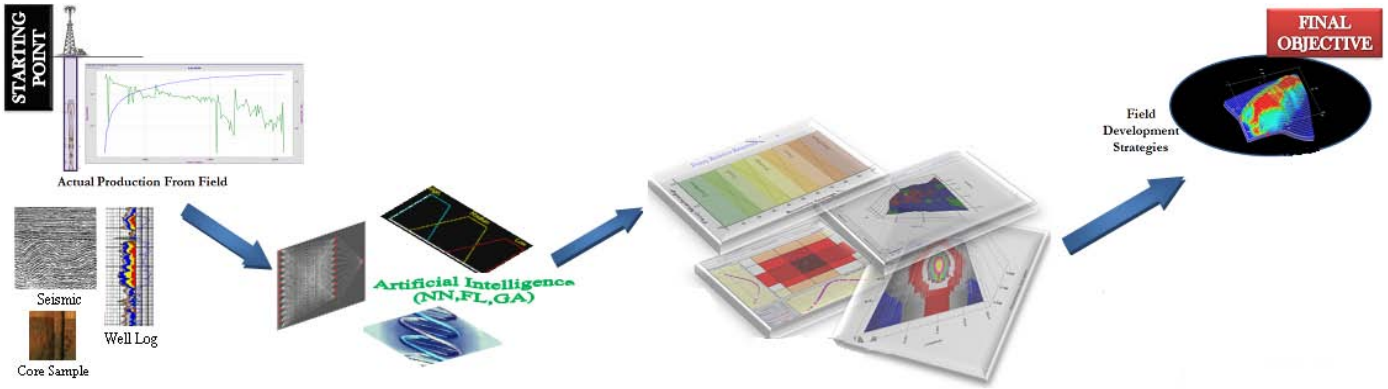


Figure 5. Top-down Intelligent Reservoir Modeling Workflow

2.2.2 Top-Down Modeling Methodology-Conceptual Approach

Top-Down Modeling is a well-designed integration of state-of-the-art in Artificial Intelligence & Data Mining (AI&DM) with solid reservoir engineering techniques and principles. It provides a unique perspective of the field and the reservoir using actual measurements. It provides qualitatively accurate reservoir characteristics that can play a key role in making important and strategic field development decisions. A brief summary of several components of this approach to reservoir modeling and management has been followed:

1. ***Decline Curve Analysis**:* Conventional hyperbolic decline curve analysis is performed on oil, gas and water production data of all the wells. Intelligent Decline Curve Analysis is used to model some production data such as GOR and Water Cut that does not usually exhibit a positive but rather a negative decline.

2. ***Type Curve Matching**:* Using the appropriate type curves, production data from all wells are analyzed. Special techniques are used to remove the inherent subjectivity associated with type curve matching process.

3. ***History Matching**:* History matching is performed on all individual wells using a single well radial numerical simulation model.

4. ***Production Statistics**:* General statistics are generated based on the available production data such as 3, 6, 9 months cumulative production and one, three, five and ten years cumulative productions. Similar data is generated for Gas Oil Ratio and water cut.

5. ***Volumetric Reserve Estimation**:* Using Voronoi graph theory in conjunction with well logs, estimated ultimate drainage area and volumetric reserves are estimated for each well, individually.

6. ***Recovery Factor Calculation**:* Using the results of Decline Curve analysis and Volumetric Reserve Estimation, a well-based Recovery Factor is calculated for all wells, individually. A field-wide Recovery Factor is also calculated. This would be an item that will be optimized in the consequent steps of the analysis.

7. ***Discrete Predictive Modeling**:* Results of the abovementioned analyses are a wealth of data and information that are generated based on individual wells. This information is indicative of reservoir/well behavior at specific time and space throughout the life of the reservoir. Using AI&DM techniques discrete, intelligent, predictive models are developed based on the large amount of data and information that has been generated. The predictive models represent all aspects of reservoir characteristics that have been analyzed.

8. ***Continuous Predictive Modeling****:* Using two-dimensional Fuzzy Pattern Recognition (FPR) technology, discrete predictive models are fused into a cohesive full-field reservoir model that is capable of providing a tool for integrated reservoir management.

9. ***Model Calibration****:* The full field model is calibrated based on classifying the reservoir into "most" to "least" prolific areas, prior to be used in the predictive mode. This is done using the latest drilled wells in the field. This practice is an analogy of history matching of the conventional reservoir simulation models. The calibrated model can then be used in predictive mode for field development strategies.

10. ***Field Development Strategies****:* Performing economic analysis, while taking into account the uncertainties associated with decision making, multiple field development strategies are examined in order to identify the optimum set of operations that would result in recovery enhancement. This process includes identification of remaining reserves, sweet spots for infill drilling as well as under-performer wells.

Figure 6 represent the general integrated workflow and steps that have been taken to model New Albany Shale reservoir in Western Kentucky.

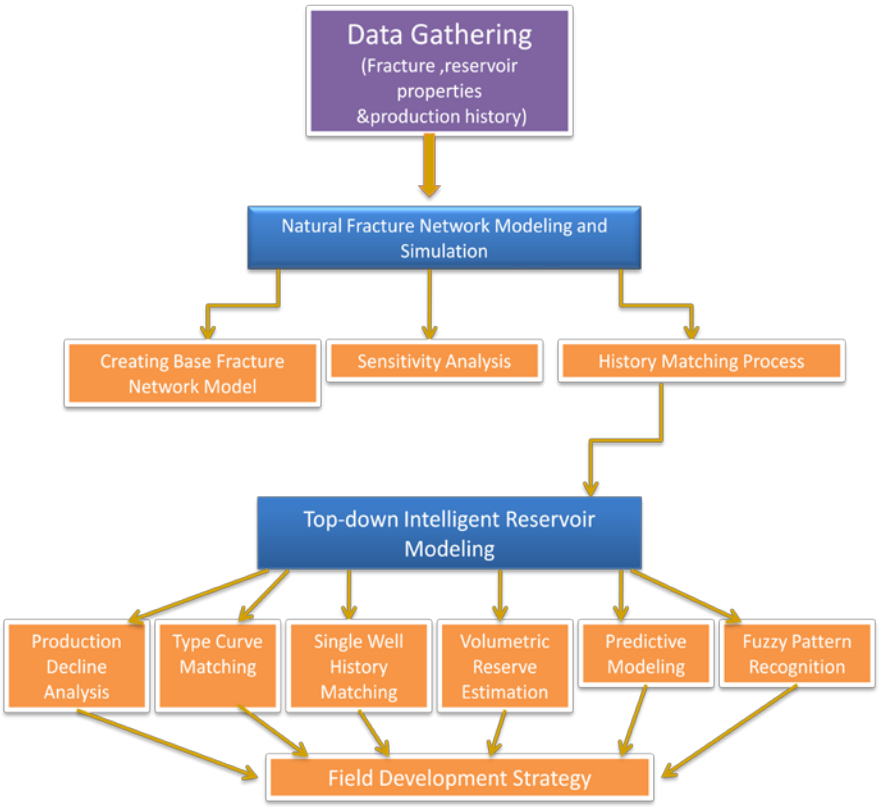


Figure 6. Integrated workflow for New Albany Shale Reservoir Modeling

Chapter 3

Results and Discussion

New Albany shale reservoir contains high-angled (vertical or nearly so) orthogonal natural fractures with non-uniform spacing that are open to unimpeded flow. The predominant fracture system is oriented east-west with spacing between joints estimated to average five feet based on outcrop studies (Figure 7) and production simulations. Based on this information, it was concluded that increases in performance could be achieved with a horizontally drilled well compared to a vertically drilled well in the same reservoir.

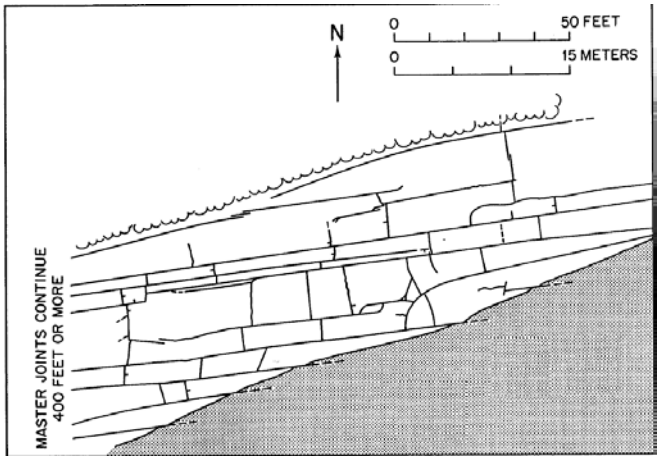


Figure 7. Schematic showing outcrop fracture features of the New Albany shale (23)

Fractures in a core of the New Albany Shale from the Energy Resources of Indiana No. 1 Phegley Farms Inc. well in Sullivan County, Indiana, were described by Kalyoncu and others (1979)(17)Twenty-one fractures were described over an interval of 104 feet. They were mainly vertical, but some had dips as low as 80 degrees. The strike of the fractures was predominantly northwest-southeast and a small secondary mode trended slightly to the north of east-west.(24)

Joint orientations in outcrops of the New Albany Shale in Indiana are parallel to this secondary east-west trend of fractures in the Phegley Farms core. (10)Fractures in a core of the New Albany Shale

from the Orbit No. 1 Clark well in Christian County, Kentucky, were described by Miller and Johnson (1979)(9). Natural fractures were regular planar sub vertical features striking northwest-southeast. They generally were filled with calcite, or less commonly with pyrite, and had apertures as

great as 3.0 millimeters (0.0098 ft). In the vertical plane, these fractures were commonly continuous for 1 or 2 feet, succeeded by sub parallel fractures offset from each other at their terminations.(24)

There is a decrease in fracture from the top of the New Albany shale to the lower members. The Clegg Creek member is clearly contains the most fractures, both natural and induced. The Blocher member typically shows half the number of natural fractures when compared to the clegg creek. Therefore the Clegg Creek member contains the most natural fractures with fracture frequency decreasing down section.Because of the problem that we had during this study to access fracture detection tools like image logs, seismic or any other tools that can be used for fracture identification and characterization, the abovementioned fracture distribution characteristics has been used to build a base fracture network model in FracGen and the flow modeling was performed in NFflow. The Fracture network characteristics used for the base model and the reservoir parameters that have been used for history matching (in NFflow) are shown in Table 4 and Table 5. Results of this model are compared with the production from a well producing from the New Albany Shale as shown in Figure 8. Meanwhile, because only last 9 years of production history was available, our production modeling (and eventually the history match) included reservoir behavior from the well completion to the last available production date. The fracture network of the base model (model providing the best history match) consists of 4sets of fractures. Three of the sets are defined in order to generate the major fracture patterns that mostly contribute to flow (the orientation of those fractures are E 95° W, E97° W and E 90°) and the remaining set are defined in order to generate the bedding.

Table 4. Fracture network properties (Base model)

	Fracture Properties	Fracture Length(ft)	Fracture Aperture(ft)	Fracture Density(ft/ft$^{2)}$	Major Fracture orientation
Major fracture generator	Set 1	2-400	0.0098	0.00003	E 95° W
	Set 2	2-400	0.0098	0.00003	E 97° W
	Set 3	5-400	0.0098	0.000003	E 90°
Minor fracture generato	Set 4	400-1000	0.00025	0.00003	E 24° N

Generations of fracture sets are based on two different models. Model 1 generates randomly located fractures, although the connectivity controls can be used to produce various degrees of clustering,

including unintended clustering. Model 2 generates fracture swarms (elongated clusters), whereby the swarms are randomly located and can overlap.

Table 5. The input variable for single well history matching

Matrix Permeability (md)	Matrix Porosity (%)	Initial Pressure (psi)	Thickness (ft)	A (Acres)
0.0000822	0.05	700	100	320

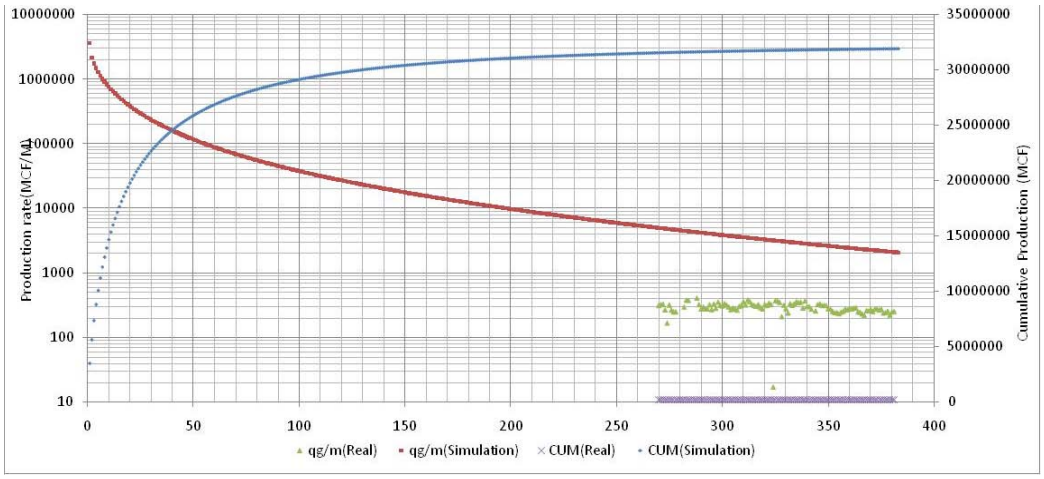


Figure 8. Simulation result examples for one history-matched New Albany Shale Gas well

The 9 years production data of a well which is completed in New Albany shale, western Kentucky has been used to verify the built fracture network and perform history matching. Figure 8 shows production rates and cumulative production from the well in green and purple dots, respectively while modeled production rate and cumulative production are shown as red and blue profiles. This figure shows that the base model has significantly overestimated the production from this well. According to the well completion report (11) the initial rate after the stimulation at July 1973 is around146 MCF/day while the model results start at 127,830 MCF/day and declines to more than 70 MCF/day in about last nine years of production.

To match the production from the New Albany Shale with the FracGen/NFflow simulator, sensitivity analysis was performed on fracture network properties (Fracture Aperture, Length, and Density) and reservoir properties (Pi, φ_m, Km, and h) in order to make the best estimation of NAS natural fracture network pattern.

3.1 Sensitivity Analysis on Reservoir and Fracture Properties

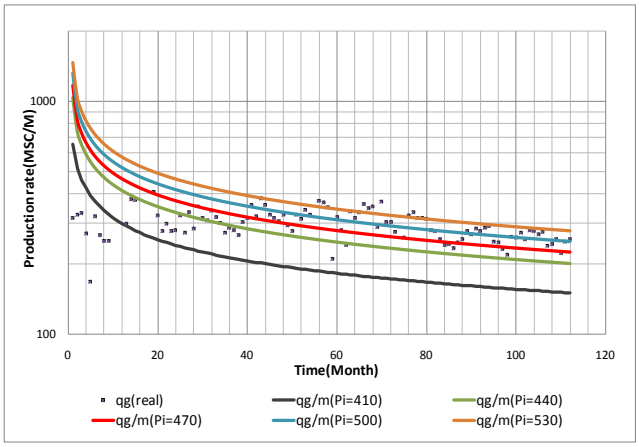
The objective of sensitivity analysis is to study the impact of different parameter and identify the factors that have the most contribution to flow.

To investigate the effect of different reservoir and fracture property on flow behavior, several studies were performed. The approach used for this analysis, starts by building the fracture network model based on the available information in literature (in FracGen). After performing the sensitivity analysis, the fracture network and reservoir properties of base model are tuned in order to match the observed production for each of the gas wells in New Albany shale.

As shown in Figure 9 through Figure 13, sensitivity analysis is performed, with the purpose of scrutinizing the influence of Initial reservoir pressure, matrix porosity, matrix permeability, net pay thickness and aperture reduction factor on flow behavior.

Aperture reduction factor is a term that has been defined as a parameter that can be used in order to shrink the hydraulic apertures of the fractures nearby the well and/or the entire drainage area of the well to further improve the history matched model. Alternatively, the fracture apertures can remain unchanged (reduction factor = 1.0).The process of reducing the aperture is a trial and- error process until the best possible match with production data or well test data is obtained for each of one or more networks.

As illustrated on Figure 9, which represent the comparison of the influence of reservoir and fracture properties on flow rate based on the sensitivity analysis results, the key parameters that have substantial effect on production behavior are initial reservoir pressure pay thickness and aperture reduction factor (ARF).



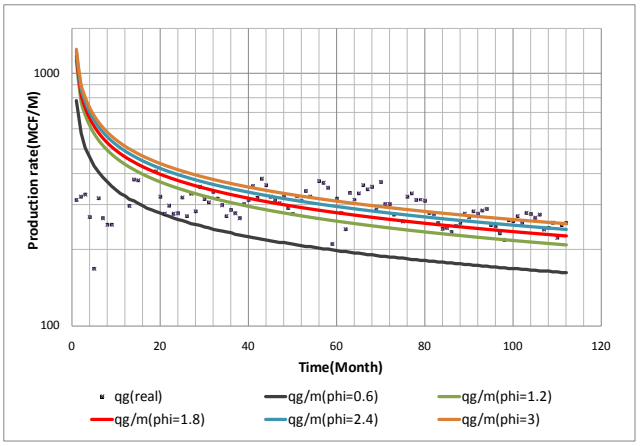


Figure 9. Sensitivity analysis on initial reservoir pressure **Figure 10. Sensitivity analysis on matrix porosity**

(Monthly gas production)

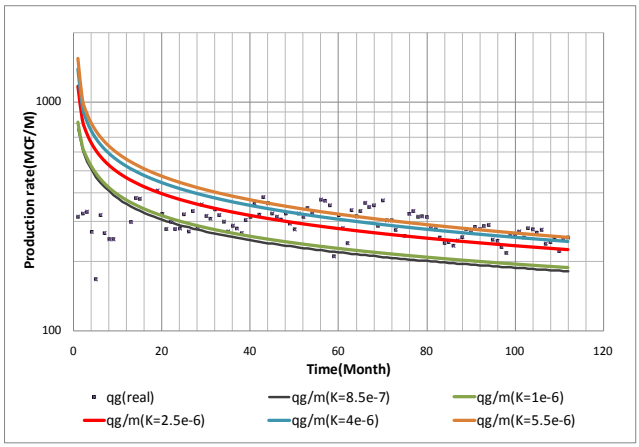


Figure 11. Sensitivity analysis on matrix permeability

(Monthly gas production)

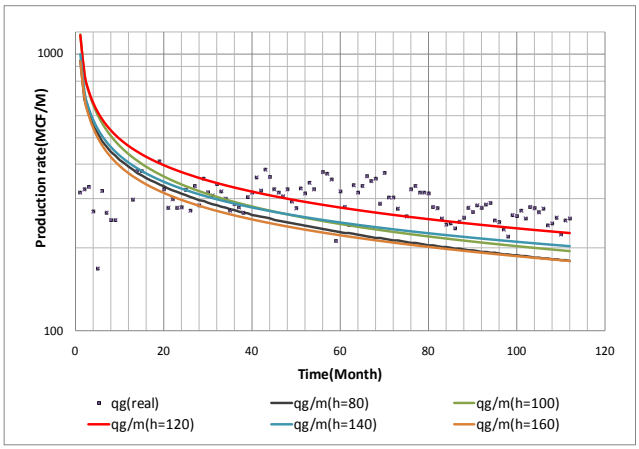


Figure 12. Sensitivity analysis on pay thickness

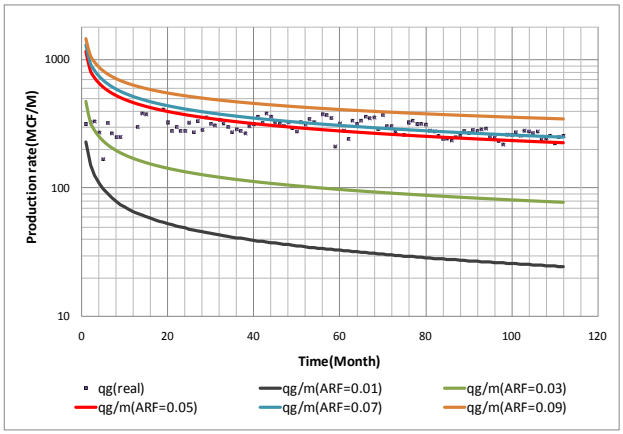


Figure 13. Sensitivity analysis on Aperture reduction factor

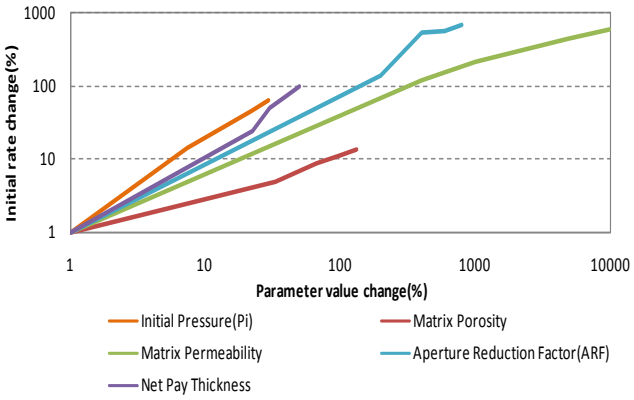


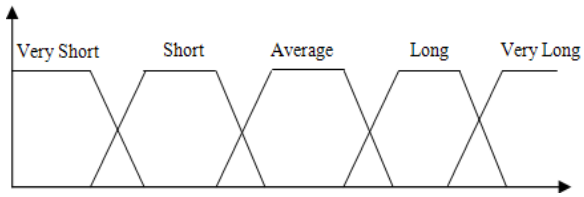
Figure 14. Sensitivity analysis - Effect of reservoir and fracture properties variation on initial gas rate

In the next part of this study, we intend to understand the effect of fracture length and density on production and reservoir behavior. Reservoir properties (h, φm, Km, Pi), fracture orientation, inner cluster fracture length & density, fractures aperture and bedding properties were assumed to remain unchanged. Therefore, the only parameters that have been changed are fracture length ad density. Hence, sensitivity analysis was performed for values of fracture length and density. Table 6 represents the suggested values for fracture length and density for one of fracture set.

Table 6. Multiple values for fracture length and density

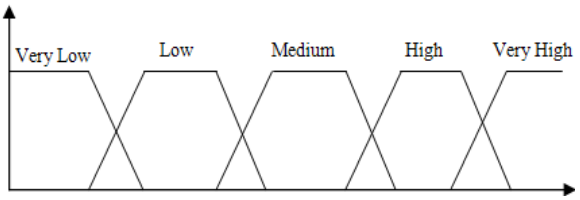
Density	Very Short (LVS)	Short (LS)	Average (LA)	Long (LL)	Very Long (LVL)
Very High (DVH)	D: e-4 L: 1-150	D: e-4 L: 1.5-200	D: e-4 L: 2-250	D: e-4 L: 3.5-325	D: e-4 L: 5-400
High (DH)	D: 8 e-5 L: 1-150	D: 8 e-5 L: 1.5-200	D: 8 e-5 L: 2-250	D: 8 e-5 L: 3.5-325	D: 8 e-5 L: 5-400
Medium (DM)	D: 6 e-5 L: 1-150	D: 6 e-5 L: 1.5-200	D: 6 e-5 L: 2-250	D: 6 e-5 L: 3.5-325	D: 6 e-5 L: 5-400
Low (DL)	D: 4 e-5 L: 1-150	D: 4 e-5 L: 1.5-200	D: 4 e-5 L: 2-250	D: 4 e-5 L: 3.5-325	D: 4 e-5 L: 5-400
Very Low (DVL)	D: 2 e-5 L: 1-150	D: 2e-5 L: 1.5-200	D: 2e-5 L: 2-250	D: 2e-5 L: 3.5-325	D: 2e-5 L: 5-400

Length



Min.Length: 1 1.5 2 3.5 5
Max.Length:150 200 250 325 400

Figure 15 . Fracture Length Values



2e-5 4e-5 6e-5 8e-5 e-4

Figure 16. Fracture Density Values

Figure 17 through Figure 21 demonstrate the results of sensitivity analysis based on different values of fracture length and fracture network density. The production data was available for just a part of well's life so the complete production profile has been generated and initial rate after stimulation has been used to verify the predicted initial rate.

According to sensitivity analysis results, with increasing fracture length or fracture density the production will be increased. In the case that fracture length and/or density are low the fracture intersection will be decreased significantly, as a result some part of the reservoir will not be depleted,

so the only way to put those parts of reservoir on production is performing some sort of stimulation (hydraulic fracturing).

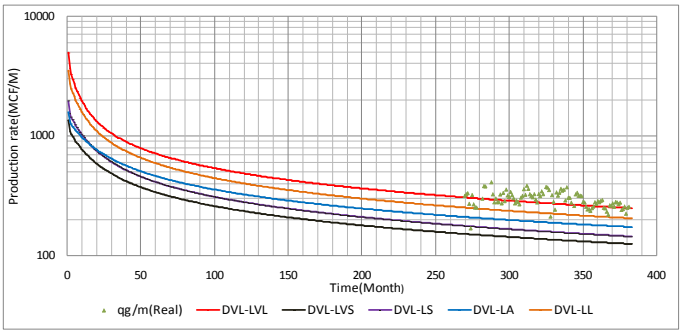


Figure 17. Sensitivity analysis results (Monthly gas production) (Very low fracture network density with variable length)

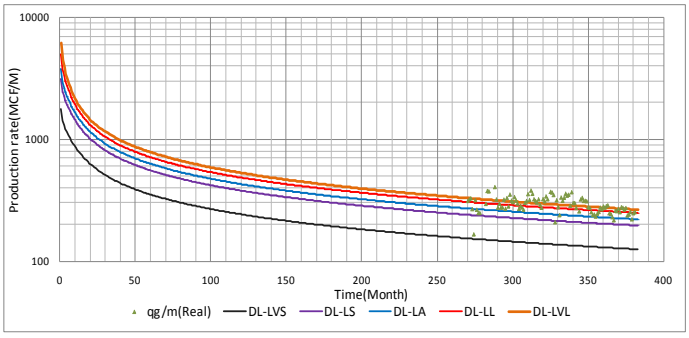


Figure 18. Sensitivity analysis results (Monthly gas production) (Low fracture network density with variable length)

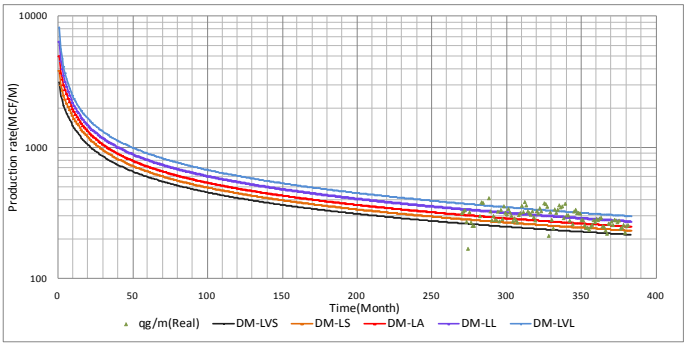


Figure 19. Sensitivity analysis results (Monthly gas production) (Medium fracture network density with variable length)

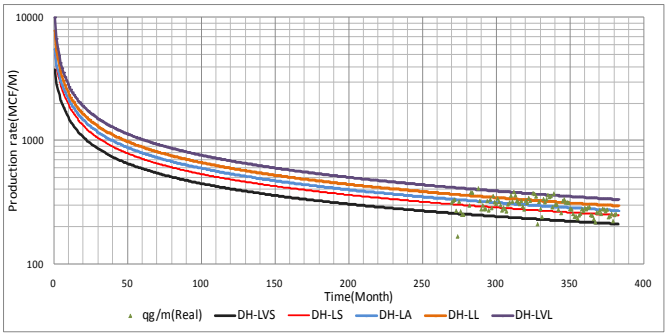


Figure 20. Sensitivity analysis results (Monthly gas production) (High fracture network density with variable length)

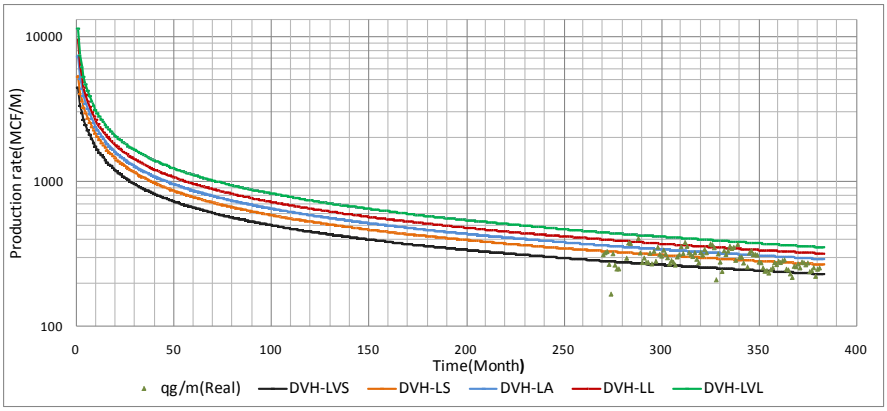


Figure 21. Sensitivity analysis results (Monthly gas production) (Very high fracture network density with variable length)

3.2 History Matched Model

Upon completion of the sensitivity, analysis and careful study of the impact of different parameters on production a new set of parameters were identified. This new set was used in the model. The result is shown in Figure 22.

According to the well completion report (10), the initial rate after the stimulation at July 1973 is 146 MCF/Day. The history matched model results in an initial production rate of 141 MCF/Day, which shows the reliability of fracture network and history matched model.

Figure 22 shows production rates and cumulative production from the well in green and purple dots, respectively while modeled production rate and cumulative production are shown as red and blue profiles.

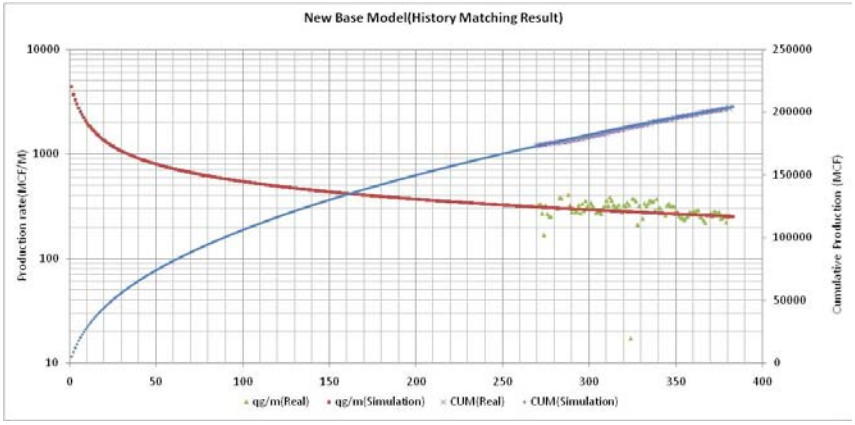


Figure 22. Single well history matching result, after changing the key

The final values of input parameters that are used in simulation (final history matching) are illustrated in Table 7.

Table 7. Shows the input parameters for single well history matching (Best match)

Matrix Permeability (md)	Matrix Porosity (%)	Initial Pressure (psi)	Thickness (ft)	A (Acres)	Aperture reduction factor(ARF)
1.5E-7	2.2	500	100	320	0.056

Fracture network characteristics used for the history-matched model are shown in Table 8 and the fracture network distribution for the base model is illustrated in Figure 23.

Table 8. Fracture network properties (History matched model)

	Fracture Properties	Fracture Length(ft)	Fracture Aperture(ft)	Fracture Density	Major Fracture orientation
Major fracture generator	Set 1	2-200	0.00055	0.00006	E 95° W
	Set 2	2-200	0.0004	0.00006	E 97°W
Minor fracture generator	Set 3	5-200	0.0004	0.000009	E 90°
	Set 4	400-1000	0.00025	0.00002	E 24° N

As shown in Table 4 and Table 8, the fracture network properties has been modified in order to get better history match is fracture aperture values.

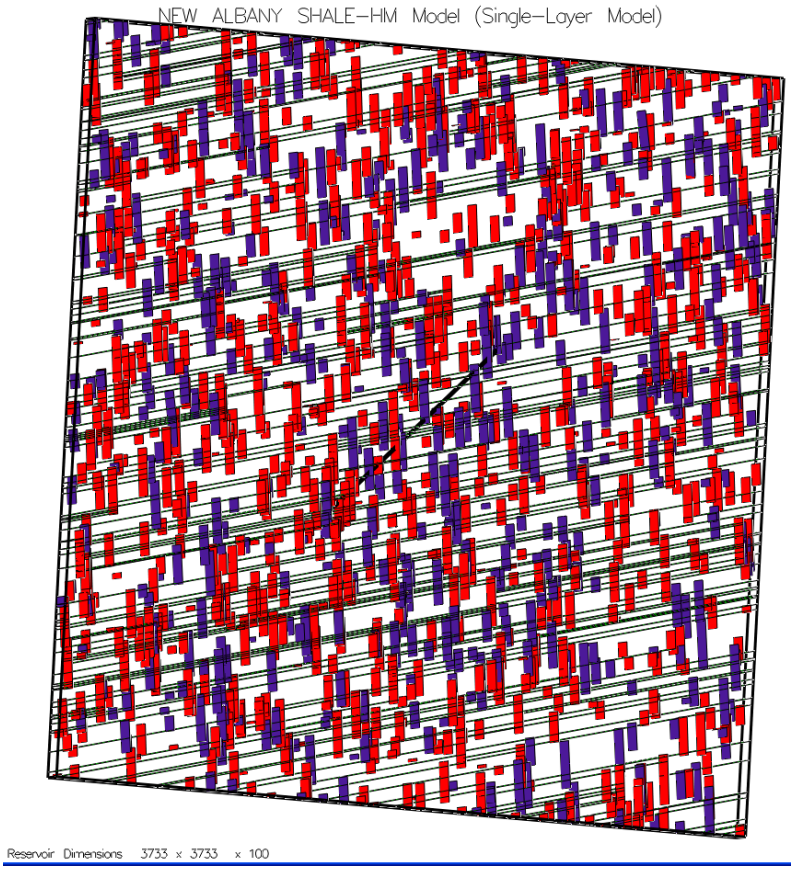




Figure 23. The well and fracture intersection for the history matched model (Based on 320 acre spacing)

3.3 Effect of lateral orientation on well productivity

In order to understand the impact of the orientation of horizontal wells on gas production in New Albany Shale the fracture network and reservoir properties are assumed to be the same for all the models to see the effect of different well orientations in horizontal plane (not Z-direction) on production and well performance.

Figure 25, shows the history match results based on different well orientations in horizontal plane (0, 30,45,60,75 and 90 degree). The result of this study shows that the history-matched models of different well orientation in X-Y plane have only slight difference in production profile (Qi, Di and b) .Therefore, horizontal well orientation has not substantial effect on well performance. (Table 9)

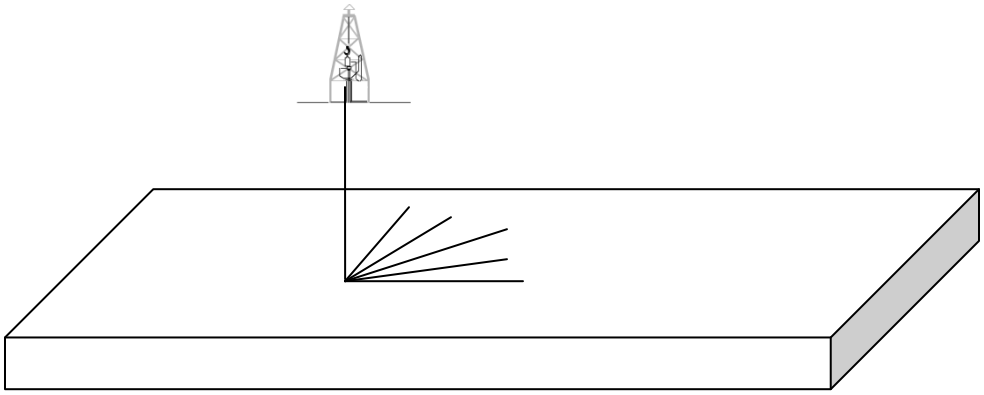


Figure 24. Horizontal well orientations in Y direction (0, 30, 45, 60, and 90 degrees)

Table 9. Initial rates based on different well orientation-History matched model

Well Orientation (degree)	Q_i (MCF/day)
0	140.13
30	140.24
45	140.56

60	140.76
75	141.19
90	140.01

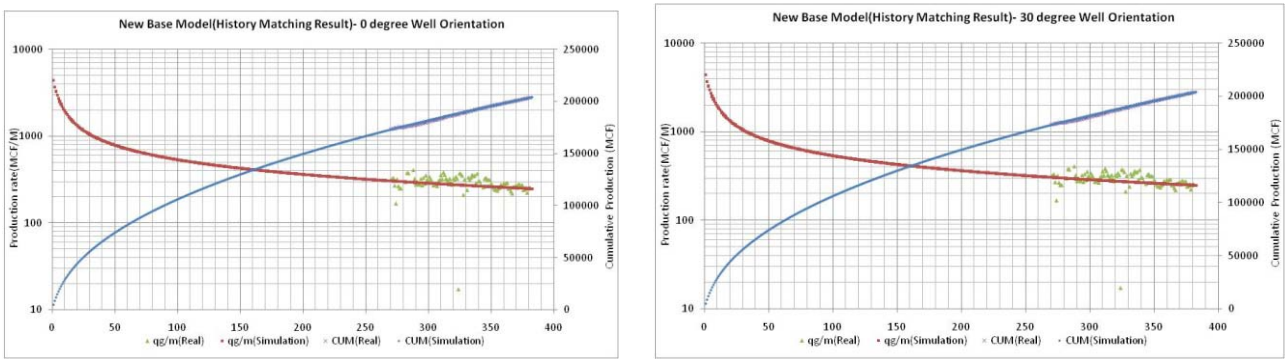


Figure 25. Single well history matching result-Zero and 30-degree well orientation (From left to right)

3.4 Horizontal Lateral Length Effect on Well Productivity

In order to indentify the effect of horizontal lateral length on well productivity from New Albany Shale, fracture network has been regenerated in order to represent the distribution of natural fracture in that formation.

NFFLOW/FRACGEN is capable to handle the drainage area of less than 100,000ft*100,000 ft (230,000 Acre). Therefore, the understudy drainage area has been selected as 99,000ft*99,000 ft (225,000 acre).

In order to have reliable results, we should perform history matching for one of the wells with 1200 ft lateral to calibrate the fracture network.

The HM process has been done. Then the History matched mode has been used as a basis for future analysis (To see the effect of different lateral length on well productivity)

The simulation study has been performed for 5, 7.5,9, and 12 miles of horizontal lateral length. Figure 26 shows clearly the monthly gas production (MCF) for 30 years.

Figure 27 shows the simulation result s as well as extrapolation results for cumulative gas production based on different lateral length.

Initial rate as a function of horizontal lateral length has been illustrated in Figure 28.

Figure 29 through Figure 33 illustrate the pressure distribution as a function of time for 2nd month and 30th years of production based on different horizontal lateral length (0.227, 5, 7.5, 9, and 12 miles)

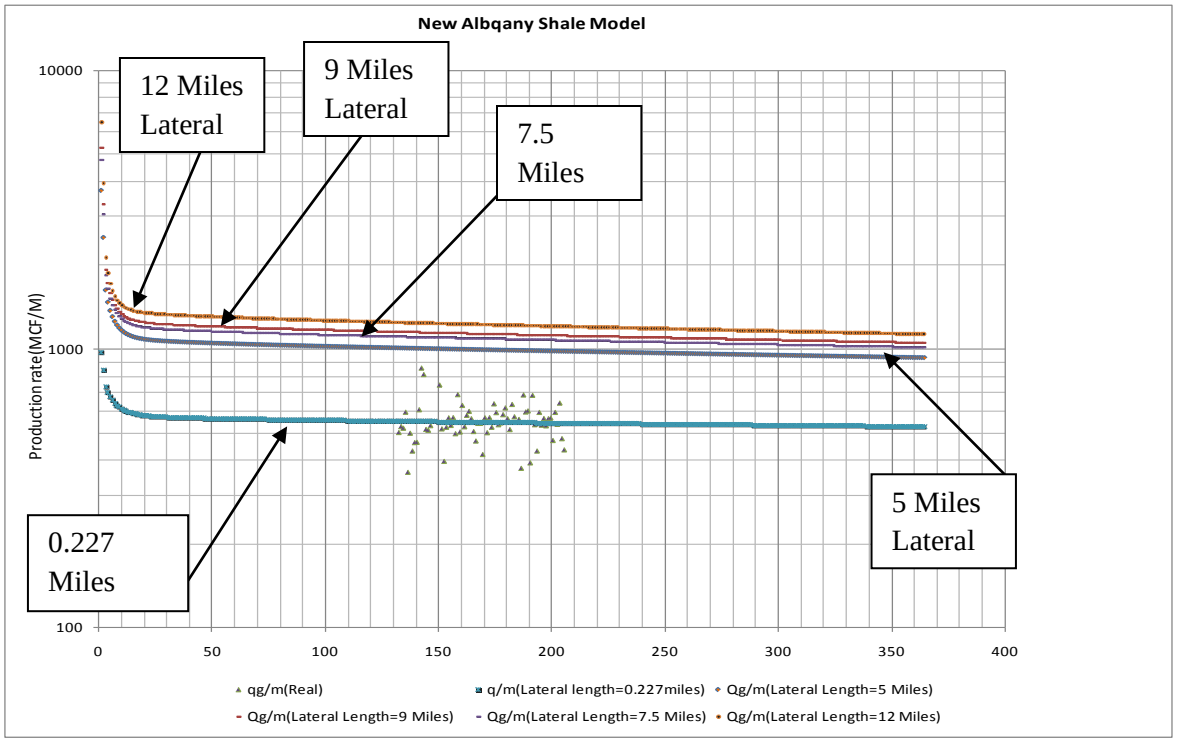


Figure 26.Effect of horizontal lateral length on well productivity from New Albany Shale

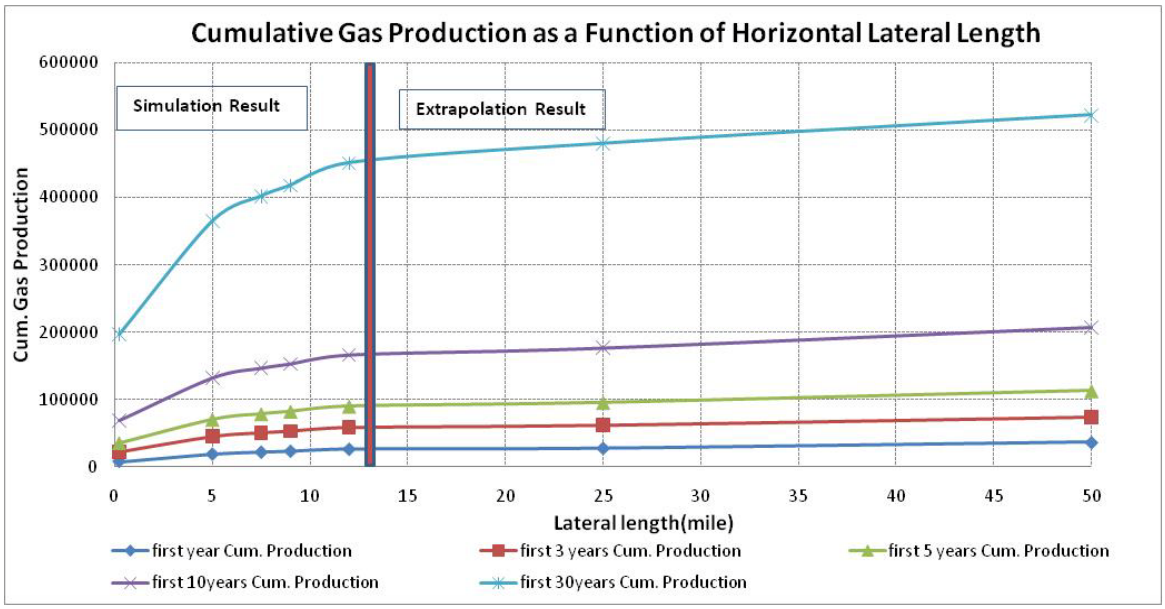


Figure 27.Cumulative gas production as a function of horizontal lateral length for 1, 3,5,10, and 30 years of Cum. Production

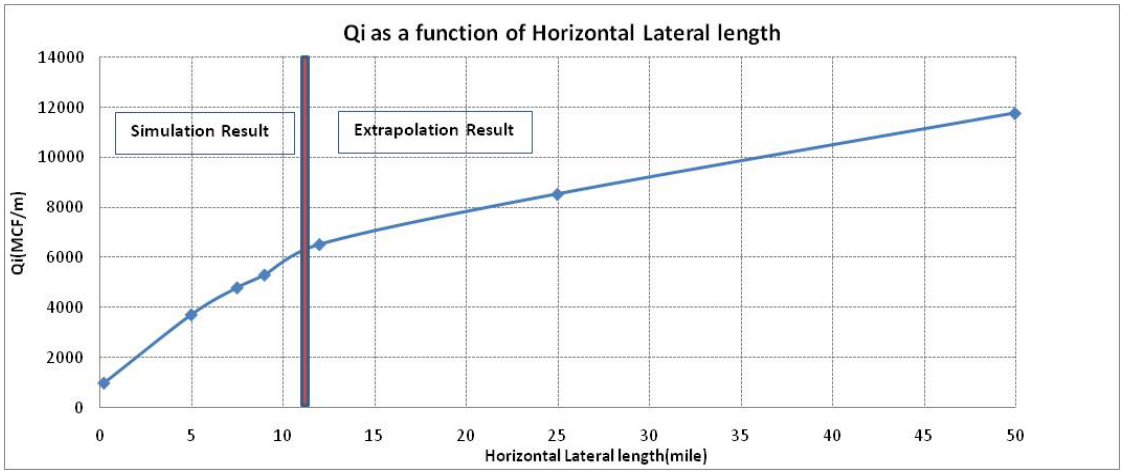
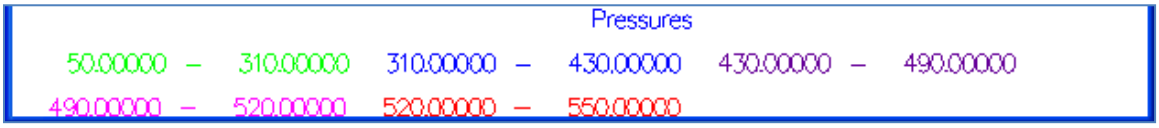


Figure 28. Initial rate as a function of horizontal lateral length



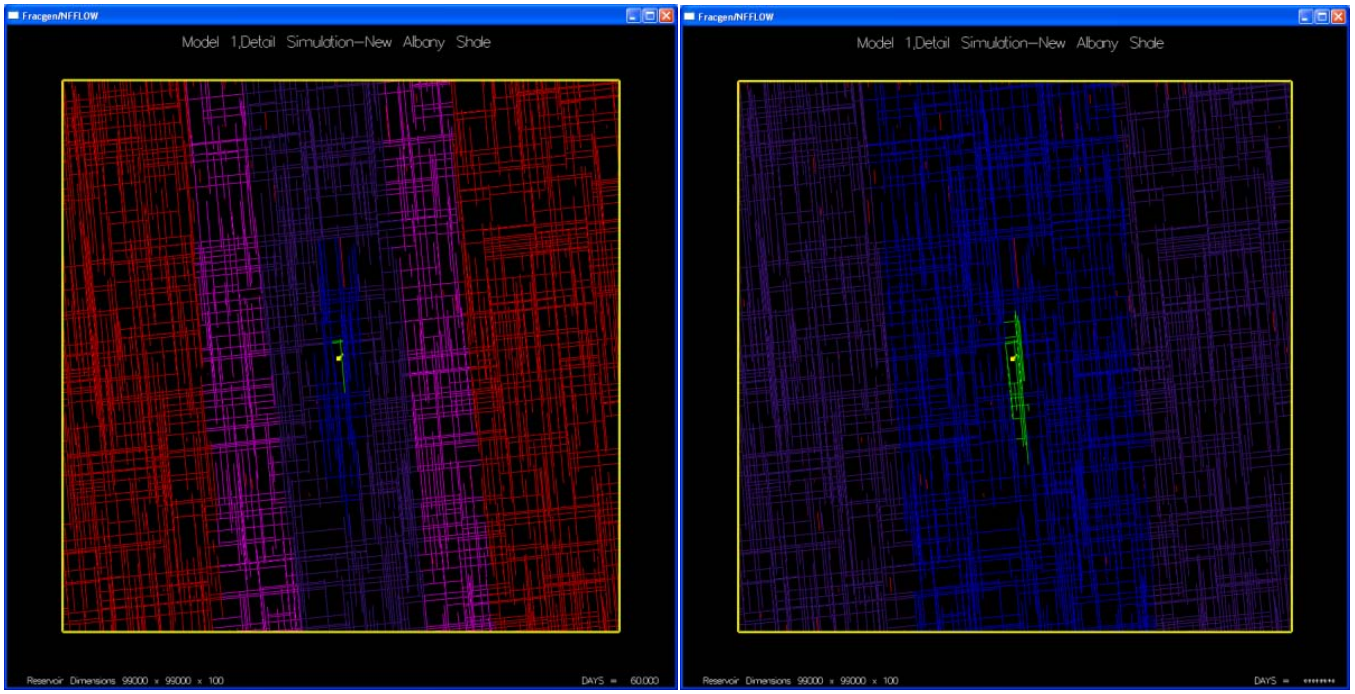


Figure 29.Pressure distribution in the reservoir as a function of time (2nd month and 30th years of production -from left to right) (Green represent the lower pressure and red shows max pressure)
(0.227 mile lateral length)

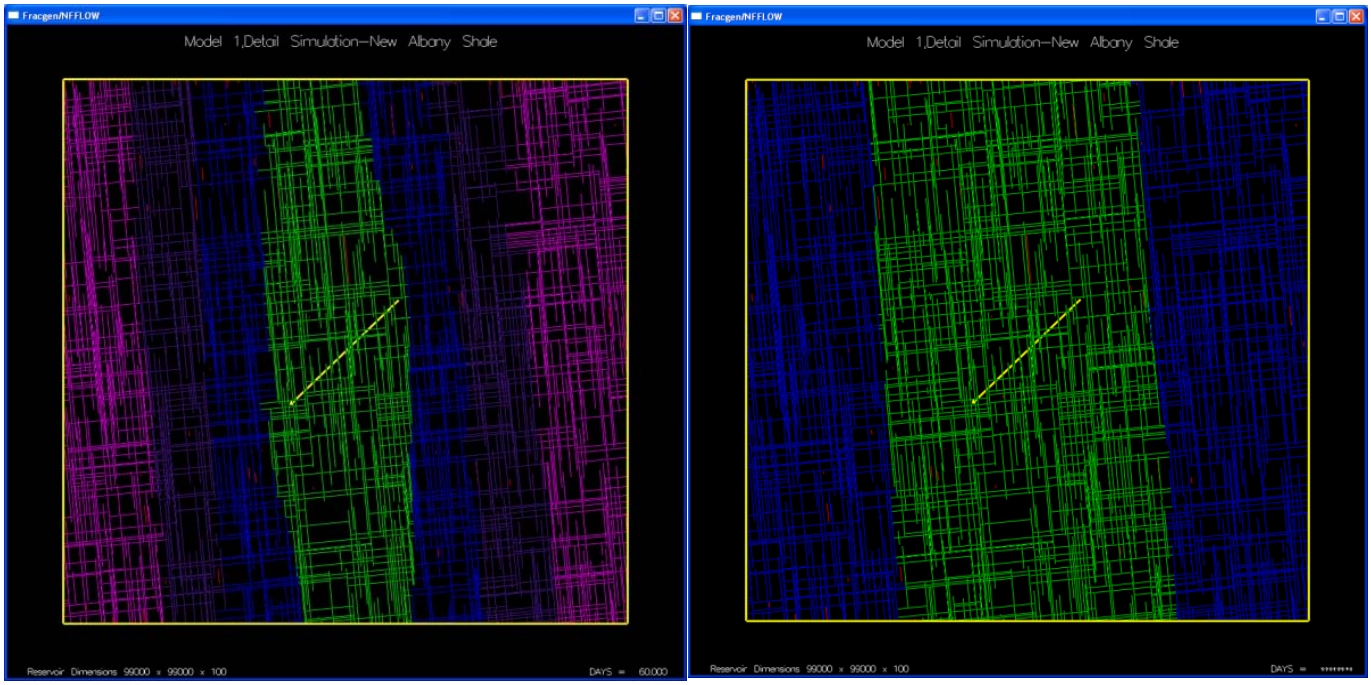


Figure 30.Pressure distribution in the reservoir as a function of time (2nd month and 30th years of production-from left to right) (Green represent the lower pressure and red shows max reservoir pressure)(5 mile lateral length)

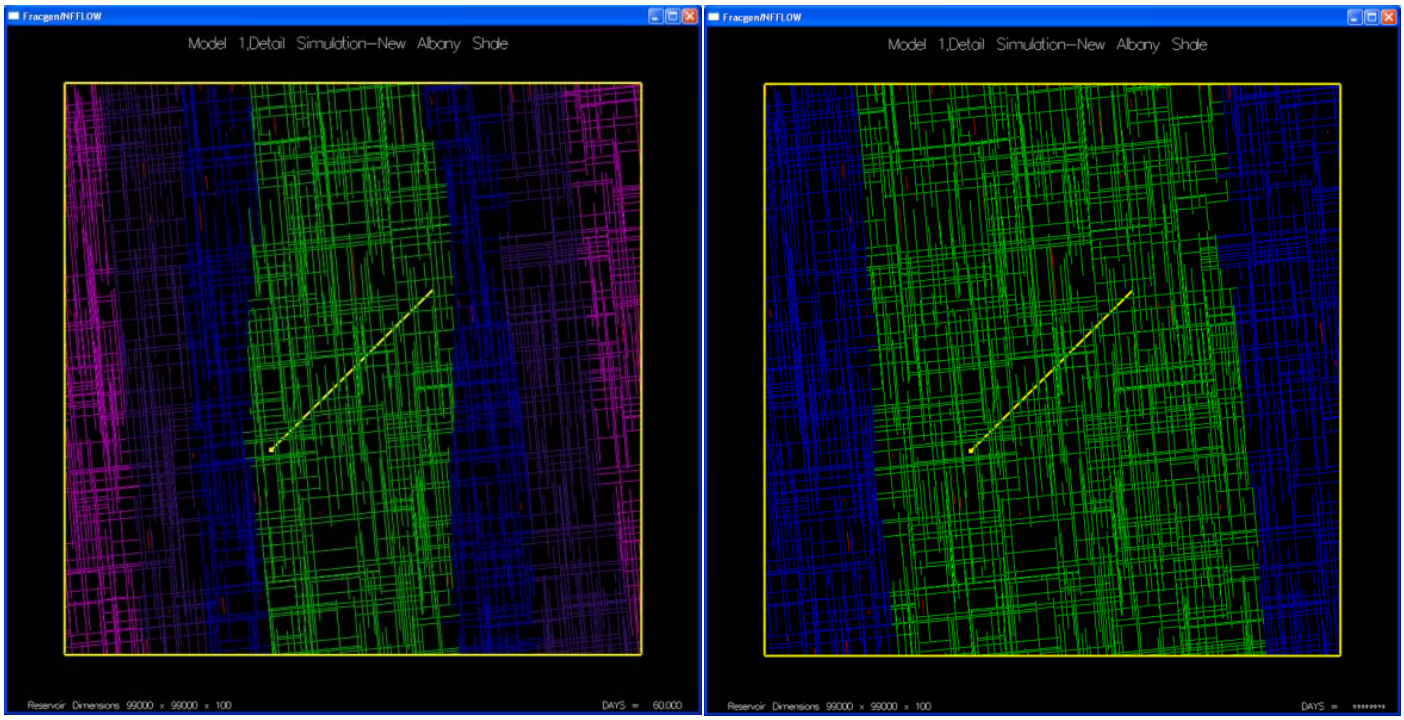


Figure 31.Pressure distribution in the reservoir as a function of time (2nd month and 30th years of production-from left to right) (Green represent the lower pressure and red shows max reservoir pressure)(7.5 mile lateral length)

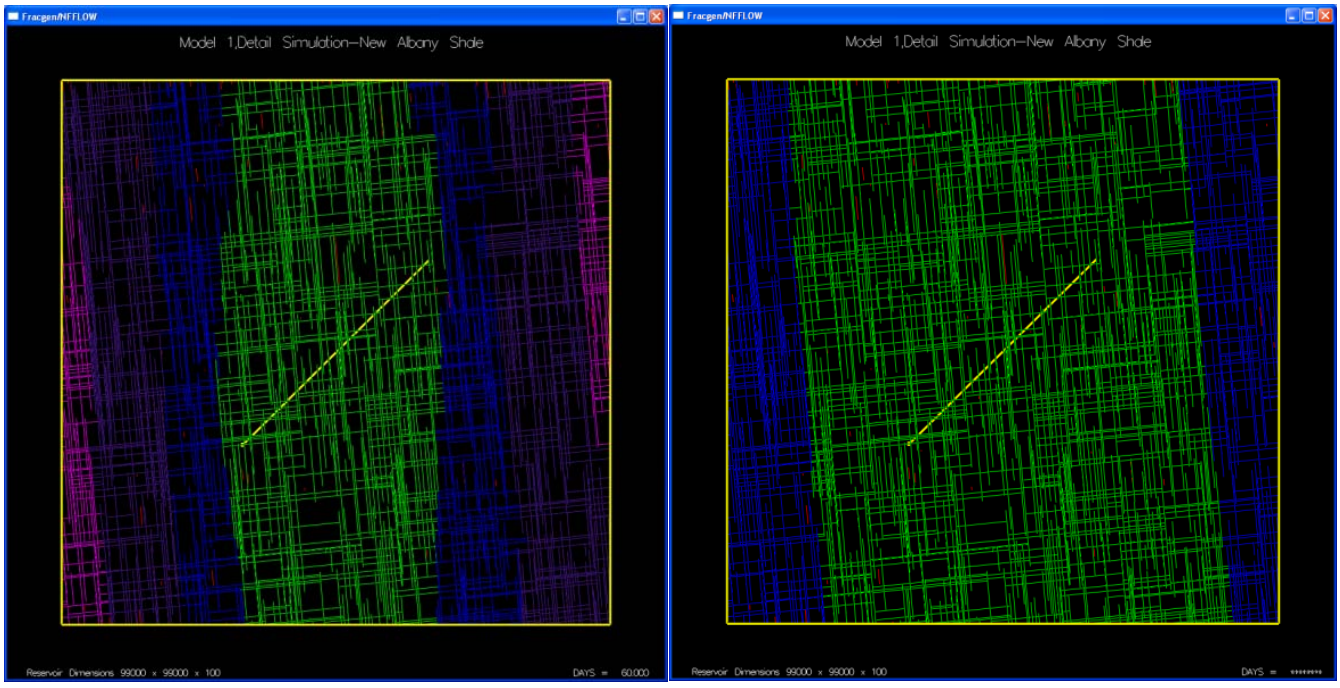


Figure 32.Pressure distribution in the reservoir as a function of time (2nd month and 30th years of production-from left to right) (Green represent the lower pressure and red shows max reservoir pressure) (9 mile lateral length)

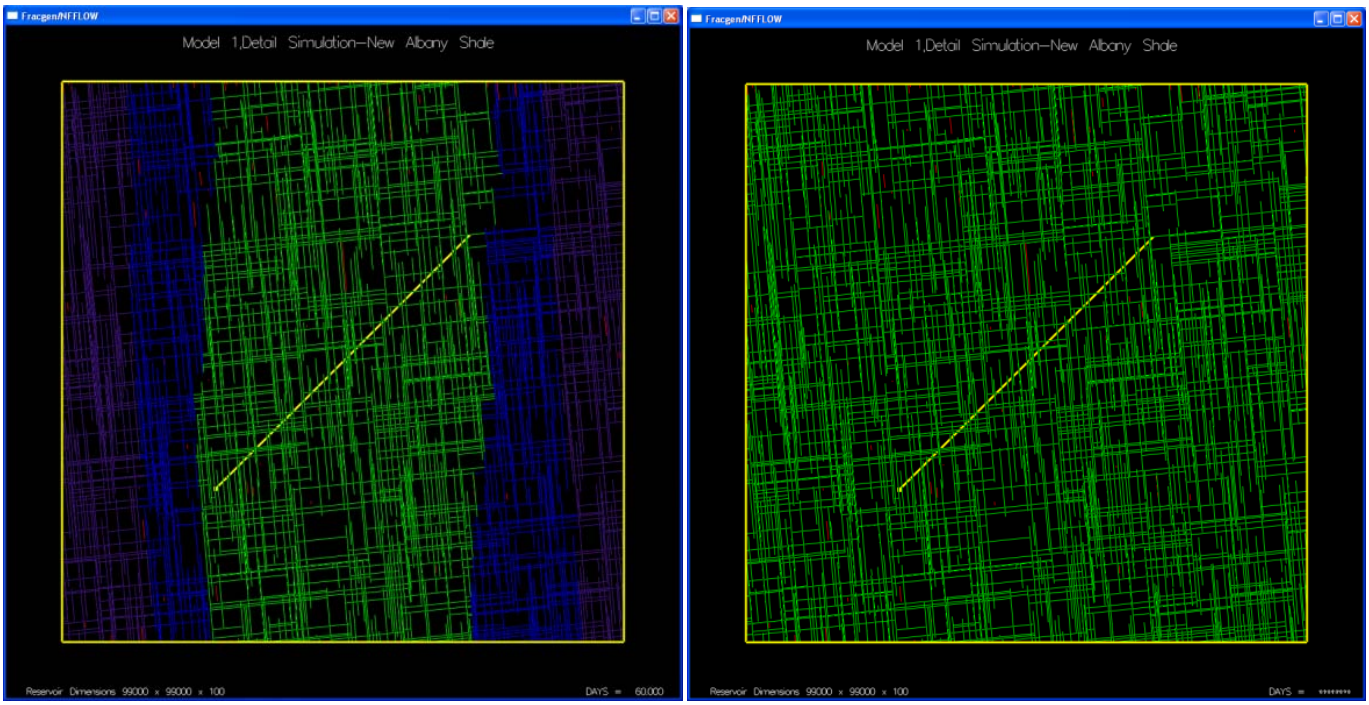


Figure 33.Pressure distribution in the reservoir as a function of time (2nd month and 30th years of production-from left to right) (Green represent the lower pressure and red shows max reservoir pressure) (12 mile lateral length)

3.5 Economic Analysis

Figure 34 summarizes the results of the sensitivity analysis simulation runs. In this Figure, initial flow rate of the well is plotted against normalized reservoir and fracture properties. This figure demonstrates that initial flow rate is most impacted by initial reservoir pressure followed by horizontal lateral length, net pay thickness, and aperture reduction factor (ARF). The parameters that are not related to the natural fracture network in the New Albany Shale such as matrix permeability and matrix porosity have the least impact on the initial flow rate among the parameters that were investigated in this study.

Economic analyses has been performed to investigate the influence of the parameters such as initial reservoir pressure, fracture aperture reduction factor, and horizontal lateral length that have most contribution in flow on the Net Present Value of benefits from producing gas wells in New Albany Shale.

The initial reservoir pressure has been changed to have values of 410,440,470 and 500 psi. Figure 35 reflects the net present values (NPV) based on $4 gas price and $0.5 operation cost per MCF and

discount rate of 10 % for this case. Figure 35 shows NPV values for different fracture aperture reduction factor. (0.01, 0.03, 0.05, and 0.07)

The same analysis has been performed on different horizontal lateral length (800, 1000, 1200, and 1400 ft) to show that the drilling horizontal wells are more favorable than drilling vertical well in New Albany Shale gas formation so horizontal wells are considered to be effective in naturally fractured reservoirs that are characterized by permeability anisotropy. (Figure 37)

As illustrated in Figure 37, the initial pressure has the higher NPV and lateral length has an NPV profile like the initial reservoir pressure.

The NPV profile for 5 years for each abovementioned case has been generated based on different discount rates. (Figure 39 through Figure 41)

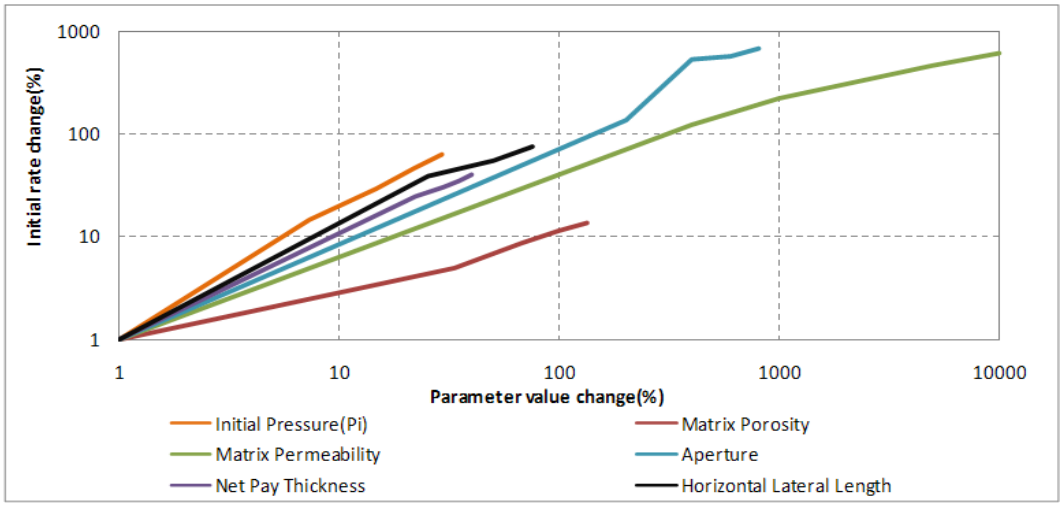


Figure 34. Sensitivity analysis on effect of normalized reservoir and fracture properties on normalized initial gas rate

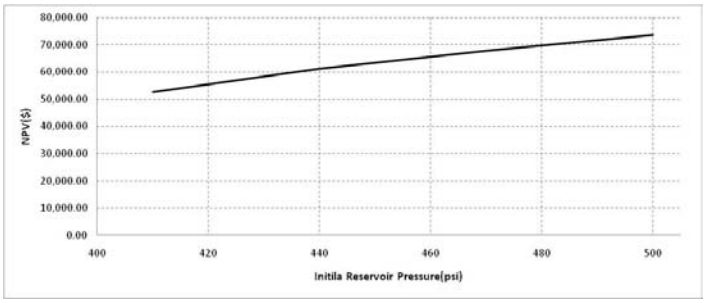


Figure 35.Effect of initial reservoir pressure on NPV factor on NPV

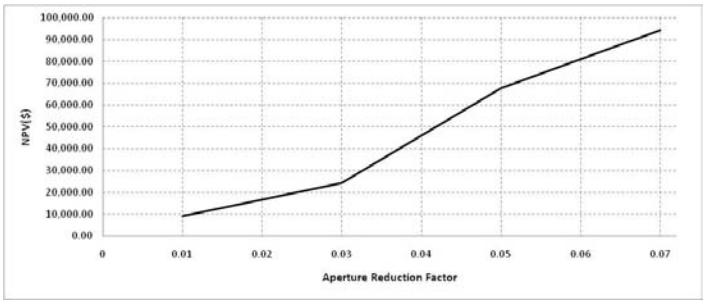


Figure 36.Effect of fracture aperture reduction

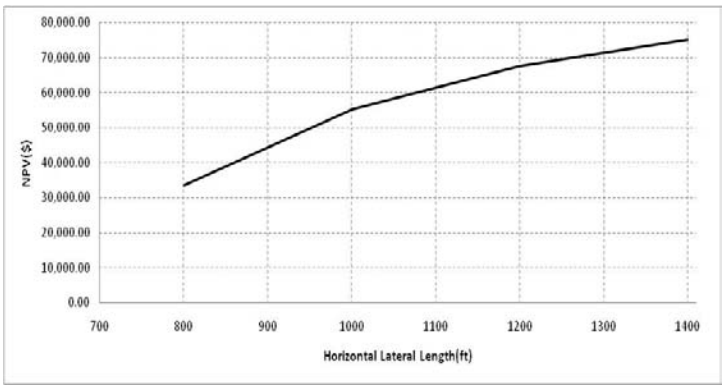


Figure 37.Effect of horizontal lateral length on NPV

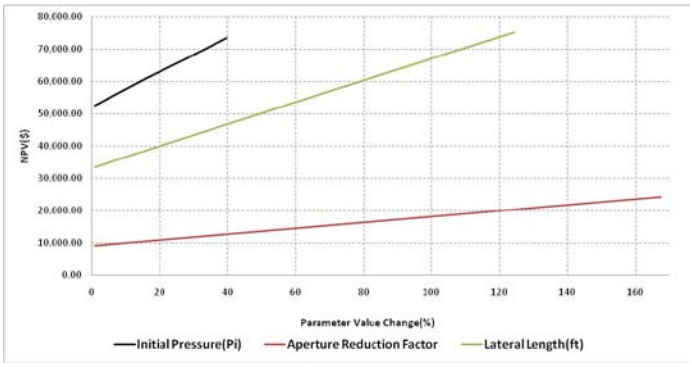


Figure 38.Comparison the effect of different parameters on NPV

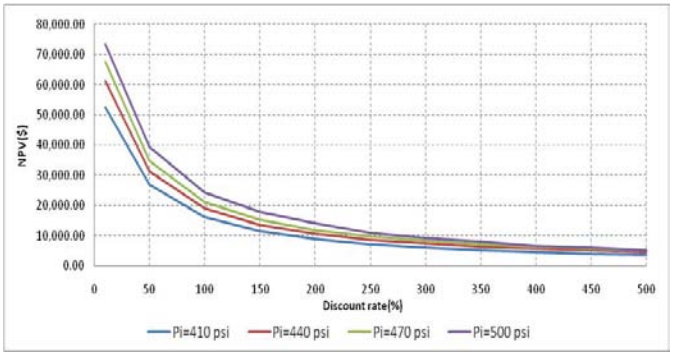


Figure 39.NPV profile for different initial reservoir pressure values

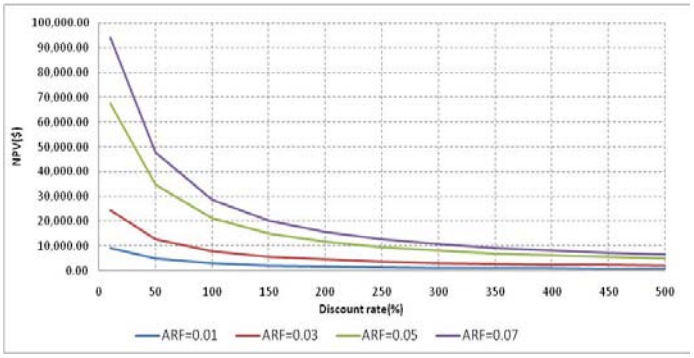


Figure 40.NPV profile for different fracture aperture reduction factor values

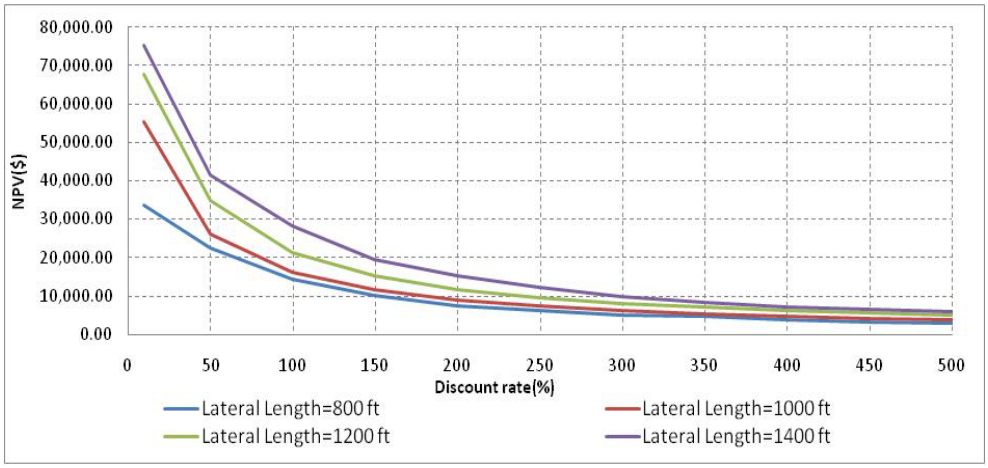


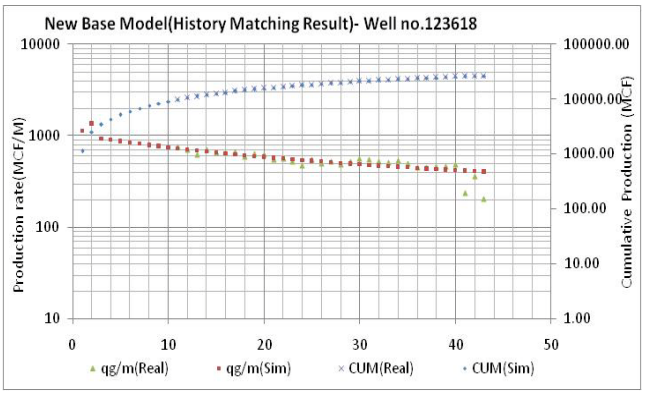
Figure 41.NPV profile for different horizontal lateral length values

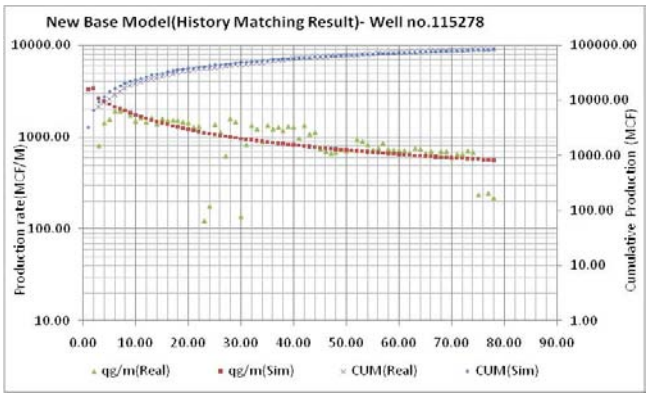
3.6 Data Preparation Procedure for Top-down Modeling

Location and monthly production rate data for all wells and well logs (not necessary for all wells) are the minimum data requirement for the Top-Down modeling. Although gas has been produced from the New Albany Shale in the Illinois Basin for more than a century, available gas production data are sparse. Production data for the older wells were either never recorded or have not been preserved. Moreover, information about recent production is difficult to obtain. The New Albany shale data for 87 wells in Western Kentucky region was extracted from Kentucky geological survey and prepared for the analysis.

Because only last 6-9 years of production history was available for the wells mentioned above, a unique natural fracture network modeling and simulation (FracGen/NFFlow) was performed in order to generate (through history matching) a relatively complete production profile for each of the 87 wells. The complete production profiles were generated using FracGen/NFFlow for the 87 wells. These production profiles were used to perform Top-Down Intelligent Reservoir Modeling for the New Albany Shale gas reservoir. Figure 42 illustrates an example of generating the complete production profile for two of the NAS wells. In this figure, the green and black dots represent the actual production rates and cumulative production data collected from the Kentucky Geological Survey while the red and blue lines represent the history matched production rate and cumulative production profiles.

In this study, FracGen/NFFlow numerical simulator has been used to model natural fracture network and simulate a single gas well in New Albany shale.





(A) (B)

Figure 42. Simulation result examples for two history-matched New Albany Shale Gas wells (Out of 87 wells)

Figure 44 represent the location of wells being studies in Western Kentucky. To enhance the resolution of the study area, the wells being analyzed were divided into 2 clusters of 55(Case1) and 32(Case 2) wells. Both cases were analyzed during this study.

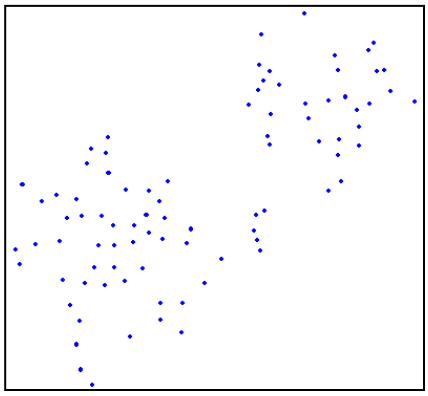


Figure 43. Location of under-study NAS gas wells

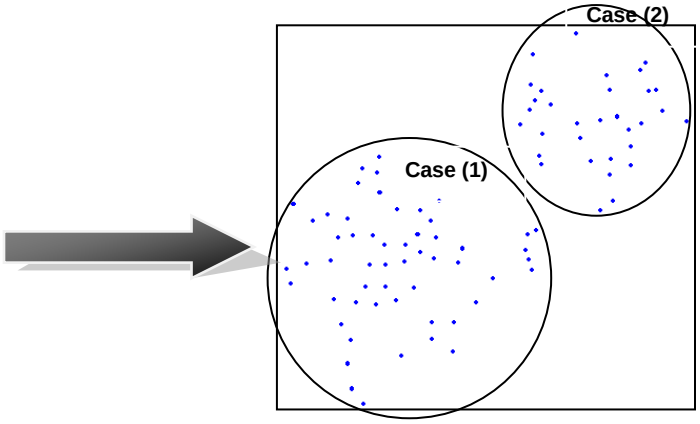


Figure 44.Two clusters of NAS wells for analysis (Case 1&2)

Case 1-The Top-Down Intelligent Reservoir Modeling begins by plotting production rate and cumulative production versus time on a semi-log scale. An automatic optimization routine based on genetic algorithms identifies the best decline curve for the given well, as both the rate versus time and the cumulative production versus time are simultaneously matched. This is demonstrated in Figure 45 for one of the NAS gas wells. Initial production rate Qi, initial decline rate Di, and hyperbolic exponent b are automatically identified. Additionally, the 30-year EUR is calculated. The information that results from the decline curve analysis is then passed to a type curve matching (TCM) procedure.

The appropriate type curves for the reservoir and fluid that is being investigated are selected. The type curves developed by Cox et al. (1995) have been used for the analysis of low-permeability shale gas reservoirs assuming constant bottom-hole pressure.

The type curve matching (TCM) has been performed by plotting the production profile using decline curve analysis results rather than the actual production data in order to minimize the subjectivity of the type curve matching. Performing decline curve and type curve analyses is an iterative process.

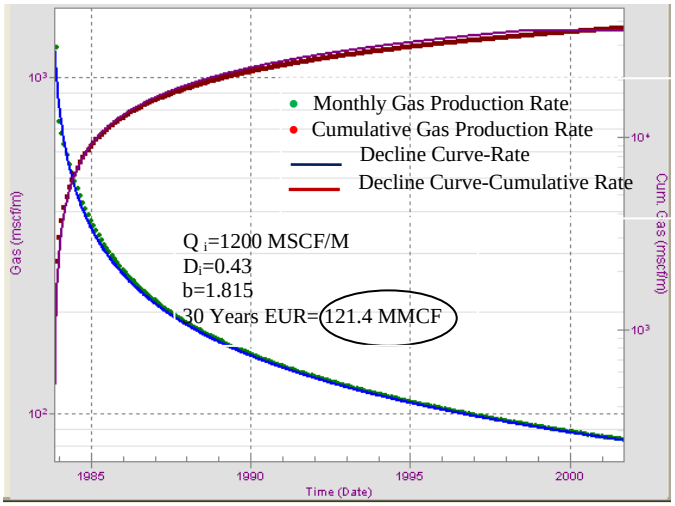


Figure 45. Decline curve analysis sample for one of NAS Gas wells

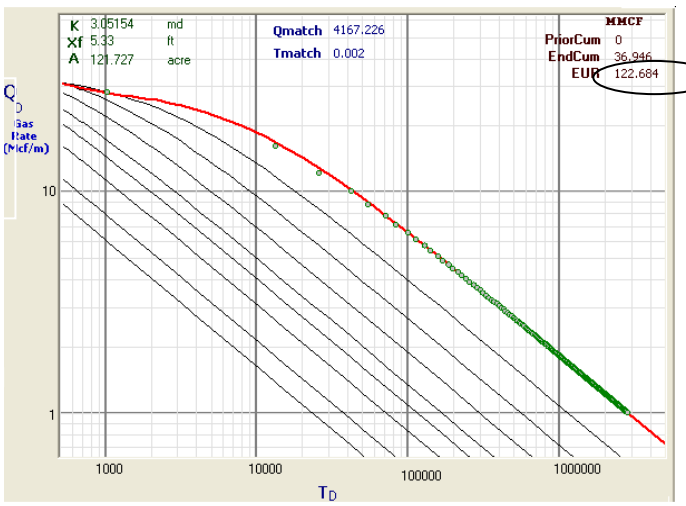


Figure 46.Type curve matching sample for one of NAS Gas wells

While following this procedure, we should always keep an eye on the 30 years EUR value calculated by these two methods as a controlling yardstick. These values should be reasonably close.

The third step of Top-down Modeling is numerical reservoir simulation using a single-well, radial numerical simulator. During history matching the production data, all of the information generated from the DCA and TCM is used to achieve an acceptable match. Decline curve analysis, type curve matching, and single well history matching are an iterative process. Figure 47 represent the qualitative comparison between the result of history matching process and decline curve analysis.

Once the individual analysis for all of the wells in the field is completed, the following information for all the wells in the field is available: initial flow rate (Qi), initial decline rate (Di), hyperbolic exponent (b), permeability (k), drainage area (A), fracture half length (Xf), and 30 Year EUR.

Figure 47 shows the well locations, followed by identification of boundary and the Voronoi grids for all the wells in the analysis for case 1.

Using the results of Decline Curve analysis and Volumetric Reserve Estimation, a well-based Recovery Factor is calculated for all wells, individually. A field-wide Recovery Factor is also calculated. Figure 49illustrates the calculate recovery factory of 17.47 % for one of the wells and Field recovery factor of 23.58%.

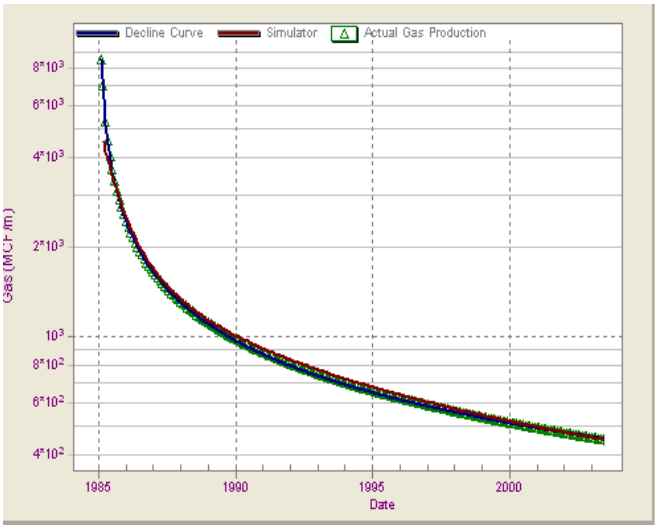


Figure 47.History matching results in comparison with DCA for one of the wells

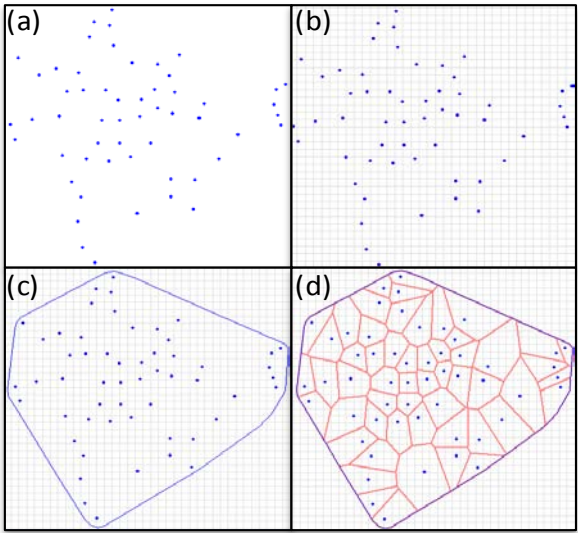


Figure 48.Generating the Voronoi cells for 55 NAS wells (Case 1)

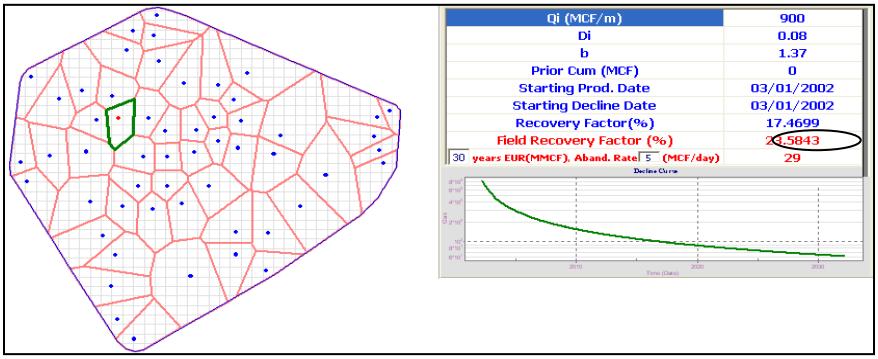
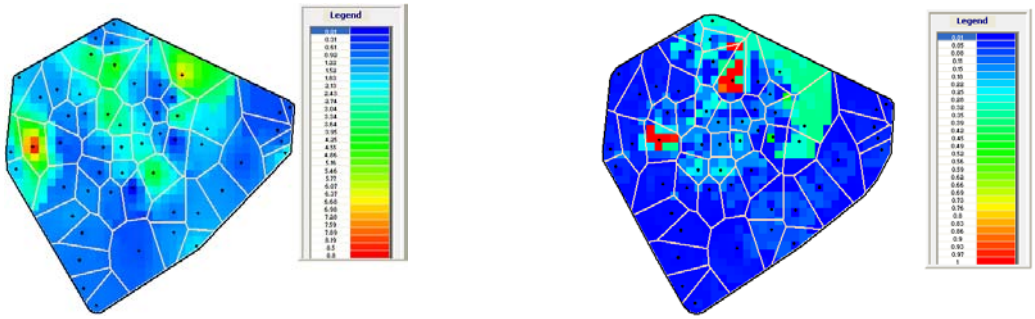


Figure 49. Calculated recovery factor for individual wells as well as field recovery factor

Once the Decline Curve Analysis and other steps mentioned above were completed, discrete, intelligent, predictive models are developed for the reservoir (production) attributes such as, first 3, 6, 9 month and 1, 3, 5, 10 years of cumulative production, decline curve information (Qi, Di and b), EUR, Fracture half length, matrix and total porosity, matrix and total permeability, net pay thickness, Initial gas in place, and well recovery factor. These sets of discrete, intelligent models are then integrated using continuous fuzzy pattern recognition in order to arrive at a cohesive model of the reservoir as a whole.

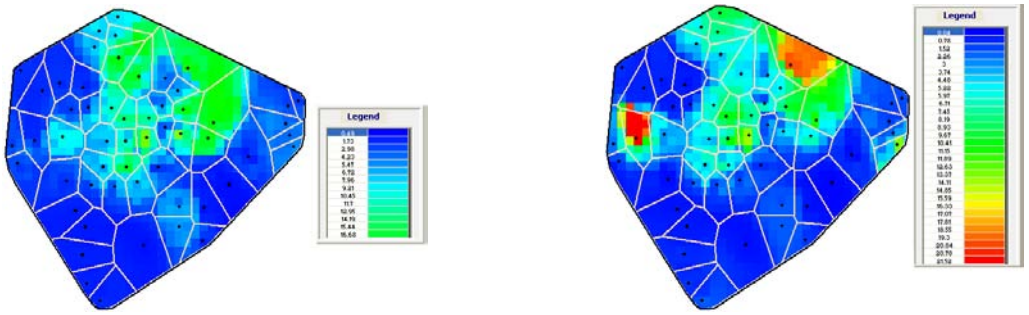
Using geostatistics a high level earth model is built. As part of the out comes of the high level earth model some of the two dimentsional maps of characteristics of the field such as porosity, permeability, and Initial Gas In Place distribution are shown in (Figure 50 and Figure 51). Another part of Top-Down, Intelligent Reservoir Modeling includes analysis of flow and production pattern characteristics usin fuzzy pattern recognition as shown in Figure 52 and Figure 53.

Upon completion of these analyses a rather complete spatio-temporal picture of the fluid flow in the reservoir emerges. The maps that are generated through these processes develop a sereis of visual guidelines that can help engineers and geo-scientist analyze reservoir behavior as a function of time and make decisions on field development strategies. Furthermore, optimum infill locations, examininig different infill scenarios and identifying potential remaining reserves based on each scenario and identifying underperformer wells are among tangible results that can be concluded from such analyses.



Matrix porosity (From simulation) Matrix Permeability ((md)*10^-6) (From simulation)

Figure 50. Results of discrete predictive modeling showing the distribution of matrix porosity, and matrix permeability for the entire field (From left to right)



Total Permeability (From type curve) Initial gas in place (IGIP)

Figure 51. Results of discrete predictive modeling showing the distribution of total permeability from type curve and initial gas in place for the entire field (From left to right)

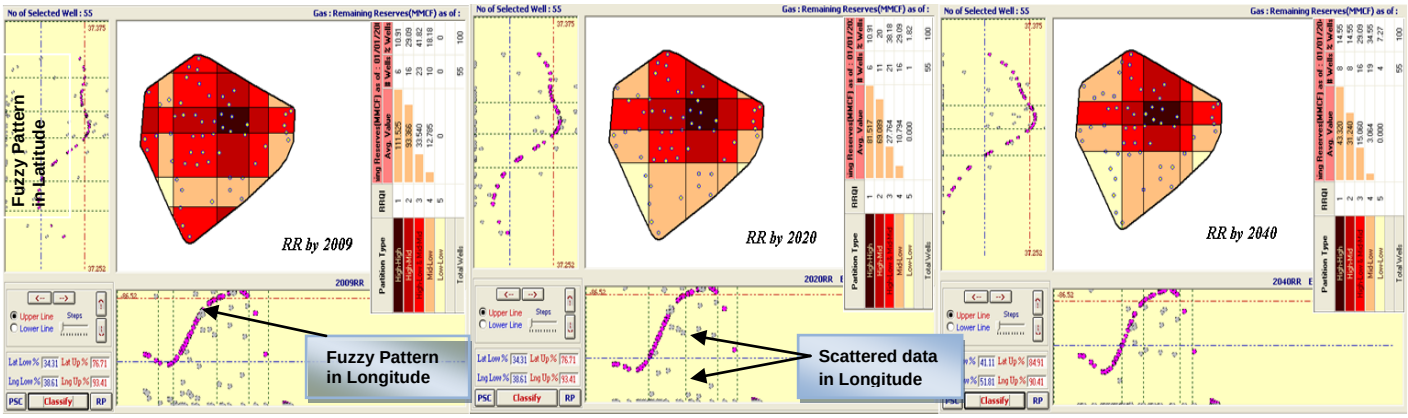
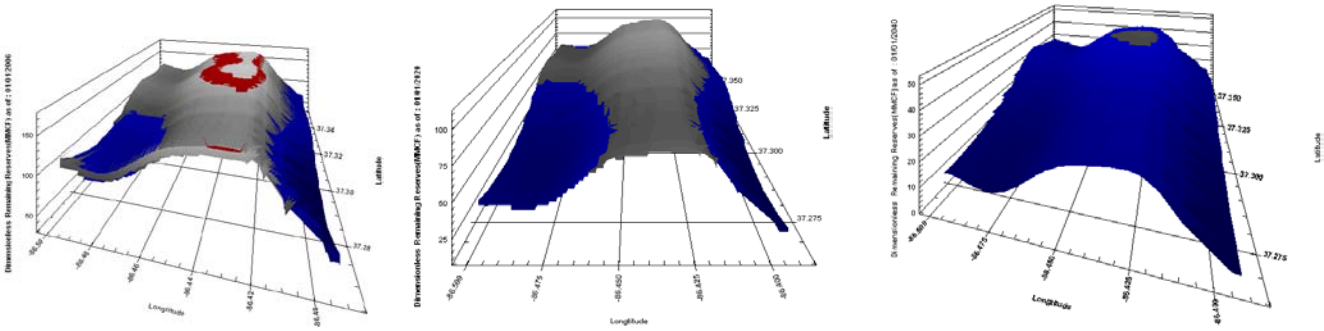


Figure 52. Results of Fuzzy Pattern Recognition showing the sweet spots in the field for the remaining reserve (MMCF) as of 2009, 2020 and 2040



Remaining Reserve, by 2009 Remaining Reserve, by 2020 Remaining Reserve, by 2040

Figure 53. Remaining reserve as a function of time

The remaining reserve as of year 2006,2020 and 2040 has been shown in Figure 52 and Figure 53. In the two dimensional maps (Figure 52) reservoir is delineated with Relative Reservori Quality Index (RRQI) being the Remaining Reserves. The delineation shown in this figure are indicated by colors. Higher quality regions (regions with high values of Remaining Reserves) are shown in darker colors and as the average value of Remaining Reserves reduces in each region, the color becomes increasing ly lighter. The difference between these three figures shows the depletion in the reservoir and identifies the parts of the field that still have potential for more recovery.

Based on the results of predictive modeling and fuzzy pattern recognition, the best spots for drilling new wells were decided. The permeability is a key parameter that plays an important role in fluid production from the reservoir. Thereby having high initial production rate in the locations which have high permeability makes sense. Another important factor while making decision about the infill

drilling locations is remaining reserves. It defines the amount of the stored fluid in the reservoir. Having both the remaining reserves and permeability, results in high storage and flow capacity. Thus, the potential spots for infill drilling can be selected, based on these parameters. Although these two parameters have considerable effect on deciding the new well locations, other parameters such as forcasted EUR for 30 years, matrix porosity,initial gas in place and also fracture half length have been taken into account.

According to these analyses, six new wells were proposed to be drilled in the reservoir. Locations of these new wells are shown in Figure 54. This figure also illustrates the change of drainage area ofter placement of new wells.

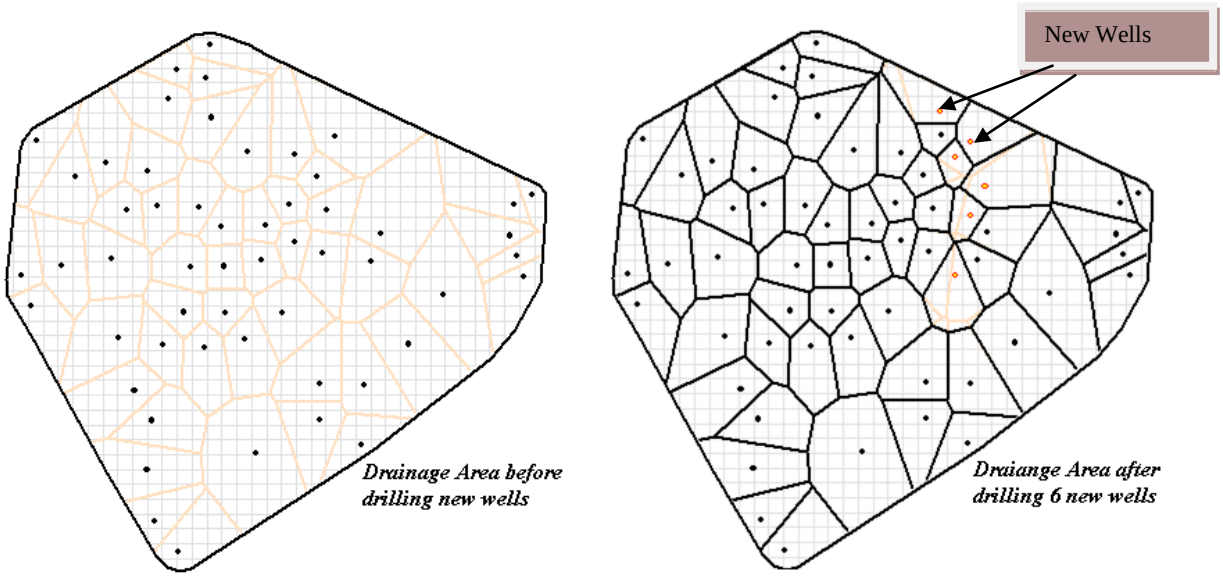


Figure 54. Proposed infill drilling locations and drainage area before and after placement of new wells (From left to right)

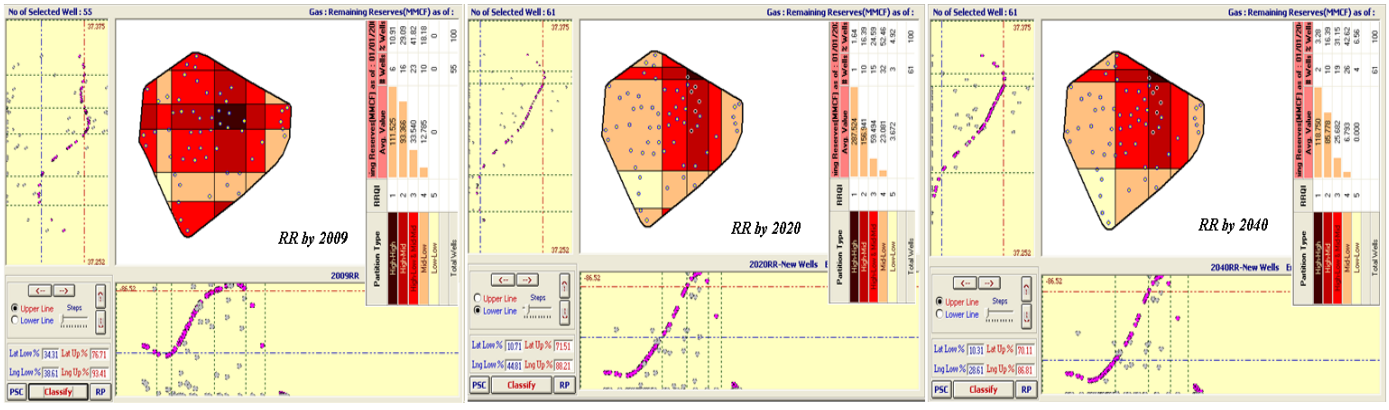
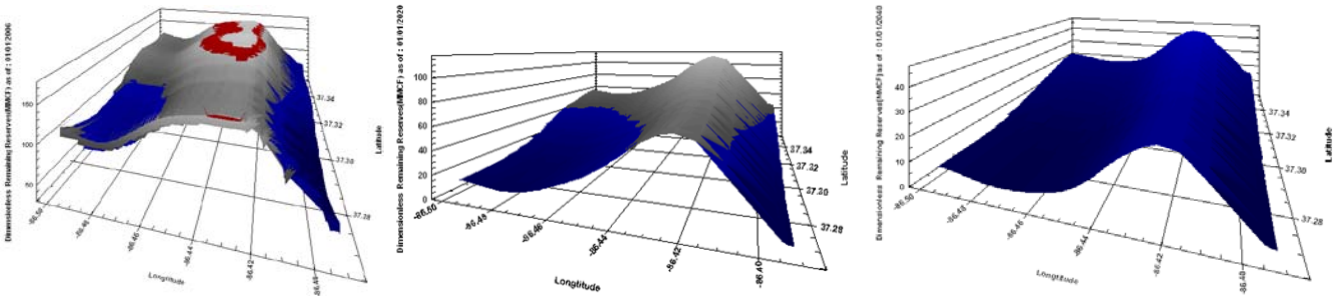


Figure 55. Results of Fuzzy Pattern Recognition showing the sweet spots in the field for the remaining reserve (MMCF) as of 2009, 2020 and 2040 (After drilling 6 extra wells)



Remaining Reserve, by 2009 Remaining Reserve, by 2020 Remaining Reserve, by 2040

Figure 56. Remaining reserve as a function of time (After drilling 6 extra wells)

Figure 55 and Figure 56 illustrates remaining reserve as of year 2006,2020 and 2040 when those 6 new wells are added to the model. New wells identified in the analyses are shown in Figure 54.By selecting new wells at different locations and repeating the analyses shown in Figure 56(observing reservoir depletion as a function of their decision on where to place new wells), engineers and geo-scientits can identify the best locations in the field that would provide the best production profiles and that satidfies their economic objectives.

Economic Analyses- The economic analyses were carried out for new infiil drilling liocations. Figure 57 demonstrates the details of economic analysis for one of proposed infill locations.The gas price that has been used in analysis was obtained from Energy Information Administriation(25) and the the vertical well cost has been estimated around $200,000 (26).The value of other parameters which are used in economic analysis are based on our best guess. The predicted Net Present Value (NPV) for each new well is listed in Table 10

Table 10. NPV for New infill drilling location

Well ID	NPV for 5 Years(USD)
1	87,054.53
2	102,207.01
3	134,870.31
4	86,170.17
5	124,827.53
6	93,311.03
Average	**104,740.10**

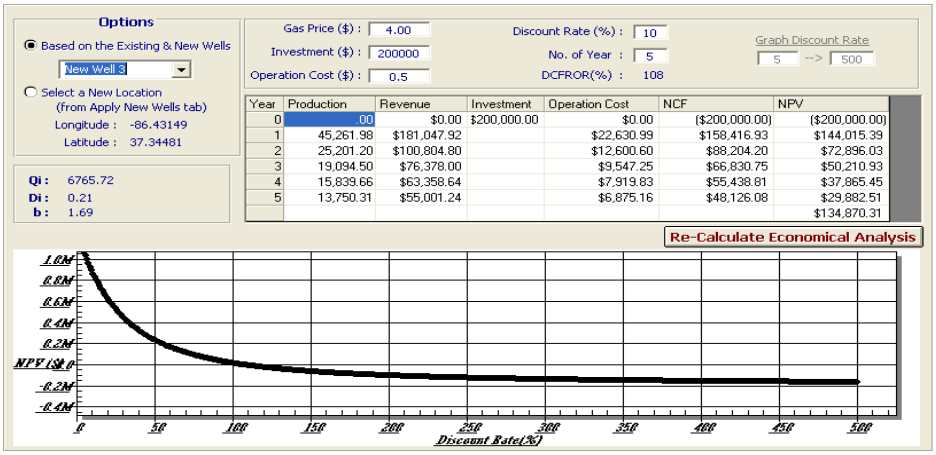


Figure 57. Economic analysis result for new well#3.

3.7 Model Calibration and Validation

One of the steps that are taken upon building the Top-Down, Intelligent Reservoir Model is to calibrate and validate the model. To calibrate the Top-Down models about 10 % of wells for are removed from the analyses. This constitutes removal of 6 wells from the analysis. The models are developed using the remaining 49 wells. The objective is to make sure that the Top-Down model can predict the 1 year cumulative production for these removed wells (blind data set). The results are shown in Table 11 and Figure 58.

For example in Table 11, four Relative Reservoir Quality Indices (RRQI) are shown as well as the model results that indicates the prediction for the blind/validation wells. As indicated in this table the Top-Down model predicted that the average 1 year cumulative production for wells drilled in the RRQI "1" (the darkest areas in Figure 58) will be more than 31.98 MMSCF. One well in RRQI "1" is removed and the average 1 year cumulative production for this well was 35.06 MMSCF **(correct prediction)**.

Furthermore, the Top-Down model predicted that the average 1 year cumulative production for well in the RRQI "2" will be between 16.9 and 31.98 MMSCF. As shown in Table 11 there was 1 well drilled in RRQI "2" and the average 1 year cumulative production for this well was 26.13 MMSCF **(correct prediction)**.

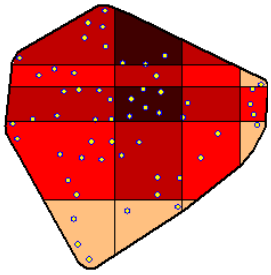
For RRQI “3” the Top-Down model over-estimates the result slightly. It predicted that the average 1 year cumulative production for wells drilled in the RRQI “3” will be between 8.45 and 16.9 MMSCF while the 1 well drilled in RRQI “2” had an average 1 year cumulative production of 18.5 MMSCF.

The Top-Down model predicted that the average 1 year cum. for one well drilled in the RRQI “4” will be between 7.69 and 8.45 MMSCF and it turned out to be 8 MMSCF **(correct prediction)**.

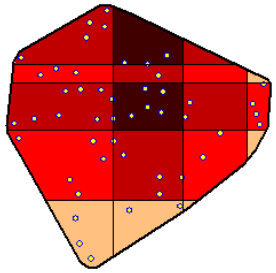
The same methodology has been performed for the second case.

Table 11. Results of Top-Down modeling (Case 1)

1 Year Cumulative Production(MSCF)					
	Model Results			Removed Wells	
RRQI	More Than	&	Less than	Average 1 Yr Cum	No. of Wells
1	31,980.55			35,062.77	1
2	16,894.13	&	31,980.55	26,130.53	2
3	8,447.53	&	16,894.13	18,553.57	2
4	7,686.24	&	8,447.53	8,006.76	1
			7,686.24	Total	6



1 Year Cumulative Production (55Wells)



1 Year Cumulative Production (49 Wells)

Figure 58. Results of Fuzzy Pattern Recognition showing the sweet spots in the field for the 1 Year cum for 55 wells (left) and 1Year cum. Production for 49 wells (right).(Case 1)

Case 2-The same analysis explained in the preceding section has been carried out for second case as well.

The generated field model besed on result of disceret intelligent modeling and fuzzy pattern recognition can be used to estimate the reserves, determine optimum infill drilling locations, follow fluid flow and depletion, verify remaining reserves,and detect underperforming wells. (Figure 63 through Figure 67)

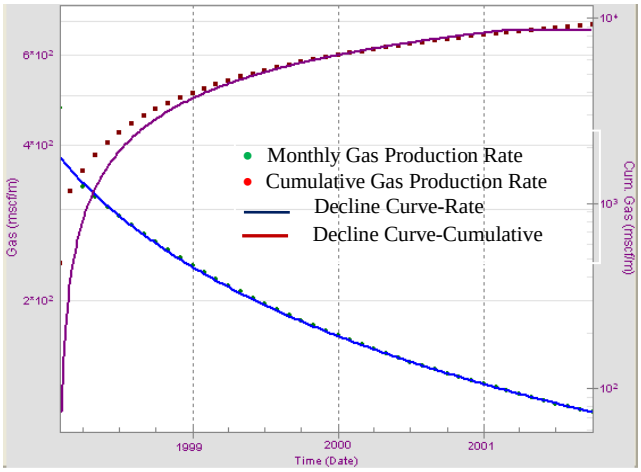


Figure 59. DCA sample for one of NAS Gas well

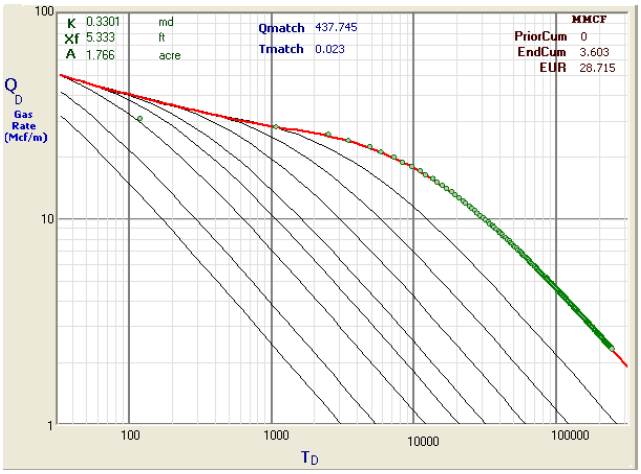


Figure 60. TCM sample for one NAS Gas wells

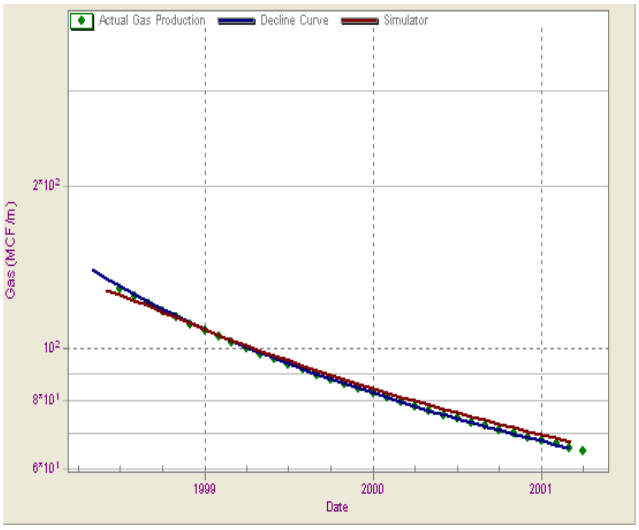


Figure 61. HM results in comparison with DCA

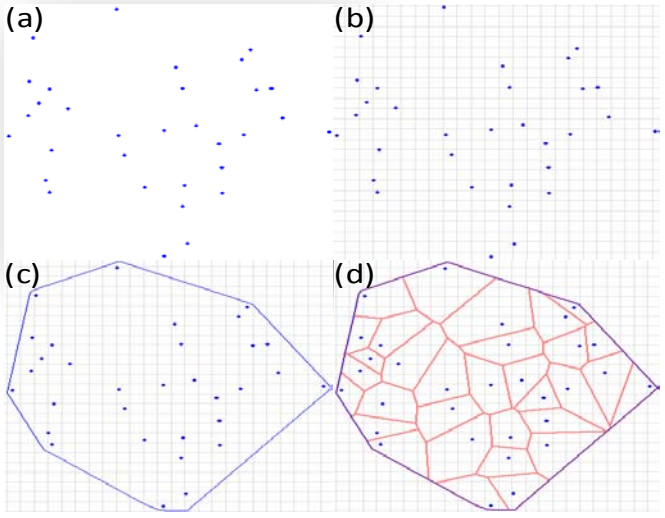
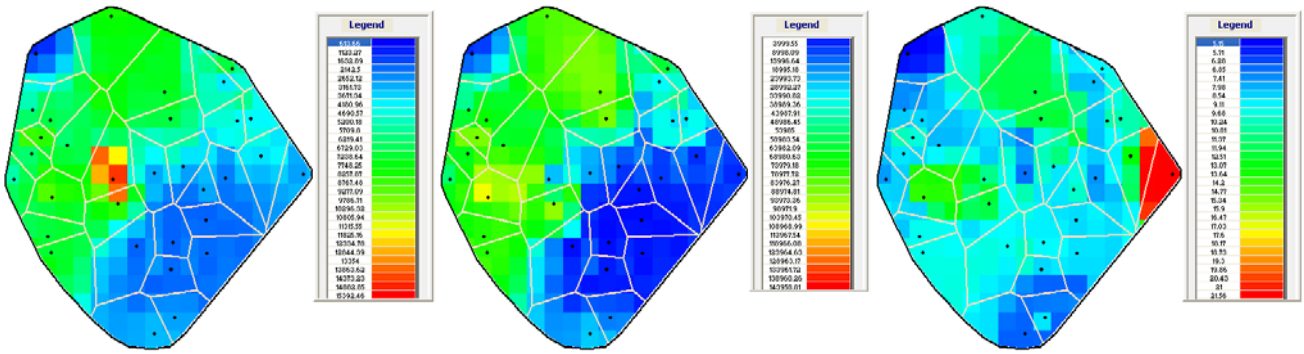


Figure 62. Generating the Voronoi cells for 32 NAS wells (Case 2)



3 Month Cumulative Production 5 Years Cumulative Production Fracture half-length

Figure 63. Results of discrete predictive modeling showing the distribution of first 3 months, 5 year cum. Production and fracture half length for the entire field (From left to right)

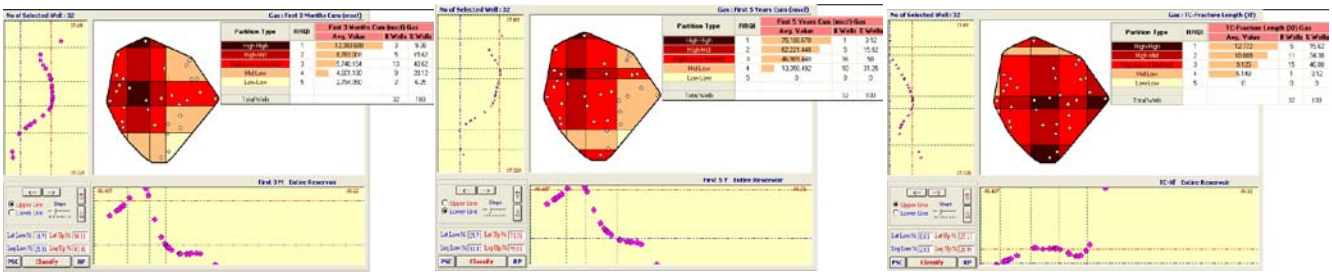
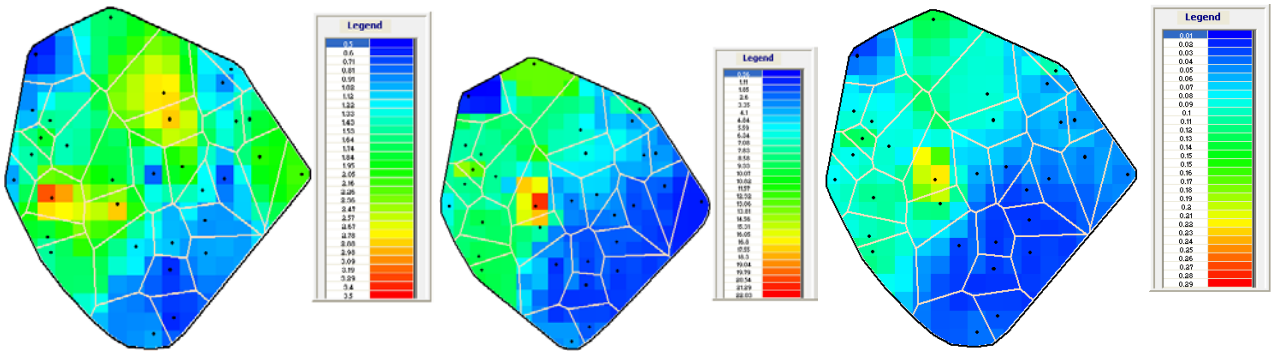


Figure 64. Results of Fuzzy Pattern Recognition showing the sweet spots in the field for the first 3 months, 5-year cum. Production, and the fracture half-length (From left to right)



Matrix porosity Total Permeability (TC) Matrix Permeability

((md)*10^-6)

Figure 65. Results of discrete predictive modeling showing the distribution of total porosity, matrix porosity, and net pay thickness for the entire field (From left to right)

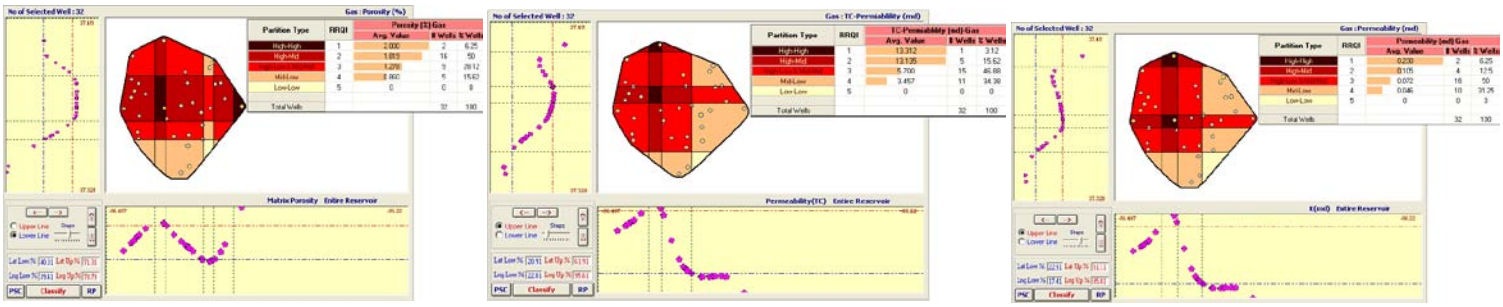
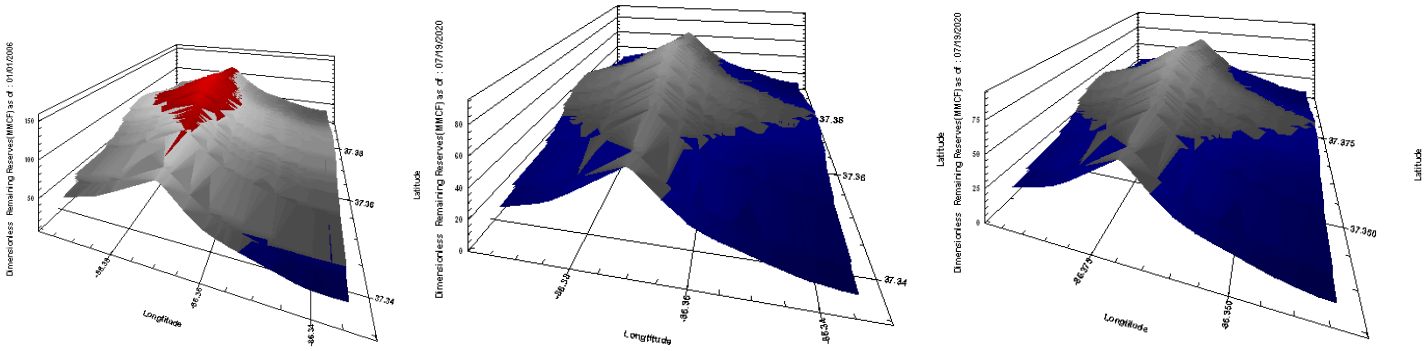


Figure 66. Results of Fuzzy Pattern Recognition showing the sweet spots in the field for the matrix porosity and total permeability from type curve and matrix permeability (From left to right)



Remaining Reserve, by 2009 Remaining Reserve, by 2020 Remaining Reserve, by 2040

Figure 67. Remaining reserve as a function of time

The remaining reserve as of year 2009,2020 and 2040 has been shown in Figure 67. The difference between these three figures shows the depletion in the reservoir and identifies the parts of the field that still have potential for more recovery.

3.8 Model Calibration and Validation

The same methodology has been performed for the second case.(Table 12 and Figure 68)

For example in table 1 the four Relative Reservoir Quality Indices (RRQI) are shown as well as the model results that indicates the prediction for the blind/validation wells. As indicated in this table the Top-Down model predicted that the average 1 year cumulative production for wells drilled in the RRQI "1" (the darkest areas in Figure 68) will be more than 29.56 MMSCF. One well in RRQI "1" is removed and the average 1 year cumulative production for this well was 32.39 MMSCF. **(correct prediction)**

Furthermore, the Top-Down model predicted that the average 1 year cumulative production for well in the RRQI "2" will be between 18.37 and 20.93 MMSCF. As shown in Table 12 there was 1 well drilled in RRQI "2" and the average 1 year cumulative production for this well was 22.33 MMSCF .(**correct prediction)**

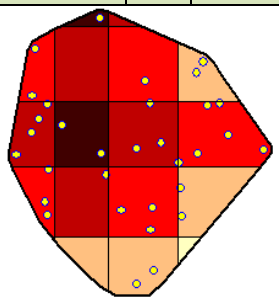
For RRQI "3" the Top-Down model predicted that the average 1 year cumulative production for wells drilled in the RRQI "3" will be between 12.92 and 18.37 MMSCF . The 1 well drilled in RRQI "2" had an average 1 year cumulative production of 14.49 MMSCF. **(correct prediction)**

The Top-Down model predicted that the average 1 year cum. for one well drilled in the RRQI "4" will be between 10.04 and 12.92 MMSCF and it turned out to be 11.5 MMSCF. **(correct prediction)**

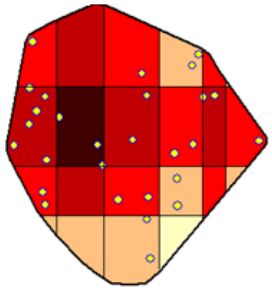
The same methodology has been performed for the second case.

Table 12. Results of Top-Down modeling (Case 2)

1 Year Cumulative Production(MSCF)					
	Model Results			Removed Wells	
RRQI	More Than	&	Less than	Average 1 Yr Cum	No. of Wells
1	29,559.87			32,391.21	1
2	18,371.65	&	20,937.61	22,332.96	1
3	12,924.83	&	18,371.65	14,492.04	1
4	10,043.96	&	12,924.83	11,507.91	1
			10,043.96	Total	4



1 Year Cumulative Production (32Wells)



1 Year Cumulative Production (28 Wells)

Figure 68. Results of Fuzzy Pattern Recognition showing the sweet spots in the field for the 1Year cum for 32 wells (left) and 1Year cum. Production for 28 wells (right).(Case 2)

3.9 New Albany Shale Subsurface Modeling-Recently Completed Gas Wells

In this part, 31 recently drilled well in Christian county Western Kentucky-Halley's Mills quadrangle have been used to perform the geological analysis using GeoGraphix®™ software Halliburton. The available well logs have been interpreted and the top and bottoms for New Albany Shale and the lower formation (Devonian LS) have been picked. The gas effect has been recognized using the neutron and density porosity logs. The structural maps for these formations have been created.

GeoGraphix® Discovery™ is an integrated suite of geophysical and geologic tools that increase asset understanding and provide the highest quality geologic maps available to the industry today.

The GeoGraphix Discovery suite is a Windows®-based geologic and geophysical interpretation system that combines industry-leading technologies supported by a common data and project architecture.

GeoGraphix® PRIZM™ software is a sophisticated log analysis application that is designed for multi-well petrophysical projects. Designed to meet the needs of both the petrophysicist and geologist, PRIZM software technology operates in a familiar Microsoft® Windows® environment. Furthermore, PRIZM software contains customizable and interactive tools for data editing, log analysis, and curve displays in multi-well, multi-zone projects. It is an ideal tool for reservoir characterization. PRIZM has tight integration with the GeoGraphix Discovery suite of mapping, cross-section, zone analysis and geophysical applications.

Zone manager feature of Geographix® software has been used .The available production data and other static reservoir properties have been imported as the attributes to generate related contour maps and have been are interpreted.

The project was built in the GeoGraphix, setting the datum as NAD 1927.Figure 69 shows the workflow of this process.

The next step was to import the well location map and corresponding well logs. The GR, Resistivity, Neutron porosity and Density porosity logs were available for almost all the wells.

Figure 70 lists the formation names. Since we are focusing on New Albany Shale for this study only this formation and the underlying formation (Devonian Limestone) are picked in the logs.

The Gamma ray was used to determine the shales using the "Area Fill" feature of the "Prizm" (Figure 71).

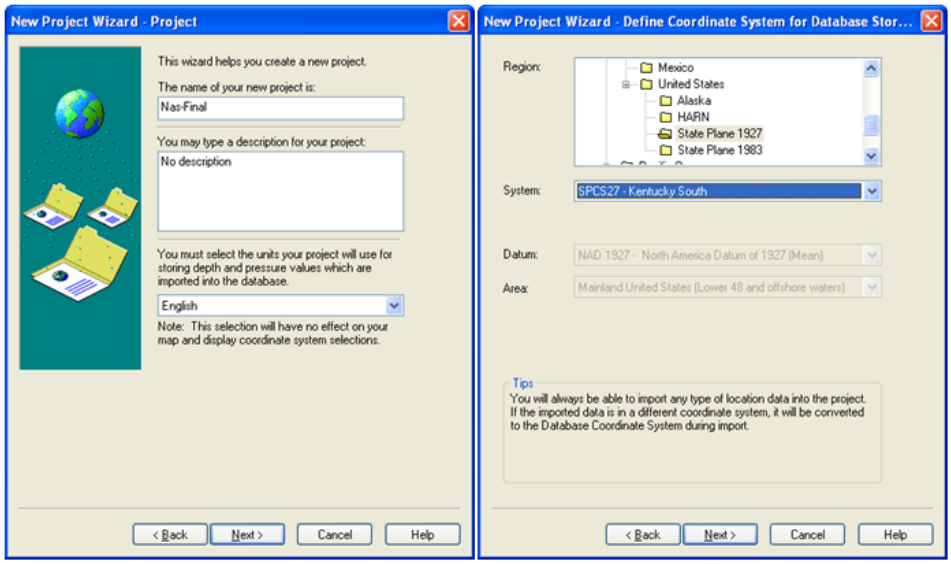


Figure 69. Making a New Project and Setting the Datum

When gas is present, the neutron log reads low porosity, and there is a big spread between the density and neutron curves. This spread is called "gas effect". The presence of sandstone also causes the two curves to spread, but not nearly so much as gas effect. This concept was used again in the "Area Fill" section of "Prizm" and by setting it to show the Gas Effect in the formations that we have the density porosity value more than the neutron porosity value we are going to have log sections as shown in Figure 71.

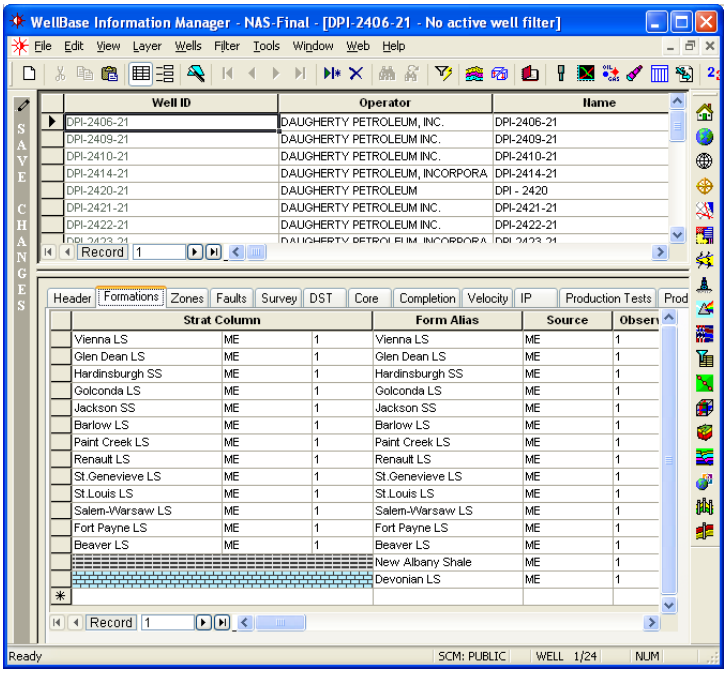


Figure 70.Well Records and Formation List.

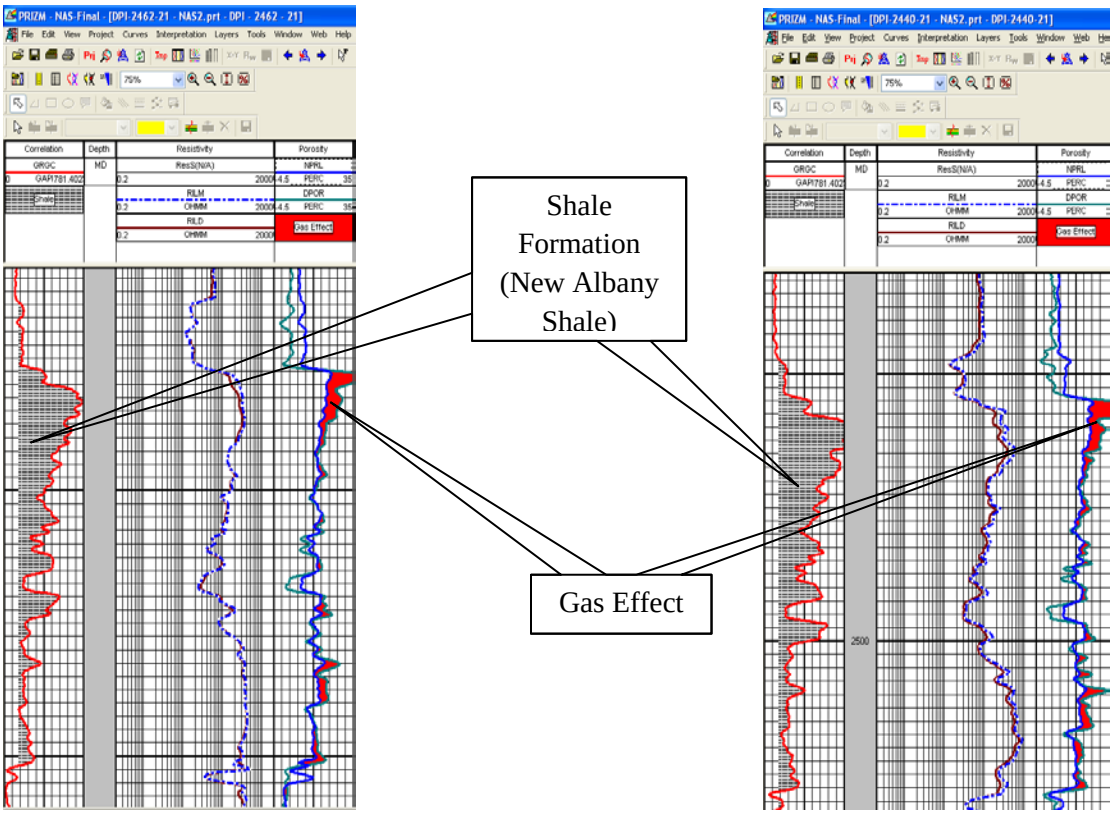


Figure 71.Interpreting the Shale Formations and Gas Effect in Prizm.

Four cross sections were created to interpret the well logs in the "X-Section" part of GeoGraphix. (Figure 72) .The New Albany Shale and Devonian Limestone tops and bottoms were picked in the well logs (Figure 73 and Figure 74). The data obtained from this step is used to build the structural maps of these formations in "GeoAtlas".

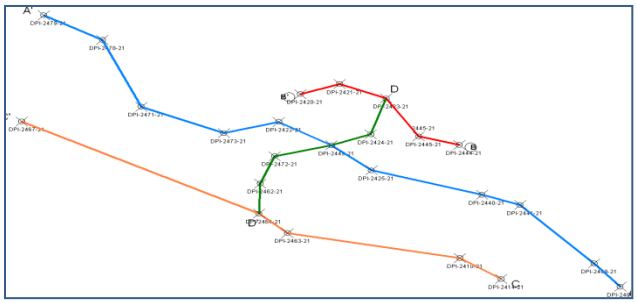


Figure 72. Four cross sections were created for analyzing the well logs.

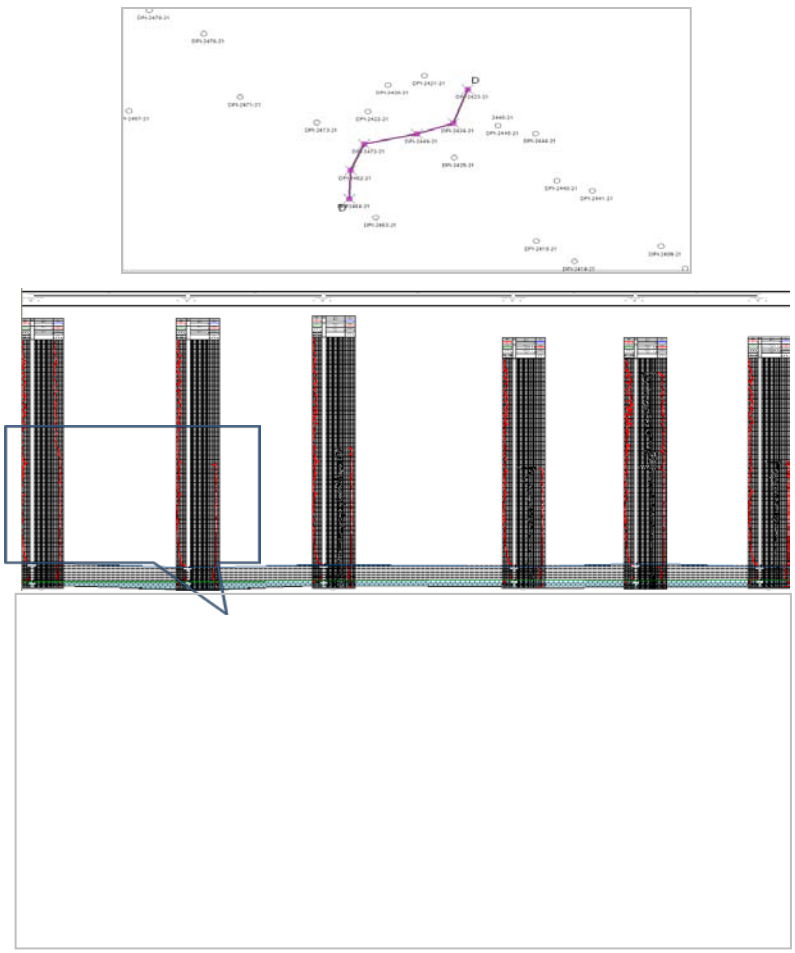


Figure 73. Picking the top and bottom of formations in Cross Section D.

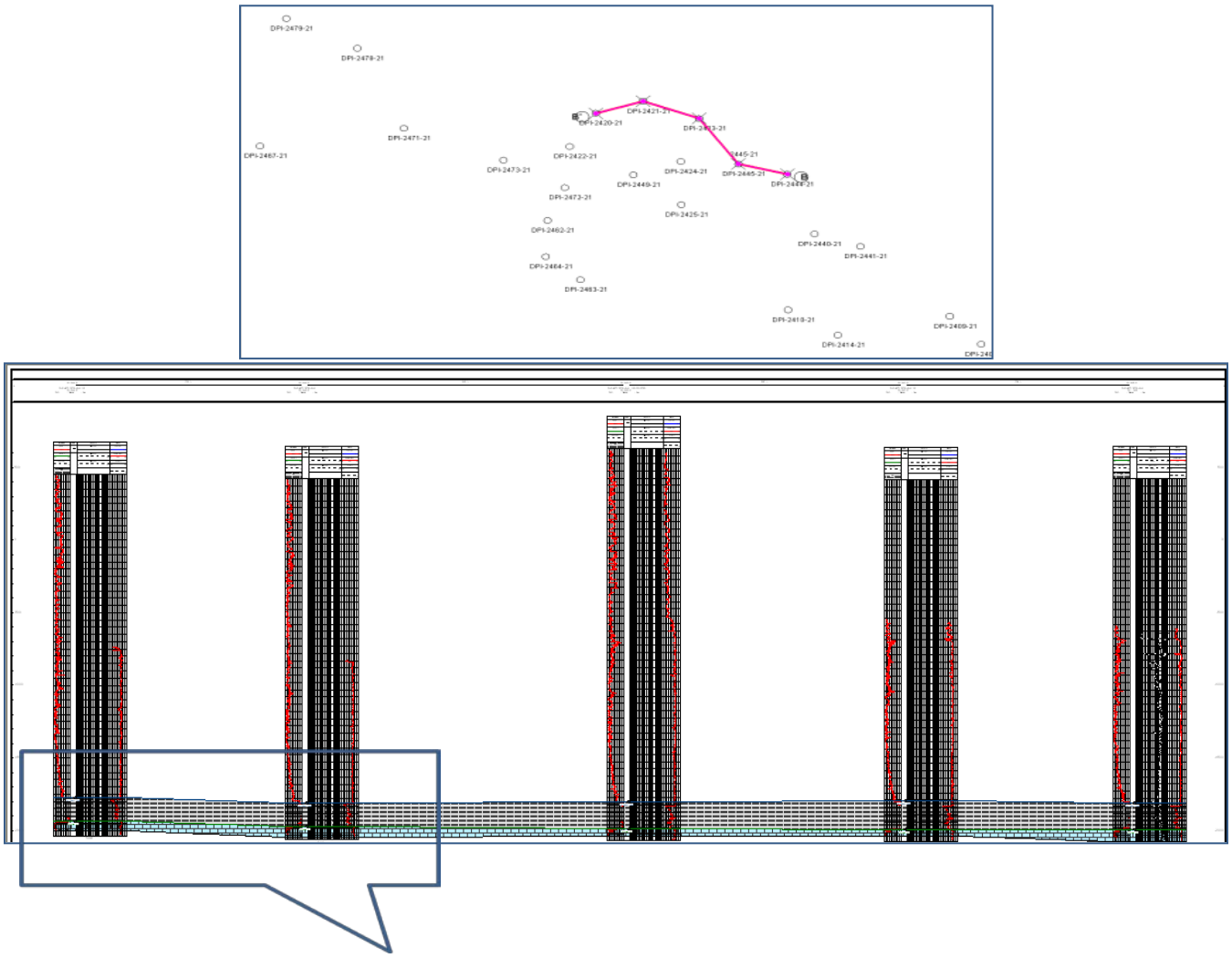


Figure 74.Picking the top and bottom of formations in Cross Section B.

The production data for the wells were imported to "Zone Manager". Resistivity logs were used to calculate the water saturation in the target formation (using the Schlumberger charts).Since New Albany Shale is only producing dry gas; the gas saturation was calculated base on the difference between 100% and the water saturation.

The average porosity was calculated by averaging the neutron and density porosity in the New Albany formation. This porosity takes into account both the matrix and fracture porosity. Since this is a Shale formation, the matrix porosity values are not significant in comparison with the fracture porosity.

A fracture network was built for New Albany Shale formation in "FracGen" software and it was history matched using the production data from these wells in "NFFlow". The matrix porosity, permeability and initial pressure calculated results from history matching process were used as import to "Zone Manager".

The formations top and bottom were used to create the structural maps. Figure 75 shows the Top Subsea map of New Albany Shale (NAS).

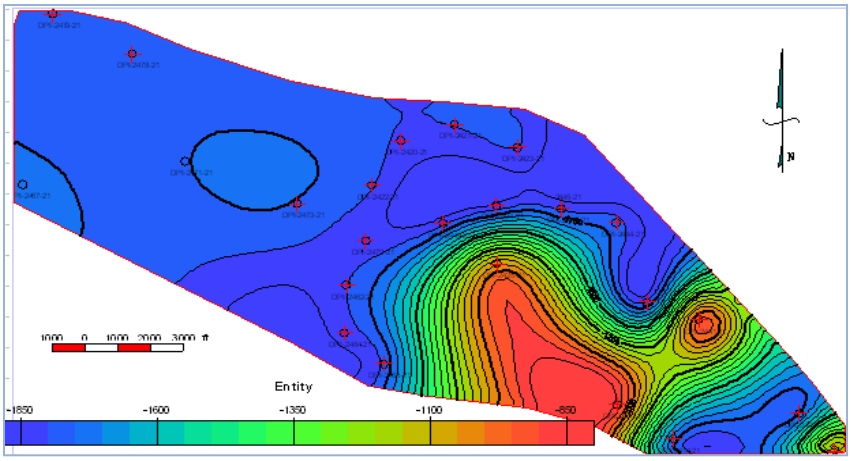


Figure 75. NAS Top Subsea

This figure shows that the formation is getting shallower in the south part, so it is dipping North-West. The top subsea map, which is, actually the NAS bottom map is shown below. (Figure 76)

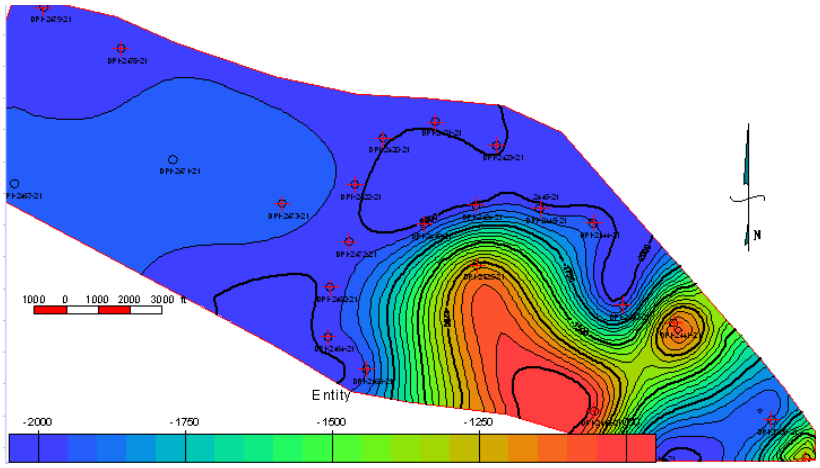


Figure 76. Devonian LS Top Subsea

According to the above figure, it can be concluded that the Devonian LS is almost following the same trend as NAS in dip.

The Gross Thickness of NAS has been mapped and shown below (Figure 77). Along with the thickness map, it is obvious that NAS formation is getting thicker in the Northern part.

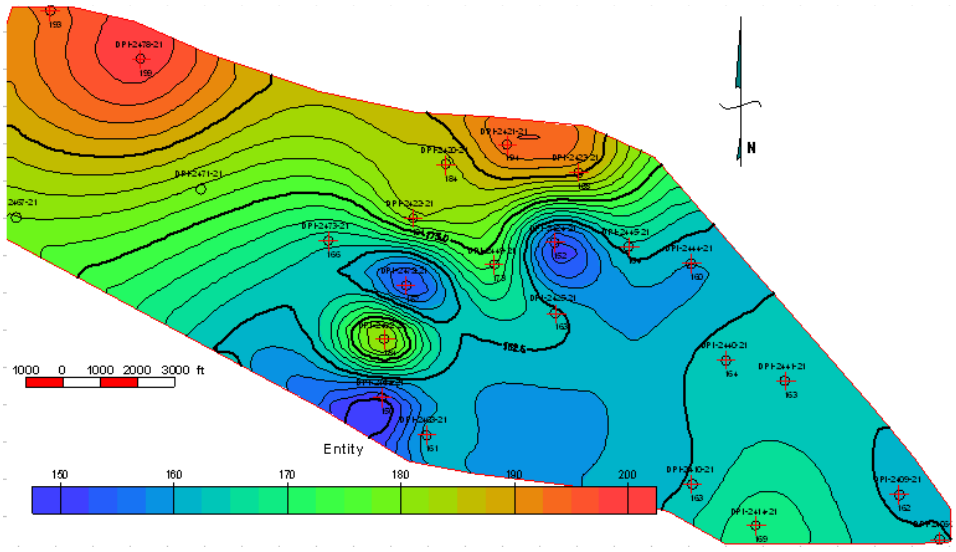


Figure 77. NAS Isochore map

The Top-Down Intelligent Reservoir Modeling workflow has been performed on recently completed wells (understudy area)

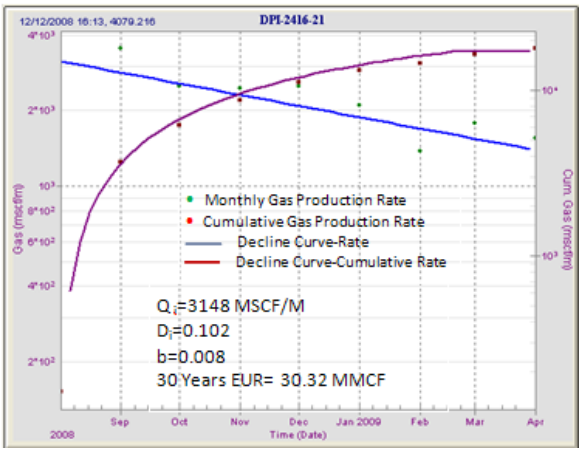


Figure 78.Decline curve analysis sample for one of NAS gas wells

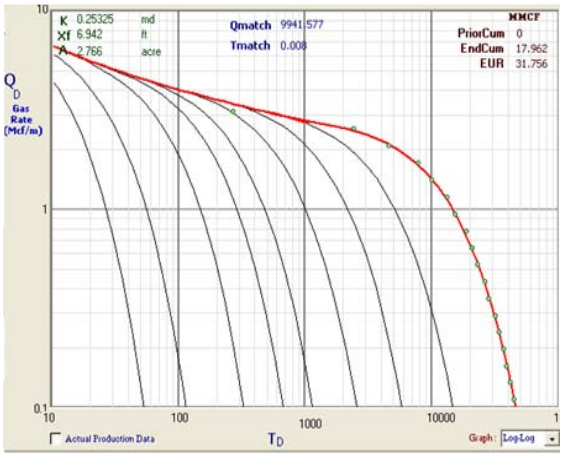


Figure 79.Type curve matching sample for one of NAS gas wells

Figure 80 represents the qualitative result of history matching process. Once the individual analysis for all of the wells in the field is completed, the following information for all the wells in the field is available: initial flow rate (Qi), initial decline rate (Di), hyperbolic exponent (b), permeability (k), drainage area (A), fracture half length (X_f), and 30 Year EUR.

Figure 80 shows the well locations, followed by identification of boundary and the Voronoi grids for all the wells in the analysis.

Using the results of Decline Curve analysis and Volumetric Reserve Estimation, a well-based Recovery Factor is calculated for all wells, individually. A field-wide Recovery Factor is also calculated. Figure 79 illustrates the calculate recovery factory of 1.0547 % for one of the wells and Field recovery factor of 0.9717%.

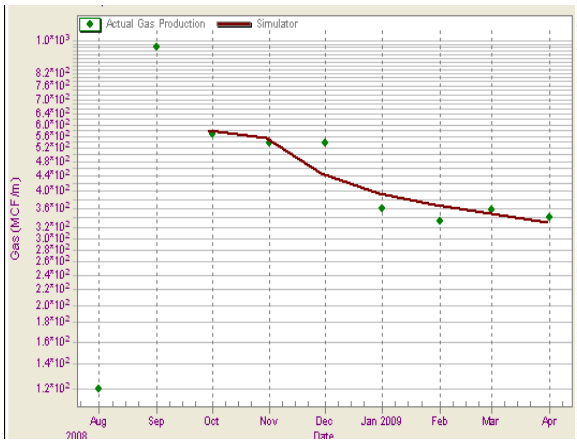


Figure 80.History matching results

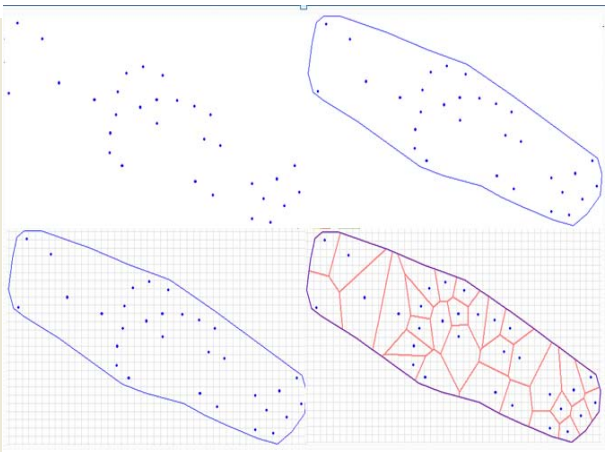


Figure 81.Generating the Voronoi cells for 31 NAS wells

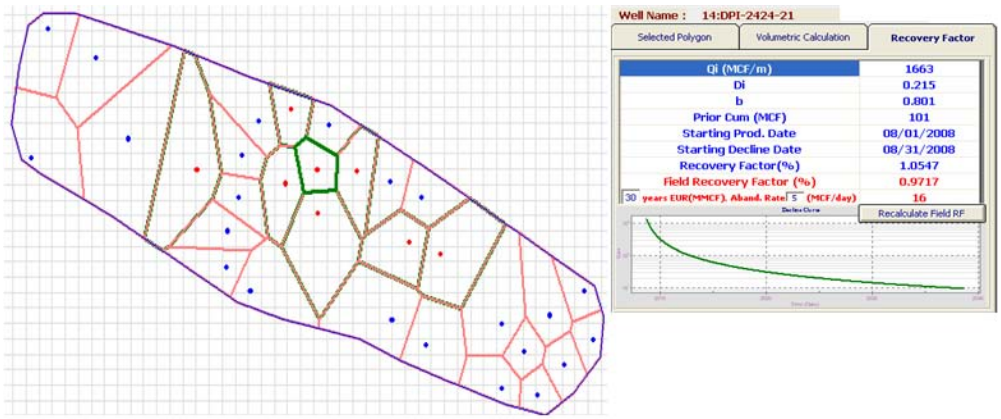
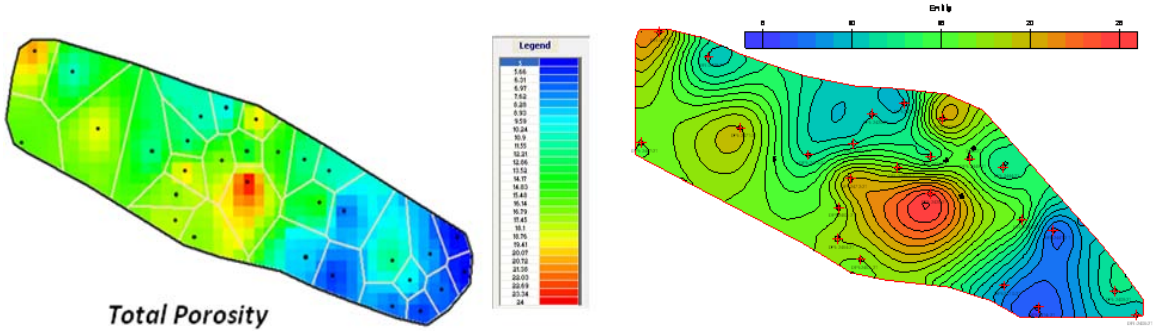


Figure 82.Calculated recovery factor for individual wells as well as field recovery factor

Once the Decline Curve Analysis and other steps mentioned above were completed, discrete, intelligent, predictive models are developed for the reservoir (production) attributes such as, first 3, 6, 9 month of cumulative production, decline curve information (Qi, Di and b), EUR, Fracture half length, matrix and total porosity, matrix and total permeability, net pay thickness, Initial gas in place, and well recovery factor. This set of discrete, intelligent models is then integrated using continuous fuzzy pattern recognition in order to arrive at a cohesive model of the reservoir as a whole.

Using geostatistics a high level earth model is built. As part of the out comes of the high level earth model some of the two dimentsional maps of characteristics of the field such as porosity, permeability, ,gas saturation and fracture aperture distribution are shown in Figure 83 and Figure 84

In addition the contour maps that are generated using geoghraphix software has been compared to the 2D geostatistical model of Top-Down Modeling and also fuzzy pattern recognition results.(Figure 83 and Figure 84).



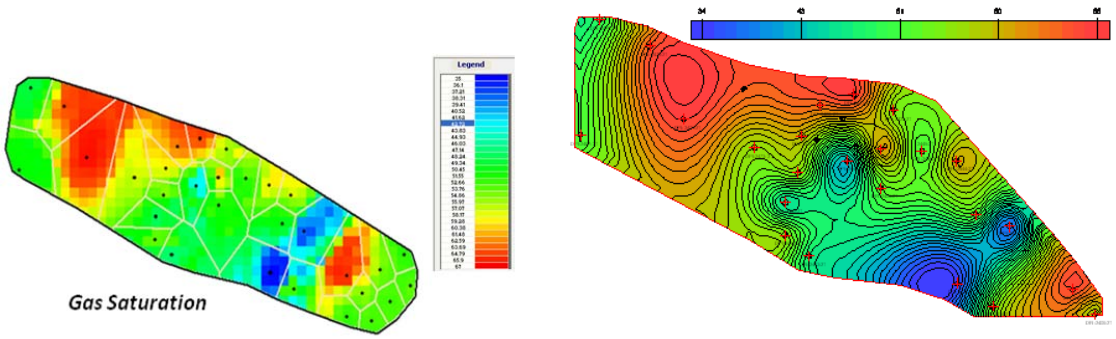


Figure 83.Results of discrete predictive modeling in comparison with contour map (Geographix result) showing the distribution of total porosity, and gas saturation for the entire field

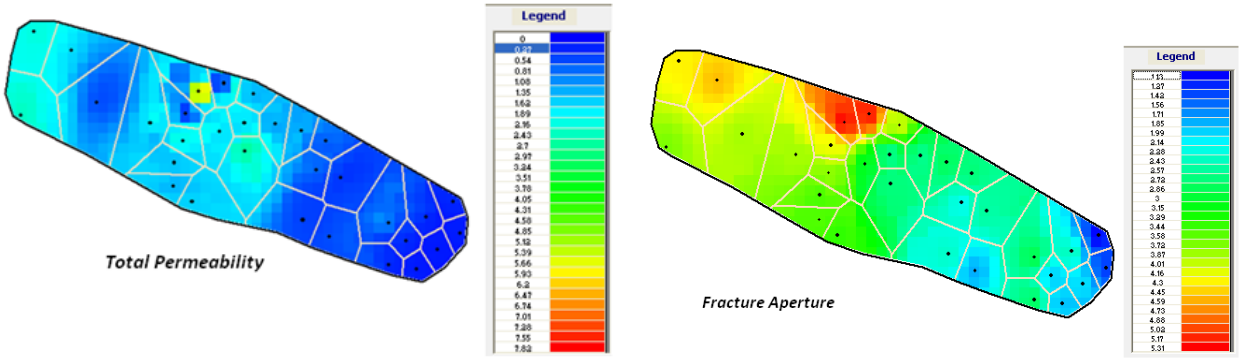


Figure 84.Results of discrete predictive modeling showing the distribution of total permeability from type curve and fracture aperture for the entire field (From left to right)

Another part of Top-down, Intelligent Reservoir Modeling includes analysis of flow and production pattern characteristics usin fuzzy pattern recognition as shown in Figure 85 through Figure 87.

Upon completion of these analyses a rather complete spatio-temporal picture of the fluid flow in the reservoir emerges. The maps that are generated through these processes develop a sereis of visual guidelines that can help engineers and geo-scientist analyze reservoir behavior as a function of time and make decisions on field development strategies. Furthermore, optimum infill locations, examininig different infill scenarios and identifying potential remaining reserves based on each scenario and identifying underperformer wells are among tangible results that can be concluded from such analyses.

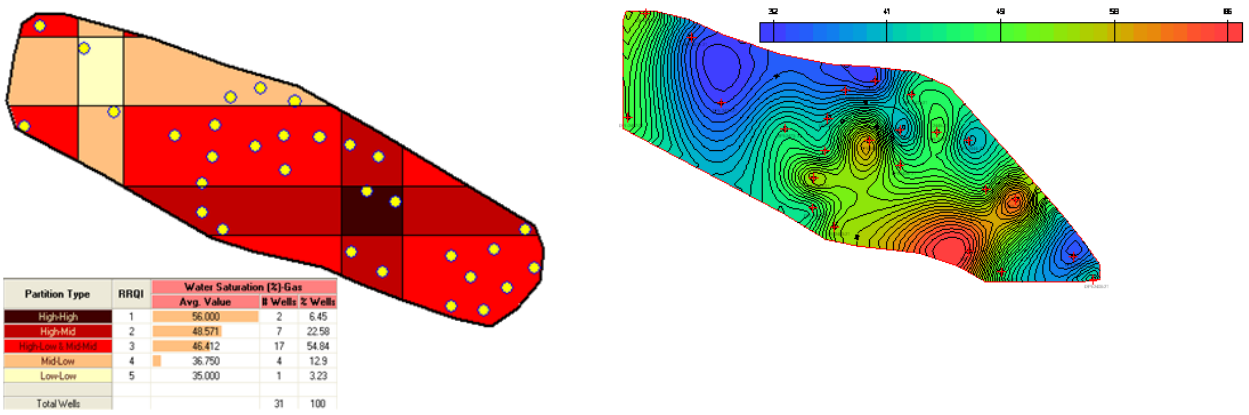


Figure 85.Results of Fuzzy Pattern Recognition showing the sweet spots in the field based on initial water saturation in comparison with the Geographix generated contour map.

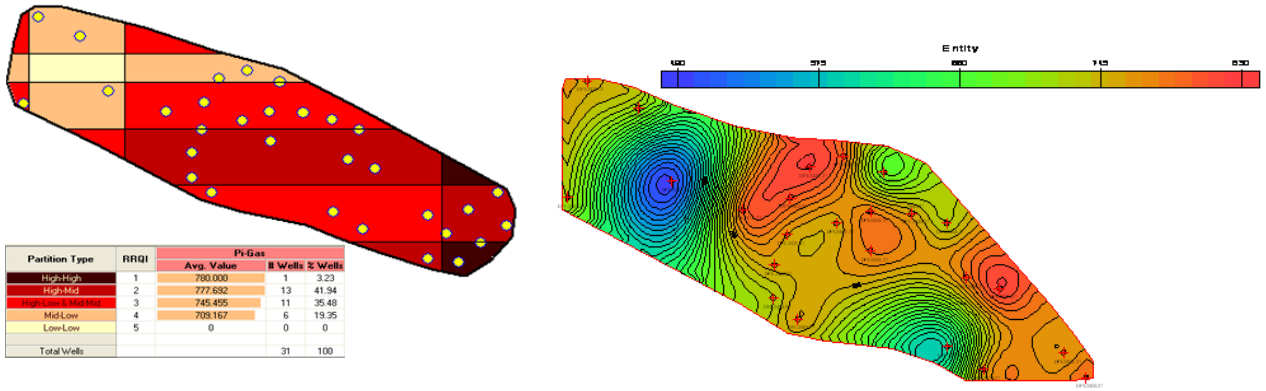


Figure 86.Results of Fuzzy Pattern Recognition showing the sweet spots in the field based on initial reservoir pressure in comparison with the Geographix generated contour map.

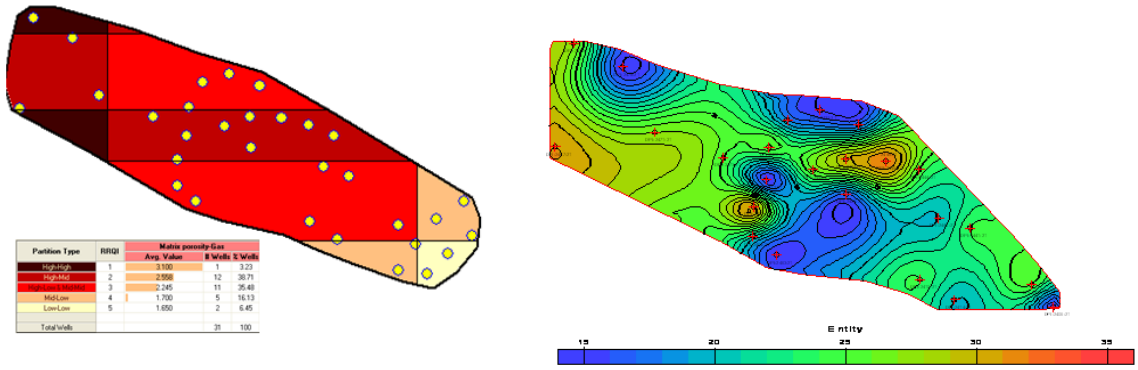
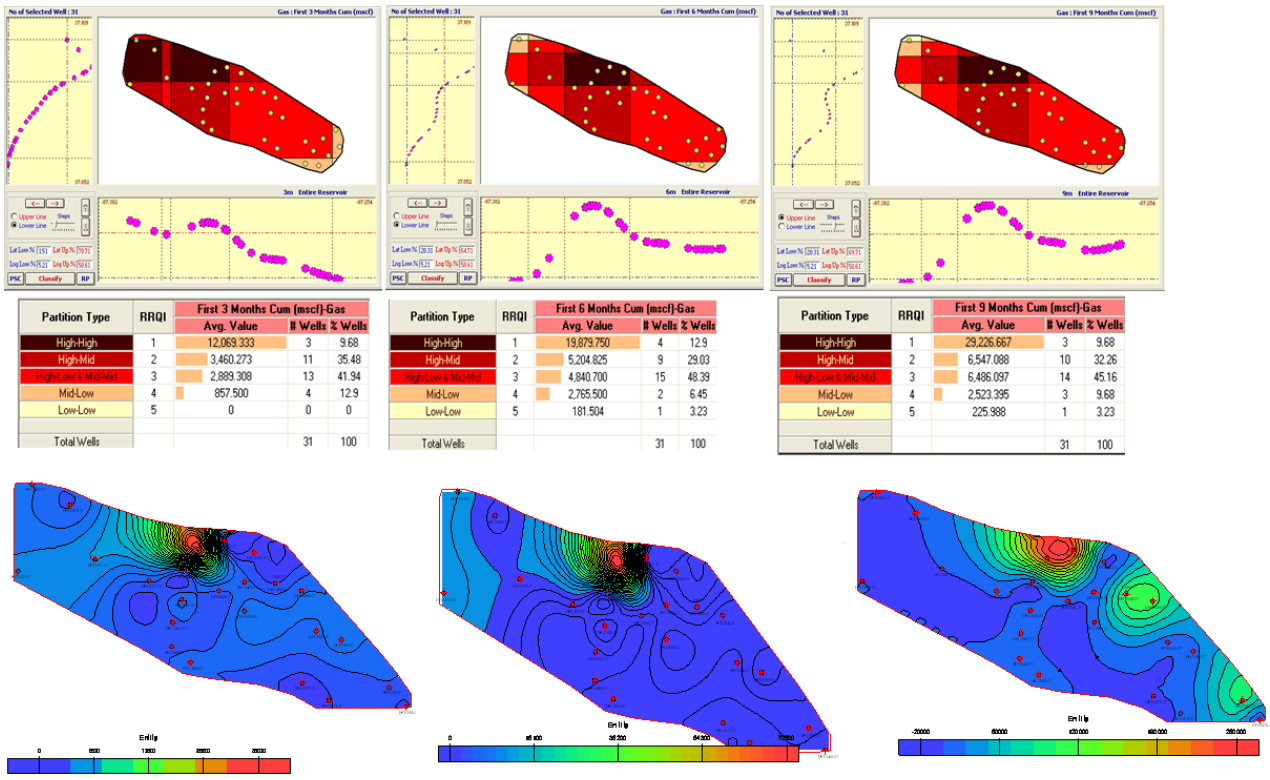


Figure 87.Results of Fuzzy Pattern Recognition showing the sweet spots in the field based on matrix porosity in comparison with the Geographix generated contour map.

Figure 85 represent the distribution of cumulative gas production for the first 3,6 and 9 month of production and the corresponding contour maps from Geoghraphix.



Partition Type	RRQI	First 3 Months Cum (mscf)-Gas		
		Avg. Value	# Wells	% Wells
High-High	1	12,069.333	3	9.68
High-Mid	2	3,460.273	11	35.48
High-Low & Mid-Mid	3	2,889.308	13	41.94
Mid-Low	4	857.500	4	12.9
Low-Low	5	0	0	0
Total Wells			31	100

Partition Type	RRQI	First 6 Months Cum (mscf)-Gas		
		Avg. Value	# Wells	% Wells
High-High	1	19,873.750	4	12.9
High-Mid	2	5,204.825	9	29.03
High-Low & Mid-Mid	3	4,840.700	15	48.39
Mid-Low	4	2,765.500	2	6.45
Low-Low	5	181.504	1	3.23
Total Wells			31	100

Partition Type	RRQI	First 9 Months Cum (mscf)-Gas		
		Avg. Value	# Wells	% Wells
High-High	1	29,226.667	3	9.68
High-Mid	2	6,547.088	10	32.26
High-Low & Mid-Mid	3	6,486.097	14	45.16
Mid-Low	4	2,523.395	3	9.68
Low-Low	5	225.988	1	3.23
Total Wells			31	100

Figure 88.Results of Fuzzy Pattern Recognition showing the sweet spots in the field for the first 3, 6 and 9 month of Cum.gas production in comparison with the corresponding contour maps from geographix.

The remaining reserve as of year 2009,2020 and 2040 has been shown in Figure 89. In the two dimensional maps (Figure 89) reservoir is delineated with Relative Reservori Quality Index (RRQI) being the Remaining Reserves. The delineation shown in this figure are indicated by colors. Higher quality regions (regions with high values of Remaining Reserves) are shown in darker colors and as the average value of Remaining Reserves reduces in each region, the color becomes increasing ly lighter. The difference between these three figures shows the depletion in the reservoir and identifies the parts of the field that still have potential for more recovery.

Based on the results of predictive modeling and fuzzy pattern recognition, the best spots for drilling can be identified. So engineers and geo-scientits can identify the best locations in the field that would provide the best production profiles and that satidfies their economic objectives.

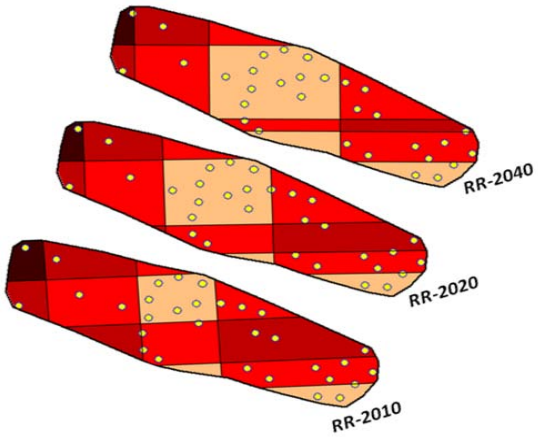


Figure 89.Results of Fuzzy Pattern Recognition showing the sweet spots in the field for the remaining reserve (MMCF) as of 2009, 2020, and 2040

The permeability is a key parameter that plays an important role in fluid production from the reservoir. Thereby having high initial production rate in the locations which have high permeability makes sense. Another important factor while making decision about the infill drilling locations is remaining reserves. It defines the amount of the stored fluid in the reservoir. Having both the remaining reserves and permeability, results in high storage and flow capacity. Thus, the potential spots for infill drilling can be selected, based on these parameters. Although these two parameters have considerable effect on deciding the new well locations, other parameters such as forcasted EUR for 30 years, matrix porosity,initial gas in place and also fracture half length have been taken into account.

3.10 Model Calibration and Validation

To calibrate the NAS Top-Down models about 10 % of wells for are removed from the analyses. This constitutes removal of 3 wells from the analysis. The models are developed using the remaining 28 wells. The objective is to make sure that the NAS Top-Down model can predict the first 3 month cumulative production for these removed wells (blind data set). The results are shown in Table 13.Results of Top-Down modeling- Model Calibrationand Figure 90.

For example in table 1 the four Relative Reservoir Quality Indices (RRQI) are shown as well as the model results that indicates the prediction for the blind/validation wells. As indicated in this table the Top-Down model predicted that the average first 3 month cumulative production for wells drilled in the RRQI “1” (the darkest areas in Figure 1) will be more than 9.7 MMSCF. One well in RRQI “1” is

removed and the average first 3 month cumulative production for this well was 13.48 MMSCF **(correct prediction)**.

Furthermore, the Top-Down model predicted that the average first 3 month cumulative production for well in the RRQI "2" will be between 2.97 and 9.7 MMSCF. As shown in Table 1 there was 1 well drilled in RRQI "2" and the average first 3 month cumulative production for this well was 4.56 MMSCF **(correct prediction)**.

For RRQI "3" the Top-Down model over-estimates the result. It predicted that the average first 3 month cumulative production for wells drilled in the RRQI "3" will be between 1.8 and 2.97 MMSCF while the 1 well drilled in RRQI "2" had an average first 3 month cumulative production of 3.9 MMSCF.

Table 13.Results of Top-Down modeling- Model Calibration

First 3 Month Cumulative Production(MSCF)					
	Model Results			Removed Wells	
RRQI	More Than	&	Less than	Average 1 Yr Cum	No. of Wells
1	9,707.85			13,488.00	1
2	2,968.89	&	9,707.85	4,566.00	1
3	1,803.29	&	2,968.89	3,906.00	1
4	857.00	&	1,803.29		0
			7,908.59	**Total no. of Wells**	3

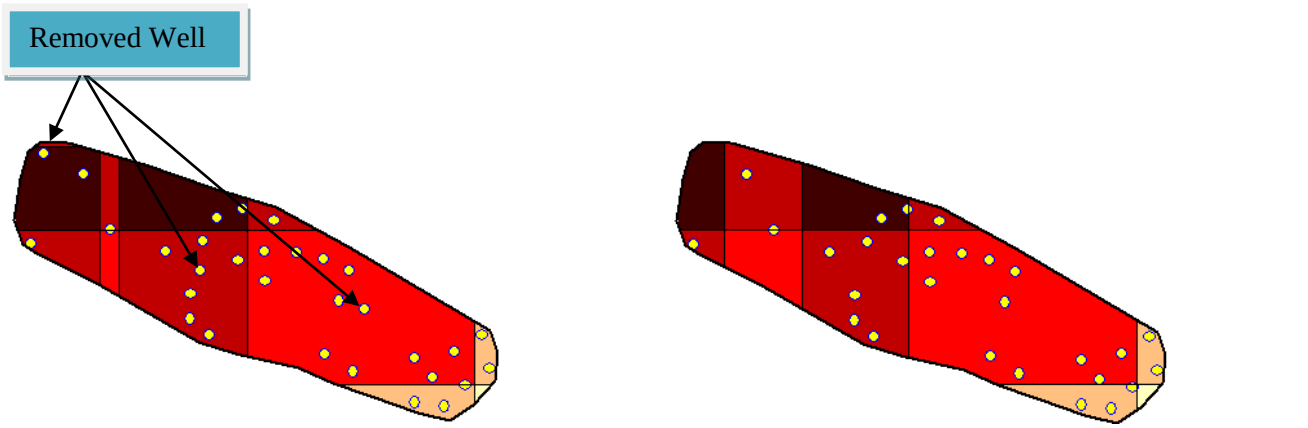


Figure 90. Results of Fuzzy Pattern Recognition showing the sweet spots in the field for the first 3-month cum. production for 31 wells (left) and first 3-month cum. Production for 28 wells (right).

Chapter 4

Concluding Remarks

In this study, natural fractures in the New Albany Shale were characterized by a comprehensive review of literature. Sensitivity analysis was performed on key reservoir and fracture parameters such as matrix porosity, matrix permeability, initial reservoir pressure, fracture aperture, fracture density, fracture length and well's lateral length .The orientation of natural fractures in New Albany Shale wells are EW and NNW-SSE and a minor ENE-SWS. Majority of natural fractures are vertical through there appears a minor set that dip between 55 to 75 degree.

A fracture network based on best available information and data was developed in FracGen. NFflow was used for fluid flow modeling based on the FracGen model. Reservoir characteristics and fracture properties were modified systematically until a reasonable history match was achieved for all the wells being studied.

The fracture model like any other geological model has a degree of uncertainty and can be updated by using additional information from fracture detection log, seismic and core analysis and any other tools that help to characterize fracture properties in order to building the more accurate model that represents the fracture network distribution of New Albany Shale.

A novel reservoir modeling technology has been applied to New Albany Shale. This relatively new modeling technology, Top-Down, Intelligent Reservoir modeling, incorporates Artificial Intelligent and Data Mining techniques such as data driven Neural network modeling and fuzzy pattern recognition in conjunction with solid reservoir engineering analyses in order to combine single well analyses into a cohesive full field model.

Top-Down intelligent reservoir modeling allows the reservoir engineer to plan and evaluate future development options for the reservoir and continuously updated the model that has been developed as new wells are drilled and more production data and well logs become available.

One of the most important advantages of Top-Down intelligent reservoir modeling is its ease of development. It is designed so that an engineer or a geologist will be able to comfortably develop a Top-Down model in a relatively short period of time with minimum amount of data (only monthly production data and some well logs are enough to start modeling). This new technique can be performed on the other types of shale and tight gas sand (Unconventional resources) as well as conventional reservoirs. (Oil and Gas)

Our Studies have shown that Intelligent Top-Down Reservoir Modeling holds much promise and can open new door for developing reservoir models using field measurement data.

This new workflow can be performed on the other types of Unconventional resources such as other shale plays and tight gas reservoirs.

Technology Transfer

The outcome of this study was a journal paper and two SPE conference papers and presentations as technology transfer which are as follows:

“A New Practical Approach in Modeling and Simulation of Shale Gas Reservoirs; Application to New Albany Shale”; which is accepted for publication in International Journal of Oil, Gas and Coal Technology.

“Top-down Intelligent Reservoir Modeling of New Albany Shale” SPE 125893, which was presented at SPE Eastern Regional Conference, Charleston, WV.2009

“Economic Impact of Reservoir Properties and Horizontal Well Length and Orientation on Production from Shale Formations: Application to New Albany Shale” SPE 125859 which was presented at SPE Eastern Regional Conference Charleston, WV.2009

Acknowledgment

Funding for this project is provided by RPSEA through the "Ultra-Deepwater and Unconventional Natural Gas and Other Petroleum Resources" program, authorized by the U.S. Energy Policy Act of 2005. RPSEA (www.rpsea.org) is a nonprofit corporation whose mission is to provide a stewardship role in ensuring the focused research, development and deployment of safe and environmentally responsible technology that can effectively deliver hydrocarbons from domestic resources to the citizens of the United States. RPSEA, operating as a consortium of premier U.S. energy research universities, industry, and independent research organizations, manages the program under a contract with the U.S. Department of Energy's National Energy Technology Laboratory.

References

1. *Some Predictions of Possible Unconventional Hydrocarbon Availability.* **Kawata Y, Fujita K.** Jakarta : SPE, 2001. SPE68755.

2. *Tight Gas Sands.* **SA, Holditch.** s.l. : SPE, 2006. SPE103356.

3. *Shale Gas Opportunities and Challenges. Search and Discovery Articles.* **Bustin, M. R., Bustin, A., Ross, D., Chalmers, G., Murthy, V., Laxmi, C., Cui, X.** San Antonio, Texas, : AAPG Annual Convention,, 2008.

4. **Browing, I.B.** *Relation of Structure to Shale Gas Accumulation. In: Devonian Shales.* Charleston,WV : Appalachian Geol.Society, 1935.

5. *Gas Occurrence in the Devonian Shale.* **Smith, E.C.** Denver : SPE Symposium on Low-Permeability Gas Reservoirs, 1979. SPE 7921.

6. *A 'New' Gas Supply – The Devonian Shales.* **Foster, J.M.** Charleston : SPE, 1975. 5451.

7. *The Barnett Shale Play; Phoenix of the Fort Worth Basin, A History.* **Steward, D.B., and Paniszczyn, F.** s.l. : The Fort Worth Geologic Society and the North Texas Geologic Society, 1977.

8. **Guidry, F.K., Luffel, D.L., and Curtis, J.B.** *Development of Laboratory and Petrophysical Techniques for Evaluating Shale Reservoirs.* 1995. GRI-95/0496..

9. *Importance of Fabric on Production of Gas Shale.* **Bustin, A.M.M., Bustin, R.M, and Cui, X.** Keystone,CO : Unconventional Reservoirs Conference, 2008. SPE 114167.

10. *Nanoscale Gas Flow in Shale Gas Sediments.* **Javadpour, F., Fiser, D., and Unsworth, M.** 10, s.l. : J. Canadian Pet. Tech., 2007, Vol. 46.

11. *Nanopores and Apparent Permeability of Gas Flow. In Mudrocks (Shales and Siltstone).* **Javadpour, F.** s.l. : JCPT Distinguished, 2009.

12. *Petrophysical Considerations in Evaluating and Producing Shale Gas Resources.* **C.H. Sondergeld, SPE, University of Oklahoma and K.E. Newsham, SPE, J.T. Comisky, SPE, and M.C. Rice,.** Pittsburgh : SPE, 2010. 131768.

13. **Joseph H.Frantz, Jr.** *Shale Gas.* s.l. : Schlumberger, 2005.

14. *New Albany Shale Project.* **Salehi, Iraj.** s.l. : Gas Technology Institute, 2009.

15. **Consortium, Illinois Basin.** *Gas Potential of the New Albany Shale (Devonian and Mississippian) in the Illinois Basin.* s.l. : Gas Research Institute, 1994.

16. **Frost, J. K., Zierath, D. L., and Shimp, N. F.** *Chemical composition and geochemistry of the New Albany Shale Group (Devonian-Mississippian)in Illinois.* s.l. : U.S. Department of Energy, 1985. DE-AC21-76ET12142.

17. **Kalyoncu, R. S., Boyer, J. P., and Snyder, M. J.** *Characterization and analysis of Devonian shales as related to release of gaseous hydrocarbons, well P-1 Sullivan County, Indiana.* Ohio : s.n., 1979.

18. **McKoy, Mark L,W. Neal Sams.** *Tight Gas Reservoir Simulation:Modeling Discrete Irregular Strata-Bound Fracture Networks and Network Flow, Including Dynamic Recharge from the Matrix.* . Morgantown : DOE, 2006.

19. **ASA, Roxar.** http://www.roxar.com/category.php?categoryID=1081. [Online]

20. *Virtual Intelligence Applications in Petroleum Engineering: Part 1; Artificial Neural Networks.* **D.Mohaghegh, Shahab.** s.l. : Journal of Petroleum Technology, 2000.

21. *Virtual Intelligence Applications in Petroleum Engineering: Part 2; Evolutionary Computing.* **D.Mohaghegh, Shahab.** s.l. : Journal of Petroleum Technology, 2000.

22. *Virtual Intelligence Applications in Petroleum Engineering: Part 3; Fuzzy Logic.* **D.Mohaghegh, Shahab.** s.l. : Journal of Petroleum Technology, 2000.

23. *A comprehensive Reservoir Evaluation of a Shale Reservoir.* **Michael D.Zober, Jeron R.Williamson,David G.Hill.** s.l. : SPE, 2002. SPE 77469.

24. **Ault, C.H.** *Directions and characteristics of jointing in the New Albany Shale (Devonian-Mississippian) of southeastern Indiana.* Kentucky : Center for Applied Energy Research, 1990. IMMR89/201.

25. Energy Information Administration(Official Eneregy Statistics From the US. Government). [Online] http://tonto.eia.doe.gov/oog/info/ngw/ngupdate.asp.

26. **David Wagman, Contributing Editor.** Shale Plays Show Growth Prospects. [Online] Hart EnergyPublishing. http://www.redorbit.com/news/science/357066/shale_plays_show_growth_prospects/.

Appendix A

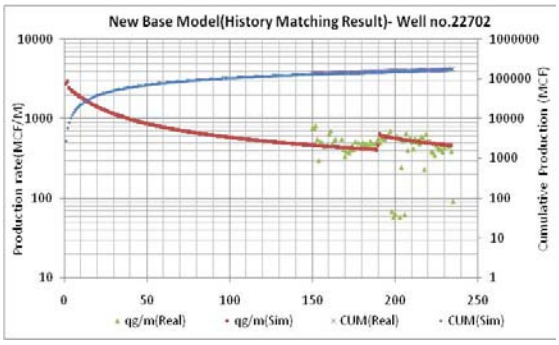


Figure A-1.History matching result - well#22702

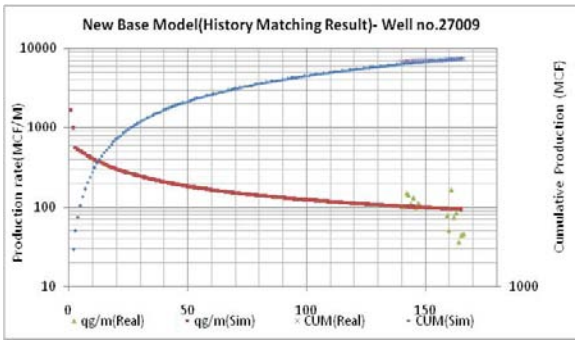


Figure A-2.History matching result-well#27009

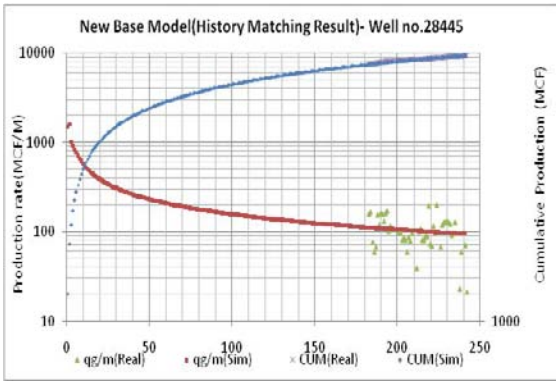


Figure A-3.History matching result-well#28445

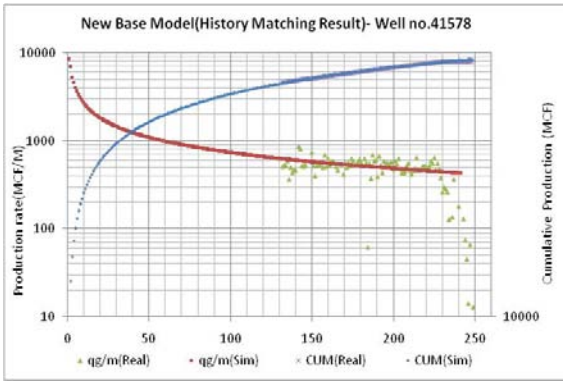


Figure A-4.History matching result well#41578

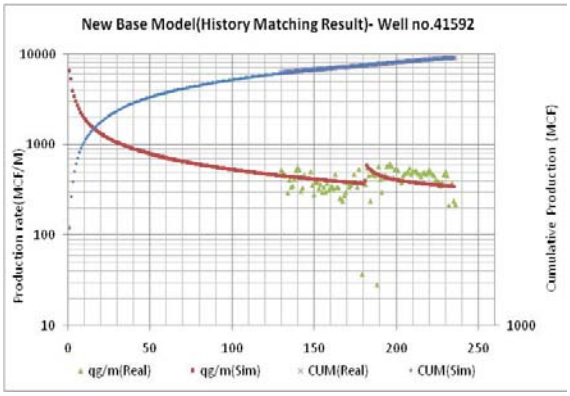


Figure A-5.History matching result well#41592

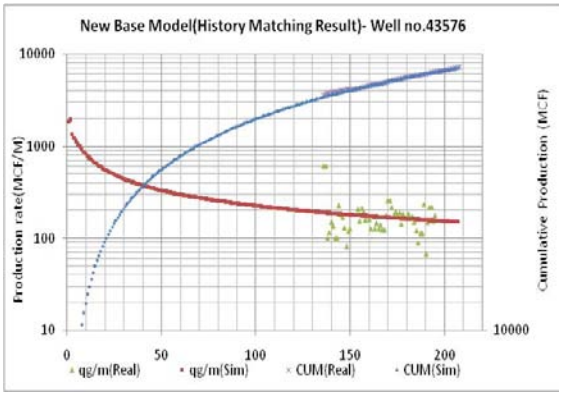


Figure A-6.History matching result well#43576

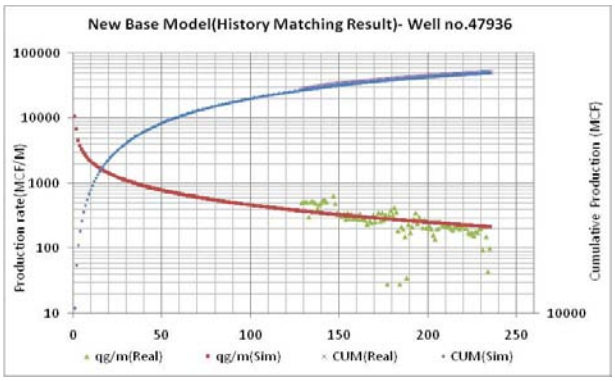


Figure A-7.History matching result well#47936

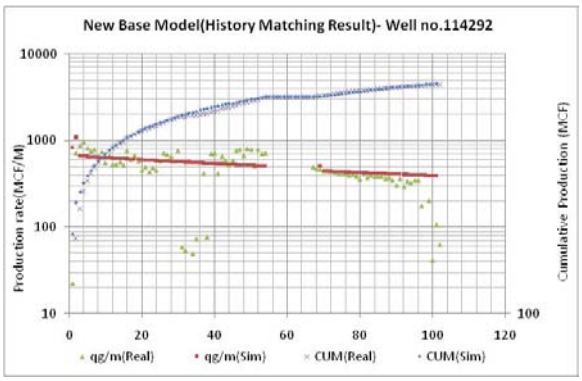


Figure A-8.History matching result well#114292

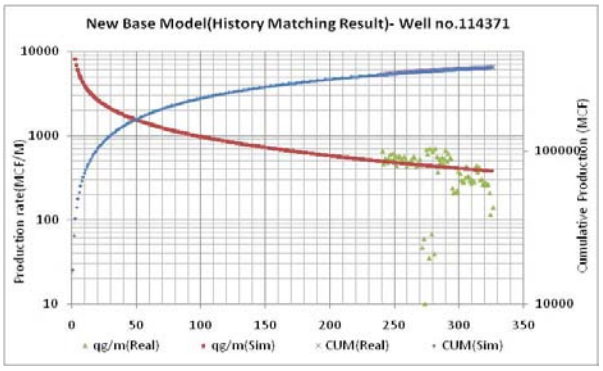


Figure A-9.History matching result well#114371

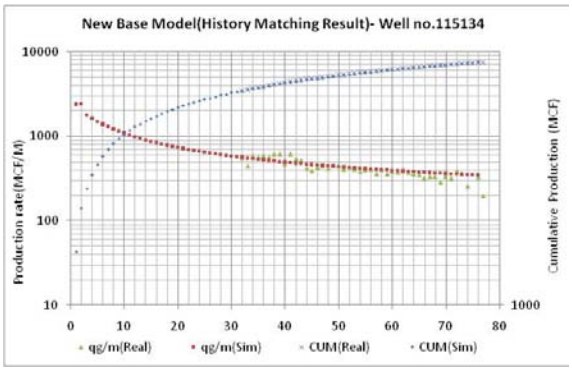


Figure A-10.History matching result well#115134

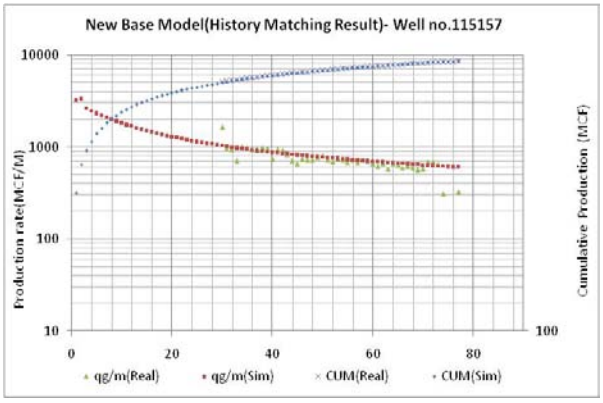


Figure A-11.History matching result well#115157

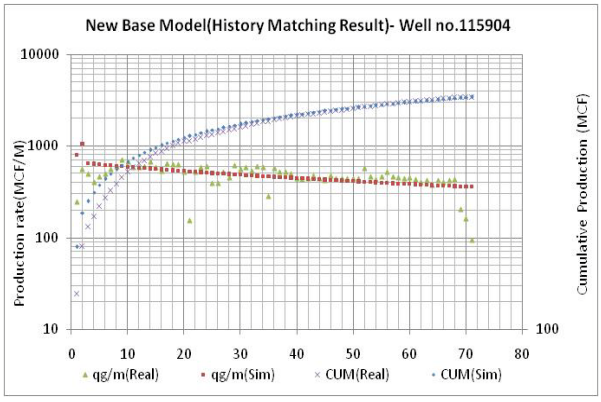


Figure A-12.History matching result well#115904

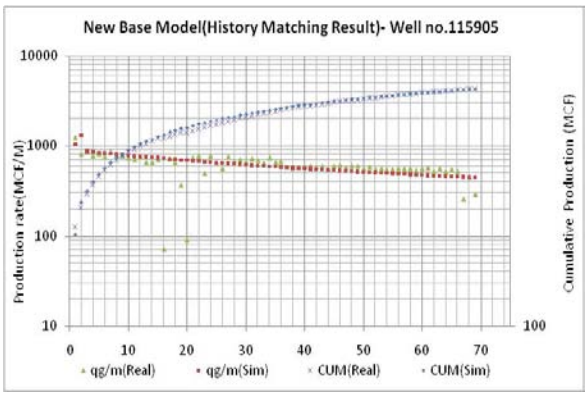


Figure A-13.History matching result well#115905

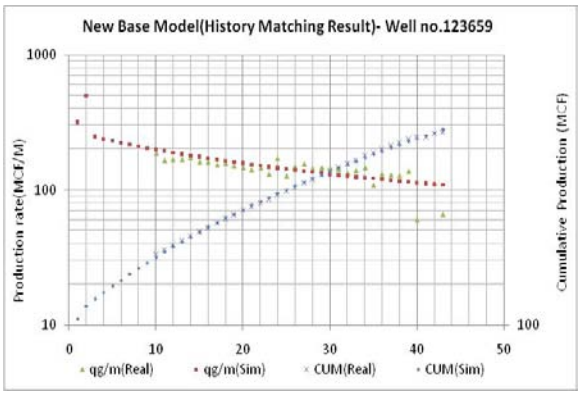


Figure A-14.History matching result well#123659

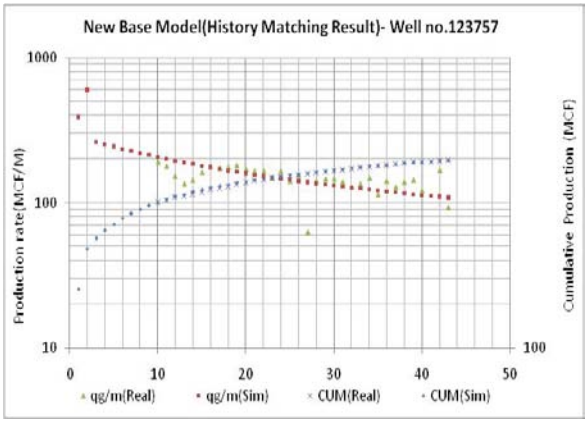


Figure A-15.History matching result well#123757

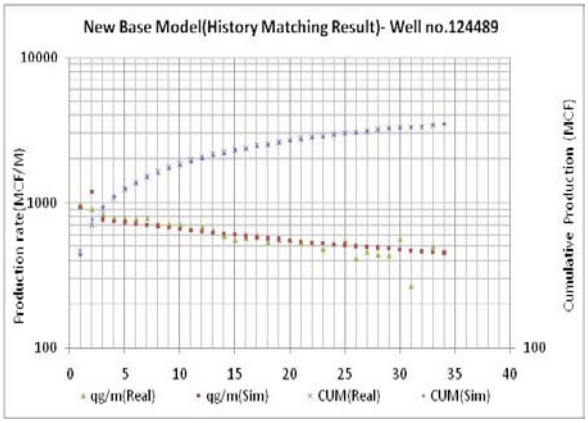


Figure A-16.History matching result well#124489

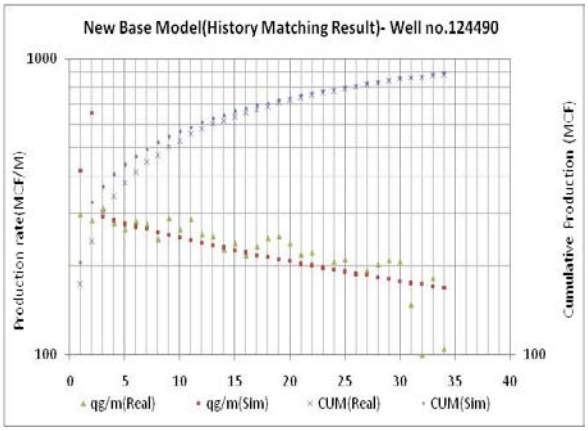


Figure A-17.History matching result well#124490

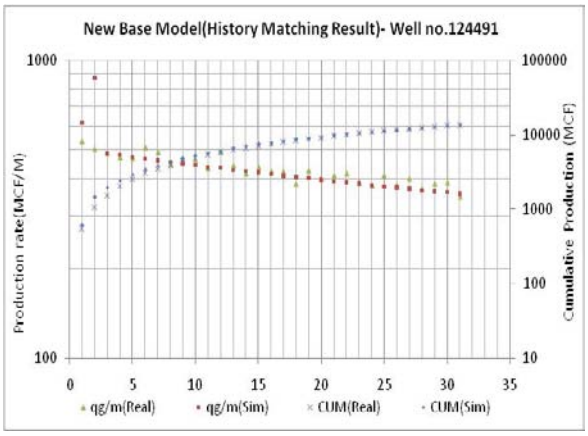


Figure A-18.History matching result well#124491

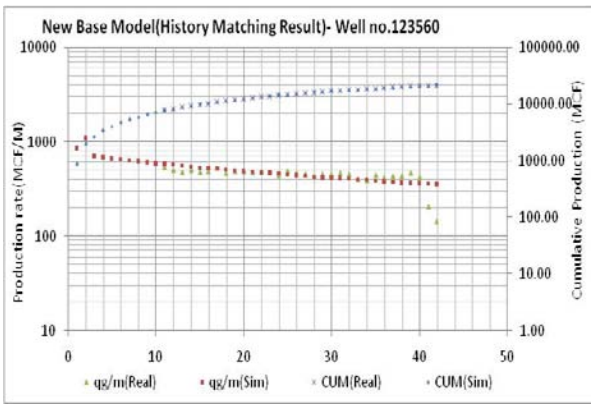


Figure A-19.History matching result well#123560

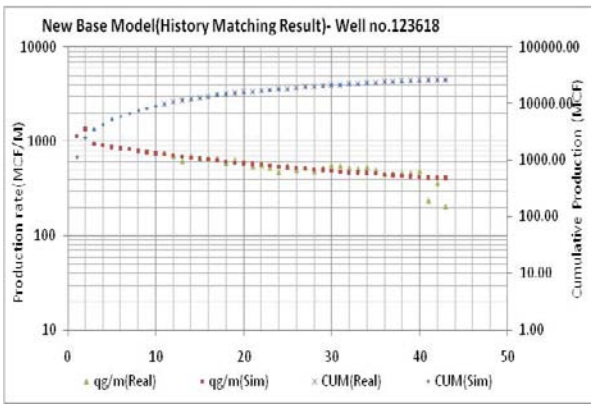


Figure A-20.History matching result well#123618

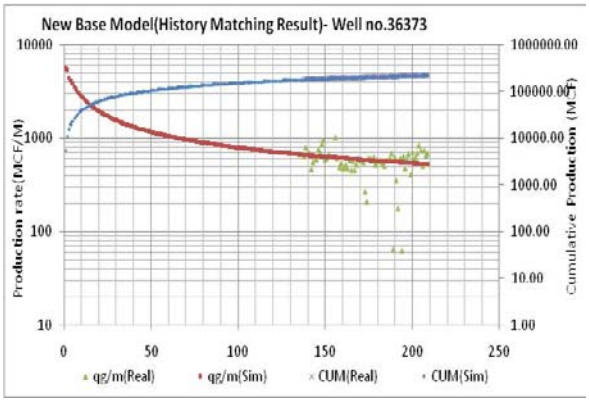


Figure A-21.History matching result well#36373

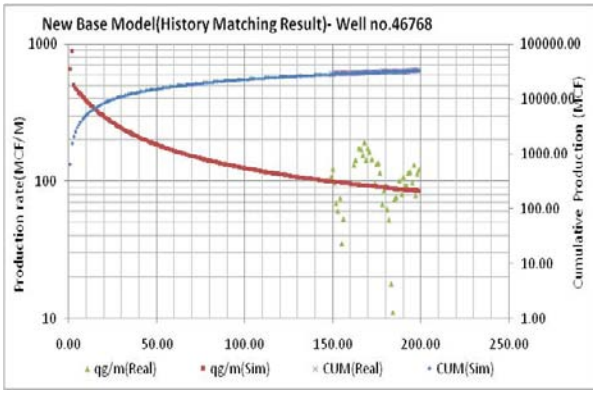


Figure A-22.History matching result well#46768

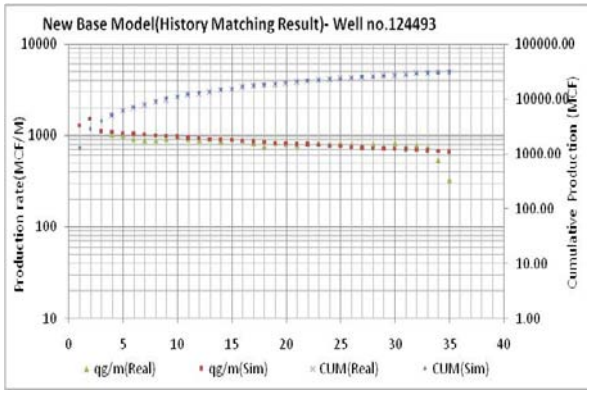


Figure A-23.History matching result well#124493

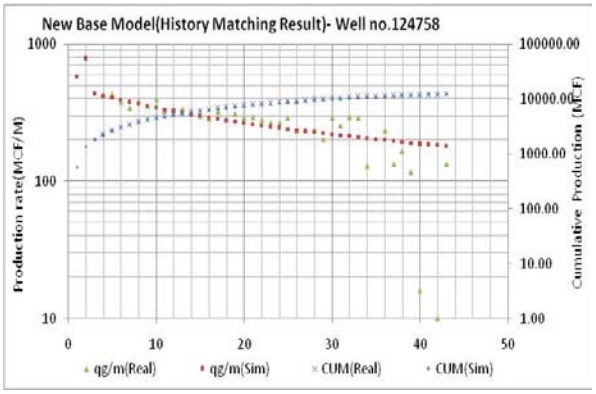


Figure A-24.History matching result well#124758

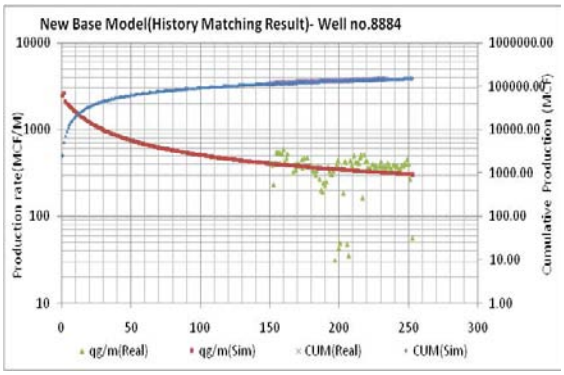


Figure A-25.History matching result well#8884

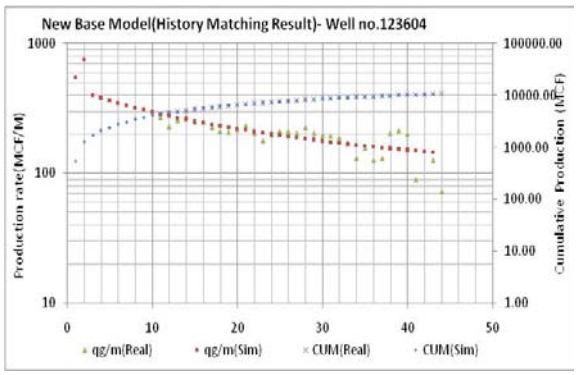


Figure A-26.History matching result well#123604

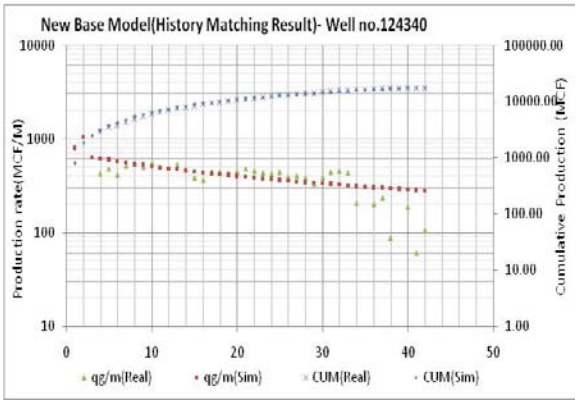


Figure A-27.History matching result well#124340

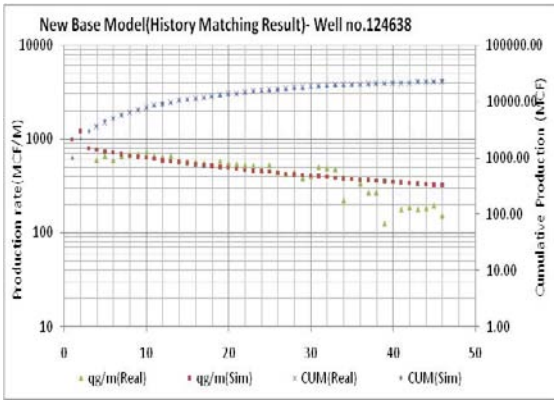


Figure A-28.History matching result well#124638

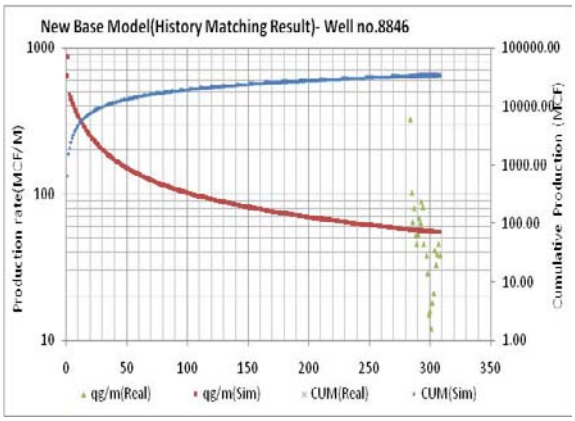


Figure A-29.History matching result well#8846

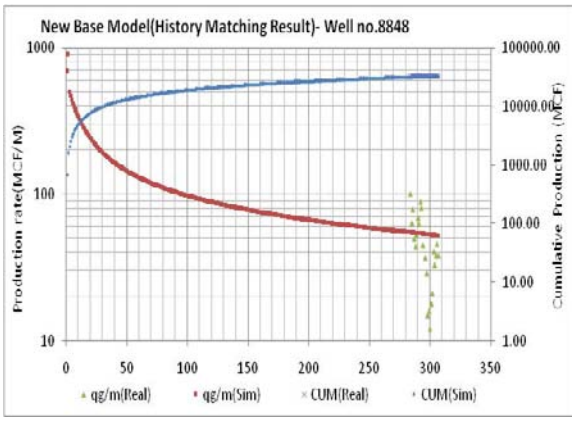


Figure A-30.History matching result well#8848

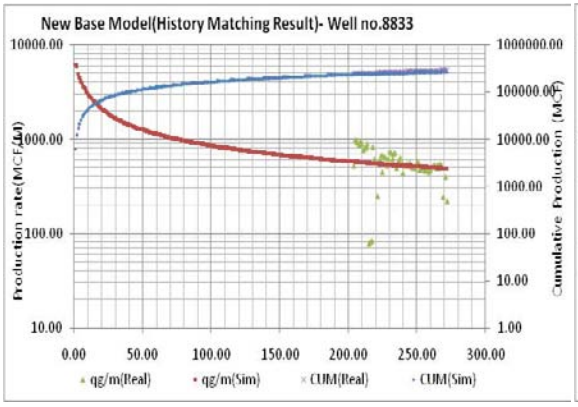


Figure A-31.History matching result well#8833

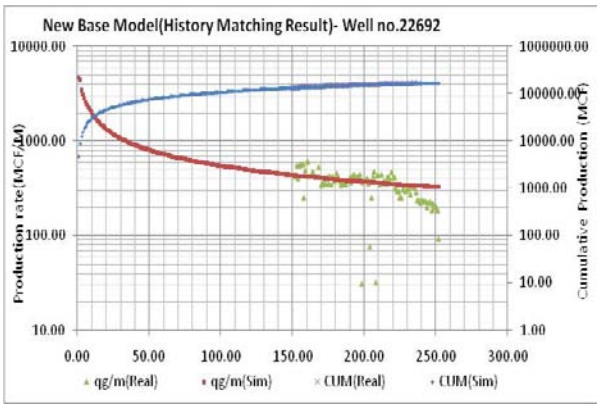


Figure A-32.History matching result well#22692

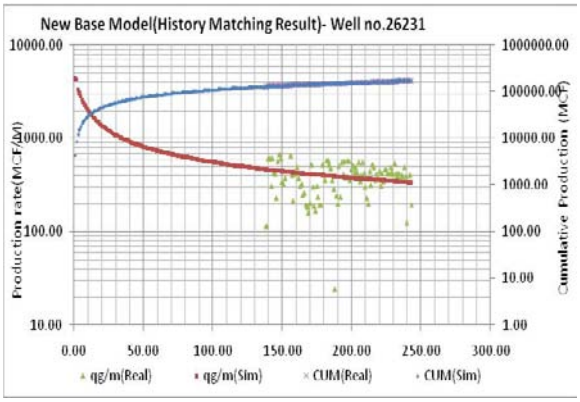


Figure A-33.History matching result well#26231

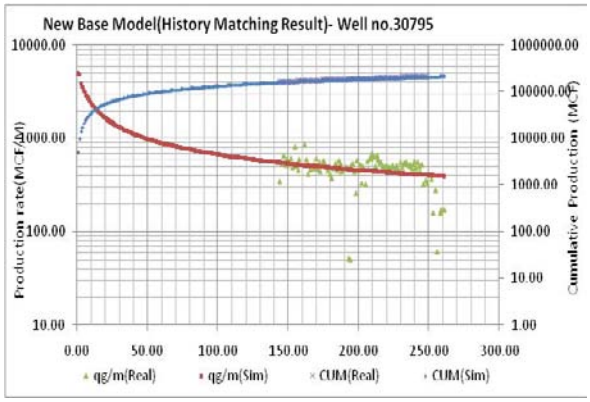


Figure A-34.History matching result well#30795

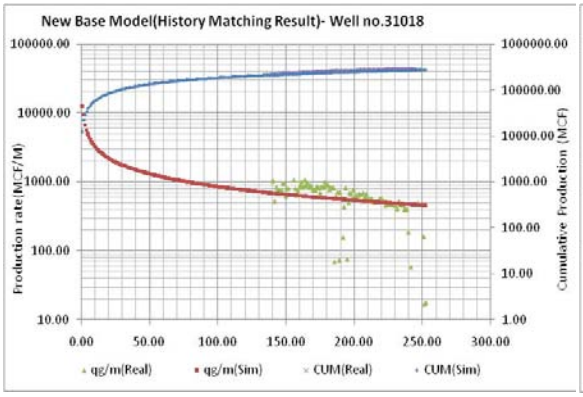


Figure A-35.History matching result well#31018

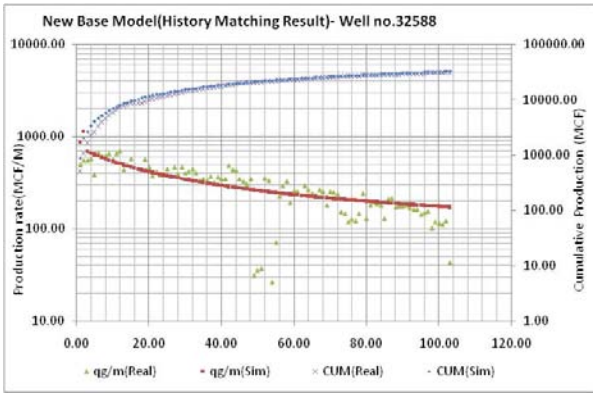


Figure A-36.History matching result well#32588

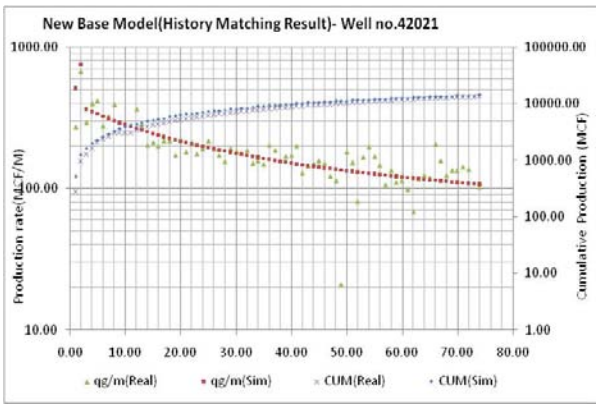


Figure A-37.History matching result well#42021

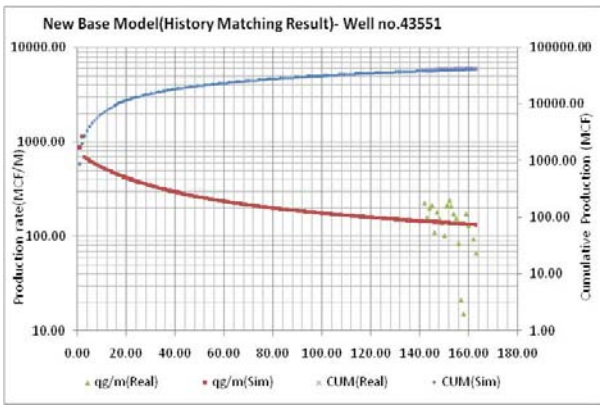


Figure A-38.History matching result well#43551

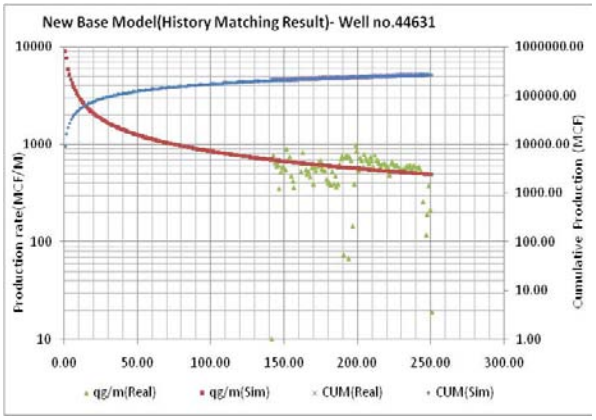


Figure A-39.History matching result well#44631

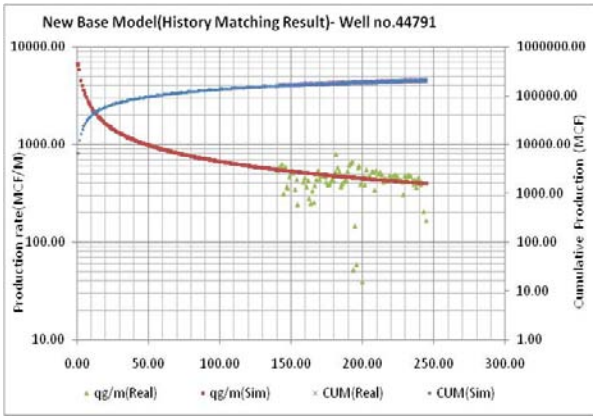


Figure A-40.History matching result well#44791

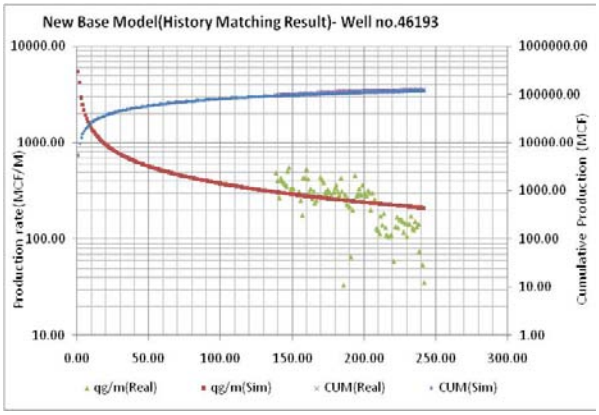


Figure A-41.History matching result well#46193

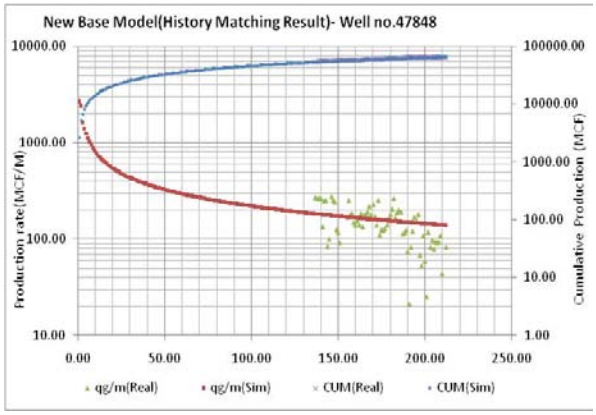


Figure A-42.History matching result well#47848

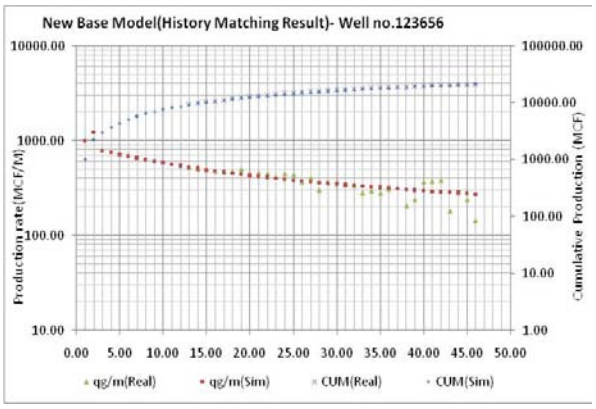


Figure A-43.History matching result well#123656

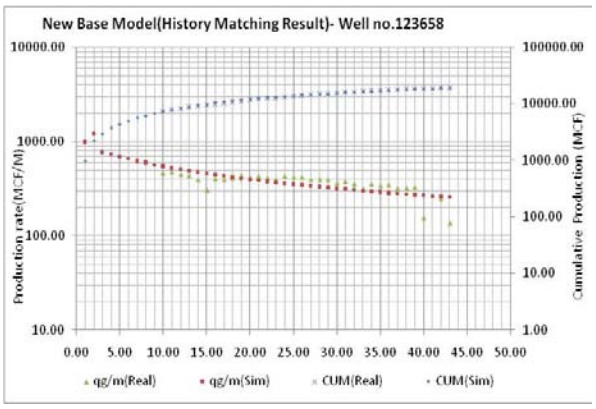


Figure A-44.History matching result well#123658

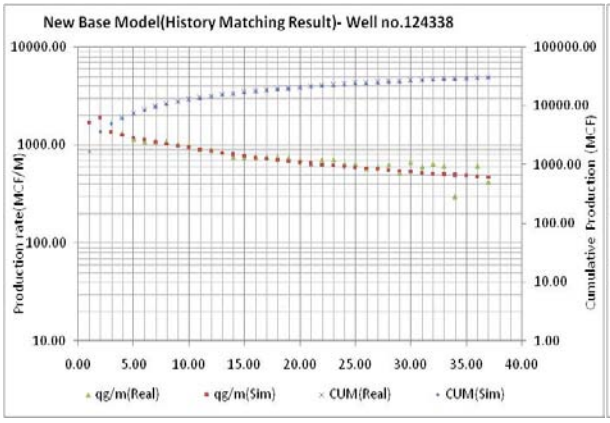


Figure A-45.History matching result well#124338

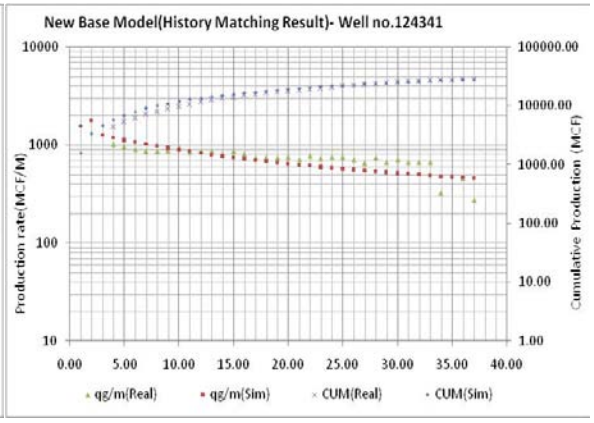


Figure A-46.History matching result well#124341

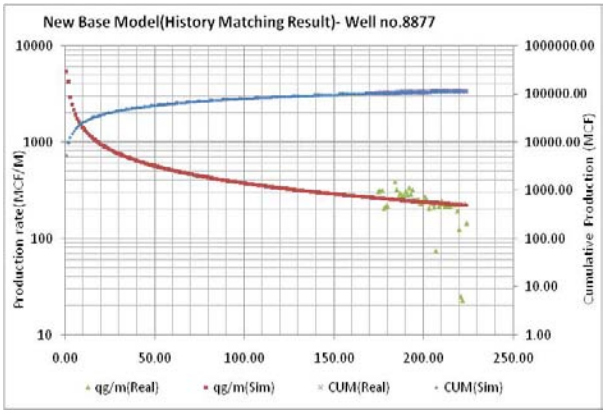


Figure A-47.History matching result well#8877

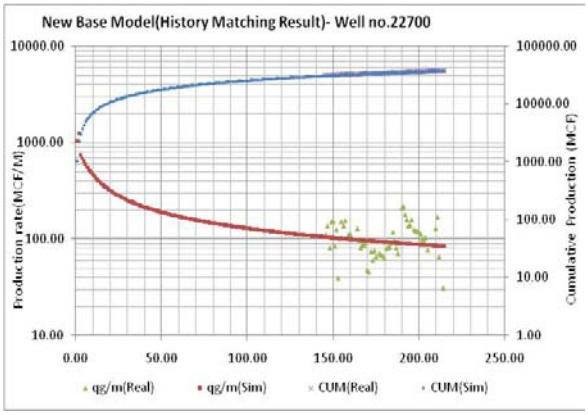


Figure A-48.History matching result well#22700

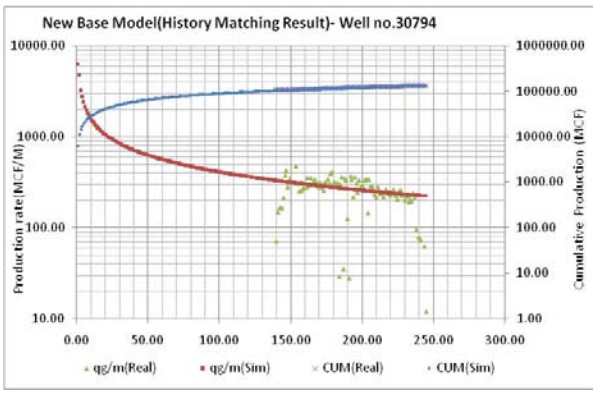


Figure A-49.History matching result well#30794

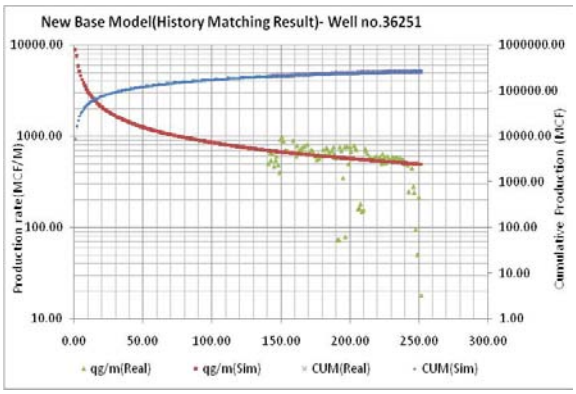


Figure A-50.History matching result well#36251

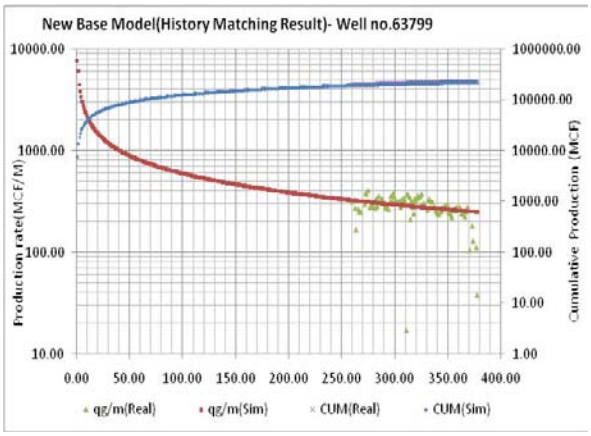


Figure A-51.History matching result well#63799

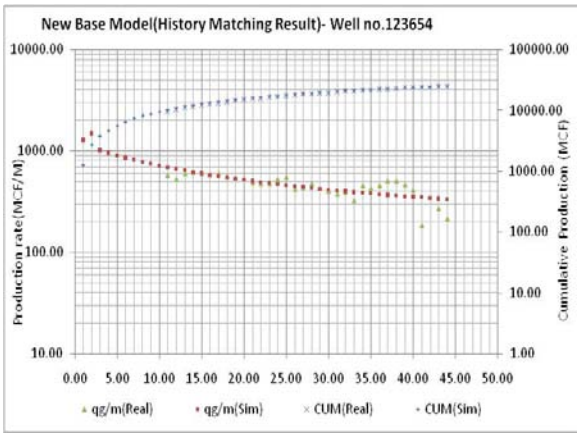


Figure A-52.History matching result well#123654

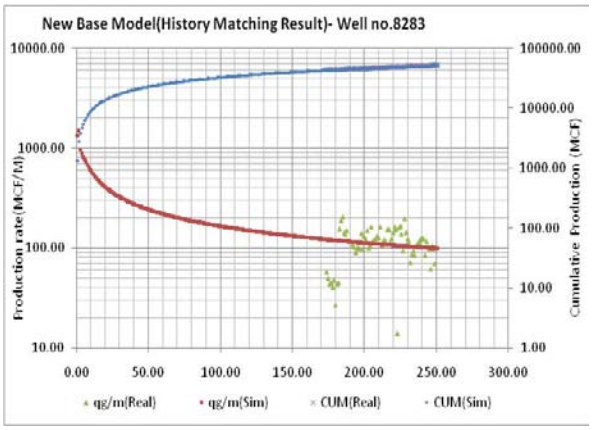


Figure A-53.History matching result well#8283

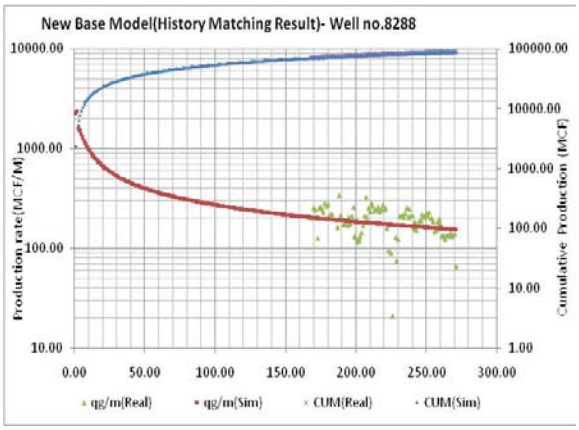


Figure A-54.History matching result well#8288

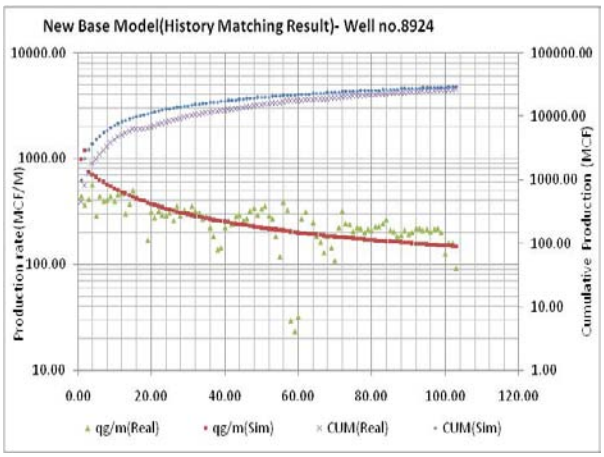


Figure A-55.History matching result well#8924

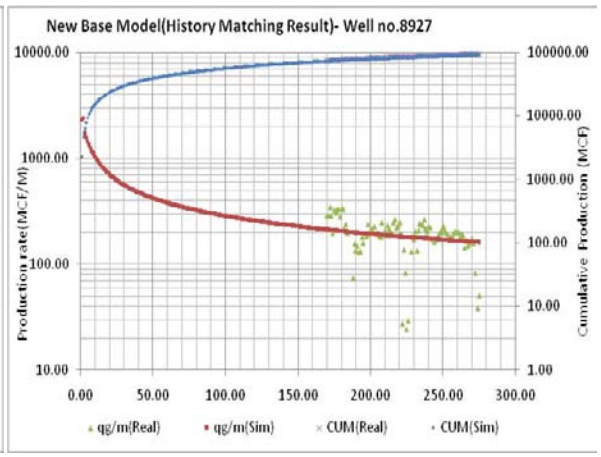


Figure A-56.History matching result well#8927

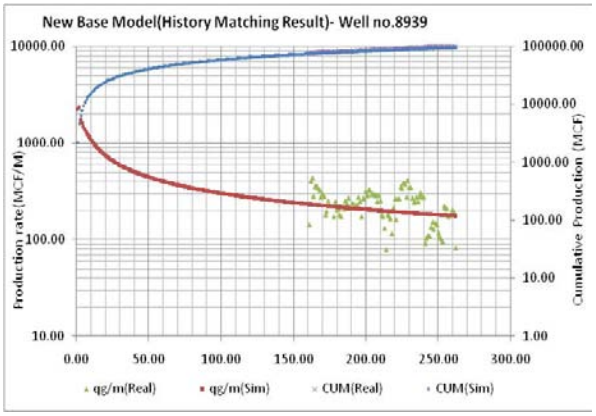


Figure A-57.History matching result well#8939

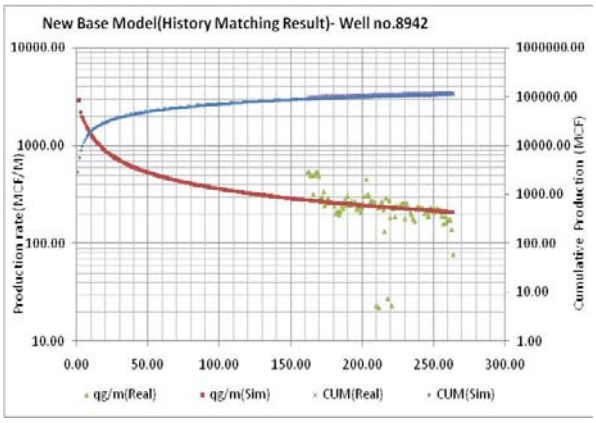


Figure A-58.History matching result well#8942

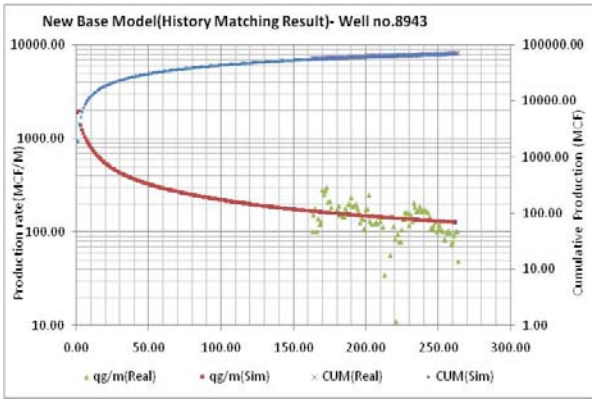


Figure A-59.History matching result well#8943

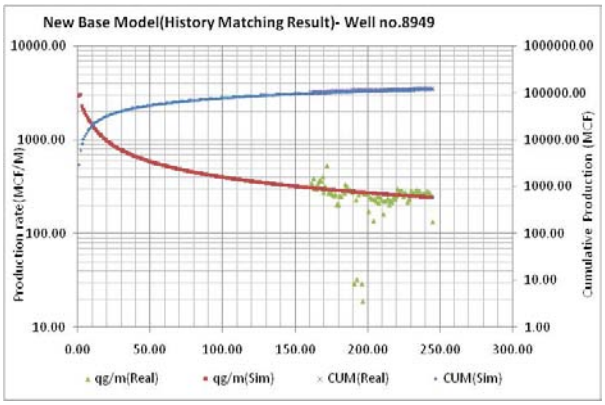


Figure A-60.History matching result well#8949

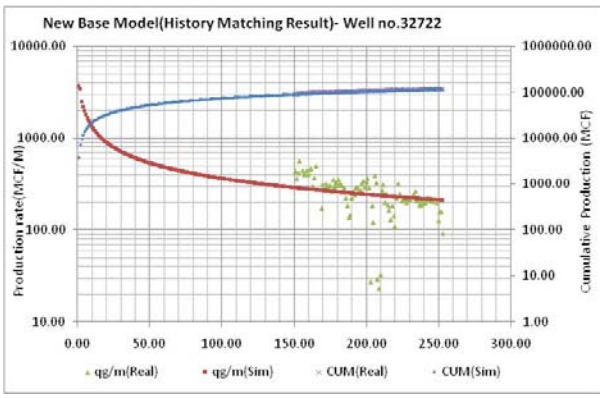


Figure A-61.History matching result well#32722

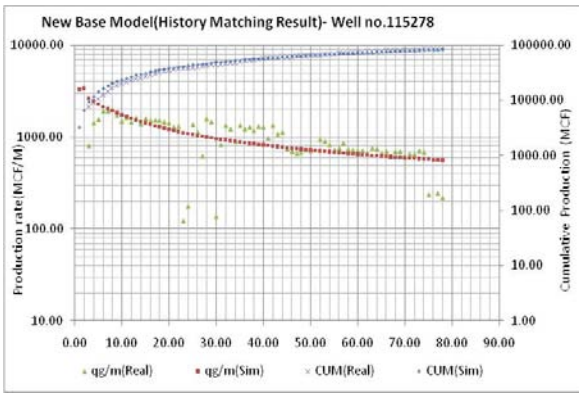


Figure A-62.History matching result well#115278

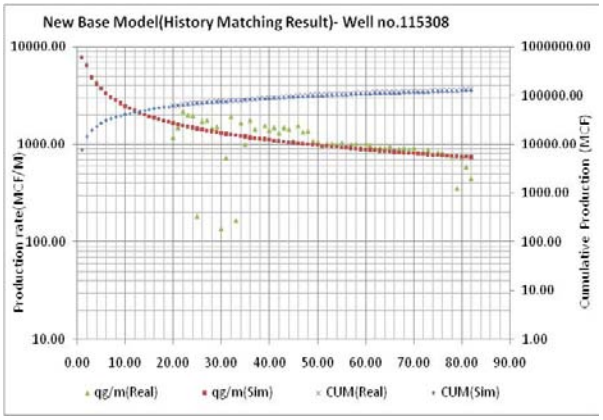


Figure A-63.History matching result well#115308

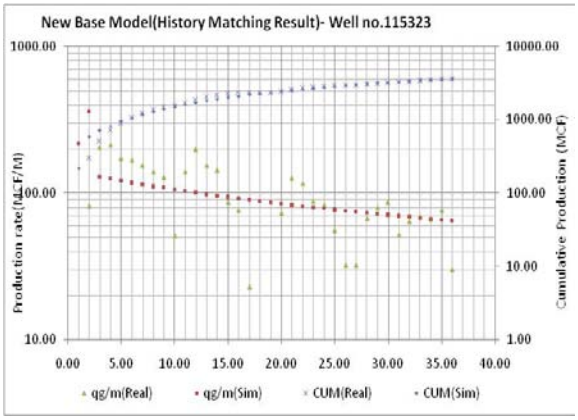


Figure A-64.History matching result well#115323

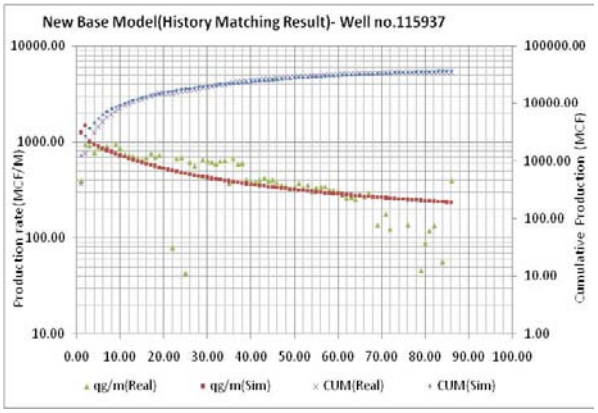


Figure A-65.History matching result well#115937

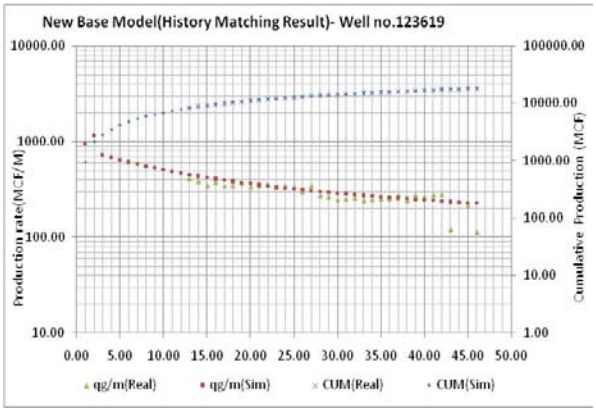


Figure A-66.History matching result well#123619

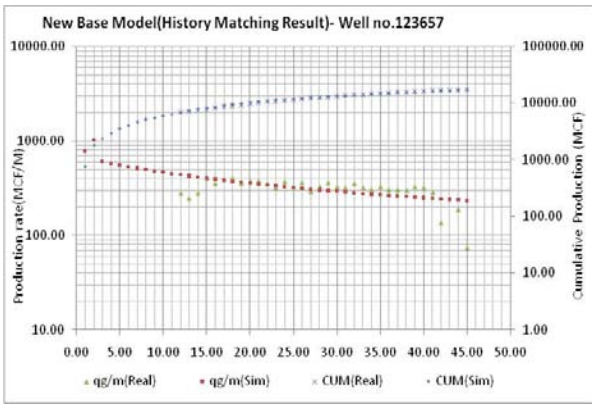


Figure A-67.History matching result well#123657

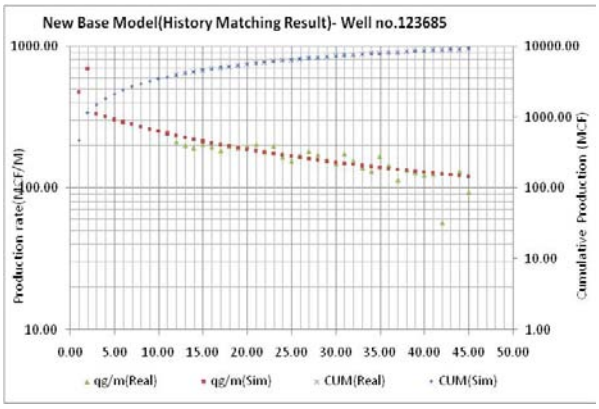


Figure A-68.History matching result well#123685

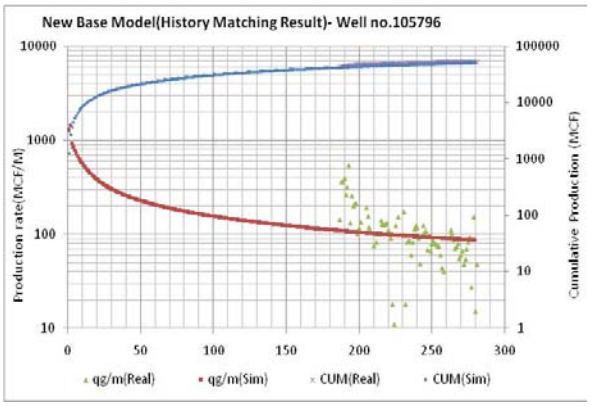


Figure A-69.History matching result well#105796

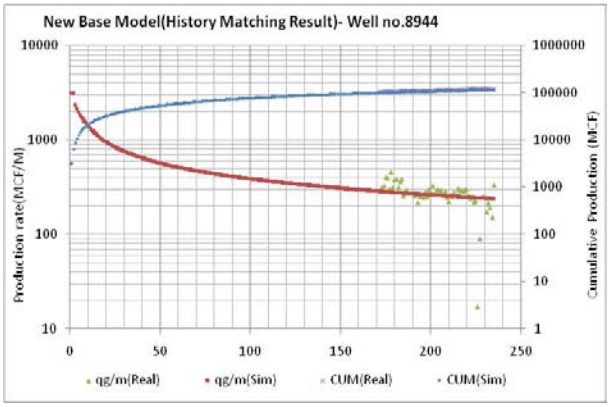


Figure A-70.History matching result well#8944

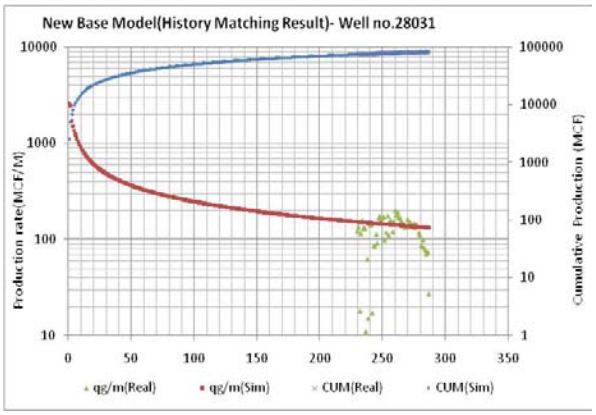


Figure A-71.History matching result well#28031

7.2

PRODUCTION ANALYSIS

New Albany Shale – Final Report on Reservoir Engineering Research

Research Team:
Thomas Blasingame, Christine Ehlig-Economides, Bo Sung; Texas A&M

Table of Contents

Main Findings 2
Technical Details 3
EUR Analysis 3
Unified PTA and PDA Analysis for Well A-7431H 4
Sensitivity Study 5
Well Design Implications 9
References 10
Appendix 11
Supplemental Material – Thesis, Bo Song – Texas A&M University 11

Main Findings

The original vision for New Albany shale emphasized the role of natural fractures, and there was an expectation that pressure transient tests might reveal characteristics of a natural fracture system. However, the only pressure buildup data acquired in this study was in the A- 7431H well. The A- 7431H well was the first well in New Albany to adopt modern shale gas exploitation techniques based on multistage fracturing of a horizontal well. Rather than depend on natural fractures, such well designs instead create a stimulated reservoir volume (SRV) defined by a hydraulic fracture network. The horizontal segment in the A- 7431H well measured 3500 ft, and 8 fracture stages spaced about 400 ft apart were created. During this project, a second well, A- 7455 was drilled with a similar design, but in this case microseismic data were acquired while fracturing that suggest the hydraulic fractures may extend in the direction normal to the horizontal well axis as much as 1200 ft in half length.

Although the pressure buildup was quite long with duration 9 days, the pressures were recorded on a daily basis; thus, early time data was missing. The data in late time do not show definitive evidence of natural fractures. Indeed, in complex well architectures it would be highly unlikely to observe pressure transients indicating the presence of natural fractures because they would be masked by transients dominated by the created fracture geometry.

The A- 7431H well also recorded the surface pressure on a daily basis, and combined pressure and rate data were processed for production data analysis. Both pressure transient analysis (PTA) from the long pressure buildup and production data analysis (PDA) showed evidence of linear flow, still with no evidence of natural fractures. An integrated interpretation incorporating fracture half length of 1200 ft indicated by microseismic data acquired from the A- 7455 well provides an estimate for permeability on the order of 180 nanodarcies (10^{-7} darcies) and an estimate for the SRV of 3.11 BSCF (assuming water saturation of 0.5 and including 2.2 BSCF adsorbed gas), which, in turn, gives an estimate of 2.6% for the gas recovery factor to-date.

An independent estimate for expected ultimate recovery (EUR) based on a power law rate decline model gave an estimate of 0.136 BSCF, which would imply ultimate recovery efficiency of 5.4%. However, if the SRV is smaller than what was hypothesized on microseismic indications from the A-7455 well, the recovery factor could be somewhat greater. Analytical analysis of the production data suggest that the created fracture half lengths must be at least 440 ft, giving a minimum SRV of 1.63 BSCF including 1.16 BSCF adsorbed gas.

EUR estimates were also done for 33 other New Albany shale wells for which production data were available. Most wells showed EUR estimates of less than 0.01 BSCF. The A- 7431H well shows considerably higher EUR than most of the other wells, indicating that the multistage fracturing approach shows promise for this resource.

For permeability of 180 nanodarcies the production forecast indicates that even after 30 years there will be gas between adjacent fracture stages still at the original reservoir pressure. This suggests that fracture stages should be spaced closer together. At a spacing of 50 ft instead of 440 ft, flow to adjacent fractures would interfere after 3.5 years, and much higher recovery of the gas in place could be achieved

during a normal well lifetime of 30 years. However, to maintain an economic rate for 30 years, the number of fractures should be increased.

Technical Details

This section will provide a summary of previously reported details. First, EUR analysis using a power law rate decline function will be provided. Second, the unified buildup-RNP analysis shows that the A- 7431H well exhibits long term linear flow behavior and shows how the integration with microseismic evidence enables permeability estimation. Third, sensitivity studies showing long term production trends for shale with properties similar to New Albany will be presented. Finally, implications for design of future New Albany wells are explored.

EUR Analysis

Production data were analyzed for 33 wells owned by a producing company referred to as company A in this report. One of the 33 wells is a horizontal well with 8 transverse fractures, and the others are hydraulically fractured vertical wells. Because publications by Valko (2009) and Ilk, et al. (2008) advocate use of a power law analysis technique for reserves estimation in shale gas wells, we have applied this technique to the wells.

As an example, Fig. 1 shows production data for Well A-7272. The circled data point was used as the initial rate, and the points shown as red square symbols were excluded in the straight line applying the power law reserves estimation technique shown for this well in Fig. 2. The power law technique computes the recover potential as

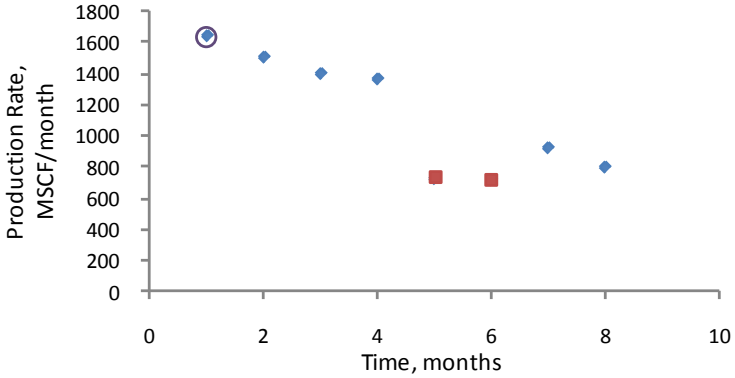


Figure 1: Production rate data for Well A- 7272.

$$rp = 1 - \frac{Q}{EUR} = \frac{1}{\Gamma\left[\frac{1}{n}\right]}\Gamma\left[\frac{1}{n}, -\ln\frac{q}{q_i}\right]$$

where q is the power law model production rate given by

$$q = q_i \exp\left[-\left(\frac{t}{\tau}\right)^n\right], \qquad (2)$$

Q is the cumulative production, EUR is the Estimated Ultimate Recovery, n is the power law exponent, and τ is a dimensionless model parameter indicating the "characteristic number of periods."

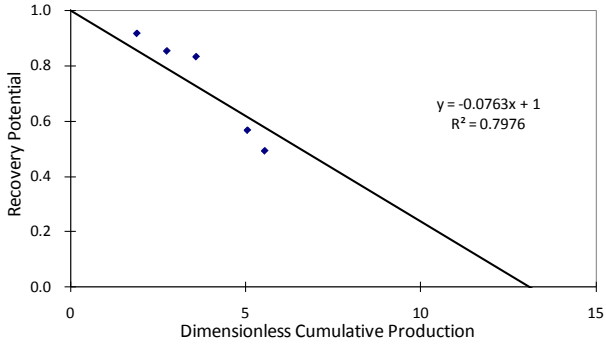
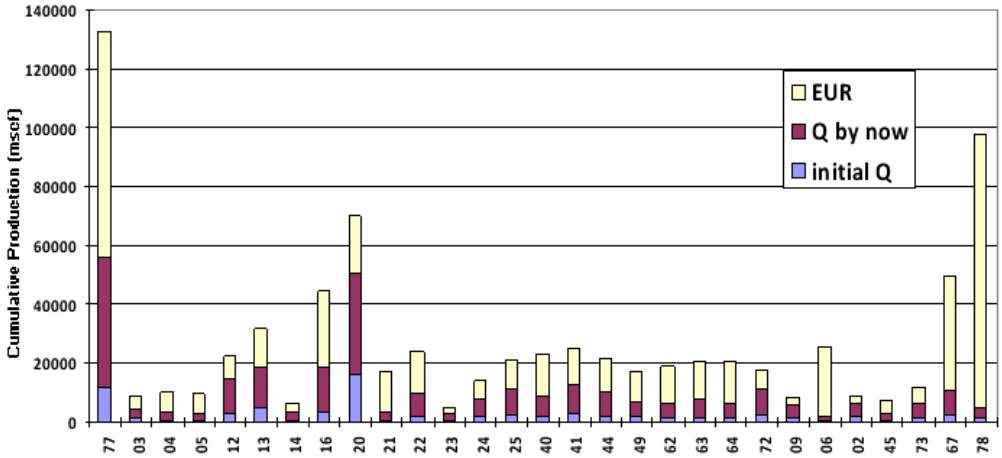


Figure 2: Reserves estimation for Well A-7272 using power law method by Valko (2009).

Results of the analyses for all the wells are shown in Fig. 3. The analysis suggests that the wells have considerable remaining reserves, and a few wells have performed much better than average, especially A-7260 and A-7431.



Unified PTA and PDA Analysis for Well A-7431H

A pressure buildup test was conducted on Well A- 7431H, the only horizontal well until Well A-7455 was drilled and completed in August, 2009. As shown in Fig. 4, Well A- 7431H was produced for 50 hr before being shut in for 192 hr. Since that time the well has been on production.

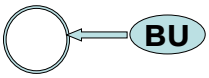


Figure 4: Rate and pressure data for Well A- 7431H.

Unlike the other wells, production data for this well includes both production rate and wellhead pressure. This enables more rigorous forms of production data analysis, including rate-normalized pressure (RNP). An improved form of the RNP analysis provides a smooth record that can be differentiated with respect to the logarithm of the production time. The result produces a virtual drawdown that can be combined with the buildup (BU) data acquired while the well was shut in.

Figure 6 shows a graph of rate-normalized pressure (RNP) and its derivative computed using the Topaz module of the Ecrin software by Kappa Engineering. As seen in Fig. 5, the extent of the apparent linear flow for essentially the entire production duration. RNP is the simplest

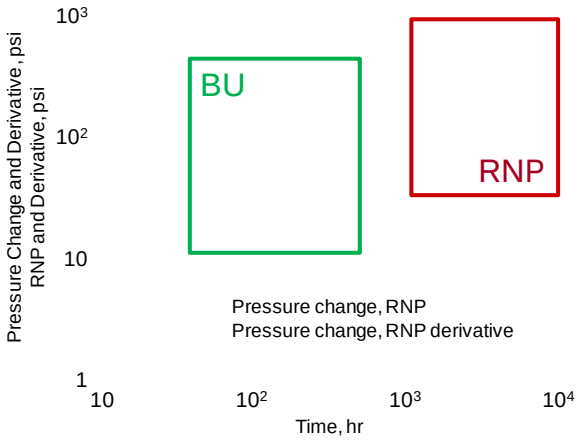


Figure 5: Rate and pressure data for Well A- 7431H.

deconvolution and represents a virtual drawdown response under constant rate production. While most analysts are attempting to interpret rate decline behavior, drawdown behavior is much more straightforward to interpret. Therefore, we are favoring interpretation using RNP instead of rate decline.

Sensitivity Study

There are 2 equations to consider for linear flow. First, during linear flow, the equation for pressure change, Δp, versus time is given by

$$\Delta p = m_{lf}\sqrt{\Delta t} + (\frac{\pi}{3})(\frac{m}{1.151})\frac{kx_f}{k_f w}, \qquad (3)$$

where the k is the formation permeability, x_f is the hydraulic fracture half length, k_f is the fracture permeability, and w the fracture width. The factor m_{lf} is the slope of a graph of pressure versus the square root of elapsed time, Δt; and the factor m is the slope of a graph of pressure versus log Δt. The equation for the pressure derivative is given by

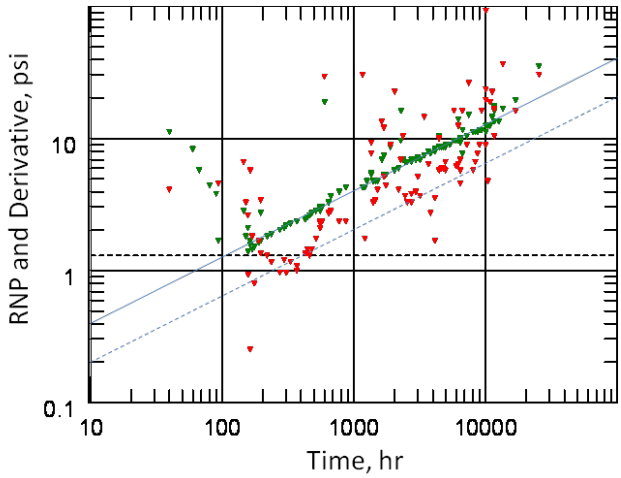


Figure 6: Rate-Normalized pressure and derivative computed for the A- 7431 H well.

$$\Delta p' = \frac{1}{2} m_{lf}\sqrt{\Delta t} \qquad (4)$$

where $\Delta p'$ is the derivative of pressure change with respect to the logarithm of elapsed time. In turn, the product of $x_f k^{0.5}$ is related to m_{lf} by

$$x_f\sqrt{k} = \left(\frac{4.064qB}{m_{lf}h}\right)\left(\frac{\mu}{\phi c_t}\right)^{1/2} \qquad (5)$$

where q is the well flow rate, B is the fluid formation volume factor, h is the formation thickness, μ is the fluid viscosity, ϕ is the formation porosity, and c_t is the total compressibility.

The second equation is the depth of pressure investigation during linear flow given by [Ehlig-Economides, 1995]

$$x_i = 2\sqrt{\frac{kt}{948\phi\mu c_t}} \qquad (6)$$

To fully appreciate the importance of Eqs. (5) and (6), Fig. 7 shows a sensitivity study of the drawdown response for the multistage fractured horizontal well shown in Fig. 8 using input variables provided in Table 1 (not shown in Table, the Langmuir pressure is 2000 psia, and the adsorption density is 0.1). The family of pressure change and derivative curves shows sensitivity to permeability, which ranges from 100 nanodarcies to 1 md. This sensitivity study reveals that the early linear flow regime associated with flow to the fracture planes can last for many log cycles, while the linear flow regime associated with compound linear flow lasts less than one log cycle for all permeability values.

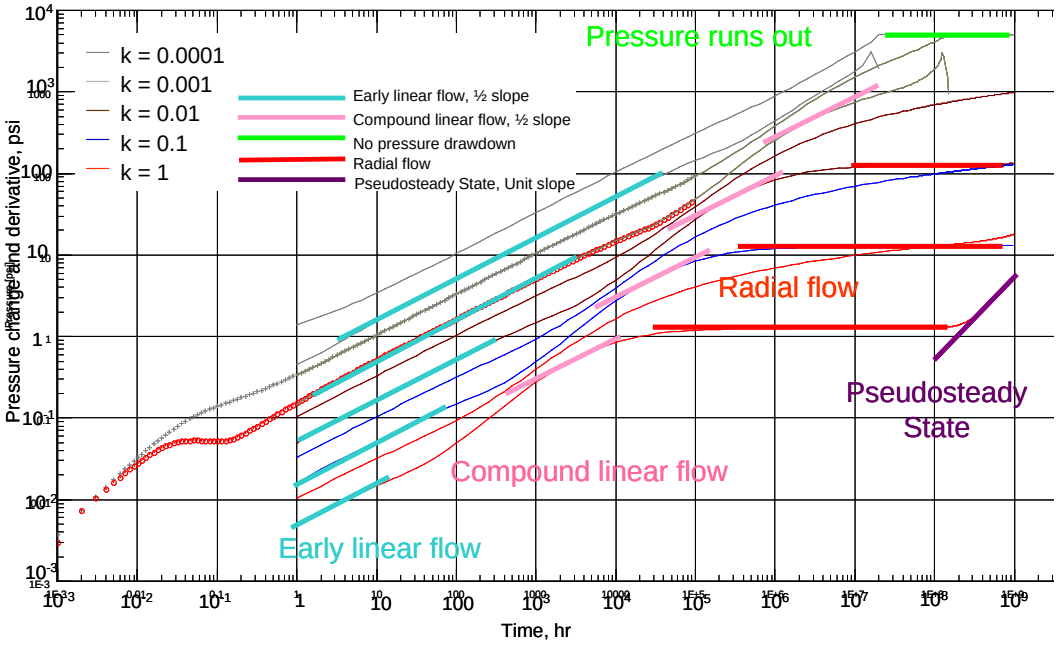


Figure 7: Sensitivity study for permeability ranging from 100 nanodarcy to 1 md for multistage fracture geometry shown in Fig. 3 and input variables provided in Table 1.

As seen in Fig2. 5 and 6, the ½ slope trend observed in the RNP response for the A- 7431H well has lasted already more than 2 log cycles. This is evidence that this trend corresponds to early linear flow and is therefore governed by Eq. 5. Noting that the RNP = 4 psi at the time of 1000 hr, and noting that the derivative is one half that of the pressure change, from Eq. 4 the slope m_{lf} = 0.126 psi/cycle. The flow rate used for the RNP graph is the value of the last flow rate, q = 156 MSCF/d. To use Eq. 5, which is intended for oil flow, we compute the gas formation volume factor at the initial formation pressure, giving B = 0.0217 cf/SCF. In turn, this indicates that

$$x_f\sqrt{k} = \left(\frac{4.064qB}{m_{lf}h}\right)\left(\frac{\mu}{\phi c_t}\right)^{1/2} = 128 \text{ ft- md}^{1/2} \qquad (5)$$

To use Eq. 4 we need the fracture spacing in the A-7431H well. If the fracture spacing is 400 ft, linear flow to fractures interferes when x_i = 200 ft. If the fractures were to show the upward trend from the linear flow trend that eventually bends into compound linear flow right after the last data

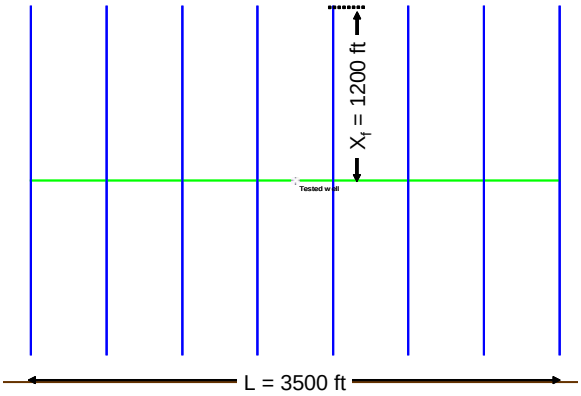


Figure 8: Diagram of well used for sensitivity study.

point at 8304 hr, this would correspond to a permeability of

$$k = \frac{948\phi\mu c_t x_i^{\,2}}{4t} = 0.0013 \text{ md}$$

This is the maximum value the permeability can be because if it were greater, the evidence of interfracture interference would be seen as an upward departure from the linear trend. Applying Eq. 5, the fracture half length corresponding to k = 0.0013 md would be 3550 ft. This corresponds to the sum of the fracture half lengths for each stage.

On the other hand, if the A- 7431H well has 8 stages with fracture half lengths on the order of those observed from the microseismic data for the recently drilled and completed A-7455 well, or ~1200 ft, then the total fracture half length would be 9600 ft. Again applying Eq. 5, this would correspond to a permeability of 0.000178 md. Also, from Eq. 4, the expected time that evidence of interfracture interference would appear would be

$$t = \frac{948\phi\mu c_t x_i^{\,2}}{4k} = 1{,}881{,}600 \text{ hr} = 215 \text{ yr for } k = 0.000178 \text{ or } 30 \text{ yr for } k = 0.0013 \text{ md.} \quad (6)$$

Table 1: Input variables for sensitivity study in Fig 2

reservoir geometry	
length, ft	1000000
width, ft	1000000
well information	
well type	multi-fractured horizontal
wellbore radius.ft	0.3
well length, ft	3500
well vertical position, ft	50
fracture number	8
fracture half length, ft	1200
reservoir properties	
payzone thickness, ft	100
porosity	0.1
temperature, F deg	212
initial pressure, psia	5000
formation compressibility, psia-1	3.00E-06
fluid, properties	
fluid type	gas
specific gravity	0.7

This analysis underscores several important points. First, if the permeability were known, it would be possible to estimate the total conductive fracture half length for the sum of the fracture stages. In contrast, if the total conductive fracture half length is estimated from microseismic data analysis, then the corresponding effective formation permeability can be estimated. Second, the analysis is only possible when both pressure and production rate are recorded over time, as they have been in the A-7431H well. Rate decline data alone do not enable estimation of the reservoir permeability. For the A-7431H well, the single extended buildup pressure transient has not provided any additional insight in part because the data rate of one pressure measurement per day is too sparse. It would be better to record pressure at a higher data rate when the well is shut in.

Another observation from this analysis pertains to the reservoir volume being drained by the multistage fractured horizontal well. Until the time of interfracture interference, the pressure investigation does not exceed 200 ft beyond the extent of the fracture tips. Assuming the total fracture half length is 3550 ft, corresponding to the maximum permeability of 0.0013 md, for 8 stages, the fracture half length for each stage is about 440 ft. If the 8 fractures are 400 ft apart, the area covered by the fractures is 1080 by 3200 sq ft including an additional 400 ft penetration in each dimension. For the thickness of 56 ft and assuming water saturation is 50%, (based on porosity report for Gohl No. 4 [Zuber, et al, 1999]) this corresponds to about 0.32 BCF free gas in place.

Analysis using the Valko power law method for estimating the Expected Ultimate Recovery (EUR) is shown in Fig. 4. This gives an EUR estimate of 0.136 BCF, which would correspond to an ultimate recovery factor of about 43%. If, instead, the fracture half lengths are 1200 ft, the recovery factor works out to less than 20% of the free gas in place.

parameters	values
Well #	DPI-2477
Initial rate, mscf/d	531
Optimal n	1
Slope absolute value	0.004
Square-R	0.5055
X-intercept	250
EUR , mscf	136154

Figure 9: Power law EUR estimation.

This analysis does not consider adsorbed gas, which for the latter case is about 2 BCF. Considering adsorbed gas, the recovery factor is 5.4%. However, the Valko EUR analysis for the A- 7431H well is problematic, as shown in Fig. 4. Late time data for this well trend to the right of the best fit line, and this may suggest that the EUR for this well will be higher than that indicated by the analysis shown in the figure.

Figure 10 shows synthetic data for 1 year on production, and after 30 years on production. The EUR estimate clearly varies with time on production. The power law decline function does not fit the synthetic data, and the nature of the discrepancy is similar to what is observed for the data from A-7431. This suggests that the EUR estimates by this technique may not be reliable. Further, this technique and other rate decline approaches designed to produce EUR do not provide any insight about the gas recovery factor within the stimulated reservoir volume.

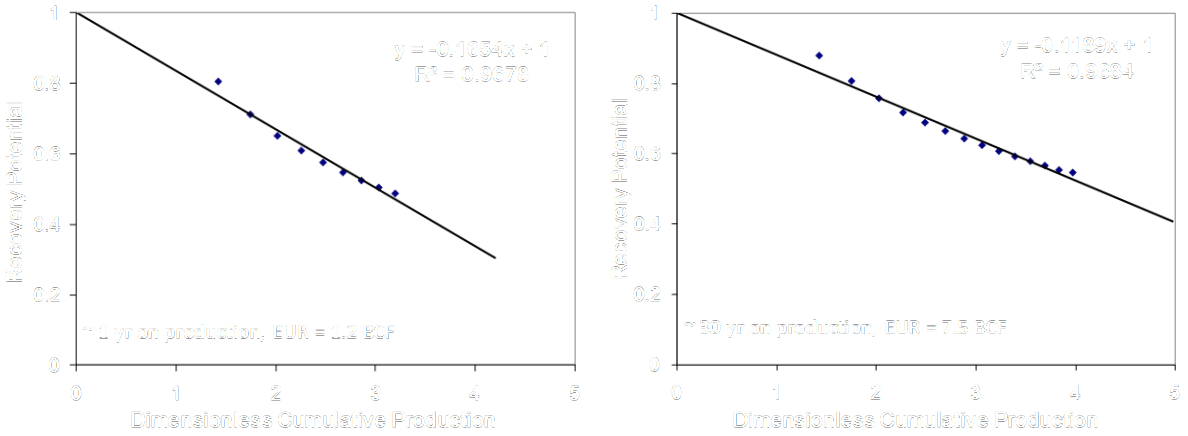


Figure 10: Power law EUR estimation on synthetic data showing dependence of EUR estimate on production time.

Well Design Implications

The sensitivity study in the previous section indicates that for the minimum permeability corresponding to 1200 ft fracture half lengths, the area investigated at the time of fracture interference occurring after about 300 years would be approximately that diagrammed in Fig. 11. Even then the recovery factor would be quite low. Unfortunately, the well rate would be less than economic in a much shorter time, and recovery efficiency would be even very much less.

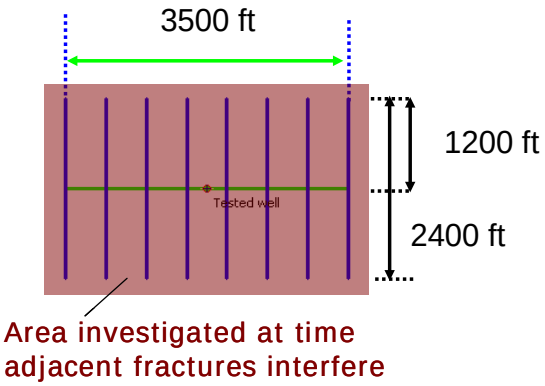


Figure 11: Diagram of A- 7431 well idealization showing area investigated after ~300 yr.

We now propose a design well methodology using permeability and the adsorption parameters (Langmuir pressure, p_L, and adsorption density ρ_{ad}). The adsorption effect is to shift the response behavior in time by a factor we call the adsorption index, I_{ad} given by the response time for a given pressure change with adsorption divided by the response time without considering adsorption. The adsorption index is always greater than or equal to one. The adsorption index depends on porosity, initial reservoir pressure and the adsorption parameters.

Our approach is to use the estimated reservoir permeability to determine what spacing between fracture stages will result in inter-fracture interference at a specified time that will, in turn, result in a recovery factor of 50% or more after a specified time on production. A key point to recognize is that until the time of inter-fracture interference production from each fracture stage is additive.

As an example, suppose we design the well for inter-fracture interference within 5 years. Considering inputs for the New Albany shale of ϕ = 0.06, pi = 714 psi, p_L = 1044 psi, and ρ_{ad} = 0.00648 g/cc, the resulting adsorption is I_{ad} = 1.5. For the permeability of 178 nd, the resulting fracture spacing should be

$$x_s = 2x_{s/2} = 2\times 2\sqrt{\frac{kt_{\text{int}} / I_{ad}}{948\phi\mu c_t}} = 51.6 \text{ ft}$$

The minimum number of fractures required for the well to pay out by a specified period of time can be determined using inputs for the basic well cost (to drill to the productive interval and build the horizontal trajectory) and for the incremental cost of drilling and fracturing each stage. If we assume the basic well cost is $1 million, the cost per fracture is $200,000, the gas price is 5$/MSCF, and the x_f is 2000 ft, for payout in 5 years, there must be at least 17 fracture stages.

The Topaze simulation indicates that the above well will recover 95.1% of the gas in place within the stimulated reservoir volume (SRV), including adsorbed gas, after 30 years on production. At 30 years the well production rate will have declined to 15.93 MSCF/d. We define the SRV as the volume investigated by the pressure after the specified well life (in this case 30 years). The pressure will penetrate as compound linear flow using the same equation as above. At this time the bulk reservoir volume of the SRV is given by $2(n_s+1)(x_f+x_t)x_t h$,

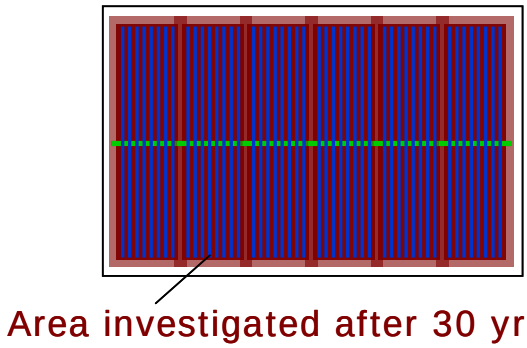


Figure1 2: Diagram of proposed well design showing SRV after 30 yr for a 48-fracture well.

where n_s is the number of fracture stages, x_f is the average fracture half-length, x_t is the linear pressure investigation after the specified well life, and h is the reservoir thickness.

For the same horizontal well length there should be many more fractures. The SRV at the end of the project is diagrammed in Fig. 12. The outer square is the area penetrated after 300 yr by the A- 7431 well. The diagrammed well would produce 6 times what A- 7431 produces from approximately the same area.

A spread sheet program has been developed to apply the approaches discussed in this report. After input of reservoir and well parameters and estimated drilling and hydraulic fracture costs as well as financial parameters, the program determines the well length and number and spacing of fracture stages that would satisfy a target payout time and computes the expected recovery efficiency for the resulting well design for the input well life. For New Albany shale, the program has difficulty finding a profitable well design. While adsorption behavior is favorable, the key problem for New Albany shale is the low reservoir pressure.

The spread sheet computes approximations for the rate decline at constant pressure production by computing the linear flow rate decline until the time of interfracture interference and then using exponential rate decline after that point to represent pseudo pseudosteady state behavior. The spread sheet also includes a correlation developed to enable estimation of the adsorption index (Song,2010).

To illustrate the importance of pressure, one need only consider the computed free gas in place. The low reservoir pressure results in much less gas in place than would be present at higher reservoir pressure. The value of the 4.7 BSCF of gas in place at $4/MSCF is about $17 million if it could be produced all at once. If the drilling cost is $1 million, and each fracture costs $200,000, the idealized well design with 48 fractures would cost $11 million. Even at 95% recovery after 30 years, this design appears to be marginal, and it is not obvious that 2000 ft fracture half lengths at 50 ft spacing are achievable. At 10 times the reservoir pressure, the gas in place would be nearly 17 BSCF, and the well design would be much more promising.

References

Ehlig-Economides, C.A.: "Computation of Test Area of Investigation in Nonradial Geometries," *H.J. Ramey, Jr., Memorial Volume, SPE Advanced Technology Series*, 1995.

Song, Bo: “Pressure Transient Analysis and Production Analysis For New Albany Shale Gas Wells,” Thesis, Texas A&M University, 2010.

Valko, P.:” Assigning Value to Stimulation in the Barnett Shale: A Simultaneous Analysis of 7000 Plus Production Histories and Well Completion Records,” paper SPE 119369, 2009.

Zuber, M. D., Frantz, J. H., Jr., and Williamson, J.: “Core Test Analysis and Correlations,” prepared for the New Albany Shale Producibility Consortium, 1999.

Appendix

Supplemental Material – Thesis, Bo Song – Texas A&M University

PRESSURE TRANSIENT ANALYSIS AND PRODUCTION ANALYSIS FOR NEW ALBANY SHALE GAS WELLS

A Thesis

by

BO SONG

Submitted to the Office of Graduate Studies of
Texas A&M University
in partial fulfillment of the requirements for the degree of

MASTER OF SCIENCE

August 2010

Major Subject: Petroleum Engineering

PRESSURE TRANSIENT ANALYSIS AND PRODUCTION ANALYSIS FOR NEW ALBANY SHALE GAS WELLS

Copyright 2010 Bo Song

PRESSURE TRANSIENT ANALYSIS AND PRODUCTION ANALYSIS FOR NEW ALBANY SHALE GAS WELLS

A Thesis

by

BO SONG

Submitted to the Office of Graduate Studies of
Texas A&M University
in partial fulfillment of the requirements for the degree of

MASTER OF SCIENCE

Approved by:

Chair of Committee,	Christine Ehlig-Economides
Committee Members,	Peter Valko
	Yuefeng Sun
Head of Department,	Stephen A. Holditch

August 2010

Major Subject: Petroleum Engineering

ABSTRACT

PRESSURE TRANSIENT ANALYSIS AND PRODUCTION ANALYSIS FOR NEW ALBANY SHALE GAS WELLS

(August 2010)

Bo Song, B.A., China University of Geosciences (Beijing);

Chair of Advisory Committee: Dr. Christine Ehlig-Economides

Shale gas has been becoming increasingly important to United States energy supply. During last decades, the mechanisms of shale gas storage and transport was gradually recognized. The special characteristic of gas desorption was realized and quantitatively described. Since the rate decline behavior of shale gas wells is different from wells in conventional reservoirs, models and approaches special for estimating rate decline and recovery of shale gas wells were developed. As the strategy of the horizontal well with multiple transverse fractures (MTFHWs) was discovered and its significance to economic shale gas production was understood, rate decline and pressure transient analysis models for this type of well were developed to shed light on the well behavior.

In this thesis, we consider a modified “Triple porosity/Dual permeability” model and performed sensitivity studies to understand long term pressure drawdown behavior of MTFHWs. A key observation from this study is that the early linear flow regime before interfracture interference gives a relationship between summed fracture half-length and permeability, from which we can estimate either of them when the other is

known. We also studied the impact of gas desorption on the time when the pressure perturbation caused by production from adjacent transference fractures (fracture interference time) and programmed an empirical method to calculate a time shift that can be used to qualify the gas desorption impact on long term production behavior.

We focused on the field case Well - 00 0077 in New Albany Shale. We estimated the EUR for it and another 32 wells using an existing analysis approach. We applied a unified BU-RNP method to process the one-year production/pressure transient data and performed pressure transient analysis to the resulting virtual constant rate pressure drawdown. Production analysis was performed meanwhile. Diagnosis plots for PTA and rate-normalized pressure analysis revealed that only the early linear flow regime was visible in the data, and permeability was estimated both from a model match and from the relationship between fracture half-length and permeability using an estimate for the total fracture length based on analogy to another well for which microseismic data provided an estimate for the transverse fracture geometry. Fracture interference time was also estimated by considering gas desorption, and the result indicated that the interference will occur only after a very long period approaching 200 years. Based on this we recommended a well design strategy to increase he gas recovery factor by decreasing the facture spacing. The higher EUR of - 0077 compared to the vertical wells encourages drilling more MTFHWs in New Albany Shale.

DEDICATION

To my parents and my wife

ACKNOWLEDGEMENTS

I would like to thank my committee chair, Dr. Christine Ehlig-Economides, and my committee members, Dr. Peter P. Valko and Dr. Yuefeng Sun, for their guidance and support to my research.

Thanks also to Dr. Walter B. Ayers for his helpful guidance. I also want to extend my appreciation to the researchers, Miss. C. Angelica and Mr. R. Hamilton in Gas Technology Institute (GTI) for their great help with providing data.

Finally, thanks to all the friends and classmates who provided me with great help with doing research in my topic.

NOMENCLATURE

a = Fraction coefficient, dimensionless

A = Drainage Area, ft^2

b = Fraction coefficient, dimensionless

B = Fluid formation volume factor, rcf/scf

BU = Build up

c_t = Total compressibility, psi^{-1}

c_t^* = Total compressibility, evaluated at average reservoir pressure, psi^{-1}

c_1 = Slope correlation coefficient, cc/g

c_2 = Slope correlation coefficient, cc/g

c_3 = Slope correlation coefficient, cc/g

c_4 = Slope correlation coefficient, cc/g

EUR = Estimated ultimate recovery, Mscf

G_i = Original (contacted) gas in place, MMscf

h = Payzone thickness, ft

I_{ads} = Adsorption Index, hour/hour

k = Formation permeability, md

k_f = Fracture permeability, md

k_m = Matrix permeability, md

k_r = Formation permeability in plane, md

k_z = Vertical formation permeability, md

L = Horizontal well length, ft

m = The slope of a graph of pressure versus log Δt, psi/cycle

m_{lf} = Slope of a graph of pressure versus square root of elapsed time, $psi/t^{0.5}$

$m(p)$ = Real gas pseudopressure, psi^2/cp

MTFHW = Multiple transverse fracture horizontal well

n = Valko new decline model parameter, dimensionless

n_f = Number of fractures

p = Pressure, psia

p_i = Initial reservoir pressure, psia

p_L = Langmuir pressure, psia

p_{wf} = Flowing bottomhole pressure, psia

PDA = Production data analysis

PTA = Pressure transient analysis

q_g = Gas production (surface) rate, Mscf/d

q_i = Initial production rate, Mscf/d

Q = Cumulative production, Mscf

r = Wellbore radius, ft

RF = Recovery factor, fraction

RNP = Rate normalized pressure, psi

RNP' = RNP derivative with respect to logarithm of material balance time

rp = Recovery potential

s = Skin factor, dimensionless

slope = The slope of the linear function of time shift versus adsorption density

SRV = Stimulated reservoir volume

S_{ex}^{surf} = The total area of exposed surface to matrix particles;

S_w = Water saturation, fraction

$S_{\phi f}$ = The area of surface of fracture space exposed to matrix particles, ft^2;

$S_{\phi m}$ = The area of surface of matrix pore space exposed to matrix particles, ft^2;

t = Elapse time, hours

t_a^* = Pseudotime, accounting for desorption, days

t_{ca}^* = Material balance pseudotime, accounting for desorption, days

t_e = Material balance time, hours

t_p = Production time, hours

T_r = Reservoir temperature, ^oF

t_{sup} = Superposition time, dimensionless

V_{ads} = Gas volume can be adsorbed by a rock of unit mass, scf/g

V_{des} = Gas volume desorbed by a rock of unit mass, scf/g

V_L = Langmuir volume, the maximum gas volume can be adsorbed, scf

V_{ph} = The adsorbed gas volume at the higher pressure, scf

V_{pl} = The adsorbed gas volume at the lower pressure, scf

$V_{\phi f}$ = Fracture space saturated by gas, scf

$V_{\phi m}$ = The pore space volume in matrix saturated by gas, scf

w = Fracture width, ft

x_f = Hydraulic fracture half length, ft

Z^* = Gas derivation factor adjusted to account for desorption, dimensionless

z_w = Horizontal well vertical position, ft

Dimensionless variables

EUR_D = Dimensionless estimated ultimate recovery

q_D = Dimensionless production rate expression

Q_D = Dimensionless cumulative production

Greek variables

α = Shape factor depending the size and geometry of matrix, dimensionless

λ = Interporosity flow coefficient, fraction

θ = Coverage fraction of the surface, dimensionless

μ = Viscosity, cp

μ_g = Gas viscosity, cp

ρ_{ads} = Adsorption density, g/cc

ρ_{ads}^{surf} = Adsorbed gas density, g/cc

ρ_{ra} = Adsorbed gas volume released from unit exposed surface area, scf/ ft^2

ρ_{rock} = Rock density, g/cc

τ = Valko new decline model parameter, dimensionless

ϕ = Porosity, fraction

ω = Storage ratio, fraction

ω_{mod} = Storage ratio accounting for desorption, fraction

Subscripts

a = Pseudo

ads = Adsorbed

c	=	Material balance
ca	=	Material balance pseudo
D	=	Dimensionless variables
des	=	Adsorbed
e	=	Material balance
ex	=	Exposed
f	=	Fracture
g	=	Gas
gas	=	Gas
i	=	Initial
L	=	Langmuir
lf	=	Linear flow
m	=	Matrix
mod	=	Modified
p	=	Production
ph	=	Higher pressure state
pl	=	Lower pressure state
r	=	Reservoir
ra	=	Release to surface area
rock	=	Reservoir
sup	=	Superposition
w	=	Water

wf	=	Sandface
z	=	Vertical direction
ϕf	=	Porous space of natural fracture system in shale gas reservoirs
ϕm	=	Porous space of matrix pore system in shale gas reservoirs

Superscripts

surf	=	Surface
¯	=	Average property
*	=	Altered variables

TABLE OF CONTENTS

Page

ABSTRACT iii
DEDICATION v
ACKNOWLEDGEMENTS v
NOMENCLATURE vi
TABLE OF CONTENTS xiii
LIST OF FIGURES xv
LIST OF TABLES xviii
CHAPTER 1. INTRODUCTION: BACKGROUND AND LITERATURE REVIEW 1
1.1 Shale Gas Resources in United States 1
1.2 Introduction of New Albany Shale Gas Play 5
1.3 Literature Review 8
CHAPTER 2. CONCEPTUAL MODEL FOR SHALE GAS 11
2.1 Gas Storage Mechanism 11
2.2 Gas Transport Mechanism 13
2.3 Gas Adsorption/Desorption Model 19
CHAPTER 3. RATE DECLINE ANALYSIS FOR NEW ALBANY SHALE GAS WELLS 26
3.1 EUR Determination from Rate Decline Analysis 26
3.2 EUR Estimates for New Albany Shale Gas Wells 29
CHAPTER 4. Drawdown Pressure Transient Behavior in Multi-Transverse Fractured Horizontal wells (MTFHWs) 30
4.1 MTFHWs in Shale Gas Reservoirs 30
4.2 Previous Models for MTFHWs 33
4.3 Rationale for Use of Long Term Drawdown Model Behavior 39
4.3.1 Rate-Normalized Pressure Analysis as Alternative to Rate Decline Analysis 40
4.3.2 Unified BU-RNP Analysis 41
4.4 Sensitivity Studies Illustrating Long Term Drawdown Behavior of MTFHWs in Shale Gas Reservoirs 43
4.4.1 Fracture Storage 48
4.4.2 Early Linear Flow 48
4.4.3 Interference between Adjacent Fractures 49
4.4.4 Compound Linear Flow 50
4.4.5 Boundary Behavior 51
4.5 Impact of Gas Desorption on the Long Term Drawdown Behavior of the MTHWF 53
4.6 Implications of the Early Linear Flow 60

4.6.1 Relationship between Permeability and Fracture Half Length 60
4.6.2 Time of Fracture Interference 63
4.6.3 Fracture Spacing Design for Interference at a Specific Time 64
CHAPTER 5. FIELD CASE STUDY: NEW ALBANY SHALE 66
5.1 Field Data and Information Collection and Synthesizing 66
5.2 Production/Pressure Data Processing by Unified BU-RNP Method 70
5.3 PTA and Production Analyses 72
5.4 EUR Estimation and Recovery Factor 77
5.5 Specialty of Low Reservoir Pressure and Comments on Well Design 80
CHAPTER 6. SUMMARY AND CONCLUSIONS 81
6.1 Summary 81
6.2 Conclusions 83
6.3 Recommendations 84
REFERENCES 86
APPENDIX A 90
VITA 102

LIST OF FIGURES

FIGURE Page

1. Gas Shale Plays in Lowe 48 United States 2

2. Illustration of Multistage Hydraulic Fracture Horizontal Well..... 5

3. Productive Area of New Albany Shale 7

4. Stratigraphy of New Albany Shale..... 7

5. Triple Porosity Storage Model in Gas Shales 12

6. Conceptual Model for Gas Shales..... 13

7. Conceptual Model for Gas storage and Transport..... 14

8. Stage Gas Production Process in Coalbed Methane..... 16

9. Gas Transport Mechanism in Gas Shales..... 17

10. Illustration of Gas Transport Mechanism in Gas Shales..... 19

11. Illustration of Typical Gas Adsorption/Desorption Isotherm..... 20

12. Model Parameter Input Dialog Window of Kappa Ecrin..... 23

13. Dialog Window for Inputting Langmuir Parameters in Kappa Ecrin 25

14.EUR Estimation of - 0077 by Valko Approach 28

15. EUR Estimation of 33 Wells in New Albany Shale..... 29

16. Illustration of Longitudinal and Transverse Fractures in Horizontal Wells..... 32

17. Pressure Profile: Half Reservoir, Linear Flow Normal to..... 33

18.Pressure Profile: Half Reservoir, Compound Linear Flow 34

19.Pressure Profile: Half Reservoir, Elliptical Flow..... 34

20. Boundary&Fracture Interference on Normalized Rate Derivative Function 35

21. Potential Flow Regimes Identified in MTFHWs 36

22. Potential Flow Regimes in MTFHW 39

23. Reservoir and Well Geometry of MTFHW_NF Test Series 45

00. Reservoir and Well Geometry of MTFHW_IA Test Series 45

25. Reservoir and Well Geometry of MTFHW_CP Test Series 46

26. PTA diagnosis plot for MTFHW_NF Test Series 46

27. PTA diagnosis plot for MTFHW_IA Test Series 47

28. PTA diagnosis plot for MTFHW_CP Test Series 47

29. Illustration of the Early Linear Flow Normal to Transverse Fractures 49

30. Pressure Interference between Two Adjacent Transverse Fractures 50

31. Compound Linear Flow Regime 51

32. Flow Regimes Revealed through Sensitivity Study 53

33. Gas Desorption Impact on Long Term Drawdown Behavior of MTFHWs 54

34. Time Shift (I_{ads}) Sensitivity Study 55

35. Illustration of Time Shift Sensitivity Study to ρ_{ads} 56

36. Illustration of Time Shift Sensitivity Study to p_L 56

37. Illustration of Relationship between the Adsorption Index and ρ_{ads} 57

38. Illustration of Relationship between Slope and Logarithm of p_L over p_i 58

39. Interface of Program for Calculating Time Shift 60

40. Application of the Relationship between k and x_f 62

41.Well Structure of - 0077 68

42. Production Rate and Pressure Data of - 0077 70

43. Unified BU-RNP Processing of PTA Data of - 0077..... 71

44. Unified BU-RNP Processing of PDA Data of - 0077 71

45. Unified BU-RNP Virtual Drawdown of - 0077 72

46. Virtual Drawdown Matching of - 0077..... 73

47. Rate and Cumulative Production Matching of - 0077..... 74

48. RNP and RNP Derivative Plot of - 0077..... 75

49. 2D Map of SRV of - 0077..... 78

50. PTA Behavior Comparison: With Desorption vs. Without Desorption..... 91

51. Gas Adsorption Density Sensitivity Result - $p_L<p_i$ 95

52. Langmuir Pressure Sensitivity Result - $p_L<p_i$ 95

53. Gas Adsorption Density Sensitivity Result - $p_L>p_i$ 96

54. Langmuir Pressure Sensitivity Result - $p_L>p_i$ 96

55. Faster Pressure Investigation Caused by Smaller Gas Desorption..... 98

56. The Smaller Desorbed Gas Volume due to ρ_{ads} (or V_L) and p_L Changes 99

57. Gas Desorption Impact on PTA Behavior of Shale Gas wells..... 101

LIST OF TABLES

TABLE Page

1. Valko EUR Estimate Approach Parameters (Valko, 2009) 27

2. Flow Regime Identification Scheme by Normalized Rate Derivative Function. 38

3. Well, Reservoir and PVT Settings for Sensitivity Study 43

4. Model Settings for Sensitivity Study 44

5. Sensitivity Study Cases 44

6. Well, fluid and reservoir information of - 0077 68

7. Gas Adsorption Parameters for - 0077 69

8. Fracture Half Length and Fracturing Used Nitrogen Volume Records 69

9. Fracture Half Length Estimation for - 0077 69

10. Recovery Factor Calculation of - 0077 79

11. Gas Desorption Impact Comparison Test Design 90

12. Basic Design Settings-Gas Desorption Impact on Dual Porosity 94

13. Sensitivity Study Design 94

14. Summary of Gas Desorption Impact on Shale Gas (Vertical) Wells 96

CHAPTER 1. INTRODUCTION: BACKGROUND AND LITERATURE REVIEW

Chapter 1 is aimed to give a brief introduction of shale gas resources in United States as well as a particular gas shale play, the New Albany Shale, as a background. Besides, the literature review including several aspects, such as gas storage and transport mechanism of shale gas, pressure transient behavior of shale gas wells and production analysis of shale gas wells, are summed to provide guidance for the research in this thesis.

1.1 Shale Gas Resources in United States

Unconventional natural gas resources, which include shale gas, tight gas sands, coalbed methane and deep basin-centered gas system, play a significant role in today's gas supply in U.S and are an important source for gas production and gas reserve growth in the future. Gas shales, the formations which are considered as both source rocks and reservoirs, are supposed to contribute a lot to the future gas production. Traditionally shale formations were only thought as source rocks or cap rocks, but not reservoir rocks where hydrocarbons accumulate. However, the success of Barnett Shale has proved that gas can be produced from shale reservoirs economically and this revolutionary success led developments of many other shale gas reservoirs (J.Daniel Authr, Brian Bohm and Mark Layne, 2008). By 2008, the natural gas resource potential for gas shale in USA was estimated to be 500-1000 Tcf. Many shale gas plays have been found (Figure 1) in the contiguous United States (Cipolla *et al* 2009). Deregulation of natural gas prices,

improvement of stimulation techniques and horizontal drilling made the economic development of shale gas reservoirs possible (J.Daniel Authr, Brian Bohm and Mark Layne, 2008).

Typically, the shale gas reservoirs exhibit a net thickness varying from 50 ft to 600 ft. Porosity varies from 2% to 8% and total organic carbon (TOC) ranges from 1% to 14 %. The depth of shale gas reservoirs also varies apparently. A shallow depth can be 1000 ft while a deep one can be up to 13000 ft (Cipolla *et al* 2009). Gas is stored as free gas in the limited pore space of the rocks, such as micro-pores and natural micro-fractures, and a sizable fraction of the gas in place is stored as adsorbed gas which is adsorbed on the surface of matrix particles (Lane, Waston and Lancaster, 1989).

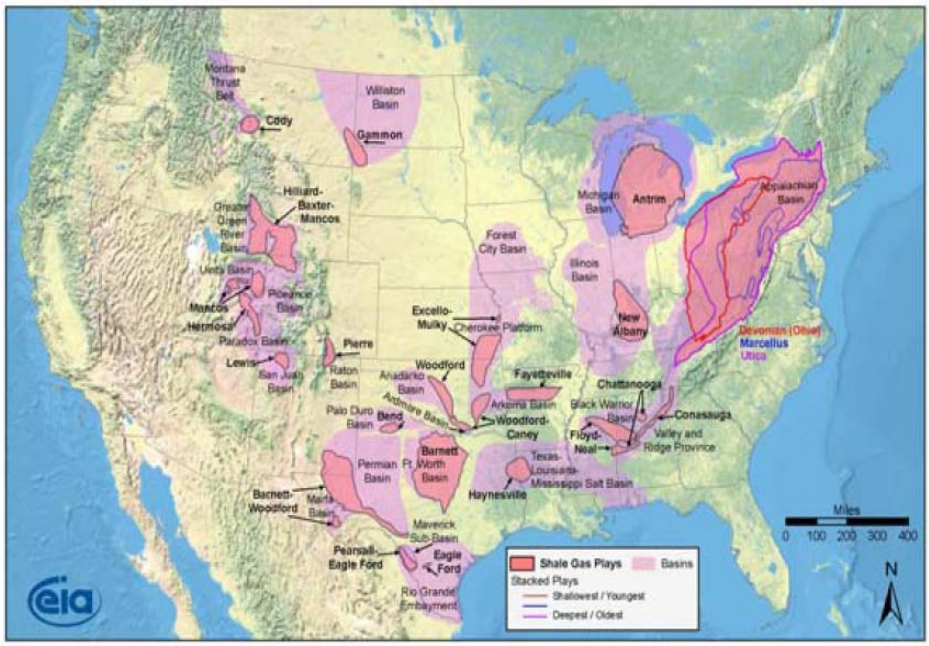


Figure 1. Gas Shale Plays in Lowe 48 United States

Unlike conventional natural gas resources, shale gas is more difficult to be produced due to extremely low effective permeability. Typically, shale permeability ranges from 10 to 100 nano-Darcy (10^{-5}-10^{-4} md) (Cipolla *et al* 2009). Though natural micro-fractures often occur in the shale formation, hydraulic fracture stimulation is still necessary to induce flow in most cases and today the strategy is to create a fracture network so that a huge reservoir surface can be effectively connected to the wellbore. However, unlike conventional hydraulic fracture treatments that use high viscosity fluids to reduce fracture complexity and promote planar fractures and allows the placement of high concentrations of large proppant, stimulation treatment in shale gas reservoirs may use low viscosity fluid to promote fracture complexity. The fracture treatment approach is totally different from conventional fracture treatment (Cipolla *et al* 2009).

In shale gas reservoirs, it is very common that water is produced with gas. Today, surface facilities designed to handle water production enable much better gas production rates (Dahaghi and Mohaghegh, 2009)

Shale gas reservoirs are typically comprised of two distinct porous media: the shale matrix containing the majority of gas storage in the formation but with a very low permeability and the fracture network with a higher permeability but low storage capacity. It is believed that in most cases shale gas is stored as “free gas” in both shale matrix and natural fracture system and as “adsorbed gas” on the surface of matrix particles. Since adsorption is considered as an unconventional mode of gas storage, its effect was usually ignored in conventional reservoir engineering analyses. However, even back to 1980’s, practical reports indicated that adsorbed gas might account for up

to over 80% of gas storage in some shale gas plays. Moreover, recent work indicates that gas desorption affects the production behavior and pressure transient behavior of gas wells significantly, particularly in the stimulated wells. Therefore, gas adsorption, which might and should be a very important gas storage mechanism, has been taken into account for modeling shale gas reservoir as shale gas exploration develops (Lane, Waston and Lancaster 1989).

The use of horizontal well drilling and multistage hydraulic fracturing appear to be key aspects for successful development of the shale gas resource. The horizontal well technology was adapted for shale gas development to provide increased wellbore exposure to the reservoir area while hydraulic fracturing, the other technology key for facilitating economical recovery of natural gas shale, is used to provide significantly more contact with reservoir which is needed because the permeability is very low. The combination of the two key aspect results in the typical well type applied in shale gas development, the multistage transverse fracture horizontal well, in which multi hydraulic fractures are produced normal to the horizontal well trajectory (Figure 2).

From a historic perspective, the shale gas development including the success of Barnett Shale has demonstrated the economic potential of shale gas through the use of horizontal well completions and hydraulic fracturing techniques. Barnett horizontal wells have laterals ranging from 1,500 to more than 5,000 feet and for these wells to be economically productive, they require hydraulic fracturing. Besides that, the development of the Marcesllus Shale has been made possible also based on the two technological advances. Although current development practices in the Marcellus shale

involve the drilling of both horizontal and vertical wells, hydraulic fractured horizontal wells are expected to become predominant for the play (J.Daniel Authr, Brian Bohm and Mark Layne, 2008). It is reasonable to believe that horizontal well completions combined with hydraulic fracturing will provide the best opportunity for producing economic volumes of natural gas from shale gas plays.

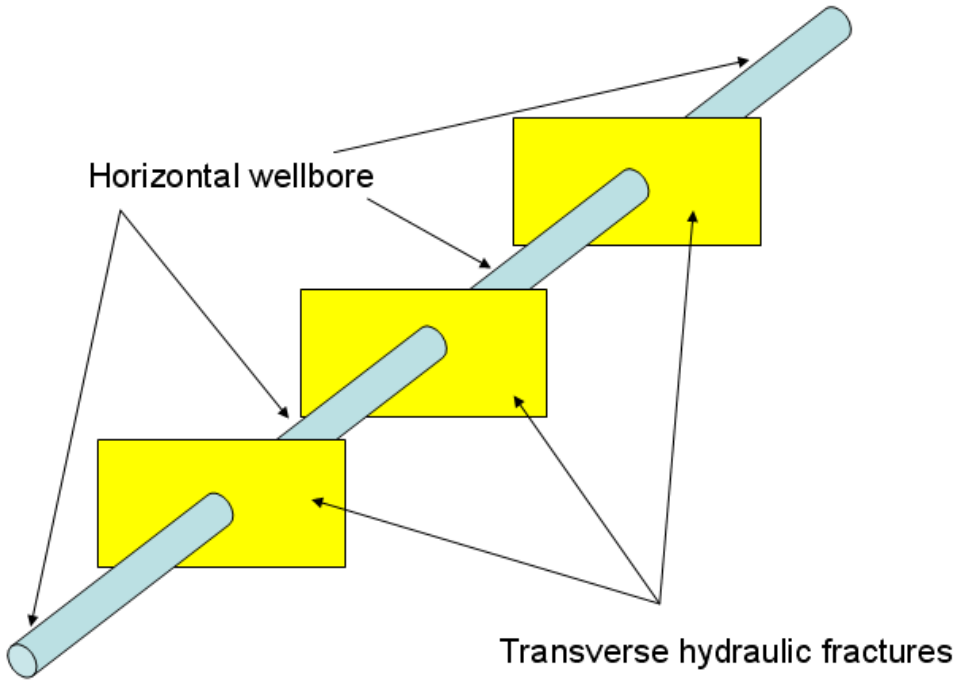


Figure 2. Illustration of Multistage Hydraulic Fracture Horizontal Well

1.2 Introduction of New Albany Shale Gas Play

The New Albany Shale is predominantly an organic-rich brownish-black and grayish-black shale, and is located over a large area in southern Indiana and Illinois and in Northern Kentucky (Figure 3). The shale is present in the subsurface throughout the

Illinois Basin (Zuber *et al* 2002). The total gas content of New Albany Shale has been estimated to be 86 TCF (Dahaghi and Mohaghegh 2009). The depth of shale appears at 500 ft to 2000 ft on average. The gross thickness of the organic shale varies form 100 ft to 150 ft, and is generally separated into 4 main stratigraphic intervals from top to bottom (Figure 4): Clegg Creek, Camp Run/Morgan Trail, Selmier and Blocher (Zuber *et al* 2002). Natural fractures occur in the shale formation and are believed to provide the effective permeability in these zones. The density of natural fractures is not very high, but this doesn't preclude the economic gas potential in New Albany Shale play (Dahaghi and Mohaghegh 2009).

New Albany Shale has been considered as a productive gas reservoir for many years. Over 200 wells had been drilled by the mid 1990s. Generally, gas production in New Albany Shale ranges from 30 to 100 Mscf/D and water production is very variable. Some wells made very little water while others made even more than 1000 B/D (Zuber *et al* 2002).

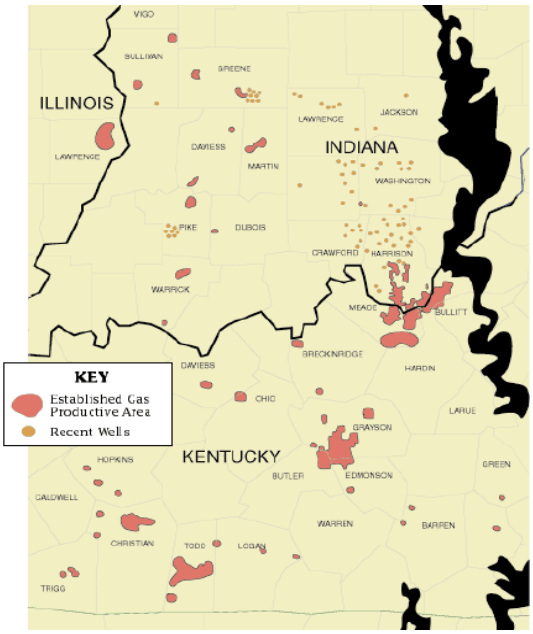


Figure 3. Productive Area of New Albany Shale

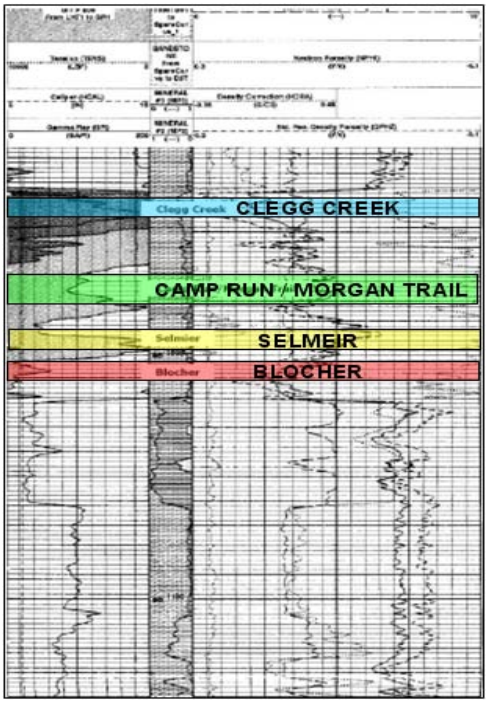


Figure 4. Stratigraphy of New Albany Shale

1.3 Literature Review

During the last tens of years, the industry has realized that the important role of gas adsorption, which makes shale gas and other unconventional gas resources such as coalbed methane different from the conventional gas resources. The storage and production mechanisms of gas in shale become a significant issue for both reserve estimation and production so that an appropriate conceptual model for shale gas reservoir is very necessary. Lane, Waston and Lancaster (1989) indicated that in shale reservoirs, gas is stored both as free gas in matrix pores and fractures and as adsorbed gas on the surface of matrix particles. Kuuskraa *et al* (1985) also indicated the importance of gas adsorption to gas recovery and behavior of shale gas wells through the investigation of Shale Gas in Ohio, West Virginia, and Kentucky. Zuber *et al* (2002) provided a conception model illustration in their paper for a comprehensive evaluation for New Albany Shale. “Triple porosity/Dual permeability Model”, which is a more detailed conceptual model including the consideration of both free gas and adsorbed gas was given by Schepers *et al* (2009). Besides those articles about gas shales, Rushing, Perogo and Blasingame (2008) provided a conceptual model for coalbed methane, which is considered to partially or totally share the same mechanism of gas storage and production with gas shales. For gas adsorption/desorption, the very important element in shale gas resources, Schepers *et al* (2009) and Lane, Lancaster and Waston (1990) indicated that Langmuir Model provides the best description. Moreover, it is also the most popular model for gas adsorption/desorption.

With the development of technology of horizontal well and hydraulic fracturing, economic production from gas shale is achieved. Though there is longitudinal and transverse fracturing for horizontal wells, almost all the recently reported fracturing application in the industry is the later option (Wei and Economides 2005) and multistage fractured horizontal wells are widely in use in shale gas development, such in the plays of Barnett Shale and Marcellus Shale (J.Daniel Authr, Brian Bohm and Mark Layne, 2008). Therefore, understanding the behavior multi-transverse-fractured horizontal well (MTFHW) is important to understand the well performance. The Flow regime issue of MTFHW was discussed several researchers: Clarkson *et al* (2009), Freeman *et al* (2009) and Al-Kobashi *et al* (2009) offered flow regimes analyses of MTFHW and a common conclusion emerges from their work: potential reservoir flow regimes appear in the sequence of linear flow normal to fracture face, then interference between fractures, then compound linear flow (linear flow normal to horizontal well axis), then pseudoradial flow around the MTFHW system (if possible), and then boundary flow (Not likely, but if present could be due to interference with adjacent similar well).

Production analysis for shale gas wells is challenging. Ilk *et al* (2008) used to develop an empirical formulation, the “Power-Law Exponential” rate decline model to perform production analysis and estimate gas-in-place/reserves for unconventional gas reservoirs. Valko (2009) developed a new decline curve model, which is both empirical and mechanical but not analytical to estimate the estimated ultimate recovery for individual well via calculating recovery potential. This approach is based on the analyses of over 7,000 gas wells in Barnett Shale and it is more direct than the former one.

The above introduction provides a general understanding of shale gas, the significant resource in today's American oil and natural gas industry. New Albany Shale is also briefly described because it is the target case on which the research work in this thesis focuses. The literature review referring to conceptual model issue, PTA issue and PA issue establishes a basis based on which the further research can be performed. The following chapters will focus on an appropriate conceptual model for the shale gas reservoir (Chapter 2), rate decline analysis for New Albany Shale Gag Wells (Chapter 3), drawdown pressure transient behavior in Multi-transverse fractured horizontal wells (MTFHWs) (Chapter 4) and the particular field case study of New Albany Shale (Chapter 5), and all the further research work described in the following chapters benefits from the previous achievements.

CHAPTER 2. CONCEPTUAL MODEL FOR SHALE GAS

Before a play is developed, it is essential to understand how mechanisms of fluid storage and transport in the reservoir affects reserves, well behavior, production performance, and even the ultimate recovery. An appropriate conceptual model can help estimate reserves and the recovery factor more accurately and forecast the well behavior and performance. Chapter 2 is aimed to describe the “Triple porosity/Dual permeability” model, and how it explains gas storage and transport mechanisms in shale gas formations.

2.1 Gas Storage Mechanism

Gas in shales is stored in two ways: free gas and adsorbed gas. The former is stored both in micro-pore space in the matrix and natural fractures in shales, and the later is stored on the surface of shale matrix particle by adsorption.

Free gas is a relative conception compared with adsorbed gas. It is essentially like the gas in conventional gas reservoirs in which pore space (or with fractures) provides the storage space. In shale gas reservoirs, natural fractures and micro-pores inside the matrix provide the storage for free gas. Therefore free gas is stored in a dual-porosity system which is like what we use for describing conventional natural fracture reservoirs. Matrix pores provide a relatively higher storage capacity than natural fractures due to their astronomically large amount though individual pore is very small and lower permeability than natural fractures due to their extremely small dimension and more complex connection.

Adsorbed gas, which might account for a big part of gas storage in gas shales, is stored by a different physical mechanism. Adsorption is the mechanism which makes this gas bound on the surface of matrix particles. A “Triple porosity” Model is appropriate to describe the gas storage mechanism (Figure 5) because it includes both the free gas and adsorbed gas. Briefly speaking, triple porosity is dual porosity system combined with gas adsorption. The reason for “Triple” is that free gas is stored in dual porosity system comprised of the matrix micro-pores (the first porosity) and natural fractures (the second porosity) and gas adsorption is considered as the third porosity though in reality the storage space is not pores or fractures but the particle surface. More will be said about gas adsorption and desorption in Section 2.3.

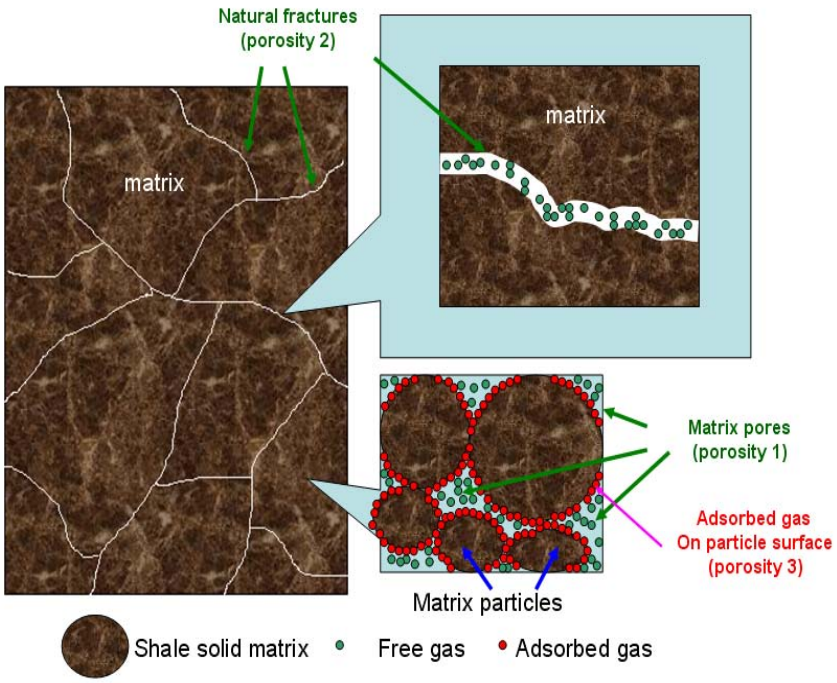


Figure 5. Triple Porosity Storage Model in Gas Shales

2.2 Gas Transport Mechanism

Schepers *et al* (2009) used to provide a conceptual model for gas shales. Apart from the similar storage consideration (dual porosity combined with gas adsorption) to other researchers, this model claims some different views of the gas flow mechanism. Figure 6 illustrates the model provided by Schepers *et al*. According to the lower part of Figure 6, two points should be highlighted: First, Schepers *et al* didn't indicate the adsorption gas will diffuse into fracture system as well when it diffuses into matrix pore system; Second, the fluid flow within matrix micro-pore system and the flow from matrix micro-pore system to fracture system is following Darcy-Flow rule which means the transport mechanism is the flow in porous media due to pressure gradient.

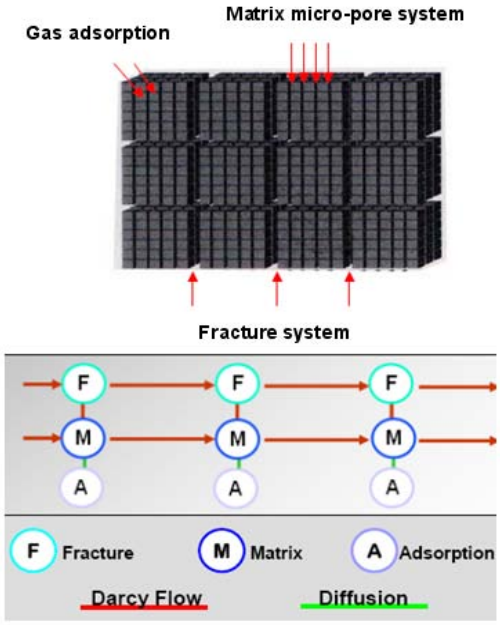


Figure 6. Conceptual Model for Gas Shales (Modified from Schepers *et al* 2009)

The “Triple porosity/Dual permeability Model” given by Schepers *et al* is an appropriate description for gas shales. However, due to the two emphasized points mentioned above, some considerations aren’t included in this model. A modified “Triple porosity/Dual permeability Mode” is provided in this thesis based on the Schepers’ great contribution to the conceptual description for gas shales. Considering the first highlighted point, it appears that adsorbed gas will also be released into the fracture system as well as into matrix pore system. Matrix solid particle surface is not only exposed to the matrix pores, but also exposed to fracture space. Though compared to the area of matrix particle surface exposed to matrix pores, that area of particles surface exposed to fractures is much smaller, its existence should not be ignored since the fact is factures are the space surrounded by the matrix. The second point is essentially about transport mechanism inside matrix pore system and from matrix to fractures. Schepers’ model indicates definitely it is a porous medium flow that controls the gas transport. Zuber *et al* (2002) also indicated the same view in their paper about New Albany Shale (Figure 7).

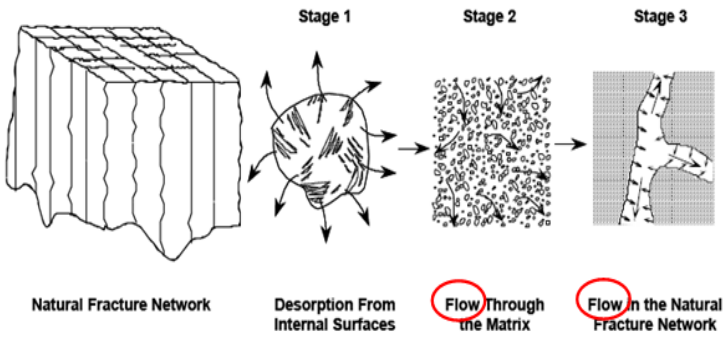


Figure 7. Conceptual Model for Gas storage and Transport (Zuber *et al* 2008)

Wang and Reed (2009) discussed this more specifically: Two main types of porous media are included in gas shales, pores and fractures. The former can be subdivided into two types as nonorganic pores and organic pores, and the later contains subtypes as natural fractures and hydraulically induced fractures. Pores formed by organic substance (organic pores) inside matrix is believed to act as a porous medium even though more detailed mechanism of gas flow through organic matters is speculative. All above, the matrix micro-system is considered as a porous media according to those researchers though common sense of shale matrix's low permeability may lead people to negate this.

However, not all agree that the matrix pore system acts like a porous medium. Rushing *et al* (2008) indicated in describing their description coalbed methane model that gas transport in matrix pore space is due to diffusion resulting from a concentration gradient (Figure 8) because the permeability is too low to activate Darcy-flow. This indirectly denies the view of porous medium. However, whether this description is also suitable for shale gas is questionable because though coalbed methane shares many aspects in common with gas shales, they are not the same.

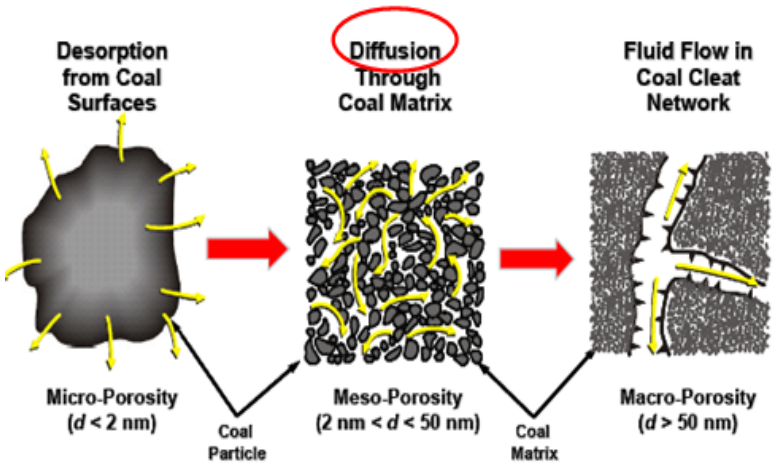


Figure 8. Stage Gas Production Process in Coalbed Methane (Rushing *et al* 2008)

Even the industry contains both the two opinions. In the commercial software "Ecrin" developed by Kappa Engineering, the reservoir model also contains two options, two porosity model and homogeneous-diffusion model for gas shales and coalbed methane. However, it is not possible to model simultaneously diffusivity and double porosity in our current implementation in Ecrin.

This analysis in this thesis assumes that the mechanism of gas flow through matrix pore system is flow in porous medium. There is not sufficient evidence to prove absolutely absence of diffusion through shale matrix and even Schepers himself stated the release and transport mechanisms are characterized by desorption, diffusion and Darcy-flow (though the diffusion is likely to occur in individual matrix pore after desorption according to Figure 6). However, flow in the porous medium is still believed to be the dominate mechanism even if diffusion does exist at the same time. This is not only because of its application in simulation work, as shown by Schepers *et al* (2009) ,

but also because of the research in more microscopic mechanics, as described by Wang and Reed (2009). In general, the concept diffusion through matrix was described based on coalbed methane and not shale gas. The gas transport mechanism through matrix in coalbed methane might be really different from that in gas shales.

To solve the above two highlighted points, a more accurate and integrate mechanism of shale gas transport can be described by flow chart shown as Figure 9.

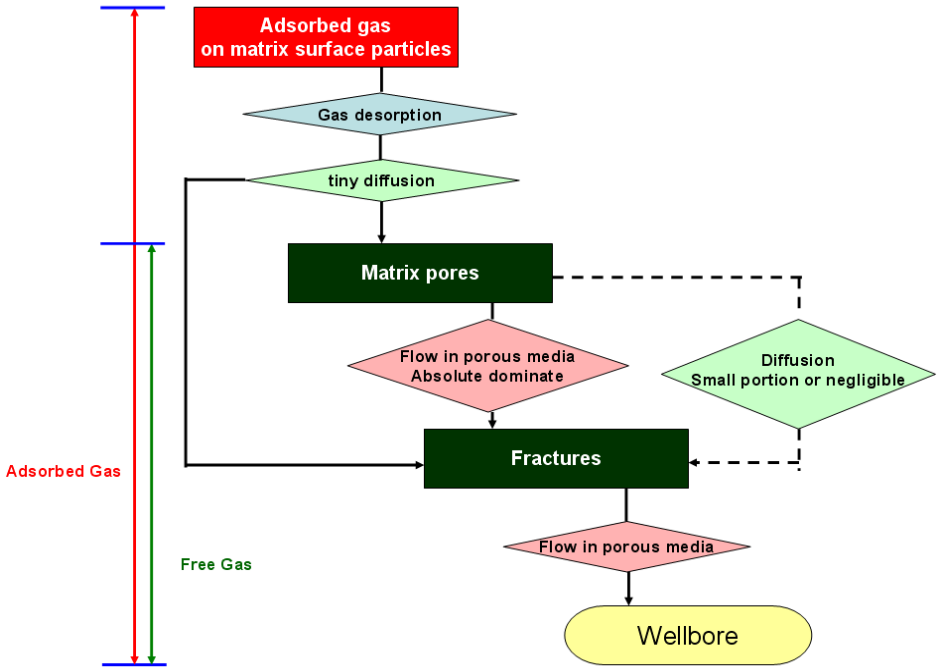


Figure 9. Gas Transport Mechanism in Gas Shales

The transport process can be described in this way: free gas will flow through matrix pores (primary porosity) into the fracture system (secondary porosity) due to pressure gradient, driven by a mechanism of fluid flow in porous media (diffusion might exist but

can be neglected); then free gas will flow to the wellbore through fractures. For adsorbed gas, desorption will occur when pore pressure decreases, and adsorbed gas molecules have the potential to move and diffuse to the pore space from particle surfaces. The duration of the diffusion (diffusion time) happening in such small pores which are usually in micro scale is considered to be negligible. After that, the adsorbed gas essentially becomes free gas and the future transport will follow the same way with the original free gas, and the mechanisms of flowing through matrix pore system and fracture system is also the same.

By now, a more appropriate conceptual model for gas shales has been described. The meaning of “Triple Porosity/Dual Permeability” in gas shales is that matrix pores, fractures and gas adsorption are the three effective porosities for storage while matrix pores and fractures are the two permeable porous media through which gas flows. Understanding the essence of the model is the basis for future research in pressure transient behavior and production performance of shale gas wells. Figure 10 provides a clear illustration.

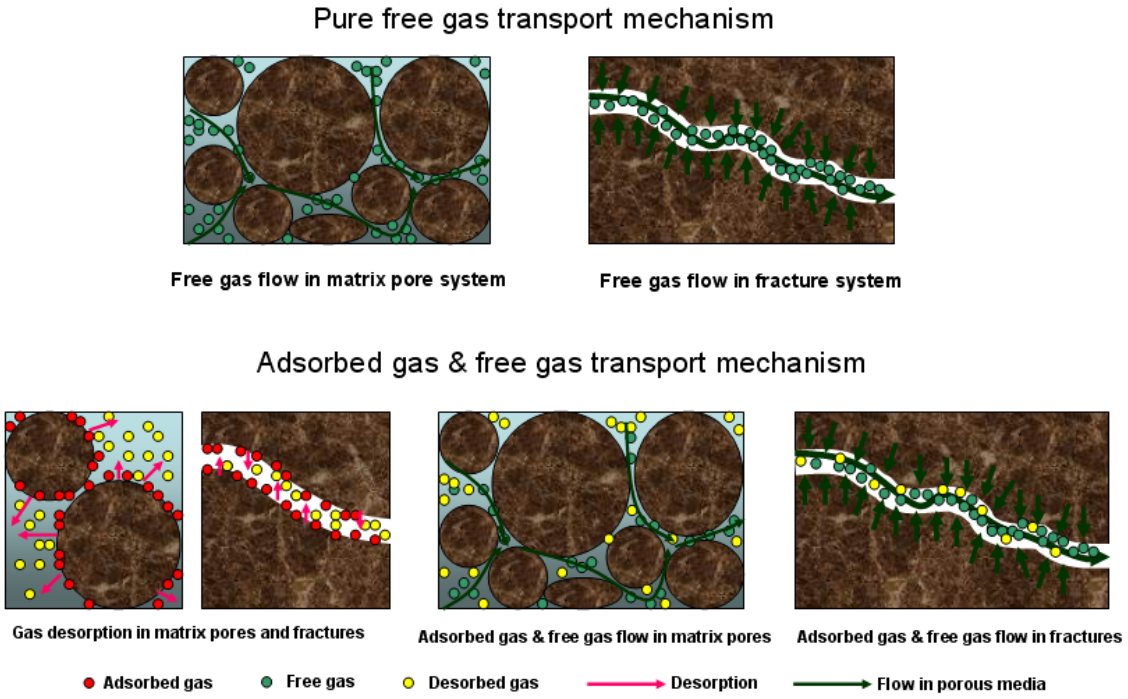


Figure 10. Illustration of Gas Transport Mechanism in Gas Shales

2.3 Gas Adsorption/Desorption Model

Gas adsorption is a surface phenomenon and is predominately a physical bond caused by the inter-molecular attractive forces (i.e., Van der Waals forces) (Rushing *et al* 2008) while desorption is the converse process of adsorption.

The Langmuir Model is the most commonly used models for quantifying the description of gas adsorption/desorption. The mathematic expression of this model is:

$$V_{ads} = \frac{V_L p}{p_L + p} \quad \text{..... (1)}$$

Where:

V_{ads}, [scf/ton], the gas volume can be adsorbed by a rock of unit mass;

V_L, [scf], Langmuir volume, the maximum gas volume can be adsorbed;

p_L, [psi], Langmuir pressure, at which half of Langmuir volume gas can be adsorbed;

p, [psi], random pressure

This model assumes there is no change in temperature. Actually, temperature will affect the gas adsorption capacity, and specifically, the higher the temperature the less gas can be adsorbed. In the Langmuir formula, temperature is not considered because of an assumption that temperature does not change for the problem under consideration. That is the reason why the plot of the Langmuir formula is called a "Sorption Isotherm". This assumption is reasonable is because reservoir flow processes are assumed to be isothermal. A typical sorption isotherm curve is illustrated as Figure 11.

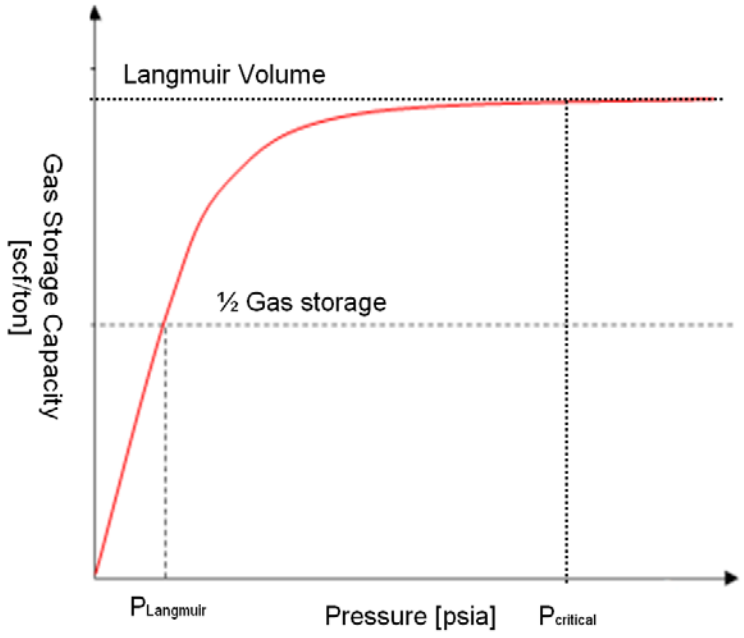


Figure 11. Illustration of Typical Gas Adsorption/Desorption Isotherm

For a fixed temperature, the Langmuir volume and Langmuir pressure control the shape of sorption isotherm. For any pressure, the quantity of adsorbed gas can be calculated. There is only one discrepancy between the mathematic and physical description of the adsorption/desorption process. From a theoretical prospective, as pressure trends to infinity, gas storage capacity is going to be infinitely close to Langmuir volume but it can never reach the Langmuir volume value theoretically. In reality, the adsorbed gas starts to be desorbed when pressure decreases from some high level to a point called the "critical pressure". Below the critical pressure the desorption process will follow the Langmuir model precisely. The small discrepancy doesn't deny the reasonability of Langmuir model because usually, the gas adsorption capacity difference between infinitely high pressure and critical pressure is so small that it can be negligible. Therefore, Langmuir model accounts for the essential gas adsorption/desorption behavior.

Besides the mathematic expression (Eq 1), Langmuir model can be expressed by some equivalent expressions. Another popular expression is as following:

$$\theta = \frac{p}{p_L + p} \quad \text{..... (2);}$$

Where,

p_L, [psi], Langmuir pressure, at which half of Langmuir volume gas can be adsorbed;

p, [psi], random pressure;

θ, [dimensionless], coverage fraction of the surface, essentially V_{ads} / V_L

$\theta \in [0,1]$.

Another issue about gas desorption is desorption time. In some circumstances, as the pressure decrease, adsorbed gas molecules are expected to be desorbed from the matrix particle surface. However, even when the pressure condition allows the occurrence of gas desorption, it might be delayed in time. The time interval between the time when pressure drops to the level for desorption and that when desorption really take place is termed desorption time. However, for convenience, assumption of instantaneous desorption is usually made.

The commercial software Kappa Ecrin uses the Langmuir model to describe the gas desorption in the shale gas model. The parameters controlling gas desorption in the model parameter input dialog window (Figure 12) include Langmuir pressure and adsorption density. As described above, it is Langmuir pressure and Langmuir volume that controls the gas desorption behavior. The later terminology called “adsorption density” could lead to some confusion.

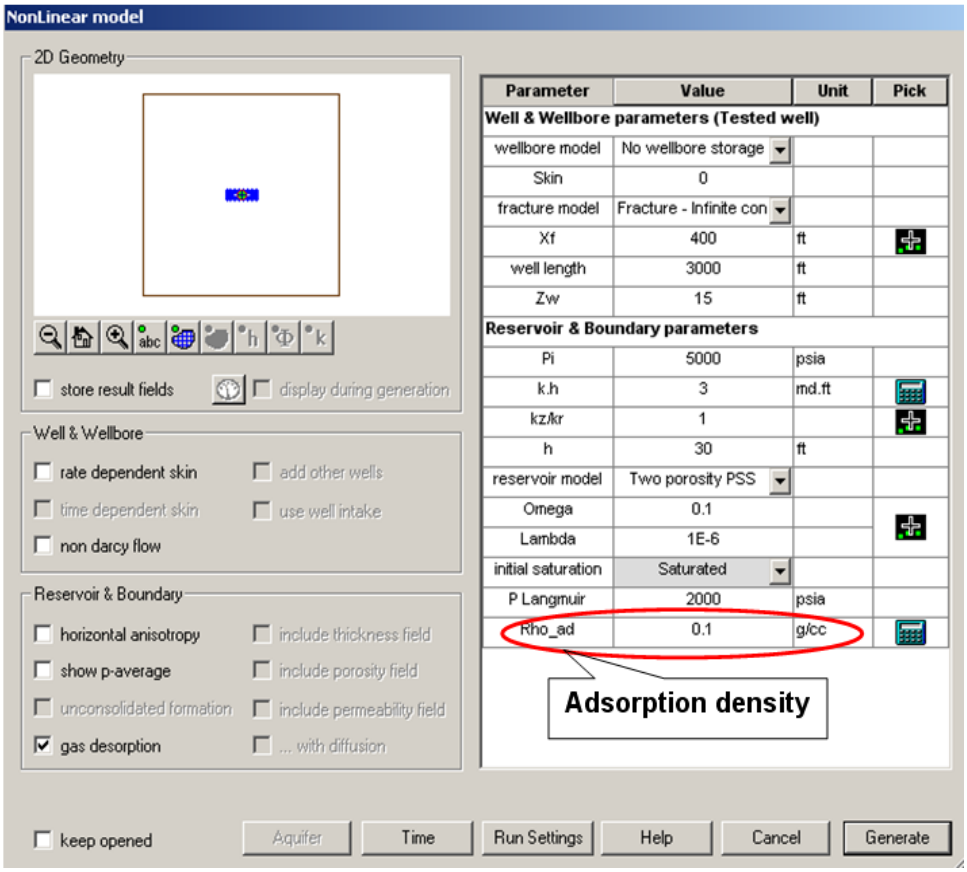


Figure 12. Model Parameter Input Dialog Window of Kappa Ecrin

The adsorption density (noted as ρ_{ads} in Ecrin) is easily related to the Langmuir Volume. Adsorption density is the product of Langmuir volume, adsorbed gas surface density and rock density:

$$\rho_{ads} = \rho_{rock}\rho_{gas}^{surf}V_L \quad \text{..... (3)}$$

Where,

ρ_{ads}, [g/cc], adsorption density;

ρ_{rock}, [g/cc], rock density;

ρ_{gas}^{surf} , [g/cc], adsorbed gas density;

V_L, [cc/g], Langmuir volume;

Gas adsorption density is not a real density but only holds a dimension of density, mass over volume. Usually, Langmuir volume tells the maximum amount of gas that can be adsorbed in terms of the gas volume per unit rock mass. Adsorption density is just converting the Langmuir volume to the gas mass per unit rock volume. The product of Langmuir volume and rock density gives gas volume per unit rock volume, and further multiplying the product by adsorbed gas density gives the gas mass per unit rock volume with a unit of density. The adsorption density is just an equivalent way of expressing Langmuir volume. The only inconvenient issue is the unit conversion. Langmuir volume is usually told with the unit of Standard Cubic Feet per Ton, so the equivalent calculation is:

$$\rho_{ads}[g/cc] = 0.3048^3 \times \rho_{rock}[g/cc]\rho_{gas}^{surf}[g/cc]V_L[SCF/TON] \quad \text{..... (4)}$$

If inputting Langmuir volume and rock density is preferred, the Langmuir volume can be converted into grams per cubic centimeter. Figure 13 shows the dialog window (inside the red circle) for inputting them separately. Adsorption gas density is automatically computed by the software according the input PVT data.

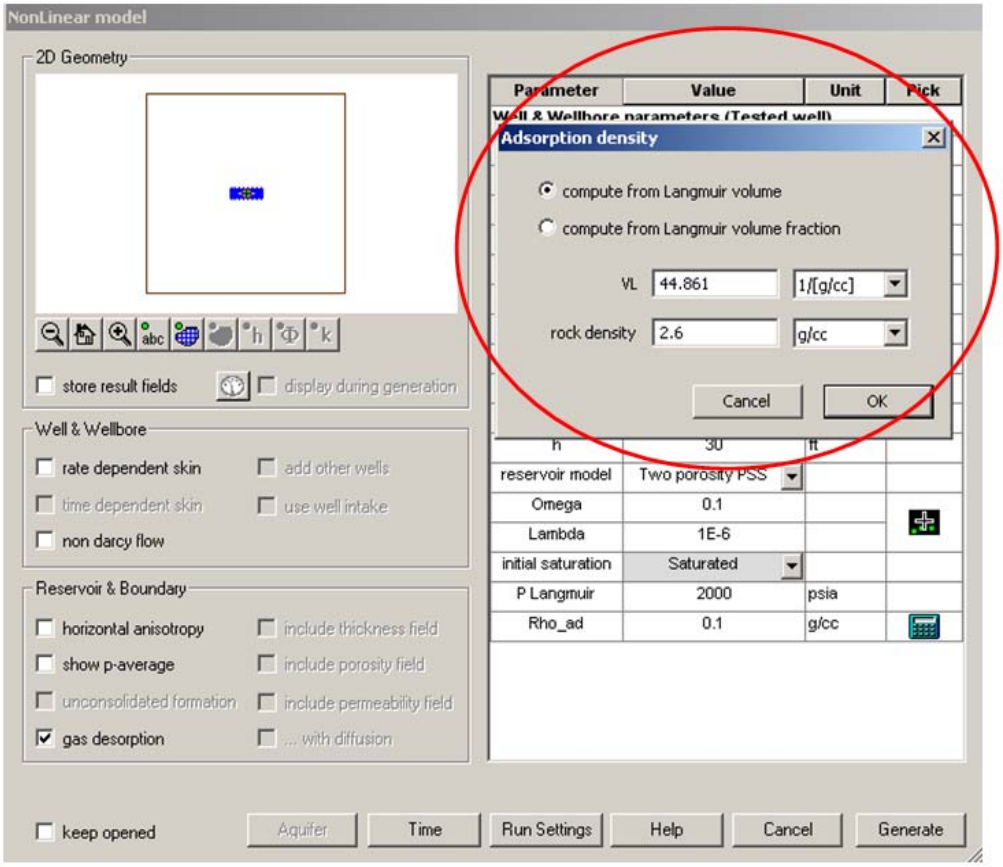


Figure 13. Dialog Window for Inputting Langmuir Parameters in Kappa Ecrin

The Ecrin model assumes instantaneous desorption, and when the adsorption option is selected in the shale gas model, there is no option to enter desorption time in the parameter input dialog window.

This chapter described a conceptual model appropriate for shale gas, and specifically and how gas is stored and flowing. The following chapter will introduce a methodology (Valko 2009) for determining estimated ultimate recovery to shale gas wells and will show EUR estimates for New Albany shale gas wells.

CHAPTER 3. RATE DECLINE ANALYSIS FOR NEW ALBANY SHALE GAS WELLS

Production rate data of 33 New Albany Shale gas wells can be used to analyze rate decline behavior of those wells in order to estimate the estimated ultimate recovery. Though other approaches exist for analyzing the rate decline and estimated ultimate recovery (EUR) of wells in gas shales and other unconventional reservoirs, this chapter will apply only the Valko (2009) technique.

3.1 EUR Determination from Rate Decline Analysis

Valko (2009) developed an empirical and mechanical approach for EUR estimation based on the research in production history of 7000 plus wells in Barnett Shale, and the application only requires production rate data.

Eq 5 shows the mathematic expression of the model and Table 1 shows the meaning of each term in this equation.

$$rp = 1 - \frac{Q}{EUR} = 1 - \frac{Q_D}{EUR_D} = \frac{1}{\Gamma(\frac{1}{n})}\Gamma[\frac{1}{n}, -\ln q_D] \quad \text{(5)}$$

This is a simple equation combined by two Gamma functions. For each rate data point, we can calculate its recovery potential by assigning a value to *n* parameter. Though the derivation of this model includes another model parameter τ, substituting expressions for q_D, Q_D and EUR_D from Table 1 can make calculation of recovery factor without τ.

Table 1. Valko EUR Estimate Approach Parameters (Valko, 2009)

Variable	*Expression*	*Remark*
t	Period, dimensionless (in case of monthly data, the number of months)	
q	Produced gas in period (eg. mscf/month)	
q_i	Model parameter, maximum (or initial) production rate	
n	Model parameter, dimensionless	
τ	Model parameter, dimensionless, 'characteristic number of periods'	
Q	$\int_0^t q\,dt$	Cumulative production
EUR	$\int_0^\infty q\,dt$	Estimated Ultimate Recovery
rp	$1-\frac{Q}{EUR}$	Recovery potential
q_D	$\frac{q}{q_i}$	Dimensionless production rate
Q_D	$\frac{Q}{q_i}$	Dimensionless cumulative production
EUR_D	$\frac{EUR}{q_i}$	Dimensionless EUR
$\frac{dq}{dt}$	$-n\left(\frac{t}{\tau}\right)^n\frac{q}{t}$	Defining differential equation of the model
q	$q_i \exp\left[-\left(\frac{t}{\tau}\right)^n\right]$	Rate expression as function of time
q_D	$\exp\left[-\left(\frac{t}{\tau}\right)^n\right]$	Dimensionless rate expression
Q_D	$\frac{\tau}{n}\left\{\Gamma\left[\frac{1}{n}\right]-\Gamma\left[\frac{1}{n},\left(\frac{t}{\tau}\right)^n\right]\right\}$	Dimensionless cumulative production expression
EUR_D	$\frac{\tau}{n}\Gamma\left[\frac{1}{n}\right]$	Dimensionless EUR expression
rp	$\frac{1}{\Gamma\left[\frac{1}{n}\right]}\Gamma\left[\frac{1}{n},-\ln q_D\right]$	Recovery potential calculated from dimensionless rate

For analyzing production data, following procedure is suggested:

1) Prepare a data series consisting of q_D and Q_D.

2) Assuming a parameter n, calculate recovery potential from Eq 5.

3) Plot of rp versus Q_D. The series should appear as a straight line, as it can be easily proven by substituting the expressions of q_D and Q_D into Eq 5.

The two intercepts of the straight line are (theoretically):

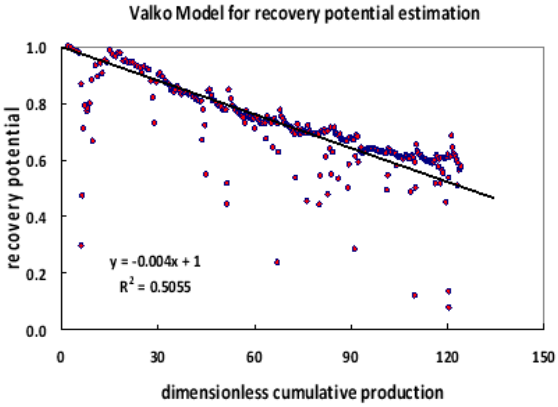
y-intercept =1

x-intercept = EUR_D

4) The estimated ultimate recovery can be obtained as the x-intercept of the straight line.

5) The actual y–intercept can be compared to the theoretical value (that is unity). If the y–intercept is not equal to 1, the parameter n should be adjusted.

Figure 14 shows the application of the above producer for New Albany shale gas well - 0077. By assigning a random value for the n parameter, we can calculate the recovery potential for each data point, and plot recovery potential versus the corresponding dimensionless cumulative production. The n parameter is adjusted until we get all the points to lie on a straight line with unit y-intercept. For - 0077, n=0.57 is the value that best satisfied these criteria. Then the dimensionless EUR is determined from as the x-intercept, 250 (not shown in the graph). Ultimately, $EUR = EUR_D \times q_i$ =123750MSCF.



parameters	values
Well #	DPI-2477
Initial rate, mscf/d	531
Optimal n	0.57
Slope absolute value	0.004
Maximum Square-R	0.5055
X-intercept	250
EUR , mscf	132750

Figure 14.EUR Estimation of - 0077 by Valko Approach

3.2 EUR Estimates for New Albany Shale Gas Wells

We applied Valko Approach to 33 wells in New Albany Shale gas wells. EUR estimation result is shown in Figure 15.

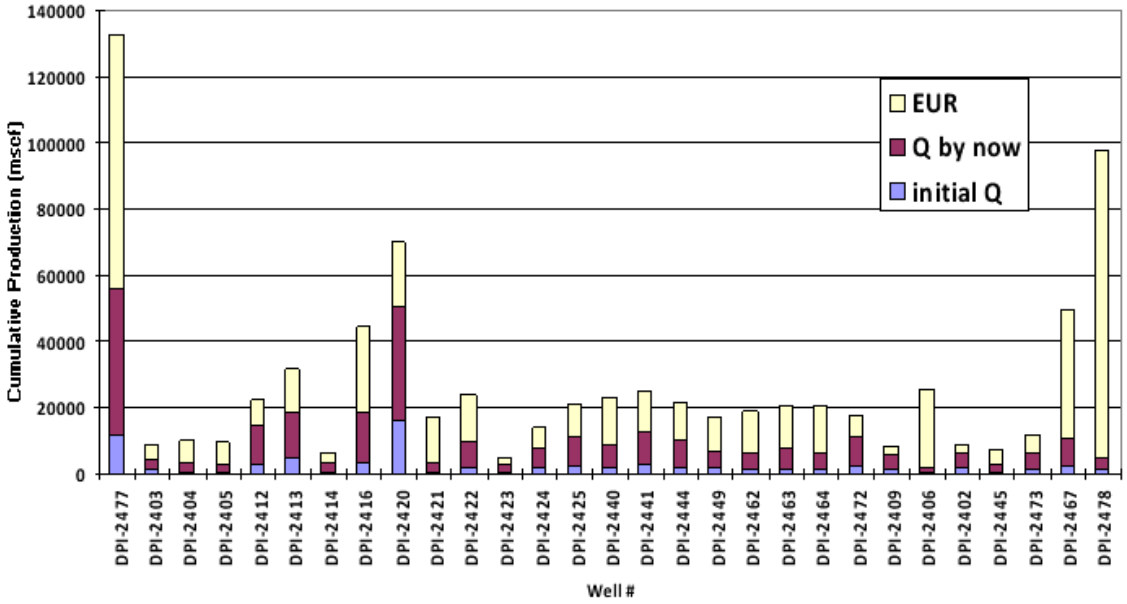


Figure 15. EUR Estimation of 33 Wells in New Albany Shale

From the EUR estimates of these 33 wells, we find though the EUR varies considerably from well to well, and some of the wells still have considerable recovery potential. - 0077 and - 0078 are multi-fracture horizontal wells, and they indicate much higher recovery potential, as might be expected because the fractures provide much more contact with the shale.

The next chapter investigates the relationship between reservoir contact and long term production.

CHAPTER 4. Drawdown Pressure Transient Behavior in Multi-Transverse Fractured Horizontal wells (MTFHWs)

This Chapter will focus on the drawdown PTA behavior of horizontal wells with multiple transverse fractures. The reason why this special well type is now widely used in shale gas development will be explained. Some previous model for MTFHWs will also be described. We will explain the rationale of using long term drawdown model behavior to reveal more information from production data. We will explain two methods for analysis of long-term production data: Rate-Normalized Pressure (RNP) Analysis and unified BU-RNP analysis. A sensitivity study helps illustrate long-term drawdown behavior of MTFHW in shale gas reservoir, and flow regime behavior will be discussed. Additionally, we will also shed light on the impact of gas desorption on the long-term drawdown behavior of the MTFHW. We will emphasize the implications of the early linear flow regime that are fundamentally important to shale gas well design.

4.1 MTFHWs in Shale Gas Reservoirs

The success of development of gas shales is dependent on recent technological advances in two key technologies: horizontal drilling and hydraulic fracturing (J.Daniel Authr, Brian Bohm and Mark Layne, 2008). The combination of these two technologies realizes the economic gas production in gas shales. However, the importance of horizontal drilling and hydraulic fracturing was not learned in just one day.

The first commercial oil well was drilled in Ignacy Lukasiewicz, Poland in 1953 and the first oil well in United States, which is known as the famous “Drake Well” was

drilled at Titusville, Pennsylvania after 6 years. As the petroleum industry developed, hydraulic fracturing was applied during 1940's. Hydraulic fracturing for stimulation of oil and natural gas wells was first used in the United States in 1947 and first used commercially in 1949. Because of its success in increasing production it was quickly adopted, and is now used worldwide in tens of thousands of oil and natural gas wells annually.

The first recorded true horizontal well, drilled near Texon, Texas, was completed in 1929. During 1980's decade, horizontal drilling technology brought a revolution to petroleum industry. Soon that horizontal drilling has become a standard industry practice (J.Daniel Authr, Brian Bohm and Mark Layne, 2008).

Since the inception of fracturing of horizontal wells in late 1980's, several field cases , for example, Lost hills Diatomite in California, upper Behariyia reservoir in Egypt and gas production in Australia, have been reported (Wei and Economides 2005). Two limiting cases exist in usual fracturing horizontal well: the longitudinal and the transverse (Figure 16). The former case means the well is drilled along the expected fracture trajectory while the later means the well and fracture face are perpendicular to each other. However, the industry reports of application of horizontal well fracturing indicated transverse case dominates (Wei and Economides 2005).

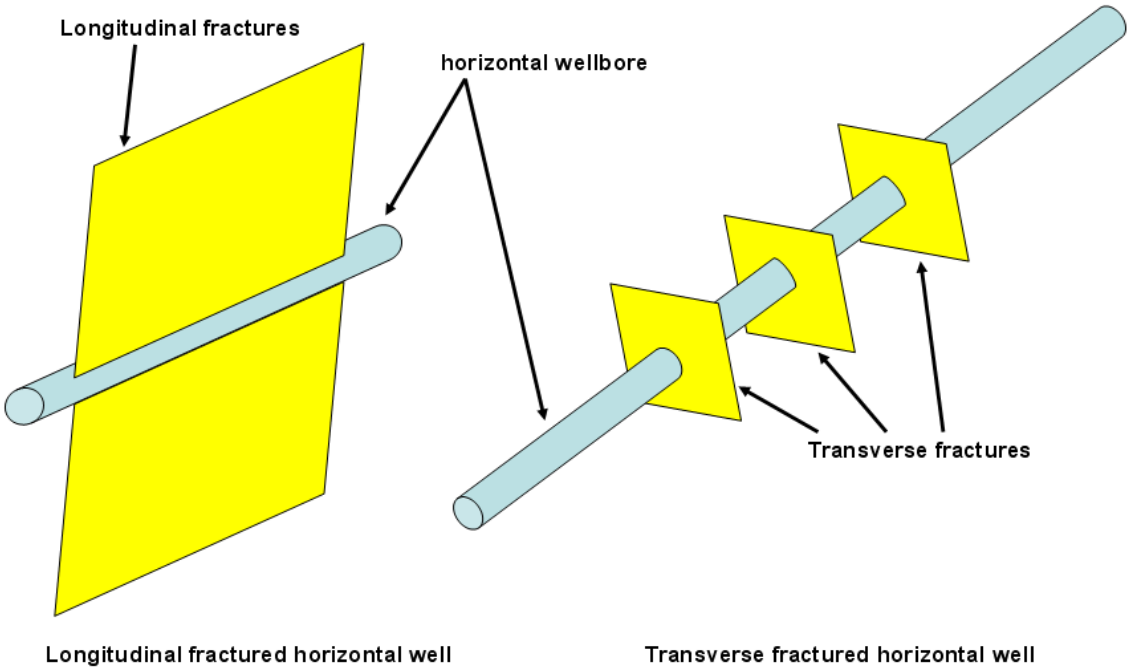


Figure 16. Illustration of Longitudinal and Transverse Fractures in Horizontal Wells

Horizontal wells with multiple transverse hydraulic fractures are believed to be the strategy for economic gas production in shale gas plays. The industry prefers MTFHWs because they can optimize the contact between the reservoir and the wellbore. The multi-stage fracture treatments in horizontal wellbores create a large stimulated reservoir volume (SRV) that increases both production and estimated ultimate recovery (EUR) (Meyer *et al* 2010).

4.2 Previous Models for MTFHWs

Freeman *et al* (2009) developed a numerical model to study the performance of MTFHWs in tight gas and shale gas reservoir system. This numerical model takes gas desorption into account and applies finite-conductivity fracture model. Simulation results reveal the reservoir flow regimes by pressure profiles shown as Figure 17, 18 and 19 in order.

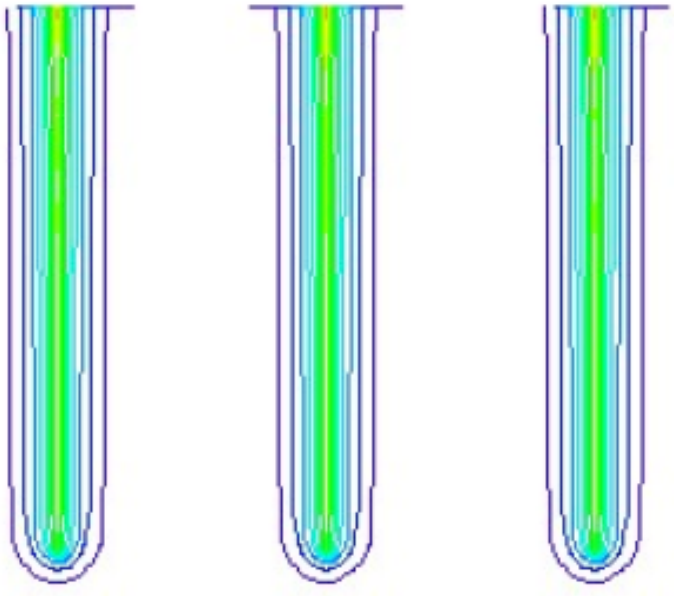


Figure 17. Pressure Profile: Half Reservoir, Linear Flow Normal to Fractures (Modified From Freeman *et al* 2009)

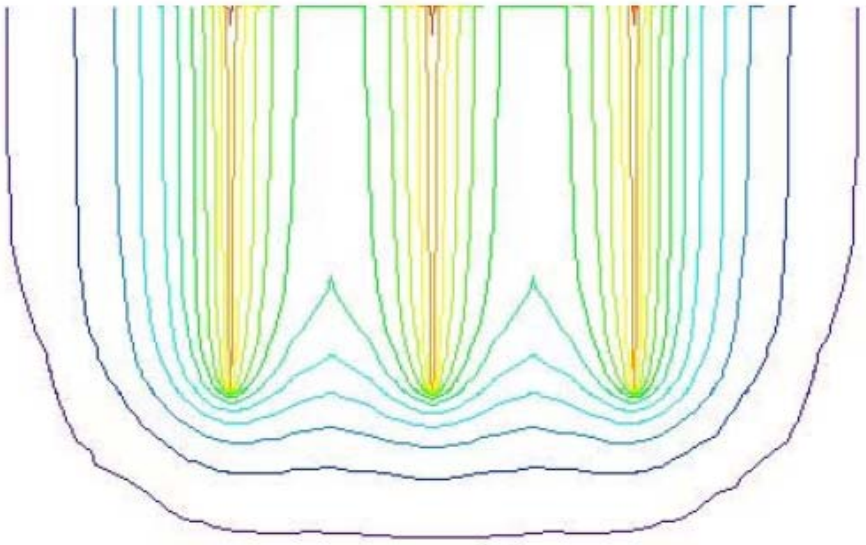


Figure 18.Pressure Profile: Half Reservoir, Compound Linear Flow

(Modified From Freeman *et al* 2009)

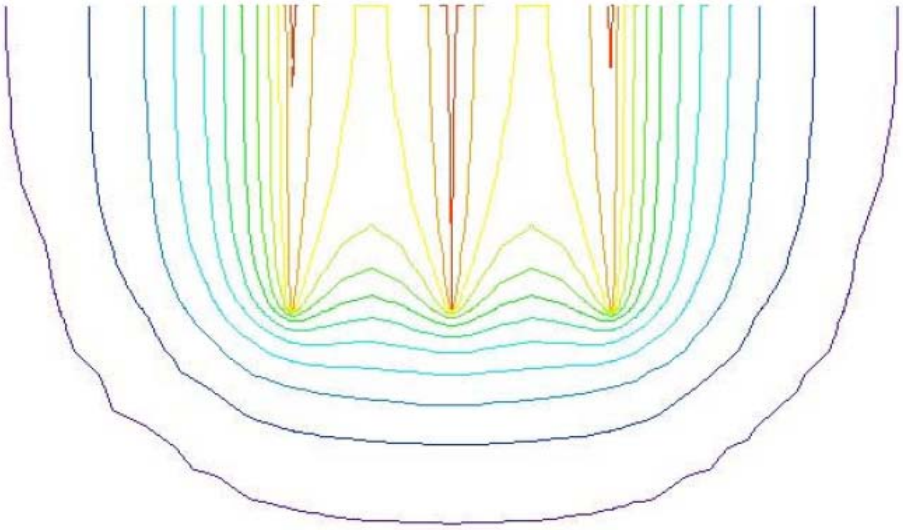


Figure 19.Pressure Profile: Half Reservoir, Elliptical Flow

(Modified From Freeman *et al* 2009)

Also, Freeman *et al* (2009) also plotted the normalize rate derivative function respect to square root of time versus time for both infinite reservoir case and finite reservoir case to reveal the flow regimes (Figure 20). The normalized rate derivative function (square root of time basis) is defined as Eq (6):

$$\frac{d(1/q)}{d\sqrt{t}} \quad \text{..... (6)}$$

(Note: this definition should be under the precondition that production is performed with constant well bottom pressure)

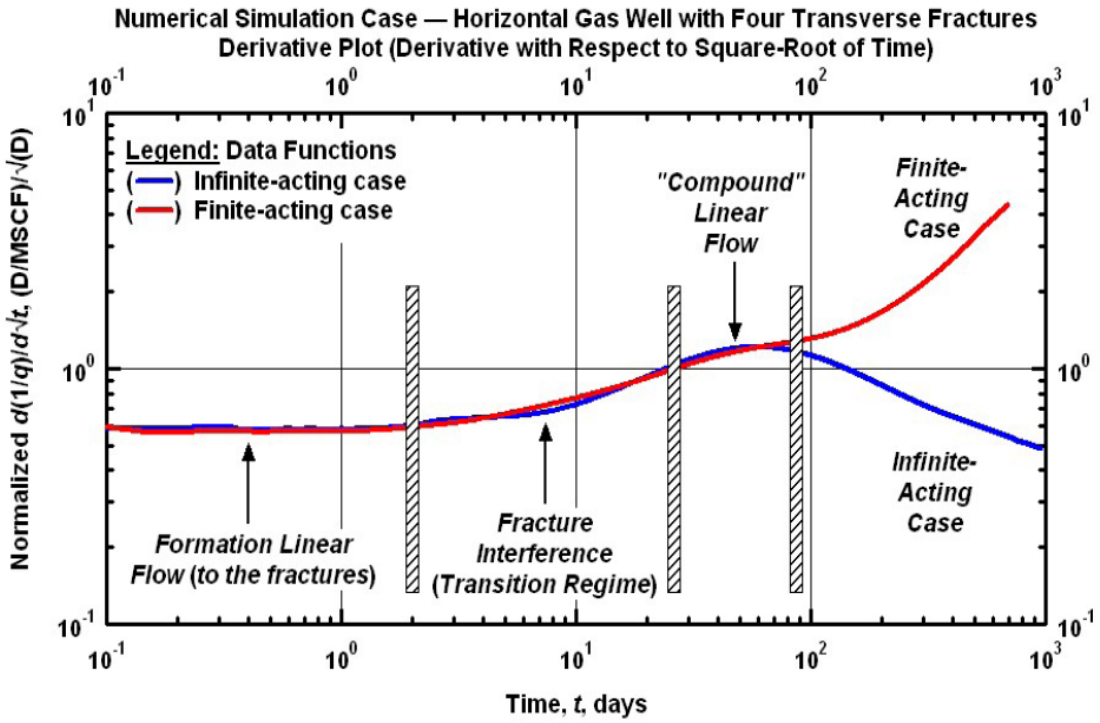


Figure 20. Boundary & Fracture Interference on Normalized Rate Derivative Function (Freeman *et al* 2009)

Al-Kobaisi *et al* (2006) also established an analytical model to study the pressure transient behavior of MTFHWs with finite-conductivity fractures. By solving the analytical partial differential equation, potential flow regimes of MTFHWs are revealed as Figure 21.

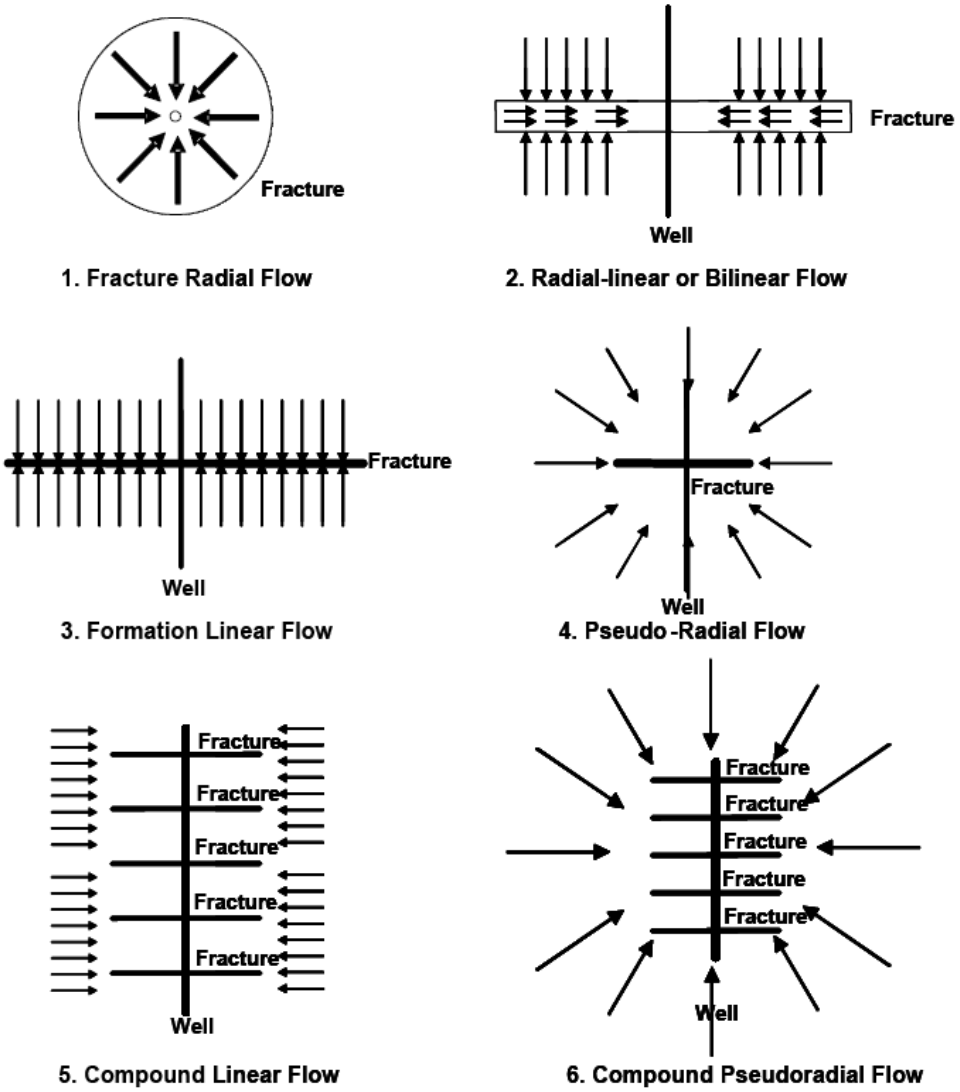


Figure 21. Potential Flow Regimes Identified in MTFHWs (Al-Kobaisi *et al* 2006)

Clarkson *et al* (2009) also studied the flow regime issue in the view of production data analysis through the normalized rate derivative function. First, they define the term "adjust time function" t^*. The specific meaning of t^* can be set as real time (t), adjust pseudotime (t_a^* defined as Eq 7) or adjust material balance time (t_{ca}^* defined as Eq 8).

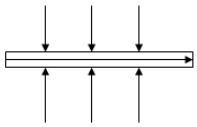
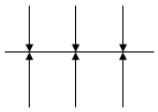
$$t_a^* = (\mu_g c_t^*)_i \int_0^t \frac{1}{\mu_g c_t^*} dt \quad \text{..... (7)}$$

$$t_{ca}^* = \frac{(\mu_g c_t^*)_i}{q_g} \int_0^t \frac{q_g}{\mu_g c_t^*} dt = \frac{(\mu_g c_t^* Z^*)_i}{q_g} \frac{G_i}{2p_i} [m(p_i) - m(p_r)] \quad \text{..... (8)}$$

Both Eqs. 7 and 8 include the altered variables c_t^* and Z^* those accounts for desorption. These variables assume instantanesous desorption, which is a reasonable assumption for long-term production in several commercial shale and coalbed methane reservoirs (Clarkson *et al* 2009). The definition of adjust time and material adjust time include the consideration of desorption through these altered variables. However, the advantage of t_{ca}^* compared to t_a^* is that it can be applied in variable rate/flowing pressure scenario while t_a^* is just for constant flowing bottomhole pressure. The flow regimes can be identified by the characterization of normalized rate derivative on a log-log diagnosis plot. Different form of the normalized rate derivative function will give different appearance of the curve, as Table 2 shows, but they represent the same flow regimes.

For the MTFHW case, they provided a brief illustration to reveal all the potential flow regimes (Figure 22).

Table 2. Flow Regime Identification Scheme by Normalized Rate Derivative Function (Modified from Clarkson *et al* 2009)

Flow regimes	Log-Log diagnostic	Plot	Derivative function characterization
 Bilinear flow	Radial derivative	$\frac{m(p_i)-m(p_{wf})}{q_g} vs. \log(t^*)$	1/4 slope
	Bilinear derivative	$\frac{m(p_i)-m(p_{wf})}{q_g} vs. \sqrt[4]{t^*}$	0 slope
 Linear flow	Radial derivative	$\frac{m(p_i)-m(p_{wf})}{q_g} vs. \log(t^*)$	1/2 slope
	Linear derivative	$\frac{m(p_i)-m(p_{wf})}{q_g} vs. \sqrt[2]{t^*}$	0 slope
 Radial flow	Radial derivative	$\frac{m(p_i)-m(p_{wf})}{q_g} vs. \log(t^*)$	0 slope
No-flow boundary flow (Pseudo-Steady State)	Radial derivative	$\frac{m(p_i)-m(p_{wf})}{q_g} vs. \log(t^*)$	1 slope

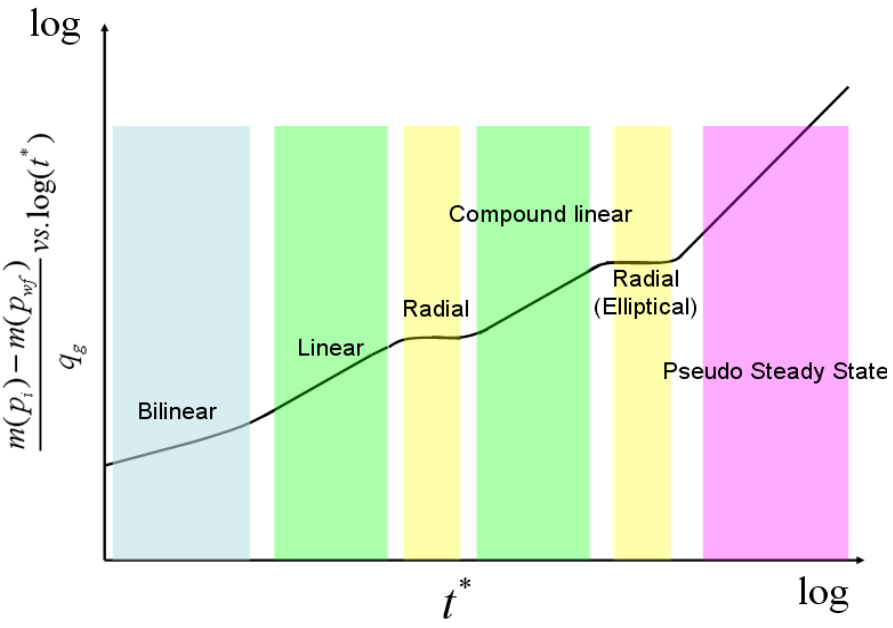


Figure 22. Potential Flow Regimes in MTFHW (Finite Conductivity Fractures)

Previous study of MTFHWs' model provided support for understanding the flow regimes of MTFHWs. Though the models study mentioned above are from different ways, including numerical model (Freeman *et al* 2009), PTA analytical (Al-Kobaisi *et al* 2006) model and production data analysis (Clarkson *et al* 2009), we can still capture a basic image of flow regimes of MTFHWs, especially reservoir flow regimes.

4.3 Rationale for Use of Long Term Drawdown Model Behavior

Models for long term rate decline behavior at a constant pressure and those for pressure drawdown at a constant production rate have been maturely developed. Matching a long term rate decline behavior or pressure drawdown behavior against an appropriate model is an effective way to diagnose well and reservoir characteristics.

However, usually neither of rate and pressure data is constant in reality. Therefore, to perform analysis to the data with the existing long term drawdown models, we need to process the varying rate and varying pressure data into a virtual long term rate decline behavior at constant pressure or a virtual pressure drawdown behavior at constant rate.

4.3.1 Rate-Normalized Pressure Analysis as Alternative to Rate Decline Analysis

In reality, the rate and pressure data recorded during the production of a well are both varying. Palacio and Blasingame (1993) provided a way to view long term production data as a single virtual rate decline at constant pressure. The graph of the instantaneous productivity index as a function of material balance time computed as the cumulative production over the last rate provides a virtual constant pressure rate decline, and this enables matching against rate decline model that represent the same well and reservoir characteristics as can be modeled for constant rate drawdown. But rate decline behavior is not as straightforward to diagnose as pressure drawdown behavior for constant rate production, which shows readily identified straight trends with characteristic slope when viewed as pressure change derivative. Therefore, we use RNP analysis to provide a virtual constant rate pressure drawdown for a well produced at variable rate and variable pressure, and it enables matching against pressure drawdown models, which is more straightforward than rate decline model for diagnosing well and reservoir characteristics (Ehlig-Economides, Martinez Barron and Okunola 2009).

Rate-normalized pressure (RNP) is simply the reciprocal of the instantaneous productivity index (Eq 9), and its derivative is defined as Eq 10. It provides virtual

constant rate drawdown behavior for arbitrary variations in rate and wellhead pressure.

$$RNP = \frac{p_i - p_{wf}}{q} \quad \text{..... (9)}$$

$$RNP' = \frac{dRNP}{d\ln t_e} = \frac{d\left(p_i - p_{wf}/q\right)}{d\ln t_e} \quad \text{..... (10)}$$

(Note: RNP' can be modified as RNP's derivative with respect to elapsed time rather than material balance time to avoid superposition effect, as discussed in Paper SPE 123042 (Ehlig-Economides, Martinez Barron and Okunola 2009)).

Plotting RNP and RNP' versus material balance time on log-log coordinate can shed lights on well behavior and flow regimes. In Ecrin Topaze this plot is also produced when rate and pressure data is input.

4.3.2 Unified BU-RNP Analysis

Pressure transient analysis (PTA) is also performed to analyze the well behavior as well as PDA. Moreover, build-up tests are preferred in the industry. However, Due to the difference in data collection between PTA and PDA, these analyses are performed independently, yielding multiple interpretations from a diverse group of people and software programs. At times the results may conflict, and creating one consistent well and reservoir characterization can be quite challenging and time consuming. A unified interpretation of both analyses would reduce analysis time and increase confidence in the results (Ehlig-Economides, Martinez Barron and Okunola 2009).

The unified BU-RNP method (Ehlig-Economides, Martinez Barron and Okunola 2009) provides a more complete analysis than either PTA or PDA alone can provide by

combining relatively short-duration PTA data and long-term PDA data. The essence of this processing is also to transferring a production process into a virtual constant-rate drawdown behavior that can be diagnosed like pressure and pressure derivative and matched against an appropriate model, but compared to pure RNP analysis this method considers both PDA and PTA (selected build up) and makes the analysis more trustable.

To perform unified BU-RNP method, the following main steps should be performed:

1. Selected a build up part, calculate pressure change and its derivative with respect to elapsed time, and back-integrate it into a drawdown behavior. The result will provide early behavior of the final unified plot.
2. Assign a constant rate used for multiplying RNP in order to combine RNP with BU in the future, and transfer PDA data into a virtual pressure drawdown behavior under this constant rate through RNP processing (there are sub-steps for deleting the redundancy (Ehlig-Economides, Martinez Barron and Okunola 2009)). This will provide the long term response of the unified plot.
3. Combine the results from PTA and PDA as the whole virtual drawdown [If the result from PDA contains the data sharing the same time domain with the result from PTA, the PTA is used because it is usually smoother, but it is also subject to superposition distortion. Overlapping the two response trends to throw off nonlinear regression in automated matching].
4. Analyze the unified plot and find an appropriate drawdown model to match it.

The procedure will also be instructed while it is applied to analyze the field case in the future chapter.

4.4 Sensitivity Studies Illustrating Long Term Drawdown Behavior of MTFHWs in Shale Gas Reservoirs

To illustrate the long term drawdown behavior of MTFHWs in shale gas reservoirs, we run a series of sensitivity studies. The sensitivity is performed to permeability. Table 3 lists the well, reservoir and PVT properties, and Table 4 shows the model settings. Table 5 lists the specific sensitivity cases we run.

We run three series of cases, each series represents one boundary condition (No flow boundary, infinite reservoir and constant pressure boundary). In each series, a sensitivity study to permeability ranging from 0.0001 md to 1 md is performed.

Table 3. Well, Reservoir and PVT Settings for Sensitivity Study

Reservoir settings		
Reservoir type	Gas shale	
h, ft	Pay zone thickness	30
ϕ	Porosity	0.1
T, ºF	Reservoir temperature	212
p_i, psia	Initial reservoir pressure	5000
Well and stimulated fracture settings		
well type	Multi-transverse fractured horizontal well	
L, ft	Well length	3200
n_f	Number of fractures	8
x_f, ft	Half length of fractures	1200
r_w, ft	Wellbore radius	0.3
z_w, ft	well vertical distance to reservoir bottom	15
PVT settings		
γ_g	Gas specific gravity	0.7

Table 4. Model Settings for Sensitivity Study

Well and wellbore parameters		
Wellbore model	No wellbore storage	
s	Skin factor	0
Fracture model	infinite-conductivity	
Reservoir parameters		
k_z/k_r	vertical/horizontal permeability anisotropy	1
Reservoir model	Homogeneous	
Desorption settings		
Adsorption saturation	Saturated	
p_L, psia	Langmuir pressure	2000
ρ_{ads}, g/cc	Adsorption density	0.1
Production design		
t_p, hr	Production time	1.00E+08
q, Mscf/d	Gas production rate	100

Table 5. Sensitivity Study Cases

Case name	Boundary condition	Permeability (md)
MTFHW_NF_k= 0.0001	No-flow boundary	0.0001
MTFHW_NF_k= 0.001	No-flow boundary	0.001
MTTHW_NF_k= 0.01	No-flow boundary	0.01
MTFHW_NF_k= 0.1	No-flow boundary	0.1
MTFHW_NF_k= 1	No-flow boundary	1
MTFHW_IA_k= 0.0001	Infinite reservoir	0.0001
MTFHW_IA_k= 0.001	Infinite reservoir	0.001
MTFHW_IA_k= 0.01	Infinite reservoir	0.01
MTFHW_IA_k= 0.1	Infinite reservoir	0.1
MTFHW_IA_k= 1	Infinite reservoir	1
MTFHW_CP_k= 0.0001	Constant pressure boundary	0.0001
MTFHW_CP_k= 0.001	Constant pressure boundary	0.001
MTFHW_CP_k= 0.01	Constant pressure boundary	0.01
MTFHW_CP_k= 0.1	Constant pressure boundary	0.1
MTFHW_CP_k= 1	Constant pressure boundary	1

Figure 23, 00 and 25 separately shows the 2-D maps of each series of cases, and Figure 26, 27 and 28 show their corresponding log-log plot of the drawdown behavior in order.

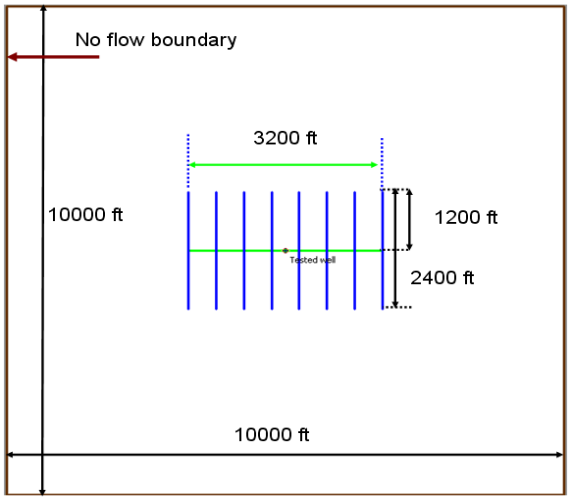


Figure 23. Reservoir and Well Geometry of MTFHW_NF Test Series

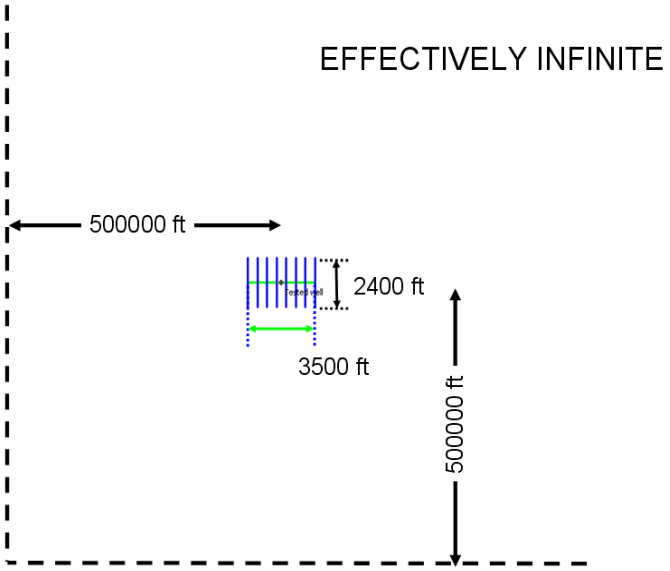


Figure 24. Reservoir and Well Geometry of MTFHW_IA Test Series

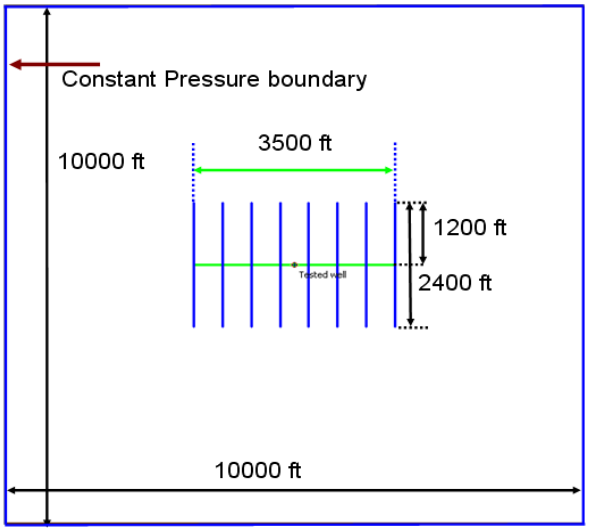


Figure 25. Reservoir and Well Geometry of MTFHW_CP Test Series

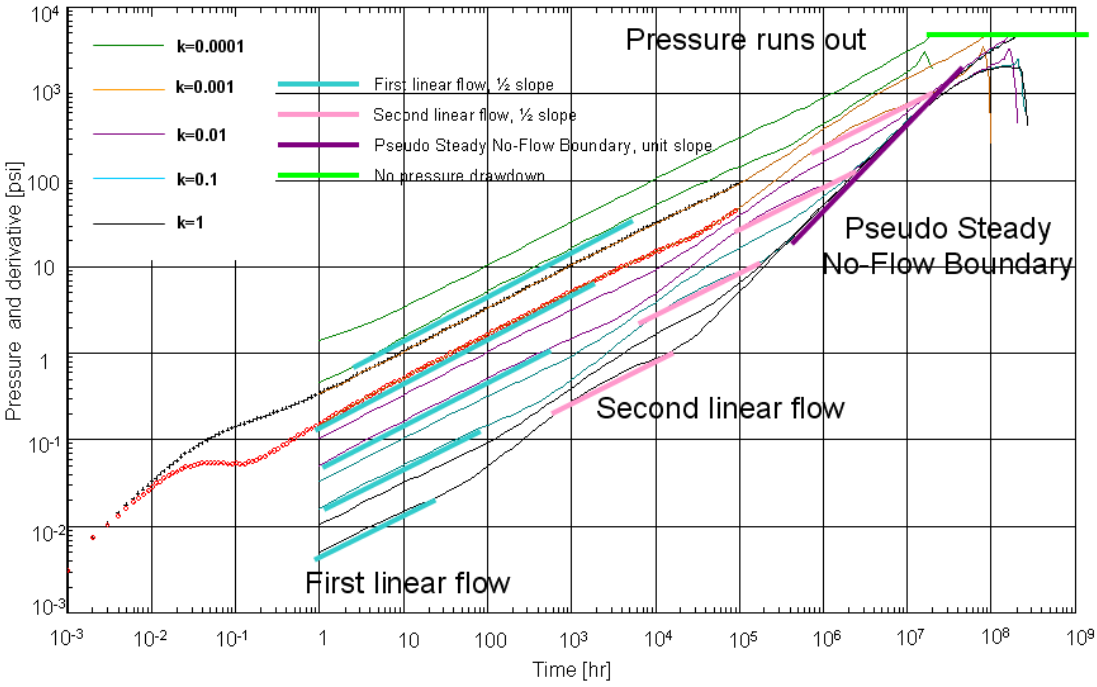


Figure 26. PTA diagnosis plot for MTFHW_NF Test Series

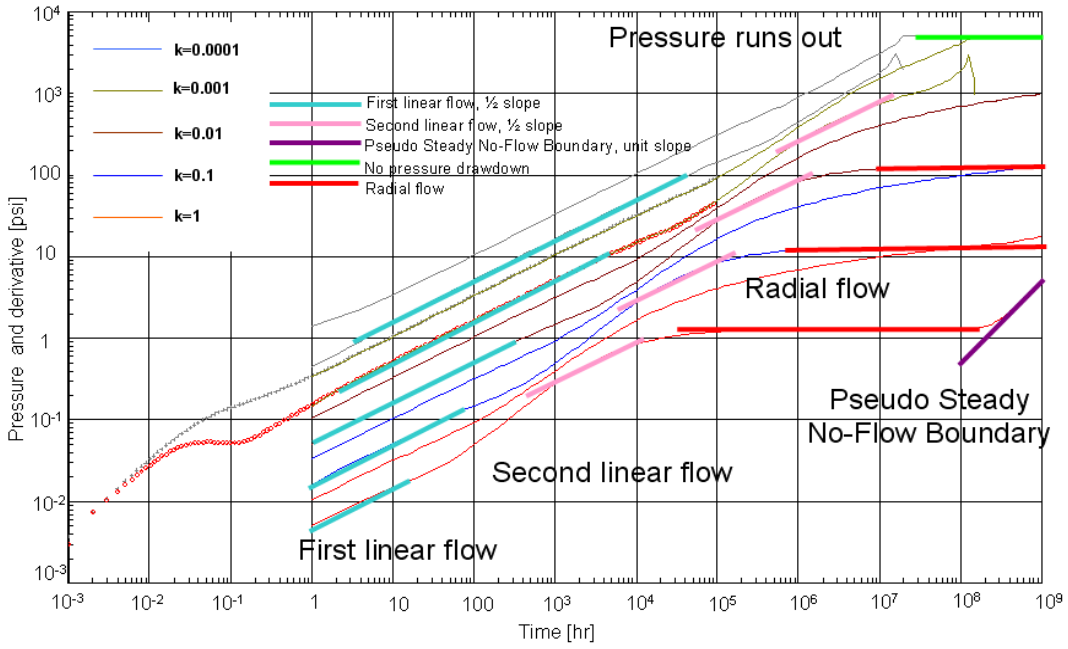


Figure 27. PTA diagnosis plot for MTFHW_IA Test Series

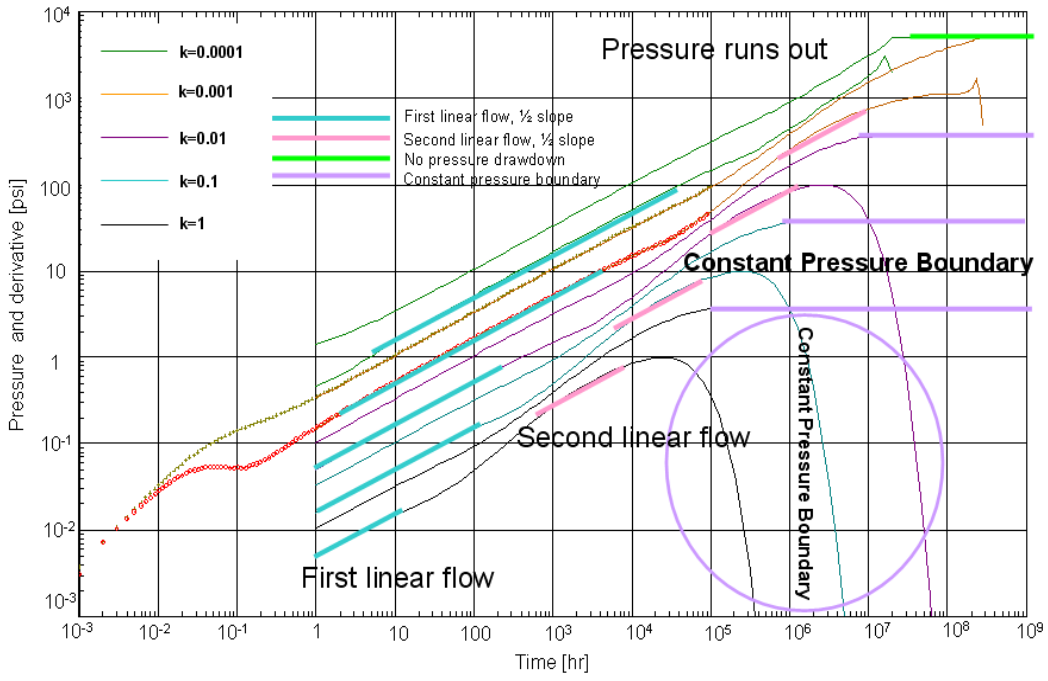


Figure 28. PTA diagnosis plot for MTFHW_CP Test Series

4.4.1 Fracture Storage

Fracture storage effect is identified by the unit slope of pressure change and pressure change derivative at very early time. On each diagnosis plot, the case of k=0.001 md shows the fracture storage effect. The fracture storage effect appears very early and usually lasts a very short time. As reservoir permeability increases, the fracture storage effect will last even shorter time and be replaced by the early reservoir flow regime sooner. Fracture storage is actually a model artifact that appears because Ecrin is using a numerical model that arbitrarily makes all fracture widths 1 cm. We should expect wellbore storage to dominate early time behavior, but this was left out of the sensitivity studies to avoid making behavior of interest.

4.4.2 Early Linear Flow

The first apparent flow regime we observed from the diagnostic plot is linear flow represented by a half-slope derivative (for linear flow, pressure change curve is also half slope). This trend is marked by light blue straight line for each case. This flow regime is the linear flow from reservoir normal to every transverse fracture (Figure 29). Since we use infinite-conductivity fracture model instead of finite conductivity fracture model, which was applied in the previous MTFHW model mentioned in Section 4.2, it is not hard to understand why we don't see bilinear flow before we see this early linear flow. With shale permeabilities in the nanodarcy range, effectively infinite conductivity fractures can be expected.

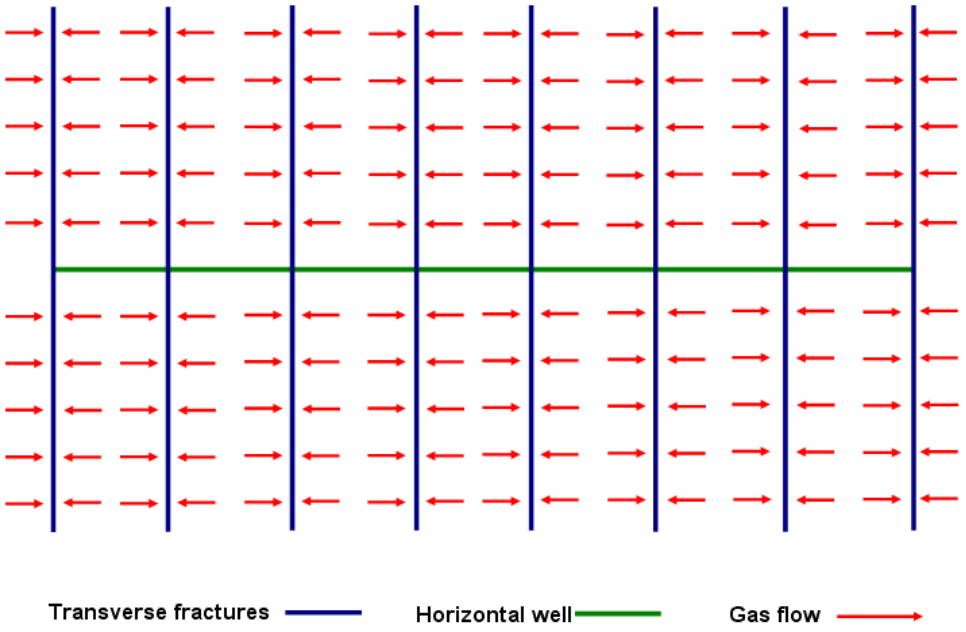


Figure 29. Illustration of the Early Linear Flow Normal to Transverse Fractures

4.4.3 Interference between Adjacent Fractures

As production continues, pressure investigation will travel further into the formation. At some time point, the pressure disturbance front between two adjacent transverse fractures will touch each other so that pressure interference will occur (Figure 30). This is also illustrated on our log-log plots. For each case, derivative curve will bend up at certain time point after the early linear flow, and the derivative departs from the one half slope trend. This interference occurs increasingly earlier with increasing permeability.

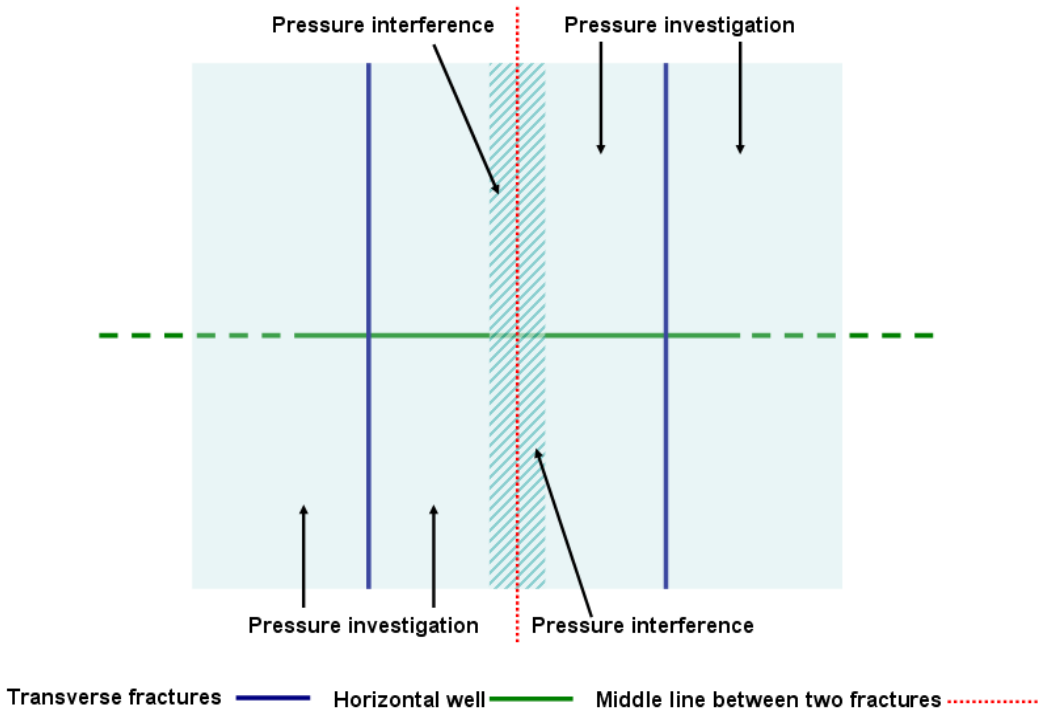


Figure 30. Pressure Interference between Two Adjacent Transverse Fractures (One Unite)

4.4.4 Compound Linear Flow

After pressure interference between two adjacent transverse fractures occurs, the pressure disturbance will cover all the stimulated reservoir volume (SRV) and extend beyond the extent in a flow regime called “compound linear flow” (Figure 31). This flow regime will is represented by the second half-slope derivative trend on the log-log plot. In our sensitivity study, we use pink straight line to mark this flow regime. This flow regime is not a pure linear flow but dominated by linear flow normal to the horizontal well. The flow on the two sides of the wellbore behaves like an elliptical shape, but its impact is weaker than the linear flow normal to the wellbore. The other characterization

of compound linear flow is that on the log-log plot, it lasts less than one square cycle, while early linear flow lasts more than two cycles for permeability less than 0.1 md.

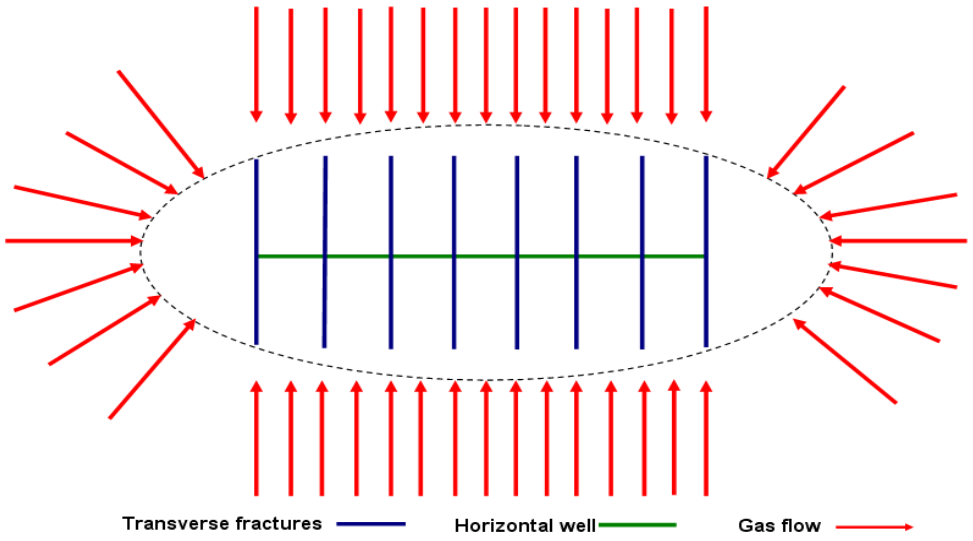


Figure 31. Compound Linear Flow Regime (Modified From Van Kruysdijk *et al* 1989)

4.4.5 Boundary Behavior

After compound linear flow, the pressure investigation may travel even further around the MTFHW system. Based on the reservoir geometry and boundary condition, we saw three kinds of following regime: pseudosteady state (no flow boundary behavior, pressure change and derivative overlap and trend unit slope, marked by violet straight line in Figure 26), infinite acting (infinite reservoir behavior, derivative curve is flat, marked by red straight line in Figure 27) and constant pressure response (constant pressure boundary behavior, pressure change curve is flat and derivative curve descends steeply, marked by the lavender circle and straight line in Figure 28).

Through our sensitivity study, we can conclude a general understanding of flow regimes of MTFHWs in shale gas reservoirs. After the fracture storage effect, which likely will be masked by wellbore storage in field PTA data, early linear flow normal to transverse fractures will form. At some time, the pressure interference between two adjacent transverse fractures occurs, at which time the pressure disturbance will cover the whole stimulated reservoir volume. After that, the pressure investigation extends beyond the SRV and compound linear flow forms. Further, boundary response will occur based on the specific well and reservoir boundary geometry and boundary condition.

Before the boundary response, all the behaviors of the three studies are identical. For typical shale reservoirs, the permeability of nanodarcy scale might encounter a boundary response only after hundreds of years. Hence boundary behavior is not likely to be seen. In reality, early linear flow normal to transverse fractures might be the only essential flow regime to MTFHWs in shale reservoirs depending on the fracture spacing. The MTFHW may just produce gas within a small distance around transverse fractures and we will not even see the pressure interference and compound linear flow regime for many decades.

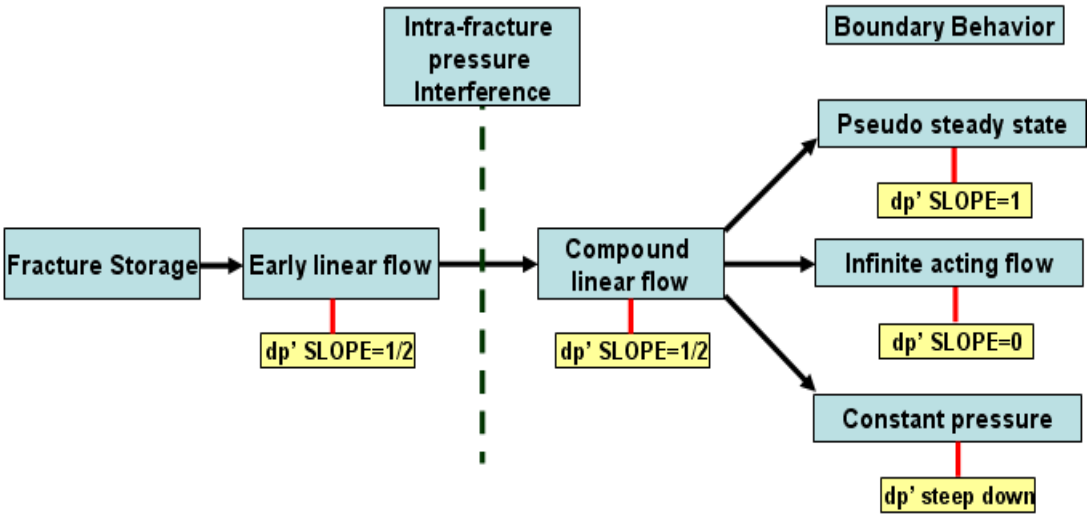


Figure 32. Flow Regimes Revealed through Sensitivity Study

4.5 Impact of Gas Desorption on the Long Term Drawdown Behavior of the MTHWF

The main impact of gas desorption is delaying pressure investigation because it provides an extra supply to gas production besides the free gas. On the log-log PTA diagnosis plot, this impact is illustrated by a parallel time shift of the flow regimes. For example, in the long term drawdown behavior of MTFHWs, gas desorption results in an apparent time shift in the early linear flow, the regime which might be the only one affecting gas production during the well life. Figure 33 illustrates gas desorption impact through a comparison between a drawdown behavior of MTFHW with gas desorption and without desorption.

The importance of gas desorption impact lies on the time when pressure interference between two adjacent transverse fractures. Interference occurrence will be delayed due to gas desorption, and this factor directly affects recovery efficiency design.

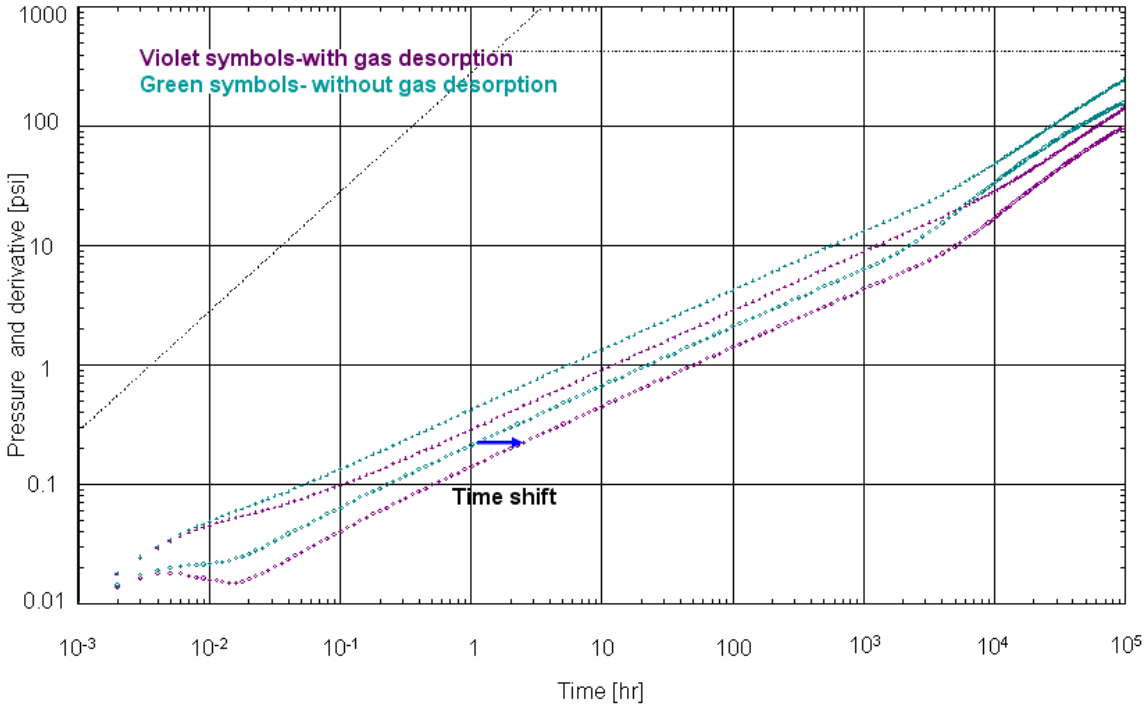


Figure 33. Gas Desorption Impact on Long Term Drawdown Behavior of MTFHWs

The time shift, which we can label the adsorption index, I_{ads} (define as the ratio of investigation time with gas desorption to that without gas desorption) depends on several parameters: ϕ, p_i, p_L and ρ_{ads}. To determine a correlation between time shift and those parameters, we did sensitivity studies to the parameters. Figure 34 shows the sensitivity study design.

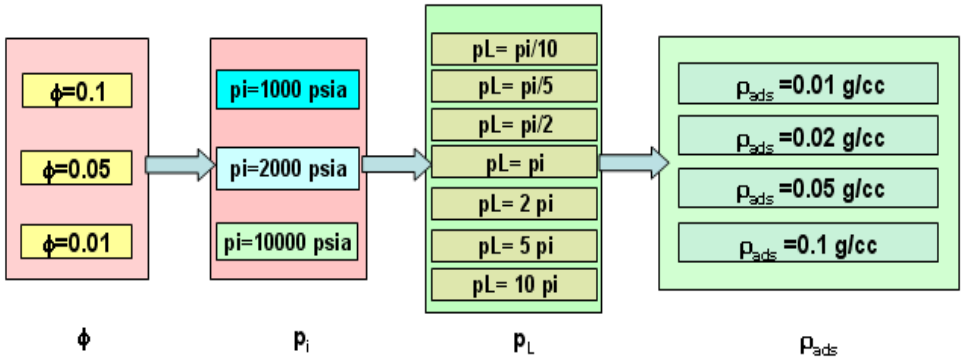


Figure 34. Time Shift (I_{ads}) Sensitivity Study

Figure 35 shows the sensitivity of the long term drawdown response to ρ_{ads} and Figure 36 shows that to p_L (symbols represent the case without gas desorption). Usually, ϕ and p_i are fixed, so we put Figure 35 and 36 to illustrate the sensitivity to ρ_{ads} and p_L. However, ϕ and p_i also impact the time shift, therefore actually, the sensitivity studies also include cases of various ϕ and p_i. The sensitivity studies give a correlation between I_{ads} and those four parameters and we made a program to calculate time shift.

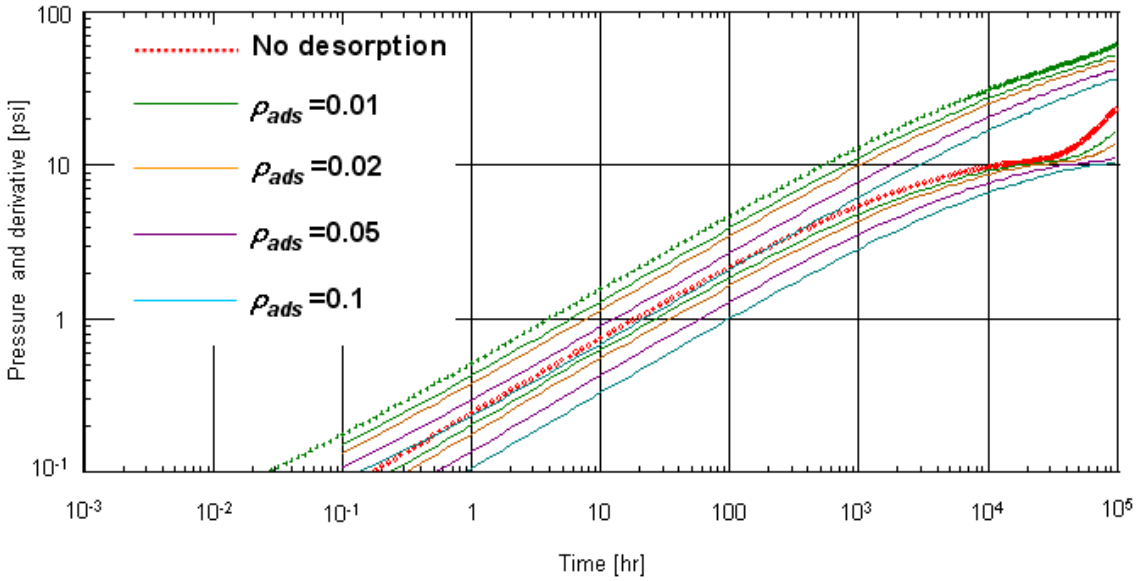


Figure 35. Illustration of Time Shift Sensitivity Study to ρ_{ads}

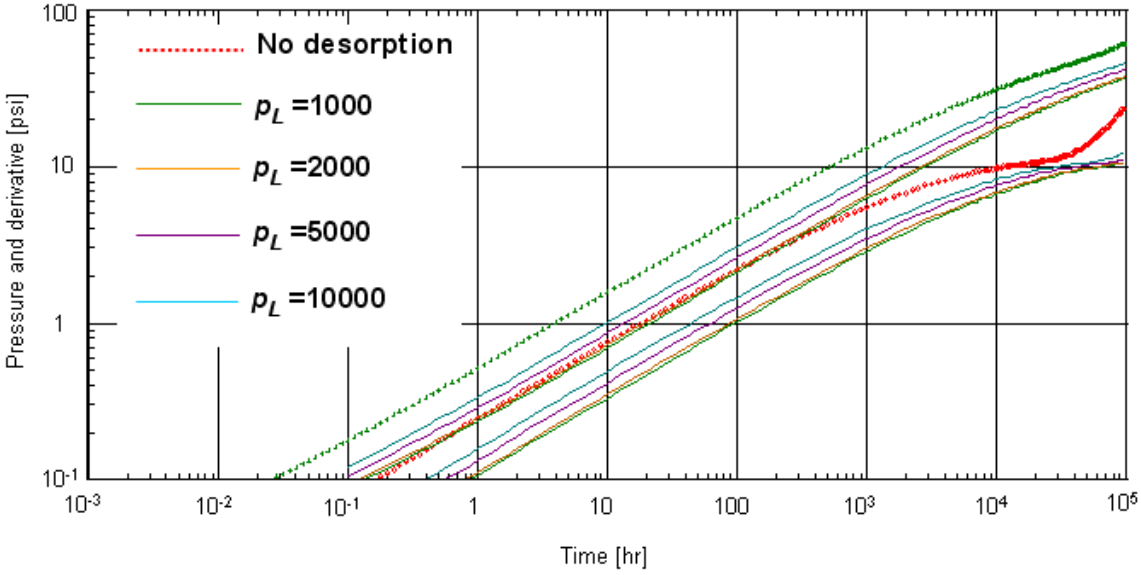


Figure 36. Illustration of Time Shift Sensitivity Study to p_L

We just use one case to illustrate how we extrapolate the relationship between time shift and the four-parameter combination.

Figure 37 shows the observed time shift versus ρ_{ads} for the case of ϕ=0.1 and p_i=1000 psia. For various p_L, time shift appears as a linear function of ρ_{ads} with unit y-intercept (Unit y-intercept is theoretical because 0 ρ_{ads} means no gas desorption, so the time shift is 1, which means investigation time with desorption equals to that without desorption). However the slope of the straight line depends on specific p_L, p_i and ϕ.

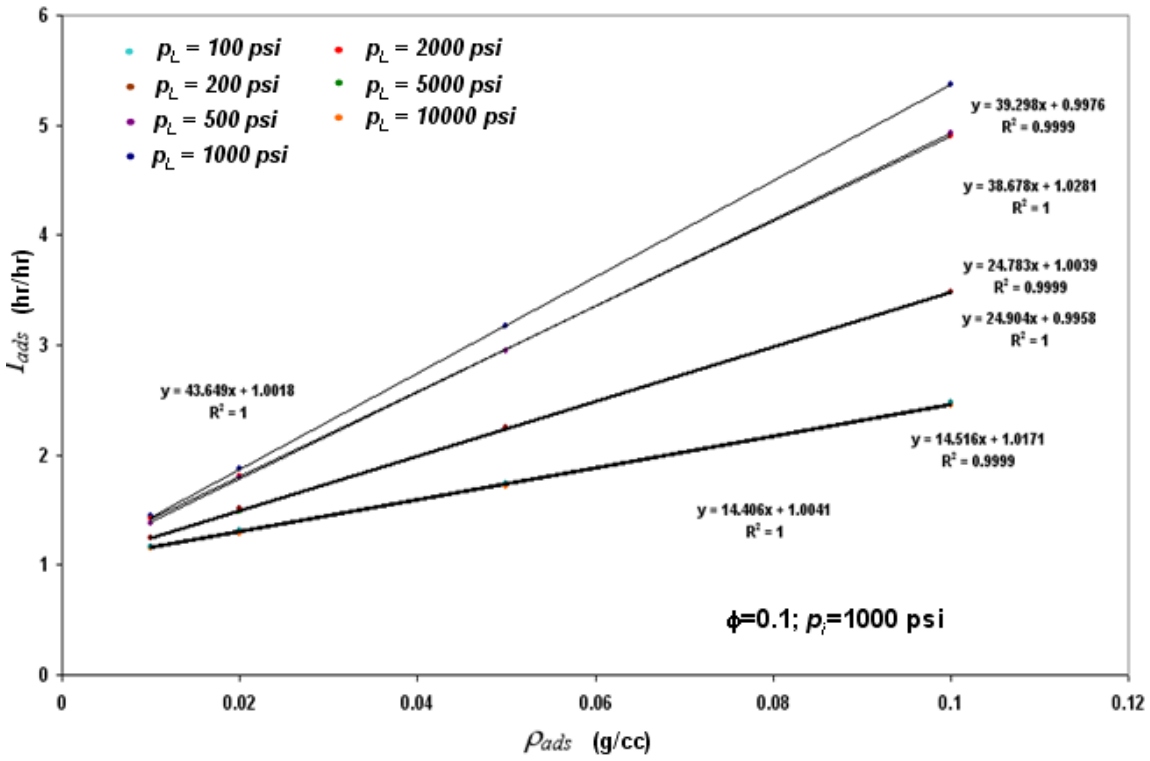


Figure 37. Illustration of Relationship between the Adsorption Index and ρ_{ads}

$$I_{ads} = t_{i,ads} / t_{i,noads} = slope \times \rho_{ads} + 1 \quad \text{..... (11)}$$

Where:

I_{ads} is the ratio of investigation time with desorption to that without desorption;

slope, the slope of the unit y-intercept linear function which correlates I_{ads} TS and ρ_{ads}.

Therefore, further we tried to correlate the slope of the linear function according to specific p_L, p_i and ϕ. Figure 38 shows the correlation.

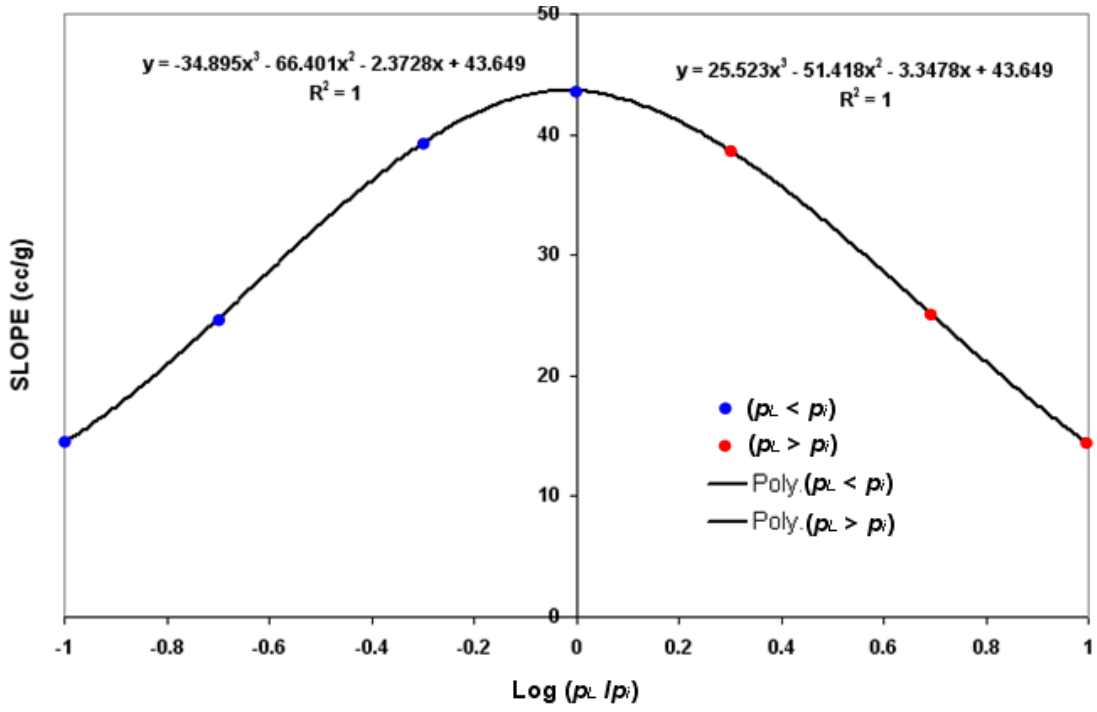


Figure 38. Illustration of Relationship between Slope and Logarithm of p_L over p_i

With a fixed ϕ, the slope is a cubic function of logarithm of p_L over p_i. However, this relationship is only applicable for the p_L with in the domain [p_i/10, 10p_i]. Theoretically, the greater the ratio between p_L and p_i is, the smaller the slope will be. The cubic function is not decreasing as p_L increases or decreases. Therefore, the extrapolation

is only effective when p_L is not very far from p_i. Additionally, the sensitivity studies are run for some certain values of ϕ and p_i, but the correlation could be completed through running more cases for other ϕ and p_i.

$$slope = c_1[\log(\frac{p_L}{p_i})]^3 + c_2[\log(\frac{p_L}{p_i})]^2 + c_3[\log(\frac{p_L}{p_i})] + c_4 \quad \text{..... (12)}$$

Where:

c_1, c_2, c_3 and c_4 are the coefficients of the cubic function for the correlation between the slope and logarithm of p_L over p_i.

Figure 39 shows the interface of the program. If we assign the specific ϕ, p_i, p_L and ρ_{ads}, I_{ads} can be calculated. The logic can be divided into two steps: first, we use ϕ, p_i and p_L to determine the so-called slope; second, determine the time shift with the calculated slope according to specific ρ_{ads}.

This program has some limitation: ϕ, p_i and ρ_{ads} should be fixed at specific values, and p_L should stay within the domain [p_i/10, 10p_i]. However, within its domain, the program does provide an accurate estimate for I_{ads} that can be used for well design purposes. A more general result may be possible with additional work.

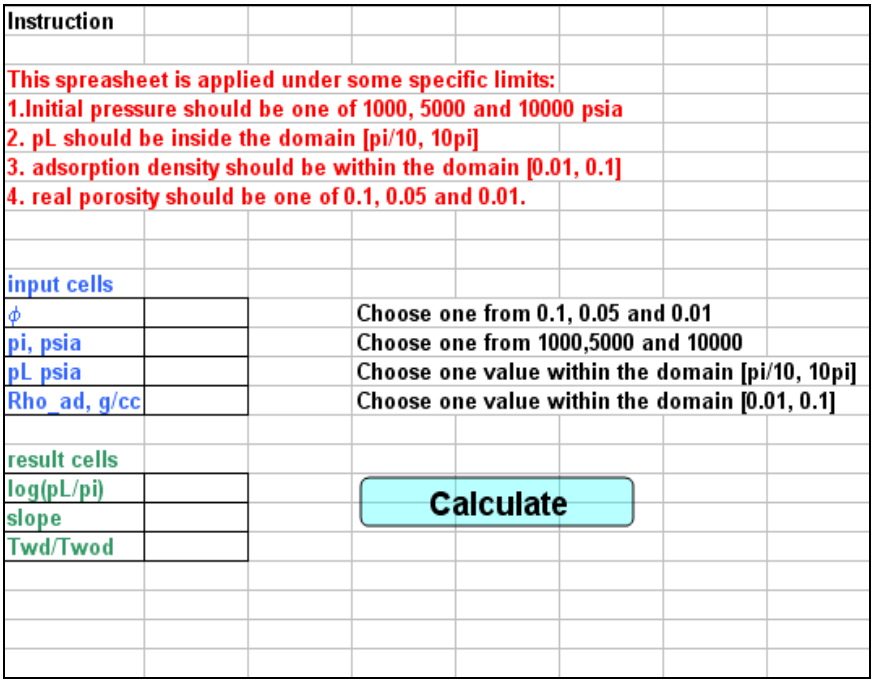


Figure 39. Interface of Program for Calculating Time Shift

4.6 Implications of the Early Linear Flow

The importance of early linear flow to MTFHWs is not only because it might be the only essential regime to the gas production, but also because during this flow regime, permeability and fracture half-length has a relationship from which either of them can be estimated when the other one were known. Furthermore, the end of early linear flow indicates the pressure interference between two adjacent transverse fractures, and this makes this flow regime important to recovery efficiency and well fracture design.

4.6.1 Relationship between Permeability and Fracture Half Length

During first linear flow before pressure interference occurs, the MTFHW actually performs like a single vertical well with a long fracture, whose length is the sum of all

the created fractures in the MTFHW. During this period, the equation for pressure change Δp versus time is:

$$\Delta p = m_{lf}\sqrt{\Delta t} + (\frac{\pi}{3})(\frac{m}{1.151})\frac{kx_f}{k_f w} \quad \text{..... (13)}$$

Where:

Δp, pressure change;

m_{lf}, the slope of a graph of pressure versus the square root of elapsed time;

Δt, elapsed time;

m, the slope of a graph of pressure versus log Δt;

k, formation permeability;

x_f, hydraulic fracture half length;

k_f, fracture permeability;

w, fracture width;

The equation for the pressure derivative is given by:

$$\Delta p' = \frac{1}{2} m_{lf}\sqrt{\Delta t} \quad \text{..... (14)}$$

Where:

$\Delta p'$, the derivative of pressure change with respect to the logarithm of elapsed time;

In turn, the product of $x_f k^{0.5}$ is related to m_{lf} by:

$$x_f\sqrt{k} = (\frac{4.064qB}{m_{lf}h})(\frac{\mu}{\phi c_t})^{1/2} \quad \text{..... (15)}$$

Where:

q, well flow rate;

B, the fluid formation volume factor;

h, the formation thickness;

μ, the fluid viscosity;

ϕ, the formation porosity;

c_t, the total compressibility;

Therefore, the product of square root of time and fracture half-length is a constant. However for MTFHWs, the x_f is not fracture half length of only one transverse fracture but the summed half length of all the transverse fractures. This relationship is valuable because if we can estimate either of these two parameters if we know the other one: if summed fracture half-length can be determined told from microseismic measurement, reservoir permeability can be estimated; in contrast, if permeability is known, summed fracture half-length can also be estimated (Figure 40).

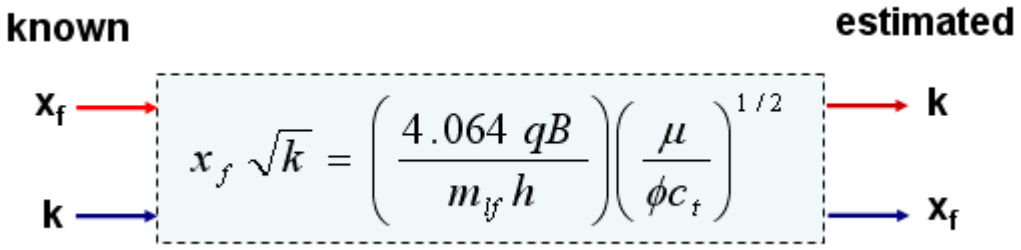


Figure 40. Application of the Relationship between k and x_f

4.6.2 Time of Fracture Interference

Ehlig-Economides (1992) provided an equation to estimate pressure investigation depth for linear flow.

$$x_i = 2\sqrt{\frac{kt}{948\phi\mu c_t}} \quad \text{..... (16)}$$

Where:

x_i, the pressure investigation depth;

μ, the fluid viscosity;

ϕ, the formation porosity;

c_t, the total compressibility;

k, formation permeability;

t, elapse time;

The transform of Eq 14 will give Eq 15, by which we can estimate the pressure investigation time at some investigation depth.

$$t = \frac{948\phi\mu c_t x_i^2}{4k} \quad \text{..... (17)}$$

For MTFHWs, if we know the fracture spacing, we can estimate the time when pressure interference between two adjacent transverse fractures occurs. However, in shale gas reservoir, gas desorption impacts the pressure investigation. For the same pressure investigation depth, the corresponding investigation time with the existence of gas desorption will be larger than that without gas desorption. Therefore, the estimation of interference time should take gas desorption impact into account.

The estimate to interference time with the consideration of gas desorption can be done by combining the pressure investigation depth calculation and time shift calculation. If we know the permeability and fracture spacing, we can apply Eq 17 to calculate a time which doesn't take gas desorption into account. Then referring back to the program we made to calculate the time shift, we can calculate the time shift according to the specific ϕ, p_i, p_L and ρ_{ads}. The product of the time we calculated from Eq 17 and time shift calculated from the program can give a fracture interference time that which takes gas desorption into account.

4.6.3 Fracture Spacing Design for Interference at a Specific Time

The pressure investigation time calculation modified by the adsorption index affects the well design. If permeability is known, the well can be designed for fractures to interfere at a specified time by spacing fractures accordingly. We can use an example to illustrate this how to use I_{ads} to determine the fracture spacing.

Assume that a formation has the following properties: ϕ=0.1; p_i=5000 psia; p_L =2500 psia; ρ_{ads} = 0.1 g/cc; k= 0.001 md at a given location, and that the well is to be designed for fractures to interfere after 3.5 years. So first, according to the parameters ϕ, p_i, p_L and ρ_{ads}, we calculate I_{ads} by the program at 2.38. Without gas desorption, the corresponding interference time without desorption is 3.5 years /2.38 = 1.47 years. Then we can use Eq 15 to calculate the pressure investigation depth after 1.47 years, and it is 200 ft. Therefore, we can design the fracture spacing at 400 ft, and we can say that a 400

ft fracture spacing will result in the fracture interference occurring after 3.5 years at this reservoir location.

Chapter 5 will now illustrate the application of what has been learned from sensitivity studies on actual field data from the New Albany shale gas wells.

CHAPTER 5. FIELD CASE STUDY: NEW ALBANY SHALE

In this Chapter, well - 0077 is used to illustrate the concepts that have been introduced in previous chapters. Both production and pressure transient data (one buildup) were collected as well as reservoir properties, fluid properties and well information. After processing the production/pressure data by unified BU-RNP method, we analyzed the data as a virtual constant rate pressure drawdown. Production analysis is also performed. We discuss the recovery facto issue based on the EUR estimation from the Valko (2009) approach. Also discussed is the special impact of gas desorption due to the low reservoir pressure in the case of - 0077.

5.1 Field Data and Information Collection and Synthesizing

Production data for and one approximately 1 year, from Oct-03-2008 to Sep-13-2009, and one pressure buildup have been recorded for the well - 0077. The well completion diagram (Figure 41), fracturing job records, fluid properties, reservoir properties and gas desorption reports are also available. Table 6 lists the well, reservoir and fluid properties.

Gas adsorption data for a core sample from another well (- 0085) is used for the analysis. It is assumed that these data are applicable for - 0077 because the 2 wells share almost the same reservoir conditions. Following is the calculation to determine ρ_{ads} from core analysis data:

$$\rho_{ads} = 0.3048^3 \times \rho_{gas}^{surf} \times \rho_{rock} \times V_L = 0.3048^3 \times 0.0008 g/cc \times 2.372 g/cc \times 125.8 scf/ton = 0.00648 g/cc \quad \text{..... (18)}$$

Table 7 synthesizes the gas adsorption information from core analysis with parameters to be loaded into Ecrin for analysis.

The estimation of fracture length of - 0077 is unavailable due to the lack of microseismic data. However, the microseismic data for well - 0085-21 drilled in summer 2009 and its fracturing job record provide an estimation of the fracture length of that well. Table 8 shows the fracturing fluid injection amount for the first three stages and their corresponding fracture half-lengths. Assuming a correlation between the amounts of fracturing fluid (Nitrogen) and the fracture length, we estimated what may be the fracture lengths for well - 0077.

Nitrogen-fracturing efficiency, the ratio of fracture half-length to nitrogen volume used in fracturing job can be captured. Under the assumption that the nitrogen-fracturing efficiency is the same for - 0077, the fracture half length of each stage of - 0077 can be estimated. Table 9 shows the estimation of half-fracture length for each stage of - 0077. By applying the nitrogen-fracturing efficiency of - 0085-21, 1.263 ft/Mscf, average fracture half length of - 0077 is estimated as approximately 1300 ft.

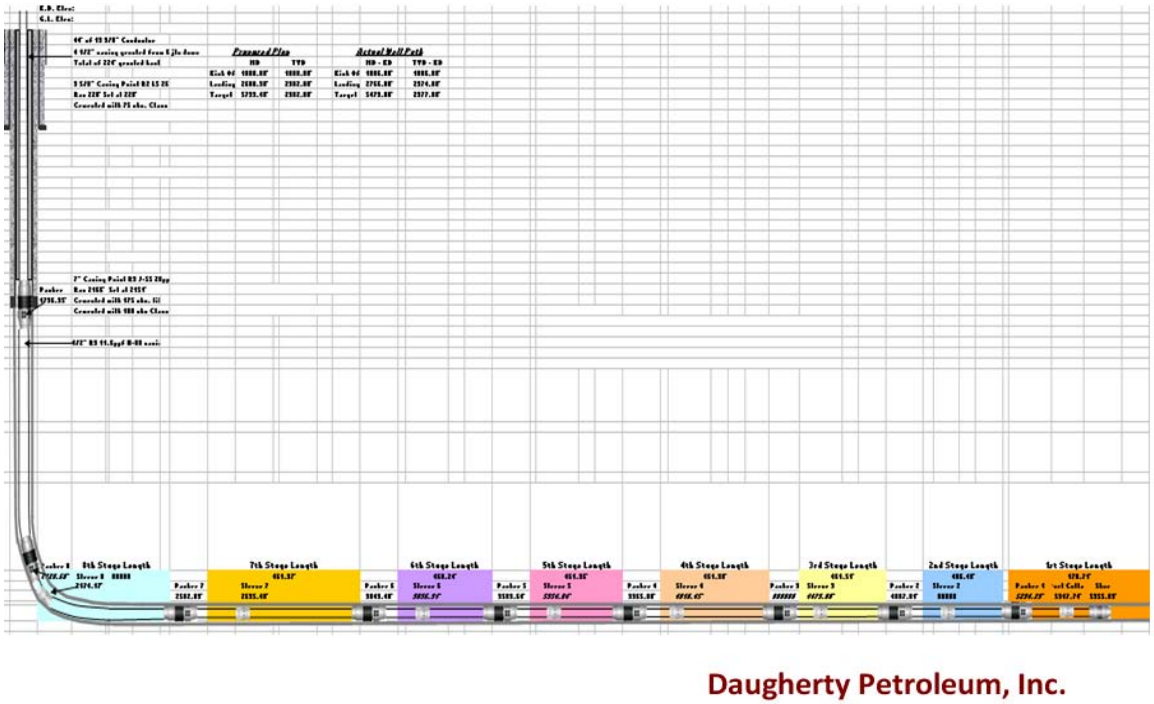


Figure 41.Well Structure of - 0077

Table 6. Well, fluid and reservoir information of - 0077

Well information (From DOE)	
well type	multi-transverse fractured horizontal well
number of well stage	8
L, well length, ft	3300
r, well radius, ft	0.375
fluid properties (From Delta Natural Gas Company)	
fluid type	gas
composition fraction	methane 84.39%; CO_2, 0.27%, N_2, 11.56%; other 3.78%
γ, specific gravity	0.626
reservoir information (From DOE and Weatherford Lab)	
reservoir depth, ft	2382
T_r, reservoir temperature, ^oF	89
P_i, reservoir pressure, psi	714
reservoir pressure gradient, psi/ft	0.3
ϕ, porosity	0.06
ρ_{rock}, rock density, g/cc	2.372

Table 7. Gas Adsorption Parameters for - 0077

p_L, Langmuir pressure, psia	1044
V_L, Langmuir volume, scf/ton	125.82
V_L, Langmuir volume, cc/g	3.563
ρ_{rock}, rock density, g/cc	2.372
ρ_{ads}, adsorption density, g/cc	0.00648

Table 8. Fracture Half Length and Fracturing Used Nitrogen Volume Records

From Pinnacle (- 0085, Stage 1,2 and 3)			
Stage #	**x_f, ft**	**total nitrogen in use, Mscf**	**ratio x_f/N2**
1	1190	1081	1.101
2	1650	1152	1.432
3	1260	1003	1.257
average nitrogen-fracturing efficiency			1.263

Table 9. Fracture Half Length Estimation for - 0077

Stage #	**total nitrogen in use, Mscf**	**x_f, ft**
1	1004.1	1268
2	1001	1264
3	1001.4	1265
4	1002	1266
5	1002.5	1266
6	1002.5	1266
7	1002.8	1267
8	1003.3	1267
average nitrogen-fracturing efficiency	1.263	1266

5.2 Production/Pressure Data Processing by Unified BU-RNP Method

About one-year production rate and pressure data of - 0077 is recorded (Figure 42).There is one pressure build up which lasted 9 days but pressure data were only recorded once a day. The buildup is supposed to be used for pressure transient analysis. However, due to its sparse data frequency, the buildup doesn't give a very satisfying result.

Therefore, we use unified BU-RNP method to transfer this production process into a virtual constant rate pressure drawdown behavior for diagnosis. We selected the only build up in the production history as the data source of PTA processing, and also processed the whole PDA data by RNP. Figure 43 and 44 separately show the process of PTA processing and PDA processing, and the sub-steps are marked by arrows. Finally, we combined the results from PTA processing and that from PDA processing, and got a diagnostic plot of the virtual constant rate pressure drawdown behavior (Figure 45).

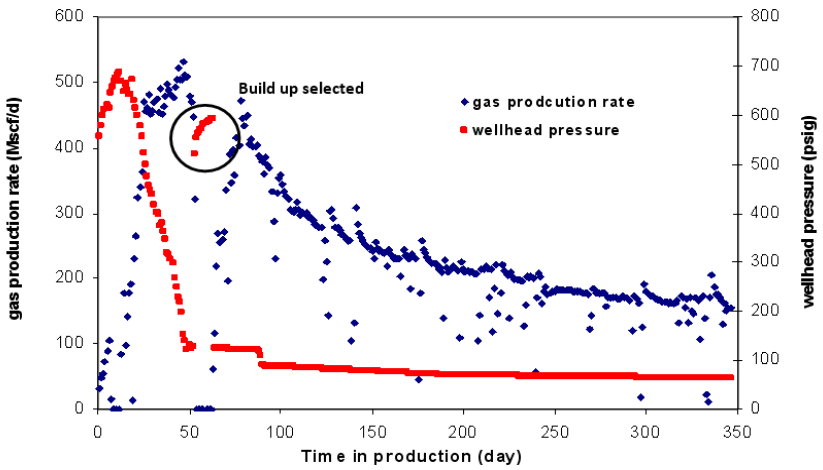


Figure 42. Production Rate and Pressure Data of - 0077

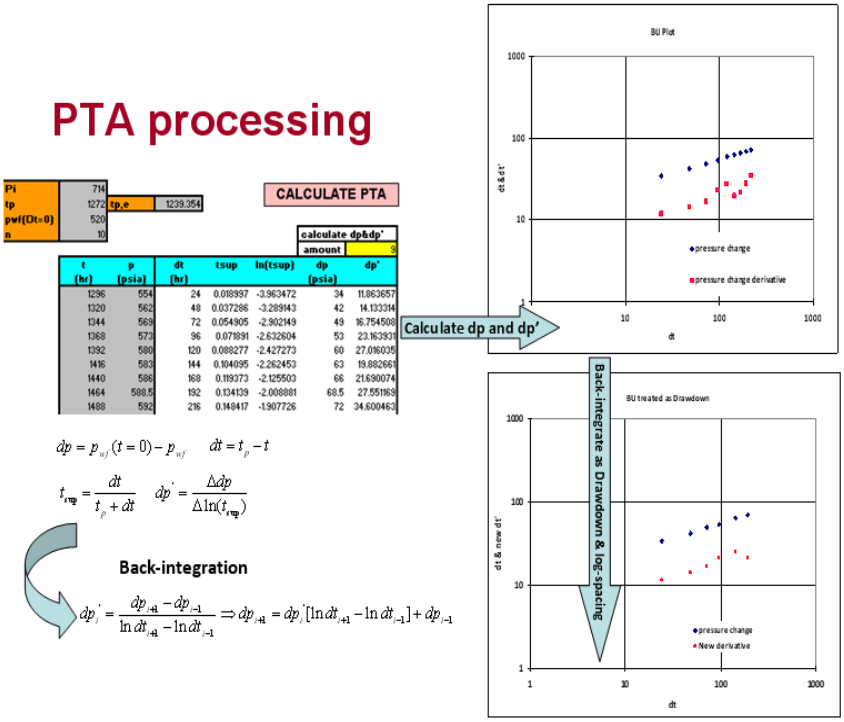


Figure 43. Unified BU-RNP Processing of PTA Data of - 0077

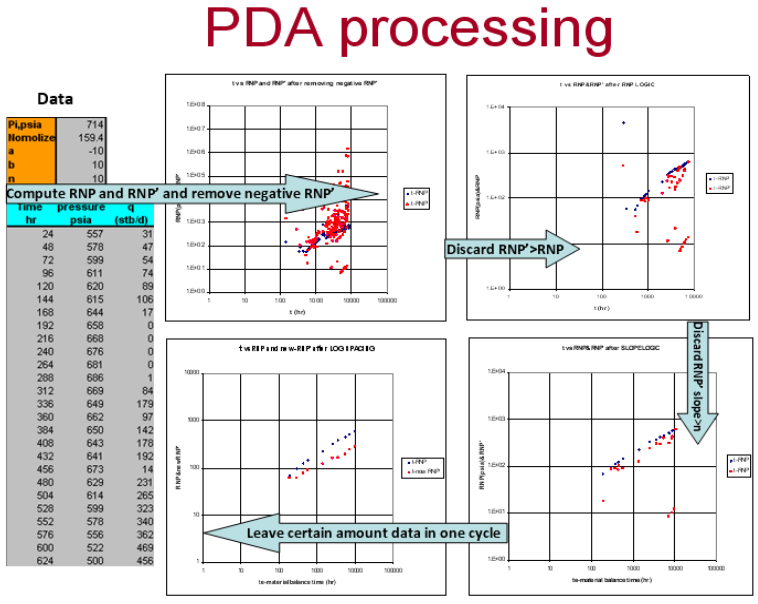


Figure 44. Unified BU-RNP Processing of PDA Data of - 0077

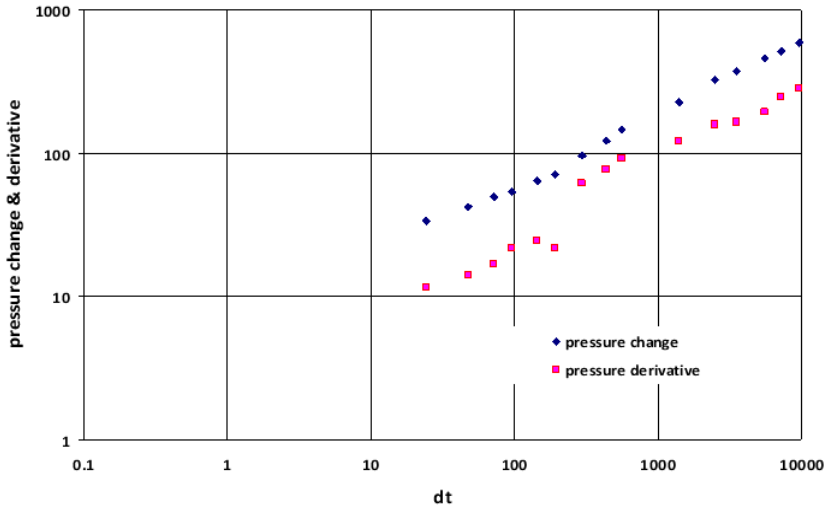


Figure 45. Unified BU-RNP Virtual Drawdown of - 0077

5.3 PTA and Production Analyses

Unified BU-RNP processing provides a unified plot, from which we can analyze the well and reservoir characteristics. On the unified plot, we can see the pressure change and derivative show a half slope extending, more than two square cycles. Half slope derivative curve last more than 1 square cycle indicates the early linear flow normal to transverse fractures, and this is the only one flow regime observable on this unified plot.

After processing the production/pressure data into a virtual constant rate drawdown behavior, we also performed the PTA analysis using commercial software. By loading the virtual drawdown data into Kappa Ecrin Saphir, we tried to find an appropriate drawdown model to match the input data. Figure 46 shows a model match for the virtual drawdown behavior.

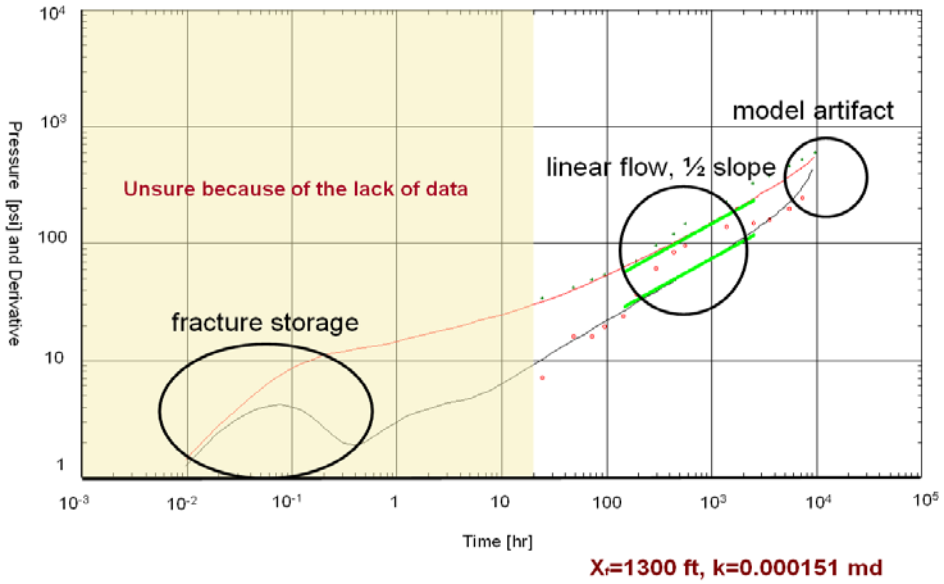


Figure 46. Virtual Drawdown Matching of - 0077

The first data after unified BU-RNP processing is from 00th hour, so though the model provides fracture storage behavior, there is no match before 1 day due to the lack of early time buildup data. After that, as on the unified plot, we see the model pressure change and its derivative with half slope lasting about 2 square cycles. As discussed in Chapter 4, this means the dominate flow geometry is linear flow normal to the fractures. The model shows an artifact at the end because constant rate drawdown exceeds the initial reservoir pressure. This model match gives the permeability of 0.000151 md and uses a fracture conductivity of infinite.

Production analysis is also performed to the production data of - 0077 by Kappa Ecrin Topaze. Figure 47 shows the matching of production rate data and

cumulative production. Figure 48 is the rate normalized pressure (RNP) and its derivative plot.

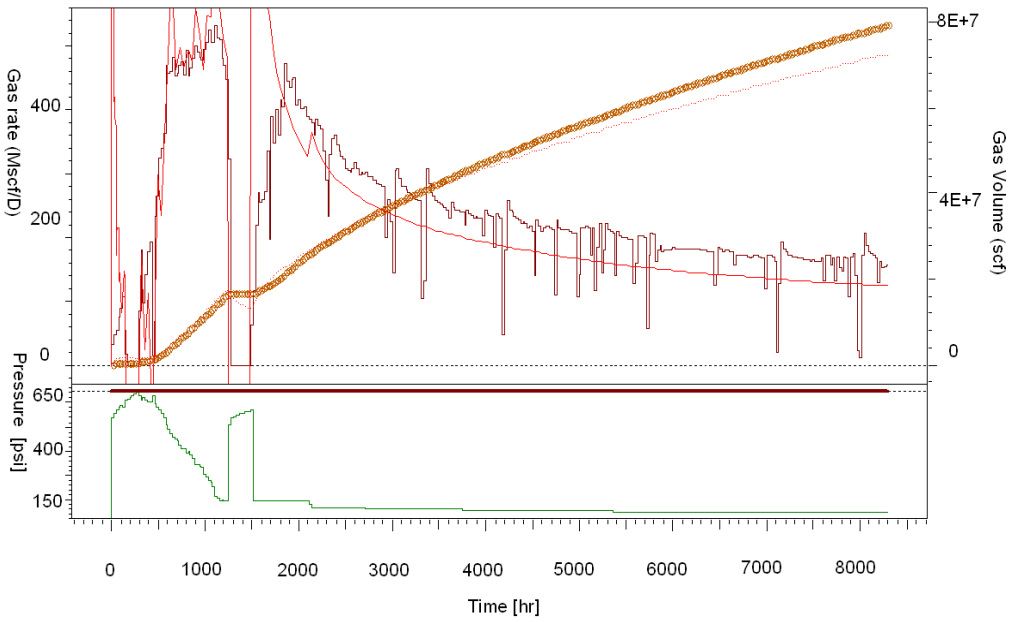


Figure 47. Rate and Cumulative Production Matching of - 0077

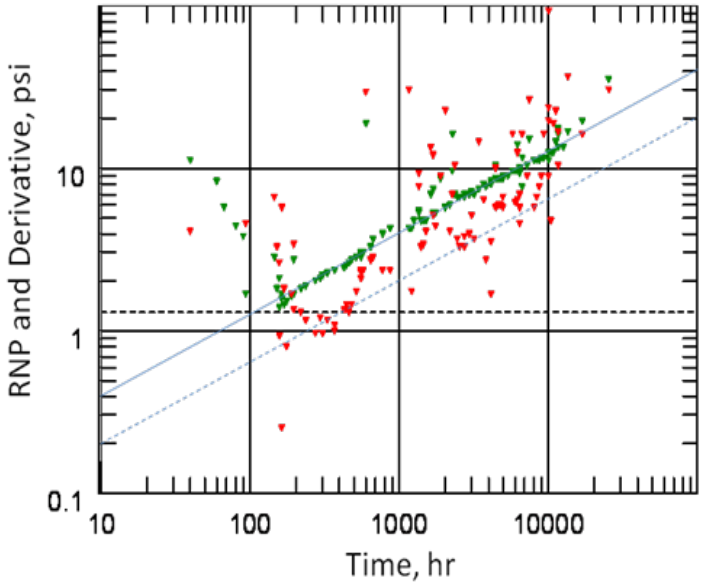


Figure 48. RNP and RNP Derivative Plot of - 0077

Though the model we used in Topaze matching doesn't make the matching of production rate and cumulative production perfect as well, the RNP and RNP derivative plot does provide useful information about the flow regime. The half slope trend of RNP and its derivative lasts more than two square cycles, as before indicating that early linear flow normal to the transverse fractures is the dominant flow regime. Therefore we are confident to say that - 0077 just revealed the early linear flow and gas was only produced within a limited extent around transverse fractures, at least by the end time of the recorded production history.

The difficulty matching rate and cumulative production with Topaze is due to the inability of Topaze to properly model inherent limits in the production rate response to a step change in pressure. Kappa Engineering suggests adding skin in order to improve the

match, but in reality this does not work very well. It may be what is needed is a rate dependent skin that accounts for flow rate restriction by the wellbore itself.

Since we have an estimation to fracture half length of - 0077, we can also apply the relationship between permeability and fracture half length to estimate the permeability. For - 0077:

$$x_f\sqrt{k}=(\frac{4.064qB}{m_{lf}h})(\frac{\mu}{\phi c_t})^{1/2}=128 \text{ ft-md}^{1/2} \quad (19)$$

where m_{lf} =0.126 psi/cycle, from the plot of pressure versus square root of time, and the flow rate used for the RNP graph is the value of the last flow rate, q =156MSCF/d. If the summed fracture half length is 1300×8=10400 ft, permeability is 0.000151 md which almost agrees with the result from Saphir matching of the unified BU-RNP response.

Pressure investigation is also studied. The fracture spacing of - 0077 is about 400 ft. Therefore, during the early linear flow period, when pressure investigation depth reaches 200 ft, pressure interference will occur. Since we have estimated the permeability at 0.000151 md, we can estimate the time when pressure interference happens:

$$x_i=2\sqrt{\frac{kt}{948\phi\mu c_t}}\Rightarrow t=\frac{948\phi\mu c_t x_i^{\,2}}{4k}=1{,}760{,}906 \text{ hr}=201.12 \text{ yr (k=0.000151md)} \quad (20)$$

This computation is conservative because it doesn't take gas desorption impact into account. Considering the specific reservoir properties, :ϕ=0.06; p_i=714 psia; p_L =1044 psia; ρ_{ads} = 0.00648 g/cc, we calculated the I_{ads} at 1.50. Therefore, if gas desorption is taken into account, the real time of interference should be 201.12 yr × 1.50= 301.68 yr.

That means in reality we can see the fracture interference after about 300 years. However, this well's life cannot be so long (surely much less than 100 years). For a given assumed time for the life of the well, the pressure investigation distance can be calculated. For example, after 100 years, the investigation distance is 115 ft.

5.4 EUR Estimation and Recovery Factor

We applied the Valko approach to estimate the EUR of Well - 0077, and the result was calculated in Chapter 3, in which the methodology was introduced. This approach indicated that the EUR of - 0077 is 132750 MSCF.

If we suppose the gas in place within the stimulated reservoir volume is the expected productive reserve, we can estimate the recovery factor by dividing EUR by the reserve in the SRV. The reserve in the SRV can be calculated through volume method, and both free gas and adsorbed gas should be considered.

Figure 49 shows the 2D map of SRV. We use volumetrics to calculate the gas in place within the SRV. Eq 21 shows how to calculate the gas in place within a certain shale gas reservoir volume.

$$GIP = GIP_{free} + GIP_{ads} = Ah\phi(1 - S_w)/B_g + Ah\rho_{rock}V_{ads} \quad \text{.....(21)}$$

Where:

GIP, gas in place

GIP_{free}, free gas in place

GIP_{ads}, adsorbed gas in place

A, drainage area

h, payzone thickness

ϕ, porosity

S_w, water saturation

B_g, gas volume factor

ρ_{rock}, rock density

V_{ads}, the gas volume can be adsorbed by a rock of unit mass;

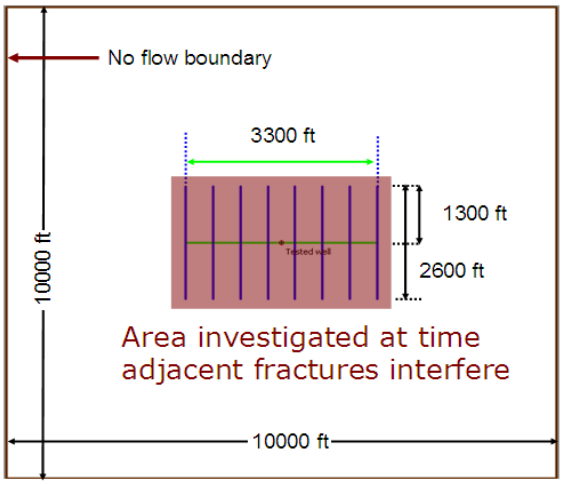


Figure 49. 2D Map of SRV of - 0077

Table 10 shows the calculation of SRV geometry, free gas and adsorbed gas volume in SRV and recovery factor. The implied recovery factor for - 0077 is about 7.10%. This is very low for a gas reservoir. Two points can be mentioned. First, the Valko extrapolation seems conservative. Referring back to Figure 14, the linear trend is more severely downward than the data, which actually seem to be leveling out. The

Valko database may not have had very many MTFHWs, and there may be a need to extend the method for these wells. Second, the calculated interference time is far too great. Our analysis suggests that the fracture spacing in future New Albany shale wells should be smaller.

If conditions for another well are similar to those for -277, using Eq 17, for a target interference time of 5 years, the spacing should be about 50 ft. The key point is that the fractures spaced closer together, the recovery factor will go up without changing the well response until the time of fracture interference. The fracture spacing should be a well design parameter. Either more fractures should be created, or for the same number of hydraulic fractures, the horizontal well length should be shorter.

Table 10. Recovery Factor Calculation of - 0077

SRV geometry			
well length, ft	3300		
fracture half-length, ft	1300		
drainage length, ft	3300		
drainage width, ft	2600		
area, ft^2	8.6×10^{6}		
pay zone thickness, ft	56		
drainage volume, ft^3	4.8×10^{8}		
Free Gas		**Adsorbed gas**	
porosity	0.06	rock density, g/cc	2.372
water saturation	0.835	rock density, ton/cf	0.0672
gas in reservoir, rf	4.76×10^{6}	mass of reservoir, ton	3.23×10^{7}
gas volume factor, rf/scf	0.0217	storage capacity, scf/ton	51.11
gas in place, scf	2.19×10^{8}	ad gas in place, scf	1.65×10^{9}
gas in place, bscf	0.219	ad gas in place, bscf	1.649
Gas in place and recovery factor			
gas in place, bscf	1.868×10^{9}		
Valko Reserve, bscf	0.1328		
Recovery Factor	7.10%		

5.5 Specialty of Low Reservoir Pressure and Comments on Well Design

The case of - 0077 is special because of its low initial reservoir pressure. Generally, New Albany Shale is normally pressured and has a shallow reservoir depth of only 0000ft. The low pressure gradient 0.3 psi/ft results in a abnormally low reservoir pressure at 714 psi. This low reservoir pressure is a barrier for pursuing high gas recovery. However, even with this low reservoir pressure, the EUR for an analogous well - 0078 is 99721 Mscf, which is more than the EUR for the vertical wells drilled in New Albany Shale. This clearly justifies drilling additional MTFHWs might be a better strategy to obtain more gas production.

For the well design, what really attracts our attention is the fracture interference time. We can design wells for fractures to interfere at a specified time by spacing the fractures accordingly. We can apply the time shift program to take gas desorption into account and use the pressure investigation depth formula to calculate a fracture spacing corresponding to the interference time we design. To pursue a higher recovery during a MTFHW's life, we recommend that the fracture spacing should not be too large. Specific strategies can be creating more transverse fractures if well length is fixed or shortening well length if the number of created fractures is fixed. The essence of the strategies actually is to increase fracture density, or rather to decrease fracture spacing. For - 0077, since the well has been already completed, what can be done to increase the recovery is stimulating more fractures between each two adjacent fractures existing there.

CHAPTER 6. SUMMARY AND CONCLUSIONS

This chapter contains the summary of the contents in this thesis and conclusions according to the research work performed in this thesis.

6.1 Summary

This thesis is focusing on several aspects about shale gas. Based on the previous work and more detailed consideration, an appropriate conceptual model for shale gas is described. The “Triple porosity/ Dual permeability” model is considered as the reasonable model which describes the mechanisms of gas storage and transport in gas shale formations.

The Valko rate decline analysis approach was applied to estimate the EUR for 33 wells in New Albany Shale. Then we focused on long term drawdown pressure transient behavior in MTFHWs in shale gas reservoirs. We adopted the unified BU-RNP method to transfer the varying rate/varying pressure pressure/production data into a virtual constant rate pressure drawdown behavior, which can be matched against the existing constant rate pressure drawdown models. Drawdown model behavior is more straightforward than rate decline behavior for diagnosing well and reservoir characteristics because of the readily identified trends of characteristic slope of pressure change derivative. Sensitivity studies illustrated long term pressure drawdown behavior of MTFHWs in shale gas reservoirs, and typical flow regimes. From the early linear flow which is of great importance to MTFHWs, we concluded a relationship between permeability and summed fracture half-length, and we also addressed the issue of time

of pressure interference between two adjacent transverse fractures, which relates to recovery efficiency and a well design issue. Moreover, we also discussed that the main impact of gas desorption on long term drawdown behavior of MTFHWs is the delay of pressure interference, which is expressed as a time shift of the pressure change and its derivative curve.

We studied a field case, Well - 0077 in New Albany Shale. We synthesized the information about reservoir, well and fluid and recorded production/pressure data for about 1 year. The unified BU-RNP method was applied to process the data into a virtual constant rate drawdown behavior for long term pressure transient analysis. PTA and production analysis only indicated the early linear flow regime and model matching gave the permeability estimation as 1.51×10^{-4} md, which agrees with an estimation from the relationship for linear flow between permeability and fracture half length. The pressure investigation study indicated that the early linear flow take 200 years (conservative estimation without considering gas desorption), which is even much longer than the well's life to see the interfracture pressure interference. If gas desorption is taken into account, the time would be nearly 10 times longer making it even less likely ever to see the interference. EUR estimation helped calculate the recovery factor, and recovery factor reaches 7.10% if we consider the gas in place within SRV as productive reserve. To pursue higher recovery, we provided the recommendation of increasing fracture density or rather decreasing fracture spacing through creating more fractures or shorter well length. The special consideration of low reservoir pressure in - 0077 case is considered as a disadvantageous factor to production recovery and performing long term

well behavior analysis, but even with this low reservoir pressure, the higher EUR for -0077 and its analogous wells compared to EUR for those vertical wells drilled in New Albany Shale offered great confidence of drilling additional MTFHWs.

6.2 Conclusions

Based on this study, the following conclusions can be drawn:

1. “Triple porosity/Dual permeability” Model is appropriate for describing gas storage and transport mechanisms in shale formations.

2. Long term pressure drawdown behavior of MTFHWs in shale gas reservoirs will encounter the following flow regimes in this order: fracture storage; early linear flow normal to the transverse fractures; interfracture pressure interference; compound linear flow; boundary flow.

3. During the early linearly flow period in MTFHWs, the system acts like a single fracture vertical well with the same total fracture length. The product of summed created fracture half-length and square root of permeability is a constant, so either of them can be estimated if the other were known.

4. In the shale gas reservoirs, the main impact of gas desorption is delaying pressure investigation, which is illustrated as a time shift of long term pressure drawdown behavior.

5. The time of interfracture pressure interference in MTFHWs is usually over hundred years because of the shale permeability in nanodarcy scale and the gas desorption impact. So the pressure interference is hard to be seen even during the whole well life

and early linear flow might be the only essential flow regime to MTFHW gas production.

6. Assuming an effective fracture half length for the transverse fractures, the formation permeability where well - 0077 is located is about 1.51×10^{-4} md. By now the flow regime is still the linear flow normal to transverse fracture and it is unlikely to see pressure interference which will probably appear after nearly 200 years.

7. To pursue higher gas recovery of - 0077, it is recommended to produce more transverse fractures or to shorten the horizontal well to reduce the fracture spacing.

8. The uncommonly low reservoir pressure in the well - 0077 case might be a disadvantageous factor to production and long term well behavior analysis, however, even with such a low pressure, the EUR for analogous wells is about 10^5 MSCF that is much higher than EUR for vertical wells in the same play and encourages drilling additional MTFHWs.

6.3 Recommendations

We also made some recommendations for the future work based on our existing work. One idea would be to find a complete generalization for determination of the adsorption index for a continuous range of input parameters. Also, finding a way to determine permeability before the well design is finalized is quite important. If that were done, it would be really good to have microseismic on a well where permeability is known because this could help understand how good is the correlation between the fracture length seen in microseismic and what is estimated from long term production.

Moreover, to perform a better pressure transient analysis, we need pressure transient data with good quality, such as a pressure buildup with higher data frequency.

REFERENCES

Al-Kobaisi, M., Ozkan, E., Kazemi, H., and Ramirez, B. 2006. Pressure-Transient Analysis of Horizontal Wells with Transverse, Finite-conductivity Fractures. Paper PETSOC 2006-126 presented at the Petroleum Society's 7th Canadian International Petroleum Conference (57th Annual Technical Meeting), Calgary, Alberta, Canada, 13-15 June.

Cipolla, C.L., Lolon, E.P., Erdle, J.C., and Rubin. B. 2009. Reservoir Modeling in Shale-Gas Reservoirs. Paper SPE 125530 presented at the 2009 SPE Eastern Regional Meeting, Charleston, West Virginia, 23-25 September.

Clarkson, C.R., Jordan, C.L., Ilk, D., and Blasingame, T.A. 2009. Production Data Analysis of Fractured and Horizontal CMB Wells. Paper SPE 125929 presented at the 2009 SPE Eastern Regional Meeting, Charleston, West Virginia, 23-25 September.

Ehlig-Economides, C.A. 1992. Computation of Test Area of Investigation in Nonradial Geometries. Paper SPE 25020 presented at the European Petroleum Conference, Cannes, France, 16-18 November.

Ehlig-Economides, C.A., Martinez Barron, H., and Okunola, D. 2009. Unified PTA and PDA Approach Enhances Well and Reservoir Characterization. Paper SPE 123042 presented at the 2009 SPE Latin American and Caribbean Petroleum Engineering Conference, Cartagena, Colombia, 31 May-3 June.

Freeman, C.M., Moridis, G., Ilk, D., and Blasingame, T.A. 2009. A Numerical Study of

Performance for Tight Gas and Shale Gas Reservoir Systems. Paper SPE 1 00961 presented at the 2009 SPE Annual Technical Conference and Exhibition, New Orleans, Louisiana, 4-7 October.

Ilk, D., Rushing, J.A., Perego, A.D., and Blasingame, T.A. 2008. Exponential vs. Hyperbolic Decline in Tight Gas Sands-Understanding the Origin and Implications for Reserve Estimates Using Arps' Decline Curve. Paper SPE 116731 presented at the 2008 SPE Annual Technical Conference and Exhibition, Denver, Colorado, 21- 00 September.

J.Daniel Arthur, P.E., Brian Bohm, P.G., and Mark Layne, P.E. 2008. Hydraulic Fracturing Considerations for Natural Gas Wells of the Marcellus Shale. Paper presented at the Ground Water Protection Council 2008 Annual Forum, Cincinnati, Ohio, 21- 00 September.

Kalantari Dahaghi, A., and Mohaghegh. S.D. 2009. Economic Impact of Reservoir Properties, Horizontal Well Length Orientation on Production from Shale Formations: Application to New Albany Shale. Paper SPE 125893 presented at the 2009 SPE Eastern Regional Meeting, Charleston, West Virginia, 23-25 September.

Kuuskraa, V.A., Sedwick, K., and Yost II, A.B. 1985. Technically Recoverable Devonian Shale Gas in Ohio, West Virginia and Kentucky. Paper SPE 14503 presented at the SPE 1985 Eastern Regional Meeting, Morgantown, West Virginia, 6-8 November.

Lane, H.S., Lancaster, D.E., and Watson, A.T. 1990. Estimating Desorption

From Devonian Shale Well Test Data. Paper SPE 21272 presented at the SPE Eastern Regional Meeting, Columbus, Ohio, 31 October - 2 November.

Lane, H.S., Watson, A.T., and Lancaster, D.E. 1989. Identifying and Estimating Desorption From Devonian Shale Gas Production Data. Paper SPE 19794 presented at the 64th Annual Technical Conference and Exhibition of the Society of Petroleum Engineers, San Antonio, TX, 8-11 October.

Meyer, B.R., Bazan, L.W., Jacot, R.H., and Lattibeaudiere, M.G. 2010. Optimization of Multiple Transverse Hydraulic Fractures in Horizontal Wellbores. Paper SPE 131732 presented at the SPE Unconventional Gas Conference, Pittsburgh, Pennsylvania, 23-25 February.

Palacio, J.C., and Blasingame, T.A. 1993. Decline-Curve Analysis Using Type Curves Analysis of Gas Well Production Data. Paper SPE 25909 presented as the SPE Joint Rocky Mountain Regional and Low Permeability Reservoir Symposium, Denver, Colorado, 26-28 April.

Rushing, J.A., Perego, A.D., and Blasingame, T.A. 2008. Applicability of the Arps Rate-Time Relationships for Evaluating Decline Behavior and Ultimate Gas Recovery of Coalbed Methane Wells. Paper SPE 114515 presented at the CIPC/SPE Gas Technology Symposium 2008 Joint Conference, Calgary, Alberta, Canada, 16-19 June.

Schepers, K.C., Gonzalez, R.J., Koperna, G.J., and Oudinot. A.Y. 2009. Reservoir

Modeling in Support of Shale Gas Exploration. Paper SPE 123057 presented at the 2009 SPE Latin American and Caribbean Petroleum Engineering Conference, Cartagena, Colombia, 31 May- 3 June.

Valko, P.P. 2009. Assigning Value to Stimulation in the Barnett Shale: A Simultaneous Analysis of 7000 Plus Production Histories and Well Completion Records. Paper SPE 119369 presented at the 2009 SPE Hydraulic Fracturing Technology Conference, Woodlands, Texas, 19-21 January.

van Kruysdijk, C.P.J.W, and Dullaert, G.M. 1989. A Boundary Element Solution of the Transient Pressure Response of Multiple Fractured Horizontal Wells. Paper presented at the 2nd European Conference on the Mathematics of Oil Recovery, Cambridge, England.

Wang, F.P., and Reed, R.M. 2009. Pore Networks and Fluid Flow in Gas Shales. Paper SPE 1 00253 presented at the 2009 SPE Annual Technical Conference and Exhibition, New Orleans, Louisiana, 4-7 October.

Wei, Y., and Economides, M.J. Transverse Hydraulic Fractures From a Horizontal Well. Paper SPE 94671 presented at the 2005 SPE Annual Technical Conference and Exhibition, Dallas, Texas, 9-12 October.

Zuber. M.D., Williamson. J.R., Hill. D.G., Sawyer, W.K., and Frantz. J.H. 2002. A Comprehensive Reservoir Evaluation of a Shale Reservoir-The New Albany Shale. Paper SPE 77469 presented at the 2002 SPE Annual Technical Conference and Exhibition, San Antonio, Texas, 29 September-2 October.

APPENDIX A

The appendix is going to reveal the specific gas desorption impact on shale gas well PTA behaviors. Also, it will explain why we use homogeneous reservoir model instead of dual porosity model in long term drawdown sensitivity study to MTFHWs and the study of New Albany Shale gas wells.

First, the conceptual model of shale gas reservoir is “Triple porosity/Dual permeability” Model. The valley on the derivative curve is a characterization of inter porosity flow, which happens in dual porosity reservoirs. We run the comparison test to illustrate the gas desorption impact on the both dual porosity characterization and pressure investigation. For convenience, we designed a simple constant rate drawdown behavior of a vertical well in shale gas reservoir (Table A-1).

Table 11. Gas Desorption Impact Comparison Test Design

	without desorption	**with desorption**
well and fracture design		
well type	vertical	fractured vertical well
r, wellbore radius ,ft	0.3	0.3
reservoir properties		
h, ft	30	30
ϕ, porosity	0.1	0.1
P_i, initial reservoir pressure, psia	5000	5000
model design		
wellbore model	no wellbore storage	no wellbore storage
s, skin	0	0
reservoir model	two porosity	two porosity+ desorption
ω, storage ratio	0.1	0.1
λ, inter-porosity coefficient	1.00E-05	1.00E-05
k, permeability, md	0.1	0.1
p_L, psia	-	2000
ρ_{ads}, adsorption density, g/cc	-	0.1

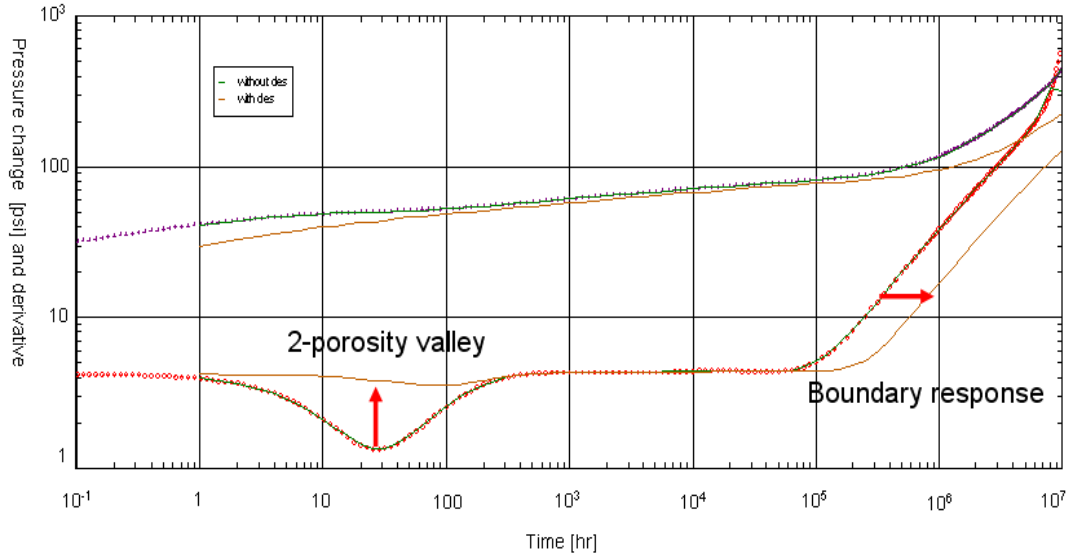


Figure 50. PTA Behavior Comparison: With Desorption vs. Without Desorption

Figure 50 shows the comparison. Visually, besides delaying pressure investigation, gas desorption eliminates the intensity of interporosity flow, which is corresponded to the smaller valley on the derivative curve.

The reasons why we don't apply dual porosity model in the context include:

1. Dual porosity doesn't affect the long term drawdown behaviors, especially the formation of certain flow regimes;
2. Dual porosity valley might mask some characteristic PTA behavior;
3. If gas desorption impact is big enough, dual porosity characterization is likely to be eliminated, so PTA behavior is almost the same with the behavior with homogeneous reservoir model.

There are two characteristic parameters describing dual porosity reservoir:

$$\omega = \frac{(\phi C_t h)_f}{(\phi C_t h)_f + (\phi C_t h)_m} \approx \frac{V_{\phi f}}{V_{\phi f} + V_{\phi m}} \quad \text{(A-1)}$$

$$\lambda = \alpha \frac{k_m}{k_f} \quad \text{(A-2)}$$

Where:

ω, storage ratio, usually from 0.1 to 0.01;

λ, interporosity flow coefficient;

$V_{\phi f}$, the fracture space saturated by gas or volume of gas in fracture space;

$V_{\phi m}$, the pore space volume in matrix saturated by gas or the gas volume in matrix pores;

Take gas desorption into account, ω can be modified as:

$$\omega_{\text{mod}} = \frac{V_{\phi f} + S_{\phi f}\rho_{ra}}{V_{\phi f} + V_{\phi m} + S_{\phi f}\rho_{ra} + S_{\phi m}\rho_{ra}} \quad \text{(A-3)}$$

Where:

$S_{\phi f}$, the area of surface of fracture space exposed to matrix particles, ft^2;

$S_{\phi m}$, the area of surface of matrix pore space exposed to matrix particles, ft^2;

ρ_{ra}, Adsorbed gas volume released from unit exposed surface area, scf/ ft^2;

Because gas desorption reduces the intensity of interporosity flow:

$$\omega_{\text{mod}} = \frac{V_{\phi f} + S_{\phi f}\rho_{ra}}{V_{\phi f} + V_{\phi m} + S_{\phi f}\rho_{ra} + S_{\phi m}\rho_{ra}} > \frac{V_{\phi f}}{V_{\phi f} + V_{\phi m}} = \omega \quad \text{(A-4)}$$

$V_{\phi f}$, fracture space saturated by gas, cf

$V_{\phi m}$, the pore space volume in matrix saturated by gas, cf

This requires a precondition:

$$\frac{S_{\phi f}}{S_{\phi m}} < \frac{V_{\phi f}}{V_{\phi m}} \quad \text{..... (A-5)}$$

Gas desorption is quantified by Langmuir model, and we want to reveal how the specific adsorption parameter, p_L and V_L affect the PTA drawdown behavior of shale gas wells.

First, we want to tell the relationship between V_{des} and ρ_{ra} and that between V_L and ρ_{ads}.

$$\rho_{ads} = \rho_{rock}\rho_{gas}^{surf}V_L \quad \text{.....(A-6)}$$

$$V_{des} = V_{ph} - V_{p_l} = \rho_{ra}S_{ex}^{surf} = \rho_{ra}(S_{\phi m} + S_{\phi f}) \quad \text{.....(A-7)}$$

Where:

V_{des}, the total volume of desorbed gas;

V_{ph}, the adsorbed gas volume at the higher pressure;

V_{pl}, the adsorbed gas volume at the volume pressure;

S_{ex}^{surf}, the total area of exposed surface to matrix particles;

ρ_{ads} is nothing but another form of V_L, it transfers the adsorbed gas volume per unit rock mass into adsorbed gas mass per unit rock volume, so the essence is the same: the maximum amount of gas can be adsorbed.

ρ_{ra} is the V_{des} per unit exposed surface area, so they are positively correlated.

The tests include two series: $p_L<p_i$ and $p_L>p_i$. We perform the sensitivity study to ρ_{ads} and p_L to each series. Table A-2 shows the basic test parameters, also we use a simple vertical well drawdown for convenience. Table A-3 shows the sensitivity study design.

Table 12. Basic Design Settings-Gas Desorption Impact on Dual Porosity

Basic design settings - two porosity & gas desorption	
Well & Reservoir Geometry	
well type	vertical
length [ft]	10000
width [ft]	10000
reservoir boundary	no-flow
reservoir type	shale gas
reservoir and well parameters	
r, wellbore radius [ft]	0.3
h, pay zone [ft]	30
ϕ, porosity	0.1
PVT	
T_r, reservoir temperature [F deg]	212
P_i, initial reservoir pressure [psia]	2000
γ, specific gravity	0.7
Model settings	
wellbore model	No wellbore storage
s, skin	0
K, md	1
reservoir model	**two porosity + desorption**
ω, storage ratio	0.1
λ, interporosity coefficient	1.E-06

Table 13. Sensitivity Study Design

$p_L<p_i$ (2000)		$p_L>p_i$ (2000)	
p_L sensitivity, ρ_{ads}=0.1	ρ_{ads} sensitivity, p_L =1500	p_L sensitivity, ρ_{ads}=0.1	ρ_{ads} sensitivity, pL=2500
1500	10	2500	10
150	1	5000	1
15	0.1	10000	0.1
	0.01		0.01
	0.001		0.001
	0.0001		0.0001

Figure 51 to 54 separately shows the sensitivity study results. Table A-4 concludes the results.

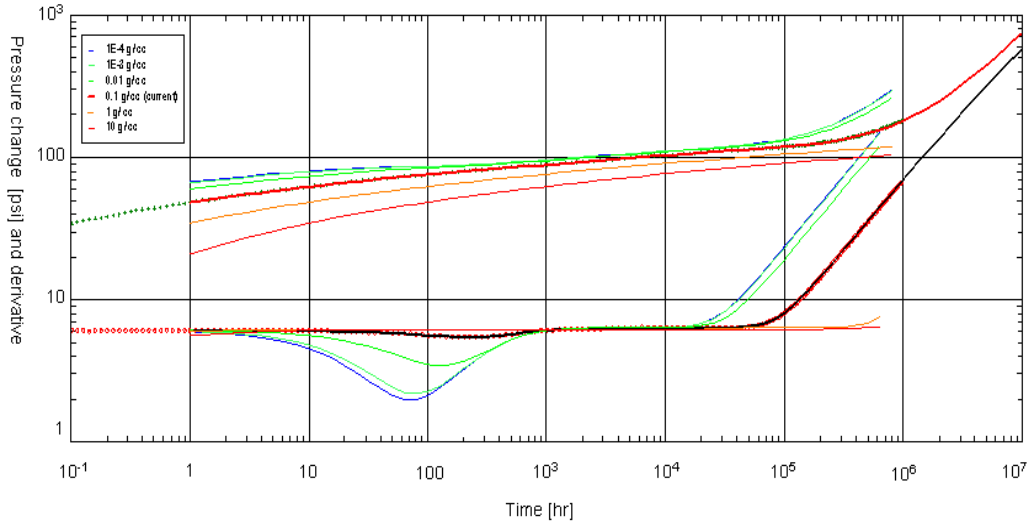


Figure 51. Gas Adsorption Density Sensitivity Result - $p_L<p_i$

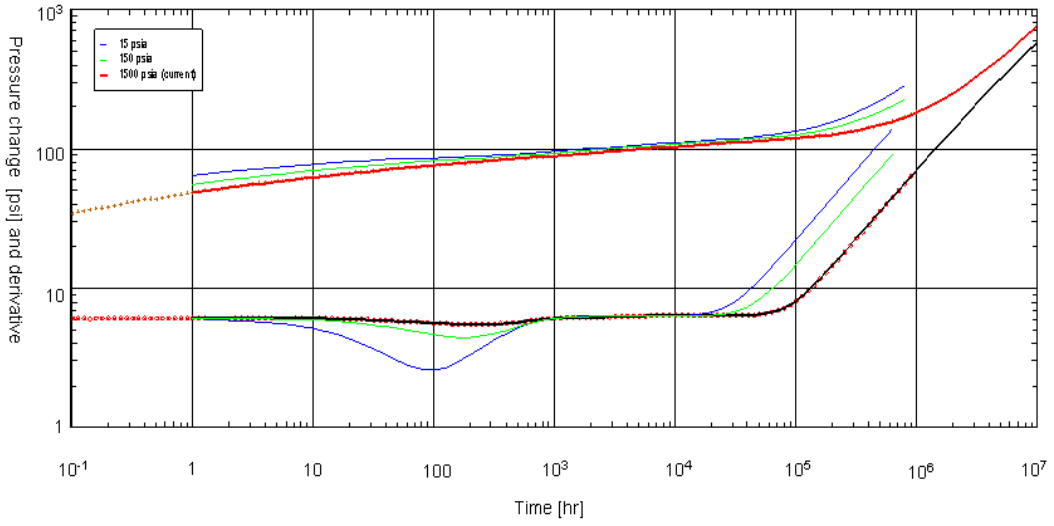


Figure 52. Langmuir Pressure Sensitivity Result - $p_L<p_i$

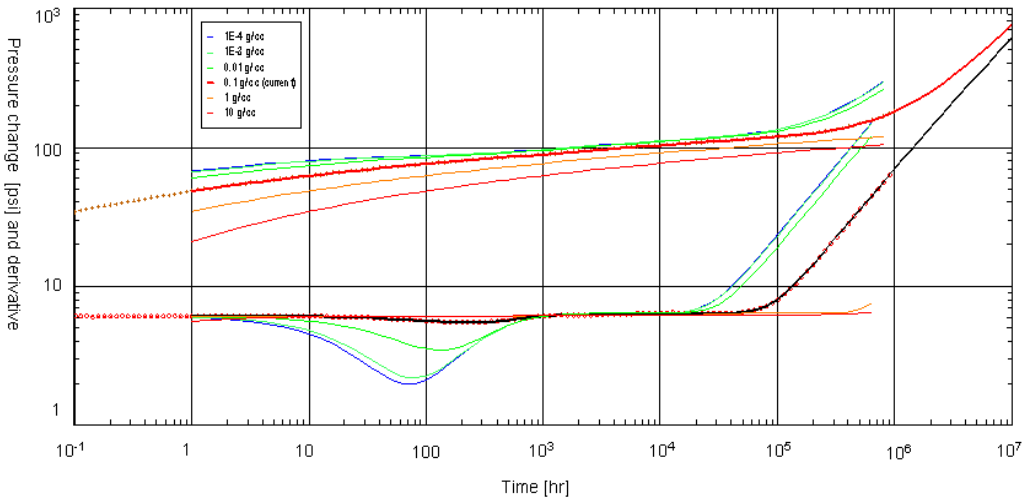


Figure 53. Gas Adsorption Density Sensitivity Result - $p_L > p_i$

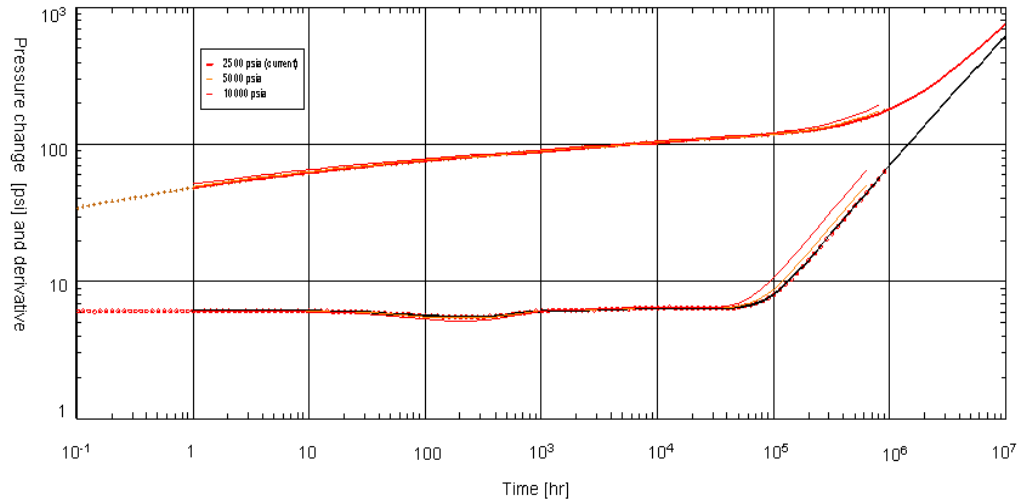


Figure 54. Langmuir Pressure Sensitivity Result - $p_L > p_i$

Table 14. Summary of Gas Desorption Impact on Shale Gas (Vertical) Wells

p_L vs. p_i	ρ_{ads} (V_L)↓	p_L ↓
$p_L < p_i$	ω_{mod} ↓, faster investigation	ω_{mod} ↓, faster investigation
$p_L > p_i$	ω_{mod} ↓, faster investigation	ω_{mod} ↑, slower investigation

No matter which of $\rho_{ads}(V_L)$ or p_L changes, the decrement in ω_{mod} which indicates higher interporosity flow and results in a bigger derivative valley and the faster pressure investigation are essentially resulted from relatively smaller desorbed gas volume V_{des}.

For the impact on dual porosity characterization:

$V_{des} \downarrow \Rightarrow \rho_{ra} \downarrow$

Assume: $V_{\phi m} = aV_{\phi f}$ and $S_{\phi m} = bS_{\phi f}$,then

$$\frac{\partial \omega_{\text{mod}}}{\partial \rho_{ra}}$$

$$= \frac{S_{\phi f}[V_{\phi f}(1+a) + S_{\phi f}\rho_{ra}(1+b)] - (V_{\phi f} + S_{\phi f}\rho_{ra})S_{\phi f}(1+b)}{[V_{\phi f}(1+a) + S_{\phi f}\rho_{ra}(1+b)]^2}$$

$$= \frac{S_{\phi f}V_{\phi f}(1+a) + S_{\phi f}^2\rho_{ra}(1+b) - V_{\phi f}S_{\phi f}(1+b) - S_{\phi f}^2\rho_{ra}(1+b)}{[V_{\phi f}(1+a) + S_{\phi f}\rho_{ra}(1+b)]^2} \quad \text{..... (A-8)}$$

$$= \frac{S_{\phi f}V_{\phi f}[1+a-(1+b)]}{[V_{\phi f}(1+a) + S_{\phi f}\rho_{ra}(1+b)]^2}$$

$$= \frac{S_{\phi f}V_{\phi f}[a-b]}{[V_{\phi f}(1+a) + S_{\phi f}\rho_{ra}(1+b)]^2}$$

According to Eq A-5 derived from the comparison test, $\frac{S_{\phi f}}{S_{\phi m}} < \frac{V_{\phi f}}{V_{\phi m}}$

recalling the assumption $V_{\phi m} = aV_{\phi f}$ and $S_{\phi m} = bS_{\phi f}$, this precondition equals to

$b < a$ or $a - b > 0$. Therefore:

$\frac{\partial \omega_{\text{mod}}}{\partial \rho_{ra}} > 0$. This indicates: $V_{des} \downarrow \longrightarrow \rho_{ra} \downarrow \xrightarrow{\frac{S_{\phi f}}{S_{\phi m}} < \frac{V_{\phi f}}{V_{\phi m}}} \omega_{\text{mod}} \downarrow$

For faster pressure investigation, Figure 55 shows the logic:

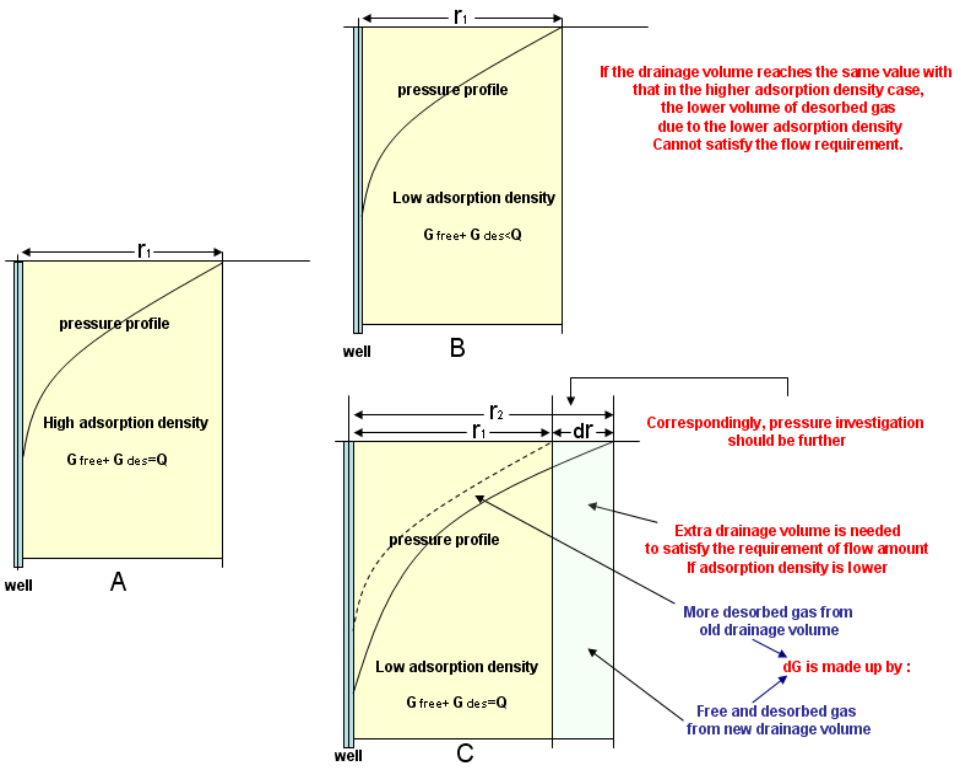


Figure 55. Faster Pressure Investigation Caused by Smaller Gas Desorption

Back to the smaller desorbed gas volume, Langmuir Isotherm comparison provides the logic for the four sensitivity studies. Figure 56 shows the smaller desorbed gas volume resulted from ρ_{ads} (or V_L) and p_L changes.

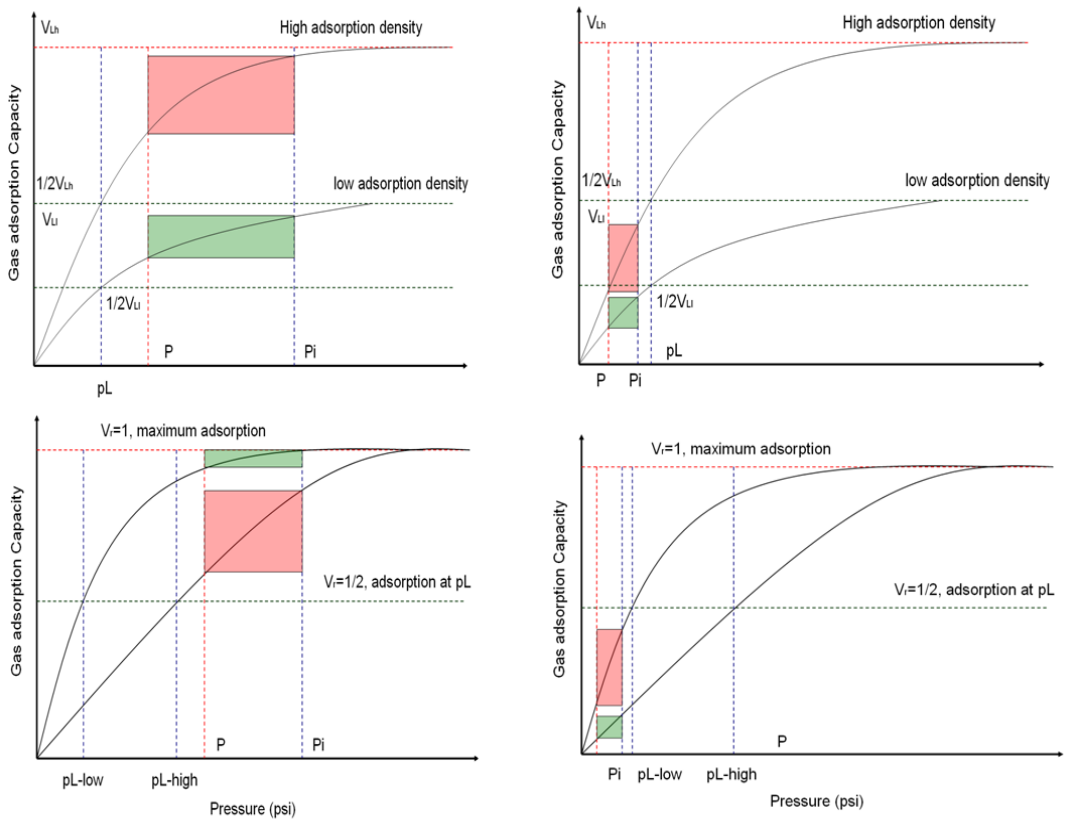


Figure 56. The Smaller Desorbed Gas Volume due to ρ_{ads} (or V_L) and p_L Changes

The logic is no matter $p_L<p_i$ or $p_L<p_i$, if p_L is the same, the lower ρ_{ads} (or V_L) isotherm gives smaller desorbed gas volume; when $p_L<p_i$, if ρ_{ads} (or V_L) is the same, the lower p_L isotherm gives smaller desorbed gas volume; when $p_L>p_i$, if ρ_{ads} (or V_L) is the same, the higher p_L isotherm gives smaller desorbed gas volume.

The Analytical derivation of this logic is shown below:

At initial pressure: $V_{p_i} = \dfrac{V_L p_i}{p_L + p_i}$

After pressure drops, at some certain pressure: $V_p = \dfrac{V_L p}{p_L + p}$;

So the gas desorption volume is:

$$V_{des} = V_{p_i} - V_p = \frac{V_L p_i}{p_L + p_i} - \frac{V_L p}{p_L + p} = \frac{V_L p_i (p_L + p) - V_L p (p_L + p_i)}{(p_L + p_i)(p_L + p)}$$
$$= \frac{V_L p_i p_L + V_L p_i p - V_L p p_L - V_L p p_i}{(p_L + p_i)(p_L + p)} = \frac{V_L p_L (p_i - p)}{(p_L + p_i)(p_L + p)} \quad \text{.....(A-9)}$$

For ρ_{ads} (or V_L):

$$\frac{\partial V_{des}}{\partial V_L} = \frac{\partial}{\partial V_L} \frac{V_L p_L (p_i - p)}{(p_L + p_i)(p_L + p)} = \frac{p_L (p_i - p)}{(p_L + p_i)(p_L + p)} \quad \text{.....(A-10)}$$

Since all parameters are positive and $p < p_i$, so $\frac{\partial V_{des}}{\partial V_L} > 0$. Here we find that no matter

$p_L < p_i$ or $p_i < p_L$, and no matter what p is ($p > p_L$ or $p < p_L$), $\frac{\partial V_{des}}{\partial V_L}$ is always positive

We can conclude this as following: the lower ρ_{ads} (or V_L) is, the smaller V_{des} will be.

For p_L :

$$\frac{\partial V_{des}}{\partial p_L} = \frac{\partial}{\partial p_L} \frac{V_L p_L (p_i - p)}{(p_L + p_i)(p_L + p)}$$
$$= \frac{\frac{\partial [V_L p_L (p_i - p)]}{\partial p_L} \times (p_L + p_i)(p_L + p) - \frac{\partial [(p_L + p_i)(p_L + p)]}{\partial p_L} \times V_L p_L (p_i - p)}{[(p_L + p_i)(p_L + p)]^2}$$
$$= \frac{V_L (p_i - p)[p_L{}^2 + p_L (p + p_i) + p_i p] - V_L (p_i - p)[2 p_L + (p + p_i)]}{[p_L{}^2 + p_L (p + p_i) + p_i p]^2} =$$
$$= \frac{V_L p_L{}^2 (p_i - p) + V_L p_L (p_i - p)(p + p_i) + V_L p_i p (p_i - p)}{[p_L{}^2 + p_L (p + p_i) + p_i p]^2} \quad \text{.....(A-11)}$$
$$- \frac{2 V_L p_L (p_i - p) + V_L p_L (p_i - p)(p + p_i)}{[p_L{}^2 + p_L (p + p_i) + p_i p]^2}$$
$$= \frac{V_L p_i p (p_i - p) - V_L p_L{}^2 (p_i - p)}{[p_L{}^2 + p_L (p + p_i) + p_i p]^2}$$
$$= \frac{V_L (p_i - p)[p_i p - p_L{}^2]}{[p_L{}^2 + p_L (p + p_i) + p_i p]^2}$$

If $p_i > p_L$, we should consider p further:

If $(p_i >) p \geq p_L$, then $p_i p - p_L{}^2 > 0 \Rightarrow \frac{\partial V_{des}}{\partial p_L} > 0 \Rightarrow p_L \downarrow, V_{des} \downarrow$;

If $p < p_L < p_i$, then $p_i p - p_L{}^2$ is not determinable. (if $p > p_L^2 / p_i$, the result is applicable.)

If $pi \leq p_L$, there is only $p < p_i < p_L$, and this will result in:

$$p_i p - p_L{}^2 < 0 \Rightarrow \frac{\partial V_{des}}{\partial p_L} < 0 \Rightarrow p_L \uparrow, V_{des} \downarrow.$$

Therefore, we can conclude a flow chart illustrating the logic of gas desorption impact on shale gas well drawdown behavior (Figure 57).

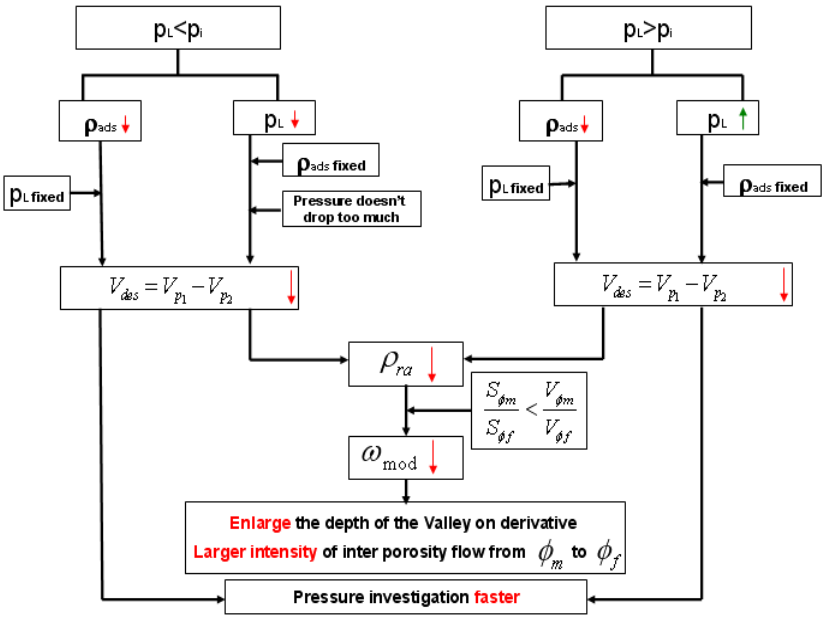


Figure 57. Gas Desorption Impact on PTA Behavior of Shale Gas wells

VITA

Name:	Bo Song
Address:	3116 TAMU - 719 Richardson Building College Station, TX 77843-3116
Email Address:	bo.song@pe.tamu.edu
Education:	B.A., Petroleum Engineering, China University of Geosciences (Beijing), 2008